MOTION PATTERNS OF GYRATING SPHEROIDS FOR VARIOUS DEGREES OF SPIN MODULATION

Daniel Abreu and Roland List

Department of Physics, University of Toronto, Toronto, Canada

1. INTRODUCTION

The fall motion of a tumbling spheroidal hailstone can be separated into three components: free fall in the direction of gravity, the secondary motion in the form of gyrations and rotations, and the sidewise particle movement. For the purpose of this paper, free fall and sidewise motion are excluded from discussion, however they can easily be incorporated; Only rotational motions will be addressed here.

The kinematic equations that describe the movement of surface points on freely falling spheroids are of importance to the understanding of hailstone growth and evolution, and allow the prediction of past, present, and future motion in space; This enhances the understanding of local growth and acceleration. While local growth will affect the evolution of shape, accelerations will control shedding, thus also representing a feedback on growth (List, Charlton & Buttels, 1968, List & Abreu, 2008). The equations will also serve as a consistency check between theoretical expectations and experimental observations.

Most natural hailstones with major diameters of 2 – 5 cm have shapes of ellipsoids with axis ratios of 1: 0.5: 0.8 (order adjusted to coordinate system). Considering that the difference between the main and the intermediate axes are relatively small, it was felt that natural hailstones could be approximated by spheroids with typical axis ratios of (1: 0.5: 1).

Kry and List (1974) established the theory of freely falling disks and spheroids. They predicted that the general motion could be described by a gyration about the horizontal axis, where the gyration of the (minor) spin axis is composed of a periodic nutation and precession of equal amplitude and frequency, but phase shifted by π/2 thereby making the minor body axis (the spin axis) follow a gyration cone. The resulting motion can be understood according to Fig. 1 of an icing experiment in a vertical wind tunnel. This motion was confirmed in free fall experiments by Stewart & List (1983).

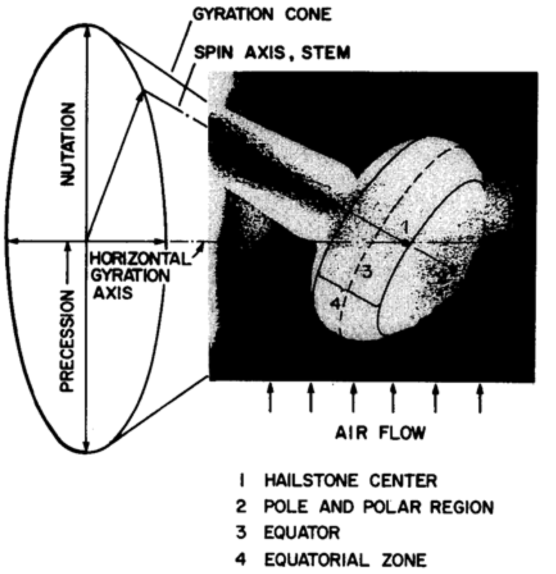

Fig. 1: Growth by cloud droplet accretion of a 2 cm spheroid gyrating in an icing tunnel (Garçia-Garçia & List, 1992)

The experiments following the free fall studies were with gyrating ice particles growing in an icing tunnel (List et al, 1987) while being forced to perform the predicted motions. This was the only way to ensure reproducible results because unsuspended particles would experience horizontal drift that would have led to continuous, irregular bouncing of the particles off the wind tunnel walls. Icing growth of gyrating, spheroidal hailstones has been studied by the Toronto group for 35 years and the major results were established by List & Lesins (1986), Garçia-Garçia & List (1992), Greenan & List (1995) and Zheng & List, (1995).

Recent developments (List & Abreu, 2008) regarding the growth of ellipsoidal hailstones has led to new insight about the cause of such complex particles; Gyration with modulated spin. This motion will expose opposite points on the equator longer to the wind field (thereby bestowing more growth) than the pair of points on the equator positioned angular distance 90º away which are exposed less to the wind field (hence will grow less); Such a situation will then allow the transition of spheroids towards ellipsoids.

Of importance will be the comparison of growth rates for points at the poles and on the equator where growth is either fastest or slowest. This is the first test before more realistic kinematic equations will be used based on double gyration – as will be briefly discussed at the end.

Nonetheless, the kinematic equations developed here will be ideal for modeling of the above proposed new concept and other ones forthcoming in the future.

In this paper, the equations of motion for any surface point on an arbitrarily shaped ellipsoid are derived, spinning at various rates (zero, constant, or modulated) and gyrating about a fixed horizontal axis. Such equations allow an exploration of the theoretically predicted three-dimensional curves traced in absolute space by any surface point (Lissajous figures), whose character is determined by the parameters that describe the motion. Such parameters are: axis ratios, spin type (zero, constant, or modulated), spin and gyration frequency, and the precession and nutation amplitudes. Modulation of the gyration frequency is also possible. In other words, the equations presented in this paper are adaptable to a very wide range of conditions.

2. DERIVING THE EQUATIONS

The ultimate goal is to describe the complete movement of any surface point on a freely falling, gyrating ellipsoid. The solutions presented here will be limited at the beginning to simple gyrations, as represented by Fig. 1. The next step, discussed later, will involve gyration with modulated spin, i.e. the *start* of the growth into ellipsoids.

The equations will be based on three different coordinate systems:

(i) A double-primed system (x”, y”, z”) describes the hailstone rotating about a fixed y”-spin axis (see Fig. 2). Note that the standard axis notation has been changed because of the positioning of the spheroid in space with its smaller spin axis in the y- and *not* in the z-direction.

(ii) A primed coordinate system (x’, y’, z’) anchors the double-primed coordinate system (x”, y”, z”) at the origin such that it gyrates about the fixed y’-axis (the primary gyration axis). Hence, the origins of both coordinate systems are identical (see Fig. 2)

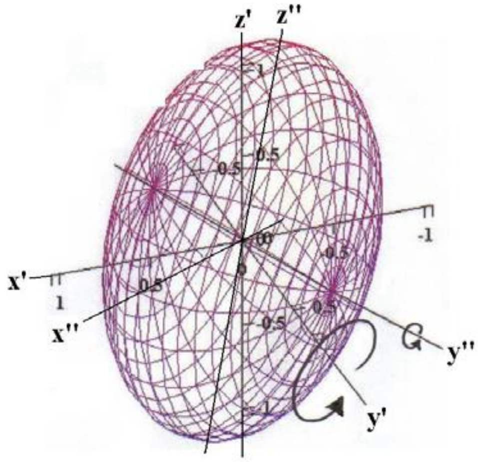

Fig. 2: Explanation of the coordinate system with clockwise spin about the y''-axis (the spin axis) and a clockwise gyration about the y'-axis (the gyration axis) of a spheroidal hailstone with axis ratios (1: 0.5: 1)

(iii) The coordinate system in absolute space (x, y, z) contains the primed coordinate system which undergoes a downward translatory motion.

The set of coordinate systems has been simplified by not assigning a system for the body itself. Furthermore, for the entirety of this paper no specification is given for vertical (fall) and horizontal (drift) particle motions so only the primed and double-primed frames will be dealt with. It should be noted however, that these components can easily be superimposed on the rotational and gyrational motions to give the full description of the motion in absolute space.

Motion in the double-primed coordinate system. It will be necessary to work with a general ellipsoid of axis ratios (a: b: c), spinning with modulation as specified by the angular, time dependent function Γ(t), about the y”-axis. The position of a point will be described by zenith angle (θ) from the y”-axis, and the azimuth angle (φ) from the x”-axis as depicted in Fig. 3.

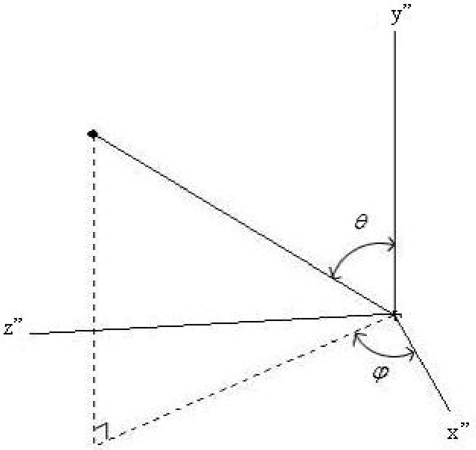

Fig. 3: Definition of the zenith (θ) and azimuth (φ) angles

Thus the following matrix completely describes a general ellipsoid surface with axes ratios (a: b: c) along the x”-, y”-, z”-axis respectively:

$$\begin{bmatrix} a\sin(\theta)\cos(\phi+\Gamma(t)) \\ b\cos(\theta) \\ c\sin(\theta)\sin(\phi+\Gamma(t)) \end{bmatrix} \tag{1}$$

where θ∈[0, π), φ∈[0, 2π)

A particular point on the surface is given by equation (1) with specified θ_o and φ_o values. The movement with time can be explored via function Γ(t) that describes the angular distance of the φ components from their original position. If the general ellipsoid has no spin then

$$\Gamma(t) = 0 \tag{2}$$

For a constant counterclockwise or clockwise spin (respectively) then

$$\Gamma(t) = \pm t \tag{3}$$

Collected samples of large hailstones, when cut open or are thin-sectioned, indicate that intermediate spheroidal shapes (diameter ~ 2 cm) develop into tri-axial ice particles with typical axis ratios of (1: 0.5: 0.8). This will be tested by investigating the initial effect of modulated spin on hailstone growth by supercooled droplets in an updraft.

In order to reflect this modulated spin in the equations, assume (without loss of generality) the points φ_o = π/2 have the fastest angular speed when they reach the x”y”-plane, and the slowest angular speed when they reach the y”z”-plane. Thus, a function Γ(t) can be defined as a piecewise, continuous, differential function formed from the increasing parts of the sine wave. This is accomplished by translating these sections horizontally and vertically. [However we could have also used parts of a different function other than the sine wave.]

It will also be necessary to control the amount of cycles as well as the speed of the modulation. Therefore, it is wise to define a piece-wise function g_o to be the following general recursion formula to accomplish these tasks:

$$\begin{array}{ll} 2\pi(l-1)+\frac{1}{2}\pi+\frac{1}{2}\pi\sin(tn-\frac{1}{2}\pi) & \frac{1}{2}\frac{(4l-4)\pi}{n}\le t\le\frac{1}{2}\frac{(4l-2)\pi}{n} \\ 2\pi(l-1)+\frac{3}{2}\pi+\frac{1}{2}\pi\sin(tn+\frac{1}{2}\pi) & \frac{1}{2}\frac{(4l-2)\pi}{n}\le t\le\frac{2l\pi}{n} \end{array} \tag{4}$$

where *l* is a dummy variable indicating the cycle being observed, and the variable *n* allows a horizontal stretch or compression of the recursion function. To get the full function Γ(t) this recursion formula must be summed over all possible *l* values which depends on the number of spin cycles, *m*, required. Consequently, for counterclockwise and clockwise spin (respectively), Γ(t) is

$$\Gamma(t) = \pm \sum_{l=1}^{m} g_o \tag{5}$$

where g_o is given in equation (4).

With equations (2), (3) and (5) the spin function Γ(t) is now obtained.

<u>*Motion in the primed system.*</u>

Equation (1) describes a ellipsoid with axes ratios (a: b: c), rotating about the fixed y”-axis with a zero, constant, or modulated spin, in the counterclockwise or clockwise directions as defined by Γ(t) in equations (2), (3) and (5). Superimposed on this motion is a gyration of the y”-axis about the fixed y’-axis (see Fig. 2).

To simulate gyration, the y”-spin axis has to rotate about the x’- and z’-axes (precession and nutation respectively) 90° out-of-phase with each other. This is accomplished using time-dependent rotation matrices applied to equation (1).

The matrix that facilitates the time dependent rotation about the z’-axis by a maximum angle ζ is:

$$\begin{bmatrix} \cos(\zeta\cos(t)) & -\sin(\zeta\cos(t)) & 0 \\ \sin(\zeta\cos(t)) & \cos(\zeta\cos(t)) & 0 \\ 0 & 0 & 1 \end{bmatrix} \tag{6}$$

While the matrix that facilitates the time dependent rotation about the x’-axis by maximum angle η is:

$$\begin{bmatrix} 1 & 0 & 0 \\ 0 & \cos(\eta\sin(t)) & -\sin(\eta\sin(t)) \\ 0 & \sin(\eta\sin(t)) & \cos(\eta\sin(t)) \end{bmatrix} \tag{7}$$

Notice that spin (equations (2), (3), and (5)) and gyration (equations (6) and (7)) are all dependent on the variable “t”, thus they are mathematically interconnected. This allows specification of relative spin-gyration frequency ratios that result in Lissajous figures in three-dimensional space.

Applying matrices (6) and (7) to equation (1), the following parametric equations are obtained that describe a zero, constant, or modulated spinning ellipsoid with axes ratios (a: b: c), gyrating about the y’-axis with maximum angle ζ with respect to the z’-axis, and η with respect to the x’-axis.

$$\begin{aligned} x =& \cos(\zeta\cos(t))\ a \sin(\theta) \cos(\varphi+\Gamma(t)) \\ & - \sin(\zeta\cos(t))\ b \cos(\theta) \end{aligned} \tag{8}$$

$$\begin{aligned} y =& \cos(\eta\sin(t)) \sin(\zeta\cos(t))\ a \sin(\theta) \cos(\varphi+\Gamma(t)) \\ & + \cos(\zeta\cos(t))\ b \cos(\theta)) \\ & - \sin(\eta\sin(t))\ c \sin(\theta) \sin(\varphi+\Gamma(t)) \end{aligned} \tag{9}$$

$$\begin{aligned} z =& \sin(\eta\sin(t)) \sin(\zeta\cos(t))\ a \sin(\theta) \cos(\varphi+\Gamma(t)) \\ & + \cos(\zeta\cos(t))\ b \cos(\theta) \\ & + \cos(\eta\sin(t))\ c \sin(\theta) \sin(\varphi+\Gamma(t)) \end{aligned} \tag{10}$$

where $\theta \in [0, \pi)$, $\varphi \in [0, 2\pi)$

To follow the path of a specific surface point, explicit θ_o and φ_o values need to be specified in (8), (9), and (10).

3. RESULTS

This section will present three dimensional Lissajous figures of surface points on spheroids (a special type of ellipsoid having axes ratios (a: b: c) = (1: 0.5: 1)) with different spin rates, gyrating about the fixed y’-axis at specified maximum angles to the x’- and z’-axes. The gyration and spin frequencies will be chosen such that a closed spatial path is produced. This is accomplished by relating the frequencies by a constant rational number. Non-rational numbers lead to open Lissajous-like tracks, particularly in all *growing* bodies.

The first three examples compare the resulting traces for zero (Fig. 4), constant (Fig. 5) and modulated spin (Fig. 6) under otherwise equal characteristics. The loop observed for zero spin is single (Fig. 4), and indicates that growth is not symmetric. No symmetry is produced if the spin frequency (constant or modulated) is equal in magnitude to that of the gyration frequency (Fig. 5 and 6.). Spin modulation at constant gyration frequency produces tri-axial bodies. The specific indicator found to distinguish between the two, are the two wiggles seen in the modulated case (one per loop, see Fig. 6).

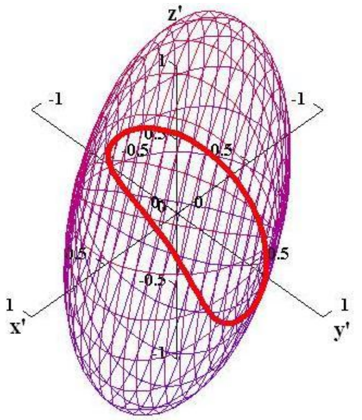

Fig. 4: Surface point $(\theta_o: \varphi_o) = (\pi/6: \pi/2)$ on spheroid with zero spin (as defined by $\Gamma(t)$ in equation (2)) and clockwise gyration with gyrational amplitudes $\zeta = \pi/6$, $\eta = \pi/6$.

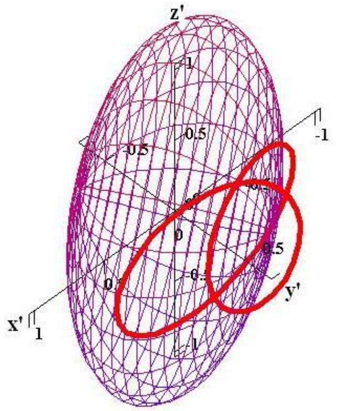

Fig. 5: Surface point $(\theta_o: \varphi_o) = (\pi/6: \pi/2)$ on spheroid with constant clockwise spin (as defined by $\Gamma(t)$ in equation (3)) and clockwise gyration, with relative gyration:spin frequency (1:2) and gyrational amplitudes $\zeta = \pi/6$, $\eta = \pi/6$.

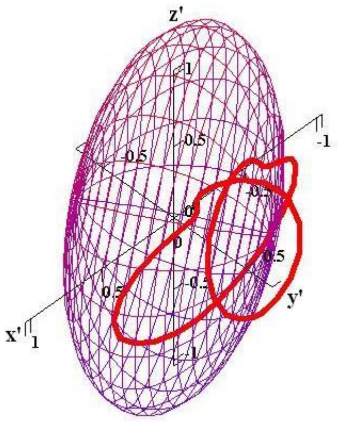

Fig. 6: Surface point $(\theta_o: \varphi_o) = (\pi/6: \pi/2)$ on spheroid with modulated clockwise spin (as defined by $\Gamma(t)$ in equation (5)) and clockwise gyration, with relative gyration:spin frequency (1:2) and gyrational amplitudes $\zeta = \pi/6$, $\eta = \pi/6$.

Additionally, it is also evident that points near the equator ($\theta \sim \pi/2$) along the same longitudinal line (having the same φ coordinate) create similarly shaped Lissajous patterns. Intuitively, this makes sense because the angular accelerations and speeds are the same for all the points, however as approaching the axis of rotation (y”-axis) the surface points experience forces that are greater in order to hold them in place. Thus, a more contorted Lissajous figure is formed but with the same general shape. Moving along the same longitudinal line toward the pole (θ smaller and smaller, approaching zero) it is observed that all the Lissajous patterns “unwind” and ultimately converge onto a simple circle at $\theta = 0$ (see Figs. 7-16); This is true for both the constant and modulated spins.

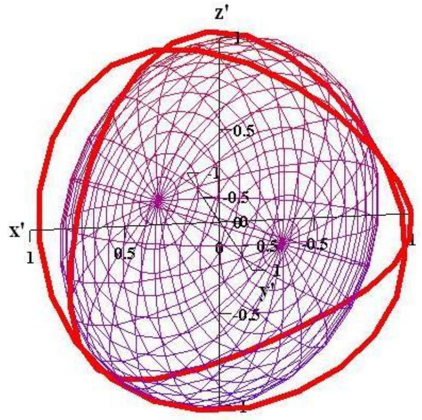

Fig. 7: Surface point $(\theta_o: \varphi_o) = (\pi/2: \pi/6)$ on spheroid with constant counterclockwise spin (as defined by $\Gamma(t)$ in equation (3)) and clockwise gyration, with relative gyration:spin frequency (1:2) and gyrational amplitudes $\zeta = \pi/6$, $\eta = \pi/6$.

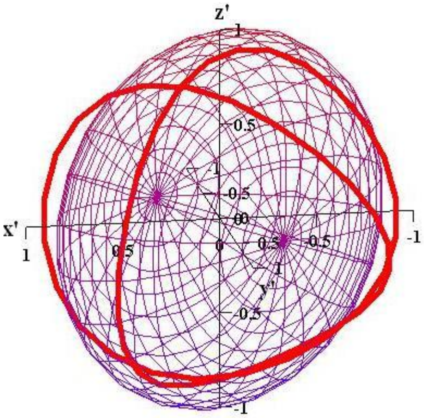

Fig. 8: Same gyration and rotation parameters as Fig. 7 but for surface point $(\theta_o: \varphi_o) = (\pi/3: \pi/6)$.

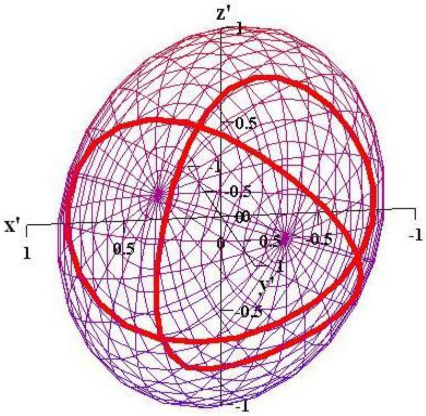

Fig. 9: Same gyration and rotation parameters as Fig. 7 but for surface point $(\theta_o: \varphi_o) = (\pi/4: \pi/6)$.

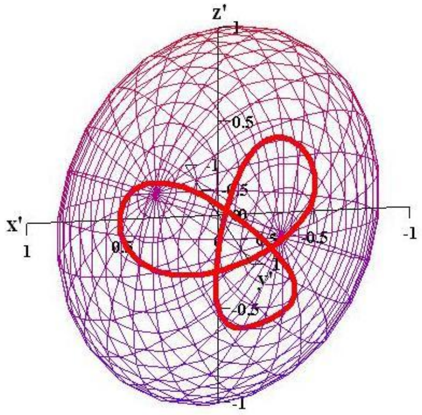

Fig. 10: Same gyration and rotation parameters as Fig. 7 but for surface point $(\theta_o: \varphi_o) = (\pi/8: \pi/6)$.

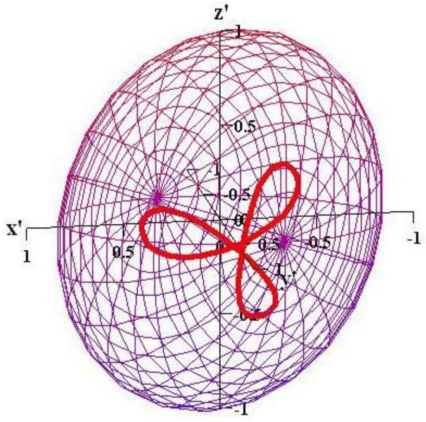

Fig. 1: Same gyration and rotation parameters as Fig. 7 but for surface point $(\theta_o: \varphi_o) = (\pi/12: \pi/6)$.

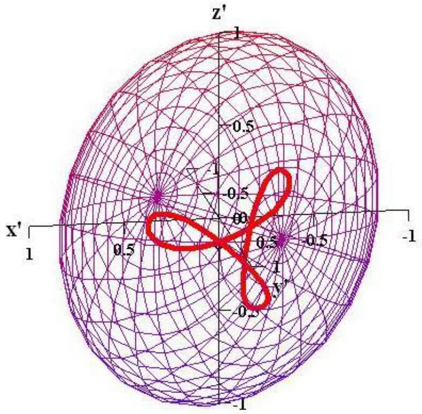

Fig. 12: Same gyration and rotation parameters as Fig. 7 but for surface point $(\theta_o: \varphi_o) = (\pi/14: \pi/6)$.

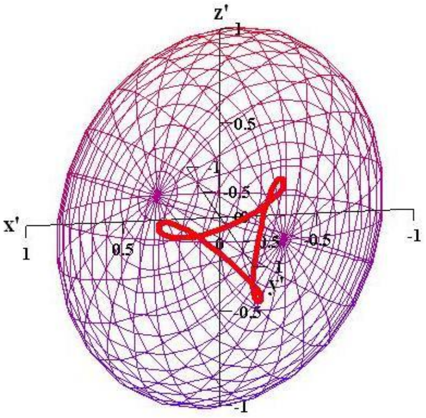

Fig. 23: Same gyration and rotation parameters as Fig. 7 but for surface point (θ$_o$: φ$_o$) = (π/19: π/6).

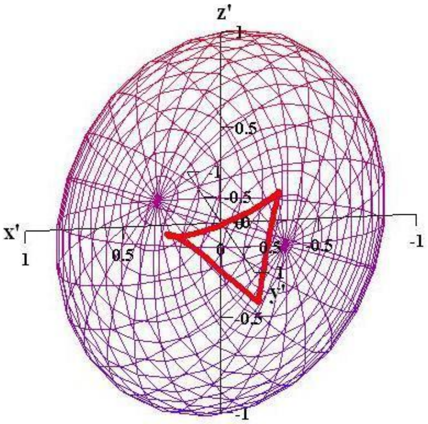

Fig. 3: Same gyration and rotation parameters as Fig. 7 but for surface point (θ$_o$: φ$_o$) = (π/27: π/6).

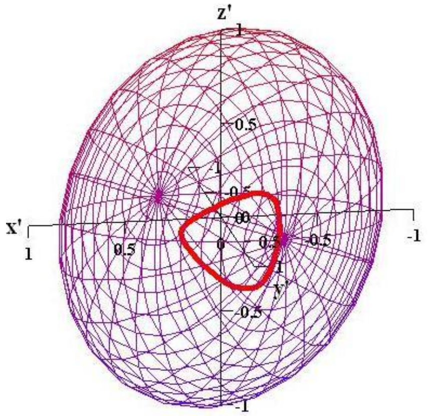

Fig. 4: Same gyration and rotation parameters as Fig. 7 but for surface point (θ$_o$: φ$_o$) = (π/75: π/6).

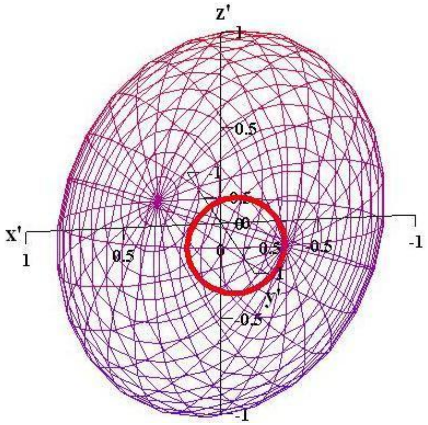

Fig. 5: Same gyration and rotation parameters as Fig. 7 but for surface point (θ$_o$: φ$_o$) = (0: π/6).

4. SUMMARY AND COMMENTS

In this paper, equations have been developed that allow the description of general ellipsoids, gyrating with constant or modulated spin. The equations also lend themselves to establish local growth and accelerations at any surface points. This is of great importance because these accelerations are a controlling factor for the shedding from surfaces of growing hailstones.

The main concern is to understand the growth transition of spheroidal to ellipsoidal hailstones. Falling while gyrating with a superimposed modulated spin may well produce hailstones with a triaxial symmetry (List and Abreu, 2008), however as those authors pointed out, spin modulation alone is not the whole solution because the angular momentum would not be conserved; Wobble of the spin axis is also required. This can be envisaged by a second, superimposed gyration as depicted in Fig. 17. This wobble, however, would produce additional inertial forces. A first line of attack is in icing experiments with a new and very flexible gyrator, much more flexible than used earlier by the group (i.e. Garçia-Garçia & List, 1992) that is presently being built in Toronto. A theoretical approach is also being explored.

It should also be mentioned here that a new gyration mode has been suggested

(List & Abreu, 2008) that might control growth of *spherical hailstones*.

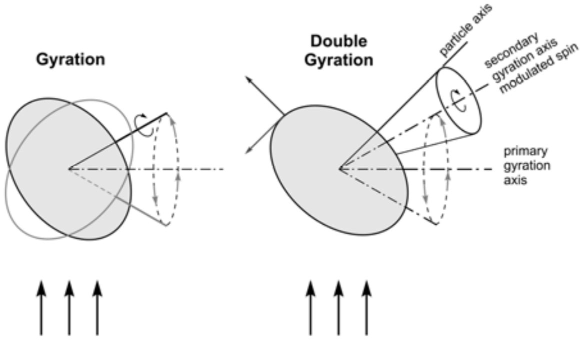

Fig. 17: Left: Single gyration with spin about minor axis. Right: Double gyration with secondary gyration, assumed to produce triaxial hailstones (for best results, requires flexible but torsion-resistant anchoring in the particle center).

The development of the kinematic equations describing the motion of a hailstone and any of its surface points is a first step towards solving the equations of motion. In addition, it allows exploration of local growth and accelerations of surface points for a growing hailstone which performs even more complex motions than discussed here. This is a window into the future and the basis for new sets of more realistic hailstone growth experiments, growth investigations, and understanding hailstone growth physics.

In this paper basic equations are being developed that describe the motion of ellipsoids, spinning with a zero, constant or modulated spin specified by a time-dependent angular function Γ(t). This function was defined and utilized to follow any surface point of a ellipsoidal body gyrating about a fixed horizontal y'-axis at angles ζ and η, and a spinning about the y" axis of a second, double-primed coordinate system.

Due to the flexibility of the equations developed here, the motions of surface points on either spheroidal or ellipsoidal hailstones can be modeled. This will lead to an increased understanding of local growth and acceleration at any surface point, which further leads to a better understanding of the transitions from spheroidal to ellipsoidal hailstones, as well as the drop shedding process which is very dependent on local accelerations, not to mention the possible application to the mass-heat transfer theory for hailstones.

Acknowledgments

The sponsoring of this research by the National Science and Engineering Research Council of Canada is gratefully recognized..

REFERENCES

Garçia-Garçia, F., and R. List, 1992: Laboratory measurements and parameterizations of supercooled water skin temperatures and bulk properties of gyrating hailstones. *J. Atmos. Sci.* 49, 2058-2073

Greenan, B.J.W., and R. List, 1995: Experimental closure of the heat and mass transfer theory of spheroidal hailstones, *J. Atmos. Sci*, 52, 3797-3815

Kry, P.R., and R. List, 1974: Angular motions of freely falling spheroidal hailstone models, *Phys. Fluids*, 17, No. 6, 1093-1102.

Lesins, G.B., and R. List, 1986: Sponginess and drop shedding of gyrating hailstones in a pressure-controlled wind tunnel. *J. Atmos. Sci.*, 43. 1 Dec., 2813-2825.

List, R. and D. Abreu, 2008: Shape evolution of growing hailstones as function of gyration parameters. Proceedings 15th International Conference on Clouds and Precipitation, Cancun, 7-11 July.

List, R., G.B. Lesins, F. Garcia-Garcia and D.B. McDonald, 1987: Pressurized icing tunnel for graupel, hail and secondary raindrop production. *J. Atmos. Ocean. Techn.*, 4, No. 3, 454-463.

Stewart, R.E., and R. List, 1983: Gyrational motions of disks during free fall. *Phys. Fluids,* 26, 920-927

Zheng Guoguang and R. List, 1995: Convective heat transfer of rotating spheres and spheroids with non uniform surface temperatures. *Intern. J. Heat Mass Transfer*, 39, 1815-1826.

A STOCHASTIC MODEL FOR THE COLLECTION GROWTH OF ICE PARTICLES IN MIXED-PHASE CLOUDS

Lester Alfonso[1], G. B. Raga[2] and Darrel Baumgardner[2]

[1]Universidad Autónoma de la Ciudad de México
[2]Centro de Ciencias de la Atmósfera, Universidad Nacional Autónoma de México, 04510 México

1. INTRODUCTION

Computational problems that arise when treating ice phase microphysics are much more complicated than those encountered in models with warm rain microphysics. Because of that there are only a few mixed phase non-parameterized cloud models based on solving the kinetic equations for size distribution functions of water drops, ice particles and aggregates.

The collection growth of ice particles is one of the most complex problems in mixed-phase microphysics, since the resulting type of particle may be of a type different from the colliding particles. Usually this process is described by a system of kinetic collection equations of great complexity (Khain and Sednev, 1995; Beheng 1978; Alheit et al., 1990; Reisin et al., 1995). For example, if only aggregates and pristine ice crystals are considered, then the quasi-stochastic equation for aggregates has the form:

$$\begin{aligned}\frac{\partial f_a(x)}{\partial t} = & \int_0^{x/2} K_a(x_c,x)\, f_a(x_c)\, f_a(x')dx' \\ & - f_a(x)\int_0^{\infty} K_a(x,x')\, f_a(x')dx' \\ & + \int_0^{x} K_{ia}(x_c,x')\, f_a(x_c)\, f_i(x')dx' \\ & + \int_0^{x/2} K_i(x_c,x')\, f_i(x_c)\, f_i(x')dx' \\ & - f_a(x)\int_0^{\infty} K_{ia}(x,x')\, f_i(x')dx' \qquad (1)\end{aligned}$$

The first term in (1) is gain term for aggregates colliding with aggregates, the second term is a loss term for aggregates colliding with aggregates, the third term is a gain term for aggregates colliding with ice crystals, term 4 is a gain term for ice crystals colliding with ice crystals and term 5 is a loss term for ice crystals colliding with aggregates.

For pristine ice crystals the quasi-stochastic equation is:

$$\begin{aligned}\frac{\partial f_i(x)}{\partial t} = & -\int_0^{x/2} K_i(x_c,x)\, f_i(x_c)\, f_i(x')dx' \\ & - f_i(x)\int_0^{\infty} K_{ia}(x,x')\, f_a(x')dx' \qquad (2)\end{aligned}$$

In (2) the first term is a loss term of ice crystals colliding with ice crystals, and the second term is a loss term of ice crystals colliding with aggregates. In equations (1) and (2) $x_c = x - x'$, $f_a(x)$ and $f_i(x)$ are the mass distributions for aggregates and pristine ice crystals and $K_i(x_c,x')$, $K_a(x_c,x')$ and $K_{ia}(x_c,x')$ are the collections kernels for the collisions of aggregates, pristine ice crystals, and aggregates with crystals.

Within the stochastic framework, the aggregation of ice crystals to form snowflakes was previously studied by Westbrook et al. (2004). In Maruyama and Fujiyoshi (2005) a stochastic model for snow aggregation was developed by adding an aggregation model to the Monte Carlo method of Gillespie (1975).

When other hydrometeor types are included in the analysis, the system of quasi-stochastic equations becomes much more complex. For example, Khain and Sednev

---

[1] *Corresponding author address:* Lester Alfonso, Universidad Autónoma de la Ciudad de México; México City, Distrito Federal 09790, México. E-Mail: lesterson@yahoo.com

(1995) included hydrometeors of seven kinds: water drops, plate-like and columnar crystals, dendrites, snowflakes, graupel and hail. To handle the problem, they formulated some rules in case of single acts of particles collisions (Khain and Sednev, 1995).

In order to avoid the solution of the complex quasi-stochastic equations, a stochastic microphysical framework for calculating the collection growth in a mixed phase cloud is proposed.

The stochastic algorithm of Gillespie (1976) for chemical reactions in the multicomponent formulation proposed by Laurenzi et al. (2002) was used to simulate the kinetic behavior of the particle population. Within this framework, reacting species are defined as ice particles of specific mass and crystal habit. The stochastic algorithm described in this work was previously used to model the evolution of a two-component droplet spectrum.

The proposed stochastic algorithm allows the study of the effect of ice crystal type on collection growth in mixed-phase clouds and could improve cloud parameterizations in models with bulk microphysics.

2. THE MONTE CARLO ALGORITHM

The stochastic framework, models the crystal aggregation as a random, discrete process. In our report, the stochastic algorithm of Gillespie (1976) for chemical reactions was adopted instead of the algorithm previously elaborated for droplet populations (Gillespie, 1975). This algorithm was reformulated to simulate the kinetic behavior of aggregating systems by Laurenzi et al. (2002). In Laurenzi et al. (2002) species are defined as a type of aggregate with a specific size and composition. In our specific case, species are defined as hydrometeors of different types (droplets, ice crystals or aggregates) with specific mass and aerosol composition.

Within this framework, there is a unique index *μ* for each pair of hydrometeors *i, j* that may react (collide). For a system with *N* species $\left(S_1,\ S_{2,}\ \ldots\ ,S_N\right)$ $\mu \in \frac{N(N+1)}{2}$. The set $\{\mu\}$ defines the total “collision” space, and is equal to the total number of possible interactions (collisions). With this set the reaction probability density function $P(\tau,\mu)$ can be determined.This quantity is defined by

$P(\tau,\mu)d\tau \equiv$ {Probability that at time the next reaction (collision) in volume V will occur in the infinitesimal interval $(t+\tau,\quad t+\tau+d\tau)$and will be a μ reaction}.

In Gillespie (1976) this probability density function has been derived for a system of *N* species as

$$P(\tau,\mu)d\tau = a_\mu \exp\left(- \sum_{j=1}^{\frac{N(N+1)}{2}} a_j \tau \right) \qquad (3)$$

Here $\mu \in \frac{N(N+1)}{2}$. The functions $a_\mu$are calculated according to

$a(i,j) = V^{-1}K(i,j)X_iX_j dt$ =Pr{Probability that two unlike particles *i* and *j* with populations (number of particles) X_i and X_j will collide within the inminent time interval} (4)

$a(i,i) = V^{-1}K(i,i)\frac{X_i(X_i-1)}{2}dt$ =Pr{Probability that two particles of the same species i with population (number of particles) X_i collide within the inminent time interval} (5)

The reaction probability density function is the basis of the Monte Carlo algorithm. For calculating the evolution of the system, two random numbers *τ* and *μ* must be generated. Equation (3) leads directly to the answers of the aforementioned questions. First, what is the probability distribution for times?. Summing $P(\tau,\mu)d\tau$ over all *μ* (all possible collisions, (reactions)) results in

$$P_1(\tau)d\tau = \sum_{\mu=1}^{\frac{N(N+1)}{2}} a_\mu \exp\left(-\sum_{\nu=1}^{\frac{N(N+1)}{2}} a_\nu \tau \right)$$
$$= \alpha \exp(-\alpha\tau)d\tau \qquad (6)$$

with $$\alpha = \sum_{\nu=1}^{\frac{N(N+1)}{2}} a_\nu$$

The probability function for reactions can be obtained in a similar way, by integrating the pdf $P(\tau,\mu)d\tau$ over all τ from 0 to ∞ results in

$$P_2(\mu) = \frac{a_\mu}{\alpha} \qquad (7)$$

Equation (4) gives the probability of a particular reaction μ given an interval $(\tau, \tau+d\tau)$. Equation (6) shows that the probability of a reaction (collision) in time follows an exponential distribution, a characteristic of a process in which events occurs randomly in time.

In order to obtain a random pair (τ, μ), according to the probability density function $P(\tau,\mu)$ we first generate a random number r_1 distributed uniformly in the interval [0,1], then, the inversion method to obtain random numbers is applied. In the inversion method this random number is taken as the probability of a reaction in the time period τ according to $P_1(\tau)$. This probability is obtained by integrating $P_1(\tau)$ from 0 to τ:

$$\begin{aligned} r_1 &= \int_0^\tau P_1(x)dx \\ &= \int_0^\tau \alpha \exp(-\alpha x)dx = 1 - \exp(-\alpha\tau) \end{aligned} \qquad (8)$$

Considering that $1\text{-}r_1\text{=}r^*_1$ is also a uniformly distributed random number in the interval [0,1], then the time τ can be calculated from (8) in the form:

$$\tau = \frac{1}{\alpha}\ln\left(\frac{1}{r_1^*}\right) \qquad (9)$$

The reaction number μ is calculated similarly. A random number r_2 uniformly distributed in the interval [0,1] is generated. Then the pdf $P_2(\nu)$ (7) must be integrated over ν until the addition of the μ probability exceeds the random number r_2. The inequality to obtain the reaction index μ has the form (Gillespie, 1976)

$$\sum_{\nu=1}^{\mu-1} a_\nu < r_2\alpha \le \sum_{\nu=1}^{\mu} a_\nu \qquad (10)$$

The former results lead to the Gillespie's direct algorithm:

1) Initialize (set initial numbers of species, set t=0, set stopping criteria).
2) Calculate the function a_μ for all μ.
3) Choose τ according to the exponential distribution $P_1(\tau) = \alpha\exp(-\alpha\tau)d\tau$
4) Calculate μ according to the distribution $P_2(\mu) = \frac{a_\mu}{\alpha}$.
5) Change the numbers of species to reflect the execution of a reaction.
6) If stopping criteria are not met, go to step 2.

3. SIMULATION RESULTS

In order to check the performance of Monte Carlo algorithm, a simulation was run considering that the only hydrometeor type is droplets. The results from the Monte Carlo algorithm are the averages over 1000 realizations of the stochastic process. For monodisperse initial conditions, we consider a cloud of 1 cm^3 volume, initially containing N_0 droplets of 10 µm. These droplets were placed in bin 1 of the size distribution. Fig.1 shows a comparison between the Monte Carlo algorithm and analytical solutions of the SCE for a constant collection kernel. The monodisperse initial distribution was set equal to N_0=100 cm^{-3}. As can be observed, the simulations, yielded the same results as the analytical solutions of the SCE.

To test the framework for the ice-phase, a simplified simulation was running with hexagonal ice plates and columnar ice crystals for the initial particles. Initial monodisperse distributions with concentrations of 50 cm^{-3} particles for both the columnar ice crystals and hexagonal plates were considered, with masses for the monomer crystals of 10^{-9} and 10^{-10}g respectively. The cloud volume was set equal to 1cm^3. Following Khain and Sednev (1996), the rules in case of single acts of particles collisions for this case are:

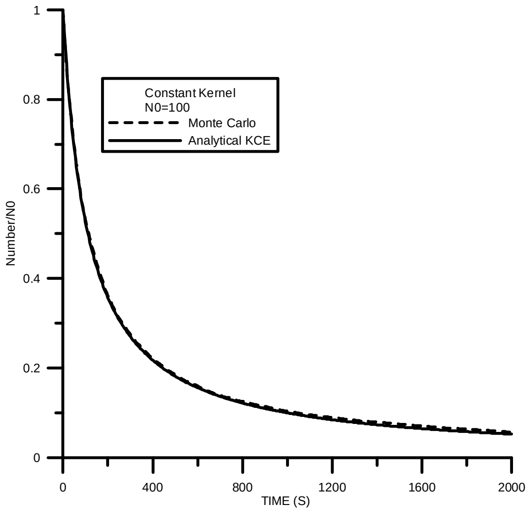

Fig.1. The number of particles averaged over 1000 simulation runs and normalized to the initial number of particles (N_0=100), versus time is shown by the dashed line. The results from the analytical solution are shown by the solid line.

- Ice crystal–ice crystal: snowflakes are formed.
- Ice crystal-snowflake: snowflakes are formed.
- Snowflake–snowflake: snowflakes are formed,

Terminal velocity of the hydrometeors were taken from Pruppacher and Klett (1997). The collection efficiency and collection kernels of crystal-ice crystal interactions were parameterized following

Khain and Sednev (1995). Simulations results are the averages over 1000 realizations of the stochastic process (Fig. 2). For the simplified simulation presented in this report, an increase in the snowflake concentration at the beginning of the simulations is observed as a result of the interaction between ice crystals. The posterior reduction is a result of the snowflake–snowflake interaction.

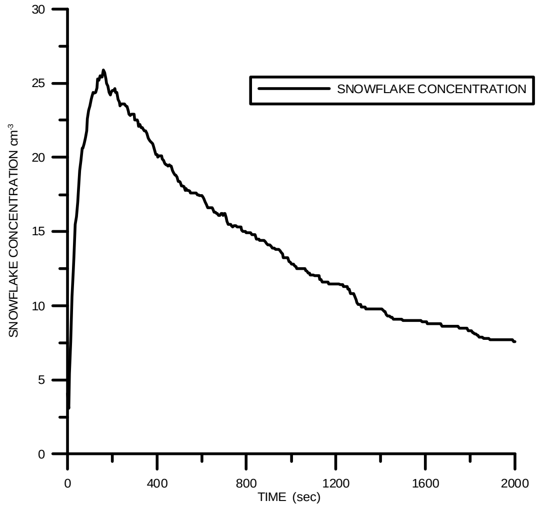

Fig.2. Snowflake concentration averaged over 1000 simulation runs versus time.

To test further the algorithm, a more detailed comparison with averages obtained from solutions of the deterministic quasi-stochastic equations is needed. The collection algorithm described in this work has to be linked with a general microphysical framework, in order to consider all the processs relevant to precipitation formation in mixed phase clouds.

4. CONCLUSIONS

The stochastic algorithm for chemical reactions developed by Gillespie (1976) in the formulation proposed by Laurenzi et al. (2002) was implemented in order to calculate the time evolution of hydrometeors in a mixed phase cloud. Within this framework, reacting species are defined as hydrometeors of specific mass and type. The collection algorithm described in this work has to be linked with a general microphysical framework, in order to consider all the processs relevant to precipitation formation in mixed phase clouds.

5. REFERENCES

Alheit, R.R., Flossmann, A.I., Pruppacher, H.R., 1990. A theoretical study of the wet removal of atmospheric pollutants. Part 4: The uptake and redistribution of AP pollutants captured through nucleation and impaction scavenging by growing cloud droplets and ice particles, J. Atmos. Sci., 47, 870-887.

Beheng, K., 1978. Numerical simulation of graupel development, J. Atmos. Sci., 35, 683-689.

Gillespie, D.T. 1975. An exact method for numerically simulating the stochastic coalescence process in a cloud. *J . Atmos. Sci*. 32: 1977-1989.

Gillespie, D.T. 1976. A general method for numerically simulating the stochastic time evolution of coupled chemical reactions. *J. Comput. Phys*. 22: 403-434.

Khain, A.P., Sednev, I., 1996. Simulation of precipitation formation in the Eastern Mediterranean coastal zone using spectral microphysics cloud ensemble model. Atmos. Res. 43, 77-110.

Laurenzi, I.J., Bartels, S.L., and Diamond, S.L.: A general algorithm for exact simulation of multicomponent aggregation, J. Comput. Phys., 177, 418, 2002.

Maruyama, K.I., Fujiyoshi, Y, 2005: Monte Carlo simulation of the formation of snowflakes. J. Atmos. Sci. 62, 1529-1544.

Reisin, T., Levin, Z., Tzvion, S., 1996. Rain production in convective clouds as simulated in an axisymmetric model with detailed microphysics. Part 1: Description of the model. J. Atmos. Sci. 53, 497–519.

C. D. Westbrook, R. C. Ball, P. R. Field and A. J. Heymsfield, 2004: A theory of growth by differential sedimentation with application to snowflake formation. Phys. Rev. E70, 021403

MONTE CARLO SIMULATIONS OF TWO-COMPONENT DROP GROWTH BY STOCHASTIC COALESCENCE

Lester Alfonso[1], G. B. Raga[2] and D. Baumgardner[2]
[1]Universidad Autónoma de la Ciudad de México, México City, 09790 México
[2]Centro de Ciencias de la Atmósfera, Universidad Nacional Autónoma de México, México City, 04510 México
Correspondence to: Lester Alfonso (lesterson@yahoo.com)

ABSTRACT

The evolution of two-dimensional drop distributions is simulated in this study using a Monte Carlo method. The stochastic algorithm of Gillespie (1976) for chemical reactions in the formulation proposed by Laurenzi et al. (2002) was used to simulate the kinetic behavior of the drop population. Within this framework species are defined as droplets of specific size and aerosol composition. The performance of the algorithm was checked by comparing the numerical with the analytical solutions found by Lushnikov (1975). Very good agreement was observed between the Monte Carlo simulations and the theoretical results.

Simulation results are presented for bi-variate constant and hydrodynamic kernels. The algorithm can be easily extended to incorporate various properties of clouds such as including several crystal habits, different types of soluble CCN, particle charging and drop breakup.

1. INTRODUCTION

The understanding of aerosol-cloud interactions contains large uncertainties that must be reduced to accurately estimate the impact of aerosols on weather and climate. One of the most problematic aspects of aerosol-cloud interactions is the collision-coalescence process that is a mechanism that modifies the aerosol distribution, i.e. the aerosol particles that are the nuclei for individual droplets are combined during the coalescence process in the same way as the mass of the individual water droplets are merged. After the evaporation of the drop formed by coalescence, the aerosol particle that remains will have the mass of the original two nuclei.

The aerosol distribution becomes important as the cloud drops evaporate and the solutes are recycled into aerosols that can serve as CCN: the larger the mass of a hygroscopic aerosol, the lower the supersaturation needed to form a cloud droplet. In the marine environment, the aerosol recycling process is believed to be the major mechanism responsible for the bimodal shape of the aerosol size distributions (Flossmann, 1994; Feingold et al., 1996). The heterogeneous chemical reactions, which add nonvolatile solute to each cloud droplet, strongly depend on the salt content and pH of the droplet (Alfonso and Raga, 2004). Since aerosols also have a significant influence on cloud microphysics and cloud radiative properties, it is necessary to simulate aerosol processes realistically and with adequate accuracy.

In general cloud models with detailed microphysics describe the aerosol and cloud droplets with two separate one-dimensional size distributions. With this approach only the average aerosol mass contained in cloud droplets of a particular size is predicted by the model and is not possible to keep track of the spectral aerosol mass distribution within the cloud droplets. For the deterministic case, the aerosol processing due to collision-coalescence was addressed by Liu (1998) and Bott (2000) by extending the flux method to two-dimensional distributions. Within this framework each particle is characterized both by the mass of its dry aerosol nucleus and by its water mass. Nevertheless, an extension of the exact stochastic framework developed by Gillespie (1976) for a two parameter droplet spectrum has never been reported in the cloud physics literature.

The main advantage of the stochastic approach, described in this paper, over deterministic methods is that it can be easily extended to include not only the solute mass, but other particle properties such as crystal habit, different populations of CCN, chemical composition and the breakup of droplets (Alfonso et al, 2006).

Here we apply the general multi-component algorithm described by Laurenzi et al. (2002) to the solution of the kinetic collection equation (KCE) in cloud models dealing with two-dimensional microphysics.

The discrete two-component KCE, which is an extension of the discrete one dimensional kinetic collection equation, is given as:

$$\frac{\partial N(m,n;t)}{\partial t} = \sum_{m'=0}^{m}\sum_{n'=0}^{n} K(m-m',n-n',m',n',t)...$$

$$...N(m-m',n-n';t)N(m',n';t)$$

$$-N(m,n;t)\sum_{m'=0}^{\infty}\sum_{n'=0}^{\infty} K(m,n;m',n';t)N(m',n';t) \qquad (1)$$

Where $N(m,n,t)$ is the average number of species with water mass from size bin *m* and aerosol mass from size bin *n*. The water mass in size bin *m* equals the volume of a droplet in the smallest (monomer droplet) bin multiplied by *m,* the aerosol mass in size bin *n* equals the volume of an aerosol in the smallest bin (monomer aerosol) multiplied by *n.* In general, $N(m,n,t)$ is the average number of particles consisting of *m* monomers of the first and *n* of the second kind, respectively. The integral (continuous) version of this equation is more familiar:

$$\frac{\partial N(n,m,t)}{\partial t} = \frac{1}{2}\int_0^m dm_1 \int_0^n dn_1 K(m-m_1,n-n_1;m_1,n_1)...$$

$$...N(m-m_1,n-n_1;t)N(m_1,n_1,t)$$

$$-N(m,n;t)\int_0^{\infty} dm_1 \int_0^{\infty} dn_1 K(m,n;m_1,n_1)N(m_1,n_1;t) \qquad (2)$$

In Eqs. (1) and (2) $K(m,n;m_1,n_1)$ is the collection kernel, now dependent on the composition of coagulating particles. The discrete KCE (1) gives the time rate of change of the average number of species with water mass from bin *m* and aerosols from bin *n* as the difference of two terms, the first term describes the average rate of production of the *(m,n)* species due to coalescence between pairs of particles whose water mass volume is in size bin *m,* and the aerosol volume is in size bin *n* and the second term describes the average rate of depletion of *(m,n)* particles due to their coalescence with particles from other species. To solve equations (1) and (2) initial conditions are needed:

$$N(m,n;0) = N_0(m,n) \qquad (3)$$

For the discrete case, we also put $N(0,0;t) = 0$ for every *t*. The numerical solution of the KCE (1) and (2) is difficult due to the double integral and nonlinear behavior of the equation and several numerical techniques can be found in the literature. In cloud physics modeling, Eq. (2) was numerically integrated by the flux method developed by Bott (2000) and independently by Liu (1998), both assuming that the probability for the collision of two cloud droplets depends only on the water mass of each one and not on the mass of the aerosol nuclei.

Other methods are computationally more expensive, such as the previously mentioned Monte Carlo (MC) algorithm developed by Laurenzi et al. (2002). This method has the advantage that it can be employed to determine both the expectations and fluctuations for multi-component aggregation. On the other hand, the KCE may not be valid at longer time periods, when a single drop acquires a mass much larger than the rest of the population and becomes separated from the continuous mass spectrum. In such a situation, the statistical fluctuations at the high-mass end of the spectrum must be taken into account. The Monte Carlo method is also very useful while investigating the role of coalescence in redistributing the aerosol mass in early warm rain stages when the artificial broadening of the drop distribution must be avoided.

2. THE STOCHASTIC ALGORITHM

A detailed description of the stochastic algorithm for multi-component aggregation of particles can be found in Gillespie (1976) and Laurenzi et al. (2002), and we briefly summarize it here. Consider a well-mixed and spatially homogeneous volume *V* in which particles belonging to N_s distinct species are present. Each species is characterized both by its water mass and by the mass of its dry aerosol nucleus, $\bar{u}_\mu = (u_m, u_n)$, such that, a droplet with composition $\bar{u}_\mu$ is a member of the *μ*th species. After time *t=0* the species will randomly coalesce according to:

$$A_{m,n} + B_{m',n'} = C_{m+m',n+n'} \qquad (4)$$

where $A_{m,n}$ and $B_{m',n'}$ are droplets with compositions $\bar{u}_\mu = (u_m, u_n)$ and $\bar{u}_\nu = (u_{m'}, u_{n'})$, respectively. The transition probabilities for coalescence events follow Laurenzi et al. (2002) and are given by:

$a(i,j) = V^{-1}K(i,j)n_i n_j dt$ ≡Pr{ Probability that two particles of species *i* and *j* (for *i* ≠ *j*) with populations (number of particles) n_i and n_j will collide within the inminent time interval} (5)

$a(i,i) = V^{-1}K(i,i)\dfrac{n_i(n_i-1)}{2}dt$ ≡Pr{Probability that two particles of the same species *i* with population (number of particles) N_i collide within the inminent time interval} (6)

In (5) and (6), $K(i,j)$ is the collection kernel, and *V* is the cloud volume. Within this framework, there is a unique index *μ* for each pair of droplets *i, j* that may collide. For a system with *N* species $(S_1, \ S_{2,} \ \ldots \ , S_N)$ $\nu \in \dfrac{N(N+1)}{2}$. The set $\{\nu\}$ defines the total collision space, and is equal to the total number of possible interactions. The transition probabilities (5) and (6) are then represented by one index (a_ν).

This stochastic model is solved using the algorithm introduced by Gillespie (1976) for chemical kinetics and modified by Laurenzi et al. (2002). The expected behavior of the system can be evaluated by averaging over many realizations of the stochastic process, described by the following steps:

1) At *t*=0, the event counter is set to zero and the initial number of species $n_1, n_{2,}\ldots, n_N$. is defined
2) The quantity *α* is calculated as:

$$\alpha = \sum_{\nu=1}^{\frac{N(N+1)}{2}} a_\nu \qquad (7)$$

Generate a random number r_1 from a uniform distribution in the interval (0,1) and considering that $1\text{-}r_1=r_1^*$ is also a uniformly distributed random number calculate

$$\tau = \frac{1}{\alpha}\ln\left(\frac{1}{r_1^*}\right) \qquad (8)$$

3) Generate a random number r_2 from a uniform distribution in the interval (0,1). Choose a collision (“chemical reaction”) with index *μ* from the inequality
4) $$\sum_{\nu=1}^{\mu-1} a_\nu < r_2\alpha \le \sum_{\nu=1}^{\mu} a_\nu \qquad (9)$$
4) Let *t=t+τ*
5) Change the number of species to reflect the execution of collision.

3. MODEL RESULTS

3.1 COMPARISON OF THE MONTE CARLO ALGORITHM WITH ANALYTICAL SOLUTIONS

In order to check the performance of the Monte Carlo algorithm, a simulation with a constant kernel was performed and compared with the analytical solution found by Lushnikov (1975). Solutions to Eqs. (1) and (2) can be obtained for an important class of collection kernels, such as when the kernel depends only on the total number of monomers (droplets and aerosols) in each colliding particle. In this case:

$$K(m,n;m_1,n_1) = K(m+n, m_1+n_1) \qquad (10)$$

Lushnikov constructed an explicit form for the composition distribution for this type of kernel, which corresponds to coagulation of initially monomeric particles. In this case $N(1,0;0) = c_1$ and $N(0,1;0) = c_2$, corresponding to the situation with initially *c₁* droplets and *c₂* aerosols. The composition distribution may be expressed as (Lushnikov, 1975):

$$N(m,n;t) = \binom{m+n}{n}\left(\frac{c_1}{c_0}\right)^m\left(\frac{c_2}{c_0}\right)^n N(m+n,t) \qquad (11)$$

With $c_0=c_1+c_2$

Where $\binom{m+n}{n}$ are the binomial coefficients, and $N(m+n,t)$ is the number of particles composed of *(m+n)* monomers (*m* monomer droplets and *n* monomer aerosols). Lushnikov (1975) showed that $N(m+n,t)$, for the type of kernels (10) is a solution of the one dimensional kinetic collection equation:

$$\frac{\partial N(i,t)}{\partial t} = \frac{1}{2}\sum_{j=1}^{i-1} K(i-j, j)N(i-j)N(j) - N(i)\sum_{j=1}^{\infty} K(i,j)N(j) \qquad (12)$$

In this case, $N(i,t) = \sum_{m+n=i} N(m,n;t)$. The initial condition for (12) is $N(i,t) = N_0\delta_{i,1}$. Analytical solutions of the continuous KCE have been obtained by Golovin (1963), Scott (1968), Drake (1972) and Drake and Wright (1972) for approximations of the hydrodynamic kernel given by the polynomials $K(i,j) = A$ $B(x_i + x_j)$ and $C(x_i x_j)$ where x_i and x_j are the masses of the droplets from bins *i* and *j*. For the constant kernel $K(x_i, x_j) = A$ and a monodisperse initial distribution with concentration *c₀*, the analytical size distribution of the discrete KCE has the form: $N(i,t) = 4c_0\dfrac{(T)^{i-1}}{(T+2)^{i+1}}$ with

$$T = Ac_0 t \qquad (13)$$

Then, the analytical solution of Eq. (1), calculated according to the expression (11) for the constant kernel $K(x_i, x_j) = A$, is compared with true stochastic averages over N_r realizations of the stochastic process (in our simulationsN_r=1000)

$$:\langle N(m,n;t)\rangle = \frac{1}{N_r}\sum_{r=1}^{N_r} N(m,n;t)^r \qquad (14)$$

where $N(m,n;t)^r$ is the number of particles for species with droplet mass from bin number *m* and dry aerosol mass from bin *n* in the *r*-realization of the stochastic algorithm at time *t*. The Monte Carlo simulation was conducted for initially monomeric particles (droplets and aerosols) with concentrations *c₁*=30 and *c₂*=30 ($N(1,0;0) = 30$ $N(1,0;0) = 30$ and $N(0,1;0) = 30$). Long (1974) calculated the coefficients for the polynomials $K(x,y) = A$, $B(x+y)$ and $C(xy)$ approximating the one dimensional collection kernel when the largest of the colliding drops is smaller than 50 µm. For the constant kernel, he found a value of *A*=1.20×10^{-4} (cm^3 sec^{-1}). We used the same value for the constant discrete two-dimensional collection kernel:

$$K(m,n;m',n') = 1.2\times10^{-4}(cm^3\sec^{-1}) \qquad (15)$$

In our simulations, the monomer droplet is 10 µm in radius (droplet mass 4.188×10^{-9}g) and the monomer aerosol is an ammonium sulfate aerosol, 0.1 µm in radius (mass 1.14×10^{-14}g).

We have defined 30 bins for the water mass grid and 30 bins for the aerosol grid. The pure monomeric species are also considered (those containing pure droplets and pure aerosols). Then, the total number of species in our numerical experimental can be calculated as:

$$N_{Total} = N_{droplets} \times N_{aerosols} + N_{droplets} + N_{aerosols} \qquad (16)$$

Where $N_{droplets}$ and $N_{aerosols}$ are the number of bins for the water mass grid and the aerosol grid respectively. The last two terms in (16) account for the monomeric species (droplets and aerosols). In our case the total number of species is 960.

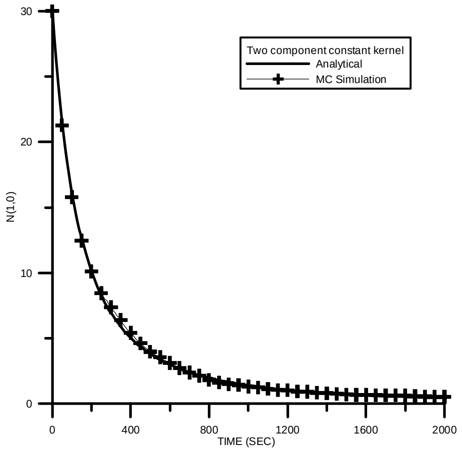

Figure 1. Time evolution (species *N(1,0)))* for a system modeled by the constant kernel, as a function of time. The solid lines are the analytical solution of the two-dimensional KCE.

Figure 1 shows the solution obtained from the Monte Carlo calculations (averaged over 1000 realizations) for the species *N(0,1;t)*. The analytical solution is also shown in Fig. 1 (represented by the solid curve), and indicates the good agreement between these solutions of the KCE (Eq. 1).

Figure 2a and 2b presents the two dimensional discrete size distributions for a) the analytical solution given by Eq.(11) and b) the average over 1000 realizations after 100 seconds. Note that the differences between the Monte Carlo averages and the analytical solution of the KCE are negligible.

The one-dimensional distribution, which is a solution of the one-dimensional kinetic collection equation (12), can be obtained from the two-dimensional spectrum by integrating over the aerosol grid for any point in time, as:

$$N(m,t) = \sum_{n=1}^{N_a} N(m,n;t), \qquad m = 1,\ldots,N_d \tag{17}$$

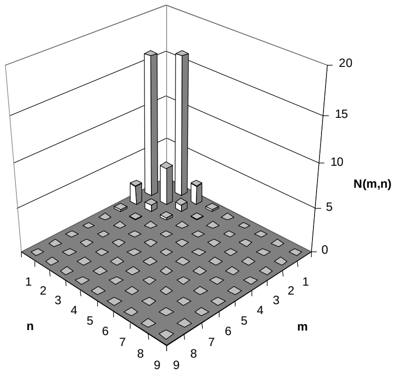

Figure 2a. Discrete two dimensional droplet distributions $N(m,n)$ resulting from the analytical solution of the two-dimensional KCE with a constant kernel at *t*=100 sec, with monomeric initial conditions: ($N(1,0;0)=30$ and $N(0,1;0)=30$**).**

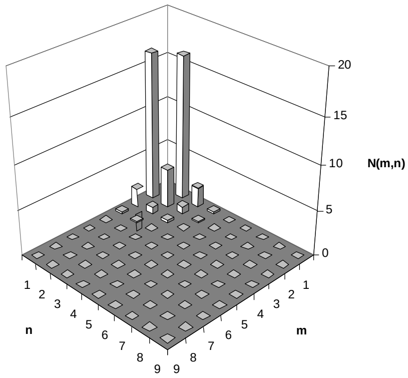

Figure 2b. Discrete two dimensional droplet distributions $N(m,n)$ resulting from the numerical solution of the two-dimensional KCE with a constant kernel at *t*=100 sec. Monte Carlo simulations were conducted with initial conditions $N(1,0;0)=30$ and $N(0,1;0)=30$.

In (17) N_a, and N_d are the number of bins (grid points) in the aerosol and water grid respectively. Two other simulations were performed with different initial conditions: $N(1,1;0)=100$ and $N(1,2;0)=150$, corresponding initially to 100 and 150 particles per cubic centimeter from species *(1,1)* and *(1,2)* respectively. From Eq (17), a monodisperse initial condition for the one-dimensional KCE can be obtained from the two-dimensional initial condition as:

$$N(1;0) = N(1,1;0) + N(1,2;0) = 250 \qquad (18)$$

For this particular case (constant kernel and monodisperse initial conditions) we can use the analytical solution (13) of the KCE in order to compare with the two-component Monte Carlo. The drop size distributions calculated from the Monte Carlo, which is obtained by integrating the particle distribution over the aerosol grid according to (17), and the analytical solution of the KCE with constant kernel (A=1.20×10^{-4} (cm^3 sec^{-1})) from a monodisperse initial condition $N_0(1)$=250 cm^{-3} are displayed in Fig. 3. Again, a good agreement between the two approaches is found.

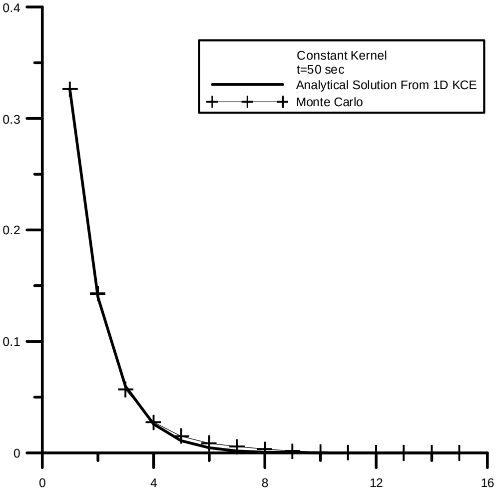

Figure 3. The number of particles averaged over 1000 realizations and normalized to initial number of particles (N_0=250) represented by the line with crosses) and the analytical solution of the one dimensional kinetic collection equation (KCE) (represented by the dark solid line) as a function of size for t=50.

As was remarked in detail by Laurenzi et al. (2002), the species accounting formalism outlined in section 2 reduces both computer storage and simulation time. This process is handled by dynamic allocation of memory permitting calculations with thousands of droplets in the initial distribution.

3.2 SIMULATIONS WITH REALISTIC INITIAL DISTRIBUTIONS AND HYDRODYNAMIC KERNEL

Simulations with the two-dimensional Monte Carlo were performed with realistic initial particle distributions and with the two-dimensional hydrodynamic kernel which is relevant to cloud physics. The two-dimensional extension of the piecewise approximation found by Long (1974) was used:

$$K(i,j) = 9.44 \times 10^9 \left(x_{species}(i)^2 + x_{species}(j)^2 \right)$$
$$\text{if } R \le 50\,\mu m \qquad (19)$$

or by

$$K(i,j) = 5.78 \times 10^3 \left(x_{species}(i) + x_{species}(j) \right)$$
$$\text{if } R > 50\,\mu m \qquad (20)$$

In (19) and (20) R is the species radius and $x_{species}(i)$ is the mass of the particle from species with index i which is calculated as:

$$x_{species}(i) = x_d(i) + x_a(i) \qquad (21)$$

where $x_d(i)$ and $x_a(i)$ are the droplet and the aerosol mass respectively.

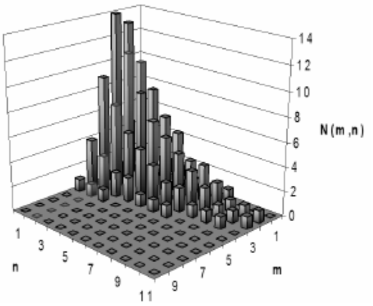

Figure 4. Initial two-component spectrum $N(m,n,0)$ with droplet concentration of 181cm^{-3} and LWC 1.87 g/kg.

Fig. 4 shows the initial two-component spectrum for our simulation. The spectrum has a droplet concentration of 158 cm^{-3}. This distribution was obtained (following Liu, 1998) by assuming a gamma distribution function for the drop coordinate and an exponential distribution for the aerosol size coordinate.

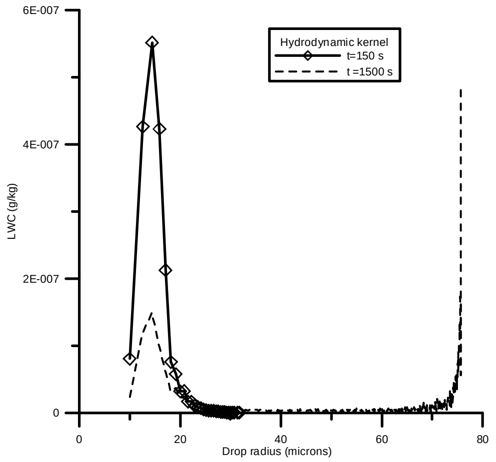

Figure 5a. Liquid water content (LWC, in g/kg) as a function of drop radius for the hydrodynamic coalescence kernel for t=150 s (solid line with diamonds) and t=1500 s dashed lines).

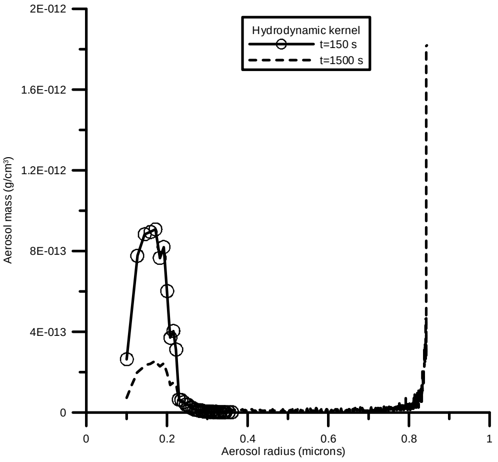

Figure 5b. Aerosol mass concentration (in g/cm^3) as a function of aerosol radius for the hydrodynamic kernel for t=150 s (solid line with circles) and t=1500 s dashed lines).

The Figs. 5a and 5b display the drop and aerosol distributions, averaged over 1000 realizations, for two durations (*t*=150 s, *t*=1500 s). As can be observed, there is a net loss for small particles and net gain for large particles. The spectrum shifts toward drops with large drop sizes and large aerosol sizes.

4. DISCUSSION AND CONCLUSIONS

The multi-component MC algorithm proposed by Laurenzi et al. (2002) and based upon Gillespie's (1976) stochastic approach to chemical reactions was implemented to simulate two-component droplet growth by stochastic coalescence. Within this framework, all assumptions included in the stochastic collection equation are avoided. Additionally it permits calculation of statistical fluctuations for two-component droplet aggregation. On the other hand, the continuous KCE may not be valid when a single drop acquires a mass much larger than the rest of the system and becomes separated from the smooth mass spectrum. In such a situation, the statistical fluctuations at the high-mass end of the spectrum must be taken into account.

For the two-dimensional case each species is characterized both by its water mass and by the mass of its dry aerosol nucleus. The simulated two-dimensional distributions were compared in detail with the predictions from mathematically exact analytical solutions. Very good agreement was observed between the MC and the theoretical results.

Moreover, the above described algorithm can be easily extended to the multi-component case in order to include various other properties of clouds. In a more general case species can be defined as types of particles with several attributes (droplet radius, CCN composition, chemical composition, electric charge, etc) as well as the breakup of droplets (Alfonso et al, 2006). For this case, the state of a *k* component system is defined by a set of drops with properties or compositions $\overline{u}_i = \left(u_{1,i}, u_{2,i}, u_{3,i}, ..., u_{k,i}\right)$ where $u_{k,i}$ denotes the amount of the component or the property *k* in species *i*. For example, for the ice phase, it may represent the crystal habit, or the ice crystal mass. Then, the transition probability (5) may be defined as the probability that a specific pair of particles (drops, ice crystals, aerosols) with set of properties $\overline{u}_i = \left(u_{1,i}, u_{2,i}, u_{3,i}, ..., u_{k,i}\right)$ and $\overline{u}_j = \left(u_{1,j}, u_{2,j}, u_{3,j}, ..., u_{k,j}\right)$ will aggregate in the next time interval.

The stochastic approach should make more feasible the modeling of highly complicated microphysical processes and offers a method to evaluate these processes in much greater detail than has been previously possible.

5. REFERENCES

Alfonso, L., Raga, G.B.: The influence of organic compounds in the development of precipitation acidity in maritime clouds, Atm. Chem. Phys., 4, 1097-1111, 2004.

Alfonso, L., Raga, G.B., and Baumgardner, D.G.: Monte Carlo simulations of drop growth by stochastic coalescence and collision-induced breakup, 12th Conference in cloud physics, Madison, Wisconsin, 2006.

Bott, A.A.: A flux method for the numerical solution of the stochastic collection equation: Extension to two-dimensional particle distribution, J. Atmos. Sci., 57, 284-294, 2000.

Drake, R.L.: The scalar transport equation of coalescence theory: Moments and kernels, J. Atmos. Sci., 29, 537-547,1972

Drake, R.L., Wright, T.J.: The scalar transport equation of coalescence theory: New families of exact solutions, J. Atmos. Sci., 29, 548-556, 1972.

Feingold, G., Kreindenweis, S.M.: Cloud processing of aerosol as modeled by a large eddy simulation with coupled microphysics and chemistry. *J. Geophys. Res.*,107, 4687, 2002.

Flossmann, A. I.: A 2-D spectral model simulation of the scavenging of gaseous and particulate sulfate by a warm marine cloud, *Atmos. Res.*, 32, 233-248, 1994.

Gillespie, D.T.: An exact method for numerically simulating the stochastic coalescence process in a cloud, J . Atmos. Sci., 32, 1977-1989, 1975.

Gillespie, D.T.:A general method for numerically simulating the stochastic time evolution of coupled chemical reactions, J. Comput. Phys., 22, 403-434, 1976.

Golovin, A.M.: The solution of the coagulating equation for cloud droplets is a rising air current, Bull. Acad. Sci. USSR, Geophys. Ser., No. 5, 482-487, 1963.

Laurenzi, I.J., Bartels, S.L., and Diamond, S.L.: A general algorithm for exact simulation of multicomponent aggregation, J. Comput. Phys., 177, 418, 2002.

Liu, Q.: Modeling of the aerosol-cloud interactions in marine stratocumulus, PhD Thesis, Cooperative Institute for Mesoscale Meteorological Studies, Norman, Oklahoma 73019, Report No. 109, 1998.

Long, A.B.: Solutions to the droplet collection equation for polynomial kernels, J. Atmos. Sci., 31, 1040-1051, 1974.

Lushnikov, A.A.: Evolution of coagulating systems III: Coagulating mixtures, J. Coll. Int. Sci., 54, 1, 94-101, 1975.

Scott, W.T.: Analytic studies of cloud droplet coalescence, J.Atmos. Sci., 25, 54-65, 1968.

THE INFLUENCE OF ICE CRYSTAL HABIT ON SIMULATIONS OF ARCTIC MIXED-PHASE CLOUDS

Alexander Avramov and Jerry Y. Harrington
The Pennsylvania State University, University Park, PA 16802

1. INTRODUCTION

One of the major problems in arctic climate model simulations is related to the simulation of arctic mixed-phase clouds. Due to their inherent colloidal instability, these clouds represent a unique challenge for any model. The ability of the current regional and climate models to correctly simulate these clouds was explored as part of the Arctic Climate Model Intercomparison Project (Curry and Lynch, 2002). While during the summer all of the models predicted liquid water paths similar to the observed, during the winter all of the models produced very little or no liquid water at all. While discrepancies like this are usually attributed to the over-simplified cloud microphysical parameterizations used in these models, a recent intercomparison study (Prenni et al., 2007) showed that more advanced schemes performed worse than the simpler models.

At present, how mixed-phase Arctic clouds can maintain significant quantities of supercooled liquid water and ice, for extended periods of times and at very low temperatures is not well understood. Because of the difference of saturation vapor pressure over ice and liquid water, the ice crystals in a mixed-phased cloud will grow at the expense of the cloud droplets. Subsequent precipitation of the ice may then cause the complete glaciation of the cloud. Pinto (1998) and Harrington et al., (1999) hypothesized that mixed-phase clouds are maintained through a balance between liquid water condensation resulting from the cloud-top radiative cooling and ice removal by precipitation. In their modeling studies Harrington et al. (1999), Harrington and Olsson (2001) and Jiang et al. (2000) found that this balance depends strongly on the ambient concentration of deposition ice nuclei (IN) and possibly on the assumed crystal habit. All of these modeling studies require low ice concentrations (through low IN concentrations) to maintain supercooled liquid water. Many recent and older measurements of IN concentrations in the Arctic tend to support this notion (Bigg, 1996, Rogers, 2001, Prenni et al., 2007) with most measurements showing IN concentrations of < 1 L-1 with some large excursions.

In the first numerical study (Prenni et al., 2007) utilizing observational data collected during the Mixed-Phase Arctic Cloud Experiment (M-PACE, Verlinde et al., 2007), the authors used a three-dimensional meso-scale model to investigate the impact of ice-nucleating aerosols on simulated arctic mixed-phase clouds. Their results showed strong sensitivity of the cloud life-time to ambient IN concentrations, similar to what have been reported before (Harrington et al., 1999; Harrington and Olsson, 2001; Jiang et al., 2000). They also demonstrated that IN must be treated prognostically in the models (i.e. advected and depleted) in order to maintain liquid water even when IN concentrations are low. In a follow-up study based on the same M-PACE case, however, Morrison et al. (2008) showed much lower sensitivities to IN concentration. Although this discrepancy in part could be explained by the different IN treatment implemented in both studies, prognostic in Prenni et al.(2007) vs diagnostic in Morrison et al. (2008), other factors that control liquid fraction depletion are also suspect.

In general, liquid water uptake by ice crystals is controlled by the crystal in-cloud residence time and their total surface area. The in-cloud residence time is controlled by the shape (habit) of the crystals (through terminal fall velocity) and the total surface area depends on their concentration and shape. Thus, liquid water depletion in mixed-phase clouds is controlled mainly by two factors – ice crystal/IN concentration and ice crystal shape. Consequently, one might expect that cloud sensitivity to IN concentration would vary depending on the assumed ice crystal shape.

To further illustrate this point, we performed several series of simulations of the same case, simulated by Prenni et al. (2007) and Morrison et al. (2008), using different ice crystal shapes.

2. CASE DESCRIPTION

We simulated the time period from 17Z on October 9 to 5Z on October 10, 2004. This is the same period chosen for case B in the M-PACE model inter-comparison study, performed jointly by the ARM Cloud Modeling Working Group and GCSS Polar Cloud Working Group (Klein et al., 2008). The synoptic situation during this period was determined mainly by the high pressure center developing over sea-ice pack to the north east of the Alaska coast. This high, coupled with the surface low over the Aleutians, intensified the pressure gradient over the area and created favorable conditions for strong northeasterly winds moving cold air off the pack ice over the relatively warm ocean surface (Figure 1). This synoptic situation persisted for several days during which the North Slope of Alaska and the adjacent ocean were covered by extensive deck of mixed-phase stratus clouds.

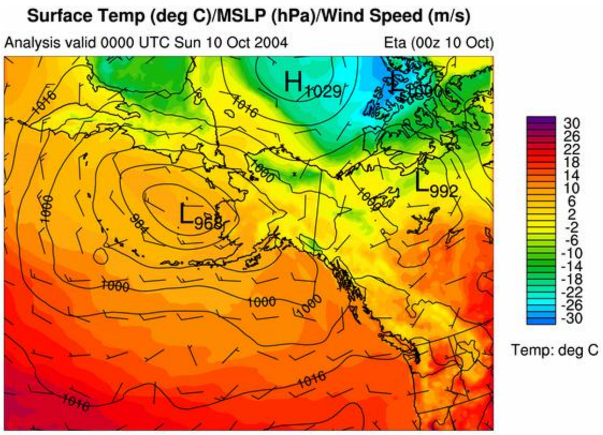

Figure 1. ETA surface analysis for 12 UTC October 10, 2004

Observed cloud top temperatures ranged between -17 and -15 ^{o}C, with cloud top height being between 1200 and 1500 m and cloud base around 800 m (Verlinde et al., 2007). Both aircraft and ground-based sensors indicated a mixed-phase cloud structure with liquid upper half and ice falling below the base of the cloud – Figure 2.

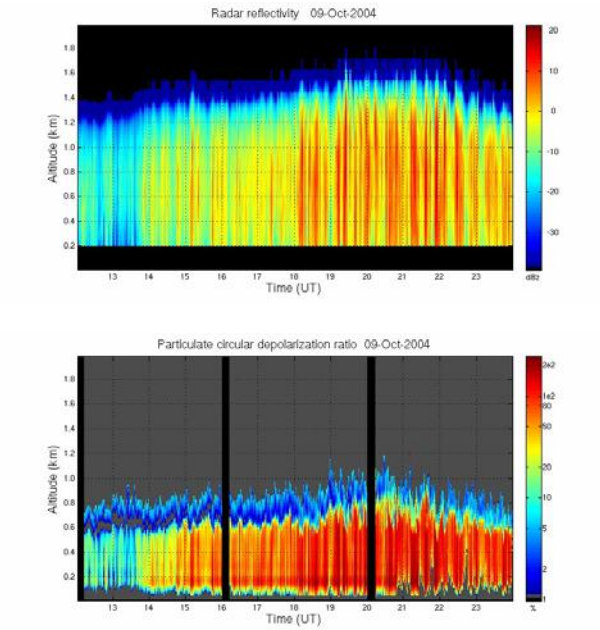

Figure 2. MMCR radar reflectivity and HSRL de-polarization ratio (<2 liquid, >2 ice) over Barrow, AK

3. MODEL CONFIGURATION

The model used in this study is the Colorado State University version of Regional Atmospheric Modeling System (RAMS@CSU) (Cotton et al., 2003) with two-moment microphysics (Walko et al., 1995; Meyers at al., 1997) and a two-stream radiation scheme (Harrington and Olsson, 2001). The microphysical package of the model has seven hydrometeor categories: cloud droplets, rain, pristine ice, snow, aggregates, graupel and hail. Three of the four heterogeneous nucleation modes are present in the model – deposition, condensation-freezing and contact nucleation. Deposition and condensation-freezing nucleation are parameterized as a function of ice supersaturation, following Meyers et al. (1992) and using IN measurement data taken during M-PACE. This parameterization has a similar functional form as Meyers et al.,

(1992) but the predicted IN concentrations are approximately 26 times lower. The initial IN concentration predicted for this case is ~0.15 L^{-1}. Contact nucleation rates due to thermophoresis, diffusiophoresis and Brownian motion are given in Cotton et al. (1986) and the number of IN available for contact freezing as a function of temperature is described in Meyers et al. (1992). Since we do not have contact nucleation data from M-PACE, we assumed that the IN available for contact nucleation should be reduced by the same factor as deposition/condensation-freezing IN. During a simulation, the model keeps track of the number of depleted and available IN for both contact and condensation-freezing nucleation modes. Once nucleated, IN are removed from the population and so additional nucleation is possible only through supersaturation increase or IN advection from another gridbox. Although this mechanism doesn't account for in-situ IN production, we believe that it allows for a relatively realistic IN depletion mechanism. The importance of IN depletion in mixed-phase clouds simulations has been emphasized in a number of studies – Harrington and Olsson (2001), Morrison et al. (2005), Prenni et al.(2007).

The model is configured as a 2-D cloud-resolving model. Computational domain has 150 X 72 grid-points with 1 km horizontal spacing and vertical spacing of 25 m in the boundary layer, stretching to 1000 m at the top of domain. The model is initialized with prescribed sounding and constant winds, large scale forcing and surface fluxes, developed specifically for the M-PACE model inter-comparison study (Klein et al., 2008). Soil-vegetation and sea-ice submodels of RAMS were not used in this study and the lower boundary was assumed to be an ocean surface.

4. RESULTS

As we discussed above, liquid water consumption by the growing ice crystals depends on their concentration, in-cloud residence time and their mass growth rate which in turn are controlled by the crystal habit.

To investigate the potential effect ice crystal habit might have on simulations of mixed-phase clouds we performed a series of sensitivity runs in which we used different ice crystal shapes. Three generic crystal shapes were used in these simulations – hexagonal plates, dendrites and spheres. In addition to the capacitance term in the mass growth equation, crystal habit manifests itself also through mass-dimensional and terminal velocity relationships. Since reported in the literature relationships exhibit large amount of scatter, we first established the range of these relationships vary (Figure 3). We use relations that span the maximum and minimum for each functional form then proceeded to investigate IN sensitivity with respect to each crystal habit. For spheres we used similar relationships to those used in Fridlind et al. (2007) and Morrison et al. (2008) who simulated the same case.

Four sets of simulations, combining lower and upper limits of mass-dimensional and terminal fall velocity relations, were then carried out for each of the crystal habits with the exception of spheres. The results are illustrated in Figure 4 and in Table 1, showing liquid and ice water path as a function of IN concentration for each of the combinations. The liquid and ice water paths for hexagonal plates do not exhibit much variation with increasing IN concentration. There is no sensitivity with regard to varying mass-dimensional or terminal velocity relationship either. This is an indication that due mostly to their small capacitance, the mass growth rate and consequently the rate of liquid water consumption by ice crystals is much smaller than the rate of liquid water production. Exactly the opposite situation is observed for "large" dendrites. (By "large" we mean that the mass dimensional relation used gives the smallest mass for a given crystal diameter.) Simulations with "large" dendritic shapes were not able to sustain enough liquid water even at low IN concentrations. In this case, condensed liquid water is rapidly consumed by the growing crystals. Figure 5 illustrates the difference in simulated cloud fields for the

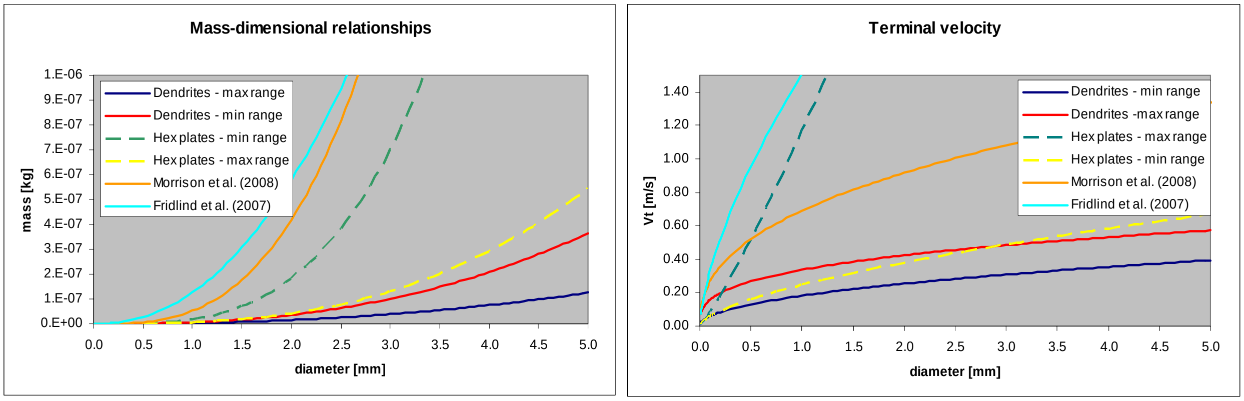

a) b)

Figure 3. Mass-dimensional (a) and terminal velocity (b) relationships for crystal habits used in the simulations

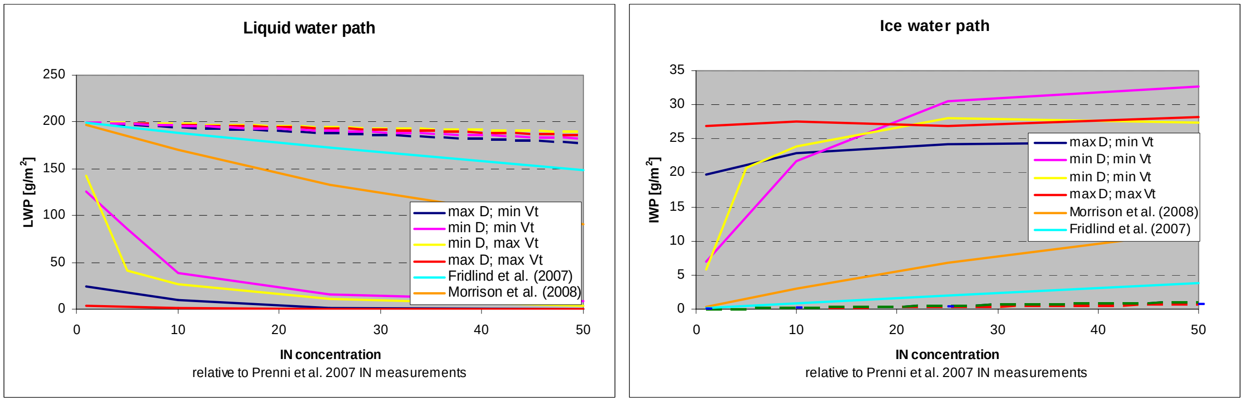

a) b)

Figure 4. Simulated liquid (a) and ice water paths (b) as a function of IN concentration (dendrites - solid line; hexagonal plates - broken line)

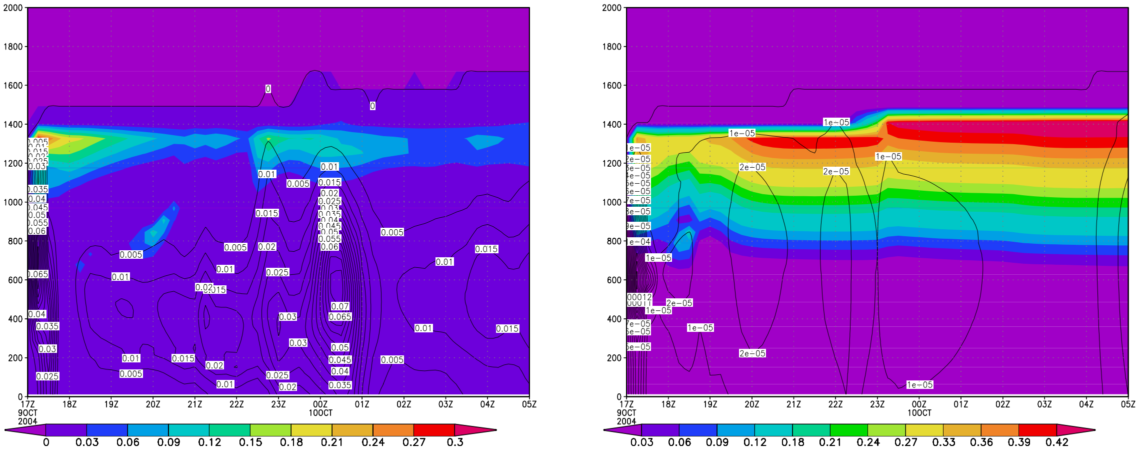

a) b)

Figure 5. Time series of simulated liquid water (shaded) and ice water (contoured) content for "small" dendrites (a) and hexagonal plates (b)

cases of “large” dendrites and hexagonal plates - thin broken liquid layer with substantial ice water content in the former, and thick solid liquid layer with almost no ice in the latter.

Of particular interest is the case of “small” dendrites, or the mass-dimensional relation that has the greatest mass for a given size. At very low IN concentrations (typical for the Arctic), the liquid water path is similar to that of hexagonal plates. Increasing IN concentration up to the values typical for mid-latitudes leads to almost complete glaciation of the simulated cloud layer, similar to what have been reported before (Harrington, 1997; Harrington and Olsson, 2001; Jiang et al., 2000; Prenni et al., 2007). The strong sensitivity to IN concentration suggests that in this case the balance between liquid water production and consumption is very delicate. Small changes in terminal fall velocity, crystal size or concentration lead to dramatic changes in simulated cloud fields.

We tried to force rapid glaciation, similar to that of “small” dendrites, using hexagonal plates, by simply increasing the IN concentration. However, instead of an abrupt change of the simulated liquid and ice water paths, we observed a gradual change with increasing IN concentration – Figure 6. This result could be explained with significantly enhanced accretion /collection processes at these extremely high IN concentrations.

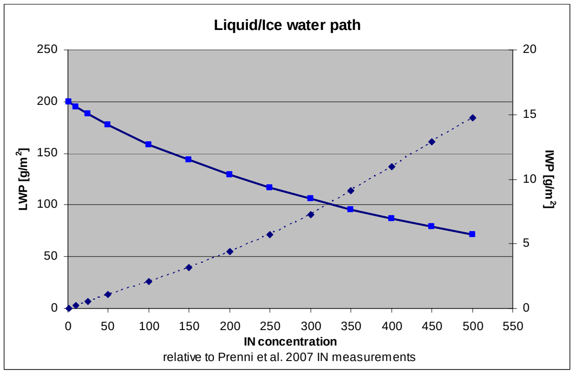

Figure 6. Liquid (solid line) and ice water path (broken line) – hexagonal plates

A similar attempt to modify rapid glaciation, this time with “large” dendrites led to rather intriguing result. We decreased liquid water depletion rate by increasing the terminal fall velocity of the “large” dendrites by using the relationship for fast falling hexagonal plates (the green broken line on Figure 3b). The results of this series of runs are shown in Table 1(maxDmaxHexVt). In contrast with the previous simulations using “large” dendrites, substantially more liquid is retained; however, the sensitivity to IN concentration is much lower, compared to that of “small” dendrites.

Even larger amounts of liquid water can be retained in the case of dendrites if the hexagonal plate capacitance is used instead of that for “large” dendrites – maxDminVtHexC run in Table 1. This “shape” can be considered as an extremely large and slowly falling hexagonal plate. Compared to the “normal” hexagonal plates, it produces lower liquid water content and higher sensitivity to IN concentration. Similar conclusions could be drawn for its counterpart – maxDminVtDendrC, which can be considered as a very small and fast falling dendrite. Compared to both “large” and “small” dendrites it produces much higher liquid water content and moderate sensitivity. It should be emphasized though, that these composite “shapes” do not have any practical meaning. However, they illustrate the relative importance of the physical factors controlling liquid water depletion. Our results show that while terminal fall speeds are certainly important for removing ice from the layer, and hence increasing the lifetime of liquid water, the crystal capacitance is of equal, or greater, importance.

As was expected, simulations using spheres showed moderate to low sensitivity to IN concentration with substantially high liquid water paths – Figure 4. Although spheres have the largest capacitance, they also have the smallest diameter and largest fall velocity (Figure 3b). The net effect of these two factors seems to neutralize to a large degree the effect of increased capacitance and IN concentration. The.

Table 1. Observed and simulated liquid and ice water path as a function of IN concentration

	LWP [g/m^2]				IWP [g/m^2]			
IN concentration	x1	X10	x25	x50	x1	x10	x25	X50
Observations – Klein et al. (2008)								
Airborne	115				7.6			
Ground-based retrievals	107-210				29.4			
Dendrites								
maxDminVt	24.30	9.49	0.95	0.33	19.72	22.90	24.23	24.50
maxDmaxVt	3.31	1.10	0.35	0.04	26.84	27.46	26.89	28.12
minDminVt	125.87	38.89	15.95	8.31	6.95	21.72	30.55	32.74
minDmaxVt	142.32	26.27	11.07	4.20	5.72	23.85	28.02	27.37
maxDmaxHexVt	136.50	114.86	86.81	53.05	2.72	3.75	6.14	10.06
maxDminVtHexC	198.70	187.94	169.63	144.10	0.05	0.49	1.28	2.99
Hexagonal plates								
maxDminVt	199.50	195.01	188.15	177.81	0.02	0.23	0.56	1.07
maxDmaxVt	199.74	196.95	192.83	185.96	0.02	0.15	0.38	0.72
minDminVt	199.63	195.97	190.45	181.82	0.02	0.22	0.54	1.04
minDmaxVt	199.83	197.66	194.50	189.50	0.01	0.12	0.30	0.59
maxDminVtDendrC	195.90	162.07	114.01	63.09	0.20	2.14	6.96	15.72
Spheres								
Fridlind	198.77	188.98	172.89	148.25	0.08	0.82	1.97	3.78
Morrison	196.60	169.72	133.32	90.92	0.32	3.00	6.87	11.46
MorrisonHexC	199.53	195.19	188.62	178.42	0.04	0.37	0.90	1.73
MorrisonDendrC	198.04	182.39	158.20	128.36	0.17	1.62	3.91	7.42

spheres used by Fridlind et al. (2007) are smaller and faster falling than those used in Morrison et al. (2008) which explains the difference in simulated liquid and ice water paths for these two series of runs. Our results suggest a reason for the weaker IN sensitivity observed by Morrison et al. (2008) and Fridlind et al. (2007) as compared to the strong IN sensitivity exhibited by the simulations of Prenni et al. (2007): Assuming a small ice category composed of faceted crystals leads to larger vapor growth rates, slower fall speeds, and hence a much greater sensitivity to IN concentrations.

It is interesting to note that despite the different modeling frameworks (3-D mesoscale model vs 2-D CRM) and the different treatment of IN (diagnosing vs. prognosing), our results track quite well those reported by Morrison et al. (2008). Also, some of the results in Table 1 correspond favorably to the airborne observational data. We should emphasize, however, that the goal of this study was not to obtain a realistic simulation that could be matched to the observations, but rather to investigate the limits in which simulated cloud liquid and ice water content could vary depending on the assumed ice crystal habit.

5. SUMMARY AND CONCLUSIONS

In this study we used high resolution 2-D cloud-resolving model to examine the influence of the assumed ice crystal habit on simulated cloud liquid and water content and their sensitivity to IN concentration. Simulated cloud fields showed strong dependence on the ice crystal shape used in the simulations. Hexagonal plate crystals produced solid thick liquid layer with very small amount of ice and virtually no sensitivity to IN concentration, crystal size and fall velocity. Dendritic shapes led to a totally opposite behavior – simulated cloud fields exhibit strong sensitivity to IN concentration and moderate sensitivity to the size and fall velocity of the crystals. The liquid water content is much lower and the ice water content much larger than in the previous case. Spherical shapes seem to be the intermediate case. They produced substantial liquid water content and at the same time significant amount of ice. Sensitivity to IN concentration is higher than that of hexagonal plates, but lower than dedndritic shapes.

Our results show that simulated liquid and ice water contents in mixed-phase clouds are highly dependent on the assumed ice crystal shape. Taking into account the strong connection between ice microphysics and cloud dynamics, we could suggest that a new approach, better reflecting the diversity of ice crystal shapes in real clouds, might lead to more realistic simulation of the arctic mixed-phase clouds.

Acknowledgements: We are thankful for support from the Office of Science (BER), U.S. Department of Energy, Grant No. DE-FG02-05ER64058

REFERENCES

Bigg, E. K., 1996: Ice forming nuclei in the high Arctic. *Tellus*, **48,** 223-233.

Cotton, W. R., G.J. Tripoli, R.M. Rauber, and E.A. Mulvihill, 1986: Numerical simulation of the effects of varying ice crystal nucleation rates and aggregation processes on orographic snowfall. *J. Clim. Apll. Meteorol*., **25**, 1658-1680

Cotton, W. R., R.A. Pielke, Sr., R.L. Walko , G.E. Liston, C.J. Tremback, H. Jiang, R. L. McAnelly, J.Y. Harrington, M.E. Nicholls, G.G. Carrió and J. P. Mc Fadden 2003: RAMS 2001: Current Status and future directions*. Meteor. Atmos. Physics* **82**, 5-29

Curry, J. A. and A. H. Lynch, 2002: Comparing Arctic regional climate models. *EOS*, **83,** 87.

Fridlind, A.M., A.S. Ackerman, G. McFarquhar, G. Zhang, M.R. Poellot, P.J. DeMott, A.J. Prenni, and A.J. Heymsfield, 2007: Ice properties of single-layer stratocumulus during the Mixed-Phase Arctic Cloud Experiment (M-PACE): Part II, Model results. *J. Geophys. Res.*, **112**, D24202, doi:10.1029/2007JD008646

Harrington, J. Y. and P. Q. Olsson, 2001a: On the potential influence of ice nuclei on surface-forced marine stratocumulus cloud dynamics. *J. Geophys. Res.,* **106**, 27473-27484

Harrington, J. Y. and P. Q. Olsson, 2001b: A method for the parameterization of cloud radiative properties within numerical models. Atmos. Res., **57**, 51-80

Harrington, J. Y., T. Reisin, W. R. Cotton, and S. M. Kreidenweis, 1999: Cloud resolving simulations of Arctic stratus. Part II: Transition-season clouds. *Atmos. Res.,* **51,** 45–75.

Jiang, H., W.R. Cotton, J.O. Pinto, J.A. Curry, and M.J. Weissbluth, 2000: Sensitivity of mixedphase Arctic stratocumulus to ice forming nuclei and large-scale heat and moisture advection. *J. Atmos. Sci.*, **57**, 2105-2117.

Klein, S., R. McCoy, H. Morrison, A. Ackerman, A. Avramov, G. deBoer, M. Chen, J. Cole, A. DelGenio, M. Falk, M. Foster, A. Fridlind, J. C. Golaz, T. Hashino, J. Harrington, C. Hoose, M. Khairoutdinov, V. Larson, X. Liu, Y. Luo, G. McFarquhar, S. Menon, R. Neggers, S. Park, M. Poellot, K. Salzen, J. Schmidt, I. Sednev, B. Shipway, M. Shupe, D. Spangenberg, Y. Sud, D. Turner, D Veron, G. Walker, Z. Wang, A. Wolf, S. Xie, K.-M. Xu, F. Yang, and G. Zhang, 2008: Intercomparison of model simulations of mixed-phase clouds observed during the ARM Mixed-Phase Arctic Cloud Experiment. Part I: Single layer cloud. *QJRMS, to be submitted*

Meyers, M.P., P.J. Demott, and W.R. Cotton, 1992: New primary ice-nucleation parameterizations in an explicit cloud model. *J. Appl. Meteor*, **31**, 708-721

Meyers, M.P., R.L. Walko, J.Y. Harrington, and W.R. Cotton, 1997: New RAMS cloud microphysics parameterization. 2. The two-moment scheme. *Atmos. Res.*, **45**, 3, 39

Morrison, H., M.D. Shupe, J.O. Pinto, and J.A. Curry, 2005: Possible roles of ice nucleation mode and ice nuclei depletion in the extended lifetime of Arctic mixed-phase clouds. *Geophys Res. Lett,* **32**, doi:10.1029/2005GL023614

Morrison, H., J.O. Pinto, J.A. Curry and Greg M. McFarquhar, 2008: Sensitivity of modeled arctic mixed-phase stratocumulus to cloud condensation and ice nuclei over regionally-varying surface conditions. *J. Geophys. Res.,*in press

Pinto, J.O., 1998: Autumnal mixed-phase cloudy boundary layers in the Arctic. *J. Atmos. Sci.*, **55**, 2016-2038

Prenni, A.J., J.Y. Harrington, M. Tjernstrom, P.J. DeMott, A. Avramov, C.N. Long, S.M. Kreidenweis, P.Q. Olsson, and J. Verlinde, 2006: Can ice-nucleating aerosols affect Arctic seasonal climate ? *Bull. Am. Meteorol. Soc.*, **88,** 541-550

Rogers, D.C., P.J. DeMott, and S.M. Kreidenweis, 2001: Airborne measurements of tropospheric ice-nucleating aerosol particles in the Arctic spring. *J. Geophys. Res.*, **106**, 15053-15063

Verlinde, J., J. Y. Harrington, G. M. McFarquhar, V.T. Yanuzzi, A. Avramov, S. Greenberg, N. Johnson, M. R. Poellot, J. H. Mather, D. D. Turner, B. D. Zak, T. Tooman, A. J. Prenni, G. L. Kok, E. W. Eloranta, M. D. Ivey, C. P. Bahrmann, K. Sassen, P. J. DeMott, A. J. Heymsfield, 2006: The mixed-phase Arctic cloud experiment (M-PACE). *Bull. Am. Meteorol. Soc.,* **88, 205-221**

Walko, R.L., W.R. Cotton, M.P. Meyers, and J.Y. Harrington, 1995: New RAMS cloud micro-physics parametrization. 1. The single-moment scheme. *Atmos. Res*., **38**, 29-62

SCAVENGING OF AEROSOL PARTICLES BY RAIN IN A CLOUD RESOLVING MODEL

Sarah BERTHET [1], Maud LERICHE [1], Jean-Pierre PINTY [1],
Juan CUESTA [2] and Grégoire PIGEON [3]

[1]Laboratoire d'Aérologie, CNRS, Université Paul Sabatier, Toulouse, France
[2]Laboratoire de Météorologie Dynamique, CNRS, Paris, France
[3]Météo-France,CNRM/4M, Toulouse, France

1. INTRODUCTION

Wet deposition is the most important sink of aerosol particles in the troposphere (Pruppacher and Klett, 1997). Wet deposition processes involve complex microphysical interactions between aerosol particles and hydrometeors. Two processes lead to wet deposition: the nucleation scavenging and the impaction scavenging. The nucleation scavenging is the scavenging of aerosol particles as cloud droplets or ice crystals are forming, respectively, on cloud condensation nuclei and on ice forming nuclei by heterogeneous nucleation. The impaction scavenging is the result of the interactions between aerosol particles and hydrometeors motions including: Brownian diffusion, interception, inertial impaction, thermophoresis, diffusionphoresis, airflow turbulence and electrostatic attraction. The impaction scavenging usually splits in two processes: in-cloud impaction scavenging, which treats the interactions between cloud droplets and raindrops with interstitial aerosol particles and below cloud scavenging, which concerns the collection of aerosol particles by falling raindrops below the cloud base. The relative importance between in-cloud scavenging processes (nucleation and impaction scavenging), also called washout, and below cloud scavenging, also called rainout, depends on meteorological conditions and on the properties of aerosol particles (size distribution and chemical composition) as well as on the stage of cloud development.

This study will focus on the below cloud scavenging (BCS) of aerosol particles although this work is embedded in a largest project, which aims at describing all processes leading to wet deposition of aerosol particles in a three-dimensional cloud resolving model. For BCS, due to the size of raindrops, the collection efficiency depends on Brownian diffusion, interception and inertial impaction (Pruppacher and Klett, 1997). A recent study (Andronache, 2003) shows that the BCS coefficient of aerosol particles increases with the rainfall rate. It has a high value for very small particles (diameters less than 0.01μm) and for the biggest ones (diameters larger than 2μm) whereas it is very low for particles in the intermediate range.

First a BCS module has been developed based upon the collision efficiency parameterization of Slinn (1983) widely used in atmospheric chemistry modeling (Tost et al., 2006). The module uses a generic Gauss quadrature method to integrate over the raindrops and aerosol particle size distributions. Then zero-dimensional tests of the module have been done on a set of rain rates and aerosol particle concentrations data of the COPS experiment, which took place in the Vosges-Black Forest area last July (see `http://www.cops2007.de/`). Finally, the module has been implemented in the three-dimensional mesoscale/cloud resolving model MesoNH (Lafore et al., 1998) and two preliminary simulations have been performed: an idealized case of a shallow tropical rainband in a 2D kinematic framework from the HaRP campaign (Cohard and Pinty, 2000) and a squall line case from the COPT81 experiment in West Africa (Lafore et al., 1989). For both simulations, sensitivity tests are performed on the initial size distributions of aerosol particles as well as on their initial vertical profile.

2.DEVELOPMENT OF THE BCS MODULE

A BCS module has been developed for the tridimensional model MesoNH in order to describe the wet removal of aerosol particles by precipitation below the cloud base. The process of aerosol particles wet scavenging is related to the aerosol particles size distribution but also to the raindrop size distribution (Andronache, 2003). So, the major difficulty to represent the aerosol particles sink by BCS is due to the polydispersed nature of both distributions. However, for simplification, one assumes a monodisperse distribution for raindrops (with a typical raindrop diameter) in order to determine the BCS coefficient $\gamma(d_p)$ between aerosol particles and falling raindrop (Tost et al., 2006 ; Loosmore et al., 2004). Because in MesoNH some information on the raindrop size distributions is available, we choose to compute the BCS coefficients by the full integral over raindrop size, in order to get an accurate estimate (Andronache, 2003 ; Feng, 2006). Then, the BCS coefficient is integrated over the aerosol particles size distribution, to obtain finally, the total size number BCS rate.

Our purpose is to implement the BCS module described below in the tridimensional cloud-resolving model MesoNH, wherein the aerosol particles are represented by the sum of several log-normal distributions $n_{pi}(d_p)$ depending on the number of modes:

$$\sum_{i=1}^{l} n_{pi}(d_p) = \sum_{i=1}^{l} \frac{N_i}{\sqrt{2\pi} d_p log\sigma_i} e^{-\left(\frac{log(d_p/\bar{d_{pi}})}{\sqrt{2} log\sigma_i}\right)^2}$$

where l is the number of mode with index i, d_p is the aerosol particle diameter, N_i, the number concentration, σ_i, the geometric standard deviation of the log-normal distribution, and $\bar{d_{pi}}$ is the modal diameter. For the moment, we use a single-moment scheme for aerosol particles in MesoNH (only the number concentration N is prognostic), so σ_i and $\bar{d_{pi}}$ are constants depending on aerosol particles types. Usually, three modes are used in order to represent the three classical modes: the Aitken mode, the accumulation mode and the coarse mode.

The raindrop size distribution $n_D(D_d)$ in MesoNH is modeled by a generalized Gamma distribution. It is reduced in this study, to the classical Marshall-Palmer law:

$$n_D(D_d) = N_0 \, exp(-\lambda_R \, D_d)$$

where $N_0 = 8\times 10^{-3} m^{-3} mm^{-1}$, λ_R is the slope parameter and D_d the drop diameter.

The method used to calculate the BCS coefficient follows the concept of the collision efficiency between an aerosol particle and a raindrop (Slinn, 1983; Pruppacher and Klett, 1997; Seinfeld and Pandis, 1998). The collision efficiency E expresses the number of aerosol particles collected by collision with the falling raindrop, in the swept out volume of the raindrop. A value of $E = 1$ implies that all particles in the geometric volume swept out by a falling drop will be collected. All the recent studies on BCS use this concept (Andronache, 2003; Loosmore et al., 2004; Henzing et al., 2006; Tost et al., 2006; Feng, 2006).

While theoretical solution of the Navier-Stokes equation for the prediction of E is not available, the accepted method uses dimensional analysis coupled with experimental data. By nondimensionalizing the equation of motion for air and for aerosol particles and raindrops, Slinn (1983) found that E depends on five dimensionless parameters :

- Re is the raindrop Reynolds number:

  $$Re \;\; = \frac{D_d \, U_t(D_d) \, \rho_a}{2 \, \mu_a}$$

  where U_t is the terminal velocity of raindrop, ρ_a is the air density and μ_a is the air viscosity.

- Sc is the aerosol particle Schmidt number:

  $$Sc \;\; = \frac{\mu_a}{\rho_a \, \mathcal{D}}$$

  where $\mathcal{D}$ is the aerosol particle diffusivity.

- St is the aerosol particle Stokes number:

$$St = \frac{2\,U_t(D_d)\,\tau_a}{D_d}$$

  where τ_a is the characteristic relaxation time of the collected aerosol particle.

- ϕ is the ratio of diameter:

$$\phi = \frac{d_p}{D_d}$$

- ω is the viscosity ratio:

$$\omega = \frac{\mu_w}{\mu_a}$$

  where μ_w is the viscosity of water.

The terminal velocity of raindrop with a diameter D_d is given by:

$$U_t(D_d) = A\,D_d^b$$

where A and b are equal to 842 and 0.8, respectively, in the MesoNH microphysical schemes but 130 and 0.5, respectively, in Andronache (2003).

The particle diffusivity $\mathcal{D}$ is defined by:

$$\mathcal{D} = \frac{k\,T\,C_c}{3\,\pi\,\mu_a\,d_p}$$

where k is the Boltzmann constant, T is the temperature, and C_c is the Cunningham slip correction factor, which depends on the aerosol particle diameter and on the mean free path of air (See Seinfeld and Pandis, 1998).

Then, Slinn (1983) propose the following analytical expression for the collision efficiency E based on correlation with experimental data:

$$\begin{aligned} E(D_d, d_p) = & \\ \frac{4}{Re\,Sc}\Big[1 + 0.4Re^{1/2}Sc^{1/3} + 0.16Re^{1/2}Sc^{1/2}\Big] & \\ +4\phi[\omega^{-1} + (1 + 2Re^{1/2})\phi] & \\ +\Big[\frac{St - St^*}{St - St^* + 0.667}\Big]^{3/2}\Big(\frac{\rho_p}{\rho_w}\Big)^{1/2} & \end{aligned} \quad (1)$$

where St^* is the critical Stokes number expressed as:

$$St^* = \frac{1.2 + (1/12ln(1 + Re))}{1 + ln(1 + Re)}$$

In our calculations, we assume that the aerosol has density ρ_p equal to 1 gcm^{-3}.

The analytical expression of the collision efficiency E has three terms with distinct physical contributions according to the aerosol particle diameter d_p:

1. The first term in Eq.(1) illustrates the Brownian diffusion that dominates for aerosol particles with $d_p < 0.01\mu m$.
2. the second term is related to collection by interception process and concerns aerosol particles with diameter between 0.01 and $1\mu m$. In this range, E has a minimum often referred to as the "Greenfield gap" (Seinfeld and Pandis, 1998).
3. The third term is due to the inertial impaction. It is efficient for large particles ($d_p > 2\mu m$). This term is included only when $St > St^*$.

Wet deposition is a 1^{st} order decay process,

$$\frac{\partial\psi(d_p, t)}{\partial t} = -\gamma(d_p)\psi(d_p, t) \quad (2)$$

where $\psi(d_p, t) = n_p(d_p, t)$ if considering the conservation of aerosol particles number distribution $[particles\mu m^{-1}m^{-3}]$ or $\psi(d_p, t) = g(d_p, t)$ if considering the conservation of aerosol particles mass distribution $[\mu gm^{-1}m^{-3}]$, and $\gamma(d_p)$ is the BCS coefficient of particles of diameter d_p already mentionned.

To compute the BCS coefficient $\gamma(d_p)$, the collision efficiency E is integrated over all raindrop diameters D_d:

$$\gamma(d_p) = \int_0^\infty \frac{\pi}{4} D_d^2\,U_t(D_d)E(D_d, d_p)n_D(D_d)dD_d \quad (3)$$

To solve the integral of Eq.(3), a Gauss quadrature method is employed (Press et al., 1992) after a change of variable. Quadrature method consists in a discretization of the integral over a number n of optimized abscissas with an assigned weight (the sum of the weights is 1). A Gauss-Laguerre variant is used to integrate over the raindrop size distribution:

$$\int_0^\infty x^\beta\,exp(-x)\,f(x)\,dx \simeq \sum_{i=1}^{n} \omega_i\,f(x_i)$$

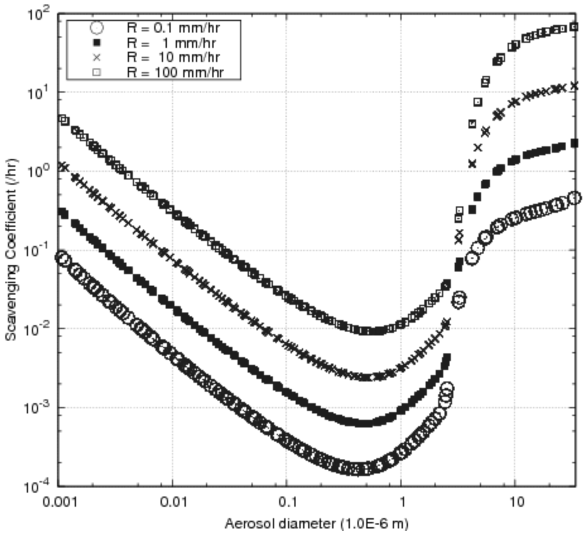

Figure 1: Scavenging coefficient as a function of particle size and rain rate (calculated with Eq.(3))

where $x = \lambda_R D_d$ and x_i is the discreted abscissa.

Finally, the BCS coefficient is integrated over all aerosol particle diameters d_p to obtain the total size number BCS rate $\frac{\partial N}{\partial t}$:

$$\begin{aligned} \frac{\partial N}{\partial t} &= \frac{\partial}{\partial t}\int_0^\infty n_p(d_p)\,dd_p \\ &= \int_0^\infty \frac{\partial n_p(d_p)}{\partial t} dd_p \\ &= -\int_0^\infty \gamma(d_p)\,n_p(d_p)\,dd_p \end{aligned} \tag{4}$$

For the integration over the aerosol particles diameters d_p, a Gauss-Hermite quadrature formula is used:

$$\int_0^\infty exp(-x^2)\,f(x)\,dx \simeq \sum_{i=1}^{n} \omega_i\,f(x_i)$$

where $x = \frac{log(d_p/\bar{d_p})}{\sqrt{2}log\sigma}$ and x_i, the abscissas. After several tests we choose to compute the sums with $n = 20$.

The BCS coefficients calculated with this method are consistent with those of Andronache (2003), Slinn (1983) and Feng (2007). Figure 1 shows that BCS coefficient $\gamma(d_p)$ varies significantly with the rain rate and the aerosol particle size. This figure illustrates the three distinct regimes of BCS corresponding to the three different physical processes involved in the collision efficiency E already described. So, coarse aerosol particles are the most efficiently scavenged, Aitken mode is moderatly scavenged and for the accumulation mode, the scavenging is low.

The Figure 1 also demonstrates that, when the rain rate increases, the corresponding BCS coefficient increases. These results are in agreement with those of the previous studies (Andronache, 2003; Loosmore et al.,2004; Tost et al., 2006; Feng, 2006).

3. 0D APPLICATION ON COPS EXPERIMENT

COPS (Convective and Orographically-induced Precipitation Study) was a 3 month international field campaign with part of a program aiming to improve precipitation forecasts and headed by the German Research Foundation. COPS took place in Summer 2007 in south-western Germany and north-eastern France. One of the goals of COPS was to collect time series of high, spatial and temporal, resolution surface flux including as many aerosol, cloud, and precipitation variables as possible, to be used as lower boundary conditions for mesoscale models.

Looking at the BCS process, we are interested by two types of COPS data that are both in situ measurements at 3 m above ground level :

- Mean rainfall rate $[mm/hr]$ calculated each 10 min from precipitation measurements with an Optical Rain Gauge (ORG)
- Time evolution of aerosol particle concentrations sampled by a Grimm optical particles counter with a time step of 1 min. The aerosol concentrations are provided for 15 classes of particles: size cut radius (μm) are $[0.15; 0.2; 0.25; 0.325; 0.4; 0.5; 0.8; 1; 1.5; 2; 2.5; 3.75; 5; 7.5; 10; 20]$

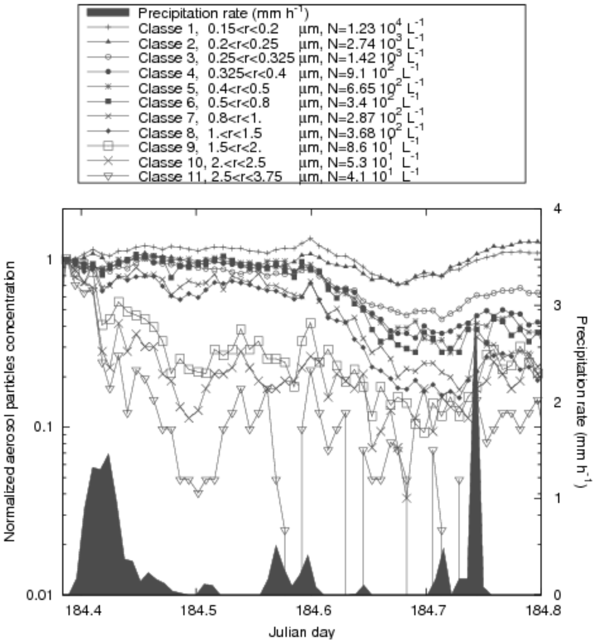

Figure 2: A short sequence of aerosol data and rainfall rate observed during COPS experiment

After comparing the two types of COPS data (precipitation intensity and aerosol particle concentrations), some sequences have been selected for which the aerosol depletion could be attributed to the wet removal by precipitation. The sequences have duration no longer than one day, and each of them contains several rainfall events. Figure 2 shows the COPS aerosol concentration data for Julian day 184.38 to 184.8 as well as the precipitation rate. This figure 2 attests the importance of scavenging on big aerosol particles.

For the moment, only the first precipitation event (between 184.38 and 184.5) is examined. During this rainfall event, aerosol concentrations of classes 1 to 8, are not perturbed. In contrast, aerosol concentrations of classes with larger diameters (classes 9 to 11) vary and are depleted in correlation with the rainfall event. This depletion seems to be partly explained by BCS process because, as shown on Fig. 1, the BCS rate is highest for large diameter and the first classes correspond to the ″Greenfield gap″. Thus, the data show the potential importance of the BCS process on the evolution of aerosol particles in the troposphere. Therefore, the implementation of this process in the aerosol continuity equation is necessary in the tridimensional model MesoNH. Looking at other rainfall event, the highest one for instance (beginning at 184.7), an increase of particle concentrations is observed for all the classes (even for the large ones) during the course of the event. Thus this event illustrates the complexity of the processes implied in the evolution of aerosol particle concentrations including dynamical transport, microphysical processes, sedimentation and scavenging.

In order to simulate the depletion of the aerosol particles by BCS using the COPS data of the first precipitation event, a mean particle diameter $\bar{d_m}$ has been defined for each class and the BCS coefficient $\gamma(\bar{d_m})$ is calculated for each $\bar{d_m}$. The method consists to initialize the concentrations at the first time step t_0, with the measured values. Then the data of mean rainfall intensity are incorporated in the BCS module for a selected rainy episode. The temporal evolution of the particle concentration of each class of size $N_i(x, y, z, t)$ is only driven by the calculated BCS rates.

For each class, the percentage of aerosol particles concentrations depleted during the rainfalll event is calculated by comparing aerosol particles concentrations at the beginning and at the end of the event. This is done for simulated and measured data. The resulting simulated percentage does not predict the entire depletion for each concentration class of COPS measurements, nevertheless, the influence of BCS is reproduced in function of diameter (as shown in Fig. 1). For instance, for the class number 3 and number 10 (defined in legend of Fig. 2), the simulated percentage of depletion is respectivly 0.1% and 87% whereas measured one is respectivly 10.8% and 54%. The discrepancy between the measured and simulated trends is attributed to other processes such as turbulent transport, microphysics, etc.

4. 2D SIMULATIONS WITH MesoNH

The numerical experiments are set to test and to evaluate the impact of the BCS on a multimodal population of particles. The particles are transported by a moist flow in which a warm or mixed-phase microphysical cycle produces rainfalls along the course of the simulation.

4.1 Warm shallow convection: the "HaRP" test case

The "HaRP" test case aims at simulating a precipitating cell forced by a time-varying non-divergent circulation during 50 min. The numerical experiments are performed with the MesoNH model using a standard Kessler scheme for the microphysics and a highly performant PPM scheme for the transport of the scalar fields (thanks to T. Maric, now at Univ. of Washington, Seattle, WA). Several simulations are run with multiple marine aerosol modes (fine, accumulation and coarse) which characteristics are given in Table 1 of Andronache (2003) and not recalled here. Each mode is advected in the 2D vertical plane and locally scavenged by rain according to the size distribution parameters of the raindrops and aerosol particles. The computational domain extends over 180×60 gridpoints with a spacing of 50 m in x and z directions. The time scale is 5 sec.

At the initial state, several mixtures of particle modes, leaving to the "Marine_A, _B, _C" cases, are filling the lowest 250 m of the atmosphere. Figure 3 illustrates the scavenging efficiency of the "Marine_B" case after 35 min of simulation. Figure 3a refers to the coarser mode ($d_{p1} = 12\mu$m) which is completely scavenged in the updraft, Fig. 3b shows that the intermediate mode, here still a coarse mode ($d_{p2} = 2\mu$mi, is partially scavenged. The finest mode, here with accumulation mode characteristics ($d_{p3} = 0.2\mu$m), remains nearly unaltered by the rainshaft (Fig. 3c). The concentrations of the particle modes (0.05, 3 and 70 cm^{-3}, respectively) are continuously resplenishing through the lateral boundaries of the lowest 250 m.

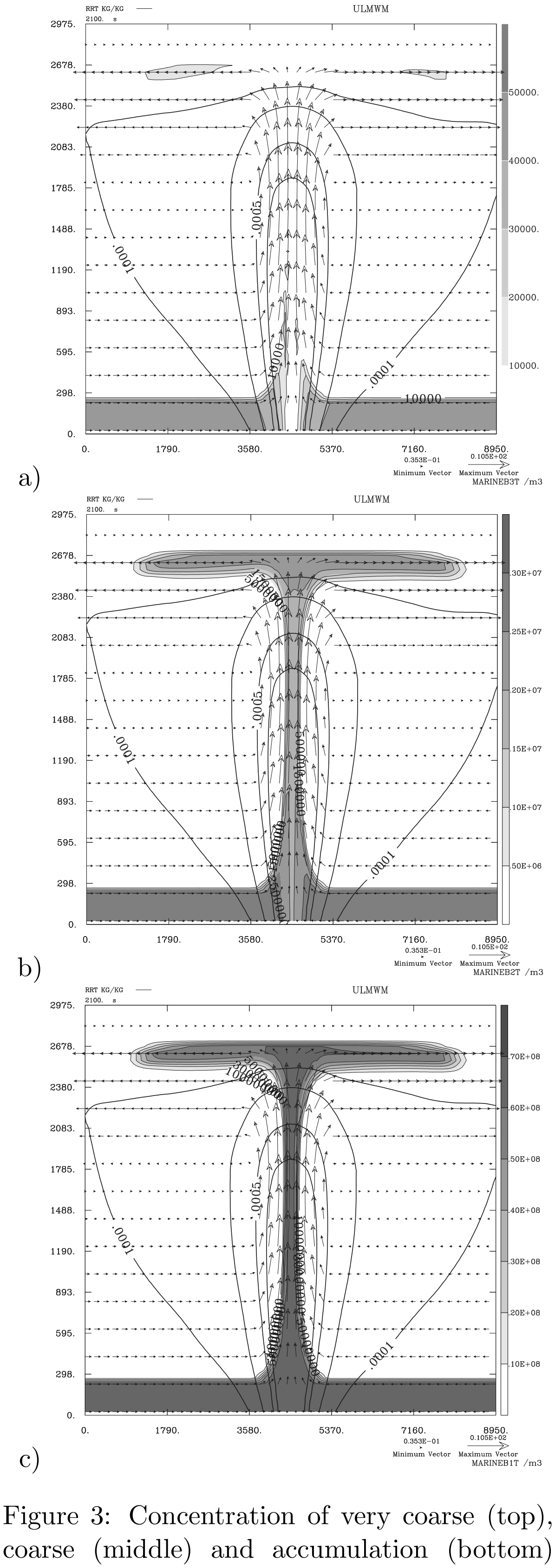

Figure 3: Concentration of very coarse (top), coarse (middle) and accumulation (bottom) particle modes after 35 min for the "HaRP" case. Rain mixing ratio contours (log scale) and flow structure (arrows) are superimposed.

The contrasted behaviour of the "Marine_A, _B, _C" cases shows up when considering the peak value of aerosol particle mass that is scavenged by the rain episode, after 50 min of simulation. For "Marine_A, _B, _C", we get an instantaneous value of 1g, 2.5g and 0.01 mg.m$^{-}-3$, respectively. The rainfall rate reaches 25 mm.h^{-1} at the same time. The very poor scavenging efficiency of the "Marine_C" case is explained by the low d_p (0.033, 0.110 and 0.540 μm) and the narrow character (σ=1.40, 1.41 and 2.02) of the size distributions.

4.2 Tropical squall line: the "COPT" test case

The "COPT" test case is typically a 12 hour simulation of a tropical squall line with a scale-resolved internal circulation, a 2D turbulence scheme and mixed-phase microphysics. The model is initialized with 3 successive layers of aerosol of 2 km depth starting from the ground level. For each layer, the same multimodal population of particles corresponding to the "Dust Layer" case of Table 1 of Andronache (2003) is used. The domain contains 320×44 gridpoints unevenly spaced in the vertical ($\Delta z = 70$ m at ground level and $\Delta z = 700$ m above 12 km). The horizontal resolution is 1.25 km. The model is integrated with a time step of 10 sec. A gravity wave damping layer is inserted between 17 km and the model top at 22.5 km. A constant speed transformation is used to compensate for the motion of the squall line. No fluxes are considered in the surface layer. Convection is initiated by forming a -0.0.1 K.s^{-1} artificial cold pool in the low levels of a small domain during 10 min.

A series of two simulations, without (SCAV$_0$) and with (SCAV$_1$) scavenging process applied to the particles, are performed. Figures 4a-c show the differences (SCAV$_0$-SCAV$_1$) relative to the coarse mode concentrations of each dust layer after 9 hours of simulation. The figures, ordered for the top, middle and bottom layers respectively, are showing the relative scavenging intensity of each layer, but plotted at

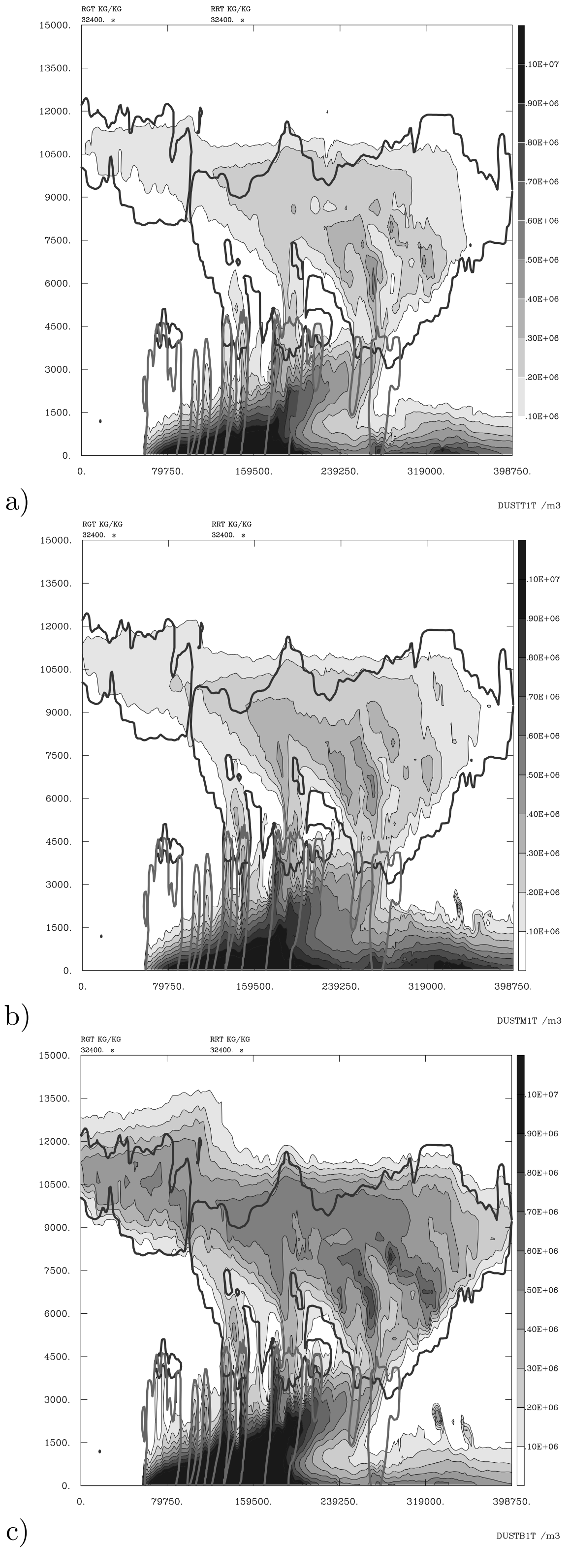

Figure 4: Concentration of scavenged coarse mode particles deduced from "COPT" simulations SCAV$_0$ and SCAV$_1$ and for 3 initial dust layers: [6,4] km (top), [4,2] km (middle) and [2, 0] km (bottom). The glaciated part of the squall line is depicted by a black solid line, the grey line shows the rainshaft contours.

the same scale. The initial concentration of the coarse mode ($d_{p1} = 0.55\mu$m) is 20 cm^{-3}. The results of Figs 4a-c indicate that all the dust layers are affected by the scavenging process which is efficient enough to eliminate much more than 1 cm^{-3} of coarse mode (here submicron) particles in the heavy precipitating convective region of the squall line. In other words, the peak value of the scavenged particle mass, obtained by summing the particle mass of the 3 modes and keeping $\rho_p = 1$g cm^{-3}, is as high as 5 mg per m^{-3} of air.

Another interesting feature displayed in Figs 4a-c is the fate of the scavenged particles in the upper glaciated region of the squall line, that is, well above 4 km high. As expected the bottom dust layer is the most affected by the scavenging removal but the 4-6 km layer is also affected because raindrops originate from altitude up to 4.5 km that corresponds to the ice melting layer.

The COPT case needs much investigation to analyse all the aspects of particle scavenging by rain in such an organized convective system. Next step will concentrate on the budget of the particle concentrations per mode and on the budget of the total mass of the particles which includes transport, scavenging and sedimentation.

5. CONCLUSIONS

A BCS module has been studied for implementation in the mesoscale/cloud resolving model MesoNH. The module is based on the collection efficiencies of Slinn (1983) and contains explicit numerical integrations over the raindrop and particle size distributions. The first numerical experiments performed with the module show that the coarse mode ($d_{p1} > 1\mu$m, approximately) of a particle population can be drastically scavenged according to the rainfall intensity and to the particle distribution modal diameters. This effect is expected to remove giant condensation nuclei and ice forming nuclei by precipitation with possible consequences on the nucleating properties of drizzling marine stratus and convective clouds with an ice phase. However more tests are needed as for instance, to examine the sensitivity to the width of the particle size distributions and the initial vertical profile of the particles with respect to the condensation and to the freezing level.

6. REFERENCES

Andronache, C., 2003: Estimated variability of below-cloud aerosol removal by rainfall for observed aerosol size distributions. *J. Atmos. Chem. Phys.,* **3**, 131-143.

Cohard, J.-M. and J.-P. Pinty, 2000: A comprehensive two-moment warm microphysical bulk scheme. II: 2D experiments with a non-hydrostatic model. *Quart. J. Roy. Meteor. Soc.,* **126**, 1843-1859.

Feng, J., 2007: A 3-mode parametrization of below-cloud scavenging of aerosols for use in atmospheric dispersion models. *J. Atmos. Env.,* **41**, 6808-6822.

Henzing, J. S., D. J. L. Olivi, and P. F. J. van Velthoven, 2006: A parametrization of size resolved below cloud scavenging of aerosols by rain. *J. Atmos. Chem. Phys.,* **6**, 3363-3375.

Jung, C. H., and Y. P. Kim, K. W. Lee, 2003: A moment model for simulating raindrop scavenging of aerosols. *J. Aeros. Sci.,* **34**, 1217-1233.

Lafore J.Ph. and coauthors, 1998: The Meso-NH atmospheric simulation system. Part I: adiabatic formulation and control simulations. *J. Ann. Geophysicae.,* **16**, 90-109.

Lafore, J.-Ph., and M.W. Moncrieff, 1989: A numerical investigation of the organization and interaction of the convective and stratiform regions of tropical squall lines. *J. Atmos. Sci.,* **46**, 531-544.

Loosmore, G. A., and R. T. Cederwall, 2004 : Precipitation scavenging of atmospheric aerosols for emergency response applications: testing an updated model with new real-time data. *J. Atmos. Env.,* **38**, 993-1003.

Press, W. H., S. A. Teukolsky, W. T. Vetterling, and B. P. Flannery, 1992: Numerical Recipes in FORTRAN: The Art of Scientific Computing, Cambridge University Press, 963 pp.

Pruppacher, H.R. and J.D. Klett, 1997: Microphysics of Clouds and Precipitation, Reidel, Dordrecht, pp. 954.

Seinfeld, J. H., and Pandis, S. N., 1998: Atmospheric Chemistry and Physics, Wiley, New York, pp. 1326

Slinn, W.G.N., 1983: Precipitation scavenging, in Atmospheric Sciences and Power Production 1979, Chap. 11. Division of Biomedical Environment Research, U.S. Department of Energy, Washington, D.C.

Tost, H., P. Jckel, A. Kerkweg, R. Sander, and J. Lelieveld, 2006: Technical note: A new comprehensive SCAVenging submodel for global atmospheric chemistry modelling. *J. Atmos. Chem. Phys.,* **6**, 565-574.

RETENTION OF TRACE GASES DURING RIMING OF ICE PARTICLES

Nadine von Blohn[1], Karoline Diehl[1], Subir K. Mitra[1] and Stephan Borrmann[1,2]
[1]Institute for Atmospheric Physics, Johannes Gutenberg University, Mainz, Germany
[2]Institute of Particle Chemistry, Max-Planck Institute for Chemistry, Mainz, Germany

1. INTRODUCTION

When ice particles and supercooled liquid droplets are present simultaneously, as in tropospheric mixed phase clouds, precipitation is mainly initiated via the ice phase. This means ice particles grow to precipitation sizes amongst others by the so called riming process. Liquid cloud droplets deposit on larger ice particles (Pruppacher and Klett, 1997) which leads to the formation of graupel or hailstones. Riming plays an important role for precipitation chemistry in mixed phase clouds because of the retention of trace gases during this process. A fraction of the trace gas is transferred to the ice phase while the rest is released back into the gas phase. Thus, the retention of trace gases is affecting their pathway into the atmosphere. In field measurements, higher amounts of trace elements were found in rimed snow samples than in unrimed samples (e.g., Collett et al., 1991; Harimaya and Nakai, 1999). Laboratory studies support this conclusion: Trace gases such as SO_2, HNO_3, and HCl are taken up directly by ice crystals in significantly lower amounts than by water drops (Mitra et al., 1990; Diehl et al., 1995; 1998; Hoog et al., 2007). Thus, riming can be considered as the major process by which these trace elements get incorporated into the ice phase.

Retention is affected by the solubility of the trace gas and by the ambient conditions during the riming process such as temperature and liquid water content. Earlier laboratory experimental studies led to controversial results (see Table 1) which were probably affected by experimental conditions. Iribarne et al. (1983) found for SO_2 a retention of 25%, Lamb and Blumenstein (1987) measured values between 1 und 12%, and Iribarne et al. (1990) obtained a value of 60% for the same gas. For H_2O_2, Iribarne and Physnov (1990) measured a retention factor around 100%, Snider et al. (1992) found it to be 24%, and later Snider and Huang (1998) found only 5%. Thus, the goal of this study was to simulate the riming process possibly in the same way as it proceeds in the real atmosphere, i.e. with ice particles and snowflakes freely falling at their terminal velocities and colliding with supercooled droplets.

2. EXPERIMENTAL METHODS

The experiments were performed in the vertical wind tunnel at the University of Mainz (Pruppacher, 1988) within a temperature range between -5 and -15°C where riming proceeds most efficiently in mixed phase clouds (Pruppacher and Klett, 1997). The air stream in the wind tunnel is laminar with a rest turbulence level of 0.5%. In the experimental section of the wind tunnel facility drops and ice particles as well as snow flakes can be freely floated in the air stream at their terminal velocities by manual control of the wind speed. Upstream of the experimental section a cloud of supercooled liquid droplets was generated by a number of sprayers. These cloud droplets caused riming on the floated ice particle when they passed by. The liquid water content was between 1 and 2 g/m^3, which are typical values for mixed phase clouds (Pruppacher und Klett, 1997).

To investigate the retention coefficients of trace gases during riming the supercooled droplets contained dissolved trace gases. The concentrations of these trace gases in the droplets were selected depending on the typically observed levels in clouds. Besides that the droplets contained Na_2SO_4 salt as a non-volatile tracer that remained entirely within the droplets during freezing so that the amount of liquid water deposited on the ice particles could be determined afterwards (Iribarne and

Physnov, 1990). After riming the ice particles were extracted from the wind tunnel and their melt water was analyzed by ion chromatography. The H_2O_2 content was measured by HPLC (high performance liquid chromatography) equipped with a fluorescence detector.

Although the final goal of the present study was to investigate riming with freely floating ice particles and snowflakes, several experimental techniques were used. In a first step the experiments were performed with captive floating ice particles of about 2 mm in diameter which were hung up using a very thin nylon fiber. The tunnel air speed was adjusted to get the ice particle floating while the thin fiber attachment prevented the particle from hitting the walls of the tunnel and also facilitated its removal from the tunnel. In the next step dendritic snow flakes were used instead of ice particles. In a special wind tunnel section these could be floated much easier than the ice particles during riming. Furthermore, the dendritic snow flakes sampled a high amount of supercooled droplets even in short time periods because of their large surface area. In the final step ice particles of 700 µm diameter were freely floated. Because completely freely floating ice particles could only be suspended for rather short time periods of 90 s, only a small amount of the trace elements were incorporated into the ice particles. Thus, in order to get enough material that allows a reasonable level of accuracy in the analyses, one needed to sample several ice particles for one analysis. Therefore, the disadvantages of the third most realistic method were the higher inaccuracies of the results.

The retention coefficients were determined from the amount of trace elements in the melt water of the ice particles and the amount of trace elements in the supercooled liquid droplets. The experimental studies started with HNO_3 and HCl which are highly soluble. Afterwards they were continued with the somewhat less soluble H_2O_2.

3. RESULTS, CONCLUSIONS, AND COMPARISONS WITH EARLIER STUDIES

All experimental techniques came to the same results. Table 1 shows the measured retention coefficients from the present studies in comparison with literature values. Investigations to determine the retention of NH_3 and SO_2 during riming are under way and will also be reported at the conference.

trace gas	literature values	measured values from wind tunnel
HNO_3	95% (1)	98 ± 2 %
HCl	100% (1)	99 ± 1 %
H_2O_2	5% (2) 24% (3) 100% (1)	58 ± 11 %
NH_3	100% (1)	under way
SO_2	1 – 12% (4) 25% (5) 60% (6)	under way

Table 1: Retention coefficients of various trace gases from the present wind tunnel studies in comparison to literature values. (1) Iribarne and Physnov (1990), (2) Snider and Huang (1998), (3) Snider et al. (1992), (4) Lamb and Blumenstein (1987), (5) Iribarne et al. (1983), (6) Iribarne et al. (1990)

Varying the temperature did not lead to different retention coefficients. Surface temperature measurements with an infrared thermograph indicated that in the investigated temperature and liquid water content range the growth proceeded in the dry growth regime. That means the amount of latent heat released during riming was insufficient to produce a significant surface temperature enhancement. Thus, the droplets froze immediately after collision with the ice particle during all experiments leading to the same retention coefficients.

For HNO_3 a retention of 98 ± 2% was measured and 99 ± 1% for HCl. These values are in good agreement with the studies of Iribarne and Physnov (1990) who found a retention of 95% for HNO_3 and 100% for HCl. Because of the high solubility of HNO_3 and

HCl, values near 100% are expected. These trace gases are strongly dissociated in water so that their release during freezing is hardly possible. Thus, independently on the experimental techniques in earlier investigations and in the present studies the results are very similar.

Earlier measurements with H_2O_2 resulted in strongly differing retention coefficients. As H_2O_2 is less soluble in water its desorption during freezing proceeds easier and is strongly affected by the experimental techniques which in some earlier studies were rather far from reality regarding the simulation of the atmospheric process. Therefore, during the present wind tunnel measurements where the riming process was simulated as it proceeds in the real atmosphere the variation of the retention was limited to values between 47 and 69%. However, the still rather wide scatter of the experimental results is caused probably by desorption of H_2O_2 from the liquid phase on the way from the sprayers to the ice particle. Experiments are under way to quantitatively determine this desorption to improve the scatter of the data.

4. ACKNOWLEDGEMENTS

The present studies are supported by the SFB 641 “The tropospheric ice phase”.

5. REFERENCES

Collett, J.L., A.S.H. Prévôt, J. Staehlin, and A. Waldvogel, 1991: Physical factors influencing winter precipitation chemistry. *Environ. Sci. Techn.*, **25**, 782-788.

Harimaya, T., and Y. Nakai, 1999: Riming growth process contributing to the formation of snowfall in orographic areas of Japan facing the Japan Sea. *J. Met. Soc. Japan*, **77**, 101-115.

Mitra, S.K., S. Barth, and H.R. Pruppacher, 1990: A laboratory study on the scavenging of SO_2 by snow crystals. *Atmos. Environ.*, **24A**, No.9, 2307-2312.

Diehl, K., S.K. Mitra, and H.R. Pruppacher, 1995: A laboratory study of the uptake of HNO_3 and HCl vapour by snow crystals and ice spheres at temperatures between 0 and -40° C. *Atmos. Environ.*, **29**, 975-981.

Diehl, K., S.K. Mitra, and H.R. Pruppacher, 1998: A laboratory study on the uptake of HCl, HNO_3, and SO_2 gas by ice crystals and the effect of these gases on the evaporation rate of the crystals. *Atmos. Res.*, **47/48**, 235-244.

Hoog, I., S. K. Mitra, K. Diehl, and S. Borrmann, 2007: Laboratory studies about the interaction of ammonia with ice crystals at temperatures between 0 and -20°C. *J. Atm. Chem.*, **57,** 73-84.

Iribarne, J.V., and T. Pyshnov, 1990: The effect of freezing on the composition of supercooled droplets. - I. Retention of HCl, HNO_3, NH_3, and H_2O_2. *Atmos. Environ.*, **24A**, 383-387.

Iribarne, J.V., L.A. Barrie, and A. Iribarne, 1983: Effect of freezing on sulphur dioxide dissolved in supercooled droplets. *Atmos. Environ.*, **17**, 1047-1050.

Iribarne, J.V., T. Pyshnov, and B. Naik, 1990: The effect of freezing on the composition of supercooled droplets. - II. Retention of S(IV). *Atmos. Environ.*, **24A**, 389-398.

Lamb, D., and R. Blumenstein, 1987: Measurement of the entrapment of sulfur dioxide by rime ice. *Atmos. Environ.*, **21**, 1765-1772.

Snider, J.R., D.C. Montague, and G. Vali, 1992: Hydrogen peroxide retention in rime ice. *J. Geophys. Res.*, **97**, 7569-7578.

Snider, J. R., and J. Huang, 1998: Factors influencing the retention of hydrogen peroxide and molecular oxygen in rime ice. *J. Geophys. Res.,* **103,** 1405-1415.

Pruppacher, H.R., 1988: Auswaschen von atmosphärischen Spurenstoffen durch Wolken und Niederschlag mittels eines vertikalen Windkanals. BMFT-Bericht 9/88, GSF München.

Pruppacher, H.R., J.D. Klett, 1997: *Microphysics of Clouds and Precipitation*, 2^{nd} rev. ed., Kluwer Academic Publishers, Dordrecht.

EXPERIMENTAL MEASUREMENTS AND NUMERICAL MODELING OF INERTIAL PARTICLES IN HIGH-REYNOLDS-NUMBER TURBULENCE

L. R. Collins[1], S. Ayyalasomayajula[1], S. Gerashchenko[1], K. Lehmann[2,3], R. A. Shaw[2,4],
H. Siebert[2], and Z. Warhaft[1]

[1] Sibley School of Mechanical and Aerospace Engineering, Cornell University, Ithaca, NY, USA
[2] Institute for Tropospheric Research, Leipzig, Germany
[3] Scripps Institution of Oceanography, University of San Diego, La Jolla, CA, USA
[4] Department of Physics, Michigan Technological University, Houghton, MI, USA

1. INTRODUCTION

The role of turbulence in the development of warm cumulus clouds remains controversial. While some have argued that turbulence can lead to droplet clustering, vapor supersaturation fluctuations and enhanced coalescence (e.g., Shaw 2003), others find little evidence of these effects in actual clouds (e.g., Brenguier and Chaumat 2001). Perhaps the most convincing argument *against* the role of turbulence is based on scaling arguments that suggest the mean levels of turbulence are simply insufficient to have much of an effect on the evolution of the cloud. These arguments implicitly assume that turbulence is a near Gaussian phenomenon that is well characterized by its mean and variance. However, turbulence is known to be highly intermittent, with statistics that deviate strongly from Gaussian statistics, and increasingly so with increasing Reynolds number. At the enormous Reynolds numbers found in the atmosphere, it is expected that there will be pockets of the cloud with conditions that are far more turbulent than the nominal levels would indicate. It is our conjecture that these highly turbulent pockets, in combination with the nature of droplet coalescence processes to exaggerate the role of the largest drops, play a disproportionate role in the evolution of the cloud to incipient rain.

In this study, we bring together field observations in clouds with laboratory experiments in a wind tunnel to estimate the distribution of droplet accelerations in the cloud. The field observations were made from a turbulence and cloud measurement system suspended from a helicopter. Cloud measurements of thermodynamic properties, including temperature and water vapor concentration, turbulent wind velocity in earth coordinates, and microphysical properties, including liquid water content and droplet size distribution, are made with high spatial resolution due to the low air speeds of the helicopter. The complementary data in the wind tunnel were obtained using particle tracking technology developed at Cornell University. Tracks of individual droplets, with time resolution of fractions of a Kolmogorov time scale, were taken and differentiated twice to obtain the droplet acceleration. By varying the size of the droplets and the turbulence conditions in the wind tunnel, it was possible to span one order of magnitude in the particle Stokes number and the Froude number. This range includes values that are relevant for the cloud. Rescaling of these data provides an estimate for the acceleration of droplets in the cloud.

We begin by presenting the cloud data, which in this paper serves to define the parameter space relevant to cloud processes. We then present laboratory measurements that lie within that parameter space, and end by presenting a model that illuminates the underlying mechanisms.

Corresponding author's address: Lance R. Collins, Sibley School of Mechanical and Aerospace Engineering, 105 Upson Hall, Cornell University, Ithaca, NY 14853, USA, email: lc246@cornell.edu

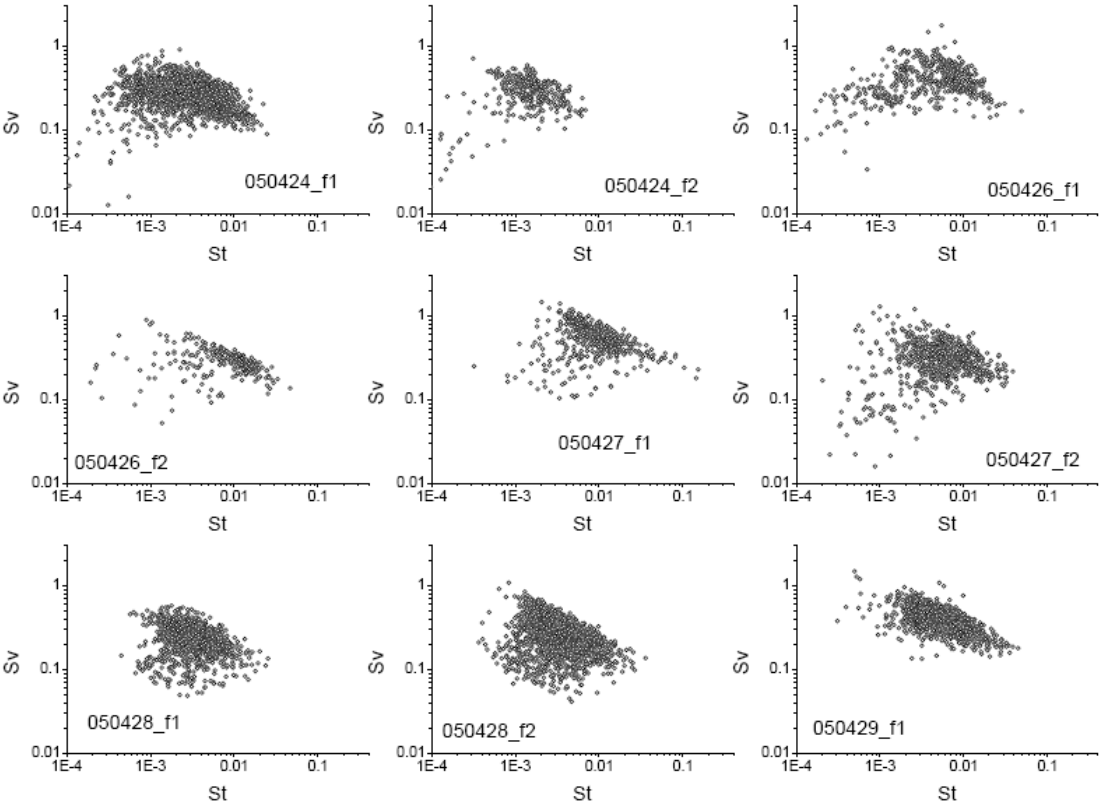

Figure 1. The distribution of cloud microphysical and turbulence properties in a dimensionless Stokes-Froude space (note that the Froude number is identical to the settling parameter, Sv, as defined by Vaillancourt and Yau (2000)). Each point represents data in a 1-second (approximately 15 meter) average.

2. CLOUD MEASUREMENTS

Cloud droplet motion can be described to reasonable approximation by the equation

$$v_i = u_i + \tau_d g_i - \tau_d \, du_i / dt ,$$

where v_i, u_i, and g_i are the i th components of the droplet velocity, the fluid velocity, and the gravitational acceleration vectors, respectively, and τ_d is the droplet inertial time scale (e.g., Shaw 2003). The derivative in the third term on the right side denotes the Lagrangian fluid acceleration. Qualitatively, the equation means that cloud droplets tend to move with the surrounding air, but with relative motion resulting from gravitational settling and from the sluggishness of droplets due to their finite inertia. Traditionally in cloud physics only the first two terms on the right side are considered: conceptually droplets are assumed to fall relative to air at a constant speed, and therefore droplets of different size approach each other solely as a result of differential gravitational settling. We know, however, that clouds are highly turbulent, so we immediately ask ourselves about the possible role of the Lagrangian acceleration term. Currently it is not possible to measure Lagrangian droplet accelerations in naturally occurring clouds due to experimental constraints, but methods for making such measurements in laboratory flows have been developed in recent years. Understanding the importance of Lagrangian droplet accelerations in real clouds through laboratory measurements is the subject of this work.

The relative roles of droplet inertia and gravitational settling can be described with two dimensionless parameters, the drop Stokes number St and the Froude number Fr (or Settling parameter):

$$St = \frac{\tau_d}{\tau_K}$$

and

$$Sv = \frac{v_T}{v_K},$$

where τ_K is the Kolmogorov time scale, v_T is the terminal velocity, and v_K is the Kolmogorov velocity (e.g., Vaillancourt and Yau 2000, Shaw 2003). We have analyzed data collected in cumulus and stratocumulus clouds to quantify the range of Stokes and Froude numbers that occur. The variability results primarily from differences in droplet diameter and the intermittent nature of the energy dissipation rate (see the accompanying conference abstract by Siebert and Shaw for further discussion of this intermittency).

The microphysical data were collected with two instruments: the Phase-Doppler Interferometer for Cloud Turbulence (PICT) and the Modified Fast Forward Scattering Spectrometer Probe (M-Fast-FSSP). The PICT instrument counts individual droplets that enter the overlapping region of two laser beams, such that the velocity component in the flight direction and the diameter are measured via frequency and phase estimated from the measured Doppler bursts (Chuang et al. 2008). The M-Fast-FSSP is a droplet counter that provides a measurement of droplet diameter based on the magnitude of light scattered to an annular detector (Schmidt et al. 2004). The turbulence data were obtained from the PICT instrument (through the droplet speed measurement) and from a sonic anemometer. All instruments were part of the Airborne Cloud-Turbulence Observation System (ACTOS), suspended from a helicopter, and moving at a flight speed sufficiently large to be safely outside the rotor downwash (Siebert et al. 2006).

Data presented here are from two field measurement campaigns: one focused on small cumulus clouds in western Germany (Winningen 2005) and one focused on weakly turbulent stratocumulus clouds over the Baltic Sea (Kiel 2007). Figure 1 shows the range of Froude and Stokes numbers that exist in small cumulus clouds sampled during all nine ACTOS flights during the first measurement campaign. The clouds were sampled in an area with high aerosol loading and therefore droplet number densities were large and droplet diameters small relative to maritime cumulus (e.g., relative to many of the clouds sampled during the SCMS or RICO experiments). It is immediately evident that clouds occupy a quite broad region of the parameter space due to variations in droplet diameter and energy dissipation rate, even though during individual flights clouds were observed to be quite homogenous from the point of view of thermodynamic, dynamic, and microphysical properties. Droplet Stokes numbers vary over approximately 2 orders of magnitude and Froude numbers vary by at least an order of magnitude.

The stratocumulus data are still being processed and therefore are not shown in the same detail as in Figure 1. Nevertheless, data from a representative flight through a shallow, weakly turbulent cloud yield Stokes numbers in the range 0.008-0.05 and Froude numbers in the range 0.2-1.4. These numbers account only for the droplet size variations, and not for the fluctuations in energy dissipation rate. The mean turbulent energy dissipation rate for the cloud was approximately a factor of 10 smaller than in the cumulus clouds previously discussed, but droplet diameters were larger due to relatively low aerosol loading. Note that the dimensionless numbers were calculated using the Stokes drag law, but in fact the Reynolds numbers for the larger drops (assuming terminal velocity) is sufficiently large that a modified drag law should be used. In that case we obtain Stokes numbers in the range 0.006-

0.04 and Froude numbers in the range 0.2-1.1. The stratocumulus values tend to have comparable Stokes numbers but larger Froude numbers because droplet sizes are larger and energy dissipation rates are lower: the two effects tend to offset each other in the Stokes number, but work in the same direction in the Froude number.

3. LABORATORY MEASUREMENTS

At Cornell we have been studying the acceleration statistics of inertial particles by injecting water droplets into a large (1 m x 0.9 m x 20 m) open circuit wind tunnel. Relatively high free-stream Reynolds numbers, up to an R_λ of 240, were attained by means of an active grid located at the tunnel inlet (Mydlarski and Warhaft 1996). The effects of Reynolds, Stokes and Froude number variations were studied in a turbulent boundary layer formed over a flat plate located 0.4 m above the tunnel floor (Geraschenko et al. 2008). Low particle Stokes numbers were achieved by feeding droplets into the boundary layer from an ultrasonic humidifier. High particle Stokes numbers were achieved by feeding the particles from sprays located downstream from the active grid. The particle mass loading was approximately 10^{-4} kg water/kg dry air. The acceleration statistics were determined by moving a high speed camera along the side of the wind tunnel at the flow speed (Ayyalasomayajula et al. 2006). A forward scatter technique, using a laser beam reflected from the far side of the tunnel back to the moving camera (from which the laser beam was introduced from a fiber optic cable) allowed us to track the droplets in a 3.3 cm x 3.3 cm sampling area. Using a single camera, 2-dimensional tracks of the particles were obtained and from these, the acceleration probability density function (pdf) was determined. Here we report the results near the top of the boundary layer where the Reynolds number is highest due to the free stream turbulence, and there are minimal shear effects.

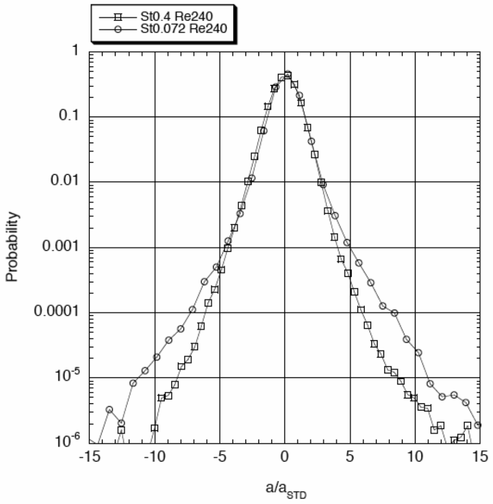

Figure 2. Probability density function of the Lagrangian acceleration of droplets in a turbulent wind-tunnel flow. The acceleration is normalized by the standard deviation and shows the stretched exponential tails characteristic of high Reynolds number flows. The two pdf's are for flows with the same Reynolds number, but droplets of different Stokes numbers.

Figure 2 shows the laboratory acceleration pdf's for the same Reynolds number but for two different Stokes numbers. At the higher Stokes number the tails of the pdf are narrower. In the atmosphere the tails will be significantly wider than for those found in Figure 2 because of the higher Reynolds number. Moreover the Stokes numbers are low, so there will be only small narrowing of the tails due to inertial effects.

It is instructive to scale the laboratory pdf's in a different way in order to elucidate the relative importance of fluid and gravitational accelerations in the atmosphere. Figure 3 shows the acceleration pdf for two different Reynolds numbers (R_λ = 100 and 240), but for the same Stokes number (0.08) and approximately the same Froude numbers (0.1 and 0.16 for the R_λ 240 and 100 cases respectively). The Reynolds numbers are an order of magnitude below those typically observed in the atmosphere, but the Froude and Stokes numbers are within atmospheric ranges. We have normalized the acceleration by the acceleration due to gravity, g, in order to compare the magnitudes of the accelerations that the particles are experiencing with that of gravity. In order to make an approximate comparison with expected atmospheric acceleration statistics we have scaled the pdf with the acceleration ratio (RMS_atmosphere)/(RMS_laboratory). The RMS acceleration measured in the laboratory is of the order 10 m s^{-2}. In the atmosphere it is of order 1 m s^{-2} in a typical cumulus cloud.

The data of Figure 3 suggest the extreme accelerations caused by the turbulent flow field may be having a significant effect on the nature of the inertial particle motion, and may compete with the gravitational acceleration. In particular, roughly one drop in 1000 has an acceleration that is equal to or greater than g, even at the modest Reynolds number of this experiment. Note that the higher R_λ case has slightly broader tails. For fluid particles ($St = 0$) the kurtosis (fourth moment) of the acceleration pdf increases with increasing Reynolds number (Voth et al. 2002) albeit slowly. This is due to the higher levels of intermittency experienced by the particles. Our data indicate a broadening of the tails for inertial particles too, but the data presented here do not allow us to determine a trend to atmospheric Reynolds numbers. The only other evidence we have for inertial particles is from the direct numerical simulations of Bec et al. (2006). But for that work the highest Reynolds number is 185, too low to determine a trend. Nevertheless, the measurements and DNS do show broadening of the tails as Reynolds number increases and it is not unreasonable to assume that this trend will hold to the high Reynolds numbers experienced in the atmosphere, significantly increasing the probability of accelerations that are large compared with those due to gravity.

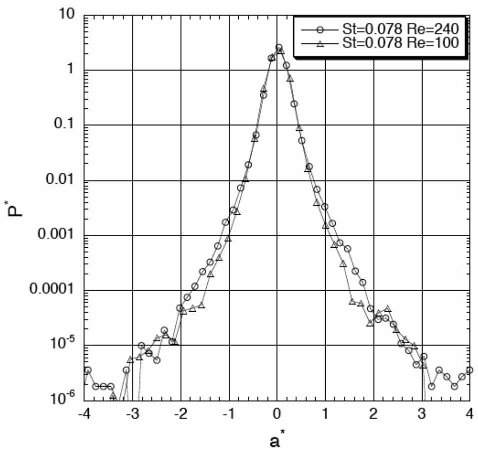

Figure 3. Probability density function of the Lagrangian acceleration of droplets in a turbulent wind-tunnel flow. The accelerations have been normalized by the gravitational acceleration and scaled to reflect atmospheric conditions (see text). Notice that the tails clearly show droplets undergoing accelerations greater than those due to gravity. The two pdf's are for flows with the same Stokes number and

Additionally, it is well established that inertial particles in a turbulent flow will be ejected by the centrifugal forces from regions of high vorticity to regions of high strain (Maxey and Riley 1983; Squires and Eaton 1991; Sundaram and Collins 1997; Shaw 2003) causing clustering of the particles. Recently there have been a number of laboratory experiments that have quantified the clustering (Wood et al. (2005), Salazar et al. (2008), Saw et al. (2008). The Saw et al. (2008) experiment was carried out in the Cornell wind tunnel described above. These experiments indicate that clustering is most dominant at the dissipation scales, but is also present in the inertial scales, particularly in the experiments of Saw et al. (2008) and Wood et al. (2005). We have observed that the tails of the acceleration pdf become narrower with increasing inertial effects, indicating that the high acceleration events are attenuated because the inertial particles selectively sample the flow.

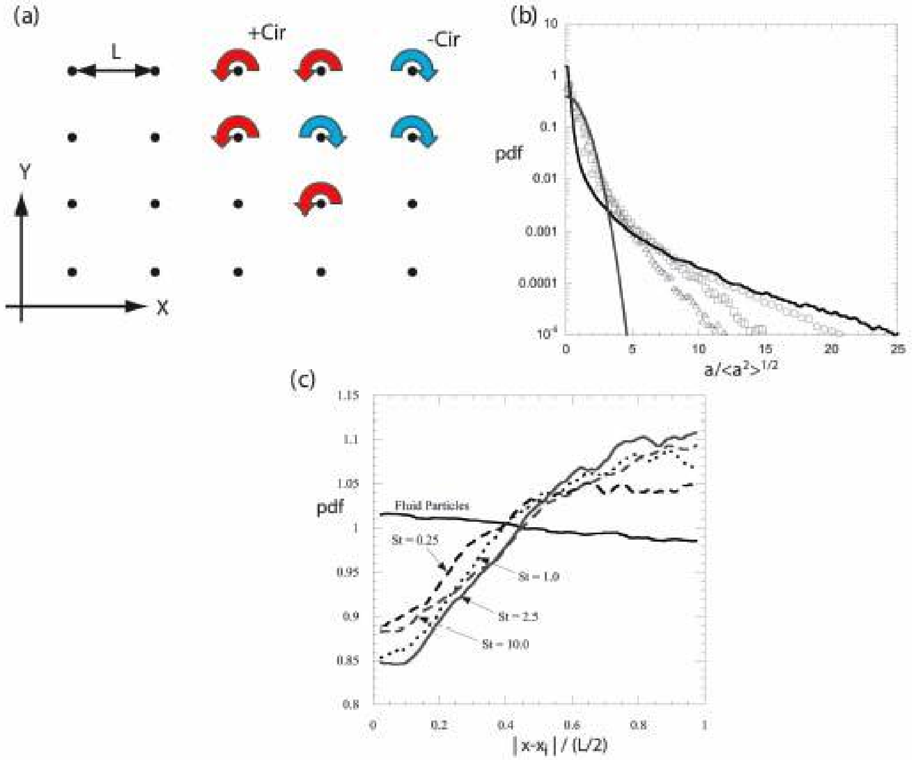

Figure 4. (a) A schematic diagram of the random vortex model. See text for details. (b) PDF's of Lagrangian particle acceleration from the random vortex model. (c). PDF's of particle separations from the random vortex model.

4. MODEL OF DROPLET ACCELERATIONS AND CLUSTERING

In order to elucidate the relationship between the acceleration pdf and the clustering, we developed a model that uses an array of potential vortices to simulate a two-dimensional flow in which fluid particles and inertial particles are tracked to obtain Lagrangian velocities and accelerations (Ayyalasomayajula et al. 2008). In contrast to earlier stochastic models (Sawford 1991; Reynolds 2003), this model allows the inertial particles to choose the fluid field it wishes to sample. An array of ten by ten vortices was used, separated by a distance L (Figure 4) which we call the integral scale. The flow field around a vortex was obtained using the two dimensional potential theory but to prevent infinite velocity near the center of each vortex, a viscous like core with radius s was added. Here, s acts like a small-scale turbulence length scale. The circulation of each of the vortices Γ_i was set using an independent Gaussian random variable whose mean is zero and standard deviation is σ_Γ. To mimic the persistence of large scale eddies as in the real turbulent flow, the circulation was randomly updated at a time-scale T. The time-scale T is associated with the slowest eddies of size L and the time-scale is constructed as L^2/σ_Γ. Similarly a small-scale time t_s is constructed as s^2/σ_Γ and it can be related to the most rapid changes in the flow which are occurring close to the core of the vortex where maximum induced velocity is expected. The inertial particle has one-way coupling to the flow through Stokes drag. The acceleration of the particle was obtained from the material derivative ($Dv(t)/Dt$) of the inertial particle velocity.

The Stokes number St for this model is defined as the ratio of particle response time, τ_d, and the flow time-scale, t_s.

The simple vortex model exhibits the stretched exponential tails for the acceleration pdf that is observed in the data (Fig. 4(b)). It also produces clustering away from the vortex centers (Fig. 4(c)) due to the selective sampling of the fluid by the inertial particles, and this is correlated with the narrowing of the shape of the pdf. Ayyalasomayajula et al. (2008) also computed the Lagrangian acceleration auto-correlation function, conditioned on the magnitude of the acceleration, for the fluid along an inertial particle trajectory, and showed that as the magnitude of the acceleration increases, the correlation time decreases. The result is that inertial particles with high acceleration are “filtered” because their response time to the turbulence is too short. This has the effect of excluding extreme acceleration events, thereby narrowing the inertial particle pdf tails Thus there is a clear link between the acceleration pdf and the clustering and filtering of the inertial particles. The pdf’s presented in Figure 3 suggest that similar mechanisms may be in play in clouds, and these may play as important a role as gravitational coalescence mechanisms.

Acknowledgements

This work has benefited greatly from our collaboration with E. Bodenschatz and other colleagues through the International Collaboration for Turbulence Research (ICTR). The work was supported by the National Science Foundation. RAS acknowledges support from the Alexander von Humboldt Society.

REFERENCES

Ayyalasomayajula, S., A. Gylfason, L. R. Collins, E. Bodenschatz, and Z. Warhaft, 2006: Lagrangian measurements of inertial particle accelerations in grid generated wind tunnel turbulence. *Phys. Rev. Lett.*, **97**, 144507.

Ayyalasomayajula, S., L. R. Collins, and Z. Warhaft, 2008: Modelling inertial particle Lagrangian acceleration statistics in turbulent flows. Submitted to *Phys. Fluids*.

Bec, J., L. Biferale, G. Boffetta, A. Celani, A. Cencini, A. Lanotte, S. Musacchio, and F. Toschi, 2006: Acceleration statistics of heavy particles in turbulence. *J. Fluid Mech.*, **550**, 349-358.

Brenguier, J.-L., and L. Chaumat, 2001: Droplet spectra broadening in cumulus clouds. Part I: Broadening in adiabatic cores. *J. Atmos. Sci.,* **58**, 628-641.

Chuang, P. Y., E. W. Saw, J. D. Small, R. A. Shaw, C. M. Sipperley, G. A. Payne, and W. D. Bachalo, 2008: Airborne phase Doppler interferometry for cloud microphysical measurements. *Aerosol Sci. Tech.*, in press.

Gerashchenko, S., N. Sharp, S. Neuscamman, and Z. Warhaft, 2008: Lagrangian measurements of inertial particle accelerations in a turbulent boundary layer. To be submitted to *J. Fluid Mech.*

Maxey, M. R., and J. J. Riley, 1983: Equation of motion for a small rigid sphere in a non-uniform flow. Phys. Fluids. 26, 883.

Mydlarski, L., and Z. Warhaft, 1996: On the onset of high-Reynolds-number grid-generated wind tunnel turbulence. *J. Fluid Mech.*, **320**, 331-368.

Salazar, J. P. L. C., de Jong, J., Cao, L., Woodward, S., Meng, H., and L. R. Collins, 2008: Experimental and numerical investigation of inertial particle clustering in isotropic turbulence. *J. Fluid Mech*., **600**, 245-256.

Saw, E. W., R. A. Shaw, S. Ayyalasomayjula, P. K. Chuang, and A.

Gylfason, 2008: Inertial clustering of particles in high Reynolds-number turbulence. *Phys. Rev. Lett.,* in press.

Schmidt, S., K. Lehmann, and M. Wendisch, 2004: Minimizing instrumental braodening of the drop size distribution with the M-Fast-FSSP. *J. Atmos. Ocean. Tech.*, **21**, 1855-1867.

Shaw, R. A., 2003: Particle-turbulence interactions in atmospheric clouds. *Ann. Rev. Fluid Mech.,* **35**, 183-227.

Siebert, H., H. Franke, K. Lehmann, R. Maser, E. W. Saw, R. A. Shaw, D. Schell, and M. Wendisch, 2006: Probing finescale dynamics and microphysics of clouds with helicopter-borne measurements. *Bull. Amer. Meteor. Soc.*, **87**, 1727-1738.

Squires, K. D., and J. K. Eaton, 1991: Preferential concentration of particles by turbulence. *Phys. Fluids A*, **3**, 1169-1178.

Sundaram, S., and L. R. Collins, 1997. Collision statistics in an isotropic particle-laden turbulent suspension. Part 1. Direct numerical simulations. *J. Fluid Mech.*, **335**, 75-109.

Voth, G.A., A. La Porta, A. M. Crawford, J. Alexander, and E. Bodenschatz, 2002: Measurement of particle accelerations in fully developed turbulence. *J. Fluid Mech*., **469**, 121-160.

Wood, A. M., W. Hwang, and J. K. Eaton, 2005: Preferential concentration of particles in homogeneous and isotropic turbulence. *Int. J. Multiphase Flow*, **31**, 1220–1230.

Vaillancourt, P., and M. K. Yau, 2000: Review of particle-turbulence interactions and consequences for cloud physics. *Bull. Amer. Meteor. Soc.* **81**, 285-298.

THE ROLE OF TRUNCATED SPECTRUM IN ACCREATIAN RATE CALCULATIONS

M. Ćurić, D. Janc, V. Vučković

Institute of Meteorology,University of Belgrade, 11000 Belgrade,Serbia

1. INTRODUCTION

Cloud-resolving mesoscale models and operational numerical models use bulk microphysical schemes instead of explicit approach due to computational expense. Improvement of such schemes is therefore always necessary. Many of microphysical processes depend on the rate at which two different classes of hydrometeors both collide and interact. These interactions are numerically presented by the integrand form of stochastic collection growth equation. It may be solved exactly, but the form involves general hypergeometric functions (Verlinde et al.,1990; Ćurić and Janc, 1997), which have not been used in praxis due to large computer requirements. Many numerical models therefore make different simplifications of collection equation in order to solve it in easier way (Mizuno,1990; Murakami, 1990).

Recently, Gaudet and Schmidt (2005) proposed another form of exact solution of collection growth equation for idealized spectra in which the hydrometeor diameters are between zero and infinity. It consists of two terms involving gamma functions and power series. For most variety of interactions between hydrometeors such solutions are far cheaper way to find out the exact solution with high precision. The shortcomings of this method was that it should lead to unrealistic values of collection rates for some interactions or it can not be applied due to divergent power series. To circumvent this problem the alternate approach is to use the truncated spectra of hydrometeors within observed boundaries instead of idealized spectra. In the text the new approach would be denoted by real spectra. To verify this statement, we tested various approximate and exact solutions of collection growth equation for both real and idealized spectra.

2. COLLECTION EQUATION

The rate of collection of hydrometeors X by hydrometeors Y is given in generalized form as

$$\frac{dQ_Y}{dt} = \frac{1}{\rho}\int_{D_1}^{D_2}\int_{D_3}^{D_4} E_{XY}\frac{\pi\left(D_X + D_Y\right)^2}{4}\left|U_X(D_X) - U_Y(D_Y)\right| m_X(D_X)N_X(D_X)N_Y(D_Y)dD_X dD_Y, \qquad (1)$$

where are dQ_Y/dt the mixing ratio $\left(Q_Y\right)$ change per unit time for species Y**;** ρ the cloud air density; E_{XY} the collection efficiency taken to be 1 for each interaction; D the equivalent particle diameter; $U(D)$ its terminal velocity; $m_X(D_X)$ the mass of collected particle; $N(D)dD$ the average number concentration of particles in diameter interval between D and D+dD; D_1, D_3, D_2, D_4 are lower and upper boundaries for spectra of X and Y particles. In numerical experiments two cases are considered: idealized spectra of particles X and Y ($D_1 = 0;\ D_3 = 0;\ D_2 = 0;\ D_4 = +\infty$) and real spectra of particles X and Y with lower and upper boundaries presented in Table 1.

Table1. Minimum and maximum diameters of hydrometeors.

	rain	snow	graupel	hail
$D_1(D_3)$	100 μm	0 cm	0 cm	0.5 cm
$D_2(D_4)$	0.5 cm	3 cm	0.5 cm	10 cm

We proposed that raindrops are distributed according to the gamma size-distribution in the form given by

$$N(D) = 0.25AD^2 \exp(-0.5BD) \qquad (2)$$

where are

$$A = 1.452 \frac{\rho Q_r}{\rho_w R_M^6} \left(1 - \frac{\Gamma(6, BD_0/2)}{\Gamma(6)}\right)^{-1}, B = \frac{3}{R_M}, \qquad (3)$$

Q_r the rainwater mixing ratio; R_M the mean radius of raindrop spectrum whose values are varied, ρ_w the liquid water density, D a raindrop diameter and $D_0 = 100 \mu m$. For snow, graupel and hail we propose the exponential size-distribution with constant intercept parameter given by

$$N_X(D_X) = N_{0X} e^{-\lambda_X D_X}, \qquad (4)$$

where the intercept parameter, N_{0X}, takes the values of 3×10^6, 1.1×10^6 and 4×10^4 m^{-4} for snow, graupel and hail, respectively. Slope parameters, λ_X, for real spectra is calculated from equation:

$$\lambda_X = \left\{ \frac{\pi \rho_X N_{0X}}{\rho Q_X} \left[\frac{\Gamma(4; \lambda_X D_1)}{\Gamma(4)} - \frac{\Gamma(4; \lambda_X D_3)}{\Gamma(4)} \right] \right\}^{0.25}, \qquad (5)$$

where $\Gamma(a,b)$ represents the incomplete gamma function.

Terminal velocities of the hydrometeors are given in form

$$U_X(D_X) = a_X D_X^{b_X} \left(\frac{\rho_0}{\rho}\right)^{c_X}, \qquad (6)$$

where is $\rho_0 = 1.2 kgm^{-3}$. Other parameters from Eq. (6) are given in Table 2.

Table 2. Parameters in Eq. (6).

	rain	snow	graupel	hail	units
a_X	842.0	4.844	193.595	164.1	$m^{1-b}s^{-1}$
b_X	0.8	0.25	0.64	0.5	-
c_X	0.5	0.5	0.8	0.5	-

Mass of collected particle X is

$$m_X(D_X) = \pi \frac{D_X^3}{6} \rho_X, \qquad (7)$$

where ρ_X is X particle density.

If we introduce fast (F) and slow (S) hydrometers then we rewrite the collection growth equation (1) as

$$\frac{dQ_Y}{dt} = \frac{1}{\rho} \int_{D_1}^{D_2} \int_{D_3}^{D_4} \frac{\pi (D_F + D_S)^2}{4} \left| U_F(D_F) - U_S(D_S) \right| m_X(D_X) N_F(D_F) N_S(D_S) dD_F dD_S. \qquad (8)$$

Exact solution for Eq.(8) can be written in shortened form as follow

$$\frac{dQ_Y}{dt} = GWA + AT, \qquad (9)$$

where the first term on the right-hand side refers to generalized Wisner approximation (marked GWA) as introduced by Gaudet and Schmidt (2005), while the additional term (marked AT) consists of convergent power series. The GWA term is derived from Eq. (8) under condition that

$$\left| U_F(D_F) - U_S(D_S) \right| = U_F(D_F) - U_S(D_S). \qquad (10)$$

For real spectra the GWA term consists of six terms sum with incomplete gamma functions calculated by algorithm of Abramowitz and Stegun (1970). The term AT also contains incomplete gamma functions within terms of power series.

2. NUMERICAL EXPERIMENTS

Differences in magnitudes of collection rates involving real spectra compared to their former values are tested through comparisons between GWA approximation for real (marked GWAR) and idealized (marked GWAI) spectra and the corresponding exact solutions (marked EXACTR and EXACTI, respectively). For the convergent AT term, two categories of interactions are analyzed: fast-falling hydrometeors collect the slow-falling ones and slow-falling hydrometeors collect the fast-falling ones. For the divergent AT term, hail/rain interaction is analyzed.

2.1. FAST-FALLING COLLECTOR, SLOW-FALLING COLLECTED

In this category we consider rain/snow, rain/graupel, graupel/snow and hail/snow interactions. If rain accretes snow, GWAR solution is largely reduced compared to EXACTR solution (Fig. 1), but less than for idealized spectra. As noted the ratios are sensitive only on snow mixing ratio. For larger their values there are more large snowflakes in snow spectrum that should lead to increased discreapancy between GWAR and EXACTR solutions, despite the fact that the terminal velocities of snow are considerably lower than those of raindrops.

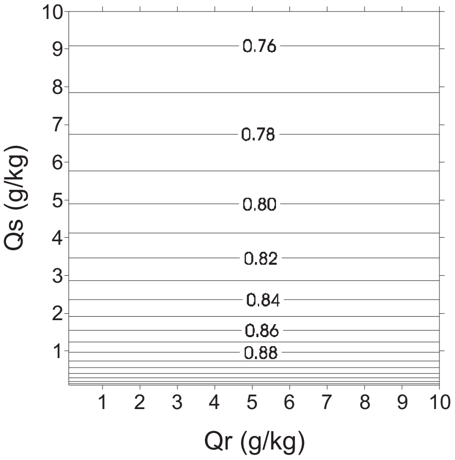

Fig.1. GWAR/EXACTR ratio for rain/snow interaction ($R_M = 300\,\mu m$).

On the other side, EXACTR solution is closed to EXACTI solution with high precision. This is due to the fact that more larger drops in spectrum is not able to modify the efficiancy of collisions with numerous slow snowflakes.

For rain/graupel interaction GWAR and GWAI solutions are negative (smaller negative values for real spectra) because of larger terminal velocities and smaller number concentrations of graupel particles compared to snowflakes. As a result, only exact solutions are proposed in praxis for this interaction. Their ratio (Fig. 2) clearly shows large reduction in their values especially for large graupel mixing ratios. This is due to the fact that there are more smaller raindrops in idealized spectrum that are capable to realize larger collection growth rates.

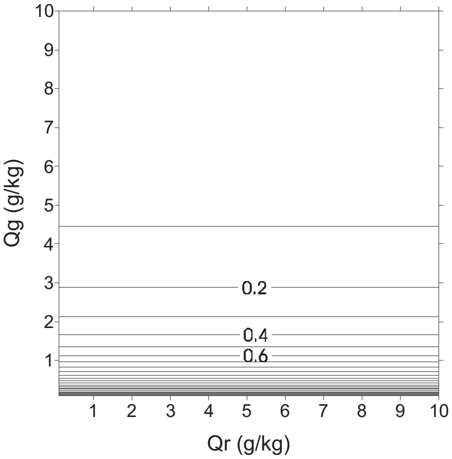

Fig. 2. As in Fig. 2 but for rain/graupel interaction.

The values of the GWAR/EXACTR ratio (Fig. 3) are larger than those for idealized counterparts for graupel/snow interaction. They decrease for smaller graupel mixing ratios due to smaller number concentration of graupel particles, despite the fact that terminal velocities of graupel are

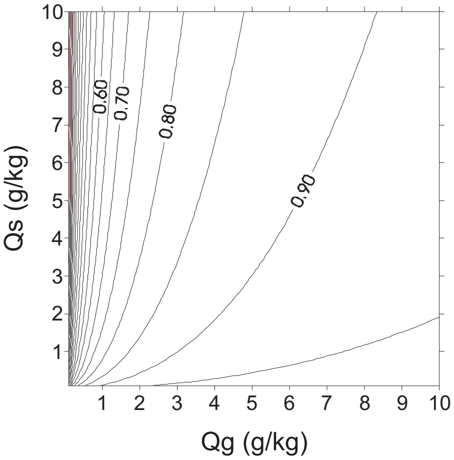

Fig. 4. As in Fig. 1 but for graupel/snow interaction.

considerable larger than those for snowflakes. On the other side, EXACTR solution is for 40% larger in magnitude compared to EXACTI one (Fig. 4) because of more large graupel particles in real spectrum.

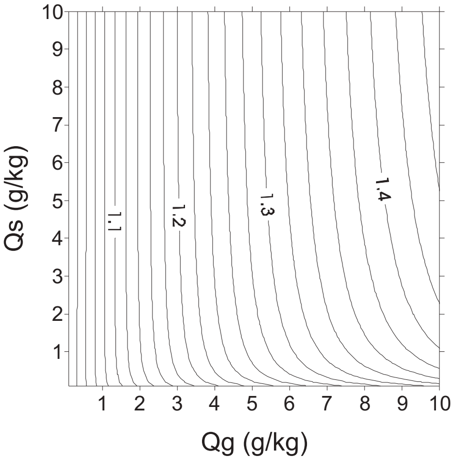

Fig. 4 As in Fig. 2 but for graupel/snow interaction.

For hail/snow interaction, difference between GWAI and EXACTI solutions is within 1% because the terminal velocities of snowflakes are always lower than 2 m/s as opposed to much larger their values for hail. The GWAR solution is equal to EXACTR one due to the fact that there are more large hailstones in such spectrum.

2.2. SLOW-FALLING COLLECTOR, FAST-FALLING COLLECTED

In this subsection we consider snow/rain and graupel/rain interactions. For snow/rain case the GWA solutions for both idealized and real spectra are closed to exact solutions within 0.1%, while the ratio EXACTR/EXACTI is equal to 1 with high precision. This scenario is due to fact that high number concentrations of snowflakes is insensitive to deficit in smaller raindrops in real spectrum.

For graupel/rain interaction GWA solutions would be also closed to EXACT ones for both spectra.

This is caused by the fact that the raindrop spectrum approximated by (2) contains higher concentrations of small and modest raindrops and smaller concentrations of large ones. In contrast, EXACTR/EXACTI ratio takes large values (>2.7) as shown in Fig. 5. This is due entirely by the fact that there are more large graupel particles and less smaller raindrops in real spectrum, which in turn, lead to increased collection rate of raindrops by graupel collector.

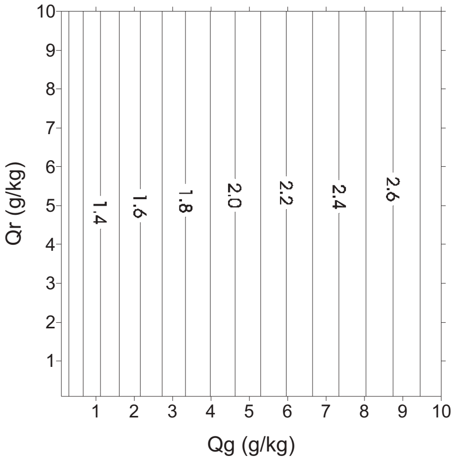

Fig. 5. As in Fig. 2 but for graupel/rain interaction.

2.3. HAIL/RAIN INTERACTION

Calculation of collection growth rate for hail/rain interaction can not be possible with Eq. (9) due to the divergence of AT term. However, our approach gives the solution of this problem. GWAR solution versus hail and rain mixing ratios is presented in Fig. 6. It is to be noted that its values are always positive. GWAI solutions shows slightly different feature. This is due to the fact that the therminal velocities of hailstones are always larger than those of raindrops smaller than 0.5 cm in diameter. Another factor is difference in number concentrations of hailstones and large raindrops. On the other side, the gamma function (2) with deficit of small drops are responsible for similar result with idealized spectrum assumption. Finally GWA solutions are equal to EXACT ones for this interaction.

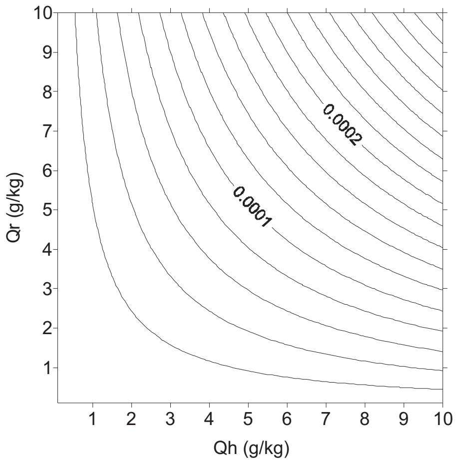

Fig. 6. GWAR solution for hail/rain interaction.

2.4. ROLE OF RAINDROP SIZE-DISTRIBUTION

Previous analisys shows that the careful selection of size-distribution is also important for success of our approach. The proposed gamma size-distributioon contains more smaller and modest but less larger raindrops compared to the Marshall-Palmer size-distribution. As a consequence our experiments with the gamma size-distribution show smaller differences between treated solutions except in EXACTR/EXACTI ratio for graupel/rain interaction.The EXACTR/EXACTI ratio for rain/snow interaction with the Marshall-Palmer distribution takes the values of over 1.5 for small rainwater mixing ratios. Ratios of analyzed solutions are insensitive to the change of rainwater mixing ratio as opposed to the case with the Marshall-Palmer size distribution. The GWAI solutions for hail/rain interaction show the wide area with negative values for small hail and large rainwater mixing ratios for exponentially-distributed raindrops as it is shown in Fig. 7. For real spectrum, it does not exist.

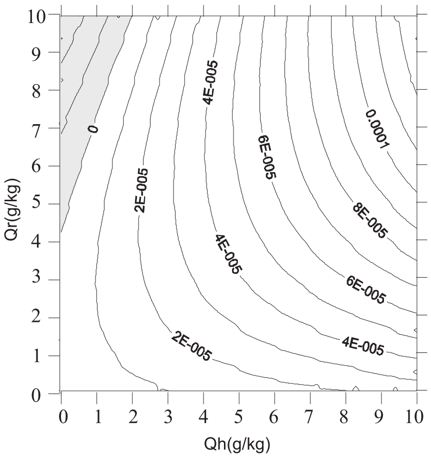

Fig. 7. As in Fig. 6 but for GWAI solution and the Marshall-Palmer size-distribution of raindrops.

3. CONCLUDING REMARKS

The goal of this paper was to prove that the real spectrum assumption that considers only sizes of hydrometeors within observed boundaries reproduces better collection growth rates between hydrometeors than idealized spectrum. This is clearly shown for the most interactions involving rain as well as for graupel/snow interaction. The advantage of the new approach is the best illustrated for hail/rain interaction because it enables the simple calculation of the exact solution. Our experiments also show that the careful selection of raindrop size-distribution may improve the quality of proposed solutions. This is due to the fact that different size-distributions generate different portions of small, modest and large raindrops.

4. BIBLIOGRAPHY

Abramowitz,M., and I.A. Stegun, 1970: Handbook of Mathematical Functions with Formulas, Graphs, and Mathematical Tables, Dover, 364 pp.

Ćurić, M., and D. Janc, 1997: The hail characteristics influence on its accretional growth. Atmos. Res., 45, 217-235.

Gaudet, B.J., and J. M. Schmidt, 2005: Assessment of hydrometeor collection rates from exact and approximate equations. Part I: A new approximate scheme. J. Atmos. Sci., 62,143-159.

Mizuno, H., 1990: Parameterization of the accretion process between different precipitation elements. J. Meteor. Soc. Japan, 68, 395-398.

Murakami, M., 1990: Numerical modeling of dynamical and microphysical evolution of an isolated convective cloud-The 19 July CCOPE cloud. J. Meteor. Soc. Japan, 68, 107-128.

Verlinde,J., P.J. Flatau, and W.R. Cotton,1990: Analytical solutions to the collection growth equation: Comparison with approximate methods and application to cloud parameterization schemes. J. Atmos. Sci., 47, 2871-2880.

Acknowledgments

This research was sponsored by the Ministry of Science of Serbia under Grant No. 146006. We gratefully acknowledge Mr. Dragomir Bulatović for tecnical preparing of the figures.

LABORATORY EXPERIMENTS ON GROWTH RATES, REGIMES, AND COLLECTION KERNELS DURING RIMING

Karoline Diehl[1], Nadine v. Blohn[1], Stephan Borrmann[1,2], and Subir K. Mitra[1]
[1]Institute for Atmospheric Physics, Johannes Gutenberg University Mainz, Germany
[2]Institute of Particle Chemistry, Max-Planck Institute for Chemistry, Mainz, Germany

1. INTRODUCTION

In tropospheric mixed phase clouds where ice particles and supercooled liquid drops are present simultaneously precipitation is mainly initiated via the ice phase. Ice particles grow to precipitation sizes amongst others by riming, i.e. the deposition of liquid droplets on ice particles (Pruppacher and Klett, 1997). This leads to the formation of graupel or hailstones. To estimate precipitation formation the knowledge of the collection kernel of involved ice particles and liquid droplets is essential (Khain et al., 1999). So far only it was studied quantitatively in one laboratory investigation only (Pflaum and Pruppacher, 1979). Because of this lack of data in most cloud model studies it is assumed that the collision efficiency of ice particles and droplets is the same as the collision efficiency of drops among themselves. This might be justified for some cases (Pflaum and Pruppacher, 1979) but still it had to be verified for other conditions. Such experiments were performed during the present studies. The temperature at the surface of rimed ice particle gives information about the growth regime: it is higher than the ambient temperature because latent heat is released. In the dry growth regime supercooled droplets freeze immediately when they collide with the ice surface but this is not the case when the surface temperature rises near 0°C so that liquid droplets may be included. Therefore, the density of graupel is dependant on the growth regime.

2. EXPERIMENTAL METHODS

The experiments were performed at the Mainz vertical wind tunnel (Pruppacher, 1988) in a temperature range between -5 and -15°C where riming proceeds most efficiently (Pruppacher and Klett, 1997). The air stream in the wind tunnel is laminar with a rest turbulence level of 0.5 %. Individual ice particles with an initial size of 700 µm were freely floated while upstream of the observation section a cloud of supercooled liquid droplets was generated by several sprayers. The size spectrum of the droplets was measured with an FSSP and the average droplet size was determined to 20 µm. During the experiments, temperature and dew point were continuously recorded to calculate the liquid water content; it was between 1 und 1.5 g/m^3 which are typical values in mixed-phase clouds (Pruppacher und Klett, 1997). Growth times were up to 90 s. Afterwards, the rimed ice particles were extracted from the wind tunnel by a suction technique and the mass increase was determined. The collection kernel *K* was calculated from the mass increase *dm/dt* and the liquid water content *LWC* by using the following relationship (Pflaum and Pruppacher, 1979):

$$K = \frac{dm/dt}{LWC}$$

To specify the conditions which determine the growth regime of the graupel the surface temperature of riming ice particles was measured with an infrared-thermograph at various temperatures and liquid water contents. For these measurements, ice particles of 1 to 2 mm diameter were hung up using a thin nylon fibre so that they were freely movable in the air stream while supported at their free fall velocities. Along the nylon fibre negligible heat conduction proceeded so that the temperature of the ice particles was not affected by the connecting fibre. The thermograph was installed at the wind tunnel in front of a double-walled (to avoid condensation) window made from polyethylene foil which has a fairly high transmission at far infrared wavelengths. Ice particles were rimed for several minutes;

during this time their surface temperatures were recordered. These studies were conducted at various ambient temperatures between 0 and -15°C and with two different liquid water contents, 1 and 2 g/m^3.

3. RESULTS AND CONCLUSIONS

According to Beard and Grover (1974) and Pflaum and Pruppacher (1979) the collection kernel shows a power law dependence (linear on a log-log scale) on the collector momentum but is independent on ambient temperature, liquid water content, and growth time. Figure 1 shows the collection kernel of rimed graupel as function of the collector momentum (mass × fall velocity). Included in Figure 1 are data from Pflaum and Pruppacher (1979) for smaller collector momentums and smaller droplet sizes. These data are shown in blue and black symbols, the new data in red symbols. The lines in Figure 1 give the collection kernels of liquid drops colliding with droplets of different average sizes. The blue and black lines are for 6 µm and 10 µm droplets, respectively (according to Pflaum and Pruppacher, 1979). The red line was calculated for the present case of 700 µm collector size and 20 µm droplet size using the collision efficiencies of Vohl et al. (2007).

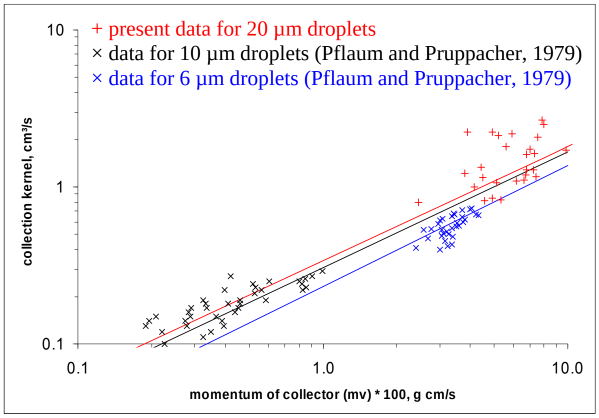

Fig. 1: Collection kernel of rimed graupel as function of collector momentum

The measurements of Pflaum und Pruppacher (1979) were for collector momentums up to 4 ×10^{-2} g cm s^{-1}. As the collection kernel for graupel matched very well with the collection kernel for liquid drops it was concluded that the use of the collection kernel of liquid drops in model simulations should not lead to large errors for the investigated size ranges. The new measurements complement the earlier measurements with data for larger collector momentums and larger riming droplets so that the range where the use of the liquid drop collection kernel in cloud models would be justified is extended.

The surface temperature of ice particles during riming T_s, the ambient temperature T_a, and the temperature difference ΔT are given in Table 1 for various liquid water contents (LWC). The error of the temperature measurements was ± 1°C which is typically for infrared-thermographs. Each value consisted of several single measurements which were averaged.

LWC (g/m^3)	T_a (°C)	T_s (°C)	ΔT (°C)
1.0	-15.6	-13.6	2.0
1.0	-12.1	-9.8	2.3
1.0	-7.6	-5.7	1.9
1.0	-3.1	-1.4	1.7
1.9	-11.8	-7.7	4.1
1.9	-7.7	-4.8	2.9
1.9	-4.3	-1.2	3.1
1.9	-3.0	-0.3	2.7

Table 1: Change of the surface temperature T_s of rimed ice particles for various ambient temperatures T_a and liquid water contents (LWC).

At higher liquid water content the surface temperature increase is approximately 3°C, at lower liquid water content around 2°C. The visual observation of the rimed graupel showed that the surface was opaque at lower temperatures but clear at temperatures above -4°C. Thus, it can be concluded that the wet growth regime is reached at ambient temperatures near 0°C only. One can estimate that with a liquid water content of 2 g/m^3 the ambient temperature must exceed -4°C, and with a liquid water content of 1 g/m^3 it must exceed -3°C to let ice particles grow in the wet growth regime. Therefore, under conditions typical for the formation of graupel, i.e. with temperatures between -5 and -15°C and liquid water contents lower than 2 g/m^3 graupel grow in the dry growth regime. Only at temperatures above -4°C and/or extremely high liquid water contents (i.e. riming with large drops) growth in the wet growth regime can be expected. This would be typical for situations where hailstones are forming. Thus, it can be concluded that the conditions during the present riming experiments produce growth in the dry growth regime only.

4. ACKNOWLEDGEMENTS

The present studies were supported by the SFB 641 "The tropospheric ice phase".

5. REFERENCES

Beard, K.V., and S.N. Grover, 1974: Numerical collision efficiencies for small rain drops colliding with micron sized particles. *J. Atmos. Sci.,* **31,** 543-550.

Khain, A., A. Pokrovsky, and I. Sednev, 1999: Effects of cloud-aerosol interaction on cloud microphysics, precipitation formation and size distribution of atmospheric aerosol particles: Numerical experiments with a spectral cloud model. *Atm. Res*., **52**, 195-220

Pflaum, J.C., and H.R. Pruppacher, 1979: A wind tunnel investigation of the growth of graupel initiated from frozen drops. *J. Atm. Sci.,* **36**, 680-689.

Pruppacher, H.R., 1988: Auswaschen von atmosphärischen Spurenstoffen durch Wolken und Niederschlag mittels eines vertikalen Windkanals. BMFT-Report 9/88, GSF München.

Pruppacher, H.R., J.D. Klett, 1997: *Microphysics of Clouds and Precipitation*, 2nd ed., Kluwer Academic Publishers, Dordrecht.

Vohl, O., S.K. Mitra, S. Wurzler, K. Diehl, and H.R. Pruppacher, 2007: Laboratory investigations of collisional growth of small raindrops in a laminar flow field and empirically determined collision efficiencies. *Atm. Res.*, **85,** 120-125.

ASSESMENT OF AEROSOL AND ENTRAINMENT-MIXING PROCESSES ON DROP SIZE DISTRIBUTIONS IN WARM CUMULUS

Graham Feingold [1], Jennifer D. Small [2], Patrick Y. Chuang [2], Hongli Jiang [3], Steven K. Krueger [4], Haflidi H. Jonsson [5]

[1]NOAA Earth Systems Research Laboratory, 325 Broadway, Boulder, CO, USA
[2]Department of Earth and Planetary Sciences, U. of California, Santa Cruz, CA, USA
[3]NOAA Earth Systems Research Laboratory/CIRA, 325 Broadway, Boulder, CO, USA
[4]Department of Meteorology, University of Utah, Salt Lake City, UT, USA
[5] CIRPAS and Naval Post Graduate School, Monterey, CA, USA

1. INTRODUCTION

Over 5 decades ago, Warner (1955) made fundamental measurements that showed that the liquid water content (LWC) of cumulus clouds is significantly subadiabatic, and that the degree of subadiabaticity increases with increasing height as progressively drier environmental air is incorporated into the cloud. The processes shaping cloud drop size distributions are both microphysical in nature (activation of aerosol, growth processes (condensation, collision-coalescence), as well as dynamical (advection, entrainment-mixing followed by evaporation). Somewhat idealized scenarios of mixing have been proposed: “homogeneous mixing” where mixing is rapid compared to droplet evaporation; and “inhomogeneous mixing” where mixing is slow relative to droplet evaporation. A number of recent studies (e.g. Chosson et al. 2007; Hill et al. 2008) have examined the sensitivity of aerosol-cloud interactions to these mixing assumptions within large eddy simulations (LES) and shown that varying the representation of mixing affects both the microphysical and radiative properties of the cloud.

The goal of this work is to explore the effects of both explicitly resolved entrainment-mixing <u>and</u> aerosol perturbations on the drop size distribution. We will apply numerical models and in-situ observations to address this question. The motivation derives from the fact that the response of cloud optical depth τ to a change in LWC can be shown to be:

$$\left.\frac{d\tau}{dLWC}\right|_{\text{homog}} = \frac{2}{3}; \quad \left.\frac{d\tau}{dLWC}\right|_{\text{inhomog}} = 1, \qquad (1)$$

whereas τ responds to aerosol number concentration perturbations (at constant LWC) according to:

$$\left.\frac{d\tau}{dN}\right|_{LWC} = \frac{1}{3}, \qquad (2)$$

(e.g., Jeffery, 2007) with the implicit assumption that drop concentration $N \propto$ aerosol number concentration N_a.Thus (a) the effects of mixing result in τ sensitivities to LWC that are at least 2 – 3 times larger than τ sensitivity to aerosol (at constant LWC), and (b) the nature of entrainment-mixing (homogeneous vs inhomogeneous) also affects the τ response.

New-generation cloud probes such as the Phase Doppler Interferometer (PDI; Chuang et al. 2008) are better suited to resolving the sizes of smaller cloud droplets (< 10 μm) than earlier instruments, and therefore, resolving the integrated effects of aerosol perturbations and mixing on the drop size distribution. Moreover, as the spatial/temporal resolution of large eddy simulations (LES) improves, and small scale motions are more faithfully represented, it becomes interesting to explore the extent to which LES that includes size-resolved microphysics can represent the evolution of drop-size distributions. While the ultimate goal of this work is to compare drop size distributions in LES to those measured by PDI, we first consider comparison between PDI and a model that explicitly simulates entrainment-mixing and droplet growth. The model is the Explicit Mixing Parcel Model (EMPM) (Krueger et al., 1997; Su et al. 1998) that, unlike LES, explicitly simulates turbulent mixing down to the smallest scales. However, it does so in a one-dimensional parcel framework with prescribed dynamics and therefore does not simulate feedbacks between aerosol/cloud particles and dynamics. For example the enhanced evaporation rates associated with small droplets do not affect mixing.

The data derive from measurements in warm convective clouds observed during the the summer of 2006, Texas Air Quality Study/Gulf of Mexico Atmospheric Composition and Climate Study (henceforth GoMACCS) field campaign in the vicinity of Houston.

2. DATA

During GoMACCS, an instrumented aircraft, the Center for Interdisciplinary Remotely-Piloted Aircraft Studies (CIRPAS) Twin Otter, outfitted with a suite of aerosol size and composition instruments, cloud drop probes, aerosol optical measurements and irradiance measurements, sampled shallow cumulus clouds during the mid-morning hours. Deep convection was avoided. The region is characterized by strong pollution from various industries and urban sources. This type of boundary layer provides an excellent environment for studying aerosol (pollution) - cloud interactions and for comparison between model results and aircraft data (Jiang et al. 2008). The focus here is on a single cloud event on September 10th described in more detail by Lu et al. 2008.

(i) Phase-Doppler Interferometer (PDI)

An airborne cloud probe based on the PDI technique has been recently developed (see Chuang et al. 2008 for more details and additional references). It measures drop size distributions in the range of 2 and 100 μm radius. One primary advantage is the ability to determine the instrument view volume as a function of drop size from the data, which minimizes uncertainties in derived concentration. It is also much less susceptible to mistaking random noise for real drops, which can be a significant issue when measuring small drops.

3. MODELS

(i) The Explicit Mixing Parcel Model (EMPM)

EMPM is a one-dimensional entraining parcel model. It differs from standard adiabatic parcel models in that it simulates entrainment and mixing events separated by periods of adiabatic growth. Turbulent mixing is simulated using the linear eddy model (Kerstein 1991) adapted by Krueger et al. (1997). The reduction of the problem to 1-D enables the model to represent all relevant length scales of mixing, down to the Kolmogorov scale. The model solves a set of equations representing 1-D molecular diffusion, droplet growth on 49 size categories of aerosol/droplets, and calculation of supersaturation. Turbulent stirring is treated stochastically by random rearrangement events of the scalar fields in the 1-D domain.

Aerosol particles are specified as a lognormal size distribution (median radius 0.06 μm, geometric standard deviation 1.8) composed of ammonium bisulfate. The model explicitly tracks individual drops and in this case the number of drops is equivalent to a concentration of ~ 700 cm^{-3}. Sensitivity to the size distribution is tested. The updraft is fixed at 2 m s^{-1}. The bulk entrainment rate (calculated from aircraft soundings) is 1 km^{-1} and the ratio of the size of the entrained blob to the domain size *d* is 0.01 (see Krueger et al. 1997 for details). The mixing is simulated as discrete events that are a random function of height. The environmental sounding is based on the aircraft data for the day in question.

(ii) Large Eddy Simulation

The LES is based on the Regional Atmospheric Modeling System (RAMS, version 6.0) coupled to a microphysical model described by Feingold et al., (2005). The model includes coupling between microphysics, dynamics, aerosol, radiation and a land surface model. The drop size distribution is resolved by 33 size bins with two moments (drop mass and number mixing ratios) in each bin. Warm processes are represented. Aerosol particles are assumed to be lognormally distributed and composed of ammonium sulfate. The domain size and resolution is varied: For fields of cumuli we use a domain of 13 km x 13 km x 5 km with Δx = Δy = 100 m; Δz = 50 m and a Δt of 2 s. Our single cloud simulations use grids as fine as Δx = Δy = Δz 5 m and Δt = 0.25 s. Only the latter will be considered here.

4. RESULTS

(i) Single Cloud: Comparison between PDI and EMPM for Houston Cloud

Figure 1 shows a number of fields sampled by the aircraft (red points), superimposed on EMPM model output of mean (black) and standard deviation (blue). Data are only shown up to a maximum cloud depth of 1500 m, although the cloud did in fact achieve a depth of 2300 m. One can see that for the model input conditions, the general features of LWC, total mixing ratio r_t, and N compare quite well.

Aircraft data are now binned into 20 height intervals. The subadiabatic factor β is of interest because it gives a general sense of the degree of cloud dilution:

$$\beta = \frac{LWC}{LWC_{ad}}, \qquad (3)$$

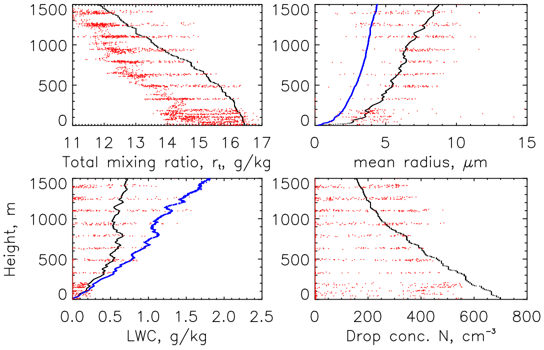

Figure 1: Comparison between aircraft data (red points) and model output with mean values in black and standard deviations in blue. The broad features of the observations are captured by the model. Height refers to height above cloud base.

where LWC$_{ad}$ is the height-dependent, adiabatic LWC calculated from cloud base conditions. A probability distribution function of β is shown in Figure 2. The disparity in counts is due to the averaging of the PDI data. Both modeled and observed clouds indicate a peak β of ~0.2.

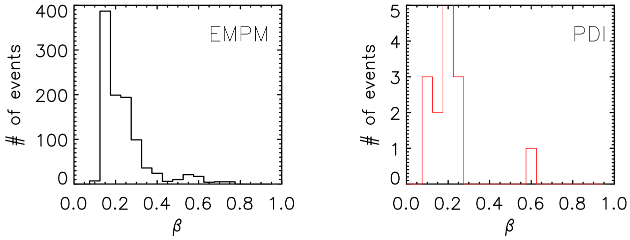

Figure 2. Frequency of occurrence of β for EMPM and PDI. Both have similar modes of ~ 0.2. The higher value of 0.6 occurs at the lower levels of the cloud.

The EMPM size distributions are representative of the mean cloud drop spectrum. Thus we compare PDI-averaged spectra at individual heights. Figure 3 shows one such comparison between PDI and EMPM. Of note is the excellent agreement between PDI and EMPM for small droplets, a region that has hitherto not been well described by cloud probes. However, in spite of the fact that the LWC, N, and β values are quite similar, there are differences between the spectral shapes, with PDI tending to exhibit a stronger peak at the drop mode and EMPM exhibiting a broader distribution comprising larger drops, and some residual unactivated aerosol in the size range 0 – 1 μm radius. This tends to be a fairly robust feature of the comparisons and is not dependent on whether entrainment events are represented in EMPM as occurring regularly or randomly with height. It is affected by the ratio of entrained blob to domain size (*d*) and the frequency of entrainment events.

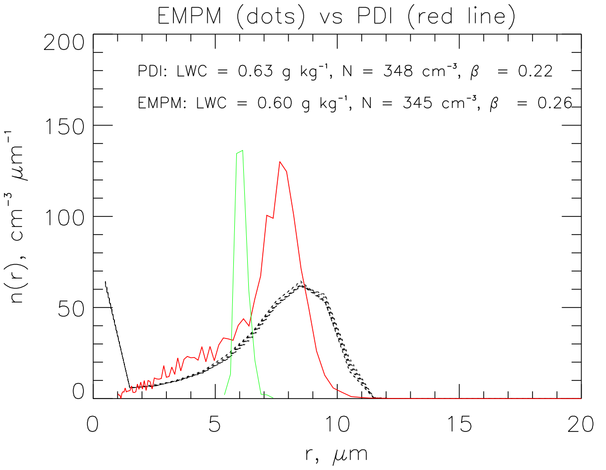

Figure 3: Comparison between averaged EMPM (black) and averaged PDI (red) drop spectra. Sampling conditions are as indicated in the legend. Aerosol input to EMPM: $r_g = 0.06\ \mu m$; $\sigma_g = 1.8$. The green line represents the shape of an undiluted adiabatic parcel with LWC = 0.60 g kg^{-1}and N = 700 cm^{-3} scaled by a factor of 7, to fit on the linear axis.

Of further interest is the extent to which the initial shape of the aerosol size distribution used as input to the model determines drop spectral shape. To this end we adjust the median radius from 0.06 μm to 0.1 μm and geometric standard deviation σ_g to 1.6, but keep N_a constant. Figure 4 shows a comparison similar to that in Fig. 3. Again there is excellent agreement at the small-drop end but PDI is still more sharply peaked at the mode than EMPM. The very small particles in the EMPM 0 – 1 μm bin are far less numerous now and the modes agree somewhat better than in Figure 3.

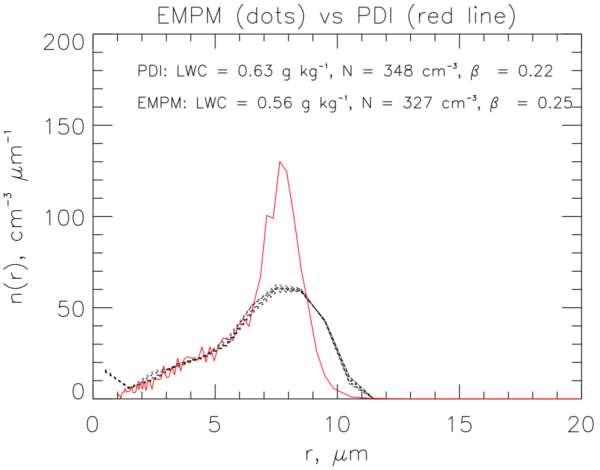

Figure 4: Comparison between averaged EMPM and averaged PDI drop spectra. Sampling conditions are as indicated in the legend. Aerosol input: $r_g = 0.1\ \mu m$; $\sigma_g = 1.6$

Overall, much greater differences in drop spectral shape are obtained via variation in mixing representation than those due to aerosol size distribution. Note, however, that the results are strongly sensitive to the number concentration of aerosol (not shown).

(ii) Single Cloud: Comparison between EMPM and LES for RICO cloud

Some very preliminary results are shown here. Further analysis will be presented at the conference.

The LES was configured to simulate a single warm cloud at high resolution (5m x 5 m x 5m) over a limited domain (1 km x 1 km x 2.5 km). The model was initialized with a warm bubble and run for about 1 h. The standard two-moment bin microphysical scheme was used to simulate activation, condensation/ evaporation and collision-coalescence.The aerosol input was 1000 cm^{-3}; r_g = 0.06 μm, and σ_g = 1.8. With drop concentrations on the order of 500 cm^{-3}, collision-coalescence is negligible, making comparison with EMPM worthwhile.

EMPM was initialized with the same aerosol size distribution and cloud base conditions as the LES. The "environmental sounding" was taken from the LES's initial conditions. An updraft velocity of 2 ms^{-1} was assumed, which was similar to that of the LES cloud. An eddy dissipation rate ε of 0.01 m^2s^{-3} and ratio of blob:domain size = 0.1 was assumed. Sensitivity to these parameters will be explored at a later date. In particular, ε will be specified based on the LES-simulated cloud.

Results are shown at 20 min during a vigorous and actively growing stage of the cloud. A comparison between horizontally-averaged LES size spectra and EMPM spectra for very similar LWC, *N*, and β conditions is shown in Figure 5. Although the general form of the spectra is similar, EMPM has both more numerous smaller, and more numerous larger drops than LES.

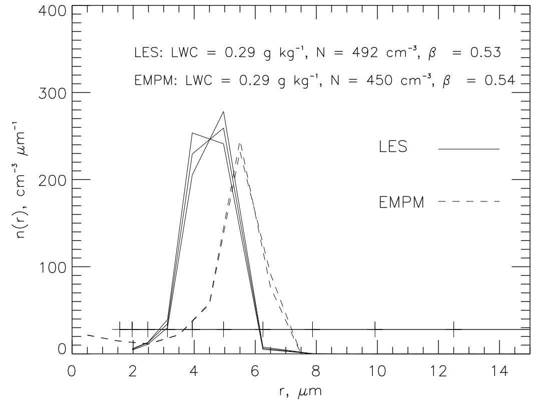

Figure 5: Comparison between LES and EMPM drop size distributions for similar N, LWC and β conditions. EMPM produces both smaller and larger drops that are not present in the LES. The horizontal grid represents the size bins in the LES microphysical model. The EMPM bins are 1 μm wide.

5. SUMMARY

We have presented some preliminary analysis addressing the question of how well we understand microphysical (aerosol and growth processes) and dynamical (entrainment-mixing) effects on cloud drop size distributions. It has been motivated by the deployment of a new generation, high resolution cloud probe, and development of models that have much higher spatial/temporal resolution than in the past.

We have considered comparison between (i) phase-Doppler Interferometer (PDI) measurements in continental cumulus and simulations of the cloud with an Explicit Mixing Parcel Model (EMPM). Results show that for similar values of LWC, N, and subadiabaticity, measured and predicted spectra exhibit good agreement, although PDI tends to measure spectra that are narrower and have a more distinct mode than EMPM. The extent to which this is dependent on model input parameters is under investigation.
(ii) Large Eddy Simulation (LES) of a single cloud, run on a 5m x 5m x 5 m grid and EMPM simulation of the same cloud. In this case some very preliminary results show that the LES modelled size distributions show fewer small and large drops than EMPM.

Further work will focus on determining the reason for these disparities and exploring how well high resolution LES simulates entrainment-mixing effects on drop spectra.

Acknowledgements: This work was supported by NOAA's Climate Goal. SKK acknowledges support from the National Science Foundation under Grant No. ATM-0346854.

REFERENCES

Chosson, F., J.-L. Brenguier, and L. Schuller, 2007: Entrainment-mixing and radiative transfer simulation in boundary layer clouds. *J. Atmos. Sci.*, **64**, 2670 – 2682.

Chuang, P. Y., J. D. Small, E. W. Saw, R. A. Shaw, C.M. Sipperley, G. A. Payne, and W. D. Bachalo, 2008: Airborne phase Doppler interferometry for cloud microphysical measurements. *Aerosol Sci. Tech.*, in press.

Feingold, G., H. Jiang, and J. Y. Harrington, 2005: On smoke suppression of clouds in Amazonia, *Geophys. Res. Lett.* **32**, L02804, doi:10.1029/2004GL021369.

Hill, A., G. Feingold, and H. Jiang, 2008: The influence of mixing on the climate forcing of non-precipitating stratocumulus. J*. Atmos. Sci*., in review.

Jeffery, C. A., 2007: Inhomogeneous cloud evaporation, invariance, and Damkohler number. *J. Geophys. Res*., **112**, doi:10.1029/ 2007JD008789, 2007

Jiang, H., G. Feingold, H. Jonsson, M.-L. Lu, P. Y. Chuang R. C. Flagan, J. H. Seinfeld, 2008: Comparison of statistical properties of simulated and observed cumulus clouds in the vicinity of Houston during the Gulf of Mexico Atmospheric Composition and Climate Study (GoMACCS). *J. Geophys. Res*., in press.

Kerstein, A. R., 1991: Linear eddy modeling of turbulent transport. Part 6. Microstructure of diffusive scalar mixing fields. *J. Fluid Mech*. **231**, 361.

Krueger, S. K., C.-W. Su, and P. A. McMurtry, 1997: Modeling entrainment and fine-scale mixing in cumulus clouds. *J. Atmos. Sci*., **54**, 2697–2712.

Lu, M-L, H. H. Jonsson, P. Y. Chuang, G. Feingold, R. C. Flagan, J. H. Seinfeld, 2008: Aerosol-cloud relationships in continental shallow cumulus, *J. Geophys. Res*., in press.

Su, C.-W., S. K. Krueger, P. A. McMurtry, and P. H. Austin, 1998: Linear eddy modeling of droplet spectral evolution during entrainment and mixing in cumulus clouds. *Atmos. Res*., **47–48**, 41–58.

Warner, J., 1955: The water content of cumiliform cloud, *Tellus*, **7**, pp. 449–457.

A WARM RAIN MICROPHYSICS PARAMETERISATION THAT INCLUDES THE EFFECTS OF TURBULENCE

Charmaine N. Franklin
Centre for Australian Weather and Climate Research
A partnership between the Australian Bureau of Meteorology and CSIRO

1. INTRODUCTION

The effect of aerosols on clouds remains one of the largest sources of uncertainty in climate studies and many of the complex aerosol-cloud interactions are associated with cloud microphysical processes. To enable greater confidence in climate projections one of the processes that requires a quantitative analysis is the second indirect aerosol effect, which is the effect from enhanced aerosol concentrations in clouds suppressing drizzle and prolonging cloud lifetimes (Albrecht 1989). To be able to quantify this effect with any real certainty, the cloud microphysical processes must be accurately represented in global climate models (GCMs), in particular the autoconversion process, which describes the collision and coalescence of small cloud droplets to form larger raindrops. Rotstayn and Liu (2005) demonstrated how changing autoconversion schemes in a GCM could decrease the globally averaged second indirect aerosol effect by 60%, highlighting the need for increased understanding and a more accurate parameterisation of autoconversion.

In clouds where the temperature does not reach freezing, it is the process of collision and coalescence that allows drops to grow to a size large enough to fall out of a cloud as rain. Observations of droplet growth tend to show a faster evolution and broader drop size distribution compared to the theoretically calculated drop spectra, where the equations are applied to a randomly distributed population of drops whose motion is governed by gravitational forcing. Several physical effects have been suggested to play an important role in the reduction of the growth times, including entrainment and mixing of dry air, turbulence and the role of giant cloud condensation nuclei (e.g. Beard and Ochs 1993). Turbulence increases the collision rate of droplets in at least three ways: by changing the droplet velocities and the spatial distribution of the droplets (e.g. Franklin et al. 2005), and by changing the collision and coalescence efficiencies between droplets. Although the effect of turbulence on cloud droplet collision-coalescence rates is yet to be quantified by observations, recent modelling studies have shown that turbulence can increase the collision rates of droplets by several times the purely gravitational rate (Franklin et al. 2005, 2007; Wang et al. 2005; Pinsky et al. 2006). Franklin et al. (2007) performed direct numerical simulations (DNS) of droplets within turbulent flow fields and developed empirically derived equations that describe the turbulent collision kernel for droplet pairs where the larger droplet is within the radius range of 10 – 30 μm and the eddy dissipation rate of turbulent kinetic energy (TKE) is between 100 and 1500 $cm^2 s^{-3}$.

Autoconversion parameterisations are derived either from analytical approximations of the collision kernel or from empirical fits to model data, where the data used is either a numerical solution of the stochastic collection equation (SCE) using an accurate collision kernel or a large eddy simulation (LES) model with explicit microphysics. Empirically based autoconversion parameterisations that use numerical solutions of the exact form of the collision kernel can simulate a range of drop size distributions that are applicable to many cloud types and at various stages of a cloud's lifetime. The model-based empirical parameterisations derive droplet growth rates due to autoconversion, accretion and self-

---

Corresponding author's address:
Charmaine N. Franklin, CSIRO Marine and Atmospheric Research, Private Bag No. 1, Aspendale, Victoria, 3195, Australia;
E-mail: Charmaine.Franklin@csiro.au

collection as functions of bulk cloud properties. This approach has been used by Beheng (1994) and Khairoutdinov and Kogan (2000) and is the one adopted in this study to develop microphysics parameterisations that include the effect of turbulence.

2. NUMERICAL METHODS

To examine the effect of turbulence on the evolution of the drop size distribution through simulations of the SCE, the gravitational geometric collision kernel has been replaced by the turbulent kernel of Franklin et al. (2007) for collector drops in the radius range of 10 – 30 μm. For the range of turbulent flow parameters examined in this study, DNS data do not exist to describe droplet collision rates for the entire drop size distribution. The DNS experiments that the turbulent collision kernel is based on in Franklin et al. (2007), cover the range of drop sizes that are believed to be the most important for the process of rain initiation in warm clouds. In the experiments that include the turbulent collision kernel the gravitational collision efficiency has been used for all collector drop sizes as it is still unclear what the effect of turbulence is on the collision efficiencies of small droplets.

In this study Bott's (1998) flux method is used to solve the SCE but with the exponential functions of Bott (2000) to describe the mass flux. This method is mass conservative, numerically efficient and accurate. The numerical solutions use a logarithmically equidistant mass grid, where the mass doubles after 3 grid cells and the time step used is 1 s. There are 160 bins with drop radii from 0.6 to 10^4 μm. Detailed numerical tests were undertaken to ensure the convergence and accuracy of the solution of the SCE. In the numerical experiments the hydrodynamic kernel of Hall (1980) is used, where the collision efficiencies come from a range of sources depending on the collector droplet size and the coalescence efficiency is set to 1.

3. EFFECT OF TURBULENCE ON THE EVOLUTION OF THE DROP SIZE DISTRIBUTION

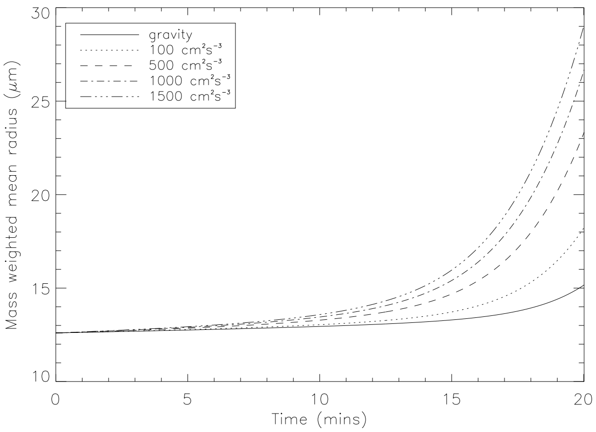

Figure 1. Temporal evolution of the mass weighted mean radius for the gravitational only and 4 turbulent cases.

It has been recognized for over half a century that the growth times of precipitation-sized drops may be significantly reduced by including the effect of turbulence in the droplet growth equation. Solving the SCE with a recently developed turbulent collision kernel allows the examination of the significance of the effect of turbulence on the evolution of the drop size distribution and the reduction in the growth times of raindrops due to turbulence. Figure 1 shows the temporal evolution of the mass weighted mean radius for the solution of the SCE that uses the gravitational collision kernel for all drop sizes, and for four cases that use the turbulent collision kernel for the droplets in the radius range of 10 – 30 μm. The four cases differ in the levels of turbulence, with the rates of eddy dissipation of TKE ranging from 100 to 1500 cm^2 s^{-3}. The initial conditions for the simulations are a liquid water content of 1 g m^{-3}, a number concentration equal to 240 drops cm^{-3} and a relative dispersion of the drop size distribution of 0.57, which implies a mean volume radius of 10 μm. During the first 10 minutes of the solution of the SCE there is little difference in the mass weighted mean radius of the gravitational and turbulence cases. However, the difference rapidly increases over the next 10 minutes and continues to increase for a further 30 minutes. It is clear from Figure 1 that the droplets grow faster as the dissipation rate of the flow is increased. The percentage of mass contained in drop sizes greater than 40 μm after 20 minutes of integration of the SCE for the case with gravitational only forcing is 0.9%, whereas for the least turbulent case the percentage is 21.4. This result shows that even a low intensity of turbulence can have a significant effect on the evolution of the drop size distribution. This percentage increases to 58.3 for the strongest turbulence case examined, highlighting the importance of the turbulent forcing on the collision-coalescence process.

4. DOUBLE MOMENT PARAMETERISATION SCHEME AND RELATIVE ROLES OF MICROPHYSICAL PROCESSES

Solutions of the SCE have been used to develop a model-based empirical double-moment parameterisation of the effect of autoconversion, accretion and self-collection on the rain and cloud water mixing ratios and the rain and cloud drop number concentrations. The SCE has been solved for liquid water contents in the range of 0.01 – 2 g kg^{-1}, number concentrations up to 500 drops cm^{-3} and relative dispersion coefficients of the initial drop size distribution between 0.25 and 0.4. The initial drop size distribution takes the form of a Gamma function and the separation radius that determines the point at which a cloud droplet becomes a raindrop is 40 µm. Only the autoconversion model is described in this paper, the equations for all of the double moment parameterisations for the processes of autoconversion, accretion and self-collection are described in Franklin (2008) and the reader is referred to that paper for the details of the full parameterisation.

The process of autoconversion has been shown to be a function of the cloud water content and cloud number concentration and can take the form (e.g. Khairoutdinov and Kogan 2000)

$$\left(\frac{\partial q_r}{\partial t}\right)_{auto} = C\, q_c^{\ \alpha}\ N_c^{\ \beta} \qquad (1)$$

where q_r is the rain water content in kg m^{-3}, q_c is the cloud water content in kg m^{-3} and N_c is the cloud droplet number concentration per cm^3. The coefficients obtained for (1) from the non-linear regression for each of the gravitational/non-turbulent and turbulent cases are given in Table 1. The exponent of the cloud water content decreases with increasing eddy dissipation rate of TKE and the exponent of the number concentration is negative and tends to zero. This reflects the decreasing dependence of the autoconversion rate on the cloud water content and the increasing dependence on the number concentration as the rate of turbulence increases.

Table 1. Coefficients for the autoconversion parameterisation as a function of cloud water content and number concentration as given by (1).

	C	α	β
Gravity	20.0 x 10^3	2.89	-1.32
100 $cm^2\,s^{-3}$	86.1 x 10^2	2.74	-1.35
500 $cm^2\,s^{-3}$	26.7 x 10^2	2.60	-1.27
1000 $cm^2\,s^{-3}$	17.8 x 10^2	2.57	-1.22
1500 $cm^2\,s^{-3}$	12.6 x 10^2	2.53	-1.18

Fitting all of the turbulence cases results in the following model of the autoconversion rate as a function of the flow Taylor based Reynolds number R_λ, the cloud water content and the cloud number concentration

$$\left(\frac{\partial q_r}{\partial t}\right)_{auto} = \left(6.5\times10^{13} R_\lambda^{\ -6.3} + 1.9\right) q_c^{\left(3.4 R_\lambda^{\ -0.23}\right)} \times N_c^{\left(-5.3 R_\lambda^{\ -0.38}\right)} \qquad (2)$$

This equation is valid for eddy dissipation rates of TKE between 100 and 1500 $cm^2\ s^{-3}$ where an appropriate Reynolds number relative to the DNS data is found from $R_\lambda = 21\varepsilon^{0.12}$, where ε is the dissipation rate in $cm^2\ s^{-3}$. The choice was made not to include the relative dispersion of the drop size distribution as a parameter in this autoconversion model because the idea of this parameterisation was to develop something general that can be used to cover all cloud types. In addition, the non-turbulent case has been fitted separately for the equations of microphysical processes. This choice was made because the effect of turbulence on the evolution of the drop size distribution, and the manifestation of that on the microphysical process rates, is a complex non-linear function of the eddy dissipation rate of TKE. As the dependence of the turbulent enhancement on dissipation rates less than 100 $cm^2 s^{-3}$ is not known from DNS experiments, the parameterisations have not been extended beyond the range for which data is available.

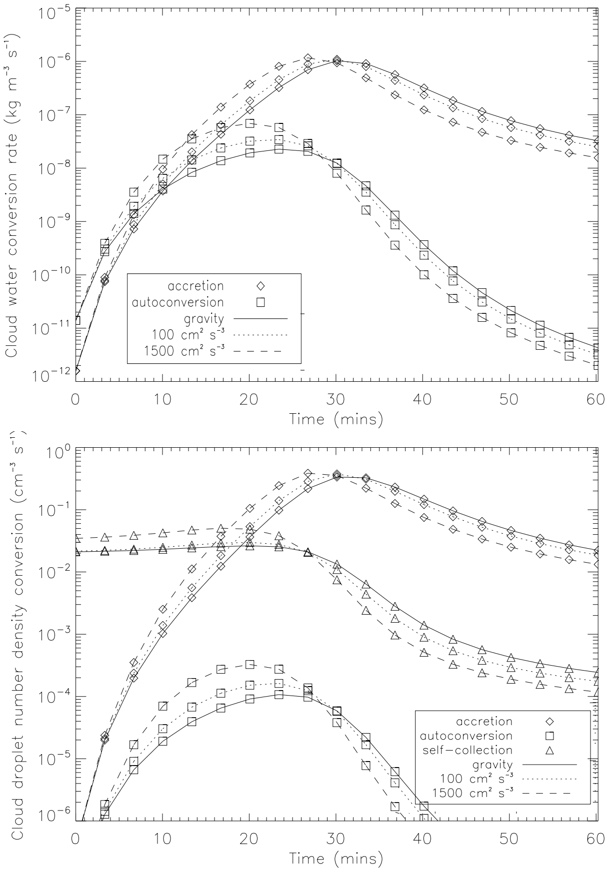

Figure 2a) Cloud water conversion rates due to the processes of autoconversion and accretion for the gravitational only case and the lowest and highest levels of turbulence. b) As for a) except for the cloud number density conversion rates due to autoconversion, accretion and self-collection.

Figure 2a shows the cloud water conversion rate due to the processes of autoconversion and accretion for a case with the initial conditions specified as a liquid water content of 1 g m^{-3}, a dispersion of the drop size distribution of 0.4 and an initial number concentration of 300 drops cm^{-3}. Plotted are the autoconversion and accretion rates as a function of time for the purely gravitational case and the least and most energetic turbulence cases (i.e. dissipation rates of TKE equal to 100 and 1500 $cm^2 s^{-3}$). Fig. 2a shows that autoconversion rates are greater than accretion rates over the first 10 minutes of the simulation for the gravity only case and this increases by a few minutes for the most turbulent case. The effect of turbulence is to increase the autoconversion and accretion rates initially as the rates are increasing, however, once the rates start to decline after about 30 minutes, the rates for the turbulent cases become less than the gravitational rate. This is because more mass has already been transferred from cloud droplets to raindrops in the turbulent cases and to maintain mass conservation the rates slow compared to the gravitational case. For the case shown in Fig. 2a turbulence increases the autoconversion rate by up to an order of magnitude, with a significant increase shown after only 5 minutes. The increase between the non-turbulent case and the turbulence cases is relatively larger for autoconversion as compared to accretion. This is due to the autoconversion rates being governed only by small droplet collisions and, therefore, being more sensitive to the increased collision rates when turbulence is included in the microphysics parameterisations.

Figure 2b shows the cloud number density conversion rates due to the processes of autoconversion, accretion and self-collection. For both cases the rate at which the number density of cloud droplets decreases is initially governed by self-collection. At the start of the simulations autoconversion and accretion are unable to change the number density significantly since large cloud droplets are few in number. Once the self-collection of cloud droplets has been acting to produce cloud drops of a larger size, then the autoconversion process can begin, and it is this process only that can generate a raindrop. Once the drop size distribution has evolved to include a reasonable number of raindrops, accretion takes over as the dominant process in deleting the cloud droplets. As for the cloud water conversion rates, the effect of turbulence on the number density conversion rates is initially to accelerate the loss of cloud droplets compared to the purely gravitational case. Similarly to the cloud water conversion rates, the number density conversion rates show that turbulence has the greatest relative increase for the autoconversion process. The difference between the non-turbulent and the least turbulent case is small for the change in number concentration due to self-collection but significant for the most turbulent case.

5. COMPARISON OF THE AUTOCONVERSION MODEL WITH OTHER SCHEMES

The autoconversion process is highly nonlinear and the typical rates cover over 14 orders of magnitude, therefore, it is a difficult task for an equation that can be easily implemented in atmospheric models to describe the autoconversion rates accurately over such a wide range of parameters and not surprisingly the predicted rates can vary significantly from the SCE rates. Due to the complexity of the problem there are many existing autoconversion models that have been developed with differing assumptions and this adds to the disparity that can be seen in the predicted autoconversion rates. With the current research focus on cloud-aerosol interactions there is a real need for more work to be done in this area to increase our understanding of the autoconversion process both in the representation of the solution of the SCE and also in the way that these parameterisations are implemented in atmospheric models.

An example of the range of predicted autoconversion rates and the comparison with the numerically calculated SCE rates is shown in Figure 3. The newly developed gravity only autoconversion parameterisation is used in this comparison since the other existing autoconversion parameterisations are based on the droplet motion being governed only by gravitational acceleration. In this figure the cloud liquid water content used is 0.5 g m^{-3}, the initial cloud droplet number concentration is 50 drops cm^{-3} and the initial value of the relative dispersion of the drop size distribution is equal to 0.4. The autoconversion rates from numerous autoconversion models have been calculated and are compared with the solution of the autoconversion rate directly computed by the SCE.

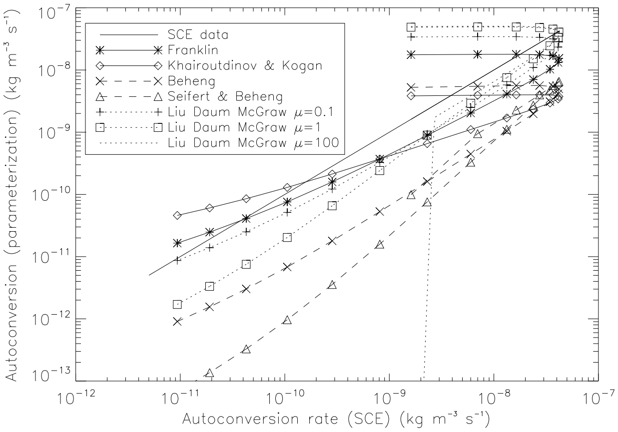

Figure 3. Comparison of the autoconversion rates derived from the SCE with various parameterisations.

It needs to be stressed here that this comparison is biased towards those models that use a separation radius of 40 µm (Franklin, Beheng, Seifert and Beheng) since this is the value that has been used to define the autoconversion process in the SCE. For a description of the autoconversion parameterisations, including details of their derivation see individual references or the summary in Franklin (2008). The approach taken by Beheng (1994) has been adopted in the development of the parameterisation herein. The differences between Beheng's model and the one here include the use of a different numerical solver, a wider range of initial states particularly lower liquid water contents in the newly developed model, the explicit parameter for the relative width of the drop spectrum in Beheng's model and the use of a turbulent collision kernel in the new model. The approach of Beheng is the only one to follow if there is no analytical approximation to the collision kernel that can be derived and as yet there is no such form of a turbulent collision kernel. Seifert and Beheng (2001) developed an autoconversion parameterisation that uses Long's (1974) polynomial approximation of the collection kernel and a correction to this in the form of a time dependent function that was estimated from numerically solving the SCE. Khairoutdinov and Kogan's (2000) model was developed from empirical fits from large eddy simulations of stratocumulus with explicit microphysics. The results of Liu et al. (2006) overestimate the autoconversion rate at the initial times when the SCE rate increases. This is mainly due to the inclusion of self collection of cloud droplets in their autoconversion formulation, which describes the total rate of mass coalescence as discussed by Wood and Blossey (2005). The newly developed parameterisation overcomes the tendency of autoconversion models to underestimate the lower range of autoconversion rates, however, this means that the new model can overestimate these rates for other sets of initial conditions (see Franklin 2008). The new model generally produces accurate autoconversion rates for a broad range of cloud conditions and in comparison with some other models has the potential to reduce the errors associated with modelling autoconversion. The inclusion of turbulence effects in the parameterisation allows for the investigation of the effect of differing turbulence intensities on cloud properties.

6. SUMMARY AND DISCUSSION

The effect of turbulence on the warm cloud microphysical processes of autoconversion, accretion and self-collection has been investigated by the use of a turbulent collision kernel (Franklin et al. 2007) in numerical solutions of the SCE. For the integrations of the SCE the effect of turbulence was applied for collector droplets in the radius range of 10 – 30 μm and outside of this range the turbulence effect was considered to be zero. While there will be some effect of turbulence outside of the range that is applied here, at the present time there is no DNS data for the turbulent flow parameters of interest in this study and applying an arbitrary function at the ends of the parameterisation of Franklin et al. (2007) to act as an asymptote was deemed unsatisfactory. It was decided that the best approach was to apply the parameterisation only where it is valid and underestimate the effects of turbulence rather than potentially overestimating these effects. The results show that turbulence can significantly reduce the time to the production of drizzle size drops. Even relatively weak turbulence with an eddy dissipation rate of TKE of 100 $cm^2 s^{-3}$ can increase the percentage of mass that is transferred to drop sizes greater than 40 μm after 20 minutes by more than 20% compared to the purely gravitational collision kernel.

Solutions of the SCE under a wide range of cloud liquid water contents, cloud droplet number concentrations and relative dispersions of the drop size distribution have been used to develop a new double moment microphysics parameterisation that includes the effect of turbulence. Using the SCE results for such a broad range of drop size distributions gives the resulting parameterisations greater statistical meaning and applicability. Although the autoconversion rates are not the highest compared to the mass and number density conversion rates from accretion and self-collection, without autoconversion there would be no initial generation of raindrops and therefore, no accretion or self-collection of raindrops. It is the process of autoconversion that is critical in the initial development of raindrops and it is, therefore, imperative to have a better understanding of this process and how it is influenced by atmospheric turbulence to enable a more accurate representation in numerical models. The developed warm rain microphysics parameterisation is a tool that allows the investigation of the effect of differing turbulence intensities on the microphysical processes and the resulting feedbacks in atmospheric models.

It needs to be emphasized that the parameterisations developed herein use the gravitational collision efficiencies in the solutions of the SCE because a parameterisation of the effect of turbulence on the collision efficiencies is yet to be developed. It was shown by Franklin (2008) that if turbulence acts to moderately increase the collision efficiencies between on average 10 and 30%, then the resulting parameterisations will not change a great deal. However, if the collision efficiencies are more strongly impacted by turbulent air flow and the increase is closer to an increase of 1.1 to 2.0 times the gravitational value, then the parameterisations will not capture the full effect of turbulence. The parameterisations developed in this study are separated into those for the gravity only or the non-turbulent case and those for the turbulent case. For the turbulent case the parameterisations are valid for the dissipations rates of TKE ranging from 100 to 1500 cm^2 s^{-3}. In addition to the above caveats, the warm rain parameterisations that include the effect of turbulence are based on a turbulent collision kernel that was developed from DNS that cannot, at this point in time, give an indication of the sensitivity of the results to increasing flow Reynolds numbers. Due to computational restraints DNS are limited in the range of Reynolds numbers that they can achieve. At the present time it is unclear if or how the collision rates will change with increasing Reynolds numbers (for a detailed discussion on the possible effects see Franklin et al. (2007)), however this uncertainty should be considered when interpreting results based on these parameterisations derived from DNS data.

7. BIBLIOGRAPHY

Albrecht, B.A., 1989: Aerosols, cloud microphysics, and fractional cloudiness. *Science*, 245, 1227-1230.

Beard, K.V. and H.T. Ochs, 1993: Warm-rain initiation: An overview of microphysical mechanisms. *J. Appl. Meteor.,* 32, 608-625.

Beheng, K.D., 1994: A parameterization of warm cloud microphysical conversion processes. *Atmos. Res.,* 33, 193-206.

Bott, A., 1998: A flux method for the numerical solution of the stochastic collection equation. *J. Atmos. Sci.,* 55, 2284-2293.

Bott, A., 2000: A flux method for the numerical solution of the stochastic collection equation: Extension to two-dimensional particle distributions. *J. Atmos. Sci.,* 57, 284-294.

Franklin, C.N., P.A. Vaillancourt, M.K. Yau, and P. Bartello, 2005: Collision rates of cloud droplets in turbulent flow. *J. Atmos. Sci.,* 62, 2451-2466.

Franklin, C.N., P.A. Vaillancourt, and M.K. Yau, 2007: Statistics and parameterizations of the effect of turbulence on the geometric collision kernel of cloud droplets. *J. Atmos. Sci.,* 64**,** 938-945.

Franklin, C.N., 2008: A warm rain microphysics parameterization that includes the effects of turbulence. *J. Atmos. Sci.,* in press.

Hall, W.D., 1980: A detailed microphysical model with a two-dimensional dynamic framework: Model description and preliminary results. *J. Atmos. Sci.,* 37, 2486-2507.

Khairoutdinov, M. and Y. Kogan, 2000: A new cloud physics parameterization in a large-eddy simulation model of marine stratocumulus. *J. Atmos. Sci.,* 57, 229-243.

Liu, Y., P.H. Daum, R. McGraw, and R. Wood, 2006: Parameterization of the autoconversion process. Part II: Generalization of Sundqvist-type parameterization. *J. Atmos. Sci.,* 63, 1103-1109.

Long, A.B., 1974: Solutions to the droplet collection equation for polynomial kernels. *J. Atmos. Sci.,* 31, 1040-1052.

Pinsky, M.B., A.P. Khain, B. Grits and M. Shapiro, 2006: Collisions of small drops in a turbulent flow. Part III: Relative droplet fluxes and swept volumes. *J. Atmos. Sci.,* 63, 2123-2139.

Rotstayn, L.D., and Y. Liu, 2005: A smaller global estimate of the second indirect aerosol effect. *Geophys. Res. Lett.,* 32, L05708, doi:10.1029/2004GL021922.

Seifert, A., and K.D. Beheng, 2001: A double-moment parameterization for simulating autoconversion, accretion and selfcollection. *Atmos. Res.,* 59-60, 265-281.

Wang, L.-P., O. Ayala, S.E. Kasprzak and W.W. Grabowski, 2005: Theoretical formulation of collision rate and collision efficiency of hydrodynamically interacting cloud droplets in turbulent atmosphere. *J. Atmos. Sci.,* 62, 2433-2450.

Wood, R., and P. Blossey, 2005: Comments on *"Parameterization of the autoconversion process. Part I: Analytical formulation of the Kessler-type parameterizations." J. Amos. Sci.,* 62, 3003-3006.

Acknowledgements

This work was supported by the Australian Greenhouse Office. I would like to thank Prof Peter Yau and Dr Paul Vaillancourt for many stimulating discussions on this subject.

LAGRANGIAN OBSERVATIONS OF INERTIAL, SETTLING CLOUD DROPLETS IN TURBULENT FLOW

J. P. Fugal[1], J. Lu[1], H. Nordsiek[1], E. W. Saw[1], and R.A. Shaw[1]

[1]Department of Physics, Michigan Technological University, Houghton, Michigan 49931, USA

1. ABSTRACT

We have designed a laboratory system for studying Lagrangian statistics of cloud droplets in homogeneous, isotropic turbulence. Turbulence is produced through the interaction of eight air jets such that the energy dissipation rate is an externally controlled parameter. With appropriate choice of droplet size we are able to match the flow and particle conditions relevant to the collision rate of cloud and drizzle droplets in turbulent clouds (e.g., particle Stokes number and gravitational settling parameter). Two methods for particle tracking are used, both based on digital in-line holography. The first is a combination of stereo-imaging and holography using two cameras. The second uses a single holographic system with depth resolution improved by temporal averaging of particle position. These approaches provide a tool for quantifying the 3-D Lagrangian properties of inertial particles with finite settling speed in homogeneous isotropic turbulence. Specifically, single-particle and particle-pair statistics, including Lagrangian velocity, relative velocity, and acceleration are obtained directly from the measured droplet trajectories. Initial results show that the distribution of Lagrangian droplet speeds relative to the quiescent settling speed broadens with increasing turbulence intensity, with values much greater than 1 observed. The distributions of speeds and angles with which droplet pairs approach each other clearly show the transition from gravitationally-dominated to turbulence-dominated regimes.

2. TURBULENCE AND GRAVITATIONAL SETTLING OF CLOUD PARTICLES

Atmospheric clouds are an important part of Earth's climate system, strongly modulating balances of visible and infrared radiation as well as the distribution of water over the globe. A primary mechanism by which cloud particle size distributions evolve is through the collision and coalescence of cloud drops. Most contemporary models of this process are based on collision rates resulting from differential gravitational sedimentation of drops: i.e., large drops sweeping up small drops. But clouds are also turbulent and there are several ways by which turbulence could modify the particle collision rate (Vaillancourt and Yau 2000, Shaw 2003). The ultimate goal of this work is to understand the transition regime between a gravitationally-dominated system (weak or nonexistent turbulence, such as in a stable fog) and a turbulence-dominated system (intense turbulence, such as in many industrial flows). The system can be described by two dimensionless parameters, the drop Stokes number St and the Settling parameter Sv, defined as

$$St = \frac{\tau_d}{\tau_K}$$

and

$$Sv = \frac{v_T}{v_K},$$

Corresponding author's address: Raymond A. Shaw, Department of Physics, 1400 Townsend Drive, Houghton, MI 49931 USA, email: rashaw@mtu.edu

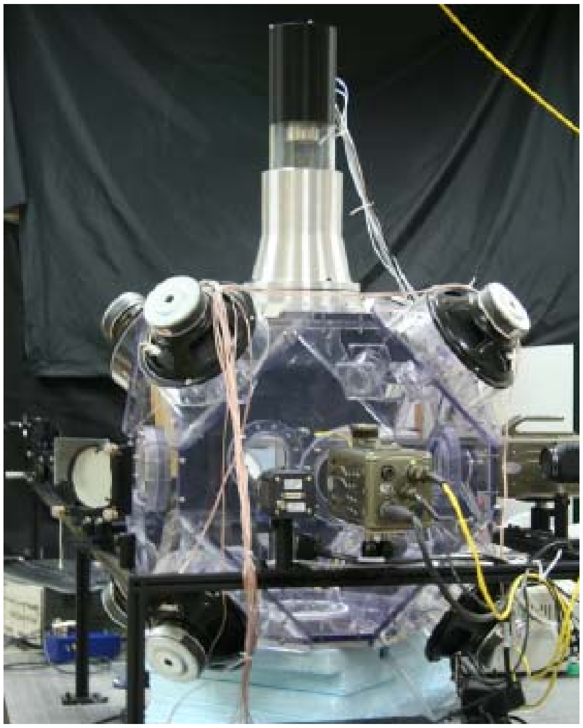

Figure 1. Photograph of the turbulence chamber (Plexiglas cube with speakers on each vertex) with the droplet generator above and the two high-frame-rate cameras (green, to the right and in front of the chamber).

where τ_d is the droplet inertial time scale, τ_K is the Kolmogorov time scale, v_T is the terminal velocity, and v_K is the Kolmogorov velocity (Vaillancourt and Yau 2000). Typical values for cloud drops with radius 2 to 50 micrometers are $10^{-4} \le St \le 2$ and $0.03 \le Sv \le 120$. In the present study we have investigated the regions of that parameter space corresponding to large cloud drops with $0.3 \le St \le 5$ and $3 \le Sv \le 13$. In this study we used 5 levels of energy to drive the turbulence, labeled Turb0 to Turb4, increasing with power level. Our estimated Stokes numbers for those levels are respectively 0.3, 0.5, 1.2, 3.0 and 4.8 and estimated settling parameters are respectively 12.9, 10.3, 6.7, 4.3, and 3.4.

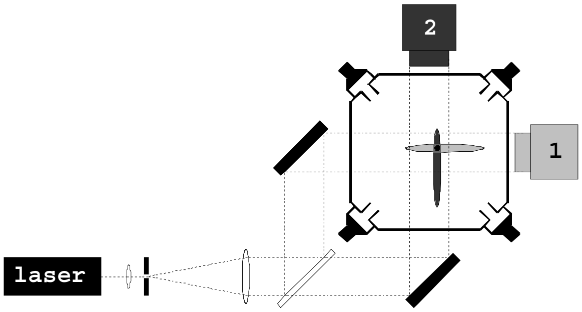

Figure 2. Schematic diagram of the optical setup for the turbulence chamber. The laser beam passes through a spatial filter and is collimated and directed through the center of the turbulence chamber to two digital cameras. Each camera provides a hologram that, upon digital reconstruction, provides an independent estimate of the particle position, shown schematically by the gray and black prolate spheroids. The actual particle position is signified by the black dot.

3. TURBULENCE CHAMBER AND HOLOGRAPHIC TRACKING

The experimental system used for obtaining Lagrangian droplet tracks is shown in Figure 1, and consists of a turbulence chamber, a droplet generator, and a dual-path digitial holographic system. The center of the chamber is designed to have nearly isotropic turbulence without a mean flow. The turbulence is produced by eight speaker-driven jets pointed at the center of the chamber. The speakers are driven with a random binary signal so as to produce uncorrelated driving vorticies. Droplets in the size range of approximately 50 to 120 μm diameter are introduced at the top of the chamber using a vibrating orifice aerosol generator (TSI Model 3450) and then fall through the turbulence in the chamber. Two high frame rate cameras (2500 fps) in a cross-beam configuration as shown in Figure 2 are illuminated by a pulsed Nd:YLF laser (20 ns pulse of wavelength 527 nm) and record holograms of the droplets in the center of the chamber. The sample volume is approximately $1.5 \times 1.7 \times 1.7$ cm^3. A computer cluster reconstructs the

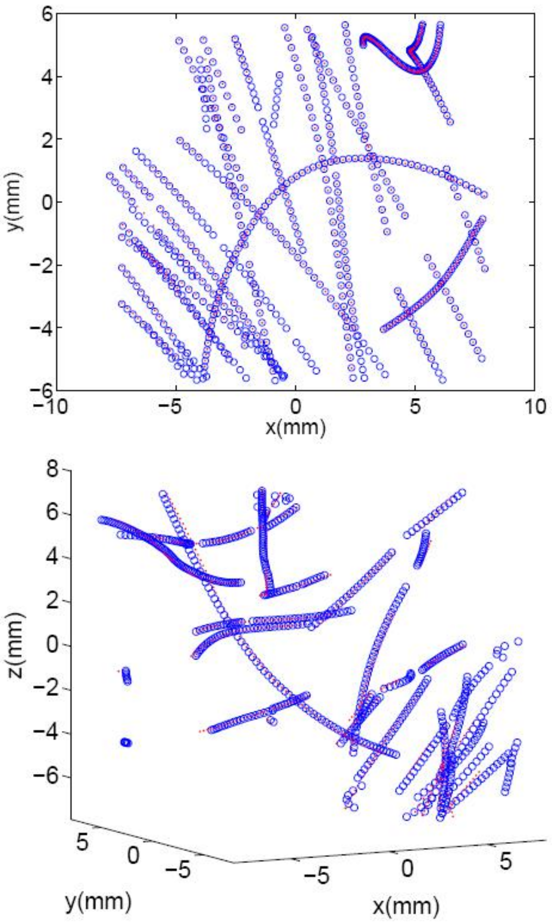

Figure 3. Examples of Lagrangian droplet tracks. Blue circles are results from the two-camera tracking and red dots are results from the one-camera tracking.

holograms and finds the positions of the particles, matches the particles as seen by each camera, and calculates the particle tracks (Lu et al. 2008).

An example of the resulting Lagrangian particle tracks is shown in Figure 3. Two tracking methods have been tested. A two-camera method allows orthogonal views to overcome the relatively poor depth resolution of holography (see Figure 2) and thereby produce particle tracks with subpixel resolution. This level of resolution is required for estimating Lagrangian accelerations. In many applications, such as outside of the laboratory, it is desirable to use only a single camera, so we also have developed a single-camera tracking algorithm that is able to overcome some of the depth resolution limitations (Lu et al. 2008). The tracks shown in Figure 3 are from both the two camera (blue circles) and the one-camera (red dots) tracking methods and it can be seen that the comparison is excellent in the two lateral directions, and acceptable in the depth direction (single camera coordinates).

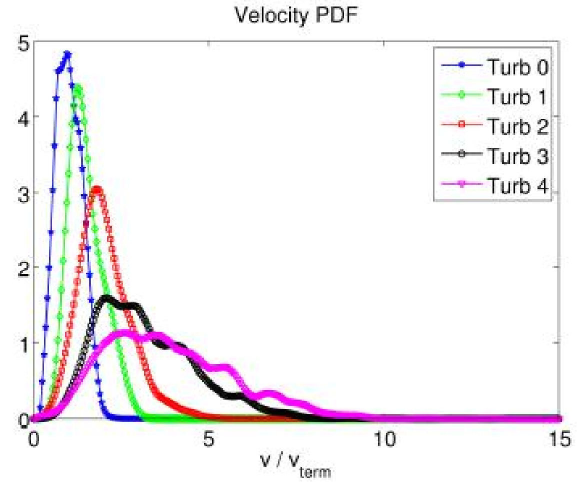

Figure 4. Magnitude of droplet Lagrangian velocity vectors normalized by the terminal speed (in a quiescent fluid).

4. LAGRANGIAN TURBULENCE STATISTICS

Results of the Lagrangian tracking experiments are summarized here in a series of figures. Each figure displays five curves, ranging from very weak to quite vigorous turbulence (see Section 2). Figure 4 shows the distribution of the Lagrangian drop velocity magnitude relative to the terminal speed for the average drop size. As turbulence intensity decreases the distribution approaches that of the terminal velocities of the size distribution. (Note that the standard deviation of droplet diameter relative to the mean diameter is approximately 10%.) Even at moderate turbulence levels velocity magnitudes several times the terminal velocity are observed with significant probability.

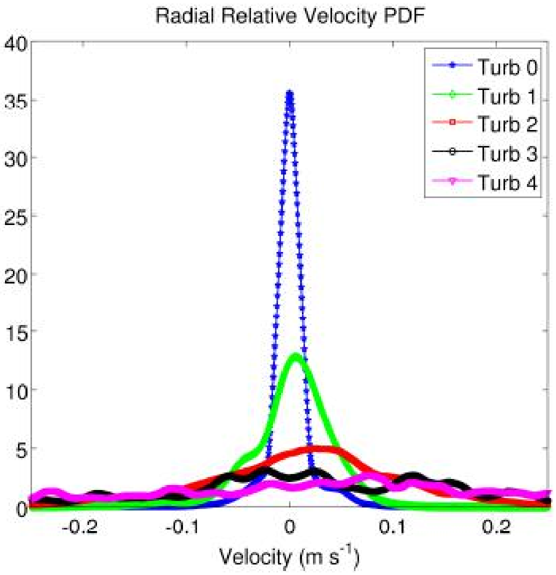

Figure 5. Distribution of the radial component of the relative Lagrangian velocity for droplet pairs within the dissipation range ($r < 20r_K$).

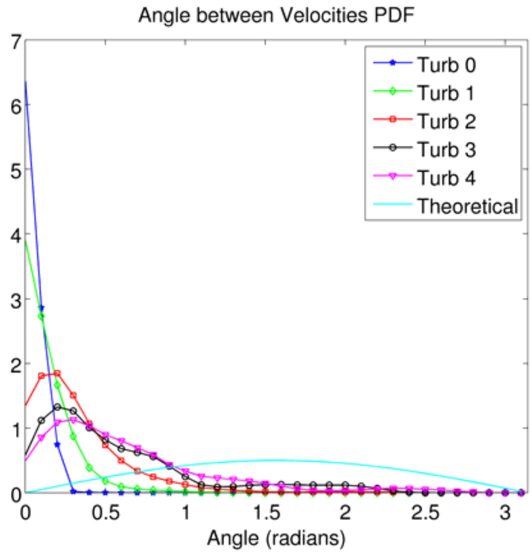

Figure 6. Distribution of angles between Lagrangian velocity vectors of droplet pairs within the dissipation range ($r < 20r_K$).

Droplet relative velocities are of direct relevance to the collision-coalescence process in clouds, but due to the very low number densities in our experiment it is not yet practical to make direct observations of the droplet collisions. We are able, however, to find statistically significant numbers of droplets separated by distances within the viscous subrange, in which droplet relative velocity should scale linearly (e.g., Kostinski and Shaw 2005). For droplets within the viscous subrange distributions of relative velocity magnitude and relative velocity angle are shown in Figure 5 and Figure 6, respectively. The "theoretical" curve for an isotropic distribution of velocity vectors, such as one might expect for a fluid element, is shown in Figure 6 for comparison. Note that for a purely gravitational system the distribution would be a delta function at an angle of zero degrees, and the transition from a delta-like distribution toward an isotropic distribution can be seen clearly as the relative role of turbulence to gravity is increased.

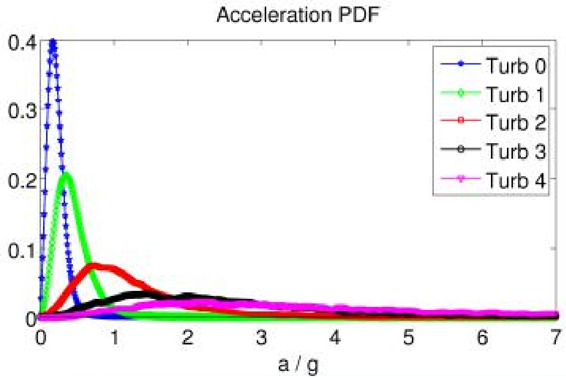

Figure 7. Magnitude of droplet Lagrangian acceleration vectors normalized by the acceleration due to gravity.

Finally, the distribution of the Lagrangian drop acceleration magnitude is shown in Figure 7, relative to the gravitational acceleration. Again, the growing role of turbulence is clearly demonstrated with increasing energy input. Accelerations more than two times that of gravity are regularly observed even for moderate turbulence levels.

Acknowledgements

We thank D. Cook and J. Nordeng for their help in building the chamber. We thank B. Suits for his advice on the circuit to drive the speakers. We are grateful our collaboration with E. Bodenschatz, L. Collins, and Z. Warhaft through the International Collaboration for Turbulence Research (ICTR) through which we obtained the high frame rate cameras to take the holograms. This work was supported by the National Science Foundation, Physical Meteorology Program.

REFERENCES

Fugal, J. P., R. A. Shaw, E. W. Saw, and A. V. Sergeyev, 2004: Airborne digital holographic system for cloud particle measurements. *Appl. Opt.* **43**, 5987-5995.

Hwang, W., and J. K. Eaton, 2004: Creating homogeneous and isotropic turbulence without a mean flow. *Exp. Fluids*, **36**, 444-454.

Kostinski, A. B. and R. A. Shaw, 2005: Fluctuations and luck in droplet growth by coalescence. *Bull. Amer. Meteor. Soc.* **86**, 235-244.

Lu, J., J. P. Fugal, H. Nordsiek, E. W. Saw, R. A. Shaw, and W. Yang, 2008: Lagrangian particle tracking in three dimensions via single-camera in-line digital holography. Submitted to *New J. Phys.*

Ouellette, N. T., H. Xu, and E. Bodenschatz, 2006: A quantitative study of three-dimensional Lagrangian particle tracking algorithms. *Exp. Fluids*, **40**, 301-313.

Shaw, R. A., 2003: Particle-turbulence interactions in atmospheric clouds. *Ann. Rev. Fluid Mech.*, **35**, 183-227.

Sheng, J., E. Malkiel, and J. Katz, 2006: Digital holographic microscope for measuring three-dimensional particle distributions and motions. *Appl. Opt.*, **45**, 3893-3901.

Vaillancourt, P., and M. K. Yau, 2000: Review of particle-turbulence interactions and consequences for cloud physics. *Bull. Amer. Meteor. Soc.* **81**, 285-298.

THE MAXIMUM SIZE OF RAINDROPS
– CAN IT BE A PROXY OF PRECIPITATION CLIMATOLOGY ? –

Y. Fujiyoshi[1], I. Yamamura[2], N. Nagumo[3], K. Nakagawa[4], K. Muramoto[5], and T. Shimomai[6]

[1]Inst. Low Temp. Sci., Hokkaido Univ., Sapporo, JAPAN
[2]Graduate School of Environmental Science, Hokkaido Univ., Sapporo, JAPAN
[3]Sendai District Meteorological Observatory, Japan Meteorological Agency, Sendai, JAPAN
[4]National Institute for Information and Communications Technology, Okinawa, JAPAN
[5]Graduate School of Natural Science & Technology, Kanazawa Univ., Kanazawa, JAPAN
[6] Department of Electronic and Control Systems Engineering, Shimane Univ., Shimane, JAPAN

1. INTRODUCTION

Recent high-resolution cloud-resolving models require a bin model because cloud dynamics, cloud life, and the timing and area of rainfall differ between bulk and bin models (e.g., Seifert et al., 2005). The number of large raindrops decreases dramatically and deviates from a Marshall-Palmer distribution when collision coalescence and breakup processes are included in microphysical models (Hu and Srivastava, 1995). However, Beard et al. (1986) measured raindrops with maximum dimensions of up to 8 mm in a shallow convective rainband. Hobbs and Rangno (2004) also reported super-large raindrops with maximum dimensions of at least 8.8 mm and possibly 10 mm. Beard et al. (1986) and Hobbs and Rangno (2004) used a PMS 2D-P and were not able to show full images of large raindrops. Using precipitation particle image sensors (PPIS), Takahashi et al. (1995) obtained clear images of large raindrops with maximum horizontal dimensions of 10 mm in tropical clouds.

There have been extensive reports and discussions about raindrop size distributions (RSD; e.g., Marshall and Palmer, 1948; Jameson and Kostinski, 2001). However, no statistical and systematic study has been conducted on the maximum size of raindrops. There are two possible reasons for this situation. First, because drops larger than approximately 10 mm in diameter break up spontaneously (Pruppacher and Pitter, 1971), the maximum diameter of raindrops should be limited and of little scientific interest. Second, because the number of raindrops decreases exponentially with size, it is quite difficult to conclude that the measured largest raindrop is the largest raindrop of a rainfall event under spatially and temporally limited observations.

The recent invention of automated

disdrometers allows the measurement of raindrop size distributions continuously whenever rainfall occurs. However, impact-type (Joss and Waldvogel, 1967) and one-dimensional optical disdrometers and remote sensors such as vertically pointing FMCW radar, wind profilers, and polarimetric radar cannot be used to determine the exact size and shape of individual raindrops. They provide only rough or statistical RSDs. However, with the advent of the two-dimensional video disdrometer (2DVD; Schönhuber et al., 1997), raindrop size, shape, drop axis ratio (oblateness), canting angle, and velocity can be measured (Kruger and Krajewski, 2002).

2. 2DVD MEASUREMENTS AND LARGE RAINDROPS AT SAPPORO, OKINAWA, AND SUMATRA

We examined three different climatic regimes: Sapporo (subarctic region) and Okinawa (subtropical region) in Japan, and Sumatra (tropical region) in Indonesia. The 2DVD data were collected over a 4-year period from 2003 to 2006 at Sapporo (subarctic region), over a 3-year period from 2004 to 2006 at Okinawa (subtropical region) and over a 2-year period from 2005 to 2006 at Sumatra (tropical region). We used 2DVD data from April to November at Sapporo because snow particles comprise most of the precipitation from December to March.

The largest raindrops (Fig. 1) were selected from several billion raindrops. The maximum equivolumetric sphere diameters were 7.42, 7.73, and 8.59 mm at Sapporo, Okinawa, and Sumatra respectively. Most of the raindrops had an oblate shape that was almost in equilibrium (Beard and Chuang, 1987), but some had pure vertical- and mixed-phase modes (Bringi et al., 2003).

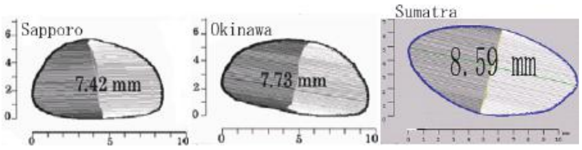

Fig. 1 Images of the largest raindrops observed at Sapporo, Okinawa, and Sumatra. The numbers indicate the equivolmetric sphere diameter.

3. APPEARANCE FREQUENCY OF THE DAILY MAXIMUM SIZE OF RAINDROPS

Because the number density of raindrops decreases exponentially with size, the detection probability decreases with increasing raindrop size. Thus, the total number of raindrops might affect the maximum size of the measured raindrops. We investigated the relationship between the maximum diameter and total number of raindrops (TNR) > 0.1 mm in diameter. Hereafter, we refer to the daily maximum diameter of raindrops as the maximum size of raindrops (MSR). The MSR increased with increasing TNR when TNR was less than approximately 5 x 10^4. In contrast, the MSR was almost independent of TNR when TNR was > 5 x 10^4. The relationship between MSR and TNR was similar at three sites of observation. We examined these large data sets to examine seasonal and diurnal variation in the MSR in the following sections only when TNR was > 5 x 10^4.

Figure 2 shows MSR appearance frequencies at Sapporo, Okinawa and Sumatra. They were well represented by a Gaussian form that peaked at approximately 3.5–4.5 mm in diameter at three sites, as reported previously (e.g., Mason, 1971). The frequency of MSR $\geq$ 5.5 mm decreased dramatically at Sapporo, but remained high at Okinawa and Sumatra. Conversely, the frequency of MSR < 3 mm decreased dramatically at Okinawa, but remained relatively high at Sapporo and Sumatra.

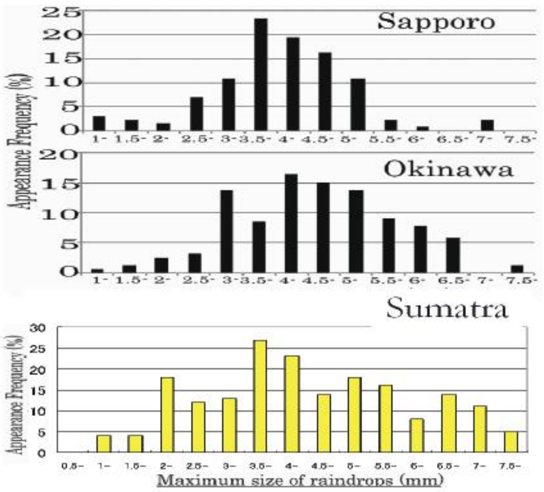

Fig. 2 Appearance frequencies (%) of the daily maximum diameter of raindrops at Sapporo, Okinawa and Sumatra.

4. SEASONAL CHNAGFES IN MAXIMUM SIZE OF RAINDROPS

The 30 largest raindrops of all raindrops measured at three sites showed a clear seasonal cycle (Fig. 3). The number of raindrops included in these 30 largest raindrops was highest in summer (June, July, and August) at Okinawa, but was highest in autumn (October) at Sapporo. This suggests that thermal (i.e., solar radiation) and dynamical (i.e., synoptic-scale disturbance) effects are the major contributors to strong convection at Okinawa and Sapporo, respectively. There are two peaks (April and September) at Sumatra, corresponding to rainy seasons.

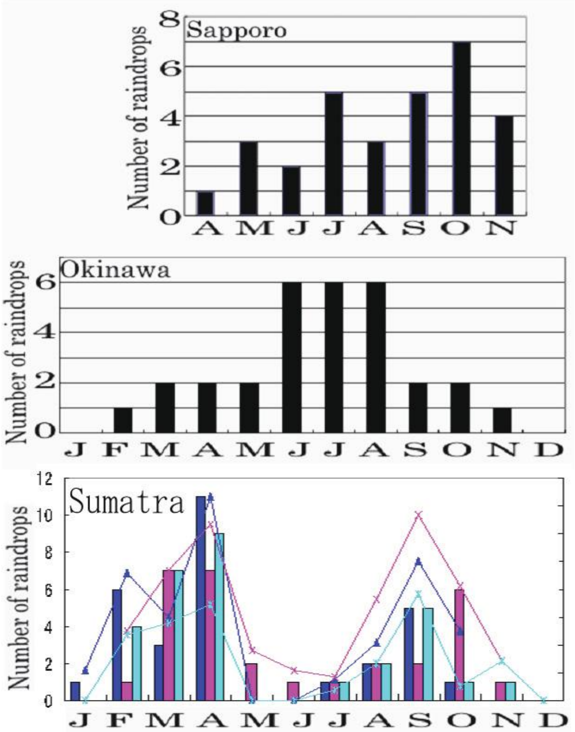

Fig. 3 Seasonal change in the number of raindrops included in the 30 largest raindrops among all raindrops measured at Sapporo, Okinawa and Sumatra.

Contrasting types of cloud create various raindrop size distributions, i.e., low-level layer clouds generate small raindrops and well-developed convective clouds generate large raindrops. Therefore, seasonal changes in the MSR might infer seasonal changes in the predominant types of rain cloud. We classified the MSR into three categories: small ($0.5\,mm \leq \mathrm{MSR} < 3.5\,mm$), medium ($3.5\,mm \leq \mathrm{MSR} < 5.5\,mm$), and large ($\mathrm{MSR} \geq 5.5\,mm$). The relative frequency of appearance of these three categories at Sapporo clearly changed seasonally: the appearance frequency of medium and large raindrops was highest in October, whereas that of small raindrops was highest in April. Okinawa showed seasonal changes that were distinct from those at Sapporo; the appearance frequency of medium and large raindrops was highest in August, whereas that of small raindrops was highest in winter. At Sumatra, the appearance frequency of medium and large raindrops was high in rainy seasons (April and September), whereas that of small raindrops was high in dry season.

5. DIURNAL CHANGES IN THE MSR

Diurnal changes in convective activity, precipitation, and raindrop size distributions have been reported for various climatic regimes (e.g., Fujibe, 1988; Nitta and Sekine, 1994; Dai, 2001; Kozu, et al., 2006). Peaks in these variables often occur in the late afternoon and between midnight and early morning, although the amplitude of peaks changes with climatic regime and season.

To study diurnal changes in the MSR, we checked the time at which the MSR was observed and counted the total number of occurrences in 3-h intervals (Fig. 4). The MSR tended to be higher between midnight and early morning (21–06 LST) at Sapporo (Fig. 4a), the MSR was higher in both the late afternoon (12–15 LST) and at around midnight (21–03 LST) at Okinawa (Fig. 4b), and the MSR was the highest in late afternoon (15– 18 LST) at Sumatra (Fig. 4c).

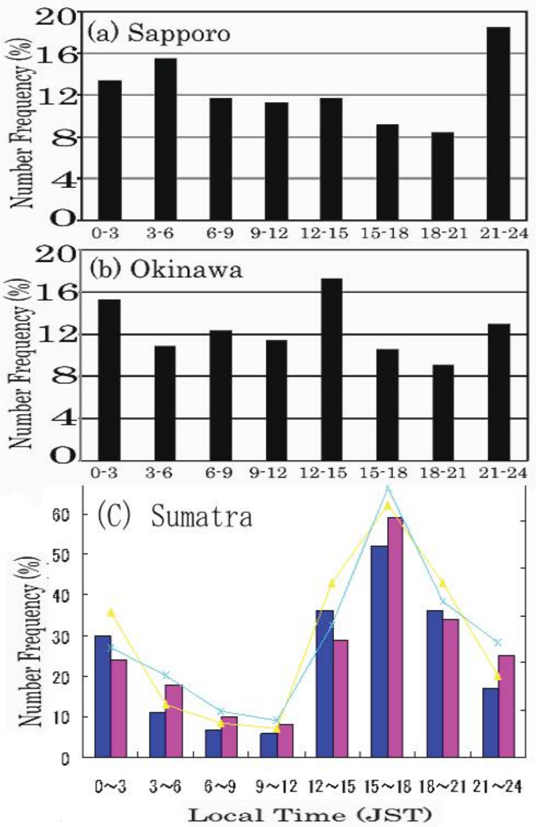

Fig. 4 Diurnal change of the occurrence frequency of the 3-h interval in which the daily maximum size of raindrops was observed at Sapporo, Okinawa, and Sumatra.

6. DISCUSSIONS

Hereafter, for convenience, we refer to raindrops with diameters between 6.5 and 7.0 mm and > 7.0 mm in equivolumetric sphere diameter as very large and super-large raindrops, respectively.

6.1 Do large raindrops fall at the very beginning of rainfall?

It is our experience that large raindrops fall at the very beginning of rainfall events, especially from shower clouds. Thus, we examined the validity of this experience. First, we selected five days on which very large raindrops were observed at Sapporo and Okinawa. Very large raindrops were not necessarily found during periods of heavy rainfall, but were often found at the beginning of rainfall events or after a pause in rainfall, as expected. Beard et al. (1986) noted that large raindrops can survive a fall of several kilometers when the concentration of small raindrops is low enough, which might explain our results.

6.2 Do large raindrops fall together?

We then checked the periods during which more than three large raindrops (≥ 6.0 mm) were found. Large raindrops fell in short periods lasting from 2 seconds at Okinawa to 149 seconds at Sapporo, when the number of large raindrops was exceptionally high from a statistical point of view. For example, the 12 largest MSRs came from raindrops that fell within 18 s (17:14:08– 17:14:26) on 10 June 2004 at Sapporo.

Beard et al. (1986) found relatively high concentrations of large raindrops within a precipitation shaft. Hobbs and Rangno (2004) surmised that super-large raindrops fall in very short-lived vertical filaments that are tens of meters across, which are known as rainshafts. Unfortunately, we made no simultaneous radar observations with 2DVD measurements. However, we succeeded in observing a rainshaft using a scanning coherent Doppler lidar (Mitsubishi Electric Co. Ltd.) at Sapporo. In vertical cross sections of S/N ratios and Doppler velocities at 14:00 JST on 23 June 2005, when a thunder cloud passed over the observation site, a strong echo 1 km in length and 200 m in width was clearly observed below the cloud base (Fig. 5). The Doppler velocity of this rainshaft exceeded 10 m s^{-1} (maximum Doppler velocity was 12.7 m s^{-1}), and time sequences of Doppler lidar images indicated that the fall velocity of this shaft was about 10 m s^{-1}. Thus, groups of large raindrops can fall from convective clouds as a narrow rainshaft. The head of the shaft forked into three branches (A, B, and C) that were somewhat similar to the high-reflectivity core that began falling approximately 10 min before each microburst (Fujita, 1992). Figures 5c and 6d indicate that Doppler velocities within branch C were larger than those within branch B, and those within branch B were larger than those within branch A. This result suggests that raindrops are sorted during their fall, even within a rainshaft, depending on their fall velocities. Interestingly, the height above ground level (AGL) of the maximum Doppler velocity (1100 m) was a few hundred meters higher than the location of the maximum value of the S/N ratio (900 m). This feature likely relates to the formation process of strong downdraft by a group of large raindrops (e.g., Feingold et al., 1991).

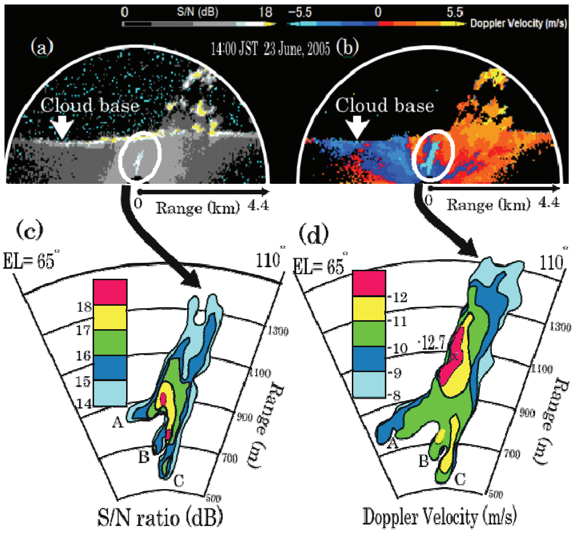

Fig. 5 Range elevation Indicator (REI) displays of (a) S/N ratios and (b) radial Doppler velocities observed by a scanning coherent Doppler lidar (Mitsubishi Electric Co. Ltd.) at 14:00 JST on 23 June 2005. Due to strong attenuation, no signals were detected above the cloud base. The lower panels show detailed structures of the (c) S/N ratios and (d) radial velocities. Negative velocity is motion downward.

6.3 How super-large raindrops are produced

It is necessary to understand how super-large raindrops are produced. Beard et al. (1986) and Hobbs and Rangno (2004) found super-large raindrops in warm, shallow convective clouds. They proposed that super-large raindrops may be produced by the rapid growth of drops that collide without breaking up, within small regions of a cloud in which the liquid water content is unusually high. At least at Sapporo, shallow, warm convective clouds were not common in October when the appearance frequency of large MSR was highest, although we cannot reject the process of collision–coalescence without break up.

Another possible process is the melting of solid hydrometeors (e.g., hailstones, graupels, and snowflakes), although the melting process of snowflakes has not yet been clarified (Fujiyoshi, 1986; Mitra et al., 1990; Fujiyoshi and Muramoto, 1996). Because large melting solid hydrometeors fall much faster than raindrops, they can survive when they fall at the very beginning of rainfall events as noted by Beard et al. (1986). They have less chance of survival when they fall during the later stages of rainfall events because of collisional break up during their fall. Using a UHF wind profiler, Kobayashi and Adachi (2001) found that raindrops > 6 mm in diameter almost disappeared during a fall from 3.25 to 3.0 km, which can be interpreted as the result of the raindrops breaking up.

We found evidence that the melting of large

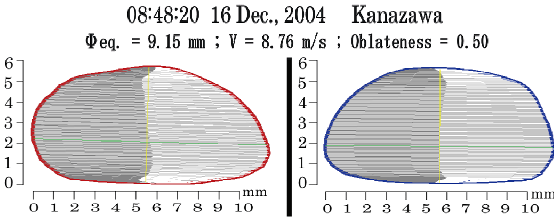

Fig. 6 The front- and side views of the largest raindrop observed at Kanazawa as well as its equivolumetric sphere diameter, vertical velocity, and oblateness.

graupels and snowflakes can produce super-large raindrops. We deployed the 2DVD disdrometer at Kanazawa, which is located in the central region of the main island of Japan facing the Sea of Japan. When the air temperature is > 0°C, melting solid hydrometeors and raindrops fall simultaneously, even in winter at Kanazawa. Super-large raindrops > 8 mm in diameter were not uncommon in winter, and the largest raindrop observed was 9.15 mm (Fig. 6).

Examples of large melting snow particles and raindrops observed on 11 and 25 January 2005 are shown in Fig. 7. On 11 January, both large melting graupels and super-large raindrops fell between 18:35 and 18:40 JST, when the surface air temperature ranged from 1 to 3°C (Fig. 7a). Most particles < 7 mm in diameter were raindrops. On 25 January, large melting snowflakes (we call the typical shape of melting snowflakes the "Mickey Mouse" shape), as well as super-large raindrops, fell between 00:24 and 00:34 JST, when the surface air temperature ranged from 7 to 8°C (Fig. 7b). Most particles < 8 mm in diameter were raindrops. The fall velocities of both melting graupels and large melting snowflakes were similar to those of super-large raindrops (approximately 8 ~ 9 m s^{-1}).

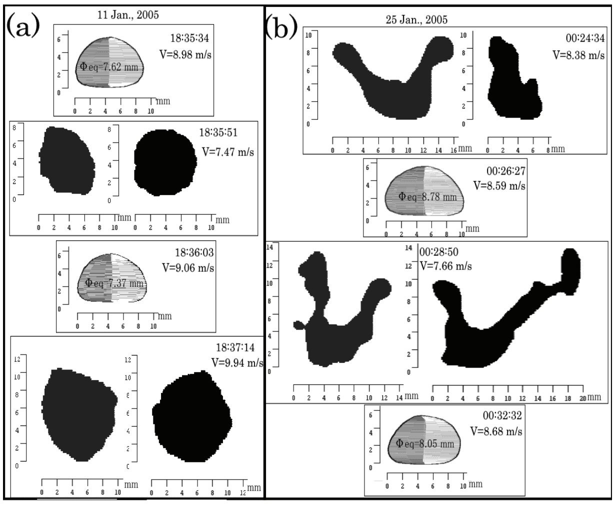

Fig. 7 2DVD images of large melting snow particles and raindrops observed on (a) 11 January 2005 and (b) 25 January 2005. The time of measurement, fall velocity, and equivolumetric sphere diameter of raindrops are also shown.

The results shown above clearly indicate that super-large raindrops can originate from melting graupels and snowflakes, which can survive a fall of several kilometers without colliding with small raindrops. The results also imply that the spontaneous break up of raindrops might limit the MSR in warm regions and seasons. Super-large raindrops > 8 mm in diameter were observed very often in winter at Kanazawa, but not at Okinawa or Sapporo. At Kanazawa, the melting level and the cloud base are usually very low in winter (< 1 km AGL). Therefore, super-large raindrops would be able to reach the ground surface before breaking up.

7. SUMMARY AND CONCLUSIONS

The maximum equivolumetric sphere diameters were 7.42, 7.73, and 8.59 mm at Sapporo, Okinawa, and Sumatra, respectively. Appearance frequencies of MSRs were well represented by a Gaussian form that peaked at approximately 3.5–4.5 mm in diameter at both regions.

MSRs > 6.0 mm occurred only in early summer (June and July) and autumn (September and October) at Sapporo, but occurred in most seasons at Okinawa. This suggests that thermal (i.e., solar radiation) and dynamical (i.e., synoptic-scale disturbance) effects are the major contributors to strong convection at Okinawa and Sapporo, respectively. At Sumatra, large raindrops fell two rainy seasons (April and September).

The MSR showed clear diurnal changes at both regions: the MSR tended to be higher between midnight and early morning (21–06 LST) at Sapporo, higher in both the late afternoon (12–15 LST) and around midnight (21–03 LST) at Okinawa, and the MSR was the highest in late afternoon (15– 18 LST) at Sumatra.

Very large raindrops (>6.5 mm) were not necessarily found during periods of heavy rainfall, but were often found at the beginning of rainfall events or after a pause in rainfall. This finding supports both our experience that large raindrops fall at the very beginning of rainfall events, and the idea that large raindrops can survive a fall when the concentration of small raindrops is low enough. Observation using a scanning coherent Doppler lidar suggests that raindrops are sorted during their fall, even within a rainshaft, depending on their fall velocities.

The 2DVD observations at Kanazawa provide evidence that the melting of large graupels and snowflakes can produce super-large raindrops. When the air temperature is > 0°C, melting solid hydrometeors and raindrops fall simultaneously, even in winter. Super-large raindrops > 8 mm in diameter were not uncommon in winter, and the largest raindrop observed was 9.15 mm.

References

Beard, K. V., D. B. Johnson, and D. Baumgardner, 1986: Aircraft observations of large raindrops in warm, shallow, convective clouds. Geophys. Res. Lett., 13, 991-994.

Beard, K. V., and C. Chuang, 1987: A new model for the equilibrium shape of raindrops. J. Atmos. Sci., 44, 1509-1524.

Bringi, V. N., V. Chandrasekar, J. Hubbert, E. Gorgucci, W. L. Randeu and M. Schöenhuber, 2003: Raindrop size distribution in different climatic regimes from disdrometer and dual-polarized radar analysis. J. Atmos. Sci., 60, 354-365.

Dai, A., 2001: Global precipitation and thunderstorm frequencies. Part II: Diurnal variations. J. Climate, 14, 1112-1128.

Feingold, G., Z. Levin, and S. Tzivion, 1991: The evolution of raindrop spectra. Part III: Downdraft generation in an axisymmetrical rainshaft model. J. Atmos. Sci., 48, 315-330.

Fujibe, F., 1988: Diurnal variations of precipitation and thunderstorm frequency in Japan in the warm season. Pap. Meteor. Geophys., 39, 79-94.

Fujita, T. T., 1992: The mystery of severe storms. WRL Research Paper 239, University of Chicago, 298 pp. [NTIS PB 92-182021]

Fujiyoshi, Y., 1986: Melting snowflakes. J. Atmos. Sci., 43, 307-311.

Fujiyoshi, Y. and K. Muramoto, 1996: The effect of breakup of melting snowflakes on the resulting size distribution of raindrops. J. Meteor. Soc. Japan, 74, 343-353.

Hobbs. P. V., and A. L. Rangno, 2004: Super-large raindrops. Geophys. Res. Lett., 31, L13102, doi:10.1029/ 2004GL020167.

Hu, Z., and R. C. Srivastava, 1995: Evolution of raindrop size distribution by coalescence, breakup, and evaporation: Theory and observations. J. Atmos. Sci., **52,** 1761–1783.

Jameson, A. R. and A. B. Kostinski, 2001: What is a raindrop size distribution? Bull. Amer. Meteor. Soc., 82, 1169-1177.

Joss, J., and A. Waldvogel, 1967: A raindrop spectrograph with automatic analysis. Pure Appl. Geophys., **68,** 240–246.

Kobayashi, T. and A. Adachi, 2001: Measurements of raindrop breakup by using UHF wind profiler. Geophys. Res. Lett., 28(21), 4071-4074.

Kozu, T., K. K. Reddy, S. Mori, M. Thurai, J. T. Ong, D. N. Rao and T. Shimomai, 2006: Seasonal and diurnal variations of raindrop size distribution in Asian Monsoon region. J. Meteor. Soc. Japan, 84A, 195-209.

Kruger, A., and W. F. Krajewski, 2002: Two-dimensional video disdrometer: A description. J. Atmos. Oceanic Technol., 19, 602-617.

Marshall, J. S. and W. M. Palmer, 1948: The distribution of raindrops with size. J. Meteor., 5, 165-66.

Mason, B. J., 1971: The Physics of Clouds, 2nd ed., 671pp, Clarendon, Oxford, U. K.

Mitra, S. K. O., V. M. Ahr and H. R. Pruppacher, 1990: A wind tunnel and theoretical study of the melting behavior of atmospheric ice particles. IV: Experiment and theory for snowflakes. J. Atmos. Sci., 47, 584-591.

Nitta, T., and S. Sekine, 1994: Diurnal variation of convective activity over the tropical western pacific. J. Meteor. Soc. Japan, 72, 627-641.

Pruppacher, H. R., and R. L. Pitter, 1971: A semi-empirical determination of the shape of cloud and rain drops. J. Atmos. Sci., 28, 86-94.

Schönhuber, M., H. E. Urban, J. P. V. P. Baptista, W. L. Randeu, and W. Riedler, 1997: Weather radar vs. 2D-video-distrometer data. Weather Radar Technology for Water Resources Management. B. Braga Jr. and O. Massambani, Eds., UNESCO Press.

Seifert, A., A. Khain, U. Blahak, and K. D. Beheng, 2005: Possible effect of collisional breakup on mixed-phase deep convection simulated by a spectral (bin) cloud model. J. Atmos. Sci., 62, .1917-1931.

Takahashi, T., K. Suzuki, M. Orita, M. Tokuno, and R. de la Mar, 1995: Videosonde observations of precipitation processes in Equatorial cloud clusters. J. Meteor. Soc. Japan, 73 (2B), 509-534.

DIFFUSION-KINETIC DROPLET GROWTH THEORY WITH THE MOVING SURFACE-BOUNDARY EFFECT (DKMB) FOR CLOUD STUDY

Norihiko Fukuta

Department of Meteorology, University of Utah, Salt Lake City, UT 84112-0110, USA

1. INTRODUCTION

Initial development of cloud properties takes place during the nucleation-growth interaction of droplets in the updraft above the cloud base. For initiation of subsequent collision-coalescence process, size spectrum broadening conducive to fall velocity difference is necessary. The classical Maxwellian theory, nevertheless, tends to produce a monodisperse size spectrum. Existing cloud condensation nuclei (CCN) alone are not sufficient to account for the broadening. Including resistance effects of thermal accommodation coefficient (α) and condensation coefficient (β), Fukuta and Walter (1970) obtained a first complete steady-state solution of the droplet growth, now called the diffusion-kinetic (DK) theory, and pointed out its size spectrum broadening effect with a small β, due to the stronger growth slow-down on the smaller end. In the DK theory, the Maxwellian corresponds to $\alpha=\beta=1$. Determination of the coefficients, β in particular, thus became crucial for cloud study. Measured data, nevertheless, exhibit a wide range of scatter centered about $\beta=1$ and 0.04. In the meantime, Zou and Fukuta (1999) showed a cloud albedo enhancing effect for a small β by modeling.

To solve the controversy, measurement was carried out by selecting all the elements so as to give the highest accuracy with simultaneous determination of the coefficients by a pressure modulation method. In the analysis, the effect of moving surface boundary (MB) on the growing droplet, which is attached to but shifts from the steady-state profiles of the temperature and vapor fields in air, was successfully derived. The effect was found as a function of supersaturation (S-1), among others, and served as the missing link to resolve the discrepancy between the two groups of β values or the problem associated with the expansion chamber measurements that reported $\beta\approx1$. With the MB effect correction, $\alpha=0.81\pm0.07$ and $\beta=0.043\pm0.016$ at T=277K and (S−1)=0.32% were determined (Fukuta and Myers, 2007). Proportional to (S−1), the DKMB growth rate sharply rises up from the DK theory in the radius range from 1 to 10 μm to further enhance the size spectrum broadening. The experimental test and the determined accommodation coefficients provide the DKMB theory with the necessary accuracy for modeling cloud albedo and precipitation element development, the latter particularly in convective clouds of low CCN concentration and high updraft, both largely contributing to the Earth's radiative and energy balance. The structure and the feature of the theory as well as the cloud application will be discussed in detail below.

2. DROPLET GROWTH SYSTEM UNDER CLOUD FORMATION

Cloud-forming air rises, expands, cools and generates (S−1) to nucleate cloud droplets. The formed droplets grow under competition with other nucleated droplets towards the $(S-1)_{max}$ where the final number concentration of droplets is decided. During the process, the formed supersaturated vapor is removed by the droplet, and the heat generated there is returned to the same cloud space.

2.1 Problem of steady-state field and the Laplacian application

Among the fields to carry the vapor and heat

Author's e-mail address: N.Fukuta@utah.edu

to and from the growing droplets, the steady-state ones persist in general the longest and normally are expressed as

$$\nabla^2 \rho = \nabla^2 T = 0, \qquad (1)$$

(for notations, see Fukuta and Myers, 2007). The formulae arise from consideration of economy of both flows in and out of an elementary volume in the cloud space, and at an arbitrary point in the space, ρ and T do not change with respect to time. This is to say that the flows are only controlled by both stationary boundaries, the droplet surface and the infinite environment, and the condition of the surface boundary is a function of α and β (DK theory). At the droplet surface, a mean-free path boundary is sometimes assumed (Fuchs and Sutugin, 1970; Pruppacher and Klett, 1997), but there is no physical evidence for the existence, and the assumption contradicts the ubiquitous chaotic thermal motions of molecules.

Nevertheless, the negligibly small air volume occupied by the highly curved and, therefore, largely deviated portion of ρ,T fields from their environmental levels is used to justify the application of the steady-state theories.

2.2 The cell-boundary-controlled droplet growth kinetics and the new moving surface-boundary effect

In the updraft of nucleation-growth interaction, a growing cloud droplet eventually reaches the stage to establish its own volume of influence, or the cell, neighboring the surrounding droplets. Droplet growth kinetics in consideration with α,β effects has been solved and found that the effect is not large under common cloud condition (Fukuta, 1992).

In the cloudy updraft of nucleation-growth interaction leading to $(S-1)_{max}$, which is known to occur slightly above the cloud base, the droplet radius remains still below a few micrometers. There, the DK effect of α,β is known to be large, and the rapid radial growth and small volume of influence make the relative movement of the droplet surface large, seriously violating the non-moving inner boundary condition of the steady-state ρ,T fields. It was the realization of this violation during the analysis for high accuracy simultaneous measurements of α and β (Fukuta and Myers, 2007) that led us to tackle the problem.

Figure 1 shows the transitional steady-state system of droplet growth under the moving surface boundary condition. Removal of water vapor from the hatched area represents the transitional mass flux, and the ratio between the flux and the steady-state ones is obtained as (see Fukuta and Myers, 2007, for detailed derivation)

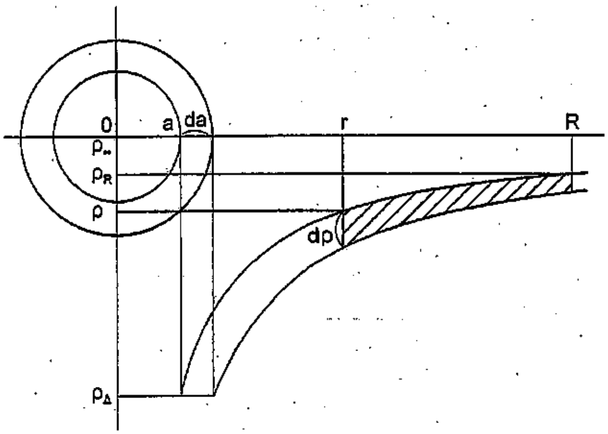

Figure 1. The system of a growing droplet in transitional steady state under the influence of moving surface boundary.

$$f_{MB} = \frac{(S-1)}{2\rho_L D[\quad]}\left(\frac{R^2}{a^2} - 1\right). \qquad (2)$$

The chief contributors to f_{MB} are thus (S - 1) and a. The [ ] term may be found in the DK theory (Fukuta and Xu, 1996);

$$\left(\frac{dm}{dt}\right)_{DK} = 4\pi a(S-1) \Big/ \left[a' + b' + \frac{1}{a}(a'l_\alpha + b'l_\beta)\right],$$

$$a' = \left(\frac{L}{R_vT} - 1\right)\frac{L}{KT}, \quad b' = \frac{1}{\rho_s D},$$

$$l_\alpha = \frac{K}{\alpha'}\frac{(2\pi R_a T)^{1/2}}{P\left(c_v + \frac{1}{2}R_a\right)}, \quad \alpha' = \frac{2\alpha}{2-\alpha},$$

$$l_\beta = \frac{D}{\beta'}\left(\frac{2\pi}{R_vT}\right)^{1/2}, \quad \beta' = \frac{2\beta}{2-\beta}. \tag{3}$$

The transitional droplet growth rate of the moving surface boundary effect is obtained as

$$\left(\frac{dm}{dt}\right)_{DK,MB} = 4\pi a(S-1) \Big/ \left[\frac{a' + b'}{1 + f_{MB}} + \frac{1}{a}(a'l_\alpha + b'l_\beta)\right], \tag{4}$$

3. APPLICATION OF DIFFUSION-KINETIC MOVING SURFACE BOUNDARY DROPLET GROWTH THEORY TO CLOUD PROCESSES

Figure 2 compares the droplet growth rate for various theories based on the Maxwellian. From the figure, it is clear that in the zone of cloud property characterization before reaching $(S-1)_{max}$ or r<10 μm, the sloping in both DK and DKMB theories indicates that the relatively slow growth and vapor removal lead to droplet size spectrum spreading (Fukuta and Walter, 1970), larger $(S-1)_{max}$, the higher droplet number concentration and cloud albedo (Zou and Fukuta, 1999).

Slow growth of droplets with DK theory does not effectively lead to large droplet formation for initiation of collision-coalescence. Whereas, the DKMB theory rises from the slow DK growth and accelerates towards the Maxwellian and even beyond if high (S−1) exists. The DKMB theory is, therefore, more suitable for formation of few large droplets to trigger the collision coalescence, in addition to describing the size spreading, droplet number concentration increase and cloud formation with higher albedo.

In experiments of α,β measurement, if a large instantaneous expansion were used, the transitional process would dominate as indicated by IE in the figure, and the resultant large (S−1) would lead to large growth rate beyond the steady-state. DK theory would describe a deceiving result as if the high growth rate were caused by large α,β close to unity with consideration of DK theory alone without MB effect. Derivation and clarification of the MB effect in the DK theory has thus been the missing link in the contemporary experimental studies for α,β determination.

The DKMB theory with the recently determined α,β values mentioned in the introduction is now believed to add major correction factors, DK, and MB effects, to the classical steady-state Maxwellian theory. It should be capable of realistically describing the main features in the cloud property characterization zone. In application for modeling of convective clouds with high updraft and low CCN concentration, the doubly (S−1)-dependent droplet growth rate of the DKMB theory is expected to describe the formation of large drops for triggering the collision-coalescence process of warm rain formation, in maritime clouds in particular. The theory is also anticipated to describe generation of embryos for graupel and hail in the high updraft of supercooled convective clouds.

4. REFERENCES

Fuchs, N.A., and A.G. Sutugin, 1970: Highly Dispersed Aerosols, Ann Arbor Science Publ., Ann Arbor, Michigan, 105 pp.

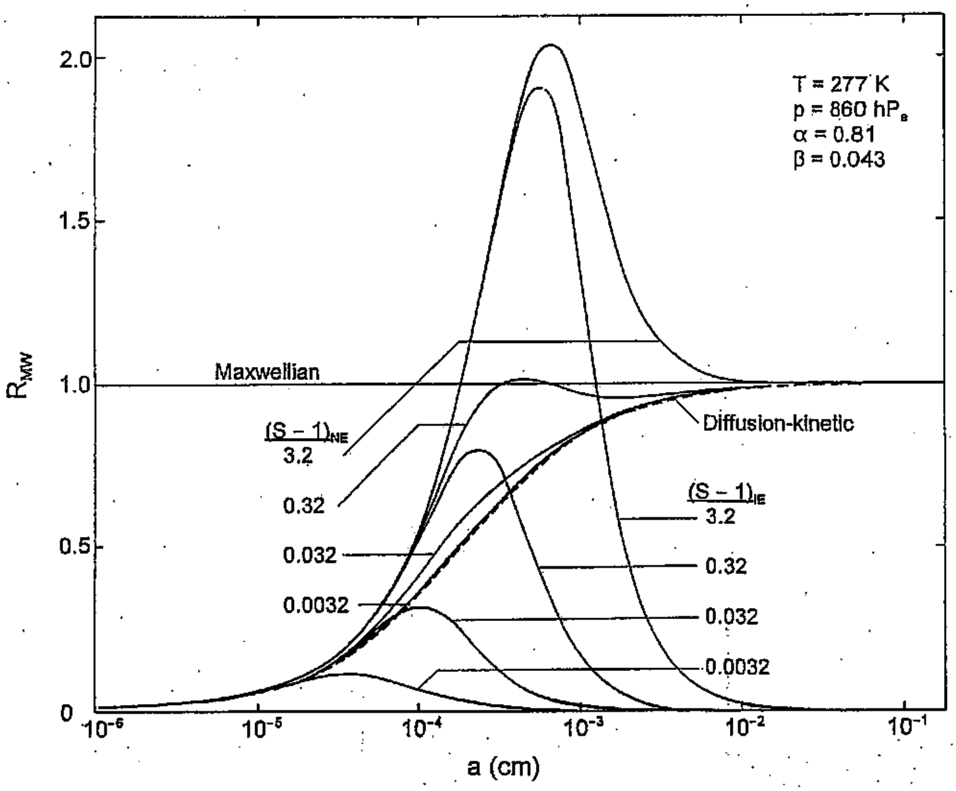

Figure 2. The mass growth rate ratio between the diffusion-kinetic with the moving boundary effect and the Maxwellian, R_{MW}, plotted as a function of droplet radius, a, for different supersaturation, (S−1). NE stands for no expansion and IE for instantaneous expansion, respectively.

Fukuta, N., 1992: Theories of competitive cloud droplet growth and their application to cloud physics studies. *J. Atmos. Sci.*, **49**, 1107-1114.

________, and L.A. Walter, 1970: Kinetics of hydrometeor growth from a vapor-spherical model. *J. Atmos. Sci.*, **27**, 1160-1172.

________, and N. Xu, 1996: Nucleation-droplet growth interactions and microphysical property development in convective clouds. *Atmos. Res.*, **41**, 1-22.

________, and M.N. Myers, 2007: Simultaneous measurement of condensation and thermal accommodation coefficients for cloud droplet growth in due consideration of new moving surface-boundary effect. *J. Atmos. Sci.*, **64**, 955-968.

Pruppacher, H.R., and J.D. Klett, 1978: *Microphysics of Clouds and Precipitation.* Kluwer Academic, 954 pp.

Zou, Y-S, and N. Fukuta, 1999: The effect of diffusion kinetics on the supersaturation in clouds. *Atmos. Res.*, **52**, 115-141.

Acknowledgments. This work was partially supported by NSF under Grant ATM-0094909.

Parameterization of the Deposition Coefficient for Bulk Microphysical Models:Influences on Simulated Cirrus.

JERRY Y. HARRINGTON[1]*, DENNIS LAMB[1], AND ROBERT CARVER[2]

[1] *Department of Meteorology, Pennsylvania State University, University Park, PA*

[2] *The Weather Underground, San Francisco, CA*

1 Introduction

The growth of ice is an important link in the macrophysical evolution of atmospheric "cold clouds." Unlike liquid drops, ice crystals can grow to large sizes by vapor deposition alone. Consequently, vapor growth strongly affects crystal sizes at which collection and sedimentation become important. Thus, vapor growth processes are intimately linked to precipitation processes and hence to cloud evolution (through mass loss and buoyancy changes). While the vapor growth of ice is clearly a key link for cold cloud evolution, important gaps exist in our knowledge about the rates and mechanisms involved. This is unfortunate because uncertainties in interlinked, but basic microphysical processes lead directly to large variability in predicted cloud structure and lifetime (Starr and Cox, 1985a,b; Harrington et al., 1999; Starr and Co-authors, 2000; Liu et al., 2003).

While all clouds that contain ice suffer from incomplete knowledge of basic physical processes, cirrus clouds are particularly pernicious because they can be long-lived, physically thin systems that are sensitive to the representation of microphysical growth processes (e.g. Starr and Co-authors, 2000). The differences in model-parameterized rates of sedimentation and growth by themselves produce vastly different cirrus-evolution scenarios. Interlinked uncertainties compound the problem. Ice nucleation modes and rates, depend on the concentration of excess vapor, which in turn depends on the concentration of crystals and their ability to take up the excess vapor (Lin et al., 2002; Liu et al., 2003; Khvorostyanov et al., 2006), competition that is critical for the simulation of cirrus. For instance, recent observations show that many cirrus, even optically thin cirrostratus, have very high concentrations of small ice crystals (Ström et al., 1997; Gayet et al., 2002; Garrett et al., 2003) and regions of high supersaturations (Gao and Co-authors, 2004; Jensen et al., 2005). These observations can be reproduced by including strong gravity waves and turbulence in modeled cirrus (Jensen and Pfister, 2004), which allows for a large vapor source and high ice nucleation rates (Jensen et al., 1994; Hoyle et al., 2005). On the other hand, kinetic limitations to ice crystal growth can also reproduce these results. Low values of the deposition coefficient (α_d) slow the early growth of ice, allowing for higher nucleation rates (Lin et al., 1998; Gierens et al., 2003; Khvorostyanov et al., 2006), slow equilibrium relaxation times (Spichtinger et al., 2004), and consequently regions of high ice supersaturation (Khvorostyanov et al., 2006). Of course, dynamic and microphysical processes work in tandem to determine the micro, and macrophysical evolution of a cloud system so deconvolving such processes can be difficult. Regardless, relatively recent measurements suggest that the deposition coefficient for ice is quite small (α_d $\sim$ 0.005) at typical cirrus temperatures ($T \sim$ -50 °C) indicating that ice vapor growth is strongly limited by surface kinetics (Magee et al., 2006).

Surface-kinetic effects, however, are generally ignored in bulk microphysical models. This is valid as long as α_d is relatively large ($>$ about 0.2) which is generally true at high supersaturations (e.g. Lamb and Chen, 1995). However, the low values of α_d recently measured suggest that including surface kinetics is necessary within bulk models. In this article, we provide a parameterization for the influence of surface kinetics on ice growth for bulk microphysical models.

2 Kinetic Corrections

The effects of surface kinetics appear as modifications to the diffusion coefficients in the standard vapor growth equation,

$$\frac{dm}{dt} = 4\pi C G(T, P, r, \alpha_d) s_i, \tag{1}$$

where s_i is the ice supersaturation, C is the capacitance, which is equal to r for an equivalent volume sphere, and from Pruppacher and Klett (1997) the function G, which acts like a diffusion coefficient, is defined as,

$$G(T, P, r, \alpha_d) = \left[\frac{R_v T}{e_i(T) D_v^*} + \frac{L_s}{K_T^* T} \left(\frac{L_s}{T R_v} - 1 \right)^{1/2} \right]^{-1} \tag{2}$$

and where T is temperature, P is pressure, R_v is the vapor gas constant, e_i is the ice equilibrium vapor pressure, L_s is the enthalpy of sublimation, and D_v^* and K_T^* are the kinetically-modified vapor and thermal diffusion coefficients. For our analysis, we have assumed spherical geometry for both simplicity and necessity. Necessity because it is yet unclear how one includes the deposition coefficient, α_d, which typically varies over each crystal face, into the capacitance model for vapor growth, which is generally used in numerical models. Second

---

[*]Corresponding author address: J.Y. Harrington, Department of Meteorology, Pennsylvania State University, 503 Walker Building, University Park, PA 16802; *e-mail*: harring@mail.meteo.psu.edu.

of all, a parameterization of α_d should provide a first-order estimate of the reduction in vapor growth due to surface kinetics, so using a simple equivalent sphere approximation may be accurate enough for bulk model computations. Finally, Chen (1992) showed that assuming an equivalent volume sphere as an approximation to the instantaneous growth of ice may provide a relatively accurate approximation, at least at water saturation.

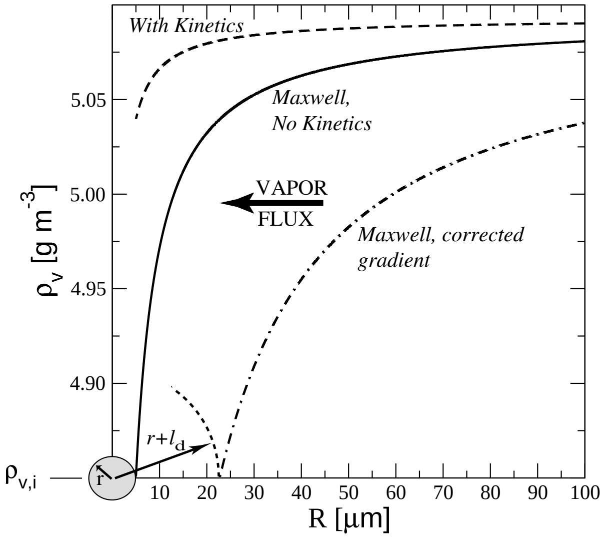

Figure 1: Density profile as a function of radial distance from the surface of an ice sphere for T = 268.15K, s_i = 5%, and α_d = 0.01. Solid line is the classical Maxwellian vapor profile, dashed line is the vapor profile for kinetically-limited growth, and the dash-dot line is the Maxwellian vapor profile for a drop of size $r + l_d$ which has the same vapor flux as that of the kinetically-limited case.

The corrections for surface kinetic effects are included through modified vapor and thermal diffusion coefficients, Pruppacher and Klett (1997),

$$D_v^* = \frac{D_v}{\frac{r}{r+\Delta_v} + \frac{l_d}{r}} \qquad \text{and} \qquad K_T^* = \frac{K_T}{\frac{r}{r+\Delta_T} + \frac{l_T}{r}} \tag{3}$$

where D_v^* and K_T^* are the diffusion coefficients for vapor and thermal energy, respectively, as modified for kinetic effects. Δ_v and Δ_T are the so-called vapor and thermal jump lengths, respectively, and each is proportional to the mean free path. The last two variables, l_d and l_d are interpreted as kinetic length scales (e.g. Mordy, 1959; Pruppacher and Klett, 1997) and are define as,

$$l_d = \frac{4D_v}{\alpha_d \overline{v}_v} \qquad \text{and} \qquad \overline{v}_v = \left(\frac{2\pi}{R_v T}\right)^{1/2}, \tag{4}$$

for the vapor kinetic length, and

$$l_T = \frac{4K_T}{\alpha_T \rho_a c_p \overline{v}_a} \qquad \text{and} \qquad \overline{v}_a = \left(\frac{2\pi}{R_d T}\right)^{1/2} \tag{5}$$

for the thermal kinetic length. In the above, $\overline{v}_v$ is the mean speed of vapor molecules, and $\overline{v}_a$ is the mean speed of "air" molecules. Since α_T is thought to be near one, its impacts on growth are relatively minor. Because of this, we do not attempt to parameterize its influence in this paper and focus our attention on the deposition coefficient. However, our approach should also be valid for α_T.

The kinetic length scales provide a useful scaling length for parameterizing α_d. The form of Eq. 3 suggests that this is the case since r/l_d appears in the modified diffusion coefficient. However, one may also interpret l_d as the length-scale necessary to correct the classical, Maxwellian vapor gradient for the influences of surface kinetics. For instance, Fig. 1 shows the profile of vapor density with distance away from the surface of an ice sphere. Classical, Maxwellian growth indicates that the surface should be at the equilibrium value. However, when surface kinetics are included, vapor uptake at the surface is reduced leading to an increase in the vapor density near the surface. A simple analysis shows that the classical Maxwellian case, with $r + l_d$ used as an effective size, leads to a vapor flux that is identical with the kinetically limited case. This is show as a corrected gradient in Fig. 1. As a result of this interpretation, we use l_d as an appropriate scaling length in the parameterization that we present next.

3 Parameterizing Kinetic Effects

In order to parameterize the effects of α_d for a bulk microphysical model, it is necessary to integrate the vapor growth rate over an assumed size distribution,

$$\frac{dM}{dt} = \int \frac{dm}{dt} n(r) dr, \tag{6}$$

where dm/dt is the vapor growth rate of a crystal of size r, and $n(r)$ is the size distribution. Many numerical models use some form of the generalized gamma distribution to approximate $n(r)$ (e.g. Walko et al., 1995),

$$n(r) = \frac{N_i}{\Gamma(\nu)} \left(\frac{r}{r_n}\right)^{\nu-1} \frac{1}{r_n} exp\left(-\frac{r}{r_n}\right), \tag{7}$$

where N_i is the ice crystal number density, ν is the distribution shape that controls the polynomial increase at small sizes, Γ is the gamma function, and r_n is the so-called characteristic size. The characteristic size has little physical meaning, but is related to the mean size through

$$\overline{r} = \frac{\int_0^\infty r n(r) dr}{\int_0^\infty n(r) dr} = r_n \frac{\Gamma(\nu+1)}{\Gamma(\nu)}. \tag{8}$$

This distribution is useful not only because it is a relatively good approximation of measured size spectra, but also because it is analytically integrable for classical Maxwellian growth eliminating costly numerical integration.

In order to develop a parameterization of surface kinetic influences, one must deal with the fact that Eq. 6 is no longer analytically integrable because G is a function of r. Figure 2 shows how G varies as a function of both r and α_d. The curves for each α_d are similar with the same limiting behavior: At

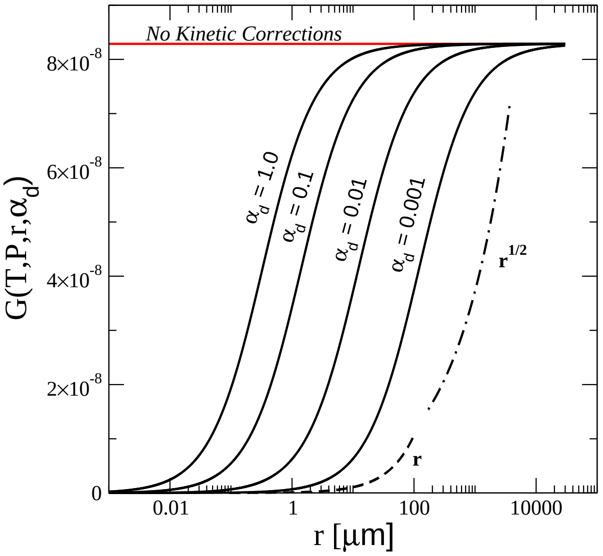

Figure 2: G as a function of radius for a variety of deposition coefficients (α_d). The classical Maxwellian case without kinetic corrections, and the inefficient, kinetically limited case which is labeled as **r**, are also shown. Intermediate cases between these two limits follow an approximately $\mathbf{r}^{1/2}$ dependence.

large sizes, G approaches the classical Maxwellian case without kinetic corrections, and at small sizes, G approaches zero (no growth). The self-similarity of these curves suggest that limiting cases may be useful in parameterization development. The two most important limits are when $r >> l_d$ (when surface kinetics produce efficient growth) and $r << l_d$ (when surface kinetics produce inefficient growth).

3.1 Efficient Growth Limit

Surface kinetics produce efficient growth when $r \rightarrow \infty$, so $r/(r + \Delta_v) \rightarrow 1$ and $l_d/r \rightarrow 0$ in Eq. 3 such that $D_v^* \rightarrow D_v$ and $G(T, P, r, \alpha_d)$ loses its functional dependence on radius (Figure 2). Hence, in the efficient limit the integrated growth equation simply becomes identical to the classical growth equation without kinetics, or

$$\frac{dM}{dt} = 4\pi G(T,P) s_i \int_0^\infty r n(r) dr = 4\pi G(T,P) s_i N_i \overline{r}. \tag{9}$$

Any parameterization of surface kinetics should be able to recover this limiting case.

3.2 Inefficient Growth Limit

When surface kinetics strongly limit growth, then $l_d/r >> r/(r + \Delta_v)$ in Eq. 3 and so $D_v^* \rightarrow D_v r/(r + l_d)$. In this limit, the function G in the vapor growth equation then becomes,

$$G(T,P,r,\alpha_d) \approx \left[\frac{R_v T}{e_i(T) D_v}\frac{r + l_d}{r} \quad + \quad \frac{L_s}{K_T^* T}\left(\frac{L_s}{T R_v} - 1\right)^{1/2}\right]^{-1} \tag{10}$$

However when growth is very inefficient $\alpha_d << 1$ and so $l_d >> r$, which means that the first term above dominates so that,

$$G(T,P,r,\alpha_d) \approx r\frac{e_i(T) D_v}{l_d R_v T} \equiv r g_\alpha. \tag{11}$$

Consequently, G is approximately a linear function of r when surface kinetics dominate vapor deposition, which is indicated in Figure 2. In this limit, the mass growth equation is easily integrated,

$$\begin{aligned} \frac{dM}{dt}_{k} &\approx 4\pi s_i \int_0^\infty r(r g_\alpha) n(r) dr \\ &= 4\pi s_i N_i g_\alpha r_n^2 \frac{\Gamma(\nu+2)}{\Gamma(\nu)}. \end{aligned} \tag{12}$$

Using the definition of the mean size ($\overline{r}$), defining $\overline{r}_2 = r_n \Gamma(\nu + 2)/\Gamma(\nu + 1)$, and using Eq. 11, we can write the kinetically-limited growth in a more revealing form,

$$\frac{dM}{dt}_{k,s} \approx 4\pi \overline{r} N_i s_i \left(\overline{r}_2 g_\alpha\right) = 4\pi \overline{r} N_i G(T,P,\alpha_d,\overline{r}_2) s_i. \tag{13}$$

Note that this equation has exactly the same form as the classical Maxwellian equation (Eq. 9), except that the radius in G is replaced with the second-moment average radius, $\overline{r}_2$. This solution should be an excellent approximation in the limit of inefficient growth, as we shall show.

3.3 Intermediate Surface Kinetics

Between the limits of inefficient and efficient growth, or where $l_d/r \sim r/(r + \Delta_v)$, is a region over which the vapor diffusion equation cannot be integrated analytically. Nevertheless, the approximate solution in the inefficient limit (Eq. 13) suggests a possible method for the parameterization of dM/dt_k within this region: Since the second-moment average radius in G may be used to good approximation in the inefficient limit, it may be possible to use an appropriate average radius in G for the intermediate case. For instance, Figure 2 shows that whereas G follows a linear, r dependence in the inefficient growth limit, it tends to roughly follow an $r^{1/2}$-dependence between the inefficient and efficient limits. This suggests that using the radius,

$$\overline{r}_{1.5} = r_n \frac{\Gamma(\nu + 1.5)}{\Gamma(\nu + 1)}, \tag{14}$$

in G between the inefficient and efficient limits. Therefore, we approximate the integrated vapor growth in this regime as,

$$\frac{dM}{dt}_{k,int} \approx 4\pi \overline{r} N_i G(T,P,\alpha_d,\overline{r}_{1.5}) s_i. \tag{15}$$

As we show below, this produces excellent agreement with accurate calculations of the growth rate.

3.4 Model Parameterization

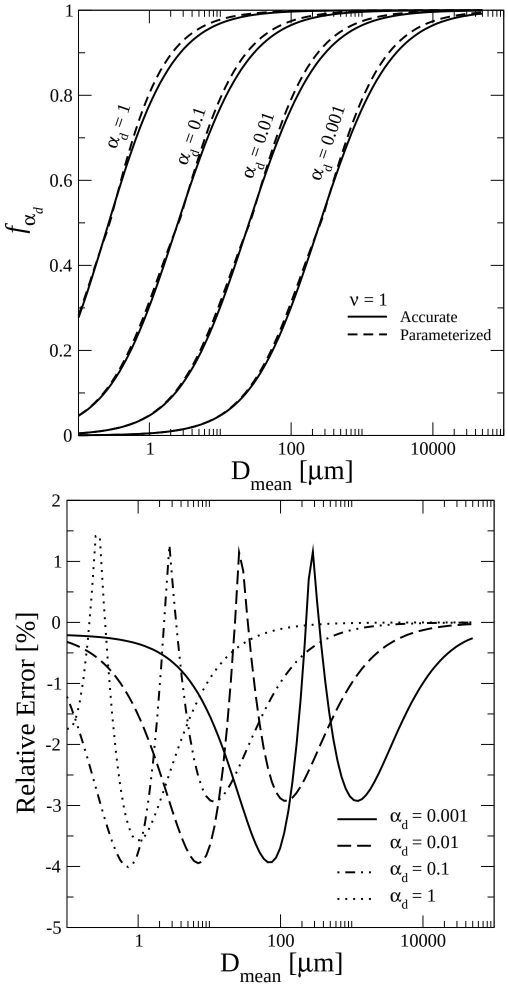

Figure 3: (a) The ratio of kinetically-limited growth and classical Maxwellian growth (f_{α_d}) as a function of the mean diameter of the size distribution. An exponential size distribution (ν = 1) was used along with a T = -20 °C and P = 500 hPa. Parameterized growth is shown with a dashed line and the numerical integration (accurate) is shown with a solid line. (b) Relative error of the parameterization in comparison to the accurate calculation.

To use the above equations in a numerical model, one needs a method to effectively choose between the three cases (Eqs. 9, 13, and 15), which requires knowledge of the growth regime (inefficient, efficient, or intermediate) for a given value of α_d. We suggest that the appropriate growth regime can be effectively chosen by comparing the average size to the kinetic length scale (l_d). A simple analytical way to make this choice is to use a weighted average size, namely,

$$\begin{aligned} w &= min\left[\frac{\overline{D}}{l_d}, 1\right] = min\left[\frac{2\overline{r}}{l_d}, 1\right] \\ \overline{r}_i &= [1-w]\overline{r}_2 + w\overline{r}_{1.5} \end{aligned} \tag{16}$$

where min is a function that chooses the minimum between $\overline{D}/l_d$ and 1. We use $\overline{D}$ in our weighting instead of $\overline{r}$ because it produces more accurate results (see below). Note that the weighted average radius, $\overline{r}_i$, recovers the appropriate limits: In the inefficient limit, $\overline{r}_i \rightarrow \overline{r}_2$ and in the intermediate regime $\overline{r}_i \rightarrow \overline{r}_{1.5}$. Note that we chose to continue using $\overline{r}_i = \overline{r}_{1.5}$ as we approach the efficient limit because kinetic effects become small regardless of which average radius we use. We can now simply use $\overline{r}_i$ in the growth equation to complete our parameterization,

$$\left.\frac{dM}{dt}\right._{k,param} \approx 4\pi\overline{r}N_iG(T, P, \alpha_d, \overline{r}_i)s_i. \tag{17}$$

Hence, computing the mass growth of a population of ice crystals now involves computing $\overline{r}_i$ based on the kinetic length scale, and then using this in growth equation above. Such a parameterization can be readily implemented into the implicit growth solution for bulk models outlined by Walko et al. (2000).

To illustrate the accuracy of Eq. 17, we have compared it to a numerical integration of the growth equation for specified gamma distributions. To remove the dependence on supersaturation, we have plotted the ratio of the kinetically-limited growth to that of the classical Maxwellian growth (f_{α_d}), as is shown in Figure 3. An exponential size distribution was used ($\nu = 1$) as we expect the errors to be greatest for this distribution: The relative number of small particles, and hence kinetic influences, are greatest for this size distribution. Even for this (worst-case) scenario, as Figure 3 shows, the parameterized growth is very accurate. The parameterization is most accurate in the efficient and inefficient limit, which is expected: The parameterization should be exact as the inefficient and efficient limits are approached. The largest relative errors (Figure 3a and b) are encountered in the intermediate regime especially as the efficient limit is approached. However, the errors are never greater than about 4%, which is roughly the maximum error that the parameterization produces over a large range of T, and P. The error decreases for non-exponential size distributions (i.e. $\nu > 1$) and are rarely greater than 1% (not shown).

4 Influence on Cirrus

To test the influence of the deposition coefficient on simulated cirrus, we implemented our new parameterization into the Regional Atmospheric Modeling System (RAMS, Cotton et al., 2003). The model domain was set up as a 2-D Eddy Resolving Model with Δx = 100 m and Δz = 100 m within the cirrus layer. The vertical domain extended from the surface to approximately 16 km. Cyclic lateral boundary conditions were used and a sponge layer 6 grid-points deep was added at the top boundary. The microphysics used was the standard bulk microphysical package following Meyers et al. (1997). The case simulated is similar to that of the “cold unstable” case of Liu et al. (2003), except that cloud top is slightly higher. Cloud top in this case is approximately 13 km with a temperature of approximately -60 °C. No large-scale forcing was applied to the simulations. Turbulent motions were initialized with random perturbations applied to the potential temperature (θ) over the cloudy grid points. Two simulations were run. One simulation used α_d = 1, or the situation in which surface kinetics offer no resistance to ice crystal growth. The second simulation, that of kinetically-limited growth, used α_d = 0.005 following the laboratory data of Magee et al. (2006).

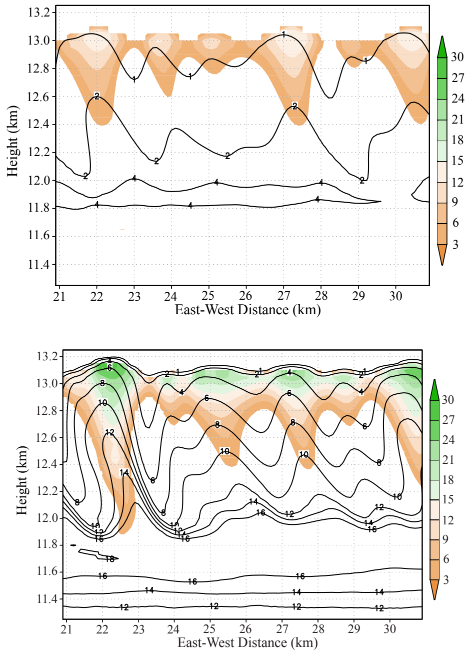

Figure 4: Simulated ice crystal concentration (contoured, cm^{-3}) and ice supersaturation (shaded, %) after 60 min of simulation time with (top panel) a deposition coefficient of α_d = 1.0 and (bottom panel) α_d = 0.005 based on the laboratory measurements of Magee et al. (2006). The same contour intervals are used in each panel.

Instantaneous x-z cross-sections showing the ice crystal concentration (N_i) and ice supersaturation (s_i) after 60 min of simulation time are shown in Fig. 4. At this time, the cloud is approximately 1 km deep and is sustained by cloud scale eddies (not shown). When vapor growth is very efficient (α_d = 1), the concentration of ice particles remains relatively low ($\sim$ 1 cm^{-3}) as does s_i ($\sim$ 6%). However, when the deposition coefficient is reduce to the laboratory-measured value of 0.005, the cloud structure changes drastically. Ice concentrations now increase to $\sim$ 15 cm^{-3} and s_i reaches maximum values of up to 30%. Note that the maximum in s_i is co-located with the top of the cloud layer and the top of upward moving eddies (not shown). This is due to at least two factors: First, strong kinetic limits on vapor growth decrease the vapor uptake and allow for larger production of supersaturation by updrafts, as compared to the α_d = 1 simulation. Second, the lower value of α_d leads to larger ice water contents at cloud top (IWC, see Fig. 5). When growth is kinetically-limited, the larger crystal concentrations, and slower growth rates, lead to smaller particles with weaker sedimentation velocities, hence the higher ice water contents. There is a feedback here in the sense that higher ice water contents produce stronger cloud top radiative cooling, and therefore stronger eddies. The maximum updraft speeds for α_d = 0.005 and α_d = 1 are 1 m s^{-1} and 0.2 m s^{-1}, respectively.

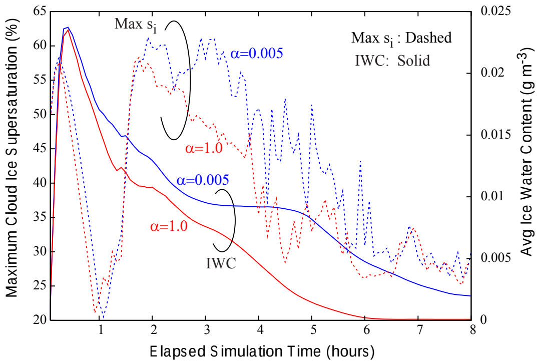

Figure 5: Domain averaged ice water path (IWP, right axis) and domain maximum ice supersaturation (left axis) as a function of time for the simulation with α_d = 1 and α_d = 0.005.

These results remain relatively consistent throughout the simulation: Smaller crystal sizes and stronger vertical motions, lead to larger maximum s_i and larger average IWCs over time for kinetically-limited growth (Fig. 5). As a consequence, cloud lifetime is also extended to over 8 hours for kinetically-limited growth as compared to 6 hours when α_d = 1. In future work, we plan to examine the importance of kinetically-limited growth to cirrus microphysical and dynamical evolution for a variety of cirriform cloud types.

Acknowledgments. J. Harrington and D. Lamb would like to thank the National Science Foundation for support under grant No. ATM-0639524.

References

Chen, J., 1992: Numerical Simulation of the Redistribution of Atmospheric Trace Chemicals Through Cloud Processes. Ph.D. thesis, The Pennsylvania State University, University Park, PA, 16802, 342pp.

Cotton, W., R. Pielke, R. Walko, G. Liston, C. Tremback, J. Harrington, and H. Jiang, 2003: Rams 2000: Current status and future directions. *MAP*, **82**, 5–29.

Gao, R. and Co-authors, 2004: Evidence that nitric acid increases relative humidity in low-temperature cirrus clouds. *Science*, **303**, 516–520.

Garrett, T., H. Gerber, D. Baumgardner, C. Twohy, and E. Weinstock, 2003: Small, highly reflective ice crystals in low latitude cirrus. *Geophys. Res. Let.*, **30(21)**, 2132, doi:10.1029/2001GL018153.

Gayet, J.-F., et al., 2002: Quantitative measurement of the microphysical and optical properties of cirrus clouds with four different in situ probes: Evidence of small ice crystals. *Geophys. Res. Let.*, **29(24)**, 2230, doi:10.1029/2001GL0014342.

Gierens, K., M. Monier, and J.-F. Gayet, 2003: The deposition coefficient and its role for cirrus. *J. Geophys. Res.*, **108(D2)**, 4069, doi:10.1029/2001JD001558.

Harrington, J. Y., T. Reisin, W. R. Cotton, and S. M. Kreidenweis, 1999: Cloud resolving simulations of Arctic stratus. part II: Transition-season clouds. *Atmos. Res.*, **51**, 45–75.

Hoyle, C., B. Luo, and T. Peter, 2005: The origin of high ice crystal number densities in cirrus. *J. Atmos. Sci.*, **62**, 2568–2579.

Jensen, E. and L. Pfister, 2004: Transport and freeze-drying in the tropical tropopause layer. *J Geophys. Res.*, **109**, D02 207, doi: 10.1029/2003JD004022.

Jensen, E., O. Toon, D. Westphal, S. Kinne, and A. Heymsfield, 1994: Microphysical modeling of cirrus, 1, comparison with 1986 FIRE IFO measurements. *J. Geophys. Res.*, **99**, 10,421–10,442.

Jensen, E., et al., 2005: Formation of a tropopause cirrus layer observed over florida during crystal-face. *J. Geophys. Res.*, **110**, D03 208, doi: 10.1029/2004JD004671.

Khvorostyanov, V., H. Morrison, J. Curry, D. Baumgardner, and P. Lawson, 2006: High supersaturation and modes of ice nulceation in thin tropopause cirrus: Simulations of the 13 july 2002 cirrus regional study of tropical anvils and cirrus layers case. *J. Geophys. Res.*, **111, D02201**, doi:doi:10.1029/2004JD005235.

Lamb, D. and J. Chen, 1995: An expanded parameterization of growth of ice crystals by vapor deposition. *Conference on Cloud Physics*, Dallas, Texas, AMS, Boston, 15-20 January, 389-392.

Lin, H., K. Noone, J. Ström, and A. J. Heymsfield, 1998: Small ice crystals in cirrus clouds: A model study and comparison with in situ observations. *J. Atmos. Sci.*, **55**, 1928–1939.

Lin, R.-F., D. O. C. Starr, P. DeMott, R. Cotton, K. Sassen, E. Jensen, B. Karcher, and X. Liu, 2002: Cirrus parcel model comparison project. phase i: The critical components to simulation cirrus initiation explicitly. *J. Atmos. Sci.*, **59**, 2305–2329.

Liu, H.-C., P. Wang, and R. Schlesinger, 2003: A numerical study of cirrus clouds. part ii: Effects of ambient temperature, stability, radiation, ice microphysics, and microdynamics on cirrus evolution. *J. Atmos. Sci.*, **60**, 1097–1119.

Magee, N., A. Moyle, and D. Lamb, 2006: Experimental determination of the deposition coefficient of small cirrus-like crystals near -50 °c. *Geophys. Res. Let.*, L17813, doi:10.1029/2006GL026665.

Meyers, M. P., R. L. Walko, J. Y. Harrington, and W. R. Cotton, 1997: New rams cloud microphysics parameterization. part ii: The two-moment scheme. *Atmos. Res.*, **45**, 3–39.

Mordy, W., 1959: Computations of the growth by condensation of a population of cloud droplets. *Tellus*, **11**, 17–44.

Pruppacher, H. R. and J. D. Klett, 1997: *Microphysics of Clouds and Precipitation*. Kluwer Academic Publishers, Boston, 954pp pp.

Spichtinger, P., K. Gierens, H. Smit, J. Ovarlez, and J.-F. Gayet, 2004: On the distribution of relative humidity in cirrus clouds. *Atmos. Chem. Phys.*, **4**, 639–647.

Starr, D. O. C. and Co-authors, 2000: Comparison of cirrus models: A project of the gewex cloud system study group (gcss) working group on cirrus cloud systems. *13th International Conf. on Clouds and Precipitation*, Reno NV, ICCP, 1–4.

Starr, D. O. C. and S. Cox, 1985a: Cirrus clouds. part i: A cirrus cloud model. *J. Atmos. Sci.*, **42**, 2663–2681.

Starr, D. O. C. and S. Cox, 1985b: Cirrus clouds. part ii: Numerical experiments on the formation and maintenance of cirrus. *J. Atmos. Sci.*, **42**, 2682–2694.

Ström, J., B. Strauss, F. Schröder, T. Anderson, J. Heintzenberg, and P. Wendling, 1997: In situ observations of the microphysical properties of young cirrus. *J. Atmos. Sci.*, **54**, 2542–2553.

Walko, R., W. R. Cotton, G. Feingold, and B. Stevens, 2000: Efficient computation of vapor and heat diffusion between hydrometeors in a numerical model. *Atmos. Res.*, **53**, 171–183.

Walko, R. L., W. R. Cotton, M. P. Meyers, and J. Y. Harrington, 1995: New RAMS cloud microphysics parameterization. Part I: The single moment scheme. *Atmos. Res.*, **38**, 29–62.

LABORATORY STUDIES ON CLOUD CHEMISTRY PROCESSES

D. Hoffmann[1], C. Weller[1], T. Schaefer[1] and H. Herrmann[1]
[1]*Leibniz-Institut für Troposphärenforschung, Permoserstr. 15, 04318 Leipzig, Germany*

Keywords: Multiphase chemistry, cloud chemistry, radical reactions

ABSTRACT Radical reactions play an important role for the degradation of organic compounds, the formation of secondary pollutants and the particle mass production within the atmosphere. These oxidation reactions take place in the gas, particle- and aqueous phase. The atmospheric aqueous phase includes not only cloud droplets but also fog, rain and aqueous particles. Important free radicals within the tropospheric multiphase system are OH, NO_3 and halogenated radicals. However, while the reactivity of free radicals in the gas phase is well investigated, reactions in the aqueous phase are not so well characterized. Moreover, aqueous phase reactions are not only influenced by the temperature but also by the pH and the ionic strength. Since these parameters are strongly variable within the atmosphere, the possible influence of them on chemical reactions must be parameterized for the implementation in atmospheric models.

In order to describe the very complex atmospheric chemistry different experimental information are necessary. The modeling of multiphase chemical processes requires besides purely kinetic data also product studies, spectroscopic studies and phase transfer parameter. However, these information are not yet available for many important atmospheric reactions and relevant compounds.

Using laser-photolysis-long-path-absorption (LP-LPA) set-ups kinetic investigation of OH, NO_3 and halogen radical reactions towards different atmospheric relevant organic compounds (e.g. alcohols, acids, carbonyls) in the aqueous phase were carried out. Radicals were generated by excimer laser photolysis of suitable precursor compounds at $\lambda = 248$ nm. While the kinetic of OH radical reactions were measured indirectly by competition kinetic technique (using the thiocyanate reference system), rate constants for NO_3 and halogen radical reactions were measured directly. Within the kinetic investigations also the influence of the ionic strength, the temperature and the pH on many rate constants was studied. Product studies were carried out by combining the LP-LPA set-up from the kinetic investigations with analytical techniques. Product studies were focused on the aqueous oxidation of phenolic compounds (phenol, p-methylphenol) in presence of OH, NO_2 and NO_3 radicals.

Recent results from the kinetic investigations and the product studies performed will be presented. The data will be discussed in terms of reactivity correlations, tropospheric lifetimes and reaction mechanisms. Since the results obtained demonstrate the importance of aqueous phase reactions for a detailed and realistic modeling of atmospheric processes, they will be implemented in the further development of the multiphase mechanism CAPRAM 3.0 (Chemical Aqueous Phase Radical Mechanism).

1 INTRODUCTION

Oxidation reactions within the troposphere play a decisive role for many important atmospheric processes. Within the tropospheric multiphase system clouds and deliquescent particles represent an important reaction medium were aqueous phase chemistry takes place (Herrmann et

---

[1] Corresponding author. Tel.: +493412352972; fax: +493412352325.
E-mail address: hoffmann@tropos.de

al., 2005). Chemical processes in the aqueous phase are strongly influenced by reactions of atmospheric radicals, such as OH, NO_3, SO_X^- and halogenated radicals. The term multiphase chemistry combines several processes including the phase transfer of volatile compounds from the gas phase into the aqueous phase, diffusion into the bulk of the solution and the subsequent reaction within the bulk phase (Ravishankara, 1997). These processes are important because they are able to influence chemical properties of tropospheric particles, degradation processes of compounds, the acidity of the aqueous phase as well as the oxidation budget within the whole troposphere. Furthermore, oxidation reactions in aqueous solution can follow reaction mechanism (e.g. electron transfer reactions), which are not possible in gas phase. This might lead to different degradation products of aqueous phase oxidation processes. In the past the conversion of S(IV) to S(VI) in the atmospheric multiphase system was intensively studied. However, there are much more reactants and oxidants present in the troposphere, which can react in aqueous solution. In order to describe these complex physcio-chemical processes within the troposphere and to evaluate their possible consequences, advanced modelling studies are required. But, the quality of atmospheric models relies strongly on experimental data from laboratory studies and field measurements. In particular laboratory studies are useful tools to study and characterize many aspects of the tropospheric chemistry under controlled experimental conditions. The following chapters give a short overview on the performed laboratory investigations concerning the kinetics and product formation of relevant photochemical reactions in aqueous solution at the Leibniz-Institute for Tropospheric research (IfT) in Leipzig, Germany. Furthermore, quantum yields of important tropospheric photolysis processes (e.g. photochemistry of Fe(III) complexes) are measured. The experimental data obtained are applied to further improve, extend and verify existing atmospheric models describing multiphase processes such as the IfT CAPRAM 3.0 mechanism (http://projects.tropos.de/capram).

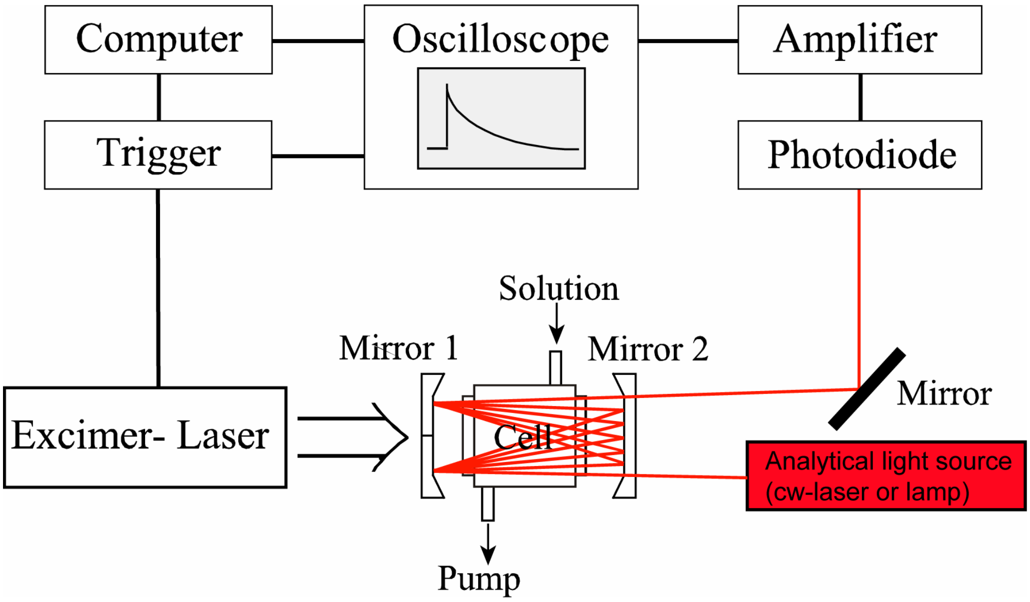

Figure 1: Laser flash photolysis – long path absorption set-up used for the kinetic investigations.

2 EXPERIMENTAL

2.1 KINETIC INVESTIGATION ON AQUEOUS PHASE REACTIONS

All kinetic measurements on reactions of atmospheric radicals in aqueous solution were carried out using different thermostated laser flash photolysis - long path absorption set-ups (LFP-LPA), as schematically shown in Figure 1. The main focus of the kinetic measurements lies on the characterization of atmospherically relevant radical reactions in aqueous solution. Radicals were generated inside the reaction cell using the Excimer laser flash photolysis of suitable radical precursor compounds. Excimer lasers were normally operated at a wavelength of λ = 248 nm. During the experiments the following radical precursors are applied (Table 1). More information concerning the detailed experimental conditions and the investigated reaction systems can be found in the listed references in Table 1.

Table 1: Overview over the applied radical precursor compounds, photolysis and analyzing wavelengths for the measurements of radical reactions in aqueous solution.

Radical	Precursor	direct/indirect method	Reference system	Photolysis wavelength	Analyzing wavelength	Literature
OH	H_2O_2	indirect	thiocyanate	248 nm	407 nm / 473 nm	a, b, c
NO_3	$NaNO_3$ (pH ≤ 0.5); $K_2S_2O_8 + NO_3^-$	direct	-	248 nm	635 nm	d, e, f, g, h, i, j, k
SO_4^-	$K_2S_2O_8$	direct	-	248 nm	407 nm / 473 nm	j, l, m
Cl	CH_3COCH_2Cl	direct	-	248 nm	312 nm	m, n
Br	CH_3COCH_2Br	direct	-	248 nm	297 nm	o
Cl_2^-	$K_2S_2O_8 + Cl^-$	direct	-	248 nm	340 nm	n, p
Br_2^-	$K_2S_2O_8 + Br^-$	direct	-	248 nm	365 nm	o

a) Ervens et al., 2003; b) Gligorovski and Herrmann, 2004; c) Morozov et al., 2008; d) Umschlag et al., 2002; e) Barzaghi and Herrmann, 2002; f) Barzaghi and Herrmann, 2004; g) de Semainville et al., 2007; h) Herrmann et al., 1994; i) Herrmann and Zellner, 1998; j) Herrmann et al., 1995; k) Exner et al., 1994; l) Grgic et al., 2007; m) Herrmann, 2007; n) Wicktor et al., 2003; o) Parajuli, 2007; p) Jacobi et al., 1999

Kinetic measurements were carried out under pseudo first order conditions, adding the organic reactants in at least ten times excess compared to the generated radical concentration inside the reaction cell. Rate constants are measured either directly, following the temporal change of the radical concentration inside the reaction cell, or indirectly, applying competition kinetic methods. To improve the sensitivity of the measurements a White cell optic is applied in order to increase the absorption path length of the analyzing light beam. Analyzing light sources are different continuous wave lasers as well as mercury xenon lamps.

Kinetic measurements in aqueous solution are routinely done at room temperature (T = 298 K). Additionally, rate constants are measured as a function of atmospherically relevant parameters like the temperature, the ionic strength and the pH of the measurement solution. The ionic strength of the solution was adjusted be adding sodium perchlorate ($NaClO_4$), a chemically inert 1:1 electrolyte. Thereby the concentration of $NaClO_4$ was varied between $0 \leq [NaClO_4]$ mol/l ≤ 3. These concentrations correspond to an effective ionic strength in the measurements solution of up to $I_{eff} \leq 2.5$ mol/l, in dependence on the experimental conditions applied.

2.2 SPECTROSCOPIC AND PRODUCT STUDIES ON AQUEOUS PHASE REACTIONS

In order to study quantum yields, short-lived reaction products or stable end products of the investigated aqueous phase reactions different spectroscopic as well as analytic methods are applied. Fast spectroscopy methods, using deuterium lamps as analytical light source and either CCD-cameras or diode array detectors, are used to study quantum yields and the formation of intermediate species (such as organic and inorganic radicals) after laser flash photolysis. For the identification of stable end products the laser flash photolysis set-up in Figure 1 is coupled off-line to different hyphenated analytical techniques (e.g. HPLC/UV, HPLC/MS and CE/UV). To enrich the formed reaction products a solid phase extraction step is carried out prior analysis (Figure 2).

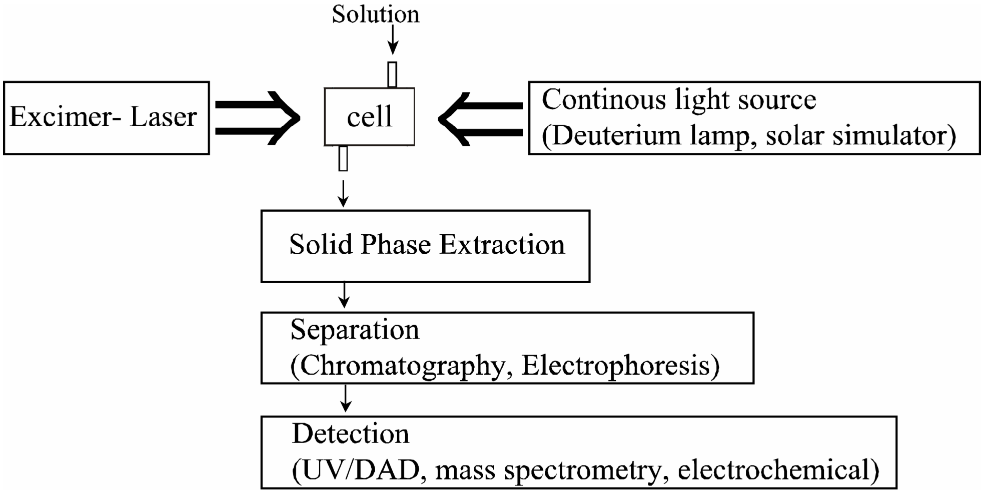

Figure 2: Off-line coupling of the laser photolysis set-up, used for the kinetic investigations, with different analytical techniques for the characterization of stable reaction products.

3 RESULTS

3.1 KINETIC INVESTIGATION ON AQUEOUS PHASE REACTIONS

Reaction kinetics of chemical reactions in the atmospheric aqueous phase are still much less investigated and understood than pure gas phase reactions. However, for the detailed description of chemical processes in clouds and deliquescent particles, these data are essential. Due to this lack of experimental data, currently applied aqueous phase chemistry mechanisms do still rely on many assumptions and approximations.

Within the laboratory investigations aqueous phase reactions of OH, NO_3, SO_X^- and halogenated radicals (e.g. Br, Cl, Br_2^-, Cl_2^-) with alcohols, carbonyl compounds, carboxylic acids, sugars and phenols have been measured. One important aspect of the kinetic measurements is the systematic characterization of temperature, pH and ionic strength effects on the kinetic data obtained. In particular measurements on pH and ionic strength effects are needed, since systematic investigations on the effect of these highly variable atmospheric parameters are limited.

An important aspect of the data evaluation is the finding of reactivity correlations between the measured reaction rates and extra-kinetic data such as bond dissociation energies, dipole moments and reaction enthalpies. These correlations can be applied to estimate unknown rate constants or activation parameter, if corresponding experimental values are not accessible. In order to establish such correlations a detailed understanding of aqueous phase chemical processes as well as an adequate experimental database is essential. The following Figure 3 shows two examples of Evans-Polyani type correlations for OH and NO_3 reactions with oxygenated organic compounds in aqueous solution. The linear dependencies between the logarithm of the rate constants (k_H) obtained and the bond dissociation energies (BDE) of the weakest H-bond in the organic reactant indicate an hydrogen-abstraction reaction mechanism for all reactants included in the correlations.

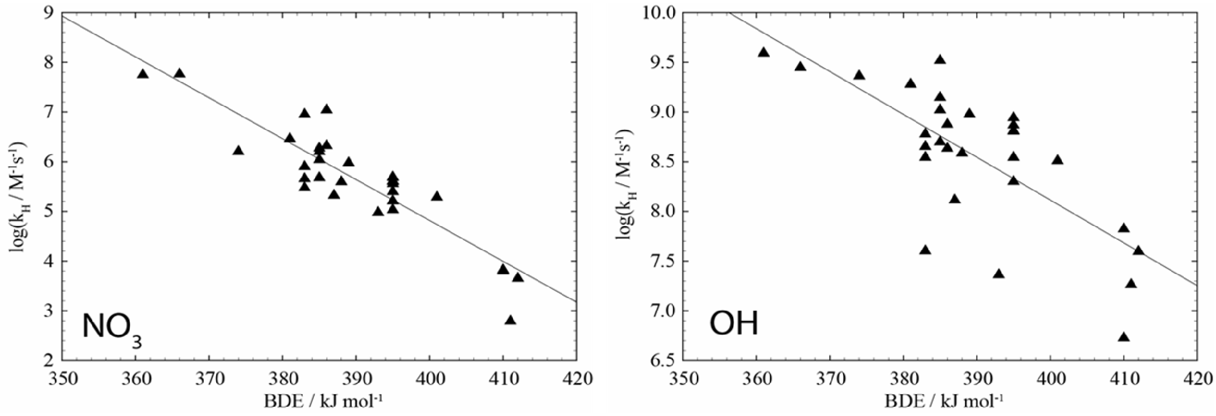

Figure 3: Evans-Polyani type correlation (logk_H vs. bond dissociation energies) for different H-abstraction of OH and NO_3 radicals in aqueous solution. Correlations are taken from de Semainville et al., 2007.

The linear regression for the OH and NO_3 reactions in Figure 3 provides the following equations (R-1 and R-2). The smaller slope of the regression equation for the OH reactions (R-2) expresses the lower selectivity of OH radicals compared to NO_3.

$$\log\left(k_{H,\,NO_3} / M^{-1}s^{-1}\right) = (37.7 \pm 5.8) + (-0.082 \pm 0.015) \cdot BDE \text{ in kJ/mol} \; ; n = 32, r = 0.90 \qquad \text{(R-1)}$$

$$\log\left(k_{H,\,OH} / M^{-1}s^{-1}\right) = (25.4 \pm 6.1) + (-0.043 \pm 0.016) \cdot BDE \text{ in kJ/mol} \; ; n = 29, r = 0.73 \qquad \text{(R-2)}$$

The influence of the pH on chemical reactions rates are shown exemplarily by the example of OH and NO_3 radical reactions with different mono- and dicarboxylic acids in Table 2. The results summarized in Table 2 demonstrate an effect off the pH value on some reactions rates, due to the different dissociation stage of the organic acids. Therefore, effects of the pH should be considered for the description of chemical processes in clouds and deliquescent particles.

Table 2: Influence of the pH on the rate constants obtained for different reactions of OH and NO_3 radicals with carboxylic acids in aqueous solution.

radical	**compound**	**pH**	**k_{2nd} ($M^{-1}s^{-1}$)**
OH	glutaric acid	1	$(5.1 \pm 1.2) \cdot 10^8$
	glutarate	9	$(8.2 \pm 0.9) \cdot 10^8$
	adipic acid	1	$(1.6 \pm 0.4) \cdot 10^9$
	adipate	9	$(1.4 \pm 0.4) \cdot 10^9$
NO_3	pyruvic acid	0.5	$(2.4 \pm 0.3) \cdot 10^6$
	pyruvate	6	$(1.9 \pm 0.5) \cdot 10^7$
	glycolic acid	0.5	$(9.1 \pm 2.3) \cdot 10^5$
	glycolate	6	$(1.0 \pm 0.2) \cdot 10^7$

Another highly variable atmospheric parameter, especially within deliquescent particles, is the ionic strength (Herrmann, 2003). A changing ionic strength can influence the rates of chemical reactions in different ways. Ionic strength effects can accelerate, decelerate or not affect chemical reaction rates depending on the nature of the reactants. Therefore, such effects need to be investigated and characterized also for atmospheric radical reactions. The following Table 3 shows few examples of measured salt effects on OH and NO_3 reactions in aqueous solution.

Table 3: Summary of measured ionic strength (I) dependent parameter of OH and NO_3 radical reactions in aqueous solution. The listed ionic strength dependent parameters ($k_{(I\rightarrow 0)}$; $k_{(I\rightarrow\infty)}$; β) in Table 3 are defined in Figure 4.

	compound	**$k_{(I\rightarrow 0)}$**	**$k_{(I\rightarrow\infty)}$**	**$k_{(I\rightarrow\infty)}$ / $k_{(I\rightarrow 0)}$**	**β**	**reference**
		$M^{-1}s^{-1}$	**$M^{-1}s^{-1}$**	**[%]**	**[M^{-1}]**	
OH	acetone	$(2.0 \pm 0.5)\cdot 10^8$	$(4.4 \pm 0.8)\cdot 10^8$	2.2	(0.13 ± 0.16)	Herrmann, 2003
	2-propanol	$(2.1 \pm 0.2)\cdot 10^9$	$(4.4 \pm 0.3)\cdot 10^9$	2.1	(0.22 ± 0.12)	Herrmann, 2003
	2-butanol	$(3.5 \pm 0.4)\cdot 10^9$	$(6.3 \pm 0.8)\cdot 10^9$	1.8	(0.25 ± 0.15)	Herrmann, 2003
NO_3	chloride	$(8.2 \pm 0.2)\cdot 10^6$	$(8.8 \pm 1.0)\cdot 10^7$	10.7	(0.82 ± 0.17)	Herrmann, 2003
	formate	$(4.2 \pm 0.2)\cdot 10^7$	$(2.3 \pm 0.3)\cdot 10^8$	5.5	(0.61 ± 0.45)	Herrmann, 2003
	oxalic acid	$(1.4 \pm 0.4)\cdot 10^8$	$(2.0 \pm 0.4)\cdot 10^8$	1.4	(0.22 ± 0.17)	Herrmann, 2003
	acetaldehyde	$(1.8 \pm 0.6)\cdot 10^6$	$(7.8 \pm 0.4)\cdot 10^6$	4.3	(0.28 ± 0.18)	Herrmann, 2003
	phenol	$(4.1 \pm 3.3)\cdot 10^8$	$(2.6 \pm 0.1)\cdot 10^9$	6.3	(0.41 ± 0.23)	Herrmann, 2003
	p-methylphenol	$(4.8 \pm 6.8)\cdot 10^8$	$(2.3 \pm 0.2)\cdot 10^9$	4.8	(0.29 ± 0.07)	this work
	p-methoxyphenol	$(0.3 \pm 2.3)\cdot 10^9$	$(2.6 \pm 0.1)\cdot 10^9$	8.1	(0.45 ± 0.59)	this work
	p-hydroxybenzoic acid	$(1.2 \pm 2.6)\cdot 10^9$	$(1.5 \pm 0.1)\cdot 10^9$	1.3	(0.13 ± 1.25)	this work
	p-nitrophenol	$(8.7 \pm 0.3)\cdot 10^8$	$(8.7 \pm 0.3)\cdot 10^8$	1.0	0.00	this work
	o-nitrophenol	$(8.9 \pm 0.4)\cdot 10^8$	$(8.9 \pm 0.4)\cdot 10^8$	1.0	0.00	this work

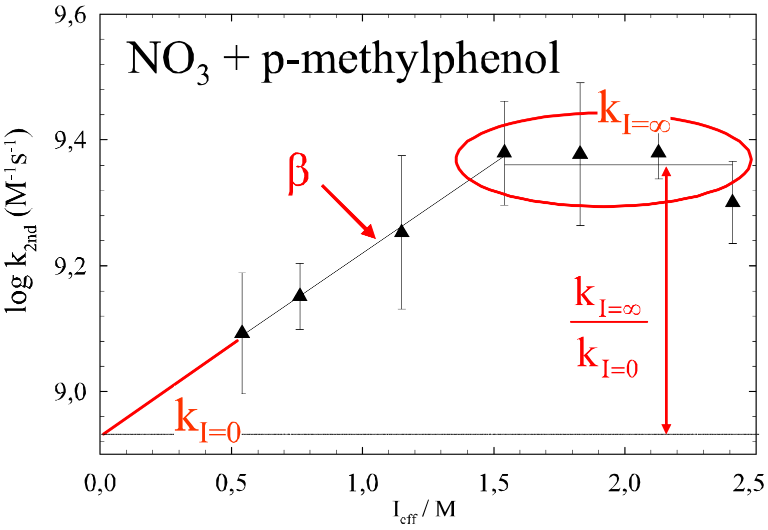

Figure 4: Measured rate constants (▲) as a function of the ionic strength for the reaction between NO_3 and p-methylphenol in aqueous solution.

As can be seen in Table 3 and Figure 4 a changing salt concentration can influence even the rate constants of reactions between neutral reactants significantly. Therefore, such salt effects should be considered in atmospheric multiphase models. However, there is so far no quantitative explanation for the measured salt effects in Table 3. That means the parameters in Table 3 can not be estimated and are purely empirical. For this reason further work on this topic will include not only measurements but also theoretical approaches in order to explain the obtained salt effects.

To evaluate the atmospheric relevance of the investigated radical reactions, the rate constants obtained can be compared with the corresponding gas phase values or with other aqueous phase oxidants. Figure 5 compares exemplarily the reactivity of OH and NO_3 radicals in aqueous solution. As can be seen in Figure 5 the OH radical reacts always faster than the NO_3 radical. However, the size of these differences does strongly depend on the considered class of organic reactants.

Similar to the gas phase chemistry is the OH radical also in the aqueous phase the most reactive and therefore most important radical for the degradation and conversion of water soluble organic compounds. However, beside the pure reactivity also atmospheric radical concentrations as well as diurnal concentration profiles needs to be consider for a detailed comparison of the atmospheric relevance.

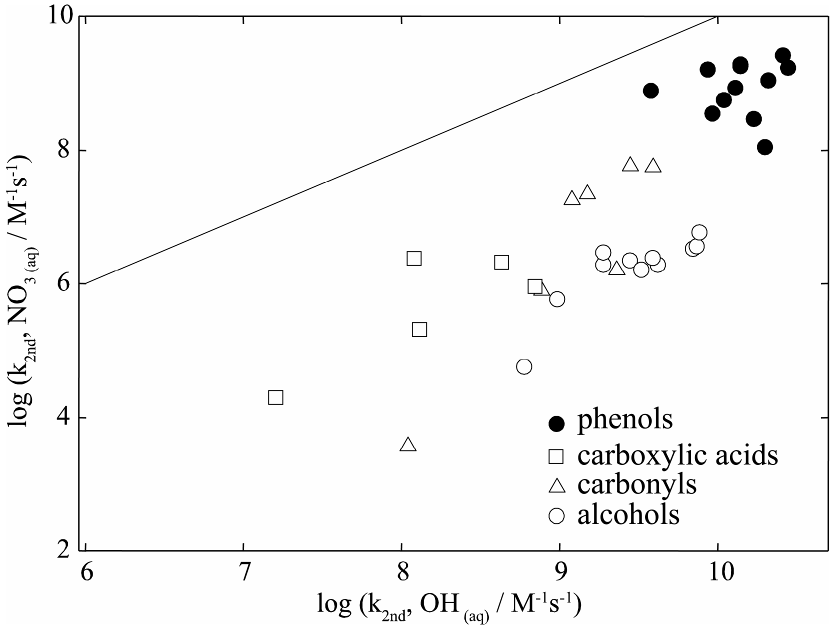

Figure 5: Comparison of the reactivity of OH and NO_3 radicals in aqueous solution. The solid line represents the line of same reactivity.

3.2 PRODUCT STUDIES ON AQUEOUS PHASE REACTIONS

In order to describe the multiphase chemistry information on reaction products, product yields and product distributions of oxidation reactions are needed as well. One investigated reaction system within the product studies performed was the oxidation of p-methylphenol in presence of atmospheric radicals (OH, NO_2 and NO_3). An overview over possible oxidation products is given in Figure 6.

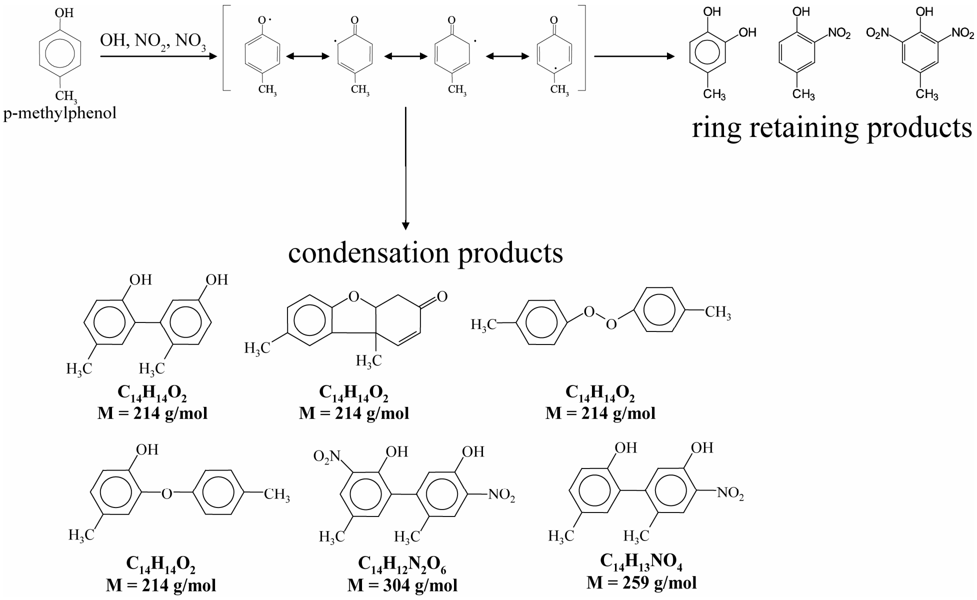

Figure 6: Possible reaction products after the aqueous phase oxidation of p-methylphenol in presence of OH/NO_2 and NO_3 radicals.

Expected reaction products in aqueous solution are ring retaining products after hydroxylation (p-methylcatechol) or nitration (2-nitro-4-methylphenol and 2,6-dinitro-4-methylphenol) of the aromatic ring as well as condensation products after the recombination of phenoxy radicals as shown in Figure 6. In this study the formation of reaction products was analyzed using the coupling of liquid chromatography-mass spectrometry after laser flash photolysis. During the experiments the number of laser pulses as well as the presence of atmospheric radicals was varied.

Identified main reaction products in presence of $OH/NO_2/NO_3$ radicals are the two nitrophenols (2-nitro-4-methylphenol and 2,6-dinitro-4-methylphenol) in Figure 6. These two compounds explain already 57 % of the observed p-methylphenol conversion. The formation of such potentially toxic and phytotoxic nitro-compounds within the atmosphere can be important for health effects and environmental aspects. Due to this possible relevance of these processes is it necessary to carefully evaluate the formation potential of nitrophenols after the aqueous phase oxidation of aromatic compounds by further laboratory studies on other systems.

Other identified p-methylphenol oxidation products are different condensation products. Due to several recombination possibilities of phenoxy radicals different condensation products (see Figure 6) with the same molecular mass were identified, as can be seen in the extracted ion chromatograms (EIC) in Figure 7. As shown in Figure 7 the number of excimer laser pulses influences clearly the number as well as the intensities of formed condensation products in the reaction cell. The formation of these high molecular weight compounds could contribute significantly to the organic mass of atmospheric particles. In order to measure the formation potential of condensation products and to characterize the atmospheric relevance, the product yields of these condensation products will be characterized with authentic standard compounds.

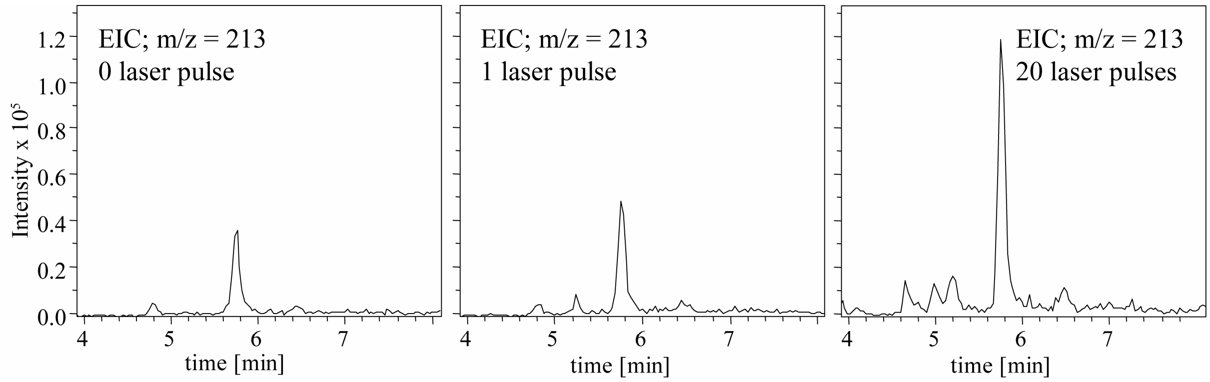

Figure 7: Extracted ion chromatograms which demonstrate the formation of condensation products after the aqueous phase oxidation of p-methylphenol in presence of $OH/NO_2/NO_3$ radicals.

4 FURTHER WORK

Further laboratory experiments concerning the better description of multiphase chemical processes will include investigation on the formation and the further chemistry of organic peroxy radicals in aqueous solution. Other investigations will be focused on the characterization of aqueous phase processes during the isoprene oxidation sequence by the combination of laboratory experiments and modeling studies. More emphasis will be placed on detailed investigations on the atmospheric stability and lifetimes of important tracer compounds for source apportionment studies.

For the implementation of the measured ionic strength effects into atmospheric models, it is planned to better investigate salt effects on atmospherically relevant reactions by further kinetic measurements and theoretical studies. Future kinetic measurements will be much more supplemented by detailed products studies.

In order to better characterize photochemical processes within the troposphere, quantum yields and photolysis products of atmospherically relevant reactions will be measured. Center of these investigations will be the photochemistry of Fe(III) complexes under atmospheric concentration. The better characterization of photochemical processes will help to reduce current discrepancies between field measurements and modeling studies

5 REFERENCES

Barzaghi, P.; Herrmann, H., “A mechanistic study of the oxidation of phenol by $OH/NO_2/NO_3$ in aqueous solution.” *Physical Chemistry Chemical Physics,* **2002,** 4, 3669-3675.

Barzaghi, P.; Herrmann, H., “Kinetics and mechanisms of reactions of the nitrate radical (NO_3) with substituted phenols in aqueous solution.” *Physical Chemistry Chemical Physics,* **2004,** 6, 5379-5388.

Exner, M.; Herrmann, H.; Zellner, R., “Rate constants for the reactions of the NO_3 radical with $HCOOH/HCOO^-$ and CH_3COOH/CH_3COO^- in aqueous solution between 278 K and 328 K.” *Journal of Atmopsheric Chemistry,* **1994,** 18, 359-378.

Ervens, B.; Gligorovski, S.; Herrmann, H., “Temperature-dependent rate constants for hydroxyl radical reactions with organic compounds in aqueous solutions.” *Physical Chemistry Chemical Physics,* **2003,** 5, 1811-1824.

de Semainville P.; Hoffmann, D.; George, C.; Herrmann, H., “Study of nitrate radical (NO_3) reactions with carbonyls and acids in aqueous solution as a function of temperature.” *Physical*

Chemistry Chemical Physics, **2007,** 9, 958-968.

Grgic, I.; Podkrajsek, B.; Barzaghi, P.; Herrmann, H., "Scavenging of SO_4^- radical anions by mono- and dicarboxylic acids in the Mn(II)-catalyzed S(IV) oxidation in aqueous solution." *Atmospheric Environment,* **2007,** 41, 9187-9194.

Gligorovski, S.; Herrmann, H., "Kinetics of reactions of OH with organic carbonyl compounds in aqueous solution." *Physical Chemistry Chemical Physics,* **2004,** 6, 4118-4126.

Herrmann, H.; Exner, M.; Zellner, R., "Reactivity trends in reactions of the nitrate radical (NO3) with inorganic and organic cloudwater constituents", *Geochimica et cosmochimica acta,* **1994**, 58, 3239-3244.

Herrmann, H.; Exner, M.; Jacobi, H. W.; Raabe, G.; Reese, A.; Zellner, R., "Laboratory studies of atmospheric aqueous-phase free-radical chemistry: Kinetic and spectroscopic studies of reactions of NO_3 and SO_4^- radicals with aromatic compounds" *Faraday Discussions*, **1995**, 100, 129-153.

Herrmann, H.; Zellner, R., "Reactions of the NO_3 Radical in Aqueous Solution", ed Alfassi, Z. B., John Wiley & Sons, New York, **1998**, 291-343.

Herrmann, H.; Tilgner, A.; Barzaghi, P.; Majdik, Z.-T.; Gligorovski, S.; Poulain, L.; Monod, A., "Towards a more detailed description of tropospheric aqueous phase organic chemistry: CAPRAM 3.0", *Atmospheric Environment,* **2005**, 39, 4351-4363.

Herrmann, H., "On the photolysis of simple anions and neutral molecules as sources of O^-/OH, SO_x^- and Cl in aqueous solution." *Physical Chemistry Chemical Physics,* **2007,** 9, 3935-3964.

Jacobi, H. W.; Wicktor, F.; Herrmann, H.; Zellner, R., "A laser flash photolysis kinetic study of reactions of the Cl_2(-) radical anion with oxygenated hydrocarbons in aqueous solution." *International Journal of Chemical Kinetics,* **1999,** 31, 169-181.

Morozov, I.; Gligorovski, S.; Barzaghi, P.; Hoffmann, D.; Lazarou, Y. G.; Vasiliev, E.; Herrmann, H., "Hydroxyl radical reactions with halogenated ethanols in aqueous solution: Kinetics and thermochemistry." *International Journal of Chemical Kinetics,* **2008,** 40, 174–188.

Parajuli, K., "Laser based kinetic investigations of halogen radicals in aqueous solution." PhD thesis, University of Leipzig, **2007**.

Ravishankara, A. R., "Heterogeneous and multiphase chemistry in the troposphere." , *Science,* **1997**, 276, 1058-1065.

Umschlag, T.; Zellner, R.; Herrmann, H., "Laser-based studies of NO_3 radical reactions with selected aromatic compounds in aqueous solution." *Physical Chemistry Chemical Physics,* **2002,** 4, 2975-2982.

Wicktor, F.; Donati, A.; Herrmann, H.; Zellner, R., "Laser based spectroscopic and kinetic investigations of reactions of the Cl atom with oxygenated hydrocarbons in aqueous solution." *Physical Chemistry Chemical Physics,* **2003,** 5, 2562-2572.

ANALYSES OF RAINDROP SIZE DISTRIBUTIONS FROM STRATIFORM AND CONVECTIVE CLOUDS OVER GUYUAN，CHINA

Xing-Can JIA [1] ,Sheng-Jie NIU[1 *],Jian-Ren SANG[2],Xiao-Li LIU[1],Jing-Jing LV[1]

1. Laboratory for Atmospheric Physics& Environment of China Meteorological Administration, Nanjing University of Information Science& Technology, Nanjing 210044, P.R.China
2. Ningxia Key Laboratory for Disaster Prevention and Reduction, Yinchuan 750002, P.R.China

1. DATA

The data were collect in Guyuan (36°N, 106°16′E), Ningxia. The climate of this area is rainless with the rainy season of three months, from early June to late August. The mean annual cumulative rainfall at Guyuan is about 490mm, while the mean evaporation is 1100mm.

Drop size distributions (DSDs) were observed with a PARSIVEL precipitation particle spectrometer during July 17th to August 26th, 2007. The PARSIVEL enables measurement of the size distribution based on single particle extinction, manufactured by PMTech AG, Pfinztal, Germany. Particles are detectable in the diameter range between 0.2 and 25mm, having velocities from 0.2 up to 20ms^{-1}. The precipitation particle size and velocity are sorted according to 32 size and velocity classes, respectively, with different width. The PARSIVEL calculates a number of related variables: drops-size and velocity distribution, rain-rate, radar reflectivity factor Z, and precipitation kinetic energy. The geometrical drop distortion is also taken into account (Loffler-Mang 2000).

The measurement time span of DSDs was 10 seconds. A total of 15893 DSDs were collected during 30 events. These 30 events were divided into stratiform and cumulus precipitation by radar and satellite observation.

2. DATA ANALYSIS

2.1 AVERAGED DSDS FROM STRATIFORM AND CONVECTIVE CLOUDS

Figure 1 presents the averaged observed drop size distributions from stratiform and convective clouds. Notably the drop number of convective rain is more than that of stratiform in the class 0.65mm<D<6mm. There are more drops with D<0.65mm in stratiform rain. The DSD breadth is broader for convective rain. The updraft is strong in convective cloud, which leads to forming large drops.

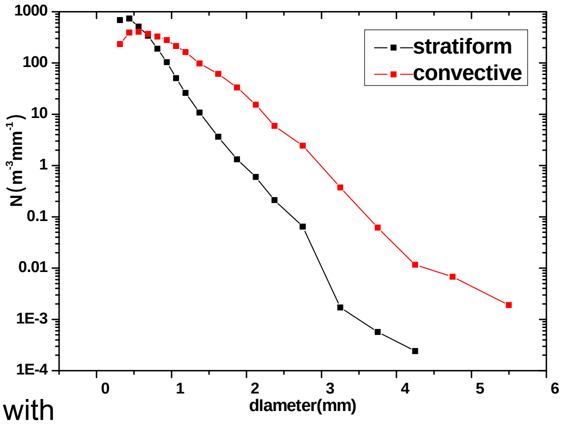

Fig.1 Averaged DSDs for stratiform and convective rain of whole dataset

The well-known gamma function (Ulbrich 1983) is used to represent the DSD given by

$$N = N_0 D^{\mu} \exp(-\lambda D)$$

where N_0 is the total number of drops, $\mu$is the shape parameter, which increases as

---

[*] Correaponding author.
E-mail address: niusj@nuist.edu.cn

the breadth of the DSD decreases, and$\lambda$is the slope parameter, which increases with the slope of the large size portion of the spectrum and also affects the DSD breadth. On average, $\mu$and λ for stratiform clouds are 0.212and 4.015, while for the convective clouds they are 1.452 and 3.369(Table 1)

Table 1 Parameters of Gamma distribution. r^2 is the correlation coefficient

	Gamma			
	N_0	λ	μ	r^2
convective	3933.5	4.015	0.212	0.931
stratiform	5832.3	3.369	1.542	0.965

2.2 ANALYSIS OF FITTING FUNCTION

Based on the skewness and kurtosis, a simple statistical method is used for a large number of spectrum data (Liu 1993). A quantitative criterion named 'Deviation Coefficients of skewness and kurtosis' (present C_s and C_k, respectively) is calculated to express the deviation of observed DSDs from an ideal gamma distribution. The equations of the C_s, and C_k are

$$C_s = \frac{S^2}{4}$$

$$C_k = \frac{K}{6}$$

where S and K are skewness and kurtosis calculated from the ten second observed DSDs, instead of widely used averaged DSDs, respectively. As calculated, the relationship of C_s, and C_k of ideal Gamma function is C_s=C_k. Figure 2 shows the data points of observed DSDs and beeline of C_s-C_k relation.It is found that the DSD from both types of clouds can be described very well with the gamma function. The mean correlation coefficient is 93.6%.

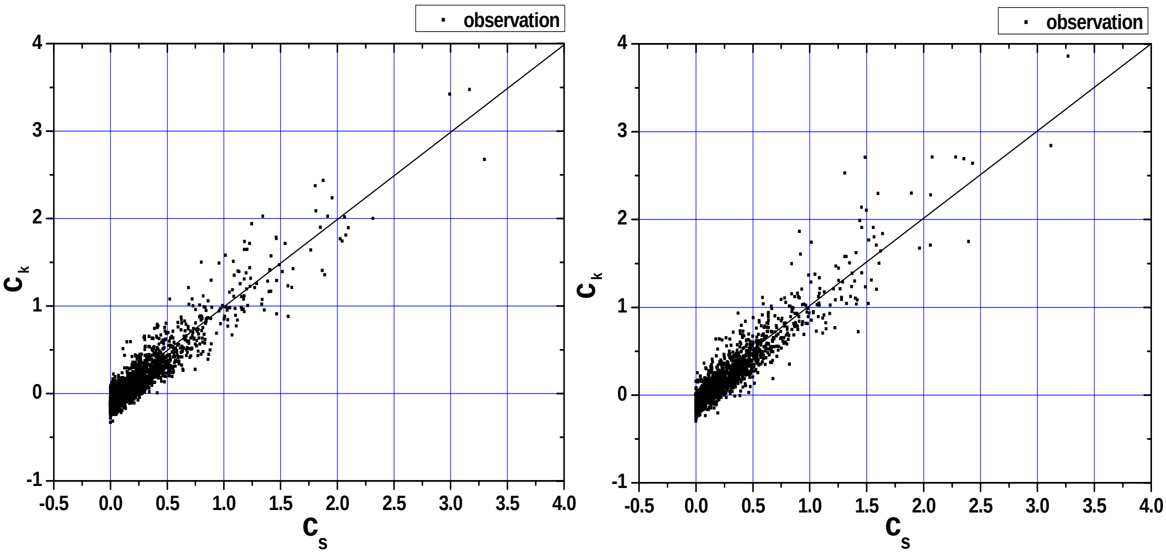

(a) (b)

Fig.2 C_s-C_k satter plot of DSDs. Each DSD results in a point. The beeline presents the C_s-C_k relation of gamma fuction (a) stratiform C_s-C_k plot (b) convective C_s-C_k plot

2.3 *Z-R* RELATIONSHIP

As is well known, the radar reflectivity factor of rain and rain-rate are linked by a relation of the form

$$Z = aR^b$$

where a and b are coefficients depending on the DSDs. The *Z-R* relation is often used to derive rain-rates from radar reflectivity. A distinction is often made between convective and stratiform *Z-R* relations owning to the cloud dynamics and microphysics. Table 2 gives the values of coefficients of a and b computed by least squares fitting. The difference of values of b between the two kinds of rain is no significant. The scatter of every values of b is small (11% and 13%for convective and stratiform, respectively). The scatter of every values of a is larger (37% and 62%for convective and stratiform, respectively). $Z=108.37R^{1.45}$ for convective, and $Z=279.02R^{1.65}$ for stratiform. The averaged value of a for convective rain is larger than the stratiform value. All values of a for stratiform is less than 200. Similar result were obtained by Liu(2006).

Table 2 Parameters of $Z=aR^b$ between stratiform and convective precipitation. r^2 is the correlation coefficient

Date	precipitation cloud	a	b	r^2
2007-7-17	c	158.60	1.50	0.49
2007-7-21	c	186.68	1.56	0.81
2007-7-22	c	278.17	1.69	0.93
2007-7-24	c	237.42	1.55	0.54
2007-7-26	c	246.63	1.52	0.94
2007-7-27	c	266.30	1.67	0.80
2007-7-29	c	403.23	1.98	0.91
2007-8-4	c	479.70	2.05	0.90
2007-8-6	c	293.13	1.63	0.95
2007-8-8	c	185.14	1.52	0.71
2007-8-12	c	417.30	1.67	0.87
2007-8-25	c	195.99	1.48	0.71
mean convective precipitation		279.02	1.65	0.80
2007-7-18	s	197.40	1.69	0.82
2007-7-19	s	160.03	1.63	0.71
2007-7-20	s	78.08	1.37	0.58
2007-8-9	s	33.85	1.23	0.98
2007-8-26	s	72.47	1.32	0.80
mean stratiform precipitation		108.37	1.45	0.78

2.4 VELOCITY

The optical disdrometer measures size and velocity of single particles, allowing a velocity–size correlation. The terminal velocities of raindrops scatter obviously around the empirical curve ($v=9.65-10.3e^{-0.6D}$). This scatter is caused by turbulence of air close to the ground, probably more important, by instrumental limitations.

The fall velocity distributions as a function of size were fit with the power law relation $V_t = cD^x$. The drop velocity distributions of both kinds of clouds show moderate differences. On average, $V_t = 3.42D^{0.71}$for convective cloud, and $V_t = 4.04D^{0.53}$ for stratiform cloud. The velocity is smaller than the empirical curve in class D>3.75mm.

3. BIBLIOGRAPHY

Atlas D. C. W. Ulbrich, An Observationally Based Conceptual Model of Warm Oceanic Convective Rain in the Tropics. J Appl Meteor.2000:2165-2181

Gunn, R., and G. D. Kinzer, The terminal velocity of fall for water droplets in stagnant air. J. Meteor, 1949 6:243–248.

Krajewski W. F. et al DEVEX-disdrometer evaluation experiment: Basic results and implications for hydrologic studies.

Advances in Water Resources 2006 29: 311–325

Loffler-Mang M, Joss J. An optical disdrometer for measuring size and velocity of hydrometeors.J Atmos Oceanic Technol 2006 17:130–139.

Liu Yangang Statistical method theory of the Marshell-Parmer distribution of raindrop Atmospheric Environment 1993:15-19

Liu Yangang Chen Wankui Investigation of aerosol partical size spectra-a simple statistical method. Acta Scientiae Circumstantiae 1993 13:22-30.

Liu Hongyan, Lei Hengchi, Characteristics of Rain from Stratiform Versus Convective Cloud Based on the Surface Raindrop Data, Chinese J Atmos Sci 2006,30:693-702

Rosenfeld, D., D. B. Wolff, and D. Atlas, General probability-matched relations between radar reflectivity and rain rate. J.Appl. Meteor.1993: 50–72.

Tokay, A., and D. A. Short, Evidence from tropical raindrop spectra of the origin of rain from stratiform and convective clouds. J. Appl. Meteor., 1998 35:355–371.

Ulbrich.C. W., Natural variations in the analytical form of the raindrop size distribution. J Climate Appl Meteor 1983 22:1764–1775.

ACKNOWLEDGEMENT

Key Technology and Instrument Development in Weather Modification （2006BAC12B01） from MOST of P.R.China.,and National Natural Science Foundation of China(Grant No. 40537034), supported this research.

THE EFFECT OF SPATIAL AVERAGING ON THE RELATIVE HUMIDITY AND PHASE COMPOSITION OF CLOUDS

Korolev A.V. and G.A. Isaac
Environment Canada, Toronto, Canada

1. Introduction

Relative humidity in clouds plays a crucial role in precipitation formation, phase transformation and life cycle of clouds. The in-cloud water vapor pressure is commonly assumed to be saturated with respect to liquid water in liquid clouds, and saturated with respect to ice in ice clouds. The humidity in mixed phase clouds has been debated in the cloud community for years. The water vapor pressure (E_w) in mixed phase clouds is generally approximated as a weighted average of the respective saturation values over liquid water (E_{ws}) and ice (E_{is})

$$E_w = fE_{ws} + (1 - f)E_{is} \qquad (1)$$

where f is the weighting factor ($0 \leq f \leq 1$). The value of f in mesoscale and global circulation models (GCM) is usually specified as a function of temperature (e.g. Fowler et al. 1996; Jakob 2002) or cloud liquid (LWC) and ice (IWC) water content (e.g. Lord et al. 1984; Wood and Field 2000, Fu and Hollars 2004). In some numerical schemes (Rostyan et al. 2000; Tremblay and Glazer 2000) the water vapor in mixed clouds assumed to be saturated with respect to liquid water, i.e. f=1.

In-situ measurements showed that the proportion between liquid and ice in mixed phase clouds is a function of temperature (Korolev et al. 2003). Besides temperature, the partitioning between ice and liquid is expected to depend on the spatial averaging scale. When the averaging scale is large enough, locally mixed phase clouds become alternated with single phase ice clouds, where relative humidity is *a priori* different from that in mixed phase clouds. Therefore, the relative humidity in clouds is anticipated to depend on the averaging scale as well. The existing humidity parameterizations do not include dependence on the averaging scale. A proper description of the relative humidity in mixed phase clouds plays an important role for accurate simulations within GCMs.

A new parameterization of the relative humidity in mixed phase clouds is discussed here. The new parameterization is based on consideration of the spatial fractions of liquid ice and mixed phase clouds. It is shown that the average relative humidity in mixed phase clouds should be weighted by the spatial fraction of ice clouds rather than by the mass fraction of ice which is frequently used in GCMs.

2. Prerequisite

There are two extreme situations which may occur in mixed phase clouds: (1) liquid droplets and ice particles are uniformly mixed and (2) liquid droplets and ice particles are separated in space and they form single-phase "ice" and "liquid" clusters. In the framework of this study the first category will be recognized as "genuinely" mixed clouds. The second category, where genuinely mixed phase and liquid clouds are mixed with ice clouds, will be referred to as "conditionally" mixed. A cartoon of a conditionally mixed phase cloud is shown in Fig.1.

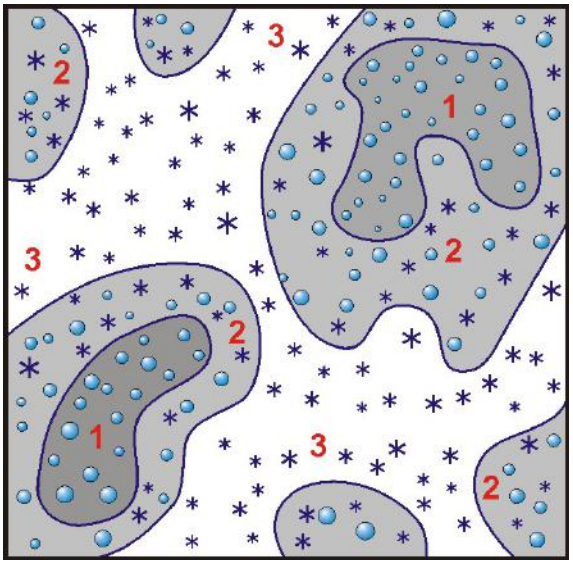

Figure 1. Conceptual diagram of conditionally mixed phase cloud. Numbers indicate genuinely mixed phase (1), liquid (2) and ice (3) clouds regions.

In a general case for the ensemble of ice, liquid and mixed phase clouds, the average humidity can be calculated as an average weighted by cloud volume fractions

$$\overline{E} = \upsilon_w \overline{E}_w + \upsilon_m \overline{E}_m + \upsilon_i \overline{E}_i \qquad (2)$$

Here $\overline{E}_w$, $\overline{E}_i$, $\overline{E}_m$ are average humidity in single phase liquid and ice, and genuinely mixed phase clouds, respectively; υ_w, υ_i, υ_m are volume fractions ($\upsilon_* = V_* / \Delta V$) of liquid, ice, liquid and mixed phase clouds, respectively; V_* is the volume of cloud regions (ice, liquid or mixed phase) sampled in a cloud with volume ΔV. The cloud volume fractions are normalized so, that $\upsilon_w+\upsilon_i+\upsilon_m=1$. It can be shown (Russ and Dehoff 2000) that for random samples $\lim_{\Delta L\to\infty} L_* / \Delta L = V_* / \Delta V$, where L_* is the length of cloud regions (ice, liquid or mixed phase) sampled along the cloud with the total length ΔL. Since in-situ techniques do not allow measurements of V_*, the ratio $L_* / \Delta L$ is used for estimation of υ. Therefore, Eq.2 can be rewritten as

$$\overline{E} = \lambda_w \overline{E}_w + \lambda_m \overline{E}_m + \lambda_i \overline{E}_i \qquad (3)$$

Here λ_w, λ_i, λ_m are spatial fractions ($\lambda_* = L_* / \Delta L$) of liquid, ice, and genuinely mixed phase clouds, respectively, and $\lambda_w+\lambda_i+\lambda_m=1$.

As was found from a theoretical analysis (Korolev and Mazin 2003) and in-situ observations (Korolev and Isaac 2006) the vapor pressure in liquid and genuinely mixed clouds is close to saturation with respect to water, i.e. $\overline{E}_w = E_{ws}$ and $\overline{E}_m = E_{ws}$. Substituting $\overline{E}_w$, $\overline{E}_w$ in Eq.3, and taking into account that $\lambda_w+\lambda_m=1-\lambda_i$ yields

$$\overline{E} = (1-\lambda_i) E_{ws} + \lambda_i \overline{E}_i \qquad (4)$$

Eq.4 can be rewritten in terms of relative humidity with respect to water as

$$\overline{RH}_w = (1-\lambda_i)100 + \lambda_i \overline{RH}_{wi} \qquad (5)$$

where $\overline{RH}_{wi}$ is the average relative humidity with respect to water in ice clouds.

Korolev and Isaac (2006) found that in ice cloud, the vapor pressure does not necessarily equal to saturation over ice, but it varies between saturation over water and that over ice, and in many cases it can be undersaturated with respect to ice. Based on the results obtained in Korolev and Isaac (2006) $\overline{RH}_{wi}$ at temperatures $-45<T<0$C can be parameterized as

$$\overline{RH}_{wi} = a_3 T^3 + a_2 T^2 + a_1 T + a_0 \qquad (6)$$

Here $a_3= 7.529*10^{-5}$; $a_2=1.408*10^{-2}$; $a_1=0.8897$; $a_0=99$; T is in degrees Celsius, and $\overline{RH}_{wi}$ is in %. Figure 2 shows measured and parameterized relative humidity in ice clouds. Eqs. 5 and 6 yield the parameterization of the average relative humidity in conditionally mixed phase clouds.

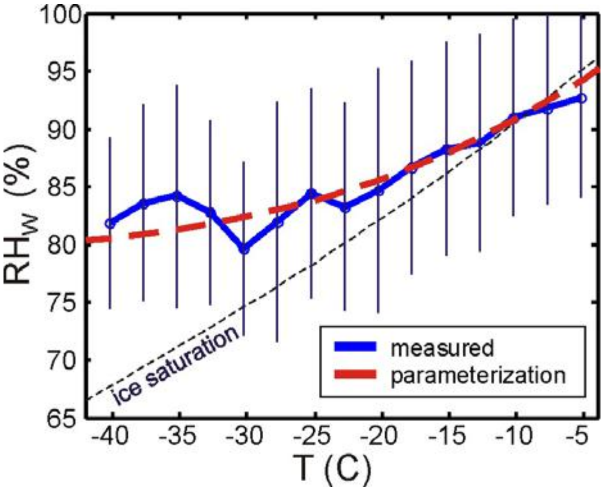

Figure 2. Average relative humidity with respect to water in ice clouds versus temperature. The red dashed line indicates the parameterization of Eq.6. Vertical lines indicate the standard deviation of the measurements. The data adapted from Korolev and Isaac (2006).

In the following sections we compare the humidity parameterization described by Eqs. 5 and 6 with that obtained from in-situ measurements in mixed phase clouds at different spatial scales.

3. Instrumentation and data set

The measurements of humidity in clouds with different phase composition were conducted using the National Research Council (NRC) Convair-580. A detailed description of the instrumentation, accuracy issues and data processing is provided in Korolev and Isaac (2006). Below we briefly describe the probes used in this study for measurements of humidity and characterization of cloud microphysics.

The air temperature was measured by the Rosemount total-air temperature probe (model 102DJ1CG). The water vapor concentration was measured by a Licor HO_2 analyzer (model LI-6262, LI-COR Inc.). The liquid water content (LWC), the ice water content (IWC) and the ice water fraction (μ=IWC/(LWC+IWC)) were deduced from the measurements of the Nevzorov probe (Korolev et al. 1998). Concentration and sizes of cloud droplets were measured by two PMS (Particle Measuring Systems) FSSP-100s (Forward Scattering Spectrometer Probe) (Knollenberg, 1981), operated in the size ranges 3 - 47 μm and 5 - 95 μm. Large cloud particles were measured by 2D-imaging optical array probes (OAP): PMS OAP-2DC (25 - 800 μm); a PMS OAP-2DP (200 - 6400 μm) (Knollenberg, 1981) and the SPEC Inc. High Volume Spectrometer Precipitation Spectrometer (HVPS) (200μm-4cm) (Lawson et al. 1998). All three instruments provided shadow binary images and concentrations of hydrometeors within their respective size ranges. The Rosemount Icing Detector (RICE) was used for identifying the presence of liquid phase in clouds with LWC>0.01g/m^3 (Cober et al. 2001; Mazin et al. 2001).

The Licor probe was calibrated every flight in liquid clouds such that the dew point deduced from its measurements was forced to be equal to the air temperature. The accuracy of the RH measurements utilizing this technique was estimated as 1% (Korolev and Isaac 2006). The Nevzorov IWC measurements were affected by bouncing of ice particles from the TWC sensor cone, which resulted in the underestimating of IWC. The IWC measurements were corrected for the ice bouncing following Korolev et al. (2008).

Because of the residual effect of ice on the Nevzorov LWC sensor, ice particles may mask the presence of a small amount of liquid water in mixed clouds. In order to reduce ambiguity in identifying low LWC in mixed clouds, the RICE probe was used as a detector of clouds with LWC>0.01g/m^3. Based on this, liquid and mixed clouds were defined from the Nevzorov and RICE measurement using the following conditions: if the ice water fraction μ<0.1, then the cloud was considered liquid; if 0.9≥ μ ≥0.1 and then the cloud was considered as mixed phase. Clouds with the concentration of ice particles N_{ice}>10m^{-3} and LWC<0.01g/m^3 were determined as ice clouds.

The data were collected during three field campaigns: FIRE.ACE in April 1998 over Canadian North and Arctic Ocean, and the Alliance Icing Research Study projects (phases 1.5 and 2) over Southern Ontario and Quebec during two winter seasons 2002/03 and 2003/04 (Isaac et al. 2001 and 2005). The bulk of the data was sampled in stratiform clouds (*St, Sc, Ns, As, Ac, Ci*), associated with frontal systems. The measurements were averaged over 1-second time intervals, which correspond to the spatial resolution of approximately 100m at the Convair-580 airspeed. The total number of flights included in the analysis is 36, with the total in-cloud portion analyzed here being approximately 22,840 km. The temperature was limited to the range -5^{o}C to -45^{o}C. The altitude of measurements ranged from 0 to 7 km.

4. Results

The data analysis of the relative humidity started from segregating cloud and cloud free regions. All cloud free measurements were excluded from the analysis. Then the clouds were sorted by temperature in three sub-ranges -35<*T*<-20^{o}C, -20<*T*<-10^{o}C and -10<*T*<-5^{o}C. After that the newly formed cloud regions were arranged in a sequence one after another in each temperature sub-range. The relative humidity, IWC, and LWC were calculated as a moving average with spatial windows 1km, 5km, 10km, 20km and 50km.

Figure 3 shows $\overline{RH_w}$ versus spatial ice cloud fraction λ_i in conditionally mixed phase clouds. The computation was done for different averaging scales in three temperature intervals. The two dashed lines indicate the theoretical values for $\overline{RH_w}$ calculated from Eqs.5 and 6 for minimum and maximum temperatures corresponding to each of the diagrams. As seen from Fig.3 the relative humidity $\overline{RH_w}$ decreases with an increase in the spatial ice fraction. The slopes of the $\overline{RH_w}$ curves are in

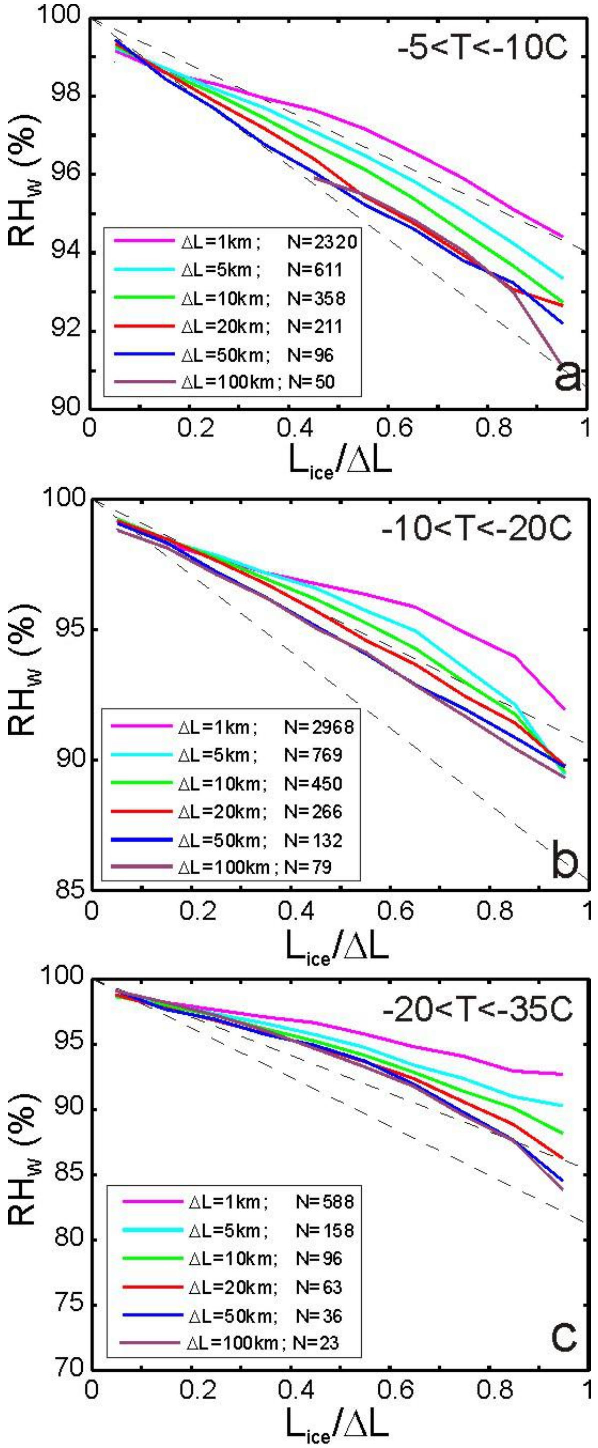

Figure 3. Relative humidity in conditionally mixed phase clouds versus ice cloud spatial fraction ($\lambda_i = L_i / \Delta L$). Dashed lines indicate the parameterization of RH_w based on Eqs. 5 and 6 for minimum and maximum temperatures corresponding to each diagram.

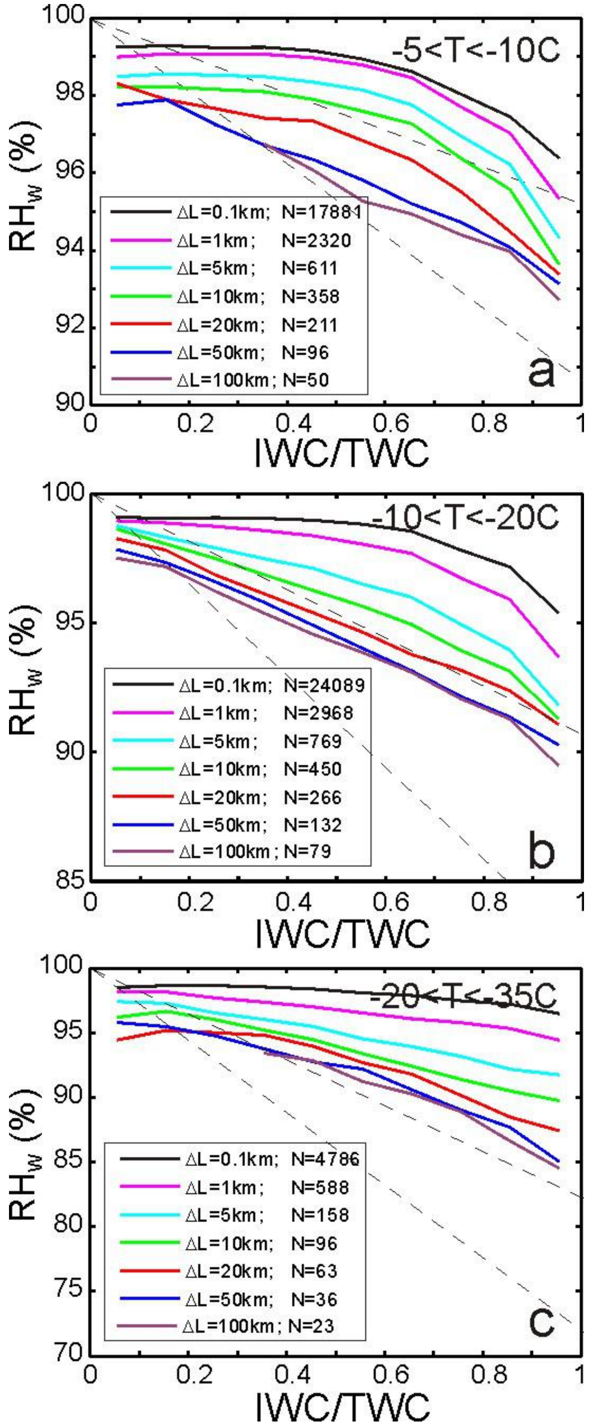

Figure 4. Relative humidity in mixed phase clouds versus ice mass fraction ($\mu_i = IWC / TWC$). Dashed lines indicate the parameterization of RH_w based on Eq. 7 for minimum and maximum temperatures corresponding to each diagram.

general agreement with that predicted by Eqs.5 and 6 (dashed lines). Fig.3 also indicates that the average relative humidity decreases when the spatial averaging increases from 1 to 20 km. However, for ΔL=50 and 100km the $\overline{RH}_w$ curves are grouped close to each other. Such behavior suggests that at the spatial scale 1 to 20km the humidity is higher in the vicinity of liquid and mixed phase clouds. Such an increase of the humidity may occur due to the horizontal transport of water vapor. At a spatial scale ΔL>50km the clouds becomes more homogenized and an increase in averaging scale does not result in changes in $\overline{RH}_w$.

Figure 4 shows $\overline{RH}_w$ versus mass ice water fraction μ_i in mixed phase clouds in three temperature intervals and different averaging scales. Two dashed lines indicate theoretical values for $\overline{RH}_w$ calculated for minimum and maximum temperatures corresponding to each of the diagrams from equation

$$RH_w = (1-\mu_i)100 + \mu_i RH_{wsi} \qquad (7)$$

Here $RH_{wsi} = 100 E_{is} / E_{ws}$ is the relative humidity over water at saturation over ice, $\mu_i = IWC / TWC$ ice mass fraction, $TWC=IWC+LWC$ is the total water content.

The general behavior of the mass weighted $\overline{RH}_w$ is generally the same as that for the spatial weighted $\overline{RH}_w$. However, simple visual comparison of Figs 3 and 4 indicate that the mass weighted $\overline{RH}_w$ have less slope and deviate more from the theoretical values than spatial weighted $\overline{RH}_w$.

In sake of better interpretation of Figs 3 and 4 it should be noted that the value of the spatial ice fraction λ_i gives an unambiguous answer whether the cloud is genuinely (λ_i=0) or conditionally (0<λ_i<1) mixed. However, the ice mass fraction μ_i does not allow any conclusions about type of mixed phase clouds. Preliminary results based on the analysis of the spatial inhomogeneity of mixed phase regions enable conclusion that most data points shown in Fig.4 for ΔL>5km are related to conditionally mixed phase clouds.

5. Conclusion

In the frame of this study we found that parameterization of the humidity weighted by spatial ice fraction agrees better with the results of in-situ measurements than humidity parameterization weighted by ice mass fraction

References

Cober, S.G., Isaac, G.A., and A.V. Korolev, 2001: Assessing the Rosemount Icing Detector with in-situ measurements. *J. Atmos. Oceanic Technol.,* **18**, 515-528

Fowler, L. D., D. A. Randall, and S. A. Rutledge, 1996: Liquid and ice cloud microphysics in the CSU general circulation model. Part I: Model description and simulated microphysical processes.

Fu, Q., and S. Hollars, 2004: Testing Mixed-Phase Cloud Water Vapor Parameterizations with SHEBA/FIRE–ACE Observations. *J. Atmos. Sci.,* **61**, 2083-2091

Knollenberg, R. G. 1981 Techniques for probing cloud microstructure. In: *Clouds, their formation, Optical properties, and Effects*, P. V Hobbs, A. Deepak, Eds. Academic Press, 495 pp

Korolev, A.V., J. W. Strapp, G.A. Isaac, and A.N. Nevzorov, 1998: The Nevzorov airborne hot-wire LWC-TWC probe: principle of operation and performance characteristics. *J. Atmos. Oceanic Technol.* **15**, 1495-1510

Korolev, A.V., G.A. Isaac, S. Cober, J.W. Strapp, and J. Hallett, 2003: Microphysical characterization of mixed-phase clouds. *Quart.J.Roy.Meteor.Soc.,* **129**, 39-66

Korolev, A.V. and I.P. Mazin, 2003: Supersaturation of water vapor in clouds. *J. Atmos. Sci.,* **60**, 2957-2974

Korolev, A.V. and G.A. Isaac, 2006: Relative Humidity in Liquid, Mixed Phase and Ice Clouds. *J. Atmos. Sci.,* **63**, 2865-2880.

Korolev, A., J. W. Strapp, G. Isaac, and E. Emery, 2008: Improved Airborne Hot-Wire Measurements of Ice Water Content in Clouds. *ibid*

Lawson, R. P., R. E. Stewart and L. J. Angus, 1998: Observations and numerical simulations of the origin and development of very large snowflakes. *J. Atmos. Sci.*, **55**, 3209-3229

Licor LI-6262 CO_2/HO_2 Analyzer. Operating and Service Manual, 1996: Publication Number 9003-59, March, 1996, LI-COR Inc., Lincoln, Nebraska, USA (http://www.licor.com/env/Products/GasAnalyzers/gas.jsp)

Lord, S. J., H. E. Willoughby, and J. M. Piotrowicz, 1984: Role of a parameterized ice-phase microphysics in an axisymmetric, nonhydrostatic tropical cyclone model. *J. Atmos. Sci.,* **41,** 2836–2848

Mazin, I. P., A. V. Korolev, A. Heymsfield, G. A. Isaac, and S. G. Cober, 2001 Thermodynamics of icing cylinder for measurements of liquid water content in supercooled clouds. *J. Atmos. Oceanic Technol.,* **18**, 543-558

Rotstayn, L.D., Ryan, B.F. and Katzfey, J.J. 2000: A Scheme for Calculation of the Liquid Fraction in Mixed-Phase Stratiform Clouds in Large-Scale Models. *Q. J. R. Meteorol. Soc.,* **128**, 1070–1088

Russ J.C. and Dehoff, R.T. 2000 Practical Stereology. 2nd edition. New York: Plenum Press.

Tremblay, A., and A. Glazer, 2000: An improved modeling scheme for freezing precipitation forecasts. *Mon. Wea. Rev.,* **128,** 1289– 1308.

Wood, R., and P. R. Field, 2000: Relationships between total water, condensed water, and cloud fraction in stratiform clouds examined using aircraft data. *J. Atmos. Sci.,* **57,** 1888–1904

ENTROPIC ASPECTS OF SUPERCOOLED DROPLET FREEZING

Alexander Kostinski and Will Cantrell
Department of Physics
Michigan Technological University
Houghton MI 44931 USA

1. INTRODUCTION

Entropy can be related to a definite quantity of heat in a reversible process but associating latent heat with a phase transition from a metastable state is less clear. However, freezing in the atmosphere is always initiated from a metastable state – supercooled water.

Measurements of the latent heat of fusion as a function of temperature are difficult and remain scarce. We have been able to locate only three such measurements – Fukuta and Gramada (2003), the Smithsonian Tables (1951), and Bertolini et al. (1985). In the two studies motivated by processes in Earth's atmosphere (Fukuta and Gramada, 2003; List, 1951) the latent heat values were obtained by using measured vapor pressures, then using the Clausius-Clapeyron equation as well as the triple point identity for the latent heats of sublimation, vaporization and fusion to extract the latent heat of fusion. In other words, the latent heat measurements are not direct and involve questionable assumptions for the supercooled (metastable) domain (see Kostinski and Cantrell (2008) for details). We re-examine the measurements and suggest a lower bound on the latent liberated during freezing of an initially supercooled water droplet. We also derive a simple estimate for the heat released in the complicated process of freezing, corresponding warming of the droplet (because of the latent heat released at the ice-water interface within the droplet as it freezes), and subsequent cooling back to ambient temperatures. Finally, we estimate the contribution of the intrinsic irreversibility of freezing to the heat production.

2. A CONSTRAINT ON THE HEAT RELEASED FROM FREEZING A SUPERCOOLED WATER DROPLET

Recall that Clausius' definition of entropy, $dS=\frac{dq}{T}$, implies reversibility. Since water freezing from a supercooled state is irreversible, the release of the latent heat of fusion to the atmosphere cannot be calculated simply from the latent heat released at the melting point, where the transition is reversible. Indeed, for the reversible case, the latent heat of fusion is simply $T\,\Delta S$, where *T* is the temperature at which the transition occurs and *ΔS* is the difference in entropy between water and ice.

Allowing for irreversible processes, the Second law of thermodynamics can be stated as $dS_{\text{system}} \geqslant \frac{dq}{T}$, where the equality applies for a reversible process. In the case of freezing, $dS_{\text{system}} < 0$ (i.e. the entropy of water decreases) and $dq < 0$ (heat is given off). Thus, the inequality implies $|L(T)| \geqslant |T\,\Delta S|$. The magnitude of the latent heat released upon freezing must equal or exceed *TΔS*, which is shown as the dashed line in the figure. The figure also shows that Bertolini et al.'s data are in agreement with the bound.

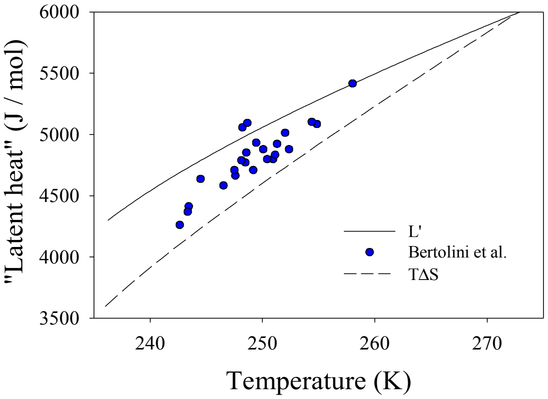

Figure 1: Bounds on the latent heat of fusion released during freezing of a supercooled droplet of water along with data from Bertolini et al. (1985).

3. A SIMPLE APPROXIMATION FOR THE LATENT HEAT RELEASED DURING FREEZING OF SUPERCOOLED WATER

Though freezing from a metastable state is not reversible, a reversible path can be constructed, linking the initial and final states. This path can then be associated with a definite quantity of heat, because it fulfills the requirement of reversibility. The reversible path connecting water at some temperature T_i, below the normal melting point, and ice at the same temperature proceeds along the following lines.

1. Warm the water (reversibly) to the melting point.
2. Freeze the water, releasing the latent heat of fusion. (This process is reversible because it is on the equilibrium phase boundary.)
3. Cool the resulting ice back to T_i.

Mathematically, the path can be written as:

$$L'(T_i)=L_m-\int_{T_i}^{T_m}[c_{\text{liquid}}(T)-c_{\text{solid}}(T)]dT \quad ,$$

where $L'(T_i)$ is the effective latent heat released by a droplet initially at the temperature T_i, L_m is the latent heat of fusion at the normal melting point, and c_{liquid} and c_{solid} are the (temperature dependent) heat capacities of liquid water and ice respectively. *L'* is plotted as the solid line in the figure. Again, Bertolini et al.'s data fall within the bounds, though (with the exception of three points), their measurements fall below the effective heat released predicted by the equation above.

Why? A thermodynamic state of ice is not fully specified by pressure and temperature. The strain also matters and depends on the history of freezing (See Kostinski and Cantrell (2008) for details.) To summarize here, we again return to the irreversibility of the process. The path we have laid out implicitly assumes that the final state is well characterized by final pressure and temperature. However, rapid freezing is likely to result in ice riddled with defects, thereby affecting it's entropy.

4. TEMPERATURE GRADIENTS WITHIN THE FREEZING DROPLET AND ASSOCIATED PRODUCTION OF ENTROPY

Release of latent heat must create temperature gradients within the droplet. Indeed, the rate at which liquid is converted to crystal at the ice-water interface is largely controlled by the rate at which the latent heat of fusion is conducted away. Note that this physical picture is consistent with the path used in the derivation of *L*', where water is warmed to the melting point and then freezes. Surprisingly, entropy production is due to the temperature gradients generated within the droplet.

We estimate the entropy created by the intrinsic irreversibility associated with temperature gradients following the reasoning that the irreversibility can be expressed as the product of the rate of entropy production, $\dot{s}$, and the droplet's thermal relaxation time, τ. (Zemansky, 1981, p. 204). In the expression,

$$\delta s_{\text{irr}}=\dot{s}\tau=kd^2\left(\frac{\Delta T^2}{d\,T^2}\right)\left(\frac{d^2}{\alpha}\right)=\rho\, c_p d^3\left(\frac{\Delta T}{T}\right)^2$$

k is the thermal conductivity of water, *d* is the diameter of the droplet, ΔT is the temperature gradient, α is the thermal diffusivity of water, ρ is the density of water and c_p is the heat capacity. Normalizing the result by the entropy of the reversible process, L/T_m, we obtain:

$$\frac{\delta s_{\text{irr}}}{\delta s_{\text{rev}}}=\frac{c_p\Delta T^2}{l\,T_m}$$

, where *l* is the specific latent heat of fusion. The contribution approaches 10% at a supercooling of 40 K. (See Kostinski and Cantrell (2008) for details.)

6. REFERENCES

Bertolini,D.,M. Cassettari, and G. Salvetti,1985: Anomalies in the “latent heat” of solidification
of supercooled water. Chem. Phys. Lett.,119, 553–555.

Fukuta,N. and C. Gramada, 2003: Vapor pressure measurement of supercooled water. J. Atmos. Sci., 60,1871–1875.

Kostinski, A. and W. Cantrell, 2008: Entropic aspects of supercooled droplet freezing. J. Atmos. Sci., in press.

List, R.,ed.,1951: Smithsonian Meteorological Tables. Smithsonian Institution, 6th edition, 527 pp.

Zemansky, M., 1981: Heat and Thermodynamics. McGraw-Hill, 6th edition, 543 pp.

Acknowledgments

This work was supported by National Science Foundation grants ATM01-06271, ATM05-54670 and CHE-0410007. Numerous helpful discussions with Gregory Ryskin are greatly appreciated. We thank Bill Conant, Keith Byers, Dennis Lamb and Raymond Shaw for useful comments and Glenn Shaw for sharing his 1968 notes of cloud physics lectures by Jim Macdonald.

FINE-SCALE MODELING OF ENTRAINMENT AND MIXING OF CLOUDY AND CLEAR AIR

Steven K. Krueger*
University of Utah, Salt Lake City, Utah, USA

1. INTRODUCTION

The EMPM (Explicit Mixing Parcel Model) predicts the evolving in-cloud variability of temperature and water vapor mixing ratio due to entrainment and finite-rate turbulent mixing using a 1D representation of a rising cloudy parcel (Krueger et al. 1997). The 1D formulation allows the model to resolve fine-scale variability down to the smallest turbulent scales (about 1 mm). The EMPM calculates the growth of thousands of individual cloud droplets based on each droplet's local environment (Su et al. 1998).

How do entrainment and mixing affect droplet spectral evolution in the EMPM? The following sequence of the events is illustrated in Fig. 1 for an isobaric entrainment and mixing event. The parcel first ascends adiabatically above cloud base, while the droplets grow by condensation. When entrainment occurs, the subsaturated entrained air replaces a a same-sized segment of the cloudy parcel. The cloudy air and the newly entrained air undergo a finite rate turbulent mixing process. During this process, many droplets encounter the entrained subsaturated air, resulting in partial or even total evaporation of some droplets.

We used the EMPM to investigate the impact on droplet spectra evolution in cumulus clouds of the following aspects of entrainment and mixing:

Parcel trajectory after entrainment: Isobaric versus ascending.

Entrained CCN concentration: Zero, half cloud base concentration, or full cloud base concentration.

We were motivated by aircraft measurements in cumulus clouds of cloud droplet number concentration (N) and mean volume radius (r_v), averaged over 10-m intervals, normalized by their adiabatic values, and plotted on a diagram with coordinates N/N_a and $V/V_a = r_v^3/r_{va}^3$. The product of the coordinates is the LWC normalized by its adiabatic value. Such a diagram (from Burnet and Brenguier 2007) for cloud traverses about 1500 m above cloud base for a case during SCMS (Small Cumulus Microphysics Study) is shown in Fig. 2. The challenge is to explain the observed distributions.

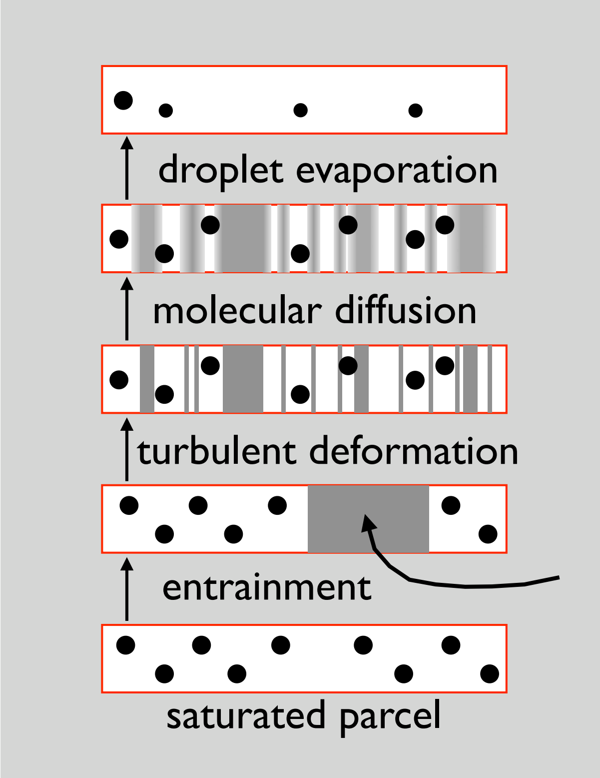

Figure 1: A parcel undergoing isobaric mixing is represented by a 1D domain in the EMPM. The parcel's internal structure evolves due to discrete entrainment events and turbulent mixing (turbulent deformation and molecular diffusion). Droplets evaporate based on each droplet's local environment.

Burnet and Brenguier proposed that isobaric

---

[*] *Corresponding author address:* Department of Meteorology, University of Utah, Salt Lake City, UT 84112. E-mail: steve.krueger@utah.edu

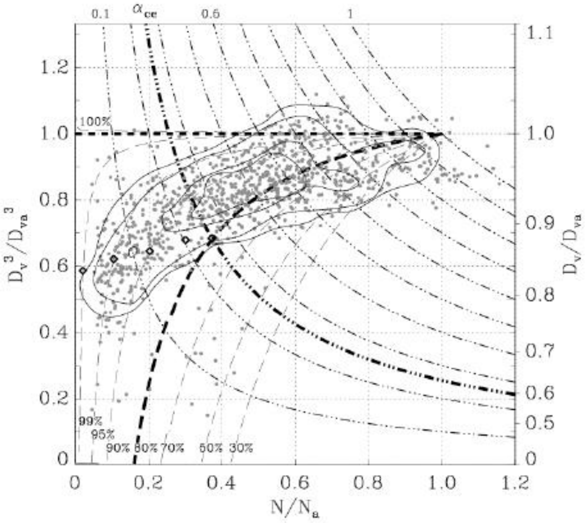

Figure 2: N-V diagram from SCMS for 10 August 1995. Plotted are 909 cloud samples, each of 10-m length. From Burnet and Brenguier (2007).

mixing, combined with buoyancy sorting, can explain the the observed distributions of N and r_v in cumulus clouds. However, we propose that additional processes (ascent of entrained air and entrainment of CCN) are likely to be important.

To explore the range of potential N-V distributions that might be encountered in cumulus clouds and to relate them to cloud processes, we applied the EMPM to a variety of realistic entrainment and mixing scenarios. The consequences of parcel trajectory after entrainment (isobaric versus ascending), and entrained CCN concentration on N-V distributions in entraining, non-precipitating cumulus clouds as predicted by the EMPM are presented in Section 2. Conclusions follow in Section 3.

2. ENTRAINMENT AND MIXING IN THE EMPM

2.1 *Isobaric mixing*

Figure 3 shows the sequence of states involved in isobaric mixing in the EMPM after an entrainment event. The states are numbered from 1 to 4. State 1 is the result of adiabatic ascent from cloud base. The variability of the droplet number concentration at this time is due to the small number of droplets (about 100) in each 1-m segment. State 2 is due to the initial breakdown of the entrained blob into smaller segments, with little droplet evaporation. This reduces N and LWC by dilution, but does not decrease r_v.

Between states 2 and 3, droplets evaporate until local saturation is achieved. This reduces the local r_v, but does not change the local N unless some droplets totally evaporate. In this case, almost no droplets totally evaporate. The blue line is the so-called "homogeneous" mixing line. It indicates all possible values of $(N$,$V)$ in *saturated* mixtures of entrained and adiabatic (undiluted cloud-base) air in which no droplets have totally evaporated. [1] Therefore, the N-V distribution moves downwards towards the blue line between states 2 and 3. In state 3, all mixtures are again saturated, due to droplet evaporation. The rate at which the adjustment to saturation occurs is limited by the rate of turbulent mixing in this case.

Between states 3 and 4, the resulting saturated parcels mix. Because the blue line is also a mixing line for saturated parcels, the N-V distribution converges towards its domain average. In state 4, the parcel is once again statistically uniform.

Burnet and Brenguier used a simple mixing model to demonstrate that isobaric entrainment and mixing events can produce $(N,\ V)$ pairs anywhere on the diagram between the "homogeneous" mixing line and $N = 0$. This result agrees with the EMPM results shown in Figure 3.

Figure 4 conceptually illustrates the sequence of states involved in isobaric mixing after an entrainment event for two parcels based on the analysis of EMPM results such as those shown in Fig. 3. The entrained air fraction is greater for the "blue" parcel (0.5) than for the "red" parcel (0.3). As a result, the LWC of the "blue" parcel is less than that of "red" parcel, both immediately after entrainment (state 2), and after saturation adjustment (state 3). In this case, no droplets totally evaporate, so the state 3 $N - V$ coordinates for both parcels lie on the same mixing line. Mixing between these the two parcels produces state 4,

---

[1] For entrainment into cumulus clouds, the mixing line depends primarily on the relative humidity (RH) of the entrained air.

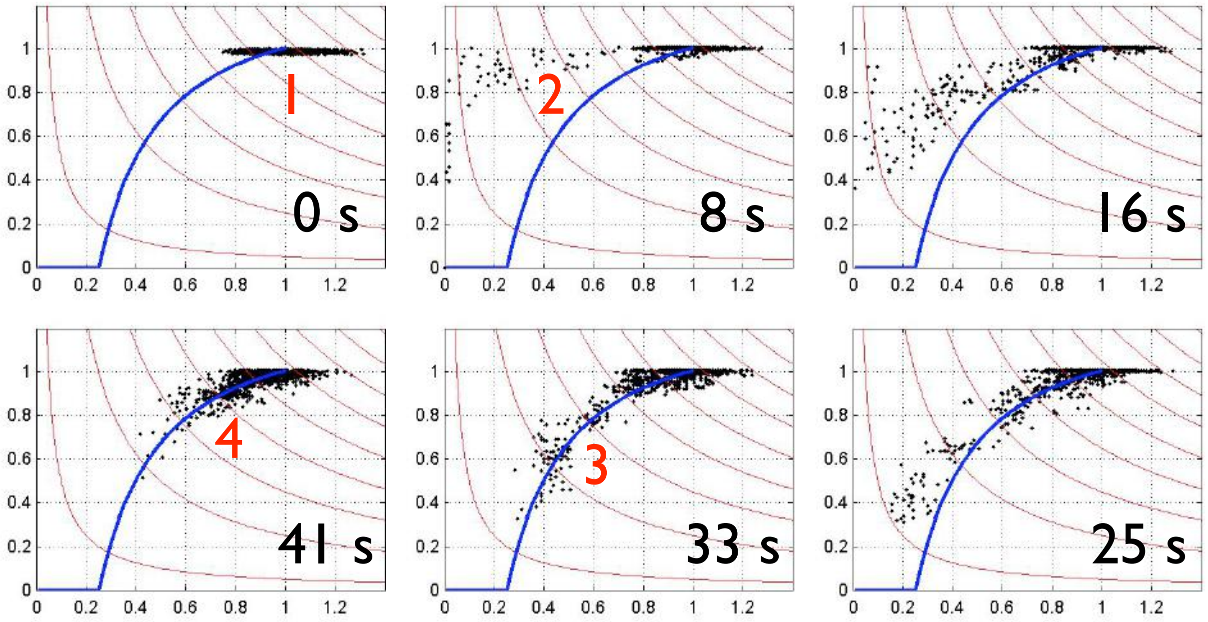

Figure 3: N-V diagram for isobaric mixing in the EMPM after an entrainment event. Each point is a 1-m average. Plotted in each panel are points from 11 "traverses" of the 80-m EMPM domain during each 8.25-s interval ending at the indicated time.

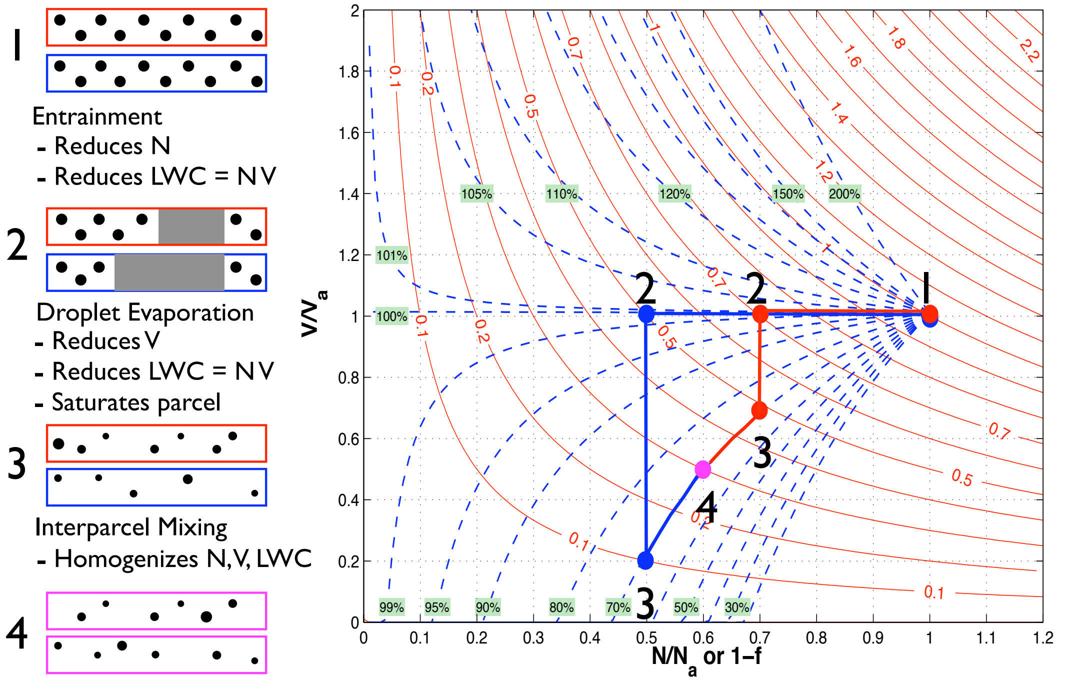

Figure 4: Entrainment and isobaric mixing for two parcels. No droplets totally evaporate.

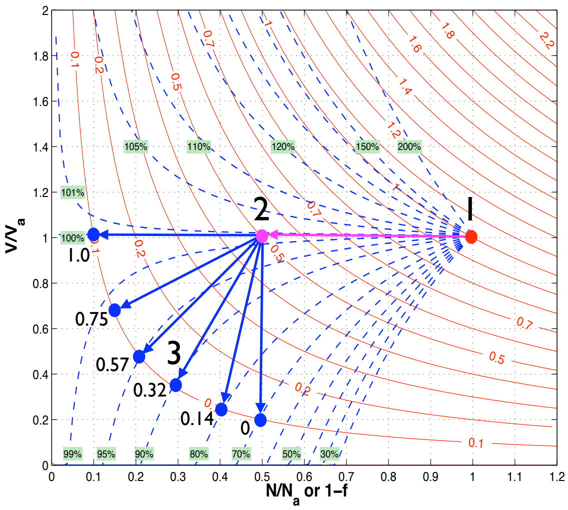

Figure 5: Entrainment and isobaric mixing when some droplets completely evaporate. The mixing parameter α is given for each mixing scenario.

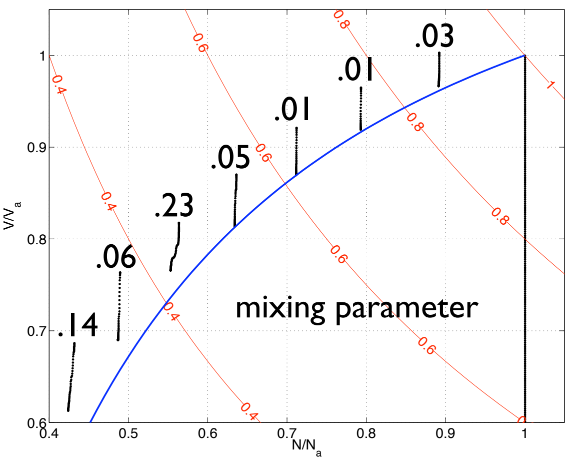

Figure 6: Time sequence of domain averages for isobaric mixing in the EMPM (80-m domain) after 7 sequential entrainment events. The mixing parameter α is given for each entrainment event.

which also lies on the mixing line.

Figure 5 is like Fig. 4 except that in this case some droplets completely evaporate between states 2 and 3, so that N decreases *after* entrainment. If V does not change during evaporation, the process is called "extreme inhomogenous mixing, and each droplet either completely evaporates, or does not evaporate at all. As before, the parcel is saturated with LWC $= NV$ when it reaches state 3.

Morrison and Grabowski (2008) proposed the following general relationship betwen N_f, the final droplet concentration after turbulent mixing and evaporation, and N_i, the droplet concentration after entrainment (for a parcel model) or after transport (for an Eulerian grid volume):

$$N_f = N_i \left(\frac{\text{LWC}_f}{\text{LWC}_i} \right)^{\alpha}, \qquad (1)$$

where LWC$_f$ and LWC$_i$ are the final and initial liquid water contents, and $0 \leq \alpha \leq 1$. For so-called homogeneous mixing, $\alpha = 0$, and for extreme inhomogeneous mixing, $\alpha = 1$.

Solving (1) for α gives

$$\alpha = \frac{\log(N_f/N_i)}{\log(\text{LWC}_f/\text{LWC}_i)}. \qquad (2)$$

Equation (2) applies equally well to ratios of normalized quantities. We used (2) to calculate α for each mixing scenario in Fig. 5, and for each entrainment and isobaric mixing event in the EMPM simulation shown in Fig. 6. The results suggest that, for given entrained air properties and mixing time scale, α increases as the LWC decreases.

Schlüter (2006) analyzed a set of more than 100 EMPM simulations of entrainment and isobaric mixing that covered a wide range of entrained air properties and mixing time scales. We have used her results to calculate α for each of the EMPM simulations. We anticipate that further analyis of her results will provide some guidance for parameterizing α in cloud-resolving models that do not resolve the entrainment and mixing process.

2.2 *Ascent with and without entrained CCN*

Figure 7 presents the distributions of the domain averages of two EMPM simulations of isobaric mixing in a 20-m domain with 7 sequential entrainment events. One had no entrained CCN, while the other entrained CCN. Note that *entrained CCN have no impact when the mixing is isobaric.*

The two plots in Fig. 8 show the dramatic impact of entrained CCN in an *ascending* parcel (80-m domain) with sequential entrainment events. Without entrained CCN (left panel), r_v^3 grows to

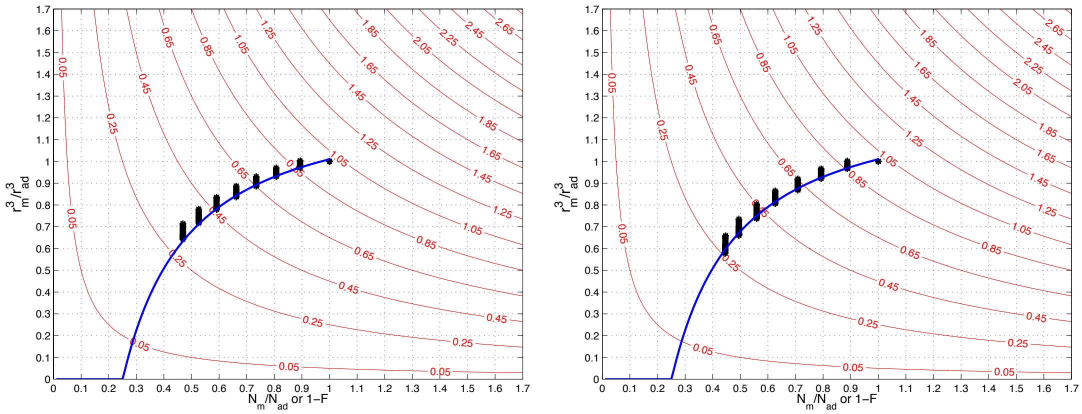

Figure 7: Time sequence of domain averages for isobaric mixing in the EMPM (20-m domain) after 7 sequential entrainment events. Left: No entrained CCN. Right: with entrained CCN.

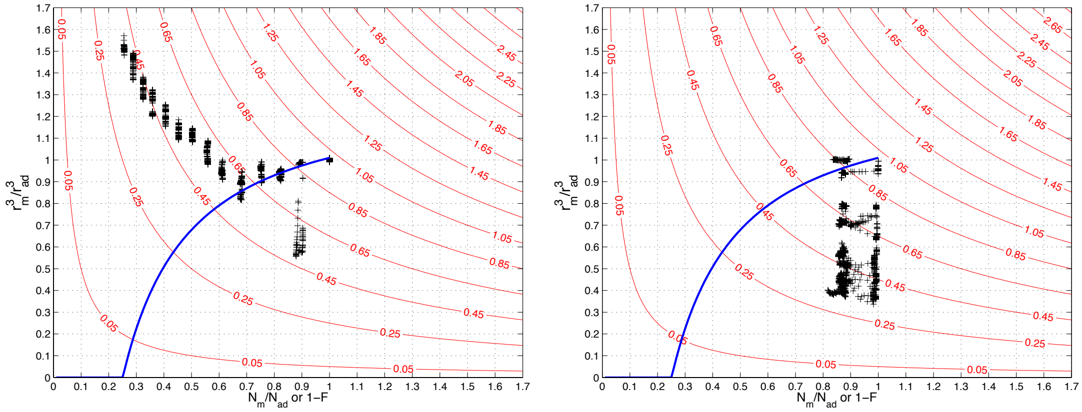

Figure 8: Like Fig. 7 except for ascent in an 80-m EMPM domain.

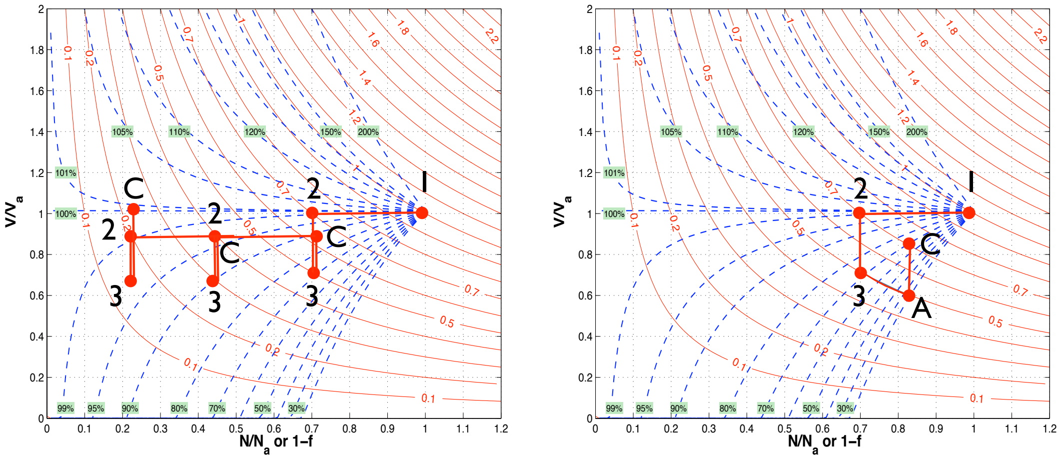

Figure 9: Left: Entrainment, mixing, and condensation (C) for a parcel that ascends after each entrainment event but entrains no CCN. Right: Entrainment, mixing, activation (A), and condensation (C) for a parcel that ascends after an entrainment event that entrains CCN.

150 percent of adiabatic at the highest level (1500 m above cloud base), while N decreases to 25 percent of adiabatic. When CCN are entrained at cloud base concentrations (right panel), r_v^3 decreases to about 40 percent of adiabatic, while N only slightly decreases, to about 90 percent of adiabatic.

If a cloudy parcel *ascends* during entrainment and mixing, the relative humidity of the entrained air will increase, thereby shifting the mixing line upwards and increasing the LWC ("feeding"). If no CCN are entrained and no droplets totally evaporate, N will remain constant after entrainment, so that r_v will also increase. This "weed and feed" scenario is illustrated in the left panel of Fig. 9.

Due to ascent and adiabatic cooling, newly entrained air may become supersaturated and some of the entrained CCN may be activated, thereby increasing N ("seeding") but decreasing r_v (for constant LWC). This "weed, seed, and feed" scenario is illustrated in the right panel of Fig. 9.

Figure 10 shows the time series of all 10-m averages for an EMPM simulation in a 200-m domain without entrained CCN. Compared to the domain-averaged results, the 10-m averages are much more variable (and realistic) because the entrained air fraction in each 10-m segment is determined by the EMPM's stochastic mixing process, rather than being specified. As a result, the 10-m averages from the 200-m domain results can be directly compared to aircraft measurements, such as those shown in Fig. 2.

Figure 11 shows the time series of all 10-m averages for an EMPM simulation in an 80-m domain with entrained CCN at one half of cloud base concentrations, while Fig. 12 shows the same for an EMPM simulation with entrained CCN at cloud base concentrations.

3. CONCLUSIONS

Entrainment followed by *isobaric* mixing reduces the droplet number concentration by dilution ("weeding") and the LWC and mean volume radius by droplet evaporation. As long as no droplets completely evaporate, the entrained air fraction determines N, and mixtures of entrained and adiabatic (undiluted cloud-base) air define the so-called "homogeneous" mixing line on the N-r_v^3 diagram.

If a cloudy parcel *ascends* during entrainment and mixing, the RH of the entrained air will increase, thereby shifting the mixing line upwards and increasing the LWC ("feeding"). If N remains constant, r_v will also increase. Due to ascent and adiabatic cooling, newly entrained air may become supersaturated and some of the entrained CCN may be activated, thereby increasing N ("seeding") but decreasing r_v (for constant LWC).

These (and other) comparisons between EMPM results and the observations of Burnet and Brenguier (2007) suggest that distributions of N and V similar to those observed can be produced in an ascending parcel by entraining air with intermediate CCN concentrations.

ACKNOWLEDGMENTS. This material is based upon work supported by the National Science Foundation under Grant No. ATM-0346854.

REFERENCES

Burnet, F., and J.-L. Brenguier, 2007: Observational study of the entrainment-mixing process in warm convective clouds *J. Atmos. Sci.*, **64,** 1995–2011.

Krueger, S. K., C.-W. Su, and P. A. McMurtry, 1997: Modeling entrainment and fine-scale mixing in cumulus clouds. *J. Atmos. Sci.,* **54,** 2697–2712.

Morrison, H., and W. W. Grabowski, 2008: Modeling supersaturation and subgrid-scale mixing with two-moment bulk warm microphysics. *J. Atmos. Sci.,* **65,** 792–812.

Schlüter, M. H., 2006: The Effects of Entrainment and Mixing Processes on the Droplet Size Distributions in Cumuli. M.S. Thesis, University of Utah, 92 pp.

Su, C.-W., S. K. Krueger, P. A. McMurtry, and P. H. Austin, 1998: Linear eddy modeling of droplet spectral evolution during entrainment and mixing in cumulus clouds. *Atmos. Res.,* **47–48,** 41–58.

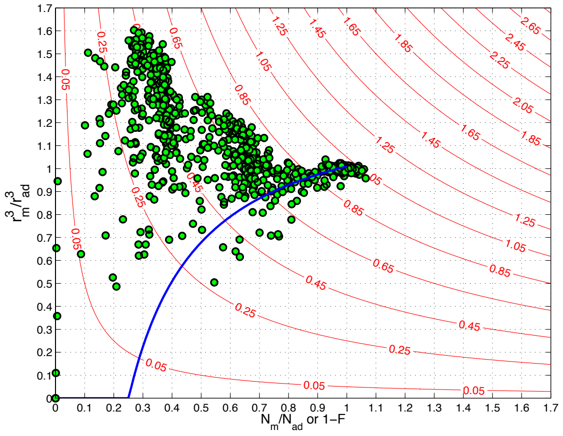

Figure 10: 10-m averages for an EMPM simulation in a 200-m ascending domain without entrained CCN. Left: All values. Right: Values for a short time interval, similar to what would be sampled by an aircraft traverse.

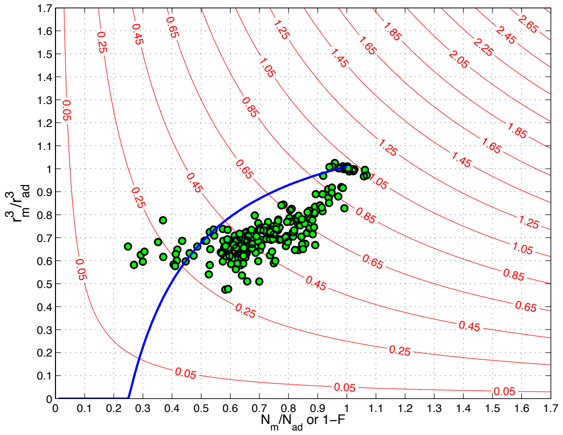

Figure 11: Like Fig. 10 but for entrained CCN at one half of cloud base concentrations.

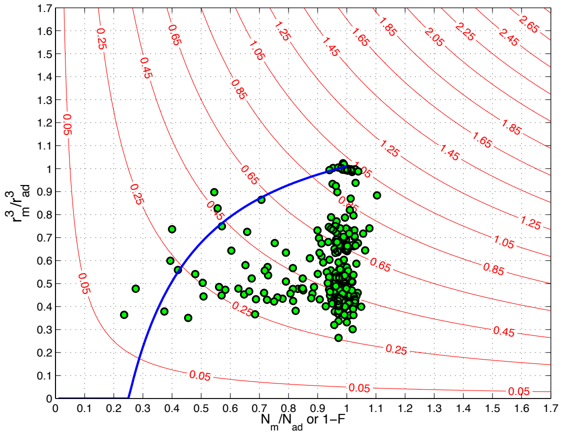

Figure 12: Like Fig. 10 but for entrained CCN at cloud base concentrations.

DROP SHEDDING FROM GROWING HAILSTONES, PROCESSES AND PREDICTIONS

Roland List and Daniel Abreu

Department of Physics, University of Toronto, Toronto M5S 1A7, Canada

1. INTRODUCTION

The shedding of drops from growing hailstones, mostly in the 1-2 mm size range (Joe et al, 1981), has an important influence on the growth of these ice particles. It affects the heat and mass transfer, HTM, and determines the density, size distribution and arrangement air bubble and single crystals of ice in the growing ice deposit as well as the shape evolution of the growing hailstone.

The first mathematically formulated hail growth theory was created by Schumann (1938), who added the heat transfer term that controls the evaporation and condensation/ deposition. He recognized, with Ludlam (1958), that growing hailstones do not always exchange sufficient heat with the environment allowing complete freezing of all the accreted water. This separation between dry and wet growth was labeled by List as the Schuman-Ludlam limit, SLL. The assumption was that growth occurred only by the water which was allowed to freeze thereby setting a limit on growth. This happened at a time when it was becoming evident that substantial hailstones had to grow fast, i.e. within 10 – 20 minutes.

List (1959) was the first to observe the growth of *spongy ice*, where the unfrozen water is incorporated into a growing ice frame – similar to a growing sponge, continuously filling with water. As a consequence all the accreted water was allowed to accumulate and contribute to growth - leading to "accelerated" growth. It will be argued in this paper that shedding will enhance growth to the degree that shedding hailstones will grow larger than hailstones that incorporate accreted water into spongy deposits.

The shedding, as it is known, will be summarized here and linked to hailstone growth and motion, while giving attention to increasing shedding with the accelerations caused by gyration.

The next section will address a higher level of simulation of hailstone growth. Gyration, as is presently known (Kry and List, 1974; Stewart & List, 1983), only explains growth of bodies with an axial symmetry, such as spheroids. The most commonly observed shape of hailstones in the size range 2-5 cm, however, is ellipsoidal. It is proposed that the controlling motion is a gyration with modulated spin or, more correctly, a double gyration.

The final section will address the link between shedding and the depletion of cloud water, LWC. It will be argued that, ultimately, shedding will be associated with less depletion and, hence, will allow faster hailstone growth. Ultimately, more sophisticated modeling will provide final proof.

The development of a warm rain process parallel to the hail process should also be looked at. The feedback, however, should not be too large.

2. SHEDDING BY GROWING HAILSTONES

Recognizing the importance of shedding, this aspect has always been included in icing experiments. However, its measurement is not trivial.

Since 1972, when the first growth experiments with gyrating hail (Joe al, 1976) were carried out by the Toronto group in the Swiss hail tunnel HVK II (List, 1966), the key suspension system was a gyrator built in Toronto in 1971. This apparatus replicated hailstone aerodynamics as predicted by Kry & List (1974). The gyrator has always been mounted in the vertical parts of the wind tunnels. These facilities provided all desirable conditions in terms of vertical velocities, temperature, pressure, and liquid water content and cloud droplet size distributions.

The gyrator suspension system mimics aerodynamic fall patterns by exposing spheroidal ice particles to icing in wind tunnels. Thereby the gyration (*Figure 1*) is composed of a spin around the minor particle axis, while this axis is rotating about a horizontal axis, the gyration axis. Thereby, the particle center is located at the apex of the gyration cone, with the apex angle chosen to be 60°. The gyrator was forcing the particle to rotate in the updraft of the wind tunnel. There was no attempt made to allow horizontal motions because they can be superimposed at will to the rotational and free fall motions. Things are happening fast with air speeds (fall speeds) up to 35 m s^{-1} and more, and gyration (nutation and precession) and spin frequencies of ≤ 30 Hz. Gyration and spin were often set in opposite directions. The wind tunnel air was held at temperatures warmer than - 35° C, pressures > 40 kPa and liquid water contents ~ < 10 g m^{-3}.

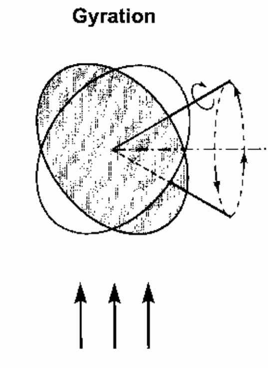

Figure 1. Model of a gyrating hailstone, i.e. rotating in a cloud updraft around a horizontal axis and spinning about an axis that follows the surface of a cone. The apex is at the center of the hailstone.

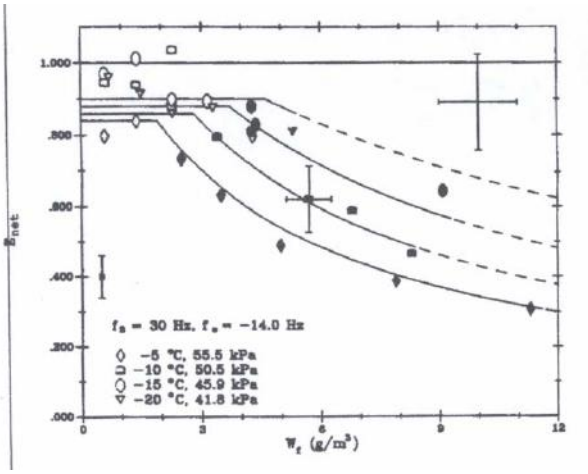

Figure 2. Net collection efficiency of a spheroidal hailstone as function of the liquid water content W_f, falling at terminal speed at temperatures correlated with pressures, at fixed gyration parameters, initial diameter 2 cm; filled symbols indicate shedding (Lesins & List, 1986). (1-E_{net}) represents the shed water.

Lesins and List (1986) carried out experiments on drop shedding and sponginess of gyrating hailstones. Necessitated by the need to keep the number of variables minimal, the free fall was calculated for freely falling spheroidal ice particles at pressures and temperatures according to hail day soundings by Beckwith (1960). *Figure 2* provides insight into the net collection efficiency E_{net} as function of LWC W_f , at gyration frequencies of 30 Hz and spin frequencies of -14 Hz. The solid curves present parameterized fittings. Note that at temperatures of -5°C shedding (black-filled symbols) occurred at liquid water contents > 2.5 g m^{-3}. E_{net} is defined as the fraction of the cloud water impacting on the hailstone water that stays on the collector particle. (1-E_{net}) represents the shed water.

The ice fraction (*Figure 3*) is < 0.5 or <50 % at a temperature of -5° C, meaning that half the accreted water is unfrozen. This presence of liquid water makes it more likely that shedding will occur. The occurrence of shedding is depicted in *Figure 4*. A dry

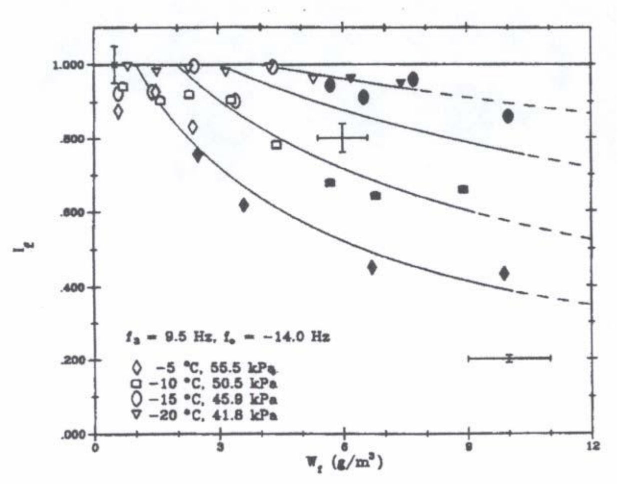

Figure 3. Ice fraction I_f of the deposit, i.e. the fraction of accreted cloud water which is frozen on the hailstone, as function of W_f and parameters indicated.

surface is observed at low W_f and is more prevalent at lower temperatures. It appears moist at slightly higher W_f values around the conditions indicated by the Schuman Ludlam Limit, SLL. Spongy growth sets in at higher W_f values. The region of soaking wet conditions is also indicated. These values were observed at laboratory pressures and at spin frequencies of 5 Hz. Note that the situation is drastically changed at frequencies > 20 Hz when the surface is always dry, and shedding occurs without the existence of a wet surface (*Figure 5*). This frequency dependence is not surprising but worrisome because it puts emphasis on the need to have a better understanding for the settings of the "real" gyration and spin frequencies of freely falling natural hailstone.

3. DOUBLE GYRATION

The complexity of the simulation of simple gyration was at the limit of what was doable in the laboratory over the past 36 years. It was also considered as more than sufficient to push the understanding of the growth of spheroidal hail stones with all its inherent complexities. However, as List & Abreu (2008) pointed out, it is now time to further improve the understanding of ice particle growth by tackling the growth of ellipsoidal hailstones, the most common shape of larger hailstones. To create a third axis and move from spheroids to elliptical growth, a double gyration is envisaged. It started with the suggestion that the spin in a simple gyration could be modulated, exposing two opposite points/areas on the equator longer to growth, while opposite points/areas perpendicular would be less exposed. This would force the formation of tri-axial (ellipsoidal) bodies. However, inspection of

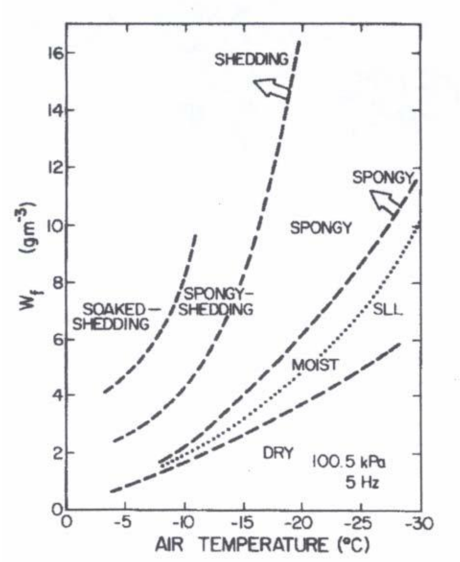

Figure 4. Surface conditions of icing spheroids at various W_f and air temperatures, separating dry surfaces from moist, with various degrees of sponginess. SLL is the Schuman-Ludlam limit where all the accreted water freezes and the temperature is 0ºC.

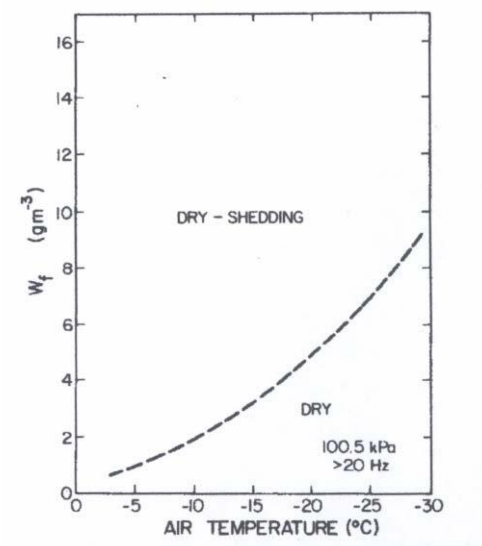

Figure 5. Shedding conditions at high rotation rates (> 20 Hz), with shedding occurring exclusively under dry ice particle surface conditions.

the physics reveals that, in order to keep the angular momentum unchanged, a “flip-flop” would have to occur, i.e. a nutation of the new spin axis about the previous spin axis – which now becomes a secondary gyration axis. This double gyration mode is depicted in *Figure 6*.

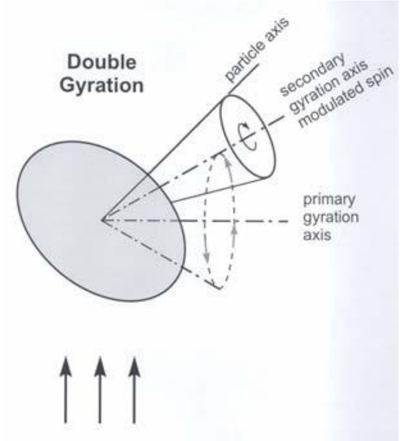

Figure 6. Double gyration, the motion proposed to create the most common ellipsoidal hailstones in the size range of 2-5 cm. Note the changing role of the original spin axis into a second gyration axis, with the final spin (particle) axis gyrating about the secondary gyration axis.

How does one check such a concept? By building a new apparatus! The modulation of the spin can be handled by stepping motors which can control rotational speeds at 200 points of one revolution at a rotation frequency of 15 Hz. Such an apparatus modulating the spin is now being built. The other parts of the second gyration will be left flexible so that nature itself can determine the resulting dynamics. Experiments are one pillar of the concept expansion, a numerical model on the kinematics as initiated by Abreu & List (2008) will help to explore the growth as well as the acceleration forces acting on the surface of the test particles. These forces are controlling the shedding. A third pillar also necessary is the development of the dynamic equations of double gyration.

4. DEPLETION OF THE LIQUID CLOUD WATER CONTENT

If a growing hailstone is considered as a separate entity, then it is obvious that shedding will decrease growth. This argument, however, needs to be expanded to include the feedback with the environment. Growing hailstones deplete the liquid cloud water content. Thus, the hailstones falling behind have less water available for growth. Hence, there will be a point where much less cloud water is left for growth. At the same time hailstones that shed water, will start to gain from bigger accretion, as caused by larger cloud water contents. Such feedback situation could be modeled in sophisticated 2- or 3-D cloud models.

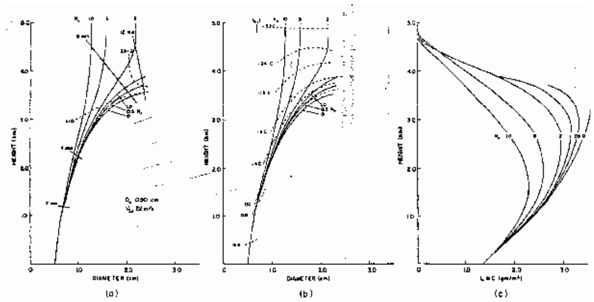

Figure 7. Hailstone and liquid water content depletion with height for hailstone concentrations of 0, 0.5, 1, 2, 5, and 10 m^{-3}; hailstones injected at 0ºC level; (a) growth in 2-min time steps up to 8 min., (b) surface temperature in 8ºC steps from 0ºC and, at lower levels, ice fractions I_f = 0.5 and 0.8; (c) depletion in function of number concentration; extreme right curve adiabatic LWC.

Due to lack of known other studies reference will be made to a paper by List et al (1968) which is about feedback of growing hailstones on a surrounding cloud and the depletion of its liquid water content. This study was carried out in a one-dimensional, steady-state model cloud. All variables are functions of height, z, only. Soundings from hail days in Denver were taken from Beckwith (1960). The continuity equation requires ρV_z = constant, a similar condition applies to number flux of hailstones. The model results are depicted in *Figures 7a, b and c*. They show the height dependent diameter and liquid water content, LWC, for a variety of number concentrations, with indications of time from injection and ice content of deposit or deposit temperature. Note that zero height is assumed at the freezing level. The consequences of this growth are shown in

Figure 7c, where number concentration values show the depletion, increasing with number concentration. *Figure 7* was introduced to discuss the strong similarity between W_f depletion by number concentration and reduced depletion by shedding. With 50% shedding (as an example) less liquid water is taken from the cloud, so that hailstones grow only by half. This is equivalent, in terms of depletion, to having only half the hailstone concentration growing to larger sizes. This reduces depletion and enhances growth of shedding hailstones. Shedding will, eventually, overtake in size the non-shedding hailstones that accreted water in spongy structures.

5. SUMMARY AND COMMENTS

The proposal is made that hailstones with ellipsoidal shape are grown by a double gyration (also List & Abreu, 2008). Larger acceleration forces at the surface of the growing hailstones are a consequence of the modulation of the spin frequency, the modulation frequency being double the spin frequency. The main effect will be increased shedding of liquid water from the hailstone surface aided by newly acting acceleration forces that are of similar size as those resulting from single gyration. Previous experiments have shown that shedding is a very complex matter. It is dependent mainly on frequency, with the remarkable result that at frequencies of > 20 Hz, no wet surface are observed during shedding. However, at lesser frequencies shedding occurred only from wet surfaces.

Shedding is closely related to gyration and double gyration. Unfortunately, insufficient information and knowledge are available about parameters (frequencies, apex angles of gyration cones) of size dependent gyrations during free fall at all atmosphere-relevant pressures. Further, nothing is known about size dependence of transitions and size dependence of ellipsoidity. Hypotheses about how the transition from spheroids to ellipsoids occurs have been developed in this paper and by List & Abreu (2008). These form but a start, together with the theory developed by Kry & List (1974). There is no question that the kinematic equations developed by Abreu & List (2008) will be an invaluable tool for exploration. Of great importance are also the new, advanced experiments planned to simulate double gyrations

The feedback of shedding to cloud liquid cloud water content is being linked to the similar issue of liquid cloud water depletion as it is increased by hailstone number concentration. There is sufficient evidence to support the conclusion that shedding enhances growth because of lesser depletion of the cloud liquid water content - as lower hailstone number concentrations unquestionably would improve growth.

There is one point which should not be overlooked. The shed water drops normally have sizes of 1-2 mm. Naturally, they can be easily collected by hailstones – with the additional benefit of having the water drops return with a temperature equal to that of the air. They are collected by the hailstones with a temperature equal to that of the air and leave the hailstones at the temperature of the hailstone surface (within ~ 0.1ºC of 0ºC). Thus, the non-freezing accreted and subsequently shed water is acting like a heat pump, removing latent heat of freezing form the “shedding” hailstones. This is an important component in the established HTM transfer equations of shedding hailstones, important because it allows more water to freeze.

There is one additional point however, which needs to be considered: The shed water consists of particles which are already raindrops. They can also grow in a supercooled cloud. They may stay liquid to as low as -30ºC. Thus, we end up with a warm rain process that is parallel and co-located with the hail evolution – with interactions. The shed water remains part of the cloud liquid water content and can – if unfrozen - be re-collected by the hailstones.

The change in relative velocity may have some effect on the models.

Acknowledgement

The support of this research by the National Science and Engineering Research Council of Canada is very much appreciated.

REFERENCES

List, R., and D. Abreu, 2008: Shape evolution of growing hailstones as function of gyration parameters. Proceedings International Conference on Clouds and Precipitation, Cancun, 7-11 July.

Beckwith, W.H., 1960: Analysis of hailstorms in the Denver network, 1949-1958. *Physics of Precipitation,* Geophys. Monogr. No 5, Amer. Geophys. Union, 348-353.

Joe, P. I., R. List and G.B. Lesins, 1981: "Ice accretions, part II: Rain production by icing assisted cloud water conversion", *J. Recherches Atmos*. 14, 3-4, 356-364 with title page of this issue from this paper.

Joe, P.I. R. List, P.R. Kry, M.R. de Quervain, P.Y.K. Lui, P.W. Stagg, J.D. McTaggart-Cowan, E.P. Lozowski, M.C. Steiner, J. Von Niederhausern, R.E., Stewart, E. Freire and G. Lesins, 1976: "Loss of accreted water from growing hailstones", Proc. Intern. Cloud Physics Conf., Boulder, 264-269.

Kry, P.R., and R. List, 1974: "Angular motions of freely falling spheroidal hailstone models", *Phys. Fluids*, 17, No. 6, 1093-1102

Lesins, G.B., and R. List, 1986: Spongyness and drop shedding of gyrating hailstones in a pressure-controlled wind tunnel. *J. Atmos. Sci.*, 43. 1 Dec., 2813-2825.

List, R., and D. Abreu, 2008: Shape evolution of growing hailstones as function of gyration parameters. Proc. 15th International Conference on Clouds and Precipitation, Cancun, 7-11 July, 2008.

List, R., F. Garcia-Garcia, R.E. Stewart and D.B. McDonald, 1984: Hail to rain conversion through melting. Proceedings, Ninth International Cloud Physics Conference, Tallinn, USSR, 21-28 August, Vol. I, 275-278.

List, R., R.B. Charlton and P.I. Buttels, 1968: A numerical experiment on the growth and feedback mechanism in a one-dimensional steady state model cloud". J. Atmos. Sci., 25, 1061-1074.

List, R., 1966: "A hail tunnel with pressure control", *J. Atmos. Sci.*, 23, No. 1, 61-66.

List, R., 1959: "Wachstum von Eis-Wassergemischen im Hagelversuchskanal", *Helv. Phys. Acta*., 32, No. 4, 293-296

Ludlam, F.H., 1958: The hail problem, Nubila, 1, 12-96.

Schumann, T.E.W., 1938: The theory of hailstone formation. Quart. J. Roy. Met. Soc., 64, 3-21.

Stewart, R.E., and R. List, 1983: Gyrational motions of disks during free fall. *Phys. Fluids,* 26, 920-927.

SHAPE EVOLUTION OF GROWING HAILSTONES AS FUNCTION OF GYRATION PARAMETERS

Roland List and Daniel Abreu

Department of Physics, University of Toronto, Toronto, Canada

1. INTRODUCTION

A “Gedankenexperiment” is presented about a new concept explaining the growth of ellipsoidal hailstones with axes ratios of 1 : 0.8 : 0.5. This shape is prevalent among atmospheric ice particles with main diameters of 2 – 5 cm. The proposed icing mode explains how such particles grow in accordance with observed hailstone properties.

First however, a review is given about the present state of knowledge and hw it was obtained. Any understanding of growth has to be based on the properties of real hailstones, their behavior in free fall, their heat and mass transfer, HTM, and their growth. This discussion wil; sketch or list observational methods, measurements of properties of the whole ice particle hierarchy, facilities, and experiments, as they have been developed by the senior author’s group over the past 56 years. The material presented is based on the consistent data sets obtained, first by the senior author and, later, by his cloud physics group. Reference will be made also to key topics of papers.

Past efforts have not been confined to the laboratory because an understanding had to be developed about the whole “environment” of growing hailstones as represented by convection in hail clouds. Also included are theories and models of the aerodynamics of free fall, HTM, basic convection and cumulus convection, including Doppler sonar and radar studies, etc.

Initially, the group’s research effort on hail concentrated on ice particle properties (***Figure 1***), while most of the relevant research of the last 35 years has been addressing the growth of gyrating spheroidal hailstones (approximating ellipsoids). (This was done parallel to the exploration of rain evolution and other topics.)

FIG. 1. Photographic examination of hailstones in the cold laboratory.

Figure 1. Samples of a hailstorm, collected at many locations, in a cold room at -10ºC (List, 1961).

Originally, the concept was developed that hailstones are a product of the icing conditions - which are imbedded in shape, air bubble and crystallographic arrangements and structures. To interpret those hailstone properties a “dictionary” is needed which allows establishment of correlations between ice structure/shape and icing conditions. Icing tunnels represent ideal utilities to develop such dictionaries. The practical application, however, is difficult because growth stages can be superimposed: porous ice can be formed directly, it may then be soaked with water and later freeze, processes which, at this time, can not be reconstructed later (List, 1961).

2. HAILSTONE PROPERTIES

Most hailstones with diameters between 2 and 5 cm have shapes of (tri-axial) ellipsoids, sometimes with indentations in the direction of the smallest axis, with varying surface roughness.

To simulate the growth of such particles Kry and List (1974) and Stewart & List (1983) established by theory and experiment that the most general motion is free fall, superimposed by gyration ***(Figure 2).***

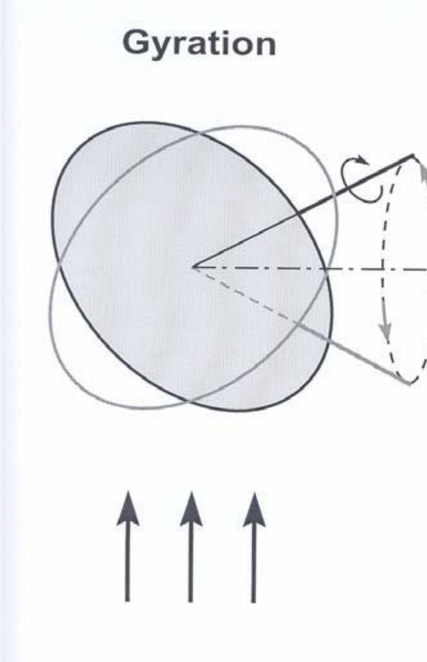

Figure 2, Spheroid i gyrating in updraft. Horizontal axis is gyration axis. The particle axis is the spin axis and moves on a cone with the particle center at the apex.

This mode, however, leads to axi-symmetric shapes, such as spheroidal forms. These shapes were acceptable for earlier experiments because the two larger axes are only different by ~ ±10 % from an average. This led to the planning and construction in Toronto of a gyrator in 1971. The apparatus was first used in by the Toronto Cloud Physics Group in experiments in the Swiss pressure-controlled icing wind tunnel (HVK II) (List, 1967). The main results of these experiments in the pressure-controlled the icing tunnel and other facilities can be found in Joe et al. (1976), Lesins & List (1986), Garcia-Garcia & List (1992), Greenan & List (1995), and Zheng & List (1995). To these studies the HMT experiments with a liquid tunnel (Schuepp & List, 1969a and b), Schemenauer & List, 1978) need to be added. The free fall behavior of ice crystals and graupel was studied in a water tank (List & Schemenauer, 1971) and hailstone free fall with a free fall tower (Kry & List, 1974; and Stewart & :List, 1983). Growth & heat and mass transfer of graupel was extended by Cober & List (1992), while ice crystal growth was explored experimentally by Schemenauer & List (1958) and theoretically by Youk et al. (2006). While many other authors worked on snow and graupel, like the Japanese groups led by Profs. Nakaya and Magono, and the Wyoming group by Prof. Vali, just to mention a few, some unique work had been done “in house” on the HTM and aerodynamics of ice crystals and graupel.

The initial studies on hail were carried out by List and List et al. - as listed under the references for the period 1955 to 1968. The paper by Aufdermauer et al (1963) also belongs to these studies in Switzerland on hailstone properties (size, shape, drag and lift coefficients, crystallographic structure, spongyness, heat and mass transfer, etc. These investigations were needed to have a basis for relating growth conditions to air bubble characteristics and crystallographic structures. These basic studies were later expanded in Toronto.

To interpret these properties, facilities were required to replicate hailstone growth under conditions as found in hail forming clouds. This was done in 5 icing wind tunnels (2 pressure controlled, 2 three stories high), 2 regular wind tunnels, one free fall tower for aerodynamic studies, and one liquid tunnel for the simulation of heat and mass transfer (HMT) of all atmospheric ice particle types (crystals, graupel and hailstones) by electrolysis (diffusion of ions or electrons [redox-electrolysis]. This is a standard method applied in mechanical and chemical engineering and is based on similarity theory. The electrolysis simulates the diffusion of water molecules from a particle surface by the diffusion of ions (electrons).

3. SHAPE EVOLUTION DURING GROWTH OF SPEHROIDAL HAILSTONES

3.1 Growth of Atmospheric Ice Particles

Based on the structure of natural hailstones List (1958) pointed to the progression of particle types from ice crystals, to conical graupel, to small hail, to spherical hailstones and spheroidal particles, to tri-axial hailstones – as expressed by air bubble arrangements and crystalline structure. This is best illustrated by ***Figure 3.*** which gives two views of the same hailstone cross section. One shows the arrangement of air bubbles, with shells and bubble lines, the other gives an indication of the size and shape of the single crystals which are associated with the air bubble arrangement.

R. List, "Physical methods and instruments for characterizing hailstones", Bull. Amer. Meteor. Soc., 42, No. 7, 452-466, 1961.

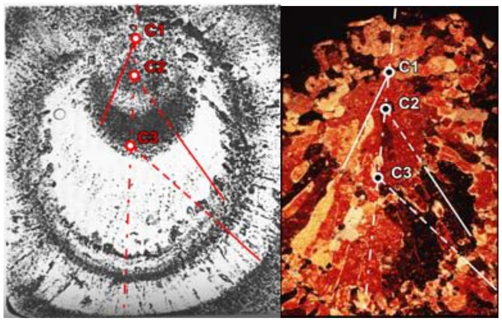

Figure 3. ***Left*** 1 mm thick section of a ellipsoidal hailstone K57.15 in translucent light, showing air bubble structure in the center of an ellipsoidal hailstone, height of photograph 2.4 cm . Upper center: conical graupel, with apex on the major hailstone axis. ***Right***: thin section (thickness 0.3 mm) of same hailstone, with same magnification, slightly rotated. . Single crystals radiating from graupel apex C1. After conical growth formation to an ellipsoidal shape, with clear ice and palisade like single crystals, radiating from a second growth center C2; interrupted by bubble shell (associated by many small single crystals), followed by clear ice and palisade-like single crystals, radiating from geometrical center C3 (List, 1958).

Each particle category is defined by the air bubble patterns (the start of graupel from dendrite had been verified in nature. Each growth stage has its specific aerodynamics with its HMT and the superimposed growth by deposition or accretion (collection of cloud droplets). Deposition can be associated with smaller graupel; growth of larger graupel, small hail and hailstones is always experiencing evaporation. Thereby, each growth stage is separated from the next by a significant change of fall behavior (and growth). Pristine ice crystals float with their biggest faces opposing free fall, graupel (size ≤ 5 mm, shape mostly conical), fall with the apex up (as observed in nature); small hail (by definition ≤ 5 mm) is close to spherical and falls as such. Small hail is a densified version of graupel growing by incorporation of accreted cloud droplets into the air capillary system of graupel, leading to rounded, spherical shapes (≤ 5 mm). Hailstones, defined as compact, lumpy particles with diameters ≥ 5 mm, then develop, with gyrations into spheroids (or spheres). It is hypothesized that the ellipsoidity increases with size. Further, once they reach diameters of 5 cm, the gyrational motion seems to become supercritical or unstable and all rotation stops in the further growth to giant hailstones, as depicted by Knigth and Knight (2005).

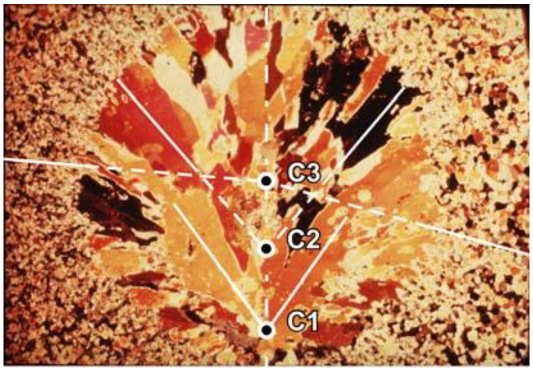

Figure 4. Thin-section, thickness 0.3 mm, of spheroidal center of another ellipsoidal hailstone. Core diameter 2 cm; tip of graupel near bottom, C1. Note the same arrangement of growth centers. As a rule they are always arranged on the main hailstone axis (List, 1958).

3.2 Free Fall and Heat and Mass Transfer, HTM

Free fall of ice crystals and graupel can easily be observed in a liquid tank at correct "atmospheric" Reynolds numbers, Re (List & Schemenauer, 1971). This is also a proper environment to observe secondary motions. For free fall of larger particles a fall tower turned invaluable.(Stewart et al, 1976).. Major studies of properties involving drag, lift and torques are best carried out in wind tunnels (Kry & List, 1974; List et al, 1973; listet al, 1969). Physical understanding is achieved by measurement of components in wind tunnels. HTM of any type of particle have been observed in a liquid tunnel (Schuepp & List, 1969-2x, Schemenauer & List, 1978).

One investigation type needs to be added: the directly observed HTM during growth of graupel and hailstones in the icing tunnel. This was facilitated by fixed-mounted and scanning radiometric microscopes – as discussed below.

3.3. Growth by Accretion in Wind Tunnels

The growth of (falling) ice particles larger than ice crystals, i.e. graupel (Cober, 1992), spheres, spheroids (Garçia-Garçia & List, 1992; Greenan & List, 1995: Zheng & List, 1995)) is best observed in vertical icing wind tunnels, the simulators of atmospheric conditions. This is particularly the case for gyrating particles which require special consideration. The rotational motion control system (gyrator) allows the collection of *reproducible* data be obtained. Restriction of sidewise motion is necessary, considering that a hailstone, falling at 30 m $s^{-1,}$ has a sidewise drift of o. 1 m s^{-1}.and could in one minute easily drift sidewise by up to 60 m. That would not be feasible in a wind tunnel. This necessitates extensive aerodynamic studies in other facilities to determine the type of *free falling* motion.

The group was fortunate because of the quick thinking of two students (S. Cober and F. Garçia-Garçia). They learned of the acquisition of a scanning radiometric microscope by a laser group of the Physics Department. They "borrowed" the instrument right away and used it in the icing tunnel to measure surface temperatures distributions of hailstones growing while gyrating. While two (fixed) radiometric microscopes had been available in the group before, the scanning opened new vistas about the HTM. This method was used ever since.

3.4 . Growth by "Simple" Gyration

For the following conceptual considerations, growth of hailstones is in the form of an accretion and freezing of supercooled cloud water droplets. It is assumed that the drops do not change shape at the location where they land on the hailstone. Further, the droplets are assumed to move at speed and direction of the free air stream. This is a first approximation because, under certain conditions, freezing may take time, thus allowing droplet deformation or spreading in thin water films.

Particles rotating about a horizontal axis are constantly experiencing maximum accelerations in the equatorial regions at the rate of $\omega \times r$, ω being the angular rotation frequency. Such accelerations forces water, often floating freely at the surface [the HMT is normally not sufficient to freeze all the accreted water] to the equator, where they are shed, also in the form of pieces of surface skins (Lesins & List, 1986). They often form radial spikes while shedding. Gyration or wobbling does not allow accumulation of free water at the equator. Thus no or only rudimentary spikes are formed and shedding is reduced.

With the above assumption of deposition a spherical particle spinning about a horizontal axis in a vertical updraft will grow into a spheroid. There will be no growth in the direction of the (horizontal) rotation axis because the cloud droplets move perpendicular to the normal of the surface at the poles. Hence, the particle will grow more and more oblate with time.

Superimposing a gyration, with the horizontal axis becoming the gyration axis, the spin axis will move on the surface of a (circular) cone with the hailstone in the apex (***Figure 2***). In all experiments using a gyrator the apex angle of the gyration cone was fixed at 60°. The nutation is key for the growth of original spheres into spheroids. These spheroids will not only grow perpendicular to the spin axis, but also along it. With an apex angle of 60°.the growth is still larger in the direction perpendicular to the spin axis than in the direction of the spin axis. Nevertheless, under otherwise unchanged conditions, the oblateness is continuously increasing. (With the chosen apex angle, the oblateness was in the expected range.)

Taking these observations into account it can concluded that the oblateness is diminishing with increasing apex angle – up to a point when it will start to reverse. If an apex angle of 180° is applied, then the growth will be limited to the equatorial region, with no growth in the direction of the spin axis. In other words, the icing product of a gyration limited to spin around a horizontal axis only (no gyration) produces the same ice growth as gyration about a cone with an apex angle of 180°, with no spin.

It is expected that oblateness reaches a minimum (growth of gyrating spheres!) at an apex angle close to 90°. Further increases of the apex angle will increase the oblateness again. There is a strong hunch that ***spherical hailstones*** are also a product of gyration and that they may form at this "reversal" point were the oblateness starts to increase. Spherical hailstones are observed in nature. Up to this point, however, no suggestion had been made about how they might grow. The only suggestion was chaotic tumbling with equal growth in all directions.

No more definite statement is made about the point of reversal because the effects of gyration (frequency and amplitude of nutation and precession) are far from being understood. It is also known that there are combinations of spin and gyration frequencies at which symmetric growth about the spin axis brakes down. It is not achieved when the two frequencies are equal in size and sense of rotation because the hailstone is then fixed relative to the gyration axis. There is also no gyrational growth symmetry when the spin frequency is zero. Note that the spin frequency is fixed to the inertial frame, i.e. the particle rotates once during one gyration. Thereby both gyration and and spin have the same sense. It is not known If there are more such conditions.

With all the investigations reported it can be stated that the growth of gyrating hailstones of spheroidal shape is more or less understood. However, growth of ellipsoidal hailstones is only known in fist approximation and many new surprises are to be expected.. Thus, the new quest for even more sophisticated experiments!

4. THE GROWTH OF TRI-AXIAL HAILSTONES

How do the most often observed ellipsoidal hailstones grow? What is their fall behavior?

The answer, based on observed particle symmetries, starts with the hypothesis that the free-fall motion is basically vertical, superimposed by a gyration [gyration axis horizontal], however the ***spin frequency*** is ***modulated.*** The spin needs to expose opposite points on the equator of an originally (spherical or) spheroidal body for a longer time than the two points 90 degrees off. Kinematic equations (Abreu & List, 2008). This assumption will be the basis for the detailed exploration and modeling of this new development. The present paper will explain how the physics of the particle motion can be dealt with by a new type of gyrator.

The new tracing of surface points during gyration with modulated spin by Abreu and List (2008) provides an appreciation of the kinematics and allows establishment of local accelerations and growth, and the linkage between initial changes in ellipsoidity of growing ice particles with modulation amplitude. Note that the modulation frequency is fixed at twice the spin frequency. The newly developed kinematic equations are, among others, also expandable to modeling of general gyrations for different apex angles of the gyration cone, and the exploration of the possibility and conditions under which gyration creates spherical shapes. Gyrations with an apex angle of 180° can also be studied in the presence of spin and a modulation of the gyration frequency. (The full implication of the generalization of gyration is not understood at this moment.)

Figure 5 visualizes simple gyration and gyration with modulated spin.. The basis for both cases is the theory and experiments of free falling discs and spheroids. Theory (Kry and List, 1974) predicted gyration about a horizontal axis. However, it took experiments (Stewart and List, 1983) to confirm these predictions and also to establish that gyration consists of 90° phase-shifted precession and nutation, both of equal amplitude – which results in a circular gyration cone. ***Figure 2*** shows a freely falling hailstone, with its center at the apex of the gyration cone, with spin about an axis moving on the surface of the cone. The original icing experiments (Lesins & List, 1986) showed that such motion of originally spheroidal particles produces axi-symmetric particles of spheroidal shape. Modulation of the spin frequency at twice the spin frequency allows longer and shorter periodic exposure of equatorial areas shifted by 90°. It is assumed that this will lead to the formation of tri-axial bodies, a hypothesis in agreement with observations, but still requiring confirmation by icing models and experiments.

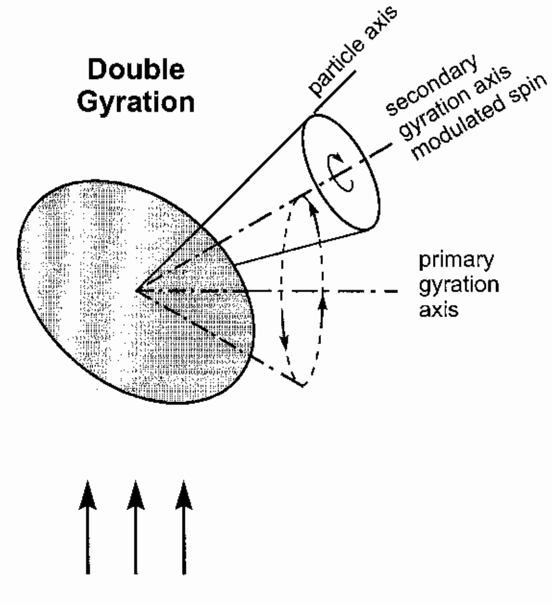

Figure 5. Double Gyration, an extension of the single gyration depicted in Figure 2. The secondary gyration occurs around the original spin axis. The second gyration allows conservation of momentum, which is necessitated by the modulation.

Periodic acceleration and deceleration of the spin, however, violates the laws of conservation of angular momentum. This can be avoided if the particle changes the tilt of its axis relative to the spin axis – which would allow conservation of angular momentum. Such a "flipping" motion can be represented by a second, superimposed gyration with a spin frequency equal to the modulation frequency. The magnitude of the secondary gyration frequency has to be determined by free fall or theory. It is expected that it would not be for from the spin fe=requency of the simple gyration. This superimposed gyration is depicted in ***Figure 5.***

There is a *caveat*: The flip-flop of the particle involves inertia. In other words, Newton's second law comes into play again. At this moment the respective implications are unknown. The solution of the (dynamic) equations of motion for double gyration is no trivial matter and will need substantial development time. Thus, the modulated-spin gyrator has been designed with flexibility and the ability to indicate where the theory may finally lead us.

The new gyrator has been designed and is being built. It allows suspended spheroids (or spheres) and tri-axial bodies to gyrate with a modulated spin – with all frequencies to be chosen as estimated. Stepping motors are the heart of the system because they will allow setting of rotational speed for 200 points of one evolution at frequencies up to 15 Hz. To give the particles freedom to "wiggle" and carry out a second superimposed gyration, their center will be flexibly connected to the forcing spin suspension axis. Thereby fiber material needs to be used which is flexible but torsion resistant. After "dry runs" in Toronto this suspension system will be tested in the Beijing icing tunnel, which is based on the facility described by List et al., 1987.

5. COMMENTS AND SUMMARY

Looking at the motion in double gyrations reveals centrifugal accelerations induced by the primary spin that are of the same magnitude as the accelerations caused by the wobble of the spin axis (secondary spin acceleration). They act in different directions. In other words, it is expected that the *shedding* of accreted cloud water will be substantially enhanced. It will further be argued that shedding will enhance hailstone growth. This will be seemingly contradictory statement will be discussed in a companion paper (List & Abreu, 2008).

The evolution of the understanding of ice particle growth over the past 56 years has been sketched, making the reader aware of the multifaceted aspects of the growth of ice particles, from ice crystals to hailstones. The present state could only be reached with a massive building of appropriate facilities and the development of related theories and models. However, another turning point has been reached: The era of icing experiments with "simple" gyrations and spheroidal hailstones is giving way to the growth of tri-axial ellipsoidal hailstones with modulated spin, invoking double gyration. The technical difficulties for mechanical motion simulation have been overcome, and the basic model describing the much more complex hailstone motions has been tested. A new world has opened up with an enormous expansion of the parameter space, setting the frame for future experiments. From the modeling point of view modeling of modulated spin frequency can also be expanded to the modulation of gyration frequency. Further, the exploration of the role of the apex angle will present new territory. In particularl, the growth of spherical hailstones by gyration presents additional excitement.

Further, the challenge of the new experiments will be to accommodate the anticipated changing of the ellipsoidity with hailstone size.

Acknowledgment. This research has been carried out with the support of the National Sciences and Engineering Research Council of Canada. Substantial experimental limitations and difficulties had to be overcome to prepare an investigation of spin modulated growth, as associated with double gyration. The technical solutions could not have been achieved without the considerable help of the manager of the technical services, Mr. Peter Hurley, and the staff of the workshop of the University of Toronto Physics Department. Many thanks are also owed Mr. Raul Cunha who drafted some of the figures and helped in many other ways.

REFERENCES

All references listing work involving the senior author are listed by year with a category indicator: **P**: properties; **A**: aerodynamics; **HTM**: heat and mass transfer; **G**: growth; **MF**: methods and facilities, DR: electromagnetic and sonic Doppler radar; **M**; numerical models; **T**: theory; **O** overviews;

The connections to the general literature can be gained by the list of references in the different papers. The only reference made here to other authors is::

Knight, C. A., and N. C. Knight, 2005: Very large hail: Growth conditions and falling behavior. *Bull. Amer. Meteor. So.*, **86**, 1773-1881.

The papers on ice particles involving the senior author are:

Abreu, D. and R. List, 2008: Motion patterns of gyrating spheroids for various degrees of spin modulation. Proceedings International Conference on Clouds and Precipitation, Cancun, 7-11 July.

List, R., and D. Abreu, 2008: Drop shedding from growing hailstones, processes and predictions. Proceedings International Conference on Clouds and Precipitation, Cancun, 7-11 July.

List, R., and D. Abreu, 2008:
Shape evolution of growing hailstones as function of gyration parameters. Proceedings International Conference on Clouds and Precipitation, Cancun, 7-11 July.

Youk, Hyun, Roland List, and Theophilus Ola, **2006**: Growth of ice crystals by molecular diffusion. *J. Atmos. Sci.,* 63**,** 1650-1657.**HTM, T**

Thomson, A.D., and R. List, **1998**: High resolution measurement of a hail region by vertically pointing Doppler radar. *J. Atmos. Sci.*, 56, 2132-2151. **DR**

Zheng Guoguang and R. List, **1996**: Local and overall convective heat transfer of rotating ice spheroids with hemispherical surface roughness. Proceedings Fifth Intern. Symposium on Thermal Engineering & Science for Cold Regions, Ottawa, Canada, May 19-22, Y. Lee and W. Hallett editors, 337-342. **HTM**

Zheng Guoguang and R. List, 1996: Thermal conductivity of porous ice in hailstone shells. *J. Glaciology,* 42, 195-200. **HTM**

Zheng Guoguang and R. List, **1995**: Convective heat transfer of rotating spheres and spheroids with non uniform surface temperatures. *Intern. J. Heat Mass Transfer*, 39, 1815-1826. **HTM, G**

Greenan, B.J.W., and R. List, 1995: Experimental closure of the heat and mass transfer theory of spheroidal hailstones, *J. Atmos. Sci*, 52, 3797-3815. **HTM, T, G**

List, R., B.J.W. Greenan and F. Garcia-Garcia, **1994**: Surface temperature variations of gyrating hailstones and effects of pressure-temperature coupling on growth. *Atmospheric Research,* 38, 161-175.**HTM, G**

Zheng Guoguang and R. List, 1994: Measurement of convective heat and mass transfer of hailstone models. *Atmospheric Research*, 32, 75-84. **HTM**

List, R., 1994: Hailstone Heat and Mass Transfer Theory and Three-Component Nusselt Numbers. *Atmospheric Research*, 32, 85-94. **HTM, T**

Cober, G.S., and R. List, **1992**: Measurements of the heat and mass transfer parameters characterizing graupel growth. *J. Atmos. Sci*., 50, 1591-1609. **P, HTM, G**

Garcia-Garcia, F., and R. List, 1992: Laboratory measurements and parameterizations of supercooled water skin temperatures and bulk properties of gyrating hailstones. *J. Atmos. Sci.* 49, 2058-2073. **HTM, G**

List, R., 1992: Properties and growth of hailstones. Chapter 12 in Thunderstorm Morphology and Dynamics, E. Kessler, ed., University of Oklahoma Press, Norman and London, 259-276. (Second Revised and enlarged edition), **O**
List, R., **1990**: The Physics of supercooling of thin water skins covering gyrating hailstones. *J. Atmos. Sci*., 47, 1919-1925. **T**

List, R., F. Garcia-Garcia, R. Kuhn and B. Greenan, **1989**: The supercooling of surface water skins of spherical and spheroidal hailstones. *Atmospheric Research*, 24, 83-87. **HTM**

List, R., 1989 Analysis of sensitivities and errors in hailstone heat and mass transfer using spreadsheets. *J. Appl. Meteor.* 28, 1118-1127. **HTM, NM**

List, R., **1988**: A linear radar reflectivity-rainfall relationship for steady tropical rain. *J. Atmos. Sci*., 45, 3564-3572. **DR**

List, R., 1988: "The supercooling of the ice sponge-to-water skin interface of gyrating hailstones", in "Atmospheric Aerosols and Nucleation", Lecture Notes in Physics, P.E. Wagner and G. Vali, editors, Springer Verlag, Berlin, pp. 689-692. **HTM, T**

List, R., G.B. Lesins, F. Garcia-Garcia and D.B. McDonald, **1987**: Pressurized icing tunnel for graupel, hail and secondary raindrop production. *J. Atmos. Ocean. Techn*., 4, No. 3, 454-463. **MF**

Joe, P., and R. List, 1987: Testing and performance of twodimensional optical array spectrometers with grey scale. *J. Atmos. Ocean. Tech.* 4, 139-150. **MF**

List, R., J. Hallett, J. Warner and R. Reinking, **1986**: The future of laboratory research and facilities for cloud physics and cloud chemistry. *Bull. Amer. Meteor. Soc*., 67, November, 1389-1397. **O, MF**

Lesins, G.B., and R. List, 1986: Spongyness and drop shedding of gyrating hailstones in a pressure-controlled wind tunnel. *J. Atmos. Sci.*, 43. 1 Dec., 2813-2825. **HTM, G, R**

List, R., **1985**: Properties and growth of hailstones. Chapter 12 in Thunderstorm Morphology and Dynamics, E. Kessler, ed., University of Oklahoma Press, Norman and London, 259-276. **O**

Stewart, R.E., and R. List, **1983**: Gyrational motions of disks during free fall. *Phys. Fluids,* 26, 920-927. **A**

List, R., 1982: Properties and growth of hailstones. Thunderstorms: A Social, Scientific and Technological Documentary. Vol. 2, Thunderstorm Morphology and Dynamics, Chapter XII, 409-445. E. Kessler, ed.; US Government Printing Office, Washington DC. **0**

List, R., 1061: "On the growth of hailstones", Nubila, 4, 29-38.

Joe, P. I., R. List and G.B. Lesins, 1981: "Ice accretions, part II: Rain production by icing assisted cloud water conversion", *J. Recherches Atmos*. 14, 3-4, 356-364 with title page of this issue from this paper. **G, T**

Lesins, G.B., R. List and P.I. Joe, **1980**: "Ice accretions, part I: testing of new atmospheric icing concepts", *J. Recherches Atmos*., 14, 3-4, 347-356. **G, T**

List, R., **1978/79**: "The cloud physics dilemma", *Riv. Ital. Geof. Sci. Aff*.; Prof. M. Bossolasco special, 5, 131-138. **O**

Melling, H., and R. List, 1978: "Acoustic Doppler sounding of falling snow", *J. Appl. Meteor.*, 17, No. 9, 1267-1273. **DR**

Melling, H., and R. List, 1978: "Doppler velocity extraction from atmospheric acoustic echoes using a zero-crossing technique", *J. Appl. Meteor.*, 17, No. 9, Sept., 1274-1285. **DR**

Schemenauer, R.S., and R. List, 1978: "Measurements of the convective mass transfer of planar and columnar ice crystals", Borovikov Memorial: "Some problems of cloud physics" (Collected papers), Academy of Sciences of the USSR, Leningrad, 217-232. **HTM**

List, R., **1976**: "Ice accretions on structures", *J. Glaciology*, 9, No. 81, 451-465. **HTM, G**

Stewart, R.E., R. List and U.W. Rentsch, 1976: "Aerodynamics of freely falling bodies", Proc. Intern. Cloud Physics Conf., Boulder, 258-262. **A**

Joe, P.I. R. List, P.R. Kry, M.R. de Quervain, P.Y.K. Lui, P.W. Stagg, J.D. McTaggart-Cowan, E.P. Lozowski, M.C. Steiner, J. Von Niederhausern, R.E. Stewart, E. Freire and G. Lesins, **1976**: "Loss of accreted water from growing hailstones", Proc. Intern. Cloud Physics Conf., Boulder, 264-269. **G**

List, R., P.I. Joe, G. Lesins, P.R. Kry, M.R. de Quervain, J.D. McTaggart-Cowan, P.W. Stagg, E.P. Lozowski, E. Freire, R.E. Stewart, C.G. List, M.C. Steiner and J. Von Niederhausern 1976: On the variation of the collection efficiencies of icing cylinders", Proc. Intern. Cloud Physics Conf., Boulder, 233-239. **G**

Girard, C., and R. List, **1975**: "Thermodynamics of falling precipitation zones", *Pure Appl. Phys.* 113, Nos. 5/6, 1035-1053. **HTM, T**

Bennett, R.C., and R. List, 1975: "Scattering of sound used to study the atmospheric boundary layer", *Acoustics and Noise Control in Canada*, Can. Acoust. Assoc., 3, No. 4, 3-6. **DR**

Bennett, R.C., and R. List, 1975: "Lake breeze detection with an acoustic radar", Proc. 16th Radar Meteor. Conf., Houston, Texas, 260-262. **DR**

List, R., and H. Melling, **1974:** "Plume convection over an urban area as observed by acoustic echo sounding", *Atmosphere*, 12, No. 4, 144-153. **DR**

Kry, P.R., and R. List, 1974: "Angular motions of freely falling spheroidal hailstone models", *Phys. Fluids*, 17, No. 6, 1093-1102. **A**

Kry, P.R., and R. List, "Aerodynamic torques on rotating oblate spheroids", *Phys. Fluids*, 17, 1087-1092, 1974. **A**

List, R., and T.L. Clark, **1973**: "The effect of particle size distributions on the dynamics of falling precipitation zones", *Atmosphere*, 11, No. 4, 179-188. **T, M**

List, R., and T.A. Agnew, 1973: "Air bubbles in artificial hailstones", *J. Atmos. Sci,* 30, 1158-1165. **P**

Charlton, R.B., and R. List, 1973: "Cloud modelling with spheroidal hailstones", *J. Rech. Atmosph*., 56-62. **M**

List, R., U.W. Rentsch, A.C. Byram and E.P. Lozowski, 1973: "On the aerodynamics of spheroidal hailstone models", *J. Atmos. Sci*., 30, No. 4, 653-661. **A, T**

Murray, W.A., and R. List, **1972**: "Freezing of water drops", *J. Glaciology*, 11, No. 63, 415-429. **G, P**

List, R., R.C. Bennett and U.W. Rentsch, 1972: "Acoustic echo soundings in urban Toronto", *Atmosphere*, 10, No. 3, 73-79. **DR**

Charlton, R.B., and R. List, 1972: "Hail size distribution and accumulation zones", *J. Atmos. Sci.*, 29, No. 6, 1182-1193. **G, T**

List, R., W.A. Murray and C. Dyck, 1972: "Air bubbles in hailstones", *J. Atmos. Sci*., 29, No. 5, 916-920. **P**

List, R., and M. Hand, **1971**: "The wakes of freely falling water drops", *Phys. Fluids*, 14, No. 8, 1648-1655. **A**

Clark, T.L., and R. List, 1971: "Dynamics of a falling particle zone", *J. Atmos. Sci*., 28, No. 5, 718-727. **A, T**

List, R., and R.S. Schemenauer, 1971: "Free fall behaviour of planar snow crystals, conical graupel and small hail", *J. Atmos. Sci.*, 28, No. 1, 110-115. **A**

List, R., J-G. Cantin and M.G. Ferland, **1970**: "Structural properties of two hailstone samples", *J. Atmos. Sci*., 27, 1080-1090. **P**

Charlton, R.B., and R. List, 1970: "On the number distributions of hail growing in updrafts", Proc. Conf. Cloud Physics, Fort Collins, Colorado, 51-52. **M**

List, R., and E.P. Lozowski, 1970: "Pressure perturbations and buoyancy in convective clouds", *J. Atmos. Sci,* 27, No. 1, 168-170. **T, A**

Schuepp, P.H., and R. List, **1969**: "Influence of molecular properties of the fluid on simulation of the total heat and mass transfer of solid precipitation particles", *J. Appl. Meteor.*, 8, No. 5, 743-746. **HTM**

List, R., R.B. Charlton and D.F. Parson, 1969: "Inertia effects on hailstones in oscillating updrafts", Proc. Sixth Conf. Severe Local Storms, Chicago, Ill., 264-266. **A**

List, R., U.W. Rentsch, P.H. Schuepp and N.W. McBurney, 1969: "The effect of surface roughness on the convective heat and mass transfer of freely falling hailstones", Proc. Sixth Conf. Severe Local Storms, Chicago, Ill., 267-269. **A, P**

Schuepp, P.H., and R. List, "Mass transfer of rough hailstone models in flows of various turbulence levels", *J. Appl. Meteor.*, 8, No. 2, 254-263, 1969. **HTM, A**

List, R., R.B. Charlton and P.I. Buttuls, **1968**: "A numerical experiment on the growth and feedback mechanisms of hailstones in a one-dimensional steady state model cloud", *J. Atmos. Sci.*, 25, No. 6, 1061-1074. **A, T**

List, R., and D.F. Parson, 1968: "Simulation of the total heat transfer of spherical hailstones", *Helv. Phys. Acta*, 41, fasc. 6-7, 1016-1020. **HTM, T**

List, R., 1968: "On the modelling of cumulus clouds", *J. Atmos. Sci.*, 25, No. 3, 529-530. **M, T**

List, R., and J-G. Dessault, **1967**: "Quasi steady state icing and melting conditions and heat and mass transfer of spherical and spheroidal hailstones", *J. Atmos. Sci.*, 24, No. 5, 522-529. **HTM, M**

List, R., **1966**: "On the simulation of physical processes occurring in clouds", *Bull. Amer. Meteor. Soc.*, 47, No. 5, 393-396. **MF**

List, R., "A hail tunnel with pressure control", *J. Atmos. Sci.*, 23, No. 1, 61-66, 1966. **MF**

List, R., **1965**: "Fall speeds on precipitation elements and aspects of similarity theory", *Quart. J., Roy. Meteor. Soc.*, 91, No. 390, 535-536. **A, T**

List, R., R.G.J. Methot and P.H. Schuepp, 1965: "Heat exchange ratios of hailstones in a model cloud and their simulation in a laboratory", *J. Atmos. Sci.*, 22, No. 6, 710-718. **HTM, M, T**

Joss, J., and R. List, **1963**: "Zur Radarrückstrahlung von Eis- und Wassergemischen", *Z. angew. Math. Phys.*, 14, No. 4, 376-380. **DR, P**

Aufdermaur, A.N., R. List, W.C. Mayes and M. de Quervain, 1963: "Kristall-achsenlagen in Hagekörnern", Z. angew. Math. Phys., 14, No. 5, 574-589. **P**

List, R., 1963: "General heat and mass exchange of spherical hailstones", *J. Atmos. Sci.*, 20, No. 3, 189-197. **T, HTM**

List, R., 1962: "Hail test tunnel", *Weather*, 17, No. 10, 317-319. **MF**

List, R., 1962: "Zur Beeinflussung des Hagelkornwachstums", *Z. angew. Math. Phys.*, 13, No. 4, 393-401. **T**

List, R., **1961**: "Entstehung und Struktur des Hagels", Die Umschau, 61, No. 17, 526-528. **O**

List, R., 1961: "Ueber einen Einfluss des AgJ auf den atmosphärischen Vereisungsprozess", *Z. angew. Math. Phys.*, 12, No. 5, 474-476. **T**

List, R., 1961: "On the growth of hailstones", *Nubila,* 4, 29-38. **G**

List, R., 1961: "Aufbau & Leistung des Hagelversuchskanals", Tech. Rundschau Sulzer, 43, 3-8. **MF**

List, R., 1961: "Physical methods and instruments for characterizing hailstones", *Bull. Amer. Meteor. Soc.*, 42, No. 7, 452-466. **MF**

List, R., **1960**: "New developments in hail research", *Science.*, 132, No. 3434, 1091-1098. **O**

List, R., 1960: "Zur Thermodynamik teilweise wässriger Hagelkörner", *Z. angew. Math. Phys.*, 11, No. 4, 273-306. **HTM, T**

List, R., 1960: "Growth and structure of graupels and hailstones", Phys. Precip., Geophys. Monograph No. 5, Amer. Geophys. U., Baltimore, 317-324. **P, GR**

List, R.,1960: "Design and operation of the Swiss hail tunnel", Phys. Precip., Geophys. Monograph No. 5, Amer. Geophys. U., Baltimore, 310-316. **MF**

List, R., **1959**: "Wachstum von Eis-Wassergemischen im Hagelversuchskanal", *Helv. Phys. Acta.*, 32, No. 4, 293-296. **P**

List, R., 1959: "Der Hagelversuchskanal", *Z. angew. Math. Phys.*, 10, No. 4, 381-415. **MF**

List, R., 1959: "Zur Aerodynamik von Hagelkörnern", *Z. angew. Math. Phys.*, 10, No. 2, 143-159. **A**

List, R., **1958**: "Kennzeichen atmosphärischer Eispartikeln, 2 Teil", *Z. angew. Math. Phys.*, 9a, No. 3, 217-234. **P**

List, R., 1958: "Kennzeichen atmosphärischer Eispartikeln, 1. Teil", *Z. angew. Math. Phys.*, 9a, No. 2, 180-192. **P**

List, R., and M. de Quervain, **1955**: "On the structure of hailstones". Nat. Res. Council Canada, Tech. Transl., TT-551, 1-7. **P**

List, R., and M. de Quervain, **1953**: "Zur Struktur von Hagelkörnern", *Z. angew. Math. Phys*., 9, No. 6, 3-7. **P**

AN EFFICIENT SEMI-DOUBLE-MOMENT BULK MICROPHYSICS SCHEME

Jason Milbrandt and Ron McTaggart-Cowan
Atmospheric Numerical Prediction Section, Environment Canada, Canada

1. INTRODUCTION

In atmospheric models, the interactions between hydrometeors in resolved clouds are simulated by cloud microphysics parameterization schemes. Due to the high computational cost of bin-resolving schemes, 3D models generally use bulk microphysics schemes (BMSs), in which the hydrometeor size distribution of each particle category is represented by an analytical function. Microphysical growth rates are then formulated for one or more moments of the distribution. Many BMSs employ the single-moment approach, in which there is one prognostic variable for each category proportional to the mass mixing ratio. There is a growing awareness in the modelling community of the advantages of the double-moment approach, in which the total number concentration is also a prognostic variable. However, the use of double-moment (or higher) schemes is more computationally costly due to the need to advect more prognostic variables as well as the cost of the additional predictive equations in the scheme itself. Consequently, many BMSs used in research models, and all schemes (to our knowledge) used in operational numerical weather prediction (NWP) models, are single-moment.

In this study, a new version of an existing bulk microphysics scheme is under development. The new version exploits the benefits of the double-moment approach for the hydrometeor categories to which the number of prognostic moments is most sensitive, while maintaining a relatively high level of efficiency by treating the remaining categories as single-moment. The resulting computational cost is expected to be comparable to that of a typical multi-category single-moment scheme. Despite its overall efficiency, the new scheme should be capable of simulating a wide range of meteorological conditions without the need for tuning of parameters for specific types of weather.

A description of the proposed BMS along with some preliminary results of high-resolution (2.5-km grid-spacing) NWP simulations of a mid-latitude squall line are presented. The following section provides a brief overview of the advantages of predicting more than one moment in a BMS. In section 2, we summarize the multi-moment scheme on which the modified semi-double-moment version is based. Section 4 describes the modifications for the proposed version of the scheme. In section 5, simulations are presented, showing results using the fully single-moment and fully double-moment versions of the BMS. Concluding remarks are given in section 6.

2. ADVANTAGES OF DOUBLE-MOMENT

a. Sedimentation

In order to motivate the incorporation of the double-moment approach into a scheme aimed at operational NWP, we briefly examine some important benefits of higher-moment bulk schemes. One of the most important benefits arises from the fact that in a multi-moment framework, the sedimentation is computed by allowing each of the prognostic variables to sediment at their respective moment-weighted terminal fall velocities (differential sedimentation). In double-moment (or higher) schemes, the result of this is to mimic the effects of gravitational size-sorting through a realistic redistribution in the vertical of the moments of the size spectrum.

This effect can be illustrated through simple calculations of pure sedimentation in a column, with no growth processes or interactions amongst particles. Figure 1 depicts the vertical profiles of hydrometeor mass content (top row) and mean-mass diameter (bottom row) that result from pure sedimentation of hail, with prescribed initial values at upper levels, as calculated by a single-moment bulk scheme, double-moment bulk schemes, and an analytic bin model. It is readily apparent that there is a fundamental improvement in the treatment of sedimentation for double-moment over single-moment schemes. Not only is the vertical redistribution of mass much more realistic, but also a double-moment scheme captures the effect of the redistribution of the largest mean-

---

Corresponding author address: Dr. Jason Milbrandt
2121 TransCanada Highway, 5th floor
Dorval, QC, H9P 1J3 Canada
e-mail: jason.milbrandt@ec.gc.ca

particle sizes towards the lower part of the profile, as in the analytic model (and nature). This is accomplished despite the fact that the entire size distribution at each level is represented by only two independent parameters. In the single-moment scheme, the mean-mass diameters (and all other moments) are directly related to the mass contents – an intrinsic limitation of the single-moment approach.

One of the problems with many double-moment schemes arises from fixing the dispersion of the hydrometeor size distribution, usually through the use of an inverse-exponential function [(i.e. with a fixed spectral dispersion parameter α=0; see Eq. (1)]. Differential sedimentation results in uncontrolled size-sorting and excessively large mean-particle sizes and fall velocities. Milbrandt and Yau (2005a) showed that this can be controlled by allowing a variable spectral dispersion, which can be realized by either predicting a third moment (such that the dispersion is effectively an independent parameter) or by allowing the dispersion parameter to vary as a diagnostic function of the predicted moments. In the middle panels of Fig. 1, the solid [dot-dashed] lines correspond to computations from a diagnostic-dispersion [fixed-dispersion, (inverse-exponential)] double-moment scheme. The fixed-dispersion solutions exhibit excessively large mean-mass diameters and sedimentation rates. In contrast, the diagnostic-dispersion approach corrects this problem.

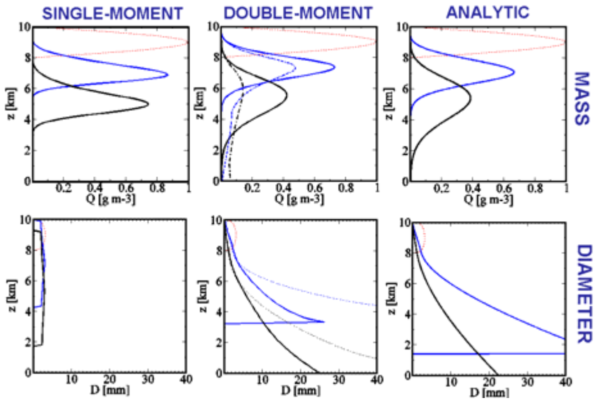

Fig. 1 Vertical profiles of hydrometeor mass content (top) and mean-mass diameter (bottom) resulting from pure sedimentation of hail with prescribed initial values at upper levels as calculated by a single-moment bulk scheme (left), double-moment bulk schemes (middle), and an analytic model (right). Profiles shown are at the initial time (red), after 4 min (blue), and after 8 min (black). For the middle panels, the solid [dot-dashed] lines correspond to computations from a diagnostic-dispersion [fixed-dispersion] double-moment approach.

Figure 2 depicts the surface precipitate rates that result from pure sedimentation corresponding to the sedimentation profiles shown in Fig. 1. The diagnostic-dispersion double-moment approach nearly reproduces the triple-moment calculation (not shown in Fig. 1), which is close to the analytic solution.

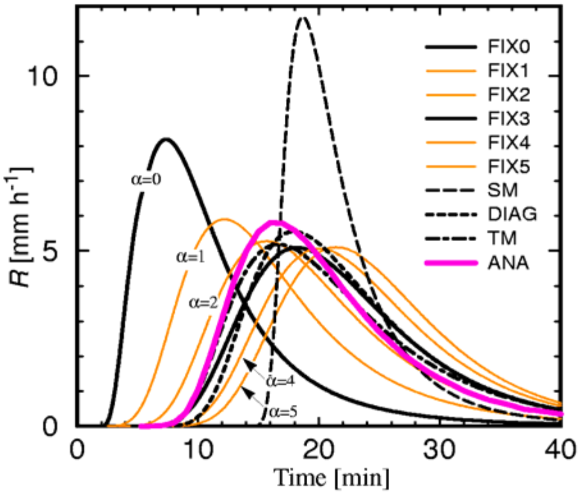

Fig. 2 Time series of surface precipitation rates from pure sedimentation computed using the indicated bulk methods. FIX(x) denotes double-moment fixed α=x; SM denotes single-moment; DIAG denotes double-moment diagnostic-dispersion, TM denotes triple-moment; and ANA denotes the analytic solution. Reproduced from Milbrandt and Yau (2005a).

The improvements for a higher-moment BMS that result from the treatment of sedimentation are not merely aesthetic nor do they simply affect only the timing of surface precipitation. The redistribution of the moments of the size distributions subsequently results in changes in the microphysical growth rates, which in turn feed back to the dynamics through latent heating and cooling during phase changes. Further, for simulations of strong convection the location of the hydrometeor mass in a vertical column can have an important impact on the amount of precipitation loading that affects the vertical air motion.

b. Other benefits of double-moment

In addition to the direct and indirect benefits due to differential sedimentation, a scheme that independently predicts the hydrometeor mass content and total number concentration can more realistically simulate certain microphysical processes. For example, the processes of accretion and diffusional growth affect the mass content while leaving the total number concentration constant. In contrast, aggregation and particle breakup affect the total number without changing the total mass. Thus, a double-moment scheme is better able to treat these processes than a single-moment scheme, which is constrained to have a monotonic relation between mass and number at all times.

3. ORIGINAL MICROPHYSICS SCHEME

a. Overview of scheme

The proposed semi-double-moment scheme is based on the multi-moment bulk microphysics scheme described in Milbrandt and Yau (hereafter MY, 2005a,b). A brief overview of the original scheme is provided here with a description of the proposed modifications given in the following section. The MY scheme has six hydrometeor categories – *cloud*, *rain*, *ice*, *snow*, *graupel*, and *hail*. The size distribution of each category *x* is represented by a gamma function of the form:

$$N_x(D) = N_{0x} D^{\alpha_x} e^{-\lambda_x D}, \qquad (1)$$

where N_{0x}, λ_x, and α_x are generally referred to as the “intercept”, “slope”, and spectral dispersion (or shape) parameters, respectively, and *D* is the particle diameter. Spherical particles are assumed. The full version of the MY scheme is triple-moment for all categories (except *cloud*, which is double-moment), with prognostic equations for the total number concentration (N_x), mass mixing ratio (q_x), and radar reflectivity (Z_x) of each category *x*, corresponding to the 0th, 3rd, and 6th moments, respectively. Thus, each of the parameters in (1) varies independently. There are also single-moment (prognostic q_x only) and double-moment (prognostic q_x and N_x) options for the scheme. One double-moment version assumes a fixed value for α_x, which is the approach in nearly all published double-moment bulk schemes. The second allows for a variable spectral dispersion by incorporating a diagnostic relation for α_x as an increasing function of the mean-mass particle diameter, D_x. This approach avoids the additional computational cost of predicting three independent moments while still retaining the benefit of the controlled size-sorting.

b. Results from previous studies

The first major test of the triple-moment version of the MY scheme was published by MY (2006a) who performed a 1-km mesoscale model simulation of a tornadic supercell. Sensitivity tests using the various versions of the scheme showed that while the diagnostic-dispersion double-moment version closely reproduced most of the important aspects of the triple-moment simulation, the fixed-dispersion simulations suffered from the problem of excessive size-sorting, exhibiting unrealistically large mean-particle sizes, reflectivities, and instantaneous precipitation rates (MY 2006b). The single-moment simulations differed from the triple-moment run in several ways, including having notably different storm structures and propagation speeds.

Milbrandt et al. (2008a,b) conducted a similar set of sensitivity tests using the MY scheme for an orographically-enhanced winter precipitation IMPROVE-2 case. In contrast to MY (2006b), there was much less variation amongst the simulations using the various versions of the schemes. This suggests that the important effects of a multi-moment scheme, at least in terms of the fields of interest for operational NWP, may be more pronounced for deep convection than for winter-type synoptically-forced weather systems.

4. SEMI-DOUBLE-MOMENT VERSION

The guiding principle in designing a new version of the MY scheme is the exploitation of the benefits of the double-moment approach with the maintenance of as much computational efficiency as possible. The goal is that the scheme be usable for operational NWP with no *a priori* assumptions about the type of weather. An important point is that not all hydrometeor categories benefit as strongly by being double-moment. Various studies have shown the importance of *hail* and *rain* being double-moment [e.g. MY (2006b)]. On the other hand, a single-moment treatment may be sufficient for categories such as *graupel*, whose range of terminal fall velocities is small.

a. General description

The size distribution of each hydrometeor category *x* in the semi-double-moment version is described by Eq. (1), as in the original BMS. The hydrometeor categories *cloud* and *graupel* are single-moment, with the q_c and q_g as the prognostic variables. *Rain* and *hail* are double-moment, with q_r, N_r, q_h, and N_h prognosed and the spectral shape parameters for each category (α_r and α_h) diagnosed (see section 2). There is also a new double-moment hybrid *ice-snow* category, with q_i and N_i predicted, which is described below. Table 1 summarizes the hydrometeor categories and prognostic variables in the proposed semi-double-moment scheme.

Hydrometeor Category	Prognostic Variables	Dispersion Parameter
cloud	q_c	fixed ($\alpha_c = 0$)
rain	q_r , N_r	diagnostic α_r
ice	q_i , N_i	diagnostic α_i
graupel	q_g	fixed ($\alpha_g = 0$)
hail	q_h , N_h	diagnostic α_h

Table 1. Summary of hydrometeor categories in the semi-double-moment version of the MY scheme.

b. New Hybrid Ice Category

For ice crystals, we combine the previously separate categories of *ice*, representing pristine crystals, and *snow*, representing large crystals and aggregates, and introduce a double-moment hybrid *ice* category. An alternative this approach, for a similar computational cost, would be to use two separate single-moment categories, as is often done in BMSs. With this double-moment single-category approach, however, it is possible to distinguish between tiny crystals and large crystals/aggregates for a given mass content, while still permitting the simulation of the observed effects of gravitational size sorting as well as the proper representation of processes such as aggregation and diffusion (i.e. with independent tendencies of mass and total number). Morrison and Grabowski (2008) recently used a similar approach for a single hydrometeor ice-phase category (but with the added sophistication of also predicting the portion of rimed mass). Also, the fall speed parameters for our hybrid *ice* category depend on the mean-mass diameter, D_i, where parameters appropriate for small crystals (aggregates) are used if D_i is small (large).

We also include the some other changes to the treatment of the *ice* category, similar to approaches recently put forward by Thompson et al. (2008) and others. Rather than assuming the *ice* to be spherical, with an exponent d_i=3 in mass-diameter relation,

$$m(D) = c_i D^{d_i} , \qquad (2)$$

and a prescribed bulk density (incorporate into c_i), as in the original MY scheme (and others) for the *ice* and *snow* categories, the new hybrid category assumes a more realistic value d_i=2, in better agreement with observed ice particles. Further, a size-dependent bulk ice density is applied, as in Thompson et al. (2008), rather than a single fixed value.

Most microphysics schemes model diffusional growth of ice following the electrostatic capacitance analogy [e.g. Rogers and Yau (1989)]. However, recent laboratory and field research has shown that due to irregularities in the shapes of real ice crystals, the electrostatic analogy overestimates diffusional growth by a factor of 2 to 8 or more (Bailey and Hallett, 2006; Field et al. 2006). This may partly account for the excessive *snow* growth in BMSs in general. The use of experimentally determined *effective* capacitances of ice may be a way of improving simulated deposition rates. Simulations of an orographic precipitation case using the MY scheme have shown that by applying a reduction factor of 0.25 to the diffusional growth equation in the scheme results in a simulated snow mass field that more closely reproduce values of mass concentration taken by *in situ* aircraft measurements (Milbrandt et al., 2008b). In view of this, the hybrid *ice* category will also include this reduction factor in the diffusional growth term, though further testing is required to determine an appropriate value to use in general.

c. Sedimentation

The calculation of hydrometeor sedimentation is one of the most computationally expensive parts of a microphysics scheme. This is particularly so for model configurations that use large time steps (i.e. compared to time steps used in cloud resolving models, which are on the order of 1 s). The bulk fall velocity for categories such as *rain* and *hail* can result in Courant numbers (*C*) much greater than 1 if the full model time step were applied on a typical vertical grid increment. This necessitates the need for either time-splitting for the sedimentation calculations or the use of numerical methods that allow for stable solutions when *C* exceeds 1. The problem is even more severe for double-moment schemes, in which gravitational size-sorting leads to large mean-mass diameters and thus large bulk fall velocities – i.e. larger than would normally occur for a single-moment scheme. Time-splitting, in addition adding computational cost, also introduces unwanted smoothing of the hydrometeor fields due to numerical diffusion.

In the original MY scheme, an Eulerian advection scheme was used to compute sedimentation. The amount of time-splitting was determined based on a worst-case scenario – computing the sedimentation time step by assuming the maximum allowable fall velocity and the minimum vertical grid-spacing. Though the scenario is seldom realized, this assumption was necessary to ensure vertical stability. The new scheme uses the box-Lagrangian advection method of Kato (1995) to compute sedimentation. Tests have shown that this modification dramatically improved the efficiency of the original scheme. Our experience has indicated that some amount of time-splitting is still required to avoid numerical noise. We have found that in general a maximum allowable C of 3 for sedimentation results in stable solutions. Also, an estimate of the maximum C is made in each column (for each category) at a given time step to determine the amount of time splitting that is required.

There are other possible approaches to optimizing the sedimentation calculations, such as the use of pre-computed look-up tables (e.g. Fiengold et al., 1998). We remark that while this topic may be essentially a technical issue, it is important since computational cost alone may prohibit the use of a double-moment microphysics for operational NWP, thereby removing the benefits.

d. Expected efficiency

Timing test have indicated that runs using the 2.5-km GEM model with the optimized fully double-moment version of the MY scheme (with 12 prognostic variables) increase the total run time by approximately 18-20% compared to runs using the fully single-moment version (with 6 prognostic variables). We estimate that the increased cost of running the semi-double-moment version (with 8 prognostic variables) will be approximately 10%. Note that the increase total cost is not identical for each variable. Although the cost of advection is the same, the cost of sedimentation is greatest for the variables of categories with the fasted fall velocities. Thus, the additional cost of having *hail* double-moment, for example, is (unfortunately) greater than the cost of adding an additional single-moment category.

5. SIMULATIONS OF A SQUALL LINE

In this section, we present the case study that will be used to evaluate the performance of the proposed semi-double-moment version of the scheme. In order to establish a baseline, fully single-moment and double-moment runs are analyzed and compared. Once the modified version of the MY scheme is finalized, the results from sensitivity tests will be evaluated in the context of the testbed developed here. We selected the 12-13 June 2002 IHOP (International H20 Project) case. During this event, thunderstorms that formed near the Oklahoma panhandle matured into a distinct squall line which passed southeastward through Oklahoma City, decaying as it approached the Oklahoma-Texas boarder. A squall line is an appropriate type of case for this study due to the presence of both convective and stratiform regions, each having distinctly different growth environments for microphysical fields. This is also one of the cases that will be investigated at the 2008 WMO Cloud Modeling Workshop, with the primary focus on the storm and cold pool initiation and morphology and on the ability of different models with different BMSs to develop the trailing stratiform rain region.

a. Model description

Simulations were conducted using the Canadian operational Global Environmental Multiscale (GEM) model (Côté et al. 1998). The GEM is based on the fully-compressible Euler equations and has a comprehensive physics package which includes a planetary boundary layer scheme based on turbulent kinetic energy, implicit (explicit) vertical (horizontal) diffusion, and a detailed land-surface scheme. The solar and infrared radiation package is fully interactive with the model clouds. The simulations used 58 terrain-following eta-like vertical levels. The regional configuration of the model (global, with Δx~15 km over North America) was first run for a 48-h integration, initialized using the Canadian Meteorological Centre regional analysis for 0000 UTC 12 June 2002. The model was then nested to a high-resolution (Δx~2.5 km) limited-area grid, centered over Oklahoma, for two 36-h integrations, one using the single-moment version of the MY scheme (SM) and the other with the double-moment (diagnostic-dispersion) version (DM) to treat grid-scale condensation. No convective parameterization scheme was used in the high-resolution runs.

b. Simulation Results

Figures 3 and 4 depict the equivalent radar reflectivity at ~2 km (above ground level) computed from the sum of the sixth moment of the hydrometeor size distributions from the SM and DM simulations, respectively, at 0600 UTC 13 June 2002, 24 h after the initial time of the 2.5-km runs. The corresponding observed reflectivity at 2 km from the WSI NOWRAD US mosaic is shown in Fig. 5. While the timing and location of the sim-

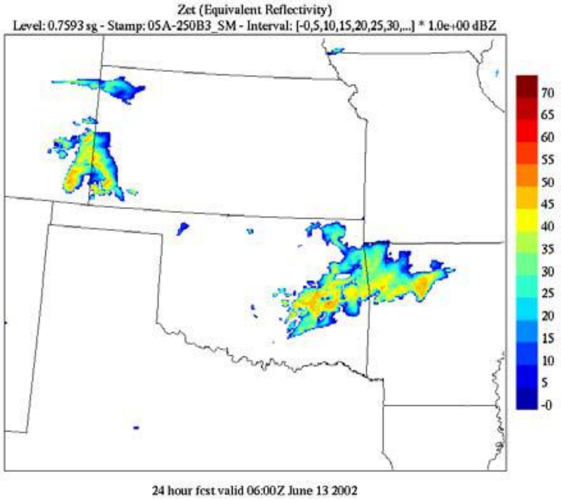

Fig. 3 Simulated reflectivity (dBZ) at ~2 km from the SM run at 13 June 0600 UTC.

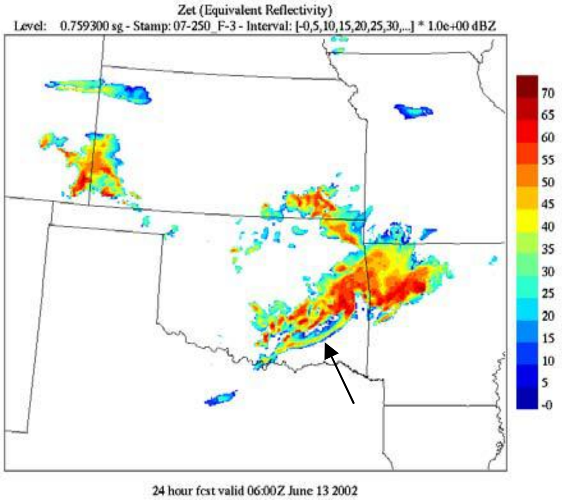

Fig. 4 As in Fig. 3 but for the DM simulation.

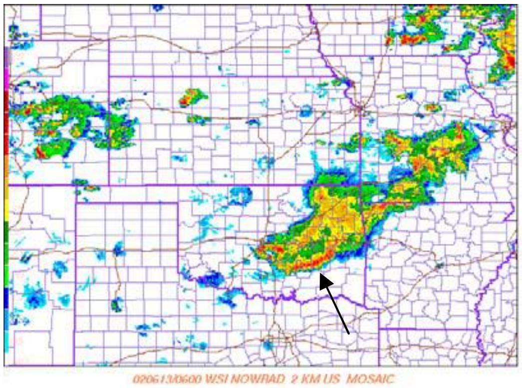

Fig. 5 Reflectivity (dBZ) at 2 km from WSI NOWRAD radar at 13 June 0600 UTC.

ulated squall lines in both runs compares well with the radar, the structures of the simulated storms are notably different. Overall, the DM simulation compares more favorably to the observations, with a more pronounced convective band along the leading edge, particularly along the south-west portion of the system (see arrows in Figs. 4 and 5), followed by a second convective region behind this band. Note that the configuration of the two simulations is identical except for the version of the BMS. Thus, the number of prognostic moments has a distinct effect on the storm structure of the convective system, not just on the instantaneous precipitation rates (not shown).

The reason for the sensitivity of storm structure to the number of moments is due to the microphysical feedbacks of the storm dynamics. The impact of changes to the microphysics scheme on the storm dynamics can be readily seen by comparing the instantaneous fields of potential temperature (θ) from the two simulations. Figure 6 depicts the mean boundary layer (lowest 10 model levels) θ from the DM simulation along with the difference in the mean θ from DM and SM, at the time corresponding to Figs. 3-5. The most conspicuous difference is the region of colder low-level air in south-central Oklahoma, along the leading edge of the squall line in the DM simulation and observed radar. A vertical cross-section of the θ difference field, along with a 3D field of cloud mixing ratio from the DM simulation, are shown in Fig. 7. The location of the temperature differences in relation to the cloud water field strongly suggests that the colder air in south-central Oklahoma in the DM simulation is due to evaporative cooling from precipitation along the leading convective portion of the system, captured in the DM run (Fig. 4) but absent in the SM run (Fig. 3).

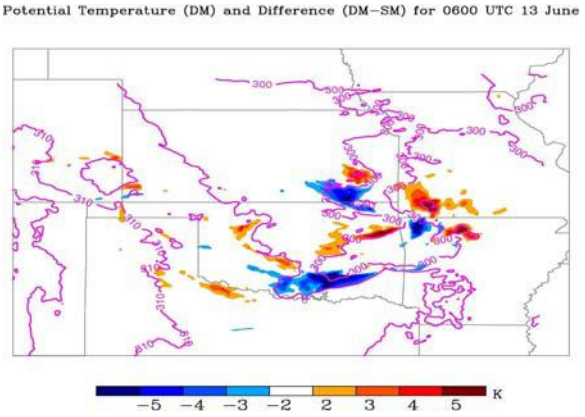

Fig. 6 Lowest model-level potential temperature from the DM simulation (purple contours, 5 K interval), valid at 13 June 0600 UTC, and the layer-averaged (lowest 10 levels) potential temperature difference field (shading) for DM-SM.

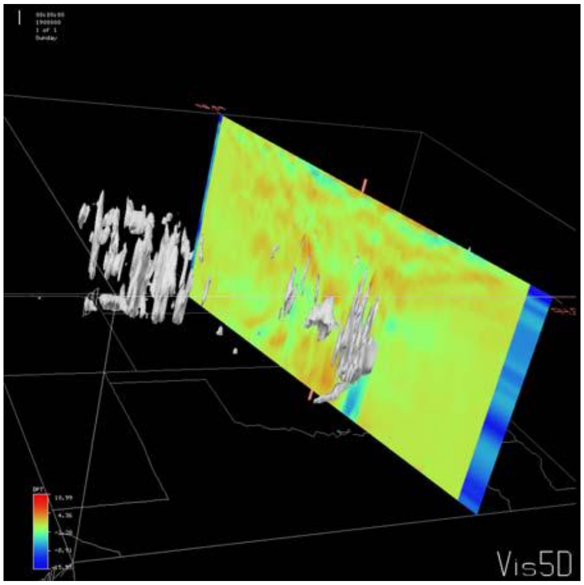

Fig. 7 Vertical cross-section of the potential temperature difference field (shading) for DM-SM and the 3D cloud water field from the DM simulation, valid at 13 June 0600 UTC.

6. CONCLUSION

An efficient semi-double-moment version of the MY multi-moment scheme is currently being developed. Some important benefits of double-moment schemes in general have been described and a description of the major modifications for the proposed scheme has been given. High-resolution simulations of the 12-13 June 2002 IHOP mid-latitude squall line using fully single-moment and double-moment versions of the BMS have been presented. The model runs illustrate that the number of moments impact on the dynamics and structure of the simulated convective system. The double-moment simulation also provides a baseline against which the semi-double-moment version will be evaluated.

For other types of cases, the effects of the microphysics can be even more pronounced, with a completely different convective mode in the simulated storm. Process studies with mesoscale models, as well as high-resolution operational NWP, would be better served with double-moment rather than single-moment BMSs, particularly for cases involving deep convection. Limitations in computational resources have, however, restricted many research and operational models to the use of single-moment schemes. In the foreseeable future, computer power will likely allow for the use of fully double-moment schemes for all atmospheric modeling applications that use bulk schemes. In the meantime, it is important to consider schemes that are at least double-moment for the hydrometeor categories for which there is the greatest impact, thus benefiting from the double-moment approach without increasing the total run time of the models prohibitively.

Simulations of the squall line case using the semi-double-moment version of the MY scheme will be presented at the conference. The success of the proposed version of the scheme will be evaluated by comparison with observations and the double-moment simulation presented here, as well as its overall efficiency. It is planned that the semi-double-moment version will be used in the high-resolution configuration of Environment Canada's operational forecast model for the 2010 Winter Olympics in Vancouver, Canada.

REFERENCES

Bailey, M. and J. Hallett, 2006: Measured ice crystal capacitances: The failure of the electrostatic analogy. *Proceedings, 12th Conference on Cloud Physics*, Madison, WI, 10-14 July 2006.

Côté, J., S. Gravel, A. Méthot, A. Patoine, M. Roch, and A. Staniforth, 1998: The operation CMC-MRB Global Environmental Multiscale (GEM) model. Part I: Design considerations and formulation. *Mon. Wea. Rev.*, **126**, 1373-1395.

Kato, T., 1995: A box-Lagrangian rain-drop scheme. *J. Meteor. Soc. Japan*, **73**, 241-245.

Feingold, G., R.L. Walko, B. Stevens, and W.R. Cotton, 1998: Simulations of marine stratocumulus using a new microphysical parameterization. *Atmos. Res.*, **47-48**, 505-528.

Field, P. R., A. J. Heymsfield, A. Bansemer and C. H. Twohy, 2006: Capacitance of snowflakes. *Proceedings, 12th Conference on Cloud Physics*, Madison, WI, 10-14 July 2006.

Milbrandt, J. A. and M. K. Yau, 2005a: A multimoment bulk microphysics parameterization. Part I: Analysis of the role of the spectral shape parameter. *J. Atmos. Sci.*, **62**, 3051-3064.

------ and ------, 2005b: A multimoment bulk microphysics parameterization. Part II: A proposed three-moment closure and scheme description. *J. Atmos. Sci.*, **62**, 3065-3081.

------ and ------, 2006a: A multimoment bulk microphysics parameterization. Part III: Control simulation of a hailstorm. J. Atmos. Sci. *J. Atmos. Sci.*, **63**, 3114-3136.

------ and ------, 2006b: A multimoment bulk microphysics parameterization. Part IV: Sensitivity experiments. *J. Atmos. Sci.*, **63**, 3137-3159.

------, ------, J. Mailhot, and S. Bélair, 2008a: Simulation of an orographic precipitation event during IMPROVE-2. Part I: Evaluation of the triple-moment run. *Mon. Wea. Rev.* (in press)

------, ------, ------,------, and McTaggart-Cowan, R., 2008b: Simulation of an orographic precipitation event during IMPROVE-2. Part II: Sensitivity experiments. (submitted to *Mon. Wea. Rev.*)

Rogers, R. R. and M. K. Yau, 1989: A Short Course on Cloud Physics. Pergamon, 293 pp.

Thompson, G. P. R. Field, R. M. Rasmussen, and W. D. Hall, 2008: Explicit forecasts of winter precipitation using an improved bulk microphysics scheme. Part II: Implementation of a new snow parameterization. *Mon. Wea. Rev.* (in press).

Morrison, H. and W. W. Grabowski, 2007: A novel approach for representing ice microphysics in models: Description and tests using a kinematic framework. *J. Atmos. Sci.* (in press).

THE MORPHOLOGY AND PROCESSES OF A DEEP, MULTI-LAYERED ARCTIC CLOUD SYSTEM

M. Rambukkange[1], J. Verlinde[1], P. Kollias[2],and E. Luke[3]

[1]Penn State University, University Park, PA
[2]McGill University, Montreal, Quebec
[3]Brookhaven National Lab, NY

1. INTRODUCTION

Mixed-phase clouds play an important role in the Arctic climate system. These clouds occur frequently in the spring and fall seasons (Pinto 1998; Intrieri et al., 2002), and also have been observed to persist for long periods of time (12 hours to days, Shupe and Matrosov, 2006). Mixed-phase clouds have been observed in temperature ranges from -3^{0}C and -34^{0}C (Witte 1968; Hobbs and Rangno, 1998; Pinto and Curry, 2001; Intrieri et al., 2002). These clouds usually contain a super-cooled liquid layer near the top with precipitating ice particles (McFarquhar et al., 2007; Intrieri et al., 2002; Pinto and Curry, 2001; Hobbs and Rangno, 1998). Despite their prevalence, detailed microphysical and dynamical descriptions of the processes involved in their formation and maintenance are not well known (Verlinde et al., 2007).

Mixed-phase cloud strongly impacts the surface energy budget in the Arctic (Persson et al, 2002). The difference in the size, shape, and refractive index between water drops and ice particles result in significantly different radiative properties (Sun and Shine, 1994). In particular, Sun and Shine (1994) demonstrated the necessity for accurately specify the liquid water content by showing that greater errors result when all ice is converted into liquid compared to totally ignoring the ice phase in the radiative transfer calculation. However, the ice phase determines the liquid water amount and longevity in mixed-phase cloud by acting as a sink (Harrington et al., 2001). Therefore, it is important to include mixed-phase clouds in climate models to reproduce the present climate realistically (e.g. Gregory and Morris 1996).

Current mixed-phase cloud parameterizations need to be improved to obtain higher levels of confidence in climate model simulations (Gregory and Morris, 1996). For example, McFarquhar et al. (2007), using in situ observations of the fine scale structure and cloud properties of mixed-phase clouds in the Arctic, showed that current climate model parameterizations which specify the liquid water fraction as a function of temperature does not match observations taken during the Mixed-Phase Arctic Cloud Experiment.

The Mixed-Phase Arctic Cloud Experiment, conducted in October 2004, contains a rich set of data capable of being used for a detailed study of mixed-phase clouds (Verlinde et al., 2007). In this paper we present an analysis of Doppler velocity spectra from the DOE-ARM millimeter wavelength cloud radar (MMCR). Shupe et al. (2004) showed how Doppler spectra may be used to identify the phase of, and quantify the microphysical characteristics of hydrometeor populations in mixed-phase clouds. The most recent work using Doppler spectra data from the Millimeter Wavelength Cloud Radar focused on obtaining vertical velocities and turbulent dissipation rates (Shupe et al., 2007). This study focuses on a detailed analysis of the Doppler spectra data to improve our knowledge of the microphysical structure, ice formation mechanisms and maintenance of liquid layer in Arctic mixed-phase stratus clouds.

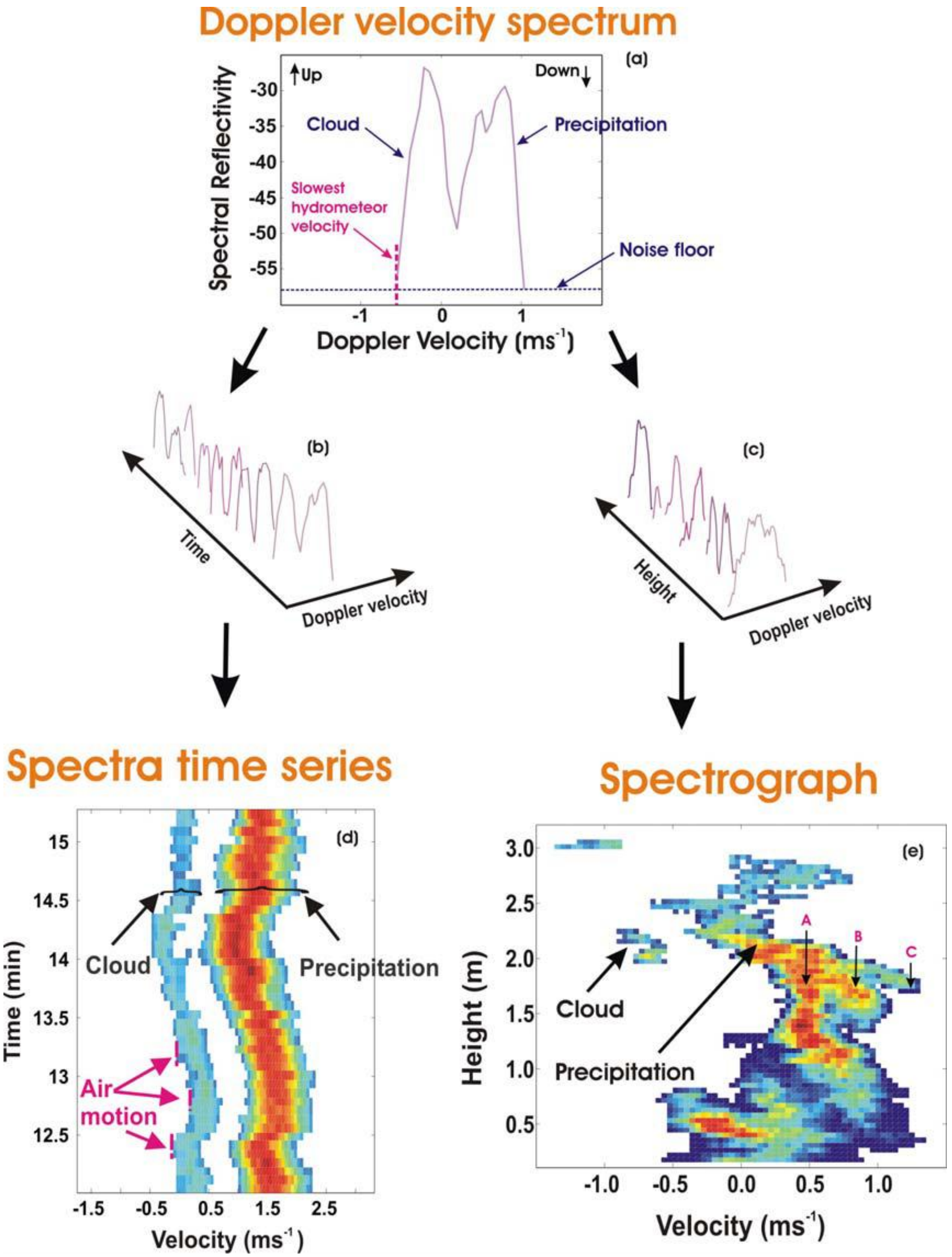

Figure 1: (a) Doppler velocity spectrum from a single range gate. The velocity of the slowest hydrometeor is found at the left edge of the spectrum. By convention use in radar meteorology, negative velocity is upward. (b) Stacking velocity spectra in time. (c) Stacking velocity spectra in height. (d) Time series plot of spectra at a single range gate: color shading represent spectral reflectivity. (e) Spectrograph obtained at single time.

2. DOPPLER VELOCITY SPECTRA

A Doppler radar spectrum is the hydrometeor backscatter power (or reflectivity) distributed in radial velocity (Fig. 1a). These spectra can then be aligned in time and velocity to obtain a spectral time series plot (Fig. 1d) which provides information about the time evolution of spectra at a particular height. Alternatively, they can be combined in height and velocity to yield a spectrograph (Fig. 1e). This point of view is ideal for keeping track of different hydrometeor modes and their velocity in height. For example, in Fig. 1e precipitation that fall into the cloud at 2 km clearly grows into three distinct modes below the cloud layer (denoted by A, B, and C). Doppler radar spectra can also be used to extract additional properties such a total reflectivity by taking its moments. The zeroth spectral moment of the Doppler spectra yields the signal mean power (integral of the spectral reflectivity yields total reflectivity), the first moment gives the mean Doppler velocity, and the second moment specifies the spectral variance (square root of this quantity is called the spectrum width). In the presence of a liquid clouds the vertical pointing MMCR measures the vertical velocities of the cloud drops which are the sum of their quiet-air terminal fall speed and air motions. These air motions can be divided into a radar volume-mean velocity that can result in shifting the whole spectrum and fluctuating part (turbulent) that can act to broaden the quiet-air spectrum (Babb et at., 1999). The quiet air terminal fall speeds of typical cloud drops (~ 10-20 µm) is less than 2 cm s^{-1}. Therefore in the presence of air velocities much larger than their terminal fall speed, drops can act as tracers of air motions, but can’t be directly used to estimate drop size distribution (Gossard et al., 1997). Under this condition the slowest hydrometeor fall speed obtained from the Doppler spectrum gives the air velocity in the presence of cloud (Fig. 1a).

3. SYNOPTIC SITUATION AND DATA

The synoptic condition over North Slope of Alaska (NSA) during Oct 4-8th was mainly controlled by a high pressure that was located over the ocean north of Barrow, Alaska. A weak disturbance that originated over the Eastern Brooks Range moved over the ocean and then moved along the coast prior to its dissipation over Deadhorse. Though the low pressure system did not cause much change in the surface winds and temperature fields, it carried with it sufficient moisture at mid level and upper levels to cause cloudiness over NSA. These upper-level clouds along with the boundary layer stratus caused the multi-layered decks that were seen over Barrow during October 6th (Yannuzzi, 2007).

The soundings at 1059 UTC and 1659 UTC were used to estimate temperature and wind information at 1300 UTC. A constant wind speed of 5 ms^{-1} flowing from east of northeast was observed between 2km and 3 km on both soundings, and also captured by the Eta model surface analysis. Therefore this wind speed will be used as wind speed at 1300 UTC. The data used for these analyses were collected by the High Spectra Resolution Lidar (HSRL) data and the 35 GHz, Millimeter Wavelength Cloud Radar (MMCR) at the NSA Atmospheric Radiation measurement (ARM) climate research facility during the Mixed Phase Arctic Cloud Experiment (M-PACE), that was conducted during 27 September – 22 October 2004 (Verlinde et al. 2007). The regions of high aerosol backscatter cross section and near zero HSRL linear depolarization are in good agreement; therefore a plot of the aerosol backscatter is not included in this study

4. Results

In Fig. 2 we present the thermodynamic profile and an instantaneous spectrograph representative of the cloud overhead the radar. The layer between 0.5 km and 2 km reveals clear bimodality in the spectra, from which one can deduce that there are two distinct populations of hydrometeors in the radar volume. The mean velocity for each of these modes differ: e.g. at 1.86 km in Fig. 2b, the mean velocity of the slow-falling mode (indicated as liquid cloud layer) is close to 0.3 m s^{-1} whereas the mean velocity of the fast-falling mode (precipitation) is about 1.0 m s^{-1}.

Therefore, the horizontal size of the domain shown is about 2.5 km. The reflectivity plot reveals evidence of vertical shear of the horizontal wind, seen as slanted streaks of maximum/minimum reflectivity. The velocity plot reveals several sharp discontinuities in height, particularly at 0.5 km and 2 km, and discontinuities in time between 3.5 km and 4 km. The linear depolarization plot shows near-zero valued layers (liquid layers) corresponding to the velocity features at 2 km and close to cloud top at 4 km, but not in the lower layers which are dominated by heavy precipitation. The higher depolarization valued regions between these layers contain precipitating ice. One may thus interpret the 2 km layer of slow moving hydrometeors as a liquid cloud layer (indicated as liquid layer in Fig. 2b. The velocity of the slowest hydrometeor may therefore be used to identify imbedded liquid layers in precipitating ice which otherwise are not visible in the reflectivity plot. The MWR plot confirms the correctness of the interpretation of these layers as liquid layers.

In Fig. 4 we present a more complete view of the evolution of this imbedded liquid layer through time-series plots of spectra at various heights spanning the cloud layer at 1.9 km. Layers well above cloud top (a & b), spanning the cloud (c & d), in the ice precipitation below this cloud layer (e & f),

the analysis period and is indicated as liquid in Fig. 4d. In contrast, the slow falling mode in Fig 4e is precipitating ice originating in the liquid layer above. The reflectivity of the ice mode precipitating through the liquid layer increases (seen at 1.9 km in Fig. 2b and also in Fig. 4c & 4d), likely the result of riming which increases the density, and hence the reflective index and the evolution of the two modes in height (g & h) are shown. Fig. 2a reveals that the altitudes spanning these layers have a generally stable temperature profile, although aircraft measurements (not shown) revealed that each liquid layer typically is found in a shallow mixed layer capped by an inversion. Looking at the mean velocity in the continuous precipitation mode, one can seen regular variations on the order of 0.7 m s^{-1}, and period about 4 minutes, at 2.5 km, becoming more damped at lower altitudes. We speculate that these variations are gravity waves forced by the radiatively driven convection in the top most cloud layer at 4 km, evidence of which can be seen from the fluctuations in speed of the slowest falling hydrometeors (Fig. 3b). Fig. 4a reveals the presence of broken cloud (liquid) at 2.5 km (between 13.22 and 13.24 UTC) with vertical motion close to 0 m s^{-1}, from which one can deduce the mean fall speed of the precipitating ice at that altitude to be 0.75 m s^{-1}, the difference between the air motion and the mean velocity of the precipitation mode.

The liquid cloud layer identified in Fig. 3b & 3c can easily be distinguished from ice below cloud base using a spectrograph. Below the base of the liquid layer as indicated by the HSRL a sharp drop-off in spectral reflectivity is clearly evident (Fig. 2b). This liquid layer persisted throughout

Fig. 3 presents profiles of the total reflectivity, the vertical speed of the slowest falling hydrometeor, the linear depolarization from the HSRL, and the liquid water path from the microwave radiometer. Data between 13.16 UTC and 13.30 UTC were used for the analysis (~ 8 minutes), during which period the mean wind speed was approximately constant at 5 m s^{-1}. of the hydrometeors. Less common, the precipitation mode separates into two or more branches (e.g., indicated by A, B, and C in Fig. 1e; three ice modes seen in Fig. 4g & 4h). This splitting suggests that there is a sub-section of the population that converts to a different terminal fall velocity class (likely a heavily rimes hydrometeor type, observed during M-PACE; McFarquhar et al., 2007).

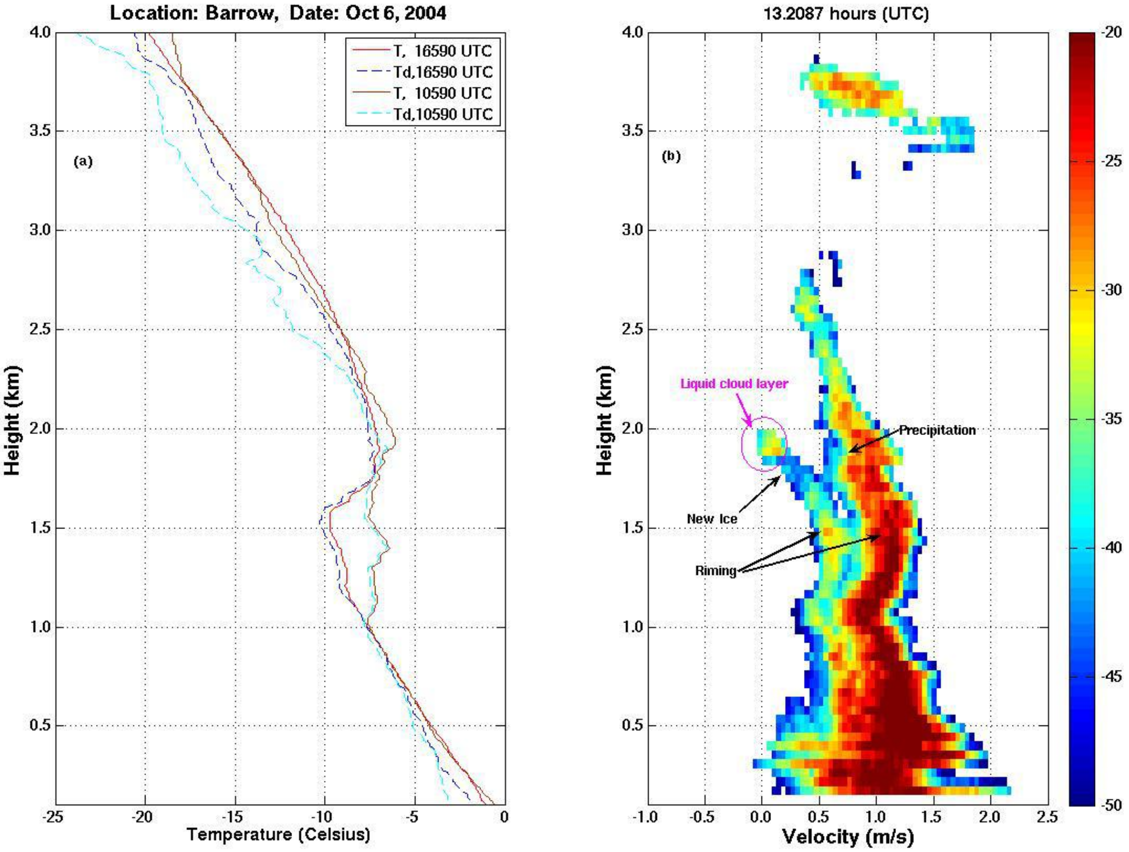

Figure 2: (a) The sounding at 1059 UTC and 1659 UTC obtained from Barrow, Alaska. (b) Spectrograph at 13.2087 UTC for the Oct 6th 2004.

The slowest falling ice mode in Fig. 2b and Fig. 4g &4h originated in the liquid layer at 1.9 km. The temperature in this liquid layer is -7ºC. Forward Scattering Spectrometer Probe mean diameters on the order of 20 micron were measured in a liquid layer at approximately the same height later in the day. Using only the liquid contribution to the reflectivity as derived from the Doppler spectra, we estimated liquid water contents of 0.1 g m^{-3} – 0.2 g m^{-3} and effective radii on the order of 11 micron during this time period, using the algorithms suggested by Shupe et al. (2005). These radar estimated values are consistent with the aircraft observations, lending confidence that this cloud layer contained drops with diameter >23 micron. Looking at individual spectra in the cloud layer, we can see that ice particles with fall speeds of ~ 1.5 m s^{-1} were present in the cloud (the difference between the velocities at the left and right edges of any spectrum in Fig. 4d is an estimate of the fastest falling hydrometeor speed). Thus, all the necessary conditions for secondary production of ice via ice splintering during riming (Hallett and Mossop, 1974) were met in this layer. This conclusion is consistent with that of Rangno and Hobbs (2001) who suggested that the conditions for ice splintering were met in localized pockets in the liquid layers. Nucleation rates via rime splintering will dominate new ice formation via heterogeneous primary ice production from ice nuclei, the rate of which are low at this temperature (Pruppacher and Klett, 1997).

Comparing the two precipitating ice modes in Fig. 2b one can see that the difference in the mean velocity of each mode decreases with distance below cloud base. This decrease may be explained by examining the effect of vapor depositional growth on the fall speed of the two populations. The fall velocity of smaller ice particle increases faster with diameter than a larger ice particle because the asymptotic dependence of the terminal fall velocity on diameter for the pristine/aggregate ice classes. One then concludes that the sub-cloud is saturated with respect to ice.

The HSRL indicates the presence of a thin liquid layer at 1.5 km early in the analysis period (Fig. 3c). The radar spectra revealed no evidence of a separate cloud mode at this altitude. This failure to detect the cloud mode may be explained by the presence of small drops in this layer and/or the shallowness of the cloud, which if less than the range gate size (45 m) will further reduce the returned power to a level below the noise level. However, a sharp increase in the reflectivity in both ice precipitation modes at this level (Fig. 2b) is evidence of riming, and thus indirect evidence of the liquid. Moreover, the expanded time window afforded by Fig. 4f – 4h shows the impact of the liquid layer on the precipitation modes. One can see a clear increase in spectral reflectivity in both precipitation modes going from 4f to 4g, and also the development of faster falling modes (4g & 4h).

5. DISCUSSION AND CONCLUSIONS

The analysis of Doppler velocity spectra presented here documented microphysical processes in a deep precipitating cloud system observed during the Mixed-Phase Arctic Cloud Experiment over the North Slope of Alaska. This cloud system consisted of ice precipitating out of a thin

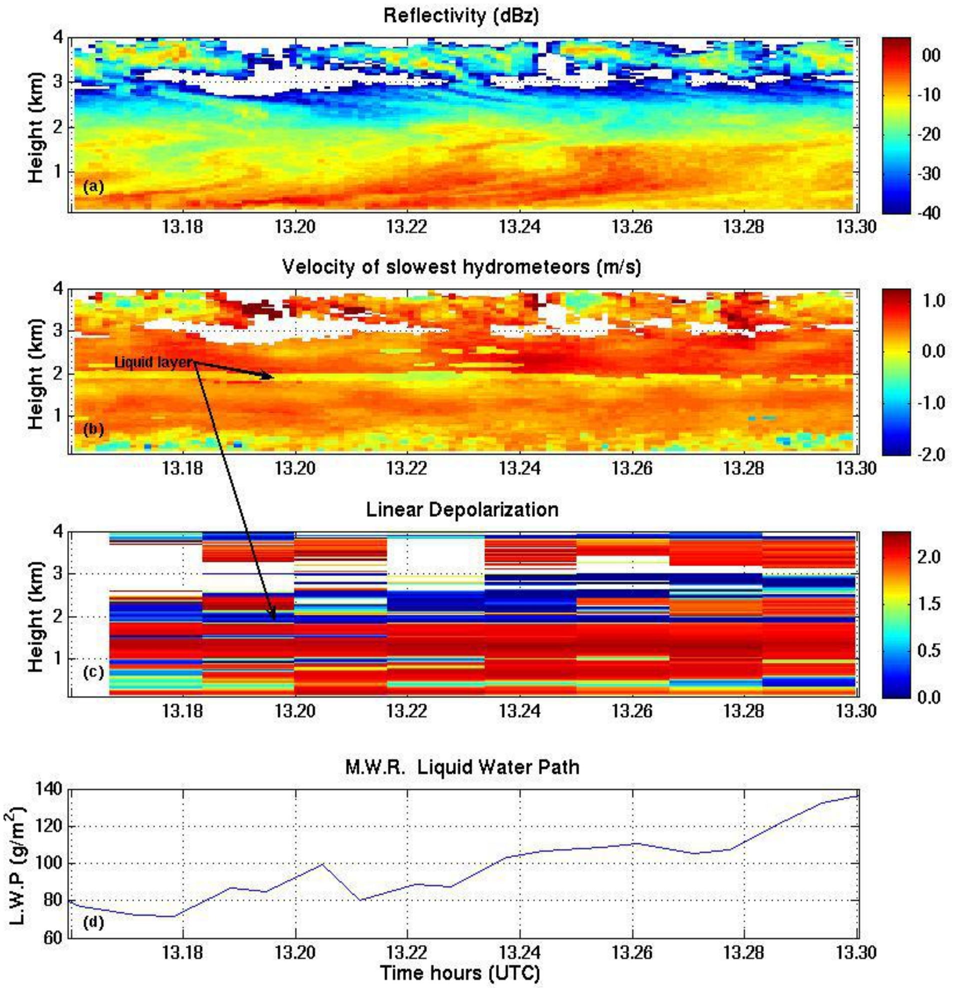

Figure 3: (a) Reflectivity plot between times 13.15 and 13.40 UTC up to a height of 4 km, (b) Slowest hydrometeor fall velocity plotted between same times and height, (c) HSRL linear depolarization (log10[percent depolarization]) for the same time period, (d) shows the liquid water path obtained from the Microwave Radiometer at Barrow for the same time period.

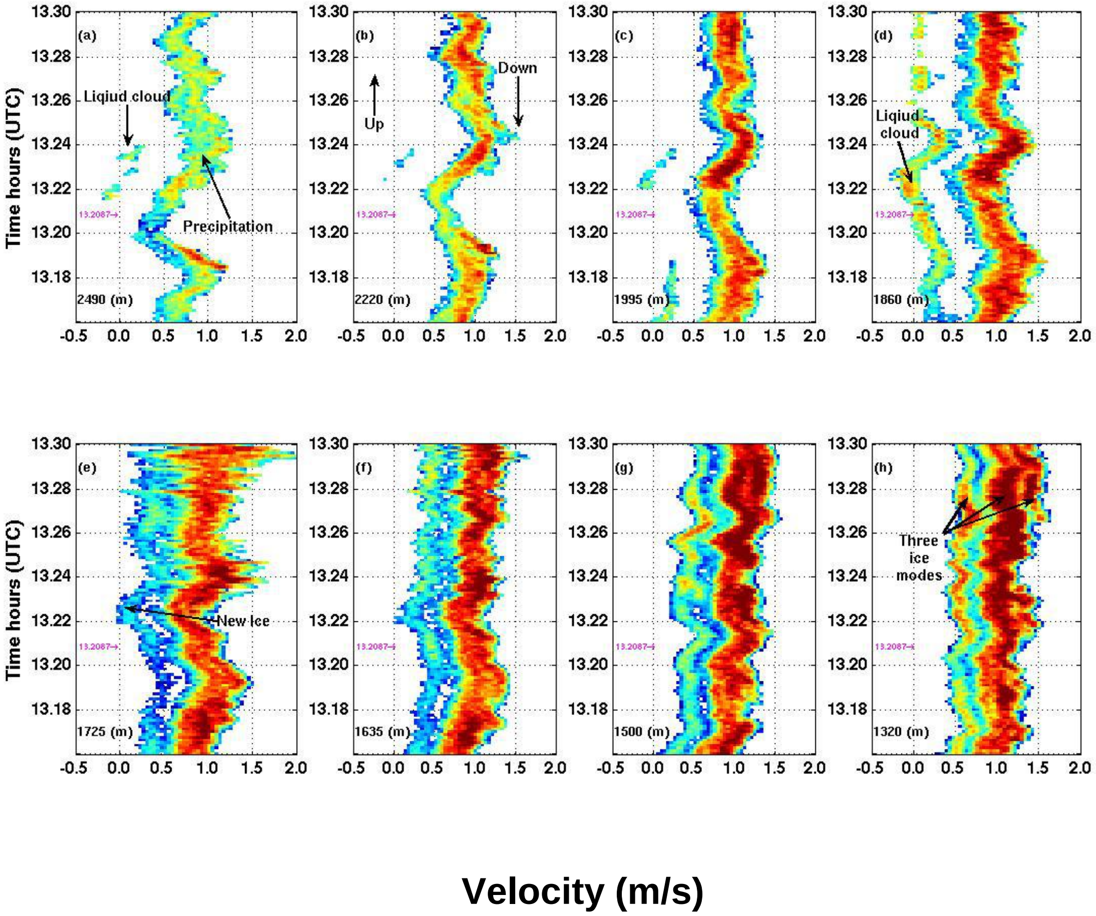

Figure 4: (a)-(h) Are times series plots of velocity at the heights indicated at bottom left. The pink arrow with text indicates the time at which the spectrograph in Fig. 1(b) was obtained. The times series plots have the same colorbar as in the spectrograph shown in Fig. 2(b).

liquid layer at 4 km, falling through multiple layers of liquid cloud.

The spectral analysis revealed the presence of these weakly reflecting liquid layers even in the presence of highly reflective ice precipitation. The formation of new ice through rime splintering was document in one of these imbedded liquid layers. The evolution of different ice modes suggests that much of the 4 km thick layer was at or above ice saturation. With most of the 4 km layer characterized by strong static stability, and perturbed by radiatively driven convection in the top-most liquid layer, much of the middle levels are strongly perturbed by gravity waves. We speculate that the intermittent clouds at 2.2 – 2.5 km (Fig. 3b, 4a, 4b; 13:22 UTC – 13.24 UTC) are formed when pockets of higher saturation experience upward forcing by these gravity waves. Further evidence for this can be seen in Fig. 3b where a maximum in upward velocity in the imbedded cloud layer is present during that period. Coincident with this vertical velocity maximum, one sees a thickening of the liquid layer in the lidar depolarization, and an increase in the total reflectivity.

Interestingly, the thin a liquid layer detected by the lidar at 1.5 km, but with reflectivity below the minimum radar sensitivity, had the strongest impact on the precipitating ice. Interaction between this thin cloud and the precipitating ice resulted in a sharp increase in reflectivity and a newly formed class of hydrometeor, characterized by faster fall speeds (Fig. 4h).

Acknowledgments. This research was supported by the Office of Biological and Environmental Research of the U.S. Department of Energy as part of the Atmospheric Radiation Measurement Program.

REFERENCES

Babb, D.M., J. Verlinde, and B. A. Albrecht 1999: Retrieval of Cloud Microphysical Parameters from 94-GHz Radar Doppler Power Spectra. *J. Atmos. Oceanic Technol. Sci*., **16**, 489–503.

Curry, J.A., and others, 2000: FIRE Arctic Clouds Experiment. *Bull. Amer. Meteorol. Soc*., **81**, 5-30.

Curry, J.A., J.O. Pinto, T. Benner, and M. Tschudi, 1997: Evolution of the cloudy boundary layer during the autumnal freezing of the Beaufort Sea. *J. Geophys. Res*., **102**, 13851-13860.

Pinto, J.O., J.A. Curry, and J. Intrieri, 2001: Cloud-aerosol interactions during autumn over the Beaufort Sea. *J. Geophys. Res.*, **106**, 15077-15098.

Gregory, D. and D. Morris, 1996: The sensitivity of climate simulations to the specification of mixed phase clouds. *Climate Dyn*., **12**, 641-651.

Gossard, E.E., J. B. Snider, E. E. Clothiaux, B. Martner J.S. Gibson, and R. A. Kropfli, and A. S. Frisch 1997: The Potential of 8-mm Radars for Remotely Sensing Cloud Drop Size Distributions. *J. Atmos. Oceanic Technol. Sci*., **14**, 76–87.

Hallett**,** J**.** and S**.** C. Mossop**,** 1974: Production of secondary ice particles during the riming process**.** *Nature***, 249,** 26-28 Harrington. J. Y., T. Reisin, W.R.

Cotton, and S. M. Kreidenweis 1999: Cloud resolving simulations of Arctic stratus Part II: Transition-season clouds, *Atmos. Res*., **51**, 45-75.

Hobbs, P. V. and A. L. Rangno 1998: Microstructures of Low and Middle-Level Clouds over the Beaufort Sea. *Q. J. Roy. Meteor. Soc.*, **124**, 2035-2071.

Intrieri, J. M., M. D. Shupe, T. Uttal, and B.J. McCarty 2002: An annual cycle of Arctic cloud characteristics observed by radar and lidar at SHEBA. *J. Geophys. Res*., **107**, SHE5.

McFarquhar, G. M., G. Zhang, M. R. Poellot, G. L. Kok, R. McCoy, T. Tooman, A. Fridlind, and A. J. Heymsfield 2007: Ice properties of single-layer stratocumulus during the Mixed-Phase Arctic Cloud Experiment: 1. Observations

. *J. Geophys. Res*., **112**, D24201.

Persson, P. O. G., C. W. Fairall, E. L. Andreas, P. S. Guest, and D. K. Perovich, 2002: Measurements near the Atmospheric Surface Flux Group tower at SHEBA: Near-surface conditions and surface energy budget, *J. Geophys. Res.*, **107***,* C10.

Pinto, J. O., 1998: Autumnal mixed-phase cloudy boundary layers in the Arctic. *J. Atmos. Sci*., **55**, 2016-2038.

Pruppacher**,** H.R**.,** and J.D**.** Klett, 1997**:** *Microphysics of Clouds and Precipitation.* 976 p.

Rangno, A.L., and P.V. Hobbs, 2001: Ice particles in stratiform clouds in the Arctic and possible mechanisms for the production of high ice concentrations. *J. Geophys. Res*., **106**, 15 056-15 075.

Shupe, M.D**.**, T. Uttal, and S.Y. Matrosov, 2005: Arctic cloud microphysics retrievals from surface-based remote sensors at SHEBA. *J. Appl. Meteor*., **44**, 1544-1562.

Shupe, M. D., and S.Y. Matrosov, 2006: Arctic mixed-phase cloud properties derived from surface-based sensors at SHEBA. *Atmos. Sci*., **63**, 697-711.

Shupe, M. D., P. Kollias, S. Y. Matrosov, and T. L. Schneider, 2004: Deriving Mixed-Phase Cloud Properties from Doppler Radar Spectra. *Atmos. Oceanic Technol Sci*., **21**, 660–670.

Sun, Z,. and K.P. Shine 1994: Studies of the radiative properties of ice and mixed-phase clouds. *Quart. .J. Roy. Meteorol. Soc*., **120**, pp. 111-137.

Verlinde, J., and others, 2007: The mixed-phase Arctic cloud experiment. *Bull. Amer. Meteor. Soc*., **88**, 205-221.

Witte, H.J., 1968: Airborne observations of cloud particles and infrared flux density in the Arctic. M.S. thesis, University of Washington, Seattle.

Yannuzzi, V.T., 2007: A Statistical Comparison of Forecasting Models across the North Slope of Alaska during the Mixed-Phase Arctic Cloud Experiment. M.S. thesis, Penn State University, UP.

ON THE PARAMETERIZATION OF EVAPORATION OF RAINDROPS BELOW CLOUD BASE

AXEL SEIFERT

German Weather Service, Offenbach, Germany

1. INTRODUCTION

Evaporation of raindrops can lead to a significant reduction of the surface precipitation compared to the precipitation flux at cloud base. A precise parameterization of this process is therefore an important issue in quantitative precipitation forecasts. Evaporation of raindrops provides also an important link between cloud microphysics and cloud dynamics. In mesoscale convective systems the evaporation of raindrops determines the strength of the cold pool and subsequently the organization and life time of convective systems. For boundary layer clouds observations show that often more than 80 % of the drizzle drops evaporate below cloud base and the associated cooling of the boundary layer has an important impact on the macroscopic cloud structure.

In cloud-resolving numerical models the evaporation of raindrops received surprisingly little attention up to now. Usually the parameterizations follow Kessler's assumptions, e.g. using an exponential drop size distribution combined with a power law relation for the fall speed. For convection-resolving models these assumptions might be insufficient as the variability of the size distribution in convective situations is much larger than in stratiform rain. Using a multi-moment approach, as it is done in some current research models, does not a-priori solve this problem but poses additional ones, like the question of size effects of evaporation. Does evaporation increase or decrease the mean size of the raindrops?

To shed some light on theses issues the process of evaporation of raindrops below cloud base is investigated by numerical simulations using a idealized one-dimensional rainshaft model with high-resolution bin microphysics. The simulations reveal a high variability of the shape of the raindrop size distributions which has important implications for the efficiency of evaporation below cloud base. A new parameterization of the shape of the raindrop size distribution as a function of the mean volume diameter is suggested and applied in a two-moment microphysical scheme. In addition, the effect of evaporation on the number concentration of raindrops is parameterized.

2. THE RAINDROP SIZE DISTRIBUTION

A crucial step for all parameterizations of evaporation of raindrops is the choice of an appropriate raindrop size distribution (RSD). Here a gamma distribution given by

$$n(D) = N_0 D^{\mu} \exp(-\lambda D) \qquad (1)$$

is assumed where $n(D)$ is the drop size distribution in m^{-4}, D is the drop diameter in m, N_0 the intercept parameter with units $\mathrm{m}^{-(\mu+4)}$, λ the slope in m^{-1} and μ the dimensionless shape parameter.

The variability of the shape parameter μ and its parameterization has been the focus of many investigations (Ulbrich 1983; Testud et al. 2001, and others). Recently Zhang et al. (2001) suggested the empirical relationship

$$\lambda = 0.0365\mu^2 + 0.735\mu + 1.935. \qquad (2)$$

between the shape parameter μ and the slope λ based on disdrometer measurements in Florida (see also Brandes et al. 2003; Zhang et al. 2003; Brandes et al. 2007). Using a simple rainshaft model Seifert (2005, S05 hereafter) showed that this μ-λ-relation is probably a result of gravitational sorting, collision/coalescence and collisional breakup.

Corresponding author's address: Dr. Axel Seifert, Deutscher Wetterdienst, GB Forschung und Entwicklung, Kaiserleistr. 42, 63067 Offenbach, Germany. E-mail: axel.seifert@dwd.de

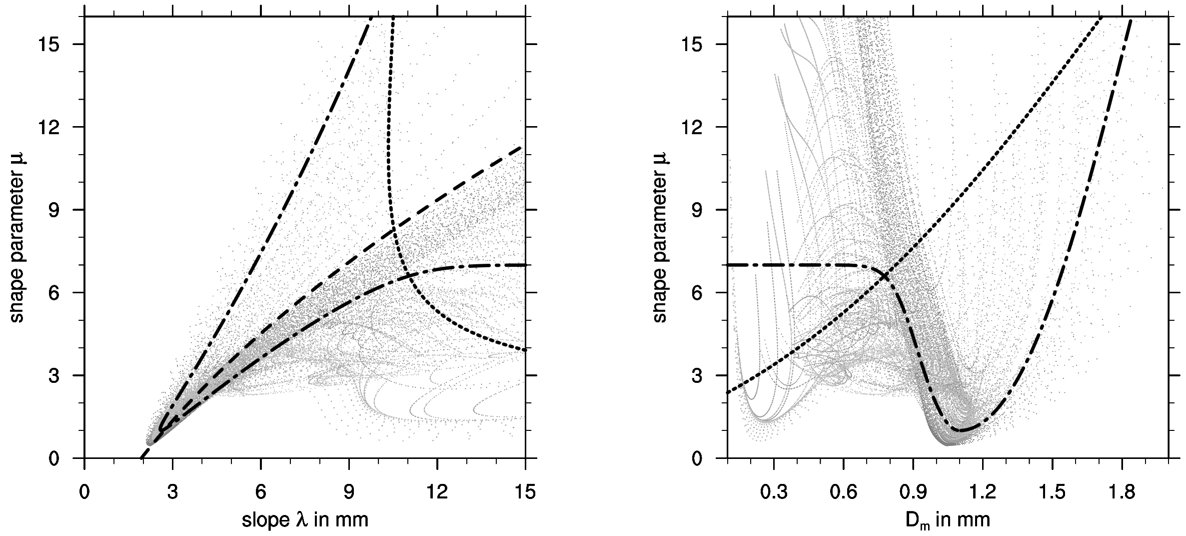

Figure 1: Shape parameter μ as a function of the slope λ (left) or mean volume diameter D_m (right). The dashed line is the μ-λ-relation of Zhang et al. (2001), the dotted line is the μ-D_m-relation of Milbrandt and Yau (2005a). The dashed-dotted line is Eq. (3).

3. NUMERICAL EXPERIMENTS USING A 1D RAINSHAFT MODEL

To investigate the variability of the shape of the RSD a simplified model of a non-stationary precipitation event is used. As in S05 a homogeneous initial cloud is assumed between a cloud base height z_{base} and a cloud top z_{top} with a initial cloud droplet distribution given by

$$f_0(x,z) = \begin{cases} Ae^{-Bx}, & z_{top} \geq z > z_{base} \\ 0, & \text{else.} \end{cases}$$

The parameters A and B are calculated from the initial liquid water content L_0 and the initial mean volume radius r_0. Below cloud base a constant temperature T_{pbl} and relative humidity RH_{pbl} is assumed. In the following all simulations assume $T_{pbl} = 20$ °C. This 1D rainshaft model is numerically solved using 130 spectral bins with a vertical grid spacing of 50 m and a timestep of 1 s.

Diagnostic relations for μ

From the bin microphysics simulation the shape of the RSD can be derived. Fig. 1 shows a scatter plot of the shape parameter μ for various initial conditions defined by L_0, r_0, z_{base}, z_{top} and RH_{pbl}. The same data is also shown as a function of the mean volume diameter D_m. The mean volume diameter has several advantages. First, it makes it easier to identify the breakup equilibrium regime around $D_m = D_{eq}$, second, it makes it possible to distinguish RSDs with smaller mean diameters from RSDs with larger mean diameters that have the same λ. For an individual 'convective' rain event the precipitation at the ground starts with large drops and high μ, then μ reaches a minimum during the precipitation maximum, maybe being close to equilibrium in strong precipitation (see Fig. 1 of S05) and then the raindrops become smaller and μ might become larger again or not depending on the relative humidity/evaporation and the rainwater content. This behavior can be roughly seen in Fig. 1. Especially when evaporation is taken into account the scatter in the μ-λ- or μ-D_m-relation becomes very large. Therefore any diagnostic parameterization of μ can only be a very crude approximation of the complicated time evolution of the RSD. A formulation which proved to be useful is

$$\mu = \begin{cases} 6\tanh[c_1\,\Delta D]^2 + 1, & D_m \leq D_{eq} \\ 30\tanh[c_2\,\Delta D]^2 + 1, & D_m > D_{eq} \end{cases} \qquad (3)$$

where $\Delta D = D_m - D_{eq}$, $c_1 = 4$ mm^{-1} and $c_2 = 1$ mm^{-1}. For $D_m \approx D_{eq} = 1.1$ mm this parameterization will give low values of μ assuming that the RSD is close to the equilibrium distribution, for small mean diameters larger values of μ will occur but the parameterization is arbitrarily constrained to a maximum value of 7. For large mean volume diameters gravitational sorting dominates which can produce very narrow size distribution and therefore very high values of μ.

Parameterization of evaporation in a two-moment bulk model

Assuming a gamma distribution the parameterization of the bulk evaporation rate of the rainwater content is quite straightforward, unfortunately this is not the case for the number concentration. A pragmatic approach to the problem is

$$\left.\frac{\partial N_r}{\partial t}\right|_{\text{eva}} = \gamma \, \frac{N_r}{L_r} \left.\frac{\partial L_r}{\partial t}\right|_{\text{eva}} \qquad (4)$$

where the coefficient γ nicely hides all unknown details. Khairoutdinov and Kogan (2000), Milbrandt and Yau (2005) as well as Morrison and Grabowski (2007) assume $\gamma = 1$, i.e. that the mean volume diameter does not change during evaporation. Khairoutdinov and Kogan (2000) show some results for drizzling stratocumulus that support this assumption in their case (their Fig. 2), but in general a compelling physical explanation of $\gamma \approx 1$ cannot easily be found. For $D_m \gg 80$ μm and $\mu \gg 1$, for example, one would expect $\gamma = 0$, since within a small time interval evaporation would only make the raindrops smaller without evaporating any of them. Therefore the assumption of $\gamma = 1$, which is equivalent to a constant D_m during evaporation, is probably only a good one for broad DSDs and/or drizzle, but not for strong convective rain.

Using Eq. (3) for the shape parameter, the evaluation of the 1D bin model suggests a parameterization for γ as

$$\gamma = \frac{D_{eq}}{D_m} \exp(-0.2\mu) \qquad (5)$$

with $D_{eq} = 1.1$ mm (see Seifert 2008, for more details). Although this parameterization points toward a delicate dependency of the size effect of evaporation on the shape parameter of the DSD, it is only a crude first attempt to model this complicated behavior.

Results of the two-moment bulk model

The parameterizations of the shape parameter μ and the evaporation coefficient γ which have been introduced in the previous sections can be combined with the warm rain scheme of Seifert and Beheng (2001) and Seifert and Beheng (2006). This scheme can now be compared with the results of the bin scheme for the idealized rain event simulated by the 1D rainshaft model. Fig. 2 shows the time evolution of the surface rainrate, the mean volume diameter and the shape parameter for an initial cloud with $L_0 = 7$ g/m^3, $r_0 = 13$ μm, $z_{base} = 3$ km, $z_{top} = 8$ km (this case differs from Fig. 1 of S05 only in the cloud base height). Again, we can see the time evolution a typical strong 'convective' rain event in three stages: During the first stage only the largest drops arrive at the surface, the second stage is characterized by strong precipitation with the DSD being close to breakup equilibrium, i.e. a broad size distribution, during the last stage the smaller drops dominate like in the stratiform region of a convective system. These three stages can be distinguished by the mean volume diameter with $D_m > D_{eq}$ during stage one, $D_m \approx D_{eq}$ during the equilibrium stage and $D_m < D_{eq}$ during the final stratiform-like period. Over the complete event the mean volume diameter decreases monotonically, although during the equilibrium stage D_m is almost constant. The shape parameter μ reaches its minimum in the equilibrium stage, and decreases (increases) during the first (last) stage. The two-moment parameterization is able to reproduce this behavior qualitatively, and for this individual event also the quantitative agreement is very good, except for the fact the μ starts to increase again too early and reaches only a value of 7 while the bin model simulates much larger values at the end of the event. In the evaporating case Fig. 2b with a relative humidity below cloud base of 70 % the maximum rainrate is reduced from about 150 mm/h to 80 mm/h, and overall about 55 % of the precipitation evaporates before reaching the ground. Compared to the simulation without evaporation the mean volume diameter drops off more rapidly during the decaying third stage of the event and the shape parameter does not increase to high values but remains low reaching only a value of 3 at the end of the event. The two-moment scheme captures

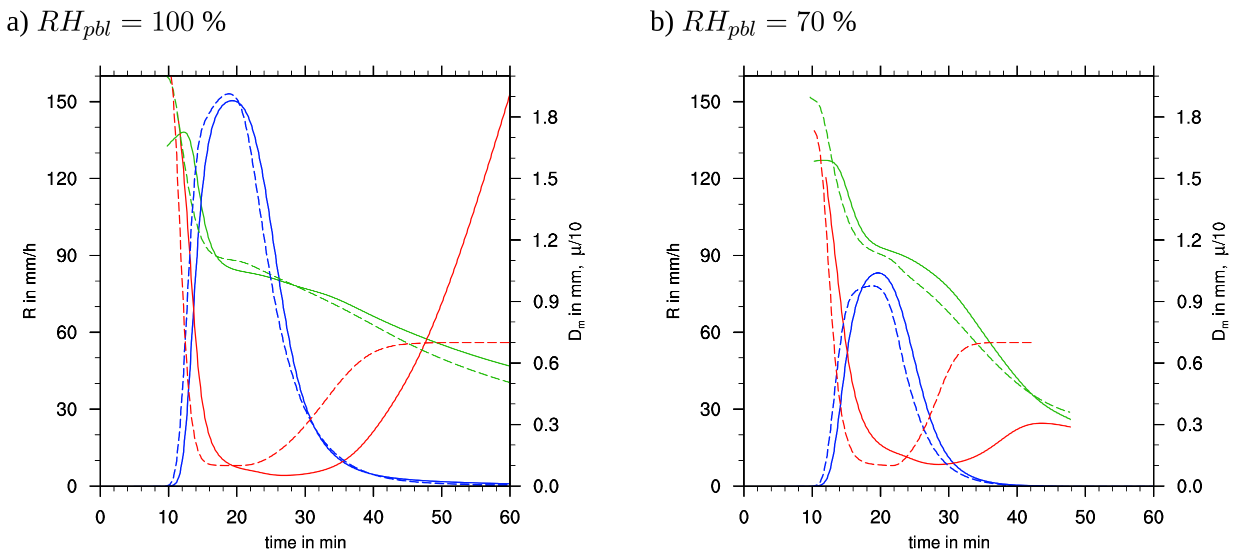
a) $RH_{pbl} = 100$ %

b) $RH_{pbl} = 70$ %

Figure 2: Time evolution of the rainrate R (blue), the shape parameter μ (red, plotted is 0.1μ) and the mean volume diameter D_m (green) for a strong rain event with $L_0 = 7$ g/m^3, $\bar{r}_c = 13$ μm, $z_{base} = 3$ km, $z_{top} = 8$ km and $RH_{pbl} = 100$ %, i.e. no evaporation, (a) as well as $RH_{pbl} = 70$ % (b). Solid lines are the results of the bin model, dashed lines represent the bulk model.

these differences to the non-evaporating case quite well, although the increase of μ in the final stage of the event is now too strong. This could only be improved by making μ a function of relative humidity. As it is now, the μ-D_m-relation Eq. (3) tries to make a compromise between non-evaporating and heavily evaporating situations. More details and a comparison with other assumptions can be found elsewhere (Seifert 2008).

4. SUMMARY AND CONCLUSIONS

An improved two-moment parameterization of raindrop evaporation below cloud base has been suggested and tested against a spectral bin reference model. It has been shown that an accurate parameterization of evaporation is a challenging problem and the suggested relations can only be a first step towards a better understanding of this complicated process. The complications arise due to the high variability of the raindrop size distribution, especially of the shape parameter μ, and the non-linear feedbacks between evaporation and breakup/coalescence as already shown by Hu and Srivastava (1995).

The suggested diagnostic relations for the shape parameter μ and the evaporation parameter γ are still very uncertain for several reasons:

- The idealized rainfall simulation is probably not realistic enough, although is reproduces the observations of Zhang et al. (2001) in a statistical sense.
- Both, the μ-D_m-relation as well as the parameterization of the evaporation coefficient γ, rely heavily on the ability of the spectral bin microphysics model to simulate the coalescence/breakup process in a realistic way. Especially for collisional breakup the uncertainties in the kernels are still significant. It is quite possible that this leads to an overestimation of evaporation in the spectral bin model, especially in moderate to heavy rain.
- In light precipitation the bin model allows high μ-values at D_m=D_{eq}, i.e. the system is not in coalescence/breakup equilibrium although the mean volume diameter is identical to the equilibrium diameter. The parameterization always predicts μ=1 for D_m=D_{eq},

since it would assume coalescence/breakup equilibrium.

- The dependency of the DSD on relative humidity is poorly understood and has, to the author's knowledge, not yet been investigated based on observations.

Overall this study shows once more that the key to an improved understanding and parameterization of the warm rain processes are reliable measurement of the drop size distribution which would be necessary to validate - of falsify - the theoretical models.

Acknowledgments The author thanks Bjorn Stevens, Klaus D. Beheng, Ed Brandes and Uli Blahak for interesting and helpful discussions.

References

Brandes, E. A., K. Ikeda, G. Zhang, M. Schönhuber, and R. M. Rasmussen, 2007: A statistical and physical description of hydrometeor distributions in Colorado snowstorms using a video disdrometer. *J. Appl. Met.*, **46**, 634–650.

Brandes, E. A., G. Zhang, and J. Vivekanandan, 2003: An evaluation of a drop distribution-based polarimetric radar rainfall estimator. *J. Appl. Met.*, **42**, 652–660.

Hu, Z. and R. C. Srivastava, 1995: Evolution of raindrop size distribution by coalescence, breakup, and evaporation: Theory and observations. *J. Atmos. Sci.*, **52**, 1761–1783.

Khairoutdinov, M. and Y. Kogan, 2000: A new cloud physics parameterization in a large-eddy simulation model of marine stratocumulus. *Mon. Wea. Rev.*, **128**, 229–243.

Milbrandt, J. and M. Yau, 2005: A multimoment bulk microphysics parameterization. Part II: A proposed three-moment closure and scheme description. *J. Atmos. Sci.*, **62**, 3065–3081.

Morrison, H. and W. Grabowski, 2007: Comparison of bulk and bin warm rain microphysics models using a kinematic framework. *J. Atmos. Sci., accepted*.

Seifert, A., 2005: A note on the shape-slope relation of the drop size distribution in convective rain. *J. Appl. Met.*, **44**, 1146–1151.

— 2008: On the parameterization of evaporation of raindrops as simulated by a one-dimensional rainshaft model. *J. Atmos. Sci., accepted*.

Seifert, A. and K. Beheng, 2006: A two-moment cloud microphysics parameterization for mixed-phase clouds. Part I: Model description. *Meteorol. Atmos. Phys.*, **92**, 45–66.

Seifert, A. and K. D. Beheng, 2001: A double-moment parameterization for simulating autoconversion, accretion and selfcollection. *Atmos. Res.*, **59-60**, 265–281.

Testud, J., S. Oury, R. A. Black, P. Amayenc, and X. Dou, 2001: The concept of "normalized" distribution to describe raindrop spectra: A tool for cloud physics and cloud remote sensing. *J. Appl. Met.*, **40**, 1118–1140.

Ulbrich, C. W., 1983: Natural variations in the analytical form of the raindrop size distribution. *J. Clim. Appl. Met.*, **22**, 1764–1775.

Zhang, G., J. Vivekanandan, and E. Brandes, 2003: The shape-slope relation in observed gamma raindrop size distributions: Statistical error or useful information? *J. Atmos. Ocean. Tech.*, **20**, 1106–1119.

Zhang, G., J. Vivekanandan, and E. A. Brandes, 2001: A method for estimating rain rate and drop size distribution from polarimetric radar measurements. *IEEE Trans. Geosci. Remote Sens.*, **39**, 830–841.

EFFECTS OF HOMOGENEOUS VERSUS INHOMOGENEOUS MIXING ON TRADE-WIND CONVECTION AS SIMULATED BY A DOUBLE-MOMENT BULK MICROPHYSICS SCHEME

Joanna Slawinska[1], Wojciech W. Grabowski[2]*, Hanna Pawlowska[1], and Hugh Morrison[2]

[1] Institute of Geophysics, University of Warsaw, Warsaw, Poland
[2] National Center for Atmospheric Research, Boulder, Colorado

1. INTRODUCTION

Recent modeling studies (e.g., Chosson et al. 2004, 2007; Grabowski 2006; Slawinska et al. 2008) demonstrate that assumptions concerning microphysical evolution of natural clouds (the homogeneity of cloud-environment mixing in particular) significantly affect the albedo of a field of shallow convective clouds, such as subtropical stratocumulus and trade-wind cumulus. It follows that modeling of microphysical properties of such clouds has important implications for the clouds-in-climate problem. In this paper, we report selected results concerning the impact of the homogeneity of mixing on microphysical properties of shallow convective clouds using two similar modeling setups, the BOMEX case and the RICO case, both recently used in large-eddy simulation (LES) model intercomparison studies.

2. THE MODEL AND MODELING SETUPS

The Eulerian version of the three-dimensional anelastic model EULAG (EUlerian/semi-LAGrangian; Smolarkiewicz and Margolin 1997, Grabowski and Smolarkiewicz 1996, and Margolin et al. 1999) is used in this work. The recently-developed double-moment warm-rain scheme of Morrison and Grabowski (2007, 2008) is included in the model. The scheme predicts number concentrations and mixing ratios for cloud water and rain. In particular, the number concentration of cloud droplets can evolve inside the cloud due to activation of CCN according to the predicted supersaturation, and also due to entrainment of environmental air. The latter affects the droplet concentration according to the prescribed mixing scenario, which can vary smoothly across the entire range, from the homogeneous mixing to the extremely inhomogeneous mixing (see Morrison and Grabowski 2008, eq. 11 in particular). In general, the current study extends that of Slawinska et al. (2008), where the impact of different mixing scenarios has been investigated in simulations of BOMEX shallow convection using a single-moment warm-rain scheme.

Both the non-precipitating shallow convection case (from the Barbados Oceanographic and Meteorological Experiment, BOMEX; Holland and Rasmusson 1973) as well as the precipitating case of trade-wind convection (from the Rain in Cumulus over the Ocean Experiment, RICO; Rauber et al. 2007) are considered in the current study. In the non-precipitating BOMEX case, the model setup follows the intercomparison study of Siebesma et al. (2003). The computational domain of 6.4 km × 6.4 km × 3.0 km is covered with a uniform grid with the horizontal/vertical gridlengths of 50/20 m. The simulations are run for six hours using a time step of 1 s and the last three hours of simulations are used in the analysis using snapshots of model fields archived every ten minutes. For the precipitating case of trade-wind convection, setup and forcings are similar to the RICO intercomparison case. The computational domain in this case is 6.4 km × 6.4 km × 4.0 km and, as in the BOMEX case, it is covered with a uniform grid with the horizontal/vertical gridlengths of 50/20 m. Simulations are run for 21 hours using a time step of 1 s. In the RICO case, the boundary layer deepens and becomes more turbulent with time. To contrast regimes at the early and late stages of the simulations, analysis is presented here for hours 3 to 6 (the early stage) and 18 to 21 (the late stage). For both BOMEX and RICO cases, simulations were run assuming either the maritime aerosol characteristics (the PRISTINE case from Morrison and Grabowski 2007; 2008) or the continental aerosols (the POLLUTED case). Here, we

---

* *Corresponding author address*: Dr. Wojciech W. Grabowski NCAR, PO Box 3000, Boulder, CO 80307; e-mail: grabow@ncar.ucar.edu.

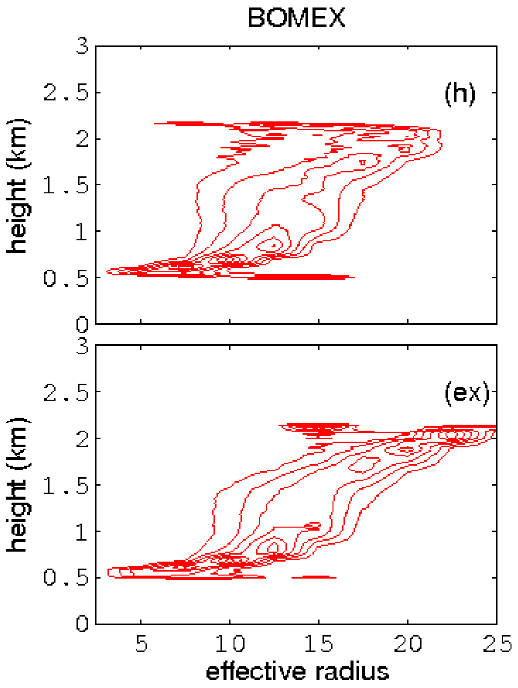

Figure 1: CFADs of the effective radius of cloud droplets for simulated BOMEX clouds assuming homogeneous (upper panel) and extremely inhomogeneous (lower panel) mixing scenarios. Contour interval is 10% and the effective radius bin size is 2.5 μm.

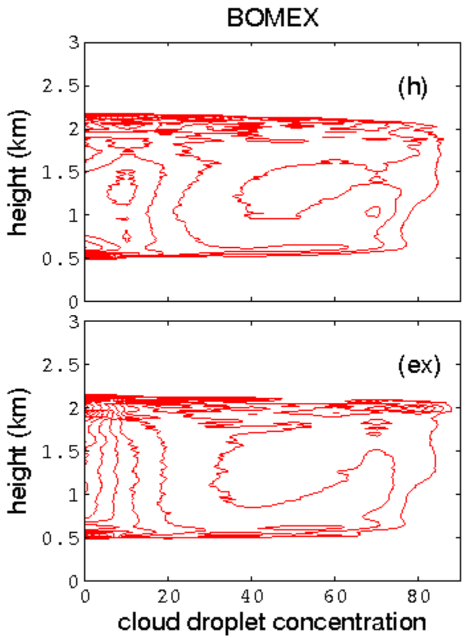

Figure 2: As Fig. 1, but for the droplet concentration. Contour interval is 4% and the concentration bin size is 10 mg−1.

present results only from the PRISTINE case as it is more relevant for the maritime environment of BOMEX and RICO observations, as well as remote sensing observations reported in McFarlane and Grabowski (2007).

In the BOMEX case, the boundary layer is well-developed, with a well-mixed layer below the cloud base (around 0.5 km) and the trade-wind capping inversion around 2 km. Cloud cover is about ten percent. The results from BOMEX simulations are in general agreement with the statistics presented in Siebesma et al. (2003). The RICO case features similar conditions, except for slightly deeper clouds (especially toward the end of the simulation period, see below). In the RICO case, the boundary layer and cloud properties can be affected by the precipitation. Preliminary results of the RICO simulations from 15 models (with various microphysical schemes, including single-moment, double-moment, and bin microphysics) are presented at http://www.knmi.nl/samenw/rico/. Earlier EULAG results obtained with the single-moment scheme are included there as well. Here, we present results applying the double-moment warm-rain scheme of Morrison and Grabowski (2007, 2008). In general, the double-moment scheme improves EULAG's results obtained with the single-moment scheme presented in the intercomparison.

3. EXAMPLE OF RESULTS: THE BOMEX CASE

Figure 1 shows the contoured frequency by altitude diagrams (CFADs) of the effective radius for simulations where the subgrid-scale mixing is always either homogeneous or extremely inhomogeneous (i.e., α in eq. 11 in Morrison and Grabowski 2008 is either 0 or 1, respectively). The results are consistent with those discussed in Slawinska et al. (2008). For instance, the homogeneous mixing case features a wider CFAD and a slightly smaller mean effective radius. An important difference is that the extremely inhomogeneous mixing resulted in a single value of the effective radius in a diagnostic study of Slawinska et al. (cf. Fig. 1 therein), but a relatively wide distribution is predicted here. This is because the adiabatic droplet concentration had to be assumed constant in Slawinska et al., whereas it is predicted by the droplet activation scheme in the current study. This is illustrated in Fig. 2 which shows CFADs of the droplet concentration predicted by the model for the cases

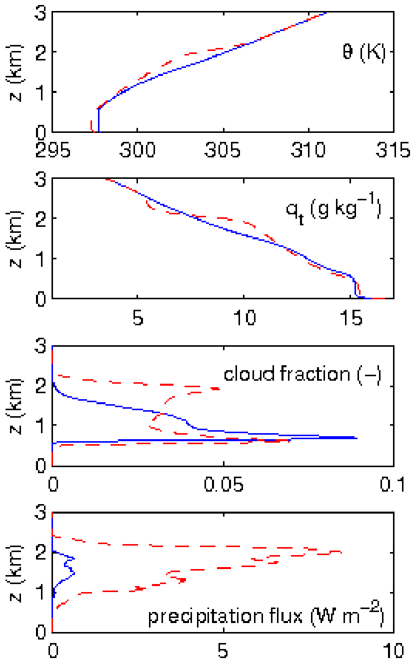

Figure 3: Profiles of the potential temperature, total water, cloud fraction, and precipitation flux for a simulation assuming extremely inhomogeneous mixing for the period of hours 3 to 6 (blue solid line) and hours 18 to 21 (red dashed line).

of the homogeneous and extremely inhomogeneous mixing. In general, the CFADs have similar shape which is because the most important source of cloud droplets is the nucleation at the cloud base, similar in both simulations. In general, CFADs of the droplet concentration are wide, perhaps even bimodal in the middle half of the cloud field. The difference between the two mixing scenarios is most evident at the lowest end of droplet concentrations.

It is unclear what impact the results highlighted above have on the albedo of a cloud field, an aspect emphasized in Chosson et al. (2004, 2007), Grabowski (2006) and Slawinska et al. (2008). Results of the application of the radiation transfer model to the simulated BOMEX clouds will be presented at the conference.

4. EXAMPLE OF RESULTS: THE RICO CASE

To contrast results from the early and late stages of the RICO simulations, Fig. 3 shows profiles of the potential temperature, total water, cloud fraction, and precipitation flux for a simulation assuming extremely inhomogeneous mixing for periods of hours 3 to 6 (the early stage) and 18 to 21 (the late stage). The results for the homogeneous mixing are similar and are not shown. As Fig. 3 illustrates, model profiles evolve significantly during the simulations and this has an important impact on simulated clouds. Since the cloud layer deepens significantly (in response to the upward shift of the initial trade-wind inversion), the amount of precipitation increases as well. The gradual increase of the surface precipitation as the simulation progresses agrees with other model results presented at http://www.knmi.nl/samenw/rico/. The upward shift of the trade-wind inversion is also accompanied by a significant increase of its strength. The stronger inversion results in the maximum of the cloud fraction profile in the upper part of the cloud field, in addition to the typical maximum near the cloud base. This is consistent with previous modeling studies (see discussion in Stevens et al. 2001 and Siebesma et al. 2003). In addition, the boundary layer is more turbulent (i.e., higher TKE) at the late stage and the updraft velocities inside clouds are higher (not shown).

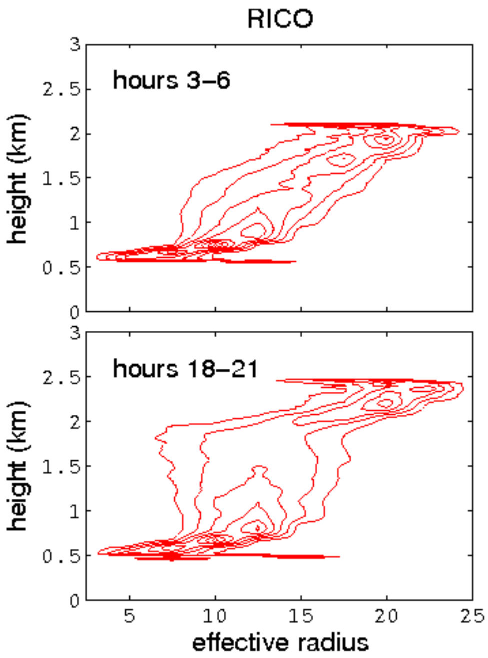

Figure 4: CFADs of the effective radius of cloud droplets for simulated RICO clouds for early (upper panel) and late (lower panel) stage of the simulation assuming extremely inhomogeneous mixing scenario. Contour interval is 10% and the effective radius bin size is 2.5 μm.

These significant changes in the macroscopic cloud features are also reflected in the changes of microphysical characteristics. Figure 4 shows CFADs of the effective radius for the early and late stages of the simulation assuming extremely inhomogeneous mixing (i.e., as in Fig. 3). At the early stage, the CFAD is similar to the BOMEX case (cf. Fig. 1). At the late stage, however, the CFAD is significantly wider, especially in the middle part of the cloud field, and the mean effective radius increases with height much slower than in the early stage. Specific reasons for these differences (e.g., modified entrainment versus precipitation flux) are currently under investigation. As in the BOMEX case, results of the application of the radiation transfer model to the simulated clouds will be presented at the conference.

BIBLIOGRAPHY

Chosson, F., J.-L. Brenguier, and M. Schröder, 2004: Radiative impact of mixing processes in boundary layer clouds. *Proceedings of the International Conference on Clouds and Precipitation*, Bologna, Italy, 371-374.

Chosson, F., J.-L. Brenguier, and L. Schüller, 2007: Entrainment-mixing and radiative transfer simulation in boundary-layer clouds. *J. Atmos. Sci.*, **54**, 2670-2682.

Grabowski, W. W., 2006: Indirect impact of atmospheric aerosols in idealized simulations of convective-radiative quasi-equilibrium. *J. Climate.*, **19**, 4664-4682.

Grabowski, W. W. and P. K. Smolarkiewicz, 1996: On two-time-level semi-Lagrangian modeling of precipitating clouds. *Mon. Wea. Rev.* **124**, 487-497.

Holland J. Z., and E. M. Rasmusson, 1973: Measurements of the atmospheric mass, energy, and momentum budgets over a 500-kilometer square of tropical ocean. *Mon. Wea. Rev.* **101**, 44-55.

Margolin, L. G., P. K. Smolarkiewicz, and Z. Sorbjan, 1999: Large-eddy simulations of convective boundary layers using nonoscillatory differencing. *Physica D*, **133**, 390-397.

McFarlane, S.A., and W. W. Grabowski, 2007: Optical properties of shallow tropical cumuli derived from ARM ground-based remote sensing. *Geophys. Res. Lett.*, **34**, L06808.

Morrison, H., and W. W. Grabowski, 2007: Comparison of bulk and bin warm rain microphysics models using a kinematic framework. *J. Atmos. Sci.*, **64**, 2839-2861.

Morrison, H., and W. W. Grabowski, 2008: Modeling supersaturation and subgrid-scale mixing with two-moment bulk warm microphysics. *J. Atmos. Sci.*, **65**, 792-812.

Rauber, R. M., and Coauthors, 2007: Rain in Shallow Cumulus Over the Ocean: The RICO Campaign. *Bull. Amer. Meteor. Soc.*, **88**, 1912-1928.

Siebesma, A.P., and Coauthors, 2003: A large eddy simulation intercomparison study of shallow cumulus convection. *J. Atmos. Sci.*, **60**, 1201-1219.

Slawinska, J., W.W. Grabowski, H. Pawlowska, and A. A. Wyszogrodzki, 2008: Optical properties of shallow convective clouds diagnosed from a bulk-microphysics large-eddy simulation. *J. Climate*, **21**, 1639-1647.

Smolarkiewicz, P. K., and L. G. Margolin, 1997: On forward-in-time differencing for fluids: An Eulerian/semi-Lagrangian nonhydrostatic model for stratified flows. *Atmos.-Ocean Special*, **35**, 127-152.

Stevens, B., and Coauthors, 2001: Simulations of trade wind cumuli under a strong inversion. *J. Atmos. Sci.*, **58**, 1870-1891.

Acknowledgments.
This work was partially supported by the NOAA Grant NA05OAR4310107. The National Center for Atmospheric Research is operated by the University Corporation for Atmospheric Research under sponsorship of the National Science Foundation. JS acknowledges the financial support for participation in the ICCP-2008 offered by the organizers.

OSCILLATION BEHAVIORS OF FREELY FALLING RAINDROPS

Miklós Szakáll[1], Karoline Diehl[1], Subir K. Mitra[1] and Stephan Borrmann[1,2]
[1]Institute for Atmospheric Physics, Johannes Gutenberg University Mainz, Germany
[2]Institute of Particle Chemistry, Max-Planck Institute for Chemistry, Mainz, Germany

1. INTRODUCTION

As the raindrop shape is a key parameter in, e.g., the remote measurement of rain fall rates and nowcasting of precipitation using dual-polarization radars, the accurate knowledge of the oscillation behaviour of the raindrops is of great importance. In particular, it needs to be clarified whether the dynamic average shape (affected by oscillation) is the same as the one in static equilibrium while the latter is assumed in calculations of the rain fall rate from radar data.

Here we present the results of our experiments on raindrop oscillations of freely suspended drops with equivalent diameters of 1 to 7 mm floating inside the Mainz vertical wind tunnel at their terminal velocities. For this purpose a high speed digital video camera was used, which allows the continuous recording of the oscillation of individual raindrops for relatively long time intervals. The comparison of the measured equilibrium raindrop shape with the theoretical model of Beard and Chuang (1987) is presented. We show how the oscillation frequency and the time averaged axis ratio of raindrops depend on the drop size. This latter one is especially of high importance, as it is still an open question whether the dynamic and the static equilibrium axis ratios of raindrops with diameters ranging from 1 to 3 mm differ. Although a few publications dealt with this question (e.g. Andsager et al. 1999), there exists no reliable experimental verification until now on the consideration of Goddard and Cherry (1984) who predicted an enhancement in the axis ratio within this size range.

2. EXPERIMENTAL SETUP

The measurements were carried out in the vertical wind tunnel at the University of Mainz where water drops and other hydrometeors can be freely floated at their terminal velocities in a vertical air stream. Wind speeds up to 40 m/s are possible so that drops of all sizes between 40 µm and 8 mm can be investigated. In the measurements presented here freely suspended raindrops within the size range of 1 to 7.5 mm were floated at their terminal velocities in the wind tunnel. The drop oscillation was continuously recorded using a high-speed digital video camera (Motion-ProX, Redlake Inc.) with a recording speed of up to 2000 frames per second. The spatial resolution of the optical system was 24 µm which together with the millisecond time resolution allows the investigation of the raindrop oscillation with very high accuracy.

3. RESULTS AND DISCUSSION

3.1 Equilibrium drop shape

First the equilibrium shapes of drops of different sizes were measured and compared to those derived from the force balance model of Beard and Chuang (1987). We considered a drop to be in the “dynamic equilibrium” state if its actual axis ratio was equal to the average axis ratio. This average was determined from the temporal variation of the axis ratio as its mathematical mean. Figure 1 shows the measured dynamic equilibrium drop shapes together with the calculated shapes for drops of 0.6, 2.6, 5 and 7 mm equivalent diameters. It is apparent from the figure that the force balance model of Beard and Chuang (1987) correctly describes the equilibrium drop shape variation with size.

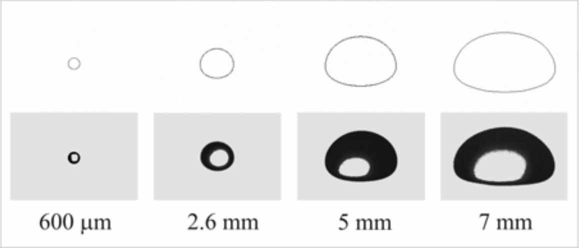

Fig. 1. Calculated drop shapes and real images of drops with different sizes floated in the Mainz vertical wind tunnel

3.2 Oscillation frequencies and modes

The oscillation frequencies of the drops were determined from the temporal variation of the axis ratio. To achieve high accuracy, the frequency of the fundamental oscillation mode (n=2, m=0) was derived from the total time of several (typically 10) oscillation periods. In the cases, where a drop floated in the field of view of the camera for a sufficiently long time (typically for 1-2 seconds), it was possible to observe the beating of two oscillation modes in the temporal variation of the axis ratio, allowing to determine the frequencies of the higher mode oscillations.

Generally the formula from Rayleigh (1879) is used to calculate the fundamental oscillation frequency of a water drop falling at its terminal velocity. However, this formula is derived by postulating that the drops have a spherical form. As raindrops larger than 1 mm in diameter are no longer spheres (see Figure 1), the formula of Rayleigh cannot be valid for raindrops in the real atmosphere. Indeed, the deformed drop shape leads to a frequency shift as shown by the asymptotic analysis of Feng and Beard (1991). The oscillation frequencies corresponding to the (n=2; m=0, 1 and 2) modes for different drop sizes derived following the calculations of Feng and Beard (1991) are plotted on Figure 2 with thick, thin, and dashed lines, respectively. The frequencies of the fundamental mode determined from our frequency analysis on the floating drops are plotted by blue rectangles on Figure 2. It is apparent from Figure 2 that our measurements validate the theoretical considerations of Feng and Beard (1991). Thus, it is reasonable to determine hereinafter the drop size from the frequency of the fundamental mode, as it is more precise and reliable (<1% error) as that from the equivalent drop volume (~2.4% error), especially in the case when the drop floated in the tunnel for several minutes. In these cases the size of the drops is reduced by evaporation. For easier computation the Rayleigh frequency formula was used as the difference between the Feng and Beard (1991) and the Rayleigh frequency for the fundamental mode is negligible.

The empirical formula from the experiments of Nelson and Gokhale (1972) is also frequently used to calculate the oscillation frequency; see the green curve in Figure 2. This curve shows slightly higher oscillation frequencies compared to those from the models and from our measurements, however, this overestimation is not significant. The reason may lie in a systematic error in the determination of the drop size by Nelson and Gokhale (1972) which is not well-described in their article.

Nine raindrops with diameters between 4.2 and 7 mm that floated stable in the field of view of the camera for a sufficiently long time to investigate higher mode oscillations.

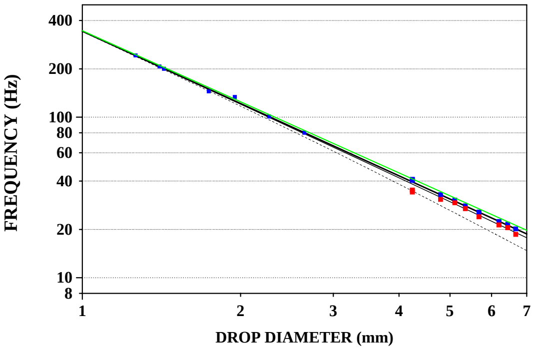

Fig. 2. The size dependence of the oscillation frequencies of different modes. Blue symbols: present result for the fundamental mode oscillation; red symbols: present results for higher mode oscillations. The theoretical curves for the n=2; m=0, 1 and 2 modes of Feng and Beard (1991) are plotted by thick, thin, and dashed lines, respectively. The empirical curve of Nelson and Gokhale (1972) is plotted by green line.

Because each oscillation mode has a different characteristic frequency corresponding to the given drop size (see Feng and Beard, 1991), it is possible to determine which oscillation modes are active by analyzing the beating frequency. The higher mode frequencies determined in this way for the nine raindrops are plotted with red symbols in Figure 2.

We found in our experiments that during the raindrop oscillation the (2,0) mode always exists (see the open symbols in Figure 2). The measured data points for drops with sizes between 4.5 and 7 mm corresponding to the higher mode frequencies calculated from the beating in the axis ratio variation lie on the curve corresponding to the (2,1) mode, indicating that the measured raindrops oscillated in this mode beside the fundamental mode. We experienced, however, the existence of the (2,2) mode and the non-existence of the (2,1) mode for drops with a diameter of 4.24 mm. Unfortunately, the difference in the frequency of the different modes decreases for small drop sizes, therefore, we could not observe the existence of higher modes for small drops. However, we can conclude from our experiments that the drops with various sizes oscillate in different modes which may depend on the drop size.

3.3 Axis ratio of the raindrops

The mean axis ratio was determined for each measured raindrop as the time-average of the varying axis ratio. The mean axis ratios as a function of the equivalent drop diameter calculated from the (2,0) mode oscillation frequency of the drop using the Rayleigh formula are plotted in Figure 3. The theoretical curve for the axis ratio calculated using the formula of Chuang and Beard (1990) is also shown in Figure 3 with a solid line, while the upper and lower bounds of the model is indicated by dashed lines.

As can be seen from Figure 3, the measured time-average axis ratios fit well to the theoretical curve which verifies the method of the equivalent diameter determination from the oscillation frequency.

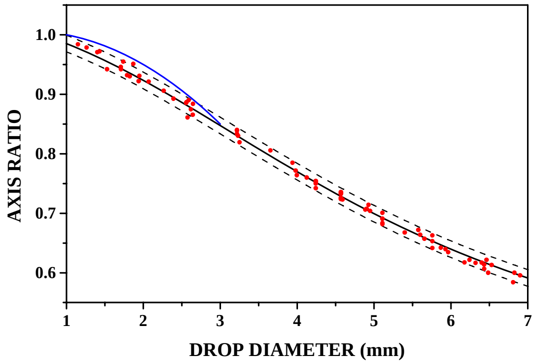

Fig. 3. Time average axis ratio of raindrops falling at their terminal velocities measured in the Mainz vertical wind tunnel (red symbols) The equilibrium axis ratio from the model of Beard and Chuang (1987) is plotted by solid, the upper and lower limit of the model with dashed line. The radar-disdrometer derived axis ratios postulated by Goddard and Cherry (1984) are plotted by blue line.

Furthermore, this agreement verifies the force balance model of Beard and Chuang (1987) which derives the shape distortion from the balance of the internal hydrostatic and the external aerodynamic pressure and the surface tension force. It can be concluded from Figure 3, that the static and dynamic equilibrium drop shape is equal within the observed size range. Our findings contradict the predictions of Goddard and Cherry (1984). They estimated the raindrop size from the radar echo signal and corresponding disdrometer-obtained drop size distributions, and obtained higher axis ratio values in the size range between 1 and 3 mm (blue curve in Figure 3) than those from the force balance model of Beard and Chuang (1987).

During oscillation the drop has different shapes, i.e. different axis ratios, which has to be considered in the backscatter ratios for the radar signal evaluations. If the drop floated in the field of view of the camera for such a long time to record several periods of beating, a reliable histogram of the axis ratio variation could be made. Figure 4 shows the distribution of the axis ratio variation for a 4.24 mm diameter drop. The distribution of the axis ratio is uniform, which is the consequence of the coexistence of different oscillation modes.

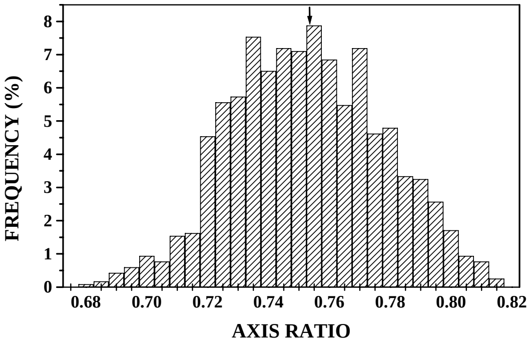

Fig. 4. Measured distribution of the axis ratio variation for a 4.24 mm diameter drop. The time average axis ratio value is signed by an arrow.

The basic problem with the experiments in the past regarding the drop oscillation was that the time evolution of the drop shape under oscillation was not recorded as a continuous time series. From our experiments, however, it was possible to determine the typical oscillation amplitude of the axis ratio, which is very important in the uncertainty analysis of the precipitation nowcasting from radar signals. To the best of our knowledge, there exists no theoretical prediction on the amplitude variation of the axis ratio of drops, therefore, we can present only our speculations. The oscillation is induced by the vortexes shedding from the rear of the drop, and the energy of the vortex shedding increases with the drop size.

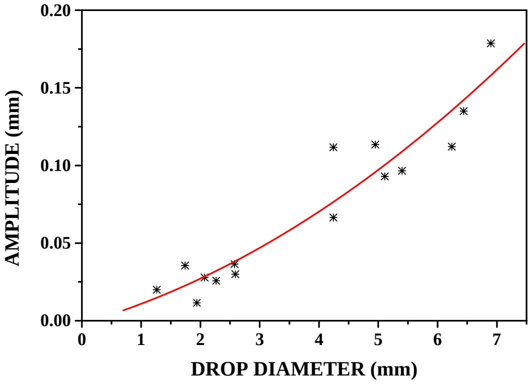

Fig. 5. The amplitude of the axis ratio for oscillating raindrops with diameter between 1 and 7 mm.

The oscillation amplitude is proportional to the energy which induces the oscillation, thus, the larger the drop, the larger is the amplitude of the oscillation. Our measurements verify this consideration, as can be seen on Figure 2, where the amplitude of the axis ratio is plotted as the function of the equivalent drop diameter. Moreover, we found that the best fit to the amplitude vs. drop diameter curve is a second order polynomial fit.

4. BIBLIOGRAPHY

Andsager, K., K. V. Beard, and N. F. Laird, 1999: Laboratory measurements of axis ratios for large raindrops. *J. Atmos. Sci*., **56**, 2673-2683.

Beard, K. V., and C. Chuang, 1987: A new model for the equilibrium shape of raindrops. *J. Atmos. Sci.*, **56** (11), 1509-1524.

Chuang, C. H., and K. V. Beard, 1990: A numerical model for the equilibrium shape of raindrops. *J. Atmos. Sci.*, **47**, 1374-1389.

Feng, J. Q., and K. V. Beard, 1991: A perturbation model of raindrop oscillation characteristics with aerodynamic effects. *J. Atmos. Sci.*, **48**, 1856-1868.

Goddard, J. W. F., and S. M. Cherry, 1984: The ability of dual-polarization radar (copular linear) to predict rainfall rate and microwave attenuation. *Radio Science*, **19** (1), 201-208.

Nelson, A. R. and N. R. Gokhale, 1972: Oscillation frequencies of freely suspended water drops. *J. Geophys. Res.*, **77**, 2724-2727.

Rayleigh, J. W. S., 1879: On the capillary phenomena of jets. *Proc. R. Soc. London*, **19**, 71-97.

ACKNOWLEDGEMENT

These studies were financed by the Deutsche Forschungsgemeinschaft (DFG) under project BO 1829/1-1/2 within the AQUARadar program and also supported by the Max-Planck Institute for Chemistry.

RECENT ADVANCES IN MODELING HYDRODYNAMIC INTERACTION AND COLLISION EFFICIENCY OF CLOUD DROPLETS

Lian-Ping Wang,[1]* Bogdan Rosa,[1] Hui Gao,[1] and Wojciech W. Grabowski[2]
[1]*Department of Mechanical Engineering, University of Delaware, Newark, Delaware 19716, U.S.A.*
[2]*Mesoscale and Microscale Meteorology Division, National Center for*
Atmospheric Research, PO Box 3000, Boulder, Colorado 80307-3000, USA

1. INTRODUCTION

In recent years an increasing number of studies have been initiated to quantify the effects of air turbulence on the collision-coalescence of cloud droplets, as it is believed that the in-cloud turbulence can enhance the rate of collision-coalescence and as such provides a mechanism to overcome the bottleneck between the diffusional growth and the gravitational collision-coalescence mechanism [31]. Much recent attention has therefore directed to the enhanced collision-coalescence rate by air turbulence for cloud droplets in the size range from 10 to 50 *μm* in radii [9, 10, 21, 22, 30]. Recently, Xue *et al.* [34] demonstrated that a moderate enhancement (*i.e.*, by a factor of two or less) of the collision kernel by air turbulence can significantly accelerate the growth of cloud droplets to form drizzle drops.

Air turbulence can enhance the collision-coalescence rate in two general ways. First, for the simplified problem of geometric collision neglecting aerodynamic interaction of cloud droplets, air turbulence can increase the collision rate by three possible mechanisms: (1) enhanced relative motion due to differential acceleration and shear effects; (2) enhanced average pair density due to local preferential concentration of droplets; and (3) enhancement due to selective alterations of the settling rate by turbulence. The level of enhancement on the geometric collision depends on two sets of key physical parameters of colliding droplets, amongst other things. The first is the Stokes number defined as the ratio of the droplet inertial response time τ_p to the Kolmogorov time τ_k of air turbulence. The second is the nondimensional settling velocity defined as the ratio of the still-fluid droplet terminal velocity v_T to the Kolmogorov velocity v_k of air turbulence. For cloud droplets, the Stokes number is on the order of 0.1 and the the nondimensional settling velocity is on the order of 1.0. This particular parameter combination implies that the relative motion between cloud droplets tends to be governed by the gravitational settling, and the enhancement on geometric collision is likely to be moderate, as shown in the recent studies by Ayala *et al.* [3], Franklin *et al.* [10], Pinsky and Khain [21], Wang *et al.* [30]. Data on the enhancement of geometric collision kernel by air turbulence have been compiled in Ayala *et al.* [3]. An analytical parameterization of turbulent geometric collision kernel for cloud droplets has also been developed in Ayala *et al.* [4].

2. COLLISION EFFICIENCY

The second way for air turbulence to impact collision-coalescence is through its effect on local droplet-droplet aerodynamic interaction and collision efficiency. Cloud droplets are typically much smaller than the Kolmogorov eddies of air turbulence. Compared to the gravitational-aerodynamic interaction problem, air turbulence affects the collision efficiency through two possible mechanisms: (1) the far-field relative motion and orientation of droplets exhibit statistical fluctuations in a turbulent background flow [19], and (2) the local fluid shear and acceleration in turbulence can alter the aerodynamic interaction forces on droplets [8]. Furthermore, for droplets of radii less than 60 *μm*, the collision efficiency is a sensitive function of droplet sizes even for the case of no air turbulence, namely, the collision efficiency can vary by three orders of magnitude [17, 23], due to the relative small inertial response time and settling rate of these droplets. It follows that air turbulence could play a stronger role in enhancing the collision efficiency than in enhancing the geometric collision rate [22, 30].

Compared to the geometric collision, however, collision efficiency is a much more difficult problem as the disturbance flows introduce another set of length and time scales in addition to the background air turbulence. While there are quite a few studies in the literature concerning the collision efficiency of cloud droplets without air turbulence, there are very few studies devoted to the collision efficiency in a turbulent flow [1, 11, 14, 19, 22, 30]. As pointed out in Wang *et al.* [30], these previous studies predicted different levels of enhancement on collision efficiency. This in part results from different kinematic formulations used to define the collision efficiency in different studies, some of which are not applicable to turbulent collisions. More importantly, there is currently a lack of accurate and consistent representations of aerodynamic interaction of many droplets in a turbulent flow.

3. A HYBRID DNS

As a first step in developing a better computational method for treating aerodynamic interaction of cloud droplets in a turbulent flow, Wang *et al.* [29] introduced an improved superposition method (ISM) to study the collision efficiency of cloud droplets in still air. The basic idea is to impose, in some average sense, the no-slip boundary condition on the surface of each droplet to better determine the magnitude and coupling of the Stokes disturbance flows in a many-droplet system. The no-slip boundary condition is specified either at the center of each droplet (the center-point formulation) or by an integral average over the droplet surface (the integral formu-

---

*Corresponding author: Department of Mechanical Engineering, 126 Spencer Laboratory, University of Delaware, Newark, Delaware 19716-3140. Phone: (302) 831-8160; Fax: (302) 831-3619; Electronic mail: LWANG@ME.UDEL.EDU

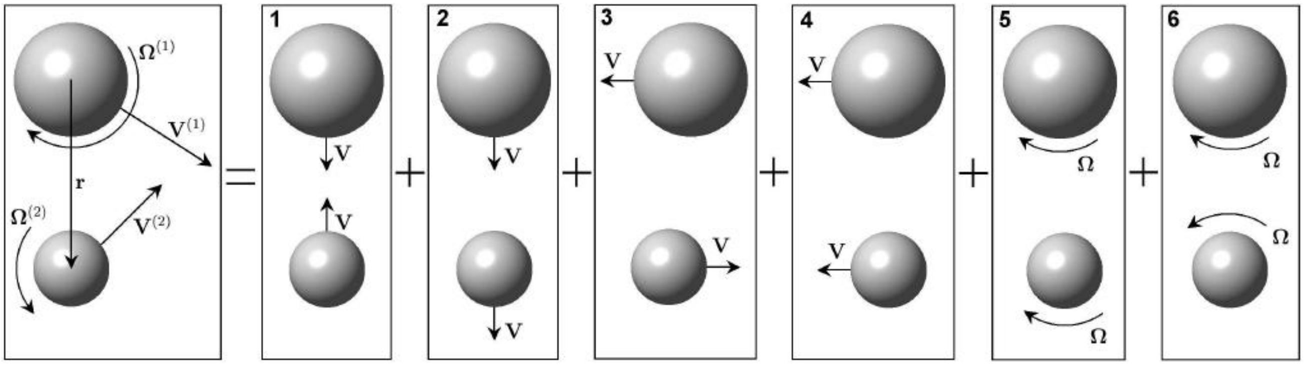

FIG. 1: Treating arbitrary short-range interaction by a combination of six elemental interactions.

lation). The advantage of ISM is that the application to many-droplet interactions in a turbulent airflow is rather straightforward leading to a hybrid direct numerical simulation (HDNS) approach [2, 30]. The HDNS approach combines direct numerical simulation of the background air turbulence with an analytical representation of the disturbance flow introduced by many droplets. The approach takes advantage of the fact that the disturbance flow due to droplets is localized in space and there is a sufficient length-scale separation between the droplet size and the Kolmogorov scale of the background turbulent flow. This hybrid approach provides, for the first time, a quantitative tool for studying the combined effects of air turbulence and aerodynamic interactions on the motion and collisional interactions of cloud droplets. The disturbance flow is coupled with the background air turbulence through the approximate implementation of the no-slip boundary conditions on each droplet. Dynamical features in three dimensions and on spatial scales ranging from a few tens of centimeters down to 10 μm are captured. Both the near-field and the far-field droplet-droplet aerodynamic interactions could be incorporated [32].

Results of turbulent collision efficiency from HDNS have been reported in Wang *et al.* [30, 33]. It was shown that the level of increase in the collision efficiency for cross-size collisions depends primarily on the flow dissipation rate and the size ratio a_2/a_1. For instance, the collision efficiency between droplets of 18 μm and 20 μm in radii is increased, relative to the gravitational collision efficiency in stagnant air, by a factor of 4 and 1.6 by air turbulence at dissipation rates of 400 cm^2/s^3 and 100 cm^2/s^3, respectively. For most cross-size collisions, aerodynamic interactions reduce the average radial relative velocity but also increase the radial distribution function. The collision efficiency for self-collisions in a bidisperse turbulent suspension can be larger than one. Such an increase in self-collisions is related to the far-field many-body aerodynamic interaction and may depend on the volumetric concentration of droplets of all sizes in the system.

HDNS provides a general framework for a systematic improvement of the approach. In this regard, the HDNS approach is closely related to the multipole expansion method of Durlofsky *et al.* [8], also in general known as the *Stokesian dynamics* approach [5]. In fact, the center-point formulation of ISM is essentially the zero-moment expansion with only monopole terms and without Faxen correction, while the integral formulation of ISM is the zero-moment expansion with the Faxen correction since the integral average of disturbance flow velocity over a droplet surface is equivalent to the center-point velocity plus the Faxen term. Durlofsky *et al.* [8] presented a multipole formulation known as the Force-Torque-Stresslet (FTS) formulation which includes moments up to the first-order plus Faxen terms. This multipole expansion method considers many-body interaction with Stokes disturbance flows superimposed onto a nonuniform background flow.

4. SHORT-RANGE INTERACTION

Both Durlofsky *et al.* [8] and Wang *et al.* [29] recognized that ISM and FTS cannot handle correctly short-range or lubrication forces. The short-range interaction forces, in principle, would require all higher-order moments to be included in the multipole expansion [15]; and the convergence to the exact lubrication forces is usually slow in the multipole expansion approach [15, 16]. To accurately treat the lubrication force, Durlofsky *et al.* [8] made use of the exact force representation of the two-sphere problem and at the same time, properly remove the redundant part from the multipole many-body representation. This procedure could be rather complicated for the many-droplet problem.

As a logical next step, we have recently developed an efficient approach for treating the hydrodynamic interaction of two spherical particles settling under gravity. Droplets are assumed to be small such that the fluid inertia in the disturbance flows may be neglected. An effort is made to ensure accuracy of the method for any inter-particle separation by considering three separation ranges. The first is the long-range interaction where a multipole method is applied. After a decomposition into six simple subproblems (Fig. 1), explicit formulae for drag force and torque are derived from the FTS formulation of Durlofsky *et al.* [8]. The FTS formulation is found to be accurate when the separation distance normalized by the average radius is larger than 5 for all cases. The second range concerns the short-range interaction where the interaction force could be very large. The leading-order lubrication expansions of Jeffrey and Onishi [16] are employed for this range and are found to be accurate when the normalized separation is

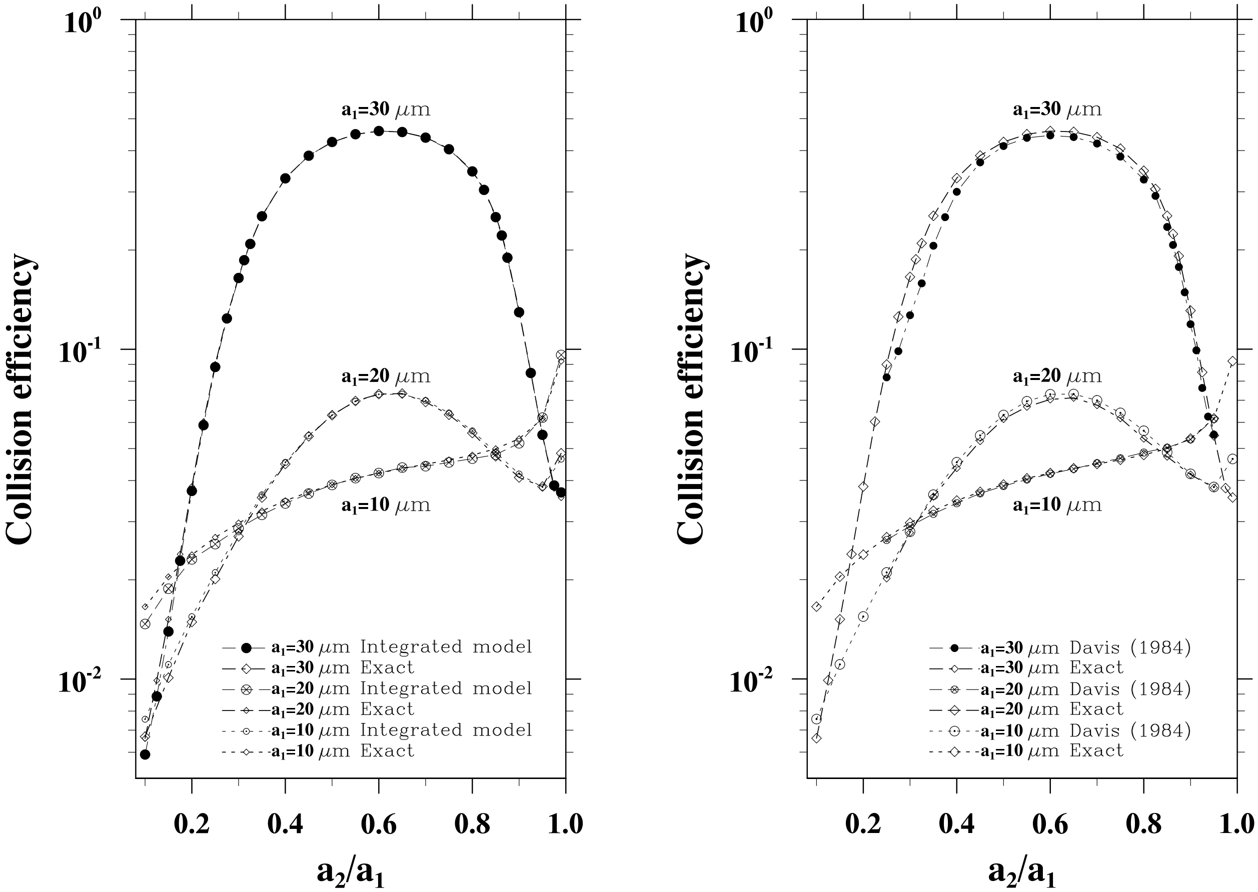

FIG. 2: Collision efficiency of droplets with the van der Waals force included. Hamaker constant is set to 5×10^{-14} erg. Left panel: Comparison of collision efficiency calculated using our integrated model with that based on the exact force/torque representation of Jeffrey and Onishi [16]. Right panel: Comparison of collision efficiency calculated using exact force/torque representation of Jeffrey and Onishi [16] and the results of Davis [7].

less than about 0.01 for all cases. Finally, for the intermediate range where no simple method is available, a third-order polynomial fitting is proposed to bridge the long-range and short-range interactions. After optimizing the exact form of polynomial fitting and the boundary locations for the three separation ranges, the force representation is found to be highly accurate when compared with the exact solution for Stokes flows. Using this efficient method, collision efficiencies for the case of gravitational interaction have been calculated. It is shown that the results of collision efficiency are in excellent agreement with previous results based on more complex treatment of the interaction force (Fig. 2). It is hoped that this method can be applied to treat hydrodynamic interactions of many particles in either stagnant or turbulent background flow.

5. TOWARDS FULLY-RESOLVED DNS

One limitation of the treatment above is the assumption of Stokes disturbance flows, which is known to become inaccurate for droplets larger than 30 *μm* in radii [17]. On the one hand, currently, no known method can treat, in an efficient manner, the problem of many-droplet interactions beyond Stokes disturbance flows. The work of Klett and Davis [17] represents the first study in which the leading-order fluid-inertia (or finite droplet Reynolds number) effect in the disturbance flows is considered for two-droplet interaction, by using Oseen flow equations. Several attempts [18, 20, 25–27] were made to handle two-droplet aerodynamic interaction at finite Reynolds numbers using a simple superposition method in which the disturbance flow due to each droplet is computed numerically by solving nonlinear Navier-Stokes equations, without any influence by the disturbance flow due to the other droplet. Unfortunately, such a simple superposition method has been widely criticized as it can result in unphysical collision efficiency [25], and it is known to be very inaccurate even for Stokes disturbance flows [29]. It is not surprising that no attempt has been made to adopt this simple superposition method to many-droplet interactions.

Recently, we started to develop size-resolved flow simulation tool [12], using the computational approach (*i.e.*, Physalis) developed by Prosperetti and co-workers [35, 36]. The ultimate goal of this work is to address collision-efficiency at finite droplet Reynolds number. The basic idea of Physalis is to recognize that, because of the no-slip boundary conditions on its surface, a droplet induces a specific local flow structure that could be used to linearize the Navier-

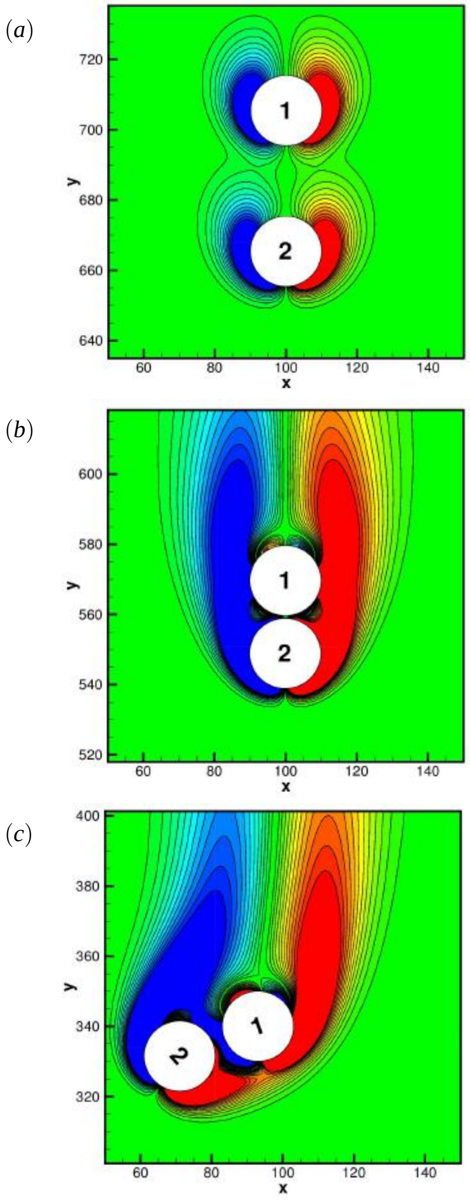

FIG. 3: A two-dimensional size-resolved simulation of particle-particle aerodynamic interaction in a confined channel of width equal to 20 particle radius, demonstrating the sequence of (a) drafting, (b) kissing, and (c) tumbling. The Reynolds number based on maximum particle sedimentation velocity was around 35. The color contours show the flow vorticity distribution. The numbers inside the particles indicate their relative location and rotation.

Stokes equations in the neighborhood of the droplet surface. The fluid velocity, pressure, and vorticity near the droplet surface can be expressed analytically using series solutions of Stokes flow equations. As a result, the geometric surface of the droplet can be replaced by a Stokes flow solution valid in a narrow but finite region near the surface, known as the cage region.

There are three main components in the hybrid method. The first component is an analytical representation of the flow within the cage region. This is obtained by the method of separation of variables applied to Stokes flow equations. The general form in 2D is given in Zhang and Prosperetti [35] and in 3D is found in [12, 36].

The second component is the numerical method for Navier-Stokes equations on a regular mesh (the flow solver). The second-order project method Brown *et al.* [6] is used. The intermediate velocity in the fractional step procedure is solved by a factorization method Kim & Moin [13], while the Poisson equation for the projection step is solved by a combination of transformation and tridiagonal inversion. This mesh extends to the interier of the particle surface. The velocity cage essentially defines an internal boundary for the viscous flow where the Stokes solution is employed to specify the boundary conditions there.

The most essential component is the coupling between the numerical solution on the regular mesh and the Stokes solution in the cage. This coupling is achieved by an iterative procedure in which (a) the numerical solution is used to refine the coefficients in the Stokes flow representation and in turn (b) the numerical solution is refined by an updated boundary conditions at the velocity cage from the refined Stokes flow. The first part is accomplished by a Singular Value Decomposition algorithm since an overspecified linear system (the number of cage nodes used for coupling is larger than the number of coefficients) is to be solved. The second part currently relies only on the specific method of defining the cage velocity nodes or the internal boundary, so the analytical nature of the Stokes solution may not be fully taken advantage of. There are more than one way to specify the cage region Takagi *et al.* [28]. For accuracy of the Stokes flow representation, it is desirable to select the cage nodes as close to the surface of the particle as possible. We are currently investigating a better strategy to locate the cage nodes used for the coupling, in order to improve the convergence behavior and the overall accuracy of the method.

An important advantage of this hybrid method is that the force and torque acting on the particle can be calculated directly from the Stokes solution, avoiding integration from the numerical solution.

Fig. 3 shows a two-dimensional simulation of particle-particle aerodynamic interaction. The well-known scenario of *drafting, kissing, and tumbling* has been reproduced. A three-dimensional simulation of particle-particle aerodynamic interaction is currently under development.

6. SUMMARY

Very little is known about droplet-droplet aerodynamic interaction in a turbulent flow or the turbulent collision efficiency. The hybrid direct numerical simulation approach [2] provides a first step to integrate the coupling of background air turbulence and local disturbance flow due to droplets. Efforts are being made to improve the representation of short-range interactions. For still background air flow, the accuracy of an integrated modeling approach has been demonstrated. The application of this integrated approach to turbulent background flow is our next step. In addition, a droplet size-resolved direct simulation approach is also being developed, but much work is needed before this approach can be applied to address the collision efficiency of large cloud droplets.

Acknowledgments

This study has been supported by the National Science Foundation through grants ATM-0114100 and ATM-0527140, and by the National Center for Atmospheric Research (NCAR).

[1] Almeida, F.C. de, 1979: The collisional problem of cloud droplets moving in a turbulent environment - Part II: turbulent collision efficiencies. *J. Atmos. Sci.*, **36**, 1564-1576.

[2] Ayala, O., Grabowski, W.W. and L.-P. Wang, 2007: A hybrid approach for simulating turbulent collisions of hydrodynamically-interacting particles. *J. Comp. Phys.* **225**, 51-73.

[3] Ayala, O., B. Rosa, L.-P. Wang, and W. W. Grabowski, 2008a, Effects of Turbulence on the Geometric Collision Rate of Sedimenting Droplets: Part 1. Results from direct numerical simulation, *New J. Physics*, in press.

[4] Ayala, A., B. Rosa, and L.-P. Wang, 2008b Effects of Turbulence on the Geometric Collision Rate of Sedimenting Droplets: Part 2. Theory and parameterization, *New J. Physics* (Focus Issue on Cloud Physics), in review.

[5] Brady J.F., G. Bossis, 1988: Stokesian Dynamics. *Annu Rev. Fluid Mech.*, **20**, 111-157.

[6] D.L. Brown, R. Cortez, and M.L. Minion, Accurate projection methods for the incompressible Navier-Stokes equations. J. Comp. Phys. 168: 464-499 (2001).

[7] Davis, R.H., 1984: The rate of coagulation of a dilute polydisperse system of sedimenting spheres. *J. Fluid. Mech.*, **145**, 179-199.

[8] Durlofsky, L., Brady, J.F. and G. Bossis, 1987: Dynamic simulation of hydrodynamically interacting particles. *J. Fluid Mech.*, **180**, 21-49.

[9] Franklin, C.N., P.A. Vaillancourt, M.K. Yau, P. Bartello, 2005: Collision rates of cloud droplets in turbulent flow. *J. Atmos. Sci.*, **62**, 2451-2466.

[10] Franklin, C.N., Vaillancourt P.A., M.K. Yau, 2007: Statistics and parameterizations of the effect of turbulence on the geometric collision kernel of cloud droplets. *J. Atmos. Sci.*, **64**, 938-954.

[11] Grover, S.N. and H.R. Pruppacher, 1985: The effect of vertical turbulent fluctuations in the atmosphere on the collection of aerosol-particles by cloud drops. *J. Atmos. Sci.*, **42**, 2305-2318.

[12] H. Gao and L.-P. Wang, Paper 713, CDROM Proceedings of the 6th International Conference on Multiphase Flow, Leipzig, Germany, July 9–17, 2007.

[13] Kim, J. and P. Moin 1985, Application of a fractional-step method to incompressible Navier-Stokes equations. J. Comp. Phys. 59: 308-323.

[14] Koziol, A.S. and H.G. Leighton, 1996: The effect of turbulence on the collision rates of small cloud drops. *J. Atmos. Sci.*, **53**(13), 1910-1920.

[15] Ichiki, K., 2002: Improvement of the Stokesian Dynamics method for systems with a finite number of particles. *J. Fluid. Mech.*, **452**, 231-262.

[16] Jeffrey, D.J. and Y. Onishi, 1984: Calculation of the resistance and mobility functions for two unequal rigid spheres in low-Reynolds-number flow. *J. Fluid. Mech.*, **139**, 261-290.

[17] Klett, J.D. and M.H. Davis, 1973: Theoretical collision efficiencies of cloud droplets at small Reynolds numbers. *J. Atmos. Sci.*, **30**, 107-117.

[18] Lin, C. and S. Lee, 1975: Collision efficiency of water drops in the atmosphere. *J. Atmos. Sci.*, **32**, 1412-1418.

[19] Pinsky, M., Khain, A. and M. Sharpio, 1999: Collision of small drops in a turbulent flow. Part I: Collision efficiency. Problem formulation and preliminary results. *J. Atmos. Sci.*, **56**, 2585-2600.

[20] Pinsky M., Khain A., M. Shapiro, 2001: Collision efficiency of drops in a wide range of Reynolds numbers: Effects of pressure on spectrum evolution. *J. Atmos. Sci.*, **58**(7), 742-764.

[21] Pinsky, M.B. and A.P. Khain, 2004: Collisions of small drops in a turbulent flow. Part II: Effects of flow accelerations. *J. Atmos. Sci.*, **61**, 1926-1939.

[22] Pinsky, M.B., Khain A.P., Grits B., and M. Shapiro, 2006: Collisions of small drops in a turbulent flow. Part III: Relative Droplet fluxes and swept volumes. *J. Atmos. Sci.*, **63**, 2123-2139.

[23] Pruppacher, H.R. and J.D. Klett, 1997: Microphysics of Clouds and Precipitation. 2nd ed. Kluwer Academic, 954 pp.

[24] Stimson, M. and G.B. Jeffery, 1926: The motion of two spheres in a viscous fluid. *Proc. Roy. Soc.*, **111A**, 110-116.

[25] Schlamp, R.J., S.N. Grover, H.R. Pruppacher, and A.E. Hamielec, 1976: *J. Atmos. Sci.*, **33**, 1747-1755.

[26] Shafrir, U. and M. Nuiburger, 1963: Collision efficiencies of two spheres falling in viscous medium. *J. Geophys. Res.*, **68**, 4141-4147.

[27] Shafrir, U. and T.A. Gal-Chen, 1971: Numerical Study of Collision Efficiencies and Coalescence Parameters for droplet Pairs with Radii up to 300 Microns. *J. Atmos. Sci.*, **28**, 741-751.

[28] S. Takagi, H.N. Oguz, Z. Zhang, A. Prosperetti, PHYSALIS: a new method for particle simulation. Part II: two-dimensional Navier-Stokes flow around cylinders. J. Comp. Phys. 187: 371-390 (2003).

[29] Wang, L.P., Ayala, O. and W.W Grabowski 2005a: Improved formulations of the superposition method. *J. Atmos. Sci.*, **62**, 1255-1266.

[30] Wang, L.P., Ayala, O., Kasprzak, S.E and W.W. Grabowski 2005b: Theoretical formulation of collision rate and collision efficiency of hydrodynamically-interacting cloud droplets in turbulent atmospheres. *J. Atmos. Sci.*, **62**, 2433-2450.

[31] Wang L.P., Xue Y., Ayala O., and W.W. Grabowski, 2006b: Effects of stochastic coalescence and air turbulence on the size distribution of cloud droplets. *Atmos. Res.*, **82**, 416-432.

[32] Wang, L.P., Ayala, O. and W.W. Grabowski, 2007: Effects of aerodynamic interactions on the motion of heavy particles in a bidisperse suspension. *J. Turbulence*, **8**, 1-28.

[33] Wang, L.-P., O. Ayala, B. Rosa, and W. W. Grabowski, 2008, Turbulent Collision Efficiency of Cloud Droplets, *New J. Physics*, in press.

[34] Xue, Y., L.P. Wang, and W.W. Grabowski, 2008: Growth of cloud droplets by turbulent collision-coalescence. *J. Atmos. Sci.*, 65, 331-356.

[35] Zhang, Z. and A. Prosperetti, A method for particle simulation. Journal of Applied Mechanics, Trans. ASME, 70: 64-74 (2003).

[36] Zhang, Z. and A. Prosperetti, A second-order method for three-dimensional particle simulation, J. Comp. Phys. 210 (2005): 292-324.

MECHANISMS OF PRECIPITATION MODIFICATION OVER COMPLEX TERRAIN

S. Wassermann, M. Kunz and C. Kottmeier

Institut für Meteorologie und Klimaforschung, Universität Karlsruhe (TH), Forschungszentrum Karlsruhe, Germany

Contact: stefanie.wassermann@imk.uka.de

1. OVERVIEW

The connection between orographically modified air flow and precipitation for stably stratified conditions is examined on the basis of idealised model studies and observations in mid-Europe. Significantly enhanced precipitation over the mountains often results in flooding of medium to large river basins. Advancing our knowledge of orographic precipitation is an important condition for further improvements of precipitation forecasts and, therefore, improvements of flood forecasts.

Orographic influences and diabatic effects due to phase transition modify the flow field in a way which is decisive for the orographically induced vertical wind field. In combination with temperature and moisture, the flow field determines the formation and composition of clouds, and, thus, the spatial distribution and intensity of precipitation. Time delays due to precipitation formation and fall distances to the ground, controlled by microphysical properties and the phases of hydrometeors, govern both precipitation efficiency and drying ratio (Smith and Evans, 2007).

We studied the relationship between precipitation patterns and dynamical effects like flow over or around a mountain or the formation of gravity waves by sensitivity studies for idealized conditions. Effects related to thermodynamics, cloud physis and precipitation formation on the amount and spatial distribution of orographic precipitation are investigated in detail. This part of the study aims at establishing a connection between the strength of precipitation enhancement and the ambient conditions upstream, combined to a single parameter (Kunz and Steller, 2005).

2. COSMO MODEL AND SETUP

COSMO-DE is the operational high-resolution weather forecast model for a lead time of 18 hr of the German Weather Service (DWD; Schättler et al., 2004). The COSMO-version used in this study is adjusted for idealized conditions. A bell-shaped mountain with a half width a = 11 km and a height of h = 1000 m is set in the middle of the domain with a size of 553 x 553 km. Inflow conditions as specified by wind velocity in x-direction, U, stability in terms of Brunt-Väisälä-frequency, N, and relative humidity, RH, are constant along the y-axis and for the lowest model levels. Aloft, U is still constant, while dry atmospheric stability, N_d, increases to very stable conditions above 10 km; RH decreases to zero at a level that is between 5 and 10 km.

We used a COSMO-setup with 40 terrain-following levels on a 200 x 200 Arakawa-C-grid in a horizontal resolution of 2.8 km that is similar to the operational version. The bulk-water-continuity cloud microphysics scheme considers cloud water, cloud snow and cloud ice, with a Runge-Kutta scheme and a 2-timelevel integration scheme (Doms et al., 2005, Schättler et al., 2004). Rayleigh damping affects disturbances above a height of approximately 11 km in order to avoid reflections at the upper model boundary.

In addition, results of idealized simulations are compared to operational analysis of DWD and observations for heavy precipitation events in a test area located over Southwest Germany with the low mountain ranges of Vosges Mountains, Black forest mountains, and Swabian Jurassic (not shown here).

3. SENSITIVITY TO WIND SPEED, RELATIVE HUMIDITY AND ATMOSPHERIC STABILITY

In earlier studies, for example, by Smith (1979), Colle (2003) and Kunz and Kottmeier (2006), it was shown that the prevailing flow regime causing flow over or around mountains, formation of gravity waves or wave breaking can be estimated by the Froude number Fr = U/(NH) or the inverse non-dimensional mountain width M = NH/U.

A dry Froude number $Fr_d < 1$ indicates that non-linear effects like wave breaking, flow blocking, or flow separation are expected, while for $Fr_d > 1$ the flow goes more or less directly over the mountains and linear theory (Smith, 1979) is applicable. The higher Fr_d, the smoother becomes the flow over the mountain. A similar theory for saturated conditions that simply considers a saturated Brunt-Väisälä-frequency, N_m (Durran and Klemp, 1982), instead of N_d is not well proofed and was only investigated by a few authors (e.g., Jiang, 2003).

In the following, sensitivity studies are presented for two different near surface temperatures: T_0 = 10°C (T10) and T_0 = -3°C (T-3). Vertical temperature profiles of are calculated from T_0 and a given constant (dry) stability, N_d. The atmospheric variables U, N_d, and RH in the control run (Ctrl) were initialized as 10 m s^{-1}, 0.01 s^{-1}, and 95%. In the model runs for the sensitivity study, one parameter was changed whereas the two others were hold as constant.

In Figure 1, each dashed line indicates one model run with precipitation (rain + snow) along the center-line through the mountain. Areas between two model runs are simply interpolated. Values of the changed parameters are indicated on the y-axis on the right hand side, corresponding dry (moist) Froude numbers are printed on the inner (outer) left y-axis.

Undisturbed velocity, U, and dry stability, N_d, are varied from 6 to 18 m s^{-1} (Fig. 1 a, b) and from 0.001 to 0.018 s^{-1}, respectively (Fig. 1 e, f). This range of parameters covers weakly nonlinear cases to weakly linear (U) and very linear (N_d) conditions. Relative humidity varies between 80 and 95% (Fig. 1 c, d).

The T10 runs mainly produce surface and vertical fluxes of rain, specific rain content and cloud water, while the T3 runs contain surface and vertical fluxes of snow, specific snow content and cloud ice mainly. The total amount of precipitation is obviously sensitive to all three parameters investigated. It increases – non-linearly – both with increasing wind speed and relative humidity, but decreases with atmospheric stability. However, a different response was found for the second precipitation maximum on the lee side that develops in the ascent of the gravity wave downstream.

Most parameter combinations considered in the study give rise to two areas with precipitation: one upstream of the mountain, the other downstream at a distance between several kilometers and up to 50 km. The first precipitation maximum corresponds to a lifting area on the windward slope of the mountain that affects only the lowest layers. The second precipitation maximum results from the ascent of the gravity wave downstream of the mountain. Depending on the ratio between U and N, the wave downstream can amplify considerably leading to the highest precipitation intensity of the domain. As can clearly be seen in the figure, this area is more sensitive to inflow parameters than the first one.

As U increases from 6 to 18 m s^{-1}, the precipitation area on the windward side stretches horizontally and intensifies (Figs. 1a and 1b). At the same time, the dry Froude number, Fr_d, increase from 0.55 to 1.63, indicating that nonlinear effects like flow blocking or flow separation vanish and wave vertical wave length of the gravity wave increases. Higher penetration ofthe mountain wave together with lifting reaching further downward to lower atmospheric layers due to less flow around the mountain extend the layer of lifted air and therefore increase windward precipitation.

The precipitation maximum downstream of the mountain crest decreases with stronger wind speeds and higher Froude numbers. Details were

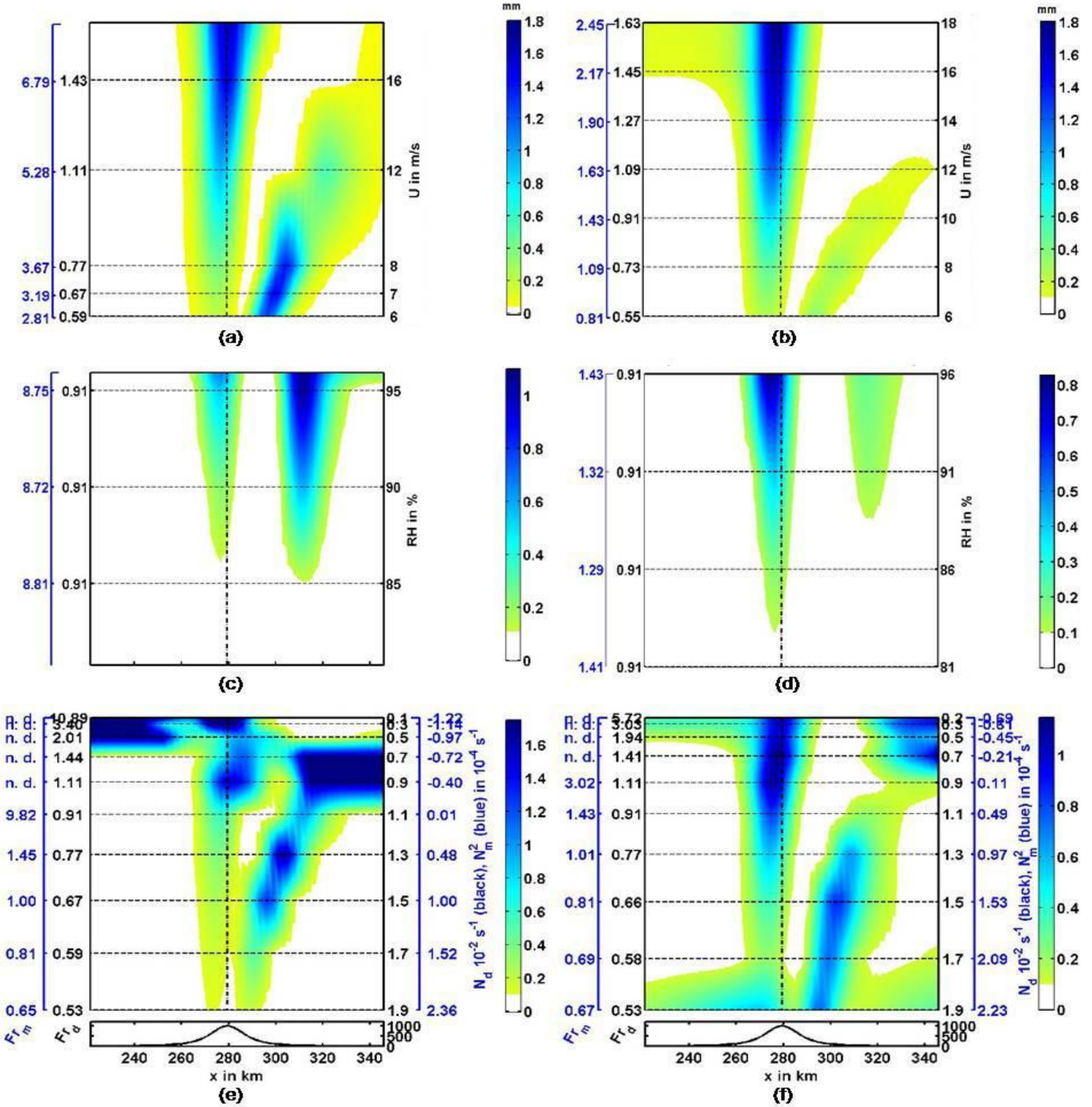

Fig. 1: *a-f: Sensitivity of precipitation to changing inflow conditions like wind speed, U, (a, b), relative humidity, RH,' (c, d), and dry Brunt-Vaisälä-frequency, N_d, (e, f) (right-hand side y-axis) for a bell-shaped mountain with H = 1000 m and a = 11 km through the center-line of the mountain. Precipitation is accumulated over one hour (after five hours of simulation). Fixed values of the control run are: U = 10 m s^{-1}, N_d = 0.011 s^{-1}, RH = 95 %, and T_0 = 10 °C (left hand side) and T_0 = -3°C (right-hand side). Dashed horizontal lines represent accumulated surface precipitation (in mm) of one simulation; colors are different from (a) to (f). y-axis on the left hand side are moist and dry Froude number on the inflow boundary of each model run.*

investigated for initial conditions with U = 16 m s^{-1} for both, T-3 and T10 runs (Fig. 1b). Although dry Froude numbers indicate equal flow conditions in both cases, the area of strong upslope precipitation is horizontally somewhat more extended in the T-3 simulations. This is surprisingly, since the T10 run contains a higher total amount of water vapor as a consequence of the Clausius-Clapeyron equation. Furthermore, the mountain wave is stronger and vertically more extended for T10 (see Fig. 2a). The reason for the higher precipitation amount in T-3 could be the formation of a light precipitating ice cloud far upstream of the mountain crest (about 150 km for U = 16 m s^{-1}). That ice clouds obviously favor and enhance precipitation formation. In contrast, in the T10 simulation mainly water clouds form directly over the windward mountain slope (not shown).

Downstream of the mountain crest, a mixed cloud with rain and snow particles develops in the T10 run, whereas an ice cloud with snow develops in the T-3 run (not shown). Mean vertical velocity increases to a factor of two compared to the upstream area, while for T10 no significant difference between both uplift areas can be found (not shown). Therefore, the downstream precipitation compared between T10 and T-3 simulations could to be connected to different cloud microphysics and stronger evaporation of snow.

The downstream precipitation area turned out to be most sensitive to relative humidity (Figs. 1c and 1d). The dry Froude number of 0.9, constant for all model runs, indicates the possibility of weak non-linear effects. Highest precipitation is found at both sides of the mountain crest, even if the initialization temperature decides about the position of the total maximum.

Details were investigated for initial conditions with RH = 95% (Fig. 1b) for T-3 and T10 runs. In both model runs, a mountain wave develops with approximately the same vertical wind speed.

For the T10 run, the wave is steeper with a higher vertical length compared to the T-3 run (Fig. 2b). Regarding mean vertical velocity (not shown), the first lifting area has similar velocity, whereas both the descent and the second ascent downstream of the mountain exhibit a higher magnitude in T10 compared to T-3. This modification in the mountain wave of T10 is caused by higher latent heat release due to more available water vapor in the warmer air of T10.

Although there is more cloud water and ice upstream of the mountain in the T10 model run (not shown), precipitation is lower there than in the T-3 run. This suggests that time scales for precipitation formation by warm rain compared to ice processes play a significant role for the location of the maximum precipitation relative to the mountain in COSMO.

The sensitivity studies for changing N_d that varies between 0.001 to 0.019 s^{-1} (Figs. 1e and 1f) comprise conditions from conditionally unstable to very stable stratification. As can clearly be seen in the Figure, the different precipitation

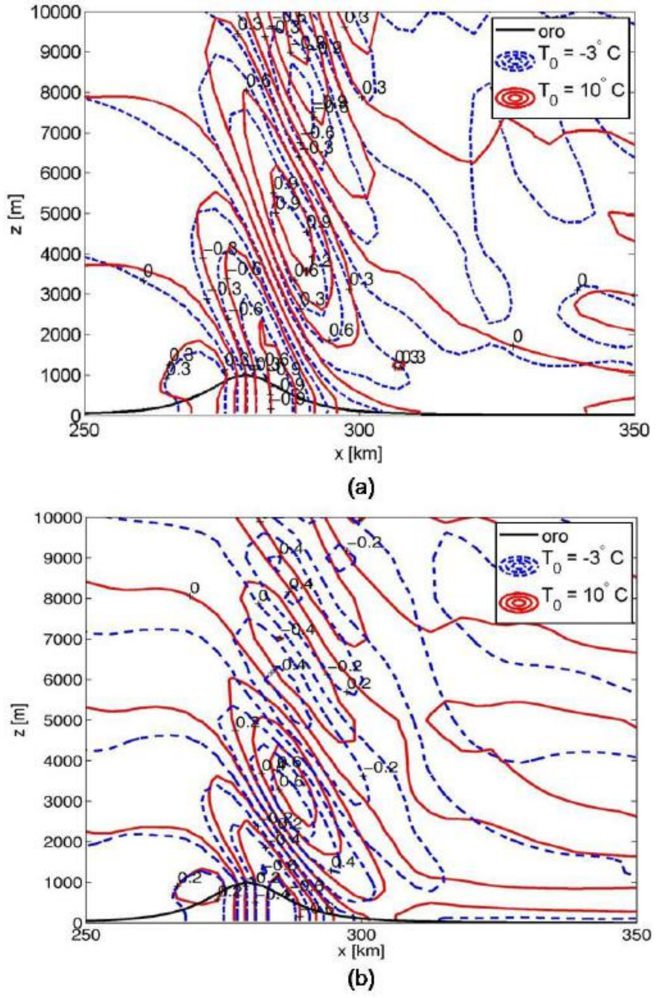

Fig. 2: *Vertical cross sections of vertical wind speed w in m s^{-1} along the center-line of the mountain for U = 16 m s^{-1} (a) and U = 10 m s^{-1} (b), initialized with T_0 = -3°C (T-3; blue dashed) and T_0 = 10°C (T10; red contoured); other parameter same as Ctrl.*

areas upstream and downstream of the mountain and their relative location (compare sensitivity to humidity, Figs. 1c and d) are also controlled by atmospheric stability. As long as stable conditions prevail (N_d >= 0.011 s^{-1}), there appear the two precipitation areas as discussed above. Both maxima increase with decreasing stability due to larger extension of lifting area. Where saturated moist Brunt-Vaisälä-frequency ($N_m^2 < 0$) indicates a conditional unstable stratification for N_d = 0.009 s^{-1} in T10 (. 2e), convection-alike structures emerge downstream of the mountain crest. This is primarily due to the release of latent heat that acts on destabilizing the stratification. In the T-3 runs, similar structures develop only for lower dry stability of N_d = 0.007 s^{-1}. Less available water vapor and more effective precipitation formation upstream of the mountain keep instability effects weak and restrict it to the area downstream of the mountain crest.

For dry conditions, the vertical wave length of the mountain wave can be estimated by $L_z = 2\pi U/N$ (Smith, 1979). From this, vertical wave lengths range between 3.4 and 10 km for the investigated velocity study (Figs. 1a and 1b), 5.7 km for the investigated relative humidity study (Figs. 1c and d), and between 3 and 62 km for the investigate

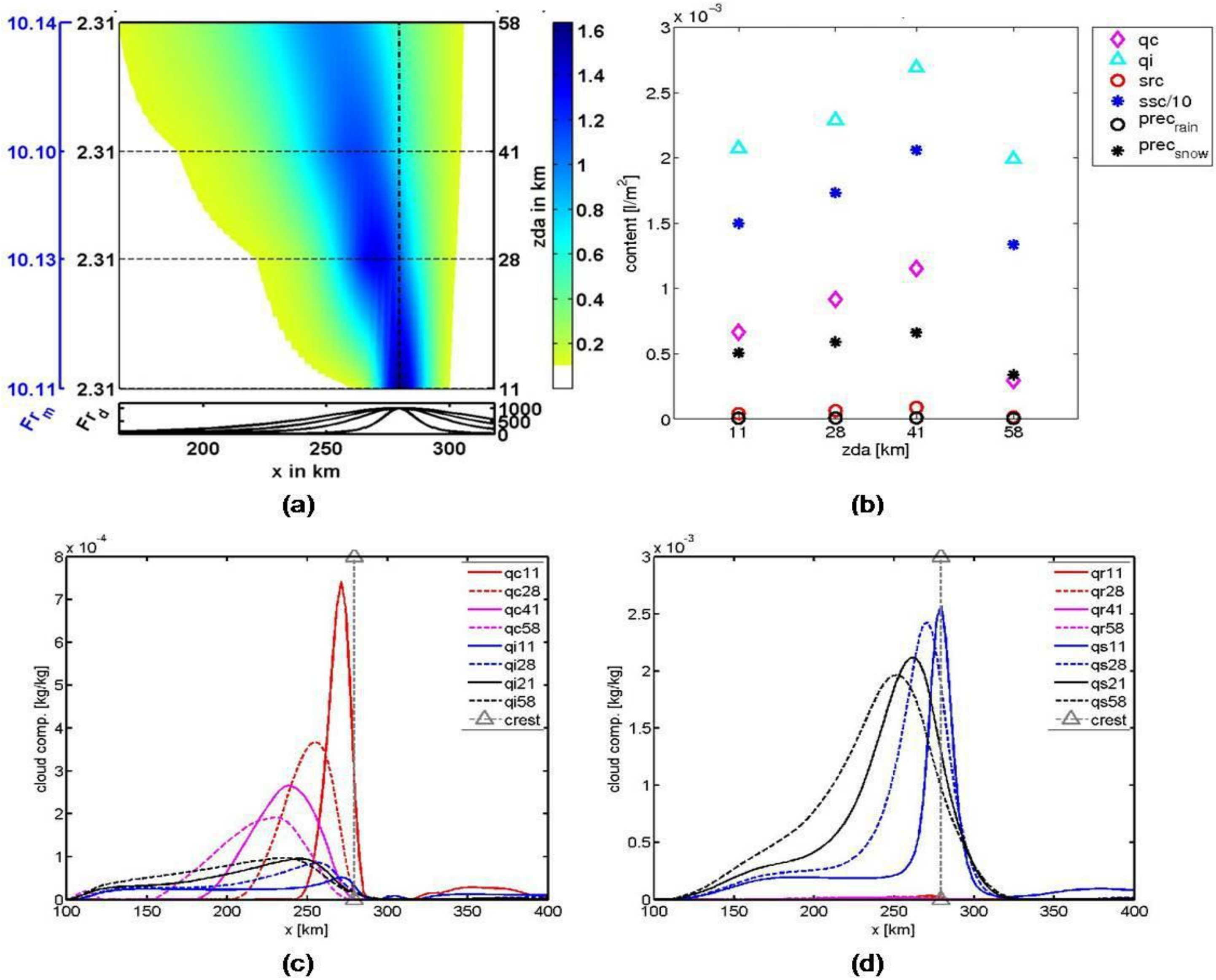

(a) (b) (c) (d)

Fig. 3: *Effect of the variation of mountain width (zda) for U = 20 m s^{-1}, RH = 95%, N_d = 0.0087 s^{-1}, T_0 = -3 °C with 1-hr accumulated precipitation after 5h of simulation time (a), 3D sum of condensate (b), vertically integrated cloud water (qc) and cloud ice content (qi) (b), and vertically integrated specific rain (qr) and snow content (qs) (d); a, c, and d are along the center-line of the mountain.*

dry atmospheric stability study (Figs. 1 e and f).

Considering saturated Brunt-Vaisälä-frequency, N_m, instead of the dry one, N_d, does not seem to be appropriate in COSMO for all case from the comparison of vertical wind fields. For U = 16 m s^{-1}, we estimate vertical wave length after linear theory from $L_z = 2\pi U/N$ (Smith, 1979).

With dry Brunt-Vaisälä-frequency it is 9 km, independent from initialization temperature. Calculation for saturated conditions using saturated Brunt-Vaisälä-Frequency gives 14 km for T3 and 33 km for T10. In comparison, in COSMO simulation, vertical wave lengths for moist conditions are closer to dry than to saturated theoretical wave lengths.

4. SENSITIVITY TO MOUNTAIN WIDTH

The location and amount of orographic precipitation obviously is controlled by the time scales of ascent in relation to that of microphysics. For effective precipitation formation, these time scales must by far exceed that for mountain overflow. If the time scales for mountain overflow are too short, condensate and hydrometeors are advected into the lee side of the mountain and evaporate without any precipitation reaching the ground.

In the next, we examine the effect of mountain width on orographic precipitation and microphysics; half width change from 11, 28, 42, to 59 km, whereas mountain height remains constant with 1 000 m. The model is initialized with U = 20 m s^{-1}, $N_d = 0.0087$ s^{-1}, RH = 95 and $T_0 = -3°C$. The set of parameter values is typical for situations with effective precipitation enhancement over Black forest mountains, as ascertain in a climatological study of Kunz (2007).

Simulation results are shown in figure 3a (analogously to Fig. 1). A dry Froude number of $Fr_d = 2.3$ that corresponds to a saturated Froude numbers $Fr_m = 10$ indicates straight flow over the mountain. As already seen in figure 1b for high wind speeds, the area of precipitation is located upstream of the mountain. Precipitation distribution of dry Froude numbers of figure 3a to figure 1 correspond well, while saturated Froude numbers of 10 was only found for very unstable conditions. Dry Froude numbers seem to be more valuable predictors for precipitation distribution compared to saturated Froude numbers.

With increasing mountain half width the windward precipitation amount decreases from 1.6 to 1.0 mm, whereas the precipitation area stretches in upstream direction. In case of the 11 km mountain, most precipitation falls close to and directly above the mountain crest. The area of maximum precipitation shifts about 20 km upstream between the narrowest and the broadest mountain. The area with significant precipitation broadens upstream for about 120 km for the investigated mountain widths. Downstream of the mountain crest, only less precipitation by spillover is found. As precipitation is mainly snow for T-3, drift and evaporation have a strong impact on precipitation advected into the lee side of the mountain, and prevent precipitation to reach the surface. This can be confirmed by the cross-sections along the center-line of the mountain for vertically integrated cloud components q_i and q_c (Fig. 3b) that show almost no cloud particles downstream of the mountain, at least for the two broader mountains.

The steepest orography is related to highest peaks of vertically integrated specific cloud water content, q_c. As already found for the precipitation maximum, q_c decrease with increasing mountain half width (Fig. 3b). At the same time, the maxima are shifted upstream. The maxima of specific cloud ice content, qi, are also shifted upstream, but are located downstream of the maxima of q_c. Interestingly, q_i upstream of the mountain crest increases whereas q_c decreases. Downstream of the crest, considerable contents of q_i and q_c (less than 10% of maximum) are found only in case of the narrowest mountain. Considering both the total specific cloud water and cloud ice as integrated vertically and horizontally over the domain, highest amounts are given for the broadest mountain.

In all simulations, the specific rain water, q_r, is almost zero due to the low temperatures (Fig. 3d). The large amount of snow combines the characteristic features of both, the distribution of cloud water as well as cloud ice (see Fig. 3b). As already seen for the cloud components, the maxima of the specific snow content, q_s, are shifted upstream for broader mountains, whereas the maxima are only slightly reduced. Again, the broadest mountain produces the highest total amount of specific snow content. Snow contents that result from very slow ascent in the domain extend approximately 180 km upstream of the mountain crest. The location, where q_s formation begins, shows almost no sensitivity to the mountain half width. Compared to q_i, the formation of q_s is shifted for about 10 km downstream. Assuming an undisturbed velocity of U = 20 m s^{-1}, this yields a formation time of approximately 500 s.

5. CONCLUSIONS

In our study, we examined the relationship between precipitation patterns over mountains, dynamical effects, and microphysics from three-dimensional sensitivity studies with the non-hydrostatic numerical model COSMO.

Precipitation distribution was strongly sensitive to changing wind speed, atmospheric stability and relative humidity and initialization temperature in our simulation. All parameters with exception to relative humidity proved to be decisive for the position of the main precipitation amount. T10 runs showed a stronger tendency to produce main precipitation downstream of the mountain crest, corresponding to the second upwind area of the mountain wave compared to T3 runs. This difference was caused by the combination several factors in our set of COSMO simulations. First, precipitation production by warm processes is slower and less effective in T10 model runs. This prevents large precipitation amounts. Second, the modification of the mountain wave by latent heat release was stronger due to more available water vapor in general. It is further amplified by latent heat release in the first cloud maximum independent from temperature. Due to higher extension of the second upwind area of the mountain wave the investigated model runs contained a mixed cloud downstream of the mountain. In what way this is conditional for precipitation increase compared to the windward side of the mountain has to be investigated in future.

Froude number Fr = U/(NH) and vertical wave length of the mountain wave $L_z = 2\pi U/N$ were applied using dry as well as saturated Brunt-Vaisälä-Frequency. Comparing dry and moist Fr and L_z were to precipitation distribution and vertical wind component from COSMO simulations, both vertical wind field as well as similarities in precipitation distribution seem to be stronger related to dry measures than to those calculated from saturated Brunt-Vaisälä-frequency. Probably, the assumption of saturation for all atmospheric layers is to rough to characterize the flow conditions. The impact of flow dynamical effects like flow blocking, flow separation and wave breaking directly from wind components has to be performed, to get more suitable relationships to predict the flow pattern.

ACKNOWLEDGMENTS

This work was funded by Deutsche Forschungsgemeinschaft (German research foundation) within the Priority Program SP1167 “Quantitative Precipitation Forecast”. The authors thank A. Seifert and J. Förstner of DWD for supporting use and modifications of COSMO-DE.

6. REFERENCES

Colle, B. A., 2003. Sensitivity of orographic precipitation to changing ambient conditions and terrain geometries: An idealized modelling perspective; J. Atm. Sci, Vol. 61, 588-606

Doms, G., J. Förstner, E. Heise, H.-J. Herzog, M. Raschendorfer, R. Schrodin, T. Reinhardt and G. Vogel, 2005. A Description of the Nonhydrostatic Regional Model LM, Part II: Physical Parameterization, Deutscher Wetterdienst, Offenbach, [available at: www.cosmo-model.org].

Durran, D. R., and J. B. Klemp, 1982. The effect of moisture on trapped mountain lee waves, J. Atm. Sci., Vol. 39, 2490-2506.

Jiang. Q., 2003. Moist dynamics and orographic precipitation, Tellus A, Vol. 55, Issue 4, 301-316.

Kunz, M., 2007. Lineare Theorie der orografisch bedingten Niederschlagszunahme am Beispiel der Mittelgebirge Südwestdeutschlands, Abstractband DACH Meteorologentagung, Hamburg, 10.09.-14.09.2007

Kunz, M. and H. Steller, 2005. Precipitation enhancement over low mountain ranges, EUG Joint Assembly, 24.-29. April 2005, Vienna

Kunz, M. and Ch. Kottmeier, 2006. Orographic Enhancement of Precipitation over Low Mountain Ranges, Part I: Model Formulation and Idealised Simulations; J. Appl. Meteor. and Climatol., 45, 1025 - 1040.

Schättler, U., G. Doms and C. Schraff, 2004. A Description of the Non-hydrostatic Regional Model LM, Part IV: User Guide, Draft Version, Deutscher Wetterdienst, Offenbach, Germany, pp. 129;

Smith, R., 1979. The influence of mountains on the atmoshpere. Adv. Geophys., 21, 87-230.

Smith R. B. and J. P. Evans, **2007**. Orographic Precipitation and Water Vapor Fractionation over the Southern Andes; J. Hydromet., Vol. 8, 3-19.

CLIMATOLOGY OF GLAZE AND RIME AT THE RUSSIAN SUB-POLAR ARCTIC STATIONS

N.A. Bezrukova

Central Aerological Observatory, Dolgoprudny, Moscow Region, 141700 Russia

1. INTRODUCTION

Glaze and rime formation on the ground surface or objects due to supercooled rain and fog deposition is one of the phenomena hazardous for surface communication lines, electric wires and poles, water transport, oil-mining platforms, and especially for aviation. Climatology of these phenomena requires more data for different regions.

This work is a continuation of the previous climatological studies of freezing precipitation and rime over the Russian territory (Bezrukova et al., 2000, 2006, 2007 [1-3]).

This paper analyzes a 10-year set of observations (1981-1990) of the frequency of such events for the Russian sub-polar region - 16 mainland and island weather stations north of 65ºN. This paper intends to draw the attention of the reader to the statistics by showing some interesting features.

2. BACKGROUND DATA

2.1 Data Sources

The author used the data provided by the network weather stations involved in the international exchange of meteorological data. The network's Monthly Meteorological Tables, comprising selected daily ground meteorological observations from 16 stations, served as a basis for the analysis.

2.2 Data type

To avoid terminology distortions [4-11], we only collected data in the form of International Weather Codes. All the types of freezing precipitation (FP) events were given as WMO Weather Codes 56, 57, 66, 67, 24 **GLAZE,** and freezing fog (FF) deposited **RIME** as WMO Weather Codes 48, 49.

2.3 Data characteristics

Weather characteristics associated with glaze and rime phenomena have also been collected and analyzed.

In particular, the following data were presented for each weather station: location (city) and station number, date and time of the observation, current weather and that between observations, temperature, dew-point temperature, relative humidity, air pressure, wind speed and direction, visibility, total and low-level cloud amounts, and cloud base height.

Thus, the collected ground observations have formed a data bank of 1023 events reported across the whole sub-polar territory north of 65ºN over a 10-year period.

The distribution of the overall number of freezing precipitation events estimated for two groups of the WMO Weather Codes by months is shown in Table 2.1. The number of fog deposited rime events is much larger than that of glaze events on the Russian polar coast, accounting for 84% of the total number. Freezing rain and drizzle occur rather seldom (16%).

Corresponding author's address: Natalia A.Bezrukova, CAO, 3 Pervomayskaya Str., Dolgoprudny, Moscow Region, 141700, Russia. E-Mail: nataly_bez@yahoo.com

Table 2.1. Distribution of freezing precipitation and rime events by months and WMO Weather Codes

Months	RIME Number of events FF (48, 49)	GLAZE Number of events FP (56, 57, 66,67,2
Jan	190 (22%)	8 (5%)
Feb	161 (19)	12 (7)
Mar	92 (10)	5 (3)
Apr	43 (5)	7 (4)
May	72 (8)	9 (6)
Jun	8 (1)	16 (10)
Jul		2 (1)
Aug	1 (0,1)	15 (9)
Sep	25 (3)	23 (14)
Oct	69 (8)	25 (15)
Nov	78 (9)	16 (10)
Dec	121 (14)	25 (15)
Year	860 (100)	163 (100)

3. DISTRIBUTION OF STATIONS BY REGIONS

The area discussed comprises all the stations north of 65°N on the Arctic coast, including the Kola Peninsula, and in the northern part of Siberia. The entire territory was divided into 4 major regions: **Western Area** (Barents Sea) (*Murmansk, Kandalaksha*), **Central Area** (Kara Sea), (*Narian-Mar, Pechora, Hoseda-Hard, Ust-Tsilma, Ostrov Dikson*), **Northern Siberia** (*Zhigansk, Verhojansk, Hatanga, Chokurdah, Olenek*) and **Eastern Area** (*Mis Shmidta, Ostrov Vrangelya*). The northern–most station is located at 73º30' N (Ostrov Dikson). The locations of the stations for the 4 sub-regions are shown on the map below (Fig. 3.1).

4. STATISTICS AND DISTRIBUTION OF CASES BY REGIONS

4.1 Glaze-deposition of freezing precipitation (Weather Codes 24, 56, 57, 66, 67)

Atmospheric glaze formation in the Arctic is due to cyclonic cold fronts and occlusion fronts in warm seasons and warm fronts in cold seasons. Generally, glaze diameter is observed to be about 5 mm. Its maximum diameter of 76 mm was measured on Uyedineniye Island, the mass being 382 g per meter length of electric wire.

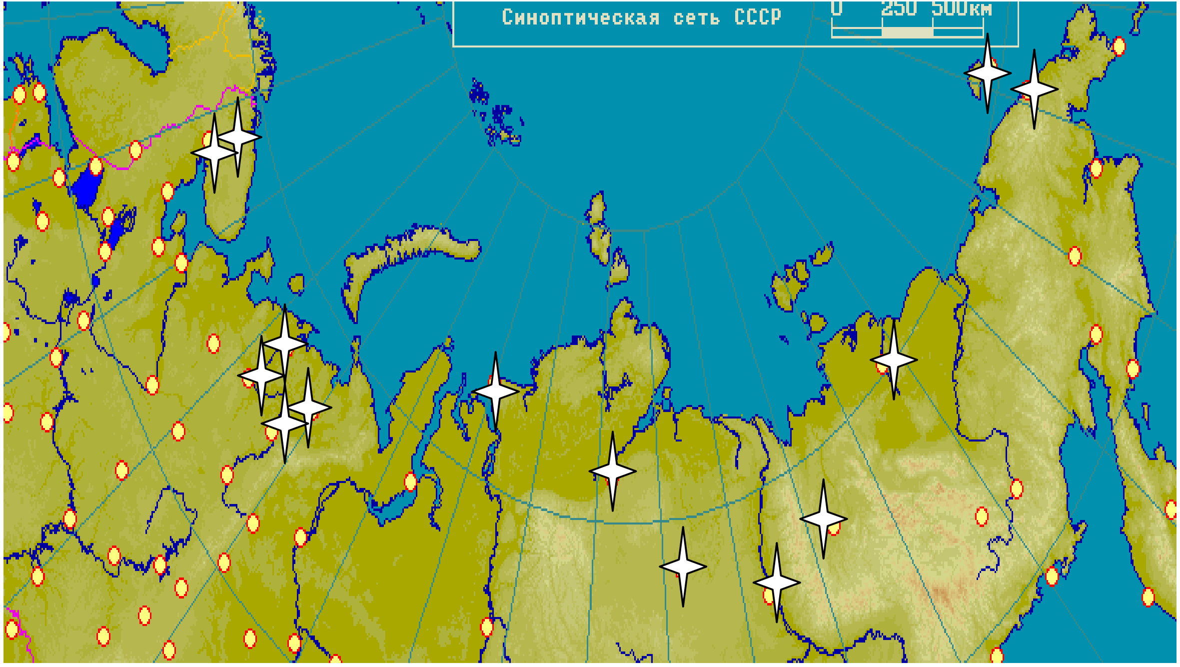

Fig. 3.1. Locations of the stations for the 4 sub-regions of the Russian polar coast.

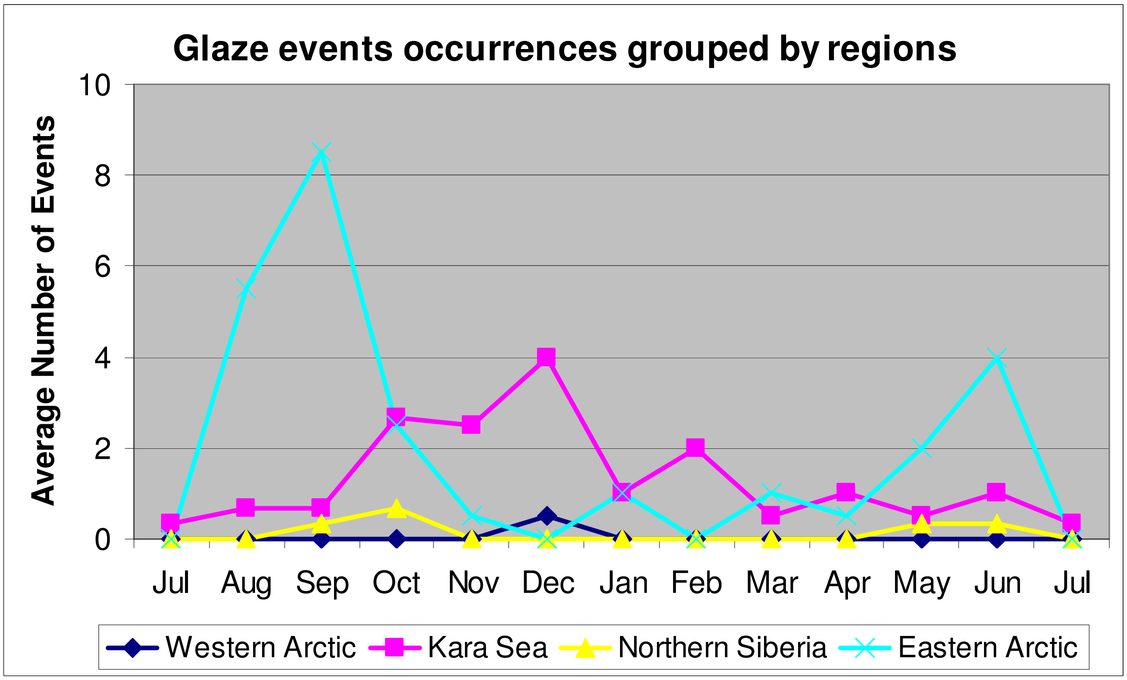

Fig. 4.1. Occurrences of glaze events grouped by regions.

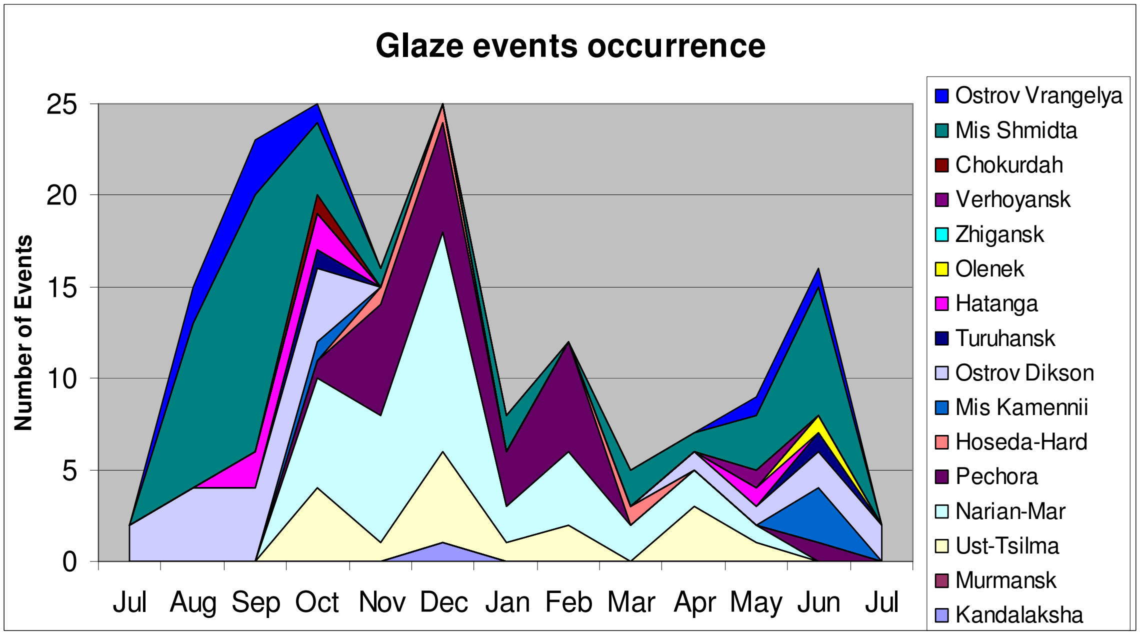

Fig. 4.2. Occurrence of glaze events by stations.

WESTERN (BARENTS) AND CENTRAL (KARA) PART OF THE ARCTIC COAST. The highest occurrence of glaze in winter (October-April), with maximum in December, is associated with cyclones on the Arctic front (two maxima in winter-spring and one in autumn-winter season). In summer, no glaze is generally observed (Fig. 4.1). The highest annual occurrence of glaze events observed in the Khibini foothills (Kola Peninsula) is up to 23 days and on the mountain slopes and tops up to 38 days. Another area with frequent glaze events in Murmansk Region is the White Sea coast, where glaze occurrence may reach 12-24 day, with 6 days on the coast of the Gulf of Kandalaksha.

EASTERN PART OF THE ARCTIC COAST. Cyclonic activity in spring and autumn results in two glaze maxima within a year. One winter minimum is observed when the influence of the Siberian anticyclone is the greatest (Fig. 4.1- 4.2).

NORTHERN PART OF SIBERIA – Glaze events are rare (1-2), generally occurring till October and in May-June, when the Siberian anticyclone already degrades. No summer glaze events are observed (Fig. 4.1).

4.1 Rime or freezing fog deposited rime (Weather Codes 48, 49)

The freezing of supercooled fog water vapor produces considerably thick rime on objects.

In Fig. 4.3 is shown the annual occurrence of rime by months. Grained rime (GR) is a deposit of ice with granular structure. It is formed by the freezing of supercooled fog drops on objects or on other freezing drops of supercooled fog, either transparent (48) or non-transparent (49). This phenomenon refers to “freezing fog” (FF). Grained rime produced by FF is a hazard to electric power and communication lines as well as railway infrastructure. In the mountains, its deposits may be as thick as 2 m. Grained rime density is 0.1-0.4 g cm-3, with a maximum of 0.6 g cm-3. The mean temperature of its formation in central Russia ranges between -2° and -8÷ -12°C.

In the Russian sub-polar region, numerous events with Codes 48, 49 were observed at very low temperature and high pressure (>1015 hPa). Below –30ºC, nearly 250 events with Code 48 (fog, deposited rime, with the sky visible) and only several ones with Code 49 (fog, deposited rime, with the sky invisible) were recorded.

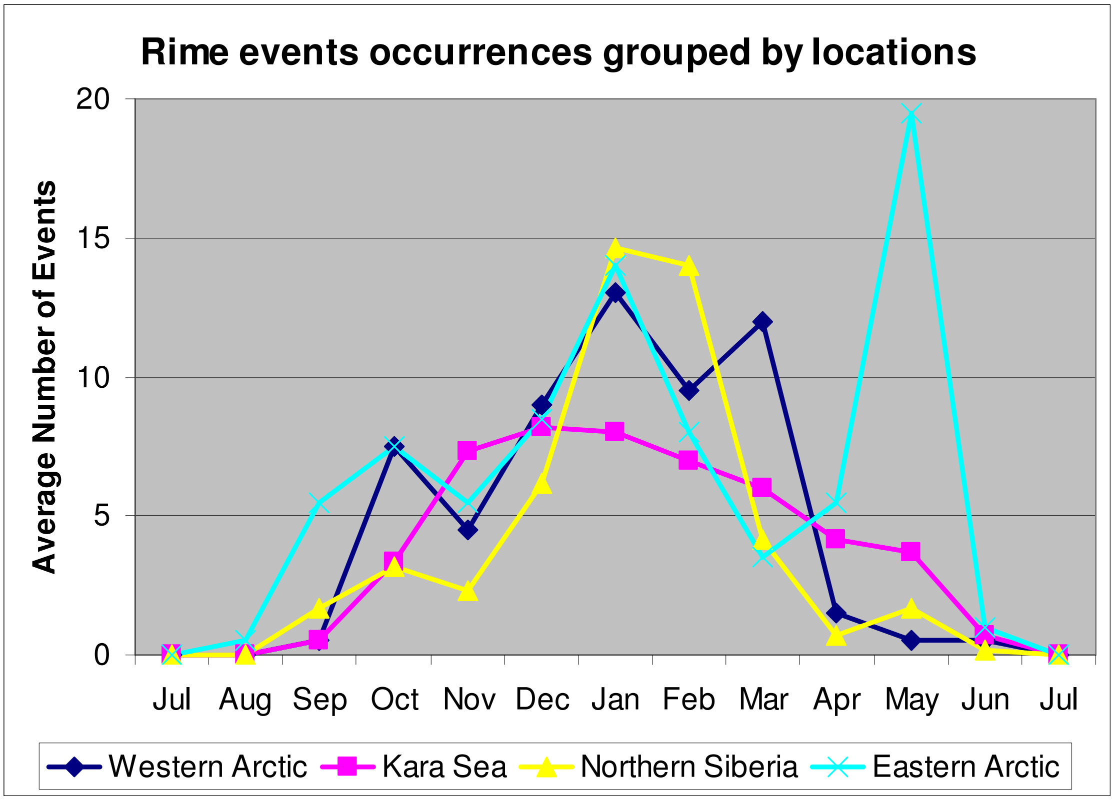

Fig. 4.3. Occurrences of rime events grouped by regions.

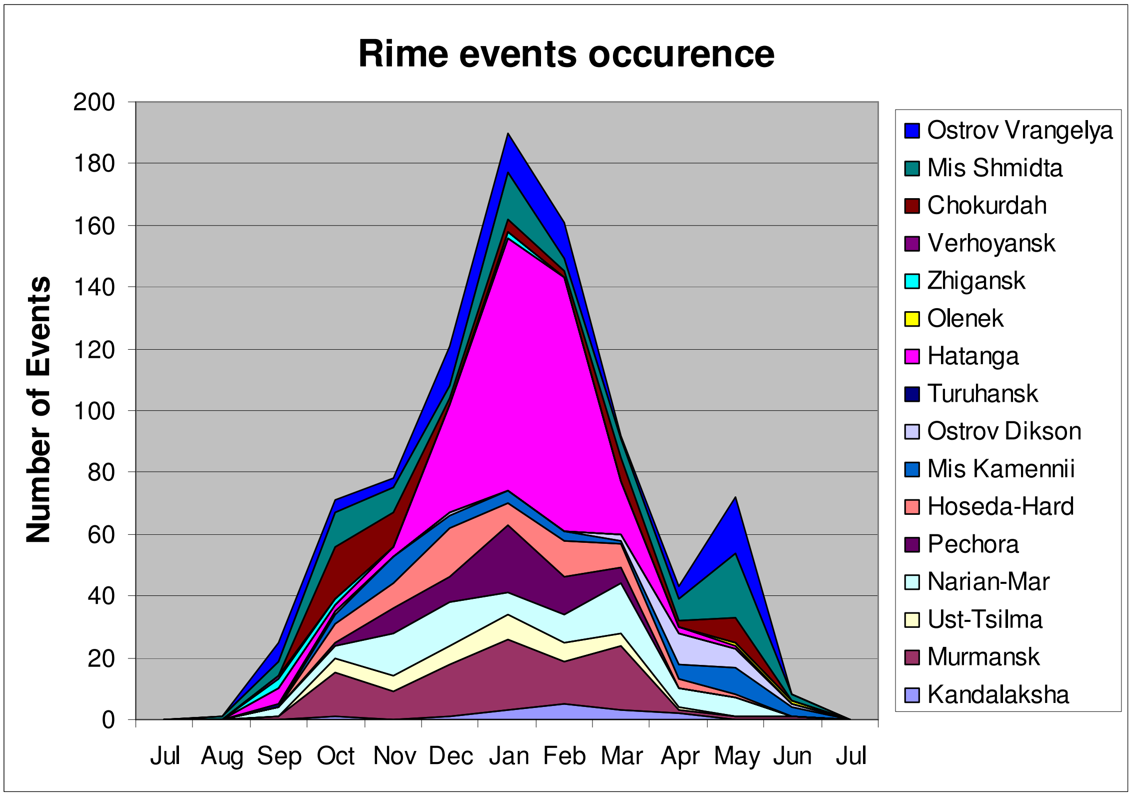

Fig. 4.4. Occurrence of rime events by stations.

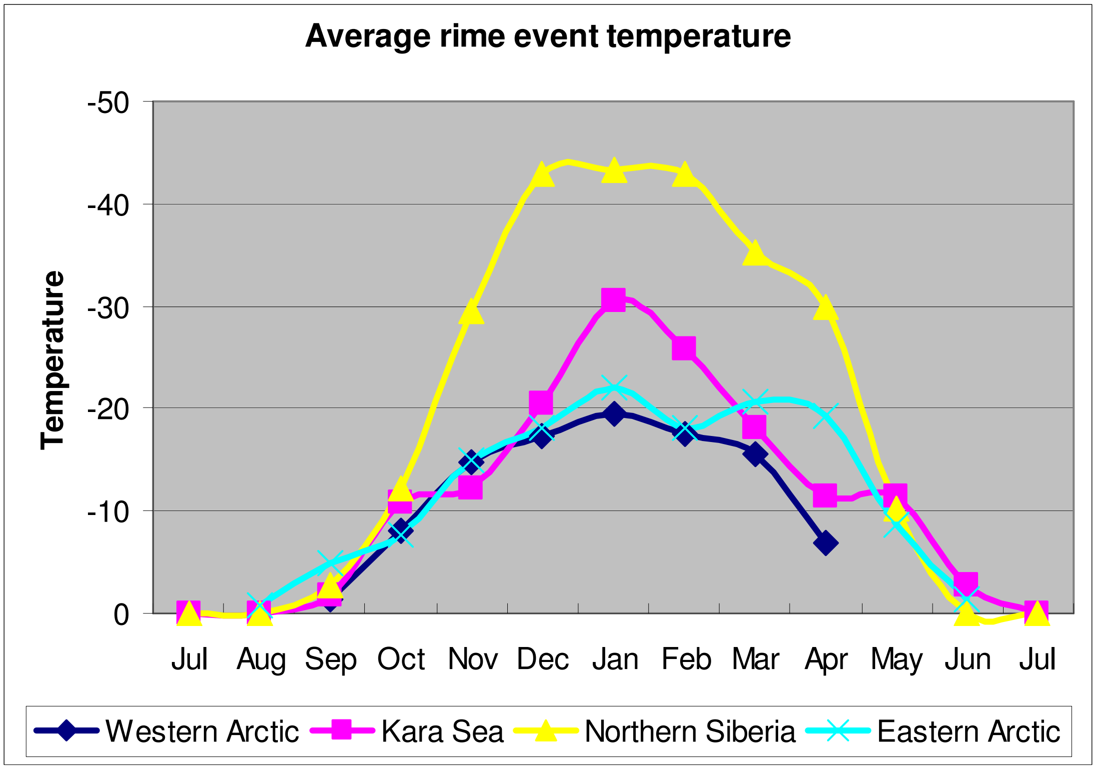

Fig. 4.5. Average rime event temperatures grouped by regions.

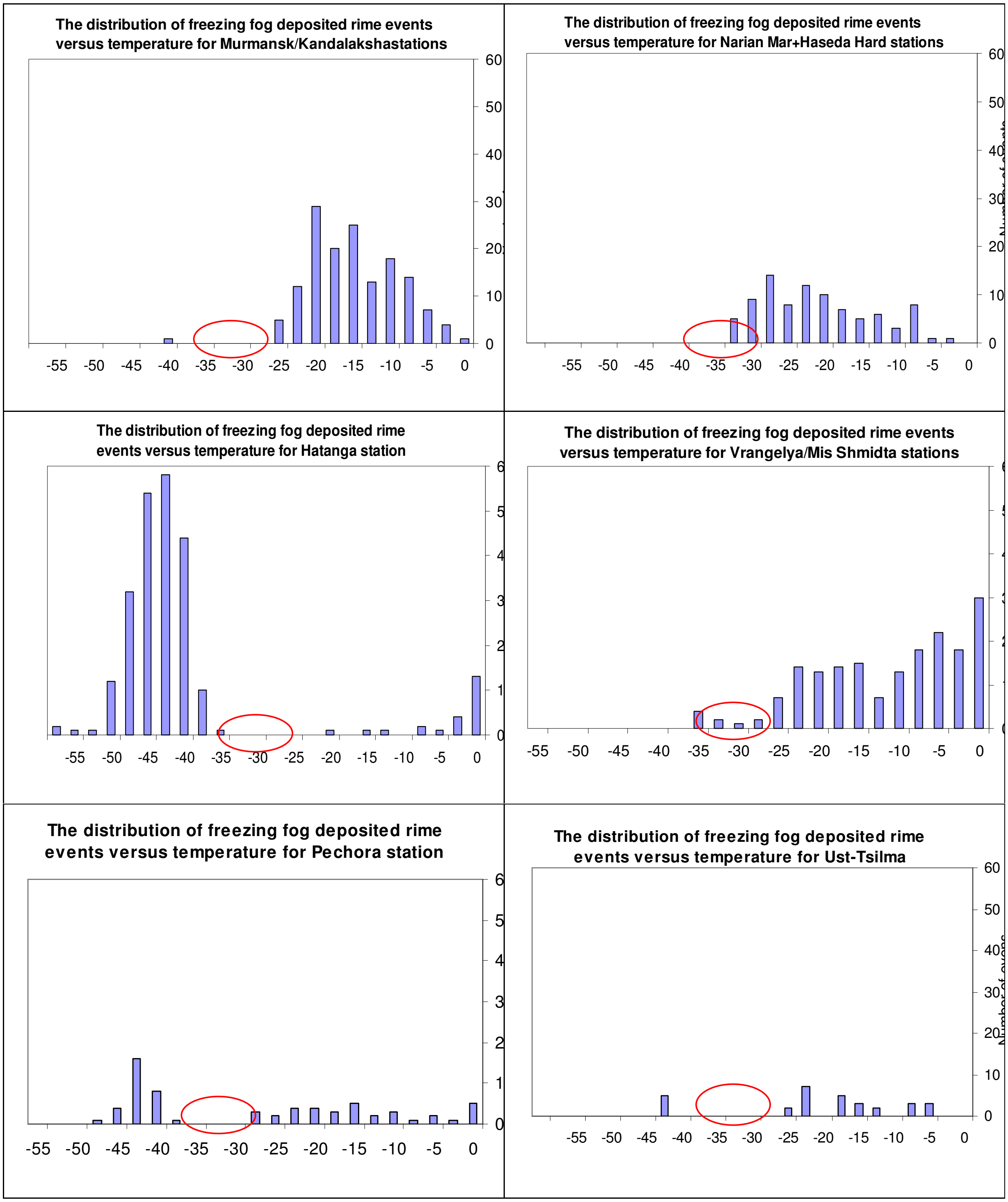
The distribution of freezing fog deposited rime events versus temperature for Murmansk/Kandalakshastations

The distribution of freezing fog deposited rime events versus temperature for Narian Mar+Haseda Hard stations

The distribution of freezing fog deposited rime events versus temperature for Hatanga station

The distribution of freezing fog deposited rime events versus temperature for Vrangelya/Mis Shmidta stations

The distribution of freezing fog deposited rime events versus temperature for Pechora station

The distribution of freezing fog deposited rime events versus temperature for Ust-Tsilma

Fig. 4.6. Occurrence of freezing fog deposited rime events versus temperature by stations.

It is noteworthy that in the variation of the dependence on temperature of the occurrence of Codes 48 and 49, one can see two maximums at the Arctic stations and two ones at North Siberia stations (Fig. 4.6). The first maximum in each case is in the range from –10 to –20 °C, while the second maximum in both regions is between –40 and –50 °C, which is characteristic of Siberian winter under anticyclone conditions. These estimates are also supported by the distribution of the number of events versus pressure. The largest number of events was observed at 1010–1015 hPa.

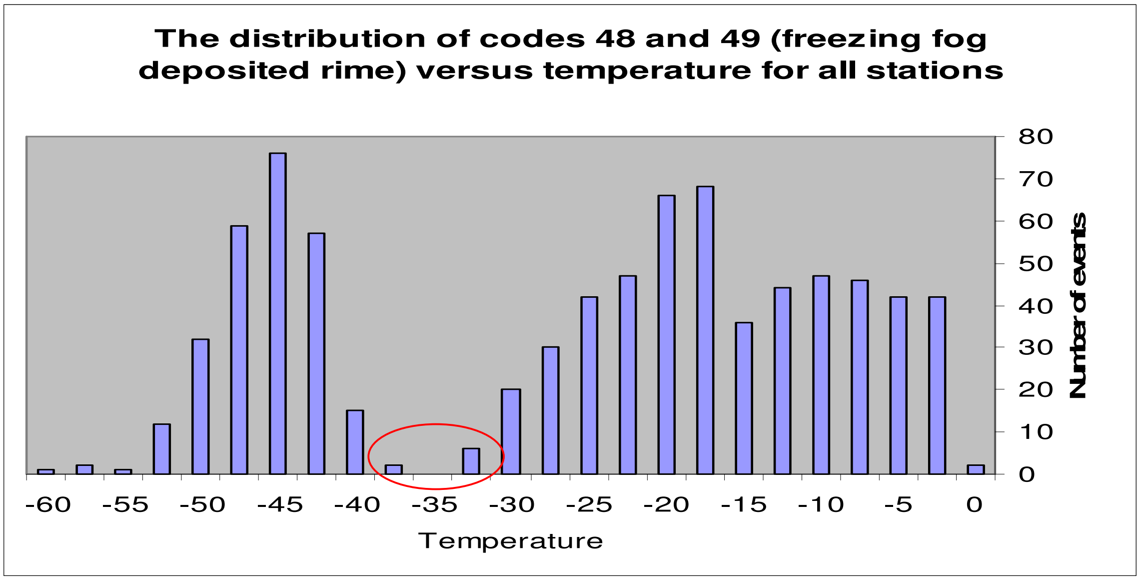

Fig. 4.7 The frequency of events by stations versus temperature.

4.4 Résumé

At all the Russian sub-polar stations, (Fig.4.7), the distribution of rime events versus temperature was typically bimodal, with the highest frequency recorded at temperatures from –40 to –50 °C. One maximum was measured between –10 and –20 °C and the other between –40 and –50 °C. Between these maximums, one can see a clear minimum of the occurrence of such events, which is the same for the two regions in a temperature range from –32 to –35 °C, i.e. practically no rime forms here. It is quite clear that the two sets of maximums are due to different microphysical rime-formation conditions.

The output of this work is the statistics and maps of the monthly occurrence of freezing precipitation over the sub-polar territory.

5. BIBLIOGRAPHY

1. Bezrukova, N.A., 1994. Winter precipitation variability over European Russia in different types of fronts originated over Arctic, Atlantic and Mediterranean regions. Atmospheric Research, V.34, pp. 153-168.

2. Bezrukova, N.A., Minina, L.S., Naumov, A.Ya., 2000. Freezing precipitation climatology in the former European USSR. Proceedings of the 13th International pp.737-739, Reno, USA, 14-18 Aug 2000.

3. Bezrukova, N.A., Jeck, R.K., Khalili, M.F., Minina, L.S., Naumov A.Ya., Stulov, E.A., 2006 Some statistics of freezing precipitation and rime for the territory of the former USSR from ground-based weather observations. Atmospheric Research, V. 82, 2006 pp. 203-221.

4. N.E. El'ianov English-Russisn Dictionary of Aviation Meteorology, Edited by B.A.Kiselev, IZOGRAF, Moscow 1996, 319p.

5. Instruction for hydrometeorological stations and posts on instrumental observations of wire icing, 1951. Issue 3, Part II. (Proizvodstvo instrumentalnih nabludenyi nad obledeneniem provodov), Gimiz, 28 p.

6. Instruction for hydrometeorological stations and posts on instrumental observations of wire icing 1985.Issue 3, Part I (Proizvodstvo instrumentalnih nabludenyi nad obledeneniem provodov) Leningrad, Gidrometeoizdat, 37 p.

7. Khromov, S.P., Mamontova L.I., 1974. Meteorological Glossary, 3rd ed., Hydrometizdat, 568 p. (in Russian).

8. Manual of Codes. WMO No. 306, Edition 1988, FM 94-IX BUFR, I-A-380, I-A-381.

9. Science Application Handbook on the USSR Climate, 1990. Ser. 3, part 1-6, V.8, Leningrad, (in Russian).

10. Surface Weather Observation and Reports, Federal Meteorological Handbook No.1, FCM-H1I, 1998.

11. WMO Four-Language International Meteorological Vocabulary WMO, 2nd ed., 1992. WMO-No.182.

Acknowledgements

The authors would like to thank the sponsors WMO, IUGG, IAMAS and ICCP for their financial support.

The authors are thankful to M.A. Khanchina for the adequate rendering of the contents of this paper in English.

PARAMETERIZATION OF ICE PARTICLE SPECTRA IN EXTRA TROPICAL CLOUDS: NORMALIZATION APPROACH

Faisal S. Boudala and George A. Isaac

Cloud Physics and Severe Weather Research Section, Environment Canada, Toronto, Ontario, Canada

1. INTRODUCTION

Numerical model simulations of clouds require a reasonable representation of ice particle size distribution (IPSD) in order to parameterize cloud microphysical processes. Many of the current climate and weather prediction models use parameterization of ice particle size distribution in their bulk microphysical schemes (e.g., *Rotstayn et al.* 2000; *Lohmann and Roeckner*, 1996; *Rutledge and Hobbs,* 1983).

Although high concentrations of small ice crystals in stratiform clouds have been measured using various optical probes such as the Forward Scattering Spectrometer Probe (FSSP) (*Lawson et al.,* 2006; Gayet et al., 2002; *Heymsfield and Platt,* 1984), and the Video Ice Particle Sampler (VIPS) probe (*McFarquhar and Heymsfield* , 1996); there are considerable uncertainties in the concentration and sizes of measured small ice crystals (D ≤ 100 µm) in ice clouds due to several reasons such as possible particle shattering on tip of the probes (*Field et al*., 2003; Korolev and Isaac, 2005; *McFarquhar et al*. ,2007). However, studies indicate that direct measurements of cloud extinction in ice clouds normally exceed that calculated from measured PSD using 2D optical array probes, particularly when the small particle sizes are ignored (*Gayet et al.,* 2002; *Heymsfield et al.,* 2006) indicating that the small particles maybe present in the natural atmosphere. However, the contribution of small ice particles to the total extinction is not well known. Therefore, in this paper, the small particle (D≤100 µm) are not considered explicitly.

There are some parameterizations of IPSD (*McFarquhar and Heymsfield,* 1997; *Heymsfield and Platt 1984*; *Ivanova et al*. 2001; *Field et al.* 2005; *Heymsfield et al.* 2002), with a varying degree of complexity based on limited aircraft observations, but their accuracy have not been tested adequately in different locations and air mass type. Nonetheless, no similar parameterization has been developed for high latitude ice clouds.

Determination of ice mass from IPSD highly depends on the particle shape as well as density. The usual practice is to use empirical mass dimensional (m-D) relationships based on data mainly collected at the ground levels (e.g., *Cunningham*,1978; *Locatelli and Hobbs*, 1974; *Mitchell et al.* 1990). These coefficients have not been adequately validated with direct observations and there may be at least a factor of 2 or 3 uncertainty in the derived ice particle mass. Therefore, in principle, there is a need to provide a parameterization of ice crystal size distributions that can be validated against independent measurements. It should be mentioned, however, that the currently available probes that measure the cloud water content, have some uncertainties, thus more research is needed to test their accuracy. The purpose of the this paper is to provide a parameterization of ice particle spectra based on available data on ice particle properties measured in extra-tropical stratiform clouds for application in regional and climate models and remote sensing.

Corresponding author : Faisal S. Boudala
Cloud Physics Research Section, Environment Canada, Toronto, Ontario, Canada , M3H 5T4
e-mail: faisal.boudala@ec.gc.ca.

2. MEAUREMENTS OF CLOUD MICROPHYSICS

2.1 *Field projects*

The data were collected during four projects using the National Research Council (NRC) Convair-580 aircraft. The Beaufort and Arctic Storms Experiment (BASE) field project was carried out in October 1994 over the Canadian Western Arctic. The FIRE Arctic Cloud Experiment (FIRE.ACE) project began in April 1998 and ended in July 1998, with the Convair-580 measurements being made in April. The Canadian Freezing Drizzle Experiment I (CFDE I) project was carried out in March 1995 mainly in maritime type clouds over Newfoundland and the Atlantic Ocean. The Canadian Freezing Drizzle Experiment III (CFDE III) started in December 1997 and ended in February 1998. During the CFDE III project, the aircraft flew mainly in continental stratiform type clouds over Southern Ontario and Quebec, and some over Lake Ontario and Lake Erie.

2.2. Instrumentation

The types of instrumentation used in these projects are described in *Isaac et al.,* (2001). The calibrations of the instruments and processing of the data are described in *Cober et al.* (2001). The main instruments used in this work are the PMS, 2D-C and 2D-P probes and other relevant meteorological instruments.

The PMS 2D-C and 2D-P probes measure concentrations in the particle size ranges of 25 – 800 µm and 200 – 6400 µm respectively. However, the first 4 channels (25-100 µm) of the 2D-C have been ignored here because of the measurement uncertainty. It has been also known for sometime that there are problems with measuring the large ice particles because of things like particle shattering due to collisions with the probes (*Cooper*, 1977). This issue has been a subject of some discussions in the latest works of *Korolev and Isaac* (2005) and Field et al. (2006). Field et al. have identified that the particle shattering effects become significant when the mass weighted mean size exceeds 1 mm and the particle size distributions are relatively broad. However, due to the fact that there are many corrections to be made as mentioned earlier, it is difficult to quantify errors associated with particle shattering. One way to exclude the shattered particles is by removing all particles crossing the sampling volume in unusually short interarrival times or short distances between two successive images as discussed by *Field et al*. (2006) and earlier by *Cooper* (1977). The precipitation probe 2D-P having a relatively larger sampling volume and course resolution tends to naturally fitter out the shattered particles, thus it is the 2D-C probe which is affected the most in the presence of shattered particles (see *Field et al.* 2006). Thus, in order to minimize the errors, shattered and elongated thin particle images ($D \geq 100$ µm) are excluded from the 2D-P and 2D-C data using image processing software. To avoid the 2D-C sample volume problem at the near end of the particle size limit (800 µm), only sizes between 125-575 µm have been included from the 2D-C measurements and the rest of the sizes greater 575 µm are obtained from 2D-P measurements. The 2D-C images were processed following a center-in scheme to increase its sampling volume. This scheme includes all partly imaged particles that have their centers within the sampling area. Their sizes are determined by reconstruction of their shapes assuming circular geometry (*Heymsfield and Parrish*,1978). The 2D-P images are processed following an entire-in scheme (*Knollenberg*, 1970). This method is based on ignoring any particle that occludes either end of the photodiode array and it is also referred as the double edge element (DEE) method. In this paper, the ice clouds are identified following the *Cober et al.,* (2001) scheme. The ice particles are categorized based on their maximum diameter (md) and projected area equivalent diameter (ad). All the microphysical data used in this study are averaged every 30 s or approximately a 3 km flight path with an average aircraft true speed of 100 ms^{-1}.

3. ICE PARTICLE SIZE DISRIBUTION

3.1 Moment method

Cloud particle size distributions can be parameterized using the moment method (e.g., *Boudala and Isaac*. 2006a, b; *Delanoe et al.* 2005; *Smith*, 2003, *Testud et al*. 2001; Heymsfield et al., 2002; *Field et al*., 2005). The moments of the observed size distribution can be derived as

$$M_n = \sum_{D_{\min}}^{D_{\max}} D^n N'(D) , \qquad \text{(8a)}$$

where D is the ad or md of a given ice particle as defined earlier, $N'(D)$ is number concentration measured at each particle bin size or D, n is the order of the moment in question that is normally related to cloud properties. For example, n=0, n=2, and n=4 can be related to number concentration, ice water content (IWC), and radar reflectivity (Z) (e.g., *Field et al*., 2005) respectively. We have also included the case n = 2.25, which would be proportional to snow precipitation rate used in the Canadian numerical weather prediction model (*Kong and Yau,* 1997), if the IWC is assumed to be proportional to M_2 as has been defined here instead of M_3. From these moments, mean particle sizes D_{32} $= M_3 / M_2$ and $D_{43} = M_4 / M_3$ can be defined.

By assuming a gamma size distribution in a form

$$N(D) = N_o D^{\mu} \exp(-\lambda D) , \qquad \text{(8b)}$$

where μ is the dispersion, N_0 is the intercept and λ is the slope parameters, and considering integration from zero to infinity, it can be shown that any moment order n associated with $N(D)$ can be derived as

$$M_n = \frac{N_o \Gamma(\mu + n + 1)}{\lambda^{\mu+n+1}} , \qquad \text{(8c)}$$

where Γ is the gamma function defined as $\Gamma(\mu + n + 1) = (\mu + n)!$. Using the definition of Γ and Eq. 8c, it can be shown that M_n can be given as

$$M_n = \frac{(\mu_n + n) M_{n-1}}{\lambda_n} . \qquad \text{(8d)}$$

With the help of Eqs. 8d and 8c, analytical solutions for λ, N_o, and μ can be obtained. It is customary, for example, M_o (concentration) to be used as one parameter to characterize the IPSD and formulate a bulk microphysics scheme (e.g., *Ferrier* 1994; *Kong and Yau*, 1997; Morrison *et al.* 2005). However, as suggested in the above equations, for a given parameter, several solutions can be obtained, and thus the accuracy of the solution depends on the chosen moments. For example, three solutions of μ, μ_1, μ_2 and μ_3 can be given as

$$\mu_1 = \frac{2M_1^2 - M_0 M_2}{M_0 M_2 - M_1^2} \qquad \text{(8e)}$$

$$\mu_2 = \frac{3M_2^2 - 2M_1 M_3}{M_1 M_3 - M_2^2} \qquad \text{(8f)}$$

$$\mu_3 = \frac{4M_3^2 - 3M_2 M_4}{M_2 M_4 - M_3^2} . \qquad \text{(8g)}$$

Similarly four different solutions of λ can be obtained using Eq. 8d, as

$$\lambda_1 = \frac{(\mu+1) M_0}{M_1} , \quad \text{(8h)} \qquad \lambda_2 = \frac{(\mu+2) M_1}{M_2} \quad \text{(8i)}$$

$$\lambda_3 = \frac{(\mu+3) M2}{M_3} , \text{(8j)} \; \lambda_4 = \frac{(\mu+4) M_3}{M_4} . \qquad \text{(8k)}$$

Using the entire observed IPSD (2050 30s averaged spectra), several moments were derived using Eq. 8d. The calculated values of μ_1 and μ_2 Eq. 8 (e and f) are plotted against μ_3 (Eq. 8g) in Fig. 1a. As indicated in the figure, there are significant differences among these three solutions and it is not always clear which pair of solutions to choose that best describe the IPSD. In panel b, the slope parameters in Eq. 8 (h, i, j and k) are plotted against the observed values based on an exponential mean square fit, that is assuming μ=0. When the higher moments are used for deriving λ, the estimated values get closer to the observed values suggesting that it is more appropriate to use higher moments than the lower moments, particularly λ_3, and λ_4 appear to be reasonable. The N_{03} and N_{04} values corresponding to λ_3 and λ_4 derived using Eq.8c as a function of M_2, M_3 and M_3, M_4 respectively are also given in panel c, and generally agree with observation although there some discrepancies at the lower and higher ends of N_0 values.

For cloud droplets, *Smith* (2003) has suggested that the appropriate moments to be used would be M_2 and M_3, or M_3 and M_4 (Eq. 8g), which seems to be consistent with the above results although the physical meanings of the moments differ for ice particles depending how the particle size is defined. Following his suggestion, the intercept (N_o) and slope (λ) parameters which would correspond to μ_3 (dropped the subscripts for simplicity) given above can be formulated respectively as

$$N_o = \frac{M_3(\mu+4)^{4+\mu}}{\Gamma(\mu+4)}\left(\frac{M_3}{M_4}\right)^{(\mu+4)} . \qquad (9a)$$

$$\lambda = \left(\frac{\Gamma(\mu+3)N_o}{M_2}\right)^{1/(3+\mu)}$$

An exponential form of Eq. (9a) can be obtained by setting μ=0

$$N_o = \frac{128 M_3^{\,5}}{3 M_4^{\,4}} \qquad (9b)$$

$$\lambda = \left(\frac{2N_o}{M_2}\right)^{1/3} ,$$

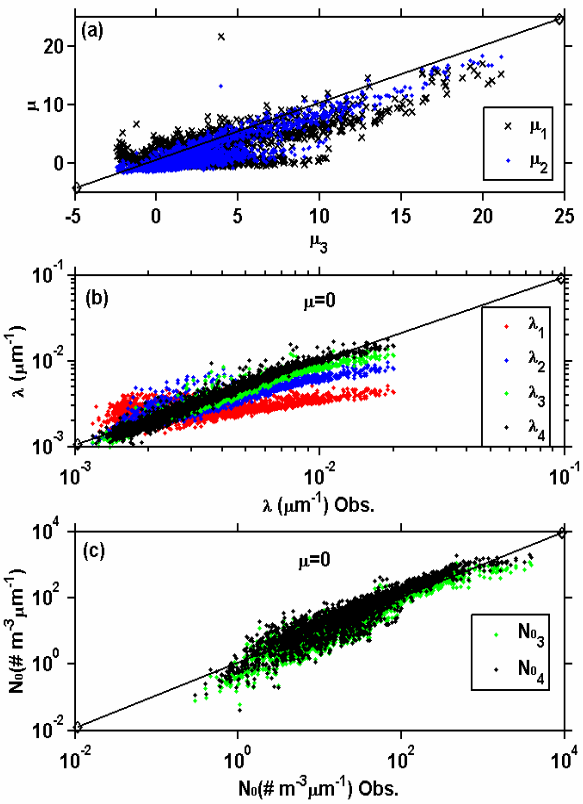

Figure 1. The dispersion parameters of μ_1, μ_2 and μ_3 derived in Eq.8 (e, f, and g) are plotted against μ_3 (panel a), slope parameters (λ_1, λ_2, λ_3, and λ_4) in Eqs. (8j, 8k, and 8l) are plotted against the observed values based on exponential mean square fit assuming μ=0 (panel b), the intercept parameter N_{03} and N_{04} associated with λ_3 and λ_4 are given in panel c .

Figure 2 shows comparisons of the gamma versus the exponential distribution as given in Eqs. 9a and 9b. The figure shows a 30s averaged spectra measured during each of the four field projects. All of the cases show that an exponential function agrees much better than the gamma distribution function for capturing the IPSD, the gamma function has a tendency to underestimate the concentration of the smaller ice particles. Therefore, based on these results a gamma distribution function does not appear to be suitable for characterization of ice particles in the size range considered in this work.

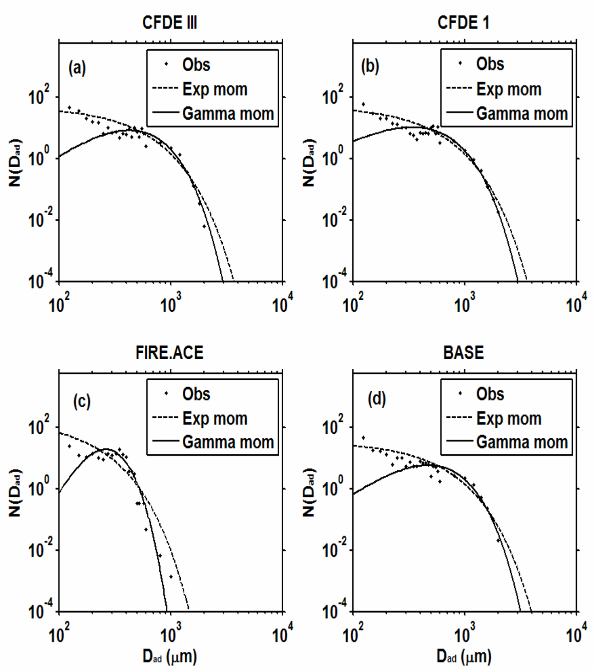

Figure 2. Comparisons of gamma (Gamma mom) and exponential distribution (Exp mom) as given in Eqs. 9a and 9b against observation.

In practice, however, knowing all these moments, the size distribution can be derived for any assumed function.

3.2 Geographical and temperature dependence of PSD

Figure 4 shows the probability distributions of N_o, λ, M_2, M_0, D_{43} and D_{32} both in the Arctic (AR) and mid-latitude (ML) clouds within similar temperature intervals of -30 ^oC ≤ T ≤ -15 ^oC and -15 ^oC ≤ T < 0 ^oC which are referenced as the colder and warmer interval respectively. It is interesting to note that all of the parameters show a Gaussian distribution within the considered temperature intervals. The mean sizes (panels e and f) and λ (panel b) vary with temperature, with no significant dependence on geographical region. On the other hand, N_o show both temperature and geographical dependence. The second moment, M_2 (related to mass) shows very little temperature dependence, but varies with location. For example, the mean values of N_o increase from 39 to 173 $\#m^{-3}\mu^{-1}$ in ML clouds and 9 to 100 $\#m^{-3}\mu^{-1}$ in AR clouds going from warmer to colder temperature interval showing both strong temperature and geographical dependence. The concentration (M_0), however, show very little temperature dependence. The mean values of M_0 vary anywhere between 9.17 and 10.17 l^{-1} within the colder and warmer temperature intervals respectively. The ML clouds, however, on average have 3 times more M_0 than the AR clouds. This may be explained partly due to difference in aerosol particle distribution between these two locations.

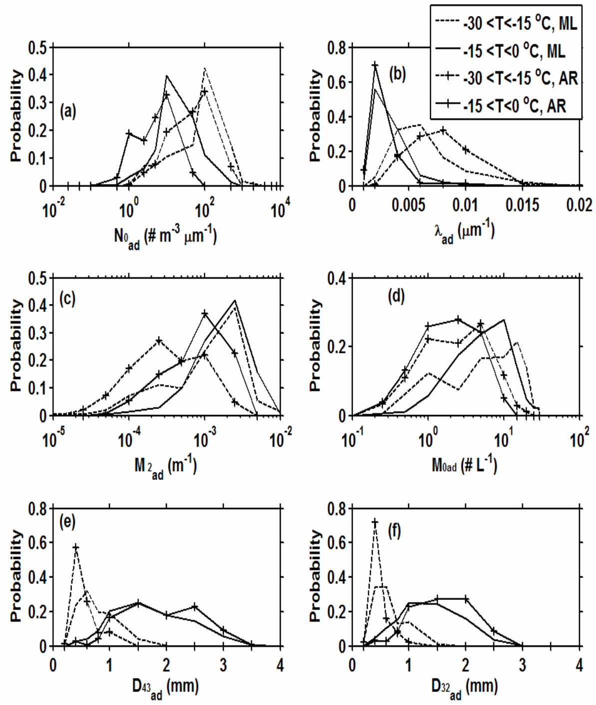

Figure 4. The probability distribution of N_0 (panel a) and λ (panel b) for exponential PSD, M_2 (panel c), M_0 (panel d), the mean particle sizes D_{43} and D_{32} (panels e and f) for both AR and ML clouds. Here only ad PSDs are shown.

The mean values of M_2 increase from 0.0018 m^{-1} to 0.0023 m^{-1} in ML cloud and from 0.0007 m^{-1} to 0.0011 m^{-1} in AR clouds going from cold to warmer temperatures showing more than a factor 2 difference between these two regions. Since the mean sizes of ice particles do not exhibit a significant dependence on geographical location, the lower M_2 values in AR clouds as compared to ML clouds maybe attributed to a change in concentration. However, as illustrated in Fig. 5 (panels a, b, c, and d), the maximum particle size measured ($D_{ad_{\max}}$ and $D_{md_{\max}}$) in a given 30s period (panels a and b), and mean sizes ($D_{43_{md}}$ and $D_{43_{ad}}$) show a temperature dependence. Since there are no significant variations in these parameters between AR and ML clouds, they are parameterized in terms of temperature alone using the averaged combined data sets and they are given in Table 2. However, as shown in the figure, there is significant scatter in the data and hence these parameterizations are merely approximations. However, the parameterization of N_o and λ requires both temperature and M_2 in order to be applied in both AL and ML ice clouds.

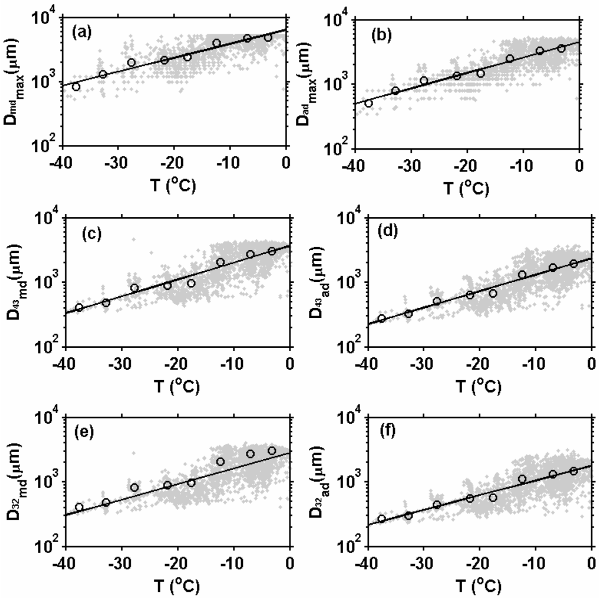

Figure 5. The maximum particle size (panel a for ad) and (panel b for md), mean sizes (panels c, d, e and f, see the text) are plotted against T. The best fit lines of the mean data are shown by the solid lines and the mean values are shown by black circles (see Table 2).

Figure 6 shows the temperature dependence of λ (panel a, b, c, d) and N_o (panel e, f, g, and h) derived based on least square fits of the observed 30s averaged data both in the mid-latitude (ML) and Arctic (AR) regions. Generally the AR data extend to colder temperatures (T < -30 °C) while the MD data sets are biased towards the warmer temperatures. Both λ and N_o show a temperature dependence regardless of where the data were collected as discussed earlier. However, it should be noted that there is considerable scatter in the data, hence temperature alone may not be sufficient for IPSD parameterization.

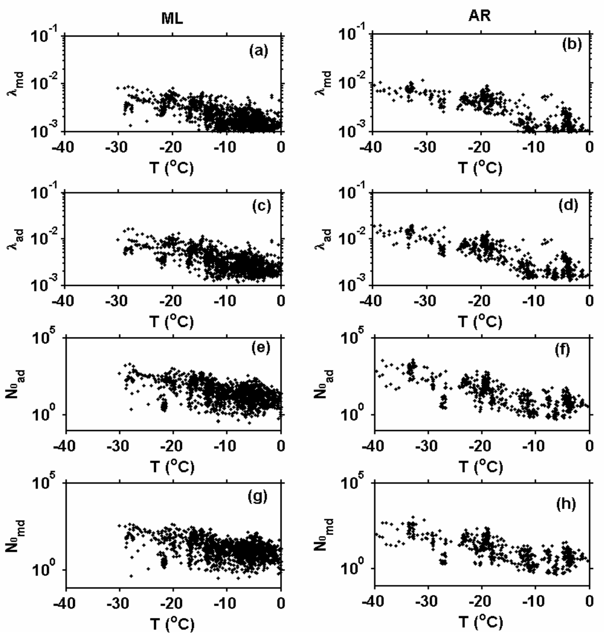

Figure 6. Temperature dependence of λ (panels a (for md) and b (for ad)) and N_o (panels c and d) for Arctic (AR) and mid-latitude (ML) clouds.

This study is consistent with earlier studies that showed λ increases with decreasing temperature for particles sizes (D>20 µm) based on measurements in mid-latitude cirrus clouds (*Heymsfield and Platt* 1984). For the same particle size rage, *Ryan* (2000) parameterized ice crystal sizes distribution using an exponential distribution function, and λ is parameterized as a function of temperature (also increases with decreasing temperature) based on several measurements including the one reported by

Heymsfield and Platt, (1984), *Ryan,* (1996), and Platt, (1997). A recent study by *Heymsfield et al.,* (2002), based on observations in deep tropical and sub-tropical stratiform clouds, also show that both λ and N_o increase with decreasing temperatures for particles sizes (D>33µm). *Field et al,* (2005) found a strong correlation between temperature and N_o. However, the *McFarquhar and Heymsfield*, (1997) parameterization of large particle mode (D>100 µm) assumes that these particles are characterized by a lognormal distribution function, and the distribution is strongly dependent on IWC, but with some weak dependence on temperature. It should also be noted that the *McFarquhar and Heymsfield*, (1997) large particle mode parameterization includes only 2D-C measurements with particle sizes (D<800 µm). The use of 2D-C probe measurements alone may be enough in the absence of large ice particles, but the 2D-C probe may give low concentrations of large particles because of its limited sample volume, which results in poor sampling. The technique of *Heymsfield and Parrish,* (1978) can be used to extend the sample volume of the 2D-C probe and improve the limitation, but it is really necessary to include data from the 2D-P probe, because of its larger sampling volume (and size range). It is worth mentioning that for exponentially distributed ice particle spectra, the total concentration is calculated as $M_o = N_o / \lambda$. Both of these parameters increase with decreasing temperature which in effect keeps M_o relatively unchanged with temperature which may partly explain the results in Fig. 4.

3.3 Least square fit method

Figure 7 shows the mean λ (panel a) and N_o (panel b) values derived using the least square fit method assuming an exponential distribution function. The data is divided into five temperature intervals for the combined data set. For a given M_2, both λ and N_o increase with decreasing temperature.

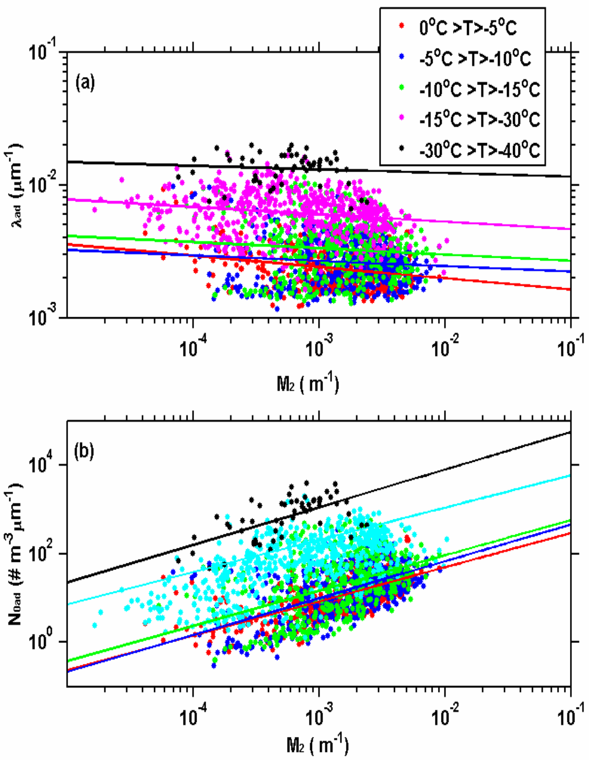

Figure 7. The slope (λ_{ad}) and intercept ($N0_{ad}$) parameters derived assuming an exponential PSD using the combined data set segregated based on temperature are plotted against the second moment ($M2_{ad}$). The symbol ad indicates that the IPSDs are arranged according to their projected area equivalent diameter (see the text).

The physical interpretation of decreasing λ with increasing temperature suggests increasing particle size as a result of aggregation or depositional growth with increasing temperature. Increasing N_o with decreasing temperature implies the production of small ice particles. For a given temperature, $\lambda(N_o)$ decrease (increase) with increasing M_2, which suggests that increasing M_2 may be associated with an increase in both ice particle production, ice particle growth via vapor deposition and aggregation processes.

Based on Fig. 7, the power law relationships (*Boudala and Isaac*, 2006a,b) are derived as

$$N_o = n_a(T) M_2^{\,n_b} \tag{11a}$$

$$\lambda = \lambda_a(T) M_2^{\,\lambda_b}\,, \tag{11b}$$

where the coefficients $n_a(T)$ and $\lambda_a(T)$ are related to temperature (T) and λ_b are n_b some constants. Table 1 defines these parameters with specified coefficients. Here T is the cloud temperature in °C, and M_2 is given in m^{-1}. Figure 8 shows some examples of comparisons of the parameterization of IPSD based on a 30s averaged observed spectra taken from each of the four projects shown earlier in Fig. 2. The parameterization (Pram.) reasonably captures the observed spectra (Obs) although there are some divergence at the small size end of the spectrum.

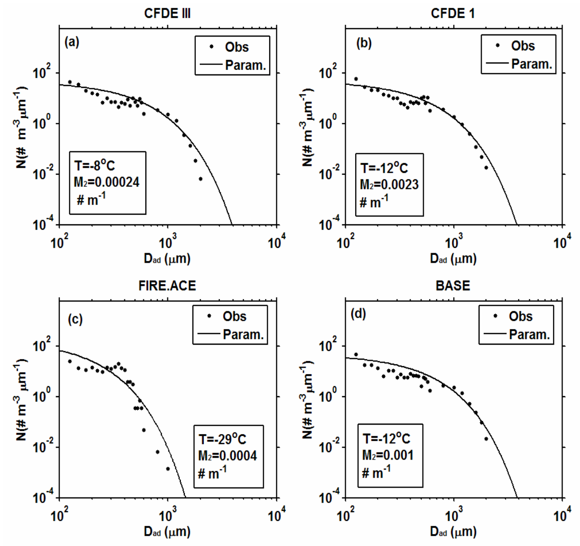

Figure 8. Comparisons of the parameterization (Param.), with the observed 30s spectra (Obs) taken from each of the four projects.

Using the new parameterization, various physical parameters such as radar reflectivity factor, and precipitation can be derived using a similar method adapted by *Boudala et al.,* (2006). For example, the radar reflectivity factor (Z) and liquid water equivalent snow fallrate (S), visible extinction coefficient (σ) can be give respectively as

$$Z = \left(\frac{6}{\pi\rho_i}\right)^2 \frac{N_0 d^2 \Gamma(2c+1)}{\lambda^{2c+1}} \tag{11c}$$

$$S = \frac{3.6 a d N_0 \Gamma(c+b+1)}{\lambda^{c+b+1}} \tag{11d}$$

$$\sigma = \frac{\pi N_0 \Gamma(3)}{2\lambda^3}\,, \tag{11e}$$

where ρ_i is the density of pure ice and the coefficients a, b, c and d are associated with particle mass ($m(D)$) and terminal velocity ($v(D)$) and the coefficients associated with the parameterization are given in Table 2. As mentioned earlier, Table 1 gives the coefficients for λ and N_0. Figure 9 shows comparisons of Z (panel a), snow precipitation (S) (panel b), and extinction coefficient (σ) (panel c) derived using the observed spectra assuming an ice particle spectra with the equivalent projected area diameter, ad .

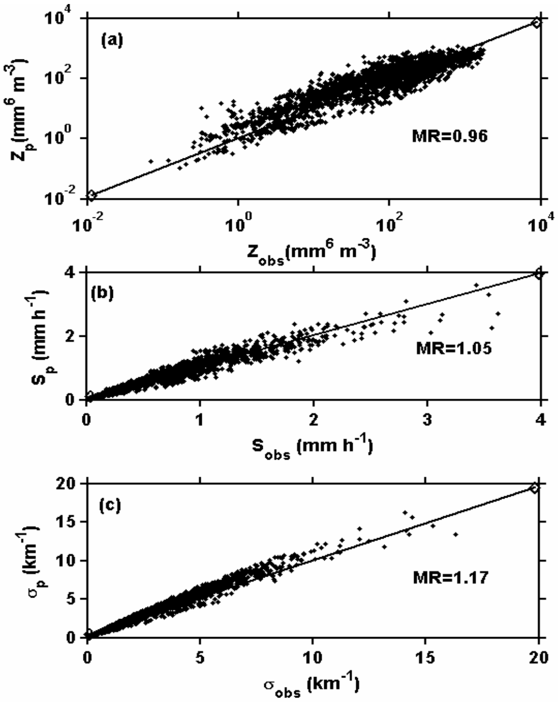

Figure 9. Radar reflectivity factor (Z_p), snow precipitation rate (S_p) and extinction coefficient (σ_p) derived using the parameterization assuming an exponential shape (see Eq. 11c,d,e) are compared to the values derived using the observed spectra .

The agreements are quite good. Based on the calculated mean ratios (MRs), both ratios Z and S are very close to unity, but for the parameterized σ, the MR is about 17% larger than the one calculated from the observed spectra. Note that in the case of the parameterization the spectra is integrated from zero to infinity, hence technically the small particles (D≤100 µm) are included and thus the 17% difference in σ is not surprising. It is worth noting here that for some practical applications, it is possible to get the upper limit of the integration by using the parameterizations $D_{mdmax}(T)$ or $D_{admax}(T)$ (see Table 2) that gives on average the maximum possible size of ice particle that can be measured at a given temperature (T).

3.4 Normalization of IPSD and the practical applications

Testud et al. (2001) have suggested a normalization approach for parameterization of droplet size distribution and this approach has been recently extended by *Delanoë et al*., (2005) to be used for IPSD by considering a melted equivalent diameter of a given ice particle size. A similar approach can be adapted here for ice particles without characterizing ice particles by their melted equivalent diameters. The normalization procedure starts with assuming the size distribution, $N(D)$ is normalized in a form

$$N(D) = N_0^* F(D/D_m)\,, \tag{12a}$$

where D_m is ad or md as defined earlier, N_0^* is the scaling parameter for concentration, D_m is the scaling parameter for diameter, which is similar to D_{43} given earlier for liquid drops (see *Testud et al*., 2001), and $F(D/D_m)$ is the shape of the normalized PSD. For spherical particles D_{43} is a mass weighted particle mean diameter. However, based on our assumption of ice particle mass, D_m can be set to D_{32} since this is how the mass weighted particle diameter is defined in this paper. Therefore, the mass weighted diameter for ice particles can be written as

$$D_m = \frac{\int_0^\infty D^3 N(D)dD}{\int_0^\infty D^2 N(D)dD}\,. \tag{12b}$$

The ice water content (IWC) can be given as

$$IWC = d\int_0^\infty D^2 N(D)dD\,, \tag{12c}$$

where d is constant (see Table 2). Using 12a and 12b, it can be concluded that

$$\int_0^\infty X^3 F(X)dX = \int_0^\infty X^2 F(X)dX \tag{12d}$$

where $X = D/D_m$. Using Eqs. (12b and 12c), the second moment of the normalized IPSD can be given as

$$\int_0^\infty X^2 F(X)dX = \frac{IWC}{dD_m^{\,3} N_0^*}\,. \tag{12e}$$

Note that no assumption about the functional shape of the IPSD have been specified in the above derivations. In order that the normalized IPSD be independent of IWC and D_m, it was chosen so that the second moment of normalized IPDS given below is assumed to be constant (con).

$$\int_0^\infty X^2 F(X)dX = con\,. \tag{12f}$$

This constant has been chosen so that the scaling parameter N_0^* is the same as N_0 of the exponential size distribution that yields $con = 2/3^3$. Note also that con is also different for cloud droplets as given by *Testud et al*.(2001) . Using Eqs. (12d and 12e), N_0^* can be given as

$$N_0^* = \frac{3^3}{2}\frac{IWC}{D_m^3 d} = \frac{3^3}{2}\frac{M_2}{D^3_m}\,. \tag{12g}$$

Knowing that for exponential PSD $D_m = 3/\lambda$ and $N_0^* = N_0$, the normalized form of exponential PSD can be given as

$$F(X) = \exp(-3X)\ . \qquad (13a)$$

For gamma type of PSD, D_m and N_0^* are given respectively as

$$D_m = \frac{\Gamma(4+\mu)}{\Gamma(3+\mu)\lambda} = \frac{3+\mu}{\lambda} \qquad (13b)$$

$$N_0^* = \frac{3^3 N_{og} D_m{}^{\mu} \Gamma(3+\mu)}{2(3+\mu)^{3+\mu}}\ . \qquad (13c)$$

With the above expressions, the normalized PSD can be given as

$$F_\mu(X) = \frac{2(3+\mu)^{3+\mu}}{3^3\Gamma(3+\mu)} X^{\mu} \exp(-X(3+\mu))\ . \qquad (13d)$$

Figure 10 shows a comparison between N_0^* for exponential PSD and N_0 directly derived from least square fit of the data, for ad (panels a and c) and N_0^* and D_m relationships (panels b and d).

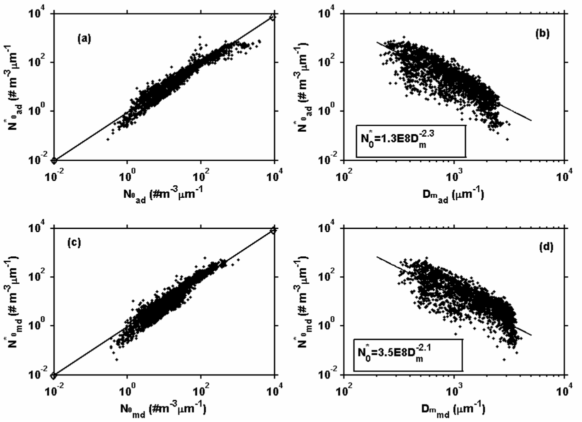

Figure 10. The normalization intercept parameters ($N^*{}_{ad}$ and $N^*{}_{md}$) and mass weighted averaged diameters ($D_{m_{ad}}$ and $D_{m_{md}}$) are compared with the corresponding parameters derived assuming an exponential function using the least mean square fit and moment methods respectively. The relationships between D_m an $N^*{}_0$ are also provided. The meaning of the symbols md and ad are given in the text.

The intercept, N_0^* reasonably agrees with N_0 although there are some discrepancies at the end points. Generally N_0^* decreases with increasing D_m as would be expected, but it is evident that there are significant scatter in the plots. Analogues to Eq. 8, the general expression for moments of order i for the normalized IPSD can be specified as

$$M_i = \int N_0^* F(D/D_m) dD \ = \ N_0^* D_m{}^{i+1} \xi_i \qquad (14a)$$

where the parameter ξ_i is given as

$$\xi_i = \int X^i F(X) dX\ . \qquad (14b)$$

Following *Testud et al*. (2001), the relation between two moments of orders of n and j similar to Eq. 8d can be defined as

$$\frac{M_n}{N_0^*} = \xi_n \xi_j{}^{[-(n+1)/(j+1)]} \left(\frac{M_j}{N_0^*}\right)^{[(n+1)/(j+1)]}\ . \qquad (14c)$$

Equation (14c) can be applied for deriving power law relationships between two meteorologically relevant quantities. For example, the radar reflectivity factor (Z) and snow precipitation rate (S) can be calculated respectively as $Z = k_1 M_4$ and $S = k_2 M_{2.25}$, where $k_1 = (6/\pi \rho_w)^2 d^2$ (see *Boudala et al.* 2006) and $k_2 = 3.6da$ (see Table 2). Using equation (14c), one can get a power low relationship between Z and S as

$$Z = N_0{}^{*-0.54} k_1 k_2{}^{-1.54} \xi_4 \xi_{2.25}{}^{-1.54} S^{1.54}\ . \qquad (15a)$$

Assuming an exponential distribution, $N_0{*} = N_0$, $\xi_{2.25} = 0.072$ and $\xi_4 = 0.099$, and using appropriate md or ad columns in Table 2, and Eq. (15a) reduces to

$$Z = 169 N_{0_{md}}{}^{-0.54} S^{1.54}$$
$$Z = 1276.91 N_{0_{ad}}{}^{-0.54} S^{1.54}\ , \qquad (15b)$$

where Z is given in $mm^6\ m^{-3}$, S is given in $mm\ h^{-1}$ and N_0 is given # $\mu m^{-1} m^{-3}$. The exponent 1.54 is similar to the one found by

Boudala et al. (2006). This expression is excellent for retrieving Z or S provided that N_0 is parameterized. For exponential PSD, Eq. (11a) can be used. However, in most cases M_2 is not known although the temperature can be measured or modeled. As shown in Fig. 4, N_0 can be related to temperature, but there is considerable scatter. It is relevant to mention that the earlier parameterizations such as *Sekhon and Strivastava,* (1970) relate N_0 to precipitation alone, but as shown in the above expression and earlier discussions it may require one other parameter to adequately estimate N_0. The other approach is to use Eq. (14a). In this case Z is linearly related to S as

$$Z = 1.36\text{x}10^{-4} D_{m_{md}}^{\ 1.75} S \quad \text{or} \qquad (15c)$$

$$Z = 9.89\text{x}10^{-4} D_{m_{ad}}^{\ 1.75} S \,,$$

where D_m is given μm and S is given in $mm\ h^{-1}$. Note that there is relatively good relationship between D_m and temperature and thus the parameterization given earlier maybe used as an approximation. Using Eqs. (14c) and (14a) one can also define many other relationships between two meteorologically relevant moments such as extinction coefficient σ (see Table 2) and Z , which may be given as

$$Z = kN_0^{\ *-2/3} \xi_4 \xi_2^{\ -5/3} \sigma^{5/3}$$

$$S = k' \frac{\xi_{2.25}}{\xi_2} D_m^{\ 1/4} \sigma \,, \qquad (15d)$$

where N_0 is associated with an exponential PSD and k' and k are constants. The units S, Z , and D_m are as before, but σ is given km^{-1}. After some simplifications using constants in Table 2, we get

$$\text{Z}{=}160.43 N_{0_{ad}}^{\ -2/3} \sigma_{ad}^{\ 5/3} \qquad (16a)$$

$$S = 0.039 D_{m_{ad}}^{\ 1/4} \sigma_{ad} \,. \qquad (16b)$$

Figure 11 shows Z calculated using Eq. (15c) with D_m (T) parameterized as a function of temperature alone (panel a) and derived D_m (panel b), and liquid water equivalent snowfall rate (S) based on Eq. 16b with D_m (T) (panel c) and with derived D_m compared with derived Z and S from observed spectra. Although D_m (T) generally gave reasonable values of Z as compared to the observation, there are considerable uncertainties at lower and higher ends of the observed Z values as compared to panel b when the observed D_m was used which for which agreement with observation is excellent. The use of D_m (T) is relatively better for estimating S (panel c) although it is quite clear from panel d that the use of D_m (T) slightly underestimates S at higher S values, and the observed D_m improves the result (panel d). The extinction coefficient can be also be calculated based on the observed ice particle spectra categorized according to their maximum diameter by assuming aggregates of planer polycrystals (*Mitchell* 1996) (see Table 2) or assuming other similar shapes. According to this study, the assumption of planar polycrystals agreed quite well with observation (not shown here).

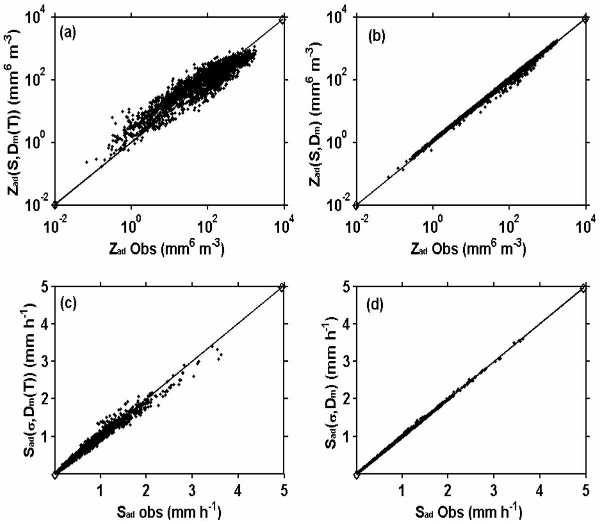

Figure 11. Z derived using Eq. 15c and $D_m(T)$ parameterized as a function of T (see Table 2) (panels a and b) and using the observed D_m (panel b), S based on Eq. 16b with $D_m(T)$ (panel c) and with D_m (panel d) are plotted against the values derived based on the observed (Obs) spectra.

We can test the relationship given in (16b) knowing $D_{m_{ad}}$ based on T, and σ_{ad} and S from observations. Figure 12 shows snow precipitation measured in a location north of Toronto, Canada during three winters between 2005 and 2007 (*Boudala and Isaac* 2007). The VAISALA FD12P probe is plotted against the estimated precipitation using Eq. (16b). The FD12P probe applies a principle of forward scattering near infrared radiation capacitance method (*Boudala and Isaac* 2007) for determination of visibility and S.

Table 1. The coefficients used for PSD parameterizations for both ice particles categorized according to their projected area equivalent and maximum diameter.

Projected area equivalent diameter (ad)

$N_0 = a_0 \exp(b_0 T) M_2^{c_0}$	$\lambda = a_\lambda \exp(b_\lambda T) M_2^{c_\lambda}$
$a_0 = 828$	$a_\lambda = 1.26\text{E-}3$
$b_0 = -0.146$	$b_\lambda = -5.45\text{E-}2$
$c_0 = 0.74$	$c_\lambda = -5.82\text{E-}2$

Maximum diameter (md)

$a_0 = 218.248$	$a_\lambda = 6.713\text{E-}4$
$b_0 = -0.123$	$b_\lambda = \text{-}4.862\ \text{E-}2$
$c_0 = 0.69$	$c_\lambda = \text{-}1.025\text{E-}1$

The mass weighted mean diameter D_m was estimated based on temperature measured at a 2 m height during the snow events. The extinction coefficient, σ is estimated from measured visibility using the FD12P probe as $\sigma = 3/vis$, where vis is the visibility in km. The mean ratio (MR) is close to unity and the correlation coefficient, r is near 0.8. However, the FD12P measurement gave slightly higher values, particularly during heavy precipitation periods. This discrepancy could be attributed to many unknown factors such as particle fall velocity, but one of the obvious reasons for this difference is that the parameter D_m is estimated from temperature alone and hence as indicated earlier this has an effect of under estimating the precipitation rate at higher S values.

Table 2: Parameterizations of various ice microphysical properties of ice clouds based on projected area equivalent and maximum diameter of PSDs and some coefficients used in this paper.

Maximum D (md)	Projected area Equivalent D (ad)
$D_{md_{max}}=6518.72\exp(0.05T)$	$D_{ad_{max}}=4574.67\exp(0.055T)$
$D_{43_{md}}=3755.86\exp(0.06T)$	$D_{43ad}=2380.59\exp(0.059T)$
$D_{32md}=2862.03\exp(0.056T)$	$D_{32ad}=1803.74\exp(0.053T)$
$m = d\ D^c$ (mass)	$m = dD^c$
$v = aD^b$ (terminal velocity)	$v = aD^b$
$A = \gamma D^\alpha$ (projected area)	$A = \pi D^2 / 4$
$\sigma = 0.2A_c$ (visible extinction)	
$k_1 = (6/\pi\ \rho_w)^2\ d^2$	$k_1 = (6/\pi\ \rho_w)^2\ d_a{}^2$
$k_2 = 3.6da,\ \sigma = \gamma M_{1.88}$	$k_2 = 3.6da,\ \sigma = 0.5\pi M_2$
$a = 0.86\ m\ s^{-1} mm^{-b},\ b = 0.25$	$a = 0.86\ m\ s^{-1} mm^{-b},\ b = 0.25$
$d = 4.23\text{x}10^{-5}\ g\ mm^{-c},\ c = 2$	$d = 1.14\text{E-}4\ g\ mm^{-c},\ c = 2$
$\gamma = 0.2285\ cm^{2-\alpha},\ \alpha = 1.88$	

The other reason could be the fact that the parameterization is highly dominated by the measured optical extinction or visibility by employing a forward scattering principle which doesn't take into account factors like absorption and diffraction of light. Although there are some uncertainties in the data, these results are very encouraging considering that the parameterizations were developed based on aircraft data and uncertainties in the measurement techniques employed by the probes.

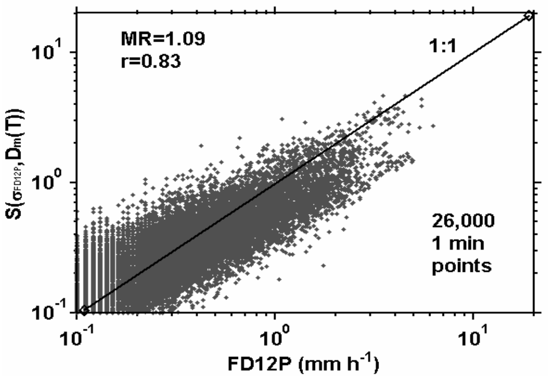

Figure 12. S derived using (Eq.16b) compared with surface observations using the FD12P precipitation probe.

4. SUMMARIES and CONCLUSIONS

Ice crystal spectra measured in continental and maritime stratiform clouds during four field projects conducted in the Arctic and mid-latitude regions have been analyzed. The ice particles sizes (D>100 µm) and concentration were measured using the PMS 2D-C and 2D-P probes. The measured ice particles were segregated based on air mass type, geographical location, and temperature (T). The IPSD were categorized in terms of their maximum and projected area equivalent diameters. Using the entire data set and employing the moment and mean square fit methods the slope (λ), intercept (N_o) and dispersion (μ) parameters have been derived assuming Gamma and exponential ($\mu = 0$) distribution functions. Mass weighted mean diameter (D_m) and maximum measured diameter ($D_{\max}$) of the IPSD for varies locations and temperatures have been derived. In this study the following observations have been made:

- It has been demonstrated that the exponential function fits the IPSD better than the Gamma distribution function for the size range considered in this study (D > 100 µm). The Gamma distribution function tends to underestimate the concentration of the small size end of the spectrum.

- For the moment method, it was better to use higher moments such as M_2, M_3, and M_4 than the lower moments such as M_0 and M_1 for characterization of IPSD.

- It was found that no significant dependence of λ or maximum ($D_{\max}$) and mean (D_m) diameters on geographical location. However, on average the values of N_o in the Arctic clouds are lower than the mid-latitude clouds by a factor of 2 or 3, depending on temperature. The ice mass derived in the Arctic clouds is smaller than the mid-latitude regions. Generally, on average, for a given temperature, λ (N_o) decrease (increase) with increasing ice mass. On average, however, both the mean particle and a maximum particle sizes are increasing with increasing T.

- In agreement with the previous observation (*Gultepe et al*. 2001), the ice particle number concentration (M_0) show very little temperature dependence, but the ML clouds on average have 3 times more M_0 than the AR clouds.

- Based the above information, parameterizations have been developed, (a) by assuming an exponential shape, (b) a gamma distribution function and (c) by adapting the normalization approach originally introduced by *Testud et al.* (2001) for cloud droplets PSD to IPSD. The relevant IPSD parameters are related to M_2 (related to mass) and temperature following *Boudala and Isaac,* (2006). These parameterizations agree reasonably well with the measured spectra. The derived quantities using these parameterizations such as extinction coefficient, reflectivity factor, and water equivalent snow precipitation rate reasonably agreed with the directly derived values.

- For the normalization approach, it has been suggested that the parameter D_m may be added into the traditional $Z-S$ and $\sigma-S$ power law relationships. The mass weighted mean diameter was related to temperature (D_m(T)). It was found that the addition of D_m derived from temperature improves the $\sigma-S$ relationship better than the $Z-S$ relationship. The comparison of the parameterization $S(\sigma, D_m(T))$ derived using surface based observations of T and σ against precipitation measured using the VAISALA FD12P precipitation probe shows reasonable agreement.

ACKNOWLEDGEMENTS

This work was funded by the National Search and Rescue Secretariat, and Transport Canada, The data were collected using the Canadian National Research Council (NRC) Convair-580 and the authors are grateful to their NRC colleagues for their assistance. These data sets were funded from the organizations listed above as well as the Panel on Energy Research and Development, as well as from U.S. sources including the Boeing Commercial Airplane Group, the National Aeronautics and Space Administration (NASA), and the Federal Aviation Administration (FAA).

5. REFERENCES

Boudala, F. and G. Isaac, 2007: Determining snowfall rate and visibility from reflectivity for winter nowcasting of precipitation and visibility. The 33rd International Conference on Radar Meteorology , Cairns, Australia, Aug. 6-10, 2007.

Boudala, F. S., G. A. Isaac, and D. Hudak 2006: Ice water content and precipitation as a function of equivalent radar reflectivity and temperature based on in- situ observations. *J. Geophy. Res*., **111**, D11202, doi:10.1029/2005JD006499.

Boudala, F. S., and A. G. Isaac ,2006a: Bulk microphysics parameterization of ice fraction for application in climate models. *Q. J. R. Meteorol. Soc*., **132**, 2377--2392

Boudala, F. S., and A. G. Isaac ,2006b: Replacing the Meyers et al. formula in bulk ice microphysics schemes in Canadian mesoscale models. Included in CD-ROM for the AMS 12th Conference on Cloud Physics Madison, Wisconsin, 10-14 July 2006

Boudala, F. S., A. G. Isaac, Q. Fu, and S. G. Cober, 2002: Parameterization of effective particle sizes for high latitude clouds. *Int. J. Climatology* , **22**, 1267-1284.

Cober, S. G., G. A. Isaac, A.V. Korolev, and J.W. Strapp , 2001: Assessing cloud-phase conditions J. Appl. Meteor., **40**, 1967-1983.

Cooper W.A., 1977. Cloud Physics Investigation by the University of Wyoming in HIPLEX 1977, by William A. Cooper. Bureau of Reclamation Report No. AS 119, Aug. 1978, 321 pp. (available from the National Technical Information Service, Oper-ations Division, Virginia, 22151)

Cunningham M. R. (1978), Analysis of particle spectral data from optical array (PMS) 1D and 2D sensors. American Meteorological Society, Fourth Symposium . Meteorol. Obs. Instrument. Denver, USA, April 10-14, 1978, 345-350.

Delanoë, J., A. Protat, J. Testud, D. Bouniol, A. J. Heymsfield, A. Bansemer and P. R. A. Brown and R. M. Forbes , 2005: Statistical properties of the normalized ice particle size distribution. J. *Geophys. Res*., **110,** D10201, doi:10.1029/2004JD005405, 2005, 1-21.

Ferrier, B. S. , 1994: A double moment multiple phase four class bulk ice scheme. Part I: Description . *J. Atmos. Sci*., **51**, 249-290.

Field P. R., A. J. Heymsfield, and A. Bansemer , 2006: Shattering and Particle interarrival times measured by optical array probes in ice clouds. *J. Atmos. Oceanic Technol* in press.

Field P. R., R. J. Hogan, P. R. Brown, A. J. Illingworth, T. W. Choulrton, and R. J. Cotton(2005), Parameterization of ice particle size distributions for mid-latitude clouds. *Q. J. R. Meteorol. Soc*., **131**, 1997-2017.

Filed, P. R., R. Wood, and A. R. P. Brown , 2003: Ice particle interval rimes measured with FSSP. J*. Atmos. Oceanic Technol*., **20**, 249-261.

Gayet, J. F, F. Auriol, A. Minikin, J. Stro¨m, M. Seifert,3R. Krejci, A. Petzold, G. Febvre, and Ul. Schumann,, 2002:

Quantitative measurement of the microphysical and optical properties of cirrus clouds with four different in situ probes: Evidence of small ice crystals *Geophy. Res. Lett*., **29**, NO. 24, 2230, doi:10.1029/2001GL014342.

Gayet, J. F. and G. Febvre ,1996: The reliability of PMS FSSP in the presence of small particles. *J. Atmos. Oceanic Technol*., *13*, 1300-1310.

Gultepe, I., G. A. Isaac, and S. G. Cober , 2001: Ice crystal number concentration versus temperature. *Int. J. Climatology*, **21**, 1281-1302.

Heymsfield, A. J.,C. Schmitt, A. Bansemer, G.-J. V. Zadelhoff M. J. McGill, C. Twohy , and D. Baumgardner (2006), Effective radius of ice cloud particle populations derived from aircraft probes, *J. Atmos. Sci.* **23**, 361-380

Heymsfield, A. J., 2003: Properties of tropical and midlatitude ice clouds particle ensembles. Part I: Median mass diameter and terminal velocities. *J. Atmos. Sci.,* **60**, 2573-2591.

Heymsfield, A. J. , A. Bansemer, P. R. Field, S. L. Durden, and J. L. Smith,2002: Observations and parameterization of particle size distribution in deep tropical cirrus and stratiform precipitating clouds: Results from in situ observations in TRMM field campaigns. *J. Atmos. Sci*., **59**, 3457-3490.

Heymsfield, A. J. and C. M. R. Platt, 984: Parameterization of particle size spectrum of ice clouds in terms of ambient temperature and ice water content. *J. Atmos. Sci*., **41**, 846-855.

Heymsfield, A. J., and J. L. Parrish, 1978: A computational technique for increasing effective sampling volume of the PMS two dimensional particle size spectrometer. *J. appl. Meteorol*., **17**, 1566-1572.

Isaac, G. A., S. G. Cober, J. W. Strapp, A.V. Korolev, A. Tremblay, and D. L. Marcotte 2001: Recent Canadian research on aircraft in-flight icing. *Canadian Aeronautics and Space Journal*, 47-3, 213-221.

Ivanova, D., D. L. Mitchell, W. P. Arnott, M. Poellot, 2001: A GCM parameterization for bimodal size spectra and ice mass removal rates in mid-latitude cirrus clouds. *Atmos. Res*., **59**, 89-113.

Knollenberg, R.G. (1970),The optical array: An alternative to scattering or extinction for airborne particle size determination. *J. Appl. Meteor*., **9**, 86-103.

Kong, F., and M.K. Yau, 1997: An Explicit Approach to Microphysics in MC2. Atmosphere-Ocean, 35, 257-291.

Korolev A.V.,and G A Isaac, 2005: Shattering during sampling by OAPs and HVPS. Part 1: Snow particles. *J. Atmos. and Oceanic Technol*., **22** (5), 528- 542.

Knollenberg, R. G., 970:The optical array: An alternative to scattering or extinction for airborne particle size determination. *J. Appl. Meteorol*., **9**, 86-103.

Lawson, R. P., B. Baker, B. Pilson, and Q. Mo , 2005: In Situ Observations of the Microphysical Properties of Wave, Cirrus, and Anvil Clouds. Part II: Cirrus Clouds. *J. Atmos. Sci*., **63**, 3186

Levkov, B. Rockel, H. Kapitza , and E. Raschke, 1992: 3D mesoscale numerical studies of cirrus and stratus clouds by their time and space evolution. *Beitr. Phys. Atmosph*., **65**, 35-58.

Lohmann, U., and E. Roeckner, 1996: , Design and performance of a new cloud microphysics scheme developed for ECHAM general circulation model. *Climate Dyn.,* **12**, 557-572.

Locatelli, J. D. and P. V. Hobbs: 1974: Fall speeds and masses of solid precipitation particles. J. *Geophys. Res*., **79**, 2185-2197.

McFarquhar, G. M. and A. J. Heymsfield, 1997: Parameterization of tropical cirrus ice crystal size distribution and implication for radiative transfer: Results from CEPEX. *J. Atmos. Sci.,* **54**, 2187-2200.

Mitchell, D. L. , 1996: Use of mass –and area – dimensional power laws for determining precipitation particle and terminal velocity. *J. Atmos. Sci*., **53**, 1710-1723.

Mitchell DL, Zhang R, Pitter R. , 1990: Mass–dimensional relationship for ice particles and the influence of riming on snowfall rates. J*. of Appl. Meteor*. **29**, 153–163.

Platt, C. M. R.,1997: A parameterization of the visible extinction coefficient of ice clouds in terms of the ice water content. *J. Atmos. Sci.*, **54**, 2083-2098.

Morrison, H, Curry, J. A., Shupe, M. D, and P. Zuidema, 2005: A new double-moment microphysics parameterization for application in cloud and climate models. Part II: Single-Column Modeling of Arctic Clouds. *J. Atmos. Sci*., **62**, 1678-1693.

Rotstayn, D. L., B. F. Ryan, and J. J. Katzfey, 2000: A scheme of calculation of liquid fraction in mixed phase stratiform clouds in large-scale models. *Month. Weath. R*., **128,** 1070-1087.

Rutledge, S. A., and P. V. Hobbs ,1983: The mesoscale and microscale structure and organization of clouds and precipitation in mid-latitude cyclones. VIII: A model for “Seeder – Feeder” process in warm frontal rainbands. *J. Atmos. Sci*., **40**,1185-1206.

Ryan, B. E., 2000: A bulk parameterization of the ice particle size parameterization and the optical properties in ice clouds. *J. Atmos. Sci*., **57**, 1436-1451.

Ryan, B. E., 1996: On the global variation of precipitating layer clouds. Bull. Amer. Meteor. Soc., 77, 53-70.

Sekhon, S. R. and R.C. Srivastava (1970), Snow size spectra and radar reflectivity. *J. Atmos. Sci*., **27**, 299-307.

Smith, L. P., 2003: Raindrop size distributions: Exponetial or gamma-Does the difference matter? J. Appl. Meteor. **42**, 1031-1034.

Testud, J., Oury, S., Black, R. A., Amayenc, P. and Dou, X. K. (2001), The concept of ‘normalized’ distribution to describe raindrop spectra: A tool for cloud physics and cloud remote sensing. *J. Appl. Meteorol.*, **40**, 1118–1140.

EVALUATION OF GROUND-BASED REMOTELY SENSED WATER CLOUD PROPERTIES USING RADIATION AND AIRCRAFT IN-SITU MEASUREMENTS

Christine Brandau[1], Herman Russchenberg[1] and Wouter Knap[2]
[1]Delft University of Technology, The Netherlands,
[2]Royal Netherlands Meteorological Institute, De Bilt, The Netherlands
Corresponding author: c.l.brandau@tudelft.nl

1. INTRODUCTION

High temporal resolution of ground-based remote sensing measurements enables long-term observations of the effect of aerosols on cloud microphysical and optical properties on a regional scale. The greatest challenge of this possibility is to retrieve and to relate the relevant parameters involved in the processes from increased anthropogenic aerosol production to changes of the cloud albedo from the observations. Our work introduces a retrieval technique of microphysical (concentration, effective radius) and optical properties (extinction, optical thickness) of low level water clouds using different ground-based observations to obtain the temporal and spatial variation of water cloud properties. The crucial parameter in this technique is the retrieval of droplet concentration, which is an important indicator related to the physics of the first indirect aerosol effect (Twomey, 1977).

2. RETRIEVAL TECHNIQUE

2.1 Method

The retrieval technique of droplet concentration combines cloud radar, microwave radiometer, lidar and radio sounding measurements with a microphysical and thermodynamic model (Boers et al., 2006). In this model the cloud is described by a single-mode droplet distribution

$$N = \int_0^\infty n(r)dr \qquad \text{(EQ 1)}$$

N is the droplet concentration with an assumed gamma function for the droplet size distribution $n(r)$:

$$n(r) = \frac{D^\nu}{\Gamma(\nu)} r^{\nu-1} e^{-Dr} \text{ for r > 0} \qquad \text{(EQ 2)}$$

$\Gamma(\nu)$ is the gamma function, ν the breadth parameter and D the size parameter.

The vertical model also includes mixing effects and considers the sub-adiabatic structure of the cloud, which can be expressed by using the following definition of liquid water content (LWC):

$$LWC = \frac{4}{3}\pi\rho_w N \left\langle r^3 \right\rangle = f(h)LWC_{ad} = f(h)\rho_a A_{ad} h \qquad \text{(EQ 3)}$$

where $\left\langle r^3 \right\rangle$ is the third moment of the assumed droplet size distribution of $n(r)$:

$$\left\langle r^3 \right\rangle = \int_0^\infty n(r)r^3 dr / \int_0^\infty n(r)dr \qquad \text{(EQ 4)}$$

h is height above cloud base, ρ_w is density of water, ρ_a is density of air, A_{ad} is the adiabatic lapse rate of liquid water content mixing ratio depending on cloud base pressure and temperature. The subscript ad refers to the adiabatic value of the variable. The function $f(h)$ represents the sub-adiabatic fraction of liquid water content and it describes the variation of LWC with height from cloud base (cb) to cloud top (ct). Furthermore it can be attributed to variations in the droplet concentration N and in the third moment of the assumed droplet size distribution $\left\langle r^3 \right\rangle$.

The measured radar reflectivity factor from the cloud radar can be expressed by

$$Z = 64N\left\langle r^6 \right\rangle \qquad \text{(EQ 5)}$$

where $\left\langle r^6 \right\rangle$ is the sixth moment of the assumed droplet size distribution of $n(r)$:

$$\left\langle r^6 \right\rangle = \int_0^\infty n(r) r^6 dr \Big/ \int_0^\infty n(r) dr \qquad \text{(EQ 6)}$$

We can relate the reflectivity factor to our description of LWC of the cloud by using the well-know relation between the third and the sixth moment of the size distribution (e.g. Atlas et al., 1954 and Frisch et al., 1998). Considering the variation of LWC with height the relation results in:

$$\left\langle r^6 \right\rangle = k_6 f^2(h) \left\langle r^3 \right\rangle^2 \qquad \text{(EQ 7)}$$

The constant coefficient k_6 depends on the breadth parameter ν of the assumed Gamma size distribution

$$k_6 = \frac{(\nu+3)(\nu+4)(\nu+5)}{\nu(\nu+1)(\nu+2)} \qquad \text{(EQ 8)}$$

It is fixed on the basis of in-situ measurements of droplet size distributions (Miles et al., 2000).

Altogether we derive a functional form of the radar reflectivity factor:

$$Z(h) = k_6 \left(\frac{6}{\pi} \frac{\rho_a}{\rho_w} A_{ad} \right)^2 \frac{1}{N} f^2(h) h^2 \qquad \text{(EQ 9)}$$

depending on the height h, the adiabatic lapse rate A_{ad}, the droplet concentration N and the sub-adiabatic fraction function $f(h)$. In this equation $f(h)$ is attributed to variations in the third moment of the assumed droplet size distribution $\left\langle r^3 \right\rangle$ and we assume a constant droplet concentration N with height. This implies a homogenous mixing process, which means that the droplets evaporate to such a degree that the total amount remains the same. The derived vertical profile of the radar reflectivity factor enables an estimation of the droplet concentration N, where the greatest uncertainty is given in the unknown sub-adiabatic fraction function $f(h)$, which is a free parameter to be fixed.

2.2 Implementation

The provided method leads to different possibilities to derive the droplet concentration N. For example a least square regression of the functional form of reflectivity (EQ 9) and the measured radar reflectivity profile could be used to estimate $f(h)$ and the droplet concentration N.

The used implementation in this work involves an integrated approach by estimating the sub-adiabatic fraction function $f(h)$ under following conditions.

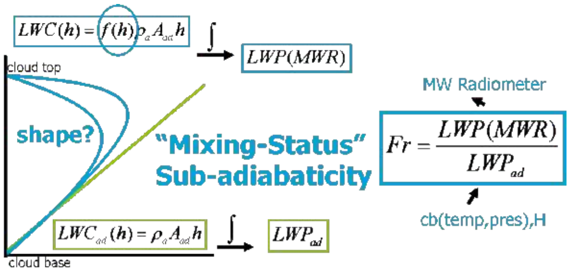

Fig 1: Schematic diagram to illustrate the estimation of the sub-adiabatic fraction function.

The adiabatic liquid water content (LWC_{ad}) is related to the maximum amount of water a cloud with a certain geometrical thickness could hold. It is a linear function with height from cloud base to cloud top and it is depending on cloud base pressure and temperature (Fig. 1 green line). But it is well-known that on average clouds are not adiabatic in nature. This can be expressed by our defined sub-adiabatic fraction function $f(h)$, which describes the variation of LWC with height and it is an unknown parameter (Fig. 1 light blue). This parameter can be fixed by using the integrated LWC from cloud base to cloud top:

$$LWP(MWR) = \int_{cb}^{ct} \rho_a A_{ad} f(h) h dh = Fr\, LWP_{ad} \qquad \text{(EQ 10)}$$

as measured by microwave radiometer (MWR) in combination with the adiabatic LWP (Fig.1). The term Fr describes the mixing-status or the degree of sub-adiabaticity in the cloud and if Fr is equal to one the cloud is assumed to be adiabatic. This ratio between the retrieved LWP from microwave radiometer and the adiabatic LWP is used to derive an estimation of the droplet concentration in combination with the integrated radar reflectivity iZ of EQ 9. The implementation results in

$$N = k_6 \left(\frac{6\rho_a A_{ad}}{\pi \rho_w} \right)^2 \frac{1}{iZ} Fr^2 \frac{1}{3} H^3 \qquad \text{(EQ 11)}$$

where H is the geometrical thickness of the cloud layer. This formulation enables the derivation of the droplet concentration in dependency of an estimation of the sub-adiabatic fraction function $f(h)$. The main remote sensing based input parameter are the radar reflectivity, the geometrical thickness derived from lidar and radar, the LWP from microwave radiometer as well as cloud base temperature and pressure from radio soundings in order to calculate the degree of adiabaticity.

3. APPLICATION

3.1 Water Cloud Case Study

The application of the retrieval of droplet concentration is restricted to non-precipitating low level water clouds without drizzle formation. The chosen water cloud case in this study on 17 May 2003 at Southern Great Plain (SGP) was presented in Feingold et al. (2006). They analyzed in detail different effective radii retrieval techniques using surface remote sensing, satellite and airborne observations in relation to changes in aerosol. During this month there was an Intensive Operations Period (IOP) to study the indirect aerosol effect in the framework of the Atmospheric Radiation Measurement (ARM) Program, supported by the U.S. Department of Energy. Referring to Feingold et al. (2006) in which a detailed cloud characterization of the 17 May 2003 is described, the following analysis is constrained as well after 17.0 UTC related to drizzle events before. This case study is used to discuss the retrieval of droplet concentration, where the results of effective radii are secondary products.

3.2 Remote sensing based input data

3.2.1 Radar Reflectivity

Fig. 2 shows the millimeter cloud radar (MMCR) reflectivity data of the cloud layer and cloud base (blue line) and cloud top (black line).

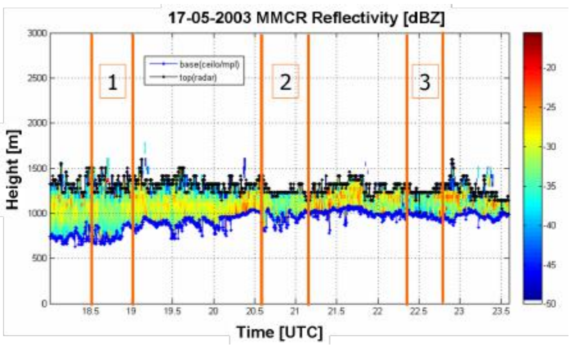

Fig 2: MMCR radar reflectivity [dBZ] 17 May 2003 SGP

The observed cloud layer is characterized by a relatively high variability, which is caused by the incipient day time heating. It became thinner and initiation of mixing processes and turbulence could be expected. There are three parts in the cloud layer (Fig 2) were the values of reflectivity became really low (< ~-35dBZ). This could be related to the transition of the cloud layer due to the day time heating. In respect to the data quality these three parts are excluded from the analysis, because the retrieval technique is only applicable for a continuous cloud layer.

3.2.2 Degree of sub-adiabaticity Fr

Fig. 3 A illustrates the microwave radiometer retrieval of LWP (black) (Turner et al., 2007) and the calculated adiabatic LWP (dark blue), which is based on the derived cloud geometrical thickness and on cloud base pressure and temperature from radio soundings. Both parameters are also influenced by the incipient day time heating. The adiabatic LWP decreases during the day, because of the influence of the variations in the geometrical thickness. The quadratic dependency on the geometrical thickness leads to a difference from about 600 to ~200g/m^2 (Fig 4) after 21.0 UTC. This has an impact on the quantification of the degree of sub-adiabaticity. Also the LWP from microwave radiometer decreases and it reached values below 100g/m^2 after 20.0 UTC.

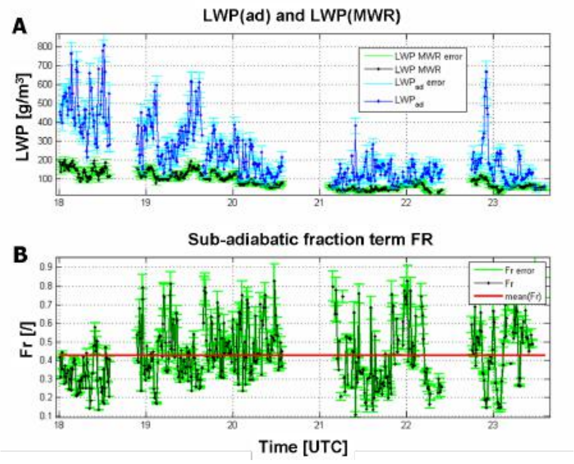

Fig 3: A) LWP retrieved from microwave radiometer (black) and adiabatic LWP [g/m^2] (blue), B) Sub-adiabatic fraction term Fr.

The variability of both parameters results in the beginning of the cloud layer in a low value of sub-adiabaticity Fr (Fig. 3 B), which tend to vary around the mean value of ~0.4 in the center of the layer (19.9 to 20.5 UTC). The variation in the end of the cloud layer is quite high, which is caused by the fluctuations of the geometrical thickness and by low values of the LWP from microwave radiometer.

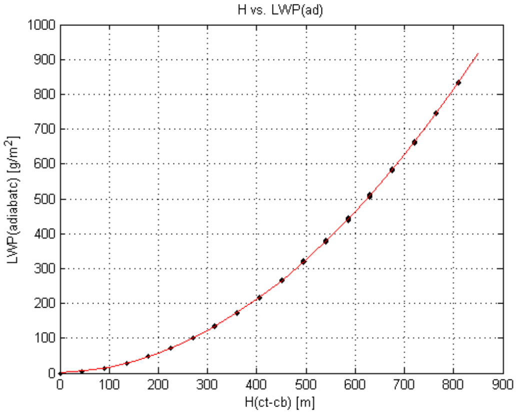

Fig 4: Dependency of geometrical thickness H on the derived adiabatic LWC.

All these effects in the measurements have a strong influence on the droplet concentration and particle size, which are depending on turbulence and mixing effects. The values of the estimated sub-adiabatic fraction term show that an adiabatic assumption ($Fr = 1$) in this case would lead to a large error source in the retrieval of droplet concentration.

3.3 Estimation of droplet concentration N

Fig 5 shows the time series of the estimated droplet concentration based on the remote sensing input data. The concentration N is varying in the beginning of the cloud layer between 400 and 1500 droplets per cubic centimeter and it decreases between 20.0 to 22.0 UTC. This behavior reflects the fluctuations in the input data, which are demonstrated again in Fig 6 A-C.

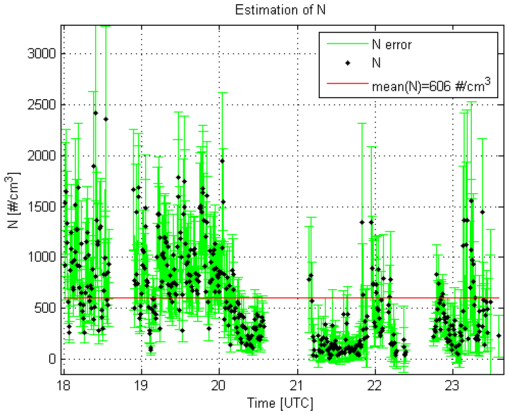

Fig 5: Retrieved droplet concentration [#/cm^3].

Between 18.0 and 20.0 UTC the integrated reflectivity (Fig 6 A) varies close to the mean value (pink line). The geometrical thickness (Fig 6 C) decreases slightly, Fr increases (Fig 6 B) and the resulting droplet concentration tend to higher values (Fig 5).

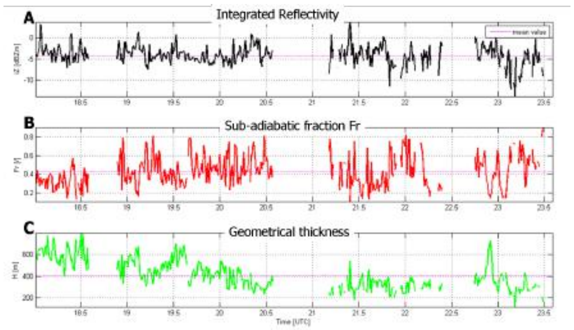

Fig 6: Remote sensing based input data:
A) integrated reflectivity iZ [dBZm], B) Sub-adiabatic fraction Fr, C) geometrical thickness H [m].

After 20.0 UTC when the cloud layer became much thinner, the concentration decreases (Fig 5) and an increase in iZ is observed (Fig 6 A). The observations related to the degree of adiabaticity and the radar reflectivity show a significant influence on the estimated droplet concentration and therefore a sensitivity analysis has been performed.

3.4 Sensitivity analysis of N

This sensitivity analysis is based on the mean values of the input data and the variation of each parameter has been performed in the range of their standard deviation. In Fig 7 the sensitivity of N referring to variations of the integrated reflectivity iZ is demonstrated. The geometrical thickness, LWP adiabatic and LWP from microwave radiometer are assumed to be constant.

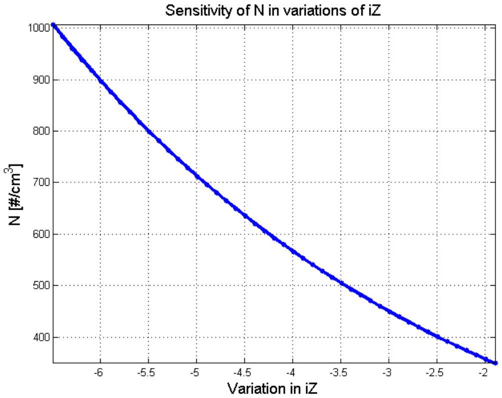

Fig 7: Sensitivity of N referring to variations of the mean value of iZ in the range of its standard deviation. H, LWP(ad), LWP(MWR) are assumed to be constant.

The droplet concentration decreases with an increase of iZ. This tendency to lower values of N is limited by the applicability of the technique on pure water clouds. Only cloud layers with reflectivity values below -17 dBZ are used, which is a proper threshold for drizzle formation. Low values in the reflectivity profiles result in a high concentration of droplets. This leads to an uncertainty in the retrieval of droplet concentration, because it is affected by the quality of the cloud radar data. The problem that has recently been identified (Russchenberg et al., 2004) is that the measured reflectivity factor of non-drizzling stratocumulus clouds can be significantly smaller than expected based on the theory of incoherent scatter, which strongly influence the standard radar reflectivity. The underestimation of the radar reflectivity could be caused by cloud mixing processes at small scales and it has a significant influence on the radar based retrieval techniques of water cloud properties.

The variation of the geometrical thickness has an impact on the sub-adiabatic fraction term Fr, because it is depending on the adiabatic LWP. An increase of 200 m in the geometrical thickness changes Fr from 0.8 (close to adiabaticity) to 0.3 (Fig 8) if LWP from MWR is assumed to be constant.

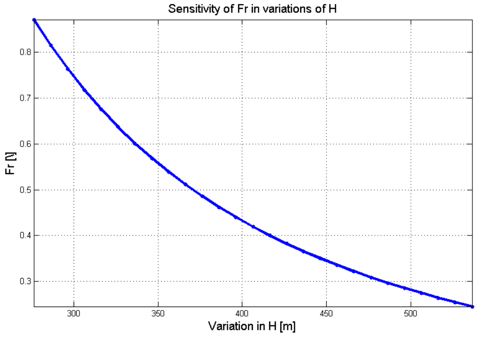

Fig 8: Sensitivity of Fr referring to variations of the mean value of H in the range of its standard deviation. LWP(MWR) and iZ are assumed to be constant.

In terms of droplet concentration it results in a difference of 300 droplets per cubic centimeter (Fig 9), which implies that the maximum amount of droplets is expected under adiabatic conditions.

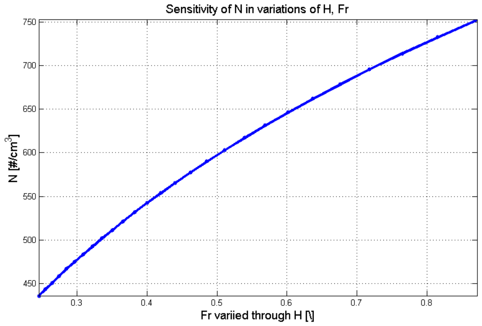

Fig 9: Sensitivity of N referring to variations of the mean value of H in the range of its standard deviation. LWP(MWR) and iZ are assumed to be constant.

The effect on the droplet concentration of assuming an adiabatic cloud layer ($Fr = 1$) for this case study is shown in Fig 10. It results in exorbitant amount of droplets (red line), which emphasizes the importance of including the degree of adiabaticity. It also confirms that the greatest uncertainty in the retrieval of droplet concentration is related to the quantification of Fr. The degree of sub-adiabaticity is depending on the cloud dimension and on LWP retrieved from the microwave radiometer and so far no systematic analysis of Fr on global water clouds have been applied (Boers et al., 2006).

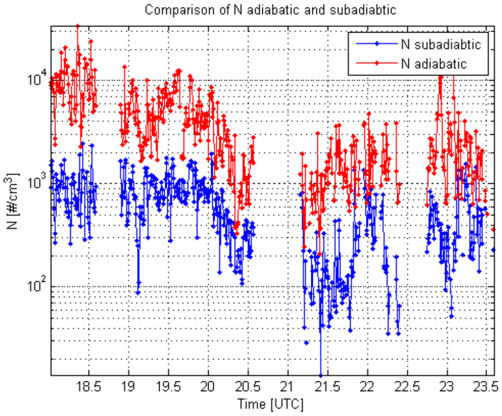

Fig 10: Estimated droplet concentration for Fr=1 (adiabaticity, red) and Fr<1 (sub-adiabaticity, blue).

4. OPTICAL PROPERTIES

The estimated droplet concentration could be used to calculate the optical properties like effective radius, extinction and optical thickness as a secondary retrieval output. These parameters are important for radiation transfer calculations.

4.1 Effective radius

The effective radius is retrieved on the basis of Frisch et al., 2002. They provide two different methods to derive profiles of effective radius using cloud radar and microwave radiometer observations. The droplet concentration in their method is fixed to be constant with height. We can combine this technique by assuming that the sub-adiabatic fraction function $f(h)$ is depending on the shape of the reflectivity profile according to the specified Gamma size distribution and breadth parameter. The estimated droplet concentrations and the measured radar profiles are used to derive profiles of effective radius.

$$r_{effective} \propto \left(\frac{Z(h)}{N_{est}} \right)^{\frac{1}{6}} \qquad \text{(EQ 12)}$$

Fig 11 A represents again the estimated droplet concentration in terms of histogram, which result in effective radii in mean about 5.2 microns (Fig 11 B). These values are in the same range of the derived effective radii in Feingold et al., 2006.

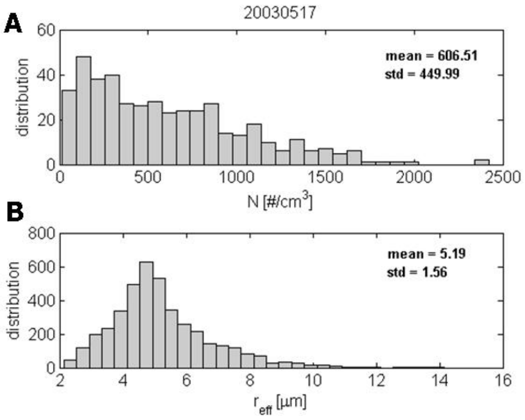

Fig 11: A) Estimated droplet concentration N [#/cm^3], B) Derived effective radius using the estimated droplet concentration and Frisch et al., 2002 approach.

According to EQ 12 and to Frisch et al., 2002 the droplet concentration is less sensitive to this retrieval method of effective radius. Fig 12 shows the sensitivity of effective radius in variations of droplet concentration using the mean radar profile of the observed cloud layer. The variation from 200 to 1000 droplets results in this case in a difference of only one micron in effective radius and therefore this parameter is inapplicable for evaluation studies of the estimated droplet concentration.

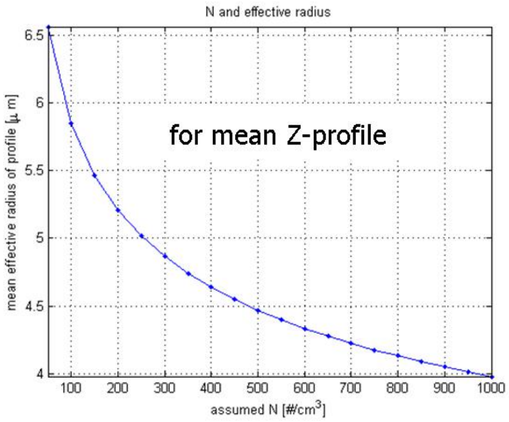

Fig 12: Sensitivity of effective radius in variations to the droplet concentration using the mean radar reflectivity profile of the observed cloud layer.

4.2 Extinction and optical thickness

The optical extinction can be expressed, assuming big particles compared to the wavelength, in the following form:

$$\sigma_{ext} \approx 2\pi N_{est} \left\langle r^2 \right\rangle \qquad \text{(EQ 13)}$$

This relation is used to calculate profiles of the optical extinction coefficient under consideration of the made assumptions in 4.1. and using the estimated droplet concentration. Fig 13 A shows the result of the optical thickness, which is the integrated value of the optical extinction profile (Fig 13 B).

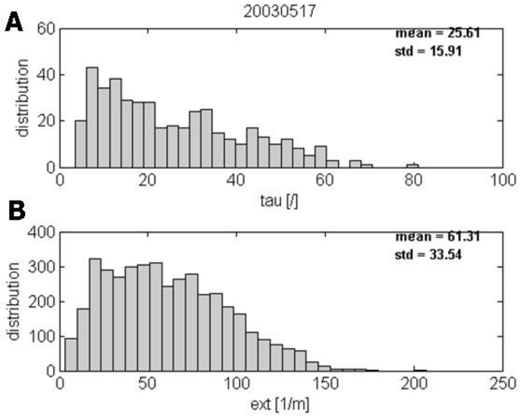

Fig 13: A) Derived optical thickness using the estimated droplet concentration, B) Derived extinction using the estimated droplet concentration.

The derived optical thickness is more sensitive to the estimated droplet concentration, which is demonstrated in Fig 14. Changes in the droplet concentration from 300 to 400 particles per cubic centimeter lead to a difference of optical thickness about 10. Consequently this parameter is an adequate input parameter for evaluation purposes of the retrieved droplet concentration using radiative transfer calculations for a closure experiment.

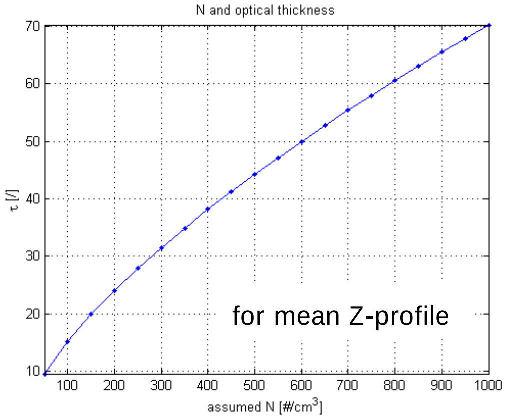

Fig 14: Sensitivity of optical thickness in variations to the droplet concentration using the mean radar reflectivity profile of the observed cloud layer.

5. EVALUATION

The quality of the retrieval products is strongly depending on the model assumptions and on the accuracy of the ground-based observations. Therefore evaluation methods are required, which are independent from the remote sensing based input parameter.

5.1 Radiative transfer calculations

In this evaluation study the derived optical thickness has been used as input for radiation transfer model calculations to simulate narrowband fluxes and to compare them with radiation measurements at the ground. The narrowband observations are used from the Multi-Filter Rotating Shadowband Radiometer (MFRSR), which is operational at Southern Great Plains (SGP). It measures global and diffuse irradiances at six wavelengths 415, 500, 615, 673, 870 and 940 nm. The first five channels are outside water vapor absorption regions and they are most suitable for the evaluation process. The simulated narrowband irradiances are calculated with the Doubling Adding KNMI (DAK) (P. Stammes et al., 2001) radiative transfer model. The monochromatic model allows for the construction of model atmospheres with plane-parallel clouds consisting of water droplets with specific particle size, size distribution and optical thickness. The radiative transfer model based input data are the mean effective radius of the retrieved profile, the assumed Gamma droplet size distribution and the retrieved optical thickness. The model environment is set by the SGP site characteristics. The simulations have been calculated for the wavelengths of 415 nm with a surface albedo of 0.05. Within the comparison of the MFRSR measured irradiances with the simulated ones an assumed Gauss spectral response function of the MFRSR at the nominal wavelength with half power width of 10nm has been considered. Fig 15 shows the comparison of the irradiances of MFRSR (blue line) and the DAK simulations including an aerosol optical thickness (AOT) of 0.3 (red line) and without aerosols (black line).

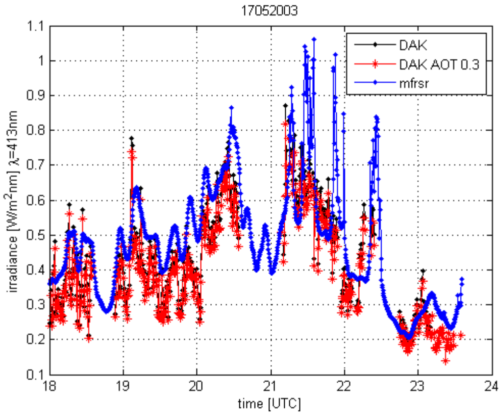

Fig 15 Comparison of MFRSR measurements (not fully calibrated!) (blue) and DAK simulated (using the optical retrievals) irradiances [W/m^2 nm] for different aerosol optical thickness (AOT), AOT=0.3 red line, AOT=0 black line.

So far no detailed evaluation studies have been done yet by using this approach, because the MFRSR data are not fully calibrated. The MFRSR is an adequate instrument to derive accurate values of transmittance without an absolute calibration and this work is in progress in order to evaluate the retrieved droplet concentration using the optical properties of the cloud layer.

5.2 In-situ observations

A more accurate evaluation of the quality of the products, also in consideration of the assumed droplet size distribution, will be analyzed by using aircraft in-situ measurements of water clouds. On the basis of an EUFAR (European Fleet for Airborne Research) proposal aircraft measurements of water cloud microphysics (liquid water content, droplet size distribution and concentration) have been performed during the measurement campaign COPS (Convective and Orographically-induced Precipitation Study). In four different flight mission simultaneous Raman lidar, cloud radar and microwave radiometer measurements at three different observation sites located in Southern Germany in the period of July 2007 could be coordinated. These data will be used for a detailed intercomparison of the in-situ and ground based measurements in order to validate the observations and to optimize the retrieval technique. Furthermore the validation process will be extended through an aircraft measurement campaign in Cabauw, Netherlands in May 2008 organized within the framework of EUCAARI (European integrated project on aerosol cloud climate air quality interactions).

6. CONCLUSIONS AND OUTLOOK

The application of the introduced retrieval technique of droplet concentration showed that an adiabatic assumption for this water cloud case would result in unrealistic, huge values of droplet concentration. The consideration of the sub-adiabatic structure of the cloud, which is closer to reality, is improving the quality of the retrieved cloud microphysical and optical properties. The sensitivity analysis pointed out that especially the degree of sub-adiabaticity (Fr) and the quality of the radar observations are the main uncertainties in the retrieval technique.

Therefore two evaluation studies are in progress in order to improve the quality of the input data and to enhance the model assumption. The closure experiment on the basis of radiation transfer calculations will be used to draw conclusions from the optical thickness to the retrieved droplet concentration, because of the determined sensitivity. The in-situ data will be analyzed in order to improve the quality of the ground-based remote sensing based input parameter. In-situ measurements of droplet size distributions will approve the model assumptions of the fixed size distribution and breadth parameter.

Altogether the enhanced droplet concentration retrieval product could be related to aerosol, vertical forcing and radiation measurements in order to cover the whole chain of processes related to the first indirect aerosol effect.

5. REFERENCES

Atlas, D., D. Short, and D. Rosenfeld, 1989: *Climatologically tuned reflectivity-rain rate relations*. Preprints, 24th Conf on Radar Meteorology, Tallahassee, FL, Amer. Meteor. Soc., 666-671.

Boers, R., J. R. Acarreta, and J. L. Gras, 2006: *Satellite Monitoring of the First Indirect Aerosol Effect: Retrieval of Droplet Concentration of Water Clouds.* J. Geophys. Res., 111, D22208, doi: 10.1029/2005JD006838, Appendix A.

Feingold, G., R. Furrer, P. Pilewsskie, L. A. Remer, Q. Min, and H. Jonsson, 2006: *Aerosol indirect effect studies at Southern Great Plains during the May 2003 Intensive Operations Period.* J. Geophys. Res., 111, D05S14, doi:10.1029/2004JD005649.

Frisch, A. S., G. Feingold, C. W. Fairall, T. Uttal, and J. B. Snider, 1998: *On cloud radar and microwave radiometer measurements of stratus cloud liquid water profiles*. J. Geophys. Res., 103, 23, 195-23, 197.

Frisch, A. S., M. Shupe, I. Djalalova, G. Feingold, and M. Poellot, 2002: *The Retrieval of Stratus Cloud Droplet Effective Radius with Cloud Radars*. J. Atmos. Oceanic Technol., 19, 835-842.

Miles, L., J. Verlinde, and E. E. Clothiaux, 2000: *Cloud droplet size distribution in low-level stratiform clouds*. J. Atmos. Sci., 57, 295-311.

Russchenberg, H., O. Krasnov, 2004: *Radar observations of stratocumulus compared with in-situ aircraft data and simulations*. Proceedings of the third European Conference on Radar Meteorology (ERAD) together with the final COST 720 seminar (Visby, Island of Gotland, Sweden, September 2004).

Stammes, P., 2001: *Spectral radiance modeling in the UV-Visible range*. IRS 2000: Current problems in Atmospheric Radiation, edited by W.L. Smith and Y. M. Timofeyev, 385-388, A. Deepak Publ., Hampton, Va.

Towmey, S., 1977: *The influence of pollution on the shortwave albedo of clouds.* J. Atmos. Sci., 34, 1149-1154.

Turner, D. D., 2007: *Improved Ground-based Liquid Water Path Retrievals using a Combined Infrared and Microwave Approach*. J. Geophys. Res., 112, D15204, doi:10.1029/2007JD008530.

Acknowledgments

The Data were obtained from the Atmospheric Radiation Measurement (ARM) Program sponsored by the U.S. Department of Energy, Office of Science, Office of Biological and Environmental Research, Environmental Sciences Division.

UNDERSTANDING OF THE FORMATION MECHANISM OF COLD WATER FOGS OFF THE WEST COAST OF THE KOREAN PENINSULA

Chang Ki Kim and Seong Soo Yum
Department of Atmospheric Sciences, Yonsei University, Seoul 120-749, Korea

1. Introduction

Fog is the condensation of water vapor near the surface. Radiative cooling at night is a major cause of fog formation over the land. Over the sea, however, direct cooling of air by cold sea surface or cold air movement over warm sea surface can lead to the saturation of air and the formation of fog. Visibility degradation by fog is a matter of great concern for some of the airports built on coastal areas, where coastal fogs and sea fogs both can affect. Leipper (1994) emphasized the importance to distinguish sea fogs from coastal fogs, suggesting that in sea fogs the relationship between the sea surface temperature and the dew point was the most useful indicator while coastal fogs were mainly associated with the low level inversion. Moreover, Cho et al. (2000) showed that in summer season, the sea surface temperature off the west coast of Korea was colder than the temperature of the lower level air due to the upwelling so that advection fogs formed frequently over this area.

The purpose of this study is to understand better the whole mechanism of cold water fogs that form over the Incheon International Airport (hereafter IIA, Fig.1).

Meteorological conditions and synoptic patterns that are relevant to fog formation are carefully examined here but numerical simulations will be presented at the conference.

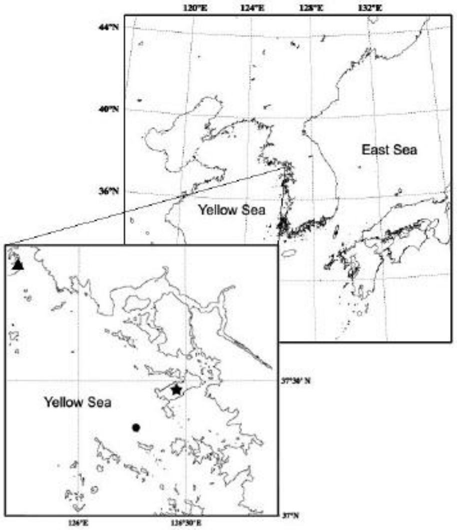

Fig. 1. The location of Incheon International Airport. The asterisk, the closed circle and the triangle indicate the location of Incheon International Airport, the buoy at Dukjeok-do and the radiosonde at Baeknyeong-do, respectively.

2. Data

Meteorological variables used in this study are visibility, wind direction (WD),

---

Corresponding author address: Chang Ki Kim, Department of Atmospheric Sciences, Yonsei University, Seoul 120-749, Korea; email: 62beatle@yonsei.ac.kr

wind speed (WS), air temperature (TAIR), dew point (TDEW), mean sea level pressure (MSLP) and weather phenomenon number, measured at IIA. Moreover, the buoy measured sea surface temperature (SST) at Dukjeok-do and the weather report from the lighthouse at Seonmi-do are added to examine the weather condition over the sea.

Synoptic patterns are investigated with the Weather charts produced from Global Data Assimilation System (GDAS) and the radiosonde at Baeknyeong-do provides the information regarding the vertical structure of the atmosphere.

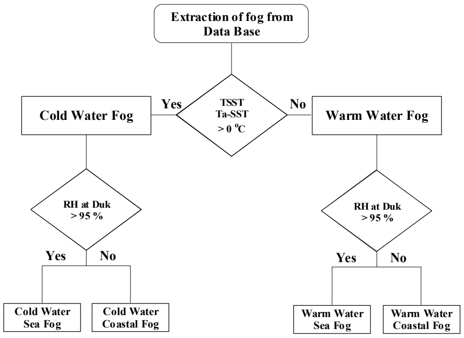

Fig. 2. The flow chart of fog classification.

3. Methodology

In this study, fog is defined when the visibility at IIA is lower than 1 km. However, precipitating cases are not considered even if they satisfy the criteria. There were 181 fog days during the investigated period of 2002 to 2006 and they are classified into cold water fogs and warm water fogs and then cold water fogs are divided into two categories, sea fogs and coastal fogs (Fig. 2). Finally synoptic patterns in each category are classified into four types, high pressure, low pressure, south high north low, and west high east low.

4. Basic features

Monthly variation of fog days

Accoring to the fog classification, cold water and warm water fog days are 100 and 81, respectively. There are 76 sea fogs are 24 coastal fogs among the cold water fog days, whereas warm water fogs are divided into 25 sea fogs and 56 coastal fogs.

Fig. 3 shows that cold water fogs occur mainly in summer season when TAIR is higher than SST while warm water fogs form mostly in winter season.

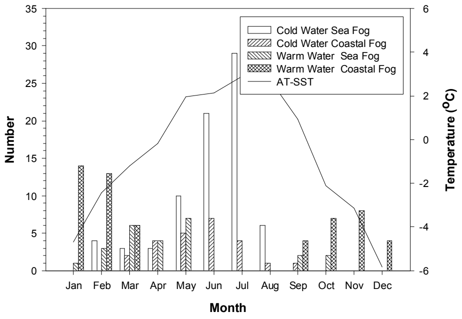

Fig. 3. Monthly fog days (vertical bar) and monthly averaged difference between the air temperature and the sea surface temperature.

Analysis of the formation and dissipation time

Now we focus on cold water fogs. Croft et al. (1997) pointed out that the investigation of the formation and dissipation times of the fog could provide useful information in the understanding of the causes to form the fog.

Fig. 4 shows the formation and dissipation time of cold water fogs as a polar plot. Cold water coastal fogs form mainly from 1800 to 0400 local time (KST) the next day while cold water sea fogs form in daytime as well as nighttime. These results indicate that the radiative cooling after sunset may be one of the main causes to form coastal fogs.

Cold water coastal fogs disappear mainly from 0500 KST to noon, suggesting that the radiative heating after sunrise helps coastal fogs to be dissipated. However, sea fogs dissipation time does not seem to be related to sunrise.

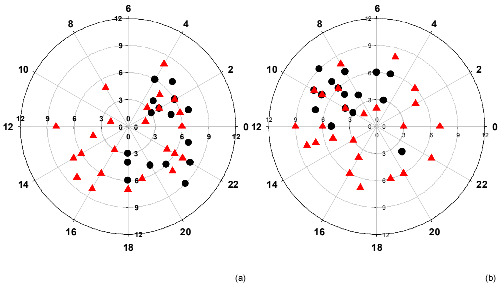

Fig. 4. The polar plot of the formation time (a) and the dissipation time (b) of cold water fogs. Closed circle and closed triangle indicate the coastal fog and the sea fog, respectively. The angle and the radius mean the hour and the month, respectively.

5. Meteorological Characteristics

Air temperature and dew point

Table 1 shows that TAIR at IIA are similar in coastal fogs and sea fogs. This may imply that both sea fogs and coastal fogs can be formed due to the cooling of low level air by cold surface.

TDEW also shows similar tendency like TAIR in Table 1.

Difference between TAIR and SST (TSST)

Analyses of TSST can provide the key to find the difference of the formation mechanism between sea fogs and coastal fogs. TSST for sea fogs and coastal fogs are 2.2 ^{o}C and 1.0 ^{o}C, respectively (Table 1). This suggests that large TSST is a key to form a sea fog for an efficient cooling of air in contact with the cold sea surface but the fog may be limited to coastal fog when TSST is small and the cooling of the air is enhanced by the radiative cooling at night.

6. Analysis of synoptic patterns

A description of pressure patterns

High pressure (HP) pattern is the case where the center of the high pressure is located to the east of the Korean peninsula and southerly winds are induced from the western sector of the high pressure. Low pressure (LP) pattern is designated when the low pressure is located to the west of the Korean peninsula and southerly winds blow from the eastern sector of the low pressure. South high north low (SHNL) pattern is the pressure pattern where the high pressure comes into contact with the low pressure in the center of the Korean peninsula and westerly or southwesterly winds blow over this region. Finally West high east low (WHEL) pattern is designated when the high pressure and the low pressure are located to the west and the east of the Korean peninsula, respectively.

Table 1. Averages of hourly mean temperatures for cold water sea fogs and coastal fogs during the investigation period. SST is observed only from the buoy at Dukjeok-do. Coastal@IIA and Coastal@Duk means observation at IIA and at the buoy, respectively.

	TAIR (°C)	SST* (°C)	TDEW (°C)	TSST (°C)	DEWD (°C)
Coastal@IIA	16.2	-	15.3	-	0.9
Coastal@Duk	14.8	13.8	12.0	1.0	2.8
Sea Fog	15.8	13.6	15.4	2.2	0.4

Table 2. Summary of synoptic pattern classification. Meaning of each synoptic pattern is described in the text.

	HP	LP	SHNL	WHEL
Sea Fog	29	14	33	2
Coastal Fog	10	5	3	5
Total	39	19	36	7

High Pressure (HP)

This pattern shows the highest frequency (Table 2). High pressure separated from North Pacific high pressure or Okhotsk high pressure seem to influence the fog formation of the fog during the summer season.

The water vapor advection chart (Fig. 5a) shows that the moisture is advected into the Yellow sea from the south by the high pressure. The veering of the wind direction (Fig. 5b) also indicates warm advection prevailing in this area.

Consequently, the warm and moist air coming from the south by the high pressure system generates a large TSST (2.6 °C, Table 4). Then the relatively much colder sea surface may cool the air in contact efficiently to form a sea fog.

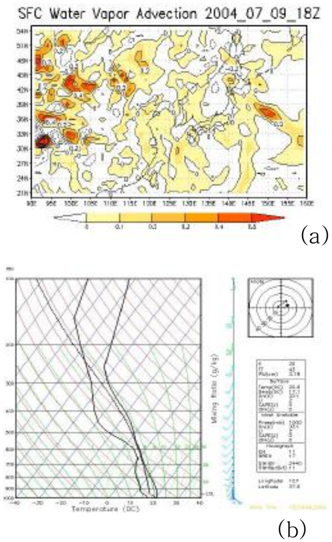

Fig. 5. The advection chart at 1000 mb of the water vapor (a) and Skew-T diagram (b) for an HP pattern.

Low Pressure (LP)

The advection chart of TAIR (Fig. 6a) indicates that the cold front exists in the western sector of the low pressure. Roach (1995) has shown that the cold advection after the passage of the cold front could cool the air and the fog occurred consequently.

This pattern also leads to the transport of the warm and moist air into the Yellow sea (Fig. 6b) so that the fog can form over cold water surface. The cold advection after the passage of the cold front may prolong the duration hour of the fog.

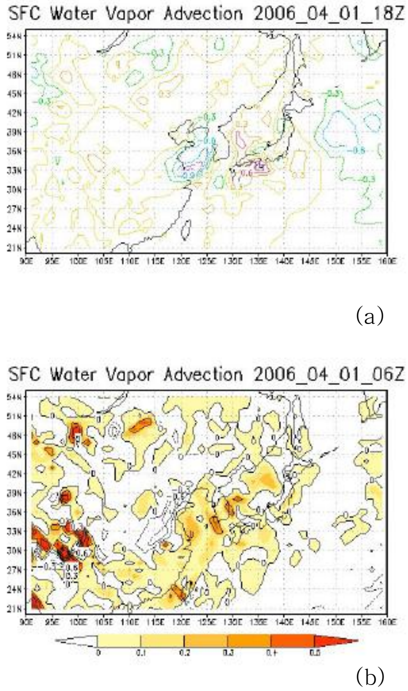

Fig. 6. The advection chart at 1000 mb of the air temperature (a) and the water vapor (b) for an LP pattern.

South High North Low (SHNL)

Fig. 7a is a typical 850 mb weather chart during the Changma monsoon season in Korea, which shows an SHNL pattern: the distribution of the wet number lies from east to west near the central Korean peninsula as a band shape. After the passage of the front, the coastal and sea area near IIA is now in the cold sector as the backing of the wind direction indicates (Fig. 7b). The moisture from the precipitation and the temperature drop in the cold sector may lead to fog formation.

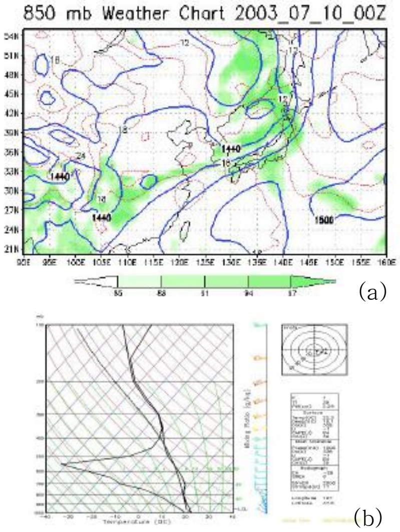

Fig. 7. The weather chart at 850 mb (a) and Skew-T diagram (b) for an SHNL pattern.

West High East Low (WHEL)

This pattern is rare in cold water fogs because WHEL pattern is a typical pressure pattern in winter season. Nevertheless, occasionally SST becomes lower than TAIR so that a sea fog can be formed. However, radiative cooling dominating coastal fogs seems more common for this pattern as Table 2 suggests.

Table 3. Averages of hourly mean meteorological variables of cold water coastal fogs and non-fog days in summer for each synoptic pattern.

	Cold Water Coastal Fog				Non Fog days			
	HP	LP	SHNL	WHEL	HP	LP	SHNL	WHEL
TAIR (°C)	18	17.0	8.2	6.7	19.5	20.6	15.8	16.2
TDEW (°C)	17.1	16.3	7.3	5.7	13.5	15.7	10.3	10.4
DEWD (°C)	0.9	0.7	0.9	1.0	6.0	4.9	5.5	5.8
τ-LON	−0.8	−6.3	−3.3	−3.6	9.1	4.4	3.6	6.3

Table 4. Same as Table 3 except cold water sea fogs and non-fog days in summer.

	Cold Water Sea Fog				Non Fog days			
	HP	LP	SHNL	WHEL	HP	LP	SHNL	WHEL
TAIR (°C)	19.9	14.4	18.8	4.1	18.3	21.5	15.6	17.2
SST (°C)	17.3	12.5	17.9	2.9	16.5	17.6	14.4	16.1
TDEW (°C)	18.6	13.8	18.5	3.0	12.1	13.6	11.4	10.6
TSST (°C)	2.6	1.9	0.9	1.2	1.8	3.9	0.8	1.1
DEWD (°C)	1.3	0.6	0.3	1.1	6.2	7.9	4.2	6.6

7. Comparison of fog days with non-fog days

Meteorological variables in non-fog days are compared with those of fog days in summer season (April to August) in Table 3 and 4.

Cold Water Coastal Fog

A new factor (τ–LON) is added in Table 3. This factor is explained in detail by Meyer and Lala (1990). Positive values of the difference between τ and LON (τ-LON) indicate that the nighttime is too short to allow the surface layer to saturate, while negative values suggest enough time is available.

Table 3 shows that all coastal fog cases have a negative (τ-LON) value, while all non-fog cases have a positive value. Therefore, the radiative cooling in non-fog days is not efficiently fast enough to saturate the surface layer as the sunrise occurs before the saturation point is achieved by the radiative cooling.

Cold Water Sea Fog

Meteorological characteristics of cold water sea fogs are compared with those of non-fog days in Table 4. Most meteorological variable for cold water sea fogs are similar to those for non-fog days but TAIR for WHEL pattern in cold water sea fogs is colder than non-fog days. This is because WHEL patterns in cold water sea fogs occur frequently in April.

According to Table 4, for sea fogs, SST is lower than TDEW so that the air in contact with the sea surface can be cooled to reach the saturation point. However, in non-fog days, SST is higher than TDEW and therefore saturation can not be achieved for the air even in contact with the cold sea surface.

Acknowledgement

This work was funded by the Korea Meteorological Administration Research and Development Program under Grant CATER 2006-2307. We really appreciate it for financial support provided from WMO, IAMAS and ICCP.

8. Reference

Cho, Y. K., M. O. Kim, and B. C. Kim, 2000: Sea fog around the Korean peninsula. *J. Appl. Meteor.*, **39,** 2473-2479.

Croft, P. J., R. L. Pfost, J. M. Medlin, and G. A. Johnson, 1997: Fog forecasting for the southern region: A conceptual model approach. *Weather. and Forecast.*, **12,** 545-556.

Leipper, D. F., 1994: Fog on the U.S. West Coast: A Review. *Bull. Amer. Meteor. Soc.*, **75,** 229-240.

SHIP OBSERVATIONS FOR CLIMATE MODEL VERIFICATION OVER THE SOUTHEASTERN TROPICAL PACIFIC

Simon P. de Szoeke and Christopher W. Fairall
Physical Sciences Division, NOAA/ESRL, Boulder, Colorado, USA.
simon.deszoeke@noaa.gov

Stratus clouds of large albedo and extent form over cold sea surface temperature (SST) in the southeastern tropical Pacific Ocean, reinforce cool SST beneath them, and contribute to air-sea interactions that influence the distribution of surface winds, the location of precipitation and upward motion in the Hadley cell, and the equatorial ocean wave guide. Despite their importance to the climate, air-sea interactions and clouds in the southeast tropical Pacific have been notoriously difficult to simulate in coupled general circulation models (GCMs).

Since 2001, NOAA ships have made 6 cruises during boreal fall to a mooring station at 20S, 85W; sampling surface meteorology, and atmosphere-ocean fluxes. Cloud properties are estimated from rawinsondes, radar, lidar, and passive microwave, infrared, and solar radiometers. The cruises provide an estimate of mean conditions and a qualitative sense of interannual variability.

An integrated data set of conditions on each cruise with 10-minute, hourly and diurnal cycle averages is available on a NOAA web site. These ship observations can be used to verify gridded data sets of upper-ocean, and atmospheric analyses and model simulations. We present an assessment of surface fluxes in the WCRP Coupled Model Intercomparison Project 3 (CMIP3) simulations.

All Stratus cruises steamed from 75W to 85W along 20S. Each cruise observed deepening of the marine boundary layer, decoupling of the cloud layer from the surface, and clearing toward the west. The most recent NOAA Stratus cruise in October-November 2007 uniquely sampled within 300 km of the shore from the equator to 20S. From the equator to 3S the SST was warmer than 20C and the atmosphere was convectively disturbed. South of 3S the SST was cooler and the clouds were mostly solid, with only occasional clearing. Particularly low aerosol concentrations were observed 18-20S, accompanied by thicker clouds. At this time the ship encountered the edge of a pocket of open cells.

1*. Constraining the surface heat budget*

Important to El Niño/Southern Oscillation, the intertropical convergence zone (ITCZ), and the seasonal cycle, the complexity of interacting processes and the paucity of observation over the eastern tropical Pacific region conspire to make it difficult to simulate properly with coupled GCMs (de Szoeke and Xie 2008). The surface heat budget simulated by GCMs in the eastern tropical Pacific region from the WCRP 3rd Coupled Model Intercomparison Project (CMIP3) are shown in Fig. 1. The quantity shaded is the sum of turbulent (sensible and latent) and radiative heat flux upward out of the ocean surface. Dark red shades above zero indicate that the ocean is cooled by the net effect of the sun and the atmosphere, while light red to blue shades indicate that the ocean surface is warmed from above. The ocean warms most where it is coolest, along the southeastern South American coast and in the equatorial cold tongue.

It is extremely difficult to observe the contribution of ocean dynamics to the surface ocean heat budget directly, and even difficult to diagnose its contribution in models. Nevertheless, assuming the storage of heat in the surface is zero in the annual average, the residual of the surface heat flux in Fig. 1 is the contribution by ocean dynamics. Therefore, the regions of strongly downward (blue) net heat flux are balanced by ocean cooling from below by upwelling and vertical mixing. These are regions where upwelling is expected along the coast and equator.

In addition to models, some researchers now produce analyses based on various combinations of limited in situ observations, satellite retrievals, and large scale budgets of the surface ocean. The lower right panel of Fig. 1 is from the Large and Yeager (2004) Common Ocean-ice Reference Experiments (CORE) surface heat flux analysis. The WHOI (Yu et al. 2004), IFREMER (Bentamy et al. 2003), and CORE surface turbulent heat flux analyses shown in Fig. 2.The IFREMER analysis is derived entirely from satellite observations. While the analyses agree qualitatively, the precise shape and magnitude of the turbulent flux has large differences among the models. The net radiative flux heating the ocean is about 20 W/m^2 stronger in ISCCP than for the CORE analysis. These analyses of surface fluxes are promising tools for more advanced assessment of model simulations and addressing model biases. Yet the analyses must be compared to direct climate-quality flux observations to resolve their differences.

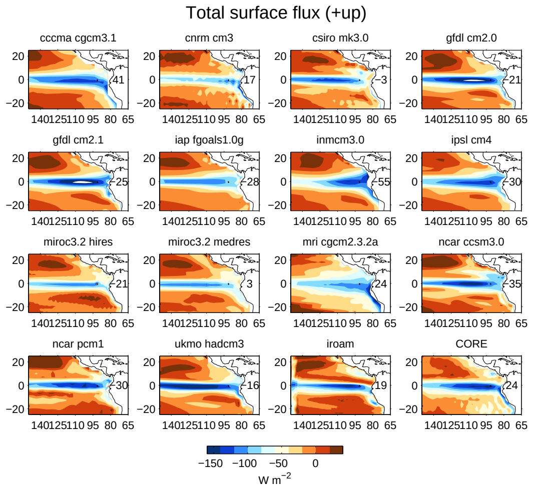

Figure 1: The annual mean total surface heat flux (upward) out of the ocean in 14 CMIP3 GCMs, one regional model (IROAM), and a global flux analysis (CORE). The numbers over South America indicate the asymmetry of the total surface flux; positive numbers indicate the ocean is being warmed by the sun and the atmosphere more in the southern hemisphere.

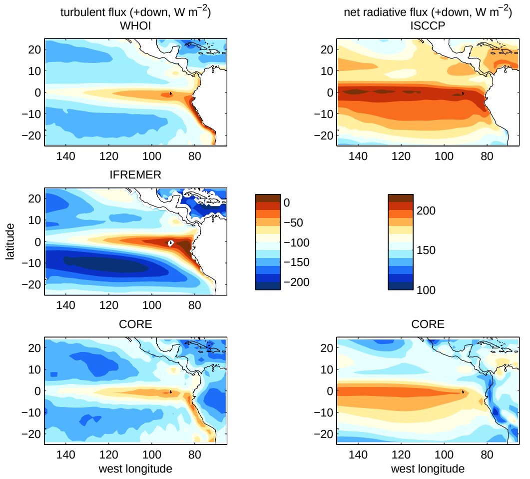

Figure 2: Turbulent (left) and radiative heat flux from surface heat flux analyses.

2. *An integrated set of ship observations*

Direct observations from autumn 2001 and 2003-2007 were made by NOAA research cruises. Each cruise serviced the Woods Hole Oceanographic Institution (WHOI) Ocean Research

Station (WORS), a moored instrument platform at 20S, 85W. In addition to comparisons with instruments on the mooring for several days on location, the ships all traveled in a longitudinal section across 20S (usually from 75-85W). The track of the 6 cruises is shown in Fig. 3. Various sensors with different data calibrations and qualities were used on the cruises, but data from the sensors has been synthesized into an integrated data set with quantities useful for climate model verification, or planning further regional experiments. These data are available as 10-minute or hourly time series, or diurnal cycles averaged in the vicinity of 20S, 85W. Rawinsonde soundings of the atmosphere are gridded to 10-m levels in the synthesis data set—suitable for verifying model PBL structure. Data are available to the community and can be retrieved from the web site, http://www.esrl.noaa.gov/psd/people/Simon.deSzoeke/synthesis.html. A summary of the instrumentation follows.

Three sets of instruments on the NOAA ship *Ronald H. Brown* (*RHB*) made measurements during the Stratus cruises (Fairall et al. 2003): NOAA PSD near surface meteorology, cloud remote sensing and aerosol number sampling from the ship, and upper-air soundings.

The NOAA/ESRL Physical Sciences Division (PSD) Weather and Climate Physics Branch (formerly ETL) has outfitted the *RHB* ship with a mobile set of accurate and fast sensors which acquire observations of the near-surface atmosphere with an accuracy suitable to compute air-sea fluxes (Fairall et al. 2003). Instruments on a jackstaff at the bow of the ship sample air temperature, humidity, wind, and ship motion. Sea surface temperature is measured by a floating “sea snake” thermometer at approximately 5 cm depth. At this depth the thermometer samples the daylight warm layer, but not the cool skin layer. Turbulent fluxes are computed from bulk quantities by the Fairall algorithm. Downward solar and infrared radiation are measured by a pyranometer and a pyrgeometer, respectively. Surface meteorology and fluxes were averaged to standard 5-minute time intervals beginning on the hour. The optical rain gauge malfunctioned and was switched off during Stratus 2007.

PSD uses an upward looking Radiometrics “mailbox” 24- and 31-MHz channel passive microwave radiometer to estimate column water vapor and liquid water (Hare et al. 2005). A Vaisala 905-nm lidar ceilometer estimates cloudiness and up to 3 cloud base heights. An active 915-MHz NOAA radar wind profiler was operated with its antenna pointed vertically. Turbulence and gradients of temperature and humidity at the MABL inversion scatter the radar pulse, from which we diagnose the height of the boundary layer to the nearest 60 m range gate. Valid returns from these three sensors are averaged to standard 10-minute intervals.

Vaisala global positioning system (GPS) digital rawinsondes were released into the atmosphere from the fantail of the ship approximately every 6 hours during the coastal transect from October 18-23, and the 20S transect on October 25-27. The rawinsonde release times and locations along the ship tracks are indicated by open circles Fig. 3. Rawinsondes measured and telemetered temperature, relative humidity, pressure, and GPS position. Profiles of temperature, humidity, and winds with height are calculated and averaged to standard 10-m altitudes.

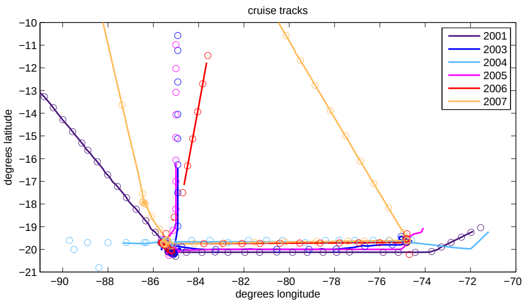

Figure 3: The track of each of the Stratus cruises. Circles represent the location that rawinsondes were launched.

3. *The 20S ship transects*

The track of all the NOAA Stratus cruises to the WORS is shown in Fig. 3. Each of the Stratus cruises contained a transect along 20S. The dates of each of these transects is listed in Table 1. Most of the cruises along 20S took place in late October, but 2001 and 2004 sampled later in the year.

Table 1. Approximate dates of the 20S transect of each of the Stratus cruises.

2001	Oct 22-25
2003	Nov 21-24
2004	Dec 5-18
2005	Oct 18-21
2006	Oct 20-23
2007	Oct 24-27

Surface meteorology along the 20S line of latitude is shown for the 6 ship transects in Fig. 4. Most cruises sampled 20S between 75-85W. The cluster of observations at 85W is from the extended time the ship spent at the buoy. In addition to spatial gradients, each cruise also sampled diurnal and interannual variability differently. Nevertheless, the aggregate of the 6 cruises gives an idea of the zonal structure along 20S. The 2007 cruise had a strong SST (thick, top panel) gradient along 20S, and a rapid transition from low marine stratocumulus to cumulus rising into stratocumulus and trade cumulus was observed that year. Most other years have a smaller increase in temperature towards the west. 2003 and 2004, which took place in late November and December show warmer temperature around 75W than the other years. On the whole, sea-air temperature difference decreased to the west.

Latent heat flux (thick upper-middle) is larger to the west, while the sensible heat flux shows no systematic gradient. Zonal wind (thick, lower-middle) shows variability around 5 m/s, but little systematic gradient. The meridional wind increases from ~3 m/s around 75W to ~8 m/s around 85W, which combined with increased saturation specific humidity at the surface, contributes to the latent heat flux. Specific humidity of the air increases slightly (thick line, bottom panel) to the west, while the integrated column water vapor changes little.

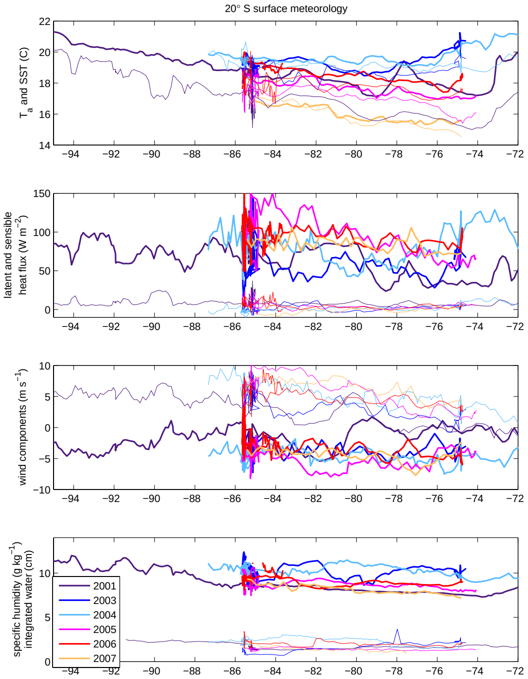

Figure 4: Cross section of surface meteorology and fluxes for all cruises along 20S.

4. *An unique coastal section*

Arrows originating from the dashed ship track in Fig. 5 are centered 6-hour averages of the surface wind. The wind was extremely constant within each 6-hour period, with speed standard deviation less than or equal to 1 m/s. The wind speed ||u|| (black dashed line) is on average 5.6 m/s, with a 0.4 m/s offshore component. The wind follows the contour of the coast with a standard deviation in direction of under 20 degrees in each 6 hour period. South of 12S winds are as much as 40 degrees offshore of parallel to the local coast, reflecting the heading of the coast upstream of the ship between Paracas Peninsula and Arica.

The SST (red) and air temperature (blue) are left of the ship track in Fig. 5. SST reaches a minimum of 15.5C at 14S and a maximum of 26.6C at 2N. Air temperature follows SST. The sea-air temperature difference is about 1.3C south of 3S, with diurnal variations of the same magnitude. On the nights of October 18, 19, and 21 local the SST cooled off to equal the air temperature, occasionally resulting in sensible heat flux from the air to the ocean. The air temperature is considerably cooler than the SST (3.5C) in the warm pool north of 3S, because advection from the south cools the surface air by ~10C/day. The largest sea-air temperature difference of 4.25C was observed in the afternoon downstream of the strong gradient at 2.5S.

At right in Fig. 5 is the profile of air-sea heat fluxes along the track. Positive (rightward) fluxes represent heat leaving the ocean. The red curves are solar (Rs) and infrared (Ri) fluxes. The solar flux is plotted on a scale one tenth of the scale of the other fluxes, and its pulses indicate the time of local daylight. The black curves are latent and sensible turbulent heat fluxes. Latent heat flux E is in the neighborhood of 100-150 W m^{-2} north of 2.5S, and about 50 W m^{-2} south of 2.5S. Sensible heat flux H is about 30 and 10 W m^{-2} north and south of 2.5S. Though solar flux has large diurnal variations, it does not appear to be noticeably different on either side of 2.5S. The variability of the infrared flux increases south of 2.5S, probably because the atmosphere has less water vapor and downward thermal radiation is more strongly modulated by clouds. To avoid diurnal sampling biases, we use the solar radiation averaged over the whole coastal leg for all of the budgets. The average solar radiation for the partial legs is nevertheless indicated in parentheses. In the warm pool to the north, the ocean surface is not losing or gaining heat within measurement error. Yet on the southern part of the leg, the cool ocean is warmed by a net 100 W m^{-2}.

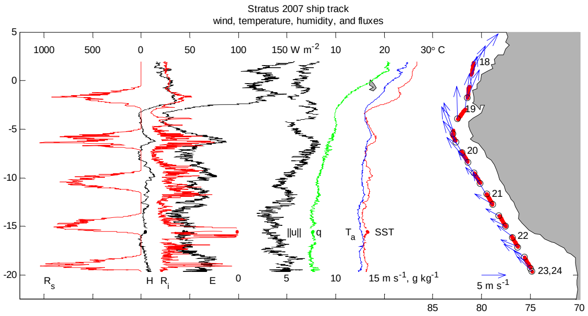

Figure 5: Track of the *RHB* along the coast of South America in 2007. Wind vectors, air temperature, SST, specific humidity, wind speed, and surface fluxes are shown at right as a function of latitude along the track.

Rawinsondes were launched from the ship every 6 hours beginning October 18, 18:00 UT, and every 4 hours on October 23, providing snapshots of the vertical temperature and humidity structure of the atmosphere. All the soundings on the coastal leg are compiled in a time-height section of potential temperature theta and specific humidity q from 0-2.5 km altitude in Fig.

6a and b. Both quantities clearly show the trade-MABL inversion after October 20, with a well-mixed layer of high humidity (7-8 g/kg) and low potential temperature (287 K). By visual inspection we picked the 4 g/kg specific humidity (black) and 296 K (green) potential temperature contours to mark the boundary layer inversion. These contours follow the strong gradient at the MABL inversion south of 8S, but the inversion is hard to diagnose north of 8S. Before October 20, the ship was under a convective weather system, with tall cumulus towers reaching far into the free troposphere. The strong humidity signal of these clouds was recorded by the soundings. The 4 g/kg contour rises more than a kilometer into the free troposphere and the stratification of the inversion and free troposphere are reduced during this stormy period. The atmosphere remained convectively disturbed above 1 km all the way to 8S, beyond the southern extent (2.5S) of warm-pool SST over 20C.

Apart from the convective period, marine atmospheric boundary layer stratocumulus clouds were quite uniform in height and thickness. We diagnose cloud top from the soundings, and compared them with other estimates from independent ship observations in Fig. 6a. (The estimates are repeated in Fig. 6b for comparison to the humidity profile.) The crosses show the height height of the minimum temperature in the sounding, assumed to be the base of the inversion. While the temperature minimum is associated with the cloud top, it is on-average 100 m below the level of the inversion indicated by strong gradients of humidity and potential temperature. The NOAA radar wind profiler receives strong signals scattered back from the gradients and turbulence at the inversion. Magenta dots show the height of maximum signal to noise ratio of the wind profiler radar returns. The wind profiler inversion height agrees well with the inversion found from the gradient in the soundings. These estimates of the inversion height agree with the level where LCL parcels would evaporate completely when mixed with 25-50% of environmental air (not shown).

The stratocumulus cloud base height observed by the laser ceilometer is plotted in green in Fig. 6a and b. The ceilometer cloud base is sometimes ~100 m higher than the LCL of a surface parcel (red), which indicates that dry air entrained from the free troposphere dilutes the water vapor in the cloud. The consistency of cloud base height from the ceilometer and the LCL, and the inversion height from the profiler and the temperature and humidity structure from the soundings gives us confidence in the accuracy of our measurements of cloud vertical structure.

The red line in Fig. 6c shows the integrated water vapor from the microwave radiometer. Integrated water vapor follows the surface humidity (Fig. 5), as most of the water vapor is trapped in the boundary layer.

The clouds are usually solid, with cloud fraction (green, Fig. 6c) rarely deviating from unity. An exception is the clear sky observed in on the first half of 19 October (UT), when the atmosphere is convective. Though partial clearing is observed on occasion, clear skies are only briefly observed in the stratocumulus region starting on the afternoons of 21-23 October (local).

The concentration of aerosol particles between 0.1 and 5 micrometers is highest late on 18 October when the ship passes closest to land offshore of Cabo San Lorenzo. The aerosol concentration dips below 100 cm-3 on October 22, with a minimum of 25 cm^{-3} on 23 October. Displacement of the ship further from shore on 22 October, after it had rounded Paracas Peninsula, could be responsible for the lower aerosol concentrations. Though clear skies were only observed briefly during these afternoons of lower aerosol concentration, the dip in aerosol concentration was similar to that in pockets of open cells (Stevens et al. 2005) observed during the remainder of the 2007 Stratus cruise.

The clearing seen from the ship in the early afternoon (local) of 22 October was associated with a thickening of the clouds, as seen from the ceilometer and the LCL in Fig. 6. Clouds remain thicker during the time of low aerosol concentrations. Satellite imagery from the NOAA-17 polar-orbiting satellite taken on 22 October, 14:25 UT (Fig. 7) shows two clear regions on either side of the ship (marked in its position at the time of the image at 18.6S, 75.4W). The clear region adjoining the coast is most likely due to the boundary layer being too shallow for parcels to reach their LCL. The clear region neighboring ship to its southwest is one of several pockets of open cells visible at this time. At the time of the image, the ship is barely outside the POC, but is headed toward its wider end. Though Fig. 7 is the only image from 22 October, on other days POCs were seen to expand during the afternoon.

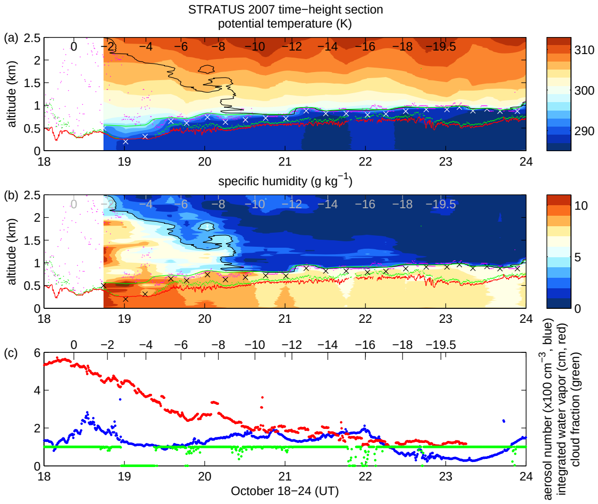

Figure 6: Vertical-time section of potential temperature (a) and specific humidity (b) from radiosondes along the 2007 coastal section. Latitude is shown along the top of each panel. Various measures of cloud base and top height, and MABL height are described in the text and shown in (a) and (b). (c) shows the cloud fraction (green), aerosol concentration (blue), and integrated water vapor (red).

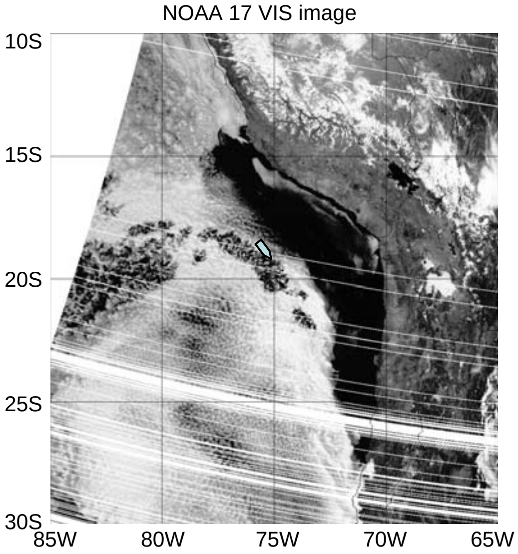

Figure 7: Visible radiance from the NOAA-17 polar-orbiting satellite on October 22 at 14:25 UT. At the time of the image, the ship was at the position marked (18.6◦ S, 75.4◦ W) between

the clear boundary layer neighboring the coast and the pocket of open cells to the southwest.

References

Bentamy, A., K. B. Katsaros, A. M. Mestas-Nunez, W. M. Drennan, E. B. Forde, and H. Roquet, 2003: Satellite estimates of wind speed and latent heat flux over the global oceans. *J. Climate*, **16,** 637-656.

de Szoeke, S. P., and S.-P. Xie, 2008: The tropical eastern Pacific seasonal cycle: Assessment of errors and mechanisms in IPCC AR4 coupled ocean-atmosphere general circulation models. *J. Climate*, in press.

Fairall, C. W., E. F. Bradley, J. E. Hare, A. A. Grachev, and J. B. Edson, 2003: Bulk parameterization of air-sea fluxes: updates and verification for the COARE algorithm. *J. Climate*, **19,** 571-591.

Hare, J., C. Fairall, T. Uttal, D. Hazen, M. F. Cronin, N. Bond, and D. Veron, 2005: Cloud, radiation, and surface forcing in the equatorial eastern Pacific.

Stevens, B., and Coauthors, 2005: Pockets of open cells and drizzle in marine stratocumulus. *Bull. Amer. Meteorol. Soc.*, **86,** 51-+.

Yu, L., R. A. Weller, and B. Sun, 2004: Mean and Variability of the WHOI Daily Latent and Sensible Heat Fluxes at In Situ Flux Measurement Sites in the Atlantic Ocean. 2096-2118.

TURBULENCE STRUCTURE OF CONTINENTAL BOUNDARY LAYER CLOUDS

Virendra P. Ghate[1] and B. A. Albrecht[1]

1. RSMAS/MPO, University of Miami

1. INTRODUCTION

Boundary layer clouds often form at the top of mixed layer and cover extensive area of earth surface. Marine boundary layer clouds are observed on the eastern side of subtropical oceans over the cold sea surface temperatures, while their continental counterparts are more variable in time and space. These clouds reflect most of the incoming radiation due to their high albedo, while due to low altitude they do not significantly alter the longwave radiation budget at the top of the atmosphere. The net effect being cooling of the underneath sea or land surface. These clouds are fundamental in regulating the vertical structure of water vapor and entropy and are also closely coupled to the turbulence in the boundary layer. Although continental boundary layer clouds cover less area than their marine counterparts, they affect the local weather and also play an important role in pollutant venting. In this study an attempt is made to characterize the turbulent structure of boundary layer clouds using Doppler cloud radar.

2. DATA & INSTRUMENTATION

The United States Department of Energy (DOE)'s Atmospheric Radiation Measurements (ARM) is a major program of atmospheric measurement and modeling, with a particular focus on the influence of clouds and the role of cloud radiative feedback. The Cloud and Radiation Test bed (CART) at the Southern Great Plains (SGP) site consists of many observing facilities. It is primarily designed to collect observations for prospective model testing in a shared data environment. There are many observing facilities present at the CART, but the complete set of instrumentation is only present at the central facility at Lamont, Oklahoma. The instrumentation at the central facility used for this study is summarized in Table 1.

Table 1: Summary of instruments at ARM SGP central facility.

INSTRUMENT	OUTPUT
W-band Doppler cloud radar	Doppler spectrum and its moments
Ka-band Doppler cloud radar	Doppler spectrum and its moments
Laser ceilometer	First three cloud base heights
Microwave radiometer	Column integrated liquid and water vapor
Flux suite	Surface longwave, shortwave and turbulent fluxes
Met station	Surface air temperature, pressure, humidity etc.

In this study, data from the W-band ARM Cloud Radar (WACR) is used to study the turbulent structure of boundary layer stratocumulus clouds.

3. TEST CASES

Presented here are turbulent characteristics of stratocumulus clouds under two different conditions. Shown in Fig. 1 is the WACR recorded mean Doppler velocity for the two test cases. The first event occurred during early hours on 8 April 2006 while the second event took place on 25 April 2006. Since the local time is 6 hours behind UTC, the first event is a night-time event, while the second is a daytime event. Also noticeable is that the first case is of decaying stratocumulus cloud with decrease in cloud thickness with time, while the second one is of cloud forming with cloud thickness increasing with time. Both cases occurred soon after the passing of a subtropical cold-front at the SGP site.

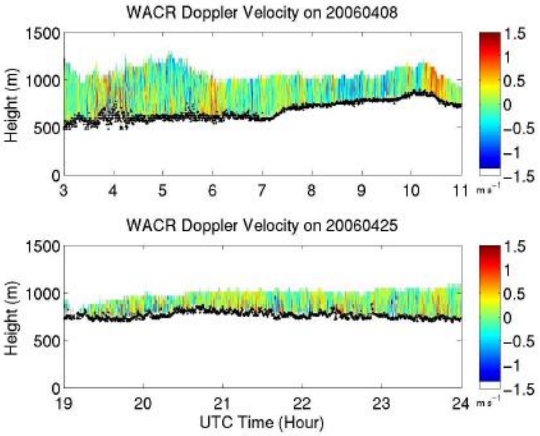

Figure 1: WACR recorded mean Doppler velocity on 8 April 2006 (top) and on 25 April 2006 (bottom). Also, shown is the ceilometer recorded first cloud base on both days.

Balloon borne soundings are made every 6 hours at the central facility. The potential temperature and mixing ratio profiles for the two events are shown in Fig. 2. Both have similar profiles with inversion base at about 1 km. The boundary layer is well mixed with the potential temperature and mixing ratio conserved within it. The surface turbulent fluxes for the two cases are shown in Fig. 3.

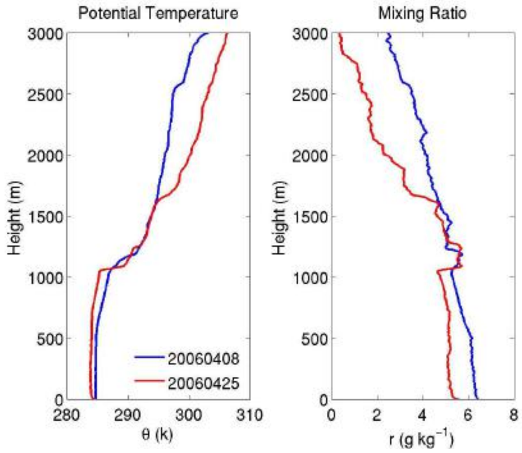

Figure 2: Potential temperature (left) and mixing ratio (right) profiles for 8 April 2006 and 25 April 2005.

During the night-time 8 April 2006 case, the absence of solar heating results in negligible surface turbulent fluxes. Hence, the turbulence in boundary layer is not due to surface buoyant production. The possible sources of turbulence in this case might be shear or cloud top radiative cooling. On the other hand for the daytime case, solar forcing results in a substantial virtual sensible heat flux and the possibility of surface production of turbulence kinetic energy by buoyancy.

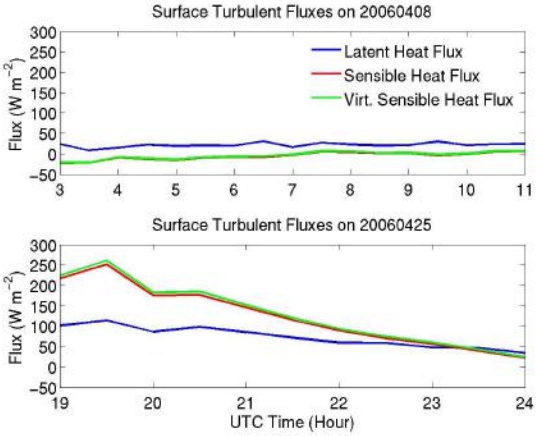

Figure 3: Surface sensible, latent and virtual sensible heat fluxes for 8 April 2006 (top) and 25 April 2006 (bottom).

4. PRELIMINARY RESULTS

Since, there are no precipitation hydrometeors observed during both the cases (dBZ<-20), it can be assumed that the cloud droplets due to their negligible fall velocity move up and down with the large eddies. Hence, the mean Doppler velocity recorded by the vertically pointing Doppler radar can be used as a surrogate for the vertical velocity and Large Eddy Observations (LEO) (Kollias & Albrecht 2000) can be carried out using the radar data. Fig. 4 shows the vertical velocity variance, skewness and fractional updraft coverage for an hour for each case. Also shown are the power spectra of cloud base and cloud top height for the chosen hours. For comparison purposes, values of these parameters were calculated at five cloud depth normalized levels. Although the cloud structure and the sources of turbulence are different for the two cases, they have a similar profile of vertical velocity variance. The variance is higher at the cloud base for the daytime case as the turbulence is surface forced.

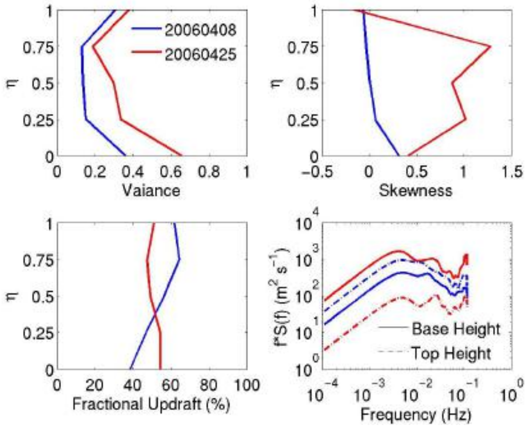

Figure 4: Vertical velocity Variance (top left), Skewness (top right), Fractional updraft area (bottom left) for hour 0600 on 8 April 2006 and hour 21 on 25 April 2006. Also shown is the spectrum of cloud top and base height (bottom right).

Positive vertical velocity skewness indicates that the updrafts are stronger but narrower than the surrounding downdrafts. A strong positive skewness is observed for the daytime case compared to an almost symmetrical distribution for the nighttime case. The fractional updraft coverage is almost 50% throughout the cloud layer for both the cases with some variations observed in the nighttime case. The power spectra of the cloud base and top height show a dominant peak and then some secondary peaks. The sources or the explanation of these peaks is not clear at this moment and will need some more data analysis.

5. FUTURE WORK

The preliminary results look promising and validate the use of radar data to carry out LEO, and study the turbulence characteristics of boundary layer clouds. The future work will be aimed to the characterize the in-cloud turbulence of boundary layer clouds under different conditions and relate it to the boundary layer properties like surface fluxes, lifting condensation level, boundary layer depth etc. An attempt will be also made to develop climatology of the vertical velocity structure of these clouds in different set of conditions.

6. BIBLIOGRAPHY

Kollias P. and B. A. Albrecht 2000: The turbulence structure in a continental stratocumulus cloud from millimeter wavelength radar observations. *J. Atmos. Sci.*, **57**, 2417-2434

Kollias P., B. A. Albrecht, R. Lhermitte and A. Savtchenko 2001: Radar observations of updrafts, downdrafts and turbulence in fair weather cumuli. *J. Atmos. Sci.*, **58**, 1750-1766.

Zhu P., B. A. Albrecht and J. Gottschlack 2000: Formation and developement of noctornal boundary layer clouds over the southern great plains. *J. Atmos. Sci.*, **58**, 1409-1426.

Acknowledgements

This research was supported by Department of Energy grant DE-F602-05SER63962

EVOLUTION OF PARTICLE SIZE DISTRIBUTION AND ICE CRYSTAL HABIT

Tempei Hashino and Greg J. Tripoli

University of Wisconsin - Madison, Wisconsin, USA

1 INTRODUCTION

Aggregation process of ice particles is the one of the most important processes that grows ice particles to precipitation size especially in stratiform clouds. Therefore, better understanding of the process is crucial, for example, to estimate life time of stratiform clouds, precipitation rate, and any impacts of anthropogenic aerosols on the clouds. The aggregation process is expected to be sensitive to ice crystal habits through cross section area and terminal velocity as well as the collision and coalescence efficiency. However, little is known quantitatively at this moment (cf., Pruppacher and Klett, 1997).

Recently Lagrangian stochastic aggregation models have simulated a fractal dimension (or mass-geometrical relationships) and aspect ratio of aggregates that agree well with observation (Westbrook et al., 2004; Maruyama and Fujiyoshi, 2005). Westbrook et al. (2004) used columns as component particle, while Maruyama and Fujiyoshi (2005), hereafter MF05, spheres. MF05 showed the growth rates of the aggregates greatly depend on the collision section of particles and discussed the sensitivity of initial Particle Size Distribution (PSD) and density of constituent particles. This paper discusses potential impacts of the habits and efficiency models on the evolution of PSD or Particle Mass Distributions (PMDs) by simulating aggregation process with the stochastic collection equation (Eulerian approach).

2 METHODOLOGY

The authors developed a new microphysical scheme called Spectral Habit Ice Prediction System (SHIPS), which is aimed to predict ice particle properties explicitly and retain the growth history in a 3D Eulerian dynamic model (see Hashino and Tripoli, 2007 and 2008). SHIPS predicts hexagonal monocrystals and polycrystals along with dendritic features, using most recent knowledge of habit growth regimes. For collection process, SHIPS solves the stochastic collection equation based on the predicted crystal habit and particle type.

The unique formulation is that SHIPS predicts the circumscribing sphere volume (or maximum dimension) of ice particles that are evolving by collection process. Mean property of component crystals is also predicted. The growth of the maximum dimension can be obtained by a simple geometric consideration of two contacting 2D rectangles. The aspect ratio and porosity of the ice particles are diagnosed based on the predicted mean crystal habit and the mass of the aggregate.

The aggregation process is tested in a simple setup where all falling particles stay in a unit volume and the evolution of PSD and ice particle properties are the results of only aggregation and riming processes (no effect of sedimentation). Five crystal habits are considered: plates, columnar crystals, dendrites, and columnar, planar, and irregular polycrystals. Following MF05, the PMD in all the simulations are initialized with exponential distribution in terms of mass (mean radius of 0.01 cm). Collision efficiency is assumed to be 1. Five different coalescence efficiency models are used: a unit efficiency model (X), a model using bulk density of two particles (P), a

---

Corresponding author's address: T. Hashino, Department of Atmospheric and Oceanic Sciences, University of Wisconsin - Madison, 1225 W. Dayton St, Madison, Wisconsin 53706 USA; Email: Hashino@wisc.edu

model using bulk density of component crystals (C), and a model using dendritic arm lengths (D).

3 RESULTS

Figure 1 shows maximum dimension, terminal velocity, bulk sphere density and aspect ratio of predicted aggregates of dendrites from X simulations. They have properties that are well compared with the limited available observations. SHIPS predicts unique property given a mass point, and the properties are subject to initial distribution and habit.

First, consider unit efficiency simulations in order to study effects of habits through cross section and terminal velocity. Figure 2 shows PMDs at 60 minutes of simulation for the five crystal habits and for the four efficiency models. Aggregation with spherical ice particles with constant density 0.3 g cm^{-3} was simulated as a reference. (a) of the figure shows results for X. The non-spherical habits predicted by SHIPS show faster growth than the constant-density sphere aggregates and aggregates of dendrites are the fastest. Figure 3 shows the collection kernel, cross section area, and velocity difference for the particle pairs where a large particle collects particles of the half mass. The aggregates of dendrites show the largest collection rate due to the largest cross section among habits. The collection kernels are largely a function of cross section area, and having different habits can lead to difference in the collection rate by factor of 10 to 100 at a given mass. It is interesting to note that the increase of cross section with mass is larger than the increase of velocity difference by factor of 10. Moreover, the velocity difference gets smaller with mass because the increase in terminal velocity declines with mass.

Compared with aggregates of sphere, the other habits compensate smaller velocity difference by having larger cross sections.

(a) Max dimension

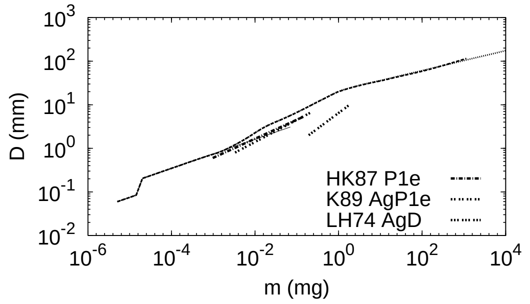

(b) Terminal velocity

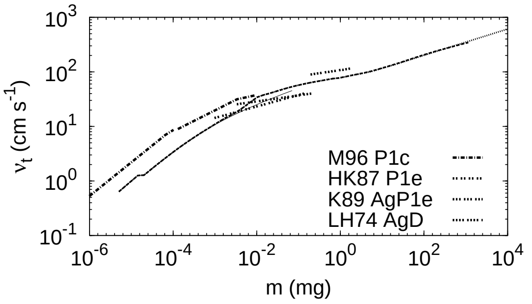

(c) Bulk sphere density

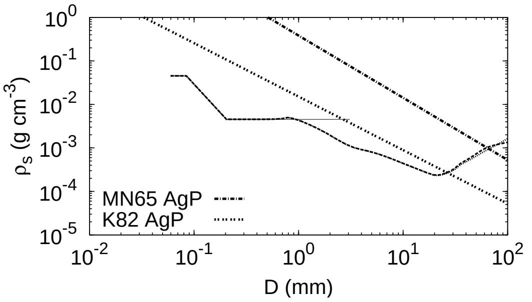

Figure 1 Predicted particle properties for aggregates of dendrites. (a) shows mass-dimensional relationship, (b) mass-terminal velocity relationship, and (c) dimension-density relationship. Each figure includes initialization (thin solid line), 20 min (thick broken line), and 60 min simulations (thick dot line). HK87 denotes Heymsfield and Kajikawa (1987), K82 Kajikawa (1982), LH74 Locatelli and Hobbs (1974), M96 Mitchell (1996). Ag indicates aggregates. MN65 AgP and K82 AgP are planar aggregates from Magono and Nakamura (1965), and Kajikawa (1982).

This is the consequence of allowing density of ice particles to decrease with mass for the non-spherical habits.

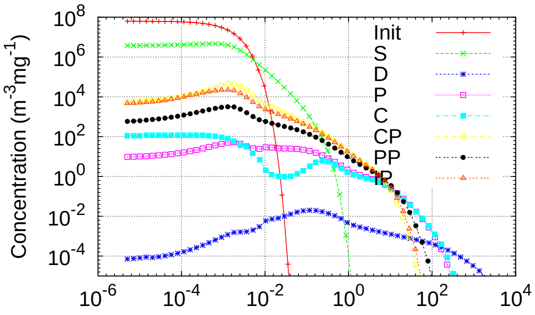

(a) Unit efficiency, X

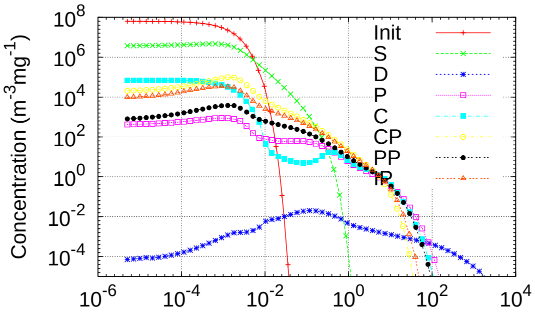

(b) Efficiency model, P

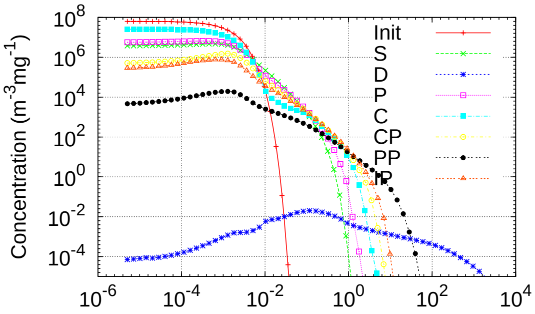

(c) Efficiency model, C

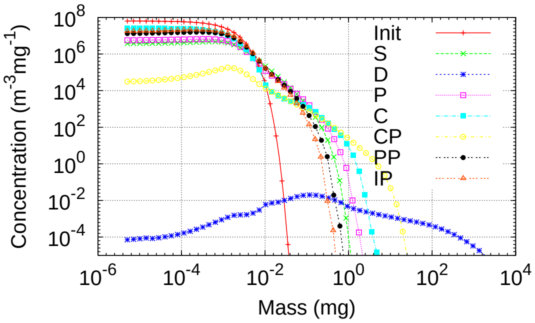

(d) Efficiency model, D

Figure 2 Comparison of particle mass distributions at 60-minute simulation for six different ice crystal habits, namely sphere (S), dendrites (D), plates (P), columns (C), columnar polycrystals (CP), planar polycrystals (PP), and irregular polycrystals (IP).

MF05 shows that the maximum difference of terminal velocities do not vary too much with time for their aggregation models, and emphasizes the importance of collision cross section in estimating snowflake growth rates. The stochastic collection model of SHIPS is qualitatively similar to the pure stochastic models of MF05 in that the cross section is more important to determine the growth rate of snowflakes than terminal velocity difference. This is the consequence of predicting density of aggregates to decrease with mass.

The three efficiency models, P, C, and D show significant differences in evolution of PMD due to nonlinear feedback ((b), (c) and (d) of Figure 2). It turned out that the predicted mass-dimension, mass-terminal velocity, and diameter-density relationships are not sensitive to the aggregation efficiency if only aggregation processes are considered, but they are sensitive to the initial PMD and habit.

4 DISCUSSIONS

A sensitivity test suggests that the growth rate of the predicted PMD is largely controlled by the separation ratio, a measure of distance between coalesced particles, and aspect ratio of the aggregates. Change of the separation ratio would be related to three dimensional growth of the aggregates and the growth has to be consistent with change of aspect ratio. These sensitive variables should be studied by direct or indirect observations of aggregation and riming processes.

The separation ratio was modeled to increase the bulk sphere density after the mass of aggregates reaches a threshold. However, the aggregation simulation, particularly with dendrites, can still produce unrealistically large aggregates within 60 minutes. Therefore, the hydrodynamic breakup of aggregates was modeled based on largely educational guess (the above results did not simulate this process). In reality, collision-breakup of aggregates is expected to occur before the hydrodynamic break, and the formulation of the breakup process should be addressed in laboratory experiments.

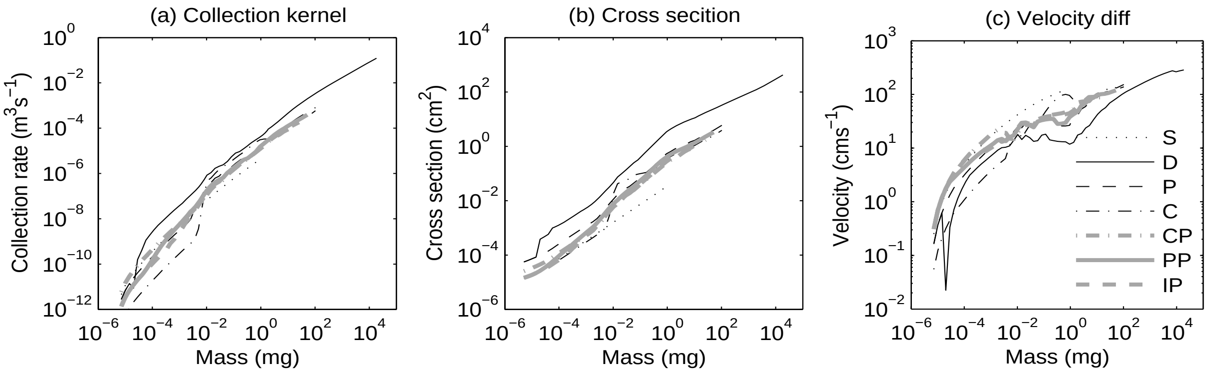

Figure 3 Comparison of (a) collection rate, (b) cross section, and (c) terminal velocity difference for the unit collection efficiency simulation.

5 CONCLUSIONS

SHIPS is able to reproduce realistic relationships between ice particle properties based on a simple growth model of maximum dimension. The simulated growth of PMS largely depends on cross section area of the given habits. The results will be compared with a Lagrangian aggregation model of MF05 in the presentation. Furthermore, effects of crystal habits on aggregation process in Eulerian dynamic models and the predicted PSDs will be discussed.

6 ACKNOWLEDGEMENT

This research was supported by NASA (NNG04GA36G and NNX07AD43G).

REFERENCES

Hashino, T. and G. Tripoli, 2007: The Spectral Ice Habit Prediction System (SHIPS). Part I: Model description and simulation of vapor deposition process. *J. Atmos. Sci.*, 64, 2210–2237.

Hashino, T. and G. Tripoli, 2008: The Spectral Ice Habit Prediction System (SHIPS). Part II: simulation of nucleation and depositional growth of polycrystals. *J. Atmos. Sci.*, (early online release).

Heymsfield, A.J., and M. Kajikawa, 1987: An improved approach to calculating terminal velocities of plate-like crystals and graupel. *J. Atmos. Sci.*, 44, 1088–1099.

Kajikawa, M., 1982: Obsrvations of the falling motion of early snowflakes. Part I: Relationship between the free-fall pattern and the number and shape of component snow crystals. *J. Meteor. Soc. Japan*, 60, 797-803.

Locatelli, J. D., and P. V. Hobbs, 1974: Fall speeds and masses of solid precipitation particles. *J. Geophys. Res.*, 79, 2185-2197.

Magono, C., and T. Nakamura, 1965: Aerodynamic studies of falling snowflakes. *J. Meteor. Soc. Japan*, 43, 139-147.

Maruyama, K. and Y. Fujiyoshi, 2005: Monte Carlo simulation of the formation of snowflakes. *J. Atmos. Sci.*, 62, 1529–1544.

Mitchell, D.L., 1996: Use of mass- and area-dimensional power laws for determining precipitation particle terminal velocities. *J. Atmos. Sci.*, 53, 1710–1723.

Pruppacher, H. R. and J. D. Klett, 1997: Microphysics of Clouds and Precipitation. Kluwer Academic, 914 pp.

Westbrook, C. D., R. C. Ball, P. R. Field, and A. J. Heymsfield, 2004: Theory of growth by differential sedimentation, with application to snowflake formation. *Phys. Rev.*, E70, 021 403.

THE STUDY ON POTENTIAL OF ARTIFICIAL PRECIPITATION ENHANCEMENT FOR STRATUS CLOUDS SYSTEM

Hong Yanchao[1]　Zhou feifei[2]　Liu Zongxiu[3]
1　Laboratory of Cloud-Precipitation Physics and Severe Storms, Institute of Atmospheric Physics, Chinese Academy of Sciences, Beijing 100029
2　Graduate School of the Chinese Academy of Sciences, Beijing 100039
3　Chinese Meteorological society，Beijing，100080

1. INTRODUCTION

Stratus Clouds System is a main precipitation system in spring and autumn in north China and a main object for artificial precipitation enhancement by the seeding. The potential of artificial precipitation enhancement is capacity of the cloud system to increase rainfall on ground by artificial influence and it must be considered in judging and directing seeding task. To understanding various factors of the potential have an important significance for opening up cloud water resource and building up effect of artificial precipitation enhancement.

At present, the potential of stratus cloud system is studied by several ways. Someone respectively taken precipitation efficiency[1] of the cloud system as the potential factor, and someone taken water vapor content, super-cooling water content, and concentration of ice crystal as other potential factors. Hu Zhijing et al.[2] think that the super-cooling water content is a favorable condition for the artificial seeding, but the clouds with little super-cooling water have still certain potential to precipitation enhancement, because water resource for artificial precipitation enhancement is not only from transform of liquid water to ice but also vapor to ice. Formation of natural precipitation is a complex processes, it is related to the structure of cloud, also the microphysical processes in cloud. Therefore, the judging potential is a complex and integrative processes, too， so that the potential should not be evaluated by one single parameter, for example, precipitation efficiency or super-cooling water content et al. In this paper, using data of a stratus cloud system simulated by the mesoscale numerical model MM5, which occurred on 19 Oct., 2002 in Henan province (Henan cloud system) and produced precipitation over a great area, we try to analyse the potential factors for artificial precipitation enhancement in cloud and precipitation physics, and taken super-cooling water content, ice crystal concentration, amount of super-saturated water vapor with respect to ice(SQV), precipitation efficiency, precipitation mechanism, cloud water content and thickness of the warm cloud region as the potential factors to advance integrative evaluation way of the potential.

2. NUMERICAL SIMULATION OF THE STRATUS CLOUD SYSTEM

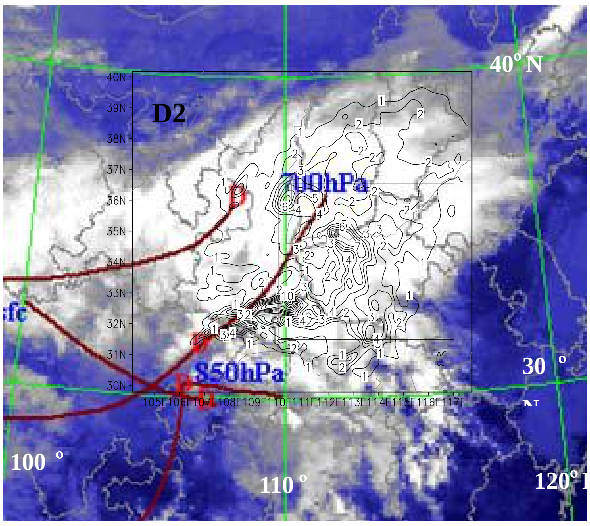

Fig.1　GMS-5 infrared satellite cloud picture at 8:00, on 18-20 October 2002 and distribution of thickness (mm) of water content in the model cloud system superimposed the cloud picture.D2 domain is noted by the large rectangle and in which the small rectangle represents Henan province area.

In this paper, mm5 of PSU/NCAR was used with graupel scheme of Reisner to simulate the stratus cloud system occurred on 19 Oct., 2002 in Henan province. The simulation time is from 08:00, 18 Oct. to 02:00, 20 Oct. Two nested-level domain with center point of (34.5°N, 109.5°E) were set. The horizontal resolution in outer domain was 45km and inner fine-mesh was 10km. The model atmosphere was divided into 23 levels from the surface to 100pha for all two domains. The model was initiated not only using the NCEP/NCAR re-analysis data but also the general ground and radio-sounding data.

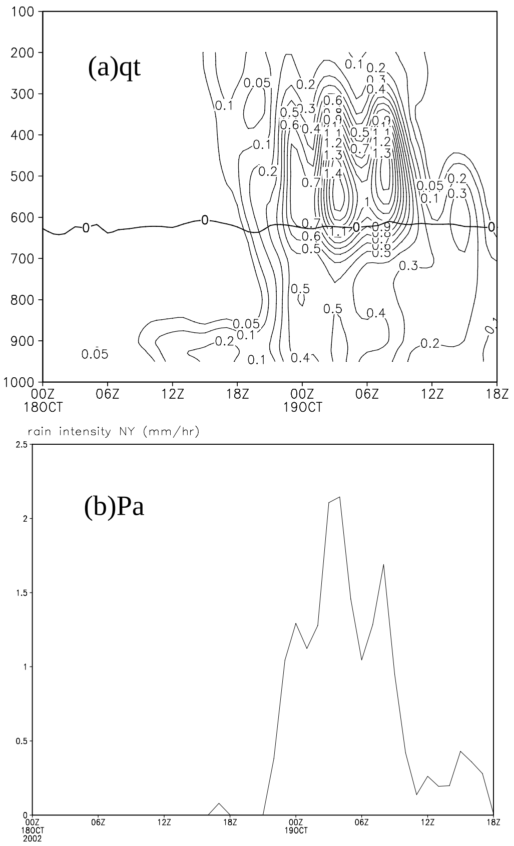

Fig.2 Time cross-section of total water content q_t (g/kg) (a) and time variation of rainfall intensity P_a (b) at Nantyang station.

Overall, simulated cloud field, temperature field, wind field, low level shear line and jet stream are all consistent with actual thing，accumulated rainfall region is consistent with observation. From fig.1, it can be seen that area of simulated cloud is same as the satellite cloud picture.

3. ANALYSIS OF POTENTIAL FACTORS FOR ARTIFICIAL PRECIPITATUION ENHANCEMENT

3.1 The Potential and Cloud Structure

Condition of the cloud water conversion is related to its distribution. In the simple cooled cloud or warm cloud processes, the cloud water is transformed hardly to precipitation，distribution of cloud water and structure of cloud system have a close relation to mechanism of the precipitation formation, therefore, to precipitation enhancement, too. Study on the cloud system structure, especially the vertical structure has an important significance for ascertaining of the potential region. Relationship of the structure and the precipitation is analyzed according to time change of water content and rainfall intensity in simulated Hena cloud system. It can be seen from fig.2 that there is warm cloud at Nantyang station during 00:00 and 18:00 on18,oct., rainfall intensity corresponding to water content region with 0.2 g/kg is lower; three maximum rainfall intensity are all corresponding to centers of the water content and they are all "seeding-feeding" clouds，in which seeding cloud joins feeding cloud . It indicates "seeding- feeding" cloud is propitious to precipitation, of course, propitious to artificial precipitation enhancement.

3.2 Precipitation Mechanism and Potential for Precipitation Enhancement

At present, artificial precipitation enhancement is operated by effecting cold cloud microphysical processes, so that only such cloud in which the cold cloud process play an important role in precipitation formation is seeded, precipitation is increased.

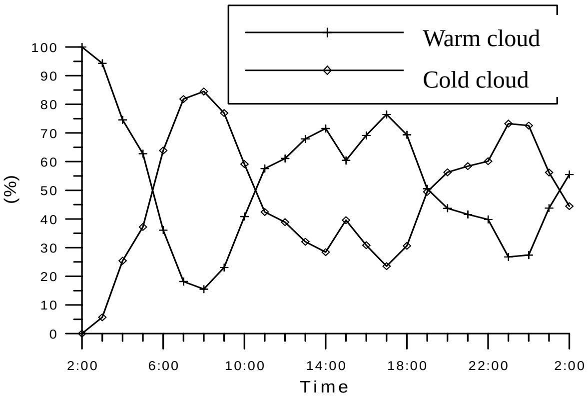

Fig.3 Time variation of ratios of hourly rainfall amount produced by warm cloud processes and cold cloud processes to hourly total rainfall amount from 02:00, on 19 to 02:00, on 20 in Zhengzhou area.

In the various stages of cloud system, the cold cloud process has different contribution for rainfall (fig.3), we should choose period of time in which cold cloud precipitation is in the ascendant for seeding, for example, from 07:00 to 09:00 on 19, oct.. so that precipitation mechanism should be a potential factor for precipitation enhancement.

3.3 Cloud Resource and Potential for Precipitation Enhancement

Here, cloud water resource is defined as vertical integral amount (mm) of cloud water content or cloud water thickness and it has a close relationship to surface precipitation (fig.4). For example, in Nanyang area the time at which maximum rainfall intensity appear consistent with that of total cloud water, suppler-cold cloud water and warm cloud water, respectively. It is shown that the cloud water, that including supper-cold cloud water and warm cloud water, is important for precipitation. From the same change trend, we think that rainfall intensity is related to thickness of supper-cold water and cloud water. The lager cloud thickness is in favor of precipitation formation, and seeding for precipitation enhancement, too. Therefore, cloud water thickness is also a potential factor for precipitation enhancement.

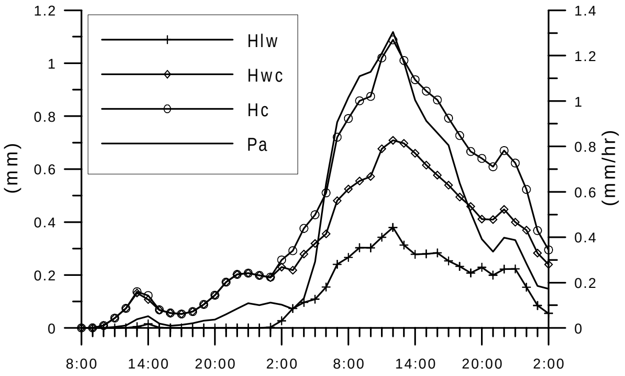

Fig.4 Time var area-mean values of super-cooling cloud water thickness (H_{lw}), cloud water thickness in the warm region (H_{wc}), cloud water thickness (H_c), and rainfall intensity (P_a) on surface from 08:00, on 18 to 02:00, on 20 in Nanyang area

3.4 Water Vapor And Potential For Precipitation Enhancement

In ice particles which have melted into liquid rain water, has the deposition process by expending water vapor or the accretion process by expending super-cooling water larger contribution to formation of rain water? It can be seen from fig.4 that, after 08:00 on 19, contribution of deposition growth to precipitation is lager than the accretion growth. This indicates that contribution of water vapor sublimation process to rain water formed by melting of ice particles larger than the accretion process and shows essentiality of water vapor in precipitation particles. Therefore, water vapor is an important potential factor.

What is called SQV, i.e., the excessive water vapor amount relative to saturation with respect to ice. Ice particle is grown by deposition in condition of supper saturation with respect to ice. In this Henan cloud system, deposition growth of ice particle by expending water vapor has lager contribution to the ice particles mass than accretion by expending supper-cold water. In some cloud system, the contribution of them are almost same, for example, in stratus cloud system [3] occurred in Henan province on 5, Apr. 2002, contributing rate of the deposition process to rain water produced by ice particles melt is 54%, and super-cold water transformation 39% at 05:00; at 08:00, they are 46% and 49%, respectively. If only cold cloud process play an important role in precipitation, deposition growth of ice particles is also important, so that supper saturation water vapor amount with ice surface related to precipitation, of course to potential for precipitation enhancement.

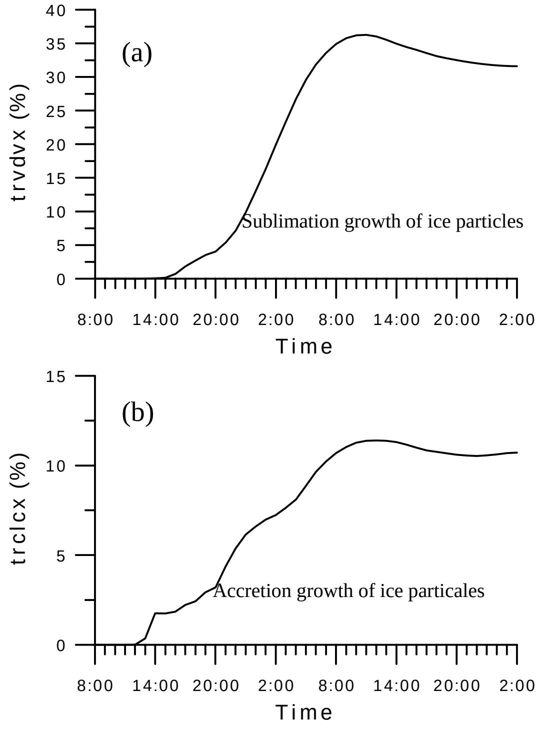

Fig.5 Time variation of contribution rate of different microphysical processes to precipitation: (a) sublimation growth of ice particles; (b) accretion growth of ice particles.

For Henan cloud system，SQV has a positive correlative with surface precipitation (fig.6), namely the lager SQV, the higher surface rainfall intensity. In fact, if the cold cloud process is main in rain water formation and deposition is main growth process of ice particle, water vapor must play an important role in cold cloud precipitation. Therefore, SQV has a close relationship to precipitation. If cold cloud process is main and deposition is an important microphysical process in the cloud system, SQV is a important potential factor.

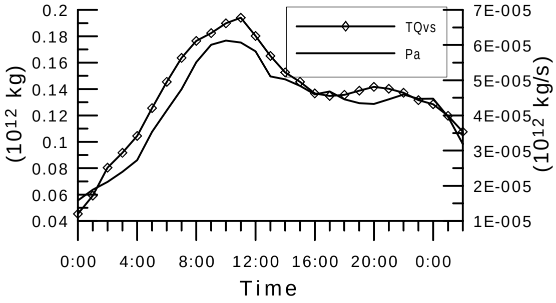

Fig.6 Time variations of super-saturation water vapor amount with respect to ice (Q_{vs}) and rainfall intensity (P_a) in D2 domain.

3.5 Precipitation Efficiency and Potential for Precipitation Enhancement

Artificial precipitation enhancement make supper-cold water surface precipitation, therefore, we need to know cloud water amount which is not transformed into rain water. The study indicate that in cloud system in which cold cloud precipitation is main, deposition of ice particle is an important microphysical process in precipitation formation, so that how much deposition-water which is not transformed precipitation should be also known. Namely, we need to work out at precipitation efficiency of condensation water and deposition water.

For Zhengzhou area, in Henan cloud system,，before 05:00 on 19（fig.7），the warm cloud precipitation is in the highest flight, precipitation efficiency of condensation water much higher than deposition；during 05:00 and 10:00，precipitation efficiency of deposition water go up quickly and exceeds condensation water and reach maximum of 71.0% at 10:00; after that, it begin to descend and average values of it is as much as precipitation efficiency of condensation water, they are 34.7% and 29.4%, respectively. Thus it can be seen that there are large numbers of condensation water and deposition water in the cloud, as a result, it has lager potential for precipitation enhancement.

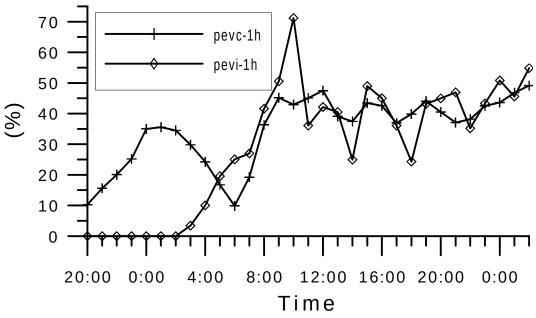

Fig.7 Time variation of precipitation efficiency of hourly condensation water (pevc-1h) and hourly sublimation water (pevi-1h) in Zhengzhou area.

4. SYNTHETICAL EVALUATION OF POTENTIAL FORPRECIPITATION ENHANCEMENT

From above analysis on the potential factors, we should use these potential factors to evaluate the potential for artificial precipitation enhancement. If cloud system and precipitation is being in developing stage, technique of synthetical evaluation potential for precipitation enhancement is as follows:

First, analyzing macrostructure of cloud system.，in general, there is potential for precipitation enhancement in the “seeding-feeding” cloud, especially the seeding layer and the feeding layer are connected，the potential is lager.

Second, for “seeding- feeding” cloud system, contribution of the cold cloud process for precipitation is needed to analyse, if the contribution is lager, the cloud system has lager potential for precipitation enhancement.

Third, analyzing precipitation efficiency of condensation water and deposition water, if they are low, the potential is lager.

Four, analyzing supper-cold water content, ice crystal concentration，cloud water content in the warm region. If the supper-cold water content is higher, ice concentration lower and water content in the warm region higher, then the potential is lager.

Fifths, analyzing water vapor condition, including vertical flux of water vapor and SQV, when updraft is lager in the cloud and SQV is lager, the potential lager.

5. CONCLUSION AND DISCUSSION

The potential factors of strtiform cloud system for artificial precipitation enhancement are studied using the simulated cloud system and consideration of synthetical evaluation of potential for precipitation enhancement is brought up. Namely, the stratus cloud system, in which there is structure of “seeding-feeding” cloud, cold cloud precipitation mechanism to be in the ascendant, higher supper-cold water content and lower ice concentration, lager SQV and lower precipitation efficiency, can be provided lager potential for precipitation enhancement.

Firstly, evaluation method of the potential proposed in the paper use many potential factors and overcome localization of evaluation by one or two factors. Secondly, some new potential factors are studied and put forward. One is the cloud structure, only “seeding-feeding” cloud structure

Secondly, some new potential factors are studied and brought forward. One is the cloud structure, only strstiform cloud system in which there is “seeding-feeding” cloud structure has seeding potential for cold cloud; the other new potential factor is precipitation mechanism and this potential factor catch hold of essential of seeding theory for artificial precipitation enhancement, namely objective of artificial precipitation enhancement is achieved by effecting cold cloud microphysical process. So that only cold cloud process has an important role in precipitation formation in the statiform cloud system, there is the lager seeding potential in the cloud system. Three is SQV, which is put forward by study growth process of ice particles in the cloud system in which cold cloud process is in the ascendant. In such cloud system, deposition growth of ice particles by expend water vapor is very important for precipitation.

Thirdly, from theory of artificial precipitation enhancement, precipitation efficiency of condensation water and deposition water which can shown ability of condensation water and deposition water to be transformed into precipitation particles and rainfall on ground. It makes the precipitation efficiency more suitable to evaluation of the potential for precipitation enhancement. If precipitation efficiency is calculated using condensation amount or sum of condensation amount and deposition mount. The former overrates precipitation efficiency because rainfall on the ground contains contribution of deposition water the latter do not distinguish contribution of condensation water and deposition to rainfall, therefore the potential evaluated is out of pertinency.

The potential factors in the paper are obtained by the numerical simulation and theory analysis, and evaluation of the potential is only based on qualitative analysis. Every potential factor has not a quantitative criterion. In fact, the quantitative criterion is very important for the evaluation of the potential. Beside, if we applied these potential factors and the evaluation consider of the potential to the practice of artificial precipitation enhancement, we have a long way to go. For example, how do we confirm the structure of “seeding-feeding” cloud? And what is the method to make sure the precipitation mechanism?

References

[1]Feng shan, Zheng shilling and Zhao peijuan. Precipitation efficiency and potential of artificial precipitation enhancement in cold frontal cloud system in spring in Henan Province. *Study on Optimal Technique for Artificial Weather Modification* (in Chinese). Beijing: Meteorology Press, 2000. 36~40

[2] Hu Zhiji，Qinyu and Wang Yubin. Numerical experimentation for stratus cold cloud. *Acta Meteorologica Sinica* (in Chinese), 1983, **41**(2):194~203

[3] Hong Yanchao, Zhoufeifei. A numerical simulation study of precipitation formation mechanism of “seeding-feeding” cloud system. *Chinese Journal of Atmospheric Sciences* (in Chinese), 2005, **29**(6): 885~896.

STUDIES OF THE STRUCTURE OF A STRATIFORM CLOUD AND THE PHYSICAL PROCESSES OF PRECIPITATION FORMATION

HU Zhao-Xia[1], LEI Heng-Chi[1], GUO Xue-Liang[1], JIN De-Zhen[2], and QI Yan-Bin[2]

1 Institute of Atmospheric Physics, Chinese Academy of Sciences, Beijing 100029

2 Jilin Weather Modification Office, Changchun 130062

1. INTRODUCTION

Precipitation of stratiform cloud is one of the important water resources on the ground. Many observational and modeling studies show that precipitation development in stratiform cloud is very complicated (Heymsfield, 1977; Rangno and Hobbs, 2001; Orville, et al., 1984). The "seeder-feeder" cloud process was first proposed by Bergeron (1950) for precipitation enhancement in orographic clouds. Similar to the "seeder-feeder" mechanism, the process of precipitation formation play an important role in the wide cold-frontal rainbands and warm-frontal rainband (Hobbs et al., 1980; Rutledge and Hobbs, 1980). You et al. (2002) also found the "seeder-feeder" process in the stratiform clouds in Northern China.

Koo Chen-Chao (1980) also proposed a three-layer conceptual model to interpret the structure and precipitation mechanism of the stratiform cloud. In this paper the structure of a stratiform cloud and physical processes of precipitation formation were analyzed by through observational data of airborne PMS, Doppler radar and rainfall in situ on 5 July 2004, in Changchun, Jilin province. A numerical simulation was also conducted using one dimensional, time-dependent stratiform cloud model with detailed microphysical processes. In the present study, the three-layer conceptual model of Koo can describe precipitation process very well including "seed-feeder" mechanism.

2. SYNOPTIC SITUATION, FLIGHT PROFILE AND INSTRUMENTATION

This paper presented here will focus on a stratiform cloud which was induced by the typhoon, Mindulle, and then evolved into a low-pressure system. The satellite IR image is shown in Fig. 1. The star marked the Jilin province, western edge of a stratiform precipitation region. The airborne and ground based observations carried out on 5 July 2004. The instrumentations aboard the Yun-12 aircraft for cloud microstructural measurements were a set of calibrated PMS probes, micro-wave radiometer, GPS, King-LWC. There were a Doppler radar and 20 rainfall stations spaced 10 km and other conventional observations.

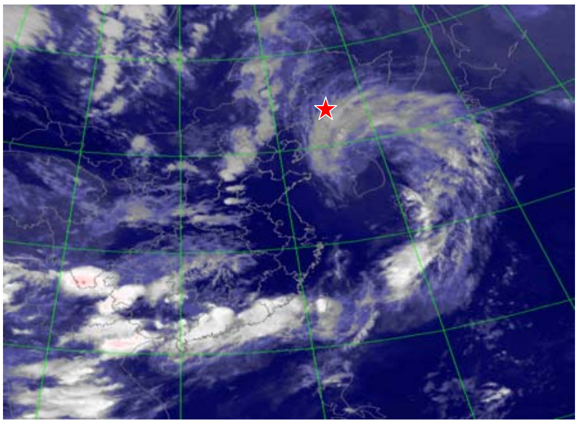

Fig.1 GOES-9 satellite infrared image taken at 19:00 BJT (Beijing Time) 4 July 2004

Fig. 2 is the flight height from aircraft taking off at 6:43 am to landing at 9:17 am. The cloud base and top are about 1400m and 6900m high respectively. 0^{o}C layer is

3900 m, which is a little difference compared with the sounding shown in Fig.3 with about 4200m high.

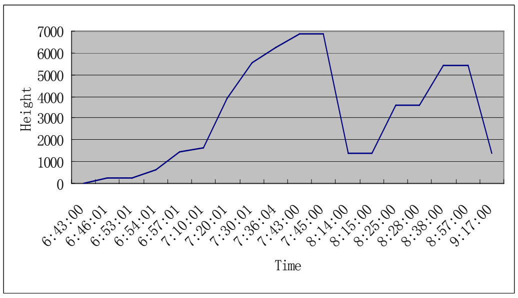

Fig.2 Variation with time of the flight height

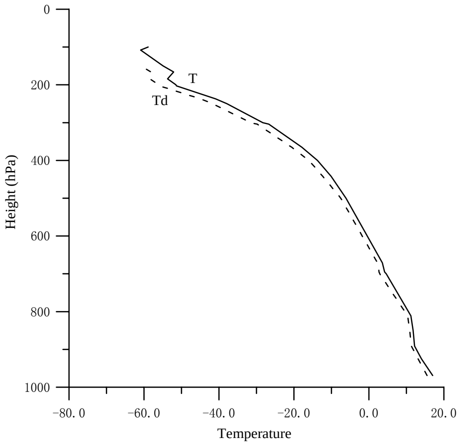

Fig. 3 Temperature (solid line) and dewpoint temperature (dashed line) sounding taken from Changchun, at 08:00 BJT 5 July 2004

3. OBSERVATIONS

3.1 Radar and Rainfall on the Ground

The radar echo (Fig. 4) shows a bright band obviously under 4 km and the maximum reflectivity is 30 dBZ.

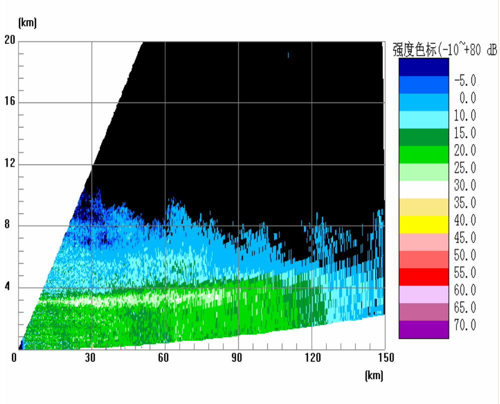

Fig.4 Radar RHI image at 179.9° azimuth at 07:20 BJT 5 July 2004

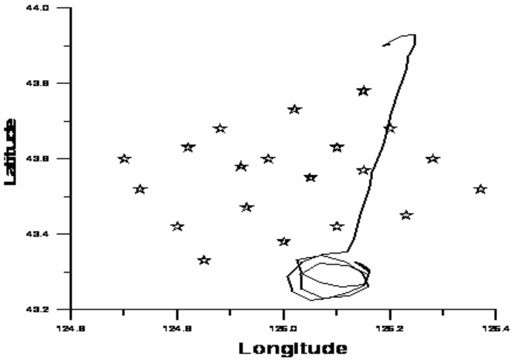

Fig. 5 Location of precipitation recorders and surface projection of flight track

The average rainfall at the surface observed by the 20 precipitation recorders is 1.33 mm/hr on 5 July 2004.

3.2 Particle Size and Concentration

Fig. 6 is the vertical distribution of the particle diameter measured by 2D-D, 2D-P and FSSP-100. The size of observed particles changed little above $0^{o}C$ layer. The mean diameters are 16.0μm, 160μm and 1100μm respectively.

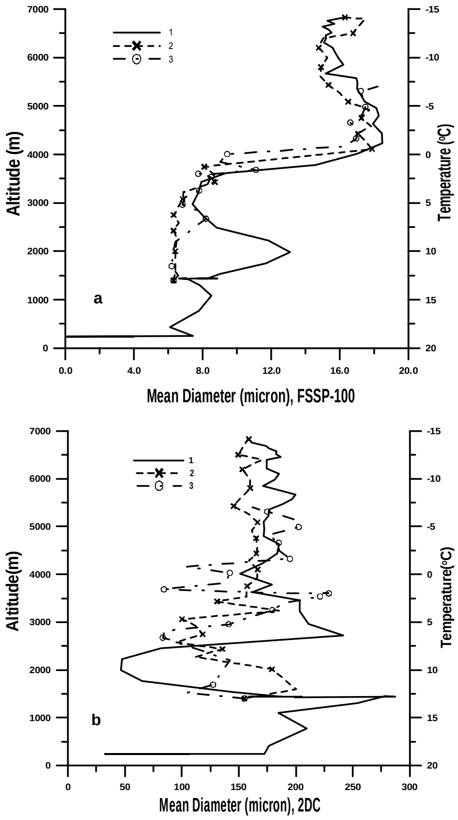

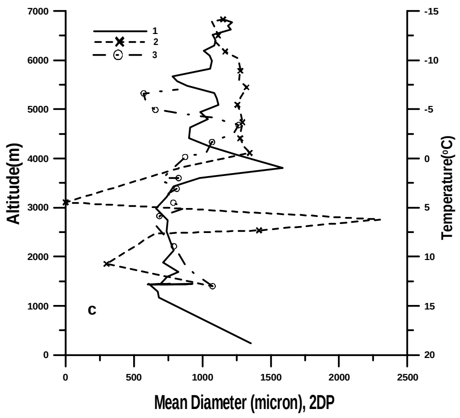

Fig. 6 Vertical distribution of the particle mean diameter (μm): (a) FSSP-100; (b) 2D-C; (c) 2D-P

Above the 0°C layer, the particle concentration changed little and the 2D-C and 2D-P probes sampled 3.0×10^4 and 2.0×10^3 per cubic meter respectively. On the other hand, the concentration varied a lot below the 0°C layer. The ice concentration above 0°C layer from 2D-C is about 2.6×10^4/m^3. There are lots of particles smaller than 25μm in the cold layer.

3.3 Water Content

The maximum of supercooled water content measured by FSSP-100 is 0.49 g/m^3 (Fig. 7). The water content is smaller in the warm layer.

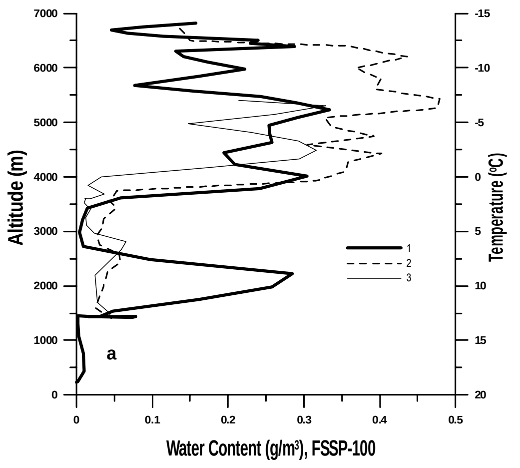

Fig. 7 Vertical distribution of water content

4 MODEL RESULTS

A one dimensional stratiform cloud model simplified from a 2-D cloud model (Hong, 1997) was employed to simulate the case. The simulated cloud water content, radar echo and rainfall intensity are shown in Fig.8-10. The other microphysical analysis will be indicated in summary.

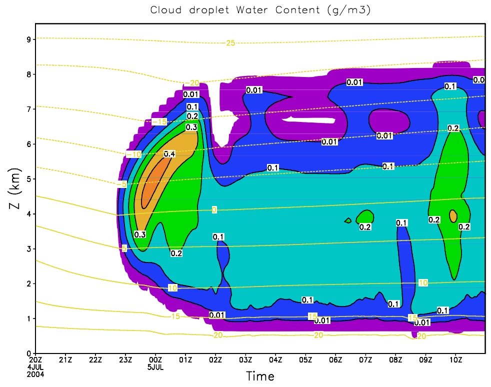

Fig. 8 Time-height cross section of the cloud water content and temperature

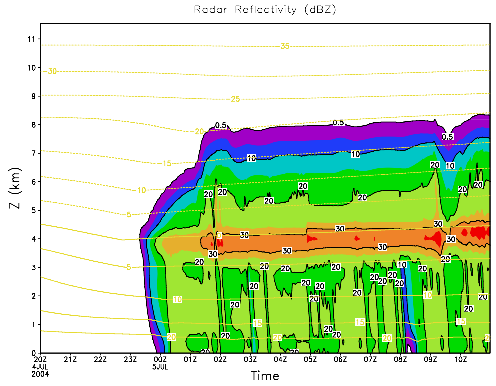

Fig. 9 Time-height cross section of the radar reflectivity (dBZ)

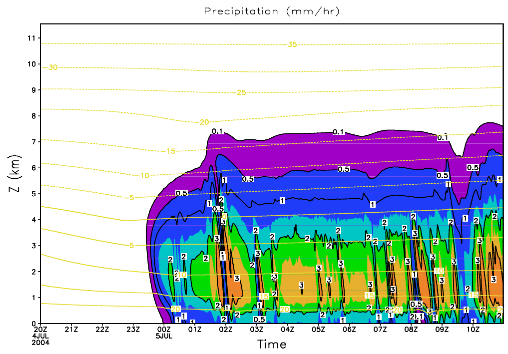

Fig. 10 Time-height cross section of the rainfall intensity (mm/h)

5 SUMMARY

The simulated results are well consistent with the observations. Koo Chen-chao’s three-layer cloud conceptual model can interpret the structure of the stratiform cloud well. In the first layer, namely ice crystal layer, the main water substance is ice crystal. The key parameter of this layer is the temperature of cloud top. In the second layer, namely supercooled water layer, there are composed by ice crystal, snow, graupel, cloud droplet and raindrop. The ice crystals grow by diffusion of water vapor to their surface due to the Bergeron process. The key parameters of the second layer are the content and thickness of supercooled water. In the third layer, namely warm water layer, the main water substances are cloud droplet, raindrop, and melting snow and graupel. The raindrops grow almost through gravitational collision. Therefore, the thickness and water content of the warm layer are the determinate factors.

The three layers, ice crystal layer, supercooled water layer and warm water layer, contribute 7%, 54% and 39% to the surface precipitation, respectively. The first layer seeds ice crystals and a little snow crystals to the feeder cloud (the second layer). And the second layer seeds snow crystals, graupel particles and raindrops to the feeder cloud (the third layer).

ACKNOWLEGEMENTS

This research was supported by the National Natural Science Foundation of China (Grant No. 40537034). The authors would also like to thank Prof. Huang Meiyuan for his helpful comments and advice.

REFERENCES

[1] Herzegh P H, Hobbs P V. The Mesoscale and Microscale Structure and Organization of Clouds and Precipitation in Midlatitude Cyclones. II: Warm-Frontal Clouds. *J. Atmos. Sci.*, 1980, **37**: 597～611

[2] Heymsfield A J. Precipitation development in stratiform ice clouds: A microphysical and dynamical study. *J. Atmos. Sci*., 1977, **34**: 367～381

[3] Hobbs P V, Matejka T J, Herzegh P H, et al. The Mesoscale and Microscale Structure and Organization of Clouds and Precipitation in Midlatitude Cyclones. I: A Case Study of a Cold Front. *J. Atmos. Sci*., 1980, **37**: 568～596

[4] Hong Y C. A Numerical Model of Mixed Convective-Stratiform Cloud. *Acta Meteorological Sinica*, 1997, **11** (4): 489～502

[5] Koo Chen-chao. *Bases of Cloud and Mist Precipitation Physics* (in Chinese). Beijing: Science Press, 1980. 173～179

[6] Orville H D, Farley R D, Hirsch J H. Some surprising results from simulated seeding of stratiform-type clouds. *J. Climate App. Meteor.*, 1984, **23**: 1585～1600

[7] Rangno A L, Hobbs P V. Ice particles in stratiform clouds in the Arctic and possible mechanisms for the production of high ice concentrations. *J. Geophys. Res*., 2001, **106**: 15065～15075

[8] Rutledge S A, Hobbs P V. The mesoscale and microscale structure and organization of clouds and precipitation in midlatitude cyclones. VIII: A model for the “seeder-feeder” process in warm-frontal rainbands. *J. Atmos. Sci*., 1983, **40:** 1185～1206

A SIMULATION OF RADAR- AND LIDAR-DERIVED VERTICAL STRUCTURES OF FRONTAL CLOUD USING A BIN-TYPE CLOUD MICROPHYSICAL MODEL

Takamichi Iguchi[1], Teruyuki Nakajima[1], Alexander P. Khain[2], Kazuo Saito[3], Takemura Toshihiko[4], Hajime Okamoto[5], and Tomoaki Nishizawa[6]

1. Center for Climate System Research, University of Tokyo
2. The Institute of Earth Sciences, The Hebrew University of Jerusalem
3. Meteorological Research Institute
4. Research Institute for Applied Mechanics, Kyushu University
5. Center for Atmospheric and Oceanic Studies, Graduate School of Science, Tohoku University
6. National Institute for Environmental Studies

1. INTRODUCTION

An active remote-sensing using radar and/or lidar can provide the vertical structure of cloud properties. *Okamoto et al*. [2007] showed the vertical cloud structure over the Pacific Ocean near Japan using radar and lidar on the Research Vessel Mirai during MR01/K02 cruise (May 2001).

In this study, we compared the vertical cloud structures simulated by the model with those conducted with a ship-board radar and lidar on the Research Vessel Mirai during a short part of MR01/K02 cruise in May 2001. The following numerical model was used: the bin cloud microphysics in Hebrew University Cloud Model is combined with a three-dimensional non-hydrostatic modeling system, Japan Meteorological Agency NonHydrostatic Model. This coupled model can predict size distributions of seven classes of hydrometeors; hence observables of radar and lidar, e.g. the radar reflectivity factor and the lidar backscattering coefficient, can be directly calculated using these size distributions.

2. MODEL DESCRIPTION

A numerical model for atmospheric dynamics used in this study is based on a multi-purpose non-hydrostatic atmospheric model developed by the Japan Meteorological Agency (JMA-NHM) [*Saito et al*., 2006]. We replaced the original bulk-type cloud microphysical scheme with a bin-type scheme based on the Hebrew University Cloud Model [e.g., *Khain et al*., 2000] [*Iguchi et al*., 2008]. The cloud microphysical tracers are size distributions of hydrometeors categorized into 7 forms (water droplets, ice plate crystals, ice dendrite crystals, ice column crystals, snow flakes, graupels and hails) (Fig. 1). This scheme treats nucleation from condensation nuclei, condensation growth, evaporation, sublimation, freezing, melting and collision coagulation growth processes.

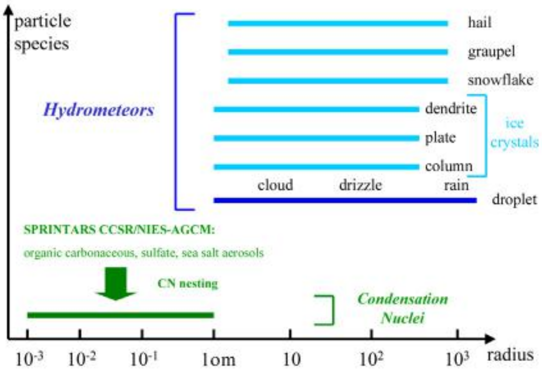

Figure 1. Schema of the bin cloud microphysical module in the model.

3. RESULT AND DISCUSSION

Numerical simulation was conducted for a region around the track of the research vessel on 22-23 May 2001. The horizontal grid intervals of 3 km is set (for 202 grid points) and the atmosphere up to 20 km is divided by 40 vertical layers with intervals increasing with altitude (40 m for the bottom layer to 1,120 m for the top layer). The values on the nearest grid to the ship track at the time is used to calculate the corresponding observables for the comparison.

Figure 2 shows the time-height cross sections of radar reflectivity factors (RRF) and lidar backscattering coefficients (LBC) obtained using 95 GHz radar and lidar at 532 nm on the vessel, MIRAI during 22-23 May 2001. The corresponding observables are calculated using prognostic size distributions of hydrometeors in the model simulation.

The model simulation can well represent the RRF and LBC of water cloud layer under the freezing level. RRF of ice cloud are overestimated, especially in the middle layer of ice cloud around the altitude of 8 km in our current simulation. The overestimation is caused by the error in prediction of vertical IWC structure and overestimation of the ice particle radius.

We will also evaluate the simulated result using IWC and effective ice radius retrieved from the radar observation data. A future work is to perform the similar study using the data of CloudSat and CALIPSO, and EarthCARE.

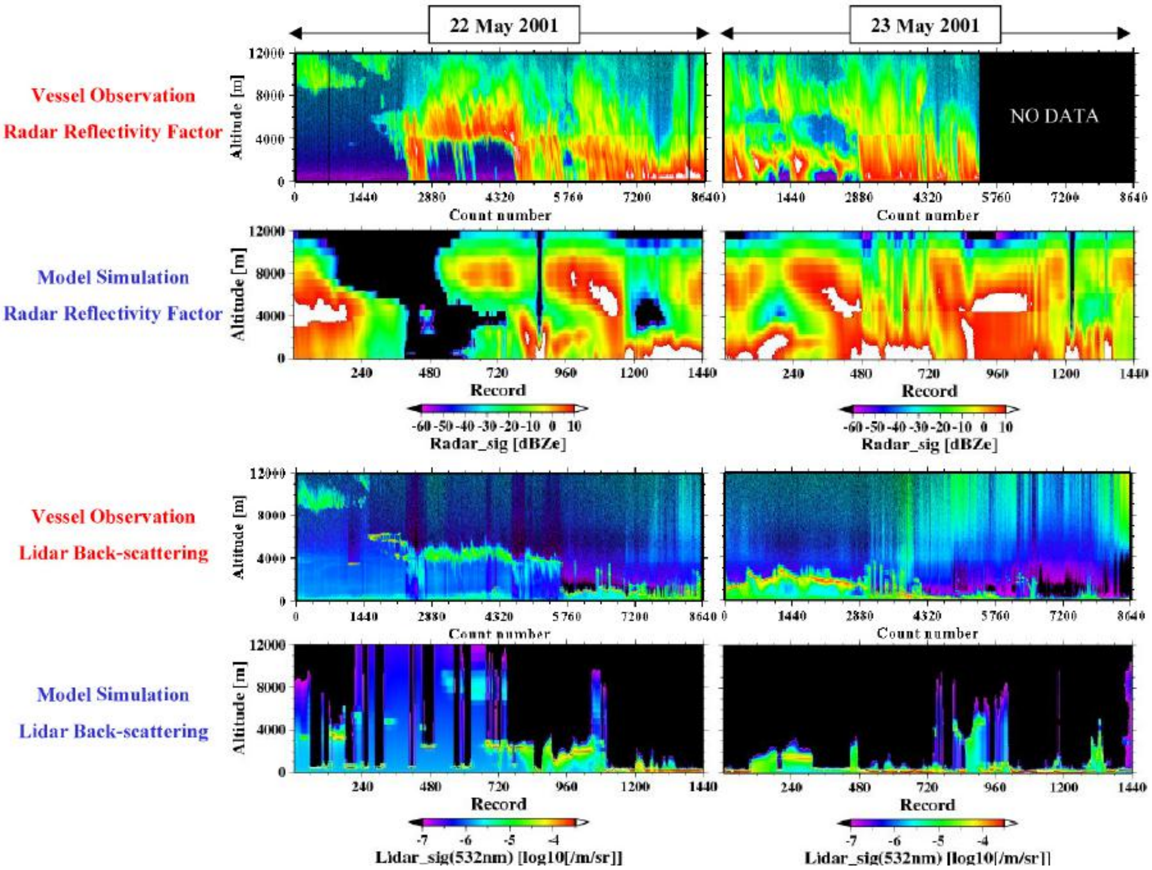

Figure 2. Time-height plots of the radar reflectivity factor dBZ at 95 GHz and backscattering coefficient at 0.532 um wavelength in the vessel observation and model simulation.

REFERENCE

Iguchi et al. (2008), A study of the cloud microphysical properties influenced by aerosols in an East Asia region using by a meso-scale model coupled with a bin cloud microphysics for clouds, J. Geophys. Res., doi:10.1029/2007JD009774, in press.

Khain et al. (2000), Notes on the state-of-the-art numerical modeling of cloud microphysics, Atmos. Res., 55, 159–224.

Okamoto et al. (2007), Vertical cloud structure observed from shipborne radar and lidar: Midlatitude case study during the MR01/K02 cruise of the research vessel Mirai, J. Geophys. Res., 112, D08216, doi:10.1029/2006JD007628.

Saito et al. (2006), The operational JMA nonhydrostatic mesoscale model, Mon. Wea. Rev. 134(4), 1266, DOI: 10.1175/MWR3120.1

Acknowledgements

This research was supported by the Global Environment Research Fund B-4 of the Ministry of Environment, Japan, by project RR2002 and the Data Integration for Earth Observation project of the Ministry of Education, Sports, Science, Culture and Technology (MEXT) of Japan, and by the JAXA/ADEOS-II GLI project. A. Khain is supported by a grant from the Israel Science

Foundation (140/07).

OBSERVATIONS AND NUMERICAL MODELING OF ENTRAINMENT AND MIXING NEAR THE TOP OF MARINE STRATOCUMULUS

Marcin J. Kurowski[1], Krzysztof E. Haman[1], Wojciech W. Grabowski[2], Szymon P. Malinowski[1]
[1]Institute of Geophysics, University of Warsaw, Warsaw, Poland
[2]National Center for Atmospheric Research, Boulder, Colorado, USA

1. INTRODUCTION

Entrainment of free-tropospheric air into stratocumulus-topped boundary layer (STBL) is of crucial importance for dynamical, microphysical, and radiative processes within STBL. The second Dynamics and Chemistry of Marine Stratocumulus field program (DYCOMS-II, Stevens et al. 2003) yielded, among other things, new data concerning the morphology of the stratocumuls (Sc) top. Gerber et al. (2005) presented detailed analysis of narrow in-cloud regions near the Sc top with lower liquid water content and cooler temperatures than averaged background values, the so-called "cloud holes". Using high resolution aircraft data, Haman et al. (2007) illustrated various ways the free-tropospheric air from above the inversion mixes with the cloudy STBL air. Their discussion illustrates the existence of a finite-thickness transition layer separating STBL from the free troposphere, the entrainment interface layer (EIL), postulated on theoretical grounds by Randall (1980) and suggested by airborne measurements discussed in Caughey et al. (1982) and Lenshow et al. (2000), among others. This layer is characterized by strong gradients of thermodynamic properties and substantial changes in the intensity of turbulence. The exchange of mass between wet and cold STBL, and dry and warm (in the potential temperature sense) free atmosphere may produce air parcels with negative buoyancy, and thus affect the dynamics of Sc top. Early studies (e.g., Lilly 1968) formulated thermodynamic conditions for such a production and a concept of cloud-top entrainment instability was introduced. The key idea is that the negative buoyancy produced through the mixing between the STBL air and the air from above the inversion can lead to a positive feedback, where the entrainment leads to buoyancy reversal and subsequently to more entrainment, and eventually to cloud dissipation.

In the present study we compare the observations from the DYCOMS-II campaign and the results from numerical simulations investigating entrainment and mixing near the top of STBL, especially concerning the EIL formation process.

2. ENTRAINMENT INTERFACE LAYER

EIL can be identified in observations and in model results as a region between the cloud top and the height of the temperature inversion. In a nutshell, EIL is a mixing zone that separates the cloudy and cold (in the potential temperature sense) boundary layer air from the dry and warm free-tropospheric air aloft. In the observations, EIL often features filaments of cloudy and clear air at different stages of stirring, mixing, and homogenization. Typical thickness of EIL is about 20m, but it varies from almost 0 to 70m. Observational results are supported by numerical modeling using the large-eddy simulations (LES) model. The model used in this study is the 3D anelastic semi-Lagrangian/Eulerian finite-difference model EULAG documented in Smolarkiewicz and Margolin (1997; model dynamics), Grabowski and Smolarkiewicz (1996; model thermodynamics) and Margolin et al.~(1999; subgrid-scale turbulent mixing). Model setup is based on RF-01 flight of the DYCOMS-II experiment, previously used in the model intercomparison study (Stevens et al. 2005). The depth of EIL is estimated as a distance between the material top of STBL and the surface of maximum static stability. The former is defined as the interface where total water mixing ratio falls below about 90% of its STBL value, i.e. 8 g/kg. The latter is simply the height of the maximum virtual potential temperature gradient. The distance between them, the EIL thickness, is shown in Fig. 1 for both model simulations and observations.

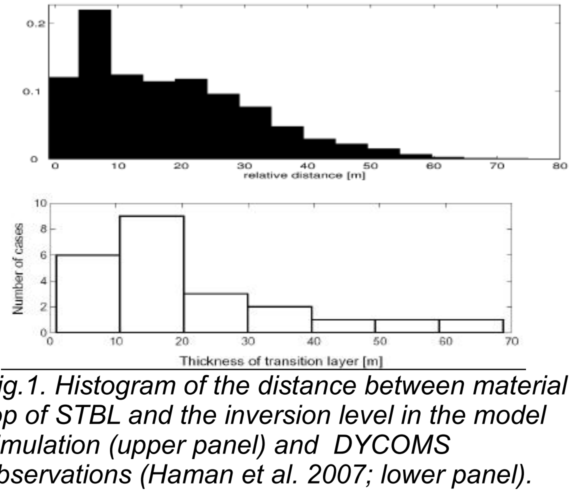

Fig.1. Histogram of the distance between material top of STBL and the inversion level in the model simulation (upper panel) and DYCOMS observations (Haman et al. 2007; lower panel).

3. ENTRAINMENT AND MIXING WITHIN STBL

In order to explain processes leading to the formation of EIL, we focus on the stability of the flow in the cloud-top region using the local gradient Richardson number at the surface of maximum static stability (maximum temperature gradient) and at the material top of STBL, defined by a threshold value of the total water mixing ratio. Boundary-layer updrafts, spanning entire depth of the STBL, impinge upon the inversion and produce a diverging horizontal flows in the upper part of the STBL. Despite the strong static stability near the cloud top, the horizontal flow is characterized by vertical shears that are strong enough to produce small-scale turbulence. This is manifested by values of the gradient Richardson number falling below the value typically associated with the onset of flow instabilities (cf. Fig. 2). Resulting turbulent mixing is responsible for the formation of the EIL and for entrainment of free-tropospheric air into the STBL.

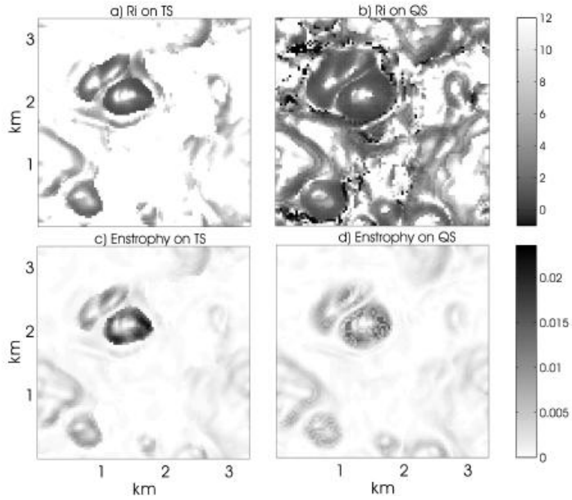

Fig.2. The gradient Richardson number Ri on the TS (a) and QS (b), as well as the enstrophy on TS (c) and QS (d) at t=3~hr. Note that the darkest shading in (a) and (b) corresponds to values of Ri suggesting flow instability. TS is a temperature inversion surface and QS is a surface defined with use of total water mixing ratio threshold (see text for details).

Mixing processes near the cloud top create finite-thickness interface layer with smoothed gradients of the temperature and humidity. The EIL is also a zone where negative buoyancy is produced and downdrafts are initiated. Injection of a passive scalar above the surface of maximum static stability after 3 hours of the model spin-up time allowed marking the free-tropospheric air that is subsequently involved in mixing with the STBL air. As expected, mixed parcels descending into STBL are characterized by the mixing proportion (i.e., the fraction of the free-tropospheric air) that corresponds to the density temperature lower than the free-tropospheric air and the STBL air. These parcels descend into STBL through "cloud holes" - trenches of cloud-free air surrounding areas of cloudy updrafts. Those cloud-free downward currents may be partially recirculated into the cloud, increasing the local cloud base height. The rest of the sinking air provides systematic dilution of the STBL.

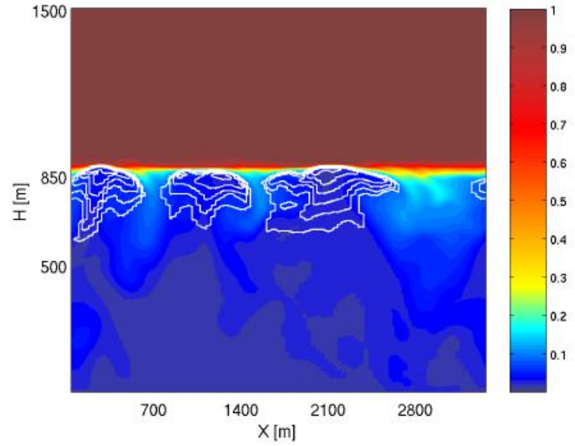

Fig.3. Vertical cross-sections of the free-tropospheric air fraction (cloud water contours shown by white lines) at t=6hrs (i.e. 3 hours after injection of the passive scalar into the free troposphere. The position of the cross-section was selected to illustrate relevant features.

An important issue is to what extent entrainment and mixing processes are driven by resolved model physics, and what effects are purely due to numerical aspects, e.g., the grid resolution. To answer this question, sensitivity simulations were performed with finer vertical resolution and modified subgrid-scale parameterizations. Results of the higher-resolution simulation show a clear dependence of main STBL characteristics on the choice of the vertical resolution, in agreement with previous results of Stevens and Bretherton (1999). Finer vertical resolution leads to smaller cloud holes (i.e., higher cloud cover) and a thicker cloud (i.e., larger liquid water path). The simulation in which the subgrid-scale mixing was switched off, similarly to one of the simulations discussed in Stevens et al. (2005), resulted in an unrealistically thick cloud, void of cloud holes, and continuously deepening without reaching the steady state.

Sensitivity simulations, perhaps in agreement with previous studies, indicate that LES modeling a Sc cloud is quite intricate. Fine model tuning is necessary to obtain results that agree with observations, arguably due to subtle interactions between resolved and subgrid-scale energy, mass, and momentum fluxes, as well as fluxes resulting from radiation parameterization. Novel representations of subgrid-scale mixing, focusing on the interactions between turbulent transport and microphysical processes, are necessary to overcome this problem. In consequence, conclusions summarized in the next section are subject of further verification. On the other hand, the agreement between modeled and measured statistical properties of EIL strongly suggests that the mechanism of entrainment and mixing described in this paper is close to the one existing in nature.

4. SUMMARY

EIL can be defined as a layer between the level of a threshold total water content and the level of the maximum static stability. Its depth is typically between of few meters and a few tens of meters, with occasional deviations close to a hundred meters. The entrainment and mixing near the STBL top occurs at upper parts of updrafts associated with convective cells spanning the entire STBL depth. The moist air rising within convective cells reaches the boundary layer top and is forced to diverge under strong capping inversion. The divergence produces significant vertical shears at the level of maximum stability, which is illustrated by the model-resolved enstrophy. Despite strong stability across the inversion, the shear can be large enough to initiate turbulent mixing as illustrated by the small Richardson number, often smaller than Ri=0.25. Small mixing fraction of the air entrained from above the inversion results in a weakly negative buoyancy of the mixture. Mixed air sinks into STBL forming cloud holes, areas void of cloud water in shape of trenches or lines, surrounding regions of diverging updraft circulations. Part of the descending air can be wrapped around the cloud edge and mixed into the updraft. The latter leads to a locally elevated cloud base and thinner cloud, as illustrated in Fig. 3. The entrained free-tropospheric air spreads across the STB relatively slowly: typical velocity of sinking motions is a few tenths of 1 m/s, with a few percent of free-tropospheric air in the downdraft.

5. BIBLIOGRAPHY

Caughey, S. J., B. A. Crease, and W. T. Roach, 1982: A field study of nocturnal stratocumulus: II. Turbulence structure and entrainment. *Quart. J. Roy. Meteor. Soc.*, **108**, 125–144.

Gerber, H., S. P. Malinowski, J.-L. Brenguier, and F. Burnet, 2005: Holes and entrainment in Stratocumulus. *J. Atmos. Sci.*, **62**, 443-459.

Grabowski, W. W. and P. K. Smolarkiewicz, 1996: On two-time-level semi-Lagrangian modeling of precipitating clouds. *Mon. Wea. Rev.,* **124**, 487-497.

Haman, K. E., S. P. Malinowski, M. J. Kurowski, H. Gerber, and J-L. Brenguier, 2007: Small scale mixing processes at the top of a marine stratocumulus - a case study. *Quart. J. Roy. Meteor. Soc.*, **133**, 213-226.

Lenschow, D. H., M. Zhou, X. Zeng, L. Chen, and X. Xu, 2000: Measurements of fine-scale structure at the top of marine stratocumulus. *Boundary-Layer Meteorol.*, **97**, 331-357.

Lilly, D. K., 1968: Models of cloud-topped mixed layers under a strong inversion . *Quart. J. Roy. Meteorol. Soc.,* **94**, 292-309.

Margolin, L. G., P. K. Smolarkiewicz, and Z. Sorbjan, 1999: Large-eddy simulations of convective boundary layers using nonoscillatory differencing. *Physica D*, **133**, 390-397.

Moeng C.-H., B. Stevens, and P. P. Sullivan, 2005: Where is the interface of the Stratocumulus-Topped PBL? *J. Atmos. Sci.*, **62**, 2626-2263.

Nicholls, S., and J. D. Turton, 1986: An observational study of the structure of stratiform cloud sheets: Part II. Entrainment. *Quart. J. Roy. Meteor. Soc.*, **112**, 461-480.

Randall, D.A., 1980: Conditional instability of the first kind upside-down. *J. Atmos. Sci.*, **37**, 125-130.

Stevens, B., and Coauthors, 2003: Dynamics and chemistry of marine Stratocumulus - DYCOMS-II. *Bull. Amer. Meteor. Soc.*, **84**, 579-593.

Smolarkiewicz, P.K., and L.G. Margolin, 1997: On forward-in-time differencing for fluids: An Eulerian/semi-Lagrangian nonhydrostatic model for stratified flows. *Atmos.-Ocean Special*, **35**, 127-152.

Stevens, B., and Coauthors, 2003: Dynamics and chemistry of marine Stratocumulus – DYCOMS-II. *Bull. Amer. Meteor. Soc.*, **84**, 579-593.

Stevens, B., and Coauthors, 2005: Evaluation of large-eddy simulations via observations of nocturnal marine stratocumulus. *Mon. Wea. Rev.*, **133**, 1443-1462.

Stevens, D. E., and C. S. Bretherton, 1999: Effects of grid resolution on large-eddy simulation of radiatively-driven entrainment through a strong inversion. *Quart. J. Roy. Meteor. Soc.*, **125**, 425-439.

ACKNOWLEDGEMENT

This work was partially supported by Polish MNiSW grant N N307 2649 33 . The National Center for Atmospheric Research is operated by the University Corporation for Atmospheric Research under sponsorship of the National Science Foundation.

Observed Macroscopical and Microphysical Structure of Clouds in Beijing

Ma XinCheng　Zhang Qiang　Huang MengYu　Li HongYu

Beijing Weather Modification Office，Beijing 100089

ABSTRACT

Beijing is one of regions for shortage of Chinese water resources. Develops the sky rain resources in Beijing is one way to solve the shortage of water resources, So it is necessary to known the cloud physics structure of Beijing in detail. Beijing Weather Modification Office (BWMO) obtained the materials of the cloud and the precipitation physics structure by the XiaYan airplane which carried on the vertical measurement in different altitude of stratus clouds. This paper analyzes airborne measurements of ten stratus clouds over the north of Beijing in 2005 and 2006 during the Spring and Summer. Four of the ten cases are Non-precipitating clouds and six of the cases are precipitating clouds.

1、Macrosocopical Structure of Stratus Clouds

Beijing stratiform is Stratus Clouds which are usually maded of Ac or As and Sc. When the stratiform is by Ac and the Sc constitution, thickness of two stratus cloud is not thick, also the middle crevice divides into the obvious two strata times greatly, often not easy to create the ground precipitation; When the stratiform is maded of As and the Sc, the boundary is fuzzy between two stratus clouds, does the level thickness to change thin, when forms a deep whole, the ground forms the precipitation generally.

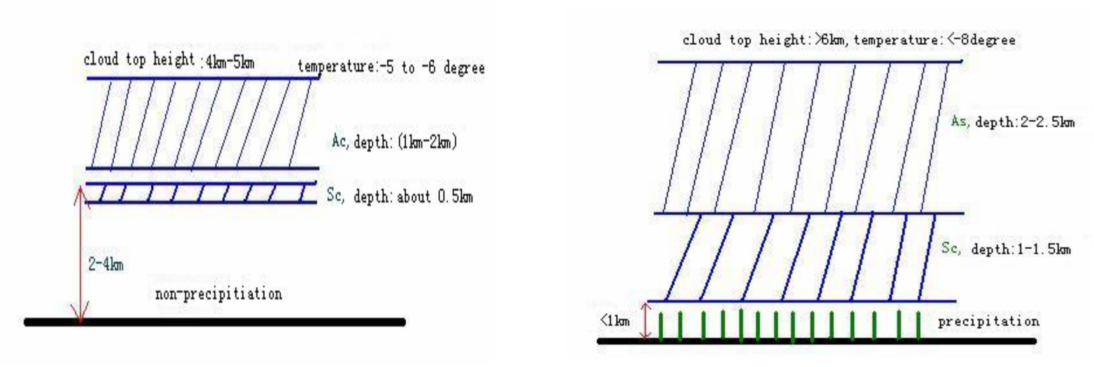

Fig 1 general macroscopic state diagram of mixed-phase clouds in Beijing

2、Microphysical Structure of Stratus Clouds

The Beijing is often the systematic precipitation which disseminates from west to east. For the further understood Beijing stratiform, we carry on the airplane vertical measurement. The stratiform is mixed-phase clouds, mainly by As, Ac and Sc constitutes; The average cloud top is highly 6000m, the corresponding temperature - 8℃; The average zero degree level altitude is 4200m; Cloud base highly >1000m,Corresponding temperature approximately > 14 degrees.

The stratus clouds have dry level, Especially the warm area has many dry levels, thickness is generally approximately 100-400m. Dry level will vanish when the process of precipitation is Forming, thickness of melted level is generally 100m-300m

.

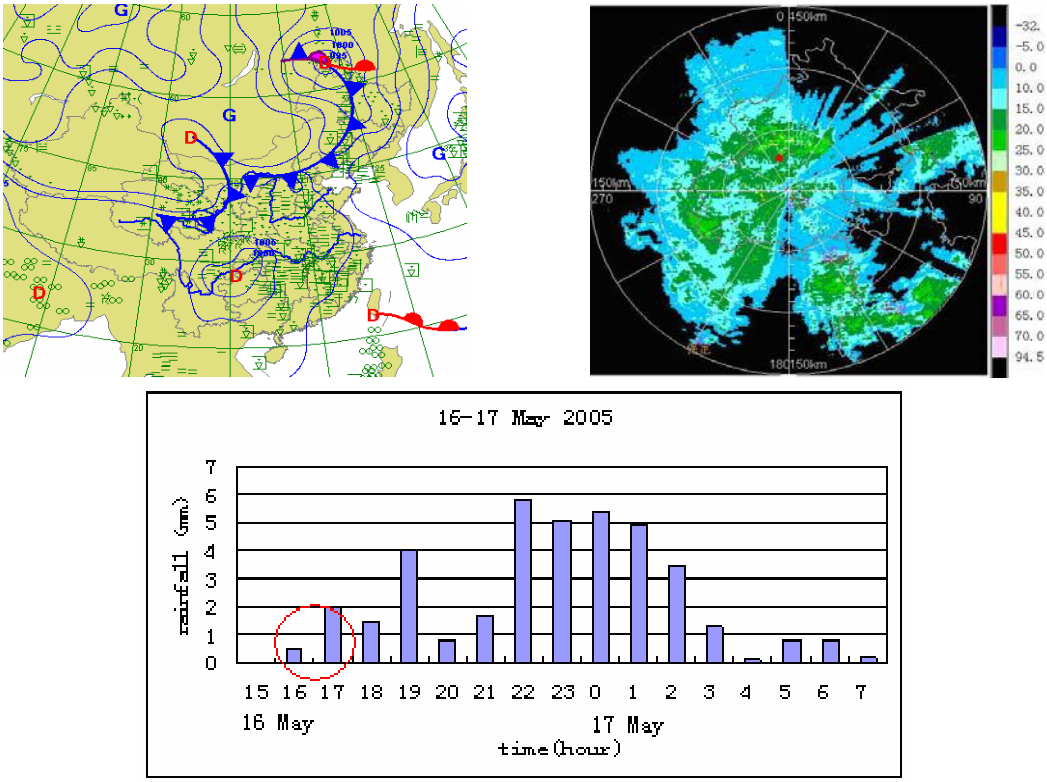

Fig 2 graph of weather, radar(Red spot is the place of vertical measurement)and rainfall amount(Red circle is the time of vertical measurement) on 16 May 2005

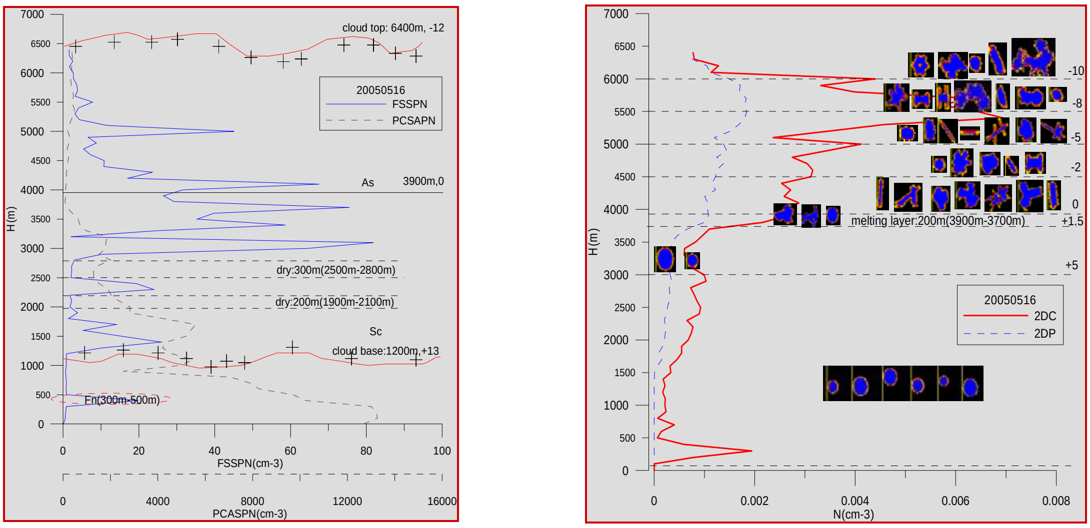

Fig 3 vertical structure of Beijing stratus cloud and precipitation on 16 May 2005

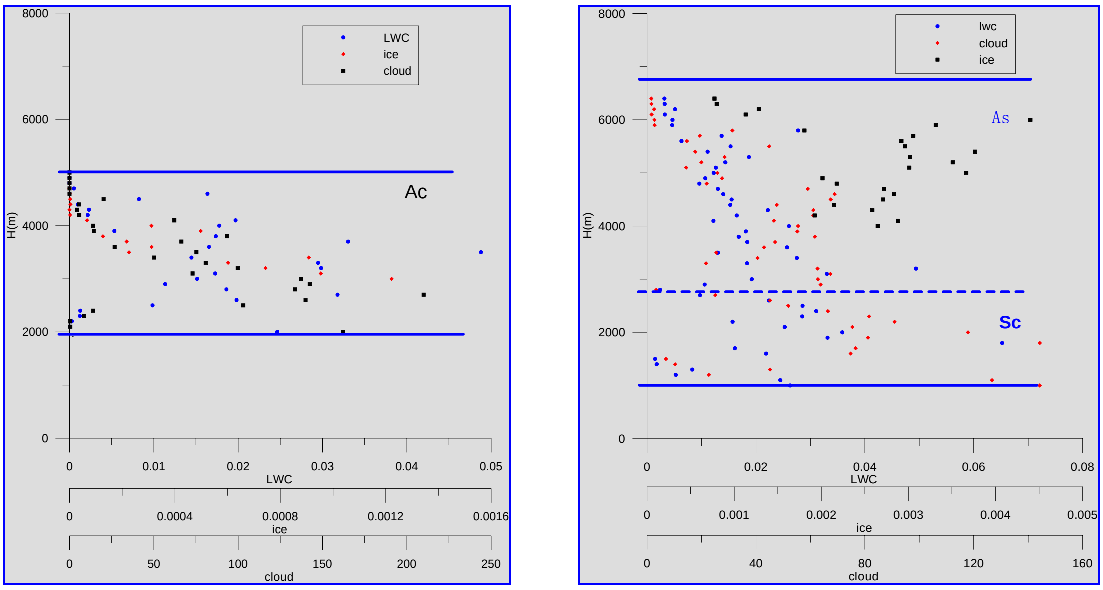

Fig 4 vertical distribution of cloud water content, cloud granule and ice crystal average density

(left : Non-precipitating of four cases; right : precipitating of six cases)

The water content distributes in cloud lower part of cold area, warm area in cloud upside, the cloud drop density is average 60 /cm3; The ice snow crystal distributes in cloud upside, the density is 1-10 /L;The ice snow crystal shape is often plate-type, acicular and columnar, between – 3℃ and - 6 ℃ there are massive acicular ice crystals, and appears the acicular polymer. Plate-type can be discovered in many temperature section.

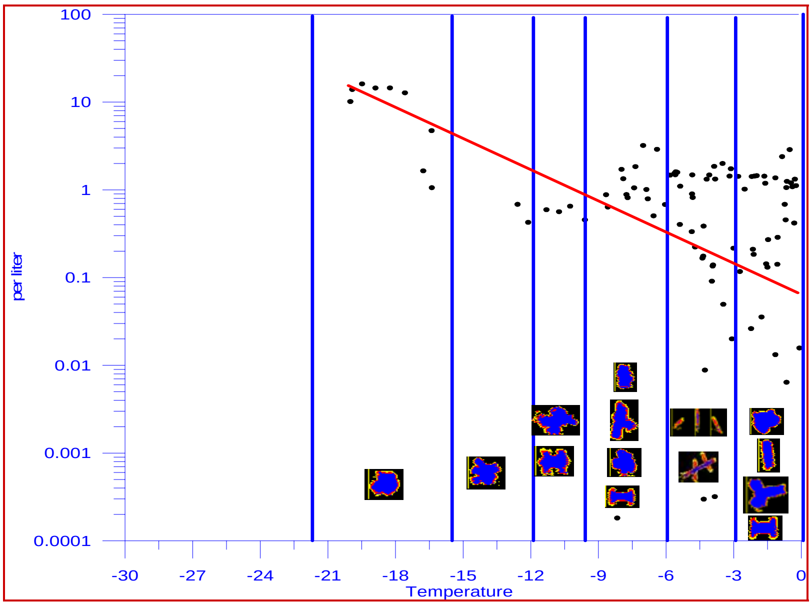

Fig 5 ice crystal density and ice crystal shape along with temperature change in stratus clouds(ten cases)

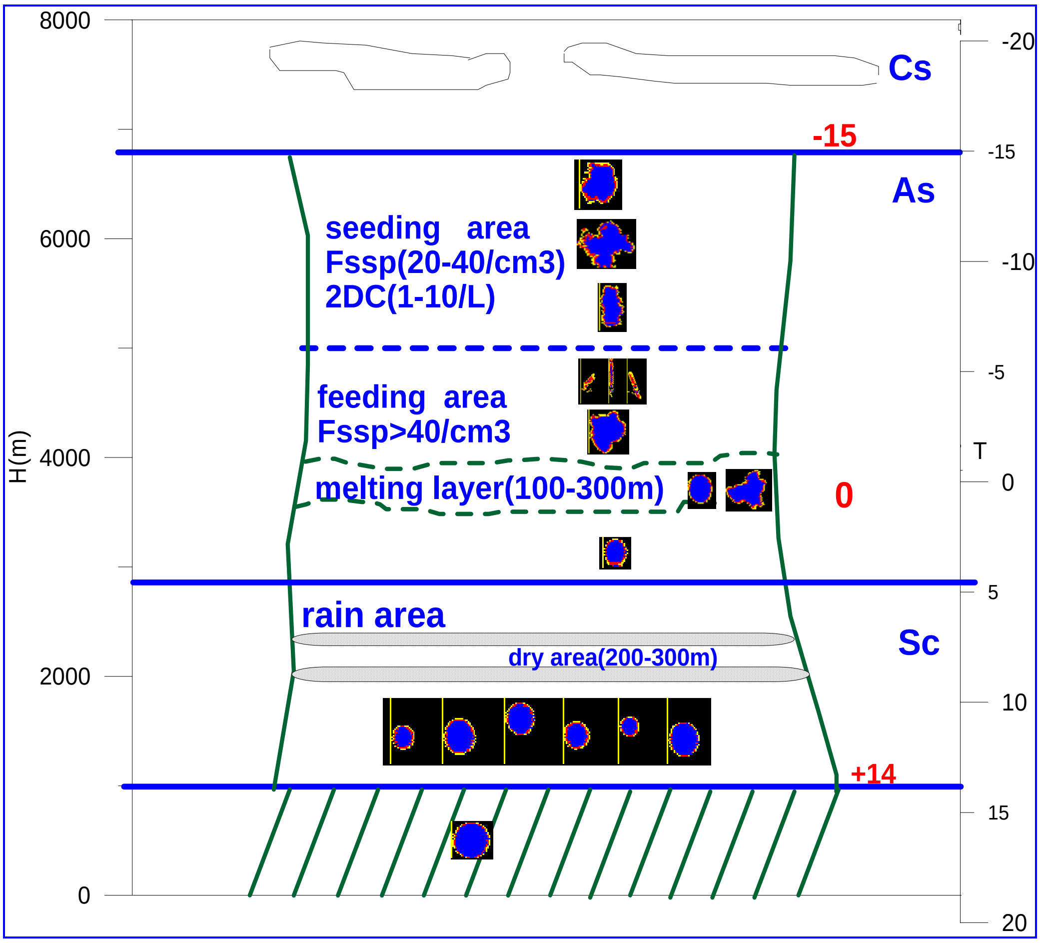

Fig 6 vertical cross-section diagram of clouds and precipitation in Beijing

Main mechanism of the Beijing stratus clouds and precipitation may be “seeder-feeder”. According to the catalyzed potential area choice standard (Fssp>20 /cm3,2DC<20 /L) the seeding region of the Beijing mixed-phase precipitating clouds is 5km-6km, The temperature is lower than - 6℃(in view of silver iodide);But when the temperature is below - 6 ℃ to 0 ℃ (5km-4km satisfies the catalyzed request approximately), it is better to use the liquid nitrogen more in order to achieve the multi-level catalyses.

Acknowledgements

This work is supported by the National Key Research Project of Ministry of Science and Technology of China “Key Technology and Equipment Research and Development on Weather Modification”(2006BAC12B00), The first author greatly thanks and appreciates to the Operating Committee of the International Conference on Clouds and Precipitation(ICCP2008) for accepting this paper and for providing partial financial support to the first author. The first author would also thanks to other donor and sponsor who has given the opportunity to the first author to attend personally in this conference.

References

Jeffrey L.Stith,James E. Dye,Aaron Bansemer,and Andrew J.Heymsfifld, Microphysical Observations of Tropical Clouds,J.A.M, 41(11), 97-117, 2002.

Houze R A,Hobbs P V.Organization and Structure of Precipitating Cloud Systems.Adv.Geophys.24:225-315,1982

THE MICROPHYSICAL CHARACTERISTICS OF FOG IN THE RIME AND GLAZE

Lei MENG, Sheng-Jie NIU[*]
Laboratory for Atmospheric Physics& Environment of China
Meteorological Administration, Nanjing University of Information Science & Technology,
Nanjing 210044, P.R.China

1. INTRODUCTION

Every winter the fog ice and glaze can be seen frequently in southeast China. As the scenery, it can abstract many visitors to improve local economy. However, it is also the severe disaster which can destroy many important electric wires even hinder the development of the local economy. So it is very significant to analyze the formation and development of the fog ice and glaze. As the process of the ice and glaze usually occur in the fog, it is very necessary to analyze the formation of fog. Many foreign and domestic scientists started these researches early. Up to now, these researches always on the survey of fog, the reaction and the impact of fog droplets and aerosols, the boundary layer in the fog, the numeric simulation of fog and so on.

This paper shows the change of the characteristics of fog ice and glaze in the development of fog in January, 1990 and February, 1991. According to the characteristic values of fog, analyze the characteristics and the evolution of the spectrum in different weather situation, whether it is fog of no fog.

2. OBSERVATIONS AND INSTRUMENT

The data come from the observation in two stations separately locate in Lou Hill and Maluojing, both belong to Zunyi city, Guizhou province. The instrument focuses on the horizontal accumulation of fog ice and glaze.

3. THE RELATIONSHIP BETWEEN FOG ICE AND THE WEATHER ELEMENTS

Generally speaking, the formation of rime and glaze depend on the low temperature, high relative humidity, moderate wind speed and wind direction. Figure 1 and figure2 show the negative correlation between ice accumulation and the average temperature in winter. They suggest the difference of rime and glaze among each winter from 1983 to 2003. (Lacking of data in 1986 and 2001)

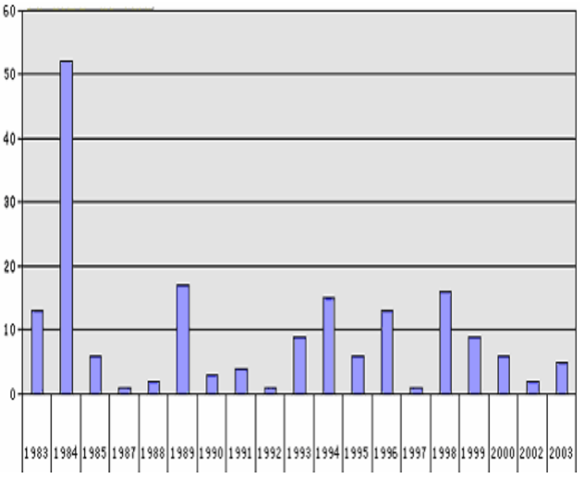

Fig.1 Rime and glaze's occurrences in the 20years

---

[*] Correaponding author.
E-mail address: niusj@nuist.edu.cn

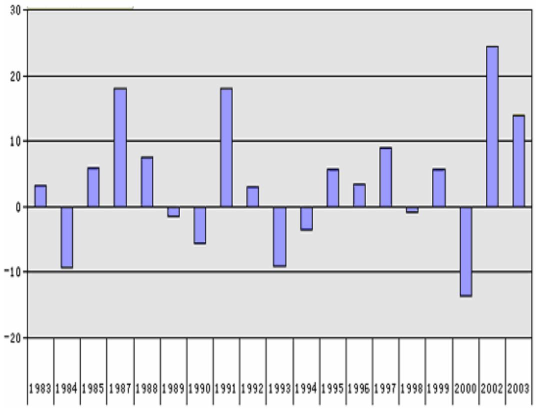

Fig.2 The average temperature of each winter in 20years

From figure 1 and figure 2, the negative correlation indicates that the accumulation of rime and glaze in winter depends on the moderate low temperature. If the monthly average temperature is higher than 1.5°C, the occurrence is usually low. From analysis, the monthly average temperature range -2~0°C or below -5.3°C can prompt the formation and development of rime and glaze. But it doesn't mean only the range of temperature is the main factor for the formation of rime and glaze. Actually, the temperature is one of the important factors of this phenomenon. When the relative humidity is up to a high level, the fog form easily and with moderate low temperature, the rime and glaze can occur. Meanwhile, the moderate wind speed is also the important factor to make fog occur. It can improve the formation of rime and glaze indirectly.

4. ANALISIS OF MICROPHYSICAL CHARACTERISTICS OF FOG

According to the researches of fog before, the size of fog droplet ranges from 2 micrometers to 10 micrometers, and the radius corresponding to the peak of size distribution spectrum is always between 3 and 4 micrometers. The size distribution spectrum of fog often shows unimodal spectrum. From these data of this observation, the spectrum corresponds with Deirmendjian distribution, no matter whether the fog occurs or not. As figure 3 indicates, the average size distribution spectra of fog droplet in different weather situation do not shows notable difference between them.

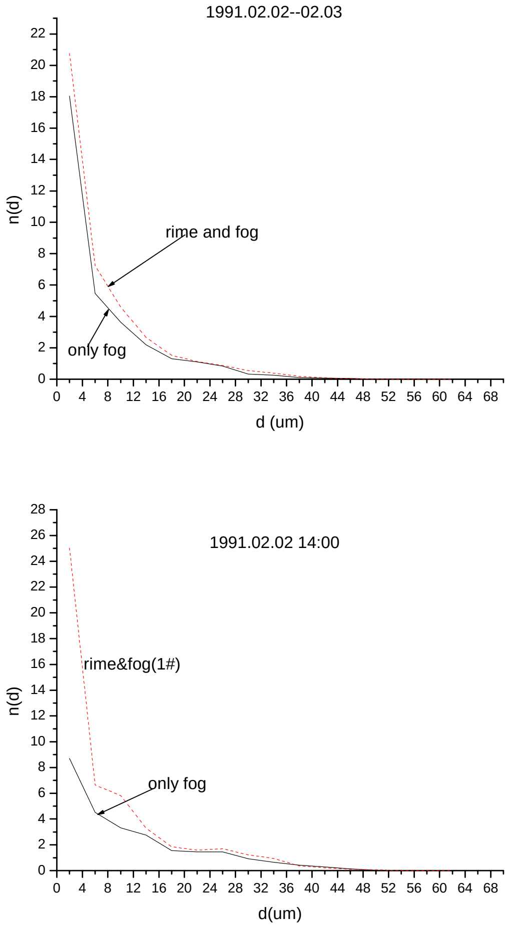

Fig.3 The average size distribution spectrum of fog droplet in different weather

However, by analyzing the micro-physical characteristic values, as table 1and table 2 show, the difference can be seen. When the rime and glaze occur in the fog, the maximum fog droplet is larger than that when no ice is accumulated. And the minimum droplet in the former situation is also larger than that of the later. It is very hard to distinguish the notable difference between the two average spectra, but the difference between them can show the impact of rime and glaze. When there is rime or glaze, it means the temperature is low enough to make ice accumulate, and the fog droplets tend to deposit on the wires or the branches of trees, and is also easy to frozen to become ice particle. The large droplets tend to collide or coagulate with each other and eventually deposit on wires. The small droplets tend to grow to larger size. So, the spectrum width of fog in the rime and glaze is narrower than that when there is no rime or glaze.

Table 1 The microphysical characteristic values,2#stands for only fog,1#stands for rime and glaze occur

station	date	Square root diameter µm	Cube root diameter µm	Peak value diameter µm	Spectrum width µm	LWC g/m^3	LWC① g/m^3
Maluojing 2 #	1991.02.02 09:00--02.03 14:00	11.0175	14.056	2	58		0.0567
Maluojing 1 #	1991.02.02 09:00--02.03 14:00	10.4001	13.569	2	58	0.229	0.0352
station	date	Value mean diameter µm	Mass mean diameter µm	Number concentration / m^3	Middle value volume diameter µm	LWC② g/ m^3	LWC③ g/ m^3
Maluojing 2 #	1991.02.02 09:00--02.03 14:00	9.5286	14.6371	118.94	27.7614	1.3943	0.2581
Maluojing 1 #	1991.02.02 09:00--02.03 14:00	9.132	14.67	164.7	28.92	2.0561	0.2438

Table 2 The microphysical characteristic values

	Peak value diameter µm	Math mean diameter µm	Mass mean diameter µm	Middle value volume diameter µm	L W C （1） g/m^3	L W C （2） g/m^3	L W C （3） g/m^3	Actual LWC g/m^3	Droplet number concentration /cm^3
1991.02.02--02.04 Maluojing1# （rime and glaze）									
Mean value	2	9.132	14.67	28.92	0.0352	2.0561	0.2438	0.2503	164.7
Maximum value	2	10.73	17.14	31.08	0.0657	4.347	0.5154	0.475	384.48
Minimum	2	6.88	11.72	26.29	0.0112	0.4487	0.065	0.057	30.04

value									
1991.02.02--02.04 Maluojing 2＃（only fog）									
Mean value	2	9.5286	14.6371	27.7614	0.0374	2.2839	0.2747		118.94
Maximum value	2	13.49	20.32	34.11	0.0657	4.347	0.5154		258.67
Minimum value	2	5.92	10.71	22.96	0.0112	0.4487	0.065		38.38

Even the observation stations have difference in the weather elements, the results are similar.

5. SUMMARY

Firstly, the rime and glaze are easy to form and develop in the low temperature when the fog occurs.

Secondly, no matter whether the fog occurs or not, the mean size droplet spectrum can not show more information about the difference between the two situations. But, analyzing the microphysical characteristic values of the droplets, the difference can take on. When the rime and glaze appear, the spectrum width is narrow than that when only fog.

6. BIBLIOGRAPHY

Jiang Yuhua, Wang Qiang, Li Zihua, etc.Characteristics of fog in Chongqing urban area, Meteorological Science and Technology. Vol.32, No.6. 2004, 450-455

Li ZIhua, Wu Jun. Winter fog droplet spectrum features in urban area of Chongqing, Journal of Nanjing Institute of Meteorology. Vol.18, No.1. 1995,46-51

Li Zihua, Huang Jianping, etc. Physical structures of the five_day sustained fog around Nanjing in 1996. ACTA METEOROLOGICA SINICA. Vol.57, No.5.1999,622-631

W. T. Roach. The formation and dissipation of land fog. Weather.Vol.50 No.1. 995, 7-11

Malcolm Walker. The science of weather: Radiation fog and steam fog. Weather.Vol.58 No.5.2003, 96-197

ACKNOWLEDGEMENT

Key Basic Research Foundation for Natural Science of the Jiangsu Higher Education Institutions of China(Grant No. 06KJA17021),and Special Foundation for Meteorological Vocation from the Ministry of Science and Technology of China(Grand No. GYHY200706026) supported this research.

ANALYSIS OF THE MICROPHYSICAL STRUCTURES OF ULTRA HEAVY FOG AROUND NANJING IN THE 2006 WINTER

Sheng-Jie NIU,Jie XU,Chun-Song LU
Laboratory for Atmospheric Physics& Environment of China Meteorological Administration,
Nanjing University of Information Science & Technology, Nanjing 210044, P.R.China

1. INTRODUCTION

Fog is a phenomenon of the vapor condensation among atmosphere, and composed of droplet or ice crystal which suspend near the ground surface. In the earlier of 20th century, Taylor had conducted the radiation fog measurement with scientific method. During 25-27 December, 2006, heavy fog occurred in Nanjing and its suburbs, which resulted in the degradation of visibility badly, and had a profound effect on human activity and the environment. In this study, fog occurred under the uniform field governed by three high pressures with distribution from southwest to northeast, moving towards the east direction during 23-27 December. In surface chart, this heavy fog developed under the allocation of the middle-high latitude's high pressure and the low latitude's low pressure with the influence of southwest air current. Under these mechanisms, the fog is lifted in the lower layer, which is benefit to the warm and moist air current from southwest, supplied and concentrated in Nanjing.

During 27-31 December, 1996, Nanjing encountered a fog sustained for 5 days, Li analyzed the characteristics of microphysical structure and the major factors which influenced the structure, and their relationship with macro developments. In their studies, fogs generally formed by radiation cooling with large variation of microphysical structure within short time. With atmospheric sounding equipment [*Vaisala*, produced by Finland], the results from sounding data including temperature, relative humidity(RH), wind speed and specific humidity along with the IR visibility detector have shown that the fog of 25-27 December, 2006 is a typical advection fog.

2. DATA AND ANALYSIS

The data used in this paper were from SPP-FM100 fog droplet spectrometer, Vaisala's wiresonde and robot weather station data in Nanjing, China during 25-27 December, 2006.

The SPP-FM100 fog droplet spectrometer is an optical detector manufactured by DMT. Based on Mie scatter theory, it accounts the fog droplet number during 2-50μm with different bin width through the light intensity when particles pass by its chamber, then we can get particle number concentration(N_c), mean diameter (D_m) and liquid water content (L_w) of each bin from the raw number data. The sample interval is 50ns, and the data output interval is 1s. The sample plane height was around 1m. In this paper, we pick up data during 25-26 to analyze the microphysical structure and the factors.

With synthesized analyses of sounding data and the synoptic background, advection process (or dynamic process) is the controlling factor for the fog development and dissipation. In the upper air, warm and moist air current with systematic descending movement arouse intensive descending thermodynamics, simultaneously, the continuous warm southwest air current supplies Nanjing with abundant water vapor, which makes this fog urge and develop. Moreover, the fog dissipation under the strength of cold air current and it's moving towards south. On the other hand, radiation balance will be changed along with fog formation and development.

Figure 1 gives the two days' fog top altitude evolution. Based on the evolution, we have this fog process partitioned into the following parts: 1) formation and development stage S1(BT00:00-07:00, 25); 2) maintenance stage S2(BT07:00, 25-20:45, 26), in this stage, it includes three sub-processes: Ⅰ.the descending period p_1 with large amplitude (BT07:00-22:45,25), Ⅱ.the explosive development period p_2(BT22:45, 25-00:00,26) and Ⅲ. the stable oscillating period p_3 (BT00:00-20:45,26); 3) the dissipation stage S3(BT20:45, 26-14:14, 27). According to the analysis of sounding data, in the sub-stage Ⅰ, due to the effects of the solar short-wave radiation warming, the warm air and the descending thermodynamics together, the fog top altitude descends to 188m from 625m in the end of this stage；in the next sub-stage, the radiation cooling is contribute to the fog explosive growth; in the sub-stage Ⅲ, fog top ascends as the temperature rising and the RH falling, while descends as temperature falling and RH rising, the intensity of warm and moist air current controls the emergence and amplitude of this oscillation process, while the short and long radiation controls the trends.

3. RESULTS

3.1 Characteristics of micro-structure parameters

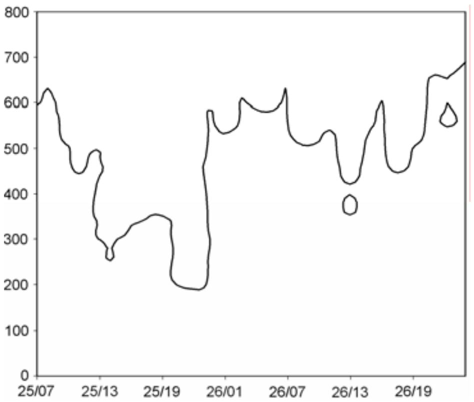

Fig.1 The time-scale evolution of the altitude of fog top from 25 to 26 December, 2006

Table 1 gives the mean values of parameters in different stages. The data in the table has been averaged over the whole period of each stage. Here, we just consider these parameters including N_c, L_w, $D_{m,}$ and the maximum diameter D_{max}. In this section, we just discuss these parameters' characters in the different stage, then, we will look for the relationships with each other and the factors which influence the changes of parameters.

As discussed above, advection process is the major mechanism for the fog formation and development, at the beginning of formation, the surface temperature do not drop enough for aerosol nucleation, so the N_c appears lower, but the abundant water vapor supplied by warm air current contributes to the integration of LWC. In S2, as fog top descending, descending thermodynamics limits the condensation growth of droplets, so D_m descends as N_c increases; then the long-wave radiation cooling of fog and surface, which makes aerosol nucleation effect become more important, and improve the condensation and coagulation processes, so at p_2 period, D_m increases simultaneously with N_c, because the explosive growth needs more water vapor, L_w decreases in this period; in the p_3, due to the effect of thermodynamics and dynamics balancing with each other and the fog body is lifted to the upper air, so the particles observed near surface decreases. In the dissipation stage, the development of cold air current makes the condensation and coagulation processes strengthened, drizzle particles is formed and drop with gravitational force.

Tabel 1 The microphysical structure of fog

stages		**N_c** **cm^{-3}**	**L_w** **$g \cdot m^{-3}$**	**D_m** **μm**	**D_{max}** **μm**
S1		220.91	0.14	6.70	39.60
S2	p_1	383.80	0.08	6.11	45.00
	p_2	661.24	0.11	7.33	50.00
	p_3	135.00	0.05	4.99	35.86
S3		374.55	0.20	4.10	30.53

Moreover, the result is very different from the results of Li's observational data in Nanjing, 1996, as the major factor for that fog development is the radiation cooling effect.

3.2 Relationship Between N_c and L_w

Figure 2 gives a good insight that there has a good correlation between N_c and L_w. Data in figure 2 has been averaged by every 10min.There exists obvious oscillation both in N_c and L_w with almost same frequency. Except for the explosive growth stage, in the other two stages, the oscillation between N_c and L_w shows a strong positive correlation.

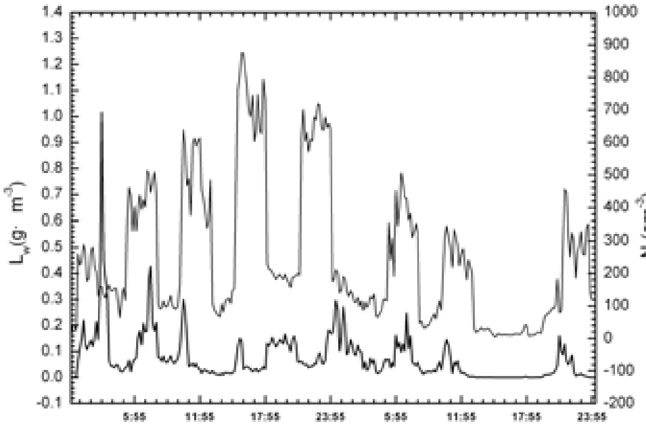

Fig.2 The time-scale evolution of liquid water content with the variation of number concentration in fog droplet

(thick solid line: L_w; thin solid line: N_c)

3.3 Fog Droplet Spectrum

Figure 3 gives the typical fog droplet spectra averaged by every 5min in the different stages. The distribution of fog droplet spectrum is a most important factor that affects the thermodynamics and dynamics of fog development.

In the stage of formation and development, surface temperature descending and the effect of warm air current are benefit to the aerosol nucleation and growth, so in this figure, we can see from BT00:05 to BT02:25, the spectrum is lifted and broadened, the maximum diameter detected also broadens from 10μm to 41μm.

Due to the descending thermodynamics, in the p_1 period, the number of small droplet increases rapidly; in the explosive growth period, long-wave radiation cooling is benefit to the aerosol nucleation and the development of condensation and coagulation processes, so each bin's particles grow enough(spectrum labeled with 22:55/25). In the oscillating period, droplet spectrum repeats between being broadened (lifted) and narrowed (descended) by the effect of balance between thermodynamics and dynamics.

In dissipation stage, the effect of nucleation makes small droplet grow fast with 10^3 magnitudes, with the drizzle formation and water vapor exhaustion, small and large particle all decrease rapidly.

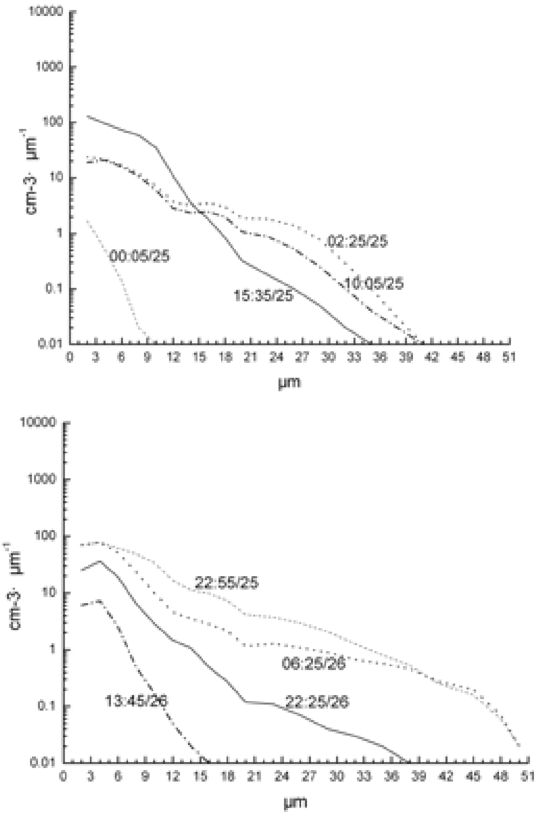

Fig.3 Fog droplet mean spectrum of 25 and 26 December, 2006

4. CONCLUSIONS AND DISCUSSION

In this study, by using atmospheric sounding data and fog droplet spectrum data, we discuss the mechanisms for the fog development and dissipation, and the factors influence microphysical parameters. Advection process is the major factor for the fog development; and there exists apparent oscillation both in N_c and $L_{w;}$ the balance between thermodynamics and dynamics make fog droplet spectrum more complex.

In this presentation, all parameters are expressed by average number. Next we will put our research on the multi-scale dependent distribution and the dispersion effect.

5. BIBLIOGRAPHY

Li Zihua, Hunag Jianping, Zhou Yuquan, et al. Physical structures of the five-day sustained fog around Nanjing in 1996[J]. Acta Meteorologica Sinica, 1999,57(5): 622-631

Taylor G.I. The formation of fog and mist[J]. Quart. J. R. Meteor. Soc., 1917, XL111: 2416-2468.

Roach, W. T., Brown, R., Caughey, S. J., GarlandJ., Garland, J. A. and Readings, C.J. The physics of Radiation fog: Part I: A field study[J]. Quart. J. R. Met. Soc., 1976, 102:313-333.

Li Zihua, Huang Jianping, Huang Yusheng, et al. Study on the physical process of winter valley fog in Xishuangbanna region[J]. Acta Meteorologica Sinica, 1999,13(4): 494-508.

Fuzzi, S., Facchini, M. C. et al. The Po Valley fog experiment 1989, An overview[J]. Tellus,1992,44B,448-468.

Li Zihua, Wu Jun. Winter fog droplet spectrum features in urban area of Chongqing[J]. Journal of Nanjing Institute of Meteorology, 1995, 18(1): 46-51

ACKNOWLEDGEMENT

Key Basic Research Foundation for Natural Science of the Jiangsu Higher Education Institutions of China (Grant No. 06KJA17021), and Special Foundation for Meteorological Vocation from the Ministry of Science and Technology of China(Grand No. GYHY200706026) supported this research.

CLOUD DROPLET NUMBER CONCENTRATION VARIABILITY OVER THE SOUTHEAST PACIFIC STRATOCUMULUS REGION

David Painemal[1] and Paquita Zuidema[1]
[1]Rosenstiel School of Marine and Atmospheric Sciences, University of Miami

1. INTRODUCTION

In spite of the important radiative role of the subtropical warm cloud (stratocumulus and stratus) deck to climate, the cloud processes remain poorly understood. This lack of understanding extends to the aerosol indirect effects. Unique features make the Southeastern Pacific stratocumulus region particularly appropriate for studying cloud-aerosol interaction processes. Variability in accumulation-mode aerosol concentrations is high, confirmed by measurements taken during 5 NOAA buoy-tending cruises (Fig. 1; see also Tomlinson et al. (2006)). While the origin of the aerosol remains uncertain, one source may be anthropogenic: oxidized sulfur emissions from the copper smelters along the coast and the Andes (Huneeus et al. 2006).

Also shown in Fig. 1 is a significant positive correlation between the ship-based aerosol concentration measurements and a satellite-derived cloud droplet number concentration (CDNC), despite the inherent difficulties to such comparisons. MODIS (MOderate Resolution Imaging Spectroradiometer) data infer large cloud droplet number concentrations (CDNCs > 200 g m^{-2}) unrepresentative of pristine marine environments along the Chile-Peru coast (Fig. 2a), corresponding to the high measured aerosol concentrations shown in Fig. 1.

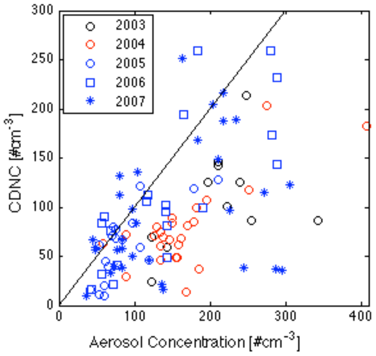

Figure 1: MODIS derived CDNC versus in situ ship-based accumulation-mode aerosol concentrations, sampled within 0-30S, 72-90W.

The increased CDNC, through the associated decreased droplet size, will increase the regional top-of-atmosphere albedo, all other cloud properties held constant (Twomey, 1977).

Dynamical processes that affect the cloud microphysics within one of the most persistent stratocumulus decks on the planet can therefore have significant climatic implications. Encouraged sufficiently by Fig. 1, we apply primarily satellite data to search for new insights on the impact of meteorological processes on CDNC variability.

2. DATA EN METHODS

We used a combined set of *in situ* observations along with satellite retrievals and reanalyzed meteorological fields from NCEP/NCAR reanalysis project. Daily mean surface winds were provided by Quikscat, level 3 products. Daily-mean MODIS retrievals of cloud optical depth (τ) and effective radius (r_e) (Terra satellite, collection 5, 1 degree resolution, overcast pixels only) were recast into CDNC and cloud depth (H) after invoking an adiabatic assumption (e.g., Schuller et al., 2005). This recasting allows a separation of the cloud microphysics from the macrophysics. The equations for deriving CDNC and cloud depth are summarized in equations (1) and (2) respectively, with ρ_w corresponding to water density and Γ_{ad} to a constant adiabatic lapse rate (0.002 gm^{-4}).

$$CDNC = \frac{\sqrt{10}}{4\pi\rho_w^{1/2}k}\Gamma_{ad}^{1/2}\frac{\tau^{1/2}}{r_e^{5/2}} \qquad (1)$$

$$H = \sqrt{\frac{2}{\Gamma_{ad}}\frac{5}{9}\rho_w r_e \tau} \qquad (2)$$

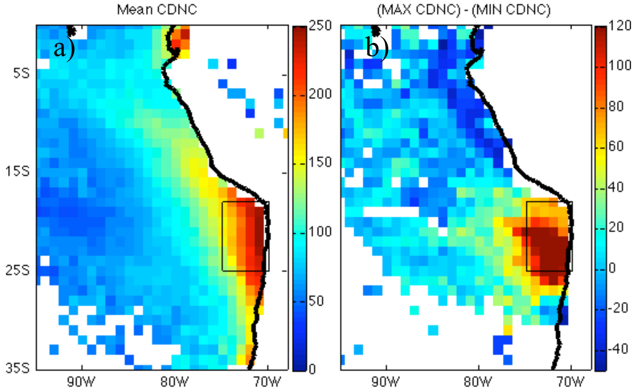

Figure 2: CDNC fields (in #cm^{-3}): a) mean CDNC, b) difference between MAX and MIN CDNC composite. The box indicates the area in which the mean CDNC was averaged and then classified into MAX or MIN CDNC.

**Corresponding author address: David Painemal, RSMAS/MPO 4600 Rickenbacker Cswy, Miami, Fl., 33149.
e-mail:dpainemal@rsmas.miami.edu*

The satellite validation through comparison to shipboard measurements collected within the southeast Pacific and to other satellite datasets is ongoing (e.g. Fig. 1), but is not the focus here. For this study we selected 3 months of the validation period: October 2001, 2005 and 2006. October (austral spring) corresponds to the climatological maximum in cloud cover (Klein and Hartmann, 1993). Daily area-averaged CDNC values were calculated for a bight known, translated from Spanish, as the Arica Elbow (70˚-75˚W and 18˚-25˚S, box in figure 2). The Arica Elbow contains the highest CDNC of the marine region. The days were composited by their CDNC values, with the highest and lowest quartiles hereafter identified as the MAX (CDNC> 250 cm^{-3}) and MIN (CDNC< 200 cm^{-3}) composites, each containing 22 days. The associated composites of the mean sea level pressure, QuikScat-derived surface winds, 850-mb NCEP winds, 500-mb geopotential heights, and MODIS-derived cloud top heights (which can serve as a proxy for the boundary-layer heights) were then examined and interpreted.

3. RESULTS

The MAX CDNC composite presents values higher than 250 [cm^{-3}] and a westward extension of the plume of 8 degrees while MIN CDNC composite is mainly confined to the coast with values lower than 200 [cm^{-3}]. Composite differences (Fig. 2.b) reveal that the maximum increase in CDNC occurs over an area between 18˚S and 27˚S and includes a westward extension of about 8˚ with values larger than 100 cm^{-3}. On the other hand, the cloud droplet number concentrations along the Peruvian coast (5˚S -15˚S) are higher during the MIN CDNC episodes than during the MAX CDNC episodes.

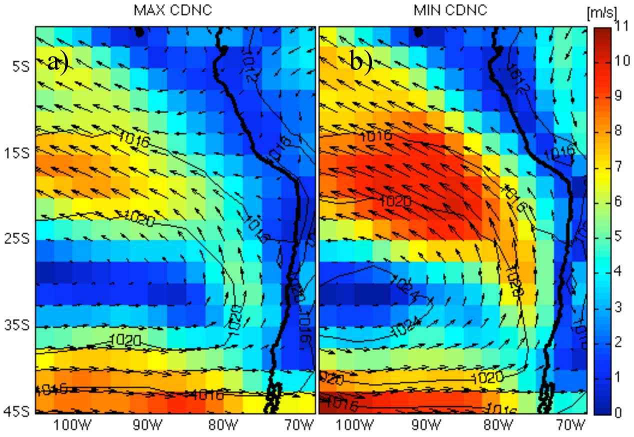

Figure 3: Wind fields at 850 mb and sea level pressure (contours) from NCEP/NCAR Reanalysis: a) composite for MAX CDNC, b) composite for MIN CDNC. Colors indicate the wind magnitude.

QuikScat (Fig. 4) and NCEP/NCAR Reanalysis data (Fig. 3) show stronger surface and 850 mb winds during the MIN-CDNC days, and weaker wind fields during the MAX-CDNC days. Changes in the subtropical high (contours in Fig. 3) are consistent: the MAX CDNC days are characterized by weaker anticyclone and a smooth trough at 500 hPa with its axis at 95˚W, while an intensified anticyclone for MIN CDNC is associated with a 500-hPa trough with its axis at 85˚W.

The MAX-CDNC days were also characterized by a slightly thinner satellite-derived mean cloud depth of 270 m accompanied by both lower cloud tops and higher lifting condensation levels, compared to the MIN-CDNC composite mean satellite-derived cloud depth of 305 m. Sonde-derived zonal winds at Antofagasta, Chile (23.43˚S, 70.43˚W, 120 m.a.s.l.) show mean easterlies below 1500 m at all times, but slightly stronger easterlies during MAX CDNC episodes.

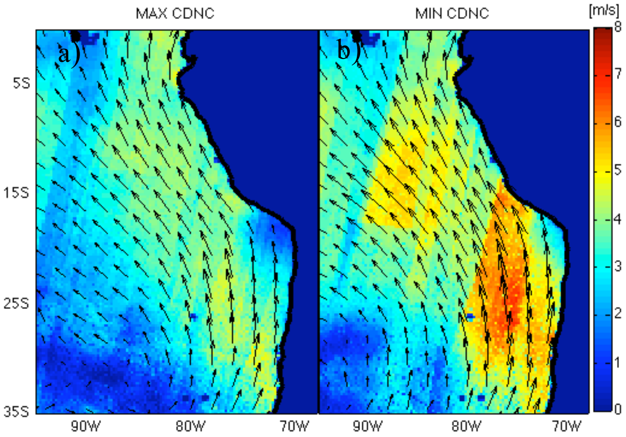

Figure 4: Winds at surface (QuikScat). : a) composite for MAX CDNC, b) composite for MIN CDNC. Colors indicate the wind magnitude.

We speculate that variability in the trade winds as well as in the boundary layer thermodynamic structure at the Arica Elbow is relevant to the aerosol longevity and/or aerosol incorporation into the southeast Pacific stratocumulus. Differences in the structure of the offshore winds during MAX/MIN CDNC episodes then help propagate different "downstream" signatures to the cloud properties characterizing each episode type. This hypothesis is guiding ongoing work. Further work is also needed to understand the cloud processes occurring over the Arica Elbow itself.

REFERENCES

Huneeus, N., L. Gallardo and J. A. Rutllant, 2006: Off-shore transport episodes of anthropogenic sulfur in northern Chile: Potential impact on the stratocumulus deck. *Geophys. Res. Lett.*, 33. doi: 10.1029/2006GL026921.

Klein, S. A., D. L. Hartmann, 1993: The seasonal cycle of low stratiform clouds. *J. Climate*, 6, 1587-1606.

Schuller,, L., R. Bennartz, J. Fischer, J.-L. Brenguier, 2005: An algorithm for the retrieval of droplet number concentration and geometrical thickness of stratiform marine boundary layer clouds applied to MODIS radiometric observations. *J. Appl. Meteor,* **44**, 28-38.

Tomlinson, J. M. R. Li, and D. R. Collins, 2007: Physical and chemical properties of the aerosol within the southeastern Pacific marine boundary layer. *J. Geophys. Res.,* **112**, doi: 10.1029/2006JD007771.

Twomey, S. 1977: The influence of pollution on the shortwave albedo of clouds, *J. Atmos. Sci.*, 34, 1149.

OBSERVATIONS OF SIZE-RESOLVED DRIZZLE RATES IN MARINE STRATOCUMULUS

D. L. Rossiter, J. D. Small, and P. Y. Chuang

Department of Earth and Planetary Sciences, University of California Santa Cruz, 1156
High Street, Santa Cruz, CA 95064

1. INTRODUCTION

While it is widely acknowledged that drizzle is a key process in the stratocumulus-topped marine boundary layer (MBL), there remain many outstanding questions regarding its quantitative impacts on the system. Here, we report in situ aircraft measurements of the size-resolved drizzle rate in marine stratocumulus using the Artium Flight Phase Doppler Interferometer (F/PDI) during the Marine Stratus Experiment in July 2005. One of the advantages of the PDI relative to previous instruments is accurate cloud drop size distribution measurements across a wide range of sizes, 4 to 150 μm diameter. The lower bound of drop size that is often considered drizzle varies substantially, with typical values ~50 μm diameter. However, Nicholls (QJRMS 1984) reports observations that suggest that the contribution of drops smaller than 50 μm to the drizzle rate can be very substantial, particularly at cloud top, although the resolution of the instrumentation allowed for only a coarse analysis.

The size distribution of drizzle is relevant to a number of processes. For example, the rate of drop evaporation after it falls below cloud base into the sub-cloud layer depends on drop size. In turn, such evaporation can be an important for the dynamics within the boundary layer and, via feedbacks, impact the cloud layer itself. Also, drop-drop interactions (such as collision-coalescence) within the cloud are strongly dependent on drop size, and therefore the development and evolution of drizzle itself is size-dependent.

2. METHODS

To compute drizzle rate, we begin with a 1-sec number drop size distribution, $\frac{dN}{d\log d}$ measured by the Phase Doppler Interferometer (PDI).

We then convert $\frac{dN}{d\log d}$ to a drizzle rate size distribution using:

$$dR_i = \frac{\pi}{6} d_i^3 \left(\frac{dN}{d\log d} \right)_i (\Delta \log d_i)\, w_T(d_i)$$

We then generate a probability distribution of 1-sec d_{50} values and compute average drizzle size distributions for each cloud leg.

3. RESULTS

We utilize these new high resolution F/PDI measurements and our calculations to examine the following questions:

a. What is the size distribution of drizzle?

Figure 1 shows significant contribution to drizzle rate at cloud top by drops between 15 and 50 μm with high variability in the fractional contribution by drops greater than 30 μm.

b. How does the size distribution vary vertically within cloud and how does this reflect cloud development?

Figure 2 and 3 show the variation in drizzle size distribution at different flight legs within cloud. This variation reflects the importance of both condensation and collision-coalescence to drizzle production.

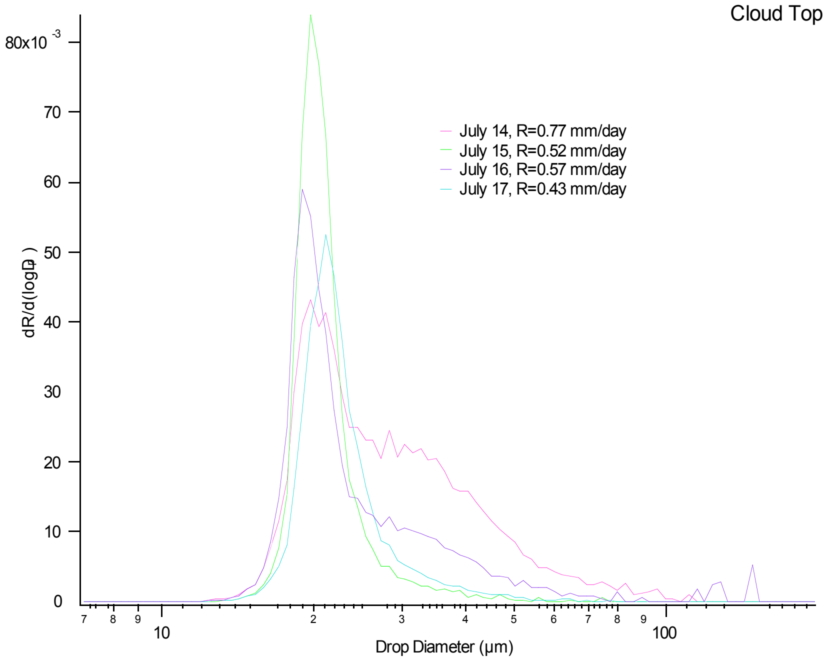

Figure 1: Drizzle distribution for cloud top legs July 14th through 17th. *R* is the integrated rain rate from the F/PDI.

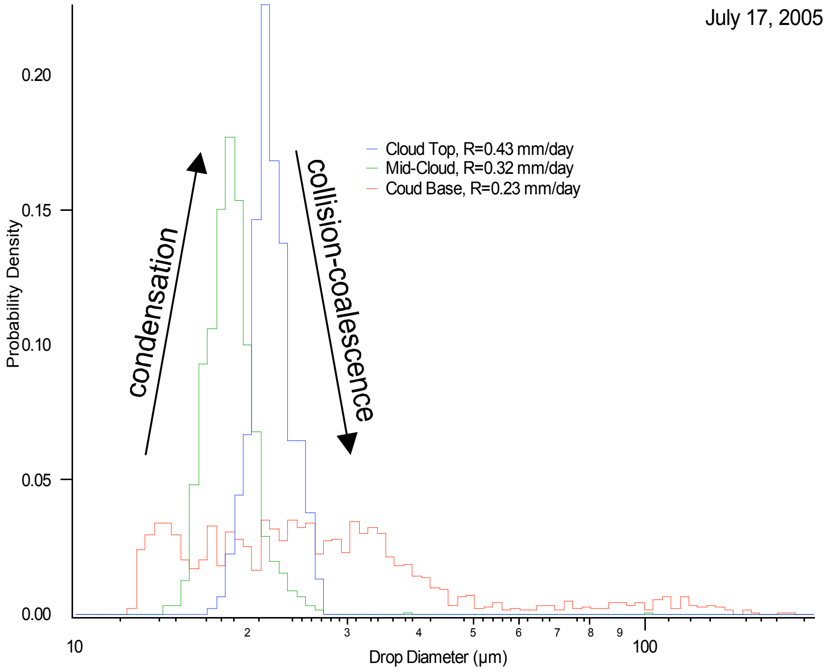

Figure 2: Histogram of median diameter of 1-s drizzle distributions for July 17th

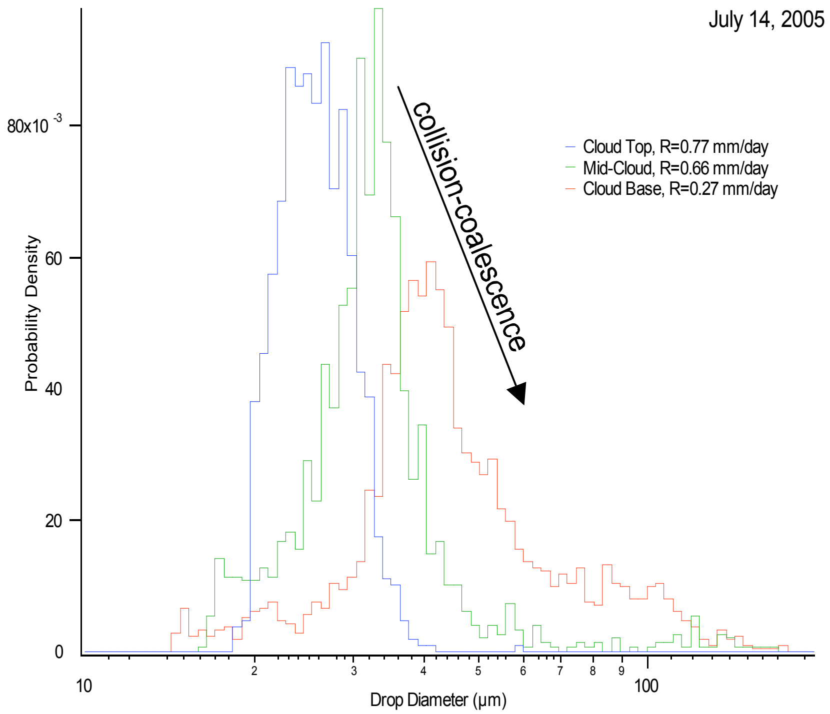

Figure 3: Histogram of median diameter of 1-s drizzle distributions for July 14th

LES MODEL SIMULATIONS OF CCN IMPACTS ON STRATOCUMULUS MICROPHYSICS AND DYNAMICS

Keun Yong Song and Seong Soo Yum

Department of Atmospheric Sciences, Yonsei University, Seoul 120-749, Korea

1. INTRODUCTION

The marine stratocumulus topped boundary layer (STBL), which prevails in the subtropical regions where the subsidence inversion associated with the descending branch of the Hadley-Walker cell dominates, is thought to be an important component of the climate system [Randall et al., 1984]. Especially, understanding the impact of the anthropogenic cloud condensation nuclei (CCN) on the cloud microphysics and dynamics of these clouds is a key to accurately assess the climatic impact of these clouds since the cloud radiative properties are determined by these properties.

Observations have shown that the diurnal evolution of marine stratocumulus to be characterized by an ascending cloud base [Vernon, 1936; Hignett, 1991]. For the daytime clouds, decoupling between the cloud layer and the surface plays an essential role in the dynamics of the STBL [Turton and Nicholls, 1987].

Here we focus on the diurnal variation of STBL, especially concerning the CCN effects on cloud. An LES model with size resolving microphysics [Kogan et al., 1995] is employed and the stratocumulus development for the three CCN loadings (maritime, continental and extreme continental) are examined.

2. MODEL SETUP

2.1. LES MODEL DESCRIPTION

The dynamical framework of the 3D LES model follows Moeng [1984]. The LES implementation uses a subgrid scheme adapted from Deardorff [1970], predicting the turbulent kinetic energy in order to evaluate eddy mixing coefficients. A 24-band solar radiation package [Slingo and Shrecker, 1982] is mounted for the shortwave radiative process calculation Longwave radiation parameterization is based on a greybody approximation for cloud drops [Herman and Goody, 1976]. The absorption coefficients for cloud drops are defined using parameterized expressions for cloud drop concentration and effective radius [Moeng and Curry, 1990].

Corresponding author's address: Keun Y. Song, Yonsei University, Dept. of Atmospheric Sciences, South Korea, Email: doitsky@yonsei.ac.kr

2.2. MODEL SETTING AND METEOROLOGICAL CONDITIONS

There are 40 grid points in x and y, and 50 in z. The grid spacing is 75 m in horizontally and 25 m in the vertical, to make the total domain size 3 km X 3 km X 1.25 km. Total simulation time is 6 hrs. The model is set up with surface temperature of 290 K. The roughness length is 0.0002 m. The initial wind field was set to be equal to zero in all grid points but thermal impulses at two locations initiate the air motion. Initial thermodynamic sounding is assumed to have inversion at 662.5 m (Fig. 1).

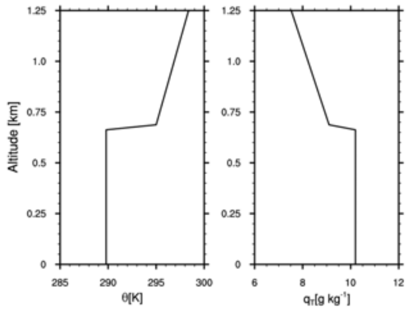

Fig. 1. Initial sounding profiles of potential temperature (θ) and total water mixing ratio (q_T).

2.3. INITIAL CCN DATA

The cumulative CCN concentrations at 1% supersaturation are 163, 1023 and 5292 cm^{-3} for the three CCN loading, maritime, continental, and extreme continental, respectively.

3. RESULTS

3.1. CCN IMPACTS ON CLOUD MICROPHYSICS, DYNAMICS, AND RADIATION

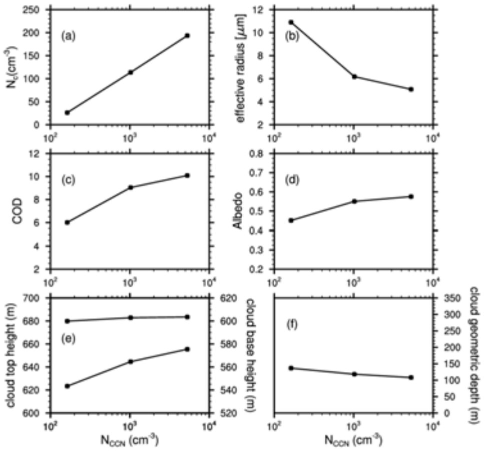

Fig. 2. Various cloud properties averaged over the last 4 h of simulations as a function of CCN loading; (a) cloud droplet concentration (N_c), (b) effective radius (R_e), (c) cloud optical depth (COD), (d) albedo, (e) cloud top and base height, and (f) cloud geometric depth for the daytime clouds.

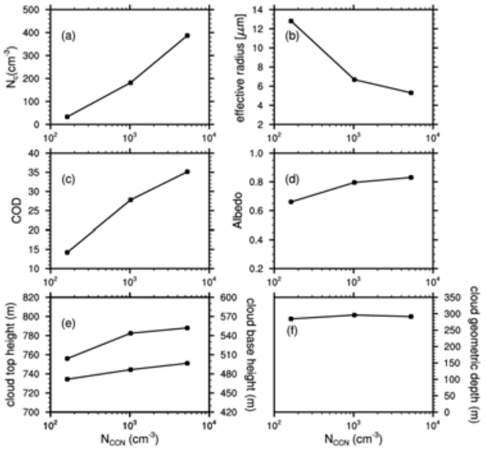

Fig. 3. Same as Fig. 2 except for the nocturnal clouds.

The cloud droplet number concentration, cloud optical depth, and albedo increase but the cloud droplet effective radius decreases with the increase of CCN concentration for both the daytime and nocturnal clouds (Figs. 2 and 3). High CCN concentration enhances cloud reflectivity (albedo) by increasing the cloud droplet number concentration, leading to a cooling effect (Table 1). Notable is that the cloud depth (top height-base height) decreases with CCN concentration for the daytime clouds (Fig. 2f). This is mainly due to the lifting of cloud base as CCN loading increases (Fig. 2e). For daytime clouds, decoupling of the cloud layer from the surface (discussed later) leads to dryness below the cloud base and strong evaporation of cloud drops in this region eventually leads to the lifting of the cloud base. The point is that this is more significant for the clouds with higher CCN concentration since evaporation is more effective for these clouds due to the smaller drop sizes (Fig. 2b). This is consistent with Lohmann and Lesins's [2003] satellite observation: cloud base height of maritime clouds is 100 hPa higher than those of continental clouds and polluted clouds were thinner than clean clouds. Since the cloud albedo depends on both the cloud droplet sizes and the cloud thickness these competing effects partly cancel each other out, making it more complex to assess indirect aerosol effects.

On the other hand, cloud thickness does not show a significant trend with CCN loading for the nocturnal clouds (Fig. 3f). Especially for the maritime cloud, strong drizzling (Fig. 4) leads to the collapse of cloud top (Fig. 3e). Light drizzling in the daytime maritime cloud, however, does not seem to affect the cloud top height.

Unlike the maritime clouds, there was virtually no surface precipitation for the continental and extreme continental clouds. Yum and Hudson [2002] provided evidence for the fact that marine stratocumulus clouds have higher drizzle liquid water content for more maritime. vanZanten et al. [2005] also showed that the precipitation rate increased with cloud drop diameter from the aircraft observation of stratocumulus topped marine boundary layers off the California coast.

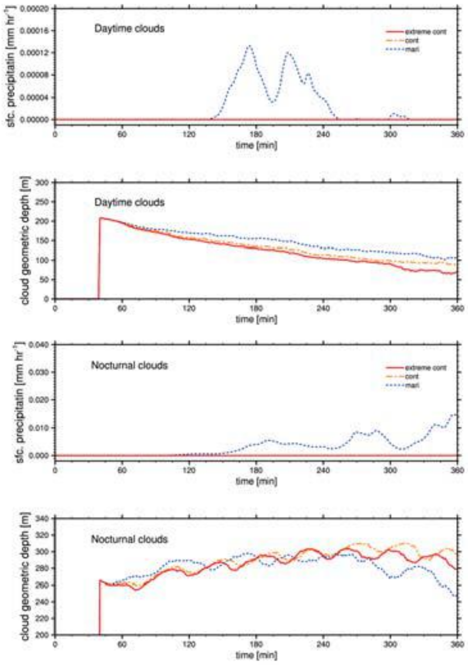

Fig. 4. Time series of surface precipitation rate and cloud geometric depth for the three CCN loadings.

3.2. CONTRAST BETWEEN DAYTIME AND NOCTURNAL CLOUDS

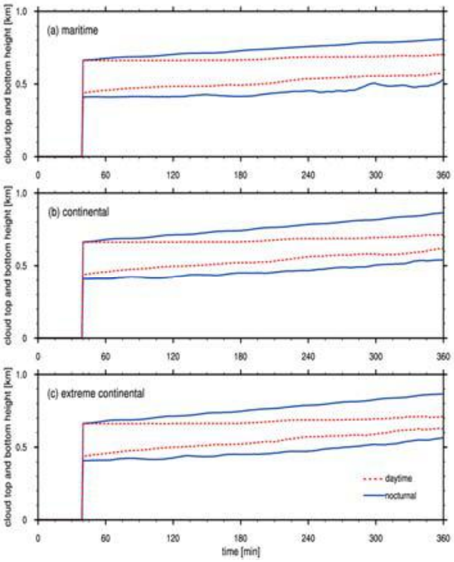

Fig. 5. Time series of cloud top and base heights for the (a) maritime, (b) continental, and (c) extreme continental cases; (dashed line—daytime; solid line--nocturnal cloud)

Cloud droplet concentration and cloud amount are consistently smaller for the daytime clouds than for the nocturnal clouds regardless of CCN loading. Daytime cloud thicknesses are also shallower than those of the nocturnal clouds for each airmass type (Fig. 5). Solar heating of the cloud layer and continued entrainment and evaporation near cloud base are responsible for the negative buoyancy flux below the bottom of the cloud layer for the daytime clouds. This leads to the decoupling of the cloud layer from the surface layer. The main effect of decoupling is to virtually cut off the cloud layer from the moisture source of the sea surface. Since entrainment drying is no longer balanced by moisture flux from the sea surface, the clouds will not be able to maintain the form before the decoupling; cloud base height rises and cloud thickness becomes thinner for the daytime clouds but no such trend is shown for the nocturnal clouds (Fig. 5). This is consistent with Turton and Nicholls [1987] observation.

3.3. CLOUD RADIATIVE FORCING (CRF)

Cloud radiative forcing (CRF) at the top of the atmosphere is calculated from the model results. The cloud radiative forcing, C, is defined

$$C = C_{cloudy} - C_{clr},$$

where C_{cloudy} is the stratocumulus cloudy-sky net heating and C_{clr} is the clear-sky net heating [Ramanathan, 1989]. The domain average of cloud radiative forcing for maritime, continental, and extreme continental clouds are shown in Table 1 for the daytime clouds. An anthropogenic net CRF can be defined as the difference in net CRF between maritime and polluted clouds. This is -103.5 W m^{-2} for the extreme continental, indicating a significant cooling effect on the global radiation balance.

Wilcox et al. [2006] estimated shortwave cloud forcing for the in-situ measurements during the Cloud Indirect Forcing Experiment (CIFEX) in North Pacific oceanic clouds. The average value of cloud radiative forcing for all overcast samples was -110.3 W m^{-2}, and the averages for the clean and polluted clouds are -103.9 W m^{-2} and -113.6 W m^{-2} at the top of atmosphere, respectively. But the strongest shortwave cloud radiative forcing was about -200 W m^{-2}. The CRF values in this study are generally larger than this measurement but are close to Hanson and Gruber [1982], who calculated average values of shortwave, longwave, and net stratocumulus cloud radiative forcing for Northern hemisphere: -228.3, 8.2, and -185.4 W m^{-2}.

Table 1. Shortwave cloud radiative forcing (CRF) at the TOA for maritime, continental, and extreme continental cases.

case	N_{CCN} (cm^{-3})	CRF_{SW} (W m^{-2})	CRF_{LW} (W m^{-2})	CRF_{NET} (W m^{-2})
mari.	163	-204.1	7.5	-196.6
conti.	1023	-283.3	7.6	-275.7
ex. cont.	5292	-308.0	7.9	-300.1

Here, N_{CCN} is CCN number concentration.

4. Acknowledgments

This work is supported by KOSEF Grant KOSEF Grant R14-2002-031-01000-0 and by Ministry of Environment as "The Eco-technopia 21 project". We really appreciate it for financial support provided from WMO, IAMAS and ICCP.

5. REFERENCES

Deardorff, J. W., 1970: A numerical study of three-dimensional turbulent channel flow at large Reynolds numbers. *J. Fluid Mech*., **41**, 453-480.

Hanson, H. P., and P. L. Gruber, 1982: Effect of marine stratocumulus clouds on the ocean-surface heat budget, *J. Atmos. Sci.,* **39**, 897-908.

Herman, G., and R. Goody, 1976: Formation and persistence of summertime Arctic stratus clouds, *J. Atmos. Sci.,* **33**, 1537-1553.

Hignett, P., 1991: Observation of diurnal variation ina cloud-capped marine boundary layer. *J. Atmos. Sci.*, **48**, 1474-1482.

Kogan, Y. L., D. K. Lilly, Z. N. Kogan, and Q. Liu, 1995: Modeling of stratocumulus cloud layers in a large eddy simulation nodel with explicit microphysics. *J. Atmos. Sci*., **52**, 2923-2940.

Lohmann, U., and G. Lesins, 2003: Comparing continental and oceanic cloud susceptibilities to aerosols, *Geophys. Res. Lett.,* **30(15)***, 1791*, doi:10.1029/2003GL017828.

Moeng, C. –H., 1984: A large-eddy simulation model for the study of planetary boundary-layer turbulence. *J. Atmos. Sci*., **41**, 2052-2062.

Meong, C.-H., and J. Curry, 1990: The sensitivity of large-eddy simulations of a stratus-topped boundary layer to cloud microphysics, *Conf. on Cloud Physics, San Francisco, CA,* *Amer. Meteor. Soc.*, 115-117.

Nicholls, S., 1984: The dynamics of stratocumulus: aircraft observations and comparisons with a mixed layer model, *Q. J. R. Meteorol. Soc.,* **110**, 783-820.

Ramanathan, V., R. D. Cess, E. F. Harrison, P. Minnis, B. R. Barkstrom, E. Ahmad, and D. Hartmann, 1989: Cloud-Radiative Forcing and Climate: Results from the Earth Radiation Budget Experiment. *Science*, **243**, 57-63.

Randall, D. A., J. A. Coakly, C. W. Fairall, R. A. Kropfli, and D. H. Lenschow, 1984: Outlook for Research on Subtropical Marine Stratiform Clouds, *Bull. Amer. Meteor. Soc.,* **65**, 1290-1301.

Slingo, A., and H. M. Schrecker, 1982: On the shorwave radiative properties of stratiform water clouds, *Q. J. R. Meteorol.,* **108**, 407-426.

Turton, J. D., and S. Nicholls, 1987: A study of the diurnal variation of stratocumulus using a multiple mixed layer model, *Q. J. R. Meteorol. Soc.,* **113**, 969–1009.

vanZaten, M. C., 2005: Observations of drizzle in nocturnal marine stratocumulus, *J. Atmos. Sci.*, **62**, 88-106.

Vernon, e. m., 1936: the diurnal variation in ceiling height beneath stratus clouds. *mon. wea. rev.*, **64**, 14-16.

Wilcox, E. M., G. Roberts, and V. Ramanathan, 2006: Influence of aerosols on the shortwave cloud radiative forcing from North Pacific oceanic clouds: Results from the Cloud Indirect Forcing Experiment (CIFEX), *Geophy. Res. Lett.,* **33***,* L21804, doi:10.1029/ 2006GL027150.

Yum, S. S. and Hudson, J. G., 2002: Maritime/ continental microphysical contrasts in stratus. *Tellus*, **54B**, 61-73.

NUMERICAL STUDY ON MICROPHYSICAL PROCESSES OF TWO DIFFERENT SNOWFALL CASES IN NORTH CHINA

Sun Jing Wang Pengyun

Chinese Academy of Meteorological Sciences, China

1. INTRODUCTION

Snowfall is very common in North China in winter and sometimes of negative effects on the traffic and power transmission in big cities. The weather systems inducing snowfall are various. Some are large scale cold frontal systems, for example the cold wave causing strong wind and snowfall during 23 - 24 Nov 1999 in Liaoning province. Some are small systems, for example the shallow trough system causing light snowfall during 7 - 8 Dec 2001 in Beijing city (Zhao et al., 2002; Sun et al., 2003). Some strong convective systems which not often occur also can bring thunder-snowstorms (Li et al., 1999). Many researches have been done about the weather and climate characteristics of snowfall (Wang et al., 1979; Yi et al., 1999; Wang et al., 1995). However, studies on snowfall are not as much as those on the rainfall. As same as the heavy rainfall in summer, it is also very complicated about the weather systems and physical processes of snowfall in winter. Nowadays the snowfall is still a challenge to weather forecast. So it is very necessary to pay more attention to the study of snowfall.

Recently some observations and simulations have shown that, the mixed-phase cloud process, in which ice phase coexisted with liquid phase, played the most important role in the development of heavy rainfall in South China and along the Yangtze River (Wang et al., 2002, 2003; Sun et al., 2003). However it is not sure whether the cloud process of snowfall in winter is the same as that of those heavy rainfalls due to lack of observations and numerical simulations. Both rainfall and snowfall are produced by the cloud microphysical processes under certain dynamical and thermal conditions. In addition to the hydrometeor phase in the cloud, the source and sinks for the generation of all hydrometeors are also very important. For heavy rainfall, the microphysical process is able to feedback significantly to the thermal and dynamical processes through latent heat and drag force. What is the feedback like for snowfall is also worthy of doing some researches.

In this paper, two different types of snowfall cases in North China are simulated, which are light snowfall during 7 - 8 Dec 2001 in Beijing city and strong wind and snowfall during 23 - 24 Nov 1999 in Liaoning province. These snowfalls brought large negative effects such as the traffic jam and power transmission break on big cities. Microphysical processes are mainly discussed. The hydrometeors and their source and sinks are analyzed and the feedback of microphysical processes to thermal and dynamical processes is preliminarily studied.

2. MODEL DESCRIPTION

In this study, the snowfalls are simulated using the PSU–NCAR non-hydrostatic, two-way interactive model MM5v3 (Grell, 1994). The model includes 6 explicit schemes, which are warm rain scheme, simple-ice scheme, mix-ice scheme, Goddard scheme, Reisner graupel scheme and Schultz scheme. The microphysical processes of Reisner graupel scheme are more complicated (Reisner et al., 1998). After analyzing the source and sinks for each hydrometeor, the primary processes to form the hydrometeor can be found. The understanding of the cloud processes is also essential to the microphysical mechanism of precipitation.

3. CASE OF BEIJING SNOWFALL

3.1 Case overview and model design

On 6 Dec 2001, a cloud system moved from Qinghai province to the east, and arrived at Beijing at 0000 UTC 7 Dec. Nine hours later it moved out of Beijing. There were two deep troughs in the east and west sides of the East Asia at 500 hPa. The west flow dominated between the troughs from 40°N to 50°N. This situation last for two days which imply no strong cold air and change of the weather. Correspondingly with the cloud image, in the west flow a shallow trough moved from north-east side of the Tibet Plateau and passed through Beijing during 0000－1200UTC 7 Dec. This trough became stronger at low levels and a close center of 1440 gpm exists at 850 hPa. It began to snowfall when the trough came close to Beijing. The southwest flow of the trough sent the moist and warm air. Updraft and convergence ahead of the trough may be one of the trigger mechanisms of this snowfall.

The non-hydrostatic model MM5v3 was used for numerical simulation. Two nested-level domains were set. The outer coarse domain included 61×61 grid points with horizontal resolution of 45km covering the area of (28.2°－52.2°N,101.0°－132.1°E); the same grid points for the fine-mesh domain but with 15km grid size covering the area of (36.0°－44.0°N,111.1°－121.6°E). The model physical processes mainly include the Anthes–Kuo convective parameterization scheme, the Reisner scheme, the MRF PBL scheme and cloud radiation scheme. The model was initiated using the USA NCEP 1°×1° grid data as a “first guess” field. The simulation was started at 0000 UTC 7 Dec and ended at 0000 UTC 8 Dec 2001.

3.2 Simulations of snowfall

Snowfall occurred around Beijing and Hebei province because of the cloud moving on 7－8 Dec 2001. The observed maximum of snowfall was 1.8 mm. Snow occurred in Beijing mainly in the period of 0600 UTC － 1200 UTC 7 Dec. The 6-hour snowfalls of observations and simulations show that the snow band moved eastward along with the cloud system (Fig. 1). The simulated snowfall was in Shanxi province at 0600 UTC 7 Dec correspondingly with observation. At 1200 UTC 7 Dec, it moved eastward to Beijing with the maximum of 1.5 mm which was a bit less than observation. At 1400 UTC 7 Dec, it moved out of Beijing. The period of the strongest snowfall simulated was 0800 UTC － 0900 UTC 7 Dec. On the whole, the simulated results reproduced the snowfall’s movement and distribution successfully.

3.3 Phases of hydrometeors

The simulated results show that the temperature of the atmosphere was below 0℃ and about -5℃ near the ground. There were no liquid phase particles and the cloud was made up of ice and snow. Fig.2 shows the vertical sections along 40°N at 0600 UTC and 0900 UTC 7 Dec. The west wind in the middle and high levels between 700 hPa and 300 hPa was stronger than that in the low levels. Ice particles were transferred by the west wind so that ice

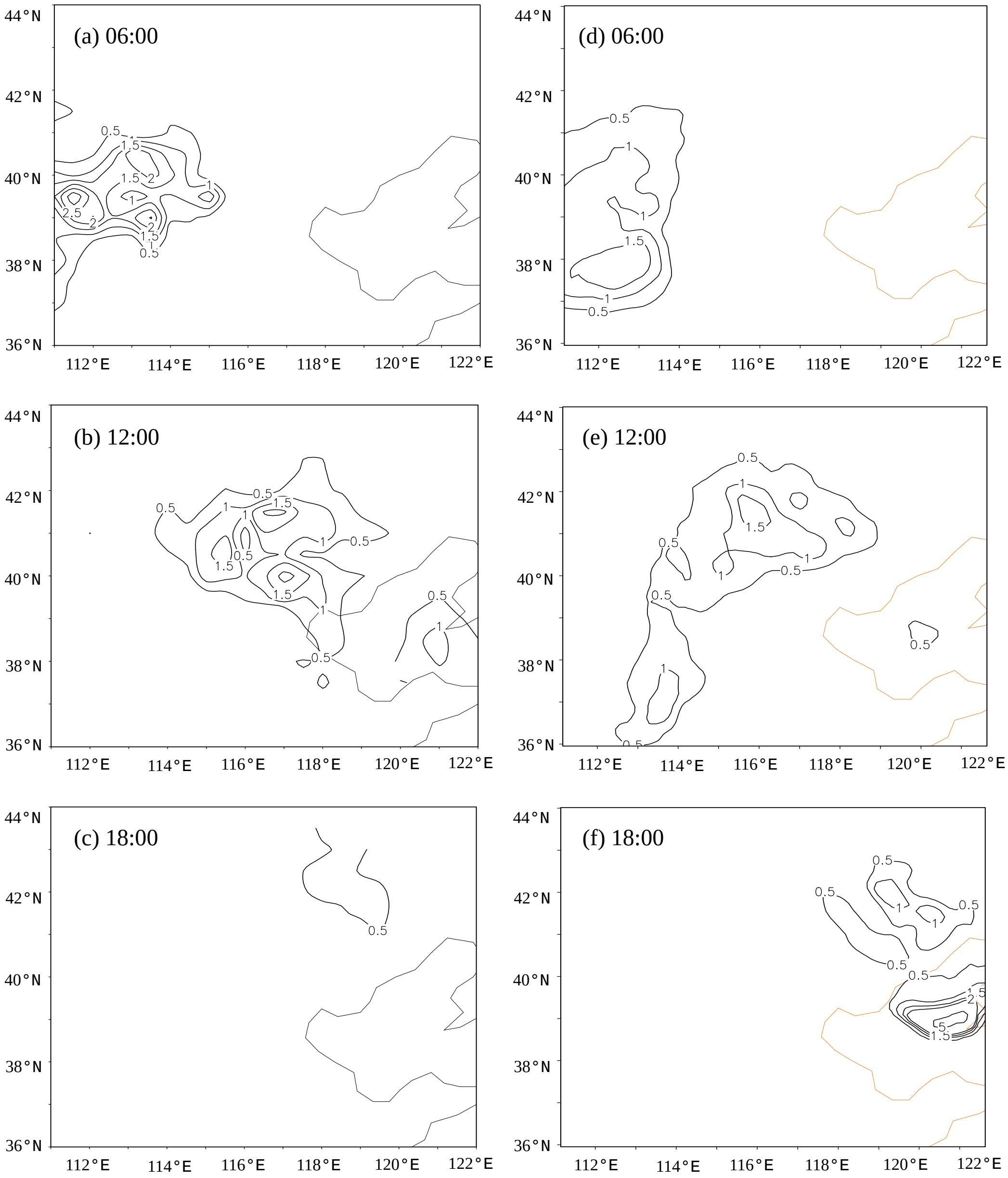

Fig1 Observed(a-c) and simulated(d-f) rainfall (mm) for every 6 hours on 7 Dec 2001.

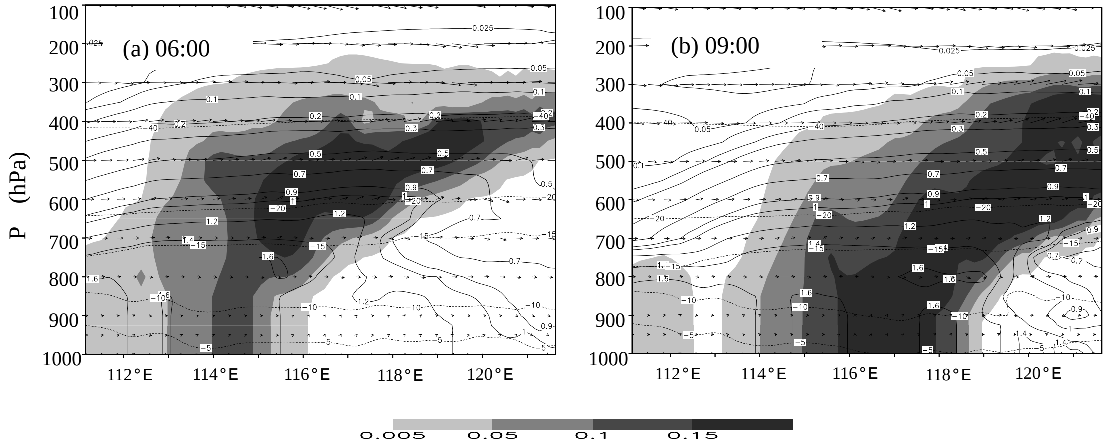

Fig.2 Cross section of ice phase particles(shaded, g/kg),water vapor(solid line, g/kg),temprature(dash line, ℃) and wind vector along 40°N on 7 Dec 2001

cloud inclined eastward with the height vertically. Ice cloud together with the snowfall center moved from the west to the east gradually. The distribution of water vapor was similar to ice particles. The maximum of water vapor was 1.6 g/kg. As for Beijing (40°N , 116.3°E), due to the vertical inclination of the cloud, it developed from the top to the bottom. The vertical section along 116.3°E shows the development clearly (Fig. 3). It did not start to snow at 0300 UTC 7 Dec. Ice particles distributed between 600—300 hPa at first. The maximum of snow was 0.035 g/kg. Correspondingly with the ice particles was the updraft with a maximum of 0.14 m/s between 750—300 hPa. At 0600 UTC, the ice cloud became thicker with the bottom at 900 hPa. The updraft sustained around the center area of ice particles. Subsequently with the eastward moving of snowfall, the center height of ice particles became lower, and ice and snow fell down to the ground at 0700 UTC indicating the start to snowfall in Beijing. Two hours later snow of Beijing became strongest with a maximum of 0.065 g/kg. The updraft turned weaker. Downdraft occurred at the north-side of snow area. At 1200 UTC, ice particles obviously became fewer. Cloud was dominated by the weak downdraft. Ice cloud began to dissipate. Snowfall stopped at 1500 UTC 7 Dec.

During this snowfall process, snow area moved from the west to the east, and the snowfall of Beijing started at 0700 UTC 7 Dec and ended at 1400 UTC 7 Dec with a maximum of 1.5 mm. The cloud was made up of ice and snow with nearly no super-cooled water and graupel. The horizontal scale of ice cloud was beyond 800 km and the magnitude of updraft was 0.1 m/s. It indicated this was a snowfall case caused by the cold stratus cloud. The layer of the cloud was a bit thin at the beginning. Afterwards the cloud's top lifted and the bottom fell so that the cloud layer became thicker. Ice cloud changed from high cloud (0300 UTC) to middle cloud (0600 UTC) and fell down to the ground at last (0900 UTC). Updraft dominated in the formation the cloud. The ice particles number and cloud thickness became larger when the updraft was stronger (0300—0900 UTC).

3.4 Snow and its sources

In order to study the source and sinks for the formation of hydrometeors in a certain period, for example the strongest precipitation period, the hour-accumulative values of hydrometeors and their sources were calculated. These values also depicted for the changes in one hour, and the unit was g/kg·h^{-1}. At last a comparison of the source and sinks were made to understand what was the most important to the formation of hydrometeors.

Simulated results have shown that one-hour precipitation in Beijing was very strong during 0800—0900 UTC 7 Dec. The center position of snowfall was (40°N, 116.3°E) with a maximum of 0.4 mm·h^{-1}. Fig.4 shows the vertical distribution of accumulative values of snow and its main sources at this center during this period. Snow increased mainly in the middle and low levels below 500 hPa. The maximum 0.236 g/kg·h^{-1} was around 985 hPa near the ground. The major microphysical processes of snow were the depositional growth (psdep) and the collection of ice by snow (psaci). Their horizontal distributions were very similar to the snow's (Figure not shown). Due to no cloud and rain water existed, the accretion of rain and cloud water did not work in the snowfall. In addition, the magnitude of conversion of ice to snow was so small that it could be ignored. The generation of the depositional growth was larger than that of the collection of ice by snow. As a result, water vapor was the most important to snow formation in the strongest snowfall period.

3.5 Feedbacks of hydrometeors to dynamical and thermal processes

Two sensitive tests were done to research the feedback effects of the microphysical processes to dynamical and

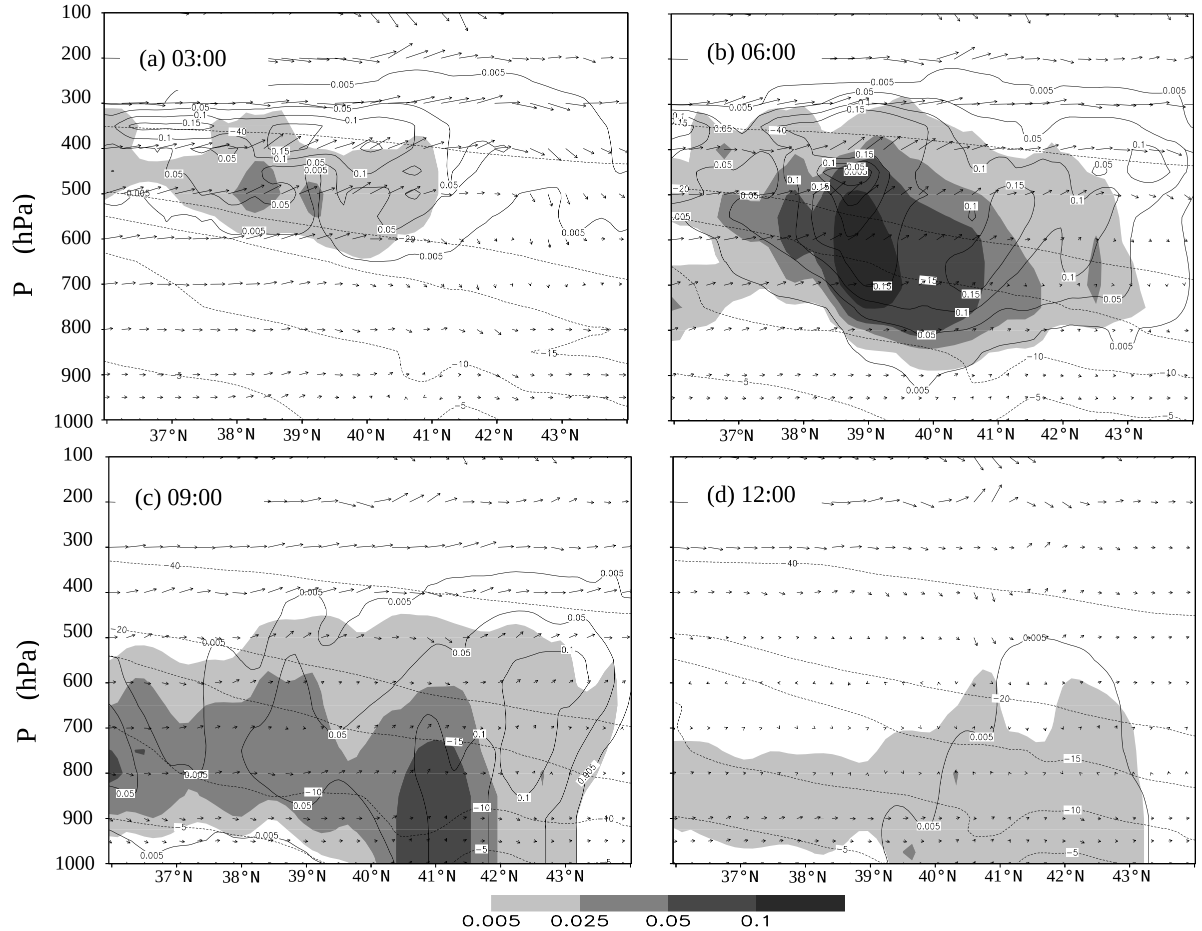

Fig.3 Cross section of ice phase particles(shaded, g/kg),water vapor(solid line, g/kg),temprature(dash line, ℃) and wind vector along 116.3°E on 7 Dec 2001

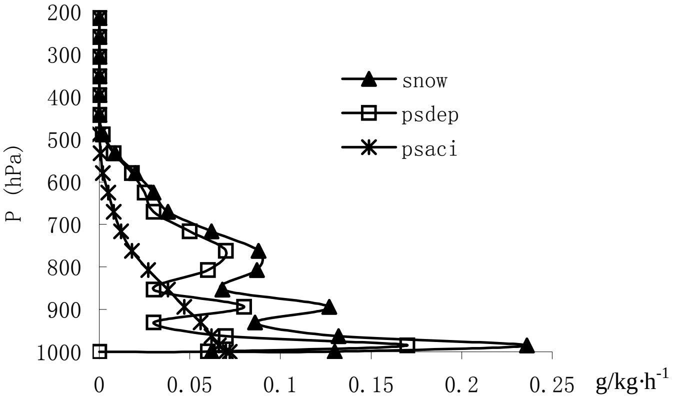

Fig.4 Vertical distribution at surface snowfall center(40°N,116.3°E) of accumulative value of snow and its main sources from 0800 UTC to 0900 UTC 7 Dec 2001

thermal processes. The “heat test” was to neglect the latent heat in thermal process. The “drag test” was to neglect the drag force in vertical velocity equation. Other model parameters kept the same in each sensitive test.

The cloud developed strong at 0600 UTC 7 Dec. θ_e (Fig. 5a) and w (Fig. 5b) of the control experiment show that, the atmosphere stratification was stable and the updraft area was in the middle-high levels between 700－200 hPa. The updraft center was around 450 hPa with a maximum of 0.12 m/s. Ice particles were at 850－300 hPa (Fig. 3b). The center area of ice was at 400－600 hPa correspondingly with updraft center. The center area of snow was a bit lower at 500－700 hPa. Using the results of two sensitive tests minus those of control experiment, the changes of thermal and dynamical values can be revealed. Below are the minus results of “heat test”. (1) As shown in Fig.5d, θ_e increased below 600 hPa and above 300 hPa, while deceased between 600－300 hPa. However the change value was very small with the maximum only 1.5 K. The vertical section for θ_e of “heat test” did not change much and still kept stable stratification (Figure not shown); (2) As for w (Fig. 5e), though there were local small centers of increase and decrease, the decrease of w in middle-high levels was the major effect. The maximum of decrease was 0.05 m/s; (3) The total precipitation decreased with a maximum of 0.5 mm (Fig. 5f). The results of “heat test” revealed that latent heat was able to enhance the updraft and precipitation. The minus results of “drag test” were described as follows. (1) θ_e decreased (Fig. 5g), but its value was smaller than that of the “heat test”. The maximum was only 0.09 K; (2) The maximum change of w was 0.02 m/s which was smaller than that of the “heat test” too (Fig. 5h); (3) The total precipitation increased with a maximum of 0.1 mm (Fig. 5i). Contrarily, the drag force of ice particles was not strong, but it was still able to weaken the precipitation. Above analyses have shown that, it was lack of liquid water during this case and the phase changes were not strong, but latent heat was still released by the depositional growth of snow. The mass content of ice particles was not large, but the falling particles could induce drag force. As a result, the latent heat and drag force induced by hydrometeors had a certain effects on thermal and dynamical processes during this snowfall case. The effect of latent heat was more obvious than that of drag force.

4. CASE OF LIAONING SNOWFALL

4.1 Case overview and model design

On 22 Nov 1999, a cold frontal cloud system moved from Xinjiang Uygur Autonomous Region to the east, passed through most of the region north of the Yellow River and arrived at the Northeast China at 0000 UTC 24 Nov. During 22－23 Nov 1999, upper-level circulation was characterized by a ridge in the west of Ural Mountain and a deep trough in the east of Lake Baikal. In the west flow from 40°N to 50°N a shallow trough moved from the west side of Xinjiang Uygur Autonomous Region to the east. The meridional circulation was strengthened on 24 Nov 1999. A blocking high was set up at Ural Mountain and a cross trough was located in the west of Lake Baikal. The Northeast China was in the unstable area in front of the moving trough. On 25－26 Nov, the cross trough developed vertically inducing the cold air southward. The cold wave with strong wind and low temperature occurred in most area of China. The trough in North

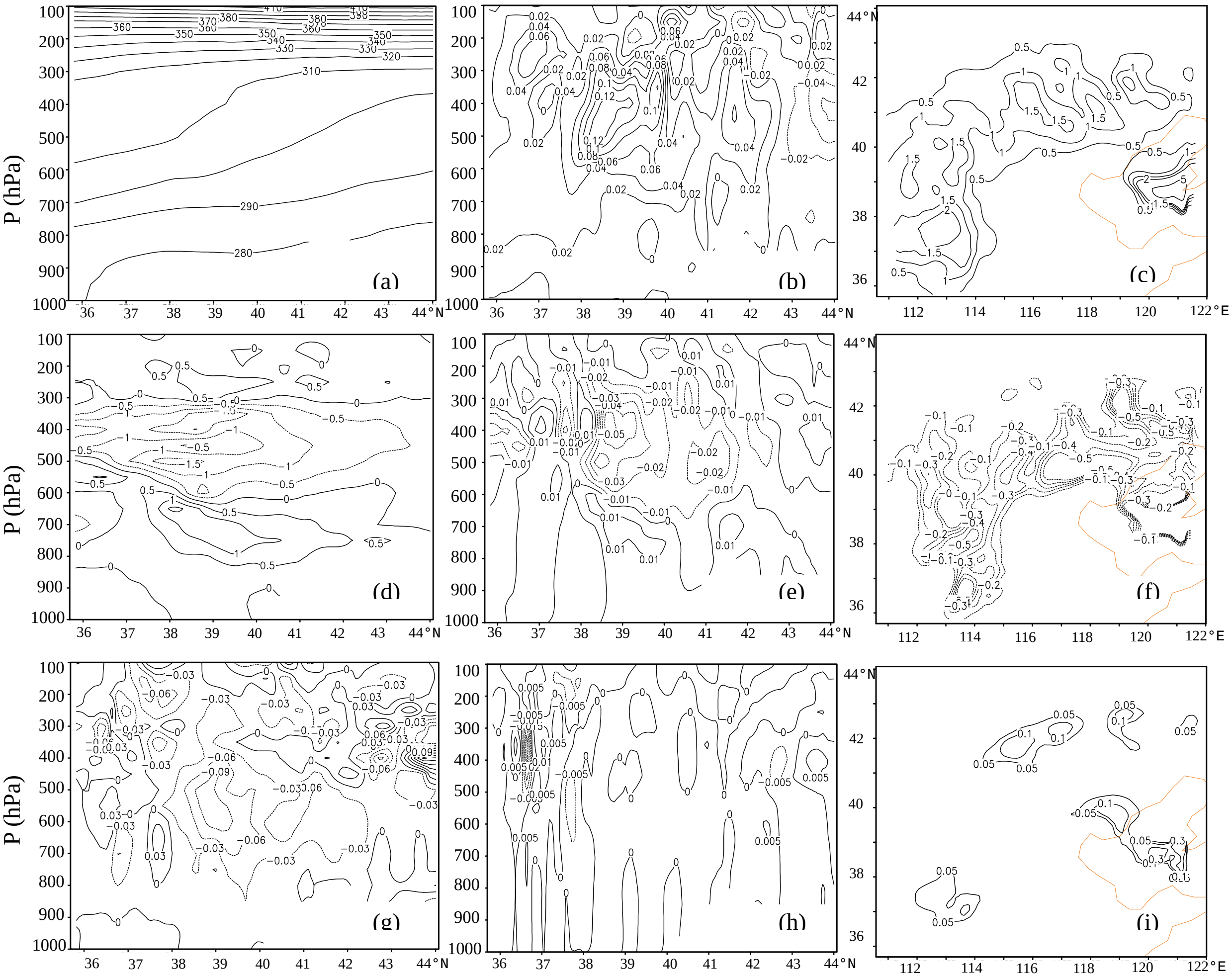

Fig.5 Cross section of equivalent potential temperature(θ e,unit:K),vertical velocity(w,unit:m/s) and 24 hours rain(rain,unit:mm) along 116.3°E at 0600 UTC 7 Dec 2001: (a,b,c) θ e, w, rain of control test respectively, (d,e,f) results of θ e, w, rain subtracted control test from heat test respectively, (g,h,i) results of θ e, w, rain subtracted control test from drag test respectively

China became stronger at 700 hPa. The southwest flow of the trough sent the moist of Bo Sea to the north. The wind at 850 hPa developed to be cyclonic flow. With the cold air enter the trough on 24－25 Nov, this cyclone moved to the northeast quickly which induced the strong wind and heavy snowfall in Liaoning province.

The non-hydrostatic model MM5v3 was used for numerical simulation. The model was initiated using the T106 of National Meteorological Center of China 1.125°×1.125° grid data as a “first guess” field. Two nested-level domains were set. The outer coarse domain included 73×73 grid points with horizontal resolution of 30km covering the area of (32.8°－52.2°N,111.0°－137.0°E); the fine-mesh domain included 91×91 grid points with 10km grid size covering the area of (38.0°－46.2N,118.0°－129.0°E). The model physical processes mainly include the Grell and KF convective parameterization scheme, the Reisner scheme, the MRF PBL scheme and cloud radiation scheme. The simulation was started at 1200 UTC 23 Nov and ended at 1200 UTC 24 Nov 1999.

4.2 Observations and simulations of snowfall

Snowfall with strong wind occurred in the most region of Liaoning province on 23 － 24 Nov 1999. This snowfall caused terrible effects on the traffic and power transmission. For example, in Shenyang city the airport was shut off and the electric power transmission stopped. From 1600 UTC 23 Nov to 0100 UTC 24 Nov was the period of rainfall or sleet-fall. Snowfall started at 0100 UTC and ended at 1000 UTC 24 Nov. Strong wind occurred near the ground. Snowfall was the main part of this precipitation. The observed precipitation increased from 1800 UTC 23 Nov (Fig.6 a-b). Snow band was of northeast-southwest orientation. The total 24-hour precipitation was 8 － 15 mm generally and 18－25 mm locally (Figure not shown). The atmosphere temperature was decreased by 20℃. Fig. 6c-d shows the simulated 6-hour precipitation. The simulated precipitation increased from 1800 UTC 23 Nov too. The simulated snowfall area was a bit south of observation, but the simulated snow-band was also of northeast-southwest orientation and its movement was basically consistent with observations. The maximum of simulated snowfall was 20 mm (Figure not shown).

4.3 Phases of hydrometeors

The cold air of this case was very strong and the atmosphere temperature decreased obviously. For example, the temperature of Xinmin station at 1200 UTC 23 was 11.2℃, while it was -11.3℃ at 1200 UTC 24. Fig.7 shows the vertical section along 125°E through the snowfall center. The isothermal lines were pushed southward by the cold air. The phase of hydrometeors was changed from the liquid to the solid.

At 1800 UTC 23, as shown in Fig. 7a-c, in the region south of 43.6°N the temperature below 750 hPa was above 0℃ and the wind blow to the north below 900 hPa; in the region north of 43.6°N the temperature was below 0℃ and the wind blow to the south below 900 hPa. The vertical 0℃ line could be seen as the frontal zone. The cloud water was in the warm region below 750 hPa. The horizontal scale of cloud water was 400 km and the maximum was 0.3 g/kg at 900 hPa. The rain water distributed correspondingly with cloud water but of smaller mass content 0.06 g/kg. Ice and snow mostly distributed in middle and high levels in the north. There existed no graupel in the simulated area. From the distributions of ice and liquid particles, ice particles were not important to precipitation at this time. Rain formation was mainly from the cloud water by warm rain processes in warm region.

At 0000 UTC 24, as shown in Fig. 7d-f, 0℃ isothermal line on the ground moved to 43°N due to the effects of cold air. The cloud top lifted to 700 hPa. The maximum of cloud water was 0.35 g/kg around 0℃ at 800 hPa. Super-cooled water emerged at this time with a small center of 0.1 g/kg at 600 hPa. Rain water moved southward with the maximum of 0.05 g/kg. The updraft in the cloud weakened to 0.08 m/s. Under the effects of cold air, ice moved southward quickly and became stronger and wider. The top of ice did not change much while the bottom extended down to 750 hPa. Several mass content centers of ice emerged, and the maximum was 0.12 g/kg at 300 hPa. As for snow, there were two mass content centers merging during its southward moving. Its horizontal scale decreased and vertical scale increased to 800－400 hPa. The maximum of snow was 0.14 g/kg at 650

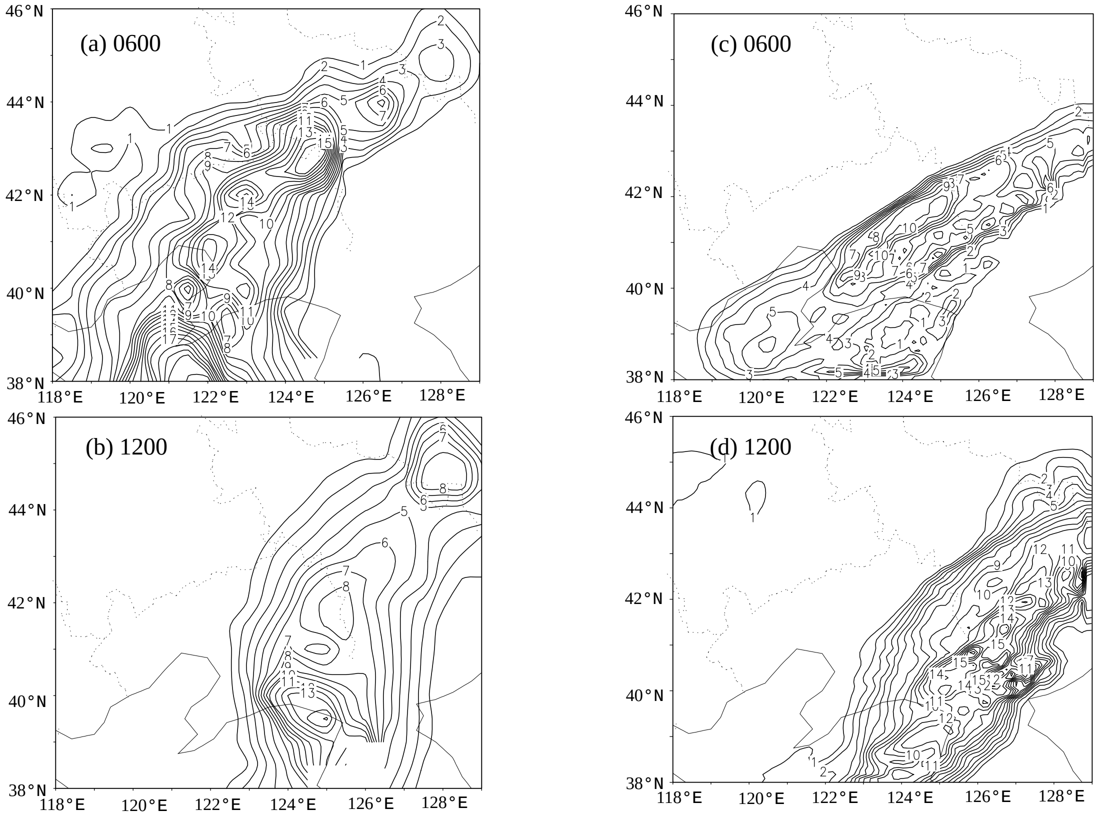

Fig.6 Rainfall (mm) for every 6 hours from 23 to 24 Nov 1999: (a-b) observed, (c-d) simulated.

hPa. Several new mass content centers of graupel emerged below 600 hPa. These centers were correspondingly with those of super-cooled water. The maximum of graupel was 0.016 g/kg. All ice particles strengthened at this time. The formation of graupel had close relationship with super-cooled cloud water.

At 0600 UTC 24, as shown in Fig. 7g-i, the strong cold air continuously moved to the south. 0℃ isothermal line on the ground moved to 42.1°N. The cloud developed strong in vertical direction. The cloud top was at 600 hPa and there was a bit super-cooled water at 500 hPa. The maximum of cloud water was 0.45 g/kg near the 0℃ layer. Rain water moved with cloud water with the maximum of 0.27 g/kg. The updraft in the cloud developed stronger with the maximum of 0.45 m/s at 700 hPa. The southward moving ice extended to the ground. The maximum of ice was 0.5 g/kg at 700 hPa. Snow fell down to the ground at 0400 UTC and increased to 0.4 g/kg. Graupel developed and merged immediately and fell down to the ground together with ice and snow. The maximum of graupel was 0.13 g/kg. Interestingly, the distributions of rain water and ice particles were divided by the 0℃ isothermal line at 41.5°N vertically. Rain water was in the warm area below the 0℃ line, while ice was in the cold area out of the 0℃ line. Most snow and graupel were in the cold area, but there were a bit of unmelted snow and graupel extending to the warm area. To the north of 41.5°N, precipitation was induced by solid particles instead of liquid particles. The cloud was full of ice particles in addition to some cloud water. The temperature was lowered under 0℃. These results revealed that it was a rainfall changing to snowfall precipitation with obvious temperature decrease, which was consistent with observations. To the south of 41.5°N, it was still rainfall. The hydrometeors of this region were of mixed-phase. The melting of ice particles played an important role in the formation of rain. The distribution of hydrometeors reflected the effects of temperature on precipitation. You et al. (2002) observed the snowfall in Xinjiang Uygur Autonomous Region and indicated that, different temperature of cloud top resulted in different types of snowfall. Some was drizzle, some was branch-shape snow and some was no liquid water. Their researches also revealed the relationship between precipitation and temperature.

After 0600 UTC 24, all hydrometeors moved southward quickly and nearly dissipated. At 1200 UTC 24, ice particles moved out of the simulated domain. Although new ice particles emerged in the north, they did not affect the snowfall in Liaoning province.

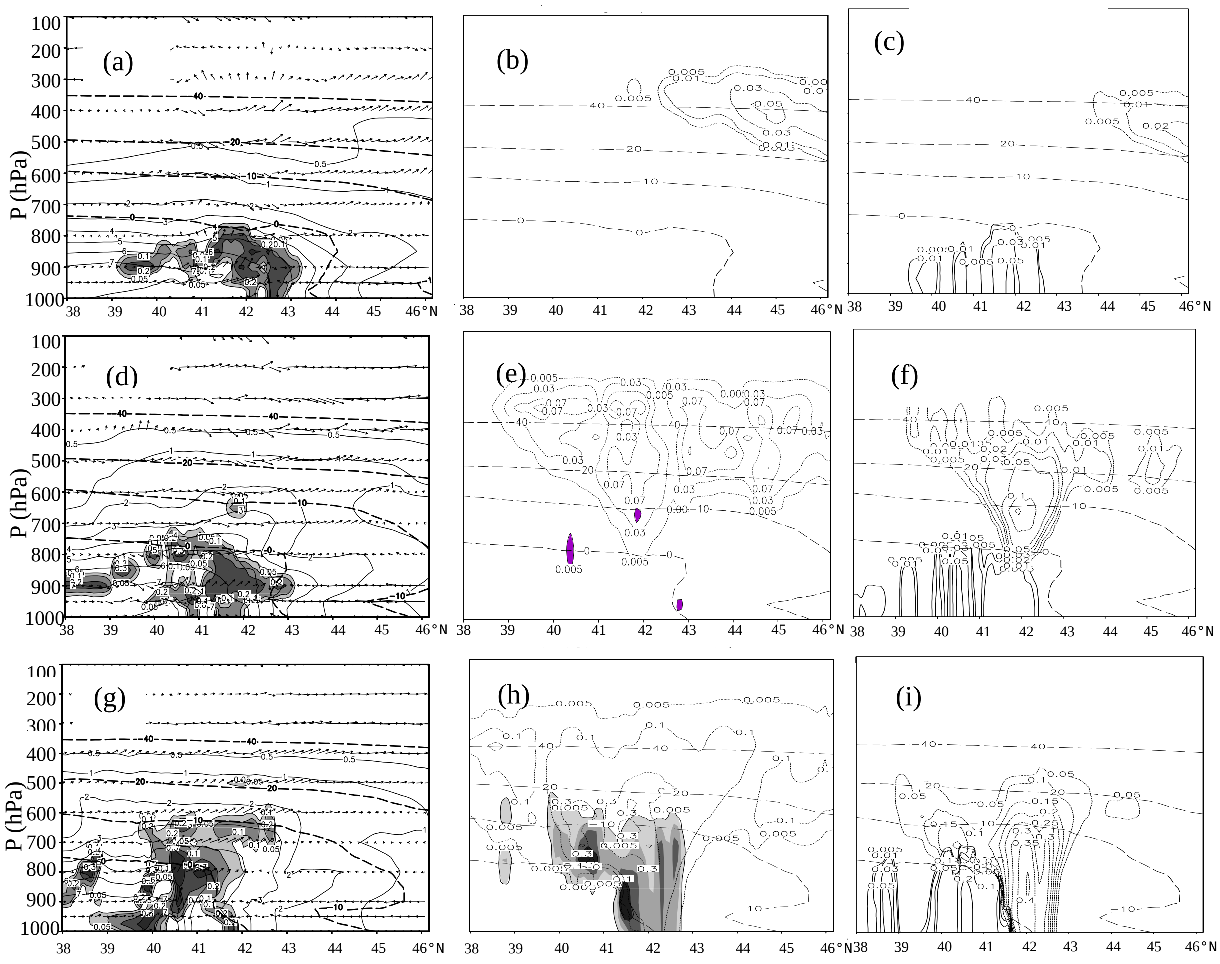

Fig.7 Cross section of water substances(g/kg),temprature(long dash line, ℃) and wind vector along 125°E at 1800 UTC 23(a-c), 0000 UTC 24(d-f), 0600 UTC 24 Nov 1999 (g-i). (a,d,g):cloud water(shaded with solid line) and water vapor(solid line), (b,e,h): graupel(shaded with solid line) and ice (dash line),(c,f,i):rain water(solid line) and snow(dash line)

4.4 Rain water, snow, graupel and its sources

The simulated rainfall became strongest during 0200－0300 UTC 24. Fig. 8 shows the distribution of rain and its sources in this period at rainfall center (41.7°N, 125°E). Rain mainly increased below 800 hPa with the maximum of 6.98 g/kg·h^{-1} near the 0℃ at 850 hPa. The melting of snow and graupel (psmlt, pgmlt) and the collection of cloud water by rain (pracw) were of the most magnitude 1g/kg·h^{-1} near the 0℃ layer. They were in the similar distribution of rain. The collection of cloud water by rain was the major process below 0℃ layer. Next were the conversion of cloud water (pccnr), the collection of cloud water by snow and graupel (psacw, pgacw). They were of the magnitude 0.1g/kg·h^{-1}. The enhanced melting of graupel by collection of rain and cloud water and the collection of snow by rain were of the smaller magnitude. These processes were not very important to rain formation.

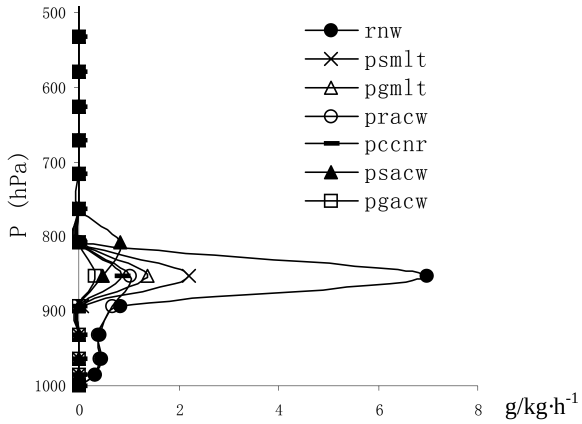

Fig.8 Vertical distribution at surface rainfall center(41.7°N,125°E) of accumulative value of rain(rnw) and its main sources from 0200 UTC to 0300 UTC 24 Nov 1999

0500—0600 UTC 24, rainfall moved to the south and the rainfall center above changed to snowfall. Ice particles developed strong. The temperature in vertical direction was under 0℃. Snow mainly increased below 500 hPa. The magnitude of snow was 0.1—1 g/kg·h^{-1} and the maximum was 1.49 g/kg·h^{-1} at 750 hPa (Fig.9). There were two negative values of the depositional growth of snow (psdep) in middle levels, because the values in the figure were the changes in one hour. Negative value depicted for the decrease of the depositional growth of snow. The depositional growth of snow, the collection of ice and cloud water by snow (psaci, pssacw) were the main processes. The processes associated with rain water were not important because there was nearly no rain water. The conversion of ice to snow was of small magnitude too. The values of snow sources of Liaoning case were larger those of Beijing case. Cloud water contributed to the formation of snow in Liaoning case while not in Beijing case. As for graupel, it mainly increased below 750 hPa. The magnitude of graupel was 0.1—1 g/kg·h^{-1} and the maximum was 1.25 g/kg·h^{-1} at 800 hPa (Fig. 10). The collection of cloud water by snow and graupel (pgsacw, pgacw) and the conversion of snow to graupel (psemb) were the main processes. They were of magnitude 0.1 g/kg·h^{-1}. Next was the collection of cloud water by ice (pgiacw) with the magnitude 0.01 g/kg·h^{-1}. Other processes such as the depositional growth of graupel were not very important to graupel formation.

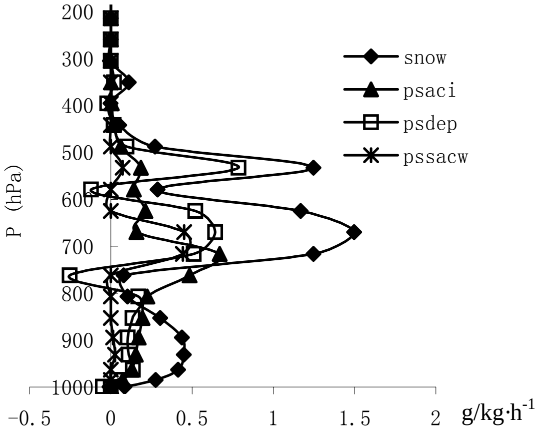

Fig.9 Vertical distribution at surface snowfall center (41.7°N,125°E) of accumulative value of snow and its main sources from 0500 UTC to 0600 UTC 24 Nov 1999

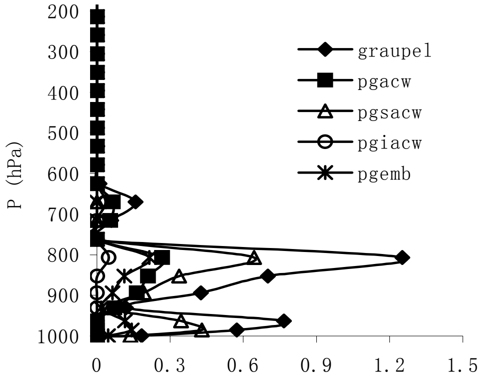

Fig.10 Vertical distribution at surface snowfall center(41.7°N,125°E) of accumulative value of graupel and its main sources from 0500 UTC to 0600 UTC 24 Nov 1999

Some researchers also have studied the microphysical processes using the Reisner scheme of MM5. Colle et al. (2005) simulated the orographic precipitation on the 13–14 December 2001 in Oregon Cascades. Their results showed that, the major processes responsible to snow formation included the depositional growth of snow, the accretion of cloud water by snow, the collection of ice by snow and the conversion of ice to snow. The major processes responsible to graupel formation included the accretion of cloud water by snow and graupel, the conversion of ice to graupel and the accretion of rain water by graupel. The major processes responsible to rain water formation included the melting of snow and graupel and the collection of cloud water by rain water. These conclusions were basically consistent with the analyses results of hydrometeors and their sources above in this paper.

4.5 Feedbacks of hydrometeors to dynamical and thermal processes

The cloud developed strong at 0600 UTC 24 Nov. θ_e (Fig. 11a) and *w* (Fig. 11b) of the control experiment show that, θ_e lines were dense in the north of 40.5°N and the atmosphere stratification was unstable in the south of 40.5°N. The maximum of updraft was at 40.5°N in low levels. Along 40.5°N, 0℃ line was at 800 hPa and mixed-phase particles co-existed to produce rainfall (Fig. 7g, h, i). Using the results of two sensitive tests minus those of control experiment, the changes of thermal and dynamical values can be revealed. Below are the minus results of “heat test”. (1) θ_e increased in the north of 40.5°N (Fig. 11d), while in the south of 40.5°N, θ_e increased at 800－600 hPa and decreased below 800 hPa. These revealed that latent heat released in the south of 40.5°N warm the air in low levels but cool in upper levels, which decreased the atmosphere stratification stability; (2) As for *w* (Fig. 11e), the updraft decreased at 40.5°N vertically. The latent heat strengthened the updraft there; (3) The total precipitation was smaller than that of control experiment (Fig. 11f). The latent heat was able to enhance precipitation. The minus results of “drag test” were described as follows. (1) θ_e did not change much with the maximum of 0.6 K (Fig. 11g); (2) As for *w* (Fig. 11h), it increased below 600 hPa at 40.5°N, which revealed that the drag force retrained the updraft; (3) The total precipitation was larger than that of control experiment (Fig. 11i). So the drag force weakened the precipitation. Above analyses have shown that, the feedback of “heat test” was larger than that of “drag test”. More latent heat was released by more cloud particles during this case. The precipitation was rainfall first and then snowfall. The mass content of particles of this case was larger than that of Beijing case. The effects of latent heat and drag force on thermal and dynamical processes during this snowfall case were more obviously than those in Beijing case.

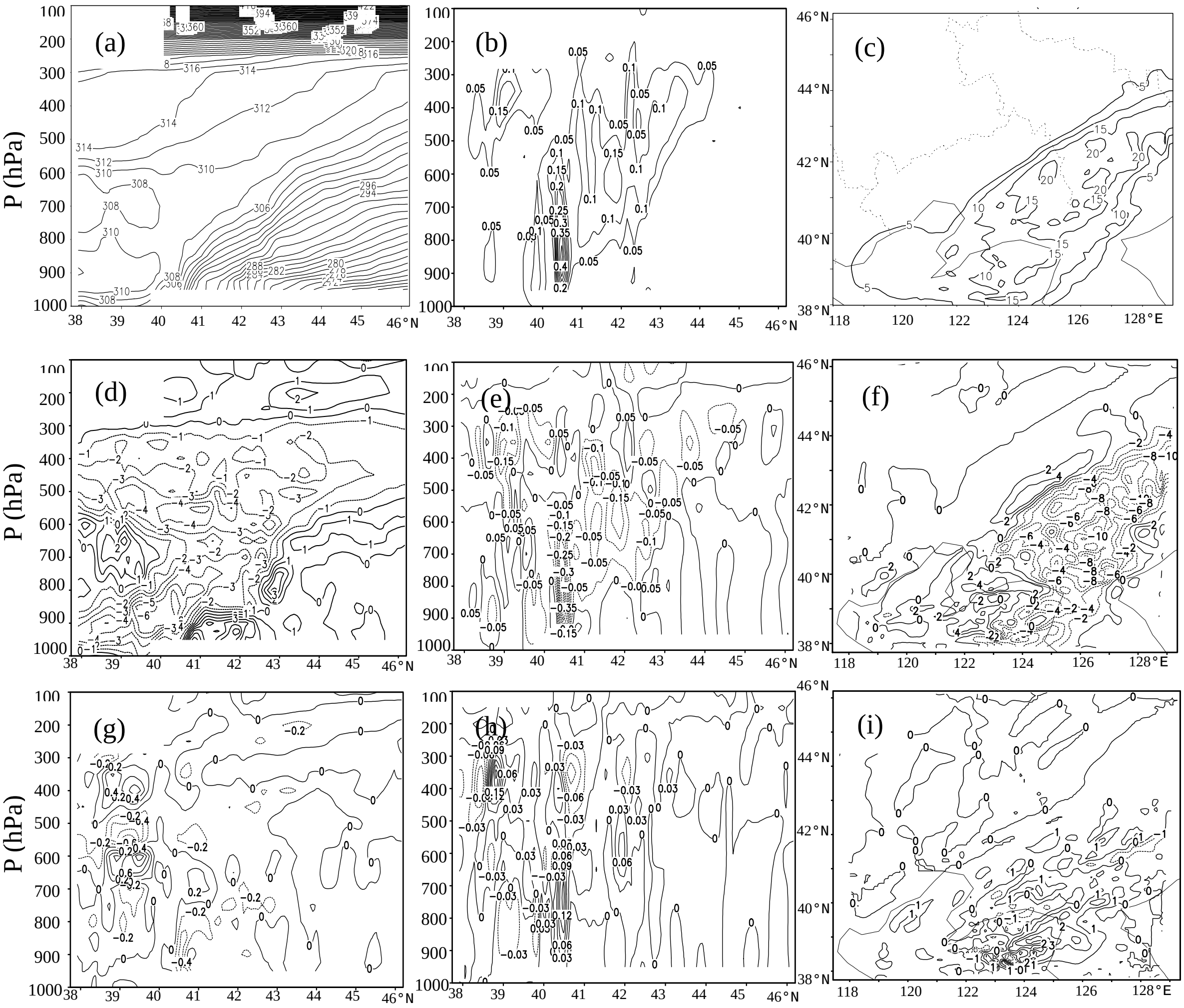

Fig.11 Cross section of equivalent potential temperature(θ e,unit:K),vertical velocity(w,unit:m/s) and 24 hours rain(rain,unit:mm) along 125°E at 0600 UTC 24 Nov 1999: (a,b,c) θ e, w, rain of control test respectively, (d,e,f) results of θ e, w, rain subtracted control test from heat test respectively, (g,h,i) results of θ e, w, rain subtracted control test from drag test respectively

5. Comparison of two cases

Simulated results have been analyzed above about the light snowfall during 7 - 8 Dec 2001 in Beijing and the snowfall during 23 - 24 Nov 1999 in Liaoning province. Although they are both snowfall cases, there are some different characteristics between them. Comparison of the two cases is helpful to understand the microphysical mechanism of the two different kinds of snowfalls. In addition, the same grid size simulation of Beijing case was also conducted as that of Liaoning case. The precipitation and distributions of hydrometeors did not change much comparing to the results of original grid size simulation. Follows are the comparing results of two cases.

(1) The weather background is not same for the two cases. Beijing light snowfall was induced by shallow trough eastward moving, while Liaoning snowfall was induced by the cold wave and strong cold air. (2) Table 1 shows the comparison of the variables such as precipitation, updraft, hydrometeors, and so on. The total precipitation and updraft of Liaoning

snowfall were larger than Beijing snowfall. The cloud developed stronger in Liaoning case. The magnitude of hydrometeors of two cases was both 0.1 g/kg. The magnitude of one-hour accumulative sources of hydrometeors was 0.1－1 g/kg·h^{-1}, but the values of Liaoning case were 2－3 times larger than those of Beijing case. (3) The atmosphere temperature was under 0℃ in Beijing snowfall. However in Liaoning case, there was a vertical interface of warm and cold air. In the north of the interface was the cold region, and in the south of the interface below 750 hPa was the warm region. The phase of particles of Beijing case was simple. There was no liquid water and graupel. The mixed-phase (vapor, liquid and solid phase) particles co-existed in Liaoning case. The precipitation included rainfall, snowfall and graupel-fall. These results reveal that the precipitation has close relationship with temperature. The cloud water and rain water are important to the formation of graupel. The temperature of Beijing case was so low that there was no liquid water and graupel. While it was of high temperature in Liaoning case so that liquid water and graupel emerged at the same time. These are the most difference between the two cases. (4) Sensitive tests have shown that the microphysical process is able to affect the thermal and dynamical processes of the two cases. The latent heat released by phase exchanging can enhance the precipitation and updraft. The drag force induced by particles falling can retrain the precipitation and updraft. The effects of latent heat are larger than that of the drag force. The atmosphere stratification was stable in Beijing case and the effect of latent heat was small. The atmosphere stratification was unstable and the latent heat strengthened the stratification stability. The microphysical processes in Liaoning case were more active than those in Beijing case. As a result, the feedback of Liaoning case was much stronger than Beijing case.

In addition, Sun et al. (2003) have done the similar analyses of the heavy rainfall on 8－9 Jun 1998 in South China. In that case the mixed-phase particles co-existed. The magnitude of updraft and hydrometeors were 1 m/s and 1－10g/kg respectively of the convective cloud. The magnitude of snowfalls in this paper was 1－2 times smaller than the heavy rainfall.

Table 1. The difference of variable maximum between Beijing case and Liaoning case

	precipitation	24h precipitation mm	0 ℃ height km	Updraft m/s	Vapor g/kg	Cloud water g/kg	Rain water g/kg	Ice g/kg	Snow g/kg	Graupel g/kg	Sources of rain g/kg·h^{-1}	Sources of snow g/kg·h^{-1}	Sources of graupel g/kg·h^{-1}
Beijing	snowfall	1.8	——	0.14	1.6	——	——	0.27	0.13	——	——	0.17	——
Liaoning	rainfall ,snowfall	20	2km	0.45	7	0.45	0.27	0.5	0.4	0.13	2.21	0.79	0.64

6. Conclusions

In this paper, two snowfall cases under different weather conditions in north China are simulated using the meso-scale model MM5. They are light snowfall during 7 - 8 Dec 2001 in Beijing city and strong wind and snowfall during 23 - 24 Nov 1999 in Liaoning province. The simulated results of microphysical processes are mainly discussed. The hydrometeors and their source and sinks under different weather backgrounds are described. The feedback effects of microphysical processes on the thermal and dynamic processes are also discussed. Comparisons were made between the results of two cases. Results have show:

(1) The distribution of hydrometeors has close relationship with temperature. In Liaoning snowfall case, liquid water was in the warm region below 0℃ layer and the ice particles were mainly in the cold region above 0℃ layer. There was also super-cooled water in cold region and unmelting snow and graupel near 0℃ layer. The mixed-phase particles co-existed in Liaoning case. While in Beijing snowfall case, the temperature was below 0℃ and there were only water vapor, ice and snow in the cloud.

(2) The same characteristics of source and sinks of two cases is that the depositional growth of snow and the collection of ice by snow are the main processes to the formation of snow. As for Liaoning case, the melting of snow and graupel and the collection of cloud water by rain water are the main processes to the formation of rain water. Graupel grows mainly through the collection of cloud water by snow and graupel and the conversion of snow to graupel. The super-cooled water is very important to graupel's growth.

(3) The latent heat and drag force induced by hydrometeors have a certain effects on thermal and dynamical processes during this two snowfall cases. The latent heat affected little on the stable atmosphere stratification of Beijing case, but strengthened the unstable atmosphere stratification of Liaoning case. The latent heat enhanced the precipitation and updraft, but the drag force induced by particles falling retrained the precipitation and updraft. The effects of latent heat are larger than that of the drag force. The microphysical processes and the feedback effects in Liaoning case were more active than those in Beijing case. The intensity of the feedback effects is consistent with the activity of microphysical processes.

(4) This paper discussed the source and sinks of hydrometeors only in the strongest precipitation period. The characteristics of the microphysical processes in other period still need to be investigated.

BIBLIOGRAPHY

Brian A. Colle, Matthew F. Garvert, Justin B. Wolfe, 2005: The 13–14 December 2001 IMPROVE-2 Event. Part III: Simulated Microphysical Budgets and Sensitivity Studies. *Journal of the Atmospheric Sciences*, 62(10), 3535-3558

Grell G A., 1994: A description of the fifth-generation Penn State/NCAR mesoscale model (MM5). *NCAR Technical Note. NCAR/TN-398+STR*.

Li Xinfang and Li Xihuai, 1999: Mechanism analyses of “thunder-snowfall” in Luoyang. *Journal of Sichuan Meteorology,*19(1), 41-42. (in Chinese)

Sun Jianhua and Zhao Sixiong, 2003: A numerical simulation of snowfall in North China on 7 December 2001. *Climate and Environmental Research,* 8(4), 387-401. (in Chinese)

Sun Jing and Wang Pengyun, 2003: Numerical study of heavy rainfall in South China with Reisner graupel scheme. *Meteorological Monthly*, 29(4), 10-13. (in Chinese)

Reisner J., Rasmussen R. M. and Bruintjes R. T., 1998: Explicit forecasting of supercooled liquid water in winter storms using the MM5 mesoscale model. *Q. J. R. Meteorol. Soc.,* 124: 1071-1107.

Wang Jianzhong and Ding Yihui, 1995: Research of moist symmetric instability in a strong snowfall in North China. *Acta Meteorologica Sinica,* 53(4), 451-459. (in Chinese)

Wang Pengyun, Ruan Zheng and Kang Hongwen, 2002: Numerical study on cloud physical processes of heavy rainfall in South China. *Journal of Applied Meteorological Science,* 13(1), 78-87. (in Chinese)

Wang Pengyun and Yang Jing, 2003: Observation and numerical simulation of cloud physical processes associated with torrential rain of the mei-yu front. *Adv. Atmos. Sci,* 20(1), 77-96

Wang Wenhui and Xu Xiangde, 1979: The heavy snow process in district Xilingele and the analysis of “77.10” snowstorm. *Acta Meteorologica Sinica,* 37(3), 80-86. (in Chinese)

Yi Qingju, Liu Yanying and Xu Chenhai, 1999: Synoptical and climatological analysis of snowfall from 1980 to 1994 in Beijing area. *Journal of Applied Meteorological Science,* 10(2), 249-254. (in Chinese)

You Laiguang, Ma Peimin and Hu Zhijin, 2002: Study on precipitation enhancement from stratiform clouds in north China. *Meteorological Science and Technology*, 30(supplement), 19-50. (in Chinese)

Zhao Sixiong, Sun jianhua, Chen hong, Qi Linlin, Zhao Yijun, Li Aiguo and Li Yunyun, 2002: A study on snowfall in Beijing on 7 December 2001. *Climate and Environmental Research,* 7(1), 7-21. (in Chinese)

Acknowledgements. The authors thank Hu Zhijin of Weather Modification Center of China for his assistance and constructive advice toward this paper. This work is supported jointly by the Dedicated Research Fund for Public Interest from the Ministry of Science and Technology of China (2002DIA20013, 2004DIB3J116) and the State Natural Science Foundation of China under Grant No 40305001

PRELIMINARY INVESTIGATIONS OF THE MANGISMS OF OROGRAPHIC CLOUD FORMATION OVER THE SOUTHERN SLOPE AREA OF QILIAN MOUNTAIN

An-Ping **Sun**[1], Guoqing **Zhang**[2], Wanfu **Zhou**[2], and Guoguang **Zheng**[3]

[1]Qinghai Provincial Weather Modification Office, Xining, Qinghai 810001, P. R. China
[2]Institute of Meteorological Research in Qinghai Province, Xining, Qinghai 810001, P. R. China
[3]China Meteorological Administration, Beijing 100081, P. R. China

1. INTRODUCTION

Many of the previous field experiments on cloud seeding ability of orographic clouds and investigation of structure and microphysics have been conducted in the world. Previous results from statistical studies on increased winter orographic precipitation by cloud seeding (Grant and Mielke, 1967; Mielke et al., 1970, 1971; Chappell, 1970), which had indicated rather clear-cut positive results is certain temperature windows, have been subject to increasingly critical review (e. g., Rangno, 1979; Hobbs and Rangno, 1979). Hill (Hill. G., 1980) indicated that, from experimental observation, winter orographic clouds over the upwind mountain base with cloud-top temperature between 0and -22 ℃ are found to be primarily composed of supercooled water and are therefore seedable and the supercooled water concentration is empirically found to depend on the updraft velocity. The potential precipitation yield is dependent on the flux of supercooled water over the barrier. Rauber (Rauber, R., 1992) showed the results from field experiments mainly investigating microphysical structure and evolution of a Central Sierra Nevada orographic cloud system. That is, the cloud system extended 130 Km upwind of the Sierra Nevada Crestline, was 4 Km deep, had a base temperature of 5 ℃, and a top temperature of approximately -15 ℃ and cloud droplets rising from cloud base grew to sizes > 50 m and first encountered dendritic ice particles descending from cloud top over the middle elevations. Uttal (Uttal, T., 1988) described the distribution of liquid, vapor, and ice in an orographic cloud from field experiment and results calculated from instrumented aircraft observation showed that, maximum vapor mass in the cloud is 2.0 g m^{-3}, which is comparable with maximum ice mass in the cloud of 1.5 g m^{-3} and maximum liquid mass is approximately one order of magnitude lower at 0.15 g m^{-3} and appears to be a small reminder between the vapor and the ice as they compete for the major portion of the cloud water mass, and that, in the cloud upwind of the mountain, the total mass of liquid, vapor, and ice to be constant, suggesting that precipitation does not deplete the water mass at the levels observed by aircraft. More studies showed that maxima in both ice and liquid mass appear just over the windward crest of the mountain, indicating a strong orographic effect on condensation of vapor to liquid and growth of ice by vapor diffusion and riming.

Qinghai Province, located in the southern slope of Qilian mountain, is one of northwestern provinces frequently suffered from natural disasters, particularly drought. The shortage of fresh water resource has been impacting the sustainable developments of economy and community in local area. Additionally, as a result of persistent drought occurred in this area, the acreage of the Qinghai Lake, which is the famous plateau salt lake, has been reduced gradually in most recent years. Recently, Chinese central and local governments have already realized the importance for alleviating this influence and made many efforts to protect environment there. As one of the most important and cheapest method to augment fresh water resource, precipitation enhancement activity has been treated a primary approach and implemented over this area in the past several years to increase natural precipitation, augment inflow of the lake, and eventually improve the ecosystem, financially supported by Chinese central government.

In order to scientifically implement cloud seeding operational works, fully realizing the general characteristics of orographic cloud, a comprehensive field experiment, which is supported by a Key National Nature Science Foundation of China, was implemented together in the southern and northern slope of Qilian mountain in July – October 2006, respectively.

2. EXPERIMENTAL FACILITIES

In order to obtain improved knowledge of the structure and properties of orographic cloud in the slope of Qilian mountain, several kinds of ground-based facilities were involved in this intensive field experiment simultaneously, including high-resolution raingage network, ground-based microwave radiometer, and sounding, etc.

3. EXPERIMENTAL DESIGN

This experiment site was focused to be placed in Menyuan county, the southern slope of Qilian mountain. The average elevation there is generally above 3000 m (ASL) (Fig. 1). Southeastern moist air flowing provides continuing uplift of approaching water vapor and promotes development of orographic clouds containing significant supercooled liquid water. Therefore, this area is most appropriate for implementing rain enhancement activity for increasing the inflow of Qinghai Lake.

The experimental unit was primarily orographic cloud. In accordance with experimental design, the sounding observation is implemented twice everyday during field observation time, and intensive observation, which is conducted in every four hours, is also designed. The observations of automatic weather stations and dual-wave microwave radiometer were observed all time during the field experiment.

The goals of this field experiment primarily include several aspects as follows:

(i) Initially understanding the structure and evolution characteristics of orographic cloud in this area.

(ii) Investigating the thermal and dynamical features of large scale circulation for orographic cloud.

(iii) Realizing the mechanisms of orographic cloud precipitation mechanism and detailed microphysics occurred in this area.

Fig. 1. Map of Experimental area in the slope of Qilian Mountain

4. PRELIMINARY RESULTS AND DISCUSSIONS

In this paper, preliminary analyses of observed data are carried out. Others will be investigated in more detailed latter in other papers.

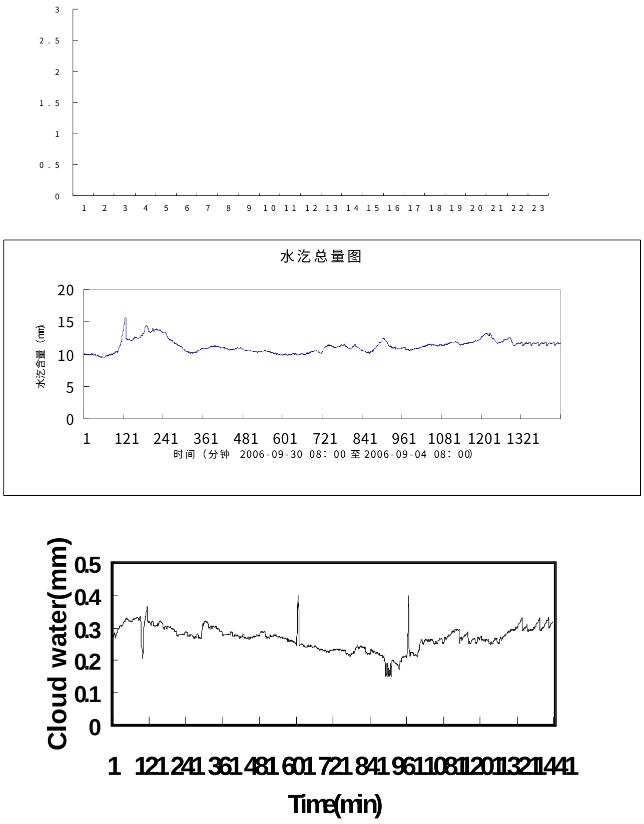

Fig. 2. Time serious distribution of rainfall (upper figure), accumulated vapor (middle figure), and accumulated cloud water (lower figure)

Fig. 2 illustrates time serious distribution of rainfall, accumulated vapor, and accumulated cloud water observed by ground-based dual-wavelength microwave radiometer for orographic cloud. It is clearly shown that the distribution of cloud water and rainfall are matched very well. When accumulated cloud water mass reached its maximum at 601min and 961min, precipitation occurred and rainfall also reached its maximum. Generally, accumulated vapor water varied not so markedly during all time. Specifically, the maximal accumulated cloud water was 0.4 mm, and accumulated vapor water was 15 mm.

The distribution of raindrop spectrum, analyzed from more than 100 samples, is given in Fig. 3. The vertical axis and horizontal axis denote number concentration and radius, respectively. It can be easily obtained that, to orographic cloud, the distribution of raindrop spectrum showed two peaks, which are 0.8 mm and 2.1 mm for radius. Generally, the radius for raindrop in orographic cloud characterized not so wide.

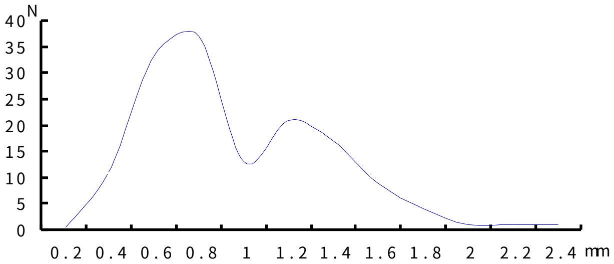

Fig. 3. Distribution of raindrop spectrum

4. SUMMARY AND CONCLUSION

Some general feature regarding orographic cloud in the southern slope of Qilian Mountain was basically analyzed. The results show that the radius for raindrop in orographic cloud characterized not so wide and accumulated cloud water was generally 0.2-0.4 mm. The time serious distribution of precipitation, accumulated vapor, and accumulated cloud water were matched very well.

It should be noted that all results presented in this paper is only preliminary investigation. Much work remains and will be done in future. More detailed analysis of observational data should be carried out to further exploit some characteristics of microphysics and dynamics particularly occurred in this area.

ACKNOWLEDGMENT: This research was supported by the Committee of National Natural Science Foundation of China through National Key Research Program.

REFERENCES

Uttal, T., 1988: Distribution of liquid, vapor, and ice in an orographic cloud from field observation. *J. Atmos. Sci.*, 45, 1110-1119.

Rauber, R., 1992: Microphysical structure and evolution of a Central Sierra Nevada orographic cloud system. *J. Appl. Meteor.*, 31, 1410-1422.

Garrett, A., 1980: Orographic cloud over the eastern slope of Mauna Loa Volcano, Hawaii, related to insolation and wind. *Mon. Wea. Rev.*, 108, 931-941.

Hill, G., 1980: Seeding-opportunity recognition in winter orographic clouds. *J. Appl. Meteor.*, 19, 1371-1381.

Grant, L. O., and R. E. Elliott, 1974: The cloud seeding temperature window. *J. Appl. Meteor.*, 13, 355-363.

Grant, L. O., and P. W. Mielke, 1967: A randomized cloud seeding experiment at Climax, CO, 1960-65.

Hobbs, P. V., R. A. Houze, Jr., and T. J. Matejka, 1975: The dynamical and microphysical structure of an occluded frontal system and its modification by orography. *J. Atmos. Sci.*, 32, 1542-1562.

Rangno, A. L., 1979: A reanalysis of the Wolf Creek Pass cloud seeding experiment. *J. Appl. Meteor.*, 18, 579-605.

Hobbs, and A. L. Rangno, 1979: Comments on the Climax and Wolf Creek Pass cloud seeding experiments. *J. Appl. Meteor.*, 18, 1233-1237.

Chappell, C. F., L. O. Grant and P. W. Mielke, 1971: Cloud seeding effects on precipitation intensity and duration of wintertime orographic clouds. *J. Appl. Meteor.*, 10, 1006-1010.

Chappell, C. F., 1970: Modification of cloud orographic clouds. Ph. D. dissertation, Colorado State University, 196pp.

MICROPHYSICAL STRUCTURES OF STRATIFORM CLOUDS ASSOCIATED WITH THE MJO OBSERVED DURING MISMO PROJECT

Kenji Suzuki[1], Shunsuke Shigeto[1], Takumi Koga[1], Kazue Morinaga[1]and Kunio Yoneyama[2]
[1]Yamaguchi University, Yamaguchi, 753-8515, Japan
[2]Japan Agency for Marine-Earth Science and Technology, Yokosuka, 237-0061, Japan

1. INTRODUCTION

Japan Agency for Marine-Earth Science and Technology (JAMSTEC) had conducted the field experiment named as MISMO (Mirai Indian Ocean cruise for the Study of the MJO-convection Onset; Yoneyama et al., 2008), by using the research vessel Mirai, moored buoy network, and land-based sites at Maldives. The aim of MISMO is to reveal the atmospheric and oceanic characteristics of the central equatorial Indian Ocean when convection in the Madden-Julian Oscillation (MJO) is initiated.

Tropical convections associated with the MJO have been discussed in many previous studies. Johnson et al. (1999) showed the trimodal cloud distribution; cumulus, congestus, and cumulonimbus and found to vary significantly on the timescale of the 30-60 day intraseasonal oscillation. Kenball-Cook and Weare (2001) showed that the build-up and discharge of the low-level moist static energy is important for the initiation of MJO convection. Kikuchi and Takayabu (2004) suggested that staged convective development associated with the MJO was strongly affected among convection, stable layers, and atmospheric moistening. Lin et al. (2004) examined stratiform precipitation associated with the MJO using TRMM PR data. Kubota et al. (2006) showed that the structure of deep convection during the MJO active phase using the satellite data and the shipboard Doppler radar data. However, in situ microphysical observation of the clouds developed over the Indian Ocean has never conducted.

In this study, microphysical structures of stratiform clouds associated with the MJO over the equatorial Indian Ocean were investigated using videosondes.

2. OBSERVATION

2.1 MISMO PROJECT

Videosonde observations were conducted as part of the MISMO project from October 16 to November 27, 2006. MISMO field experiment was taken place in the central equatorial Indian Ocean under the relatively strong Indian Ocean Dipole event. The R/V Mirai maintained a fixed position on 0º, 80.5ºE during observation period. We could monitor the onset stage of MJO-convection. Convective activity abruptly became active in mid-November. At that time, the drastic change of the upper tropospheric zonal wind from westerlies to easterlies was also observed (JAMSTEC, 2006; Yoneyama et al., 2008). Figure 1 shows the rainfall intensity observed every minute on the R/V Mirai from Oct.25 to Nov. 26, 2006.

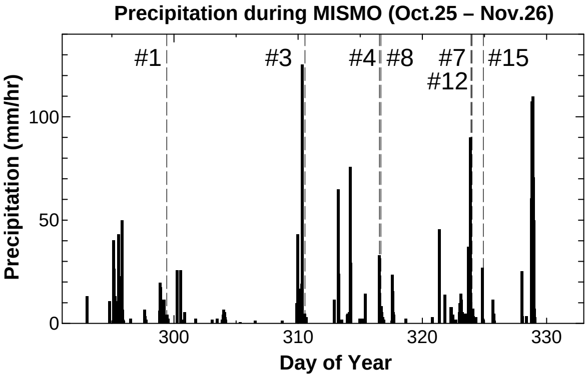

Figure 1. Precipitation observed on the R/V Mirai during the MISMO project. Dashed lines indicate the launches of videosonde #1, 3, 4, 7, 8, 12, and 15.

Corresponding author address: Kenji Suzuki, Yamaguchi University, Yamaguchi 753-8515, Japan; E-mail: kenjis@yamaguchi-u.ac.jp

2.2 VIDEOSONDE

The videosonde used in the present study was an improved version of that designed by Takahashi (1990), being lighter and less expensive while providing the same level of performance. Videosonde is a balloon-borne radiosonde that acquires images of precipitation particles via a CCD camera. The videosonde system consists of a CCD camera, a video amplifier, an infrared sensor, a transmitter, batteries, and a control circuit. The system has a stroboscopic illumination that provides information on particle size and shape. Interruption of the infrared beam by particles triggers a flash lamp and particle images are then captured by the CCD camera. Images of particles were converted to frequencies between 10 Hz and 1 MHz and transmitted by a 1680 MHz carrier wave (bandwidth 4 MHz, transmission power 0.5 W) to the receiving system located on the navigation deck of the R/V Mirai before being displayed and recorded onto videotapes and DVDs. Recorded precipitation particles were classified as either raindrops, frozen drops, graupel, ice crystals, or snowflakes on the basis of transparency and shape, as described by Takahashi and Keenan (2004). Information concerning atmospheric pressure, temperature, humidity, and wind was obtained from a Vaisala RS-92 radiosonde attached to the videosonde. Seven videosondes were launched into one convective cloud and six stratiform cloud systems during the MISMO project.

3. RESULTS AND DISCUSSION

Six videosondes were launched into the stratiform clouds developed over the central equatorial Indian Ocean. Convective activity abruptly became active in mid-November, which it can be said it is the initiation of deep MJO-convection (Yoneyama et al., 2008). We launched three videosondes respectively before and after that. In the latter case, the R/V Mirai was completely covered by thick stratiform clouds with gentle rain. Doppler radar images showed a clear bright band at that time. Satellite images showed a broad cloud that was several hundred kilometers wide. Particle images transmitted from videosondes were ice crystals, graupel, and aggregate (snowflakes) near and above the freezing level (Fig.2). The shapes of these aggregates were different from aggregations of nearly round graupel observed in the maritime stratiform clouds during TOGA-COARE (Takahashi et al., 1995) and the R/V Mirai MR04-08 cruise over the western Pacific Ocean (Suzuki et al., 2006).

The number concentrations of ice crystal and graupel were greater than that observed in the maritime stratiform clouds over the western Pacific region. It was found that the stronger ice crystal formation process in the upper level of stratiform clouds was characteristic over the Indian Ocean.

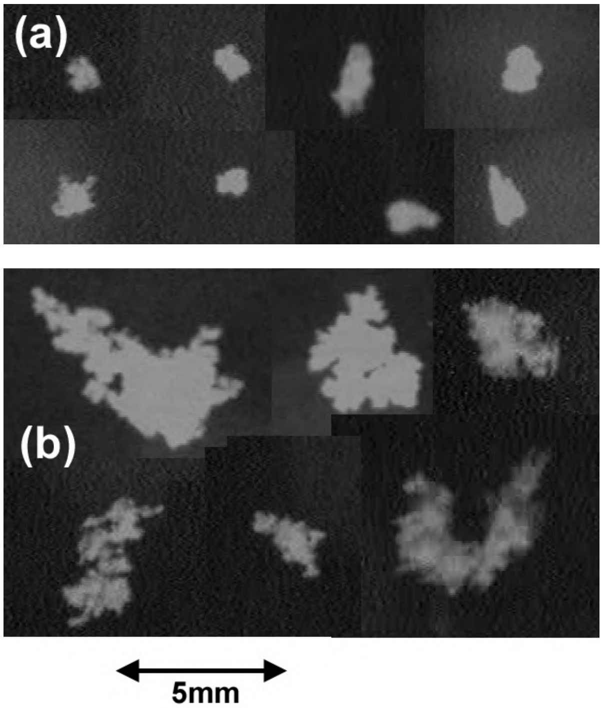

Figure 2. Precipitation particle images of (a) graupel and (b) aggregates observed during the MISMO project.

During the MISMO observation period, we experienced the drastic enhancement of convective activity that may be related to the onset of deep convection in the MJO after mid-November, and the large-scale upper air circulation had been dramatically changed. Before and after that, the vertical precipitation particle distributions were greatly different. Figure 3 shows the vertical distribution of precipitation particles observed on Nov. 12 (before the initiation of deep MJO-convection) and Nov. 20 (after the initiation of deep MJO-convection). The number concentrations of ice crystal and graupel that had been observed in the latter half was greater than that observed in the first half (Fig.4).

Figure 5 shows the 10-days backward trajectories from Nov. 5, 10, 15, 20, 25, 30 at 1500m ASL. For computation of trajectories, the JRA-25 data provided by the cooperative research project for the JRA-25 long-term reanalysis of the Japan Meteorological Agency (JMA) and the Central Research Institute of Electric Power Industry (CRIEPI) and the National Institute of Polar Research (NIPR) trajectory model (Tomikawa and Sato, 2005) were used. The backward trajectory analysis shows that the air mass from the northern hemisphere was dominant after the initiation of the deep MJO-convection, while the air mass from the southern hemisphere before that. There is a continent in the north of the Indian Ocean, and, on the other hand, the large ocean spreads out in the south. It suggested that this high concentration of ice crystal in the upper-level was greatly affected by the high concentration of CCN from the northern continent.

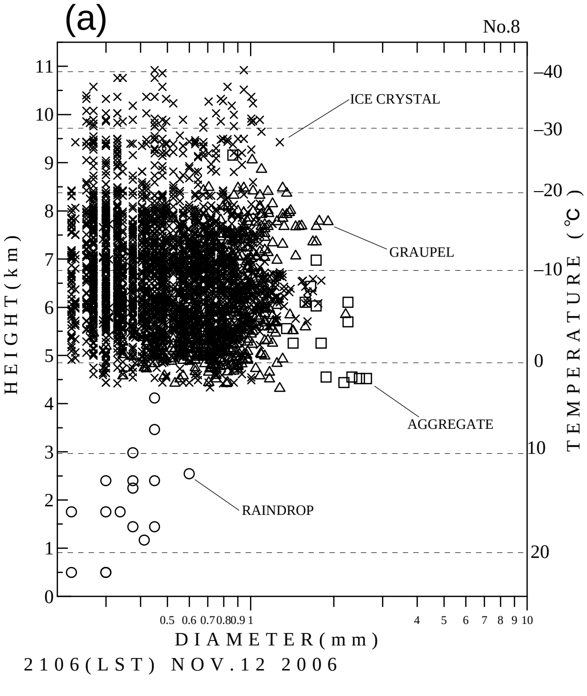

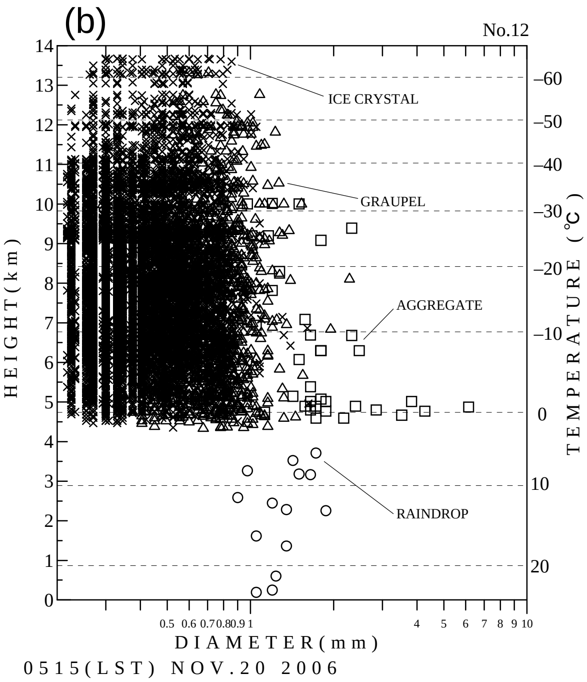

Figure 3. Precipitation particle size-height diagram of videosonde (a) #8, ascent at 2106LST, November 12, 2006, (b) #12, 0515LST, November 20, 2006. Open circle (raindrop), triangle (graupel), cross (ice crystal), square (aggregate).

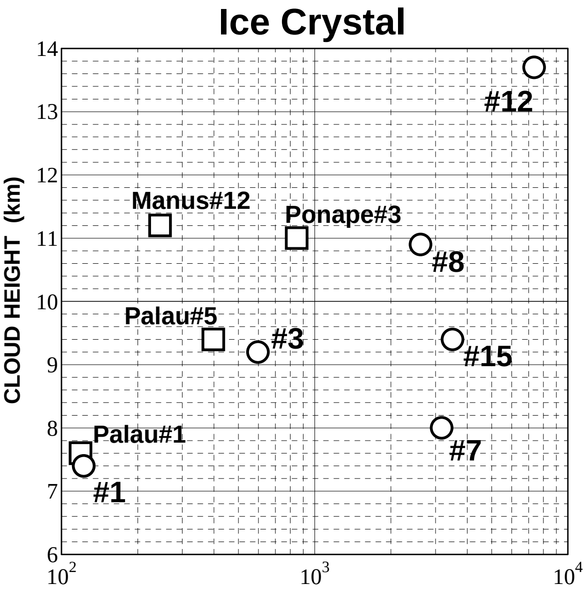

Figure 4. Relationship between the maximum ice crystal number concentration and the cloud height. Open circles indicate videosondes launched during the MISMO project. Squares indicate videosonde launchings into the stratiform clouds at Ponape (Takahashi and Kuhara, 1993), Manus (Takahashi et al., 1995), and Palau (Suzuki et al., 2006).

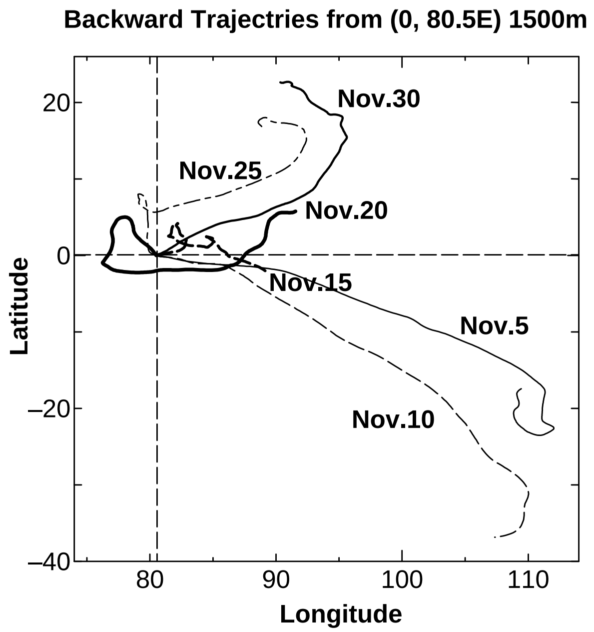

Figure 5. Backward trajectories from (0º, 80.5ºE) at 1500m on Nov. 5, 10, 15, 20, 25, and 30.

Acknowledgements

This study was conducted as a part of the R/V Mirai cruise conducted by the Japan Agency for Marine-Earth Science and Technology. We sincerely appreciate Captain Akamine and his crew for running the ship during this cruise. Thanks are also due to the technical staff of Global Ocean Development Inc. for their support in conducting the videosonde observations. Many researchers who joined the cruise are also acknowledged for their help with observations.

References

JAMSTEC, 2006: R/V Mirai cruise report –MR06-05 leg-1 (MISMO), pp134.

Johnson, R. H., T. M. Rickenbach, S. A. Rutledge, P. E. Ciesielski and W. H. Schubert, 1999: Trimodal characteristics of tropical convection. J. Clim., **12**, 2397-2418.

Kemball-Cook, S. R. and B. C. Weare, 2001: The onset of convection in the Madden-Julianoscillation. J. Clim., **14**, 780-793.

Kikuchi, K. and Y. N. Takayabu, 2004: The development of organized convection associated with the MJO during TOGA COARE IOP: Trimodal characteristics. Geophys. Res. Lett., **31**, L10101, doi:10.1029/2004GL019601.

Kubota, H., R. Shirooka, T. Ushiyama, J. Chen, T. Chuda, K. Takeuchi, K. Yoneyama and M. Katsumata, 2006: Observations of the structures of deep convections and their environment during the active phase of an Madden-Julian Oscillation event over the equatorial western Pacific. J. Meteor. Soc. Japan, **84**, 115-128.

Lin, J., B. Mapes, M. Zhang and M. Newman, 2004: Stratiform precipitation, vertical heating profiles, and the Madden-Julian Oscillation. J. Atmos. Sci., **61**, 296-307.

Suzuki, K., Y. Shigenaga, T. Kawano and K. Yoneyama, 2006: Videosonde Observation during the R/V Mirai MR04-08 Cruise. J. Marine Meteor. (Umi to Sora), **82** (2), 29-38.

Takahashi, T. 1990: Near absence of lightning in torrential rainfall producing Micronesian thunderstorms. Geophys. Res. Lett., **17**, 2381-2384.

Takahashi, T. and K. Kuhara, 1993: Precipitation mechanisms of cumulonimbus clouds at Pohnpei, Mirconesia. J. Meteor. Soc. Japan, **71**, 21-31.

Takahashi, T., K. Suzuki, M. Orita, M. Tokuno and R. de la Mar, 1995: Videosonde observations of precipitation processes in equatorial cloud clusters. J. Meteor. Soc. Japan, **73**, 509-534.

Takahashi, T. and T. D. Keenan, 2004: Hydrometeor mass, number, and space charge distribution in a “Hector” squall line. J. Geophys. Res., **109**, D16208, 10.1029/2004JD004667.

Takahashi, T.,2006: Precipitation mechanisms in east Asia monsoon: Videosonde study. J. Geophys. Res., **111**, D09202, 10.1029/2005JD006268.

Takayabu, Y. N. 2002: Spectral representation of rain profiles and diurnal variations observed with TRMM PR over the equatorial area. Geophys. Res. Lett., **29**, 30-1, doi:10.1029/2001GL014113.

Yoneyama, K., and Coauthors, 2008: Overview and early results of the MISMO field experiment. Bull. Amer. Meteor. Soc., in press.

THE CONDITIONS AND DEPTH OF RELATIVE HOMOGENUES CLOUD LAYER IN THE STRATUS CLOUDS

Zlatko Vukovic
Environment Canada, Toronto, Ontario, Canada

1. INTRODUCTION

The main purpose of this study is to establish a procedure for analyzing conditions for a relatively homogenous cloud layer in the stratus clouds. Consequently, the depth and vertical position of the relative homogenous layer can be better defined and more accuracy used in the models and applications where it is needed.

During the Canadian ClaudSat /CALIPSO Validation Program (C3VP, http://c3vp.org) the 2D cloud (2D-C and 2D-G) and 2D precipitation (2D-P) probes were used to measure shape, size and concentrations for cloud particles. The original 2D images data set was analyzed as a function of various parameters. The sensitivity of the crystal habits was examined with respect to the variation of the selected parameters. Based on the results of the analysis it was determined when the range and values of the parameters would be considered a cloud layer consisting of similar crystal content.

2. DATA SET

During the C3VP project approximately 35 hours of 2D in-situ Convair-580 aircraft measurements was realized. The data from each flight was averaged in sequential 30-s intervals, corresponding to a horizontal length scale of about 3km. In total, there were 4125 30-s in-cloud data points, which are named as the original data set.

Following the technique of Cober et al. (2001) the segregation of 2D particle images into drops and ice crystals was preformed. The original data set was divided in 11 subsets of data according on the Cober's 2D based phase estimation:

1- small drizzle
2- large drizzle
3- drizzle and rain
4- drizzle with the occasional crystal
5- mixed rain and ice crystals
6- mixed drizzle and ice crystals
7- semi circular ice crystals
8- unclear, probably ice
9- irregular ice crystals dominate
10- needles dominate
11- dendrites dominates.

3. RESULTS AND ANALYSE

In order to approximate the conditions for the listed cloud phase categories, each subset of data was analyzed with regards to the following parameters: altitude (h), temperature (T), dew point difference (ΔTdw=T-Tdw), Nevzorov total water content (NevTWC), King Liquid Water (KingLWC), 2D-C and 2D-P concentrations (2DCcnc and 2DPcnc), aerosol concentrations (PCASPcnc) and mean volume diameter (PCASPmvd).

The mean values of the chosen parameters, the standard deviation (σ), and the number of 30-s data points for each of the cloud phases are summarized in Table 1.

As examples, two phase categories, dendrites and semi circular ice, are shown in more detail.

The graphical presentation of the relative frequency distribution of dendrites with altitude for different range of (a) temperature, (b) dew point difference, (c) total condensable liquid water content, (d) liquid water content, (e) 2D-C concentration, (f) 2D-P concentration, (g) aerosol counts, and (h) aerosol MVD are shown in Figure 1a-h. The black solid line represents distribution without the parameter separation, while the blue, red and green dashed lines are the first three ranges of the parameters with the highest percentage of occurrence. The cloud layer equal 2σ is marked with the light blue area. Similar graphs for semi circular ice are shown in Figure 2a-h.

Table 1.The statistic summary for cloud phase categories.

Phase category →	1	2	3	4	5	6	7	8	9	10	11
avAltitude (km)	1.5	2.1	1.7	1.7	1.6	1.8	1.8	1.6	1.7	1.6	1.7
σ (km)	0.6	0.0	0.5	0.4	0.2	0.6	0.4	0.5	0.7	0.7	0.6
Points	91	1	97	49	16	178	61	12	1031	38	203
avT (C)	-3.3	-1.8	3.8	-7.2	1.2	-7.8	-12.7	-8.0	-18.5	-6.4	-12.0
σ (C)	4.8	2.6	2.4	3.5	0.3	7.7	6.5	1.3	8.8	5.1	3.9
Points	114	14	98	72	16	246	75	12	2636	45	279
Av ΔTdw (C)	-1.5	-2.0	-1.3	-1.1	-0.1	-0.7	-0.6	-0.8	0.2	-2.4	-0.8
σ (C)	1.1	0.8	1.2	1.4	0.5	2.2	3.4	1.6	6.2	1.5	1.4
Points	114	14	98	72	16	246	75	12	2636	45	279
avNevTWC (g/m^3)	0.3	0.4	0.1	0.2	0.1	0.1	0.1	0.2	0.0	0.2	0.0
σ (g/m^3)	0.1	0.2	0.1	0.1	0.0	0.1	0.1	0.1	0.1	0.1	0.1
Points	114	14	98	72	16	246	75	12	2600	45	278
avKingLWC (g/m^3)	0.3	0.4	0.1	0.2	0.1	0.1	0.1	0.2	0.0	0.1	0.0
σ (g/m^3)	0.1	0.2	0.1	0.1	0.0	0.1	0.1	0.1	0.0	0.1	0.0
Points	111	14	91	72	16	246	75	12	2555	24	277
av2DCcnc (#/cm^3)	397.6	643.9	78.9	493.9	40.2	151.5	87.4	105.3	100.6	76.4	23.7
σ (#/cm^3)	534.3	521.0	208.4	603.3	15.1	208.6	116.9	76.8	122.6	287.3	46.8
Points	114	14	98	72	16	246	75	12	2636	45	279
av2DPcnc (#/cm^3)	1524.5	213.4	133.1	72.6	195.9	482.0	60.1	1.3	614.1	494.1	115.8
σ (#/cm^3)	9285.2	190.5	102.8	154.2	84.7	643.2	123.2	1.1	800.1	2573.0	270.1
Points	114	14	98	72	16	246	75	12	2636	45	279
av PCASPcnc (#/cm^3)	374.0	387.4	873.4	210.2	641.1	264.5	176.0	241.2	119.0	113.8	202.9
σ (#/cm^3)	200.2	187.7	484.9	214.6	241.9	290.0	140.6	71.4	150.3	107.4	204.2
Points	111	14	91	72	16	246	75	12	2555	45	277
av PCASPmvd (µm)	1.1	1.1	0.7	1.2	0.7	1.0	0.8	0.9	0.8	1.1	0.6
σ (µm)	0.3	0.3	0.3	0.3	0.3	0.4	0.4	0.3	0.4	0.5	0.4
Points	111	14	91	72	16	246	75	12	2555	45	277

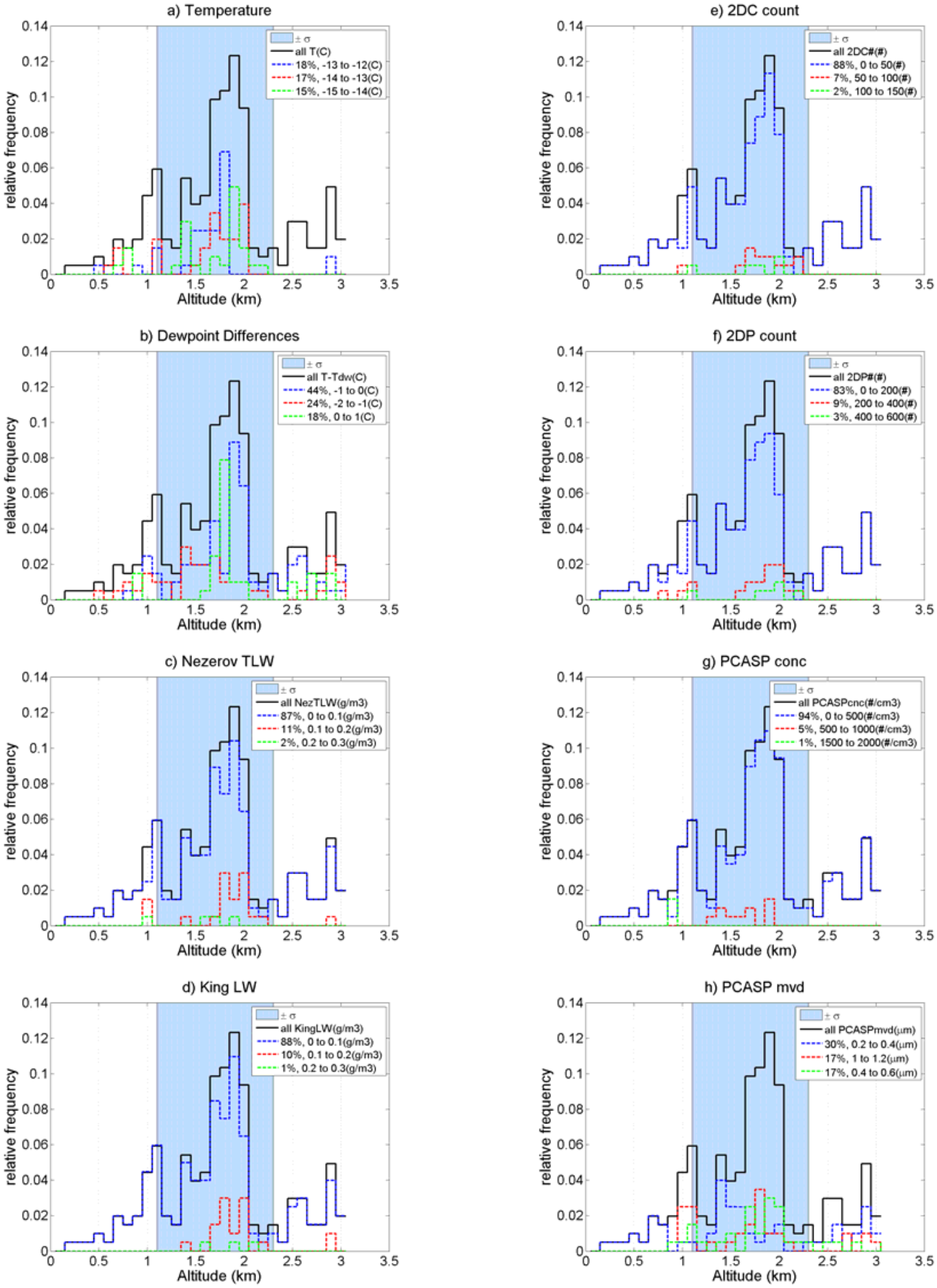

Figure 1. The relative frequency distribution of dendrites with altitude for different ranges of (a) temperature, (b) dew point difference, (c) total liquid water content, (d) liquid water content, (e) 2D cloud particle number, (f) 2D precipitation particle number, (g) aerosol concentration, (h) aerosol MVD. The black solid line represents distribution without parameter separation, while the blue, red and green dashed lines are the first three ranges of the parameters with the highest percentage of occurrence. The cloud layer equal to 2σ is marked with the light blue area.

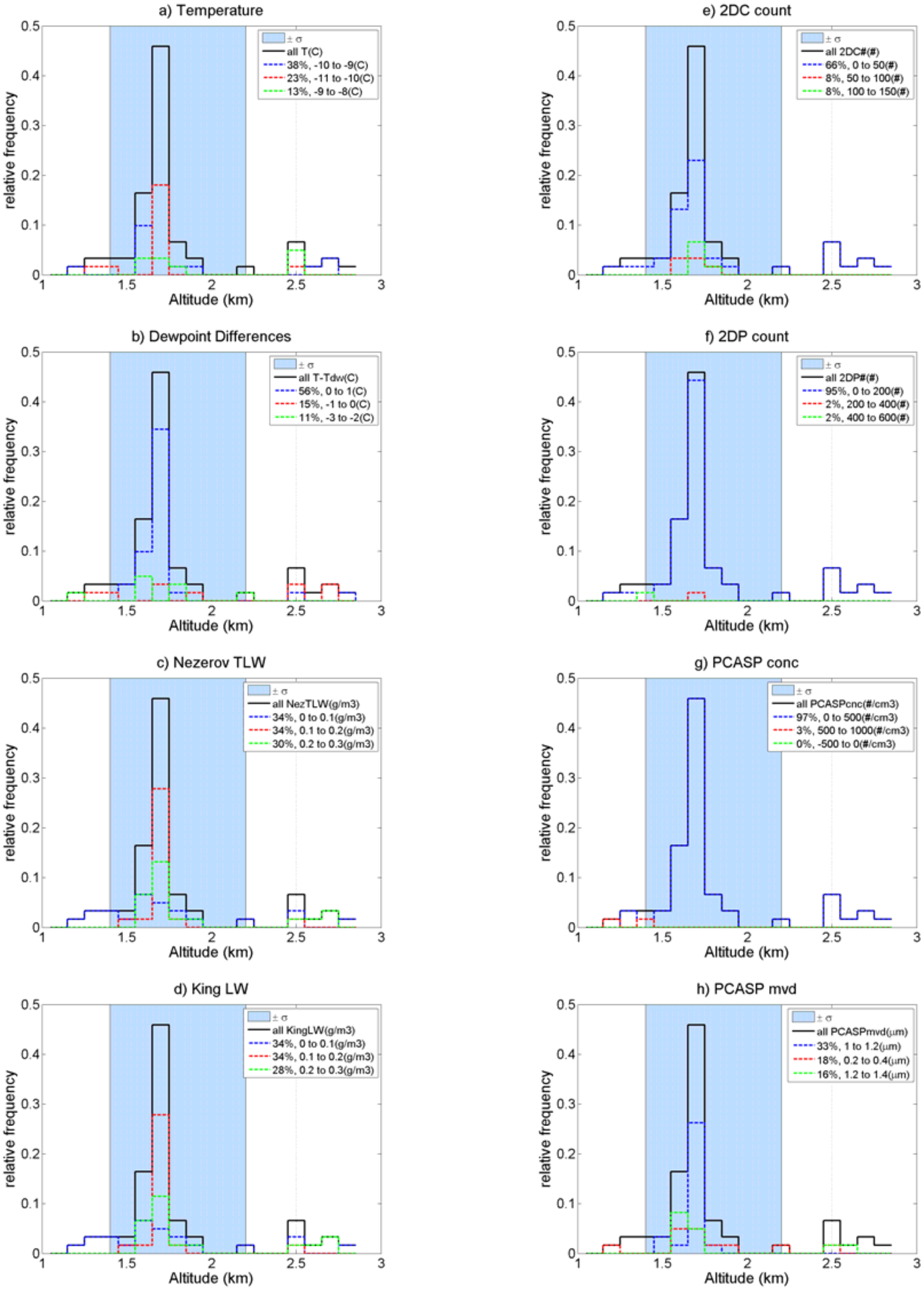

Figure 2. Same as for Figure 1 except for semi circular ice.

From the presented table data and the graphs we can see that during the C3VP project the average altitude of the cloud layer with dominate dendrite crystals was about 1.8km (the same as for the semi circular ice) and the most likely range of altitude was between 1.2km and 2.4km (1.4km-2.1km).

The distributions of the selected parameters indicate the most likely conditions of the cloud layer where dendrite crystals or semi circular ice were measured. In general the dendrite crystals (semi circular ice) are in the:

- temperature range between -15°C to -12°C (-11°C to -8°C);
- the thinner, warmer and more restricted temperature range layer than the dendrite cloud layer;
- in about 25% of cases the cloud layer was slightly super saturated (more supersaturated, 10%);
- neglected amount of liquid water, ~90% case it was less than 0.1g/m^3, (significant, ~65% cases greater than 0.1 g/m^3);
- very rear, 95%, small number (less than 500) of aerosol particle with size in range 0.2-1.2μm, (97%, 0.2-1.4μm);

The number of 2D cloud particles was in ~90% (65%) of cases less than 50, while the number of perceptible 2D particles was in ~80% (95%) no more than 200 for dendrite crystals and semi circular ice.

4. DISCUSION AND CONCLUSION

Since the main aim of the study was to preliminarily investigate the possibility of classification of size, structure and conditions of the layers in the stratus cloud, the quantitative aspect of the results was not the primary objective.

For a more reliable analysis a much bigger data set from a dozen of field projects is needed so that the measured samples could better represent a variety of stratus clouds.

5. REFERENCE

Cober, S.G., G.A. Isaac, and A.V. Korolev, 2001: Assessing the Rosemount Icing Detector with In Situ Measurements. J. Atmos. Oceanic Technol., **18**, 515-528.

AN ANALYSIS OF CHARACTERISTIC FOG-DROPLET SIZE DISTRIBUTION ON GUIZHOU YUNWU MOUNTAIN

Ling-Ling WANG[1], Sheng-Jie NIU[1*], Chun-Song LU[1], Jie XU[1], Ning LUO[2], Jun-Wei YU[2]
1. Laboratory for Atmospheric Physics& Environment of China
Meteorological Administration, Nanjing University of Information Science & Technology,
Nanjing 210044, P.R.China
2. Guizhou weather modification office, Guiyang 550002, P.R.China

1. TIME, PLACE AND APPARATUS OF OBSERVATION

Guizhou Province is located in the east of Yungui altiplano in China, it is a typical mountainous area. The site of observation--Yunwu mountain which height is more than 1700 meters is in the center of Guizhou Province. The microphysical characteristics of winter fog on Guizhou Yunwu mountain has been analyzed for a two week period in January and February of 2007. During this period, the fog on Jan.25th was most heavy and lasted for a long time, so take fog on this day as an example.

The droplet size distribution of the fog was measured at one sample per second with an optical particle spectrometer (the DMT fog monitor) so that the evolution of the cloud microphysics could be evaluated at high time resolution. High rate measurements are important since many of the physical processes that determine fog lifetime are highly inhomogeneous, e.g. turbulent mixing with drier air and evaporation, and cannot be captured with longer sampling times.

1. EVOLUTION OF CHARACTERISTIC PARAMETERS

The observation of fog on Jan.25th as an example shows the evolution of some characteristic parameters, such as number concentration, diameter, liquid water content and visibility.

Thus it can be seen from the charts below (Fig.1-4) that the number concentration and average diameter are inversely correlated, that the liquid water content and diameter are positively correlated and that visibility is anti-correlated with number concentration and liquid water content. All of these relationships are what would be expected, but the magnitudes and slopes of these correlations are quite different when comparing the mountain case with the urban case.

Comparing the fog characteristics in the clean environment with measurements made in some polluted urban environments in this country shows that when meteorological conditions are similar, the droplet size distributions are different as a result of the background cloud condensation nuclei (CCN) population. The number concentration of fog in urban case is much greater, from which it can be seen the pollutions in cities.

---

[*] Correaponding author.
E-mail address: niusj@nuist.edu.cn

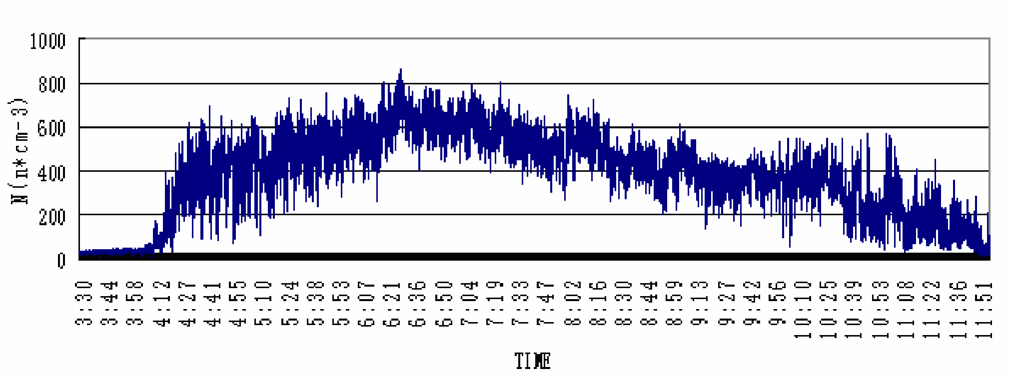

Fig.1 Evolution of number concentration

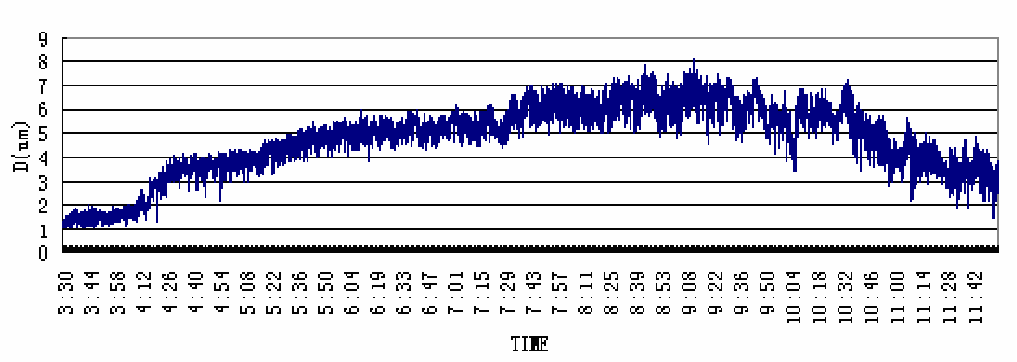

Fig.2 Evolution of average diameter

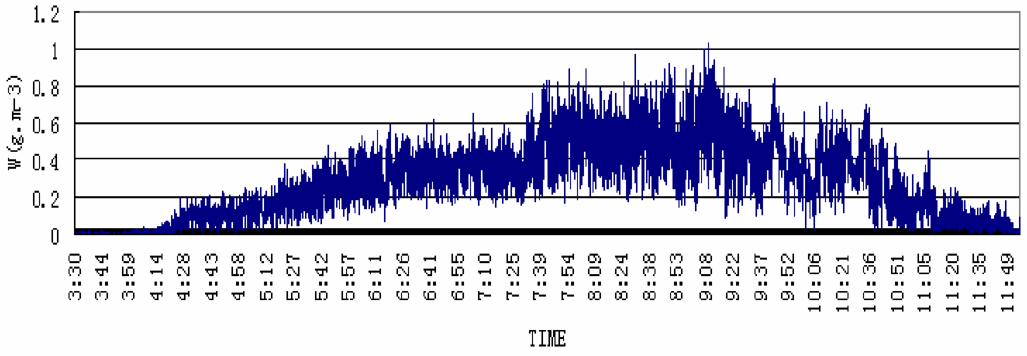

Fig.3 Evolution of liquid water content

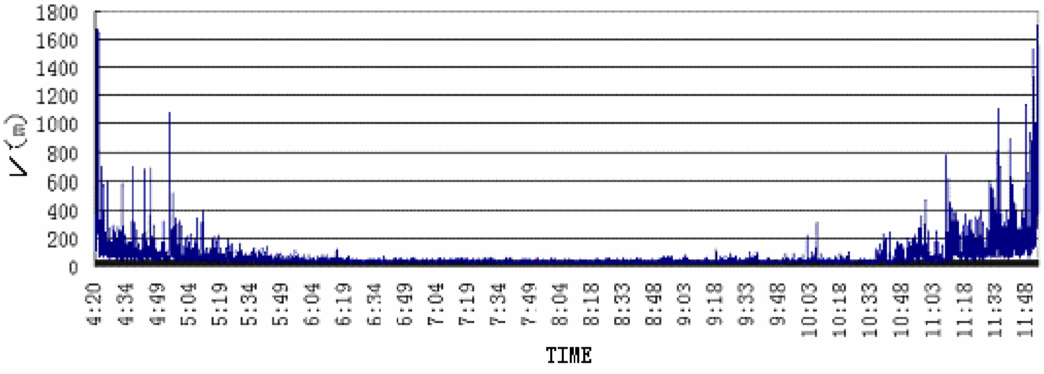

Fig.4 Evolution of visibility

3. EVOLUTION OF FOG-DROPLET SIZE DISTRIBUTION

With the objective of understanding how fog forms, evolution and dissipation in a relatively pristine environment in China, the fog on Jan.25th is taken as an example to show the evolvement of fog-droplet size distribution in different stages (Fig5).

The five different lines show the different stages of forming, first evolving, second evolving, maturating and dissipating.

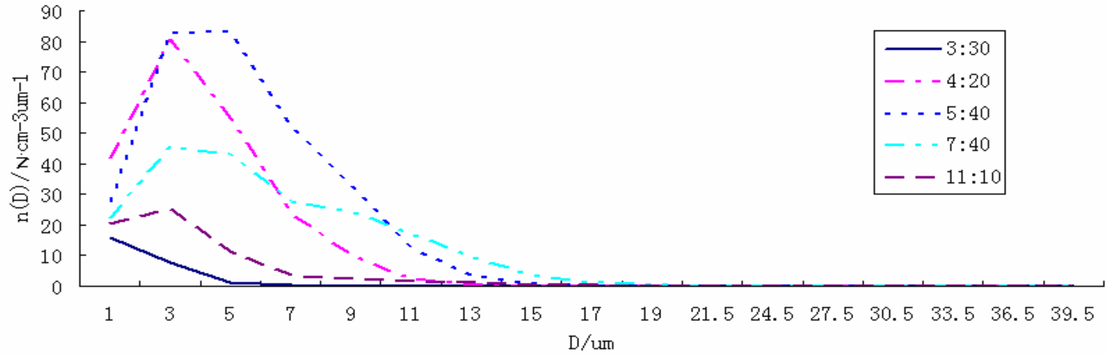

Fig.5 Fog-droplet size distribution

Form Fig.5, and also combining Fig.1-4, it can be seen that in the forming stage from 3:30, the number concentration is very little, the width of drop-size distribution is very narrow, the size of fog-droplet is also very small, and the liquid water content is nearly zero, this stage is short; in the evolving stage from 4:20, the number concentration grows rapidly and reaches a large numerical value, the width of drop-size distribution becomes wider, the size of fog-droplet and the liquid water content also grow rapidly, but the visibility reduces rapidly; in the maturating stage from 7:40, although the number concentration falls, the number of bigger droplets still grows, the size of fog-droplet still become wider; and in the dissipating stage from 11:10, the number concentration, the size of fog-droplet and the liquid water content all decrease, the visibility increases, the fog dissipates.

4. COMPARISON OF FOG-DROPLET SIZE DISTRIBUTION AND AEROSOL SIZE DISTRIBUTION

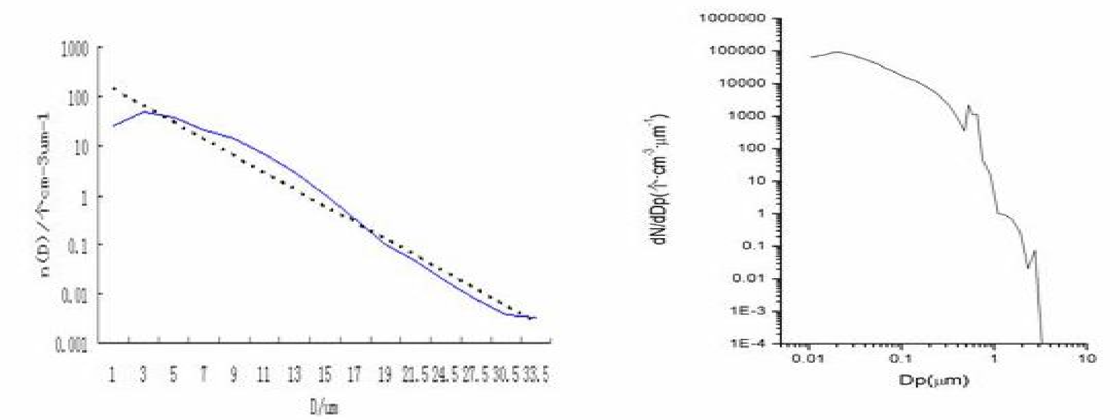

Fig.6 The average fog-droplet size distribution and the aerosol size distribution

In the above two charts (Fig.6), the left one is the average fog-droplet size distribution, it almost meets an index rule, the number of the particles decreases rapidly along with the diameter's increasing. The right one is the aerosol size distribution. Compare the two charts, it can be seen that they are similar, both decrease rapidly, but the fog-droplet size distribution moves right and down evidently.

5. **BIBLIOGRAPHY**

Roach W T, et al The physics of radiation fog I, A field study.Quart J Roy Meteor Soc,1976,102,313- 333

Jiusto J E, Lara G G Radiation fog field programs, recent studies A SRC- SUN Y,1983,Publ No.869

Noone K J, et al Changes in aerosol size and phase distributions due to physical and chemical processes in fog. Tellus, 1992, 44B, 489- 504

Wendisch M, et al Drop size distribution and LWC in Po valley fog. Contril Atmos Phys, 1998, 71, 87- 100

Li Zihua, Studies of fog in China over the past 40 years, Acta meteorological scinca, 2001, 59(5), 616-624

Deng Xuejiao, et al Physical characteristics of dense fog at Nanling Mountain region, Journal of tropical meteorology, 2002, 18(3), 227-236

Huang Yusheng, et al The microphysical structure and evolution of winter fog in Xishuangbanna, Acta meteorologica scinca, 2000, 58(6), 715-725

Li Zihua, et al Physical structures of the five-day sustained fog around Nanjing in 1996,Acta meteorologica scinca, 1999, 57(5), 622-631

Zhou Tao, et al Temporal and spatial distribution of fog in Guizhou, Journal of Guizhou Meteorology, 2005, S1, 32-34

ACKNOWLEDGEMENT

Key Basic Research Foundation for Natural Science of the Jiangsu Higher Education Institutions of China (Grant No. 06KJA17021), and Special Foundation for Meteorological Vocation from the Ministry of Science and Technology of China(Grand No. GYHY200706026) supported this research.

Study on the Stratiform Cloud Numerical Model and Actual Observation

YANG Jie-Fan$^{1,\,2}$*, LEI Heng-Chi*^{1}*, HU Zhao-Xia*^{1}*, GUO Xue-Liang*^{1}*, and XIAO Wen-An*^{2}
$^{(1)}$ *Institute of Atmospheric Physics, Chinese Academy of Sciences, Beijing 100029*
$^{(2)}$ *Najing University of Information Science and Technology, Najing 210044*

1. Introduction

As known to all, nowadays there are two modes to describe the drop spectra. One is parameterisation, and the other divides the drop spectra into many categories and focuses on the interactions between the categories.

In the early 1960s, scientists such as Berry[1] and Kovert[2] did researches on the evolution of the raindrop spectra with the drop category model. In the 1980s, Xiao Hui[3] *et.al* used a cloud drop category model to simulate the evolution of drop spectra in the process of condensation and coalescence. Meanwhile, Xu Huibin[4] in his paper particularly covered the problems of the applicability of the category model.

In this paper, with the help of the improved one-dimensional stratiform cloud raindrop category model developed by the Chinese Institute of Atmospheric Science, we have simulated the three different precipitations in Changchun, Jilin Province, on June 21, 2005 and made a comparison between the results and the data obtained through actual observation, taking advantage of the stratiform cloud raindrop category model in calculating the raindrop spectrum and the natural development of the precipitation intensity.

2. Improvement of model microphysical processes

The microphysical processes are introduced in paper 1 and 2 in detail. In this part, we aim to introduce the improvement of the microphysical processes.

2.1 The automatic cloud transformation method

In the original model, the Kessler case is used to describe the cloud automatically transforming to raindrops, such as

$$\begin{cases} A_{\mathrm{cr}} = K(q_{\mathrm{c}} - q_{\mathrm{c0}}) & q_{\mathrm{c}} > q_{\mathrm{c0}} \\ A_{\mathrm{cr}} = 0 & q_{\mathrm{c}} \leqslant q_{\mathrm{c0}} \end{cases}$$

We changed the q_{c0} from 0.75 to 0.35 g • kg^{-1}. And the liquid water transforming from the cloud is distributed into raindrop categories through the following method:

$$Q_{\mathrm{cr}} = \frac{1}{\rho_{\mathrm{a}}} \int_{D_1}^{\infty} m(D) N_{\mathrm{or}} \mathrm{e}^{-\lambda D} \mathrm{d}D$$

In this equation, Q_{cr} denotes the liquid water content of raindrops, which transforms from the cloud drops during the automatically changing process. $m(D)$ is the raindrop mass with the diameter D. ρ_a is air density. λ is a constant equated to 90. And the unit of raindrop diameter is centimetre. We can easily derivate the following equation:

$$Q_{\mathrm{cr}} = \frac{\pi}{6\rho_{\mathrm{a}}} \int_{D_1}^{\infty} N_{\mathrm{or}} D^3 \mathrm{e}^{-\lambda D} \mathrm{d}D$$

$$Q_{\mathrm{cr}} = \frac{\rho_{\mathrm{w}} \pi}{6\rho_{\mathrm{a}}} N_{\mathrm{or}} \left\{ \frac{1}{\lambda^4} \exp(-\lambda) \left[(\lambda D_1)^3 + 3(3D_1)^2 + 6(3D_1) + 6 \right] \right\}$$

$$N_{\mathrm{or}} = \frac{\rho_{\mathrm{w}} \pi}{6 Q_{\mathrm{cr}} \rho_{\mathrm{a}}} \left\{ \frac{1}{\lambda^4} \exp(-\lambda) \left[(\lambda D_1)^3 + 3(3D_1)^2 + 6(3D_1) + 6 \right] \right\}$$

2.2 Numerical solution of the raindrop spectra evolution

The diameters in each category, defining a series of length interval, were chosen to form an exponential progression, which is denoted as $D(I) = D_0 \exp[(I-1)/\mathrm{I}_0]$. In order to keep the conservation of mass and quality of whole raindrops, we reprogrammed the numerical solution of the raindrop spectra evolution by means of a simple method derived from the K-0 case, which can be simply written as:

$$N'_{\mathrm{j}} = N_{\mathrm{j}} + N_{\mathrm{j-1}} \frac{D'^3_{\mathrm{j-1}} - D^3_{\mathrm{j}}}{D^3_{\mathrm{j}} - D^3_{\mathrm{j-1}}} - N_{\mathrm{j}} \frac{D'^3_{\mathrm{j}} - D^3_{\mathrm{j}}}{D^3_{\mathrm{j+1}} - D^3_{\mathrm{j}}}$$

N'_{j} is the quantity of raindrop in category j after collecting with cloud, and N_{j} is the one before collecting. D'_{j} denotes the raindrop diameter in category j after collecting with cloud, and D_j is the one before collecting.

3. Comparison between the numerical simulation and actual observation

In this part, we simulated three stratiform precipitations in Changchun, Jilin Province, China, on June 21, 2005, comparing between the results and the data observed by Doppler radar, vessel of rain gauge and the raindrop size distribution.

As is shown in Fig.1, the top of the cloud is about 7000m, with the 0℃ level of 3500m.

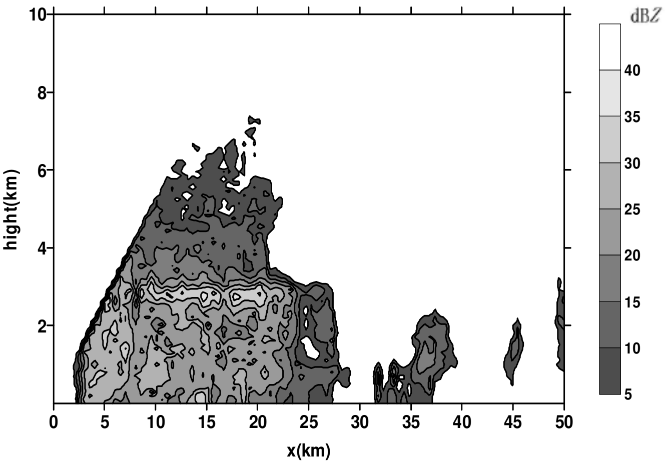

Fig.1 The contour chart of the Doppler radar echo at 0808 BT on June 21, in Changchun, Jilin Province

The sounding data of Changchun, Jilin province at 0808 BT on June 21 is used as the initial field of the model simulation. The time step is set to 2s and the vertical grid length to 100m. And the updraft is supposed to be invariable during the numerical simulation

Fig.2 indicates the evolution of the distribution of the ice crystal concentration and the water content at different periods of time. The three updrafts are set to 0.12m·s^{-1}, 0.18m·s^{-1}and 0.28m·s^{-1}; the evolutions of ice crystal above zero-temperature level with different updrafts is alike: a high ice crystal concentration area formed at 6000 m height after IN nucleation, and then ice crystals fell into the lower layer and kept growing by collecting the super cooling water near the zero-temperature level.

Finally, the ice crystals melted after falling into the warm area. The IN nucleation rata and other microphysical processes changed significantly with different updrafts. The concentration of the ice crystal near the 0℃ level is 1.2L^{-1}、0.8L^{-1}and0.5L^{-1}, while the water content of ice crystal is about 0.6g • kg^{-1}、0.3g • kg^{-1}and 0.2g • kg^{-1}. From the fig3 we can see that the dB*Z* profiles simulated by the model and that of the actual radar observation under the zero - temperature level is similar when the updraft is set to 0.12 m·s^{-1}、0.18 m·s^{-1}and 0.28 m·s^{-1}, and the radar echo simulated by the model near the ground is 21.86 dB*Z*、26.51 dB*Z*、28.56 dB*Z* after 80 min which are similar to the radar echo calculated by the raindrop size distribution observed on the ground.

Fig 5 shows the evolution of the raindrop size distribution from zero-temperature level to the ground. Which indicates the raindrop spectra changed a little under the 0℃ level. The collection between the raindrops and cloud contribute to the rain intensity is about 10% in this case

4. Conclusion

a. In this paper, an improved 1-D stratiform cloud model is used to simulate three precipitations in Changchun, Jilin Province, China, on June 21, 2005. The results show that the improved model tends to be much more stable in calculating and it can simulate the raindrop spectrum closest to the actual precipitation spectrum.

b. It is shown in the comparison between the actual observation and the modelling that the rain intensity could increase about 10% after collecting with cloud water in the warm area.

c. In this model, we only focus on the collection with cloud drops and evolution of raindrop, both of which lead to the great variation of raindrop spectra from zero-temperature level to the ground.

d. The method of parameterisation remains to be used in the cold cloud processes, including the nucleation, multiplication and accretion of ice particles, all of which remain intangible.

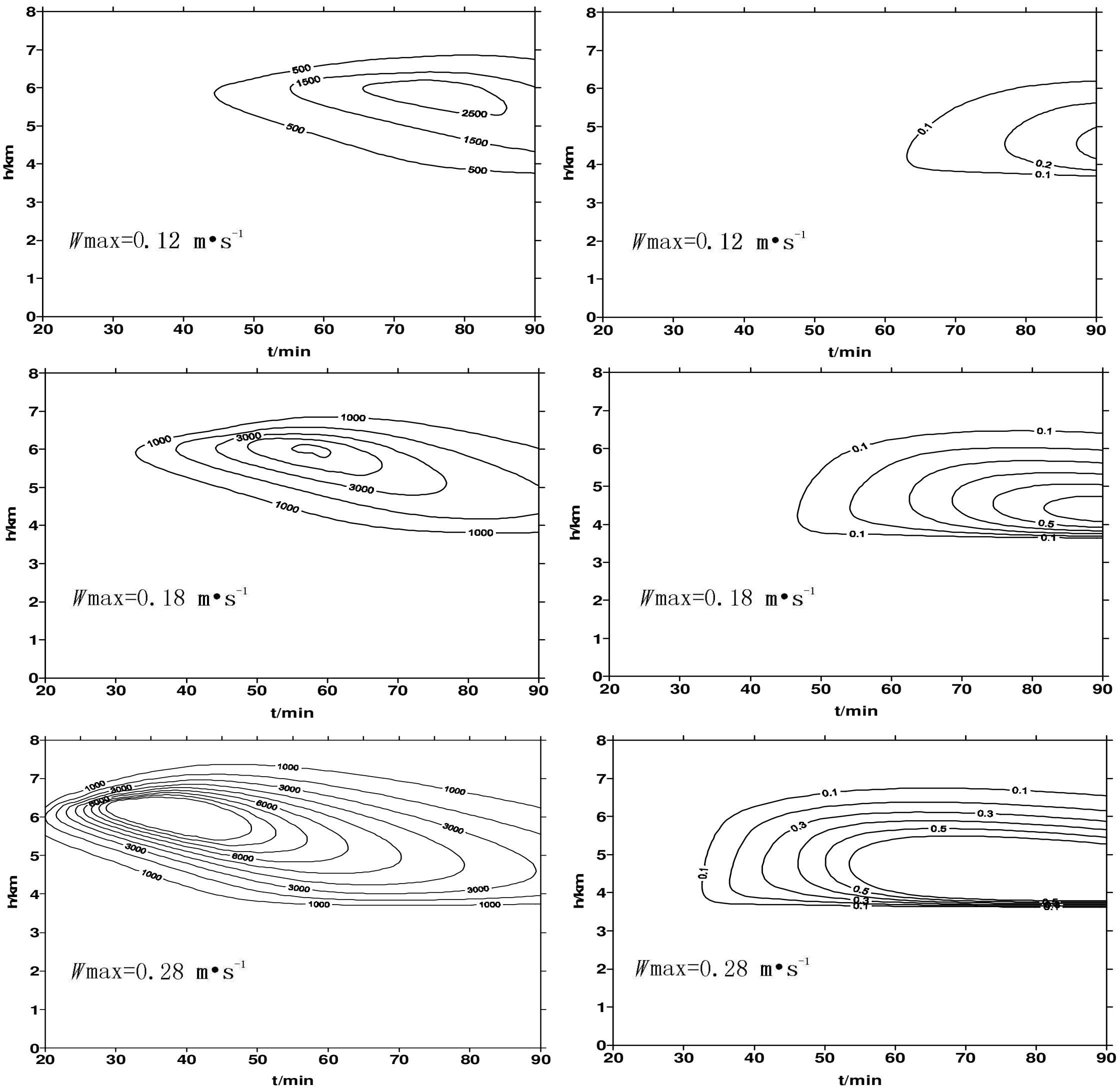

Fig.2 The coutour chart of water content and density of ice particle in three schemes of updraft

(Left graphics are coutour charts of density of ice particles, m^{-3}

Right graphics are coutour charts of water content of ice particles, g•kg^{-1})

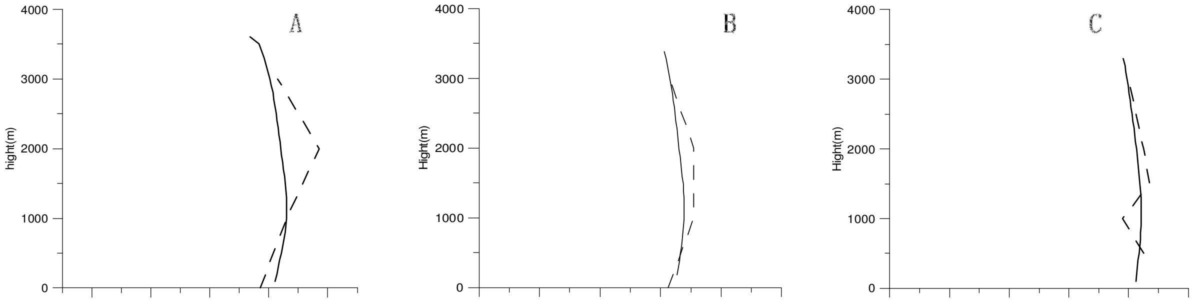

Fig. 3 The comparison between the dBZ profile simulated by the model and that of the actual radar observation

(a). 0720 LST on 21 Jun , Wmax=0.12 m•s^{-1} (b).0845 LST on 21 Jun, Wmax=0.28 m•s^{-1}

(c). 0905 LST on 21 Jun, Wmax=0.18 m•s^{-1}

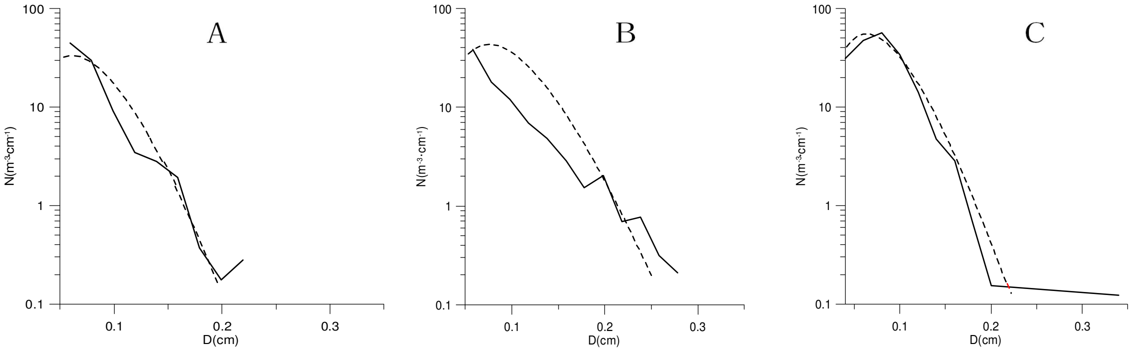

Fig.4 the ground raindrop size distribution simulated and observed. D for diameter of raindrop, N for then concentration of raindrop

(a). 0720 LST on 21 Jun , *W*max=0.12 $m\cdot s^{-1}$ (b). 0845 LST on 21 Jun, *W*max=0.28 $m\cdot s^{-1}$ (c). 0905 LST on21 Jun 21, *W*max=0.18 $m\cdot s^{-1}$

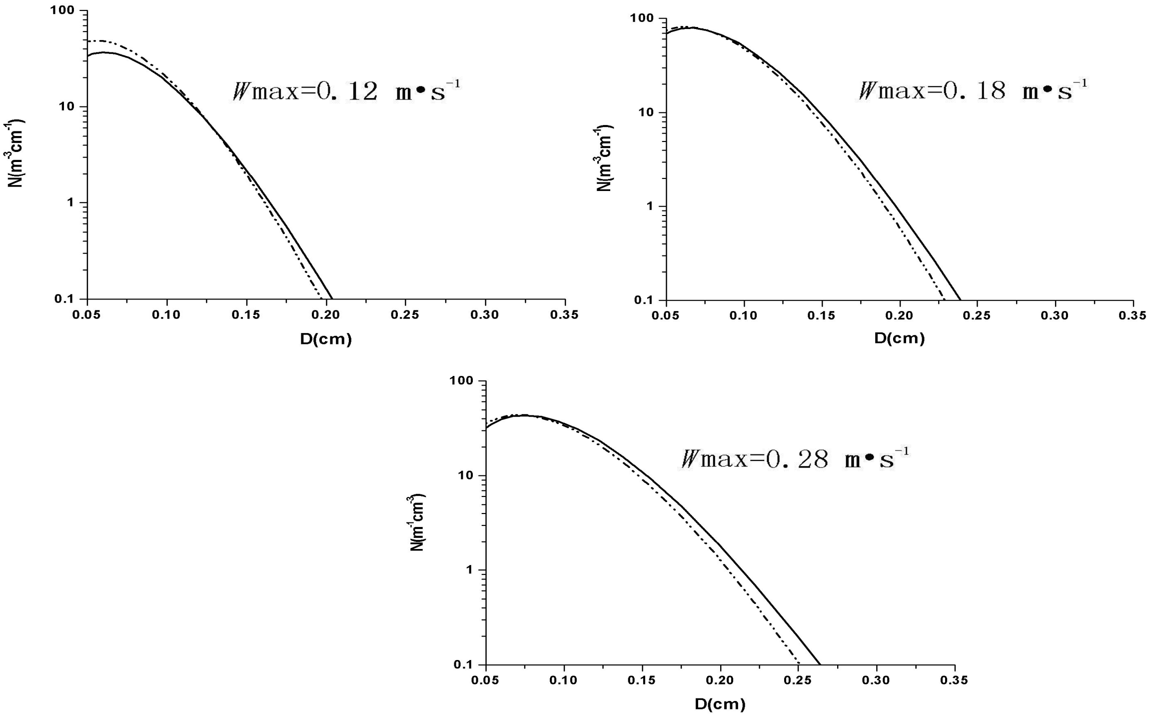

Fig.5 The comparison between raindrop size distribution in the bottom of cloud and 0℃ level Real line for the spectrum of rain drops at cloud base and the dashed for the spectrum of rain drops at 0℃ level

Acknowledgements

We grateful to my teachers for their helpful suggestions and comments. This research partially funded by the Chinese academy of Sciences Knowledge Innovation Program under contract KZCX3-SW-22

References

1. Berry E X. Cloud droplet growth by collection. J. *Atmos. Sci.*, **24**, 688-701, 1967
2. Kovetz A and Olund B. The effect of coalescence and condensation on rain formation in a cloud of finite vertical extent, J. *Atmos. Sci.*, **26**, 1060-1065,1969
3. Xiao Hui, Xu Huangying and Huang Meiyuan. The numerical simulation study of drops distributor in cumulus Part Ⅰ : The effect of salt nuclei spectrum and density. *Scientia Atomospherica Sinica*(in Chinese), **12**, 121-130,1988
4. Xu Huanbin, Duan Ying. Some question in studying the evolution of size-distribution spectrum of hydrometers particles. *Acta.Meteorologica. Sinica*(in Chinese), **57**, 450-460, 1999

Analysis on the 2004 Jiang Su temperature decrease by rocket artificial enhance precipitation

Bai Ka-wa, Wang Jia, Wang Ke-fa, Zong Peng-cheng
Jiang Su Artificial Modification Weather Office, Nan Jing 210008

1. Introduction

In 2004 the South of Huai He in Jiang Su was in hot summer just after end of mei-yu period. According to the statistic from automatic weather station , from July 16th to 31st the average temperature over the province was between 28.0 and 32.2 ℃ , higher 0.7~4.0℃ than the same time of the normal years. The average temperature between Chang Jiang and Huai He and South of Jiang Su reached the maximum after 1961. The Jiang Su electricity charge broke through the 24 million KWA at 10:41 on July 28th, reaching the history maximum. In order to relieve the summer high temperature condition and reduce the consumption of electricity power, from July 25th to August 10th , Jiang Su Weather Modification Office launched 27 times rocket artificial precipitation stimulation for detemperature with the strong assistance of army and civil aviation.

According to the statistic from the Energy Source Department in Jiang Su Economy and Commerce Committee, the average detemperature of the five cities in South of Jiang Su province was 7℃ during the time of the artificial precipitation stimulation, and the electricity charge reduced by 3.9 million KWA. The electricity charge all over the province was ensured, the living environment was improved, and the air quality became better. The social and economical benefit was significant.

2. Synoptic background of artificial precipitation stimulation for detemperature

Between July and August, the formulation of precipitation in Jiang Su was relative to the weakness ,east and south movement of the West Pacific Semi-tropical high. When the cold air from the north go towards to the south or there is the sheer line in Jiang Su, the West Pacific Semi-tropical high may change and induces the precipitation.

Table 1 The statistic days of the synoptic background of precipitation stimulation for detemperature

Synoptic background	Cold air towards to the South	Sheer line	Boundary of Semi-tropical high
Days	4	4	3

3. Analysis on the precipitation and temperature descent before and after seeding

(1) The variation of the radar echo before and after seeding indicates that seeding to the developing and rape cloud ,if the seeding time and amount are proper, after seeding the echo changes in some extent. The echo area enlarges ,the echo intensity becomes stronger and the echo top increases.

(2) According to all the data observed on the ground and weather real condition, when there is rainfall on the ground (no matter in the city or around the city), in short time the ground temperature will decrease, but the descent extent is not direct ratio to the rainfall amount. Because the reason of detemperature is that the evaporation absorbs the ground energy, however the amount of absorbed energy is limited, when in some extent the evaporation reaches saturated, even if the precipitation amount becomes larger, there is no effective of temperature decrease. Therefore the temperature decrease from the evaporation is limited, but the main factor of detemperature are the cold air advection and the downward transmission of the cold air momentum enforced by the downdraft result from the short heavy rain. Therefore, the key to rock precipitation stimulation for detemperature is seeding to force the convection cloud to develop, so that the strong downdraft bring the clod air to the ground.

4. Case study of Chang Zhou precipitation stimulation in August 5th,2004

4.1 Radar echo and precipitation

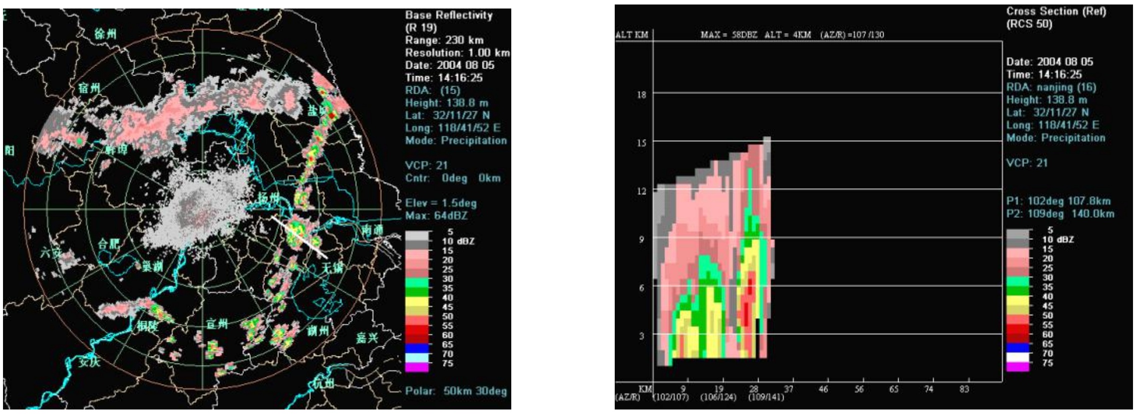

(a) (b)

Fig.1 Radar echo with base reflectivity observed (a, the white line is instead of the location of RCS chart)and with RCS observed(b) Nanjing Station at 14:16 Aug 05th ,2004

The Nan Jing Doppler radar data showed that there was a convective cloud echo band corresponding to the cloud band in infrared image. The echo in the band developed and dissipated quickly. The echo cell moved towards to the eastnorth along steering flow at 700hpa. At 9:30 the convective cloud echo in the eastsouth of echo band developed. By the end of 11:35, a short convective cloud band was formed from Bao Ying to Dan Yang(called cloud band 1). In the south of cloud band 1 the new convective cell developed, corresponding to the real-time rainfall from 11:00 to 12:00 when the center of rainfall was in Bao Ying and an hour rainfall amount reached 5.3mm. At 12:25, the 0.5 ° PPI chart indicated that some fragmentary cloud echo appeared in Chang Zhou. Until to 12:56, we found that the convective cloud echo had developed from the 2.4 ° and 3.4 ° PPI charts. The maximum echo intensity reaching 20dBz nearby 119 ° 58′E, 31° 50′ N formed another short cloud band(called cloud band 2) together with the convective cloud in Yi Xing. The rainfall center which is 7.5mm in an hour moved south to Gao You between 12:00 and 13:00. At 13:21 the south of the cloud band 1 and the north of the cloud band 2 connected, forming a eastnorth-westsouth long cloud echo band. At 13:58 the two bands incorporated together nearby Chan Zhou. After incorporating there is still two convective center, the 40km horizontal scale , 15km top echo and the maximum echo intensity reached 50dBz. Chang Zhou Weather Bureau launched 4 rockets in 60° elevation and 180° azimuth at Xue town. After seeding the echo developed rapidly, the maximum echo reached 60dBz, the area of 40dBz echo enlarged significantly, the echo top reached at least 15km and the area of 15km echo top became larger. The same conclusion can be found from the RCS chart(Fig.1b). Besides before seeding 10 min(13:30-13:40) the maximum rainfall amount was 6.3mm, however, after seeding 10 min(14:10-14:20) the maximum rainfall amount reached 8.7mm. From 14:00 to 15:00 an hour rainfall amount in Chan Zhou was 10.0mm more 6.8mm than around Chan Zhou

4.2 Analysis on the temperature descent

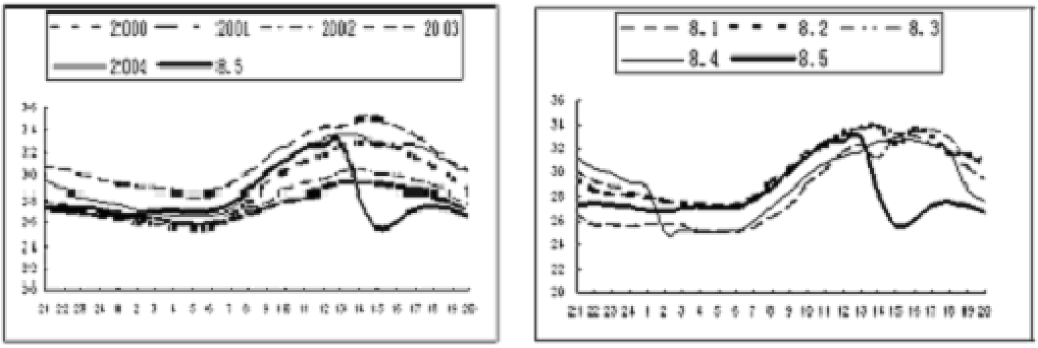

(a) (b)

Fig. 2 The change of 1 day's temperature

We can concluded from 2000~2004 daily variation chart of the average temperature(Fig.2a) that on the first ten days of August the daily temperature started ascent all the time after 6:00, reached the maximum between 14:00 and 16:00, and then after 16:00 the trend went towards to descend slowly. However, the chart of daily temperature trend on August 5th show that at 12:49 the temperature reached the maximum of 33.3℃, then the temperature descend rapidly, and at 14:16 the temperature decreased to the minimum of 24.2℃. The total decreasing temperature reached 9.1℃ within 2 hours. After then the temperature increased slowly, by 15:00 the temperature reached 25.6℃. At this time although the temperature trend was ascent, the increasing speed was slow and the amplitude was small. Meanwhile, through analysis on the 24 hours temperature variation from August 1st to 5th (Fig.2b), we can find that the temperature variation was normal in nature, but on August 5th the temperature decreased rapidly within short time after seeding.

The table 2 lists the temperature descent amplitude after rainfall within 2 hours from automatic weather station. Judging from the table, when the precipitation forms, the temperature decreases within short time. The table shows the detemperature condition in the 10 areas. Except for Chang Zhou, the maximum descent amplitude reach 23.7%, the minimum is 0.4%, the average detemperature is 3.4℃, and the average detemperature amplitude is 11.0%. However, after rainfall In Chang Zhou the detemperature is 9.1℃, and the amplitude reached 27.3%, more 16.3% than the average, which is relative to the heavy rain (31.6mm) with 22m/s thunder strong wind after the rocket precipitation stimulation in Chang Zhou

Table 2 The fall of temperature in 10 area

Station	Hong Ze	Bao Ying	Gao You	Jiang Du	Dan Yang	Chang Zhou	Yi Xing	Tian Xing	Hai An	Ru Ben
Temperature before rainfall（℃）	25.6	28.8	28.8	30.1	31.5	33.3	33.6	32.1	28.7	31.6
Temperature before rainfall（℃）	25.5	27.1	27.5	28.6	28.8	24.2	28.6	24.6	24.9	24.1
Difference（℃）	－0.1	－1.7	－1.2	－1.5	－2.7	－9.1	－5.0	－7.5	－3.8	－7.5
Amplitude（%）	－0.4	－5.9	－4.2	－5.0	－8.6	－27.3	－14.9	－23.4	－13.2	－23.7

4.3 Numerical simulation

1) Nature cloud simulation

The Nature cloud is simulated by the IAP 3–dimension cloud model. The corrected sounding data in Nan Jing at 8:00BST input to the model as the initial condition.

The simulated nature cloud shows that rainfall appears on the ground at 15 min. At 34 min the updraft in the cloud reaches the maximum of 18.35m/s, and the total water content in the cloud reaches maximum at 44 min. The total amount rainfall within an hour is 11231.30 kton.

2) Seeding cloud simulation

We seed 40g AgI into the cloud by rocket. After seeding the total amount of rainfall reaches 15445.86kton, increasing by 4214.56kton. The area of the storm cloud enlarges and the water content in the up of the cloud increases(Fig.3b)

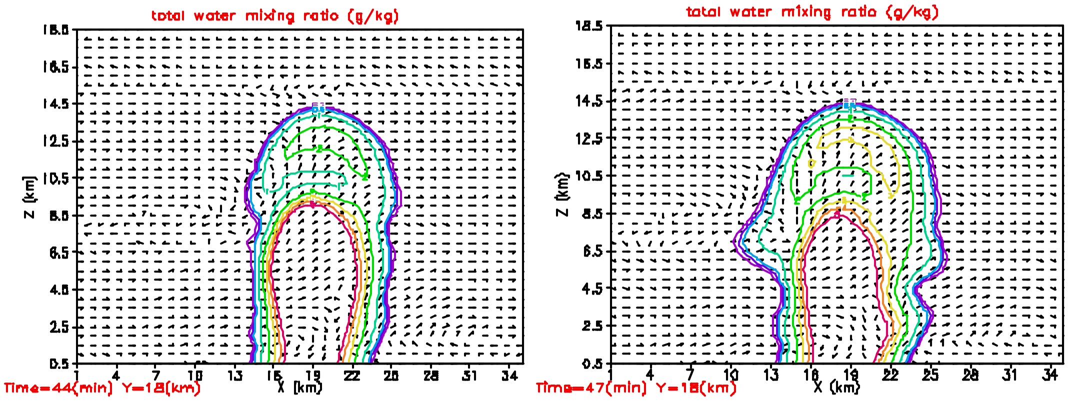

(a) (b)

Fig.3 The convective cloud by simulation in nature and in catalyzed state (total specific water content,unit:g/m^3) at time 44 muinute(a),47 minute(b)

5. Conclusion

The Doppler radar data , all the data observed on the ground and the numerical simulation analysis show that :

(1) After seeding AgI into the cloud in the development and mature stage, the reflectivity area enlarged , the reflectivity and echo top increased, the updraft in the cloud enhanced, the rain on the ground increased, so that the temperature decreased significantly.

(2) The seeding numerical simulation of convective cloud in the Chang Zhou on August 5th in 2004 show that after seeding the area of the storm cloud increases, the water content on the top of the cloud increases, the total rain on the ground is 15445.86 kton, more than nature cloud 4214.56 kton, the increasing amplify reaches 27.4%

(3) When the rain on the ground forms (no matter in the city or around the city), the temperature on the gourd decreases within short time. However, the real factors of ground temperature decrease are the cold advection and the downward transmission of the cold air momentum enforced by the downdraft result from the short heavy rain. Therefore, the key to detemperature by rocket artificial precipitation stimulation is to seeding the developing cloud, enhance the violent development of the cloud, so that the strong and lasting downdraft bring the cold air to the ground.

THE 26TH SEPTEMBER 2007 VENICE EXTREME CONVECTIVE RAINFALL EVENT

Adriano Barbi[1], Gabriele Formentini[1] and Marco Monai[1]
[1] ARPAV – DRST – CMT, Italy

1. INTRODUCTION

In the framework of the Regional Agency for Environmental Prevention and Protection of the Veneto (ARPAV), the Meteorological Centre of Teolo (CMT) is the operational regional meteorological service in Veneto, the region of Venice, in Northeastern Italy (Fig. 1). Activities of CMT (a branch of Land Safety Department–DRST) include:

- operational forecasting;
- specific support to Civil Defence, tourism, agriculture, etc;
- participation in national and international projects.

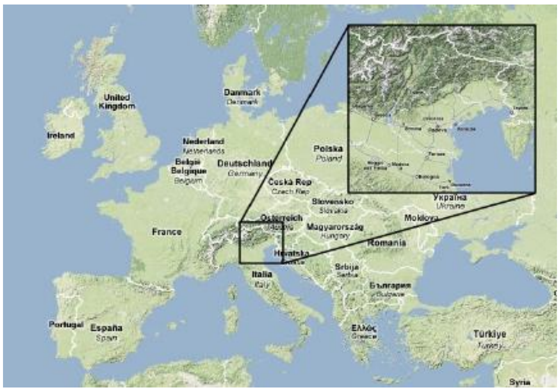

Fig. 1: Veneto region in Europe.

In the early and morning hours of the 26th September 2007 surrounding areas of Venice were hit by extreme rainfall caused by severe thunderstorms which developed close to the central-southern coastline of the north-eastern Italian region Veneto. The multisensor network of ARPAV includes two meteorological C-band radars, Meteosat-9 satellite data, and a high-resolution surface network of automatic weather stations, analysis of which allowed to find some interesting features of the storm environment.

The main effects of the event were the exceptionally high rainfall rates and large amounts of accumulated precipitation in short time intervals. Some different raingauges observed 250 mm in three hours and 300 mm in six hours, numbers close to the 40% of annual total rainfall (700-800 mm).

The specific position of the area of interest close to the western Veneto radar site allows a detailed analysis of the convective event. The area invested by the thunderstorms is densely populated so that many people experience the effects of floods in urban area.

2. GENERAL FRAMEWORK AND LOCAL EVOLUTION

In the following a more detailed analysis will be carried on considering:

- synoptic situation;
- satellite and radar records;
- ground stations measurements.

A surface low formed in the very first hours of September the 26th on the Gulf of Genoa in northern Italy. Aloft a trough deepened advecting cold air from North Europe to South France towards the Alps (Fig. 2).

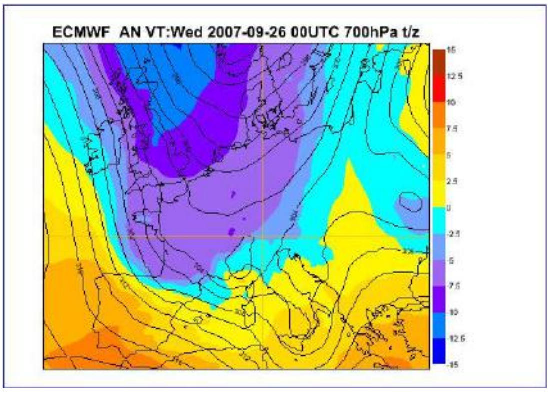

Fig. 2: ECMWF Analysis of geopotential height (dam) and temperatures (°C) at 500hPa valid for 00UTC of 26 September 2007.

Surface winds intensified during the night from southeast on the North Adriatic Sea and from northeast on the Veneto region inland.

The first convective cell formed just after midnight between the Padua and Venice provinces border and developed moving northwards over some areas close to the Lagoon of Venice.

In the following hours three more cells grew in the western part of the Province of Venice. Teolo radar images show that these cells were organized in a linear structure and moved north-westwards over the Province of Padua.

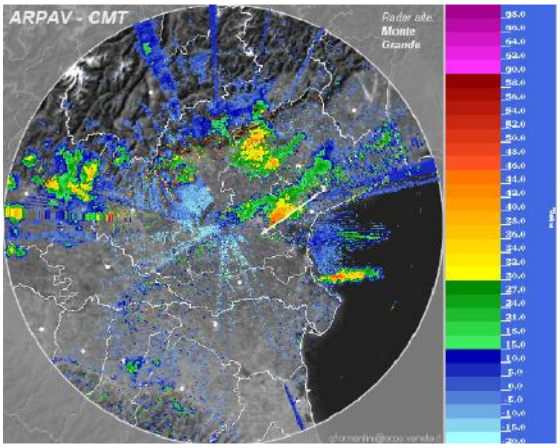

Fig. 3: Reflectivity of the Teolo radar PPI 0.8° product valid for 00:40UTC 26 September 2007.

Following these cells, the two most interesting events took place. At first a low topped supercell (echo-top below the height of 6-7km) formed with the typical weak echo region and mini hook echo as nicely visible in the radar data (Fig. 3 and 4). The main effect of this low-topped supercell was the high precipitation rate.

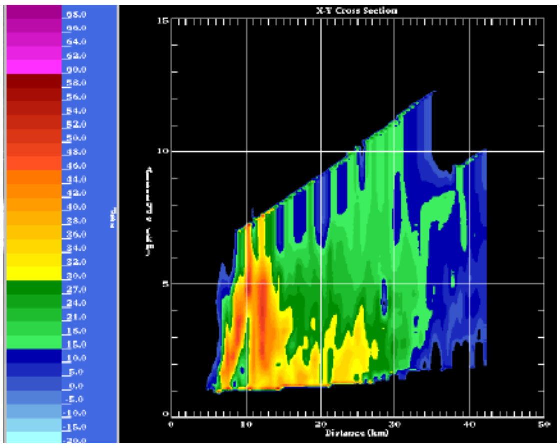

Fig. 4: Vertical cross section of reflectivity of the Teolo radar along A-B segment in Fig. 3.

At 3:50 the supercell dissipated moving westwards but the convergence between its outflow and the south-easterly winds over the north Adriatic Sea gave rise to a second low-topped supercell. The evolution of this second cell was disturbed by a number of small cells present in southern Veneto at that time.

Between 4-5UTC convection changed its characteristics from supercellular to multicellular. The main contribution was provided by the injection of very humid and unstable air from east, enhancing both the convergence effect and instability.

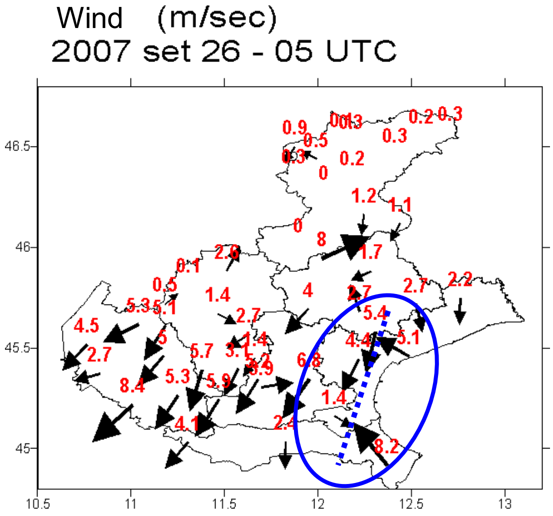

Fig. 5: Wind vectors from automatic surface station network valid for 05UTC 26 September 2007. The blue dashed line denotes the low-level wind convergence.

A very strong convergence between northeastern cold continental and warm and humid southeastern air formed close to the shoreline and became the focus point that triggered and drove the convection from this time onward (Fig. 5).

For many hours different cells originated, developed and dissipated much over the same geographical area. The main system took the form of a multicell convective system with very low translation velocity causing large amounts of rain accumulations.

In the morning the surface winds were opposite to the winds at medium-high levels for many hours supporting the continuous regeneration of cumulonimbus clouds in the same geographical area and limiting the eastward propagation of the system. Satellite images confirmed the severity of the convective activity displaying a typical V-shape multicell thunderstorms complex.

All the cells were organized along the north-south direction and continued regenerating for hours. After 05UTC the system reached its maximum intensity as shown also by MET-9 satellite images with top infrared temperature below -55°C (Fig. 6).

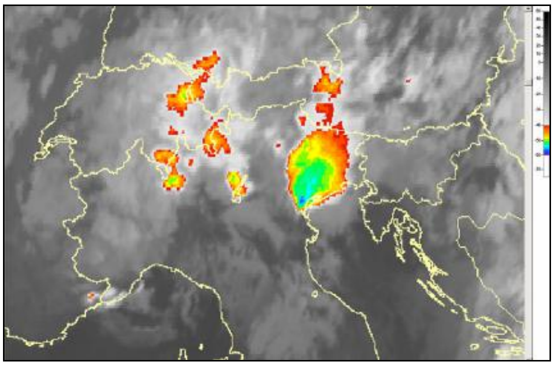

Fig. 6: Infrared 10.8 MSG image in false colours at 05UTC 26 September 2007. Temperatures below -55°C are depicted in blue.

During these hours a number of rain gauges measured very high rain rates: more than 90mm in 30 minutes, 120mm in one hour and 200mm in three hours.

From 07UTC the system became a V-shape mesoscale convective system causing floods in the very densely populated Mestre-Venice metropolitan area (Fig. 7).

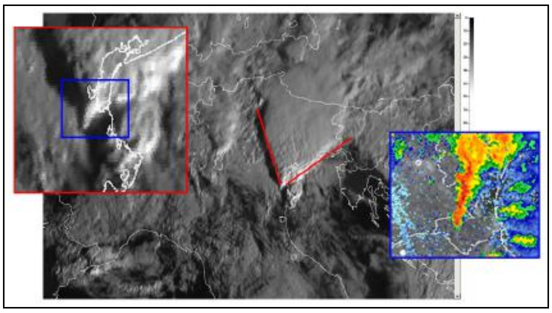

Fig. 7: HRV MSG satellite image with superimposed radar image at 07:00 26 September 2007 in which V-shape of thunderstorms system is evident.

During the morning the multicell system started to evolve moving eastwards and showing progressively decreasing rain rates.

A second multicell system developed in the Po river delta area but moving east onto the sea thus not hitting populated areas (Fig. 9).

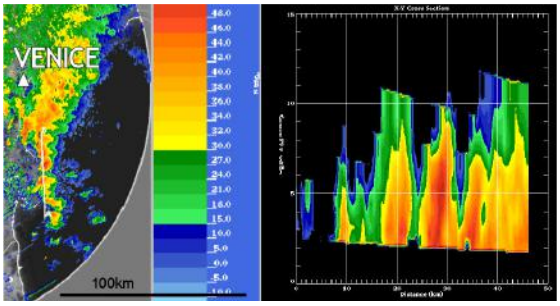

Fig. 9: Reflectivity of the Teolo radar at 08:50 UTC 26 September 2007 showing the multicell structure of precipitation.

From a qualitative point of view, positioning of reflectivity maximum didn’t match with raingauges. This suggests that locally even larger precipitation amounts could be fallen compared to raingauge data.

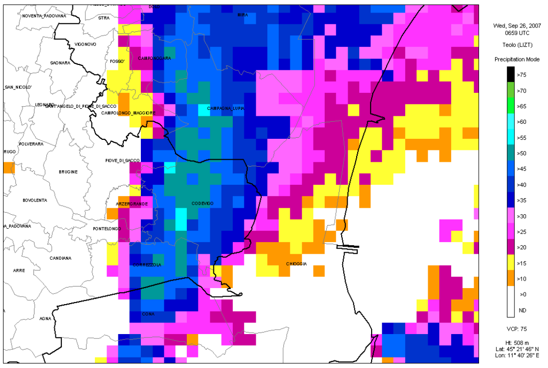

Fig. 10: detailed image of Teolo Radar CMAX product at 06:50UTC 26 September 2007 with villages and towns borders superimposed.

In summary the main points of the precipitation event were:

- low level convergence, with strong southeasterly winds on the sea and shoreline and moderate-strong northeasterly winds inland kept system stationary.
- advection of very humid and warm air from the sea that contributed to enhance instability, also due to the

contrast between the sea and land temperature;

- moderate shear supported the multicell organization of the convection;
- moderate medium troposphere winds (3000-5000m) supported continuous regeneration of cumulonimbus clouds in the same area (flanking line);
- divergence in the left-exit region of the jet stream at high levels enhanced the convergence in the low levels.

3. PRECIPITATION MEASUREMENTS

The main effects of the event were the very high rainfall rates and large amounts of precipitation accumulated in short time intervals in a restricted area of the region invested by the thunderstorms. This area, on the central-southern coastline of Veneto, is close to Venice and densely populated so that many people experienced the effects of floods in urban area. Figure11 shows the isolines of total daily precipitation measured for the day of 26 September 2007 by 161 ARPAV raingauges in Veneto.

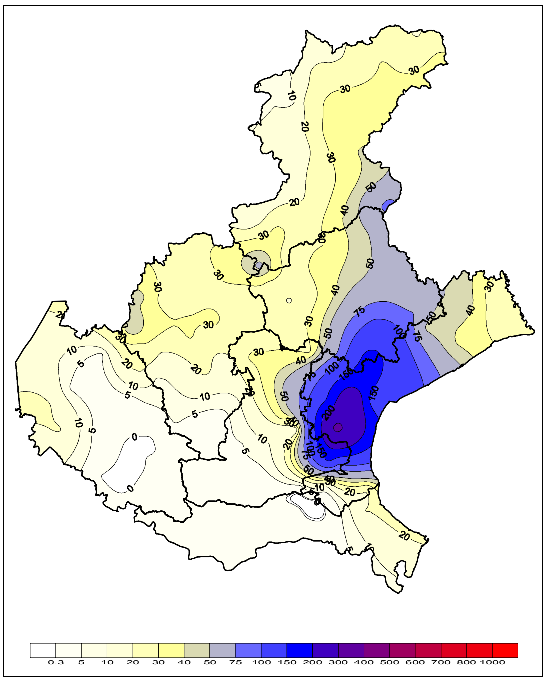

Fig. 11: Daily precipitation accumulation for 26 September 2007 for Veneto based on the 161 rain gauges ARPAV network.

The rainiest area is the central and southern part of Venice Province, close to the lagoon, where 5 rain gauges measured more than 160mm, with maximum values of 260.4mm (Mestre rain station) and 324.6mm (Valle Averto rain station). The extreme behaviour of the 26 September event is described in the maps of Figs. 12-13-14, where a composite map of the maximum 30 minutes, 1 hour and 6 hours precipitation accumulation recorded at each station is shown. Note that the maximum did not necessarily happen in the same time.

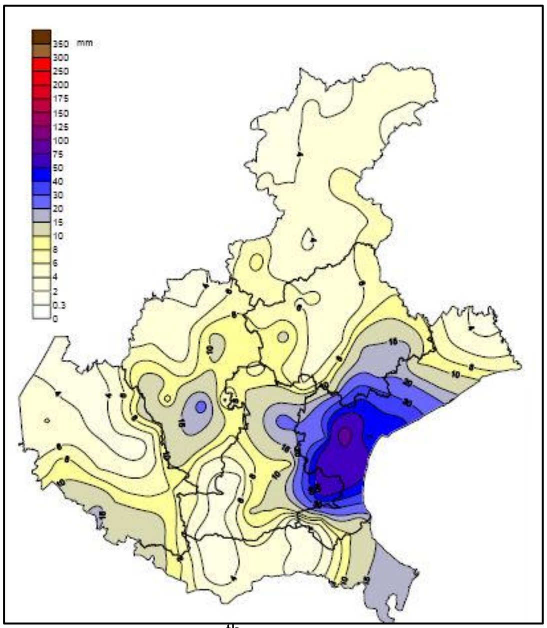

Fig.12: the 26th September composite map of the maximum 30 minutes precipitation accumulation recorded at each station: the highest value monitored is 91.2mm registered in Mestre rain station.

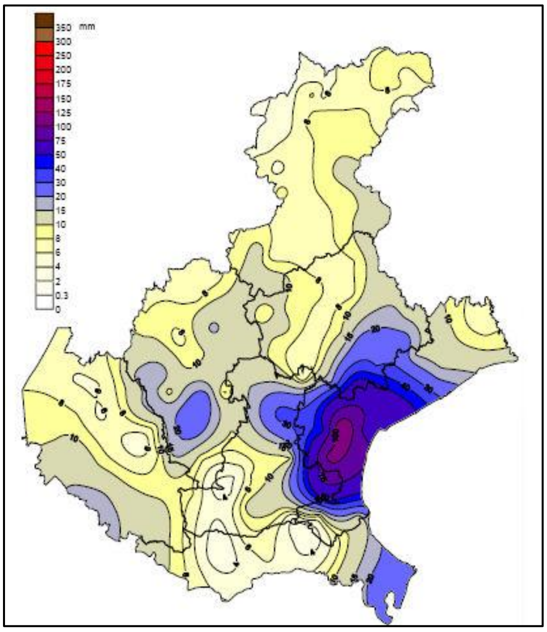

Fig.13: as in Fig.12 but for accumulation time of 1 hour: the highest value monitored is 126.6mm registered in Mestre rain station.

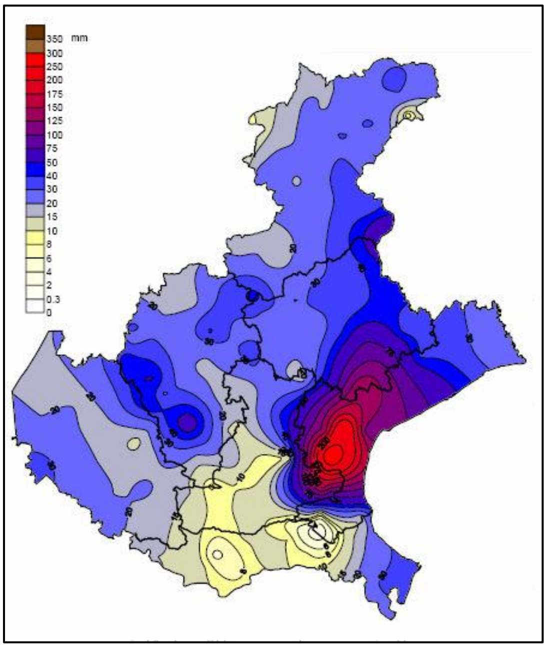

Fig.14: as in Fig.12 but for accumulation time of 6 hours: the highest value monitored is 301.4 mm registered in Valle Averto rain station.

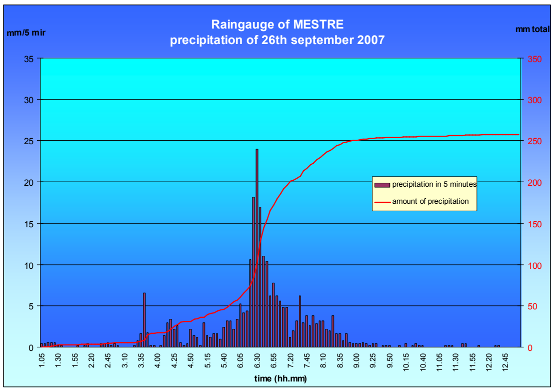

Fig.15: Time series of the rain gauge station Mestre from 01-13UTC 26 September 2007 for 5-minute intervals (histogram) and accumulated (red line).

Figures 15-16 show the precipitation for 26 September registered every 5 minutes and the corresponding cumulated value from 1am to 1pm in Mestre and Valle Averto stations: the first weak precipitation started shortly after 01UTC, and intensified at 04UTC; between 6.30 and 6.45UTC the total precipitation reached 100 mm, after half an hour the total increased already to 150 mm, while between 7.15UTC and 7.50UTC it reached 200mm. Around 9UTC the monitored values were for the Mestre and Valle Averto rain gauges 250 and 300 mm, respectively.

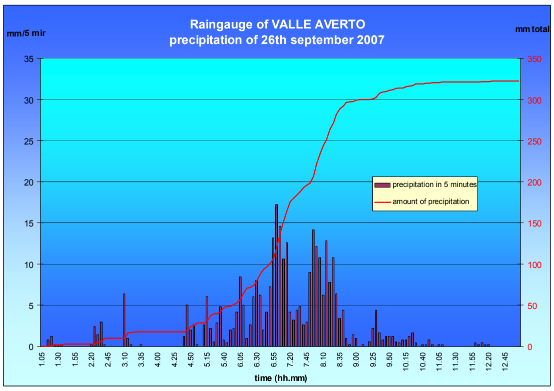

Fig.16: Time series of the rain gauge station Valle Averto from 01-13UTC 26 September 2007 for 5-minute intervals (histogram) and accumulated (red line).

Table 1 shows the maximum precipitation for various accumulation periods recorded by the two rain gauges with the highest values in the event; 100 years return time precipitation amounts (calculated with the Gumbel method) are indicated in parenthesis for historical stations of Mestre and Codevigo (1956-1996 period data set). Owing to availability of data, this comparison is possible only for 1 hour and longer time intervals.

	26/09/2007 [TR 100 yr]	26/09/2007 [TR 100 yr]
time	**Raingauge Mestre**	**Raingauge Valle Averto**
5 minutes	**24 mm**	**17.2 mm**
10 minutes	**42.2 mm**	**31.8 mm**
15 minutes	**59.2 mm**	**45 mm**
30 minutes	**91.2 mm**	**75.4 mm**
45 minutes	**111.4 mm**	**90.2 mm**
1 hour	**126.6 mm [60 mm]**	**106 mm [70 mm]**
3 hours	**201 mm [90 mm]**	**248.4 mm [100 mm]**
6 hours	**246.8 mm [120 mm]**	**301.4 mm [110 mm]**
12 hours	**257.6 mm [140 mm]**	**322.2 mm [130 mm]**

Table 1: maximum precipitation for different accumulation periods (5’ to 12 hours), recorded by the two rain gauges with the highest values for the event (Mestre and Valle Averto, Province of Venice). In parentheses the almost 100 years return time precipitation amounts are indicated.

Note that for this event for periods shorter or equal than an hour the Mestre rain gauge recorded the highest precipitation values with 24mm in 5 minutes, 91.2mm in 30 minutes and 126.6mm in 1 hour. For periods longer than one hour the Valle Averto rain gauge measured the highest values with 248.8mm in 3 hours, 301.4mm in 6 hours and 322.2mm in 12 hours.
The extremely high intensity of the events registered in this area are further evidenced by the comparison with the 100 years return time precipitation reference values in that for both stations the 1 to 12 hours maximum precipitation accumulation are two to three times higher than the reference values.

4. CONCLUSIONS

- The area surrounding Venice experienced an extremely strong precipitation event on the 26 September 2007;
- Within a few hours 40% of the total annual precipitation amount was recorded.
- Severe weather events frequently happen in September and October in the areas close to the Adriatic sea. The water basin with relative high temperatures plays a crucial role in the triggering and/or enhancement of convection.
- Key factors for the event have been studied thanks to the availability of a very detailed observing system (radar, satellite, dense network of automatic surface weather stations).
- To better understand the convective dynamics and its interplay with the mesoscale environment, further studies should be carried on, including numerical simulations with proper resolution and parametrisation.

EVALUATION OF A NEW LIGHTNING-PRODUCED NO_x PARAMETERIZATION FOR CLOUD-RESOLVING MODELS

Christelle Barthe[1,*], and Mary C. Barth[1]

[1] National Center for Atmospheric Research, Boulder, Colorado
[*] Now at: Laboratoire d'Aérologie, CNRS/Université Paul Sabatier, Toulouse, France

1 INTRODUCTION

Lightning flashes are considered to be a major source for nitrogen oxides ($NO_x = NO + NO_2$) in the upper troposphere. However, large uncertainties remain for the NO lightning production rate. Previous studies have examined different storms finding the lightning-produced NO_x (LNOx) source to be 33 to 665 moles NO per flash (*Schumann and Huntrieser*, 2007). An intercomparison of several cloud resolving chemistry models that simulated the same storm used an LNOx source anywhere from 36 to 495 moles NO per flash (*Barth et al.*, 2007b). One explanation for the large LNOx production range is the size of the volume in which the LNOx is placed. The objectives of this study are to introduce a new LNOx parameterization and to evaluate the sensitivity of the LNOx parameterization to the spatial distribution of the NO lightning source.

2 THE LNOx PARAMETERIZATION

The goal of this new parameterization is to predict the temporal and spatial distribution of individual lightning flashes without using an explicit electrical scheme.

When several convective cells are present, they may not all produce lightning flashes. An algorithm has been developed to detect potentially electrified cells. In order for lightning flashes to occur, the updraft speed must exceed 15 m s^{-1} which is similar to the 10-12 m s^{-1} threshold estimated by *Zipser and Lutz* (1994).

Unique to this parameterization is the prediction of lightning flash rate based on the fluxes of non-precipitating and precipitating ice. Through theoretical and observational investigations, *Blyth et al.* (2001) and *Deierling* (2006) have shown a strong correlation between the total flash rate and the precipitation and non-precipitation ice mass flux product. *Barthe et al.* (2007a) (hereinafter referred to as BDB07) showed that simulated ice mass flux product for the entire storm is quite similar to the ice mass flux product derived from radar observations. In this study, the parameterization is improved by calculating the non-precipitation and precipitation ice mass flux product for each convective cell. It is then associated to a total flash rate per cell:

$$F_{MF} = 1.13 \times 10^{-15} \times f_{np} \times f_p \qquad (1)$$

where F_{MF} is the total flash rate (fl. $\min^{-1}$) computed from the precipitation and non-precipitation ice mass fluxes, f_p (kg m s^{-1}) and f_{np} (kg s^{-1}) respectively. The 1.13×10^{-15} coefficient has been determined from comparisons between model results and lightning and radar data in two STERAO storms.

The flash triggering and propagation is based on *Ott et al.* (2007). Flashes can be triggered in the region defined by the convective core and by the region extending 10 km downwind of the maximum vertical velocity (C_{trig}). A 4 km radius cylinder C_{prop} where a lightning flash can propagate is centered on the randomly chosen point. The points of C_{prop} where the discharge can propagate are restricted to the region of the cloud where ice particles can be found since the hydrometeors that carry most of the electric charges are the ice particles (*Barthe and Pinty*, 2007).

The vertical distribution of the flash channel follows a bimodal distribution (*DeCaria et al.*, 2005). For each altitude level, the grid points reached by the lightning channel are chosen randomly among the possible points in C_{prop} to mimic the filamentary aspect of a lightning flash

(*Ott et al.*, 2007). The flash length is prescribed either to be constant or to have a lognormal distribution (*Defer et al.*, 2001).

The amount of NO produced per flash is assumed to depend on the flash length and on the altitude (*Wang et al.*, 1998):

$$n_{NO}(P) = a + bP \tag{2}$$

with n_{NO} the number of NO molecules produced per flash length (molecules m^{-1}), P the pressure (Pa). *Wang et al.* (1998) set the coefficients to $a = 0.34 \times 10^{21}$ and $b = 1.30 \times 10^{16}$.

The aim of this new parameterization is to reproduce the global morphology of a discharge to avoid the instantaneous dilution of the NO in the storm. This is important for the redistribution of the chemical species and for the comparison between model results and observations.

3 MODEL DESIGN

The LNOx parameterization described above has been implemented in the Weather Research and Forecasting (WRF) model. The WRF model solves the conservative (flux-form), nonhydrostatic compressible equations using a split-explicit time-integration method based on a 3^{rd} order Runge-Kutta scheme (*Wicker and Skamarock*, 2002). Scalar transport is integrated with the Runge-Kutta scheme using 5^{th} order (horizontal) and 3^{rd} order (vertical) upwind-biased advection operators. Transported scalars include water vapor, the different hydrometeor categories and the chemical species. The cloud microphysics is described by the single moment (bulk water) approach (*Lin et al.*, 1983). Mass mixing ratios of cloud water, rain, ice, snow, and graupel/hail are predicted. Cloud water and ice are monodispersed and rain, snow, and hail have prescribed inverse exponential size distributions. For the graupel/hail category, the intercept parameter of the exponential distribution is 4×10^4 m^{-4} and the density is 917 kg m^{-3} which corresponds to characteristics of hail particles.

The model also predicts the mixing ratios of methane, carbon monoxide, ozone, hydroxyl radical, hydroperoxy radical, methyl hydroperoxy radical, nitrogen dioxide (NO_2), nitric oxide (NO), nitric acid, hydrogen peroxide, methyl hydrogen peroxide, formaldehyde, formic acid, sulfur dioxide, ammonia, and aerosol sulfate. Details on the gas-phase and aqueous chemistry scheme can be found in *Barth et al.* (2007a).

4 CONTROL EXPERIMENT

The LNOx production in the 10 July 1996 STERAO storm has been widely studied (*Skamarock et al.*, 2003; *Barthe et al.*, 2007b; *Barth et al.*, 2007a,b) but large differences are found in LNOx estimates that range from 36 to 465 moles per flash (*Barth et al.*, 2007b). Thus, it is interesting to investigate the origin of such discrepancies. There is also a unique set of data for this storm: storm structure and kinematics from radar data, lightning flash characteristics and in-situ chemical species measurements from two aircraft (*Dye et al.*, 2000).

4.1 Initialization

The simulation performed is similar to those described by *Skamarock et al.* (2003) and *Barth et al.* (2007b). The environment was assumed to be homogeneous, thus a single profile was used for initialization. The initial profiles of the meteorological data were obtained from sonde and aircraft data (*Skamarock et al.*, 2000). The convection was initiated with three warm (3°C) bubbles oriented in a NW to SE line. WRF is configured to a 160 × 160 × 20 km^3 domain with 1 km horizontal resolution and 51 grid points in the vertical direction with a variable resolution beginning at 50 m at the surface and stretching to 1200 m at the top of the domain. The simulation was integrated at a 10 s time step for a 3-hour period. To keep the convection near the center of the model domain, the grid is moved at 1.5 m s^{-1} eastward and 5.5 m s^{-1} southward. While the observed storm lasted from 2130 to 0300, only the period 2315-0215 UTC is simulated. Initial mixing ratios of the chemical species follow *Barth et al.* (2007a).

The total flash rate is computed from the non-precipitation and precipitation ice mass flux product. The cloud-to-ground (CG) flash rate is considered null all along the simulation since very few CG flashes were observed in this storm. The lower and upper modes of the bimodal distribution correspond to the -15°C and the -50°C isotherms respectively. The flash length is assumed to be lognormal in the range 1 to 400 km. As in the observations (*Defer et al.*, 2001), the percentage of the short flashes (< 1 km) is set to 47%. Among these short flashes, 36% are considered as short duration flashes (< 1 ms). It is assumed that the short duration flashes produce the same amount of NO per flash length as a normal short flash. The original a and b parameters are multiplied by 5 to best match with observations. This simulation is called REF thereafter.

4.2 Results

Skamarock et al. (2000) and BDB07 showed that the dynamics and the microphysics structure of this storm simulated by WRF compare well to the radar data. Based on the storm structure and dynamics, three different stages have been identified in this storm: a multicell (0-80 min corresponding to 2315-0030 UTC), a transition (80-110 min corresponding to 0030-0105 UTC) and a supercell (110-180 min corresponding to 0105-0230 UTC).

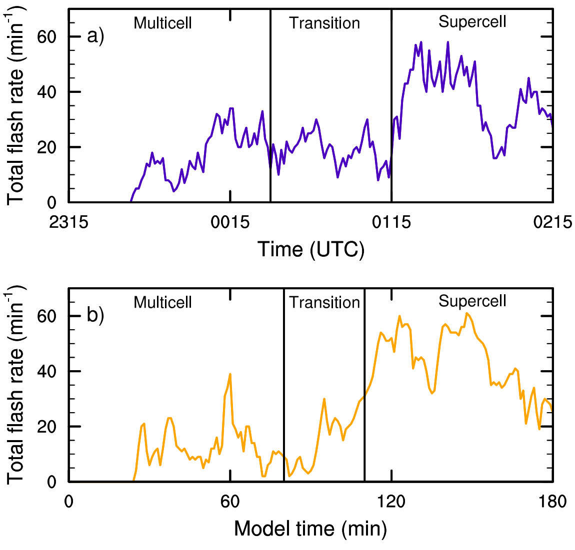

Figure 1: Temporal evolution of the total flash rate (a) from observations and (b) from the non-precipitation and precipitation ice mass flux product. The different stages of the storm are indicated both for the observed (a) and the simulated storms (b).

First, the flash rate computed from the ice mass fluxes is compared to observations (Figure 1). The number of flashes observed between 2340 and 0215 UTC was 3728, while that simulated was 4253 flashes. The mean flash rate during the multicell stage is 9.2 fl. min^{-1} for the simulated flash rate, which is similar to the 10.5 fl. min^{-1} observed. During the transition stage, the ice mass flux parameterization underestimates the mean flash rate (15.7 vs. 20.4 fl. min^{-1}) and overestimates it in the supercellular stage (43.8 vs. 33.8 fl. min^{-1}). There is a good agreement between the observed and simulated flash rate. The differences in the simulated and observed microphysics and dynamics features cause the differences in the observed and simulated mass flux and flash rate. Using observed flash rate when available is desirable but the modeled storm dynamics and physics must also reproduce the observations well.

Figure 2 shows horizontal cross sections of the NO mixing ratio during the different stages of the storm. During the multicell stage, LNOx production occurs mainly in the convective cores. Peaks of NO up to 3000 pmol mol^{-1} are colocated with the cells along a NW-SE axis (Fig. 2a). NO mixing ratios higher than 1000 pmol mol^{-1} are related to fresh LNOx production. Downwind of the convective cores (SE of the storm cores), NO values lower than 1000 pmol mol^{-1} are due to the transport and dilution of NO produced by lightning earlier in the simulation. At 5400 s, the flash rate is lower than in the multicell stage (Fig. 1) which can explain why peak NO values decrease (Fig. 2b). In the supercell stage, the flash rate is higher than in the two other stages leading to high values of the NO mixing ratio. NO mixing ratios up to 1000 pmol mol^{-1} can be found 100 km downwind of the updraft maximum. Even though the LNOx parameterization produces LNOx only in a small region in and downwind of the convective core, NO molecules are transported and diluted throughout the anvil.

To evaluate the simulated NO with aircraft observations, a transect across the anvil during the multicell stage of the storm is used. The transect is 10 km downwind of the SE cell at t = 1

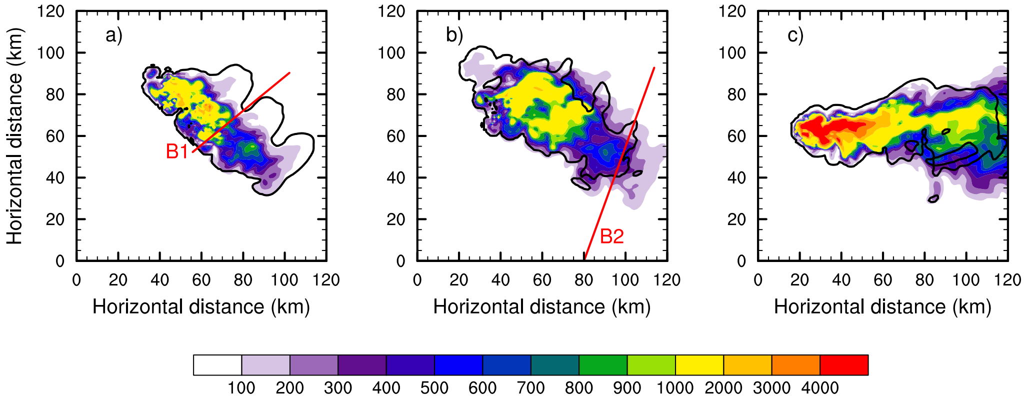

Figure 2: NO mixing ratio (in pmol mol^{-1}) at 11.5 km msl. The results are shown during the multicell (t = 3600 s; a), the transition (t = 5400 s; b) and the supercell (t = 7200 s; c) stages. Results are for the reference simulation (REF). The red line segments B1, and B2 correspond to the transects across the anvil 10 km downwind of the convective core at t = 3600 s (Fig.s 3) and to the transect across the anvil 60 km downwind of the convective core at t = 6000 s (Fig. 4) respectively.

h for the simulation (B1 in Fig. 2a). The simulated transect compares well with observations. A peak of 1800 pmol mol^{-1} is simulated and NO $>$ 500 pmol mol^{-1} extends over a distance of 20 km in the simulation. The distance over which the observed NO mixing ratio is higher than 500 pmol mol^{-1} is 30 km. Thus, WRF with its new LNOx parameterization is able to simulate peaks of NO $>$ 1000 pmol mol^{-1} in the region where lightning flashes are mostly triggered and propagate from.

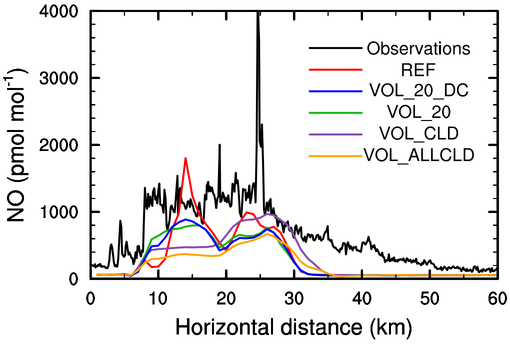

Figure 3: NO (pmol mol^{-1}) transects across the anvil during the multicell stage (t = 3600 s) at 11.6 km msl. The location of the transect B1 is shown in Fig. 2.

Downwind of the convective core, several regions of NO mixing ratio higher than 540 pmol mol^{-1} can be seen at the altitude of 11.5 km and up to 13 km which is in agreement with the UND Citation aircraft measurements (Fig. 4). In summary, the WRF model coupled with the new LNOx scheme gives results in good agreement with observations both near the convective cores and in the anvil.

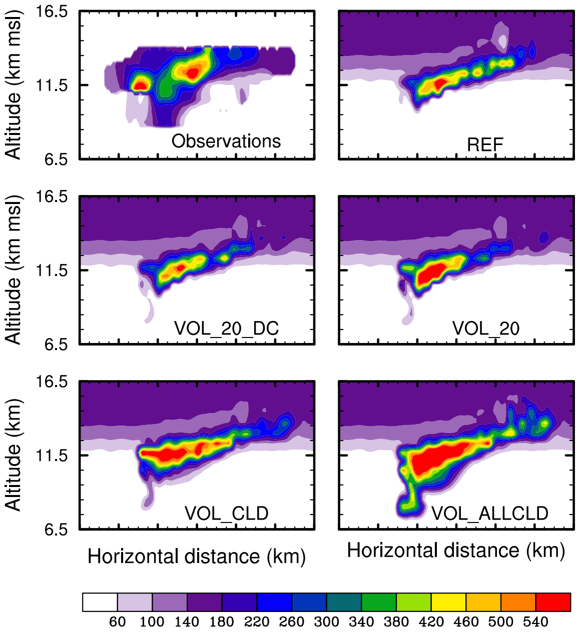

Figure 4: Vertical cross sections 60 km downwind of the convective core of the NO mixing ratio (pmol mol^{-1}) across the anvil at 6000 s. Observations are a composite from airbone measurements between 2316 and 0036 UTC (*Skamarock et al.*, 2003). The location of the transect B2 is shown on Fig. 2.

For this simulation, the mean production per flash is 121.3 moles of NO (7.3 × 10^{25} molecules

NO). This NO production is in the lower range of the estimates from the last 5 years as reported by *Schumann and Huntrieser* (2007).

5 IMPACT OF THE LNOx SPATIAL DISTRIBUTION

Previous parameterizations (*Pickering et al.*, 1998; *DeCaria et al.*, 2005) assumed that the NO molecules produced by the lightning flashes are instantly diluted over a large volume. This instant dilution does not produce the NO peaks observed by instruments onboard airplanes (*Barth et al.*, 2007b; *Ott et al.*, 2007).

Four sensitivity tests are compared to the REF simulation to investigate how the NO mixing ratio is affected by an instantaneous dilution of the LNOx source. First, the approach of *DeCaria et al.* (2005) is followed (VOL_20_DC). The NO molecules are distributed vertically following two modes in the volume where the radar reflectivity exceeds 20 dBZ. Second, the NO molecules are distributed uniformly in the 20 dBZ volume above the -15°C isotherm (VOL_20). Third, the LNOx is distributed over the entire cloud above the -15°C isotherm (*Pickering et al.*, 1998, VOL_CLD). In these first three simulations the LNOx source is only distributed in the detected electrified cell in proportion to the flash rate of each cell. Finally, the last simulation follows *Pickering et al.* (1998) but there is no cell identification (VOL_ALLCLD). In the REF, VOL_20_DC, VOL_20, VOL_CLD and VOL_ALLCLD, the NO molecules produced by a single flash are distributed over ∼20, 9400, 4300, 17700 and 23400 grid points on average, respectively.

To identify the impact of the bimodal distribution on the NO mixing ratio, the results of the VOL_20_DC and VOL_20 simulations are compared. In Figure 4, the cross section of NO mixing ratio across the anvil for VOL_20_DC is fairly similar to REF. The region of high NO mixing ratio is much larger in VOL_20 than in VOL_20_DC. Examining the VOL_CLD and VOL_ALLCLD results gives some insight on the impact of the cell identification. Three different spots of NO mixing ratio higher than 540 pmol mol^{-1} are visible for VOL_CLD, while in VOL_ALLCLD there is only one large region where the NO mixing ratio exceeds 540 pmol mol^{-1}. When the vertical distribution of the NO molecules is uniform (VOL_20, VOL_CLD, VOL_ALLCLD), the region with high NO mixing ratio across the anvil increases with the volume in which NO molecules are instantly diluted (e.g., compare VOL_20_DC to VOL_20). Furthermore, the larger volumetric distributions of the NO source do not allow the peaks in the transects to be well reproduced near the convective core where an enhancement in the NO mixing ratio is observed (Fig. 3).

6 CONCLUSIONS

A new LNOx parameterization has been developed for use in cloud resolving models. It has has three unique characteristics. First, a vertical velocity threshold is used to identify the cells that can produce lightning. Second, the flash rate is estimated from the non-precipitation and precipitation ice mass flux product, which has the benefit of containing information on both the dynamical and microphysical state of the storm. Third, the source location of the NO is filamentary using the approach of *Ott et al.* (2007). This parameterization has been tested on the 10 July 1996 STERAO storm. The predicted flash rate is in good agreement with observations for both the magnitude and trend. The distribution of the NO mixing ratio in the anvil, and the NO mixing ratio values near the convective core and in the anvil agree well with the aircraft measurements taken in the 10 July 1996 STERAO storm. The spatial placement of the LNOx source has been shown to be an important factor.

These sensitivity simulations can provide guidance for both future modeling and measurement strategies.

Acknowledgments

This research has been financially supported by NCAR's Advanced Study Program. The National Center for Atmospheric Research is operated by the University Corporation for Atmospheric Research under the sponsorship of the National Science Foundation.

BIBLIOGRAPHY

Barth, M. C., S.-W. Kim, W. C. Skamarock, A. L. Stuart, K. E. Pickering, and L. E. Ott, Simulations of the redistribution of formaldehyde, formic acid, and peroxides in the july 10, 1996 STERAO deep convection storm, *J. Geophys. Res.*, *112*(D13310), doi:10.1029/2006JD008046, 2007a.

Barth, M. C., et al., Cloud-scale model intercomparison of chemical constituent transport in deep convection, *Atmos. Chem. Phys.*, *7*, 4709–4731, 2007b.

Barthe, C., and J.-P. Pinty, Simulation of electrified storms with comparison of the charge structure and lightning efficiency, *J. Geophys. Res.*, *112*(D19204), doi:10.1029/2006JD008241, 2007.

Barthe, C., W. Deierling, and M. C. Barth, On the use of ice mass fluxes to estimate total lightning in cloud resolving models, *Eos Trans. AGU*, *88(52)*, Fall Meeting Suppl., Abstract AE43A–02, 2007a.

Barthe, C., J.-P. Pinty, and C. Mari, Lightning-produced NO_x in an explicit electrical scheme: a STERAO case study, *J. Geophys. Res.*, *112*(D04302), doi:10.1029/2006JD007402, 2007b.

Blyth, A. M., H. J. C. Jr., K. Driscoll, A. M. Gadian, and J. Latham, Determination of ice precipitation rates and thunderstorm anvil ice contents from satellite observations of lightning, *Atmospheric Research*, *59-60*, 217–229, 2001.

DeCaria, A. J., K. E. Pickering, G. L. Stenchikov, and L. E. Ott, Lightning-generated NO_x and its impact on tropospheric ozone production: A three-dimensional modeling study of a Stratosphere-Troposphere Experiment: Radiation, Aerosols and Ozone (STERAO-A) thunderstorm, *J. Geophys. Res.*, *110*, doi:10.1029/2004JD005,556, 2005.

Defer, E., P. Blanchet, C. Théry, P. Laroche, J. E. Dye, M. Venticinque, and K. L. Cummins, Lightning activity for the July 10, 1996, storm during the Stratosphere-Troposphere Experiment: Radiation, Aerosol, and Ozone-A (STERAO-A) experiment, *J. Geophys. Res.*, *106*(D10), 10,151–10,172, doi:10.1029/2000JD900849, 2001.

Deierling, W., The relationship between total lightning and ice fluxes, Ph.D. thesis, University of Alabama, Huntsville, Alabama, 2006.

Dye, J. E., et al., An overview of the Stratospheric-Tropospheric Experiment: Radiation, Aerosols, and Ozone (STERAO)-Deep Convection experiment with results for the July 10, 1996 storm, *J. Geophys. Res.*, *105*(D8), 10,023–10,045, doi:10.1029/1999JD901116, 2000.

Lin, Y.-L., R. D. Farley, and H. D. Orville, Bulk parameterization of the snow field in a cloud model, *J. Clim. Appl. Meteor.*, *22*, 1065–1092, 1983.

Ott, L. E., K. E. Pickering, G. Stenchikov, H. Huntrieser, and U. Schumann, Effects of lightning NO_x production during the 21 July European Lightning Nitrogen Oxides Project storm studied with a three-dimensional cloud-scale chemical transport model, *J. Geophys. Res.*, *112*, doi:1029/2006JD007,365, 2007.

Pickering, K. E., Y. Wang, W. K. Tao, C. Price, and J.-F. Müller, Vertical distributions of lightning NO_x for use in regional and global chemical transport models, *J. Geophys. Res.*, *103*(D23), 31,203–31,216, 1998.

Schumann, U., and H. Huntrieser, The global lightning-induced nitrogen oxides source, *Atmos. Chem. Phys.*, *7*, 3823–3907, 2007.

Skamarock, W. C., J. E. Dye, E. Defer, M. C. Barth, J. L. Stith, and B. A. Ridley, Observational- and modeling-based budget of lightning-produced NO_x in a continental thunderstorm, *J. Geophys. Res.*, *108*(10), doi:10.1029/2002JD002,163, 2003.

Skamarock, W. C., et al., Numerical simulations of the July 10 Stratospheric-Tropospheric Experiment: Radiation, Aerosol, and Ozone/Deep Convection Experiment convective system: Kinematics and transport, *J. Geophys. Res.*, *105*, 19,973–19,990, 2000.

Wang, C., and R. Prinn, On the roles of deep convection clouds in tropospheric chemistry, *J. Geophys. Res.*, *105*(D17), 3399–3418, 2000.

Wang, Y. A., W. DeSilva, G. C. Goldenbaum, and R. R. Dickerson, Nitric oxide production by simulated lightning : Dependance on current, energy and pressure, *J. Geophys. Res.*, *103*, 19,149–19,159, 1998.

Wicker, L. J., and W. C. Skamarock, Time-splitting methods for elastic models using forward time schemes, *Mon. Wea. Rev.*, *130*, 2088–2097, 2002.

Zhang, X., J. H. Helsdon, and R. D. Farley, Numerical modeling of lightning-produced NO_x using an explicit l ightning scheme: 2. Three-dimensional simulation and expanded chemistry, *J. Geophys. Res.*, *108*(D18), doi:10.1029/2002JD003,225, 2003.

Zipser, E. J., and K. R. Lutz, The vertical profile of radar reflectivity of convective cells: a strong indicator of storm intensity and lightning probability?, *Mon. Wea. Rev.*, *122*, 1751–1759, 1994.

EVALUATION OF ETA MODEL FORECASTS WITH PARAMETERIZED CONVECTIVE MOMENTUM FLUXES FOR A RAINY PERIOD IN SOUTHEAST BRAZIL

Paulo Roberto Bastos1 and Sin Chan Chou2

1.Brazilian Air Force,
2.National Institute for Space Research INPE
Cachoeira Paulista, SP, CP.01, Brazil
Email: chou@cptec.inpe.br

1.INTRODUCTION

The role of cumulus parameterization is to provide the subgrid effects of the convective fluxes to the grid environment, precipitation and evaporation. The mixing effects of heating and moistening fluxes cause stabilization of the environment. Convective parameterizations mass flux type can extend the mixing effects to other cloud properties. The momentum fluxes are generally excluded from the parameterization schemes, which are more focused on the thermodynamic variables. However, the presence of deep convective clouds produces strong impact on the environment winds by mixing momentum.

Objective of this work is to insert the convective momentum fluxes into the Eta Model (Black, 1994; Mesinger et al, 1988) which uses the Kain-Fritsch scheme (Kain, 2004) to parameterize convection. The forecast is evaluated for a case and for December 2006 which is a rainy month over the Southeastern part of Brazil.

2.METHODOLOGY

The Eta Model is run operationally to produce weather and climate forecasts over South America. In this work. the Eta Model was configured to run at high resolution, 5km and 50 layers, over the Southeast Brazil. The approximate domain is shown in Figure 1. The Eta Model uses the Kain-Fritsch cumulus parameterization scheme (Kain, 2004).

The momentum fluxes were parameterized following the mass flux basis applied to the heat fluxes of the scheme. The cloud base mass fluxes, entrainment and detrainment rate values were the same applied to the heat and moisture fluxes. Linear distribution of the fluxes from the cloud base toward the surface was applied. At the cloud top, the momentum fluxes also decreased linearly toward the layer immediately above. The momentum fluxes were only applied in the presence of deep convective clouds.

The runs used NCEP 12z analyses as initial conditions. The lateral boundary conditions were taken from the Eta-40km resolution runs, updated every 6 hours. Initial soil moisture was taken from monthly climatology.

The evaluations the Equitable Threat Score for the one month period for 24, 48 and 72-hours forecasts.

3.RESULTS

During the rainy season, the precipitation of the Southeast Brazil region receives contribution from organized deep convective systems, cold fronts and the South Atlantic Convergence Zone. The proximity to the coast favours the moisture load. A mountain range that runs along the coast provides additional ascent to the sea breeze.

The Kain-Fritsch scheme closure is based on the Convective Available Potential Energy. The closure reduces the initial CAPE by 90%. The inclusion of the convective momentum flux caused an additional stabilization to the atmosphere by providing more mixing. Figure 2 shows the difference between the 24-hour forecasts of CAPE from the run with momentum flux parameterization and original scheme. The reduction of CAPE is mostly located in the rainy regions where the scheme was activated. These forecasts are valid on the 05 December 2006, 1200 UTC.

The inclusion of the momentum flux clearly caused a change of the timing of the convection and of the position of the maximum centers of precipitation. In most of the cases, the new scheme moved ahead the position of the maximum precipitation. Figures 3a and 3b show the 24-h accumulated precipitation observed on the 5 December 2006. The major precipitation band is located to the north of the state of Sao Paulo, reaching the southern part of Rio de Janeiro and Minas Gerais states. The 24-h forecast of daily precipitation from the original version of the model (Eta/KF) (Figure 4a) shows the band to the southern part of Sao Paulo, and clearly lags behind the forecast from the version with convective momentum fluxes included (Eta/KFM) (Figure 4b).

The 2-m temperature difference between the 24-h forecasts from the two versions of the Eta Model (Figure 5) shows negative values in the raining area of the Eta/KFM version. This cooling is the result from the evaporation of precipitation which stabilizes the environmental boundary layer air. The 10-m wind difference between the 24-h forecasts of the two versions of the Eta Model shows increase in the magnitude of the winds near the raining region (Figure 6). This increase is enhanced near higher topography. The divergent winds near the raining area of the Eta/KFM suggest near-surface outflow produced from downdrafts of deep convective clouds.

The 1-month precipitation evaluation is based on the Equitable Threat Score (ETS) and Bias Score (BIAS) for 24-, 48- and 72-hour forecasts (Figure 7). The ETS of precipitation forecasts show no clear difference between the two versions of the scheme. The decrease of forecast performance at heavier precipitation rates is typical as extreme rain events are more difficult to forecast. The Eta Model with Kain-Fritsch scheme tends to show large precipitation bias over the region. The inclusion of the convective momentum fluxes increased the bias at heavier precipitation rates and at longer forecast lead hours, 48 and 72h forecasts. Adjustsments to the scheme parameters are still necessary.

4.CONCLUSIONS

Convective momentum fluxes were included to the Kain-Fristch convective scheme of the Eta Model. The impacts are clear on advancing the position of the precipitation maxima and therefore advancing the timing of the heavier precipitation events. The domain total amount does not show clear increase although the BIAS scores show values greater than 1 in most of evaluated precipitation thresholds. Additional stabilization to the environment is provided by the inclusion of the momentum fluxes. The evaluation period is being increased and change to some parameters is being carried out to adjust the scheme.

References

BLACK, T.L. The new NMC mesoscale Eta model: description and forecast examples. **Wea. Forecasting**, v. 9, n. 2, p. 265-278, 1994.

KAIN, J. S. The Kain–Fritsch Convective Parameterization: An Update. **Journal of Applied Meteorology**. v. 43, n. 1, p.170-181, 2004.

MESINGER, F.; JANJIC,Z.I.NICKOVIC, S.; GAVRILOV, D.; DEAVEN, D.G. The step-mountain coordinate: model description and performance for cases of Alpine lee cyclogenesis and for a case of an Appalachian redevelopment. **Monthly Weather Review**, v. 116, n. 7, p. 1493-1518, 1988.

Acknowledgments

This work is partially funded by the Sao Paulo Science Support Foundation (FAPESP) under the grant: 04/09469-0, and partially funded by CNPq under the grant AT 503883/2005-0.

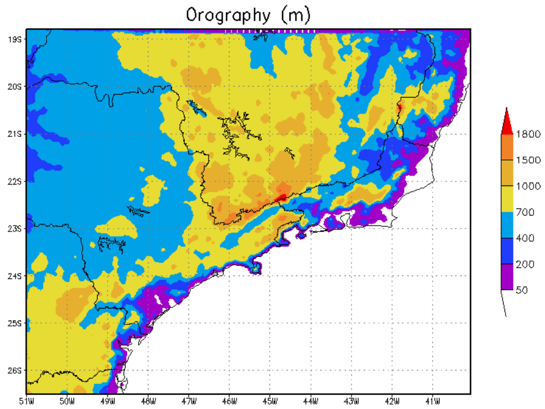

Figure 1 - Topograpjy (m) in the study domain.

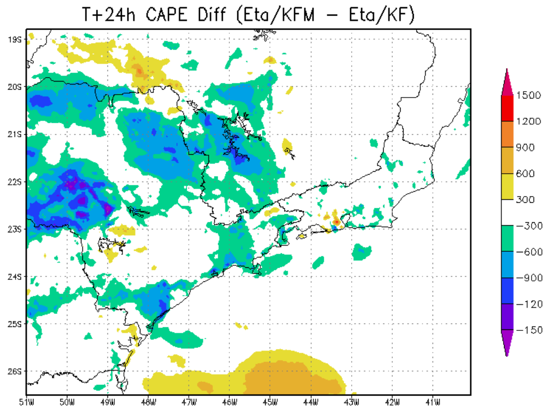

Figure 2 – Difference between CAPE from Eta/KF-momentum fluxes and Eta/KF-original.

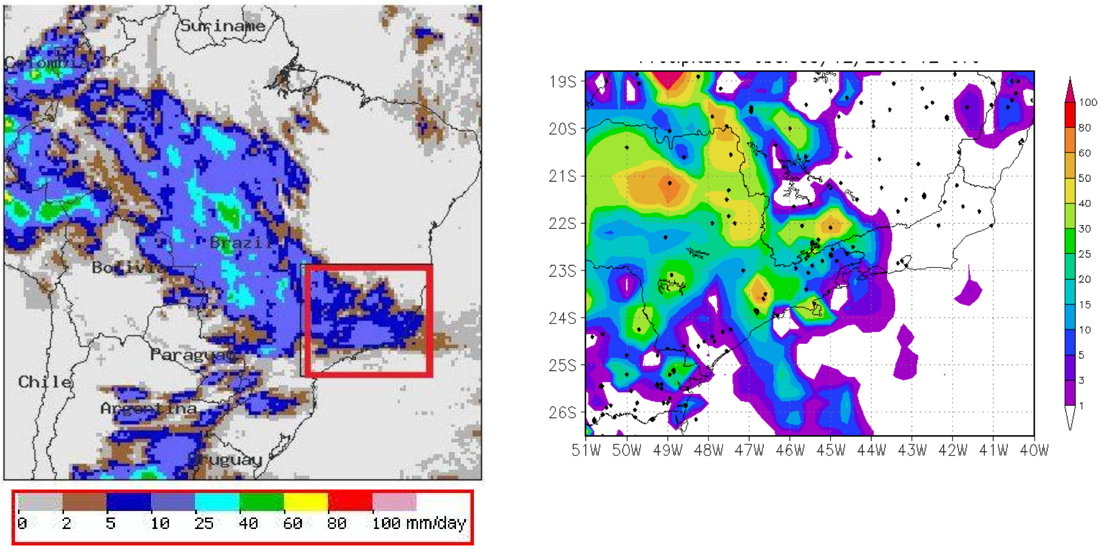

Figure 3 – Observed precipitation on 5 December 2006 (a) PERSIANN data (b) Surface observed data). Units are in meters.

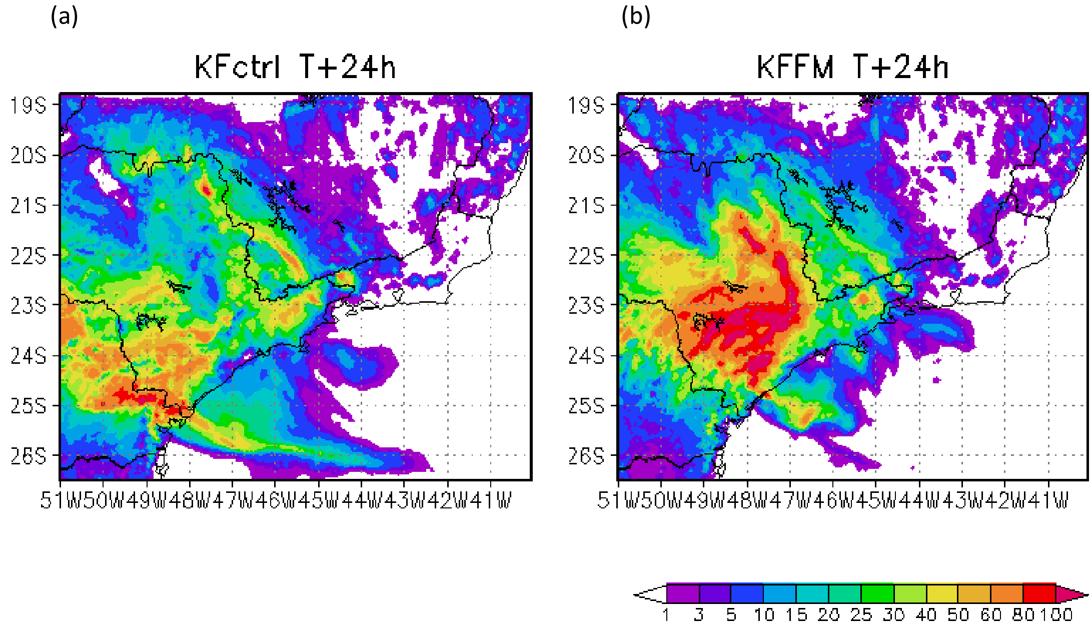

Figure 4 – 24-h precipitation forecast verifying on the 5 December 2006, 1200 UTC. Left: Eta with Kain-Fritsch scheme. Right: Eta with Kain-Fritsch and momentum fluxes. (units: mm accumulated in 24 hours)

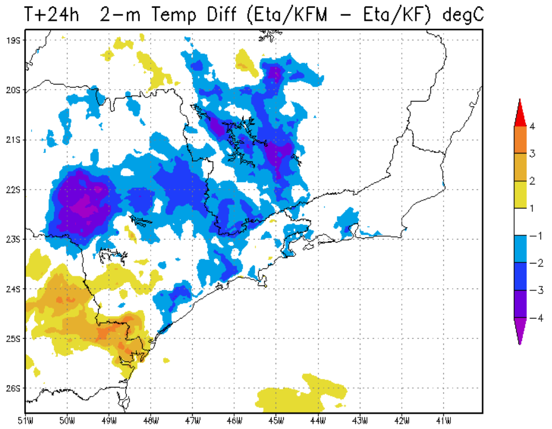

Figure 5 - 2-m temperature difference between the 24-h forecasts Eta/KF and Eta/KFM, verifying on 5 Dec 2006, 1200 UTC.

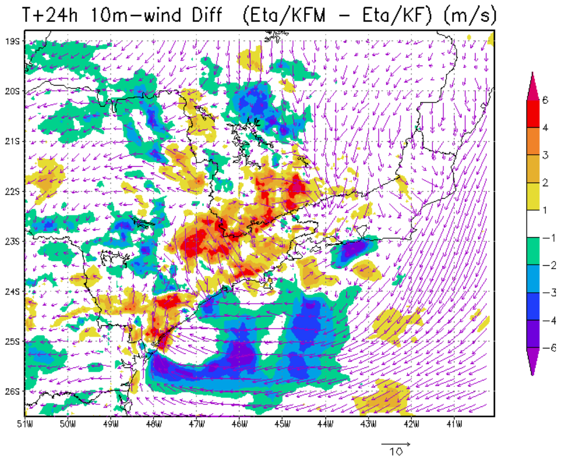

Figure 6 –24-h forecast of 10-meter wind from Eta/KFM, and difference between Eta/KF and Eta/KFM.

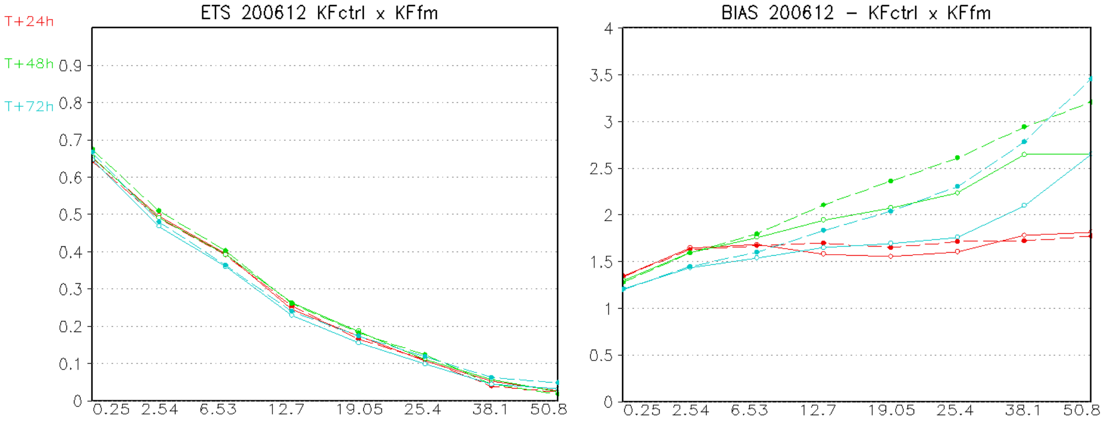

Figure 7 – Comparison of Eta/Kain-Fritsch (solid line) against Eta/Kain-Fritsch-Momentum (dashed line) precipitation forecasts for December 2006: (a) Equitable Threat Score and (b) Bias score of 24, 48 and 72-hour forecasts.

DOES TURBULENCE CONTROL THE RAIN FORMATION IN CONVECTIVE CLOUDS?

N. Benmoshe, A. Khain and M. Pinsky

Department of the Atmospheric Sciences, The Hebrew University of Jerusalem, Israel

Email: khain@vms.huji.ac.il

ABSTRACT

The spectral bin microphysics Hebrew University cloud model (HUCM) with spatial resolution of 50 m is used to simulate deep convective clouds under maritime and continental aerosol concentrations. The model calculates turbulent dissipation rate and the Taylor microscale Reynolds numbers in each grid points and at each time step. These values are used to choose the turbulent induced collision enhancement factor given in the form of lookup tables calculated in recent study by Pinsky et al (2008). High model resolution allowed us to represent "fractal" cloud structure resembling that of real clouds.

Parameters characterizing the turbulent intensity vary within a wide range, so that maximum values can significantly exceed the cloud averaged ones. It is shown that first raindrops tend to form in zones of intense turbulence. Turbulence accelerates the rain formation in cumulus clouds. Its role is especially important in clouds with continental aerosols, where the pure gravity collision kernels do not lead to the formation of raindrops by droplet collisions.

1. INTRODUCTION

Clouds are known as areas of enhanced turbulence as compared with the cloud-free atmosphere. At the same time there are only few in situ measurements of turbulence in clouds. The mean kinetic energy dissipation rate (hereafter, dissipation rate ε) in stratocumulus clouds (Sc) is estimated as $\varepsilon \sim 1 \text{ } to \text{ } 10 \text{ } cm^2 s^{-3}$ (Siebert et al. 2006), in small cumuli $\varepsilon \sim 50 \text{ } - 200 \text{ } cm^2 s^{-3}$ (MacPherson and Isaac, 1977; Mazin et al 1989; Pinsky and Khain 2003). The values of ε measured in deep cumulus clouds range from several hundred to $\sim 2 \cdot 10^3 \text{ } cm^2 s^{-3}$ (Panchev 1971; Weil et al 1993). Recent measurements of turbulent structure of the boundary layer using a helicopter (Siebert et al 2006) indicated a dramatic spatial imhomogeneity of ε: while the typical mean values of $\varepsilon \sim 1 - 10 \text{ } cm^2 s^{-3}$, in some zones of Sc clouds (possibly in the zones of imbedded convection) the values ε were measured as high as $1000 \text{ } cm^2 s^{-3}$. Specific feature of atmospheric turbulence is that it is characterized by enormously high values of the Taylor microscale Reynolds number $\mathrm{Re}_\lambda = 15 \tilde{w} \lambda / \nu$ ($\tilde{w}$ is the r.m.s. velocity fluctuation, and $\lambda = \tilde{w}(15\nu / \varepsilon)^{1/2}$ is the Taylor microscale, ν is the air viscosity). Using the data presented by Mazin et al (1989) the values of Re_λ were estimated as ranged from $\sim 5 \cdot 10^3$ in stratiform clouds to $\sim 2 \cdot 10^4$ in strong deep convective clouds. The high values of Re_λ indicate that atmospheric turbulence is highly intermittent, i.e. the values of the dissipation rate mentioned above represent some averages while the local values of dissipation rate vary dramatically at small scales. To our knowledge, there were no regular measurements of the spatial distribution of ε and Re_λ in cumulus clouds.

At the same time turbulence plays a very important role in cloud evolution affecting both cloud dynamics and microphysics. Turbulence responsible for process of cloud mixing with environment determining the rate of entrainment and detrainment at small scales and affects the buoyancy and droplet size (e.g., Grabowski, 1993, 1995; 2007; Andrejczuk, et al 2004, 2006). It is often assumed that the turbulence can affect droplet size distributions (hereafter, DSD) via homogeneous or inhomogeneous mixing affecting diffusion growth/evaporation of drops (e.g., Jensen and Baker, 1989). In many studies treating clouds as turbulent jets, the turbulent entrainment rate is assumed to be inversely proportional of the jet radius (e.g., Prupacher and Klett 1997). An increase in the entrainment of dry air leads to a dilution and a decrease in the cloud top height. Arakawa and Shubert (1974) used this dependence to determine the cloud top height in their convective parameterization scheme. In many cases turbulence plays the role of friction, leading to spatial smoothing of different quantities.

A special branch of the Cloud physics is related to turbulence effects on drop collisions. Historically this problem has arisen in relation to the necessity to explain the wide DSD (e.g., Brenguier and Chaumat, 2001) and the rain formation in clouds, which takes place faster than one could be obtain using pure gravity collision kernels (Jonas 1996). The main question was whether turbulence can serve as a plausible mechanism of the DSD broadening and rain formation acceleration or not. The first theoretical attempts to evaluate different aspects of turbulent effects on collisions of cloud droplets were performed by Arenberg (1939), Saffman and Turner (1956), Ivanovsky and Mazin (1960), Almeida (1976, 1979), Manton (1977); Grover and Pruppacher (1985), Reuter et al (1988) and others.

Different turbulent mechanisms were analyzed, and the conclusions reached were quite different. In some studies (e.g. Ivanovsky and Mazin 1960) the effect of turbulence on droplet collision rate was found much weaker than that of gravity, while Almeida reported a dramatic increase in the collision rate. The results obtained in many of these studies were successively criticized both from the point of view of the methods used in the investigations, and the validity of turbulent flow description (e.g., Pruppacher and Klett, 1997). Studies by Khain and Pinsky (1995), Pinsky and Khain (1996) reinforced the interest to turbulence effects on drop collisions. Vohl et al (1999) performed laboratory experiments indicating the increase in the collision rate between small rain drops and smallest cloud droplets in turbulent flow. The results obtained in the course of further theoretical and laboratory investigations, as well as in situ observations were overviewed by Pinsky et al (2000); Khain et al (2000, 2007); Vaillancourt and Yau (2000); Shaw (2003); Riemer and Wexler (2005). It seems that the fact that turbulence enhances the rate of droplet collisions can be considered as established. Pinsky and Khain (1998) presented arguments according to which turbulence increases collision rate between droplets and ice hydrometeors and well as between ice particles even to a larger degree than between cloud droplets.

Turbulence affects collisions by means of three main mechanisms: a) formation of turbulent-induced relative droplet velocity (so called transport effect); b) formation of turbulent-induced inhomogeneity of the droplet concentration, and c) increase in the efficiency of the droplet hydrodynamic interactions.

During recent few years a significant progress has been achieved in the understanding and of quantification of the turbulent effects. The quantitative results were obtained, especially as concerns collisions between small cloud droplets with radii below 25 μm (Pinsky et al, 2005, 2007, 2008; Franklin et al, 2005; 2007; Wang et al 2006, Xue et al, 2008). It should be noted that while in the earlier studies the estimations of the collision enhancement factor varied from zero to several hundred, there is an obvious convergence of the results in the recent studies of 2006-2008.

Evolution of droplet size distribution due to droplet collisions is usually calculated using the stochastic collision equation, which traditional form is:

$$\frac{d\langle f\rangle}{dt} = \int_0^{m/2} \langle f(m')\rangle\langle f(m-m')\rangle K\ (m-m')dm' \\ -\int_0^{\infty} \langle f(m)\rangle\langle f(m')\rangle K\ (m,m')dm' \qquad (1)$$

where $f(m)$ is the size distribution of droplets, m is the droplet mass, K is the collision kernel in a turbulent flow depending on the turbulent intensity, symbols < > denotes the volume averaging. The problems of the time and spatial averaging leading to (1) are still unresolved. However, in several studies (e.g., Falkovich et al 2000; Pinsky et al 1997; 2008; Xue et al, 2008) the effects of turbulence are taken into account in this equation by implementation of collision enhancement factors P_{kern} *and* P_{clast} as compared to pure gravity case. The factor P_{kern} describes the increase in the collision kernel due to increase in relative velocity between droplets (transport effect) and increase in the collision efficiency (the drop hydrodynamic interaction). The factor P_{clust} describes the effect of more frequent collisions in a turbulent flow because drop concentration inhomogeneity (the droplet clusters formation). As a result, the corrected equation for collisions is written as follows:

$$\frac{d\langle f\rangle}{dt} = \int_0^{m/2} \langle f(m')\rangle\langle f(m-m')\rangle P_{clust}P_{kern}K_g(m-m')dm' \\ -\int_0^{\infty} \langle f(m)\rangle\langle f(m')\rangle P_{clust}P_{kern}K_g(m,m')dm' \qquad (2)$$

where K_g is the gravitational collision kernel The factors P_{kern} *and* P_{clast} being known, this equation allows one to evaluate the effects of different turbulent mechanisms of the DSD evolution and rain formation.

Pinsky et al (2008) presented 11 tables of the collision kernel enhancement factor P_{kern} between cloud droplets calculated for a wide range of turbulent intensities: from those expected in stratiform clouds to those estimated for Cb. The tables have been calculated with the resolution of drop radii of $1\,\mu m$. According to results by Pinsky et al (2007a,b, 2008), the collision rate enhancement dramatically depends on the turbulent intensity, which is characterized by two main parameters: dissipation rate, ε and Reynolds number Re_{λ}. An example of a collision kernel enhancement factors calculated for conditions typical of different cloud types is presented in **Figure 1**. The tables are calculated with the accuracy close to that with which the gravity collision kernels are calculated. The utilization of these tables for DSD simulation evolution by solving the stochastic collision equation showed a significant acceleration of the formation of raindrops (Pinsky et al 2008). A parameterization of clustering effect described by the factor P_{clust} was presented by Pinsky et al (2008). It is a natural next step is to use these tables in numerical cloud models to investigate turbulent effects on precipitation formation.

Some preliminary comments are required as regards the suitability of different clouds models for investigations of turbulent structure of clouds and its effect on precipitation formation. There are problems of both dynamical and microphysical nature.

The first problem to describe turbulence in clouds adequately. This problem is closely related to the model resolution. It is clear that the finite-difference grid increment should be smaller than the external turbulent scale. At a very few exceptions where small warm microphysics (no ice) cumuli (Grabowski 2007) and boundary layer stratocumulus clouds (Stevens et al, 2005) are simulated with resolution of ~10 m, the most numerical cloud models have spatial resolution varying from several hundred meters to a few kilometers.

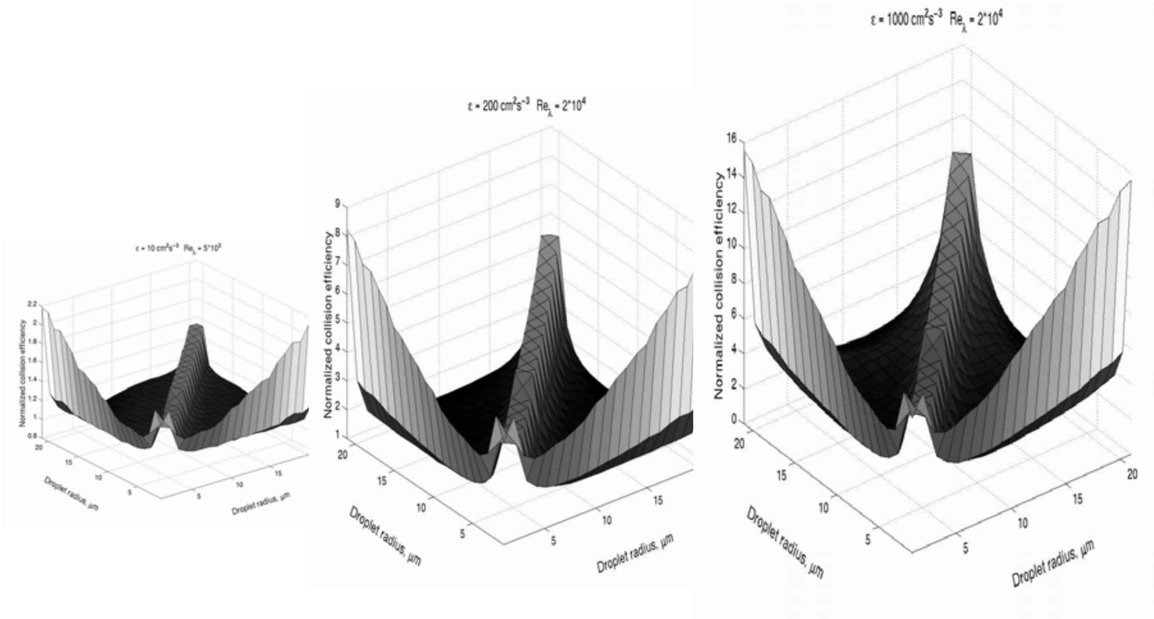

Figure 1. Mean normalized collision efficiency in turbulent flow for three cases: stratiform clouds ($\varepsilon = 0.001\ m^2s^{-3}$, $\mathrm{Re}_\lambda = 5\cdot 10^3$) (left panel), cumulus clouds ($\varepsilon = 0.02\ m^2s^{-3}$, $\mathrm{Re}_\lambda = 2\cdot 10^4$) (middle) and cumulonimbus ($\varepsilon = 0.1\ m^2s^{-3}$, $\mathrm{Re}_\lambda = 2\cdot 10^4$) (right panel).Pressure is equal to 1000mb.(After Pinsky et al, 2008)

It means that the scales resolved by the most models are significantly larger than the external turbulent scale. As a result, subgrid processes include not only turbulent scale motions, but also motions of not turbulent nature. In this case parameterization of subgrid fluxes using the K-theory is not well grounded. The terms responsible for the parameterization of turbulent viscosity and heat transfer play often the role of filters damping the motion of small wavelengths to prevent the numerical instability. The turbulent diffusion coefficient values in this case do not reflect real turbulent intensity in clouds.

The values of the dissipation rate are usually calculated within the boundary layer only (e.g. LES models used for simulation of stratocumulus clouds) within the frame of k-ε 1.5 order closure. The values of Re_λ are as a rule not calculated in the numerical models.

It is clear that the description of dynamical and microphysical processes should be consistent. For instance, the cloud structure is determined by the relationship between vertical air velocity and gravity sedimentation velocity. At the same time vertical velocities in numerical models depend on the model resolution, while the sedimentation velocities do not. The crude resolution leads to a decrease in the vertical velocity and underestimates the effect of the dry air entrainment (Khain et al 2004). As a result, the crude resolution leads to earlier raindrop fall, instead if their ascending within cloud updrafts. Thus, a decrease in the resolution accelerates the rain formation.

The second comment concerns the description of microphysical processes in the state-of the art cloud models. It is known that most cloud models have no problems to simulate precipitation without any turbulent effects included explicitly. Moreover, many models tend to overestimate the rain intensity (e.g., Lynn et al, 2005). The reason of this is that the raindrop formation process is crudely parameterized in these models. For instance, in large scale models any excess of humidity above the saturation value is immediately transferred to the precipitating mass. In more sophisticated bulk-parameterization models the rate of rain production is often assumed to be proportional to cloud drop mass content (e.g. Kessler 1969; Lin et al 1983). The later means that production of cloud drop mass is the sufficient condition for raindrop formation in such models. In more sophisticated two-moment bulk-parameterization schemes the rate autoconversion (raindrop formation by collisions of cloud droplets) is calculated using more comprehensive formulas, which take into account the droplet concentration. Parameters of these formulas are tuned to provide more or less reasonable rates of raindrop formation rates under a given shape of drop size distribution (DSD). Thus, the applicability of such models for investigation of turbulent effects on precipitation is questionable.

Spectral (bin) microphysics (hereafter SBM) cloud models calculate raindrop formation solving the stochastic collision equation for DSD (1) defined on a given mass grid containing, as a rule, several tens of mass bins (e.g., Khain et al, 2004, 2008). However, direct utilization of these models for investigation of turbulent effects also faces difficulties both of numerical and physical nature. It is known that SBM schemes face the problem of artificial spectrum broadening, when DSD obtained after a time step after diffusion growth of droplets and collisions is interpolated on the regular mass grid (see Khain et al 2000 for detail). As a result of such remapping, raindrops turn out in the bins corresponding to drop sizes larger than the maximum drop size of the DSD before the remapping. This numerically induced broadening accelerates the raindrop formation mimicking the effects of turbulence. The implementation of a new remapping scheme (Khain et al 2008) decreased significantly the artificial DSD broadening, opening the way to investigate the physical mechanisms of the DSD broadening.

To our knowledge there are only a few studies (e.g., Khain et al 2004, 2008), in which an attempt to account for the turbulence effects on collision has been made using the SBM cloud model. In these studies, however, the collision rate enhancement factor does vary in space and with time, so that neither the spatial nor the time variability of turbulence intensity was taken into account. Hence, in spite of the fact that the state-of-the art theoretical studies indicate the substantial effect of turbulence on cloud particle collisions (which for conditions typical of convective clouds significantly exceeds the effect of gravity), these effects were not taken into account in cloud models.

In this study the following questions are addressed:

a) How does cloud turbulence look like?

b) What are characteristic parameters of the turbulent structure of cumulus clouds?

c) What is the effect of turbulence on cloud microphysical structure and rain drop formation in cumulus clouds?

d) To what extent do the turbulence effects depend on the cloud type (continental vs. maritime)?

e) How does the cloud microphysical structure affects the cloud turbulence?

It is clear that such questions cannot be answered within the frame of one paper. In the study we present preliminary results, which will be elaborated in deeper details in future.

2. THE MODEL AND SIMULATION DESIGN

2.1 The model update

An updated version of the spectral (bin) microphysics Hebrew University Cloud Model (HUCM) (Khain 2004, 2008) has been used. The HUCM is 2-D non-hydrostatic non-elastic model in the z-coordinate framework, in which the vorticity and the stream function are used as computational variables. The model microphysics is based on the solution of the equation system for size distribution functions of cloud hydrometeors of seven types (water drops, plate-, columnar-, and branch-like ice crystals, aggregates, graupel, and hail/frozen drops) as well as for the size distribution function of aerosol particles playing the role of cloud condensational nuclei (CCN). The later allows simulation of both maritime and continental clouds with different aerosol loadings and distributions. Each size distribution function contains 43 doubling mass bins. The model is described in detail by Khain et al (2004, 2008), so that we focus on description of new features of the model. Note only that the gravitational water-water collision kernel K_g was taken from the study by Pinsky et al (2001). We consider these values of K_g as very accurate ones. The collision kernels increase with height according to Pinsky et al (2001) and Khain et al.(2001). According to Pinsky et al (2007) collision enhancement factor depends on height only slightly. Thus, the turbulent collision kernels increase with height with nearly the same rate as the gravitational ones. To simulate turbulent cloud structure adequately and to calculate turbulent parameters the following improvements have been done. First, *the model resolution has been improved*, so the resolution of 50 m in both horizontal and the vertical direction is used instead of the standard model resolution of 250 m x 125m. Such spatial finite-difference grid increment is located within the inertial turbulence sub range. Second, *turbulent diffusion coefficients and the dissipation rate* ε *have been calculated.* In spite of the fact the grid resolution was chosen within the inertial turbulent range, the techniques of the scale separation between turbulent fluctuations and the time dependent mean flow varying in space is not developed. Even an extremely high resolution LES models use the k-ε closure (the 1.5 order closure) to calculate the turbulent fluxes (Stevens et al, 2005). In this study we use the same approach, according to which the turbulence kinetic energy E in each grid point using the well known equation was calculated as (e.g., Skamarock et al., 2005):

$$\frac{\partial E}{\partial t}+U\frac{\partial E}{\partial x}+W\frac{\partial E}{\partial z}=$$
$$K\left[2\left(\frac{\partial U}{\partial x}\right)^2+2\left(\frac{\partial W}{\partial z}\right)^2+2\left(\frac{\partial U}{\partial z}+\frac{\partial W}{\partial x}\right)^2\right]$$
$$-\alpha K N^2-\varepsilon \qquad (3)$$

where U and W is the wind velocity components in the x and the z-directions, respectively. In (3) $\alpha=\mathrm{Pr}^{-1}=3$ (Pr is the turbulent Prandtl number), $N^2=\frac{g}{\theta}\frac{\partial\theta}{\partial z}$ is the square of the Brunt-Vaisala frequency (N^2 can be positive or negative depending on the stratification), θ is the potential temperature, g is the gravity acceleration. K is the coefficient of turbulent viscosity (hereafter, turbulent coefficient). According to similarity theory (e.g., Monin and Yaglom 1975)

$$K=C_k l E^{0.5} \qquad (4)$$

$$\varepsilon=\frac{CE^{3/2}}{l}, \qquad (5)$$

where the mixing length l is calculated as (Skamarock et al., 2005)

$$l=\begin{cases}\sqrt{\Delta x\Delta z} & if \quad N^2\le 0\\ \min\left(\sqrt{\Delta x\Delta z},0.76\frac{\sqrt{E}}{N}\right) & if \quad N^2\rangle 0\end{cases} \qquad (6)$$

$C_k=0.2$ and $C=1.9C_k+\frac{(0.93-1.9C_k)l}{\sqrt{\Delta x\Delta z}}$

For utilization of tables of turbulent collision enhancement factors, the value of Re_λ should be calculated. Note that the turbulence kinetic energy E in (2) is the measure of intensity of subgrid turbulence with scales below 50 m. At the same time the total turbulent kinetic energy TKE_{tot} should be determined by the external turbulent scale L (Pope 2000, pp. 234):

$$TKE_{tot}=(\varepsilon L)^{2/3} \qquad (7)$$

To determine the external turbulent scale we use the results of study by Elperin et al.

(2002), according to which an effect of self-organization in a turbulent flow under convective conditions leads to the energy separation between large scale "convective" structures (e.g., large eddies) and small scale turbulence. In our case the large scale is the cloud size calculated as

$$L_{cl} = 1/\left(\frac{1}{L_x^2} + \frac{1}{L_z^2}\right)^{1/2} \qquad (8)$$

where L_x *and* L_z are the cloud sizes in the horizontal and the vertical directions, respectively. The external turbulent scale was estimated as $L \approx L_{cl}/10$ (Elperin et al., 2002). The characteristic turbulent velocity fluctuation u' can be evaluated as

$$u' = \sqrt{\frac{1}{2}TKE_{tot}}\ , \qquad (9)$$

The Reynolds number Re_λ required for the determination of the collision enhancement factor was calculated using the expression:

$$\mathrm{Re}_\lambda = \frac{u'\lambda}{\nu}\,, \qquad (10)$$

where λ is the Taylor microscale. The value of λ was calculated as (Monin and Yaglom 1975)

$$\lambda = u'\sqrt{\frac{15\nu}{\varepsilon}} \qquad (11)$$

The expressions presented above allow calculation of ε and Re_λ needed to evaluate collision enhancement factor.

The most important model improvement was the *utilization of turbulent collision kernels*. Pinsky et al (2008) presented eleven tables of the collision rate enhancement factors P_{kern} due to increase in the collision efficiency and increase in the relative velocity. The tables are presented for different values of dissipation rates and the Reynolds numbers, corresponding to different turbulent intensities. Each table contains values for collision rate enhancement for cloud droplets with radii ranged from 1 to 21 μm.

Many theoretical studies are dedicated to the clustering of inertial particles in a turbulent medium and its effect on the collision rate. Most results, however, were obtained for conditions far from those in atmospheric clouds, for instance, the sedimentation effect was neglected, turbulent flows were assumed frozen, Reynolds numbers were several orders of magnitude smaller than those typical of atmospheric turbulence. Because of these reasons the application of the results to atmospheric clouds is questionable (this problem is discussed in detail by Khain et al 2007). In spite of the fact that in recent DNS studies (Wang et al, 2005a,b; Franklin et al, 2005, 2007) differential droplet sedimentation is taken into account, utilization of small Reynolds numbers in DNS (50-100 in DNS versus 10^4 in real clouds) results in too low Lagrangian accelerations. The latter overestimates the clustering effect (the clustering is caused by velocity shears, but accelerations and sedimentation hinder or destroy it (see Chun et al 2005; Khain et al 2007; Franklin et al. 2007). In case droplets are of different size both factors foster decrease the rate of concentration inhomogeneity of large cloud droplets and raindrops.

As regards cloud droplets, the DNS provide collision enhancement factors of the same order of magnitude as the simple parameterization formula derived by Pinsky and Khain (2003) who derived the empirical dependence of the clustering rate on the Stokes number *St*. The dependence has been obtained as the result of statistical analysis of a long series of drop arrival times measured in situ by Fast FFSP in ~60 cumulus clouds. The parameterization formula is as follows:

$$\frac{\left\langle N'^2\right\rangle^{1/2}}{\left\langle N\right\rangle} = F(St) = 0.577\cdot St^{0.317}\,, \qquad (12)$$

where $\langle N\rangle$ is the mean droplet concentration, $\left\langle N'^2\right\rangle^{1/2}$ is the r.m.s. of the concentration fluctuations, the St number is normally below $0.1-0.2$ for cloud droplets. The value $\langle N_1 N_2 \rangle$ that appears in the stochastic collision equation can be written as $\langle N_1 N_2 \rangle = \langle N_1 \rangle \langle N_2 \rangle + R \langle N_1^{'2} \rangle^{1/2} \langle N_2^{'2} \rangle^{1/2}$ (here N_1 and N_2 are concentrations of droplets of different radii). One can expect a strong spatial correlation between concentration fluctuations of cloud droplets of different size (the correlation coefficient was taken $R=1$), because the zones of positive and negative drop velocity flux divergence coincide for small droplets (Pinsky et al 1999b). Using this simplified assumption we have introduced the collision enhancement factor P_{clust} caused by the clustering effect, which is characterized by the Stokes numbers St_1 and St_2 as follows:

$$P_{clust}(St_1, St_2) = \frac{\langle N_1 N_2 \rangle}{\langle N_1 \rangle \langle N_2 \rangle} =$$
$$= 1 + F(St_1) F(St_2) = 1 + 0.333 \cdot (St_1 St_2)^{0.317} \quad (13)$$

The factor $P_{clust}(St_1, St_2)$ depends on both the droplet sizes and on the intensity of turbulence (on the dissipation rate), and usually does not exceed 1.3. This factor is used in the stochastic collision equation. In spite of the fact that formula (13) is based on some limiting assumptions (resulting from the limitations in the observational data used), we believe that it produces reasonable evaluation of the clustering effect as compared to other factors (i.e. the increase in the collision kernel) affecting DSD formation. The total enhancement factor was calculated as

$$P_{tot} = P_{kern} P_{clast} \quad (14)$$

The results show that in Cu and Cb clouds P_{tot} is several times larger than one for most droplet pairs. *It means that turbulence is the dominating factor as regards droplet collisions and formation of rain drops* at least in cumulus clouds. In the simulations the collision enhancement factor P_{tot} was applied for cloud droplets with radii $\le 21 \mu m$. This upper size was chosen because of many uncertainties as regards turbulence effects on collision of larger droplets in spite of that fact that the laboratory experiments do indicate the collision enhancement between small raindrops and small cloud droplets (Vohl et al, 1999). Besides, no effects of turbulence on water –ice and ice-ice collisions are taken into account. Thus, the role of turbulence on clouds is underestimated in the present study.

2.2. Simulations

For the simulations the thermodynamical conditions typical of Amazon region during the LBA-SMOCC campaign were chosen (Andreae et al 2004; Khain et al 2008). Sounding for these conditions is presented in these studies. Clouds were triggered by a short temperature pulse located in near the surface in the middle of the computational area which contained 257 x 257 grid points. Th*e initial* (at t=0) Cloud Condensational Nuclei (CCN) size distribution is calculated (see Khain et al 2000) using the empirical dependence

$$N = N_o S_1^k , \quad (15)$$

where N is the concentration of activated AP (nucleated droplets) at the supersaturation S_1 (in %) with respect to water, N_o and k are the measured constants. In all simulations k=0.72. At t>0 the prognostic equation for the size distribution of non-activated AP is solved. Using the value of S_1 calculated at each time step, the critical AP radius is calculated according to the Kohler theory. The APs with the radii exceeding the critical value are activated and new droplets are nucleated. The corresponding bins of the CCN size distributions become empty.

In the simulation representing "green-ocean" clouds developing in clean air the values of N_o were chosen equal to 200 cm^{-3} (experiment E-200). For comparison a simulation with typical continental aerosol concentration has been carried out with N_O= 2000 cm^{-3} (experiment E-2000). The results are compared to those obtained in cases when only gravity kernels were used. These corresponding simulations will be referred to as E-200_grav, and E-2000_grav, respectively.

3. TURBULENT CLOUD STRUCTURE AND ITS TIME EVOLUTION

Figure 2 shows the vertical velocities, cloud droplet concentration and cloud drop mass at several height levels in simulation E-2000 at t=1600s. One can see significant variability of the values in the horizontal direction indicating the formation of several convective bubbles. This structure differs dramatically from that simulated by models with cruder resolution and larger values of turbulent coefficients (Khain et al, 2005, 2008; Lynn et al, 2005). The cloud structure obtained in simulations of 350 m x 125m at the development stage is characterized, as a rule, by existence of one maximum of the variables located at the cloud axis. It means that the spatial structure of cloud simulated with the high resolution becomes highly imhomogeneous with significant fluctuations in droplet concentration, CWC, RWC and other parameters. The vertical velocity maximum in the simulation reaches 15 m/s, which is typical value for continental clouds of such type.

Note that the maximum vertical velocity in the E-2000 is significantly (by ~5 m/s) higher than in E-200 (not shown). This effect reflects the convection invigoration caused by higher release of latent heat in the course of cloud droplet growth by diffusion and ice deposition in case of high aerosol concentration (Khain et al 2005, 2008). However, the absolute difference between the maxima of the vertical velocity is larger in the present simulations as compared to those in Khain et al (2008), supposedly because the higher resolution.

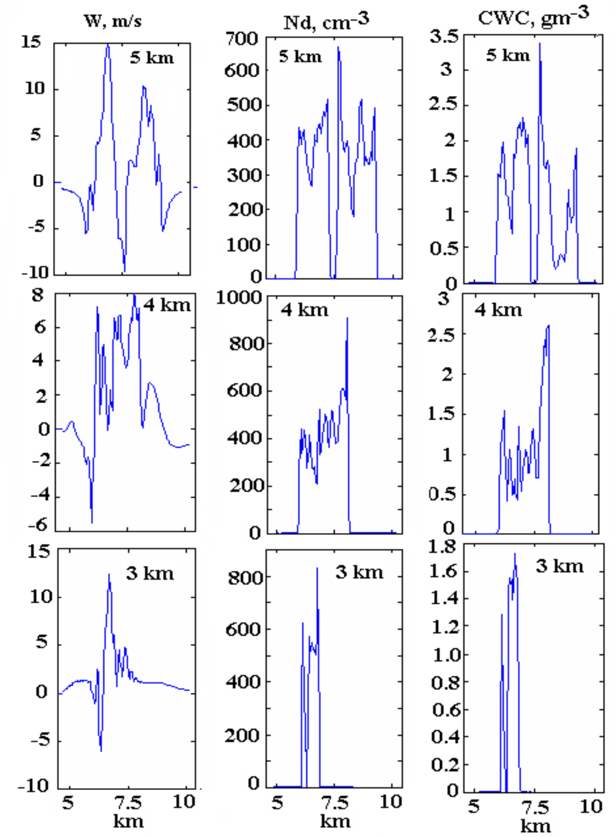

Figure 2 *The vertical velocities, cloud droplet concentration and cloud drop content at several height levels in simulation E-2000 at t=1600s.*

Figure 3 shows the fields of TKE_{tot}, the dissipation rate ε, and Re_λ in the simulations E-200 and E-2000 at t=45 min. One can see that the turbulent values vary within the wide ranges indicating high inhomogeneity of the turbulent structure in clouds. The averaged values of ε correspond to the measured values discussed above. It is interesting that the calculated values of Re_λ agree well with the evaluations of Re_λ used by Pinsky et al (2008) for calculation of the collision enhancement factors. We would like to stress several points following from Figure 3: a) the maximum values of turbulent parameters significantly exceed the cloud averaged values; and b) there is a high correlation between the fields of the turbulent parameters. It means that the maximum values of ε and Re_λ are located in the same cloud volumes. The latter fact is of significant importance, because the collision enhancement rate increases both with the dissipation rate and Re_λ.

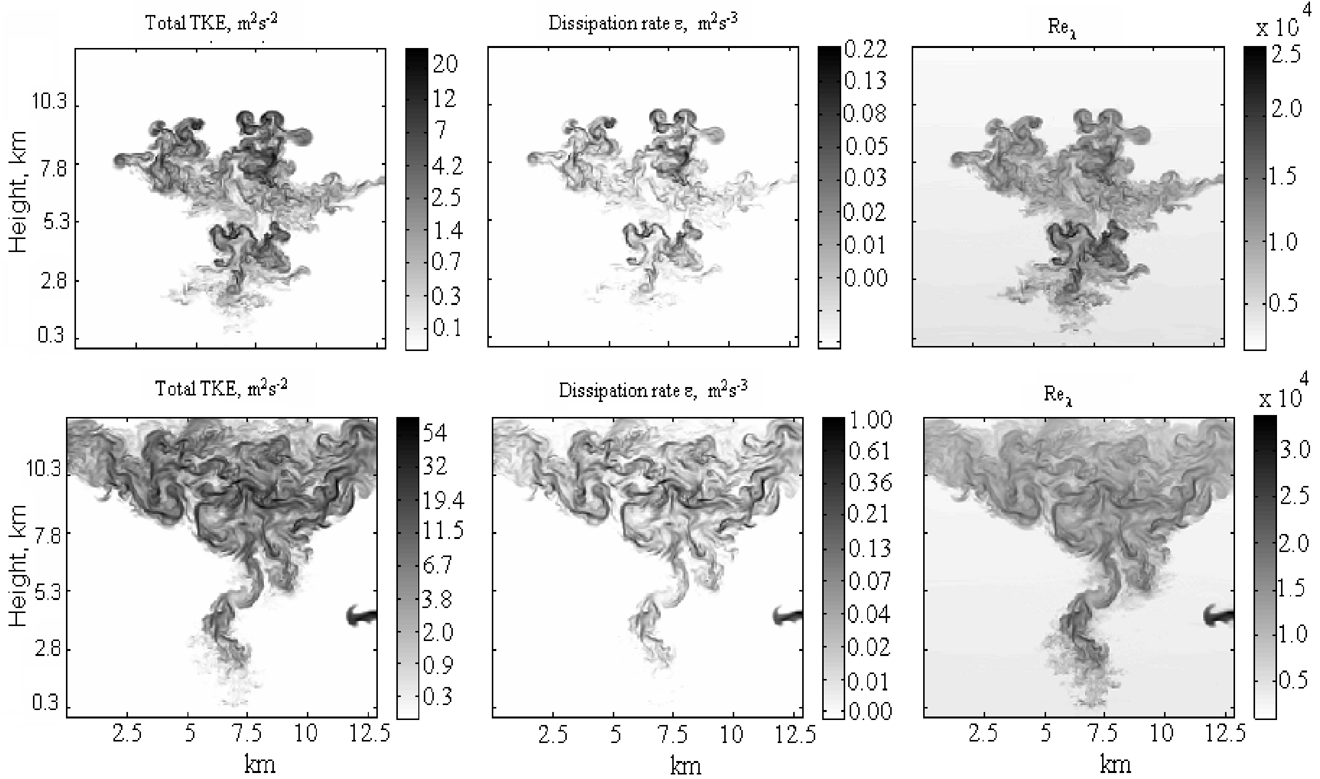

Figure 3 *The fields of the* TKE_{tot}*, the dissipation rate, and* Re_λ *in the simulations E-200 (upper panels) and E-2000 (lower panels) at t=45 min.*

Thus, the results indicate nonlinearity of the raindrop formation process, i.e. under other parameters being similar, the formation of the first raindrops in zones of intense turbulence are much more probable that in the others.

The second important point that can be seen in Figure 3 is that turbulence in the cloud developing in the continental surrounding (high aerosol concentration) is much more intense. While maximum values of TKE_{tot}, ε and Re_λ are $25\,m^2s^{-2}$, to $0.2\,m^2s^{-3}$, and $2.5\cdot 10^4$ in microphysically maritime clouds, in microphysically continental cloud these values are $70\,m^2s^{-2}$, 1.0 m^2s^{-3} and $3\cdot 10^4$.

Besides, the area of the highly turbuliezed air is larger in the continental cloud. Thus, under similar thermodynamic conditions, the continental cloud is much more turbulent.

Figure 4 shows the time dependence of cloud averaged values of TKE_{tot}, ε and Re_λ in the simulations of maritime (E200) and continental (E2000) clouds. One can see again that averaged values are much lower than the maximum ones. Note that polluted clouds are much more turbulent. The reasons of this will be discussed in more detail below. We notice only that aerosols increase the turbulence intensity of clouds, indicating the existence of the strong relationship between microphysical and dynamical cloud properties.

4. EFFECTS OF TURBULENCE ON MICROPHYSICS, RAINDROP FORMATION AND PRECIPITATION

Figs. 5 and 6 show effects of turbulence on the cloud microphysical structure by comparing cloud properties in simulations of the maritime (E-200-grav and E-200) and the continental (E-2000-grav and E-2000)

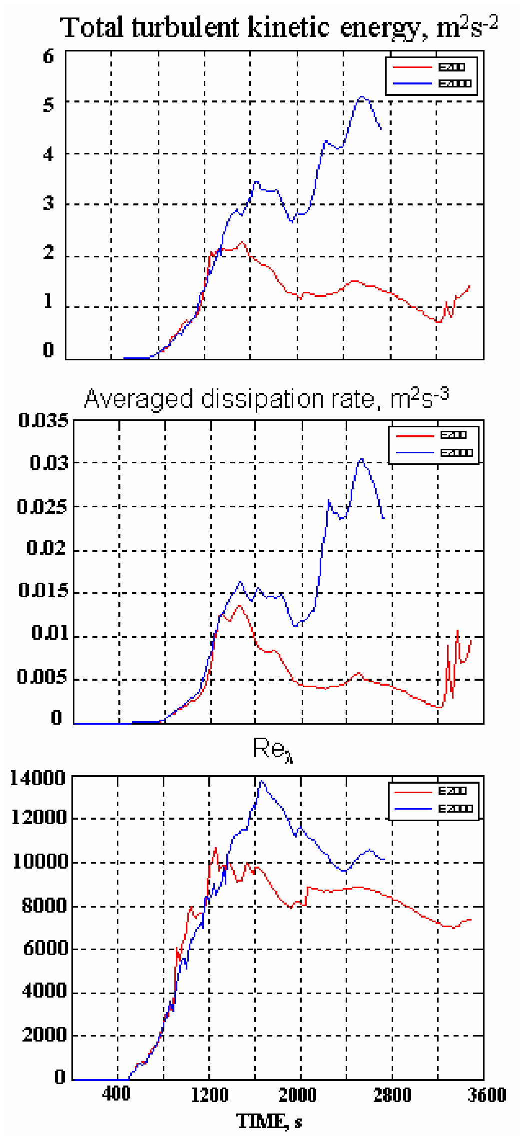

Figure 4 *Time dependence of cloud averaged values of* TKE_{tot}, ε *and* Re_{λ} *in the simulations of maritime (E200) and continental (E2000) clouds.*

clouds, respectively. One can see that increase in the collision rate between cloud droplets slightly decreases the maximum values CWC and the total ice content. The latter is related to the fact that turbulence accelerates the formation of

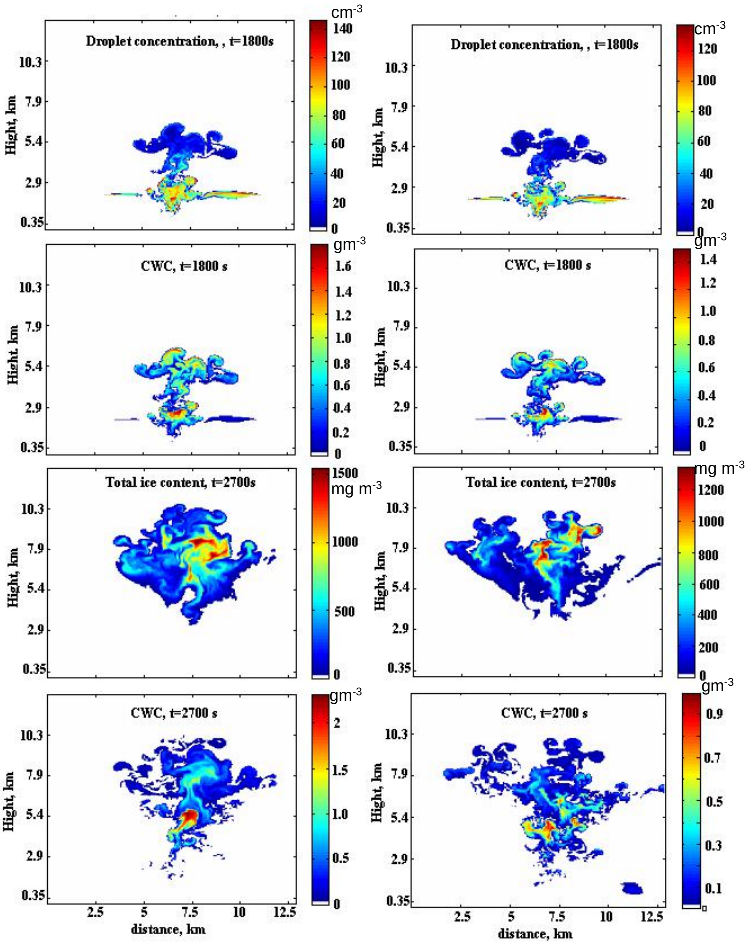

raindrops (see Fig.5 and below), which fall down, decreasing, therefore, the amount of ascending liquid water.

Figure 5 Fields of droplet concentration, CWC, RWC, and total ice content at t=1800s and 2700s in simulation E-200-grav (left panels) (pure gravity collision kernel) and E-200 (turbulent collision kernel) (right panels)

It is interesting that turbulence-induced intensification of collisions significantly increases the cloud volume covered by liquid water and ice. We speculate that the increase in drop size caused by turbulence leads to the fact that larger drops cover the larger cloud volume (we remind that collision kernels increase with height) which intensifies the processes of freezing and riming within larger cloud volume. Freezing (including that during riming) leads to an extra latent heat release intensifying the turbulence at upper cloud levels. The ice formation (graupel) begins at lower levels because in turbulent clouds larger drops are produced and freeze at lower levels. Comparison of the corresponding fields in Figs. 5 and 6 indicates that the increase in the aerosol concentration leads to a dramatic convection invigoration which includes the increase in the cloud top height and the horizontal cloud sizes. As was discussed in detail by Khain et al (2008), this invigoration is caused by the extra latent heat release due to condensation of water vapor on ascending more cloud droplets (higher CWC) and the formation of the larger ice amount. A comparison with the results presented in Khain et al (2008) shows that the convection invigoration is more pronounced in the model with higher resolution. The latter is possibly related to the absence of strong smoothing of the fields (including the field of the latent heat release) in the case of crude resolution.

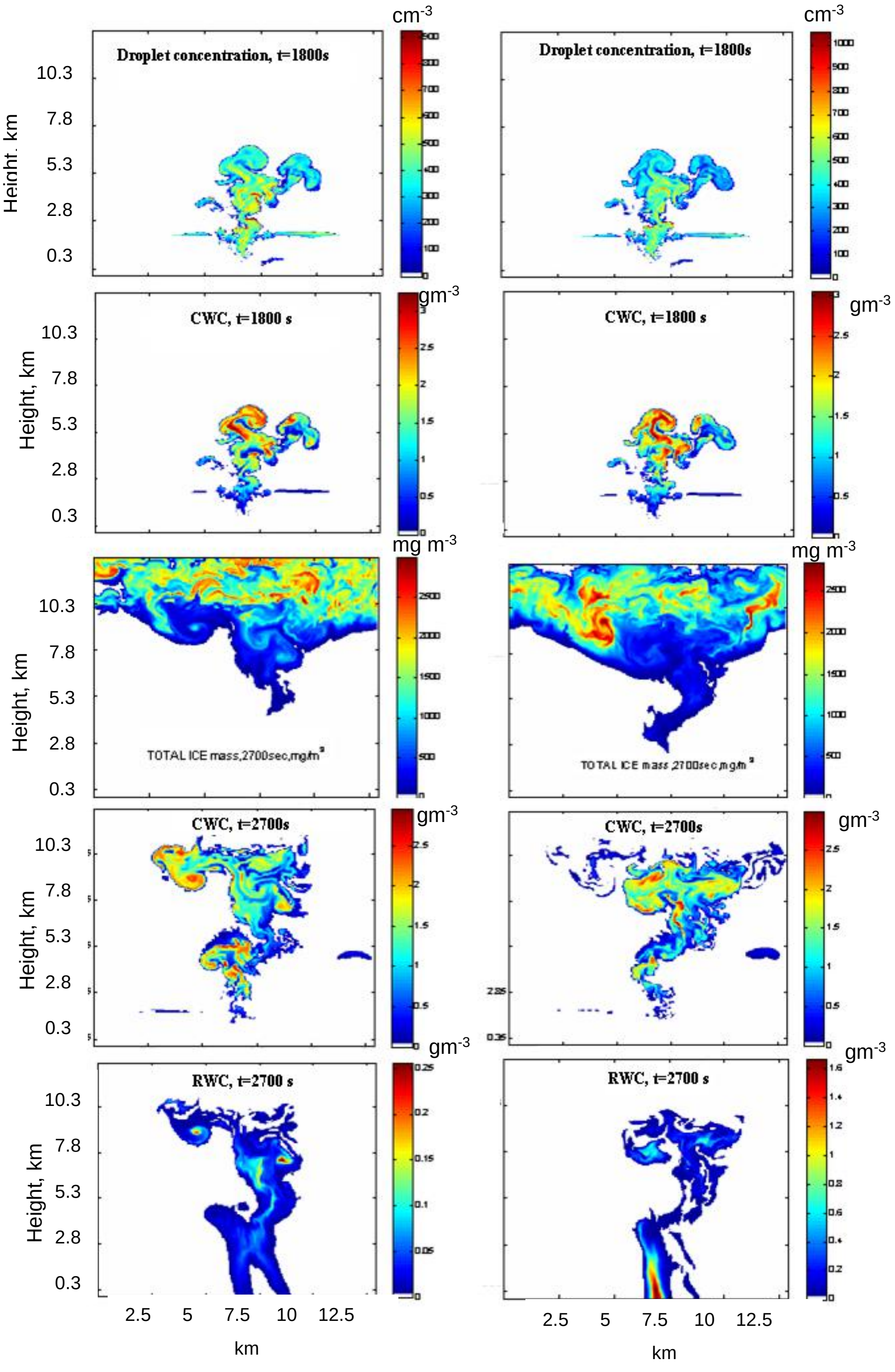

Figure 6. The same as in figure 5, but simulation of continental cloud: E-2000-grav (left panels) (pure gravity collision kernel) and E-2000 (turbulent collision kernel) (right panels)

Effects of turbulence on the location and rate of raindrop formation are of special interest. **Figure 7** shows the fields of RWC and the dissipation rates in developing clouds with low (left) and high (right) aerosol concentrations at the stage of the formation of first rain drops. One can see that first raindrops form in cloud developing in clean air earlier, as was observed and simulated in many studies. For the purposes of the present study it is more important that first raindrops arise in zones of intense turbulence.

This conclusion is supported by **Figure 8** showing the dissipation rate-radar reflectivity scattering diagrams indicating the relationship between the dissipation rate and the radar reflectivity

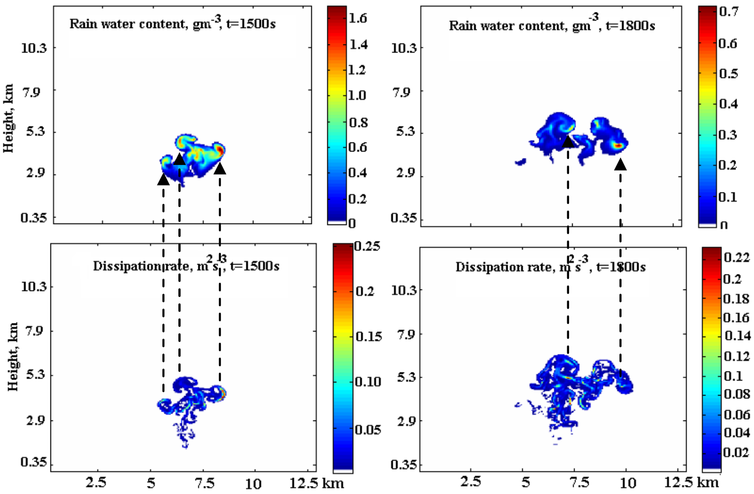

Figure 7 *Fields of RWC and the dissipation rates in clouds with low (left) and high (right) aerosol concentrations at the stage of the formation of first rain drops. Arrows show that first raindrops arise in zones of intense turbulence.*

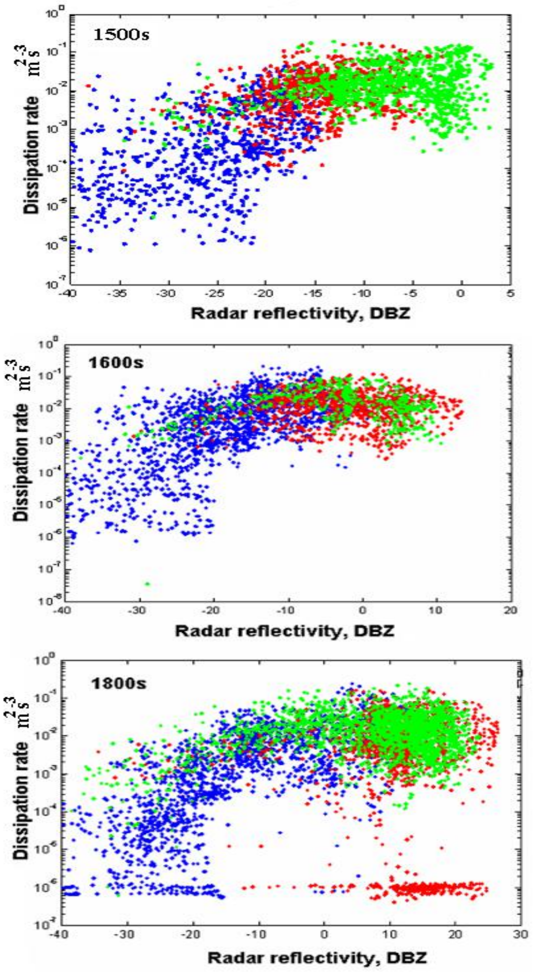

Figure 8. *The dissipation rate-radar reflectivity scattering diagrams in the E-200 run at the stage of first rain drop formation. Blue dots correspond to levels below 4 km, red dots denote grid points within the layer 4 km to 5 km, and green dots correspond to the grid points located above the 5 km level.*

which is proportional to six power of drop size) characterizing raindrop formation at t=1500s, 1600s and 1800s in the simulation E-200. One can see that the first raindrops form in zones of enhanced turbulence. In the upper two panels one can see that there are points where the dissipation rate is high, but RWC is low. However, at t=1400s-1600s there are no points where there are raindrops (high radar reflectivity), but the dissipation rate is low. At the later stage (1800 s) raindrops sediment and the correlation between the raindrop mass and the dissipation rate decreases. For instance, some largest raindrops producing radar reflectivity as high as 20 dBZ turn out in zones with a very low dissipation rate.

Figure 9 shows dependencies W(x), CWC(x), RWC(x), ε and Re_{λ} at z= 4 km; at t=1400 s in simulation E200. One can see that a) the first raindrops form in the areas where ε and Re_{λ} are maximal. It is interesting that RWC maximum also coincides with the maximum of CWC.

Figure 10 shows the CWC-dissipation rate scattering diagram. In spite of the fact that small values of the CWC can take place in grid points at large turbulent intensities, large CWC magnitudes take place largely at high ε. The result shown in Figs 9 and 10 indicate a synergetic effect of both factors: the RWC forms where both the CWC and turbulence intensity are maximal. Raindrops form at x=7.6 km, but do not form at x=6.5 km, in spite of the CWC peak in this point. We attribute this results to the fact that the turbulence intensity is significantly lower at x=6.5 km than at x=7.6 km.

Figure 9 shows also that the maximum turbulent intensity takes place not within of updraft peaks, but rather within the zones of the maximum wind shears ($\partial W / \partial x$), indicating a significant role of shear production term in the TKE equation (3).

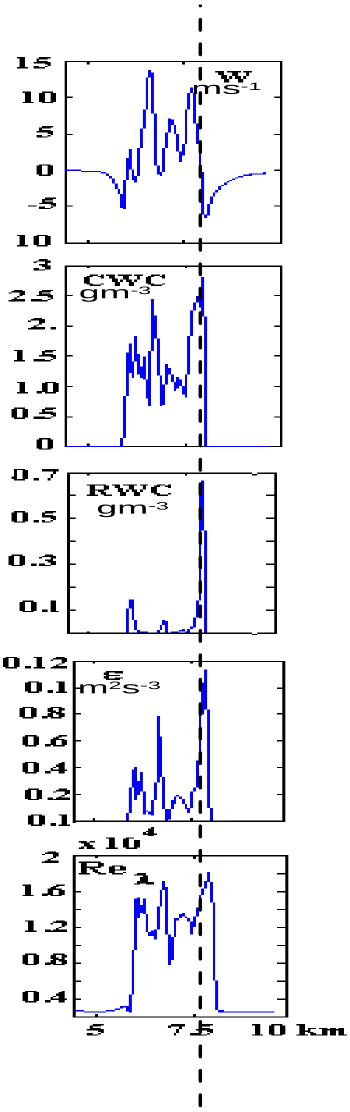

Figure 9. Dependencies W(x), CWC(x), RWC(x), ε and Re_λ at z= 4 km; at t=1400 s in simulation E200. The dashed line is plotted at the x-value, where RWC reaches its maximum and first raindrops arise.

Figure 11 compares the rain water content (RWC) fields in the E-200-grav and E-200 cases. One can see that turbulence accelerates the raindrops formation and decreases the upper height level of suppercooled raindrops.

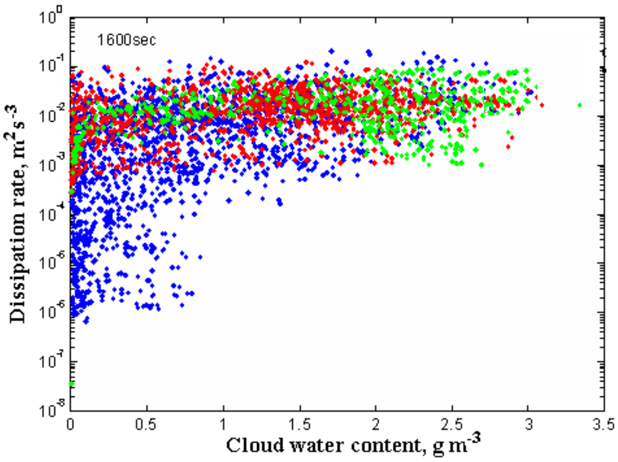

***Figure 10.** The CWC-dissipation rate scattering diagram. One can see that large CWC take place at high ε*

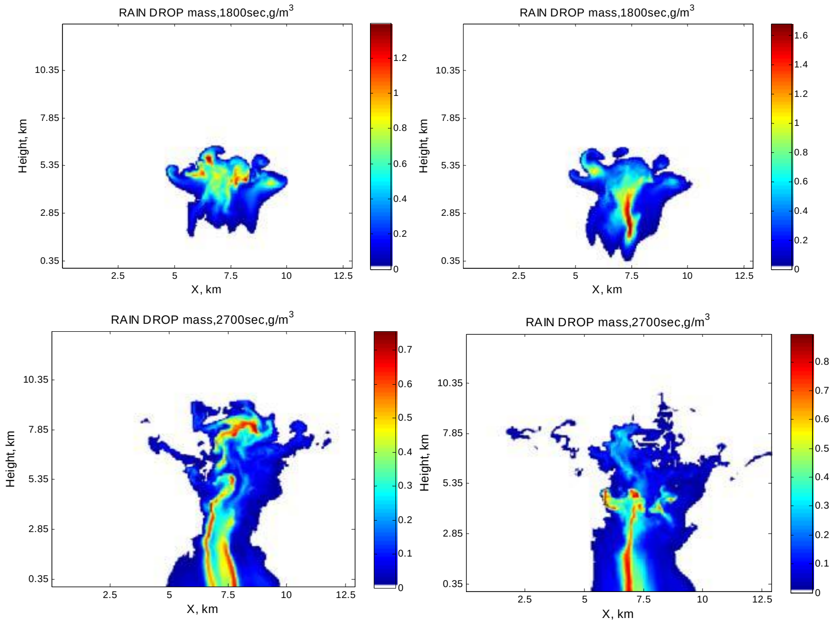

***Figure 11** The RWC fields in the E-200-grav (left panels) and E-200 cases at 1800 s and 2700s.*

As concerns continental clouds, effects of turbulence on rain drop formation even more important. For instance, Fig. 6 (low panel) shows that while in the pure gravity case the mass of raindrops is negligible at t=2700 s, the RWC is significant in the case the turbulent effects are taken into account.

Figure 12 shows the time dependences of the RWC in the case of pure gravity and turbulent collision kernels in the simulations E-200 and E-200_grav. One can see that turbulent induced collision enhancement accelerates raindrop formation and increases the RWC maximum. The acceleration of the raindrop formation in the case of low aerosol concentration is of several minutes.

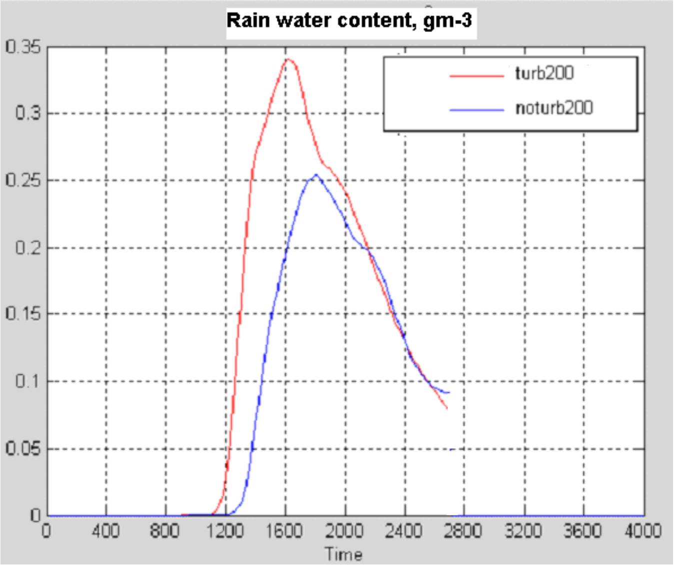

Figure 12. The time dependences of the RWC in the case of pure gravity and turbulent collision kernels in simulations E-200 and E-200_grav.

Figure 13 shows the accumulated rain amount at the surface in the simulations discussed. One can see that turbulence significantly accelerates the beginning of the precipitation. For instance, in case of low aerosol concentration precipitation at the surface falls ~15 min after the convection triggering. This time seems to be typical of such kind of clouds. In case when the pure gravity collision kernel was applied, precipitation at the surface begins 10 min later. Taken into account the spin-up time before the cloud formation, we see that turbulence shortens the time before the beginning of the rain twice. So, turbulence is the plausible mechanism of rapid rain formation in clouds. As was mentioned above, the role of turbulence in case of high aerosol concentration turns out to be even more pronounced. In case of pure gravity collision kernel, the rain at the surface is actually suppressed (at least during the first hour of the simulation). In case the turbulence-induced collision enhancement factor is taken into account, precipitation at the surface begins at ~45 min. Note that the increase aerosols from 200 cm^{-3} to 2000 cm^{-3} led to a precipitation delay by about 20 min.

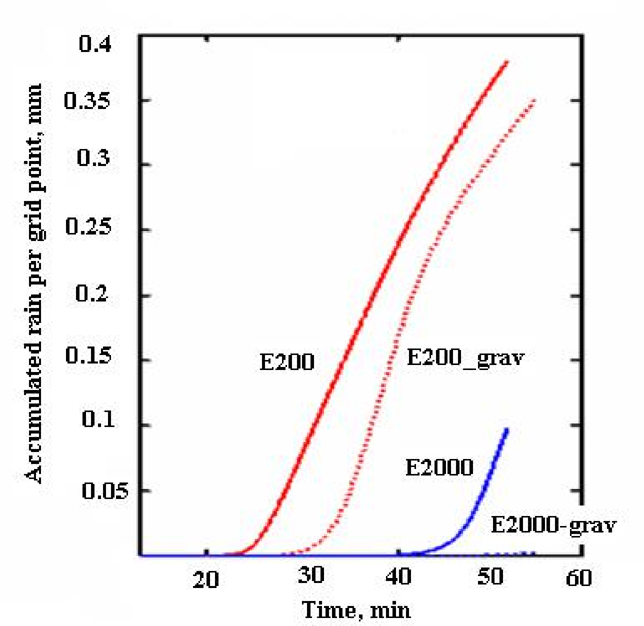

Figure 13. *Accumulated rain amount in different simulations*

It is of interest to see whether turbulence effects on collisions affect the turbulent intensity in clouds. **Figure 14** shows that increase in the collision rate slightly affects the cloud averaged values of the dissipation rate. Collision enhancement decreases the cloud averaged intensity of turbulence in maritime cloud and increases the intensity in continental clouds. At the same time the increase in the collision rate increases cloud volume, as it was shown above.

We attribute this result to the following. In case of maritime cloud ice processes are not efficient and the turbulence-induced acceleration of the warm rain formation leads to a decrease in the latent heat release aloft. In continental clouds considered drops ascend above the freezing level in both gravity and turbulent simulation. In this case turbulence intensifies the processes of drop freezing and riming leading to extra latent heat release and turbulent intensification.

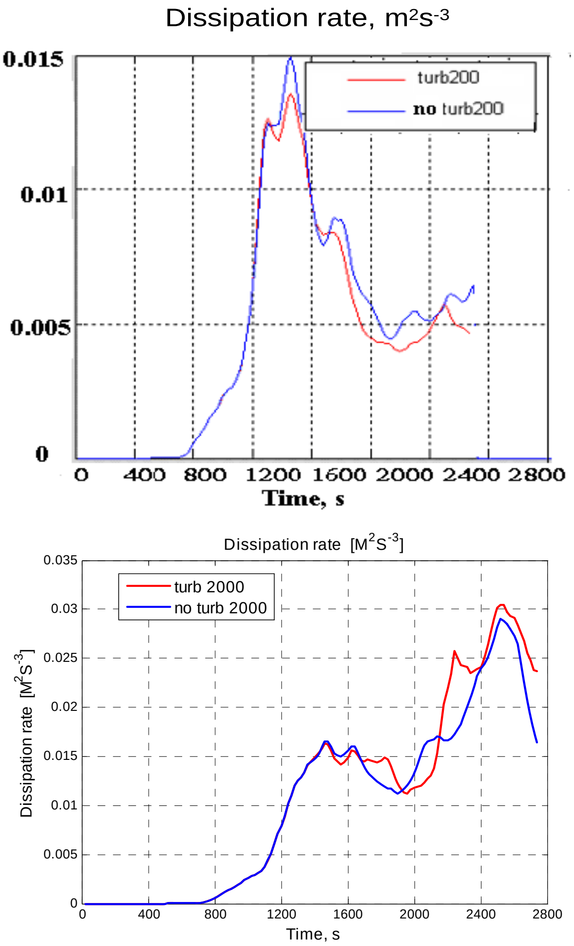

Figure 14. *Time dependence of dissipation rate in simulations with low aerosol concentration with and without turbulent collision enhancement taken into account.*

8. CONCLUSIONS

In the present study we investigate turbulent structure of continental and maritime clouds. The study represents the important step forward as regards the application of a long set of theoretical studies dedicated to turbulent effects on drop collisions to the cloud modeling. For the first time spatial and time dependent turbulent collision rate enhancement factors for cloud droplets were included into a spectral (bin) microphysics cloud model.

To accomplish this task, the model simulations were performed using the spatial resolution as high as 50 m. Calculations of the dissipation rate in each grid point and each time step were performed using the k-ε 1.5 order closure. A method of calculation of the Taylor microscale Reynolds number is proposed. It is shown that the utilization of the high resolution allowed us to reproduce "fractal" cloud structure consisting of many convective bubbles which a typical feature of real convective clouds. The averaged values of the dissipation rate and Re_λ calculated in simulations agree well with the observations available and implicit previous estimations. At the same time turbulence in clouds turns out to be highly inhomogeneous, so that maximum values of dissipation rate and Re_λ are significantly higher than the horizontally averaged (or averaged over the entire cloud) values. This fact is of high importance, because it shows that in some zones of clouds the collision rate enhancement can be much higher than the averaged value.

Using these turbulent parameters the collision enhancement factors were calculated at each time step and in each grid point of the cloud using the look up tables of the collision enhancement factors calculated in previous study (Pinsky et al 2008) for different dissipation rates and Reynolds numbers.

It is shown that raindrops tend to form in zones of enhanced turbulence. A interesting feature of cloud structure is that zones of the maximum cloud water content often coincide with zones of enhanced turbulence. Further investigations are required to figure out the reasons of such structure. We speculate that such structure can be related to the buoyancy caused by latent heat release within turbulent bubbles. In any case, the formation of the first raindrops turns out to be the synergetic effect of enhanced turbulence and large CWC.

Since the effects of turbulence on collisions are quite non-linear, the utilization of spatially averaged turbulent parameters and kernels should underestimate turbulent effects.

The results show that turbulence is the plausible mechanism responsible for a comparatively rapid realistic rain formation in convective clouds. The turbulent effects being taken into account, precipitation at the surface starts in 15 minutes in microphysically maritime clouds without any contribution of giant and ultragiant CCN. Effects of turbulence are of special importance in case of continental clouds. In the continental cloud simulated the application of pure gravity kernels do not lead to precipitation on the surface (at least during the first hour of cloud evolution). At the same time, this cloud precipitates when the turbulence effects on droplet collision was taken into account.

It is shown that aerosols affect dramatically the cloud evolution leading to the convection invigoration, increasing the cloud volume and turbulizing the cloud. Thus, clouds developing in polluted atmosphere are much more turbulent than typical maritime clouds. It is shown also that the intensification of droplet collisions leads to the cloud turbulization and to increase the cloud volume.

As follows from the simulations, the effects of turbulence and small aerosols (small CCN) on surface precipitation are somewhat opposite. Intense turbulence in continental clouds shortens the delay in raindrop formation caused by aerosols. An increase in the rate of cloud "continentality" leads to the increase in the turbulence intensity. In case this feedback is strong enough, the results of many simulations of aerosol effects on precipitation performed in neglecting turbulent effects on collision should be, possibly, reconsidered.

It seems that this study opens a new direction in the numerical cloud physics in several aspects. The first one is related to the relationship between dynamical and microphysical cloud properties. For instance, high model resolution allows the investigation of processes entrainment of the cloud microphysics, as well as of drop and ice particles recycling. It is well known, for instance, that hailstones contain several layers of different densities, indicating that these particles ascend and descend within a cloud several times during their growth. Crude resolution does not allow one to resolve such recycling. We suppose that the hydrometeor exchange between different bubbles having different vertical velocities and different microphysical properties will affect significantly the size distributions of hydrometeors and, as a result, the precipitation formation process. In particular, the efficiency (inefficiency) of the in-cloud recycling can determine success/ (no success) of cloud seeding when only a small fraction of cloud volume is seeded, so that the earlier formation of raindrops can be expected only in a comparatively small cloud volume. Note that the analogy between the effects of the decrease in the aerosol concentration and increase in the turbulence intensity mentioned above is not exact. For instance, turbulence intensifies processes of riming accompanying by an extra latent heat. Thus, turbulence can lead to convection invigoration like aerosols. It is possible, that both high aerosol concentrations and high turbulent intensity are the necessary conditions for the heavy hail formation.

It is clear that the processes of entrainment-detrainment in clouds having small scale "fractal" structure is more efficient than in "smoothed" clouds. At the same time, fluctuations of vertical velocities in "fractal" clouds can be quite significant, which can lead to new drop nucleation, etc. The "bubbled" cloud structure allows us to suspect significant fluctuations of supersaturation with respect to water and ice, in-cloud evaporation, and related IN nucleation, affecting the process of ice formation and cloud glaciation.

As concerns the turbulent effects on precipitation formation in cumulus clouds, the present study represents only the first step in this direction. Simulations should be performed for longer period of time to allow the reproduction of effects of turbulence on ice precipitation. It requires a significant increase in the computational volume. We would remind that the effects reported here are obtained by the increase of the collision rates between small cloud droplets only. At the same time laboratory experiments (Vohl et al 1999) indicate the increase in the collision rate between small cloud and small rain drops. Besides, turbulent effects on water-ice and ice-ice collisions were not taken into account. The topic is "terra incognito" in the Cloud Physics. However, one can expect that turbulent effects on ice collisions are even stronger than those in case of cloud droplets. Thus, the present study significantly underestimates turbulent effects on cloud dynamics and microphysics. Significant theoretical, observational and numerical efforts are required to reach further progress in this direction.

Acknowledgements. The study was supported by the Israel Science Foundation, grant 140/07.

References

Andrejczuk, M, W.W. Grabowski, S.P. Malinowski, and P.K. Smolarkiewicz, 2004: Numerical simulation of cloud-clear air interfractal mixing. *J. Atmos. Sci.* 61, 1726-1739.

Andrejczuk, M, W.W. Grabowski, S.P. Malinowski, and P.K. Smolarkiewicz, 2006: Numerical simulation of cloud-clear air interfractal mixing: effects on cloud microphysics. *J. Atmos. Sci*. 63, 3204-3225.

Andreae, M.O., D. Rosenfeld, P. Artaxo, A.A. Costa. G.P. Frank, K.M. Longlo, and M.A.F. Silva-Dias, 2004: Smoking rain clouds over the Amazon. Science, 303, 1337-1342.

Arenberg, D., 1939: Turbulence as the major factor in the growth of cloud drops 1939. Bull. Amer. Meteor. Soc. **20**, 444-448.

Almeida, F. C., 1976: The collisional problem of cloud droplets moving in a turbulent environment-Part I: A method of solution. *J. Atmos. Sci.*, **33**, 1571-1578.

Almeida, F. C., 1979: The collisional problem of cloud droplets moving in a turbulent environment-part II: Turbulent collision efficiencies. *J. Atmos. Sci.*, **36**, 1564-1576.

Beard, K.V., 1976: Terminal velocity and shape of cloud and precipitation drops aloft. *J. Atmos. Sci.* 33, 851-864.

Bott, A., 1998: A flux method for the numerical solution of the stochastic collection equation *J. Atmos. Sci.*, 55, 2284-2293.

Brenguier J-L. and Chaumat, 2001: Droplet spectra broadening in cumulus clouds. Part 1: Broadening in adiabatic cores. *J. Atmos. Sci.*, **58**, 628-641

Elperin T., Kleeorin N., Rogachevskii I., 2002: Formation of large scale semiorginized structures in turbulent convection, *Physical Review E* 66, 066305, 5-10.

Falkovich G., A. Fouxon and M.G. Stepanov, 2002: Acceleration of rain initiation by cloud turbulence, *Nature*, **419**, 151-154

Franklin C.N., Vaillancourt P.A., Yau M.K. and Bartello P., 2005: Collision rates of cloud droplets in turbulent flow. *J. Atmos. Sci.*, **62**, 2451-2466.

Franklin C. N, P.A. Vaillancourt and M.K. Yau, 2007: Statistics and parameterizations of the effect of turbulence on the geometric collision kernel of cloud droplets. *J. Atmos. Sci.* 64, 938-954.

Grabowski W.W., 1993: Cumulus entrainment, fine scale mixing and buoyancy reversal. Quart. J. Roy. Met. Soc., 119, 935-956.

Grabowski W.W., 1995: Entrainment and mixing in buoyancy reversing convection with application to cloud-top entrainment instability. Quart. J. Roy. Met. Soc., 121, 231-253.

Grabowski W.W, 2007: Representation of turbulent mixing and buoyancy reversal in bulk cloud models. J. Atmos. Sci., 64, 3666-3680.

Grover S.N. and H.R. Pruppacher, 1985: The effect of vertical turbulent fluctuations in the atmosphere on the collection of aerosol particles by cloud drops.*J. Atmos. Sci.*, **42**, 2305-2318.

Ivanovsky A. and I. Mazin, 1960: Turbulent coagulation and its role in drop growth. *Proceed. Central Aerological Observatory*, N 35, 21-35 (in Russian)

Jensen, J. B., and M. Baker, 1989: A simple model of droplet spectral evolution during turbulent mixing. *J. Atmos. Sci.*, **46**, 2812-2829.

Jonas, P.R., 1996: Turbulence and cloud microphysics. *Atmos. Res.*, 40, 283-306.

Kessler, E., 1969: On the distribution and continuity of water substance in atmospheric circulation. *Met. Monographs* 10, 84.

Khain A. P. and M. B. Pinsky, 1995: Drops' inertia and its contribution to turbulent coalescence in convective clouds: Part 1: drops' fall in the flow with random horizontal velocity, *J. Atmos. Sci.* , 52, 196-206.

Khain, A. P. and M. Pinsky, 1997: Turbulence effects on the collision kernel, Part 2: Increase of swept volume of colliding drops. *Quart. J. Roy. Meteor. Soc.*, 123, 1543-1560.

Khain, A. P., M. Ovtchinnikov, M. Pinsky, A. Pokrovsky, and H. Krugliak, 2000: Notes on the state-of-the-art numerical modeling of cloud microphysics. *Atmos. Res.* 55, 159-224.

Khain A.P., Pinsky, M.B., M. Shapiro and A. Pokrovsky, 2001a: Graupel-drop collision efficiencies. *J. Atmos. Sci.*, 58, 2571-2595.

Khain A. P., D. Rosenfeld and A. Pokrovsky, 2001b: Simulation of deep convective clouds with sustained supercooled liquid water down to –37.5 C using a spectral microphysics model. *Geophys. Res. Lett*, 3887-3890.

Khain A., M. Pinsky, T. Elperin, N. Kleeorin and I. Rogachevskii, and Kostinski, 2007: Critical analysis of results concerning droplet collisions in turbulent clouds . *Atmos. Res* 86, 1-20.

Khain, A. P., N. BenMoshe, A. Pokrovsky, 2008. Factors determining the impact of aerosols on surface precipitation from clouds: attempt of classification. *J. Atmos. Sci.* (in press)

Lynn *B.*, A. Khain, J. Dudhia, D. Rosenfeld, A. Pokrovsky, and A. Seifert *2005:* Spectral (bin) microphysics coupled with a mesoscale model (MM5). Part 2: Simulation of a CaPe rain event with squall line *Mon. Wea. Rev.*, 133, 59-71.

MacPherson, J.I., and G.A. Isaac, 1977: Turbulent characteristics of some Canadian cumulus clouds. J. Appl. Meteorol. , 16, 81-90.

Mazin, I. P., A. Kh. Khrgian, and I. M. Imyanitov, 1989: Handbook *of Clouds and Cloudy atmosphere*. Gidrometeoizdat, 647p

Monin, A.S. and Yaglom, A.M. 1975: "*Statistical Fluid Mechanics: Mechanics of Turbulence*", vol. 2, MIT Press.

Panchev, S., 1971: *Random fluctuations in turbulence.* Pergamon Press, 256 p

Pinsky, M. and Khain, A.P., 1996: Simulations of drops' fall in a homogeneous isotropic turbulence flow. *Atmos. Res.*, 40: 223-259.

Pinsky, M., and A. P. Khain, 1997: Turbulence effects on droplet growth and size distribution in clouds- A review. *J. Aeros. Sci.,* 28, 1177-1214. (1.508, 11/37, 3)

Pinsky, M. and A.P. Khain, 1997: Formation of inhomogeneity in drop concentration induced by drop inertia and their contribution to the drop spectrum broadening. *Quart. J. Roy. Meteor. Soc.*, 123: 165-186.

Pinsky, M. and A. P. Khain, 1997: Turbulence effects on the collision kernel, Part 1: Formation of velocity deviations of drops falling within a turbulent three-dimensional flow. *Quart. J. Roy. Meteor. Soc.* 123, 1517-1542.

Pinsky, M., and A. P. Khain, 1998: Some effects of cloud turbulence on water-ice and ice-ice collisions, *Atmos. Res.*, 47-48, 69-86.

Pinsky, M., A. P. Khain, and M. Shapiro, 1999a: Collisions of small drops in a turbulent flow. Pt.1: Collision efficiency: problem formulation and preliminary results. *J. Atmos. Sci.* , 56, 2585-2600.

Pinsky, M.B., A.P. Khain and Z. Levin, 1999b: The role of the inertia of cloud drops in the evolution of the spectra during drop growth by diffusion. *Quart. J. Roy. Meteor. Soc*., 125, 553-581.

Pinsky, M., A. P. Khain, and M. Shapiro, 2000: Stochastic effects on cloud droplet hydrodynamic interaction in a turbulent flow. *Atmos. Res.*, 53, 131-169.

Pinsky, M., A. P. Khain, and M. Shapiro 2001: Collision efficiency of drops in a wide range of Reynolds numbers: Effects of pressure on spectrum evolution. *J. Atmos. Sci.* 58, 742-764.

Pinsky, M. B., and A. P. Khain, 2003: Fine structure of cloud droplet concentration as seen from the Fast-FSSP measurements. Part 2: Results of in-situ observations, *J. Appl. Meteor*., **42**, 65-73.

Pinsky M.B., and A.P. Khain, 2004: Collisions of small drops in a turbulent flow. Part 2. Effects of flow accelerations, *J. Atmos. Sci.,* **61**, 1926-1939.

Pinsky, M., A. P. Khain, and M. Shapiro 2001: Collision efficiency of drops in a wide range of Reynolds numbers: Effects of pressure on spectrum evolution. *J. Atmos. Sci*. **58**, 742-764

Pinsky M., Shapiro M., Khain A. and Wirzberger H., 2004: A statistical model of strains in homogeneous and isotropic turbulence, Physica D, **191**, 297-313

Pinsky M. B., A. P. Khain , B. Grits and M. Shapiro, 2006: "Collisions of cloud droplets in a turbulent flow. Part 3. Relative droplet fluxes and swept volumes", *J. Atmos. Sci* 63, 2123-2139.

Pinsky M. B., A.P. Khain**,** and M. Shapiro, 2007: Collisions of cloud droplets in a turbulent flow. Part 4. Droplet hydrodynamic interaction. *J. Atmos. Sci , 64, 2462-2482.*

Pinsky M., A. Khain and H. Krugliak, 2007: Collisions of cloud droplets in a turbulent flow. Part 5: Application of detailed tables of turbulent collision rate enhancement to simulation of droplet spectra evolution. *J. Atmos. Sci.* (in press).

Pope B. 2000: *Turbulent Flows*. Cambridge University Press; 771 pp.

Pruppacher, H. R., and J. D. Klett, 1997: *Microphysics of clouds and precipitation.* 2-nd edition, Oxford Press, 1997, 963p.

Riemer N. and Wexler A.S. 2005: Droplet to Drops by turbulent coagulation. *J. Atmos. Sci.*, **62**, 1962-1975

Saffman P.G. and Turner J.S, 1956: On the collision of drops in turbulent clouds. *J. Fluid Mech.* **1**, 16.

Shaw R.A., 2003: Particle-turbulence interactions in atmospheric clouds, *Annu. Rev. Fluid Mech*., **35**, 183-227.

Siebert H, K. Lehmann, and M. Wendisch, 2006: Observations of small-scale turbulence and energy dissipation rates in the cloudy boundary layer. *J. Atmos. Sci*., 63, 1451-1466.

Stevens, B, G and COAUTHORS, 2005a: Evaluation of large-eddy simulations via observations of nocturnal marine stratocumulus. Mon. Wea. Rev., 133, 1443-1455.

Xue Y. L-P.Wang, and W. W. Grabowski, 2008: Growth of cloud droplets by turbulent collision-coalescence. J. Atmos. Sci., 331-356

Wang, L-P, O. Ayala, S.E. Kasprzak, and W.W. Grabowski, 2005a: Theoretical formulation of collision rate and collision efficiency of hydrodynamically interacting cloud droplets in turbulent atmosphere. *J. Atmos. Sci*. **62**, 2433-2450.

Wang, L-P., O. Ayala, and W.W. Grabowski, 2005b: On improved formulations of the superposition method, *J. Atmos. Sci*. ,**62**, 1255-1266.

Weil, J.C., R. P. Lawson,A. R. Rodi, 1993: Relative dispersion of ice crystals in seeded cumuli. *J. Appl. Meteor.,* **32**, 1055-1073.

Vaillancourt P.A., and Yau M. K., 2000: Review of particle-turbulence interactions and consequences for Cloud Physics, *Bull. Am. Met. Soc.*, **81**, 285-298

Vohl, O., S.K. Mitra, S.C. Wurzler and H.R. Pruppacher, 1999: A wind tunnel study on the effects of turbulence on the growth of cloud drops by collision and coalescence. *J. Atmos. Sci*., **56**, 4088-4099.

IDEALIZED NUMERICAL SENSITIVITY STUDIES ON SHALLOW-CONVECTION-TRIGGERED STORMS

Ulrich Blahak*
Institut für Meteorologie und Klimaforschung, Universität Karlsruhe / Forschungszentrum Karlsruhe

1 INTRODUCTION

The forecast of convective storms, their triggering, life cycle and precipitationstill present a challenge to todays weather forecasting systems. Even with the newest generation high resolution nonhydrostatic models including sophisticated data assimilation schemes, often the processes which contribute to trigger convective systems (e.g., smallscale convergence lines, shallow convection, anabatic valley winds) are not adequately resolved and thus forecast more or less fails, even in a statistical sense over a larger area.

Once convection starts in the model, the treatment of cloud microphysical processes determines the further evolution of the clouds via the microphysical/dynamical feedback processes (latent heat release, development of cold pools). Explicit forecasting of severe threats, e.g., large hail or heavy wind gusts, also critically depends on microphysics. Especially hail formation is difficult to simulate due to its highly nonlinear and very small-scale nature.

In order to better understand those physical processes, idealized high resolution cloud resolving simulations with the COSMO-model of the German Weather Service (DWD) are performed, using the 2-moment cloud microphysical scheme of Seifert and Beheng (2006) with an additional class of high density particles (”hail”, Noppel et al., 2006) in a newly modified version (Blahak, 2008). The goal is to study the influence of ambient atmospheric environmental conditions (aerosols, profile of temperature, humidity and wind) and orography on the development, life cycle and precipitation efficiency of convective cells in order to elaborate parameters crucially influencing the characteristics of convective cells.

In past idealized simulations, single convective systems have been artificially triggered either by the classical "warm bubble" approach or by wave flow over idealized orography (Blahak et al., 2006; from now on BL06). The numerical results often exhibited rather strong maximum updraft speeds ($w > 60$ m s^{-1}) and a rather quick lateral spreading of multicell/supercell type systems over the entire model domain. This was often accompanied by a comparatively low precipitation efficiency and low simulated radar reflectivity in the upper part of the cells.

An improvement has been obtained by changing microphysical parameters and process descriptions, described in Blahak (2008).

Another reason for the low efficiency could be the simulated vigorous and thus fast development, leaving only a short time for precipitation formation mechanisms (e.g., riming) to be active during a single pass through the updraft region. We believe that this behaviour may partly be attributed to the fact that the simulated systems developed isolated and in a rather "pristine" environment, lacking interactions with neighbouring circulation patterns.

Accordingly, simulations are altered by specifying an idealized daily cycle of the surface fluxes, repesentative for a sunny summer day, such that a broad spectrum of convective structures simultaneously appears. Effects of sloping terrain and slant cloud shadows are taken into account. In this way, the relevant circulation scales (shallow convection) spin up by themselves and, after removal of CIN, deep convective cells develop. To resolve the necessary spatial scales, we use model resolutions down to 100 m horizontally and approx. 50 m vertically within the PBL.

This kind of ”quasi” LES simulations has been performed in the past by various authors, e.g., to investigate warm shallow cumulus clouds. However, most of them did not apply such a detailed cloud microphysical parameterization and did not focus on sensitivity studies on deep convective mixed phase clouds. The work of Balaji and Clark (1988), one of the few who simulated the development of a deep convective cloud in a very similar fashion (but with coarser grid spacing), has been very influential to the author.

Similar to BL06, results of four simulations are presented in section 4, combining a low- and high-CCN regime with a colder and a warmer environment at same values of CAPE, vertical buoancy distribution and (weak) wind speed and shear. However, this time shallow convective motions trigger the deep cells, in contrast to the formerly case of wave flow over a gaussian mountain. But before that, in the next section the numerical model will described, and in section 3, the simulation of pure shallow convection (clouds are turned off) is analyzed in more detail, since it constitutes the basis for our deep convective simulations.

---

*Corresponding author address: Ulrich Blahak, Institut für Meteorologie und Klimaforschung, Universität Karlsruhe / Forschungszentrum Karlsruhe, Postfach 3640, D-76021 Karlsruhe, Germany;
e-mail: ulrich.blahak@imk.fzk.de.

2 Description of the numerical model

The fully compressible and nonhydrostatic COSMO-model (Doms and Schättler, 2002; (Doms et al. 2005)) of DWD is used as dynamical core for the simulations presented in this paper, to which the abovementioned modified two-moment bulk cloud microphysical scheme of Seifert and Beheng (2006) is coupled. Numerical methods comprise a 3rd order Runge-Kutta method for time integration and 5th order upwind scheme for the horizontal advection of the dynamical variables, together with the usual time splitting into fast (sound-) processes and slow modes. Advection of moisture quantities is done by 2nd order Bott's scheme.

For our idealized simulations, the original soil- and radiation modules are turned off. Instead, an idealized daily cycle of sensible and latent heat fluxes H and E is imposed at the lower boundary, taking into account the effects of sloping terrain, slant cloud shadows and precipitation, as mentioned in the introduction. Only in case of flat orography and clear sky conditions, these fluxes are horizontally homogeneous. This daily cycle is based on an analytic solution to the surface energy balance equation, which includes simple and well-known parameterizations of the radiation balance (Q) components (direct insolation as function of geographical latitude and time of day, diffuse shortwave radiation, up- and downwelling longwave radiation; Goody, 1964; Kondratjev, 1976; Adrian and Fiedler, 1991) and is applicable during daytime. To enable this analytic solution, a constant Bowen ratio and a constant ratio of surface heat flux B to radiation balance Q are assumed and have to be pre-specified. All soil- and vegetation properties are hidden in these two parameters. Figure 1 shows an example of such an idealized daily cycle under clear sky conditions for a latitude of 49° and Julian day 180 for the parameters given in the figure. In this case, H has a maximum of 300 $\mathrm{W m^{-2}}$ at noon. As a simple alternative, fixed values of H and E may be specified as well.

For the momentum transfer at the lower boundary, a no-slip boundary condition is applied.

Fully periodic lateral boundary conditions are used together with a sponge layer at the upper model boundary to prevent spurious vertical wave reflections.

Typical horizontal grid spacings for our simulations range from 100 m to 1 km. A suitable 3D turbulence closure is used which combines a Smagorinsky-type LES formulation of the turbulent lenght scale with a 1.5th order TKE closure for the turbulent diffusion coefficients (Herzog et al., 2002). Moist effects are taken into account by using the virtual-potential temperature in the equation for TKE instead of ordinary potential temperature. The ratio of the horizontal to vertical turbulent diffusion coefficients is chosen to be 3.

For these "quasi" LES simulations, no parameterizations of deep and shallow convection resp. boundary layer schemes are used.

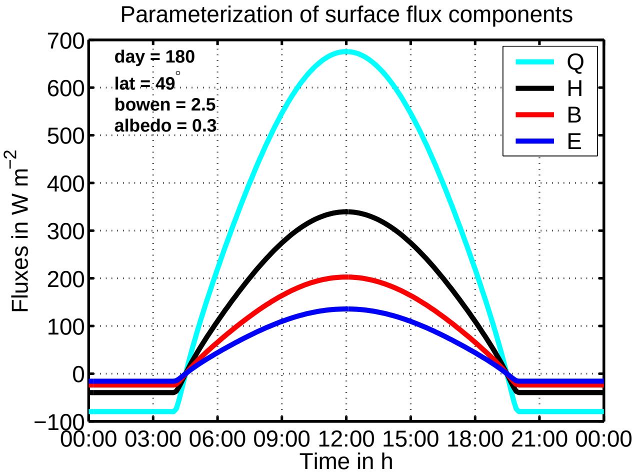

Fig. 1: Exemplary idealized daily cycle of the surface energy balance components Q, B, H and E in $\mathrm{Wm^{-2}}$ as function of time of day in h, for a geogr. latitude of 49°, Julian day 180, Bowen ratio 2.5, ratio B/Q = 0.3. From these, H and E are specified at the lower model boundary.

3 REPRESENTATION OF SHALLOW CONVECTION

Using horizontal grid spacings in the range of up to a few hundred meters together with appropriate initial vertical temperature and humidity profiles and specifying H and E in the manner shown in Figure 1, shallow convection patterns spin up explicitly in the boundary layer from pre-specified weak random noise on W and T fields and will eventually trigger deep convective cells after removal of CIN. These shallow convection circulation patterns are briefly analyzed in this section before the focus turns to deep clouds in the next section.

To this end, various simulations have been performed with cloud microphysics parameterization turned off. Immediate and important questions to answer are:

1. Necessary grid resolution?
2. How does the turbulence parameterization perform in that kind of simulation?

To this end, a set of 3 simulations with grid spacings 100, 200 and 500 m, each with 125 x 125 x 80 grid points in X-, Y- and Z-direction is shown in the following. The vertical grid spacing is quite dense in the boundary layer and decreases with height: the lowest model level is in 20 m and the model domain has a height of 9 km (ΔX = 100 m) resp. 15 km (200 m, 500 m). For simplicity, initial conditions are taken from the classical idealized soundings of Weisman and Klemp (1982) for moist unstable conditions,

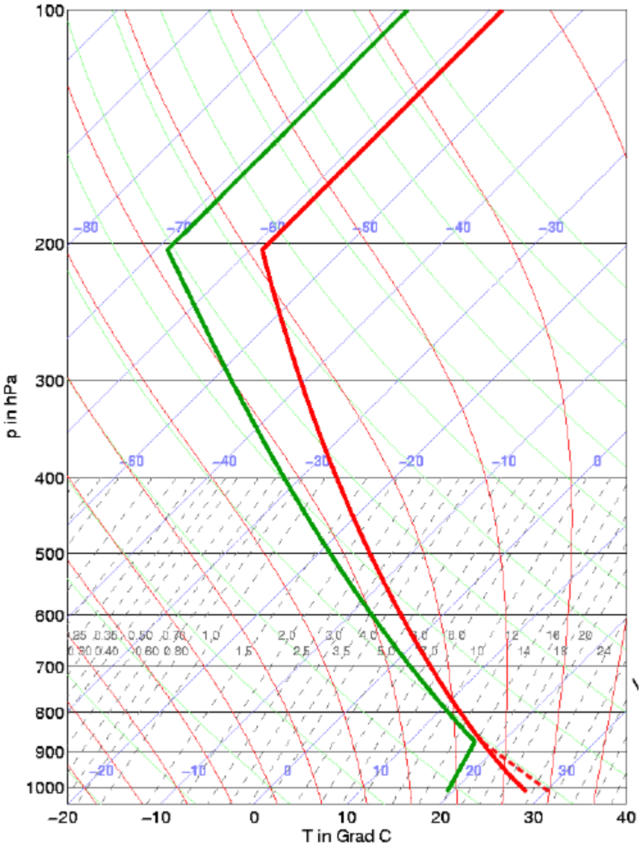

Fig. 2: Log-p/skew-T diagram of initial temperature (red) and dew point (green) profiles for the simulations of pure shallow convection. Dashed red line represents a well-mixed boundary layer, which builds up gradually after model start.

see Figure 2. Wind speed U is 5 m s^{-1} in the free troposphere in positive X-direction and decreases towards the ground with no directional wind shear ($U(z) = U_\infty \tanh(z/z_s)$ with $z_s = 3000$ m). The temperature profile exhibits a stable boundary layer, which is qualitatively representative of the morning hours on a sunny day. The solid red is the initial temperature profile and the short dashed red line shows the temperature in a well-mixed boundary layer, which builds up in the simulations after some time. Consistent to that, the specified daily cylce of H and E at the lower boundary starts at 10 o'clock.

Figure 3 shows simulated vertical velocity at $Z = 1000$ m after 3 h time for the simulation with ΔX = 200 m. Active thermal circulation patterns with maximum updrafts of about 7 m s^{-1} and with mean distance between the thermals of about 5 – 8 km are visible which equals about 3 times the boundary layer height. Thermals itself have diameters of about 500 – 1000 m. Similar results are obtained with ΔX = 100 m, but for ΔX = 500 m maximum mean thermal's diameter and distance is larger and maximum updraft speeds are lower, which can be seen from the time series of domain maximum/minimum W plotted in Figure 4.

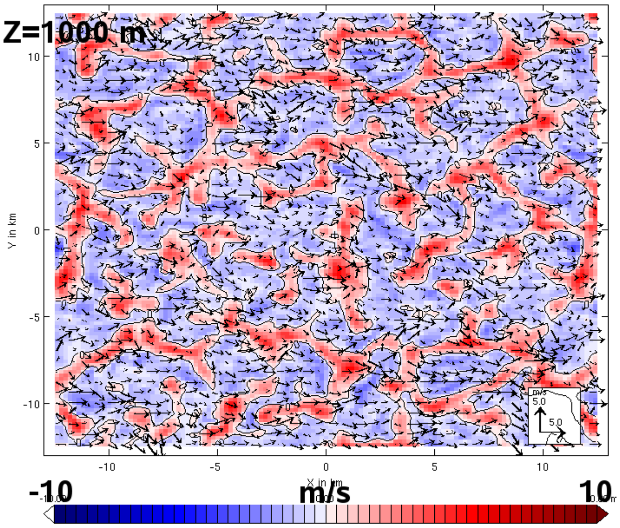

Fig. 3: Example of a simulation with $\Delta X = 200$ m: W in m s^{-1} at $Z = 1000$ m after 3 h simulation time

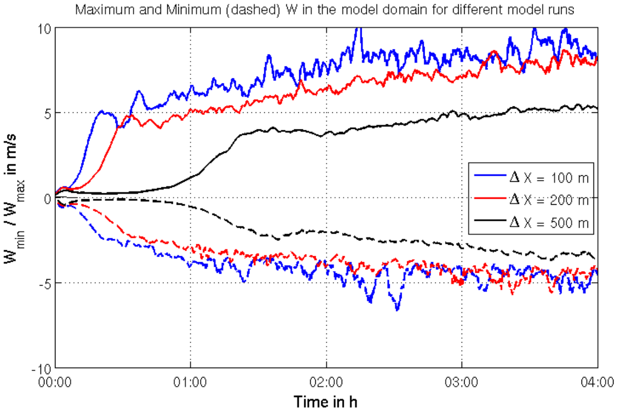

Fig. 4: Maximum/minimum W in the model domain in m s^{-1} as function of time in h for 3 exemplary simulations with $\Delta X = 100$ m, 200 m and 500 m.

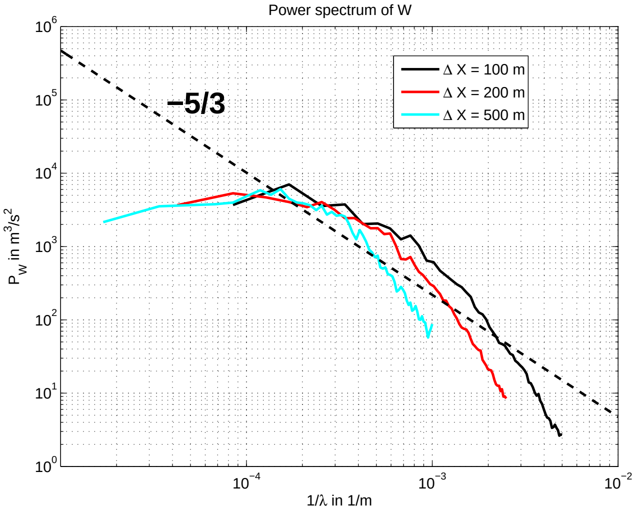

Fig. 5: Mean horizontal power spectra of W in Y-direction in m^{3}s^{-2} as function of inverse wavelength in m^{-1} for the simulations with $\Delta X = 100$ m, 200 m and 500 m. Averaging has been done over the boundary layer and over simulation hours 2 – 4.

Also, the coarser the resolution, the longer it takes for large and strong coherent convective patterns to develop, consistent with the LES assumption of division into resolved an non-resolved (parameterized) turbulent scales depending on the grid spacing.

To round out the picture, mean horizontal power spectra of W in Y-direction (perpendicular to the flow) are presented in Figure 5. These are averaged in space over the boundary layer and in time over hours 2 to 4 of the simulations. A distinct maximum at $1/\lambda \approx 1.2 \times 10^{-4}$ m is observed ($\equiv \lambda = 8$ km). Towards higher frequencies, the spectra first follow more or less a -5/3-law and then, above a frequency which corresponds to about 6ΔX, fall off faster. This shows that poorly- and non-resolved turbulent scales, whose contribution to the turbulent fluxes is parameterized (LES), are efficiently damped out but are not too aggressively suppressed. Especially, there is no spurious buildup of energy at the lowest resolved wavelength 2ΔX, indicating that turbulent mixing is large enough and parameters of the turbulence scheme are properly chosen. At the same time, there is still significant energy at the scales of shallow convection ($\lambda = 500 - 1000$ m) for the simulations with 100 and 200 m grid spacing, but not with 500 m. It is however clear that even at our $\Delta X = 100$ m the scales of shallow convection lie within the over-5/3-spectral fall-off and not all details of this phenomenon are realistically simulated.

However, it seems that for our purpose (which is triggering of deep convective cells with realistic mutual distances), the coarsest possible grid spacing may be in the range of 200 m to 500 m.

4 DEEP CONVECTION WITH VARYING CCN AND TEMPERATURE LEVEL

Now we turn our focus on what happens if cloud microphysics processes are turned on in the model. In continuation of the work presented in BL06, the effect of different temperature levels in combination with low-CCN- and high-CCN-aerosol regimes on shallow-convection-triggered cells is investigated. For that, four simulations are presented, which constitute all possible combinations of a ”warm” and ”cold” environment with ”high-CCN” and ”low-CCN” conditions. For the ”warm” case, the initial vertical profiles of temperature, humidity and wind equal those previously described in section 3 (see Figure 2). The surface temperature T_B equals 28°C, $CAPE$ is 2800 J kg^{-1}, and due to the very low wind shear a multicellular behaviour of the convective cells is to be expected. From this, the ”cold” case initial profiles are constructed in a way that the surface temperature T_B is lowered by 6°C, and the temperature profile as a whole is shifted towards lower temperatures in a way that preserves $CAPE$, LCL, LFC, LNB and the vertical buoancy distribution (see also BL06). The wind profile remains unchanged. ”High-CCN” and ”low-CCN” conditions are imposed by adjusting the cloud number concentration N_c as a function of the resolved supersaturation S w.r.t. water, if there is less N_c as required by the curves shown in Figure 6.

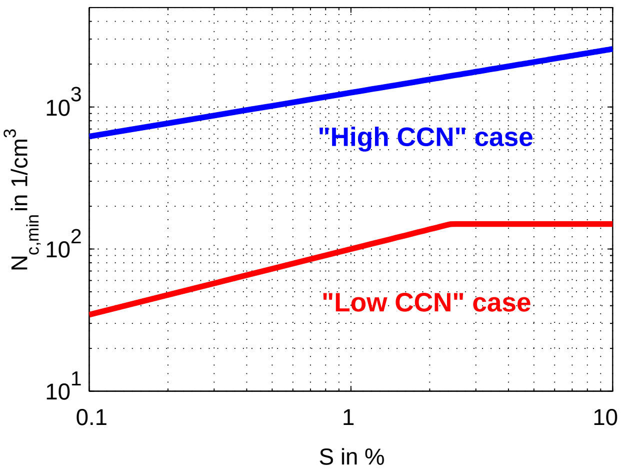

Fig. 6: Imposed minimum number concentration of cloud droplets as function of explicitly resolved supersaturation S for the ”low-CCN” and ”high-CCN” cases.

Akin to BL06, the orography consists of a single gaussian mountain (height 500 m, halfwidth 20 km) in the center of the model domain, which, together with the fully periodic boundary conditions, represents a laterally infinite hilly terrain. Aside from the orographic effects of the mountain, surface properties are horizontally homogeneous. Horizontal grid spacing is 300 m.

Figure 7 provides an overview of the cloud fields after 1:10 h by showing transparent isosurfaces of 0.1 g m^{-3} hydrometeor mass densities. In each of the 4 cases, an early cumulonimbus cloud has developed over the sunny (southeast) slope of the mountain due to its exposition to the sunlight. The cloud’s main updraft contains cloud droplets and rain drops in the low-CCN case and only cloud drops in the high-CCN cases. The upper cloud part is composed mainly of graupel in the low-CCN- and mainly of snow and cloud ice in the high-CCN cases. At the time 1:10 h, also first low cumulus clouds appear over the surrouding plains, triggered by shallow convective vertical motions. These subsequently grow into cumuli congesti and cumulonimbi, and their cloud tops reach the tropopause within the next 20 min.

The accumulated precipitation from these clouds after 2:00 h as function of location is depicted in Figure 8 for each simulation. Precipitation amounts are generally higher in the warm cases compared to the cold ones. Note also the more widespread precipitation in the low-CCN cases (steming from the cells over the plains), which is lacking in the high-CCN cases – although the corresponging clouds are present.

This behaviour has changed completely after 3:30 h (Figure 9). Now the differences in precipitation amount between the four simulations are very much smaller,

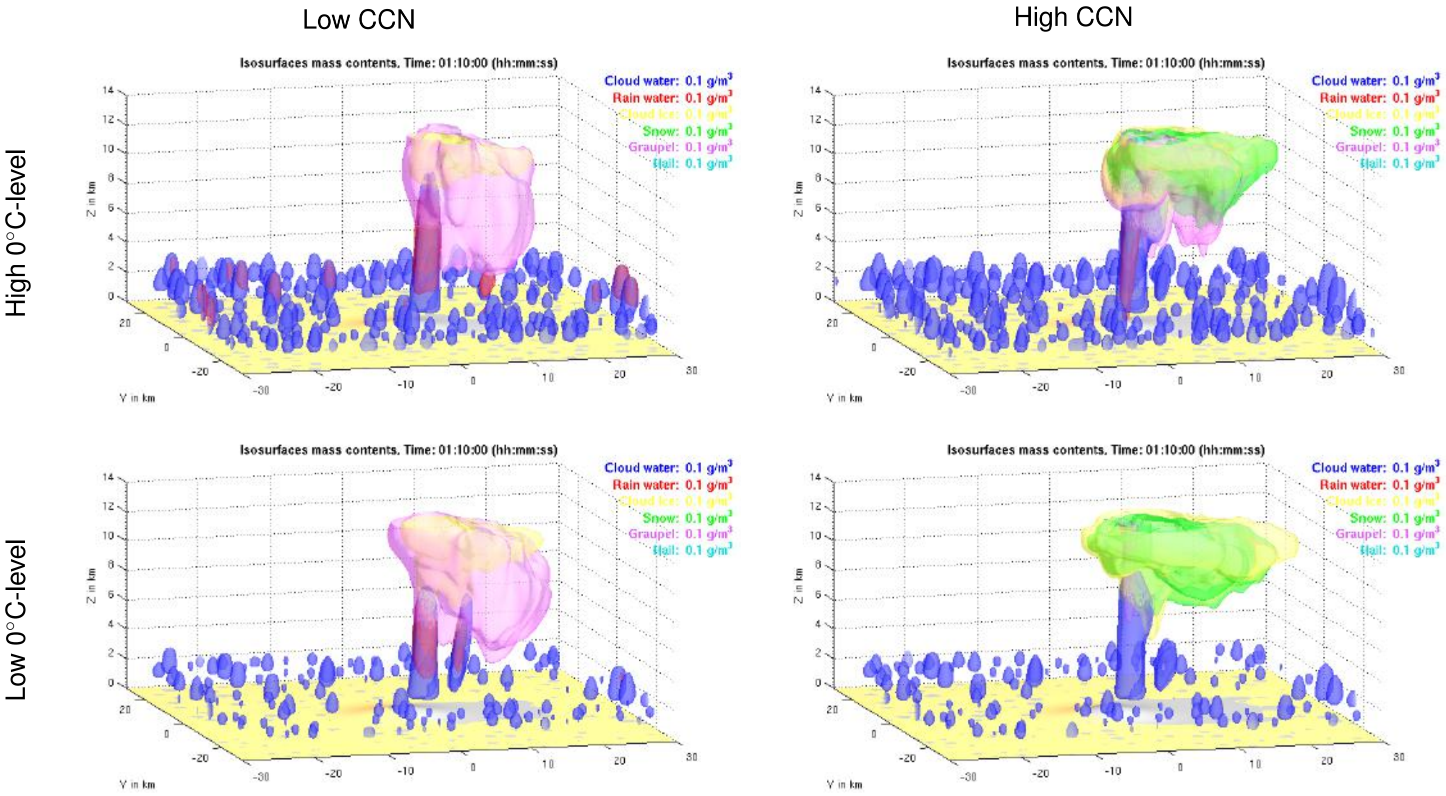

Fig. 7: 3D isosurfaces of the mass content 0.1 $g m^{-3}$ for each considered hydrometeor category after 1:10 h for each of the 4 simulations. Blue = cloud water, red = rain, yellow = ice, green = snow, purple = graupel, magenta = hail. The environmental flow is from left to right. Note the (barely visible) isolated bell-shaped mountain in the domain centers.

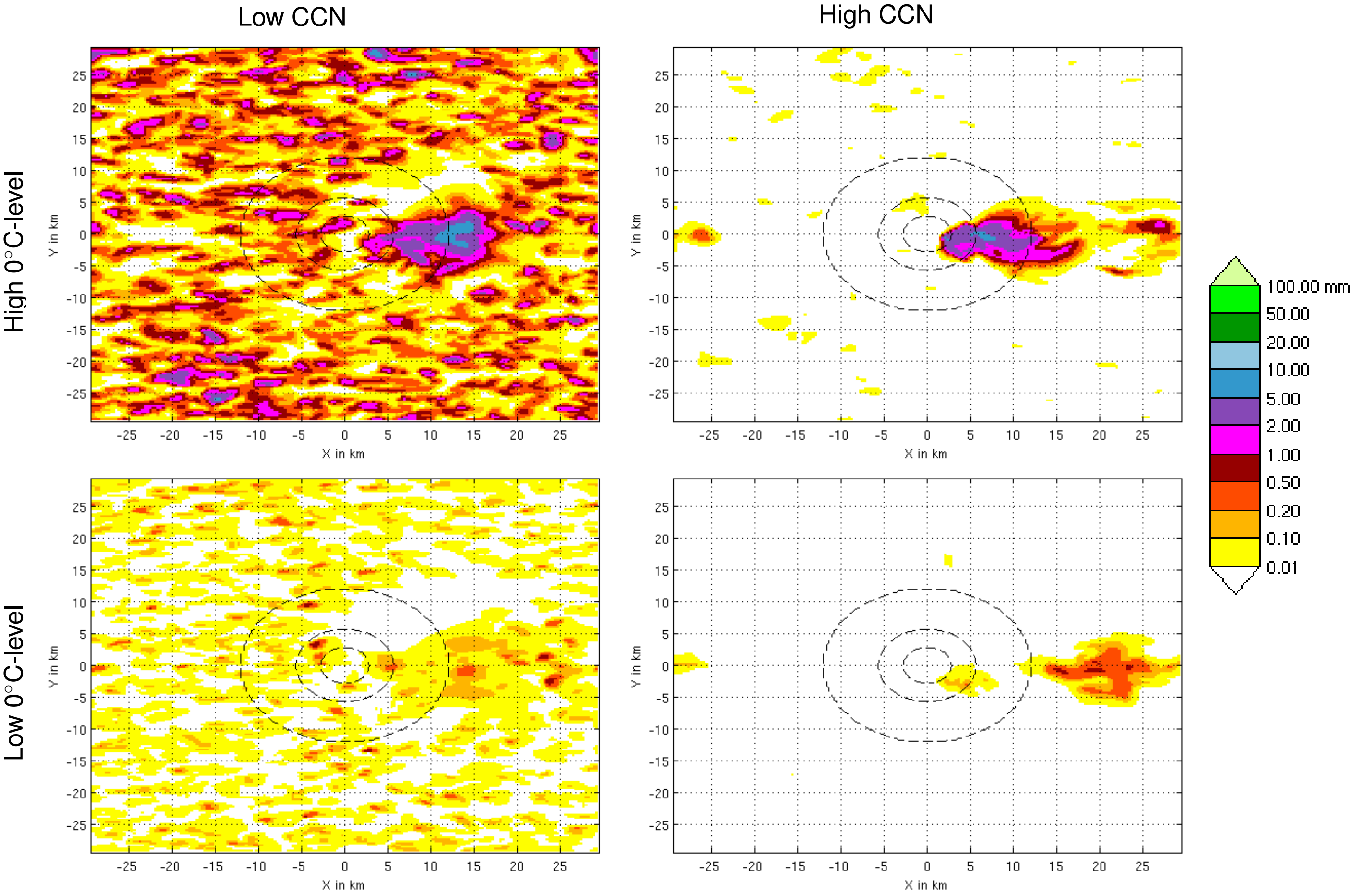

Fig. 8: Plan views of accumulated precipitation at ground in mm after 2:00 h for each of the 4 simulations. The dashed lines are height contours with 200 m spacing. The outer contour marks the transition between zero- and non-zero terrain heights.

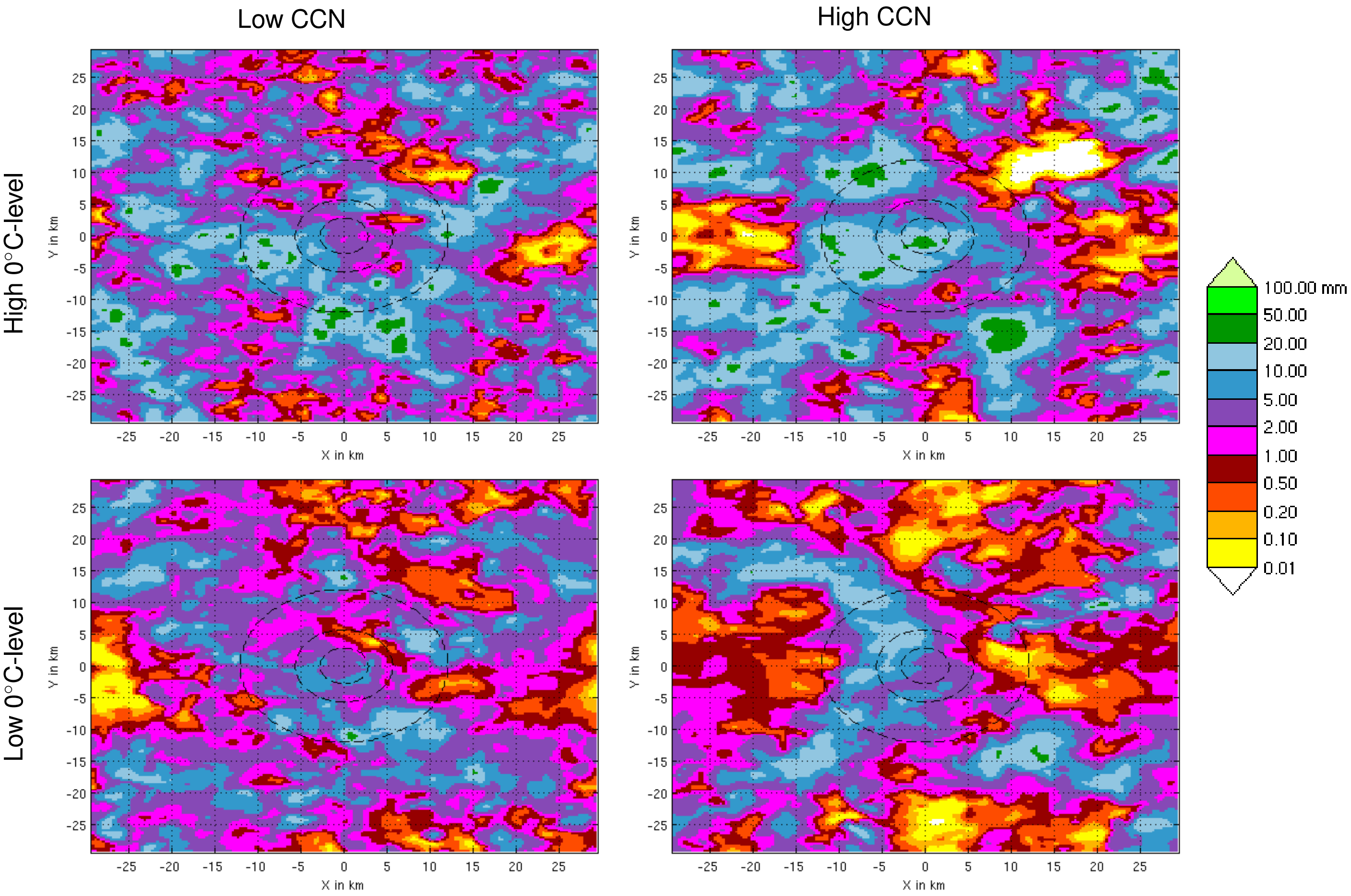

Fig. 9: Same as Figure 8, but after 3:30 h.

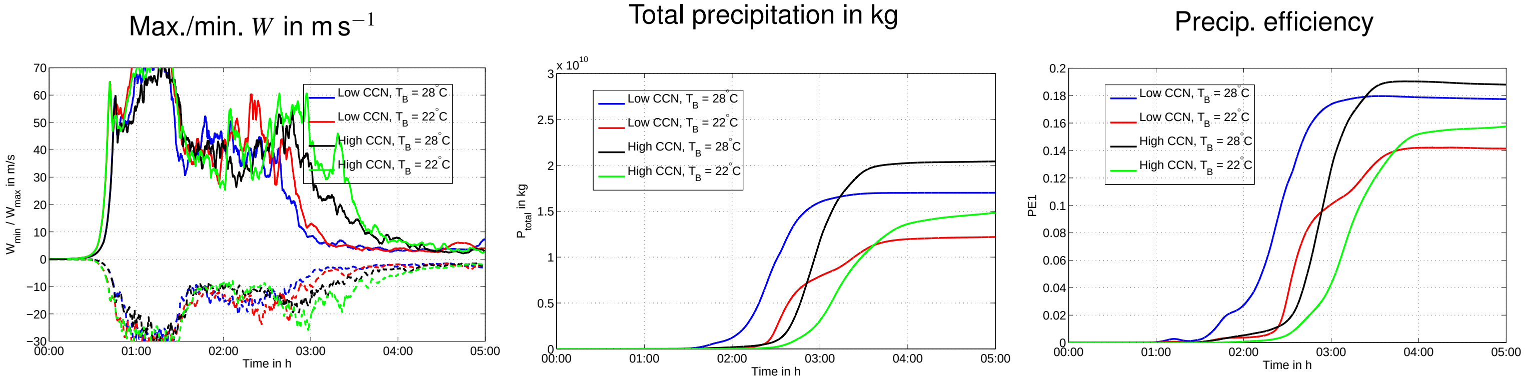

Fig. 10: Timeseries of minimum/maximum vertical velocity in m s^{-1} (left figure), total accumulated precipitation in kg (middle), and precipitation efficiency (right) for the 4 simulations.

and it seems that the high-CCN resp. cold clouds very much ”caught up” in producing precipitation.

The timeseries of maximum/minimum vertical velocity W_{max}/W_{min}, of total precipitation P and of the precipitation efficiency PE (ratio of P to the total condensed/sublimated mass) in Figure 10 illustrates this behaviour. The first updraft (single cell over the sunny mountain slope) spins up after about 30 min and is slightly stronger in the cold cases (maybe due to increased release of latent heat of freezing at lower altitudes). This first cell does not spread infinitely anymore as in our earlier simulations shown in BL06, but interacts with and is retarded by the later forming neighbouring cells. No secondary cells seem to be initiated by this primary cell. After about 1:30 h, W_{max} starts to be dominated by the ensemble of surrounding cells, which exhibits much lower W_{max} ($\approx$ 40 m s^{-1} compared to 70 m s^{-1} in the first cell. Further, between 2:00 h and 3:00 h, the two ”cold” simulations and the ”warm, high-CCN” run show a secondary maximum in W_{max}, leading to the interpretation, that secondary cells are generated by the precipitation induced downdrafts of the earlier cells. In these three cases, the main precipitation amount is produced by the secondary cells, not the primary ones as in ”warm, low-CCN” conditions. Lateron, the upper troposphere has been heated so much by the convective heat transport that all instability is removed and no further tertiary cells emanate. In the end, the high-CCN respectively warm cases exhibit slightly higher P and PE-values compared to low-CCN respectively cold conditions. In our four simulations, higher CCN values merely delay the onset of precipitation at same amount, whereas at colder temperatures lower amounts are observed.

Panels of MAX-CAPPI views of simulated radar reflectivity after 1:40 h in Figure 11 and 2:50 h in Figure 12 complement our discussion. After 1:40 h, the typical ”convective cores” indicating the presence of large hydrometeors (rain, graupel, hail) are only visible at low-CCN conditions, aside from the mountain induced first cell for the high-CCN cases. In the latter cases, the surrounding ensemble of primary cells creates a very ”inefficient” thick and slowly sedimenting cloud layer in the upper troposphere, which mainly consists of small ice and snow particles. Not until the secondary cells spin up, strong convective cores also form in high-CCN conditions, clearly visible at 2:50 h.

A first inspection of the microphysical conversion rates (processes) showed that, for the high-CCN cases, the autoconversion rate (cloud drops → rain drops) is lower by 1 - 2 orders of magnitude for the primary cells compared to the secondary cells, which explains the dramatic difference in their precipitation efficiency. Riming and the initiation and formation of larger solid hydrometeors is stronly enhanced by the presence or larger supercooled droplets compared to small cloud drops only. The obvious question is, why the autoconversion rate is so different at nominally the ”same” prescribed aerosol conditions (note that the model does not include an aerosol budget). This seems to have to do with the strong nonlinear dependence of our autoconversion parameterization from L_c (cloud mass density), N_c, L_r (rain mass density) and the assumed shape parameters of the underlying generalized gamma distribution of cloud droplets. Now, the conditions in the cloud updrafts only seem to be ”autoconversion friendly” for the secondary cells, which in turn ”flips the switch” for the formation of rain, graupel, and hail. This is currently under investigation.

5 CONCLUSIONS AND OUTLOOK

In this paper, the direct numerical simulation of shallow convective motions and subsequent triggering of an ensemble of interacting convective cells using the COSMO-model and the newly modified Seifert-Beheng two moment bulk microphysical scheme has been investigated, applying horizontal grid spacings of 100 - 500 m. Shallow convection has been forced by specifying suitable sensible and latent heatfluxes at the surface. The used model setup and turbulence parameterization are adequate to simulate the spin-up of an

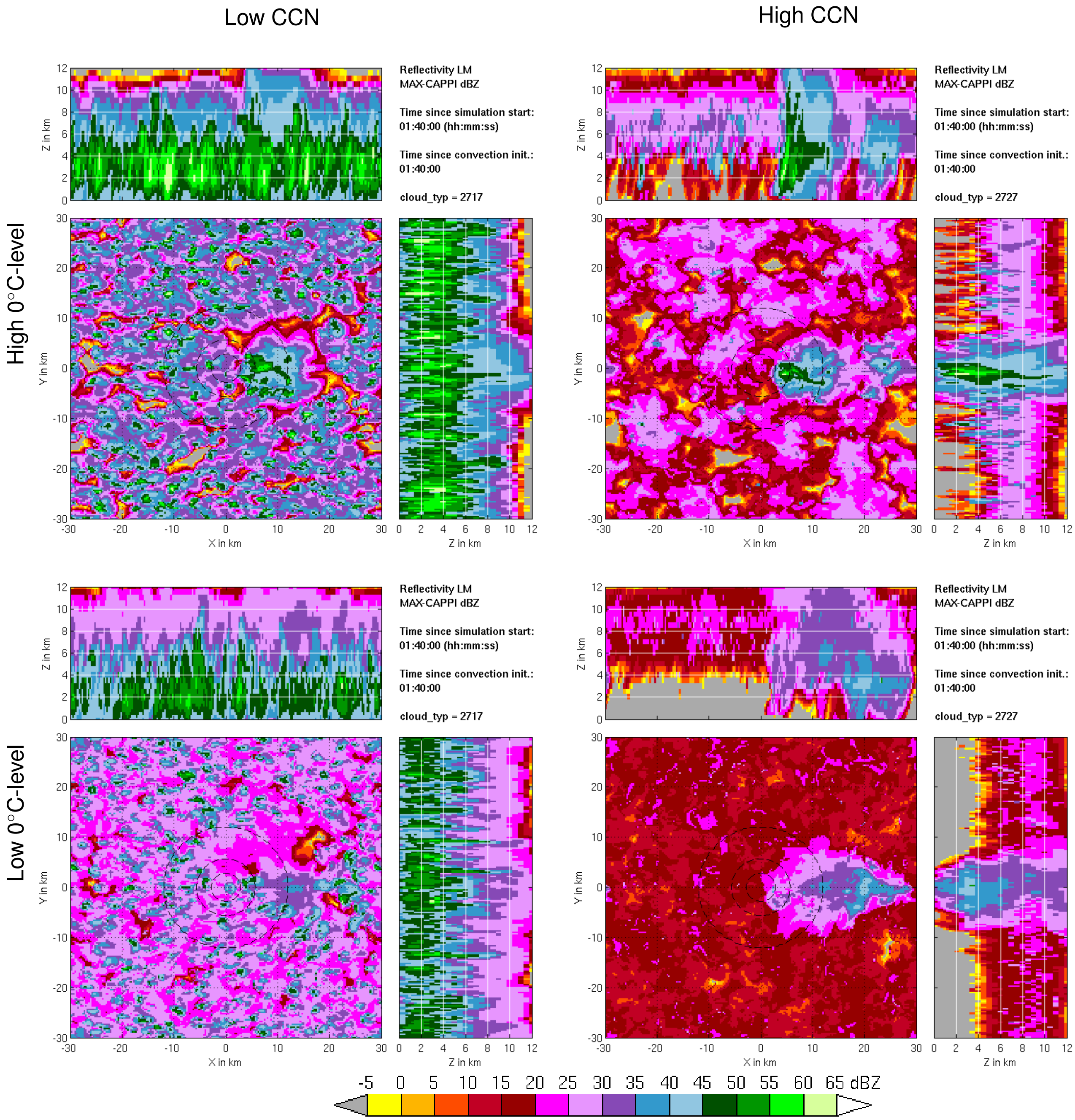

Fig. 11: MAX-CAPPI (top- and side views of vertical and horizontal column maxima) of simulated radar reflectivity in dBZ after 1:40 h for each of the 4 simulations.

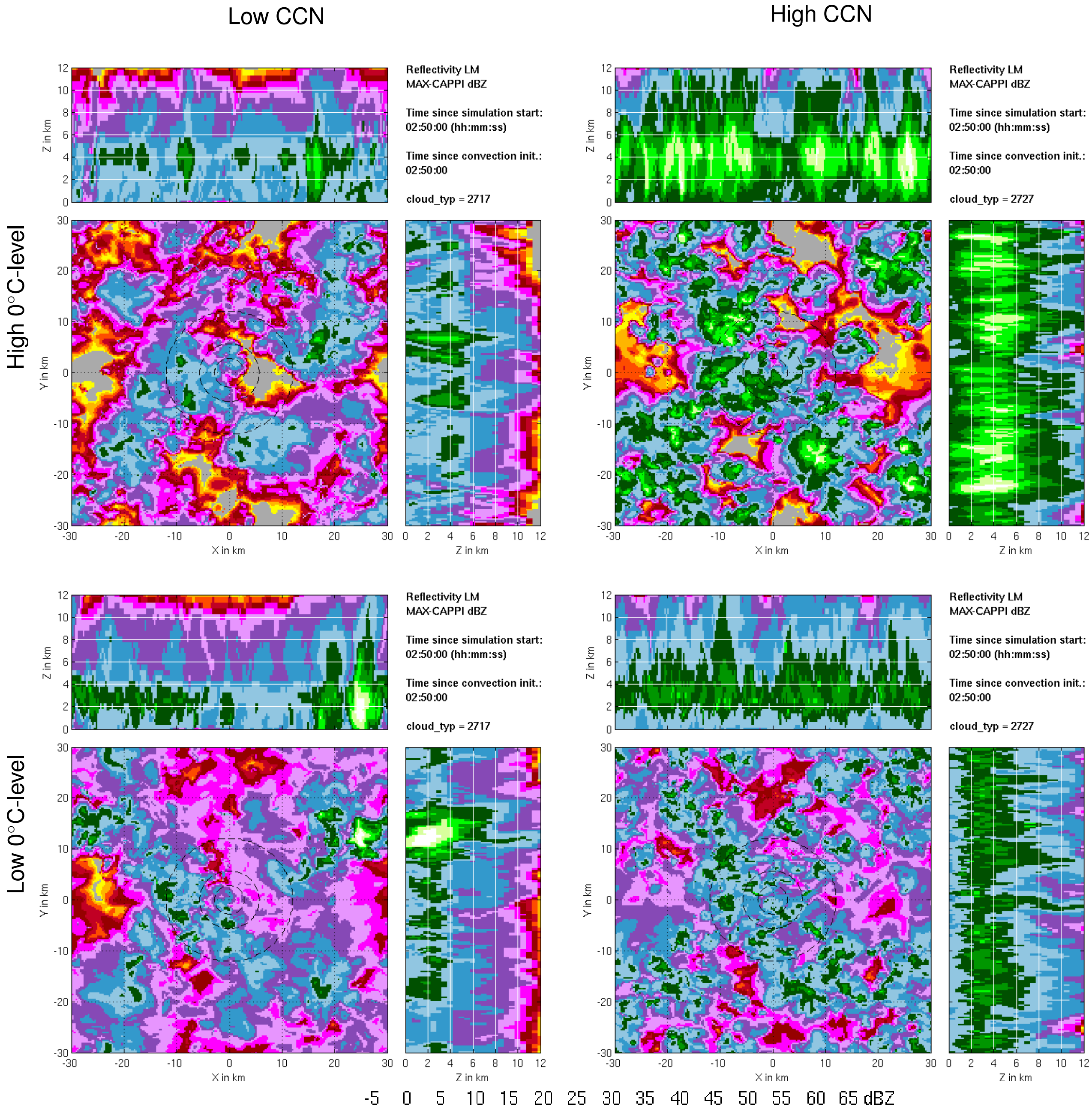

Fig. 12: Same as Figure 11, but after 2:50 h.

ensemble of cells with, after a certain time of self-organization, take on realistic mutual distances and maximum vertical updraft speeds. However, the transition from shallow to deep convection is quite fast, which may be due to ”extremely favorable” initial temperature and humidity profiles with very large $CAPE$.

Compared to the earlier study BL06, in which a single multicellular cell system has been initiated by pure mountain wave flow at same environmental conditions, now the former vigorous spreading of such a system is hindered by interactions with neighbouring cells. Such interaction-effects will be explored in more detail in the future. In this case, the assumption of ”high-CCN” conditions leeds to a time delay of precipitation accompagnied by a slight increase in precipitation amount and efficiency, in comparison with a ”low-CCN” regime. Prespecifying a colder environment at same $CAPE$) leeds to slightly lower simulated precipitation amount and efficiency. However, this sensitivity strongly depends on details of the parameterizations of autoconversion and cloud nucleation (and maybe others), which means that our results may not be generalized, and further investigations are necessary.

REFERENCES

Adrian, G. and F. Fiedler, 1991: Simulation of unstationary wind and temperature fields over complex terrain and comparison with observations, *Beitr. Phys. Atmos.*, **64**, 27–48.

Balaji, V. and T. L. Clark, 1988: Scale selection in locally forced convective fields and the initiation of deep cumulus, *J. Atmos. Sci.*, **45**, 3188–3211.

Blahak, U., Towards a better representation of high density ice particles in a state-of-the-art two-moment bulk microphysical scheme, Extended Abstract, 15th International Conference on Clouds and Precipitation, CANCUN, 7.7. – 11.7.2008.

Blahak, U., H. Noppel and K. D. Beheng, Influence of ambient environmental conditions and orography on the characteristics of deep convective cells as simulated with a sophisticated two-moment (bulk) microphysical scheme, 12th AMS Conference on Cloud Physics, 10. – 14.7.2006, Madison, Wisconsin, available online: http://ams.confex.com/ams/pdfpapers/113531.pdf.

Doms, G., J. Förstner, E. Heise, H.-J. Herzog, M. Raschendorfer, R. Schrodin, T. Reinhardt and G. Vogel, 2005: *A Description of the Nonhydrostatic Regional Model LM. Part II: Physical Parameterization*, Consortium for Smallscale Modeling (COSMO), available online: http://www.cosmo-model.org/content/model/documentation/core/cosmoPhysParamtr.pdf, 133 pp.

Doms, G. and U. Schättler, 2002: *A Description of the Nonhydrostatic Regional Model LM. Part I: Dynamics and Numerics*, Consortium for Smallscale Modeling (COSMO), available online: http://www.cosmo-model.org/content/model/documentation/core/cosmoDyncsNumcs.pdf, 134 pp.

Goody, R. M., *Atmospheric Radiation*, Clarendon Press, Oxford, 1964.

Herzog, H.-J., G. Vogel and U. Schubert, 2002: LLM – a nonhydrostatic model applied to high-resolving simulations of turbulent fluxes over heterogeneous terrain, *Theor. Appl. Climatol.*, **73**, 67–86, doi: 10.1007/s00704–002–0694–4.

Kondratjev, K. Y., *Radiation Characteristics of the Atmosphere and the Earth's Surface*, Amerind Publishing, New Delhi, 1976.

Noppel, H., U. Blahak, K. D. Beheng and A. Seifert, A two-moment cloud microphysics scheme with two process-separated modes of graupel, 12th AMS Conference on Cloud Physics, 10. – 14.7.2006, Madison, Wisconsin, available online: http://ams.confex.com/ams/pdfpapers/113532.pdf.

Seifert, A. and K. D. Beheng, 2006: A two-moment cloud microphysics parameterization for mixed-phase clouds. part I: Model description, *Meteorol. Atmos. Phys.*, **92**, 45–66.

Weisman, M. L. and J. B. Klemp, 1982: The dependence of numerically simulated convective storms on vertical wind shear and buoyancy, *Mon. Wea. Rev.*, **110**, 504–520.

THE SENSITIVITY OF MICROPHYSICS AND DYNAMICS OF SIMULATED CONVECTIVE STORM DUE TO THE ALTERED CLOUD DROP SIZE-DISTRIBUTION

M. Ćurić, D. Janc, V. Vučković, and N. Kovačević
Institute of Meteorology, University of Belgrade, Serbia

1. INTRODUCTION

Generally operational numerical models and the cloud-resolving mesoscale models use bulk microphysical schemes. Until it becomes feasible to replace bulk microphysics with explicit schemes, careful selection of a size distribution of hydrometeors with adjustable parameters will always be necessary. Recently some sensitivity studies with cloud-resolving models appear in literature (Van den Heever and Cotton, 2004; Cohen and McCaul, 2006) in which the arbitrarly specified parameters of the particle size-distribution are varied. The general conclusion is that the models are sensitive to variations of size-distribution parameters.

In present paper we focus on sensitivity study of cloud-resolving model outputs on the altered cloud drop size-distribution function. The Marshall-Palmer and various gamma size distributions are most widely used approximations of the raindrop spectrum. The Marshall-Palmer exponential size-distribution tends to overestimate the number of both the smallest and the largest drops (Torres et al., 1994). One of the alternate analytical function for fitting the observed cloud drop datasets is the Khrgian-Mazin size-distribution of gamma-type as proposed by Mazin et al. (1989) and Pruppacher and Klett (1997).

Most numerical models of convective storms with bulk microphysics (Murakami, 1990; Xue et al., 2001; Ćurić et al.,2003) consider that the cloud droplets are distributed according to the monodisperse size distribution while the Marshall-Palmer size distribution (marked MP) is applied to raindrops. The Khrgian-Mazin size distribution was mainly used in numerical models to approximate the cloud droplet spectra (Hu and He, 1988; Ćurić and Vuković, 1991) despite the fact that it represents also the raindrop spectrum. We therefore proposed the unified Khrgian-Mazin size distribution (marked KM) for entire liquid water (both cloud droplets and raindrops) instead of conventional approach. The size-distribution function may be written (Prupacher and Klett 1997; Ćurić and Janc 1998) as

$$N(D) = \frac{AD^2}{4}\exp\left(-\frac{BD}{2}\right), \qquad (1)$$

where

$$A = 1.452\frac{\rho Q}{\rho_w R_M^6}; B = \frac{3}{R_M}. \qquad (2)$$

Above, Q is the total liquid water mixing ratio; R_M is the mean radius of drop spectrum, ρ and ρ_w are the cloud air and the liquid water densities, while D is a drop diameter. Such type of a distribution generates only minor concentrations of raindrops over 0.5 cm in diameter (Ćurić and Janc, 1998) that is a case in reality. The unified Khrgian-Mazin size-distribution generates for 1-3 orders of magnitude higher number concentrations of raindrops than those for the Marshall-Palmer size distribution. We have tested the impacts of the unified KM size distribution on microphysics, dynamics and precipitation characteristics of simulated convective storm by utilizing the cloud-resolving mesoscale model (Ćurić and Janc, 2003). In sensitivity tests two model versions with respect to cloud drop spectrum treatment are used: one with conventional approach (marked MMP) and the one with the unified KM size distribution (marked KM). Primary aim of our investigation is to show that the substitution of the former cloud drop size distributions with the unified Khrgian-Mazin size-distribution produces essential changes in microphysics, dynamics and precipitation characteristics of simulated convective storm.

2. MODEL CHARACTERISTICS

The model used is the cloud-resolving mesoscale one (Ćurić et al., 2003; 2007). The model numerically integrates the time-dependent, nonhydrostatic and fully compressible equations. Dependent variables of the model are: Cartesian wind components, perturbation potential temperature and pressure, turbulent kinetic energy and mixing ratios for water vapor, cloud water and ice, rain, snow and hail. The model uses the generalized terrain-following coordinate in the vertical, while the horizontal coordinates are the same as in the Cartesian system. The turbulence is treated by 1.5-order turbulent kinetic energy formulation. Coriolis force is neglected.

The model was configured with the domain $64\,\mathrm{km} \times 64\,\mathrm{km} \times 17\,\mathrm{km}$ with a 600 m grid-spacing in horizontal direction and 300 m in vertical. The simulations were terminated at t=120 min. Long and short time steps were 3 and 0.5 s, respectively. The wave-radiating condition was applied for lateral boundaries. An upper boundary with a Rayleigh spongy layer was used, while the lower boundary was a free slip boundary.

The reference state is homogeneous in the horizontal direction, with constant values of temperature, humidity, pressure, wind velocity and direction. The model cloud is initiated by introducing an ellipsoidal warm bubble with 1.5 K amplitude at the center, with a horizontal radius of 10 km and a vertical radius of 1.5 km. The coordinates of the bubble center are (x=16, y=40, z=1.5) km. The sounding is characterized by 1800 J of available convective potential energy and veering winds from the surface to roughly 1 km in height. This represents typical environmental conditions in which individual cumulonimbus clouds are initialized. The wind speed varies from 7 m/s near the ground to about 17 m/s at 9 km height. The water vapor mixing ratio increases to 13.3 $\mathrm{g/kg}$ at p=900 mb.

For purpose of this study we use the single-moment bulk microphysics in which one moment of the size distribution would be held fixed. The mixing ratios of cloud water, cloud ice, rain, hail and snow are predicted. For KM model version cloud droplets and raindrops are represented by the unified Khrgian-Mazin size spectrum with constant mean radius of drop spectrum while the total liquid water mixing ratio is predicted. For MMP model version cloud water spectrum is monodispersive, while rain is represented by the Marshall-Palmer size spectrum. Hail and snow follow exponential size-distributions with constant intercept parameters while the cloud ice is monodispersive. The model uses a noniterative saturation-adjustment scheme introduced by Tao et al. (1989). Cloud ice initiation and its depositional growth are taken from Murakami (1990).

In the model, hail can be initiated by probabilistic freezing of raindrops, collisions between rain and cloud ice, collisions between rain and snow and aggregation of snow crystals. Hail grows by accretion of cloud water, cloud ice, rain and snow, or can be melted or sublimated. Snow can be initiated by the Bergeron-Findeisen process, autoconversion of cloud ice to snow, or collisions between raindrops and cloud ice crystals. Production terms for snow include various accretion terms (collisions of snow crystals with cloud ice, cloud water, raindrops, hail), snow melting and sublimation. Rainwater can be initiated by autoconversion of cloud droplets to raindrops, melting of precipitating ice or collisions with ice crystals at temperatures higher than 0 ℃.

3. SENSITIVITY EXPERIMENTS

Tests with the KM and MMP model versions are conducted in order to determine the impact of altered cloud drop size-distribution on model storm characteristics. We progressively increase the mean radius of cloud drop spectra (R_M) from 10 to $50\,\mu m$ with a step of $10\,\mu m$. Sensitivity tests with the KM model version are denoted subsequently by KMN $(N=1,2,3,4,5)$.

After being initialized, the model storm propagates roughly in NW-SE direction. Three cells are formed within the cloud at t=40 min. The first one is occurred at the front part of a cloud. Two other cells are at right and left cloud flanks. They are characterized by positive and negative vertical vorticities. In Figures, they would be marked A and B, respectively. Their formation is due to the sharp sheared environmental wind close to the ground. The model cloud top grows up to $\sim$13 km, while the averaged vertical velocity maximum (with respect to different tests) is $\sim 40\,ms^{-1}$.

3. 1. MICROPHYSICS

At first we shall investigate the influence of altered drop size-distribution to particular microphysical terms involving rainwater. The KM rates of rain accreting cloud water are larger than the MMP ones except for $R_M = 10\mu m$. The KM rates of rain collecting cloud ice are larger, while those of cloud ice accreting rain are lower than their MMP counterparts. The KM probabilistic freezing term is reduced for several orders of magnitude compared to the MP one because of smaller raindrop volumes in this case. Evaporation of the KM distributed raindrops is also reduced compared to the MP one, because of smaller surface of raindrops available for evaporation. This effect is the most expressed for $R_M = 10\mu m$ and small rainwater mixing ratios. The KM rates of rain accreting snow are lower than their MP counterparts. On the other side the rates of hail accreting rain as well as those of snow accreting rain would be larger or lower than the MMP values. Difference in magnitude of particular microphysical terms is caused mainly by different number concentrations and sizes of raindrops between KM and MP size-distributions. The other factors are different number concentrations, terminal velocities and total cross-section areas of particles interacting with raindrops.

Figs. 1 shows the visual appearance as viewed from the west of cloud water field at t=90 min for KM1 and MMP tests if the corresponding mixing ratios are greater and equal to $10^{-4} kgkg^{-1}$. Larger vertical extent in MMP test is induced by higher number concentration of smaller cloud drops in MMP test than in KM1 one.

Fig. 2 represents differences in rain water fields between KM1 and MMP tests. Raindrops are present at high levels (over 12 km) for KM1 test. Such scenario is affected by two principle factors: larger number concentrations of small raindrops (mainly below 0.1 cm in diameter) and lower values of probabilistic freezing term than in MMP test. As noted, the storm propagates faster in MMP case than in KM one. If $R_M > 20$ µm, the vertical extent of rainwater is below that for cloud water.

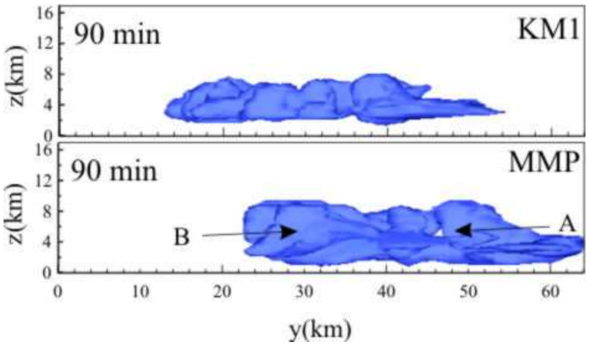

Fig. 1.Cloud water field as viewed from the west for two tests.

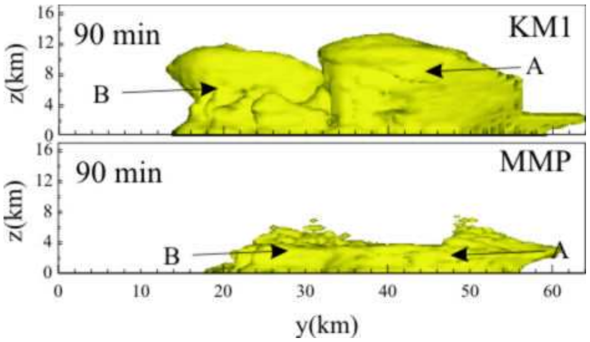

Fig. 2. Same as in Fig. 1 but for rainwater field.

Fig. 3 represents the maximum values of cloud water (a) and rainwater (b) mixing ratios versus time. Absolute maximum in cloud water mixing ratio is for KM5 test (12.6 g/kg). The smallest maximum is detected for MMP test (4.9 g/kg). These magnitudes are due mainly to the fact that the monodispersive cloud drop spectrum contains larger number concentration of smaller droplets as opposed to KM tests. The rainwater maximum values shows more complex feature: that for MMP test (13.0 g/kg) is lower than that for KM1 test (14.8 g/kg) but larger than that for KM5 test (6.8 g/kg).

3.2. DYNAMICS

In this section we would discuss about the influence of cloud drop size distribution on dynamics of simulated storm. In order to detect maximum differences in vertical velocity fields among KMN and MMP tests we represent their horizontal cross-sections for KM5 (Fig. 4) and MMP tests (Fig. 5) at t=80 min and height of 6 km.

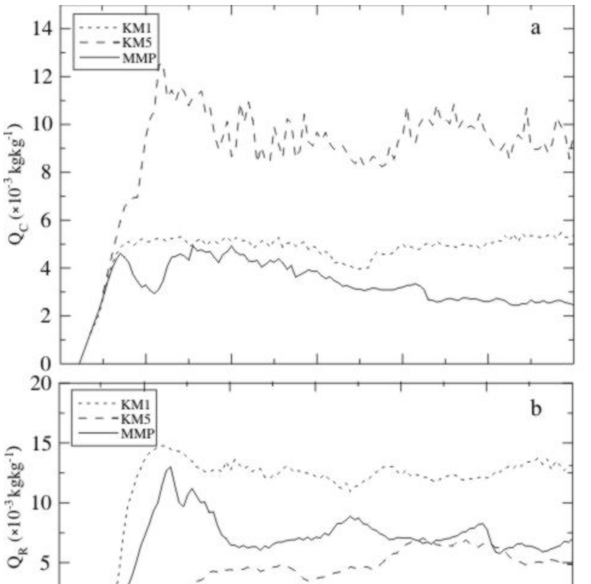

Fig. 3. Maximum values of cloud water (a) and rainwater (b) mixing ratios versus time.

Besides cells A and B another cell C is also formed behind the simulated cloud. As noted, the new cell (denoted by D) is initialized north-easterly from C cell for KM5 test (Fig. 4). This cell is not initiated, while the cell C has smaller area in MMP test (Fig. 5). This is due to the fact that more large raindrops within MP spectrum imply faster evaporation of rain water for the same environmental conditions. This should lead to stronger precipitation-laden downdrafts.

3.3. PRECIPITATION CHARACTERISTICS

Precipitations are the final product of interactions between microphysics and dynamics. We show the cumulative surface total precipitation (in mm) for KM1 and MMP tests at t=120 min whose amounts are greater or equal to 30 mm in Figs. 6 and 7, respectively. As noted, KM1 test is able to produce larger amount of total precipitation over larger area and in shorter time interval

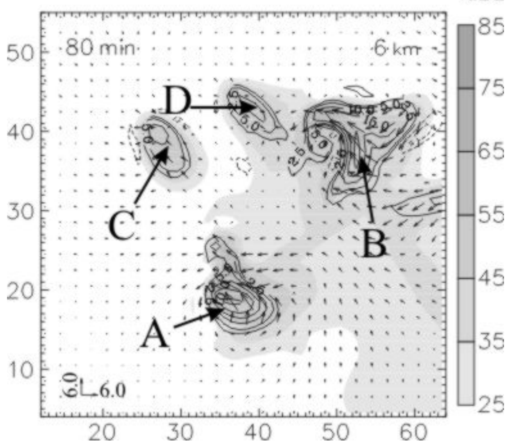

Fig.4.The zoomed horizontal cross sections of vertical velocity for KM1 test at t=80 min and 6 km height. Positive and negative values of vertical velocity are presented by solid and dash lines, respectively. The contour interval is 2.5 $m s^{-1}$ starting at 2.5 $m s^{-1}$. Streamlines represent the perturbation of horizontal velocity whose scale is given at left lower corner of each figure. Simulated radar reflectivity (dBZ) is represented by shadowed contours whose scale are denoted at the right side of the figure.

than MMP test. The distance between A and B cells are also larger in KM1 test. As a consequence the low-level downdrafts are then mainly stronger.

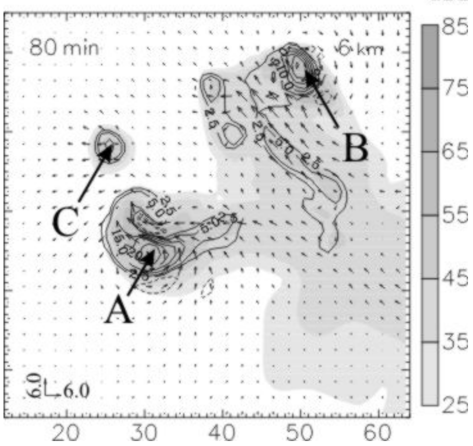

Fig. 5. As in Fig. 4 but for MMP test.

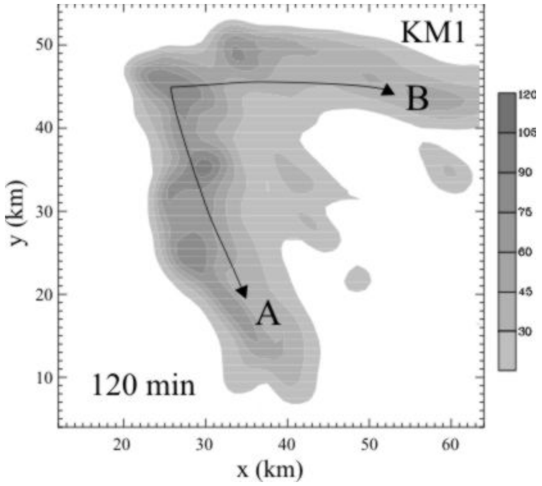

Fig. 6. Model values of surface cumulative total precipitation (in mm) for KM1 case at t=120 min represented by shadowed contours whose scale are denoted at the right side of the figure. Curved arrows denote tracks of A and B cells.

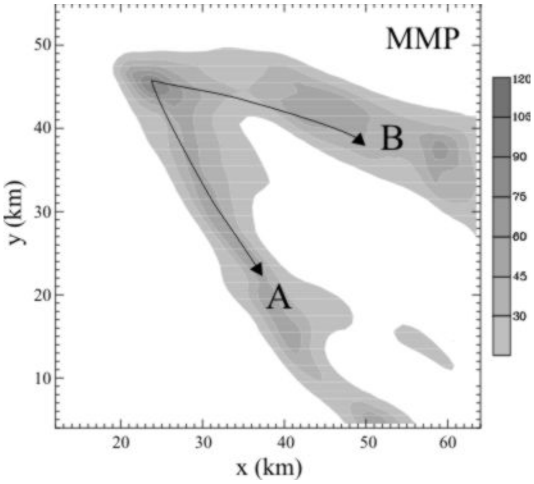

Fig. 7. As in Fig. 6 but for MMP test.

4. CONCLUDING REMARKS

In this paper the cloud drop spectrum is treated by the unified KM size distribution of a gamma type in the cloud-resolving mesoscale model. The purpose of this research is to investigate the sensitivity of model storm on altered cloud drop size distribution. Five sensitivity tests are conducted with KM size-distribution and one with conventional approach (MMP test). A summary of our findings concerning the comparison of model outputs follows.

Sensitivity tests show clearly that KM model version are capable to produce larger contents of cloud water, rain, hail, cloud ice and snow than MMP counterpart. Vertical extents of cloud water and rain fields are very sensitive to altered cloud drop size distribution.

KM model version is capable to produce larger total precipitation amount over larger area and in shorter time interval than the MMP counterpart. Consequences are that the downdrafts are mainly stronger for KM tests, while the model cloud propagates more slowly than for former approach. The new cell is initialized behind the main cloud for the KM model version that is not present in the MMP one as a result of smaller evaporation rate in that case. Results given by the model show clearly that the altered cloud drop size distribution lead to essential changes in microphysical, dynamical and precipitation characteristics of model convective storm. This should be important in operational use and analysis of convective storms.

5. BIBLIOGRAPHY

Cohen,C., E.W. McCaul Jr., 2006: The sensitivity of simulated convective storms to variations in prescribed single-moment mycrophysics parameters that describe particle distributions, sizes, and numbers. Mon. Wea. Rev. 134, 2547-2565.

Ćurić, M., D. Janc, V. Vučković, 1998: On the sensitivity of cloud microphysics under influence of cloud drop size distribution. Atmos. Res. 47-48, 1-14.

Ćurić, M., D. Janc, V. Vučković, 2007: Cloud seeding impact on precipitation as revealed by cloud-resolving mesoscale model. Meteorol. Atmos. Phys. 97, 179-193.

Ćurić, M., D. Janc,D., D. Vujović, V. Vučković, 2003: The effects of a river valley on an isolated cumulonimbus cloud development. Atmos. Res. 66, 123-139.

Ćurić, M., Z. Vuković, 1991: The influence of thunderstorm-generated acoustic waves on coagulation. Part I: Mathematical formulation. Z. Meteorol., 41,164-169.

Hu, Z., G. He, 1988: Numerical simulation of microphysical processes in cumulonimbus- Part I: Microphysical model. Acta Meteorologica Sinica 2, 471-489.

Mazin, I.P., A.K. Khrgian, I.M. Imianitov, 1989: Clouds and cloud atmosphere (in Russian). Leningrad, Gidrometeoizdat, 648pp.

Murakami, M., 1990: Numerical modeling of dynamical and microphysical evolution of an isolated convective cloud-The 19 July 1981 CCOPE cloud-. J. Meteor. Soc. Japan 68, 107-128.

Pruppacher, H. R., J. D. Klett, 1997: Microphysics of clouds and precipitation (second edition). Kluwer Academic Publishers, 954 pp.

Tao,W.K., J. Simpson, M. McCumber, 1989: An ice-water saturation adjustment. Mon. Wea. Rev. 117, 231-235

Torres,D.S., J.M. Porra, J.-D. Creutin, 1994: A general formulation for raindrop size distribution. J. Appl. Meteor. 33, 1494-1502.

Van den Heever, S.C., W. R. Cotton, 2004: The impact of hail size on simulated supercell storms. J. Atmos. Sci. 61, 1596-1609.

Xue, M., et al., 2001: The Advanced Regional Prediction System (ARPS)-a multi-scale nonhydrostatic atmospheric simulation and prediction model: Part II. Model physics and applications. Meteorol. Atmos. Phys. 76,143-165.

Acknowledgments

This research was sponsored by the Ministry of Science of Serbia under Grant No. 146006. We gratefully acknowledge Mr. Dragomir Bulatović for his assistence in preparing of the figures.

Description of the cloud hydrometeors observed in the Amazon region during the wet and dry season.

Maria Eugenia Baruzzi Frediani and Carlos Augusto Morales
Department of Atmospheric Sciences – IAG - University of São Paulo.
frediani@model.iag.usp.br and morales@model.iag.usp.br

ABSTRACT

This study aims to improve the description of the Amazonian clouds observed during the WET AMC 1999 and DRY TO WET RACCI 2002 field campaigns. A total amount of 188 clouds, of which 48 corresponds to the wet period and 140 to the dry and transition period, were measured by cloud microphysics instrumented aircrafts, mainly the CITATION of University of Dakota during the TRMM/LBA and ALPA of Ceará State University during the DrytoWet. The two field campaigns were conducted during the wet and dry season respectively and present a unique opportunity to investigate the impact of the aerosols, i.e., during the dry season several forest fires were observed with high concentration of cloud condensation nuclei (CCN), while in the wet season it was observed low concentrations of CCN. This study presents a characterization of the hydrometeors size distribution as a function of height (temperature), season and the presence of lightning, in order to understand the differences on the droplets formation and how the aerosols load plays in the formation of inhibition of the precipitation. Results obtained during the dry and transition seasons showed a suppression of the coalescence process, while the wet season showed distributions, where both modes, diffusion and coalescence, appeared very clear.

INTRODUCTION

Precipitation is a complex process responsible for the closure of the hydrological and energetic cycle. Although it is known that the convective systems that produce the major amount of the global precipitation are found in the tropics (Petersen et al. 2002, Rickenbach et al. 2001, Carey et al. 2001), it is also known that the study of precipitation is extremely challenging considering its wide time and spatial variability. Remote sensing studies have been extensively used to increase spatial and time accuracy of numerical model results (Kingsmill et al. 2004), however, this kind of study does not provide enough information on intra-cloud physics (Andreae et al. 2004), which leads to weak models parameterizations (Laurent et al. 2002). Therefore, to improve precipitation evaluation and predictability it is crucial to understand the physics inside the cloud, such as the hydrometeors size distribution and how it may change seasonally and according to human interference.

In order to accomplish such study, in situ measurements are essential to evaluate the intra-cloud processes (Vali 1997). Recently, two field campaigns promoted aircraft measurements over the Amazon, the 1999 WetAMC - TRMM/LBA (Artaxo et al. 2002, Silva Dias et al. 2002) and the 2002 Dry-to-Wet/RACCI (Silva Dias et al. 2003). The aircrafts used in these campaigns were instrumented with cloud characterization sensors and ground meteorological radars were used complement the tri-dimensional measurements of precipitation.

A considerable number of studies have been performed employing the data obtained on these campaigns.

Most of them concentrated to show that the systems observed over the Amazon exhibit remarkable seasonal patterns (Rickenbach et al. 2001, Williams et al. 2002, Petersen et al. 2002, Carey et al. 2001), related to the mean wind field circulation pattern (Easterly and Westerly flow).

During the wet period, particularly the westerly (easterly) wind regime, the observed clouds presented weak (strong) updrafts, low (high) CCN concentration and modest (excessive) amount of lightning flashes. From these perceptions, Williams et al (2002) suggested that the west regime presents vast similarities to maritime clouds, calling it ”Green Ocean” regime. In addition, according to Petersen et al. (2002), these same systems presented lower (higher) vertical development, lower (higher) vertical extension of precipitation cores above 30dBZ, warmer (colder) brightness temperature and lower (higher) precipitation rates.

When tropical systems develop under pollution generated by biomass burning, as occurs over the western Amazon during the dry to wet period, the high concentration of CCN produces clouds with high amount of small droplets. Williams et al. (2002) stated that this stage is the pre-monsoon season and presents extremer conditions than those seen in the Easterly regime during the wet season. Artaxo et al. (2002) observed a mean aerosol concentration of 8,000cm^{-3}, reaching 40,000cm^{-3}, whereas the average observed during the wet season was about ten times lower.

The drop size distributions of the dry to wet period modeled by Martins (2006) appeared narrower than those for pristine environment. Martins (2006) simulations also showed the mean precipitation rate is higher in clean atmosphere although isolated extreme rain peaks are found within high CCN concentration. According to Andreae et al. (2004), the droplet size reduction in polluted environment is related to the change of the altitude where precipitation begins, consequently intensifying the updrafts and promoting severe thunderstorms. Stith et al. (2002) showed that the shallow clouds in the wet season with weak updrafts generate mainly warm rain due to the altitude of the level where precipitation is formed. As the updrafts get stronger the concentration of droplets increases while its size decreases.

Nevertheless, the shape of droplets size distribution depends on the cloud stage of development. According to Pruppacher and Klett (1978), in the mature stage, the spectrum is larger than in the early and decay stages. In the early stage, the coalescence processes are only beginning, showing narrower spectra with high concentration of small droplets. In the decay stage the larger drops have already precipitated, generating a spectrum with low concentration of non-precipitating size droplets. Generally, the distributions show a sharp decrease in concentration with increasing size, since the collision and coalescence processes promotes the break up of large size drops. Essentially, the droplets growth is a non-linear function of the condensed water content that increases with the altitude, reaching its peak in the superior mean portion of the cloud and then decreases towards the top.

Although many studies have been produced in order to explore the general microphysics of Amazonian clouds and impacts of aerosols in the formation of precipitation, only a few, approach the subject through in situ measurements performed by aircrafts. Moreover, the characterization of the wet and dry to wet seasons, in terms of particle size distribution, have not yet been compiled in one single study. In this manner, this study aims on improve the hydrometeors description and characterize its size distribution over the Amazon, seeking to help the development of enhanced cloud parameterizations for weather and climate prediction models.

DATA

The WetAMC - TRMM/LBA campaign, performed during the wet season, from January to February 1999, aimed to evaluate the products of precipitation estimation from the meteorological radar and from the microwave algorithms of the TRMM satellite.The experiment accounted with aircraft measurements obtained by the UND CITATION II from the North Dakota University. This platform comprised sensors able to measure hydrometeors size distribution from 5 to 25000µm, air temperature, dew point, liquid and ice water content, vertical speed and atmosphere pressure. The measurements of hydrometeors size distribution used on this study were obtained with a set of probes, composed by a Forward Scattering Spectrometer Probe (FSSP), a Two Dimensional Cloud Probe (2DC) and a Two Dimensional Precipitation Probe (2DP); as well as a Rosemount Total Temperature, Hygrometer EG&G, Rosemount Static and Dynamic Pressure, Hot Wire Csiro King, for measurements of temperature, dew point, pressure and liquid water content, respectively. The dataset presented 48 processed cloud cases, available online in the TRMM Global Validation Campaigns website.

The Dry-to-Wet /RACCI campaign was accomplished between September and November 2002 and its main scope was the comprehension of convection during the transition of dry to wet season, besides the evaluation of the impact of aerosols from biomass burning in the formation of clouds and precipitation. The campaign had the microphysics aircraft measurements performed by the ALPA aircraft, from Universidade Estadual do Ceará. The same instrument models used in the first campaign performed some of the measures, like temperature, dew point, liquid water content and pressure. The measurements of hydrometeors size distribution were obtained by a FSSP, and two One Dimensional Optical Array Probe (OAP 1D 200x and 200y).

Although similar models of FSSP were used in both campaigns, they were set to measure different sizes spectra. The first had the FSSP set from 5 to 40µm with 5µm of diameter interval, while the second was set from 2.5 to 47µm with 1.5 µm of interval. Likewise, the probes used for larger diameters had diverse sets: The 2DC measured from 150 to 1,000µm with 50µm of interval, the 2DP, from 1,000 25,000µm with 400µm interval, the OAP 1D 200x, from 20 to 300µm with 30µm interval and finally the OAP 1D 200y that measured from 300 to 4,500µm with 300µm interval. The dataset presented 21 unprocessed continuous samples, i.e., in and out cloud.

In addition to the aircraft data, the analysis methodology comprised the satellite images from GOES-8, channel 4 infrared, and the Lightning data from the ALDF (Advanced Lightning Direction Finder) Network.

METHODOLOGY

The unprocessed dataset from Dry-to-Wet/RACCI were reduced from measurements at 20Hz sampling to 1Hz and the FSSP data had to be synchronized to the rest of the measurements due to its independent acquisition system. The offset of the liquid water content (LWC) was removed by a linear adjustment function of the true air speed.

Once one of the campaign scopes were to investigate the role of the aerosols in the formation of precipitation, the dataset contained measurements from inside and outside clouds. Therefore, each flight dataset was broken into many samples, considering only the periods that the aircraft was inside a cloud. The selection criteria was based on the time series of temperature, dew point, LWC and droplets concentration from the FSSP. Changes in the pattern of the parameters along the time represents the conditions of that aircraft were outside (inside) and then inside (outside) a cloud environment. Analysis of altitude and trajectory were useful to identify measurements of an isolated cloud and multiple measurements of a cloud system. The selection into the 21 flight datasets resulted in 265 cloud samples.

The characterization of the clouds was based on the hydrometeors size distribution and on the liquid water content size distribution, both segmented by temperature intervals representing the vertical structure of the cloud. A classifying method was defined to join similar datasets and generate a single representation of each resulting group. The adopted method was built concerning the following criteria:

a) Dominating clouds
b) Type of the sampled area
c) Conditions of the atmosphere, polluted or pristine
d) Wind regime (considered only for the wet season)
e) Lightning flashes

The clouds were identified using the GOES-8 satellite image, selected considering the time of the image available and the time of the sampling. The longest time gap between image and sampling was no longer than 15 minutes. The satellite images were used to define the (a) and (b) criteria.

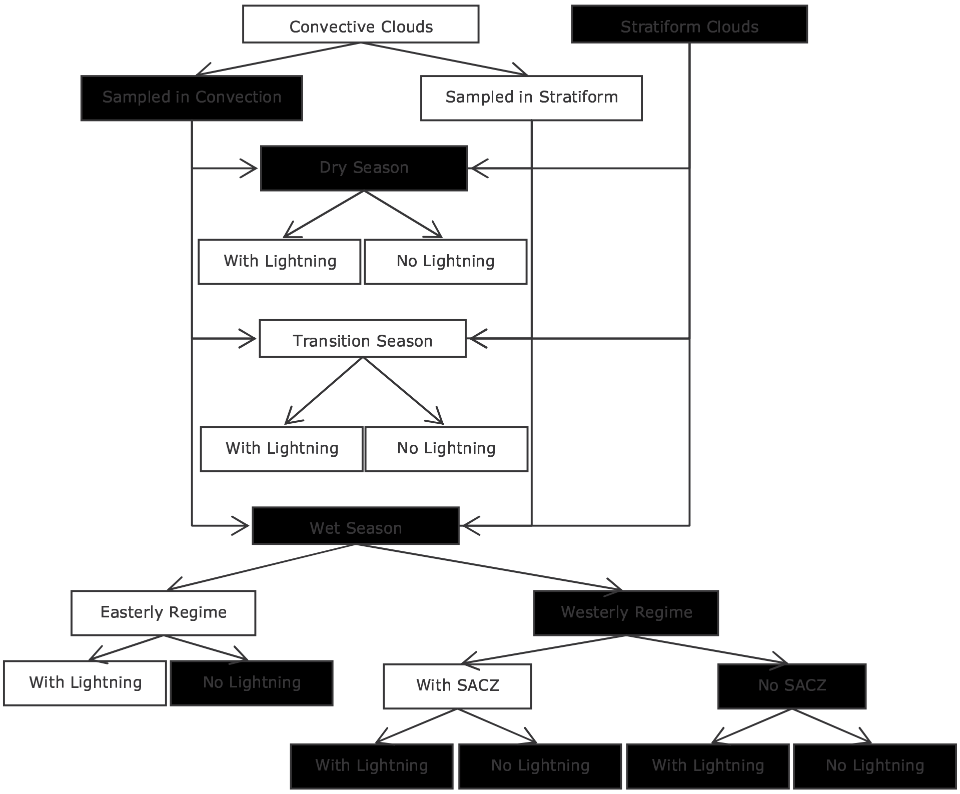

Figure 1: Scheme of the classifying method defined to join similar datasets and generate a single representation of each resulting group

The conditions of the atmosphere, (c), followed Vestin (2007) that stated

- Dry season: from September 11th to October 8th
- Transition period, from October 9th to 30th

The Wind regime, (d), followed Rickenbach (2001) definitions, which consisted of the evaluation of the 1,000 - 800mb wind regime as well as the presence of the South Atlantic Convergence Zone (SACZ):

- Easterly regime: from January 19th to

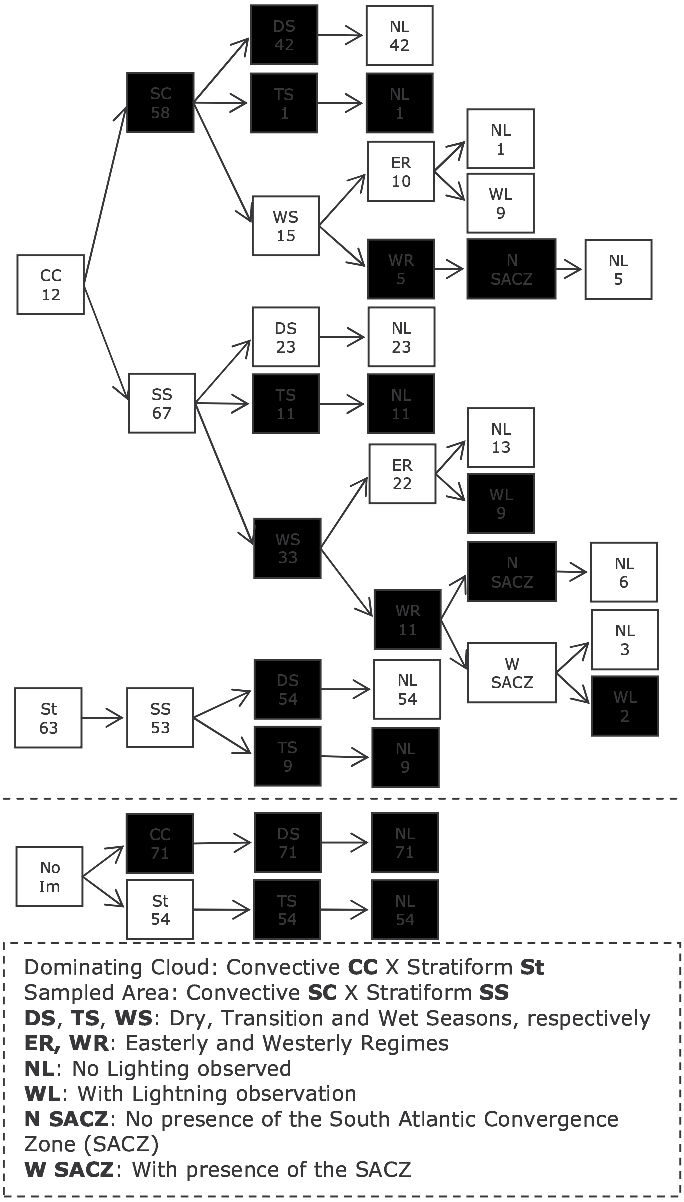

Class #	Class Name
1	CC SC DS NL
2	CC SS DS NL
3	St SS DS NL
4	CC SC TS NL
5	CC SS TS NL
6	St SS TS NL
7	CC SC WS ER NL
8	CC SC WS ER WL
9	CC SC WS WR NSACZ NL
10	CC SS WS ER NL
11	CC SS WS ER WL
12	CC SS WS WR NSACZ NL
13	CC SS WS WR WSACZ NL
14	CC SS WS WR WSACZ WL

Figure 2: Result of the application of the classifying method. Each step of the classification shows the number of samples

29th and February 8th to 22nd.

- Westerly regime: from January 29th to February 8th, without SACZ, and from February 22nd to March 1st, with well-defined SACZ.

Finally, the lightning flashes, (e), were gathered before and after the 15 minutes the sampling time range. *Figure 1* shows the diagram of the applied method.

The *Figure 1* diagram provided 14 final classes of 24 possibilities. As it can be seen in *Figure 2*, some samples were not completely classified due to missing satellite images around the sampling time. Therefore, they were partially classified and will not account for the present characterization. Because of that, the dataset was reduced from 265 samples, from dry to wet season, to 140, plus the initial 48 samples from the wet season.

For each one of the 14 resulting classes, four mean distributions were created. The first presented the mean hydrometeors concentration per diameter interval (HSD), and the second, presented the mean liquid water content per diameter interval (LWD). Both of these distributions displayed the mean values for every single temperature level observed in the respective classes. The temperature levels were shown on a color scale where red represented warmer temperatures, and blue, colder temperatures. Temperatures below 0°C ($-5 \le T < 0$) were represented by yellow and above or equal to 0°C ($0 \le T < 5$) were represented by light orange. The third and fourth distributions also showed the HSD, and LWD, except that these do not consider the temperature levels and also displayed the mean standard deviation.

Figures 3 to *16* show the distributions for all the 14 classes. On the left side of each figure are the HSD's, where the one on the top shows the distribution according to the temperature levels, and the one on the bottom shows the general mean value as well as the mean standard deviation. On the right side are the LWD's, respecting the same organization for top and bottom positions.

ANALYSIS

The majority of samples belonged to the dry season, with 119 samples, followed by the wet season, with 48, and at last, the transition season, with 21 samples. The numbers of samples of each classifying step are shown in *Figure 2*, as well as the representing indexes for each final class.

Noticing yet the classifications of the samples, it is seen that lightings were only observed during the WS and happened during the WR as well as during the SACZ in the ER. In the ER 56% of the samples presented lightning against 12% of the WR.

If the rate of lightning flashes may be considered as an indicator of thunderstorms intensity, the observations, then, agree with Richenback et al. (2001) and Williams et al. (2002) that stated that the systems of the WR are less intense than those in the ER.

The HSDs of the dry season (Figures 3 to 5), were all very similar, presented a narrow spectrum, and confirmed the dominance of diffusion growth over coalescence. Growth by diffusion was clearly detected until sizes of around 20μm, while vestiges of the coalescence mode could be noticed only from 30 to 50μm. They all showed higher concentrations at warmer temperatures (10 – 25^{o}C). The maximum concentration of droplets reached 93.1 $cm^{-3}dD\mu m^{-1}$, at 5.75μm (Figure 5), but all the spectra experienced a steep reduction of their concentration around 10μm. Precipitating-sizes, over 1,000μm, were observed in very low concentration (maximum of ~2x10^{-7} $cm^{-3}dD\mu m^{-1}$). The LWD distribution showed that the location of droplets with superior water volume and diameter was preferably at colder temperatures, i.e., larger droplets were found at higher levels. Considering the robust efficacy of diffusion growth, the presence of these large droplets at colder levels may be explained by the occurrence of strong updrafts. That way, the updrafts would have caused the enhancement of supersaturation conditions, and consequently droplets growth at higher levels. The highest LWD mean values were around 0.1 g cm^{-3}, and remained between 16.25 - 22.25μm, at -5 to 15°C.

The distributions of the classes during the transition season (Figure 6 to 8) showed more explicit differences concerning stratiform and convective conditions. The stratiform distribution (Figure 8) presented its highest concentration at smaller diameters (72.3 $cm^{-3}dD\mu m^{-1}$ at 5.75 μm), while the convective distribution presented its maximum at slightly larger diameters (14.75 μm) and consequently a comparatively broader spectrum. The distributions from the TS do not exhibit considerable differences from those of DS. Affirmations stating differences between the shapes of TS and DS spectra, so far, are inconclusive. A more detailed analysis of these distributions would require an inspection of the aerosols loading in the atmosphere. So far, the characteristics found in the TS were very similar to the DS, such as the dominance of diffusion growth and low concentration of precipitating-size drops.

In the wet season (Figures 9 to 16), the displayed HSDs revealed a minor variation on concentration. The spectra shifted slightly along the axis, however, the main shape of the spectra remained unchanged. The classes of the WS presented a clear development of the coalescence process around 25μm. Generally, colder temperatures hold higher concentrations, particularly after coalescence and before precipitation. Spectra were broader than dry and transition seasons, with lower concentrations up to 20μm, but revealed higher concentration of particles ranging from 20μm to 7mm. The concentration maximum reached 3.82 $cm^{-3}dD\mu m^{-1}$ at 17.5μm and drops larger than 10mm were detected. Precipitating sizes achieved 1.5x10^{-4} $cm^{-3}dD\mu m^{-1}$, an elevated value compared to dry and transition seasons. The LWDs showed constantly increasing values, stating the efficiency of the coalescence process over diffusion. The peak of the coalescence mode only appeared, in the FSSP measured spectrum, at temperatures warmer than 0°C. For those levels, coalescence attained its maximum between 30 – 40μm. Additionally all classes exhibited a well-defined diffusion growth mode, situated between 10 – 20μm. Finally, no relevant differences were detected between cases with and without lightning.

DISCUSSIONS

At the present moment, the classes belonging to the dry season have not appeared to be different of those from the transition season. Future studies including aerosols concentration will permit a better distinction of pollution and clean conditions, providing more resources to classify each sample. In this manner, DS and TS may be evaluated as a single period.

The DS and TS period clearly exhibited the dominance of diffusion growth over coalescence. Mainly, high concentration values at smaller sizes (up to 20μm), followed by a sharp decrease in concentration with increasing diameter, thus characterizing a narrow spectrum. Larger drops, over 1mm, appeared in very low concentration. The majority of the liquid water volume were distributed among droplets below 30µm.The concentration of liquid water mostly at higher levels, suggested the presence of strong updrafts.

The WS presented a slightly shifting of the spectra among its classes. However, the differences among each other were not significant to particularize any of the classes. The presence of lightning did not affect the distributions, neither the spectra nor the concentrations of droplets. The processes of growth by diffusion and coalescence were clearly visible, being the coalescence the responsible for the spectrum enlargement. The greater amount of liquid water was retained by larger droplets, over 30µm.

HSD's from DS and TS exhibited over 20 fold higher concentration than the WS's, at small diameters. Despite of the initial lower concentration, the WS revealed a broader spectrum with higher concentration after the coalescence mode.

REFERENCES

Andreae, M. O., D. Rosenfeld, P. Artaxo, A. A. Costa, G. P. Frank, K. M. Longo, and M. A. F. Silva Dias, 2004. Smoking Rain Clouds over the Amazon. *Science* **303** (5662), 1337. [DOI: 10.1126/science.1092779].

Artaxo, P., J. V. Vanderlei Martins, M. A. Yamasoe, A. S. Procópio, T. M. Pauliquevis, M. O. Andreae, P. Guyon, L. V. Gatti, and A. M. Cordova Leal, 2002. Physical and chemical properties of aerosols in the wet and dry seasons in Rondônia, Amazônia. *J. Geophys. Res*., 107, doi: 10.1029/2001JD000666.

Carey, L.D., R. Cifelli, W.A. Petersen, and S.A. Rutledge, 2001. Characteristics of Amazonian Rain Measured During TRMM-LBA. Preprint Volume, American Meteorological Society 30th International Radar Conference, Munich, Germany, 19-24 July.

Laurent, H.; Machado, L.A.T.; Morales, C.A.; Durieux, L., 2002. Characteristics of the Amazonian mesoscale convective systems observed from satellite and radar during the WETAMC/LBA experiment. *J. Geophys. Res* 107, (D20).

Martins, J. A., 2006. Efeitos dos núcleos de condensação na formação de nuvens e o desenvolvimento da precipitação na Região Amazônica durante a estação seca. Dissertação de Mestrado, IAG-USP.

Pruppacher, H. R., e J. D. Klett, 1978. *Microphysics of cloud and precipitation*. Reidel Publishing Company 1st ed., 9-44.

Petersen, W.A., S.W. Nesbitt, R.J. Blakeslee, R. Cifelli, P. Hein, and S.A. Rutledge, 2002: TRMM Observations of Intraseasonal Variability in Convective Regimes over the Amazon. *J. Climate*, 15, 1278–1294.

Rickenbach, T. M., R. N. Ferreira, J. Halverson, and M .A.F. Silva Dias, 2001: Mesoscale properties of convection in western Amazonia in the context of large-scale wind regimes. *J. Geophys. Res.*

Silva-Dias, M. A. F., Rutledge, S., Kabat, P., Silva-Dias, P. L., Nobre, C., Fisch, G., Dolman, A. J., Zipser, E., Garstang, M., Manzi, A. O., Fuentes, J. D., Rocha, H. R., Marengo, J., Plana-Fattori, A., Sá, L. D. A., Alvalá, R. C. S., Andreae, M. O., Artaxo, P., Gielow, R. & Gatti, L. (2002) Cloud and rain processes in a biosphere-atmosphere interaction context in the Amazon Region, *Journal of Geophysical Research. 107*, 8072.

Silva-Dias, M. A. F., Fisch, G., Plana-Fattori, A., Silva-Dias, P. L., Machado, L. A. T., Morales, C. R., Manzi, A. O., Yamasoe, M., Marengo, J., Ambrizzi, T., Andreae, M. O., Artaxo, P., Freitas, S., Longo, K. M., Costa, A. A., Betts, A. K. & Williams, E. (2003) Radiation, cloud and climate interactions in SW Amazon during the dry-to-wet transition season/LBA in pp. 13683-13683 Geophysical Research Abstracts.

Stith, J. L., J. E. Dye, A. Bansemer, A.J. Heymsfield, C.A. Grainger, W.A. Petersen, and R. Cifelli, 2002: Microphysical Observations of Tropical Clouds. *Journal of Applied Meteorology*, 41, 97-117.

Vali, G., 1997: Cloud Properties Measured From Aircraft – An Assessment. *Proc. of WMO Workshop on Measurements of Cloud Properties for Forecasts of Weather and Climate,* WMP Report 30, WMO/TD 852, pp. 37-55.

Vestin, A., J. Rissler, E. Swietlicki, G. P. Frank, and M. O. Andreae, 2007. Cloud_nucleating_properties_of_the_amazon_biomass_burning_aerosol_ CCN_measurements_and_modeling. *Journal of Geophysical Research*, Vol. 112, D14201, doi:10.1029/2006JD008104, 2007.

Williams E., et al. 2002. Contrasting convective regimes over the Amazon: Implications for cloud electrification. *J. Geophys. Res.* 107(D20), doi: 10.1029/2001JD000380.

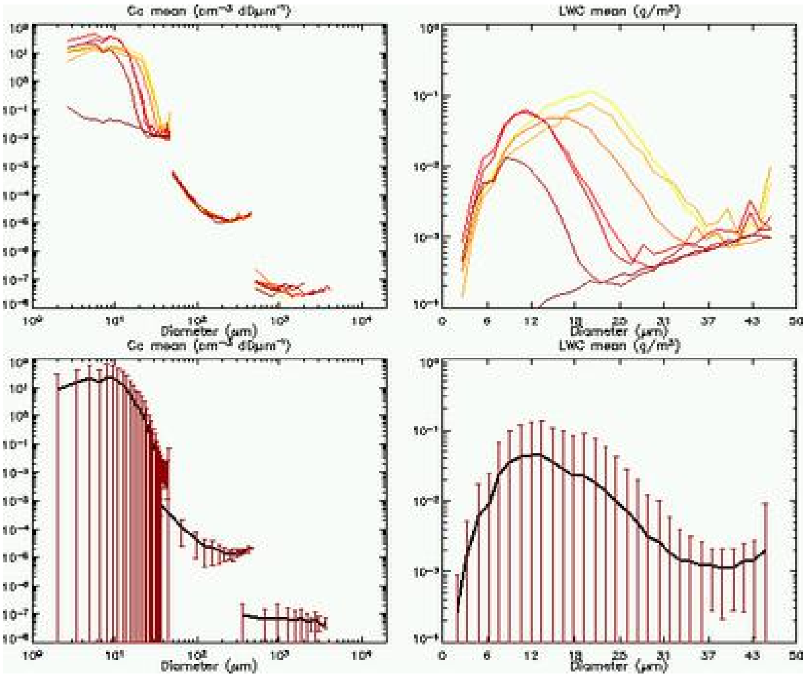

Figure 3: Convective Clouds, Sampled in Convection, Dry Season, No Lightning.

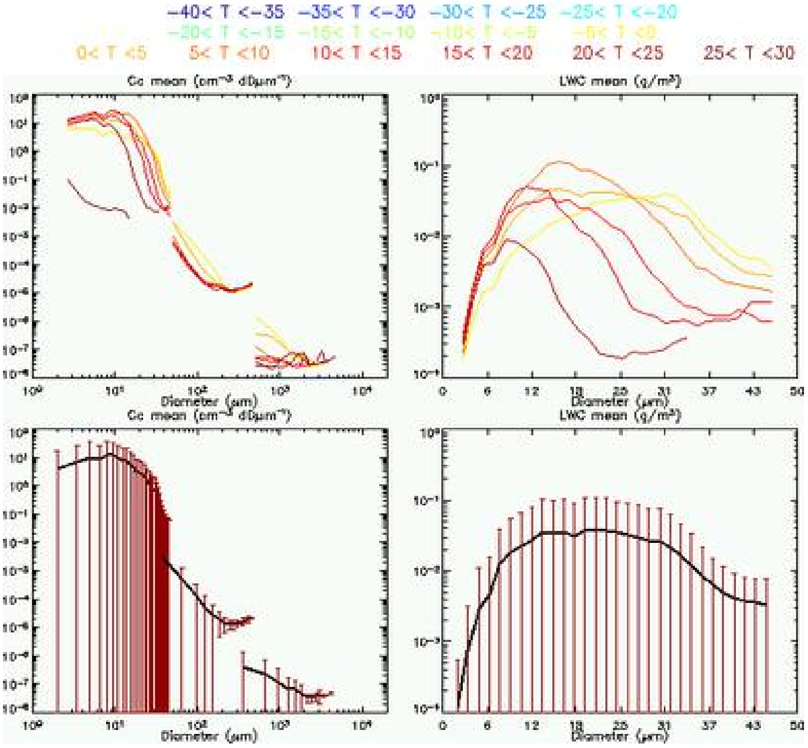

Figure 4: Convective Clouds, Sampled in Stratiform, Dry Season, No Lightning

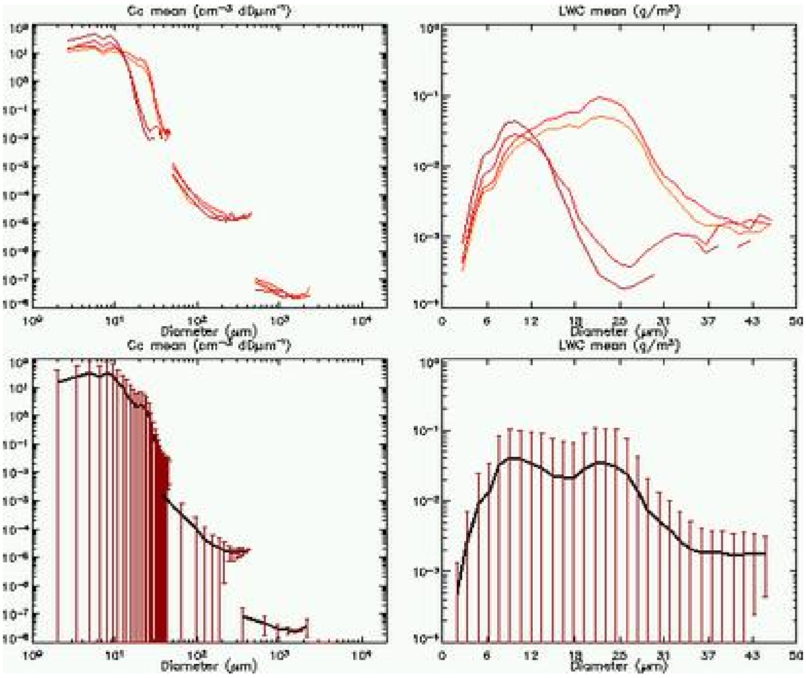

Figure 5: Stratiform Clouds, Sampled in Stratiform, Dry Season, No Lightning.

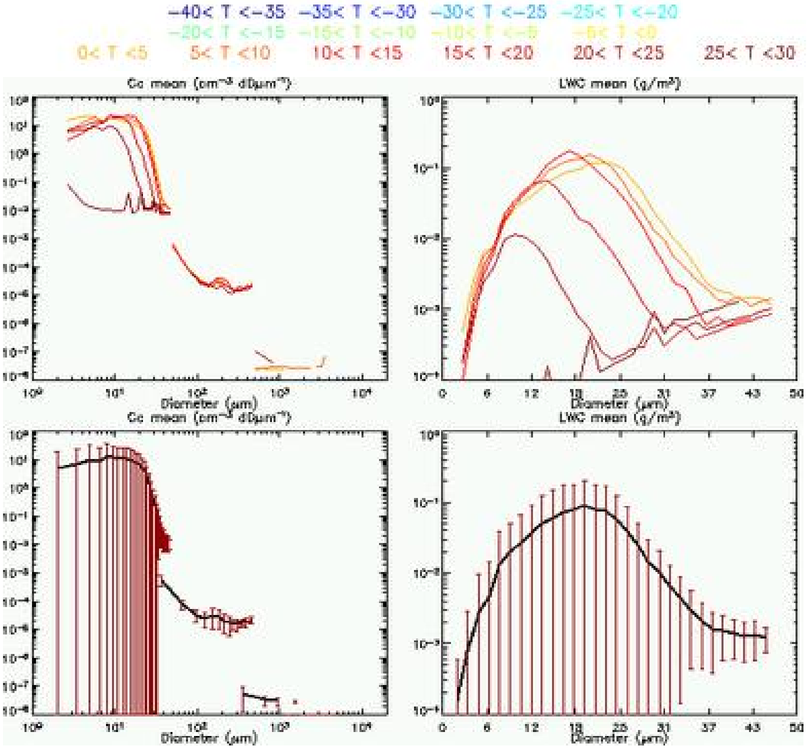

Figure 6: Convective Clouds, Sampled in Convection, Transition Season, No Lightning.

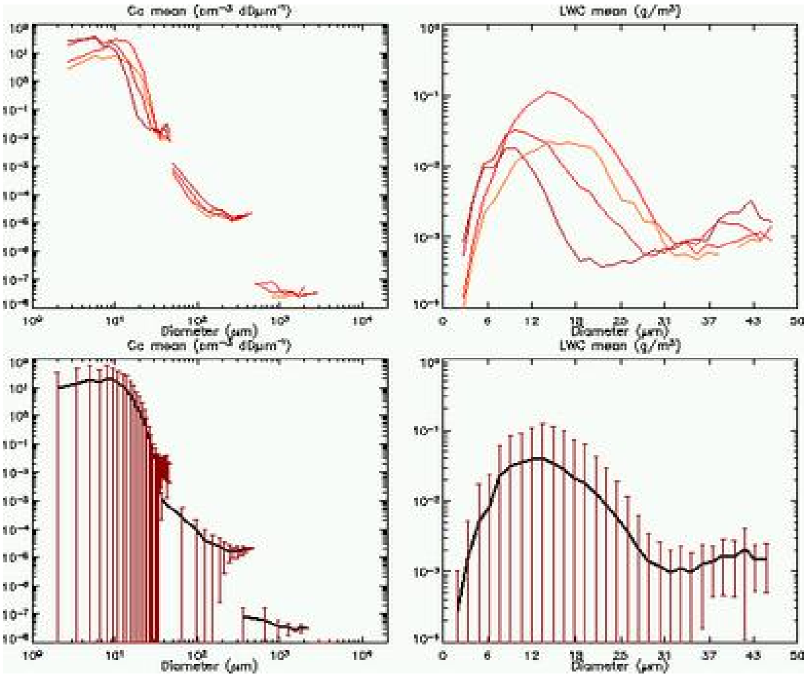

Figure 7: Convective Clouds, Sampled in Stratiform, Transition Season, No Lightning

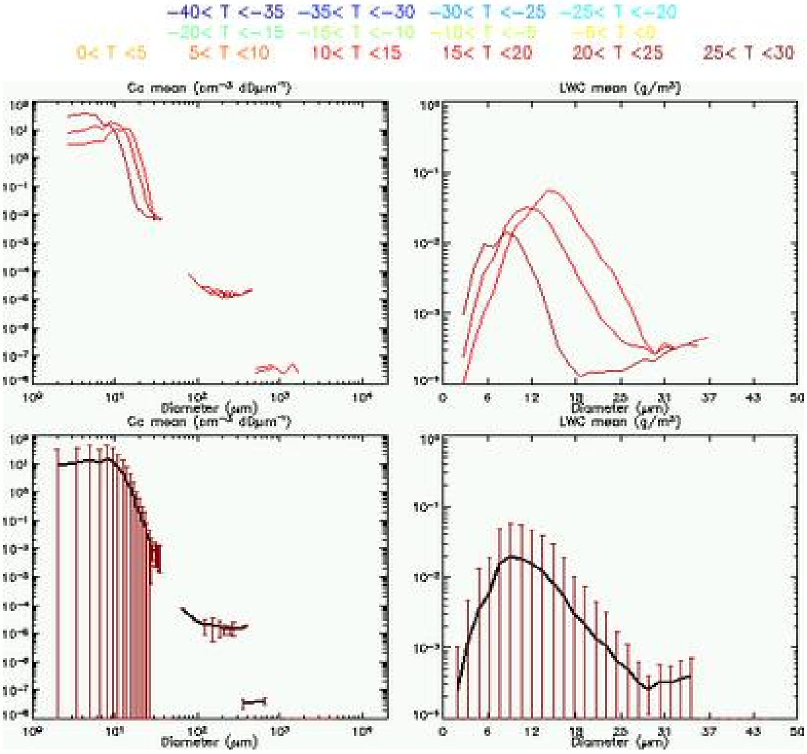

Figure 8: Stratiform Clouds, Sampled in Stratiform, Transition Season, No Lightning.

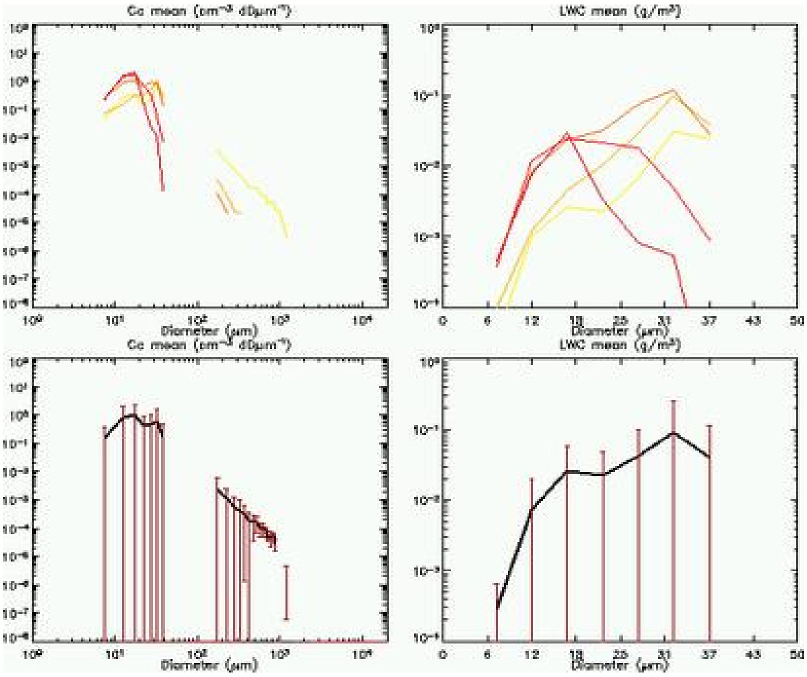

Figure 9: Convective Clouds, Sampled in Convection, Wet Season, East Regime, No Lightning.

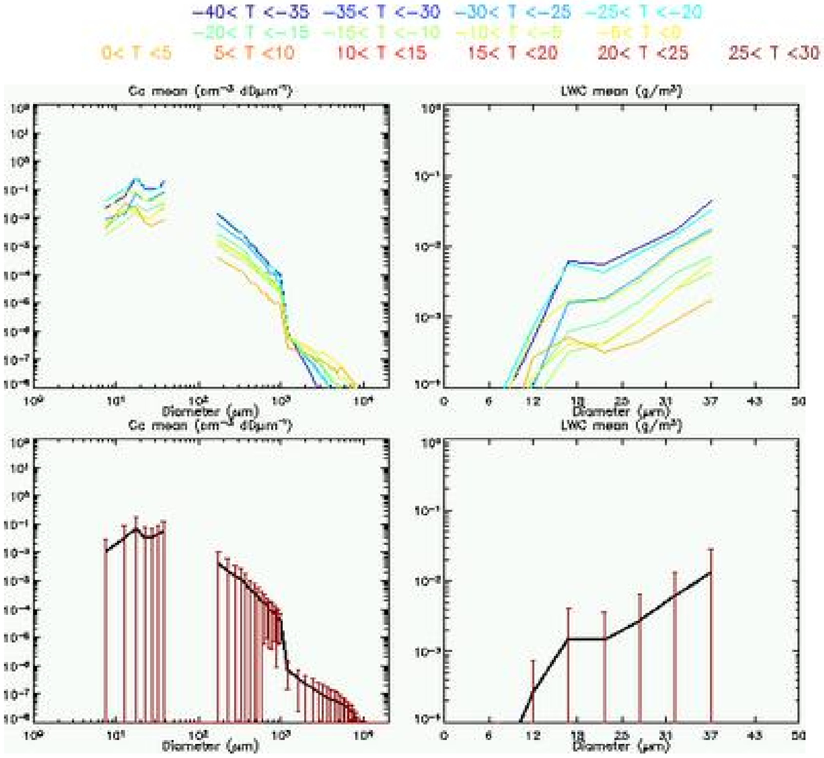

Figure 10: Convective Clouds, Sampled in Convection, Wet Season, Easterly Regime, With Lightning.

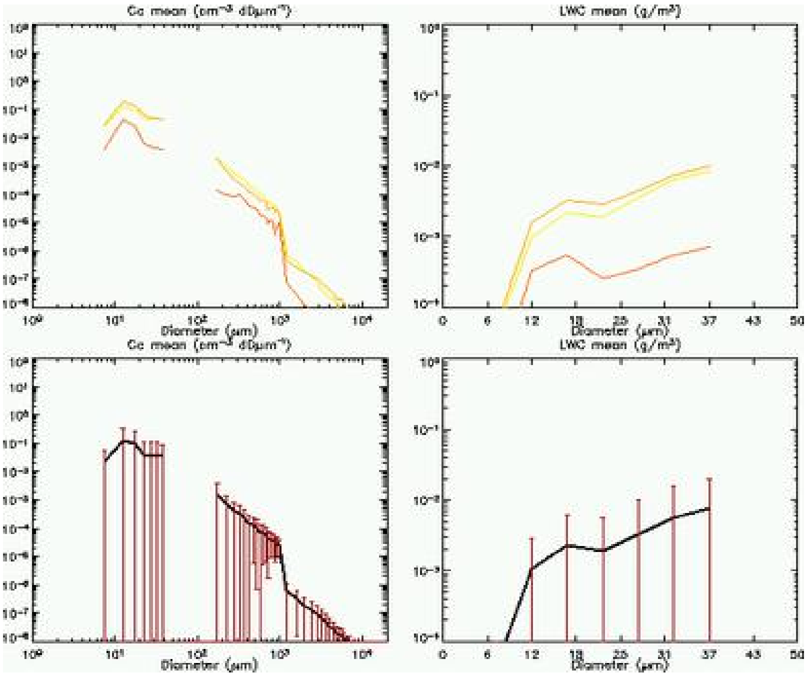

Figure 11: Convective Clouds, Sampled in Convection, Wet Season, Westerly Regime, No SACZ, No Lightning.

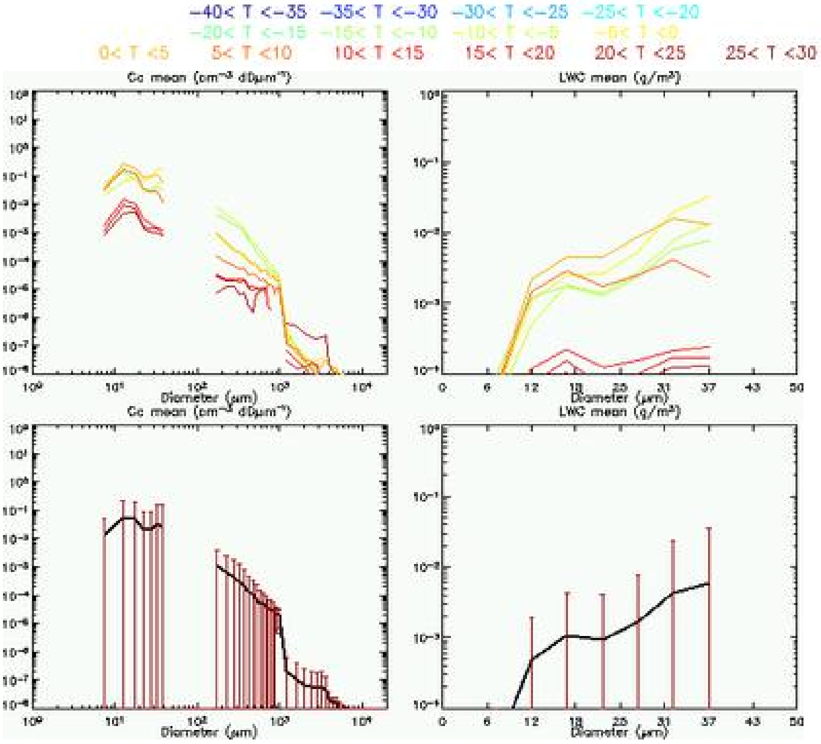

Figure 12: Convective Clouds, Sampled in Stratiform, Wet Season, Easterly Regime, No Lightning.

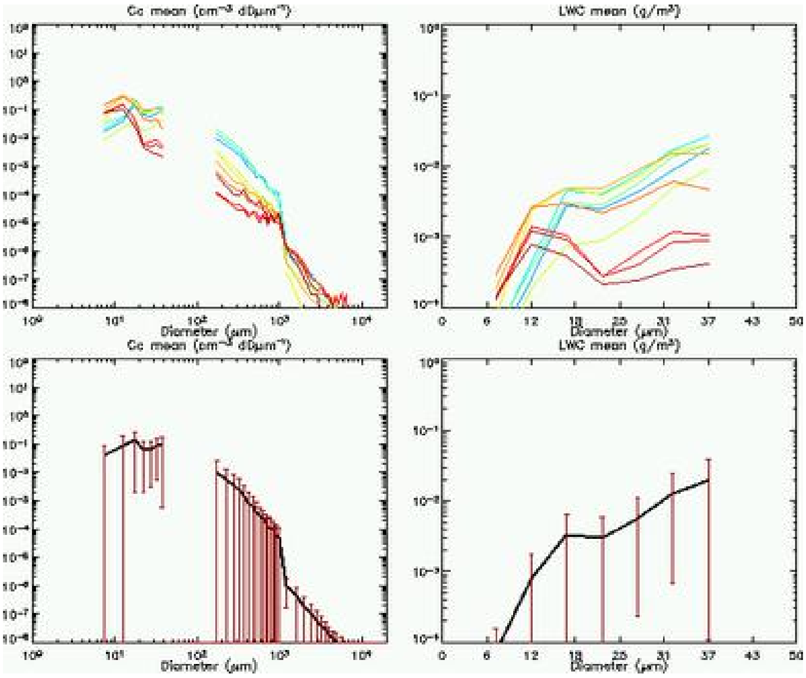

Figure 13: Convective Clouds, Sampled in Stratiform, Wet Season, Easterly Regime, and With Lightning.

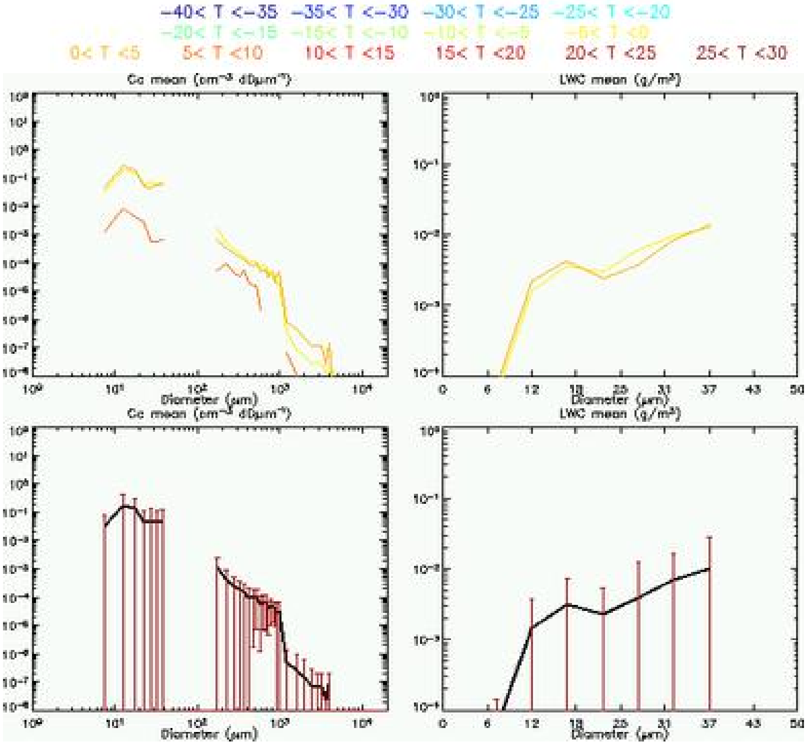

Figure 14: Convective Clouds, Sampled in Stratiform, Wet Season, Westerly Regime, No SACZ and No Lightning.

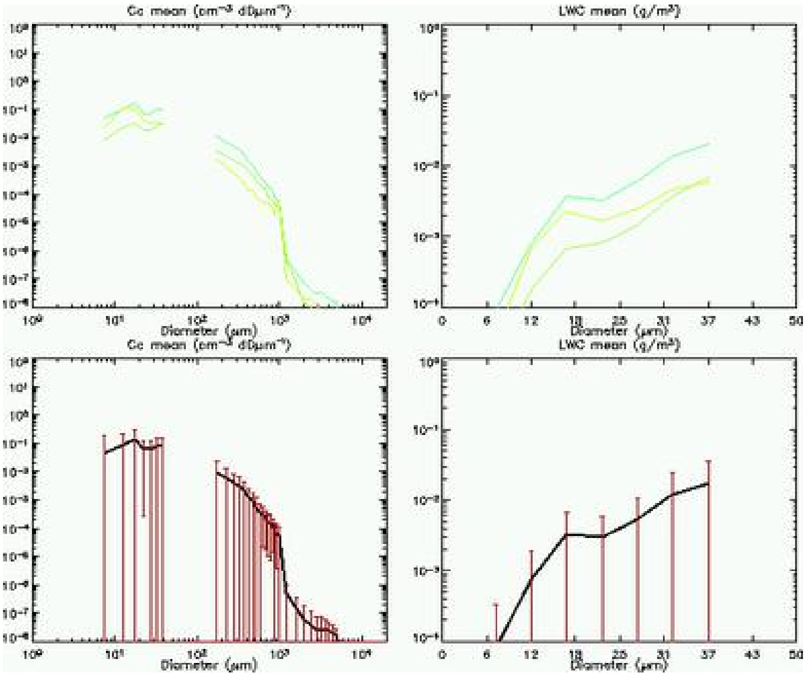

Figure 15: Convective Clouds, Sampled in Stratiform, Wet Season, Westerly Regime, With SACZ and No Lightning.

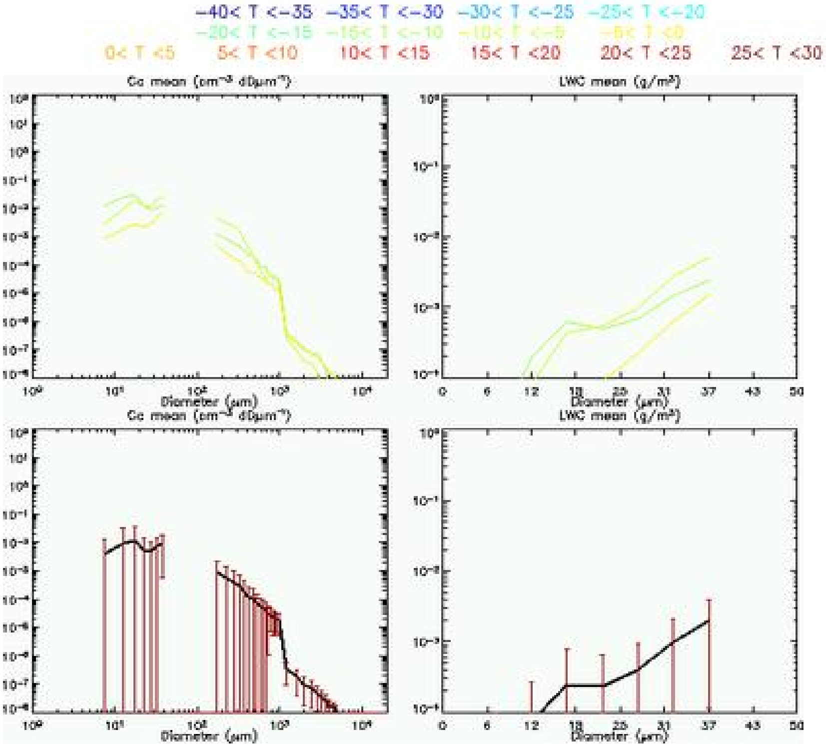

Figure 16: Convective Clouds, Sampled in Stratiform, Wet Season, Westerly Regime, With SACZ and With Lightning.

RAINFALL PROCESSES AND CLOUD MICROPHYSICS OF MONSOON CONVECTIVE SYSTEM OVER THE OCEAN

Danhong Fu[1], Xueliang Guo[1,2], and Changhai Liu[3]

1. Institute of Atmospheric Physics, Chinese Academy of Sciences, Beijing, China
2. Chinese Academy of Meteorological Science, Beijing, China
3. National Center for Atmospheric Research, Boulder, Colorado, USA

1. INTRODUCTION

The East Asian monsoon plays an important role in the regional and global climate, and is a major component of the Northern Hemisphere summertime circulation system. The initial onset of the East Asian summer monsoon starts over the South China Sea (SCS) region in early to mid-May, and triggers the formation of the convective systems over the northern SCS. Some studies found that tropical precipitating cloud systems interact with the large-scale environment through precipitation, latent heating; eddy fluxes of heat, moisture, momentum, microphysical processes; and air-sea interaction. In addition, the clouds also affect the incoming and outgoing radiant energy through processes of reflection, absorption, and emission. This study reported the results obtained by a mesoscale numerical simulation study on cloud microphysics and precipitation processes over the South China Sea Monsoon Experiment.

2. METHODOLOGY

The nonhydrostatic version of the Weather Research and Forecasting (WRF) model was used in this study. There are 80 vertical η levels, and the grid spacing in horizontal is 2000m with 302 grid points. We used the WRF Single-Moment (WMS) 6-class scheme which includes ice, snow and graupel processes as microphysical scheme. The Mellor-Yamada-Janjic scheme was used for planetary boundary layer (PBL). The CAM scheme, which was from the Community Atmosphere Model (CAM) and allows for aerosol and trace gases, was used for longwave and shortwave radiation. The WRF was modified to run with periodic boundary conditions in both north-south and east-west boundaries, which ensured that there was no additional heat, moisture, or momentum forcing inside the domain apart from the large-scale forcing. The time step was 10 s, and integral time was from 0000 UTC 15 May 1998 to 0000 UTC 11 June 1998.

The average of gridded data fields over the South China Sea Monsoon Experiment (SCSMEX) as the main forcing, such as horizontal wind field, potential temperature, and water vapor mixing ratio, are imposed into the model.

3. RESULTS

Figure 1 shows the time series of domain-averaged rainfall rate over the SCSMEX region that were simulated by the model and estimated from Tropical Rainfall Measuring Mission (TRMM), Global Precipitation Climatology Project (GPCP) and Japan Meteorological Agency (JMA/GAME). The temporal variation of the WRF model-simulated rainfall rate is good agreement with the observed data. The agreement is due to the fact that the WRF was forced by large-scale tendencies in temperature and water vapor computed from the sounding network. When the imposed large-scale forcing cools and moistens the environment, the model responds by producing clouds, and then produces surface rainfall. Two precipitating processes occur over the northern SCS. The first period was around 15-22 May, and the second was around 2-8 June. The rainfall in June was stronger than in May due to the stronger large-scale forcing in water vapor in June.

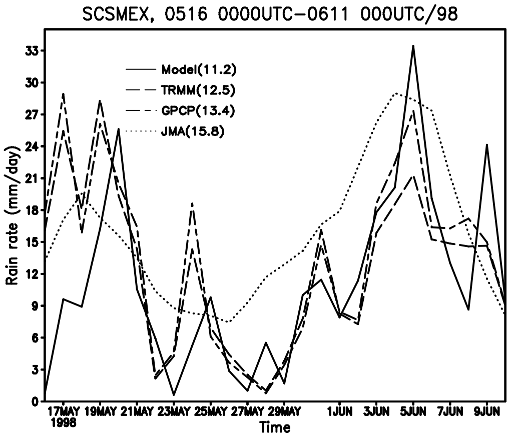

Fig.1 Time sequence of the domain-averaged rainfall rate (mm day^{-1}) produced by the WRF model, TRMM, GPCP, and JMA.

The surface rain rate is contributed by the large-scale forcing in water vapor mixing (Q_{forcing}), the local vapor change (Q_{vt}), the cloud source/sink (Q_{ct}), and the surface evaporation flux (E_{s}). Table 1 indicates the correlation coefficient between the each term contributed for rainfall and rain rate. The correlation coefficient is 0.87 between the large-scale forcing in water vapor. The rainfall contributed by the local water vapor is smaller, which the correlation coefficient only is 0.09. This indicates that the large-scale forcing in water vapor is very important for convective precipitation processes in the SCSMEX There are the negative correlations coefficient between cloud sink/source and rain rate and between the surface evaporation flux and rain rate.

Table1. The correlation coefficient between the large-scale forcing, local water vapor, cloud, cloud, surface evaporation and rain rate, respectively

	Q_{forcing}	Q_{vt}	Q_{ct}	E_{s}
Correlation coefficient	0.87	0.09	-0.03	-0.28

Figure 2a shows Convective Available Potential Energy (CAPE) during May and June. There were strong CAPE before the convective periods in May and in June, and the maximum CAPE reaches 3000 J kg^{-1} and 3500 J kg^{-1} in May and in June, respectively. The reduction in CAPE occurs due to the vertical mixing by deep convection after the convective periods. The strong convection occurred around 18 May, and the maximum updraft reached about 14 m s^{-1}, and the other obvious convectively active periods were from 1 to 10 June, and the maximum updraft was about 20 m s^{-1} (Fig 2b). From 23 to 30 May, the convection was weak. Two convectively active periods occurred at the onset and break period of the monsoon. The convection in June was stronger than in May. The maximum downdraft reached -4 m s^{-1} and -8 m s^{-1} at the upper levels in May and June, respectively (Fig 2c). This suggests that the loading of ice particles was strong in June. The maximum downdraft was -3 m s^{-1} and -5 m s^{-1} below the melting level in May and June, respectively.

A sensitivity test was performed to examine the relation between the microphysics processes in tropical convective systems over SCSEMX with the radiant energy and the heat flux at the surface.

The differences (ice runs – ice-free) of the rain rate is showed in Figure 3. The difference in the average rain rate is -0.7 mm day^{-1}, and the ice-free processes produces more surface rain fall during the monsoon.

Table 2 indicates the difference in the physical processes which are responsible for the rainfall variation between ice run and ice free. The difference in the average local water vapor reaches -0.24 mm day^{-1}, which suggests that there is more water vapor change to rain fall in the ice-free processes. The difference in the average cloud sink/source is 0.005 mm day^{-1}, which suggests that there is more cloud sink/source change to rain fall in the ice-free processes. The difference in the average surface evaporation is -0.47 mm day^{-1}, which suggest that more rain fall in ice-free processes is produced by the surface evaporation processes.

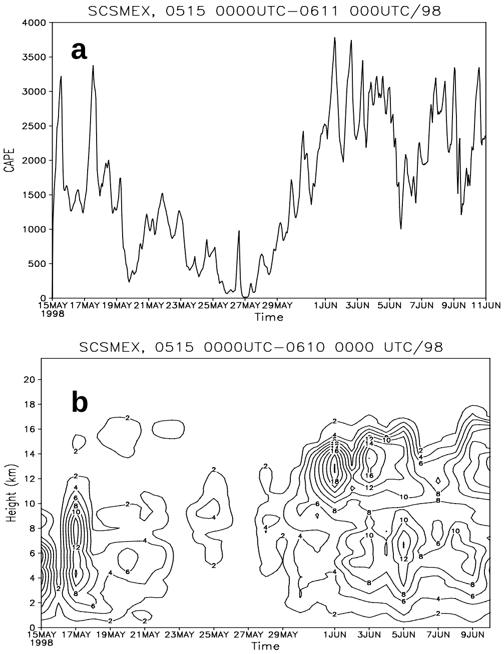

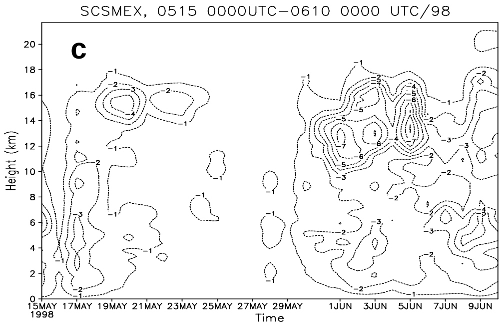

Fig.2 Temporal distribution of the maximum updraft and maximum downdraft

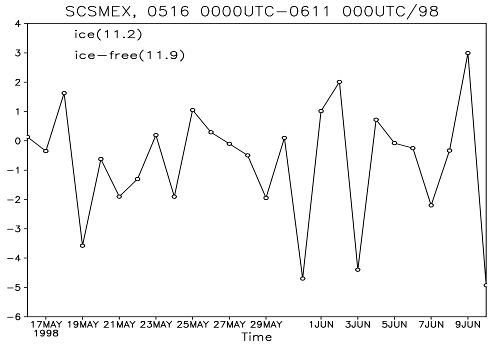

Fig. 3 Temporal distribution of difference in rain rate between the ice and the ice-free,

Table 2. The difference in time mean rain rate, local water vapor change (advection), cloud sink/source, and surface evaporation flux between ice run and ice free

	Q_{vt}	Q_{ct}	E_S
Difference	-0.24	0.005	-0.47

Figure 4 shows the evolution of the average outgoing longwave radiation (OLR) in ice runs and ice-free runs. The 27-day means of OLR in the ice runs and the ice-free runs are 216.08W m^{-2} and 267.61W m^{-2}, respectively. One of the major differences between the ice runs and the ice-free runs was the smaller OLR in the ice runs during the convective periods in May and June. This reveals that the cloud top temperature in ice runs is lower due to the ice particles.

The downward shortwave flux at the surface in both experiments show similar evolution (Figure 5a), and is smaller in the ice runs when the convective actions develop over the SCS. This suggests the cold clouds processes reduce the shortwave radiation at the surface, which means solar reflection is larger. The 27-day means of the downward longwave flux at the surface in the two experiments are 429.11W m^{-2} and 422.01W m^{-2}, respectively (Figure 5b). The downward longwave flux at the surface in the ice runs is larger during the convective periods. This is because the condensation and deposition processes in the ice runs produce more latent heat in the clouds.

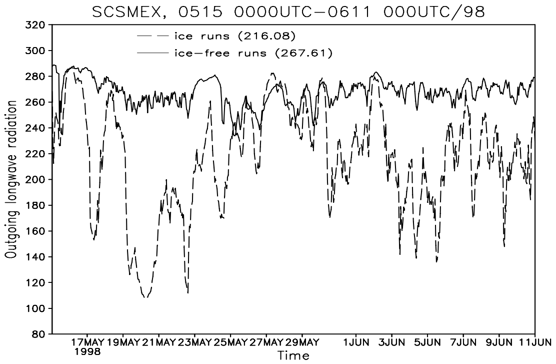

Fig. 4 The evolution of the averaged outgoing longwave radiation (OLR) in ice runs and ice-free runs from model

The latent heat and sensible heat flux at the surface in both experiments show similar evolution, and are smaller in the ice runs when the convective actions develop over the SCS (Figure 6). The differences are mainly contributed by the differences of the downward shortwave and longwave flux at the surface.

Figure 7 shows the temporal distribution of the domain maximum updraft. The convection without ice microphysics processes is stronger, and the maximum updrafts in ice runs and ice-free runs are 20.19 m s^{-1} and 23.68 m s^{-1}, respectively. This is due to the lager latent and sensible heat flux at the surface. This suggests that the interaction of the microphysics processes in the cloud and the radiation is very important for the development of the convection over the SCS.

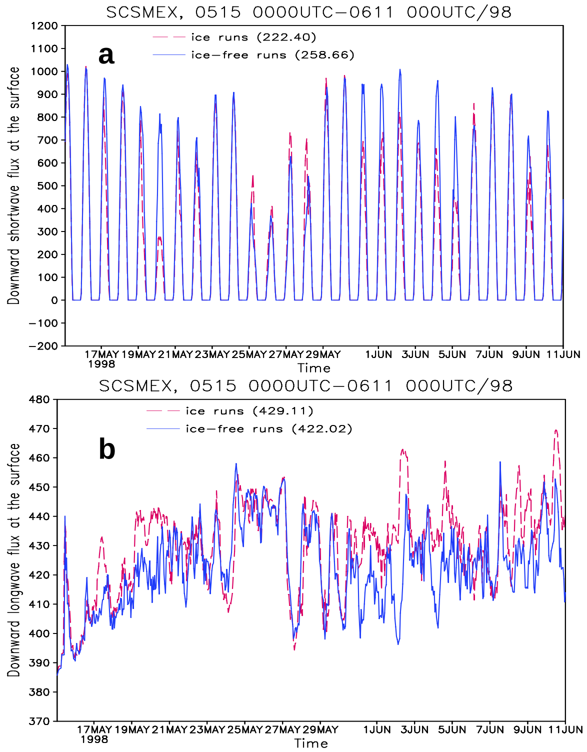

Fig. 5 The evolution of the average (a) downward shortwave flux and (b) downward longwave flux at the surface

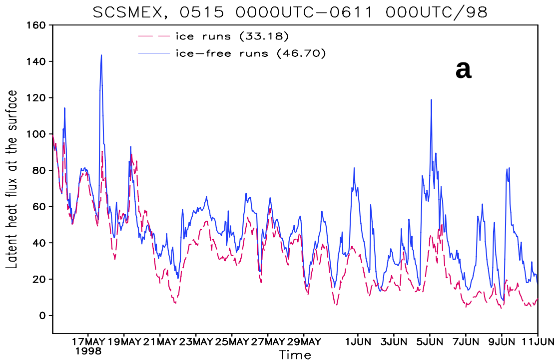

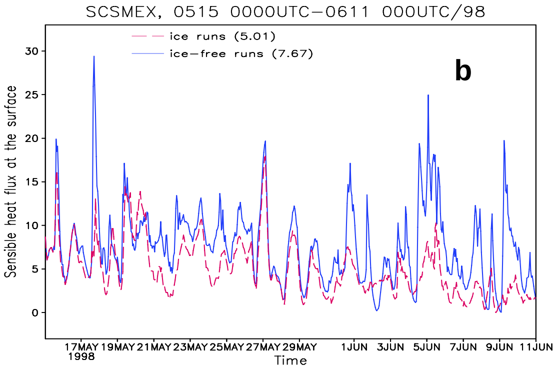

Fig. 6 The evolution of the average (a) latent heat flux and (b) sensible heat flux at the surface

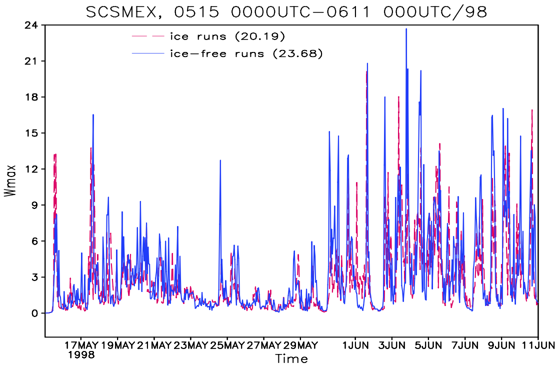

Fig. 7 Temporal distribution of the maximum updraft in ice runs and in ice-free runs

4. CONCLUSION

The nonhydrostatic version of the Weather Research and Forecasting (WRF) model is used to simulate the tropical cloud systems during SCSMEX.

The temporal variation of the simulated rainfall is in good agreement with the observed data. Two convectively active periods occurred over the northern South China Sea in May and June 1998. The first convective periods occurred during the onset of the monsoon and the second period was during the monsoon period. The convective processes were stronger in June than in May.

The surface rain rate is composed of the large-scale forcing in water vapor, moisture source/sink, cloud source/sink, and surface evaporation fluxes, and the imposed large-scale forcing in water vapor is very important for convective precipitation processes in the SCSMEX.

Sensitivity tests were performed to examine the microphysical processes in clouds. The ice-free processes produce more rain fall during the monsoon. The more rain fall in ice-free processes is produced by the surface evaporation processes. The interaction of the microphysics processes in the cloud and the radiation is very important for the development of the convection over the SCS.

ACKNOWLEDGMENTS

This research was jointly sponsored by the Chinese Natural Science Foundation (Grant No. 40575003 and 40333033) and the Key Sci & Tech Supporting Project of the Ministry of Science and Technology of China (Grant No. 2006BAC12B03).

REFERENCES

Johnson, R. H. and P. E. Ciesielski, 2002: Characteristics of the 1998 summer monsoon onset over the Northern South China Sea, *J. Meteor. Soc. Japan*, *80*, 561-578.

Johnson, R. H., S. L. Aves, and P. E. Ciesielski, 2005: Organization of oceanic convection during the onset of the 1998 East Asian summer monsoon, *Mon. Wea. Rev.*, *133*, 131-148.

Tao, W.–K., C.-L. Shie, J. Simpson, S. Braun, R. H. Johnson, and P. E. Ciesielski ,2003: Convective systems over the South China Sea: Cloud –resolving model simulations, *J. Atmos. Sci.*, *60*, 2929-2956.

MODEL CONVECTIVE AND STRATIFORM PRECIPITATION PARTITION DEPENDENCE ON HORIZONTAL RESOLUTION

Gomes, Jorge Luís [1], Chou, Sin Chan [1]
1. Centro de Previsão de Tempo e Estudos Climáticos – Instituto Nacional de Pesquisas Espaciais - Cachoeira Paulista - Brazil
gomes@cptec.inpe.br, chou@cptec.inpe.br

ABSTRACT

Model precipitation can be produced explicitly or through convective parameterization schemes. Different types of precipitation produce distinct vertical profiles of latent heat to the atmosphere, however, to estimate the effect of these different profiles of heating it is important to know accurately the partition between convective and stratiform precipitation.

Models with resolution coarser than 20 km are able to reproduce the cumulus convection with some skill through parameterization schemes. On the other hand, models with grid-size resolution smaller than 1 km should solve the convection explicitly. Within the range of these two resolutions hybrid solutions are suggested, with cumulus convection acting together with the explicit form of representation. In the present work, the Eta model was used to simulate a precipitation event associated with the South Atlantic Convergence Zone (SACZ). This type of system exhibits a large band of stratiform cloudiness with embedded convective cells. The Eta Model uses the Kain-Fritsch cumulus parameterization scheme. Cloud microphysics was treated by Ferrier scheme. The convective scheme has a parameter that controls the fraction of condensate that goes into rain and snow in each layer. A change is proposed to the parameter to include resolution dependence. The convective scheme converts less condensed water into precipitation, part of the condensed water is made available to cloud microphysics scheme and another part evaporates. In grid resolution higher than 1 km, convective scheme still acts in removing convective instability and all precipitation is produced by cloud microphysics. Simulations with different horizontal resolutions, 20, 10 and 5 km, have been carried out up to 5-day integrations which is the average duration of SACZ events. The changes produced two major impacts: the position of maximum precipitation area was better simulated and the amount of total precipitation became closer to the observations. The simulations showed that the increase of horizontal resolution

changed the distribution of stratiform and convective precipitation.

1. INTRODUCTION.

The precipitation of the NWP models may be generated implicit by though convective parameterization scheme and explicitly though excess of water vapor over a prescribed threshold. Convective parameterization schemes work in a model grid where convective instability is found. The cloud microphysics schemes, such as Lin et al. (1983), Zhao (1997), Eta-Ferrier (2002), etc. produce precipitation explicitly. According with the model resolution it is expected greater or lesser activity of each of these two schemes. According Molinare (1993) models with resolution greater than 20 km the precipitation would be simulated by implicit convective schemes with reasonable skill. Models with resolutions lesser than 3 km, where the model grid approaches the scale of cloud development, the precipitation would be simulated by explicit schemes. Adequate representations of implicit and explicit precipitation partition by NWP are essential to get a better representation of precipitation. With increasing the resolution the explicit scheme becomes more important. In this case, the clouds processes become more sensitive with respect to the model grid scale. In this paper the objective is to evaluate the precipitation production and partition at different horizontal resolution for a case of SACZ.

2. THE ETA MODEL.

The Eta Model was first developed in Belgrade University by Mesinger (1988) and a comprehensive physical package has been incorporated into the model by Janjic (1990, 1994). It is a hydrostatic/no hydrostatic model with an accurate treatment of complex topography using eta vertical coordinate system (Mesinger, 1984). The model topography is represented as discrete steps whose tops coincide exactly with one of the model vertical layer interfaces (BLACK, 1994). The model uses a semistaggered Arakawa E grid as a horizontal grid. The radiation package used in the model is one developed at GFDL. Planetary boundary layer (PBL) uses a modified Mellor-Yamada Level 2.5 scheme (Black 1994). The prognostics variables of the model are: temperature, specific humidity, zonal and meridional components of the wind, surface pressure, turbulent kinetic energy and cloud hidrometeores. The explicit precipitation is generated by cloud microphysics Eta-Ferrier scheme Ferrier (2002), hereafter referred to FR, and implicit precipitation generated by Kain-Fritsch cumulus parameterization scheme (Kain and Fritsch, 1990 and 1993; Kain, 2004), hereafter referred as KF. Further details of the model can be found at Mesinger et al. 1988 and Black, 1994.

2.1. PRECIPITATION SCHEMES

In this section a brief review of the precipitation schemes used in this work are show and a new modification in Kain-Fritsh scheme is proposed.

- The Eta-Ferrier scheme (FR). The scheme predicts changes in water vapor and condensate in the forms of cloud water, rain, cloud ice, and precipitation ice (snow/graupel/sleet). The individual hydrometeors are combined into total condensate. The water vapor and total condensate that are advected in the model.
- Kain-Fritsch scheme (KF): uses a Lagrangian Parcel method along with vertical momentum dynamics to estimate the properties of cumulus convection, It incorporates a trigger function, a mass flux formulation and closure assumption. The trigger function identifies the potential updraft source layers associated with convection, whereas the mass flux formulation calculates the updraft, downdraft and associated environmental mass flux. The scheme assumes conservation of mass, thermal energy, total moisture and momentum. The efficiency Productions of rain and snow are controlled by a parameter that specifies the fraction of the precipitation mass to be transferred from KF to the host model.

3. METHODOLOGY

The Eta model was configured with 20, 10 and 5 km of horizontal resolutions. In the first and second cases the vertical resolution used was 38 layers and the model run in a hydrostatic mode. The time steps were 40 and 20 seconds respectively. With 5 km resolution the model was run in non-hydrostatic mode 50 layers, with time step set to 10 seconds. The domain was centered at -23.5S, -48.0W. The domain of the 3 resolution was the same to avoid any possible differences in the simulations. Initial and lateral boundary conditions were taken from NCEP (National Centers for Environmental Prediction) global analyses with T126L28 resolution. The lateral conditions were updated every 6 hours. The domains for all experiments are shown in Figure 2. The model was integrated up to 132 hours. The resolution dependence was introduced into the scheme through the F parameter. This parameter varies between 0 and 1. When the model resolution is 3 km or higher the parameter is set to 1; between 3 and 40 km the parameter follows a function given by Figure 1; and when the model grid size is 40km or smaller, the parameter is set to 0. The F parameter included the horizontal resolutions dependence into the precipitation efficiency and the convective adjustment through temperature and moisture profiles. In the 20 km experiment where F parameter was set to 0.4, 60% of cloud water is converted to rain. In this case, the convective activity was reduced by 40%. For the resolutions 10 and 5km the convective efficiency and the convective activity were reduced by 60% and 80%.

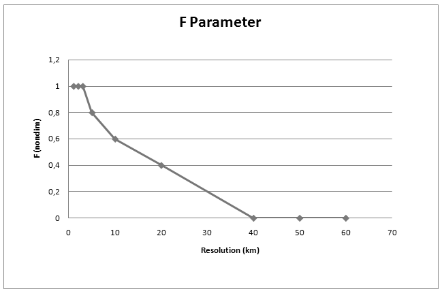

Figura 1: F parameter (non dimensional).

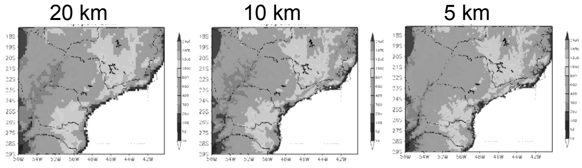

a) b) c)

Figure 2: Topography and domains of the experiments for: a) 20 km; b) 10 km and c) 5 km

3.1. CASE ANALYSIS

The case chosen for this study was the SACZ event from January 24-29, 2004. The JAN24 cloud band exhibited a meridional orientation and significant rainfall over southeast Brazil, mainly in the southern part of São Paulo State, where the maximum of the precipitation between 200-300 mm was observed (Figure 3 a and b). The Figure 2b shows the PERSIANN (Precipitation Estimation from Remotely Sensed Information using Artificial Neural Networks) accumulated precipitation for JAN24 period. The precipitation band exhibited southern orientation, with axis that extends from Triângulo Mineiro through the extreme south of the São Paulo State and followed by the Atlantic Ocean. The sequence of IR images from GOES-8 shows that the system was acting over the region between January 24-29, 2004. The streamlines at high levels showed a cyclonic vortex positioned closer to the coastline of Northeast of Brazil which kept the SACZ over the southern and southeast region. The cold front over the ocean was maintained by upper level trough.

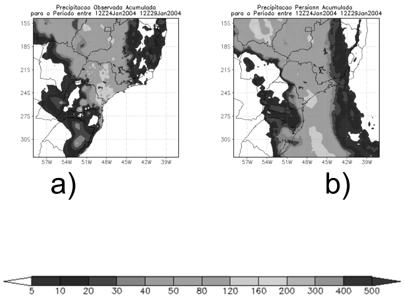

a) b)

Figure 3: Observed precipitation accumulated for SACZ event: a) surface observations and b) PERSIANN data

4. RESULTS

4.1. CONTROL RUN

In the 20 km simulated maximum precipitation was positioned too south (Figure 5a) when compared with the observations (Figure 5a and 5b). In the C20, the precipitation band was positioned over Santa Catarina and Paraná States, whereas the observations showed the cloud band to the north. In this case, the maximum accumulated precipitation was 400 mm over Santa Catarina State, whereas in the observations the amounts were smaller and the cloud band positioned to the north, over São Paulo State. The comparison between the Figures 5g and 5n shows that most part of precipitation was generated by the implicit scheme. The runs with different resolutions showed the same distribution of implicit and explicit precipitation (Figures 5 c, j and p; Figures 5e, l and r). The differences between C10-C20 and C05-C20 where showed a little shift in the precipitation band toward north but a significant increase in the maximum precipitation when increased the horizontal resolution was increased. However, the increase in the total precipitation is associated with an increase of convective scheme (Figures 5g, j and l), although it would be expected that the explicit scheme acted more strongly with resolution increase.

4.2. F PARAMETER

The comparison between the 20-km runs, control and F experiment showed that the position of the precipitation band is further north, closer to the observation (Figure 3a and b). One can note in Figure 5b and h that there was a reduction in the amount of precipitation produced by the implicit scheme. The greater availability of liquid water for the explicit scheme contributed to an increase in the amount and area of precipitation produced by the explicit scheme. The explicit scheme became more active and contributed to positioni the precipitation maximum to the north (Figures 5n and o). With the increase of resolution, the liquid water produced by the convective scheme and the temperature and humidity tendencies were reduced by 60% and 80% in the 10-km and 5-km runs, respectively. Comparison among the Figures 5b, d and f against the Figures 5a and b one can note that the resolution increase improved the simulated position of precipitation band.

5. CONCLUSIONS

Experiments carried out with the Eta Model at 20, 10 and 5-km resolutions with original KF and FR setups) showed that the model produced heavy precipitation and had some position error in the precipitation band associated with the SACZ event. The KF scheme produced the largest contribution to the total precipitation in the control runs. Despite the resolution increase, the precipitation maximum was intensified due to greater activity of the KF convective scheme.

The inclusion of resolution dependence to the F parameter caused the reduction of the convective activity, the reduction in the precipitation amount generated by the scheme and an increase of the explicit precipitation. This new precipitation partition reduced the overprediction and resolution insensitive of the schemes in the control runs. As the horizontal resolution increases the position of the precipitation band associated with the SACZ event was also better positioned.

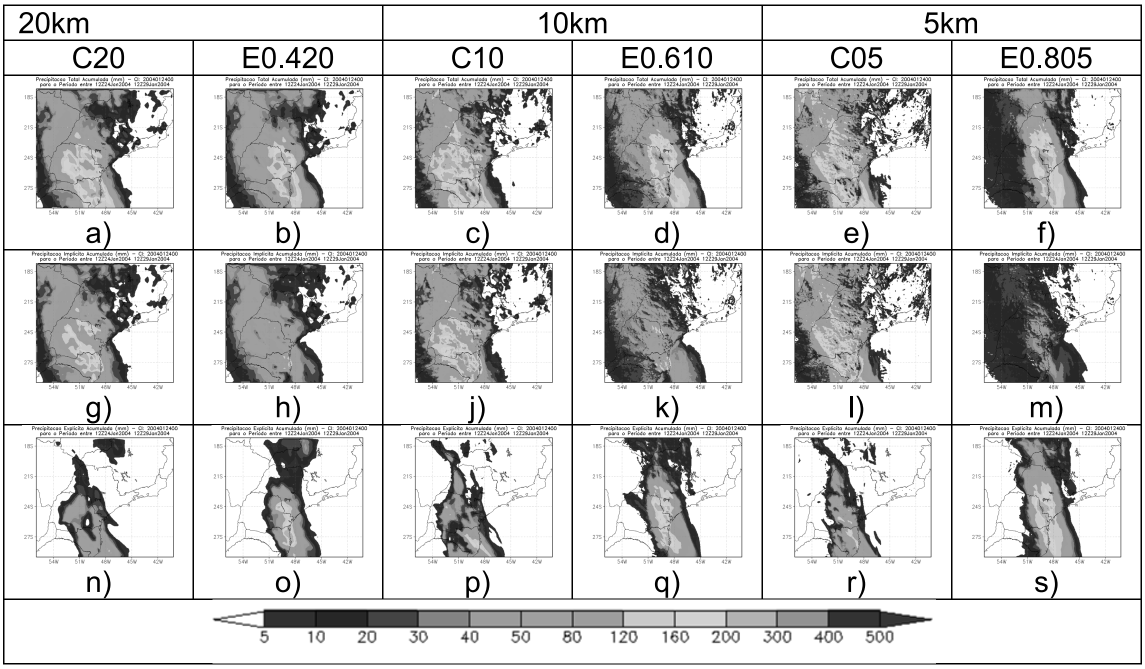

Figure 5: 5-day accumulated precipitation for the control and F-parameter experiment runs. The different resolutions are shown in columns. The first row is the total precipitation, the second row is the implicit precipitation and the third row is explicit precipitation.

6. REFERENCES

BLACK, T. L., 1994: The new NMC mesoscale Eta model: Description ad forecast examples. *Wea. Forecasting*, **9**, 265-278.

FERRIER, B. S., Y. LIN, T. BLACK, E. ROGERS, AND G. DiMEGO, 2002: Implementation of a new grid-scale cloud and precipitation scheme in the NCEP Eta model. Preprints, 15th Conference on Numerical Weather Prediction, San Antonio, TX, *Amer. Meteor. Soc.*, 280-283.

KAIN, J. S. 2004: The Kain-Fritsch convective parameterization: An update. J. Appl. Meteor., 43, 170-181.

___, and J. M. FRITSCH, 1993: Convective parameterization for mesoscale models: The Kain-Fritsch scheme. The Representation of Cumulus Convection in Numerical Models, Meteor. Monogr., No. 46, Amer. Meteor. Soc., 165-170.

___, AND ___, 1990: A one-dimensional entraining/detraining plume model and its application in convective parameterization. J. Atmos. Sci., 47, 2784-2802.

MESINGER, F., 1984: A blocking technique for representation of mountains in atmospheric models. *Riv. Meteor. Aeronaut*., **44**, 195-202.

___, JANJIC, Z. I., NICKOVIC, S., GAVRILOV, D. AND DEAVEN, D. G. 1988: The step-mountain coordinate: Model description description and performance for cases of Alpine lee cyclogenesis and for a case of Appalachian redevelopment. *Mon. Wea. Rev*., **116**, 1493-1518.

MOLINARI, J., 1993: Na overview of cumulus parameterization in mesoescale models. The Representation of Cumulus Convection In Numerical Models. *Amer. Meteor. Soc.,* **Vol. 24**, **46**, 155-158.

ZHAO, Q., T. BLACK AND M. E. Baldwin, 1997: Cloud prediction scheme in the Eta model at NCEP. Wea. Forecasting, 12, 697-712.

Acknowlegments**:** This work is partially funded by FAPESP under grant no. 04/09649-0 and partially by CNPq under grant no 308725/2007-7

THE EFFECT OF OVERSHOOTING DEEP CONVECTION ON THE WATER CONTENT OF THE TTL AND LOWER STRATOSPHERE FROM CLOUD RESOLVING MODEL SIMULATIONS.

Daniel Grosvenor[1] and Thomas Choularton[1].
[1]The University of Manchester, UK.

1. INTRODUCTION

Water vapour is the most potent greenhouse gas in the atmosphere. Its concentration in the upper troposphere and lower stratosphere plays a key role in the Earth's radiative balance. Here it is one of the primary sources of hydrogen oxides, which control ozone production and destruction in the lower stratosphere. It also forms Polar Stratospheric Clouds (PSCs) that are involved in ozone destruction.

Understanding what affects the stratospheric water vapour content is therefore vitally important, even more so in light of observations that suggest that it has been increasing by ~1 % per year between 1954 and 2000 (Rosenlof et al., 2001). Climate models suggest that this may have had a significant positive radiative forcing on the Earth (e.g. Forster & Shine, 2002). About half of the increase can be attributed to methane increases with rest thought to be due to unexplained changes in the transport of water from the troposphere to the stratosphere.

At present the relative importance of the different mechanisms that transport water from the troposphere to the stratosphere are poorly understood. Traditionally, water transport through slow ascent across the tropopause as part of the Brewer Dobson circulation was thought to account for most of the transport. In this scenario the amount of water entering the stratosphere is controlled by the tropopause temperature through freeze drying. However, this is at odds with observations of decreasing tropopause temperatures (Seidel et al., 2001; Zhou et al., 2001) at the same time as stratospheric vapour was seen to increase, which is the opposite of what would be expected if temperature was the controlling factor, suggesting a role for trends in other mechanisms.

One possibility for such a mechanism is the transport of water into the stratosphere by overshooting deep convection. Recent aircraft and balloon observations in the tropics and mid-latitudes have provided compelling evidence that clouds overshoot the tropopause and deposit ice into the stratosphere (Nielsen et al., 2007; Hanisco et al., 2007; Peter, 2008). Peter (2008) provided one of the only estimates based on observations of the amount of water input into the stratosphere by an overshoot, quoting a permanent input of ~100 tonnes. However, it remains very difficult to estimate a global effect since knowledge of the frequencies of overshoots is limited and generally extrapolations based on single clouds have to be made. Modelling should be able to increase the number of case studies examined, although there is a need to ensure model accuracy.

Here, a Cloud Resolving Model (CRM) is used to estimate the stratospheric water input provided by overshoots of various vigour, based on clouds observed over southern Brazil. A global estimate of stratospheric water input is extrapolated from these cases using estimates of overshoot frequencies based on satellite observations. These provide some insight into whether long term trends in the moistening provided by overshoots could have caused the long term trend in stratospheric water vapour.

2. CRM SIMULATIONS OF DIFFERENT STRENGTHS.

The 3D CRM used is the non-hydrostatic UK Met Office LEM (Large Eddy Model) v2.3 (Shutts & Gray, 1994). This model has a bulk microphysics scheme (size spectra are assumed gamma distributions), which is double moment for the ice hydrometeors. The model is initialised using a sounding from Bauru, Brazil (22.3° S, 49.03° W) taken as part of the HIBISCUS campaign. Convection was initialised using a warm and moist bubble of 3 different degrees of heating and moistening to produce separate simulations of overshoots of different strengths. The 10 dBZ simulated radar echo of the strongest overshoot reached 18.2, 17.4 and 16.4 km in the strong medium and weakest cases respectively; these heights are likely to be close to cloud top. These were above the tropopause in all cases, which was located at 15.9 km. This was consistent with, respectively, 322, 124 and 75 real clouds observed by the radar in Bauru during the 51 day campaign period, indicating that such overshoots occur regularly in the region.

It was found that in all cases the clouds mixed some of the ice-laden air carried in them with stratospheric air. The warming experienced as a result caused some of the ice to evaporate thus leaving moist air plumes in the stratosphere with vapour values of >10 ppmv (e.g. see Figure 1) in the most vigorous case. The mixing and warming also meant that the air attained stratospheric potential temperatures and thus would be likely to remain in the stratosphere.

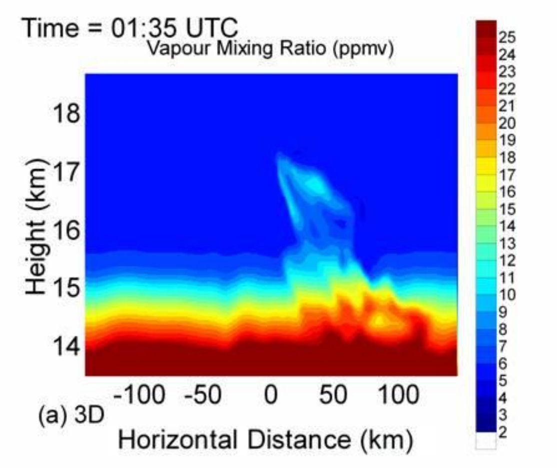

Figure 1. 2D cross section of the vapour mixing ratio in the plume produced by the overshoot in the most vigorous case after 1hr 35 mins of simulation time. At this time the plume air was stable in the stratosphere having attained stratospheric potential temperatures through mixing with stratospheric air.

The mass of extra water vapour inputted into the stratosphere was calculated for the three different cases and came to 1116, 194 and 86 tonnes in the strong, medium and weak cases respectively. Thus, there was a large difference between the different cases indicating that a small change in overshooting distance can produce a large difference in the amount of water deposited in the stratosphere. One estimate for the amount of water input into the stratosphere by an overshoot from aircraft observations of ice remnants after an overshoot has been made (Peter, 2008), giving a value of ~100 tonnes. However, this was in a different region (N. Australia) and thus may not be representative of the clouds here. Nevertheless, this hints that the weak and medium case may be more realistic.

3. CCN SENSITIVITY

A microphysical sensitivity case was also performed since the ice size distribution in the overshoot is likely to be very important in determining how much of the ice falls from the stratosphere and how much evaporates within it. This was based on the strongest case but with the number of CCN at cloud base increased from 240 to 960 cm^{-3}. This had the effect of increasing the number of droplets that survived the riming process within the main updraught to freeze at the -38 ^{o}C homogeneous freezing level at ~11 km. Smaller ice crystals were therefore present in the overshooting cloud and this resulted in more evaporation of ice, due to their lower fall speeds, producing an extra 118 tonnes of stratospheric vapour increase.

In addition, a lot more of the water transported into the stratosphere remained as ice in this case (505 tonnes compared to 131 tonnes in the normal CCN case) due to the slow ice fall speeds. Hence, if the remaining ice can later evaporate before falling from the stratosphere, a significant increase in the total moistening of 45 % is predicted due to the CCN increase. This suggests that anthropogenic aerosol emissions may play some role in determining the amount of moistening produced by overshoots and possibly therefore the water input into the stratosphere if the overall effect of overshoots is globally important.

4. A GLOBAL ESTIMATE OF THE INPUT OF WATER INTO THE STRATOSPHERE BY OVERSHOOTING CONVECTION.

In order to put these results into context, a global estimate of overshoot moistening on the stratosphere is made here based on an estimate of global overshoot frequency and by assuming that all of these clouds deposit the same amount of water into the stratosphere as in the various simulations. Overshoot frequency is estimated from the TRMM satellite data presented in Liu & Zipser (2005) where the number of observations of clouds whose 20 dBZ echo top reached above the tropopause were counted from 46 months of data. Based on the limited coverage provided by the satellite there were on average ~22 clouds whose 20 dBZ radar echo was above the local tropopause present at any one time in the tropics (20 ^{o}S to 20 ^{o}N). In order to estimate a frequency of occurrence of these clouds it is necessary to assume a lifetime (T_{20} hours) of the 20 dBZ signal above the tropopause. Then the frequency becomes $22/T_{20}$ hour^{-1} since if each event was visible for T_{20} hours then there will have had to have been 22 new events in each T_{20} time period to replace the ones that subsided below the tropopause in order for the satellite to have observed 22 events at any one time.

A value for T_{20} was taken from the time that the 20 dBZ echo spent above the tropopause in the simulations in the most vigorous case, which was 16.7 minutess. In the other cases T_{20} was lower and hence this estimate represents the value that will result in the lowest overshoot frequencies and hence the lowest global moistening estimates. Since this value is critical to the calculation it is desirable that it is also estimated from radar observations in various different locations in future studies.

This frequency is multiplied by the mass of water input into the stratosphere from the simulated clouds in order to produce a global convective flux of water into the stratosphere. This is then expressed as a percentage of the flux of water entering the stratosphere through slow ascent in the Brewer Dobson circulation as calculated from an average entry mixing ratio of 3.8 ppmv suggested in Dessler (1998) and the global mass flux of air across the 100 hPa level of ~85x10^{8} kg s^{-1} quoted in Holton et al. (1995). For the strongest case it was estimated that, based on only the vapour increases seen in the simulations, convective overshoot input of moisture into the stratosphere would provide 120 % of the Brewer Dobson flux of moisture; i.e., overshoots would be the most important source of water entering the stratosphere. The observations of Peter (2008) suggest that the moistening from this case is an overestimate. For the cases more inline with that observation, the medium and weak cases, percentages of 21 and 9 % are produced respectively, which still represent an important, although not dominant, input from overshoots.

Given these predictions for a high stratospheric input from convective overshoots it seems possible that any trends in the amount of moistening provided by overshoots could produce trends in the stratospheric vapour mixing ratio and may therefore be able to provide an explanation for the unexplained portion of the observed long term stratospheric vapour trend, which amounts to a ~23 % increase over a 46 year period. Such convective moistening trends may have been possible if there were trends in the number of clouds overshooting the tropopause over the same period. The results here suggest that a small change in the distance that a cloud overshoots the tropopause by can result in large moistening differences and so it is likely that even moderate changes in the pattern of cloud severity may produce large trends in the amount of overshoot moistening. In order for a convective trend to have caused a 23 % trend in stratospheric water vapour, overshoots must have provided at least this amount of the Brewer Dobson flux of vapour into the stratosphere at the end of the trend period with the assumption that the convective input increased to this amount from zero over the trend period. Hence, the 23 % stratospheric vapour trend might easily be explained by convective overshoot moistening trends if the overshoot frequency is reasonable and if all of the clouds deposit as much water into the stratosphere as in the strongest simulation. For the medium case the convective flux is just below that required and for the weak case a trend of the magnitude observed is only possible over ~18 years.

Since CCN concentrations were shown to have produced a large sensitivity in the amount of moistening in the strongest case it is conceivable that trends in CCN may have also led to stratospheric vapour trends. The simulation for which the highest percentage of the Brewer Dobson moisture flux was predicted to be produced was the high CCN case of the strongest storm simulated, which produced an estimate of 194 % when including moistening from ice as well as vapour. The normal CCN case gave a value of 134 %, representing a 45 % increase in moistening due to the CCN increase. To estimate whether CCN increases could have been responsible for the observed increase in stratospheric moisture it could be assumed that in previous years there were on average fewer CCN in the atmosphere with the '3D' case being representative of CCN values 46 years ago and that 134 % was the percentage of the Brewer Dobson flux provided by convection. The Brewer Dobson flux is assumed here to have been constant over the 46 years. The simulations would then predict that a CCN increase over the past 46 years from 240 cm^{-3} to a level of 960 cm^{-3} would lead to a ~26 % increase in stratospheric vapour. Thus this increase due to CCN trends might be large enough to provide the observed 23 % increase in total stratospheric water vapour.

However, if only vapour increases due to CCN in the most vigorous case are considered then the possible increase due to CCN increases drops to only 9.2 %, which is only large enough to explain an ~18 year trend. Since the convection percentage becomes much smaller for the weaker cases it is likely that moistening increases in these cases due to CCN increases (not tested here) would not be enough to allow a stratospheric trend on a par with that observed unless the moistening increase due to the CCN increase was much larger in these clouds.

The results suggest that only clouds that moisten the stratosphere by a similar amount to the strongest case simulated here would be able to produce a trend in stratospheric water vapour similar to that actually observed due to increases in CCN only and then only if the ice remaining in that simulation evaporated in the stratosphere.

5. CONCLUSIONS AND OUTLOOK

The amount of permanent water input into the stratosphere by the overshooting convection simulated here is suggested to be globally significant if similar overshoots occur throughout the tropics with a frequency on a par with that estimated here from satellite observations. In the strongest case (most moistening) convective input of water into the stratosphere by deep convection is predicted to be the most important source and is ~5.2 times larger than the minimum required for trends in overshoot moistening to have been able to have caused the unexplained portion of the observed stratospheric vapour trend. The amount of moistening in the medium case is slightly too low to have produced the 46 year trend and that in the weakest case is only enough for an ~18 year trend. An observed overshoot case (Peter, 2008) suggests that the water input in the medium and weak cases is more realistic, although the observations were in a different region (N. Australia compared to S. Brazil).

The extra moistening in the high CCN case of the strongest cloud could be enough to allow CCN increases to have caused the 46 year trend if the ice moistening in the simulation is also included; only an ~18 year trend is possible if not. However, extra moistening due to CCN increases in weaker clouds would seem unlikely to be enough (although this was not tested here) given the large reduction in the mass of water deposited into the stratosphere in these cases.

It is unknown whether the majority of overshooting clouds would produce as much moistening as in the strongest case with the observed case (Peter, 2008) suggesting against this. Therefore, this indicates that if trends in stratospheric vapour are to be explained by trends in moistening due to overshooting convection it is more likely that trends in the frequency of overshoots or the degree of overshooting will be the main cause rather than changes to the aerosol loadings of the clouds. This is also suggested by the sensitivity of the amount of moistening to the overshooting distance above the tropopause in the simulations.

Of course, extrapolating from one cloud to a global convective overshoot flux will introduce a large degree of error. The intention here was to asses the significance of the moistening produced in the clouds simulated rather than obtaining an accurate global estimate. In order to do the latter studies of overshooting clouds from all over the tropics need to be made utilizing combinations of observations and modelling that has been tested against observations. In order to be able to use satellite data to give a more accurate estimate of overshoot frequency a more reliable estimate of the lifetime of the 20 dBZ radar echo top above the tropopause needs to be made for such cases, with the most feasible way of doing this being from ground based radar statistics.

REFERENCES

Dessler, A. E.: A reexamination of the "stratospheric fountain" hypothesis, Geophysical Research Letters, 25, 4165-4168, 1998.

Forster, P. M. D., Shine, K. P.: Assessing the climate impact of trends in stratospheric water vapor, Geophysical Research Letters, 29, -, 2002.

Hanisco, T. F., Moyer, E. J., Weinstock, E. M., St Clair, J. M., Sayres, D. S.,et al.: Observations of deep convective influence on stratospheric water vapor and its isotopic composition, Geophysical Research Letters, 34, -, 2007.

Holton, J. R., Haynes, P. H., Mcintyre, M. E., Douglass, A. R., Rood, R. B., Pfister, L.: Stratosphere-Troposphere Exchange, Reviews of Geophysics, 33, 403-439, 1995.

Liu, C. T., Zipser, E. J.: Global distribution of convection penetrating the tropical tropopause, Journal of Geophysical Research-Atmospheres, 110, D23104, doi:10.1029/2005JD006063, 2005.

Nielsen, J. K., Larsen, N., Cairo, F., Di Donfrancesco, G.: Solid particles in the tropical lowest stratosphere, Atmos. Chem. Phys., 7, 685-695, 2007.

Peter, T. 2008. Upscaling results from Hector measurements to global convective H_2O input into the tropical stratosphere. Presented at SCOUT-O3 /ACTIVE / TWP-ICE workshop on tropical UTLS, The University of Manchester, 8-11th January 2008. http://www.ozone-sec.ch.cam.ac.uk/scout_o3/meetings/manchester/presentations/Peter.pdf.

Rosenlof, K. H., Oltmans, S. J., Kley, D., Russell, J. M., Chiou, E. W.,et al.: Stratospheric water vapor increases over the past half-century, Geophysical Research Letters, 28, 1195-1198, 2001.

Seidel, D. J., Ross, R. J., Angell, J. K., Reid, G. C.: Climatological characteristics of the tropical tropopause as revealed by radiosondes, Journal of Geophysical Research-Atmospheres, 106, 7857-7878, 2001.

Shutts, G. J., Gray, M. E. B.: A numerical modelling study of the geostrophic adjustment process following deep convection., Quart. J. Roy. Meteor. Soc., 120, 1145-1178, 1994.

Zhou, X. L., Geller, M. A., Zhang, M. H.: Cooling trend of the tropical cold point tropopause temperatures and its implications, Journal of Geophysical Research-Atmospheres, 106, 1511-1522, 2001.

CASE STUDIES OF THE DEVELOPMENT OF ICE AND PRECIPITATION IN UK CUMULUS CLOUDS DURING ICEPIC

Yahui Huang[1], Alan Blyth[1], Phil Brown[2], Paul Connolly[3], Tom Choularton[3], and Hazel Jones[3]

[1]University of Leeds, UK
[2]Met Office, UK
[3]University of Manchester, UK

1. SUMMARY OF OBSERVATIONS OF CASES

ICEPIC (ICE and Precipitation Initiation in Cumulus) is a project aiming to understand and quantify the formation and growth of ice particles in cumulus clouds in the UK and therefore to improve the parameterizations of the formation and development of ice particles and precipitation in numerical models.

Detailed measurements were made with cloud physics instruments on board the FAAM BAe- 146 aircraft, such as the Cloud Particle Imager (CPI). Observations made in the tops of clouds on 4 Jul (B107) and 13 Jul (B110) 2005 and 18 May 2006 (B200) are summarized in Table 1.

In the cases on 4 Jul and 18 May, high concentrations of ice particles were observed at relatively high temperatures (T > -10 C). The high concentration far exceeds the value estimated with the formula of Meyers et al. (1992) derived from typical IN measurements suggesting that some secondary ice production process operated.

For the cases B107 and B200, the observations of numerous ice particles and the co-existence of small ($d < 13$ µm) and large ($d > 24$ µm) cloud droplets, pristine ice columns and graupel pellets within the temperature zone of -3 to -9 °C strongly suggest that the Hallett-Mossop process of splintering during riming (Hallett and Mossop, 1974; Mossop and Hallett, 1974; Mossop, 1978) may be responsible for the observed high concentrations of ice. Figures 1 and 2 are two examples of the observations.

In contrast, the concentration of ice particles observed in the case on 13 Jul was low. There were plenty of large and small drops but the concentration of particles with diameters larger than 1mm was very low (Figure 3). We will discuss likely reasons for this in Section 4.

2. ICE PRODUCTION RATES

Following Harris-Hobbs and Cooper (1987) we calculated the observed and predicted ice production rates for the three cases. The results (Table 2) show that the observed rates are high for the cases B107 and B200 and they are in good agreement with the predicted rates of the H-M process. This indicates that the H-M process is responsible for the observed high concentrations of ice particles in the two cases. Both the observed and predicted rates are much lower in case B110, however, than the others, which suggests that there was no effective operation of the H-M process.

Table 1. Max concentration of drops (Nm) and LWC (Lm) from FFSSP, vertical velocity (Wm), and concentration of ice particles (Ni,m) from combined 2DC and 2DP

	Run	Z (km)	T (°C)	Nm (cm^{-3})	Lm (gm^{-3})	Wm (m/s)	Ni,m (L^{-1})
B 1 0 7	11	2.7	-5.4	80	0.8	6.0	3
	12	3.0	-7.0	65	0.6	7.5	27
	13	3.1	-7.6	62	0.6	5.0	42
	14	3.3	-8.6	120	0.7	5.0	70
B 2 0 0	2	2.1	-1.0	130	0.6	6.0	8
	3	2.4	-3.0	110	0.8	10.0	60
	4	2.7	-5.0	80	0.6	6.0	110
B 1 1 0	4.3	4.0	-3.1	240	0.9	8.0	0.2
	4.4	4.3	-6.0	220	1.3	10.0	6
	4.5	4.9	-7.8	160	1.1	6.4	6

Table 2. Ice production rates

	Run12 (B107)	Run 4 (B200)	Run 4.4 (B110)
Observed rate (L^{-1} s^{-1})	0.43	1.49	0.04
Predicted rate (L^{-1} s^{-1})	0.31	1.40	0.09

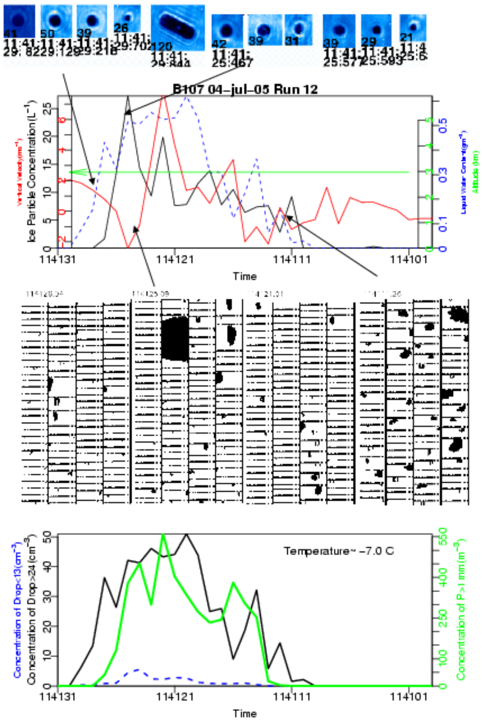

Figure 1. Ice particle concentration (black line in upper panel), concentrations of large, small drops, and graupel particles (black, dashed blue, and green lines in lower panel, respectively). The examples of particle images from CPI and 2DC are included.

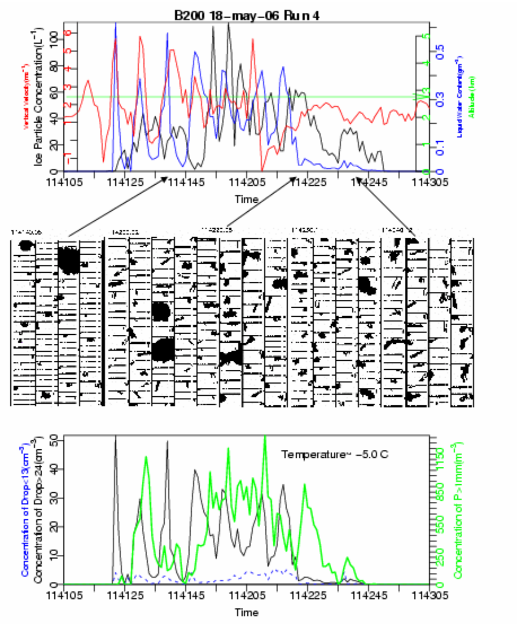

Figure 2. Same as Fig. 1 but for B200.

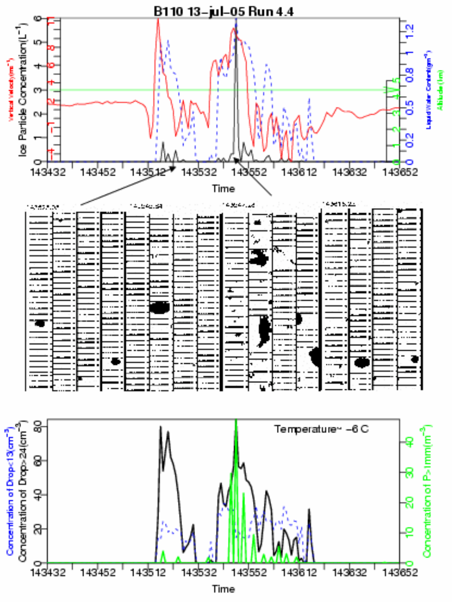

Figure 3. Same as Fig. 1 but for B110.

3. MODEL SIMULATIONS

A 2-D, axisymmetric, non-hydrostatic, bin-resolved cloud model, MAC3 (Model of

Aerosols and Chemistry in Convective Clouds, Reisin et al., 1996; Yin et al., 2005) was employed to simulate the three cases. The model results for the three clouds shown in Figs 4-6 agree well with the observations in all cases. The simulated high concentrations of ice crystals at an altitude of about 3 km for cases B107 and B200 (Figs 4b and 5b) are due to the H-M process. In sharp contrast, the simulated concentration of ice crystals is very low in case B110 (Fig. 6b). The ice particles were produced mainly by the primary ice production.

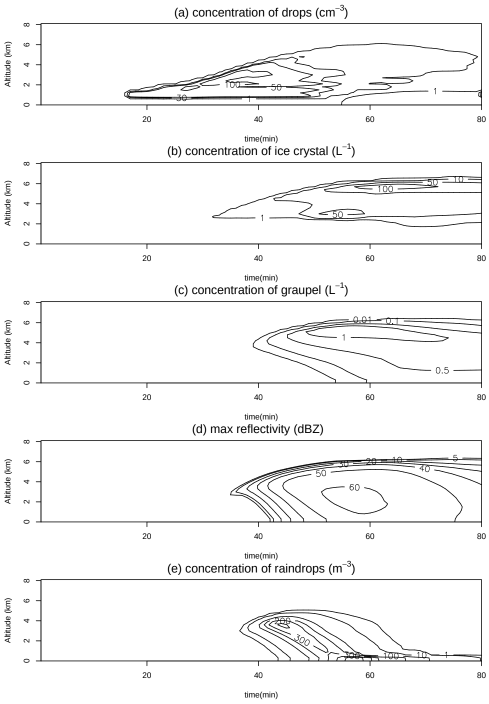

Figure 4. The evolution of model-produced values of the maximum concentration of: a) drops; b) ice crystals; c) graupel; and e) raindrops, and the reflectivity (d) for case B107.

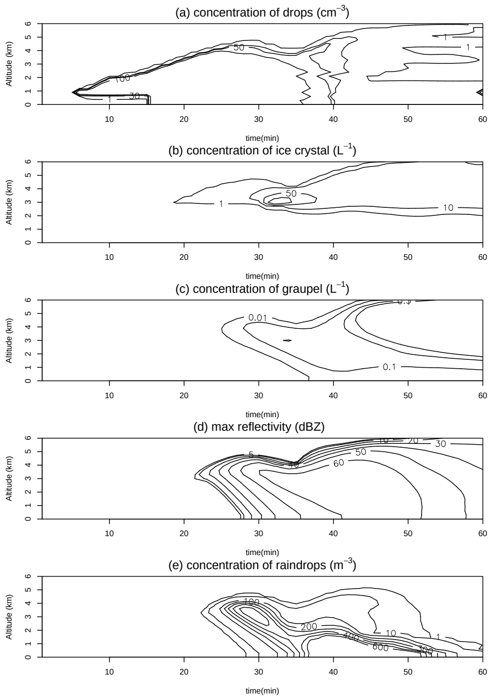

Figure 5. Same as Fig. 4 but for case B200.

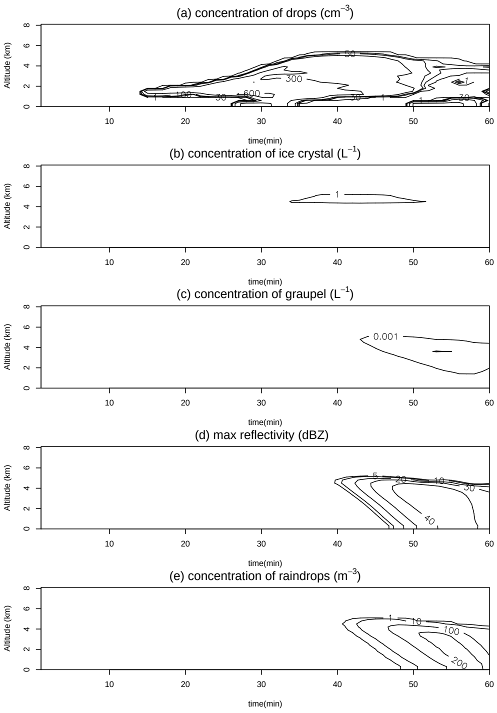

Figure 6. Same as Fig. 4 but for case B110.

4. COMPARISON OF CASES B110 AND B107

Figure 7 shows the comparison of cases B110 and B107. The total loading of aerosols in case B110 is about two times higher than in B107, so the concentration of nucleated droplets (here represented by the concentration of droplets with diameters smaller than 10 µm in Fig. 7a) is much higher for B110 and fewer raindrops formed (Fig. 7c). The freezing of supercooled raindrops by interacting with small ice crystals is an effective mechanism for the formation of graupel in the other two cases. The larger concentration of aerosol particles resulted in a delay in the production of raindrops (Fig. 6e) and hence of graupel particles (Fig. 6c). There was also a lower concentration of raindrops. The cloud had begun to decay by the time the raindrops and graupel particles had formed. In addition, the concentration of ice crystals near the cloud top decreased (Fig. 6b) with the decay of the cloud, even making it more difficult for the formation of graupel. The extremely low concentrations of graupel particles meant that the H-M process was unable to operate effectively in B110.

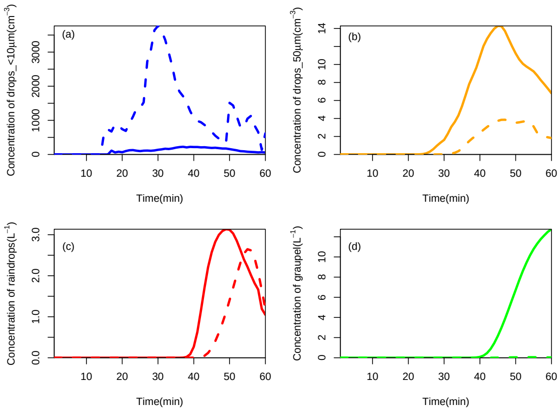

Figure 7. The time evolution of the sum over the whole depth of the clouds of the maximum concentrations of: a) drops with diameters less than 10 µm; b) drops with diameter of 50 µm; c) raindrops; and d) graupel. The solid lines represent case B107 and the dashed lines B110.

5. CONCLUSIONS

Observations of the development of ice made in the tops of growing cumulus clouds and corresponding model results were presented for three different cases. Relatively high concentrations of ice particles were observed in the 4 July 2005 and 18 May 2006 clouds. The observations of numerous ice particles and the co-existence of small (d < 13 µm) and large (d > 24 µm) cloud droplets, pristine ice columns and graupel pellets within the temperature zone of -3 to -9 °C suggest that the H-M process was responsible for the development of ice particles. Calculations and simulations support this conclusion.

In contrast, low concentrations of ice particles were observed in the cloud measured on 13 Jul 2005. Analysis and simulations revealed that the low concentration was due to the small concentration of graupel particles and the delay in the production of these particles until the cloud was decaying and therefore the lack of H-M process. The model results showed that the high aerosol loading was responsible for the reduced numbers and delay in production of supercooled raindrops that formed the graupel particles. Hence, it seems that aerosols can play an important role in the H-M process of splintering during riming.

References

1. Hallett, J. and S. C. Mossop, 1974. Nature, 249, 26-28.
2. Harris-Hobbs, R. L., and W. A. Cooper, 1987. J. Atmos. Sci., 44, 1071-1082.
3. Meyers, M. P., P. J. DeMott, and W. R. Cotton, 1992. J. Appl. Meteor., 31, 708-721.
4. Mossop, S. C. and J. Hallett, 1974. Science, 186, 632-634.
5. Mossop, S. C., 1978. Quart. J. R. Met. Soc., 104, 323-330.

6. Reisin, T., Z. Levin, and S. Tzivion, 1996. J. Atmos. Sci., 53, 497-519.
7. Yin, Y., K. S. Carslaw, and G. Feingold, 2005. Quart. J. R. Met. Soc., 131, 221-245.

Acknowledgement

We thank the pilots of the FAAM BAe aircraft for making the flights and the staff of FAAM and Dr. Jonathan Smith for assistance of the data. We also thank Drs. Justin Peter, Jason Lowenstein, and Zhiqiang Cui for many fruitful discussions and help with the model and with the flights. Both the FAAM aircraft and the ICEPIC project are jointly supported by the Natural Environment Research Council and the Met Office.

The Mechanism and Echo Analysis of the Hail Storm Moving and Evolution on Yachi River in Guizhou Province

HUANG Haojuan[1,2], WEI Ming[2] , WANG Li[1], ZHOU Lina[1]

(1．Weather Modification Office of Guizhou Meteorological Bureau，Guiyang 55002,China；

2．China—America Cooperative Remote Sensing Center，NUIST．Nan]ing 210044，China)

1. Introduction

Guizhou province is a complex mountainous plateau. As the important region in the multi-hail belt of China south, its water vapor is abundant. Discussing the evolution characteristic of Guizhou hail storm has the vital significance.

In order to improve the forecast and the operation effect of weather modification in some area, the special plateau topography results in the phenomenon that times of falling hail in eastern bank is different from that in western bank on Yachi River based on many observation facts.

In the same synoptic process, the hail damage at the east bank is more serious than West bank.

2. Complex topography

As shown in Figure 1 used 1: 250,000 DEM data, Yachi River located at Guiyang's west side, flowing from north to south, is a dividing line between the Guiyang area and the Bijie area.

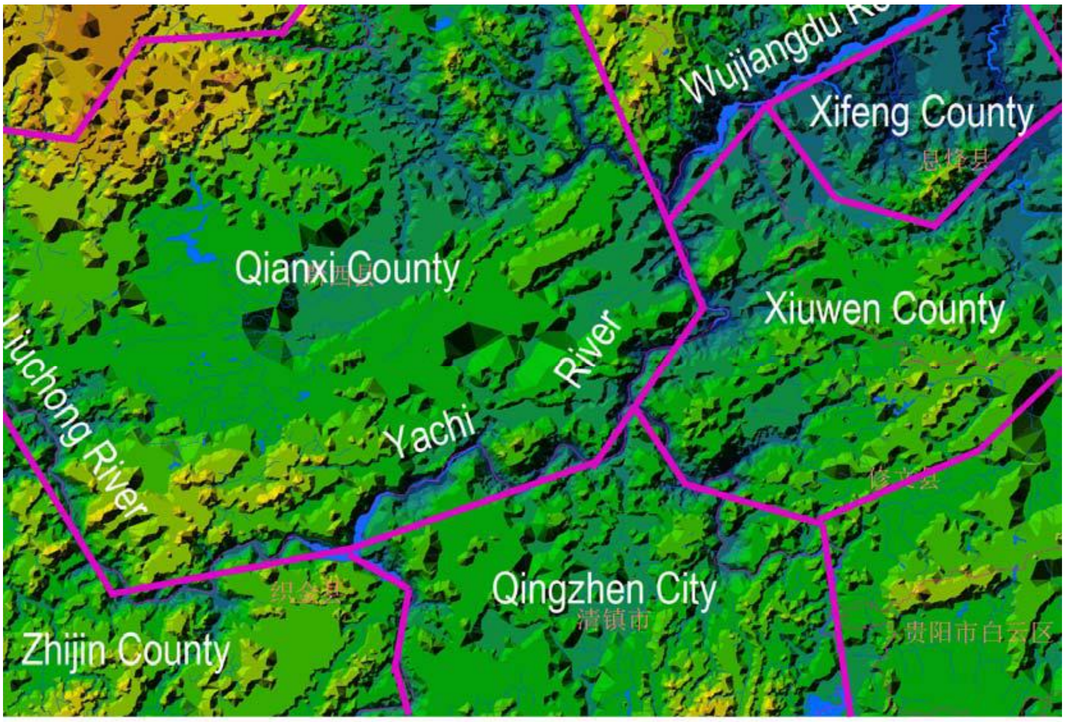

Fig 1 The topographic map of Yachi River area

The river surface width is about 30 meters in April and in May. The west bank's elevation is quite high, it’s a multi-mountainous regions. The eastern bank is a gentle slope, its topography is open.

3.Hail storm characteristics

We compare various features of the observed hail storm between the different banks of Yachi River in table 1.

Hail storm produced in Guizhou western always moves to the west, acrosses this river, then arrives at the Guiyang area. The hail storm often moves along with the certain rout, this can explain that some certain region's topography play an important role in the system's production or enhancement.

Year	western bank （time）	eastern bank （time）
1996	5	8
1997	4	7
1998	0	3
1999	1	3
2000	3	4
2001	0	0
2002	4	11
2003	0	1
2004	0	6
2005	0	0

Table 1 Comparison the number of times with hail record between the western bank and the eastern bank in April and May from 1996 to 2005

4. Echo analysis

As observed at Guiyang on May 10, 2004 in Fig.5, after acrossing river, cell A rapidly growth, the echo area increased, the max radar reflectivity increased. After cell B cross river, its corner is intensely, echo area increases. The two cells approaches each other after acrossing the river which advantageous to the multi-cell’s downdraft air collide, thus form “the cloud bridge” , promotes various cells connect. After cell A cross river, the strong echo drops highly (see Table 2), meanwhile the hail are observed at eastern bank.

Table 2 Comparison echo of the hail cloud A and hail cloud B between the hail clouds on different reaches of Yachi River

Evolution time	Hail cloud A		Hail cloud B	
	15：56	17：26	15：56	17：26
Max radar reflectivity (dBZ)	50	50	45	50
Echo area (km^2)	618	1031	570	914
Max cloud-top height(km)	13	11	11	14

On May 10, 2004 Yachi River banks region's the hail falling times as shown in table 3. Three counties at western bank do not have the hail report, but simultaneously three counties at eastern bank have.

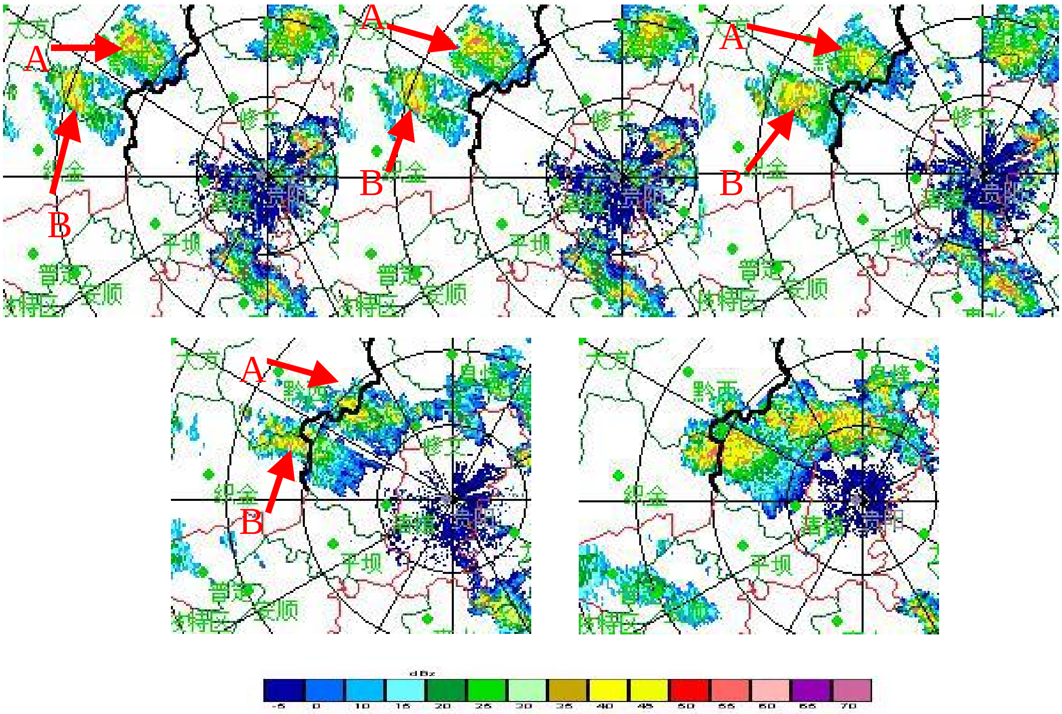

Fig 5 The evolution of hail cloud echo, the elevations are 0.5°on May 10,2004(each distance circle 30km, black line indicates where Yachi River is)

Table 3 Compare the number of times with hail record between the western bank and the eastern bank of Yachi River on April 22,2004

western bank (time)		eastern bank (time)	
Zhijin	0	Xiuwen	3
Qianxi	0	Qingzhen	1
Jinsha	0	Xifeng	2

Diagram of Reflectivity of velocity shows that the hail storm's center is composed of several small convective cell [image omitted]. It also has been found that Guizhou local hail storm has this characteristic generally.

5. Summary and conclusions

The purpose of this paper is to analyze the mechanism and echo of the hail storm moving and evolution on Yachi River observed in Guizhou province. Major finding of analysis include the following.

◆ It is found that down-slope wind, mesoscale leeward slope low- pressure and environment heating play important roles. The reason of strong wind and the RHI echo character of falling hail at Dongfeng Lake, which is at the join of rivers area, are analyzed.

◆ In this paper, through the analysis of two case of the hailstorm moving and evolution on Yachi river, it shows that there is different development when thunderstorm across different reach of Yachi river.

◆ Hailstorms always move along advantageous route that accelerates their development. It proves the mechanism of the hail storm moving and evolution on Yachi River as this paper reveals.

MODELING OF SUBGRID-SCALE MIXING IN LARGE-EDDY SIMULATION OF SHALLOW CONVECTION

Dorota Jarecka[1], Wojciech W. Grabowski[2] *, and Hanna Pawlowska[1]

[1] Institute of Geophysics, University of Warsaw, Warsaw, Poland
[2] National Center for Atmospheric Research, Boulder, Colorado, USA

1. INTRODUCTION

Recent modeling studies (e.g., Chosson et al. 2004, 2007; Grabowski 2006; Slawinska et al. 2008) demonstrate that assumptions concerning microphysical evolution of natural clouds (the homogeneity of cloud-environment mixing in particular) significantly affect the albedo of a field of shallow convective clouds, such as subtropical stratocumulus and trade-wind cumulus. It follows that modeling of microphysical properties of such clouds has important implications for the clouds-in-climate problem. Since such clouds are strongly diluted by entrainment, the focus should be on modeling dynamical, thermodynamical, and microphysical processes associated with entrainment. This paper discusses a novel approach to model subgrid-scale processes associated with entrainment and mixing. It extends the approach advocated in Grabowski (2007; hereinafter G07). As in G07, we limit the discussion to the bulk representation of cloud microphysics, and present analysis of a series of simulations of shallow convective clouds using the same modeling setup as in the section 4b of G07. The longer-term goal is to combine the approach discussed here with the two-moment microphysics scheme of Morrison and Grabowski (2007; 2008) to locally *predict* the homogeneity of mixing (i.e., the parameter α in Morrison and Grabowski 2008; eq. 11).

The next section provides a brief summary of the method developed in G07 and presents a slight modification (or extension) of this approach. Selected results from a series of numerical simulations of shallow nonprecipitating convection are discussed in section 3. Brief summary in section 4 concludes the paper.

2. MODELING EVAPORATION OF CLOUD WATER RESULTING FROM ENTRAINMENT AND MIXING

As in G07, we start with the thermodynamic grid-averaged equations for the advection-diffusion-condensation problem:

$$\frac{\partial \theta}{\partial t} + \frac{1}{\rho_o}\nabla \cdot (\rho_o \mathbf{u}\theta) = \frac{L_v}{\Pi c_p} C + D_\theta \ , \qquad (1a)$$

$$\frac{\partial q_v}{\partial t} + \frac{1}{\rho_o}\nabla \cdot (\rho_o \mathbf{u} q_v) = -C + D_v \ , \qquad (1b)$$

$$\frac{\partial q_c}{\partial t} + \frac{1}{\rho_o}\nabla \cdot (\rho_o \mathbf{u} q_c) = C + D_c \ , \qquad (1c)$$

where θ, q_v, and q_c are the potential temperature, the water vapor and cloud water mixing ratios; $\rho_o(z)$ is the base state density profile; $\Pi = (p/p_o)^{R/c_p}$ is the Exner function (p is the ambient pressure profile and $p_o = 1000\,\text{hPa}$); L_v and c_p denote the latent heat of condensation and specific heat at constant pressure, respectively; C is the condensation rate, and the last terms on the rhs of (1a,b,c) represent subgrid-scale turbulent (eddy-diffusion) transport terms, typically represented by a divergence of parameterized turbulent fluxes.

In the bulk condensation model, the condensation rate C is defined by constraints that the cloud water can exist only in saturated conditions and that supersaturations are not allowed ["all-or-nothing" scheme; cf. (3) and (4) in Grabowski and Smolarkiewicz 1990]. For the uniformly saturated and adiabatic air parcel, the condensation rate C can be derived from the rate of change of the saturated water vapor mixing ratio (see Appendix in G07); it is marked as C^a (a for *adiabatic*). For the system (1), C is derived by the saturation adjustment after calculation of advection and eddy diffusion. The adjustment brings the gridbox back to saturation, provided there is enough cloud water in the case of evaporation. The condensation rate calculated in such a way is marked as C^{sa} (*sa* for *saturation adjustment*).

---

* *Corresponding author address*: Dr. Wojciech W. Grabowski NCAR, PO Box 3000, Boulder, CO 80307; e-mail: grabow@ncar.ucar.edu.

A critical aspect of the saturation adjustment is that the cloud water can exist only in a saturated gridbox. However, for the turbulent mixing such an assumption is often invalid because the turbulent mixing involves a gradual filamentation (i.e, stirring) of initially coarse mixtures of cloudy air and cloud-free air. As the turbulent mixing progresses, cloud water can exist in a gridbox that is an average subsaturated. Turbulent stirring may take up to a few minutes if the volume to be homogenized is relatively large [for instance, a volume corresponding to a typical large-eddy simulation model gridbox ($\sim$ 50 m)^3] and turbulence intensity is low (see G07 for a detailed discussion). Only when the microscale mixing is finalized and the gridbox becomes homogeneous, the saturation adjustment is justifiable.

To represent the chain of events characterizing turbulent mixing—from the initial engulfment of the ambient fluid by an entraining eddy, to the small-scale homogenization—and to include a corresponding delay in the saturation adjustment, G07 proposed to include an additional model variable that describes the progress of turbulent mixing towards the small-scale homogenization. This variable is the scale of cloudy filaments, λ. Following the discussion in Broadwell and Breidenthal (1982), the evolution equation for λ was proposed in G07 to take the form:

$$\frac{\partial \lambda}{\partial t} + \frac{1}{\rho_o} \nabla \cdot (\rho_o \mathbf{u} \lambda) = -\gamma \epsilon^{1/3} \lambda^{1/3} + S_\lambda + D_\lambda \ , \quad (2)$$

where the first term on the rhs describes the decrease of the filament scale λ as the turbulent mixing progresses [$\gamma \sim 1$ is a nondimensional parameter and ϵ is the local dissipation rate of the turbulent kinetic energy (TKE); see Broadwell and Breidenthal 1982], S_λ is the source/sink term, and D_λ is the subgrid transport term.

The source/sink term S_λ considers three processes that affect the scale λ. These are: (a) formation of cloudy volumes due to grid-scale condensation; (b) disappearance of cloudy volumes due to complete evaporation of cloud water; and (c) homogenization of a cloudy volume. Since it is assumed that condensation due to saturation adjustment occurs always over the entire gridbox, (a) is represented by simply reseting current value of λ to the scale comparable to the size of the the gridbox, say, $\Lambda \equiv (\Delta x \ \Delta y \ \Delta z)^{1/3}$ (where Δx, Δy, Δz are model gridlength in x, y, and z direction, respectively). Complete evaporation of cloud water [i.e., process (b)] is represented by reseting λ to zero. Finally, microscale homogenization of the cloudy gridbox (i.e., homogenization that results in a saturated gridbox containing some cloud water and with $\lambda < \lambda_0$) is represented by resetting $\lambda = \Lambda$. Here, λ_0 is the threshold value of λ that represents scale at which molecular homogenization occurs (say, $\lambda_0 = 1$ cm).

With λ predicted by the model, it is possible to represent the delay of cloud water evaporation associated with the entrainment and turbulent mixing. In the case of evaporation, the saturation adjustment is delayed until the gridbox can be assumed as homogenized. In practice, when $\lambda = \Lambda$ or $\lambda \leq \lambda_0$, the evaporation rate is exactly the same as in the standard bulk model: $C = C^{sa}$. However, when $\Lambda > \lambda > \lambda_0$, i.e., the turbulent mixing has not reached scales characterizing the small-scale homogenization, the adiabatic rate is used but only over the cloudy part of the gridbox: $C = \beta C^a$, where β is the fraction of the gridbox covered by the cloudy air.

It was suggested in G07 that β can be diagnosed locally based on the mean relative humidity of a gridbox RH and of the environmental relative humidity RH^e at this level as:

$$\beta = \max\left(0., \min\left(1., \frac{RH - RH^e}{1 - RH^e}\right)\right) \ , \quad (3)$$

where the additional limiting is used to avoid unphysical values of β. Arguably, (3) may provides a reasonable approach for the case of a convective cloud. For the stratocumulus, on the other hand, entrainment and cloud-environment mixing takes place primarily at the cloud top where environmental profiles evolve rapidly due to the presence of boundary-layer inversion. It follows that (3) is most likely of limited use when modeling the stratocumulus. Since the accuracy of (3) is uncertain, we decided to make β an additional model variable and to locally predict its value together with λ. The advection-diffusion equation for β is:

$$\frac{\partial \beta}{\partial t} + \frac{1}{\rho_o} \nabla \cdot (\rho_o \mathbf{u} \beta) = S_\beta + D_\beta \ , \quad (4)$$

where S_β is the source/sink term and D_β is the subgrid transport term. Similarly to the source term for λ in (2), S_β resets β to 1 if either the grid-scale condensation or microscale homogenization takes place. Otherwise, β is advected and diffused in a manner similar to λ. The justification for the approach where β is predicted rather than diagnosed comes from *a posteriori* comparison between the values of β obtained from the diagnostic formulation (3) and the prognostic formulation (4); see Fig. 1 herein to be discussed later.

In the next section, we present selected results from the modified G07 model (which will be referred to as the $\lambda - \beta$ model) and compare them to the traditional bulk cloud model.

3. APPLICATION OF THE $\lambda - \beta$ MODEL TO BOMEX SHALLOW CONVECTION

Eqs. (3) and (4) were included in the anelastic semi-Lagrangian/Eulerian cloud model EULAG documented in Smolarkiewicz and Margolin (1997; model dynamics), Grabowski and Smolarkiewicz (1996; model thermodynamics), and Margolin et al. (1999; subgrid-scale model). Eulerian version of the model is used to simulate quasi-steady-state trade-wind shallow nonprecipitating convection observed during the Barbados Oceanographic and Meteorological Experiment (BOMEX; Holland and Rasmusson 1973) and recently used in the model intercomparison study described in Siebesma et al. (2003). In BOMEX observations, the 1.5-km-deep trade-wind convection layer overlays 0.5-km-deep mixed layer near the ocean surface and is covered by 500-m-deep trade-wind inversion layer. The cloud cover is about 10% and quasi-steady conditions are maintained by the prescribed large-scale subsidence, large-scale moisture advection, surface heat fluxes, and radiative cooling. The model setup is as described in Siebesma et al. (2003) but applying different domain sizes and model gridlengths (i.e., increasing the model resolution but keeping the same number of gridpoints in the horizontal, 128×128; and adjusting the number of gridpoints in the vertical to maintain the 3-km vertical extent of the domain). Three different model gridlengths were considered: 100 m/40 m in the horizontal/vertical (i.e., as in Siebesma et al. 2003), 50 m/40 m, and 25 m/25 m. Note that increasing the horizontal resolution with the same number of gridpoints results in progressively decreasing horizontal domain size and thus poorer cloud statistics. This, however, does not seem to affect the results discussed below. Results from the lowest and the highest resolution will be discussed in this paper, using both the traditional bulk model and the $\lambda - \beta$ model. As in Siebesma et al. (2003) and G07, the model is run for 6 hours and snapshots of model results for hours 2 to 6 archived every 4 minutes are used in the analysis.

Figure 1 shows results from the simulation applying the $\lambda - \beta$ model with the gridlength of 25 m in the horizontal and vertical directions. The figure compares values of β predicted by (4) to corresponding values obtained using the diagnostic relationship (3) at 1250 m level (i.e. about half of the cloud field depth). As the figure illustrates, there is a significant scatter between predicted and diagnosed values of β, most likely reflecting the fact that assumptions leading to (3) are seldom justified. More importantly, however, the diagnostic approach leads to a significant overestimation of β. This is likely because the air entrained into the cloud is typically more humid than the environmental profile, that is, the environmental air is premoistened before it is entrained into a cloud. This is consistent with the fact that reducing RH^e in (3) indeed results in the increase of the diagnosed β. Another way to show that the entrained air is premoistened is to consider the plot of the ratio RH/RH^e versus β. Eq. (3) implies that $RH/RH^e \rightarrow 1$ (i.e., RH approaches RH^e) when

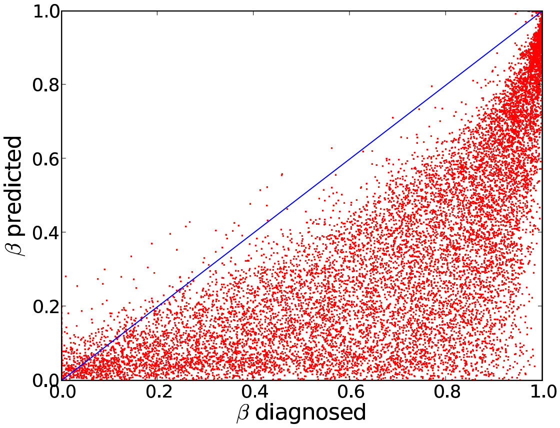

Figure 1: Predicted β versus diagnosed β at an altitude of 1250 m in simulation with 25 m gridlength and averaged over hours 2-6.

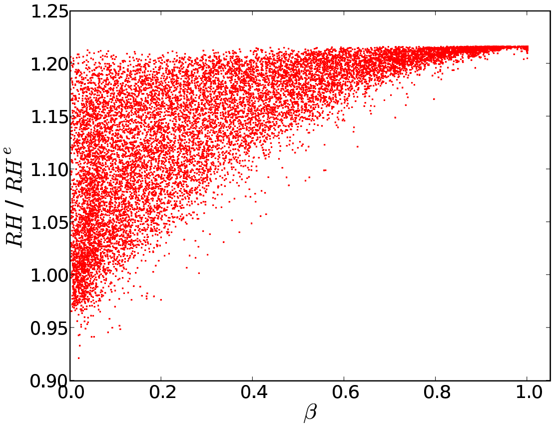

Figure 2: RH/RH^e versus β for the simulation as in Fig. 1.

$\beta \rightarrow 0$. Figure 2 shows that this is not true because the ratio RH/RH^e is typically larger than 1 when β is close to 0. This implies that the air entrained into the cloud is, on average, more humid than environmental air at this level. Similar analysis can be performed separately for the temperature and water vapor mixing ratio. It shows that the water vapor is typically higher near the cloud than the environmental value at a given level, whereas the temperature close to the cloud is usually lower than the environmental temperature. The latter seems consistent with the fact that premoistening is associated with the evaporative cooling.

In general, the above results provide *a posteriori* support for the $\lambda-\beta$ model. Hence, in the following analysis, results of the traditional bulk model are compared to the $\lambda - \beta$ model, in the spirit of the discussion in section 4b of G07.

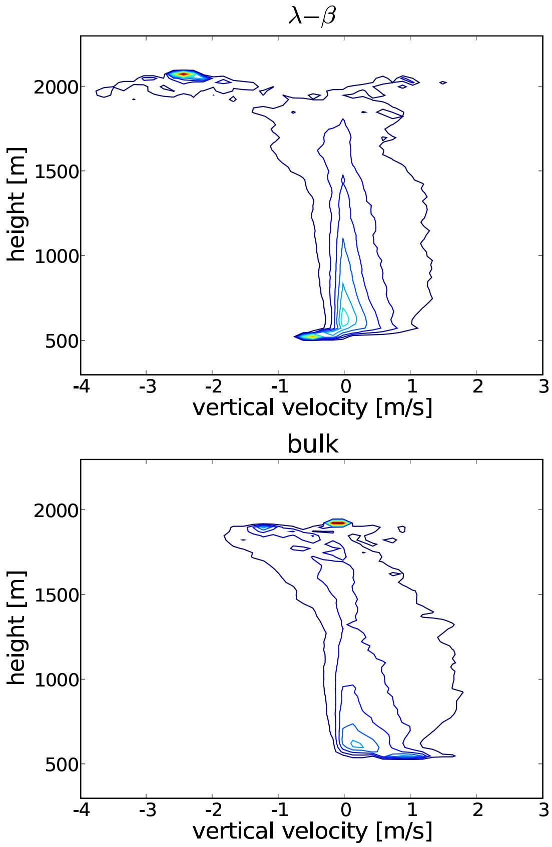

Figure 3: CFADs of the vertical velocity for the $\lambda-\beta$ model (upper panel) and the traditional bulk (lower panel) in simulation with 25 m gridlength and averaged over hours 2-6.

Figure 3 presents the contoured frequency by altitude diagrams (CFADs) of the vertical velocity for simulations with the traditional bulk model and the $\lambda - \beta$ model using the 25-m gridlengths. Only cloudy gridpoints (i.e., those with the cloud water mixing ratio larger than 10^{-2} g kg^{-1}) are included in the analysis. Although both CFADs seem similar, there are significant differences. First, clouds in the $\lambda - \beta$ model seem slightly deeper than in the bulk approach (noisy pattern close to the cloud layer top comes from poor statistics there). This is consistent with the lower-resolution results discussed in section 4b of G07. Second, there seem to be more points with positive vertical velocities in the range of 0 to 1 m s^{-1} in the $\lambda - \beta$ model across most of the depth of the cloud field. This is consistent with the expectation that cloud evaporation (and thus buoyancy reversal and subsequent downward acceleration) is delayed when the $\lambda - \beta$ approach is used. Arguably, the delayed evaporation is also responsible for a more erect shape of the CFAD in the $\lambda-\beta$ case, whereas the CFAD for the bulk model tilts towards the negative velocities, especially in the upper half of the cloud field.

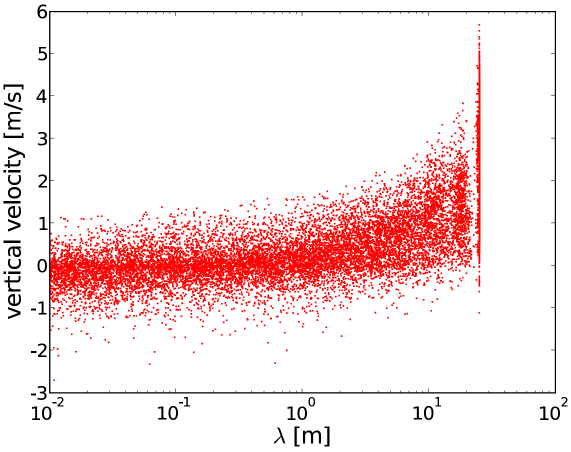

Figure 4: Vertical velocity versus λ for the simulation as in Fig. 1.

To document the impact of the $\lambda - \beta$ approach on the vertical velocity field inside clouds, Fig. 4 shows a scatterplot of the vertical velocity versus λ at an altitude of 1250 m for the simulation using the 25 m gridlengths (i.e., as in Figs. 1–3). It needs to be kept in mind that the cloud water in a grid box with $\lambda_0 < \lambda < \Lambda = 25$ m would be immediately evaporated in the traditional bulk model. As the Fig 4 shows, the gridboxes with intermediate values of λ are characterized by small positive and negative values, with the mean around zero. A clear tendency toward positive bias is apparent for

λ values approaching Λ. The values at $\lambda = \Lambda$ correspond to the homogeneous cloudy gridboxes and thus are characterized by both positive and negative values. Arguably, these are the values that the traditional bulk model would have at this height.

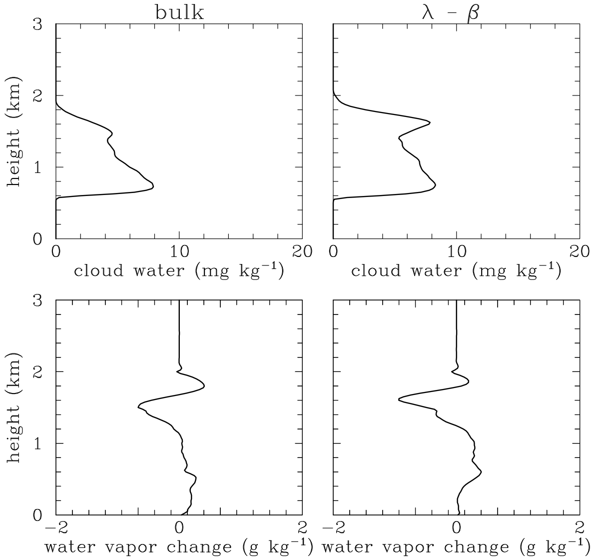

Figure 5: Profiles of the cloud water mixing ratio (4-hr averages; upper panels) and the difference between q_v profiles at hour 2 and 6 (lower panels) for resolution (100 m/40 m) and either the traditional bulk model (left panels) or the $\lambda - \beta$ model (right panels).

Finally, Figs. 5 and 6 show profiles of the horizontally-averaged cloud water mixing ratios (also averaged in time between hour 2 and 6) and profiles of the difference between horizontally-averaged water vapor mixing ratios at hour 2 and 6 for simulations with the lowest (100 m/40 m horizontal/vertical) and the highest (25 m in horizontal and vertical) resolutions, respectively, and for simulations applying the traditional bulk model and the $\lambda - \beta$ model. These figures are similar to Fig. 10 in G07 except that rather than showing the water vapor profiles at hour 2 and 6, a difference between them is plotted (this allows a better evaluation of the change in the profiles). As the figure shows, the differences between the traditional bulk model and the $\lambda - \beta$ model decrease as the model resolution increases. In agreement with the discussion in G07, the $\lambda - \beta$ approach predicts deeper clouds and larger changes of the water vapor mixing ratio during the last 4 hours of the simulation than the traditional bulk model. As far as overall characteristics of the BOMEX shallow convection are concerned, the differences between G07 approach (i.e., when λ was predicted and β was diagnosed) and the $\lambda - \beta$ model are insignificant (not shown).

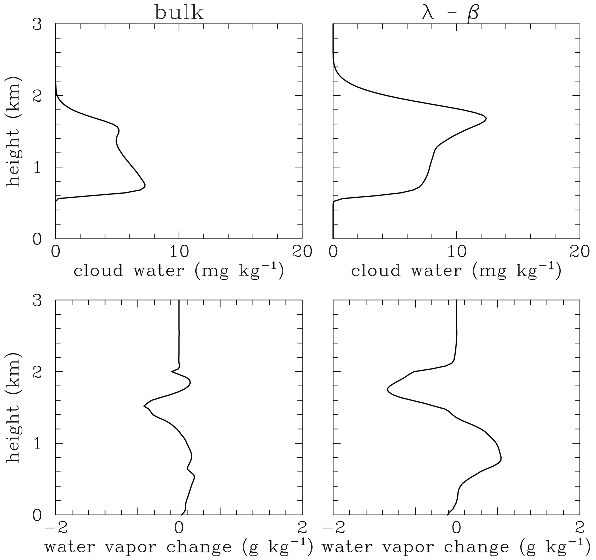

Figure 6: As Fig. 5 but for resolution (25 m/25 m).

4. SUMMARY

This paper presents results using the approach developed in G07 to represent the delay of cloud water evaporation and buoyancy reversal associated with the cloud-environment mixing. This is accomplished by including an equation for the horizontal scale of cloudy filaments, λ. A conceptual picture is that turbulent mixing is initiated by an engulfment of environmental fluid by an entraining eddy, it progresses through the gradual filamentation of the initial coarse mixture of cloudy and cloud-free air (which is represented by the decrease of λ), and reaches the final homogenization once λ approaches spatial scales not far from the Kolmogorov microscale. Using the new approach, evaporation of cloud water (i.e., the saturation adjustment) is delayed until the homogenization stage. Here, we extend the approach of G07 and include one additional model variable, the fraction of the gridbox covered by the cloudy air, β. The parameter β was diagnosed in G07, but here we show that the diagnostic approach results in significant inaccuracies when modeling shallow convective clouds. These inaccuracies exist because the air entrained into the cloud has thermodynamic properties significantly different than the environmental air at this level, in contrast to the assumptions underlying the diagnostic approach. The diagnostic approach is also unlikely to work in the case of stratocumulus, where rapid changes of environmental profiles in the vicinity of boundary-layer inversion make the validity of (3) questionable. We refer to the extended approach as the $\lambda - \beta$ model.

Application of the $\lambda - \beta$ model to the same BOMEX case as in G07 shows that predicting β in addition to λ results in small changes of the results when β is diagnosed. The reason for predicting β, perhaps not obvious in the current study, is that β will play an important role when the $\lambda - \beta$ model is combined with the 2-moment bulk microphysics scheme developed by Morrison and Grabowski (2007, 2008). The overall idea is to locally predict the homogeneity of mixing (i.e., decreasing only the number of droplets for the extremely inhomogeneous mixing or only their size in the case of homogeneous mixing). These developments will be presented in forthcoming publications.

ACKNOWLEDGMENTS.

This work was partially supported by the NOAA Grant NA05OAR4310107 (DJ and WWG) and by Polish MNiSW grant ACCENT/295/2006 (DJ). The National Center for Atmospheric Research is operated by the University Corporation for Atmospheric Research under sponsorship of the National Science Foundation. DJ acknowledges the financial support for participation in the ICCP-2008 offered by the organizers.

BIBLIOGRAPHY

Broadwell, J. E., and R. E. Breidenthal, 1982: A simple model of mixing and chemical reaction in turbulent shear layer. *J. Fluid. Mech.*, **125**, 397-410.

Chosson, F., J.-L. Brenguier, and M. Schröder, 2004: Radiative impact of mixing processes in boundary layer clouds. *Proceedings of the International Conference on Clouds and Precipitation*, Bologna, Italy, 371-374.

Chosson, F., J.-L. Brenguier, and L. Schüller, 2007: Entrainment-mixing and radiative transfer simulation in boundary-layer clouds. *J. Atmos. Sci.*, **64**, 2670-2682.

Grabowski, W. W., 2006: Indirect impact of atmospheric aerosols in idealized simulations of convective-radiative quasi-equilibrium. *J. Climate*, **19**, 4664-4682.

Grabowski, W. W., 2007: Representation of turbulent mixing and buoyancy reversal in bulk cloud models. *J. Atmos. Sci.*, **64**, 3666-3680.

Grabowski, W. W. and P. K. Smolarkiewicz, 1990: Monotone finite difference approximations to the advection-condensation problem, *Mon. Wea. Rev.*, **118**, 2082–2097.

Grabowski, W. W. and P. K. Smolarkiewicz, 1996: On two-time-level semi-Lagrangian modeling of precipitating clouds. *Mon. Wea. Rev.* **124**, 487-497.

Holland, J. Z. and E. M. Rasmusson, 1973: Measurements of the atmospheric mass, energy, and momentum budgets over a 500-kilometer square of tropical ocean. *Mon. Wea. Rev.* **101**, 44-55.

Margolin, L. G., P. K. Smolarkiewicz, and Z. Sorbjan, 1999: Large-eddy simulations of convective boundary layers using nonoscillatory differencing. *Physica D*, **133**, 390-397.

Morrison, H., and W. W. Grabowski, 2007: Comparison of bulk and bin warm rain microphysics models using a kinematic framework. *J. Atmos. Sci.*, **64**, 2839-2861.

Morrison, H., and W. W. Grabowski, 2008: Modeling supersaturation and subgrid-scale mixing with two-moment bulk warm microphysics. *J. Atmos. Sci.*, **65**, 792-812.

Siebesma, A. P., and Coauthors, 2003: A large eddy simulation intercomparison study of shallow cumulus convection. *J. Atmos. Sci.*, **60**, 1201-1219.

Slawinska, J., W. W. Grabowski, H. Pawlowska, and A. A. Wyszogrodzki, 2008: Optical properties of shallow convective clouds diagnosed from a bulk-microphysics large-eddy simulation. *J. Climate*, **21**, 1639-1647.

Smolarkiewicz, P. K., and L. G. Margolin, 1997: On forward-in-time differencing for fluids: An Eulerian/semi-Lagrangian nonhydrostatic model for stratified flows. *Atmos.-Ocean Special*, **35**, 127-152.

ANALYSIS ON RADAR ECHO CHARACTERISTICS OF MESO-γ SCALE CONVECTIVE CLOUDS IN SUMMER IN ANHUI AREA, CHINA

Jiang Nianchong[1] Liu Juan[2] Hu Wen[3] Lu Hai[2] and Song Zizhong[2]
1. Weather Modification Office of Anhui Province, 230061
2. Fuyang Meteorological Observatory, Anhui Province
3. Anhui Meteorological Bureau

1. INTRODUCTION

Convective cloud system is an important precipitating system and main target for weather modification. Effect of different synoptic systems is important to understand cloud and precipitation process in the Anhui region. The new generation weather radar (CINRAD) provides much better data for study of convective cloud properties. Radar echo features of intense convective storm producing hail and torrential rain have been studied by many researchers, and precipitation property and precipitation distribution of the convective cloud and their motion and intensity change have been understood well (Guo et al., 2005; Zhou et al., 2006). Cheng et al. (2002) studied radar echo characteristics of convective clouds and their life cycle, and obtained some significant results. The life cycle, scale, intensity and liquid water content of convective cloud in summer in south of China were analyzed statistically by Jiang et al (2005), and to obtain dynamic features of convective cells in different developing stages and at different levels.

In this paper, structure of meso-γ scale convective clouds under different synoptic system was analyzed and studied using this new generation weather radar data. Basic characteristics of convective cloud were analyzed statistically in order to study precipitation mechanism, structure of convective cloud in summer and to provide some parameters for artificial precipitation enhancement operation.

2. DATA

The data used for statistic analysis are from production (62 mark) provided by new generation weather radar at Hehui station. The radar production can give multiple properties such as storm number, azimuth and distance of storm, height of the cloud base and top, Vertically Integrated Liquid Water Content (VIL) of the storm cell, radar maximum reflectivity factor and its height. All these parameters are in favor of structure analysis for meso-γ scale convective clouds. The storm number can mark every storm cell and distinguish and track, azimuth and distance can show position relative to the radar of storm cell, i.e., the position of center of storm mass, etc.

3. CONVECTIVE CLOUD FEATURES IN SUMMER

In general, structure of radar echo from precipitating convective cloud is close-grained, and the variation of the radar reflectivity is lager and the intensity is more than 35dBZ. Moreover, minimum threshold of distinguishing automatically from convective cells by the radar is 30dBZ, and in view of when radar echo intensity of convective cloud to be seeded for artificial precipitation enhancement is generally more than 30dBZ. Therefore, various features of convective cloud studied in this paper are all those of convective cloud with intensity greater than 30dBZ.

3.1 FREQUNCEY OF CONVECTIVE ACTIVITITY AND LIFE CYCLE OF CONVECTIVE CELL

Table 1. Frequency（%） of convective clouds with different life cycles（min）

synoptic system	6	7～17	18～60	61～90	91～120
A	51	17	28	3	1
B	44	16	34	5	1
C	48	19	29	3	1
D	39	14	37	8	2
E	50	18	27	4	1

Note：A, stands for around Subtropical high, sample number 7009. B, north trough of china, sample number 3448. C, trough along the sea, sample number 1561. D, subtropical high control, sample number 1378. E, subtropical high control, sample number 528. Synoptic system and sample number in the other tables are same as table 1.

From table 1, convective clouds that life cycle less than 1 hour is 90%-95% of the total number and they are absolute majority in five synoptic systems. Those convective clouds with life cycle from 1-1.5 hours is 3%-8% of the total number and convective clouds having life cycle of 2.5-2 hours only is 1%-2% in total. It may be known from total number of the cell that number of convective cell occurring around subtropical high is the most and the cell number is taken second place in north trough of china. Under the condition of south branch trough, convective cloud is the least.

3.2 WARM TOP AND COLD TOP OF CONVECTIVE CLOUD

In order to understand property of convective cloud and easy to choose tool for artificial precipitation enhancement, radar echo top height of convective cloud with 30dBZ is defined as initial cloud top height and that below 0℃ level is warm cloud top and that over 0℃ level and near 0℃ cold cloud top or mixed cloud top. It may be seen from table 2 that over 80% of convective clouds are the cold clouds or the mixed cloud in summer in Hanhui area. In the influence of subtropical high, heights of 0 ℃ level are greater than 5km, high big gun and rocket can be act as seeding tool; In the condition of other synoptic system, because 0 ℃ levels are lower than 5km, the airplane is a suitable seeding tool.

Table2. Frequency (%) of convective clouds with warm and cold top and their average height (km)

Synoptic System	warm top /frequency	0℃ level /frequency	cold top /frequency
A	4.5/6.0	5.4/54.8	6.3/39.2
B	3.5/5.5	4.5/29.6	5./ 64.9
C	4.2/7.9	4.9/32.2	6.1/59.9
D	4.4/19.0	5.3/16.7	7.7/64.3
E	3.8/17.0	4.8/28.0	5.9/55.0

3.3 RADAR ECHO INTENSITY OF CONVECTIVE CLOUD

There are convective cells with different radar reflectivity under the influence of different synoptic systems and frequency of intense convective cloud is also different.

Table 3. Frequency(%） of convective clouds with different radar echo intensity (dBZ)

Synoptic System	<35	≤40	≤45	≤50	≤55	≤60	>60	max.
A	5	26	39	24	5	0.9	0.1	69
B	18	34	24	14	6	3	1	65
C	8	30.6	38	19	4	0.3	0.1	66
D	3	8.7	15	26.7	28.3	14.3	4	72
E	25	46	26	3	/	/	/	51

It can be seen from table 3 that in subtropical high control, intensity of convective cell of 70% may achieve 45-60dBZ and the maximum is 72dBZ. Under influence of round subtropical high and trough along the sea, radar reflectivity of convective cells of over 80% is from 35 to 50dBZ, the maximums are 69 and 66dBZ, respectively. While north trough of China appears, the convective cell intensity is mainly between 30 and 50dBZ and the maximum is 65dBZ. In the condition of south branch trough, convection is the most infirmness and the intensity of a most of convective cells is less than 45dBZ, their maximum is only 51dBZ.

3.4 TOP HEIGHT OF RADAR ECHO OF CONVECTIVE CLOUD

Top height of radar echo of convective cloud is used to judged precipitation property. Statistical features of top height of convective cloud under the condition of various synoptic systems are listed in table 4.

Table 4. Frequency (%) of convective cloud with different top heights (km)

Synoptic System	≤3	≤5	≤6	≤ 8	≤10	≤12	≤15	h > 15
A	1.9	28.4	30.5	34.5	3.8	0.7	0.2	/
B	5.5	29.6	26.4	27.4	6.9	2.6	1.3	0.3
C	3.7	36.4	31.1	25.2	3.3	0.3	/	/
D	3.4	15.6	16.6	32.7	15.6	7.6	5.5	3
E	6.1	39	26.9	27	1	/	/	/

It may be seen from table 4 that in the condition of subtropical high control and around subtropical high, the top heights greater than 70% convective cloud are all over height of 0℃ level. Especially under the influence of subtropical high, top heights of convective cloud of 3% are lager 15km, and for other three synoptic systems, top heights of most convective cloud are below height of 0℃ level。This shows that under the influence of subtropical high，the cloud to producing rainfall is in deed the mixed cloud or the cold cloud, and the warm convective cloud do not produce effective precipitation. As north trough of China, top heights of the cloud which produce easy rainfall are from 5 to 8km。

3.5 DEPTH OF CONVECTIVE CELL

The depth of convective cloud is an important index for seeding of artificial precipitation enhancement. In table, the depth of convective cloud in five synoptic systems is given. It can be seen from table 5 that in the around subtropical high, depth of convective clouds to be more than 85% is region of 2 and 6 km, and about 3% of the convective clouds lager 6km; in situation of north trough of China, depth of most convective clouds is less than 5km, depth from 5km to 10km account for 8.5% of the total and convective clouds with depth of over 10km only is 1.3%; under the condition of trough along the sea, the depth of convective cells are main less than 5km and the maximum depth is not more than 8km; in view of subtropical high control, convective cells with between 2km and 5km depth occupy 59% and that of more than 10km only is 7.3%; in south branch trough, depths of 92% in convective clouds less than 4km, the maximum is not lager than 5km.

Table5. Frequency (%) of convective clouds with different depths (km)

Synoptic System	≤2	≤3	≤4	≤5	≤6	≤7	≤8	≤10	> 10
A	12.4	24.4	35.8	19.3	5.3	2	0.5	0.2	0.1
B	20.3	32.6	26.4	10.9	2.8	2.9	1.5	1.3	1.3
C	17.7	38.1	33.4	9.	0.3	0.3	0.3	/	/
C	8.1	19.8	29.6	9.7	8.6	6	5.3	5.6	7.3
D	20.8	38.3	32.9	8	/	/	/	/	/

3.6 VERTICALLY INTERGRATED LIQUID WATER CONTENT OF CONVECTIVE CELL

Vertically Integrated Liquid Water Content （VIL）is a very important parameter judging convection intensity. In the condition of different synoptic system and different seasons and area, VIL values is different (table 6). From table 6, around subtropical high, VIL of convective cells of 72.9% is less than 5kg/m^2, convective cells with VIL of 6-10kg/m2 are account for 20.4%, other few convective clouds have VIL greater than 1kg/m2. For north trough of China, although maximum VIL of convective clouds are changes from 1 to 60 kg/m2, the most of them are between 1 and 5kg/m2 and it accounts for 74.6%; under the situation of trough along the sea, VIL of the most of convective clouds are 6～20 kg/m2 and occupy 71.5%; in control of subtropical high, the VIL arrive at up to 60kg/m2 and that of 7.3% is between 50 and 60kg/m2; if the south branch trough appears, maximum of VIL of convective cells do not exceed 20kg/m2, VIL of 92% is from 1 to 15kg/m2.

Table 6. Frequency(%) of convective clouds with different VIL(kg/m2）

Synoptic System	1～5	≤10	≤15	≤20	≤25	≤30	≤40	≤50	≤60
A	72.9	20.4	4.8	1.4	0.3	0.1	0.1	/	/
B	74.6	13.4	5.3	2.6	0.7	0.6	1.4	1	0.4
C	17.7	38.1	33.4	9.9	0.3	0.3	0.3	/	/
D	8.1	19.8	29.6	9.7	8.6	6	5.3	5.6	7.3
E	20.8	38.3	32.9	8	/	/	/	/	/

4. SUMMARY

According to analysis of Doppler radar productions for over 5 synoptic systems, results obtained are as follows.

In the 5 synoptic systems, convective clouds with life cycle less than 1 hour occupy 90%～95% of total. There are the most convective cells in around subtropical high. Under the condition of subtropical high, seeding tools for artificial precipitation enhancement are main Archibald and rocket ; In other synoptic systems, the airplane is generally used. In subtropical high control, radar reflectivity of convective clouds greater than 70% can reach 45～60dBz .The radar reflectivity is the lowest and less than 45dBZ in the south branch trough, and in the other synoptic system, greater 80% of them can reach 35-50dBZ. In the subtropical high, top height of convective clouds greater 70% is higher than 0℃ level. Depth of the convective cell is generally from 2km to 5km. In around subtropical high and north trough of China, VIL of most convective cells is between 1 and 5 kg/m2;and trough along sea, the VIL is generally from 6 to 20 kg/m2 and it occupy 71.5％; in subtropical high control, VIL of the most convective cells is about 50 kg/m2, and the VIL do not exceed 20 kg/m2.

REFERENCES

Cheng Qiuping, Zeng Guangping and Sui Ping， 2002：Discussion on convective cloud precipitation in summer using radar echo data . Quarterly Journal of applied Meteorology. 12(3), 339-346.

Guo yan, Yin Dongmei and Liu Dongmei， 2005: Doppler radar data analysis of “4.12”hail event in Jiangxi Province. Meteorology, 31(11), 47-51.

Jiang Niancong, Cheng Qiuping and Lu Dachun et al., 2005: Analysis on Basic characteristic of convective precipitation cloud using CINRAD radar data. Quarterly Journal of applied Meteorology,16(2), 264-266.

Zhou Yuhua, Huang Xiaoyu and Li Zhuxian， 2006: Analysis of Doppler radar echo feature of heavy rain events at the edge of west pacific subtropical high. Meteorology, 32(1),12-16

A NEW PERSPECTIVE ON DROPLET SPECTRAL BROADENING OF CUMULUS CLOUDS

Jiming Sun[1], Parisa A. Ariya [1,2], Henry G. Leighton[1] & M. K. Yau[1]

[1]Department of Atmospheric and Oceanic Sciences, and [2]Department of Chemistry McGill
University, 805 Sherbrooke St. W., Montreal, PQ, H3A 2K6, CANADA

1. SUMMARY

Temperatures and liquid water contents less than the adiabatic values associated with moist air ascending from cloud base are routinely observed in cumulus clouds. Cloud droplet spectra are also routinely observed to broader than is predicted from diffusional growth in a parcel of adiabatically ascending air. Entrainment of dry air has been considered as a way to explain these observations. However, the dynamic and kinematic structures of cumulus clouds show that entrainment cannot completely explain the spectral broadening observed near cloud top. We have developed a 1.5-D non-hydrostatic cumulus cloud model with bin-resolved microphysics to investigate the evolution of cloud spectra. Our study shows that the updraughts induced by the pressure gradient force of dynamic pressure result in new activation of cloud droplets at the cloud-clear air interface. Our finding will help clarify warm rain formation and improve understanding of atmospheric moisture cycling with respect to the Earth' s climate system.

2. BACKGROUND

The interaction between cloud dynamics and microphysical processes determines the droplet spectra in cumulus clouds. The mechanisms that are responsible for spectral broadening of cloud droplets in cumulus clouds may have an important influence on the rate of precipitation formation and on the Earth's radiation budget.

A crucial issue in cloud physics is why the observed cloud droplet spectra are broader, both on the small and large droplets sides of the spectra than those predicted by condensational growth in adiabatically ascending parcels. Collision and coalescence processes involving large cloud droplets play a key role in the initiation of warm rain. The initiation of warm rain in a short time is due to enhanced collision kernel, which may be explained by the existence of ultra-giant aerosols (diameter greater than 10 μm), cloud turbulence, and entrainment of dry air into cloud with inhomogeneous mixing. Entrainment mixing (both inhomogeneous and homogeneous mixing) alone explains small cloud droplet formation in cumulus clouds and smaller liquid water contents (LWCs) compared with adiabatic values. Although entrainment mixing can lead to the dilution of clouds and the fresh activation of cloud droplets, how entrainment is triggered remains controversial[1-5]. Furthermore, current theories cannot completely explain the spectral broadening of cloud droplets at the cloud top if we consider the dynamics and kinematics of simulated cumulus clouds[3-5].

The cloud top has been considered a key location to study the structure of cumulus clouds [1-6]. The original reason is that downdraughts originate at the cloud top [1, 2]. Since mixing of cloudy air with dry cloud-free air above the cloud top leads to evaporation of cloud droplets, evaporative cooling can result in buoyancy reversal. Therefore, it has been generally believed that evaporative cooling and buoyancy reversal play a significant role in cloud top entrainment [7, 8]. The positive feedback between buoyancy reversal and the rate of entrainment results in the formation of penetrative downdraughts which bring dry cloud-free air deep into cumulus clouds. This proposed process has a dramatic impact on the evolution of cloud droplet spectra and the vertical transport of mass in cumulus clouds. However, numerical experiments [3, 4, 9-11] and laboratory experiments [12] have suggested that buoyancy reversal due to evaporative cooling is actually an effect rather than the cause of entrainment [10, 11] and, furthermore, that buoyancy reversal has a negligible effect on the rate of mixing between cloudy air and cloud-free air [4]. Therefore, the positive feedback between buoyancy reversal and the rate of entrainment is very weak.

The instability of the cloud-environment interface, rather than buoyancy reversal, may drive cumulus entrainment [10, 11, 13-15]. Dynamical instabilities near the cloud top may be another mechanism responsible for the cloud-top entrainment [10, 11, 13, 15]. Two-dimensional anelastic, non-hydrostatic simulation shows that such entrainment occurs at the periphery of the main updraught with vortex-like structures in upper part of the cloud, leading to fresh activation of cloud droplets and multimodal cloud spectra [16]. Recently, three-dimensional numerical studies have demonstrated that vortical circulation at the cloud top results in entrainment and mixing from the sides of clouds [5, 17, 18]. However, in the above studies dry air above the cloud top become a part of clouds before the fully vortical circulations are formed [5, 16] and the multimodal cloud spectra appear at the top of the main updraught [16]. Thus, the new activation of cloud droplets at the summit of clouds with upward motion cannot be explained by the above mechanism because the trajectory of air parcels implies that the entrained dry air reaches this height after the multimodal cloud spectra occur. Furthermore, recent study showed that wind shear could also induce the entrainment mixing at the cloud top and result in multimodal of cloud spectra [6]. This result indicated that the development of cumulus clouds should be more complicated than we know.

3. HYPOTHESIS AND RESULTS

It is generally believed that entrainment and mixing are only responsible for the fresh activation of cloud droplets in cumulus clouds. Without entrainment, the cloud top air with continuous upward motion would have to come from the cloud base and have a narrow mono-modal cloud spectrum due to condensational growth. In other words, the altitudes that updraughts can reach also represent those of air parcels from the cloud base. This concept is based on the parcel theory that the air parcel is driven only by buoyancy. However, if we take into account the pressure gradient force induced by pressure perturbations in cloud parcel movement in addition to buoyancy, what will happen to the air above the cloud top? When this kind of pressure gradient force is exerted upwards on the air parcels above the cloud top, the upward movement can result in the fresh activation of cloud droplets even if there is no occurrence of the entrainment mixing. The phenomenon that small cloud droplets occur at the cloud top is consistent with observations.

The sizes of cloud droplets affect the Earth's radiation budget and onset of precipitation. Understanding the spectral broadening mechanism of cloud droplets in warm cumulus clouds against the background of cloud dynamics helps us understand how precipitation is initiated and how cumulus clouds impact the Earth's radiation budget. Therefore, we hypothesize that the spatial distribution of updraughts produced by cumulus cloud dynamics mainly determines the formation of the cumulus cloud spectra. The cause of this distribution by the pressure gradient force of dynamic pressure, one kind of the pressure gradient forces of pressure perturbations, should be considered in the evolution of cumulus cloud spectra. To diagnose the role of these dynamic effects on cloud formation, we developed a one-and-a-half-dimensional non-hydrostatic aerosol and cloud interaction model to simulate cumulus cloud formation. We have found that the fresh activation of cloud droplets at the cloud top can also be attributed to the subsaturated air parcel upward movement driven by the pressure gradient force of the dynamic pressure under no consideration of the vortex-like wind mixing and wind shear mixing. Furthermore, This finding can explain the warm rain formation in a short time without considering the impacts of ultra-giant aerosols and turbulence.

4. BIBLIOGRAPHY

1. Squires, P. Penetrative downdraughts in cumuli. *Tellus* **10**, 381-389 (1958).
2. Paluch, I. R. The entrainment mechanism in Colorado cumuli. *J. Atmos. Sci.* **36**. 2467-2478 (1979).

3. Grabowski, W. W. Cumulus entrainment, fine-scale mixing and buoyancy reversal. *Q. J. R. Meteorol. Soc.* **119**, 935-856 (1993).

4. Grabowski, W. W. Entrainment and mixing in buoyancy-reversing convection with applications to cloud-top entrainment instability. *Q. J. R. Meteorol. Soc.* **121**, 231-253 (1995).

5. Zhao, M. & Austin. P. H. Life cycle of numerically simulated shallow cumulus clouds. *J. Atmos. Sci.* **62**, 1291-1310 (2005).

6. Vaillancourt, P. A., Yau, M. K. & Grabowski W. W. Upshear and downshear evolution of cloud structure and spectral properties. *J. Atmos. Sci.* **54**, 1203-1217 (1997).

7. Reuter, G. W. A historical review of cumulus entrainment studies. *Bull. Am. Meteorol. Soc.* **67**, 151-154 (1986).

8. Blyth, A. M. Entrainment in cumulus clouds. *J. Appl. Meteorol.* **32**, 626-640 (1993).

9. Haman, K. E. and Malinowski, S. P. 'Formation of downdrafts in cumulus clouds' . Pp. 527-530 in {reprints, 9th International cloud physics conference, Tallinn (USSR) (1984).

10. Grabowski, W. W. and Clark, T. L. Cloud-environment interface instability: Rising thermal calculations in two spatial dimensions. *J. Atmos. Sci.*, **48**, 527-546 (1991).

11. Grabowski, W. W. and Clark, T. L. Cloud-environment interface instability. Part II: Extension to three spatial dimensions. *J. Atmos. Sci.* **50**, 555-573 (1993).

12. Johari, H. Mixing in thermals with and without buoyancy reversal. *J. Atmos. Sci.* **49**, 1412-1426 (1992).

13. Klaassen, G. P. & Clark, T. L. Dynamics of the cloud-environment interface and entrainment in small cumuli: Two-dimensional simulations in the absence of ambient shear. *J. Atmos. Sci.* **42**, 2621-2642 (1985).

14. Clark, T. L. Smolarkiewicz, P. K. & Hall, W. D. 'Three-dimensional cumulus entrainment studies' . Pp. 88-90 in Preprints, 10th International cloud physics conference, Bad Homburg (FRG) (1988).

15. Grabowski, W. W. & Clark, T. L. Cloud-environment interface instability. Part III : Direct influence of environmental shear. *J. Atmos. Sci.* **50**, 3821-3828 (1993).

16. Brenguier, J. E. & Grabowski, W. W. Cumulus entrainment and cloud droplet spectra: A numerical model within a two-dimensional dynamical framework. *J. Atmos. Sci.* **50**, 120-136 (1993).

17. Carpenter, R. L., Droegemeier, J. K. K. & Blyth, A. M. Entrainment and detrainment in numerically simulated cumulus congestus clouds. Part1: Geral results. *J. Atmos. Sci.* **55**, 3417-3432 (1998).

18. Carpenter, R. L., Droegemeier, J. K. K. & Blyth, A. M. Entrainment and detrainment in numerically simulated cumulus congestus clouds. Part III: Parcel analysis. *J. Atmos. Sci.* **55**, 3440-3455 (1998).

Acknowledgements

We appreciate financial support from the Natural Science and Engineering Research Council of Canada (NSERC), C-SOLAS, Centre for Climate and Global Change Research, and McGill University for the William Dawson Research Chair to PAA. We also appreciate financial support from WMO, IUGG, IAMAS and ICCP to attend ICCP2008 conference.

THE MYSTERY OF ICE MULTIPLICATION IN WARM-BASED CUMULUS CLOUDS

Jiming Sun[1], Parisa A. Ariya [1,2], Henry G. Leighton[1] & M. K. Yau[1]

[1]Department of Atmospheric and Oceanic Sciences, and [2]Department of Chemistry McGill University, 805 Sherbrooke St. W., Montreal, PQ, H3A 2K6, CANADA

1. SUMMARY

High concentrations of ice crystals exceeding those of background ice nuclei have often been observed in warm-based precipitation cumulus clouds. Laboratory experiments reveal that such ice multiplication can occur when graupel collides with cloud droplets (Hallett-Mossop mechanism). However, further studies suggested that the Hallett-Mossop mechanism is unable to account for the exceedingly high ice concentrations in some precipitating cumulus clouds. We have developed a novel 1.5-D non-hydrostatic cumulus cloud model with bin-resolved microphysics to investigate ice crystal multiplication via the Hallett-Mossop mechanism. Our study shows that the ice multiplication phenomena in warm-based cumulus clouds can indeed be explained by the Hallett-Mossop mechanism. A supercooled small raindrop band plays a central role in ice multiplication.

2. BACKGROUND

One of the outstanding unsolved problems in cloud microphysics is the rapid formation of exceptionally high ice particle concentrations in warm-based cumulus clouds (cloud base temperatures greater than 0°C) [*Hobbs and Rangno*, 1998]. Ice particle concentrations can increase from < 0.01 L^{-1} to more than 100 L^{-1} within 10 minutes at cloud top temperatures warmer than -10°C [*Hobbs and Rangno*, 1990]. The mechanism producing ice particle concentrations two or more orders of magnitude greater than typical concentrations of ice nuclei is not very well understood and it is therefore difficult to represent it in global climate models. Laboratory experiments reveal that ice multiplication occurs when graupel collides with cloud droplets [*Hallett and Mossop*, 1974; *Mossop and Hallett*, 1974]. The well-known Hallett-Mossop (H-M) mechanism requires: (1) cloud temperatures between -3 and -8°C; (2) large cloud droplets (diameters greater than 24 μm) in concentrations of more than a few drops per cm^3 [*Hobbs and Rangno*, 1998]; (3) the ratio of the concentration of droplets with diameters less than 13 μm and those with diameters greater than 24 μm to be greater than 0.1 [*Mossop*, 1985]. Although the H-M mechanism has been known for several decades, the formation of ice bursts in warm-based cumulus clouds is still a mystery [*Hobbs and Rangno*, 1998]. The main argument against the H-M mechanism is the rapid formation of ice crystal bursts. Previous studies suggest that to produce such significant ice particle concentrations through this mechanism requires a minimum of 25 minutes [*Mossop*, 1985; *Beheng*, 1987; *Mason*, 1996], although a shorter time might be required when new cumulus clouds develop from the debris of an adjacent turret [*Blyth and Latham*, 1997; *Phillips et al.*, 2002].

We argue that the previous studies did not adequately take into account the dynamics and thermal structures of cumulus clouds, or the evolution of water droplets in them. The previous studies were based on too many assumptions concerning the evolution of water droplets, such as the constant vertical profile of the updraught velocity, the constant sizes of cloud droplets as well as the unrealistic assumption of constant total water contents (liquid and ice) in rain drop formation and evolution processes [Beheng, 1998], or the role of rain droplets in the graupel formation was ignored [Mason, 1996, Mossop, 1985]. Consequently, the riming process could be largely prohibited due to the expense of cloud droplets [Beheng, 1987} or the ice splinter production was underestimated [Mason, 1996; Mossop, 1985}. The H-M mechanism is always postulated to operate in cumulus clouds as follows [*Hobbs and Rangno*, 1998]. Primary graupel particles form in the upper level of a supercooled cloud through ice crystals nucleated by primary ice nuclei. Graupel has fall speeds much larger than those of cloud droplets. These particles fall through the temperature zone between -3 and -8°C and intercept both cloud droplets greater than 24 μm and less than 13 μm diameter. During the riming process ice splinters are ejected. The ice splinters grow through water vapor deposition over a period of a few minutes to sizes where they can rime and produce more ice splinters while still in the H-M temperature zone. This process continues until conditions are inappropriate for ice-splinter production. Application of this procedure to cumulus clouds with assumed fields of dynamics and thermodynamics cannot explain the observed characteristics of ice multiplication phenomena. The salient features of observations in both maritime and continental cumulus clouds [*Hobbs and Rangno*, 1998; *Rangno and Hobbs*, 2005] may be summarized as follows. (1) The highest ice particle concentrations generally appeared within 10 minutes and the entire cloud turret head glaciated spontaneously when the cloud top resided at or near its maximum level for more than a few minutes, but ice particles were absent from newly rising cloud towers. (2) The high concentrations of ice particles occurred almost simultaneously with the appearance of frozen drizzle drops (100 to 600 μm diameter) and small raindrops (600 to 2000 μm diameter). (3) The occurrence of high ice particle concentrations was strongly correlated with the breadth of the cloud droplet spectra near the cloud top with large cloud droplets (25 μm diameter) present in concentrations of a few per cm^3. (4) Near the cloud top water drops with diameters greater than 0.1 mm were observed in concentrations of more than 1 L^{-1} or even more than 100 L^{-1} for typical cases before ice bursts and precipitation was present when the ice crystal concentration in the ice bursts was exceptionally high. (5) Cloud depth appeared to be a more important determinant of ice-crystal development than cloud-top temperature. These complicated conditions for ice multiplication processes suggest that cloud dynamics and thermodynamics as well as the evolution of water droplets play important roles. Therefore, they should be taken into account in any effort to fully understand the role of the H-M mechanism in this type of clouds. The time variation of vertical velocities, heights of the H-M temperature zone and the spatial distribution of the water drop spectra are all factors that may influence the ability of the H-M mechanism to explain the observations.

3. RESULTS

Ice multiplication in warm-based precipitation convective clouds can in fact be explained by the Hallett-Mossop mechanism. Ice initiation processes at the cloud top or in the inner cloud both can trigger the ice bursts. The concentration of IN at the temperature above -10 ^{0}C can influence the total concentration of ice particles. But this change is just significant when a concentration change of IN in orders of magnitude occurs. Our simulations indicate that supercooled precipitation sized drops play a central role in this process. The most active ice nuclei, such as bioaerosols, especially bacteria, may act as a trigger for this process through condensation, immersion and contact freezing modes. Therefore, the issue of ice multiplication can indeed be regarded as issues of warm rain initiation and ice nucleation. The large ice crystal concentrations generated in the present simulations are not necessarily limited to cumulus clouds but may also occur in large scale stratiform clouds in which supercooled raindrops form as a result of some small scale convection within them.

4. BIBLIOGRAPHY

1. Koenig, L. R. The glaciating behavior of small cumulonimbus clouds. *J. Atmos. Sci.* **20**, 27-47 (1963).

2. Mossop, S. C. Comparison between concentration of ice crystals in cloud and the concentration of ice nulei. *J. Rech. Atmos.* **3**, 119-124 (1968).

3. Hobbs, P. V., and A. L. Rangno (1998), Reply to “comments by Alan M. Blyth and John Latham on 'Cumulus glaciation papers by P. V. Hobbs and A. L. Rangno' ” . *Q. J. R. Meteorol. Soc.* **124**, 1009-1011.

4. Baker, M. (2001), Cloud phyics: Inside history on droplets. *Nature* **413**, 586-587.

5. Hobbs, P. V., and A. L. Rangno (1990), Rapid development of ice particle concentrations in small, polar maritime cumuliform clouds. *J. Atmos. Sci.* **47**, 2710-2722.

6. Hallett, J., and S. C. Mossop (1974), Production of secondary particles during the riming process. *Nature*, **249**, 26-28.

7. Mossop, S. C., and J. Hallett (1974), Ice crystal concentration in cumulus clouds: influence of the drop spectrum. *Science*, **186**, 632-634.

8. Mossop, S. C. (1985), Secondary ice particle production during rime growth: The effect of drop size distribution and rimer velocity. *Q. J. R. Meteorol. Soc.* **111**, 1113-1124.

9. Mossop, S. C. (1985), The origin and concentration of ice crystals in clouds. *Bull. Am. Meteorol. Soc.* **66**, 264-273.

10. Beheng, K. D. (1987), Microphysical properties of glaciating cumulus clouds: Comparison of measurements with a numerical simulation. *Q. J. R. Meteorol. Soc.* **113**, 1377-1382.

11. Mason, B. J. (1996), The rapid glaciation of slightly supercooled cumulus clouds. *Q. J. R. Meteorol. Soc.* **122**, 357-365.

12. Blyth, A. M., and J. Latham (1997). A multi-thermal model of cumulus glaciation via the Hallett-Mossop process. *Q. J. R. Meteorol. Soc.* **123**, 1185-1198.

13. Phillips, V. T. J., T. W. Choularton, A. M. Blyth, and J. Latham (2002), The influence of aerosol concentrations on the glaciation and precipitation of a

cumulus cloud. *Q. J. R. Meteorol. Soc.* **128**, 951-971.

14. Hallett, J., I. Robert, J. R. Sax, D. Lamb, and A. S. R. Murty (1978), Aircraft measurements of ice in Florida cumuli. *Q. J. R. Meteorol. Soc.* **104**, 631-651.

15. Mossop, S. C. (1985), Microphysical properties of supercooled cumulus clouds in which an ice particle multiplication process operated. *Q. J. R. Met. Soc.* **111**, 183-198.

16. Hobbs, P. V., and A. L. Rangno (1985), Ice particle concentrations in clouds. *J. Atmos. Sci.* **42**, 2523-2549.

17. Rangno, A. L., and P. V. Hobbs (1991), Ice particle concentrations and precipitation development in small polar maritime cumuliform clouds. *Q. J. R. Meteorol. Soc.* **117**, 207-241.

18. Blyth, A. M., and J. Latham (1993), Development of ice and precipitation on New Mexican summer time cumulus clouds. *Q. J. R. Meteorol. Soc.* **123**, 1185-1198.

19. Rangno A. L., and P. V. Hobbs (2005), Microstructures and precipitation development in cumulus and small cumulonimbus clouds over the warm pool of the tropical Pacific Ocean. *Q. J. R. Meteorol. Soc.* **131**, 639-673.

20. Mossop, S. C. (1976), Production of secondary ice particles during the growth of graupel by riming. *Q. J. R. Meteorol. Soc.* **102**, 45-57.

21. Mossop, S. C. (1978), The influence of drop size distribution on the production of secondary ice particles during graupel growth. *Q. J. R. Meteorol. Soc.* **102**, 45-57.

22. Mossop, S. C. (1978), Some factors governing ice particle multiplication in cumulus clouds. *J. Atmos. Sci.* **35**, 2033-2037.

Acknowledgements

We appreciate financial support from the Natural Science and Engineering Research Council of Canada (NSERC), C-SOLAS, Centre for Climate and Global Change Research, and McGill University for the William Dawson Research Chair to PAA. We also appreciate financial support from WMO, IUGG, IAMAS and ICCP to attend ICCP2008 conference.

RESEARCH ON INTERACTION OF MICROPHYSICAL AND ELECTRIC PROCESSES IN CUMULUS CLOUDS: NUMERIC SIMULATION.

Kortchagina Elena, Shapovalov Alexander
High-mountainous Geophysical Institute of Roshydromet, Nalchik, Russia
helena.a.k@km.ru

1. INTRODUCTION

Last years many works are devoted to development of numerical models of convective clouds. Contemporary models reproduce thermodynamic, microphysical and electric structure of a cloud. However, the influence of electric characteristics of a cloud on its microstructure formation is seldom taken into account in models. In the present study research of influence of electric characteristics of a cloud on process of precipitations formation is presented. Research was spent by means of the two-dimensional version of convective cloud numerical model, developed in High-mountainous geophysical institute.

2. MODEL DESCRIPTION

The model consists of three blocks: thermodynamic, microphysical and electric.

Thermodynamics described with equations of moist convection.

The model uses a detailed description of microphysics. That enables to consider influence of an electric field of a cloud on process of coagulation without parametrization. As is known, the collision factor for cloud particles depends on their sizes, charge and an external electric field. Magnitudes of collision factor for cloud particles which have the close sizes are taken from experimental and theoretical researches by *N.V. Krasnogorskaya (1965).* For particles of greatly differing sizes - from works of *L.M Levin* (1961).

The electric part of the model consist of the equations for noninductive charge separation, concentration of small ions, Poisson's equation and equation for electric field vector.

More detailed description of the model can be found in (Kortchagina et al. 2004)

Numerical simulations were spent for a summer cloud on the basis of atmospheric sounding in the "Mineral Waters" airport (Northern Caucasus). The dependence of coagulation rate of cloud drops on an external electric field was investigated. Numerical simulations of development of a cumulus cloud were provided in two modes: without and with taking into account microphysics dependence on electric field of a cloud. In the latter case acceleration of precipitation formation is observed

3. SUMMARY

The results of the simulations shows that at calculation of thermodynamic, microphysical and electric structure of cumulus clouds influence of its electric field on its microphysics should not be neglect.

From the other hand, electrization mechanisms depend on characteristics of a cloud particles spectrum (the positive feedback is observed). It is obvious, that both at qualitative, and at the quantitative analysis of the contribution of various electrization mechanisms in formation of an electric field of a cloud it is necessary to consider mutual influence of these structures.

BIBLIOGRAPHY

Kortchagina E.A., Shapovalov A.V. The numerical research of interaction of microphysical and electrical processes in convective clouds at their evolution. Proceedings of institutes of higher education. North Caucasus. Natural Sciences. № 3, pp. 56-62. 2004

Krasnogorskaya N.V. The electric forces influence on the coalescence of particles of close sizes. IAS USSR, Physics of the atmosphere and ocean, V.I, pp. 339-345, 1965

Levin L.M. The Electrical coagulation of cloud particles. Proceedings of Elbrus high-mountainous expedition. V.2, pp.5-42, 1961.

ACKNOWLEDGMENTS

This work is provided with support of RFBR, grant № 06-05-96646.

EVALUATION OF PRECIPITATION CHARACTERISTICS OBSERVED IN PANAMA DURING TC4

Paul A. Kucera(1), Andrew J. Newman(1,2), and John C. Gerlach(3)
(1)National Center for Atmospheric Research/Research Applications Laboratory, P.O. Box 3000, Boulder, CO, 80307, USA, pkucera@ucar.edu
(2) Colorado State University, Department of Atmospheric Science, Fort Collins, CO, USA, anewman@atmos.colostate.edu
(3) National Aeronautical Space Administration, Goddard Space Flight Center, Greenbelt, MD, USA, john.c.gerlach@nasa.gov

1. Introduction

During July and August 2007, NASA sponsored a field campaign called Tropical Composition, Cloud and Climate Coupling (TC4) experiment. The experiment was centered on the countries of Costa Rica and Panama. One of the goals of TC4 was to better understand the relationship between convection and associated anvil generation. A variety of instruments were deployed during TC4 to sample the atmosphere in this region. One of the instruments was the NASA 10-cm polarimetric Doppler weather radar (NPOL). NPOL measurements along with data from a high resolution rain gauge network that was deployed in southern Panama during TC4 was used to characterize the convection in this study.

A variety of events were observed during TC4. Events ranged from short-lived unorganized convection to long-lived mesoscale convective systems (MCSs). It was observed that systems often developed over the Gulf of Panama in the late evening, but often weakened or dissipated before reaching land in the mid-morning hours. However, as result of strong diurnal heating, a second maximum in convection was often observed over the mountainous regions of Panama during midday.

The study provides an overview of the observed convection, which includes storm area, vertical structure, evolution, diurnal variability, and spatial distribution of the events. A description of the instrumentation is provided in the next section. The methodology is discussed in Section 3. Section 4 highlights the results and Section 5 presents a summary and future direction for this research.

2. Data

NPOL operated almost continuously between 16 July and 12 August 2007. The only data gap was between 18 UTC 19 July and 02 UTC 21 July. As result, nearly 3500 volume scans are available for studying the convective properties in Panama. NPOL was located at a latitude of 7° 45’ 13.32” N and longitude of 80° 15’ 9.84” W. The site was located near the city of Las Tablas in the southern peninsula of Panama along the eastern coast (see Fig. 1). A picture of NPOL deployed during TC4 is shown in Fig. 2.

NPOL scanned with a temporal resolution of 10 min and spatial resolution of 200 m. A scanning strategy of a 12 tilt, ranging from 0.7° to 23.3°, volume scan with a maximum range of 150 km was followed by a long range surveillance scan out to maximum range of 275 km. NPOL observables included radar reflectivity, Doppler velocity, spectral width and variety of polarimetric variables including differential reflectivity, differential phase, specific differential phase and correlation. However, initial analysis indicates the polarimetric fields were noisy; hence there were not included in this study. An evaluation of the reflectivity calibration indicated that a +3.6 dB correction was required.

Rain gauge observations were collected from high resolution MetOne tipping bucket rain gauges. A total of ten sites (one site located at NPOL) were deployed (see Fig. 1 for locations). The sites were chosen to capture the variability of precipitation observed in the mountain, inland, and coastal regimes. Also, they were placed at a variety of distances from NPOL to provide range dependent reference for the NPOL rainfall estimates. The rain gauges were deployed in pairs to ensure data quality, Problems with single rain gauge measurements are often difficult to detect. An example rain gauge site deployed during TC4 is shown in Fig. 3.

Fig. 1: A map showing the location of NPOL and the deployed rain gauge network during TC4. NPOL is indicated by a star and the rain gauge locations are indicated by plus symbols.

Fig. 2: A picture of NPOL deployed near Las Tablas, Panama during TC4.

3. Methodology

Radar data were processed into a variety of products including diurnal cycle of echo frequency, echo area, etc. A quality control program was run on the radar data using all available fields to determine and remove and spurious echo (i.e., ground clutter, second trip echo, etc). The data were then transformed onto a 2 km (horizontal and vertical) resolution Cartesian grid. These Cartesian products were used to produce Figs. 6-8 and Figs. 12-13. Figure 5 was produced directly from the quality controlled volume scan files.

Rain gauge data were compared between the two gauges at each site. Any discrepancies between gauges were highlighted and only gauges determined to be properly operating were used in this analysis.

Fig. 3: An example rain gauge site (TC4_Gauge1) deployed during TC4. A dual rain gauge network was deployed to improve data quality.

4. Results and Discussion

The results are shown in the following figures. A typical day of convection is shown in Fig. 4. An area of convection was located over the Gulf of Panama at 12 UTC (7 am local time) on 09 Aug. As can be seen from Fig. 8, this corresponds to near the time of maximum echo frequency over the gulf for the entirety of the campaign.

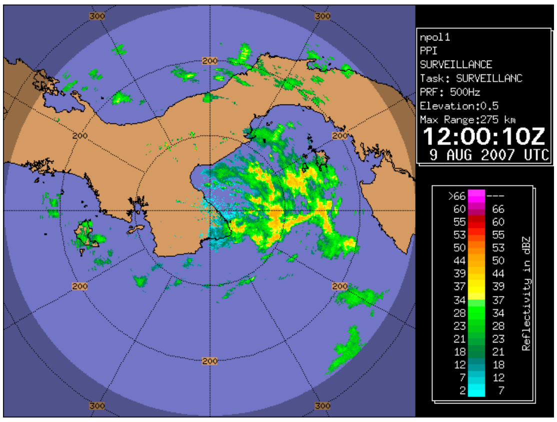

Fig. 4: A typical observation of convection developing in the Gulf of Panama. This particular example was observed at 12 UTC 09 August 2007.

Figure 5 presents a time series of fractional echo area for thresholds of 10 and 40 dBZ (times 10) during the field campaign. This plot indicates that convection was present nearly every day of the project with several days having a large organized convective event with maximum echo coverage of approximately 35-45 percent of the NPOL domain at minimum echo threshold of 10 dBZ. Figures 6 and 7 display the frequency of reflectivity for thresholds ≥ 10 and 40 dBZ, respectively, over the NPOL domain (maximum range of 150 km). Figure 6 shows there is a maximum of occurrence over the gulf to the east of NPOL with the observation of reflectivity ≥ 10 dBZ occurring in 16-18 percent of the scans. Some beam blockage occurred to the SW of NPOL, resulting in a lack of echo occurrences in that area.

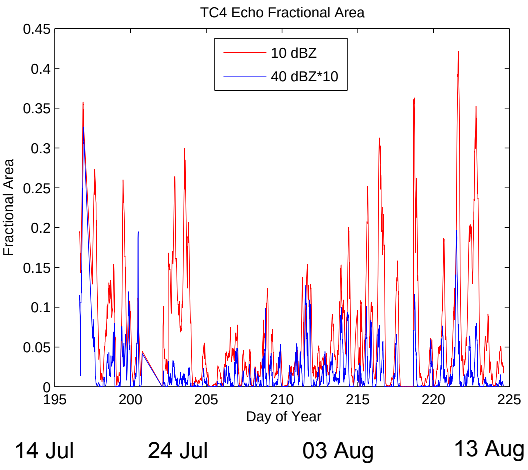

Fig 5: Time series of echo area.

There appears to be a minimum in echo occurrence to the north of NPOL, which corresponds to the relative flat region between the northern mountains and the higher terrain along the southern coast of Panama. The 40 dBZ maximum (Fig. 7) over the far Eastern gulf with less frequent intense echo to the west indicates a weakening trend towards the western extent. Also, a secondary maximum in more intense echo can be seen over the elevated terrain in northern Panama, which can be seen as southwest to northeast line north of NPOL. Correspondingly, Fig. 8 shows the maximum time of occurrence of echo ≥ 10 dBZ over the elevated terrain is near and slightly after local noon while the maximum over the gulf is in the early morning hours. This corresponds well to the satellite observed and modeled convective trends in papers by Mapes et al. (2003a,b).

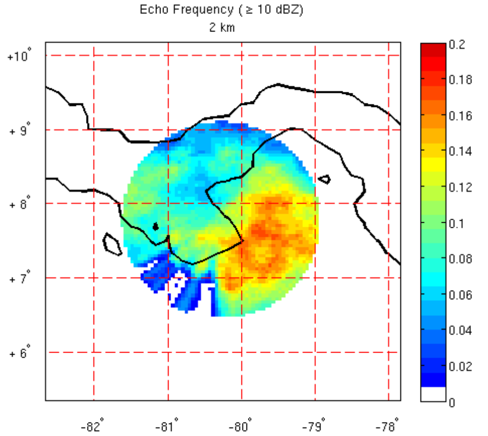

Fig 6: Distribution of echo frequency for reflectivity ≥10 dBZ at height of 2 km above ground.

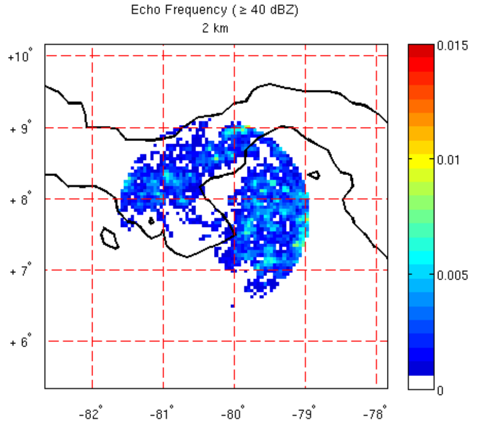

Fig 7: Same as Fig. 6 except for reflectivity ≥40 dBZ.

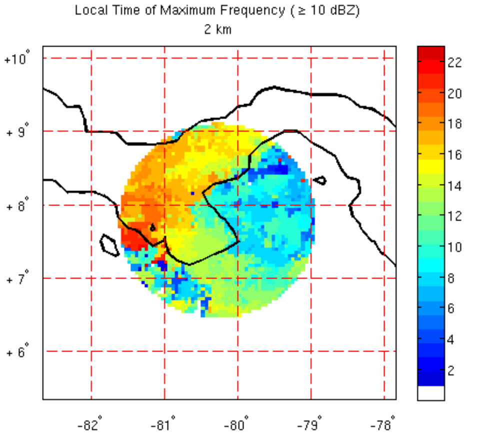

Fig. 8: Diurnal cycle of echo frequency in local time.

Gauge analysis from two gauges in the elevated terrain (Figures 9 and 10) shows a late morning and slightly after local noon maximum in precipitation. Figure 9 shows the diurnal cycle for rainfall observed at site TC4_Gauge5. The diurnal cycle shown in Fig. 10 corresponds to a rain gauge located at site TC4_Gauge8. The diurnal cycle plot in Fig. 11 corresponds to a rain gauge located at NPOL (TC4_Gauge1). The diurnal cycle near the coast indicates an early morning maximum, which is similar to what is observed over the ocean. Overall, the rainfall maxima observed by the rain gauges correspond well with the radar observed time of maximum occurrence of echo ≥ 10 dBZ.

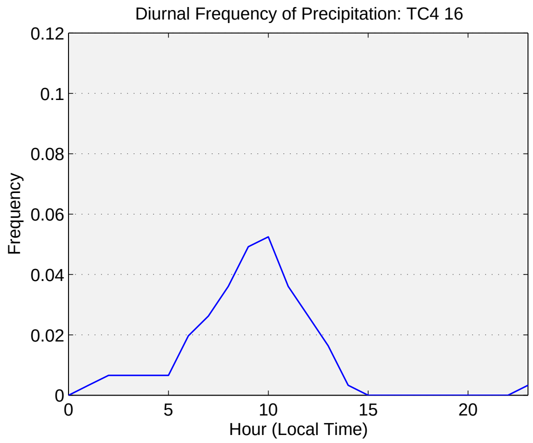

Fig 9: Diurnal cycle of precipitation observed from rain gauge site TC4_Gauge5 (see Fig. 1 for location).

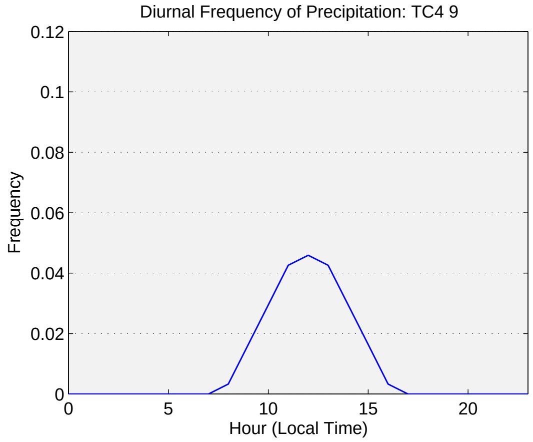

Fig. 10: Same as Fig. 9 except for rain gauge site: TC4_Gauge8.

Constant frequency altitude diagrams (CFAD) were produced over all scans in the 09-10 LT and 19-20 LT hours. The results are displayed in Figs. 12-13. From this analysis, the results indicate a slight increase in intensity in the 09-10 LT CFAD compared to the later time period. However, the mean reflectivity above 8 km is larger for the 19-20 LT time period. There are also more occurrences of ≥ 40 dBZ in the 19-20 LT time period. This makes physical sense as the 19-20 hour is near or shortly after the maximum intensity of the afternoon mountain convection. The 09-10 LT time period is near the convective minimum, which corresponds to the dissipation stage of the overnight convection. However, these differences are slight and may relate to the fact that all areas were used; there was no separation between land and ocean in this analysis.

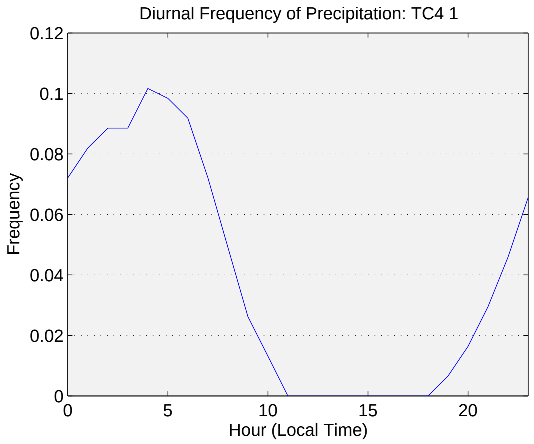

Fig. 11: Same as Fig. 9 except for rain gauge site: TC4_Gauge1.

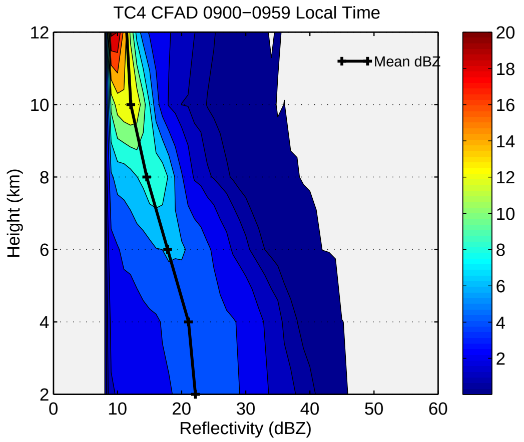

Fig 12: CFAD analysis over all areas for 09-10 LT time period.

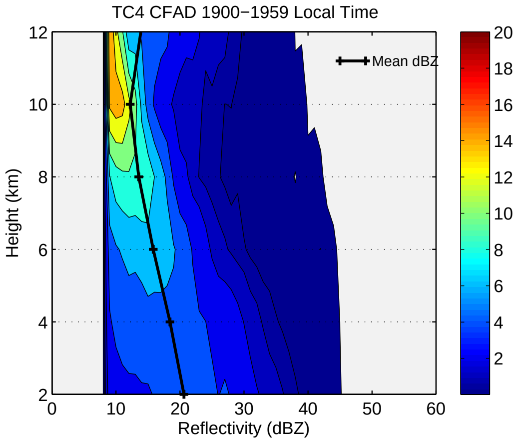

Fig 13: Same as Fig. 12 except for the 19-20 LT time period.

5. Conclusions and Future Analysis

The results of study show that the greatest occurrence of convection was observed over the Gulf of Panama. A secondary maximum occurred over the mountains. An interesting feature of a local minimum was observed near the coast. Diurnal cycle analysis indicated an early morning maximum over the Gulf with an afternoon maximum over the mountains. CFAD analysis included that vertical structure was nearly the same for evening and morning with slightly more deep convection in late afternoon.

Future analysis will examine the generation of cirrus anvils as result of the convective activity. Also, we plan to use a mesoscale model to better understand the convective distribution. Segregation of coast, land and ocean pixels will also be done and then CFAD analysis will be redone to examine the differences in vertical structure between the different regions. We would also like to understand the observed minimum of precipitation near the coast.

6. References

Mapes, B. E., T. T. Warner, M. Xu, and A. J. Negri, 2003a: Diurnal Patterns of Rainfall in Northwestern South America. Part I: Observations and Context. *Mon. Wea. Rev.*, **131**, 799–812.

Mapes, B. E., T. T. Warner, M. Xu, 2003b: Diurnal Patterns of Rainfall in Northwestern South America. Part III: Diurnal Gravity Waves and Nocturnal Convection Offshore. *Mon. Wea. Rev.*, **131**, 830-844.

Acknowledgements

This work was supported by the NASA Grant: NNX07AL11G.

A NUMERICAL STUDY OF TROPICAL DEEP CONVECTION AND THE SENSITIVITY TO PBL PARAMETERIZATIONS

Jiapeng Li   Yan Yin
Key Laboratory of Atmospheric Physics and Environment
Nanjing University of Information Science & Technology, Nanjing, China

1. INTRODUCTION

Tropical deep convective (TDC hereafter) systems provide the primary mechanism whereby solar heating of the ocean is moved upward into the free troposphere where it can be transported poleward and eventually emitted to space. In the process, these great engines of the global climate produce precipitation and drive the global-scale circulation. TDC is the source of water vapor for the upper troposphere in the tropics. This upper-tropospheric humidity plays an important role in maintaining the natural greenhouse effect in the atmosphere and also has an important diurnal variation.

In order to understand the forming mechanism, a typical kind of TDC named Hector that developed regularly over the Tiwi islands (130.8°E, 11.6°S), which are located at the northwest of Australia, during the transition seasons (Nov.-Dec. and Feb.-Mar.) have been studied using observational data and models. The Island Thunderstorm Experiment (ITEX) [1] and the Maritime Continent Thunderstorm Experiment (MCTEX) [2] are two such field campaigns conducted in 1988 and 1995, respectively, in this region. These experiments presented the structure of convection over the Tiwi islands and gave an idea of the functional relationship between convective strength and other external parameters. Keenan et al. [3] classified the process of the convection observed during ITEX into three phases: the initial cells, merger and rapid growth phase, and the mature squall line phase. After analyzing the data from MCTEX, Carbone et al. [2] proposed a model to describe two different modes of the forming processes of the TDC over Tiwi islands.

Besides of these field experiments, some numerical simulations have also been carried out. Golding et al.[4] utilized a mesoscale model established by Met. Office of U. K. to simulate two cases observed during the ITEX field experiment. Although their results showed the development of the TDC over the Tiwi islands, but the 3 km resolution they used was not fine enough to resolve the clouds and the use of a single point sounding data, instead of the real external forcing and lateral boundary condition, also limited the ability of their model.

Saito et al.[5] used the Japanese Meteorological Research Institute mesoscale model (MRI NHM) with 1km resolution to simulate a case from MCTEX. This study showed a good agreement between the simulation and observed evolution of the TDC over the Tiwi islands. The sensitivity experiments to land scale and orographic effects showed that the intensity of TDC was not only determined by the stability of the atmosphere but also significantly impacted by the island-scale circulations. Although this work revealed several interesting characteristics of TDC, the model failed to simulate properly the timing of the cloud merger process and the location of the TDC.

Based on the studies above, Crook[6] used linear and nonlinear models to examine the development of TDC over the Tiwi islands. The sensitivities of the convective strength to wind speed and direction, and low-level moisture showed that the strength of convection increases when the wind speed decreases and the wind direction turns toward the major axis of the islands, and that the low-level moisture was an important predictor of convective development.

As has been noticed above, simulations of the TDC using real time data are rare, so numerical prediction of TDC is still proved to be challenging. Here we expect to find a mesoscale model using real time data to represent the TDC over the Tiwi islands with high horizontal resolution and to test whether the problems encountered in previous studies can be solved using this new model system. Meanwhile, the development of the TDC is influenced by the land-sea breeze, orographic distribution, low-level moisture and surface flux etc.[5] [6] which are closely related to the planetary boundary layer (PBL). It is therefore necessary to find an appropriate PBL parameterization to resolve the TDC before simulating it using a mesoscale model. Some experiments according to PBL parameterizations have been conducted before using some popular mesoscale models. Braun and Tao[7] studied sensitivity of hurricane to different PBL parameterizations, significant sensitivity was presented in the simulation and suggested that accurate forecasts of precipitation in hurricanes can be just as sensitivity to the formulation of the PBL as they are to the cloud microphysical parameterizations. Berg and Zhong [8] compared the results simulated by MM5 model using BK, MRF and GS PBL schemes to the observed datasets. Bright and Mullen[9] did sensitivity experiments of the southwest monsoon boundary layer to PBL schemes and Mao et al.[10] carried out experiments on MM5-CMAQ sensitivity to various PBL schemes. The above three studies proposed similar results that the various PBL schemes did not appreciably affected the model performance and PBL features also these works are all focused on mid-latitude but not tropical area. Srinivas et al. [11] gave an experiment of land-sea breeze to PBL schemes at tropical area in India and presented that all the schemes shown similar ability in simulating the boundary layer temperature, humidity and winds and the land-sea breeze could be simulated by all the schemes. These works above all based on MM5 model gave similar outcome that there is little improvement in overall accuracy of predictions with more complex PBL schemes and just cared about these PBL characteristics but did not consider the impact to the convection. Besides, an experiment using the new generation mesoscale model WRF (Weather Research and Forecast) was conducted by Jankov et al.[12] but this work was studied different physical parameterizations and their interactions on warm season MCS rainfall. However, studies using the WRF model with high horizontal resolution real-case run are rare. So this study will focus on the impact of different PBL parameterizations on the intensity of the TDC over Tiwi island in high resolution real-case simulation using WRF model, and expecting to find a most appropriate scheme to resolve the TDC and fix some problems presented by previous work [5]. The experiment setting will present in section 2, the analysis of results will be given in section 3 and the summary will present in section 4.

2. EXPERIMENT DESCRIPTION

In this experiment, we simulated TDC case happened in 16 Nov. 2005 using the up to date version WRF model v2.1.2. The initial and boundary conditions are provided by the NCEP 1°×1°final analysis data. The details of experiment setting are shown in table 1.

TABLE 1 Details of the grids and the physics options used in the WRF model

Dynamics	Vertical resolutions	Horizontal resolutions	Radiation schemes	PBL schemes	Microphysics scheme
Primitive equation, non-hydrostatic	40 sigma levels	9km 3km 1km	Dudhia scheme for short-wave, RRTM scheme for long-wave	YSU MYJ MRF	Purdue Lin scheme

For checking the effect of the different PBL scheme in simulating TDC in WRF model, the observed radar reflectivity datum from the international project ACTIVE

(Aerosol and Chemical Transport In Tropical Convection) cooperated by the UK, Canada, Australia etc. will be used to have a comparison with the simulated outcomes.

3. RESULTS

A. Intensity of the TDC

The cross section of the strongest convection is given by fig 1c. From the observed radar echo, we found the strongest convection happened at -45km in west-east direction, 0km in south-north direction. The top of reflectivity reached the height of 17km and the area greater than 45dBz exceeded 11km (fig 1d). The horizontal range of reflectivity spread almost 30km wide. All the simulated convections were located at the middle area of the island in south-north direction, this characteristic is similar to the observed results, but the position of convections using three schemes all have deflections in west-east direction compare with the observed fact and the departure using three schemes are 9km (MRF), 19km (YSU), 17km (MYJ) respectively. Here we are more care about the intensity of convection, so from this aspect we find that the reflectivity using MYJ (fig 1c) scheme is the most similar to the reality, the top of reflectivity reached about 17km and the area greater than 45dBz exceeded 12km, but the wide spread of reflectivity is significant smaller than the observed. The convection simulated by the YSU (fig 1b) scheme is stronger than by the MRF (fig 1a) scheme, but these two are distinct smaller than the reality. So for this aspect of convection intensity, the MYJ scheme behaved a significant advantage compare to the other two schemes.

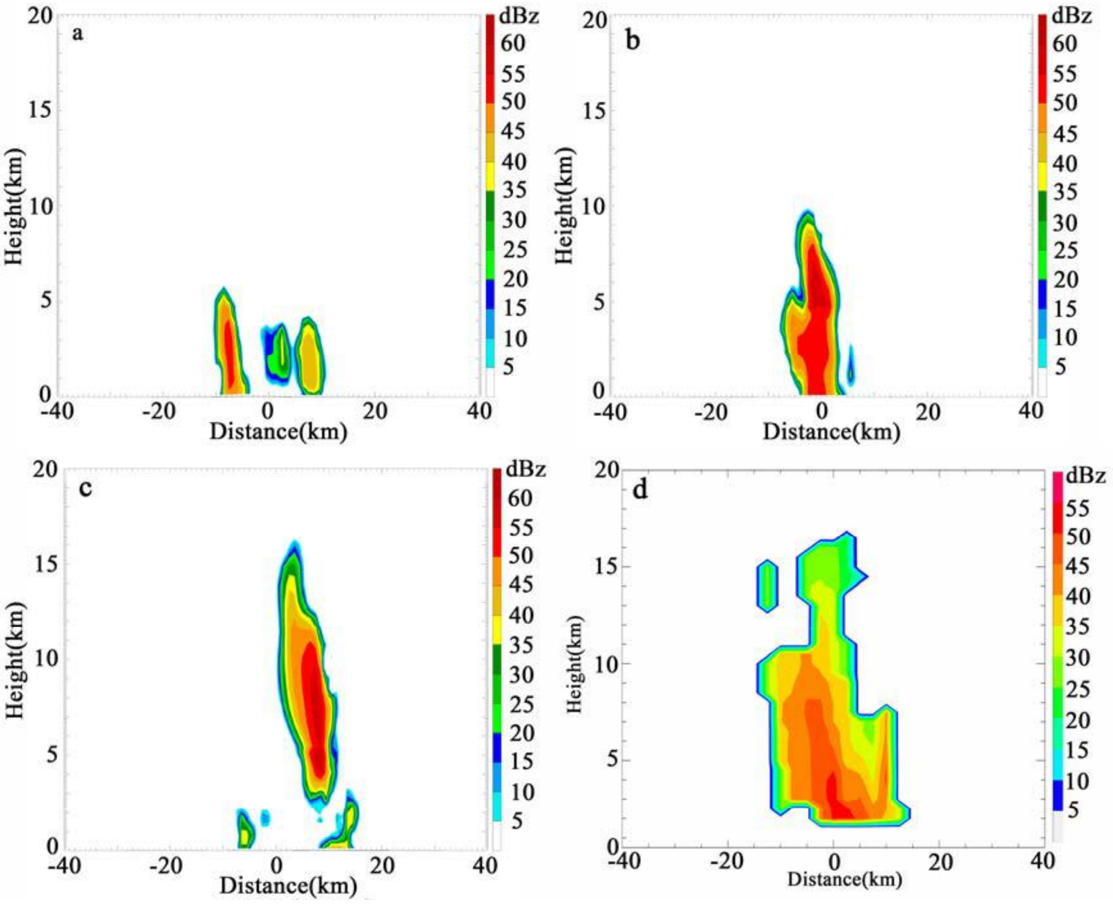

Figure 1.Cross section of Strongest radar echo simulated using different PBL schemes (a: MRF, b: YSU, c: MYJ) and observation (d) in south-north direction range from -40km to 40km

B. Vertical velocity

Vertical velocity is an important aspect in impacting the intensity of the TDC, and the comparisons of time evolution of max vertical velocity using three schemes is shown in Fig 2. We can find the max vertical velocity using MYJ scheme is the most powerful during the all daytime and the land area averaged vertical velocity (the figure is omitted) indicated the MYJ scheme made the strongest vertical motion after about 11:00LST. Besides, the MRF scheme made the smallest value in both max and averaged vertical velocity. The phenomena indicate that the PBL scheme makes a distinct influence of vertical motion and the convection intensity. This phenomena indicates that the PBL parameterization process can make great impact on the vertical velocity then the intensity of the convections.

C. PBL height and surface flux

The development and intensity of convection over the Tiwi island is greatly impacted by low-level moisture and surface flux etc.[6], so the difference of these characteristic simulated by various PBL schemes are critical to the ability of representing the intensity of convections. The time evolution of the maximum PBL height simulated using different schemes are shown in Fig 3. The max value of PBL height using MYJ scheme is the highest than the others, but the land area averaged (fig omitted) PBL height is smaller than the MRF scheme in most of the daytime. These phenomena indicate that the intensity of turbulence motion using MRF scheme is more symmetrical in the whole land area than the one using MYJ scheme, and this is why the MRF scheme made many small similar convection during the daytime but the MYJ and YSU schemes made stronger convection but had fewer amounts. The HFX (surface heat flux) and MFX (surface moisture flux) indicate similar feature to the PBL. The result using MYJ scheme provides the strongest surface heat and moisture flux all the time, the sufficient supply of heat and moisture from the low-level produces the strongest convection. All the characteristics above show that the outcome which is simulated by MYJ scheme has a more asymmetrical distributing of energy provided by PBL than the other two schemes. This feature made the surface heat and moisture flux using MYJ scheme give the strongest value all through the daytime and these also give a reasonable explanation of different intensity of convection simulated by diverse PBL schemes. The discussion also gives support of the point proposed by Crook [6] that the surface flux seriously influences the development of the convection over Tiwi island.

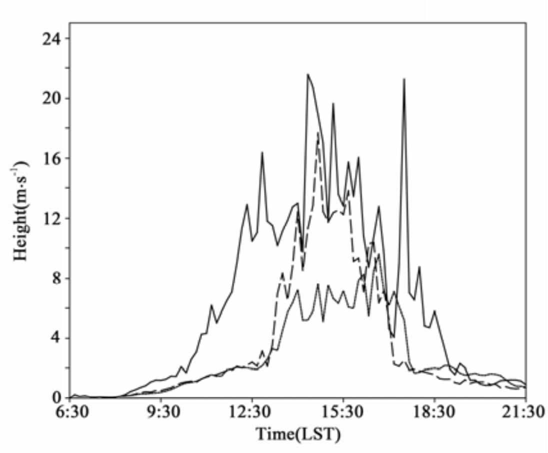

Figure 2.Time evolution of comparisons of max vertical velocity simulated using different schemes. (MRF: short dash, YSU: long dash, MYJ: solid)

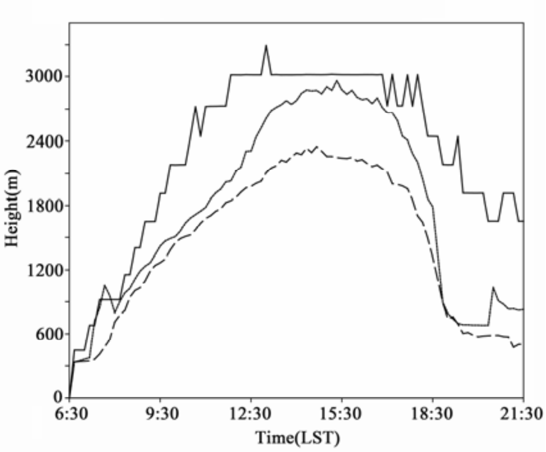

Figure 3.Time evolution of comparisons of max height of PBL simulated by different schemes. (MRF: short dash, YSU: long dash, MYJ: solid)

Considered all the features, the more complex MYJ scheme with a prognostic equation for TKE plays a distinct advantage in reproduce a similar TDC to the observed reality. The analysis of vertical velocity, PBL height, HFX and MFX give a reasonable explanation to the advantage. But lacks of position and time of convection appearance and the wide spread of convection are exposed by all the simulations.

4. CONCLUSIONS

All the schemes play similar skill in represented the land-sea breeze circulation process, but the MYJ scheme produced a relatively stronger circulation compared to the MRF and YSU schemes which produced similar results. Meanwhile, the results using MYJ scheme indicates relatively significant process of the interaction of sea breeze front and gust front which MRF and YSU do not present clearly. For the simulation of intensity of convection, the MYJ scheme show significant advantages compared to the other two schemes, the results simulated by the MYJ scheme is closest to the observations.

The analysis of vertical velocity, PBL height, surface heat and moisture flux gives a reasonable verification of different intensity of convection using various PBL schemes and indicates that the surface flux greatly impact the development of the TDC. The MYJ scheme presented the most powerful vertical velocity, surface heat and moisture flux all through the daytime corresponding to the strongest convection which is the most similar to the observed. This experiment suggests that in simulating deep convection in tropical regions the utilization of complex turbulence parameterization of MYJ scheme plays a relative well capacity to represent the intensity, but all these three schemes exposed drawbacks in simulating the position, time and horizontal spread of the appearance of convection and the above results suggest that more work should be carried out to solve existing problems and improve accuracy of resolving using mesoscale model.

5. BIBLIOGRAPHY

[1] Skinner, T., and N. Tapper, “Preliminary sea breeze studies over Bathurst and Melville Islands, Northern Australia, sa part of the Island Thunderstorm Experiment (ITEX),” Meteor. Atmos. Phy., 53, pp. 77-94. 1994.

[2] Carbone, R. E., J. W. Wilson, T. D. Keenan, and J. M. Hacker, “Tropical island convection in the absence of significant topography. Part I: Life cycle of diurnally forced convection,” Mon. Wea. Rev., 128, pp, 3459-3480. 2000.

[3] Keenan, T. D., B. Ferrier, and J. Simpson, “Development and structure of a maritime continent thunderstorm,” Meteor. Atmos. Phy., 53, 185-222, 1994a.

[4] Golding, B. W., “A numerical investigation of tropical island thunderstorms.” Mon. Wea. Rev., 121, pp, 1417-1433, 1993.

[5] Saito, K., Keenan, T., Holland, G., and Puri, K., “Numerical simulation of the diurnal evolution of tropical island convection over the maritime continent,” Mon. Wea. Rev., 129, pp,237-400, 2001.

[6] Crook, N. A., “Understanding Hector: the dynamics of island thunderstorms,” Mon. Wea. Rev., 129, pp, 1550-1563, 2001.

[7] Braun, S. A., and W. Tao, “Sensitivity of high-resolution simulations of hurricane Bob (1991) to planetary boundary layer parameterizations,” Mon. Wea. Rev., 128, pp, 3941-3961, 2000.

[8] Berg, L. K., and S. Zhong, “Sensitivity of MM5-simulated boundary layer characteristics to turbulence parameterizations,” J. Appl. Meteor., 44, pp, 1467-1483, 2005.

[9] Bright, D. R., and S. R. “Mullen, The sensitivity of the numerical simulation of the southwest monsoon boundary layer to the choice of PBL turbulence parameterization in MM5,” Wea. Forecasting, 17, pp, 99-114, 2002.

[10] Mao, Q., L. L. Gautney, T. M. Cook, M. E. Jacobs, S. N. Smith, and J. J. Kelsoe, “Numerical experiments on MM5–CMAQ sensitivity to various PBL schemes. Atmos. Environ.,” 40, pp, 3092-3110, 2006.

[11] Srinivas, C. V., R. Venkatesan, and A. Bagavath Singh, “Sensitivity of mesoscale simulations of land–sea breeze to boundary layer turbulence parameterization,” Atmos. Environ., 41, pp, 2534-2548, 2007.

[12] Jankov, I., W. A. Gallus Jr., M. Segal, B. Shaw, and S. E. Koch, “The impact of different WRF model physical parameterizations and their interactions on warm season MCS rainfall,” Wea Forecasting, 20, pp, 1048-1060, 2005.

SATELLITE RETRIEVAL OF A STRONG HAILSTORM PROCESSES

Liu Guihua[1] Yu Xing[2] Dai Jin[2] Daniel Rosenfeld[3]
[1] Weather Modification Center of Shaanxi Province, Xi`an, China
[2]Meteorological Institute of Shaanxi Province, Xi`an, China
[3]Institute of Earth Sciences, The Hebrew University of Jerusalem, Israel

1. INTRODUCTION

The cloud microphysical properties, such as the temperature, the composition and phase of cloud, and the effective radii, can be retrieved by satellite multiple spectral data.

With the polar-orbit satellite retrieval methodologies and software developed by D. Rosenfeld, taking the hailstorm as an example occurred in the Northwestern part of China on 24 June 2006, the cloud effective radii (Re) at the cloud top were retrieved. The cloud microphysical properties were vividly presented by RGB visual multispectral classification scheme. The microphysical zones of clouds were inferred by the cloud top temperature (T) versus Re relation for convective clouds, combing the surface observations and synoptic situation, the micro- and macro-physical properties and the precipitation process of this hail were analyzed.

2. SYNOPTIC SITUATION

On the Eurasian synoptic map of 500 hPa, the cold air influenced by the Mongolia depression, moved southward along the northwest current. Strong regional precipitation and hail occurred at the northwest in the afternoon. The diameter of hail was about 15 mm with the maximum of 30 mm in the northern part of Shaanxi Province.

3. MULTIPLE SPECTRAL IMAGE

Composite image of RGB visual multispectral classification scheme can reflect the cloud microstructures. Figure 1 was the one from NOAA-18 satellite on 07:13 UTC June 24 2006. The color of convective clouds was red, which suggest that the large particles absorb strongly at the 3.7μm. Some small cell in the yellow indicated that the cloud top temperature was rather higher and the particle size was smaller. While the in the cloud top temperature was rather lower and the particle size was smaller in the orange area.

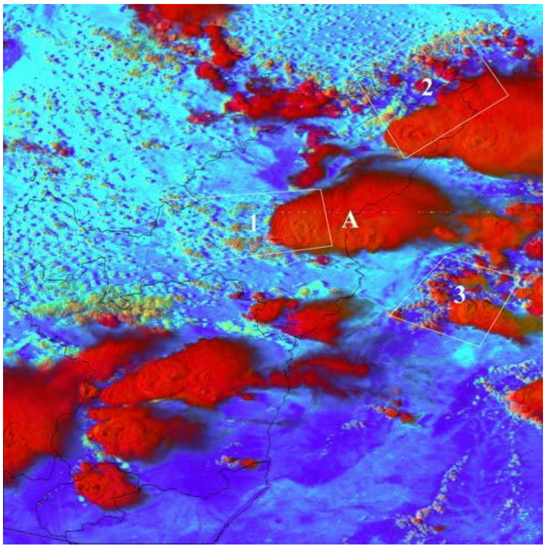

Fig. 1 RGB composite image from NOAA-16 satellite on 07:13 LST June 24 2006 of 0.6 μm reflectance (red), 3.7 μm reflectance (green) and 10.8 μm brightness temperature (blue), the numbered areas framed with white are the study areas.

4. MICROPHYSICAL PROCESS OF CLOUDS

Based on the cloud top temperature (T) versus Re relation (Fig. 2), the microphysical process and microstructure can be revealed. The analyses show that: (1) At the start of convective formation, effective radius is rather small, about 10μm, which suggest that there existed CCN in the low level. (2) There existed a deep zone of diffusional droplet growth, and the growth of particle was slow maybe firstly due to the coalescence of small drops in the low level leading to the insufficient conversion between ice and water, and secondly due to the uplift which cause small cloud drops were brought to higher level before they grew to large. (3) The glaciation temperature was low, about -30°C. The low glaciation temperature suggested that the zone of super cooled water was deep, which supplied suitable environments for hail growth. (4) There existed obvious small ice particles on the cloud tops, which suggested that the strong uplift made the clouds develop to the level of -40℃, where the super-cooled cloud droplets freeze to form plentiful ice particles via homogeneous nucleation.. All those suggested that the super cooled water was rich, exceeded amount needed in the ice phase growth, and therefore were lifted to the cloud top by the uplift. (5) there did not exist the zones of droplet coalescence growth and rainout, which were may due to the strong uplift in the low level brought the particles grown insufficiently in the zone of diffusional droplet growth, to the zone of mixed phase.

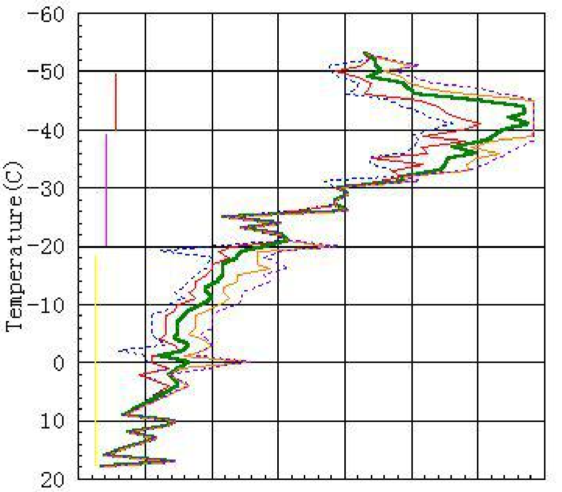

Fig. 2 Temperature(T) versus R_e relations for convective clouds in the study areas 2 in Fig. 1. The vertical lines stand for different zones of microphysical process, the red, purple, and yellow lines represent the zones of glaciation, mixed-phase and diffusional growth. The curves of blue, red, green, brown and pink indicate T-R_e relations for 10, 25, 50, 75 and 90% available samples.

Another important fact is that the satellite observation can obtain many cloud properties tending to form hailstorm, and warn the occurrence of hail ahead to 90 minutes by the satellite retrieval methodologies. These are very vital to the early identification and mitigation of hail.

5. ACKNOWLEDGMENTS

We are grateful to Prof. Daniel Rosenfeld who supply the methodologies and software of satellite retrieval, and a lot of instructions. This work was supported by and National Natural Science Foundation of China under Grant No. 40575004.

6. REFERENCES

Rosenfeld D and Gutman G. Retrieving microphysical properties near the tops of potential rain clouds by multispectral analysis of AVHRR data. Atmos. Res., 1994, 34: 259—283.

Rosenfeld D, Lensky I M. Spaceborne sensed insights into precipitation formation processes in continental and maritime clouds. Bulletin of American Meteorological Society, 1998, 79: 2457—2476.

Lensky I M and Rosenfeld D. The time-space exchangeability of satellite retrieved relations between cloud top temperature and particle effective radius. Atmos. Chem. Phys., 2006, 6: 2887—2894.

NUMERICAL SIMULATION OF THT EVOLUTION OF PARTICLES IN A CONVECTIVE CLOUD USING BIN SPECTRAL MICROPHYSICS

Xiao-Li LIU, Sheng-Jie NIU*
Laboratory for Atmospheric Physics& Environment of China
Meteorological Administration, Nanjing University of Information Science&
Technology, Nanjing 210044, P.R.China

1. THE MODEL

A convective cloud model has been developed based on 3-D compressible non-hydrostatic dynamics (IAP,China) and the spectral bin microphysics of a 2-D slab-symmetric model (Tel vel).

2. ACTUAL WEATHER

This model has been used to simulate an actual cloud that occurred on the 29th of June, 2000 near Bird City, Kansas(Sun, 2005). This was a cloud being studied as part of the STEPS(Severe Thunderstorm Electrification and Precipitation Study), and its evolution was within the coverage area of the STEPS triple-radar network. The three S-band Doppler Radars consist of the operational WSR-88D located at Goodland, Kansas(KGLD), and two multi-parameter research radars: the National Center for Atmospheric Research(NCAR) S-Pol and the Colorado State University(CSU) CHILL.

3. THE SIMULATION OF THE RADAR REFLECTIVITIES AND TOTAL WATER CONTENT

The main object of the present study is to explore the evolution of particles in this convective cloud with bin spectral microphysics. The results of the simulation with the 3-D convective bin cloud model are compared with the IAP 3-D hailstorm numerical model (with bulk microphysics). Figure 1 presents the x-z cross section of radar reflectivity and vertical velocity at 24 min, 28 min and 32 min along center grid of longitude direction. The bin model accurately depicts the updraft velocities and spatial structure of the reflectivity that was observed with the Doppler radar. The simulated radar reflectivity of 60 dBZ appears on both sides and upper areas of the main updraft.

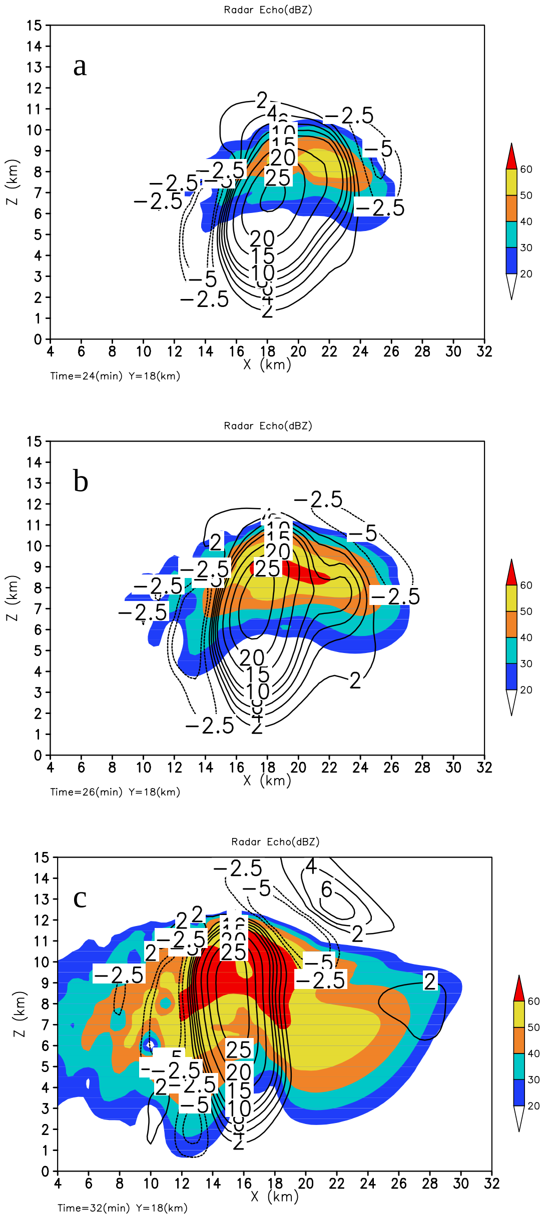

---

[*] Correaponding author.
E-mail address: niusj@nuist.edu.cn

Fig.1 x-z cross section of radar reflectivity (shading with a 10 dBZ increment starting from 20 dBZ), vertical velocity(dashed represent the negative contours start from -2.5 m·s^{-1} with an increment of -2.5 and solid lines represent the positive contours with an increment of 2 m·s^{-1} from 2 to 10,and an increment of 5 m·s^{-1} from 10 m·s^{-1}) along center grid of longitude direction: a. at 24 min; b. at 28 min;c. at 32 min

Figure 2 presents the x-z cross section of total water content at 24 min,28 min and 32 min along center grid of longitude direction. The spatial distribution does not completely correspond with that of total water content.

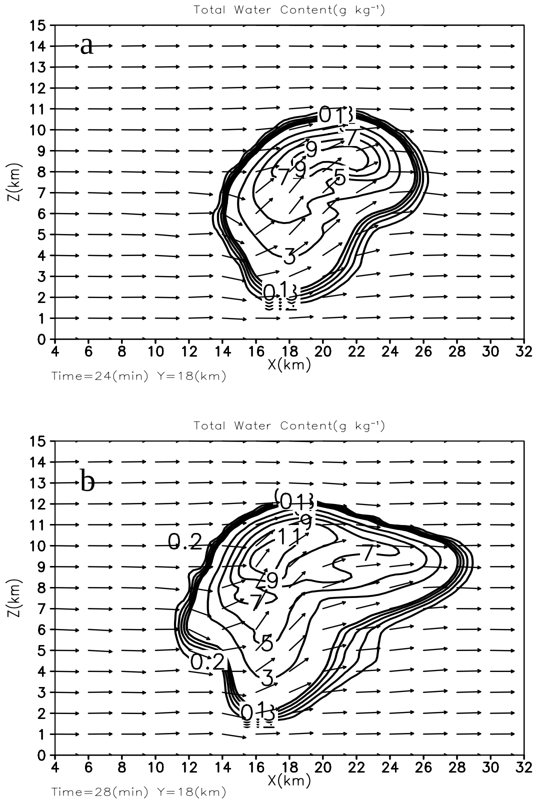

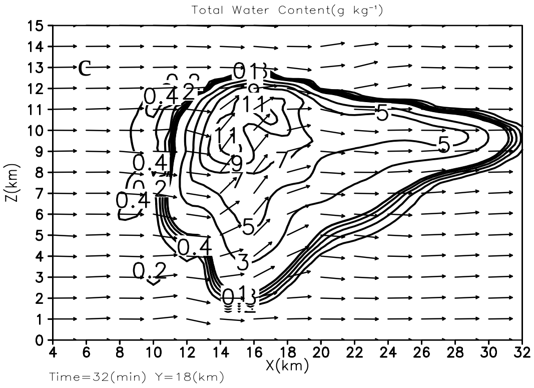

Fig.2 x-z cross section of total water content(start from 0.1 g kg^{-1} with increment of 1 for contours larger than 1 g·kg^{-1}) along center grid of longitude direction: a. at 24 min;b. at 28 min;c. at 32 min

4. THE SIMULATION OF THE ICE,WATER AND GRAUPEL CONTENT

A cloud anvil forms on the outflow side of the cell and the downdraft is most apparent on the inflow side where most of the precipitation is occurring. The total water content in the middle and lower part of the updraft is composed mostly of liquid water. In the upper part of the updraft and in the anvil, the water is in the form of ice and graupel. Two maxima in the graupel water mass form, one on either side of the updraft.(figure omitted)

5. THE SIMULATION OF THE MASS DISTRIBUTION FUNCTION OF GRAUPEL

Figure 3,4 and 5 separately presents the x-z cross section of the mass distribution function of graupel at 24 min,28 min and 32 min on the inflow side, over the main updraft, and on the outflow side. It can be concluded that both depositional and coalescence processes participate in the growth processes of graupel particles, although coalescence seems to dominate, particularly for diameters larger than a millimeter.

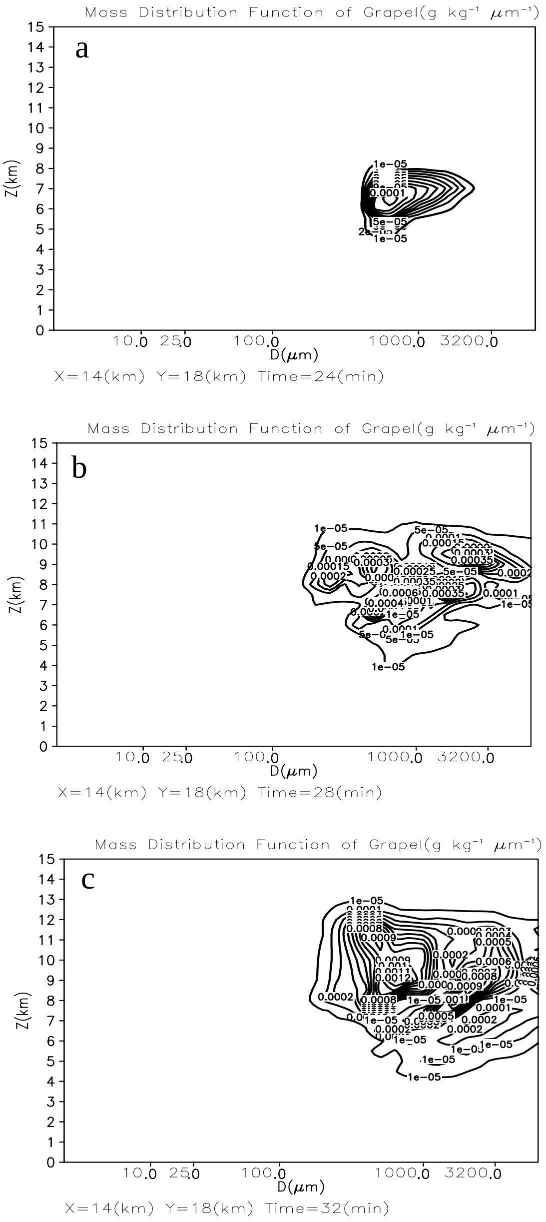

Fig.3 x-z cross section of mass distribution function of graupel total water content on the inflow side: a. at 24 min; b. at 28 min; c. at 32 min

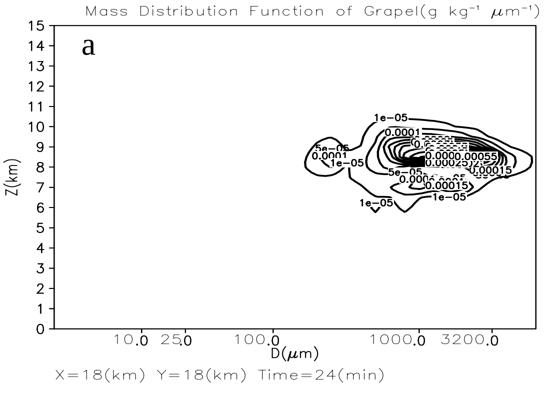

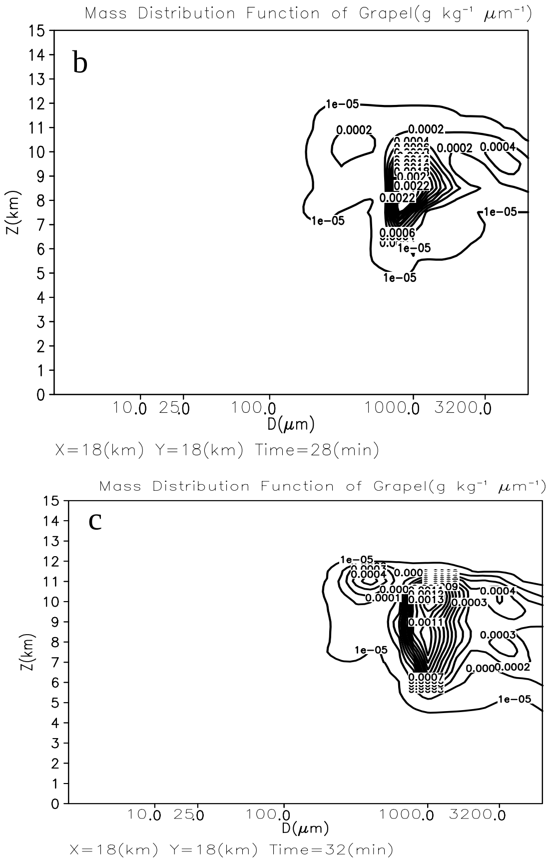

Fig.4 x-z cross section of mass distribution function of graupel total water content over the main updraft: a. at 24 min; b. at 28 min; c. at 32 min

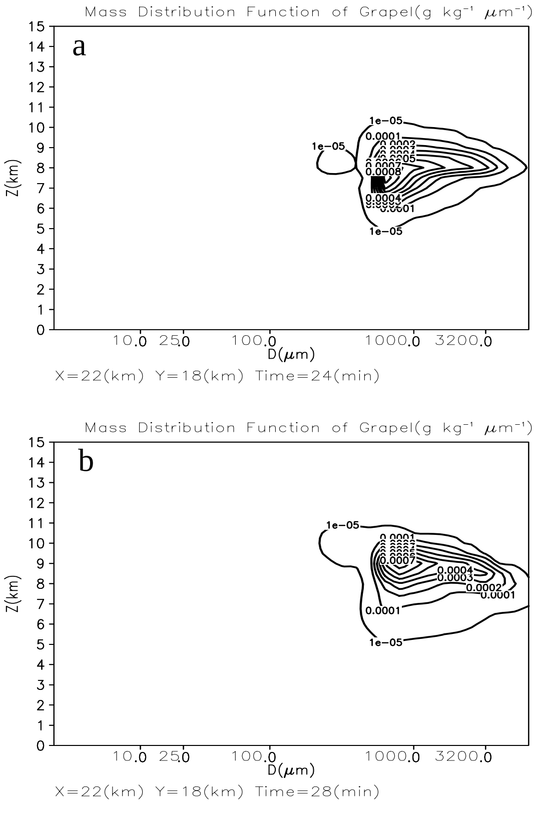

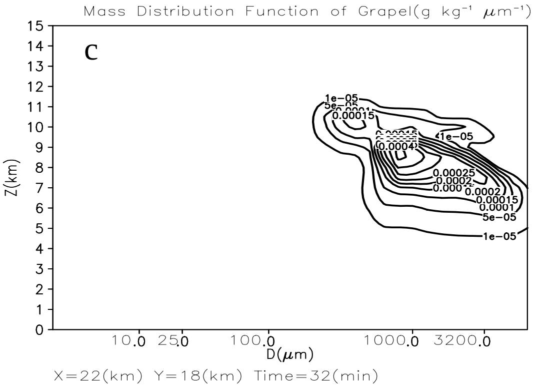

Fig.5 x-z cross section of mass distribution function of graupel total water content on the outflow side: a. at 24 min; b. at 28 min; c. at 32 min

6. SUMMARY AND CONCLUSIONS

From these results we conclude that there is a cyclic growth process in inflow region and the mass distribution of graupel, in the developing stage of the convective cell, has a relatively larger value in the outflow region. In general, the bin spectral microphysics depict the distribution and evolution characteristics of precipitation particles in convective clouds in good agreement with radar observations.

7. BIBLIOGRAPHY

Reisin T,Levin Z,Tzvion S.Rain production in convective clouds as simulated in an axisymmetric model with detailed microphysics. Part I: Description of the model. J Atmos Sci, 1996,53(3):497-519

Reisin T,Levin Z,Tzvion S. Rain production in convective clouds as simulated in an axisymmetric model with detailed microphysics. Part II: Effects of varying drops and ice initiation.J Atmos Sci, 1996, 53(13):1815-1837

Yin Y,Levin Z,Reisin T,et al.The effects of giant cloud condensational nuclei on the development of precipitation in convective clouds: A numerical study. Atmos Res, 2000, 53:91-116

Yin Y,Levin Z,Reisin T,et al.Seeding convective clouds with hygroscopic flares: Numerical simulations using a cloud model with detailed microphysics. J Appl Meteor, 2000, 39(9):1460-1472

Sun J.Initialization and numerical forecasting of a supercell storm observed during STEPS. Mon Wea Rev, 2005,133(4):793-81

ACKNOWLEDGEMENT

National Natural Science Foundation of China (Grant No. 40537034), and Key Technology and Instrument Development in Weather Modification（2006BAC12B02）from MOST of P. R. China supported this research.

NUMERICAL SIMULATION OF THE FORMATION OF A MIXED CONVECTIVE AND STRATIFORM CLOUD SYSTEM IN GUIZHOU PROVINCE

Yan-Wei LI[1], Sheng-Jie NIU[1*], Ning LUO[2], Ji-Fen WEN[2], Hao-Jun HUANG[2]
1、Laboratory for Atmospheric Physics& Environment of China Meteorological Administration, Nanjing University of Information Science & Technology, Nanjing 210044, P.R.China
2、Weather Modification Office of GuiZhou Province, GuiYang 550002, P.R.China

1. INTRODUCTION

The mixture of convective and stratiform clouds is an important precipitation system and also a major focus of weather modification studies. In these types of systems, the radar PPI images show that many convective cells or bands can exist within the stratiform background. But their formation, evolution mechanism and physical characteristics are not clearly understood. In this presentation, the formation and evolution of a mixed convective and stratiform cloud system is analyzed in detail.

A process of mixed convective and stratiform cloud system happened in Guizhou province is very typical. The favorable weather situation is that the north area in Guizhou province is influenced by cold airflow from leaning north direction, and at the same time, south-west airflow invade Guizhou and meet with the cold air, so a convergence line is formed at 850hpa (lon:104-112,lat:22-28). Accordingly, a stationary front is emerged on the ground, and Guizhou is almost in the cold area of the front. Influenced by this weather situation, an obvious process of mixed convective and stratiform cloud system emerged. Besides, another favorable condition is that there is vertical wind shear between 700hpa and 850hpa.

2. SIMULATION SCHEME

Using the mesoscale model WRF(2.1.2), we simulated the process happened in May 17-18th, 2005. The initial data are from the NCEP data based on 1°×1° resolution. Two nested grid domains were used in the current simulation, which have a grid resolution of 18km and 6km. The Kain-Fritsch scheme for convective parameterization was used for domain 1 and the Lin cloud microphysics parameterization is used for the second domain 2.

3. CONTRAST OF SIMULATION RESULTS WITH OBSERVING DATA

The simulated rain band of 24hr is basically consistent with the observation. As shown in fig.1, the simulated total water content distribution(fig.1a) is very similar with the cloud system in the black rectangle in the satellite cloud picture(fig.1b). Fig.1c is radar cloud system distribution in Guiyang, we find that the simulated radar echo distribution and intensity(fig.1d) are almost same with those in fig.1c. The simulated rainfall(fig.1f) is similar with the observations (fig.1e). These prove that the simulation results is very well and we can analyze the process in detail.

Fig.1.a

---

[*] Correaponding author.
E-mail address: niusj@nuist.edu.cn

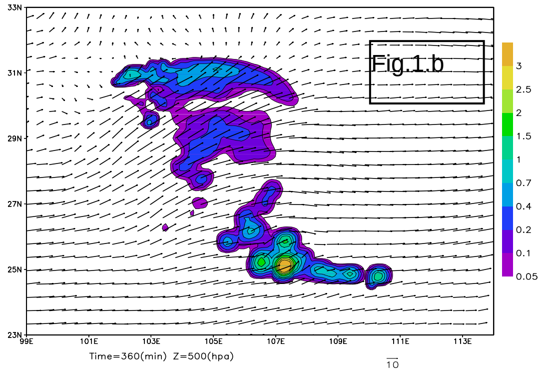

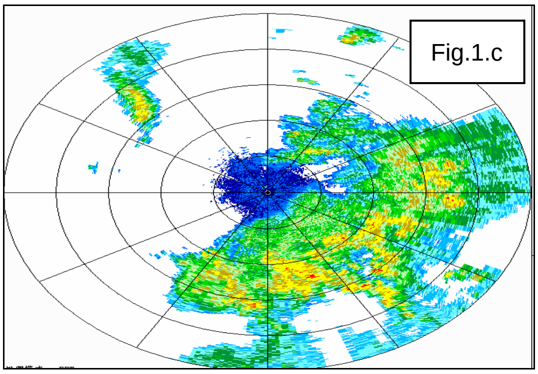

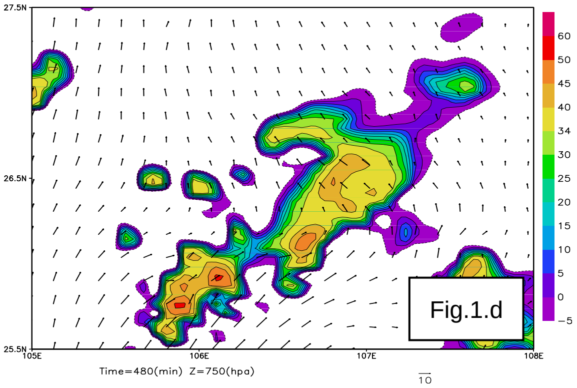

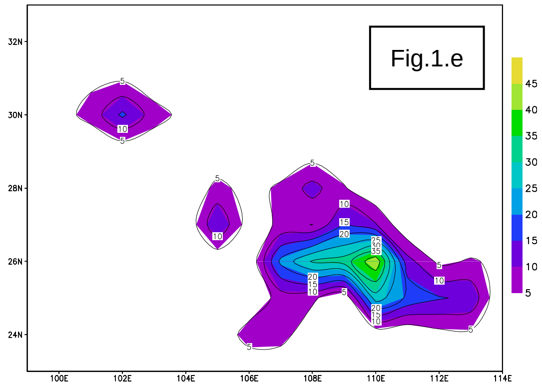

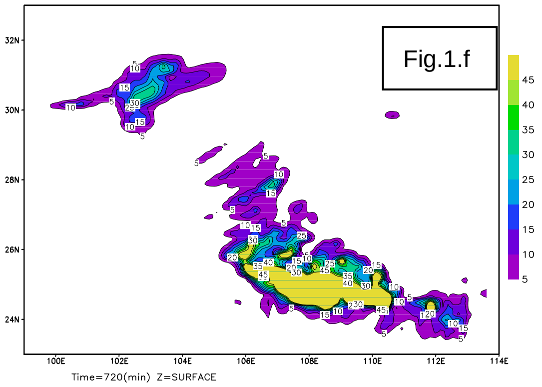

Fig.1 simulation and observed results(1a. satellite picture at 02:00 18th ; 1b. simulated total water content at 500hpa at 02:00 18th; 1c. radar echo picture at 1.5°of PPI at 03:00; 1d. simulated radar echo at 03:00; 1e. observed precipitation distribution; 1f. simulated precipitation distribution)

4. ANALYSIS OF THE FORMATION PROCESS

Judged by radar echo pictures and simulation results, this process of mixed convective and stratiform mixed clouds happened in May 17-18th 2005 is caused by convection merger. There are 3stages: (1)convective cells merge into a big convective cloud; (2)convective clouds merge into convective cluster; (3)convective clusters merge into the mixed convective and stratiform mixed cloud system.

4.1 CONVECTIVE CELLS MERGE INTO A BIG CONVECTIVE CLOUD

In the vicinity of the convective line, many convective cells come forth, and in their moving process, they may span and connect, and then they may turn stronger and higher. The merging process often begins from the middle and lower part between clouds. Fig.2 shows the merging process of three convective cells. Along the moving direction, it seems that the back convection can absorb energy and water vapor of the front one, so the back convection will turn stronger and the others will turn weaker. At last, they merge into a one bigger convective cloud.

At the same time, the similar merging process happens at other areas of Guizhou province, so many bigger convective clouds form.

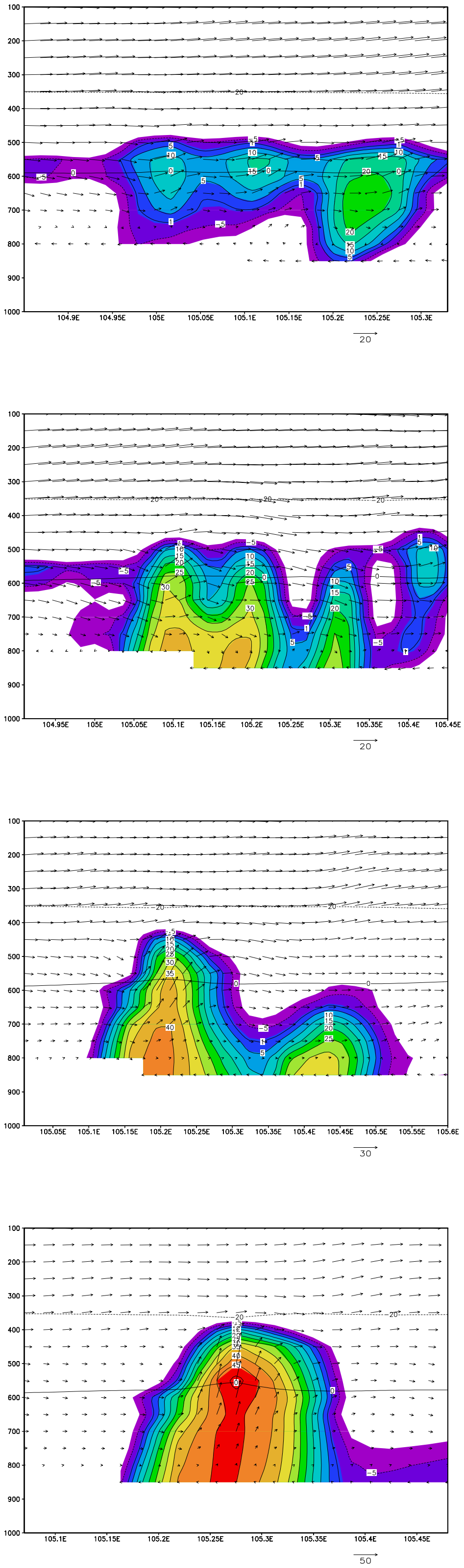

Fig.2 merging process of 3 convective cells

4.2 CONVECTIVE CLOUDS MERGE INTO CONVECTIVE CLUSTER

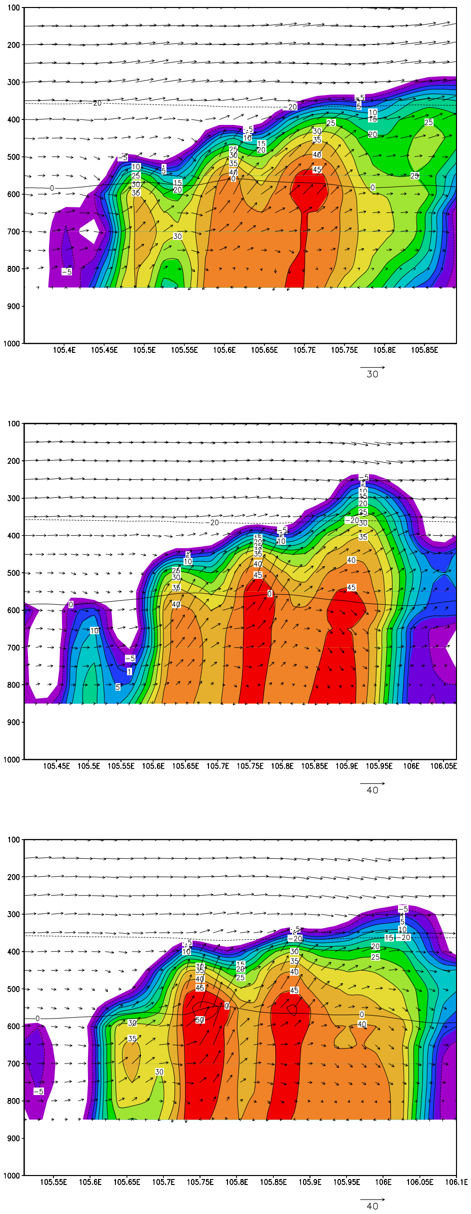

Fig.3 merging process of convective clouds

In the moving process of many bigger convective clouds, the front convections are often be absorbed and the back convections develops. Herein, convective cells will constantly supply the convective cluster, as shown in fig.3.

4.3 CONVECTIVE CLUSTERS MERGE INTO THE MIXED CONVECTIVE AND STRATIFORM CLOUD SYSTEM

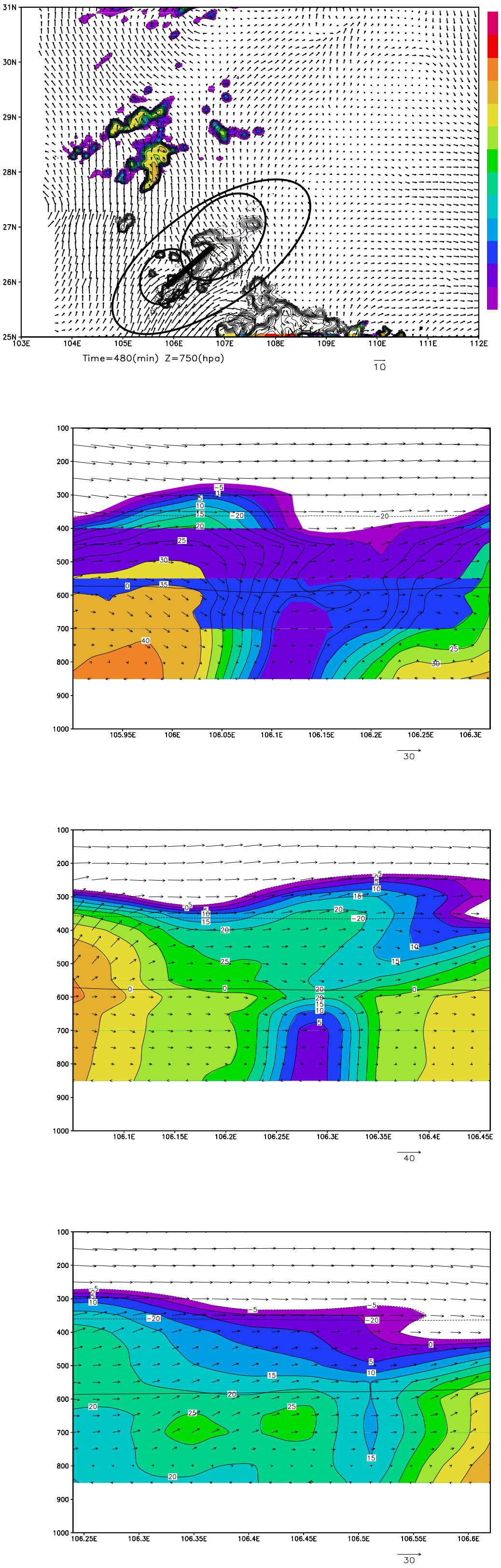

Fig.4 merging process of convective cluster

In this precipitation process, there are 2 big convective clusters in Guizhou province. Fig.4 shows the merging process of two convective clusters into the mixed convective and stratiform cloud system. The merging process begins from the upper part because vertical wind wear and also the quicker airflow in the upper level.

4.4 STAGE OF MIXED CONVECTIVE AND STATIFORM CLOUD SYSTEM

With the development of merger, evolution, the cloud system exhibits obvious mixed state. Fig.4 show one part of the cloud system.

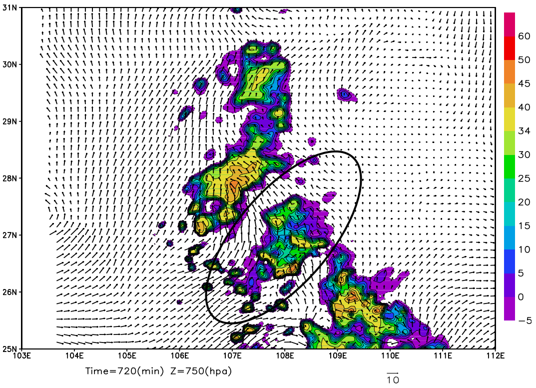

fig5.a. the mixture at 750hpa

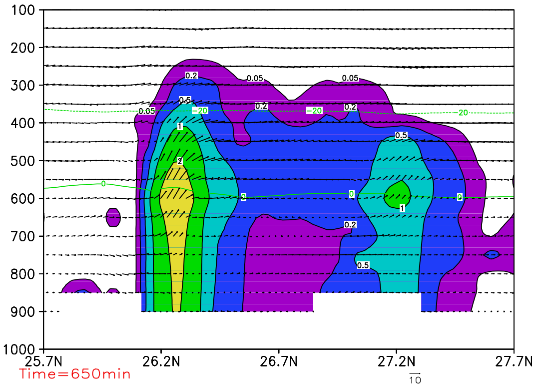

Fig5.b. vertival section along lon 107.6°

ACKNOWLEDGEMENT

This work is supported by Key Technology and Instrument Development in Weather Modification（2006BAC12B02）from MOST of P.R.China.

CONVECTIVE CLOUDS CHARACTERISTICS IN THE SOUTHWESTERN AMAZONIA DURING WET AND THE PRE-WET SEASON.

Luiz A. T, Machado* and Rafael C. G. Martins**

* - Instituto Nacional de Pesquisas Espaciais - Brazil
** - Fundação Cearense de Meteorologia - Brazil

1 – ABSTRACT

This study uses the volume scan from S band radar, operating during the LBA dry to wet season field campaign, and the 915 MHz Doppler profiler radar and a Joss-Waldvogel impact disdrometer measured during the LBA wet season campaign to characterize the convective processes of Amazon convection. Two main points were explored in this study, a) the typical reflectivity profiles of the convective clouds and the associated cloud droplets distribution at the surface and the diurnal variation of those characteristics; b) the typical variation of the reflectivity profiles during the convective cells life cycle and the use of the cloud top time rate as an indicator of cloud severity and life cycle. Results show typical diurnal evolution of reflectivity profiles and the associated rain droplet distribution. We have computed the mean reflectivity profile and cloud height top rate as function of the life time showing the increase in the ice phase as the cloud evolves to the mature stage.

2 – INTRODUCTION

The understanding of the cloud processes is a key question to many applications as climate change, precipitation estimation and nowcasting. Clouds constitute one of the major components of the climate system in determining and modulating the quantity of solar radiation absorbed by the surface, the terrestrial radiation lost to space, and radiative feedbacks. However the cloud processes is fairly known and very difficult to be estimated. The cloud microphysics, the ice morphology, the quantity of ice, mixed ice-water, cloud droplet, rain droplet distributions are very important to be known.

This study uses the LBA experiment in Amazonia to try to give a contribution about the cloud processes from the point of view of the rain cell lifecycle.

Machado and Laurent (2004) showed that is possible to estimate the probable lifetime duration of a convective system, within certain error bar, considering only its initial area expansion. They also have shown that the area increase in the initial stage is mainly due to the condensation process then afterwards, in the mature stage, the upper air wind divergence increases. They deduced an equation to describe this process discarding the term describing the ascend/descend rate of the top of clouds. They considered that the top of the convective system, detected using a cold satellite threshold, is close to the tropopause and therefore its variations are relatively small and can be neglected. It is reasonable when satellite data and cold threshold are used. In that case, satellite data commonly show a nearly stable height of the cloud deck and does not give much information about the evolution of cloud dynamic. When radar high time resolution data is employed, the importance of the term describing ascend/descend rate of the top of clouds should be of first order.

The goal of this study is to evaluate the evolution of the reflectivity profiles as function of the rain cell lifecycle, the diurnal cycle and the importance of the cloud top height rate as a tool for nowcasting.

3 – DATA AND METHODOLOGY

3.1 Data

The dataset employed in this analysis was collected during LBA/RACCI (Radiation Cloud and Climate Interaction). The RACCI experiment was designed to understand the transition between the dry to wet season and the impact of the aerosols produced by forest burning in the development of clouds. The experiment was held in the central part of Rondonia State in the southwestern part of the Amazon basin. A Brazilian weather radar manufactured by the TECTELCOM was used in this campaign. This radar is a Doppler S-Band (2.7-3 GHz), with 2 degrees antenna aperture. The radar was installed in Rondonia State in the following coordinates: longitude of 62.4 W, latitude of 10.9 S and altitude of 433 meter. During the experiment, 10 minutes interval volume scans with 24 elevations were realized to better describe the horizontal and vertical distribution of the precipitating systems. The period of measurements concentrated during September 16th through November 7th of 2002.

An intercomparison with the Tropical Rainfall Measuring Mission (TRMM) Precipitation Radar (PR) was performed to depict an existence of a bias offset. The retrieval of the bias offset is described in Morales et al. (2004).

The second part of this study used the data from the LBA wet Season (see Silva Dias, 2002, for details). Basically two measures were used, a Joss-Waldvogel disdrometer and a vertical pointing radar (915 MHz). The radar data was used with 210 m resolution each minute. Both dataset were pre processed by Albrecht (2005). The disdrometer and the radar were installed in the Ji-Paraná airport (61,81W and 10,88S), and the data were recorded from 17 January up to 01 de March 1999. During this period the disdrometer recorded 288 mm distributed in 4787 samples.

3.2 Methodology

The tracking technique employed in this study is called as ForTraCC (Forcasting and Tracking Cloud Cluster). The main steps of the ForTraCC algorithm are the following ones: (1) a rain cell detection method based on a size and reflectivity threshold; (2) a statistical module to perform morphological and radiative parameters of each rain cell; (3) a tracking technique based on rain cell overlapping areas between successive images. ForTraCC has also a module for nowcasting but it was not used in this study, for more details see Vila et al. (2008).

A rain cell was defined as neighbor pixels, at the CAPPI 2 km, having reflectivity larger than 20 dBZ.

In the second part of this study we have computed the average reflectivity profile for different rain rates and for different local time. The droplet size distributions (DSD) were computed and organize in classes of precipitation intensity and by classes showing maximum in 0,5 mm, 1.0 mm and 2.0 mm *(details are presented in the result section)*.

4 – RESULTS

4.1 – The Average Reflectivity Profile

Following the rain cells as defined above, we were able to classify the life cycle duration and the typical vertical structures. The long lived rain cells (larger than 160 m), where the lifecycle is very clear, we computed the average reflectivity vertical profile for different phases of the life cycles. We have considered the first detection, when the system has more than 4 pixels, as representative of the initiation phase. The phase - before maturation - was defined as the middle time between initiation and mature phase (mature is defined as the time of maxima area). The other two phases were defined as after-mature and dissipation. Dissipation was defined as the last time a cluster of 4 pixels were tracked, and after-mature as the middle time between mature and dissipation.

Figure 1 shows the typical reflectivity profile of the long lived rain cells as function the lifecycle. In the initiation stage the precipitation (reflectivity in the lower levels) are closer to the one in the mature stage, however, we can note that the reflectivity in the upper levels, in the initiation is much smaller than in the mature stage. This has important implication for the algorithms that exploit the relationship between ice aloft and rainfall at the surface. Figure 1 clear shows the increase of ice phase as the rain cells pass to the mature stage. In the dissipation stage, the rain cells have smaller ice amount and rainfall at the surface.

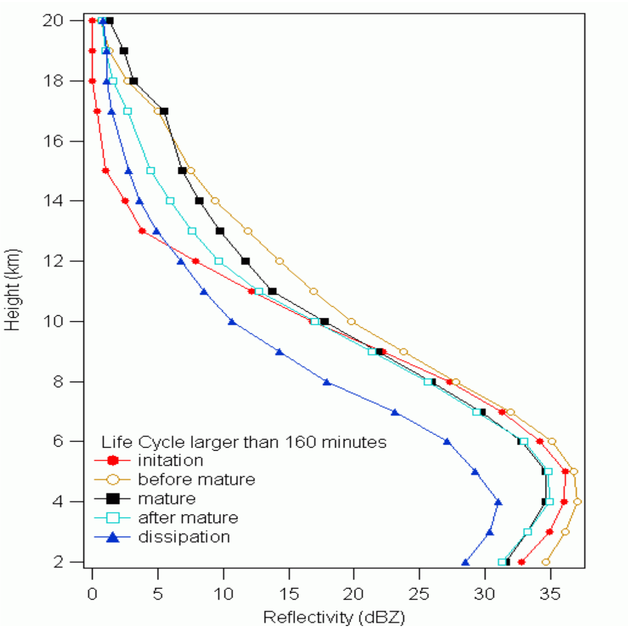

Figure 1 – The mean vertical reflectivity profile as function of the long lived (>160 minutes) rain cell life cycle

4.2 – The Cloud top height rate

Using radar data and a rain cells tracking technique we were able to compute the cloud top height time variation. This cloud top height rate can be an useful parameter to describe the vigor of the convection, because this term, during the development phase, represents an average vertical velocity (w) that is closely associated with the mass flux inside the convective cores.

Using the radar volume scan data, every ten minutes, we computed the CAPPI from 2 to 19 km every 1 km. Using the CAPPI at 2 km we computed the trajectories of each rain cell (defined by the threshold of 20 dBZ). For each rain cell and time step, the average cloud top height and reflectivity profile was calculated using all CAPPIs levels. Based in this calculation, we have for each rain cell life cycle, the reflectivity profile and the cloud top height variation in 10 minutes, what we called as:

$$W = \Delta h / \Delta t, \text{ in m/s} \qquad (1)$$

Where *h* is the average 20 dBZ reflectivity threshold height for all the pixels belonging to the rain cell and Δt is the time interval between successive measurements (10 minutes).

Using the rain cells lifecycle information we calculated the mean cloud top height rate as function of the life cycle, using the same definition as described above.

We can note (Figure 2) that this rate decrease as function the lifetime. The maximum cloud top height rate occurs in the initiation stage, during the mature the cloud top is nearly unchanged, decreasing in the dissipation phase. This behavior is similar to that one obtained by Machado and Laurent (2004) using satellite to define the cloud are expansion, The cloud area expansion can be also related to the vertical mass flux inside the cumulus towers.

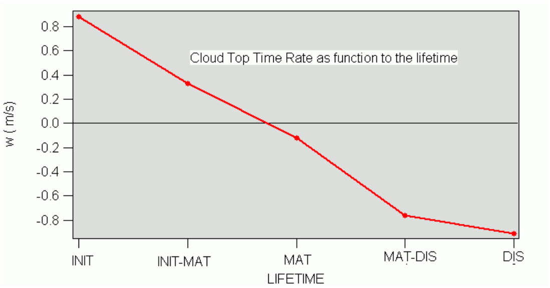

Figure 2 – The mean cloud top rate (assigned as w in m/s) as function of the lifetime

The cloud top height rate, mainly in the initiation phase, seems to be related to the dynamic inside clouds, and can be used as proxy of the convective activity, severity and the trend of the convective activity. To verify the potentiality of the cloud top height rate (here after called as W) to nowcasting the evolution of the convective activity dh/dt (top here define by 20 dBZ) was separated in 4 classes as following: 1) -1.5 m/s > dh/dt , 2) -1.5 m/s< dh/dt < 0 m/s, 3) 0 m/s< dh/dt < 1.5 m/s, 4) 1.5 m/s < dh/dt. We have computed the average change in the radar reflectivity profile, after 10 minutes (Figure 3), for each class of W. After 10 minutes the average variation in the reflectivity profile for the class of largest W shows an increase in the radar reflectivity for all levels. This behavior is prominent near the surface (precipitation increase) and at the high levels (ice particles aloft). For the dh/dt class between 1.5 and 0 m/s, we observe that reflectivity values in the lower levels increases after 10 minutes, however a clear decreasing is observed in the higher levels indicating the beginning of the decaying stage. For the classes showing dh/dt smaller than zero, we observe a process of convection decaying in all levels.

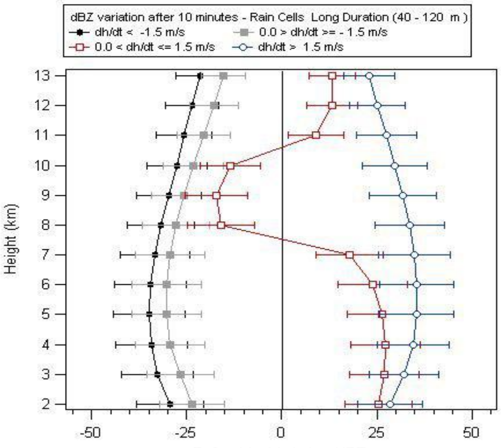

Figure 3 – The mean vertical reflectivity profile variation as function of the cloud top rate 10 minutes before.

This result presents a typical time evolution of the vertical reflectivity profiles for different range of the cloud top height time variations. Large values of cloud top increasing are associated with a clear increasing of ice phase (ice particles aloft) and surface precipitation in the next few minutes. For the situation when the cloud top rapidly decreases, the reflectivity profile in the next few minutes presents the collapse of the ice phase and a significant decrease of the precipitation.

4.2 – The DSD and the associated reflectivity Profile

Using the measurement from vertical pointing radar and a disdrometer, operating during the LBA wet season we were able to evaluate the cloud droplet distribution and the diurnal cycle of the reflectivity profiles. Looking the individual DSD samples we observed typical profiles presenting a maximum in 0,5 mm, 1,0 mm and 2,0 mm. Using an algorithm that computed the size of maximum DSD, we have separated these three classes of DSD. Figure 4 presents the average distribution of these three classes, over 4423 samples, 51,9% has maximum in 0,5 mm, 32,6% in 1,0 mm and 2,7% pics in 2,0 mm. 87,2% of the DSD can be roughly described by these three DSD presented in Fig. 4. These distributions are related basically with three vertical reflectivity profiles that are represented in Figure 5. These profiles are associated to the Stratiform precipitation that mainly occurs during the night and early morning, convective clouds in the developing stage, in the afternoon, and with the intense precipitation in the late afternoon – evening, probably corresponding to the end of the mature stage.

Precipitation, DSD and the reflectivity profile are strongly modulated by the diurnal cycle and the lifecycle of the rain cell. These three patterns accounts for 87% of all measured cases. It corresponds to a well simplification of the complex system describing the cloud process.

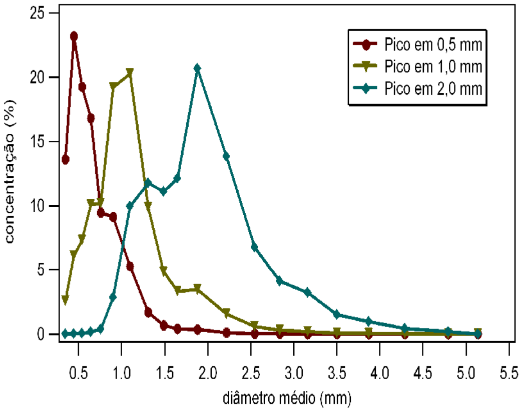

Figure 4 – Typical droplet size distribution for the Amazon rainfall during the wet season.

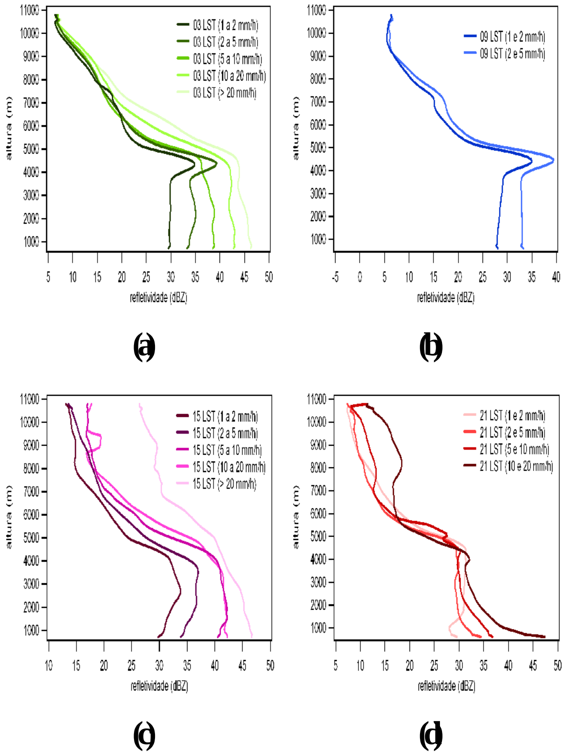

(a) (b)

(c) (d)

Figure 5 – Mean reflectivity profiles as function of the precipitation rate for 03, 09, 15 and 21 LST

.

5) Conclusion

This study uses radar data to describe the lifecycle and the diurnal cycle evolution of the rain cells.

The rain cell shows an increase of ice phase as it evolves to the mature stage. In the dissipation stage the rain cells have smaller ice amount and rainfall.

The use of the cloud top height time variations can help to describe the dynamic of the cloud/ice droplets. dh/dt value seems to be an useful parameter to describe the lifetime of raining cells and to forecast their evolutions.

The wet season Amazon raining clouds shows three typical DSD and reflectivity profiles that are modulated by the diurnal cycle and the lifecycle.

6 - References

Morales C.A., Machado L.A.T., Silva Dias M.A.F., Amorim W., Frediani M.e.B. Characteristics of teh precipitating systems during the 2002 dry-to-wet field campaign in the Amazon region. ICCP, Bologna, 2004.

Albrecht, Rachel Ifanger; Silva Dias, Maria Assunção Faus da *Microphysical evidence of the transition between predominant convective/stratiform rainfall associated with the intraseasonal oscillation in the Southwest Amazon.* Acta Amazonica, 2005,vol.35, n2

Machado L. A. T. E Laurent, H.: The convective system area expansion over Amazonia and its relationships with convective system life duration and high-level wind divergence. Monthly Weather Review, vol 132, 714-725, 2004.

Silva Dias, M.A.F. da; Rutledge, S.; Kabat, P.; Silva Dias, P.L.da; Nobre, C.A.; Fisch, G.; Dolman, A.J.; Zipser, E.; Garstang, M.; Manzi, A.O.; Fuentes, J.D.; Rocha, H.R.; Marengo, J.A.; Plana-Fattori, A.; Sa L.D.A.; Alvala, R.C. dos Santos; Aandrea M.O.; Artaxo, P.; Gielow, R; Gatti, L. 2002. Cloud and Rain processes in a biosphere-atmosphere interaction context in the Amazon Region. *Journal of Geophysical Research*, 107(D20): 8072- 8090

Vila D. L.A.T.Machado, H. Laurent, I. Velasco, 2008: Forecast and Tracking the Evolution of Cloud Clusters (ForTraCC) Using Satellite Infrared Imagery: Methodology and Validation. Weather and Forecasting, vol 23, 233-245.

IMPACT OF CLOUD MICROPHYSICS ON THE DEVELOPMENT OF TRAILING STRATIFORM PRECIPITATION IN SQUALL LINES

Hugh Morrison*, George Bryan, and Greg Thompson

National Center for Atmospheric Research, Boulder, Colorado, USA

1. INTRODUCTION

Squall lines with trailing stratiform precipitation are common in both mid-latitude and tropical environments, and have been extensively studied by numerous researchers (e.g., Zipser 1969; Biggerstaff and Houze 1991). These studies have suggested several common morphological features described by the conceptual model of Biggerstaff and Houze (1991, see Fig. 18 therein). These features include an upshear-tilted, multicellular convective region with heavy precipitation and active updraft cell generation along the gust front, a transition zone of lighter precipitation and a low-level radar reflectivity minimum between the convective and stratiform regions, followed by a region of moderate precipitation in the trailing stratiform region.

Numerous studies have attempted to simulate squall lines with an enhanced region of trailing stratiform precipitation using cloud-system resolving models (e.g., Fovell and Ogura 1988; McCumber et al. 1991; Ferrier et al. 1995). In general, models have not been very successful at replicating commonly-observed squall line features, the transition zone and trailing stratiform region in particular.

In this paper, we examine the role of cloud microphysics in idealized 2D and 3D simulations of squall lines, focusing on the development of stratiform precipitation. The focus is on a comparison of one- and two-moment bulk microphysics schemes. One-moment schemes predict the mixing ratios of the hydrometeor species only, while two-moment schemes predict both mixing ratios and number concentrations, allowing for a more robust treatment of the particle size distributions. We also examine the impact of assuming that the dense precipitating ice species consists of either graupel or hail.

2. MODEL DESCRIPTION AND EXPERIMENTAL DESIGN

The Advanced Research Weather Research and Forecasting model (WRF) Version 2.2 (Skamarock et al. 2007) is the fully compressible, nonhydrostatic, two-dimensional cloud model used for the 2D simulations. The numerical model of Bryan and Fritsch (2002) is used for the 3D simulations. In both models the governing equations are solved on a horizontal staggered Arakawa C-grid using time-split integration with third-order Runge-Kutta scheme and sub-steps for the acoustic and gravity wave modes. Lateral boundary conditions are open in the 2D simulations. In the 3D simulations, lateral boundary conditions are open in the X direction and periodic in the Y direction. Upper and lower boundaries are free slip, with zero surface fluxes, and radiative transfer neglected. A Rayleigh damper is used near the model top to damp spurious waves in the stratosphere. The 2D simulations have a domain size of 600 x 20 km, while the 3D simulations have a domain size of 512 x 128 x 18 km. Both the 2D and 3D simulations are initialized with the thermodynamic sounding of Weisman and Klemp (1982), which has a convective available potential energy (CAPE) of about 2200 J kg^{-1}. The ambient wind has a weak low level shear (10-12 m/s over the lowest 2.5

---

*Corresponding author address: Dr. Hugh Morrison, NCAR, 3450 Mitchell Lane, Boulder, CO, 80307 km). The horizontal and vertical grid spacings are 1 and 0.25 km, respectively.

The bulk cloud microphysics scheme used here is described by Morrison et al. (2008; hereafter M08). It predicts five hydrometeor species: cloud droplets, cloud ice, snow, rain, and either graupel or hail. The hydrometeor size distributions N(D) are treated using gamma functions as

$$N(D) = N_0 D^{\mu} e^{-\lambda D}$$

where D is the particle diameter, and N_0, μ, and λ, are the intercept, shape, and slope parameters, respectively. For the precipitation species, we assume that $\mu = 0$ (i.e., an exponential distribution). In the two-moment version of the scheme, N_0 and λ are free parameters that are determined from the predicted mixing ratio and number concentration. In the one-moment version of the scheme, N_0 is specified as a constant for each species (this is the approach used in most one-moment schemes), and λ is determined from the predicted mixing ratio and specified N_0. A key point is that all other aspects of the one- and two-moment versions of the scheme are the same. Hereafter, the one-moment and two-moment schemes are referred to as '1-M' and '2-M', respectively.

For the tests using either graupel or hail, the dense precipitating ice species has a bulk particle density set to either a lower value for graupel (400 kg m^{-3}) or higher value for hail (900 kg m^{-3}). Fallspeed parameters are also modified to correspond to either graupel or hail following Locatelli and Hobbs (1974). All of the 2D WRF simulations assume graupel. Differences using either graupel or hail are explored in the 3D BF simulations.

3. RESULTS

Moist deep convection is initiated within the first 15 min of the 2D simulations and, over the next several hours, organizes into features that are characteristic of many observed squall lines. An example of the storm structure using 2-M in terms of synthetic radar reflectivity and 2D wind vectors during the mature phase of the squall line is shown in Figure 1. Several features of the simulated squall line, including well-developed storm-relative front-to-rear flow at mid- and upper-levels and rear-to-front flow at mid- and lower-levels, are consistent with observed squall lines (e.g., Biggerstaff and Houze, 1991, Fig. 18 therein).

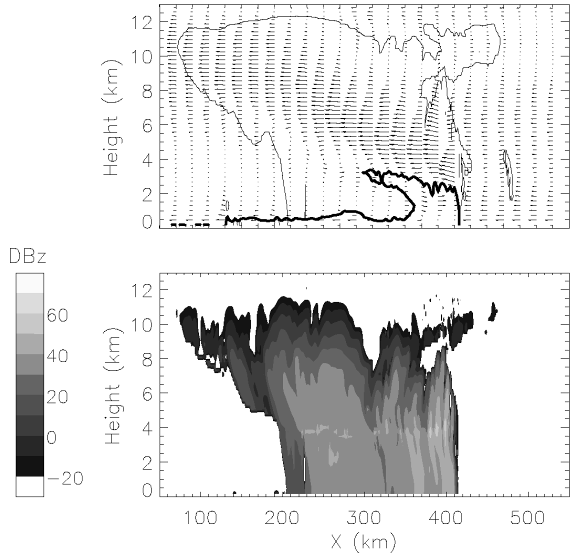

Figure 1. Storm-relative 2-D wind vectors (arrows), cold pool region defined by the -2 K isotherm of potential temperature perturbation (thick solid line), and boundary of hydrometeors with mixing ratio greater than 0.01 g kg^{-1} (thin solid line) (top), and radar reflectivity (bottom), for the 2D two-moment simulation (2-M) at t = 6 hr. For clarity, the wind vectors are plotted every 20 km horizontally and the vertical component is exaggerated by a factor of 2.

While the overall storm structure is similar between 1-M and 2-M, there are some significant differences. Namely, 1-M produces significantly less stratiform rainfall at the surface and weaker reflectivities in the stratiform region both above and below the melting level (~ 4 km), as seen by a comparison of Figs. 1 and 2, as well as in Fig. 3.

The primary reason for this difference in stratiform precipitation between 1-M and 2-M is a reduced rain evaporation rate in the stratiform region in 2-M. This directly contributes to the greater stratiform rainfall at the surface, as well as the reduced vertical

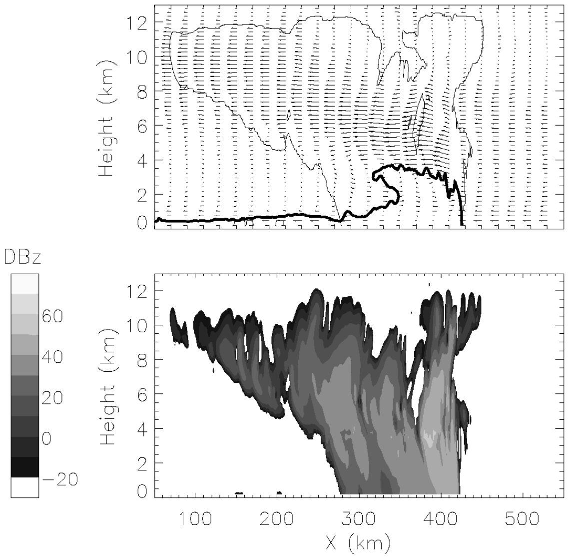

Figure 2. Same as Figure 1, except for the 2D one-moment simulation (1-M).

gradient of reflectivity with height in the stratiform region. It also results in a weaker cold pool, although the gust front propagation speed is only slightly reduced in 2-M. The lower rain evaporation rate results from a smaller N_0 parameter for rain, N_{0r}, predicted in 2-M in the stratiform region, compared with the specified value in 1-M. As shown in Fig. 4, the predicted N_{0r} in 2-M varies widely between the stratiform and convective regions of the squall line, with values of about 10^6 m^{-4} in the stratiform region and 10^8 m^{-4} in the convective region. In 1-M, N_{0r} is constant at 10^7 m^{-4}. The large difference in N_{0r} between the stratiform and convective regions in 2-M is consistent with disdrometer measurements in observed mesoscale convective systems (e.g., Waldvogel 1974; Tokay and Short 1996). This sharp decrease of N_{0r} between the convective and stratiform regions has been referred to as the "N_0 jump" in the literature.

In the convective region, N_{0r} is larger in 2-M than the specified value in 1-M. This results in *increased* rain evaporation in the convective region in 2-M. The increased rain evaporation leads to reduced updraft strength and increased detrainment of momentum and buoyancy at

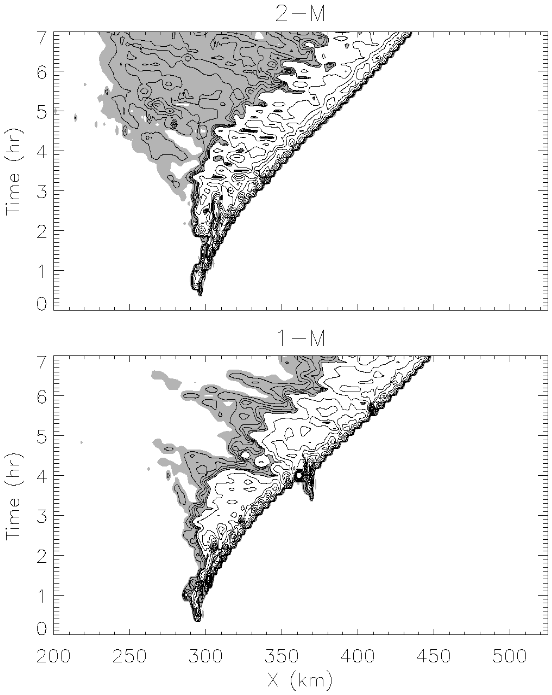

Figure 3. X-time plot of the surface rainfall rate for the 2D two-moment (2-M) and one-moment (1-M) simulations. Contour interval is every 1 mm/hr for rates between 0 and 5 mm/hr and every 10 mm/hr for rates greater than 10 mm/hr. To highlight the stratiform rain precipitation region, moderate precipitation rates between 0.5 and 5 mm/hr are gray-shaded.

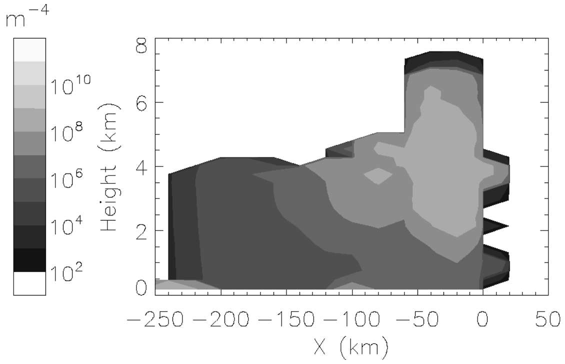

Figure 4. Rain intercept parameter, N_{0r}, predicted in the 2D two-moment simulation (2-M) as a function of distance from the leading edge of precipitation, averaged between 6 and 7 h.

midlevel, which in turn is associated with a stronger mesoscale updraft over the stratiform region (see Morrison et al. 2008 for details).

A key point is that no single value of constant N_{0r} specified in 1-M is able to reproduce the 2-M results. A sensitivity test using 1-M but with N_{0r} reduced to the value of 2 x 10^6 m^{-4} (typical of the value produced by 2-M in the stratiform region) results in greater stratiform rainfall due to the reduced evaporation (not shown). However, reduced evaporation in the convective region produces stronger convective drafts, reduced detrainment of buoyancy at mid-levels, and a weaker mesoscale updraft relative to 2-M. Another sensitivity test using 1-M but with N_{0r} increased to the value of 2 x 10^8 m^{-4} (typical of the value produced by 2-M in the convective region) results in increased mid-level detrainment of buoyancy and a stronger mesoscale updraft relative to 1-M, but increased rain evaporation in the stratiform region and very little stratiform rainfall at the surface. Prediction of two moments versus one moment for snow and graupel has much less impact than prediction of two moments for rain in 2-M.

Moist deep convection in the 3D simulations rapidly organizes into typical squall line features. The 1-M and 2-M simulations with graupel (hereafter '1-MG' and '2-MG', respectively) exhibit many features in common with the corresponding 2D simulations (Fig. 5). However, the simulations with hail ('1-MH' and '2-MH') show substantial differences from 1-MG and 2-MG. Namely, there are higher reflectivities in the stratiform region, and a distinct transition zone of lighter precipitation between the stratiform and convective regions. Because of the higher fallspeed of hail compared with graupel, much of the hail falls to the surface within the convective region. In contrast, graupel remains lofted much longer and subsequently detrains from the convective updrafts. Once it is detrained from the convective region it falls out rapidly, producing enhanced reflectivity between the stratiform and convective regions (see Fig. 5), in contrast to observations of mid-latitude squall lines that often show a transition region of lighter precipitation between the stratiform and convective regions (e.g., Biggerstaff and Houze 1991). In contrast, detrained snow is transported much farther from the convective region because its fallspeed is lower than that of graupel. These results suggest the importance of the representation of dense precipitating ice. Similar conclusions were reached in the 2D simulations of Fovell and Ogura (1988).

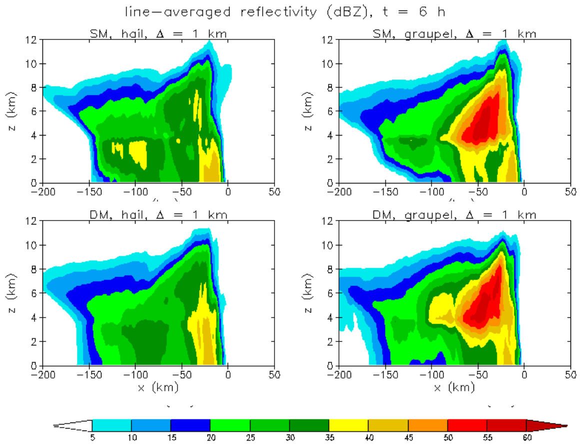

Figure 5. Line-averaged radar reflectivity (DBz) as a function of height and distance from leading storm edge, for 3D one-moment (SM) and two-moment (DM) simulations with either graupel (right) or hail (left). Results are shown at t = 6 hr.

There is less difference between 1-MH and 2-MH compared with 1-MG and 2-MG. Thus, prediction of two moments versus one moment has more impact when the dense precipitating ice is treated as graupel rather than hail. However, differences are still noted between 1-MH and 2-MH. In particular, radar reflectivity increases rapidly with height in 1-MH in the stratiform region due to significant evaporation of rain below the melting layer. This is due to the relatively large N_{0r} compared to 2-MH in the stratiform region, similar to the 2D results with graupel. The greater rain evaporation rate in 2-MH produces a wider and deeper cold pool than in 1-MH, although the minimum perturbation potential temperature is similar between the runs. Higher reflectivity (> 40 DBz) also extends higher in the convective region in

2-MH than 1-MH, due to the larger N_{0r} and hence lower rain fallspeed in 2-MH in this region.

4. SUMMARY AND CONCLUSIONS

Several 2D and 3D simulations were performed to assess the role of cloud microphysics on modeled squall line morphology and precipitation. All of the simulations produce features characteristic of observed squall lines, including storm-relative front-to-rear outflow at midlevels and rear-to-front inflow at lower levels, enhanced precipitation in the convective region at the leading edge of the storm, and lighter precipitation in the stratiform region. The 2D and 3D simulations were also generally similar. However, significant differences were apparent in terms of some aspects of the storm structure among the simulations with the different microphysical configurations that were tested. Most notably, the two-moment microphysics scheme produced more stratiform rainfall than the one-moment scheme, especially when the dense precipitating ice was treated as graupel instead of hail. This was mostly due to a reduced rain evaporation rate in the stratiform region in the two-moment simulation, as a result of the smaller N_{0r} predicted by the scheme compared with the specified value in the one-moment scheme. In contrast, the two-moment scheme predicted larger N_{0r} in the convective region. These differences in N_{0r} between the stratiform and convective regions were consistent with observations (e.g., Waldvogel 1974; Tokay and Short 1996).

Even more significant differences were seen between the hail and graupel simulations, due mostly to large differences in the respective particle fallspeeds. The slower-falling graupel remained lofted and subsequently detrained from the convective region, producing enhanced rainfall between the stratiform and convective regions. In contrast, fast-falling hail fell to the surface within the convective region, while snow was detrained to the stratiform region, producing a transition zone of weak precipitation between the stratiform and convective regions.

We note that several other microphysical parameters may impact squall line structure that were not tested here. For example, the assumed shape parameter of the rain size distribution, μ, can impact rain evaporation rate and hence cold pool development, surface precipitation rate, etc. Future work will focus on testing these additional parameters. We will also investigate the model using real case studies, including comparison with observations.

Acknowledgments. This work was supported by NOAA Grant NAOAR4310107 (W. Grabowski, PI), U.S. D.O.E. Atmospheric Radiation Measurement (ARM) Grant DE-FG02-03ER63539 (J. Curry, PI), NASA MAP NNG06GBB1G (J. Curry, PI), and by the NSF Science and Technology Center for Multi-Scale Modeling of Atmospheric Processes (CMMAP), managed by Colorado State University under cooperative agreement ATM-0425247. National Center for Atmospheric Research is sponsored by the National Science Foundation.

References.

Biggerstaff, M. I., and R. A. Houze, Jr., 1991: Kinematic and precipitation structure of the 10-11 June 1985 squall line. *Mon. Wea. Rev.*, **119**, 3034-3064.

Bryan, G. H., and J. M. Fritsch, 2002: A benchmark simulation for most nonhydrostatic numerical models. *Mon. Wea. Rev.,* **130**, 2917-2928.

Ferrier, B. S., W.-K. Tao, and J. Simpson, 1995: A double-moment multiple-phase four-class bulk ice scheme. Part II: Simulations of convectgive storms in different large-scale environments and comparisons with other bulk parameterizations. *J. Atmos. Sci.*, **52**, 1001-1033.

Fovell, R. G., and Y. Ogura, 1988: Numerical simulation of a mid-latitude squall line in two dimensions. *J. Atmos. Sci.*, **45**, 3846-3879.

Locatelli, J. D., and P. V. Hobbs, 1974: Fallspeeds and masses of solid precipitation particles, *J. Geophys. Res.,* **79**, 2185-2197.

McCumber, M., W.-K. Tao, J. Simpson, R. Penc, and S.-T. Soong, 1991: Comparison of ice-phase microphysical parameterization schemes using numerical simulations of tropical convection. *J. Appl. Meteor.*, **30**, 985-1004.

Morrison, H., G. Thompson, and V. Tatarskii, 2008: Impact of cloud microphysics on the development of trailing stratiform precipitation in a simulated squall line: Comparison of one- and two-moment schemes. *Mon. Wea. Rev.* (submitted)

Skamarock, W. C., J. B. Klemp, J. Dudhia, D. O. Gill, D. M. Barker, W. Wang, J. G. Powers, 2007: A description of the Advanced Research WRF Version 2. *NCAR Technical Note NCAR/TN-468+STR*.

Tokay, A., and D. A. Short, 1996: Evidence from tropical raindrop spectra of the origin of rain from stratiform versus convective clouds. *J. Appl. Meteor*., **35**, 355-371.

Waldvogel, A., 1974: The N_0 jump of raindrop spectra*. J. Atmos. Sci*., **31**, 1067-1077.

Weisman, M. L., and J. B. Klemp, 1982: The dependence of numerically simulated convective storms on wind shear and buoyancy. *Mon. Wea. Rev.*, **110**, 504-520.

Zipser, E. J., 1969: The role of organized unsaturated convective downdrafts in the structure and rapid decay of an equatorial disturbance. *J. Appl. Meteor.*, **8**, 799-814.

DEEP CONVECTION GENESIS AND MESOSCALE CIRCULATIONS OVER NORTHERN AND CENTRAL ARGENTINA DURING SUMMER

Matilde Nicolini(1) and Yanina García Skabar(2)

(1)Departamento de Ciencias de la Atmósfera y los Océanos. UBA.
Centro de Investigaciones del Mar y la Atmósfera. CONICET/UBA.
(2)Servicio Meteorológico Nacional
Cátedra de Climatología y Fenología Agrícolas. FA - UBA
Buenos Aires. Argentina.
email: nicolini@cima.fcen.uba.ar

1. INTRODUCTION

Maximum frequency of moist deep convection at night over northern central Argentina during summer is found both for environments dominated by convergence related to the presence of different types of low level jets to the east of the Andes (Nicolini et al. 2006) but also when this feature is not present (Torres, 2003, Nicolini and Saulo, 2006, Salio and Nicolini, 2006, Salio et al. 2007). Different processes related to the Andes mountain range as well as west-east gradients in surface characteristics influence the generation of mesoscale circulations that interact with surface friction and large-scale pressure gradients and may gradually force deep moist convection (Nicolini et al, 1987, Borque et al., 2006, Garcia Skabar, 2008). These mesoscale circulations are associated with divergence/convergence patterns in the boundary layer (Segal and Arrit, 1992, Pan et al., 2004 and references therein).

This study addresses different genesis mechanisms of organized convection in the mentioned region. With this objective case studies have been selected in weakly and strongly forced environments and both circulation patterns and deep convection systems are described and related in each case.

2. DATA AND METHODOLOGY

This work has been done using an enriched analysis for the summer 2002-2003, during which the South American Low-Level Jet Experiment (SALLJEX) was performed in Southeastern South America (Vera et al., 2006). SALLJEX aimed to monitor, quantify and analyze the low-level circulation over this region and its related precipitation. SALLJEX data set provides a quantitative improvement in both spatial and temporal resolution over that of the operational network. Enriched analyses were generated ingesting all available data with a higher spatial and temporal resolution than that available for the region, following a downscaling methodology, using Brazilian Regional Atmospheric Modeling System (BRAMS, see Cotton et al., 2003).

This model was applied to obtain analysis every three hours, with a horizontal resolution of 80 km covering mostly South America and an enhanced domain with 20 km resolution for the region encompassing Central and Northern Argentina, southern Brazil, Bolivia, Paraguay and Uruguay (García Skabar and Nicolini, 2006).

In order to identify the convective systems and their life cycle IR brightness temperature data was employed at half hourly intervals with a horizontal resolution of 4km over the area between 10ºS-40ºS and 40ºW- 75ºW for the same period Janowiak et al. (2001); data online at http://lake.nascom.nasa.gov/).

3. RESULTS

Previous studies and a detailed analysis of the synoptic situations and circulations in the selected region during SALLJEX using the enriched and higher resolution analyses identified the following processes preceding and forcing convective events in a moist unstable environment:

- Low level convergence related to mesoscale circulations associated with a complex non homogeneous surface roughly described by a steep mountain-broad valley terrain and to horizontal gradients in surface properties. This circulations dominate in weaker synoptic environments and typically is responsible of generating shallower and less extended convection more frequently over the higher western regions that may intensify and enlarge its horizontal dimension when propagates later to the east over central Argentina.
- Low level convergence related to a frontal zone that usually remains quasi-stationary between 35 and 40S during a couple of days or more and before starting to propagate across the region forces initial convection closely linked with the synoptic front. This mechanism is also responsible of the genesis of organized convection over the northernmost provinces of Argentina and over southern Bolivia when the frontal zone reaches these latitudes (some of these events are described in Torres, 2003).
- An upper level short trough approaching and destabilizing the environment in the study area.
- Low level convergence related to the SALLJ downwind of the jet maximum in the warm and moist air mass ahead of a quasi-stationary front. This mechanism may force organized convection particularly intense (in terms of horizontal extension, duration and convective tops high) and the convergence in this strong synoptic situation affects a deeper layer that dominates over the nocturnal mesoscale circulations limited to a usually shallower nocturnal boundary layer. These cases have been analyzed by Nicolini and Saulo, 2006, Borque et al., 2006 and Salio et al., 2007, among others.

Follows the analysis of selected convective cases during which one of the before mentioned processes or a combination of them have been recognized during the SALLJEX warm season.

3.1. CASE STUDY: November 16, 2002

Deep intense convection initiates during this day over an area located in the southern part of the Cordoba province characterized by the presence of low orography around 19 UTC (not shown). This convective system increases in size and eventually merges with another mesoscale system simultaneously generated over Buenos Aires province related to a quasi-stationary front. This merging evolves in a convective line at 23 UTC. The focus of this analysis is in the organized convection at 22 UTC around 27ºS and 65ºW westward and near higher mountains than the previously mentioned system. Figure 1 displays the evolution of this system from the initial to the dissipation stages with a clear eastward propagation ending in the early morning on November 17 over Uruguay and southern Brazil. Later in the afternoon a similar convective cycle starts over Cordoba.

The synoptic situation was dominated by an upper level short trough approaching northwestern Argentina preceded by divergence at 200 hPa (see Fig. 2c) and a cloudy pattern clearly distinguishable in the satellite images at 18 UTC (not shown). Rising motions related to this upper level trough are evident earlier along the meridionally oriented western high terrain since 14 UTC, generating weak convective areas along this mountain range. Figure 2a denotes the northeasterly flow that supports warm and moist advection (temperatures near the surface higher than 32C) and the pressure pattern insinuate a thermal low that deepens at this time with pressure values lower than 993 hPa. Both the fields of temperatures at 2m above the surface and the equivalent potential temperature denote the presence of a frontal zone and of warm air penetrating almost up to 40ºS. The northerly flow is also apparent at 850 hPa and the presence of a particularly strong and meridionally extended low level jet is shown in Figure 3. It is interesting to remark the intensification and displacement of the axis of the low-level jet during the period displayed in Figure 3. The mesocale convective system also displays this intensification and displacement.

.

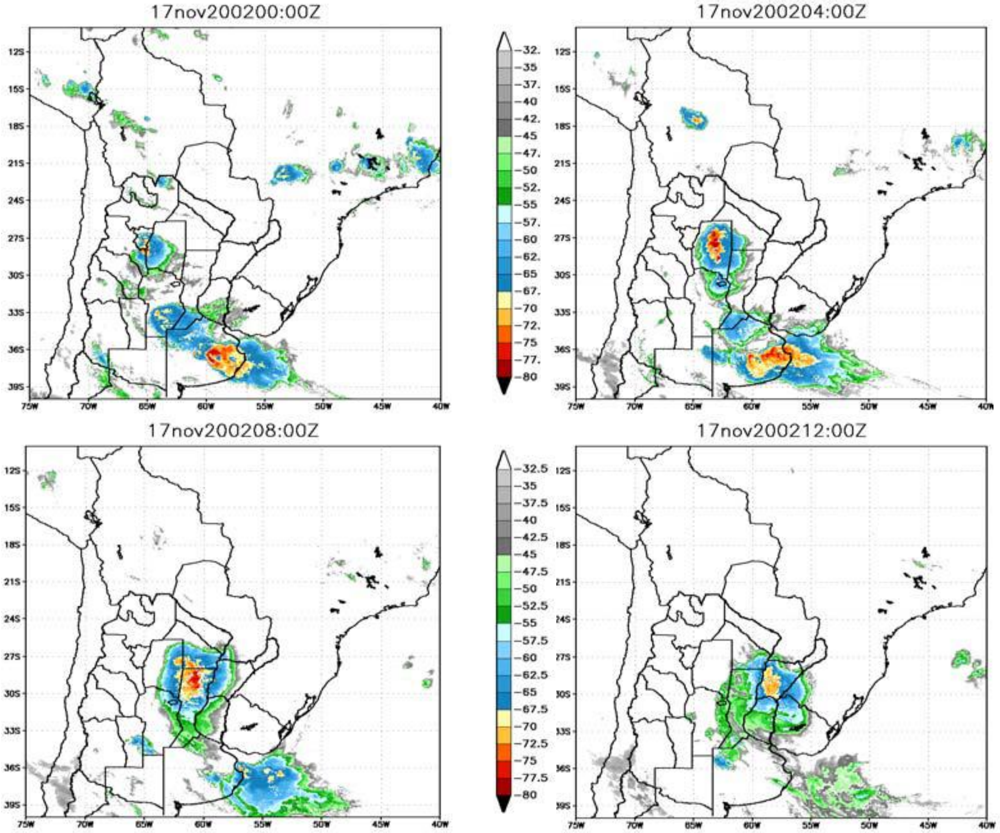

Figure 1: IR brightness temperature from satellite image for November 17, 2002 at 00, 04, 08 and 12 UTC

The genesis of convection over Cordoba seems to be partially mechanically forced by the presence of the mountains as the horizontal flux convergence and rising motions at the time convection originates in this area are constrained very near the high terrain (Fig. 4a and b) and partially related to convergence related to the frontal zone (more clear to the south of the cross section as depicted in Fig. 3 at 850 hPa), whereas the convergence centered at 2 km and at 63W (also Fig. 4a) is presumably more related to the desacceleration at the leading edge of the northerly current that at this time (afternoon) is weaker.

As to the system that starts at 22 UTC it is more clearly bounded to the orography in its genesis as is evident in Figure 4c and d while the maximum in water vapor flux convergence present around 2km high dominates later as the convective system intensifies and propagates while it stays linked to the low-level jet convergence area.

Figure 5 displays the evolution of the divergence in the boundary layer in the period 18 UTC November 16 (afternoon time) and 9 UTC, November 17 (sunrise time) to highlight the presence of a diurnal cycle in the boundary layer related to a mesoscale breeze related to the presence of a particular topography dominated by the presence of the Andes to the west and broad valleys eastward this mountain range. The height of the boundary layer has been determined using a threshold criterion for the potential temperature vertical gradient and the divergence is estimated at each grid point as a vertical average weighted at each level by the thickness of the layer that represents the corresponding divergence value.

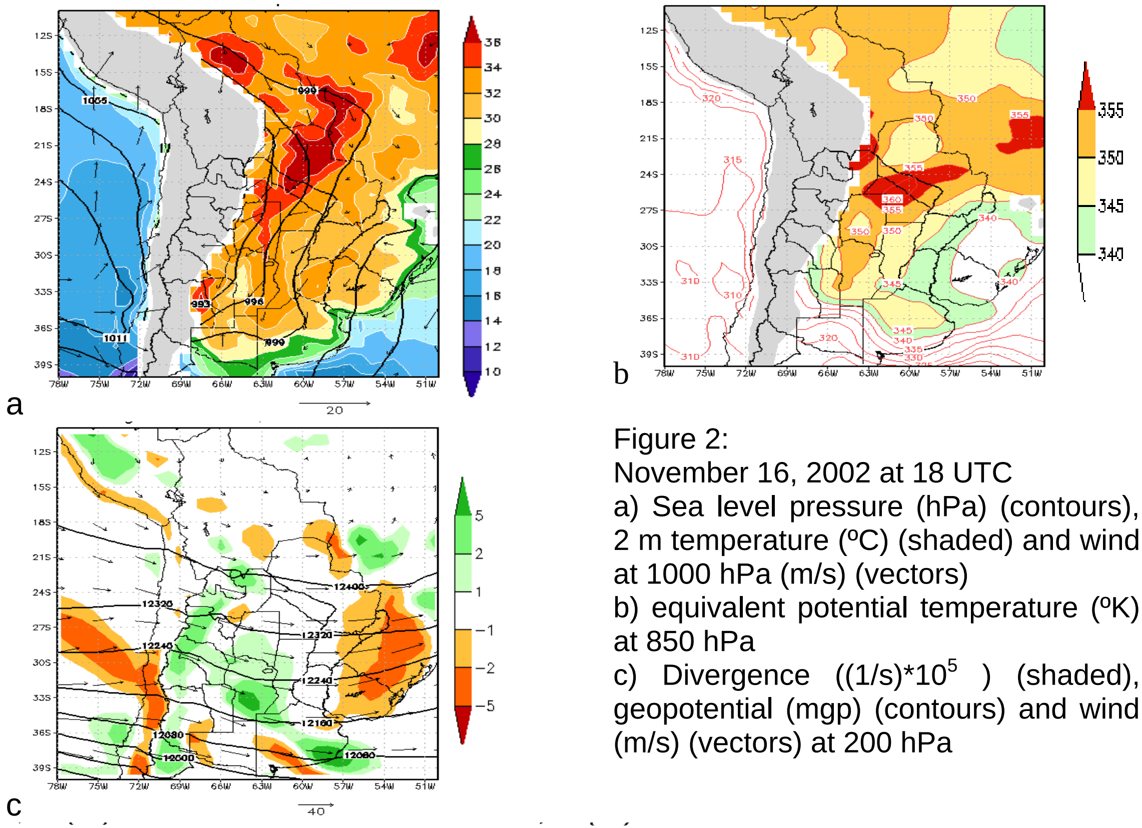

Figure 2:
November 16, 2002 at 18 UTC
a) Sea level pressure (hPa) (contours), 2 m temperature (ºC) (shaded) and wind at 1000 hPa (m/s) (vectors)
b) equivalent potential temperature (ºK) at 850 hPa
c) Divergence ((1/s)*10^5) (shaded), geopotential (mgp) (contours) and wind (m/s) (vectors) at 200 hPa

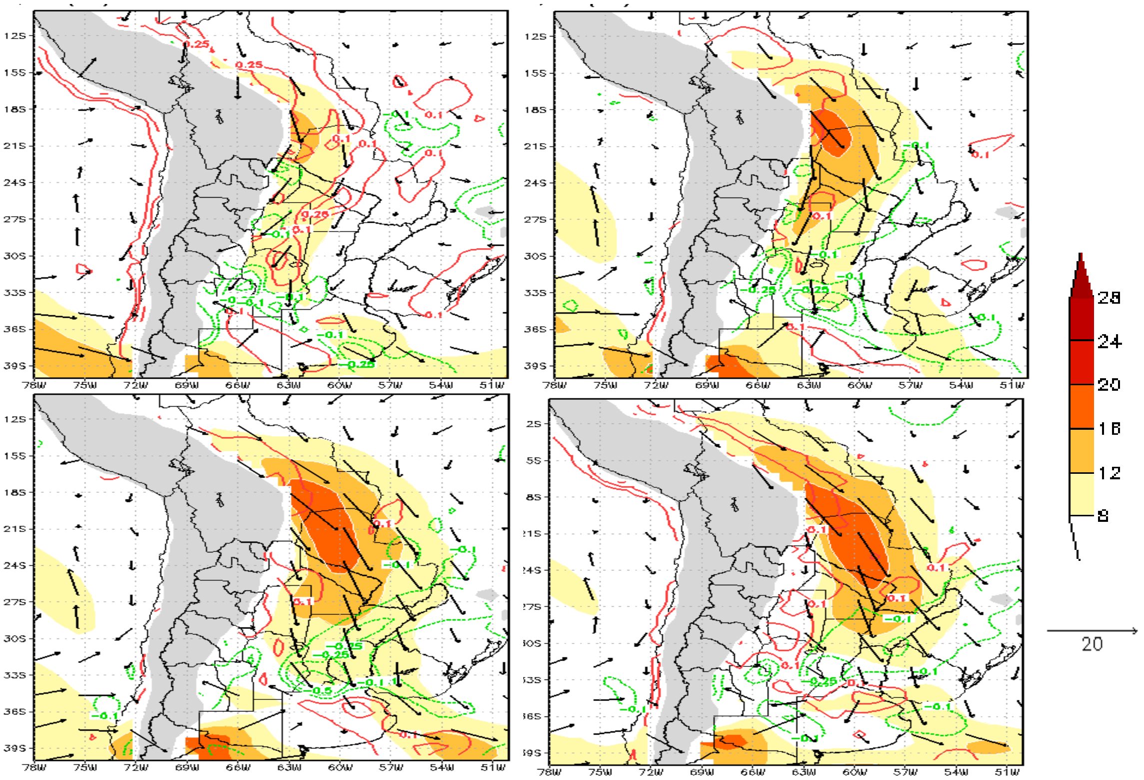

Figure 3: water vapor flux divergence ((1/s)*10^6) (contours), wind speed (m/s) (shaded), and wind (m/s) (vectors) at 850 hPa for November 16, 2002 at 18 UTC, and November 17, 2002 at 00,06 and 12 UTC.

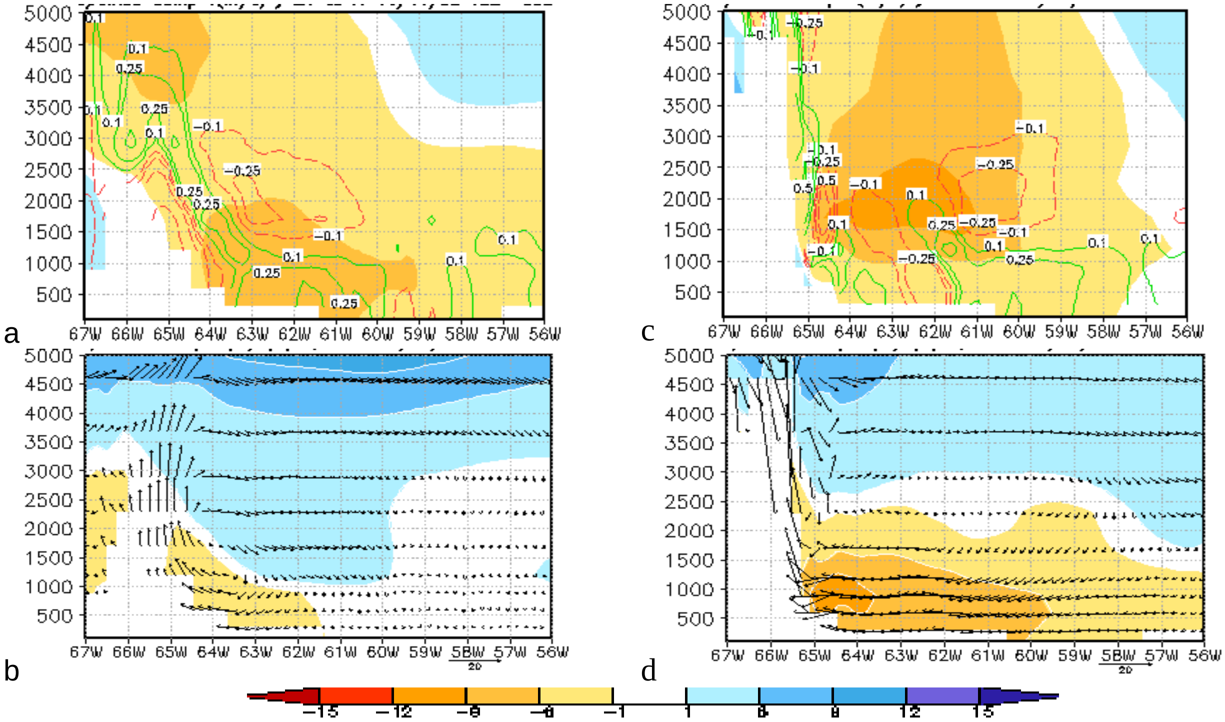

Figure 4: a) Meridional wind component (m/s) (shaded), horizontal water flux divergence (1/s)*10^6) (contours), b) zonal wind component (m/s) (shaded) and U, W*100 vectors (m/s) (for 18 UTC November 16 at 33ºS. c) and d) idem for 21 UTC November 16 at 27ºS

Divergence is prevalent eastward 65W before convection initiates and is replaced by convergence that starts first near the mountains to force convection at low levels. Once this mechanism is activated and the nocturnal convergence pattern spreads out over the plains convection is favored eastward and goes through the rest of its life cycle in phase with the low-level jet convergence that dominates above the estimated boundary layer and attains its maximum during nighttime as is apparent in Figure 3.

3.2. CASE STUDY: December 13-14, 2002

This situation is characterized by weak convection over the mountains and in the eastern slopes in the afternoon (not shown) until 00 UTC December 14, when a system starts to develop near 28S, 65W in the mountain area and another more intense system originates almost simultaneously northward near the frontier between Argentina, Bolivia and Paraguay. These systems evolve during the night propagating to the northeast and while the first one starts to dissipate at 9UTC the second one lasts longer initiating dissipation around 12UTC (see Fig. 6).

The synoptic situation is dominated by an anticyclonic circulation being the convective systems positioned in the western flank where an east-northeastern flow prevails while the rest of the country is dominated by southerly winds behind a cold frontal zone. A short wave is propagating at middle and upper levels from the Pacific (see Fig. 7b) proceeded by divergence. Also temperatures near the surface exceed 30 C (see Fig. 7a). These patterns and unstable conditions for vertical motions originating in low levels (see the CAPE values in an extended and narrow tongue parallel to the mountains in Fig. 7b) favor convection. Stable conditions related to the migratory anticyclone constrains convection to develop within the limited domain near the mountain region as evident in Figure 6.

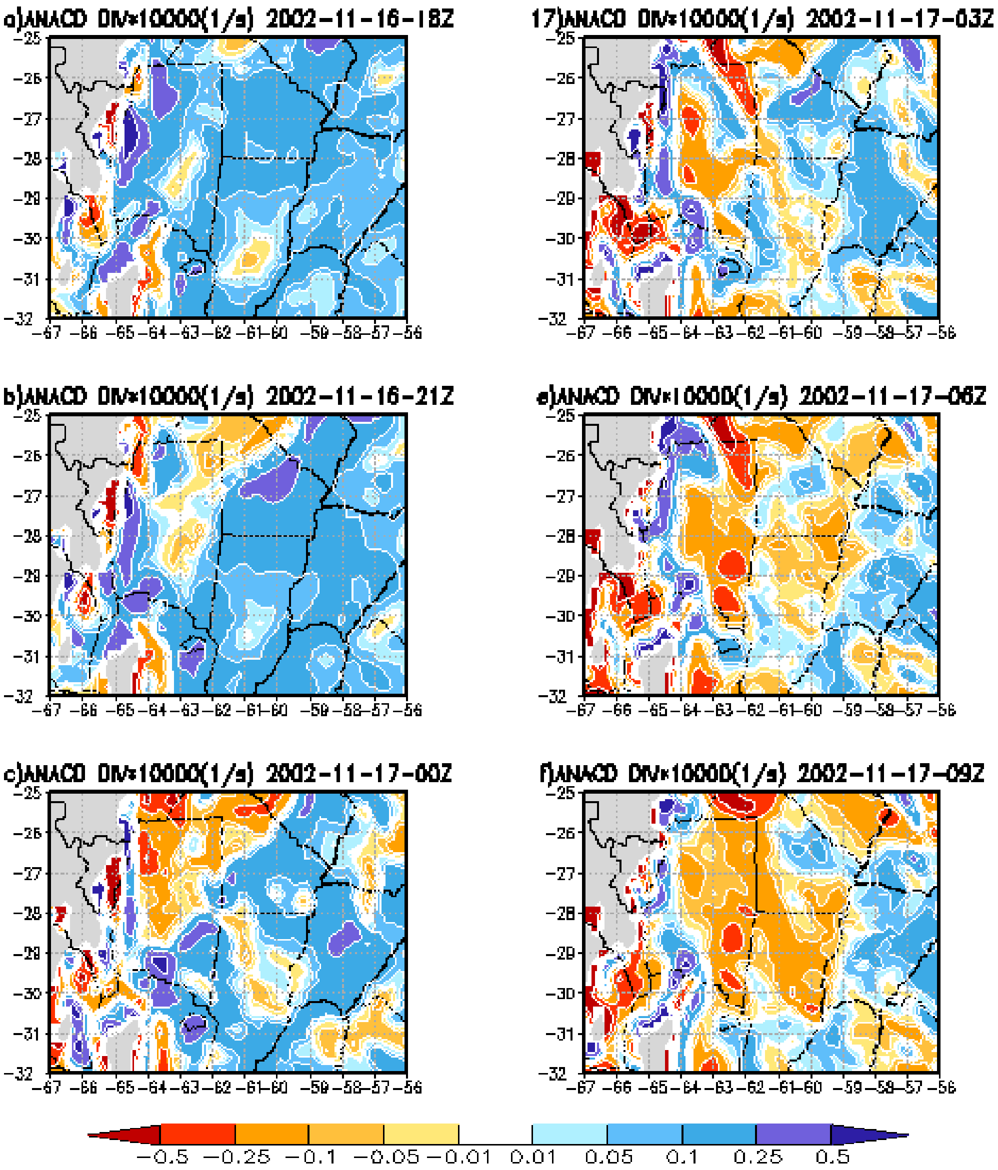

Figure 5: Divergence in the boundary layer (1/s*10^4): a) 18UTC, b) 21UTC for November 16, 2002 and c) 0UTC, d) 3UTC, e) 6UTC and f) 9 UTC for November 17, 2002.

In contrast with the situation of November 16, 2002, this case is characterized by the absence of a forced lifting due to the presence of frontal zone and of a low-level jet originating in tropical latitudes. Warm and moist advection is weaker in this case and restricted to extratropical latitudes instead. This environment is more prone to be controlled by mesoscale circulations driven by a radiative diurnal cycle. Figure 8 displays the 12 hours cycle of divergence patterns in the boundary layer. As in the previous case afternoon hours are characterized by divergence until 00 UTC when convergence starts to be apparent near the mountains in the region where convection initiates. Divergent pattern eastward is perturbed by convergence areas that develop related to cyclonic vorticity advection associated with an extended upper level trough that appears at low levels as a cyclonic curvature in the pressure pattern (see Fig. 7a). .

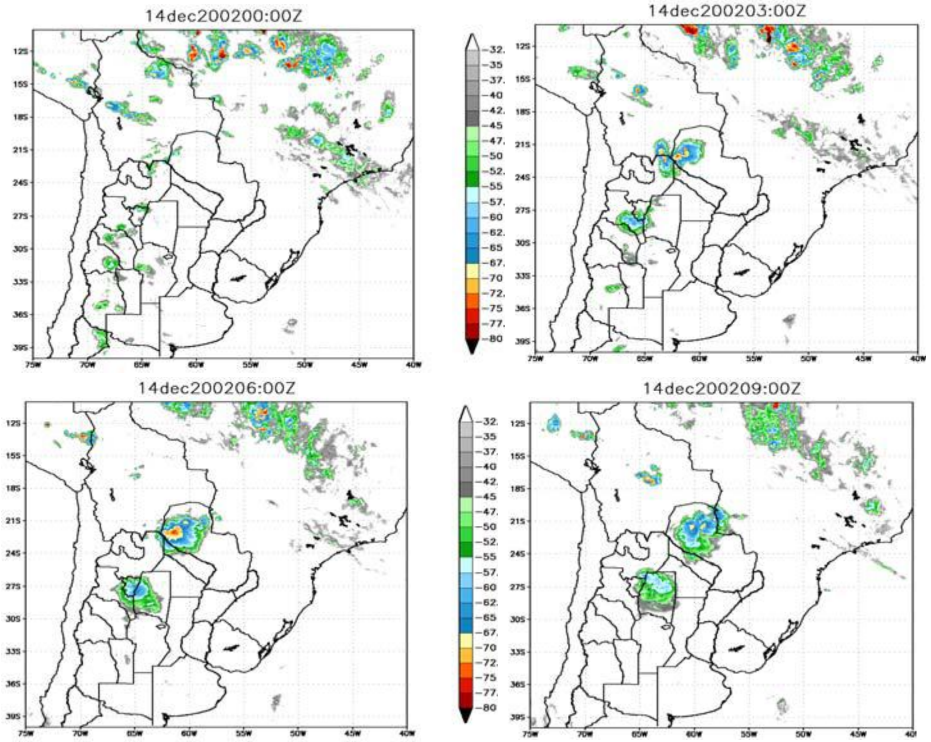

Figure 6: IR brightness temperature from satellite image for December 14, 2002 at 00, 03, 06 and 09 UTC

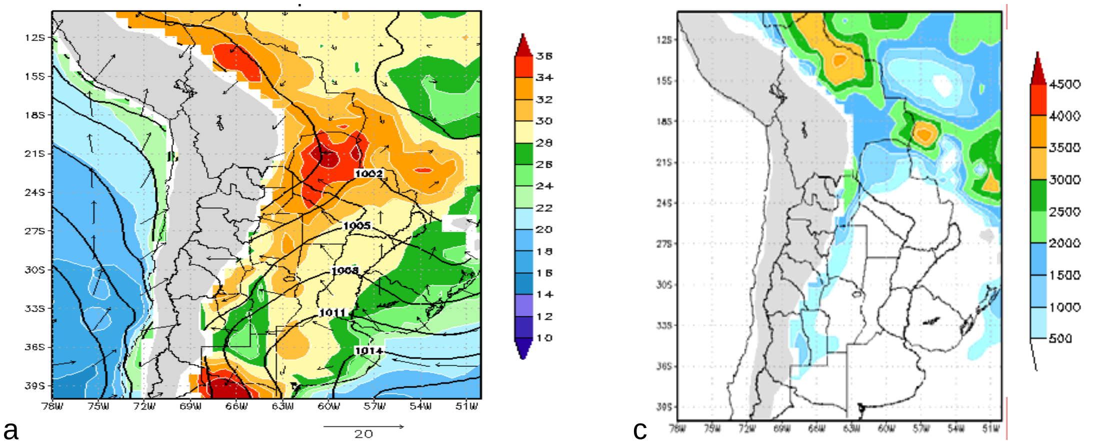

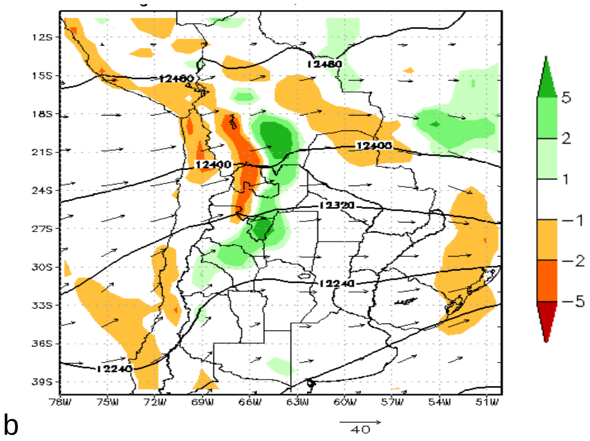

Figure 7:
December 13, 2002 at 18 UTC
a) Sea level pressure (hPa) (contours), 2 m temperature (ºC) (shaded) and wind at 1000 hPa (m/s) (vectors)
b) Divergence ((1/s)*10^{5}) (shaded), geopotential (mgp) (contours) and wind (m/s) (vectors) at 200 hPa
December 14, 2002 at 00 UTC
c) CAPE

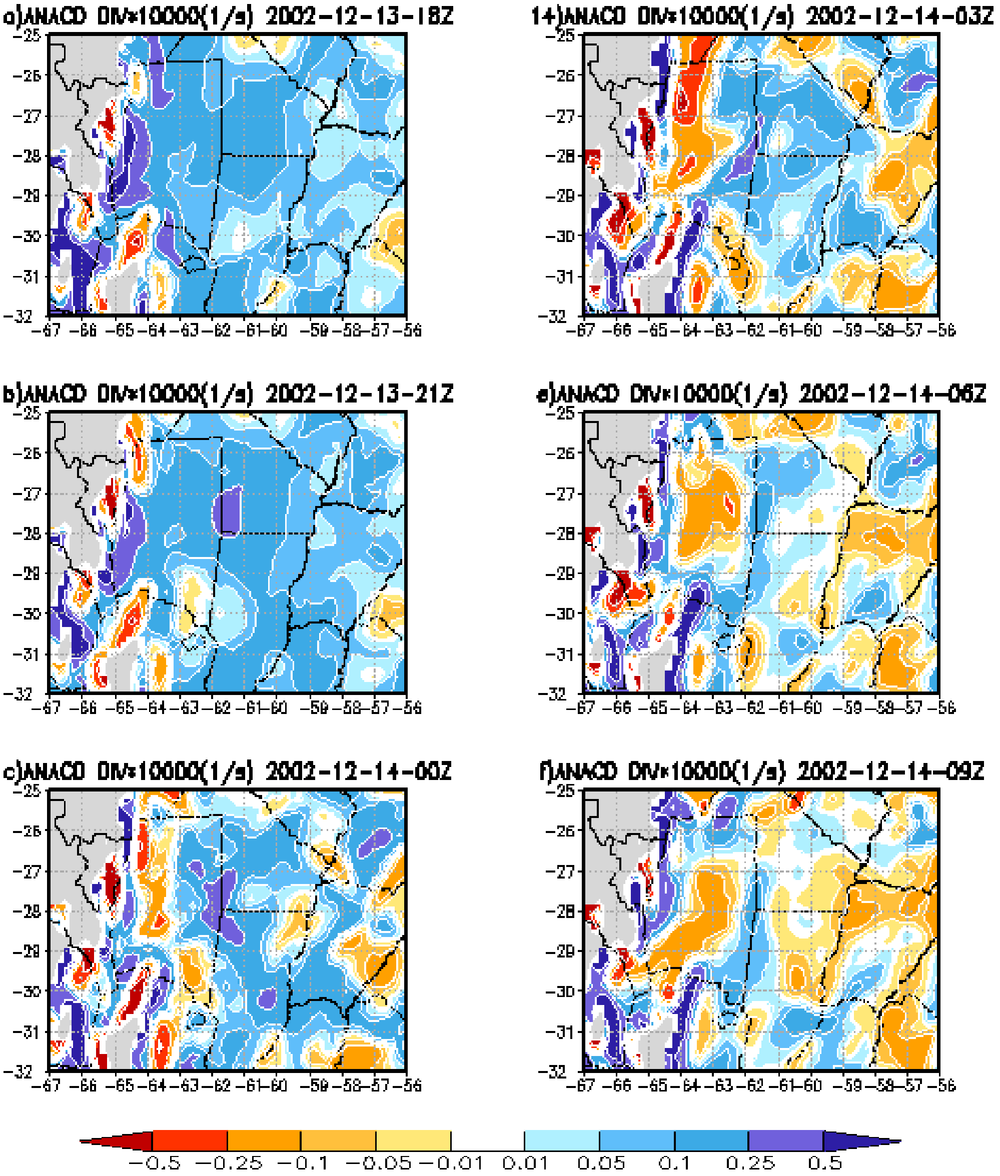

Figure 8: Divergences in the boundary layer (1/s*10^4): a) 18UTC, b) 21UTC for December 13, 2002 and c) 0UTC, d) 3UTC, e) 6UTC and f) 9 UTC for December 14, 2002.

The genesis of the system developed within Argentina is related to this mesoscale circulation and the presence of the orography as displayed in Figure 9 three hours earlier.

4. DISCUSSION

Processes preceding and forcing convective events in a moist unstable environment have been identified in two case studies: Low level convergence related to the SALLJ downwind of the jet maximum in the warm and moist air mass ahead of a quasi-stationary front is the dominant mechanism on the November 16, 2002 case as found in previous studies. This case was also controlled by the presence of a short wave trough and a frontal zone. A deep thermal low pressure system develops to the lee of the Andes over Northwestern Argentina enhancing the low-level jet. Mesoscale circulations are altered once convection develops and dominates the different patterns.

The effect of a diurnal cycle in a divergence pattern within the boundary layer to the east of the Andes is investigated. This pattern is characterized by convergence and upward motions at night, and divergence and downward motions at daytime. An orogenic mesoscale convective system initiates at early evening on December 13-14, 2002 in phase with convergence and develops and decays during nighttime not supported by a low-level jet during its life cycle.

Results provide insight to perform further numerical experiments to isolate and find interaction between factors that control both the mesoscale circulations and the convection.,

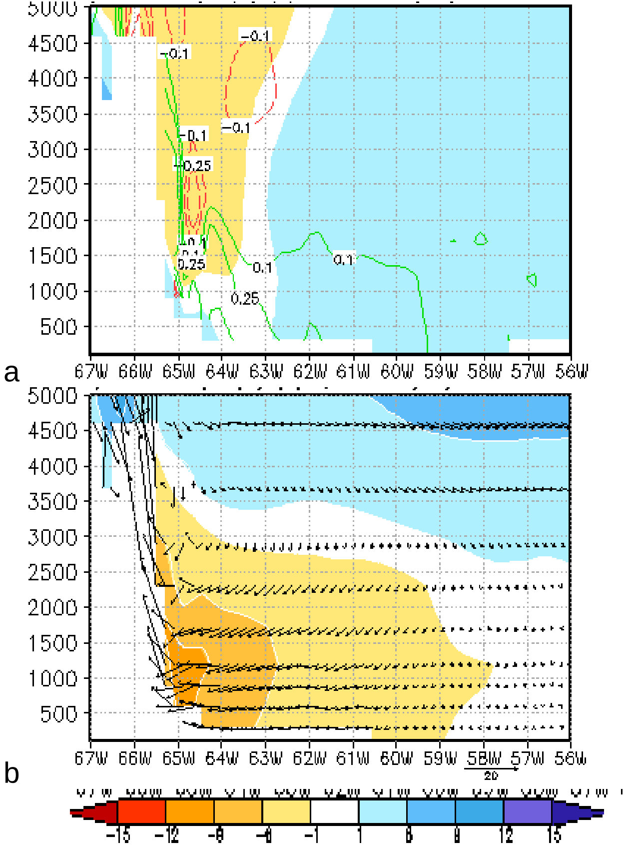

Figure 9: a) Meridional wind component (m/s) (shaded), horizontal water flux divergence (1/s)*10^6) (contours), b) zonal wind component(m/s) (shaded) and U,W*100 vectors (m/s) (vectors) for 18 UTC December 13 at 27ºS.

ACKNOWLEDGMENTS

The authors thanks de Previsão de Tempo e Estudos Climáticos (CPTEC) and Universidade de São Paulo (USP) for providing version BRams 3.2, particulary to Dr. Pedro Leite Silva Dias. We also thanks SALLJEX, that was supported by NOAA/OGP, NSF ATM 0106776 (USA), FAPESP Grant 01/13816-1 (Brasil),ANPCYT PICT 07-06671 and UBACYT 055 (Argentina). NCEP GDAS analysis data were provided by the NOAA and the soil moisture fields by USP/CPTEC. This research was partially supported by ANPCYT through Project PICT 2003 07-14420, by Univ. de Buenos Aires through Project X266, and by CONICET through Project PIP 5582.

REFERENCES

Borque, P. C.; Vidal, R.; Salio, P.; Nicolini, M; García Skabar, Yanina, 2006: Previous conditions associated to a development of a mesoscale convective system under South American Low-Level Jet event: A case study.8thInternational Conference on Southern Hemisphere Meteorology and Oceanography (8ICSHMO). Foz do Iguaçu, Brazil, April 24-28, 2006. 1677- 1682.

García Skabar, Y. y M. Nicolini, 2006: Downscaling and assimilation of an enhanced data base in Southeastern South America. 8th International Conference on Southern Hemisphere Meteorology and Oceanography(8ICSHMO). Foz do Iguaçu, Brazil, April 24-28, 2006, pág. 23-27.

García Skabar, Y. ,2008: Análisis enriquecidos, evaluación de su impacto en el pronóstico y su aplicación para describir circulaciones de mesoescala en el centro y norte de Argentina (Enriched analyses, evaluation of their impact on the forecast and its application to describe mesoscale circulations in central and northern Argentina. Doctoral Dissertation. University of Buenos Aires, 168 pp.

Janowiak J., R. Joyce, and Y. Yarosh, 2001: A real time global half hourly pixel resolution infrared dataset and its applications. B. Am. Met. Soc., **82**, N° 2, 205–217.

Nicolini, M., J. Paegle y M. L. Altinger, 1987: Numerical simulation of convection and boundary layer convergence. Preprints, Second Int. Congress of Meteorology, Buenos Aires, Argentina, Latin Amer. Meteor. Fed. and Meteor.Soc., pages 8.5.1-8.5.7.

Nicolini, M. y A. C. Saulo, 2006: Modeled Chaco low-level jets and related precipitation patterns during the 1997-1998 warm season. Meteorology and Atmospheric Physics, vol. 94, 129-143.

Nicolini, M., P. Salio and P. Borque, 2006: Thermodynamic and kinematic characterization of the low-level troposphere during SALLJEX in different large-scale environments. 8th International Conference on Southern Hemisphere Meteorology and Oceanography (8ICSHMO). Foz do Iguaçu, Brazil, April 24-28, 2006, p.1141-1148.

Pan, Z. ,M. Segal y R.W. Arritt, 2004: Role of Topography in Forcing Low-Level Jets in the Central United States during the 1993 Flood-Altered Terrain Simulations. Mon. Wea. Rev., Vol.132, Nº1,pp. 396-403.

Salio, P. y M. Nicolini, 2006: Seasonal characterization on the diurnal cycle of convection frequency over Southeastern South America under different low-jet conditions. 8th International Conference on Southern Hemisphere Meteorology and Oceanography (8ICSHMO). Foz do Iguaçu, Brazil, April 24-28, 2006, p. 1157-1162.

Salio, P., Nicolini, M. and E. J. Zipser, 2007: Mesoscale Convective Systems over Southeastern South America and their relationship with the South American Low Level Jet. Mon. Wea. Rev, Vol. 135, 4, 1290-1309.

Segal, M. and R.W. Arritt, 1992: Nonclassical mesoscale circulations caused by surface sensible heat-flux gradients. Bull. Amer. Meteor. Soc., Vol. 73, Nº 10, 1593-1604.

Torres, 2003: Sistemas convectivos en mesoescala altamente precipitantes en el norte y centro de Argentina (Heavily precipitating mesoscale convective systems over central and northern Argentina). Doctoral Dissertation. University of Buenos Aires, 132 pp.

Vera, C., and Coauthors, 2006: The South American low-level jet experiment. Bull. Amer. Meteor. Soc., 87, 63-77.

HOW WELL CAN A BULK SCHEME REPRODUCE THE MICROPHYSICAL PROCESSES WITHIN A CONVECTIVE STORM? - COMPARISONS TO A SPECTRAL BIN MODEL

Heike Noppel*, Alexander Khain†, Andrei Pokrovsky†, Ulrich Blahak*, and Klaus D. Beheng*
∗ Institut für Meteorologie und Klimaforschung,Universität/Forschungszentrum Karlsruhe, Germany
† Institute of Earth Sciences, Hebrew University of Jerusalem, Israel

1 INTRODUCTION

Recent studies of cloud interactions with particulate air pollution, performed mostly on a conceptual level, suggest that pollution aerosols can invigorate convection into severe storms by slowing down the conversion of cloud drops into precipitation.

The aim of the EU-project ANTISTORM (Anthropogenic Aerosols Triggering and Invigorating Severe Storms) was to study the impact of aerosols on the severity of convective storms and to develop models that should help to improve forecasting of such storms.

Especially for forecasting severe storms, 3D-simulations using a sufficiently large model domain and a high horizontal resolution are necessary while at the same time computing time is limited. Consequently, bin parameterizations of cloud microphysics are computationally too costly for this purpose; only bulk schemes are feasible. But bulk microphysical models comprise many simplifications, especially when only one moment of the particle size distribution (e.g., mass density) is predicted while further assumptions have to be made to derive other moments (e.g number density) as well. However, bulk schemes using more than one moment as a prognostic variable seem to be a good compromise.

Comparisons between the 2-moment scheme by Seifert and Beheng (2006) and the spectral bin scheme by Khain et al. (2004) using the the same 2D-dynamical framework were performed in order to show how well the bulk scheme can reproduce the microphysical processes within a convective storm including the impact of aerosol concentration.

2 MODEL AND MODEL SETUP

The 2-moment scheme was implemented into the 2-dimensional model HUCM (Hebrew University Cloud Model, Khain et al., 2004). HUCM includes a spectral bin model with 8 particle categories (CCN, drops, plates, columns, dendrites, snow, graupel, hail) with 43 bins each. The bulk model was implemented in a way that allows to run both microphysical schemes in parallel, where only bin microphysics feed back on dynamics, i.e. wind and temperature fields are determined by the bin model and the bulk model only reacts on them. However, it was necessary to introduce an extra specific humidity for the bulk model, that performs saturation adjustment at the end of the microphysical part while the bin scheme allows for non-zero supersaturation at each time step. Hence, if the bulk model was driven by bin humidity this would mean that in every microphysical time step water vapor would be added to the bulk model, leading to unrealistically high LWC values.

Originally the bulk scheme had included 5 particle categories (cloud droplets, raindrops, cloud ice, snow, and graupel) but was recently extended by a hail class (Blahak, 2008). Additionally, a new cloud droplet nucleation scheme based on look-up tables by Segal and Khain (2006) was implemented and the shape parameter of the assumed raindrop size distribution has been made dependent on mean particle size for sedimentation and evaporation (Seifert, 2008).

Main differences between the bin and the bulk scheme are listed in Tab. 1. Additionally the particles have different characteristics, e.g., bulk density and terminal fall velocity.

In adjustment to the bin scheme, shedding was completely switched off in the bulk scheme for the model runs presented in this paper. However, shed-

---

[*] *Corresp. author address:* Heike Noppel, Institut für Meteorologie und Klimaforschung, Universität / Forschungszentrum Karlsruhe, P.O.Box 3640, D-76021 Karlsruhe, Germany; e-mail: heike.noppel@imk.fzk.de.

Table 1: *Main differences between the bin and the bulk scheme.*

spectral bin	**2-moment bulk**
8 particle categories (drops, plates, columns, dendrites, snow, graupel, hail, CCN)	6 particle categories (cloud droplets, raindrops, cloud ice, snow, graupel, hail)
prognostic variables: masses in 43 bins for each of the 8 categories + liquid water fraction for each bin for ice particles → $(8+6) \times 43 = 602$ prognostic variables	prognostic variables: mass density (q) and number density (n) for each of the 6 categories → 12 prognostic variables
43 bins for each category → size distribution calculated explicitly	size distributions assumed to be a generalized gamma distribution $f(x) = Ax^{\nu}\exp(-\lambda x^{\mu})$ with A and λ determined by the 0th and 1st moment, (q and n), $x =$ particle mass, and μ and ν prescribed for each particle class (as a constant or a function of mean particle size)
full CCN budget (no sources)	no CCN budget (no sources, no sinks, no transport)

ding has recently been implemented into the bin scheme, and further improvements are currently undertaken.

A HUCM standard setup was used with a grid spacing of Δx = 350 m and Δz = 125 m, 513 grid points in the horizontal and 129 in the vertical. Model runs with idealized initial soundings were performed. All have same CAPE (2200 J kg$^-1$) but different cloud base temperature. As an example Fig. 1 shows the sounding with a cloud base temperature of 20 °C. The same initial wind profile was assumed for all runs (Fig. 2) and convection was triggered by a cold bubble situated at a higher level.

Simulations with low and high aerosol concentration were performed leading to typical maximum cloud droplet concentrations of about 100 cm^{-3} and 1000 cm^{-3}, respectively.

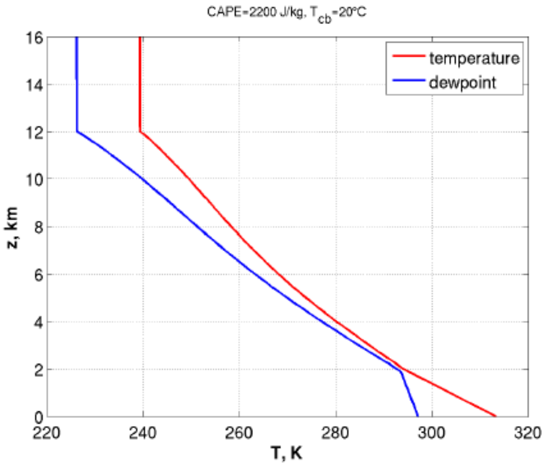

Fig. 1: Profiles of air temperature and dewpoint used to initialize the model for the warm case (20 °C at cloud base).

3 RESULTS

As an example, preliminary results for the run with a cloud base temperature of 20 °C are presented here.

Updrafts are very similar for low and high CCN concentration, with maximum values of about 30 m s^{-1} and typical downdrafts of -10 to -20 m s^{-1} (Fig. 3) with the first cell being rather weak and the secondary and further cells more intense. Please remember that the wind and temperature fields are exactly the same for the spectral bin and the 2-moment

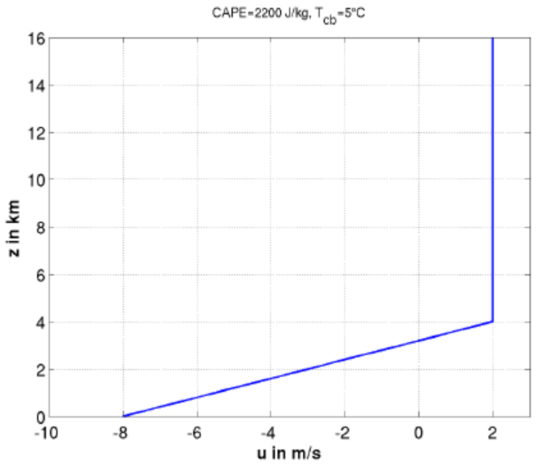

Fig. 2: Initial wind profile used for all model runs..

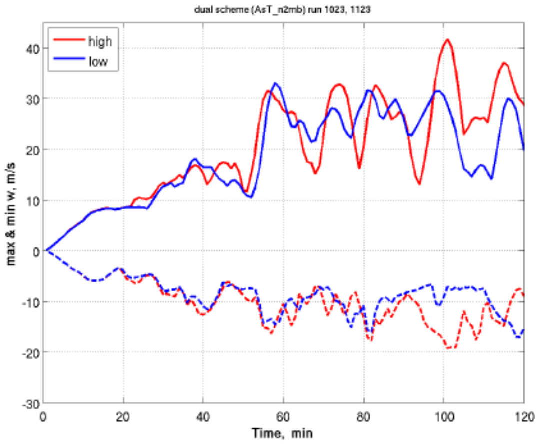

Fig. 3: Maximum and minimum vertical wind speed for high (red) and low (blue) aerosol concentration.

bulk scheme.

Precipitation starts slightly later with the bulk scheme and as precipitation rates are about the same for the first 90 min, the accumulated amount remains lower than with the bin scheme (Fig. 4). In both microphysical schemes higher aerosol (CCN) concentration leads to a higher amount of total accumulated precipitation at ground. For the low aerosol case bin and bulk microphysics yield about the same amount of hail at ground and in both schemes CCN concentration affects the partitioning of the accumulated precipitation between rain and hail, but in the opposite direction: with the bin scheme an increase from low to high CCN concentration results in a strong increase in accumulated hail, while with the bulk scheme it leads to a decrease.

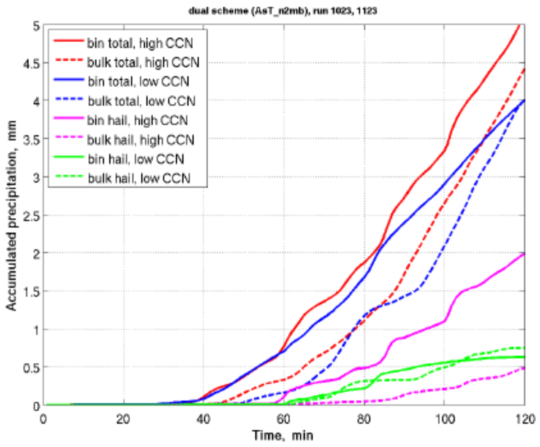

Fig. 4: Grid average of accumulated precipitation at ground by the spectral bin scheme (solid lines) and the two-moment bulk scheme (dashed lines); red: *total, high CCN concentration,* blue*: total, low CCN,* magenta: *hail, high CCN,* green*: hail, low CCN.*

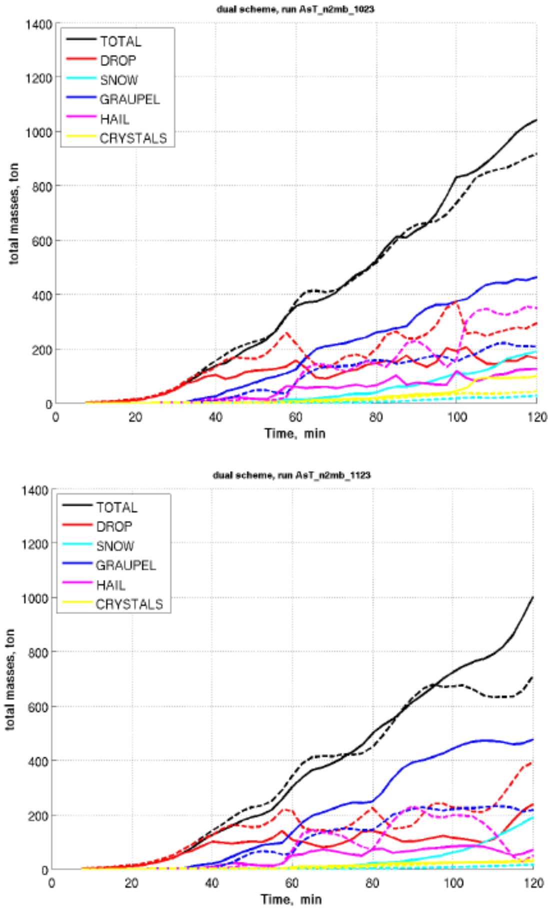

Fig. 5: Time series of total hydrometeor masses for high (top) and low (bottom) CCN concentration; black: *total of all categories,* red*: drops,* cyan*: snow,* blue: *graupel,* magenta*: hail,* yellow*: ice crystals.*

Temporal evolution of total hydrometeor mass agrees very well (Fig. 5). However, masses of the single particle classes show some differences. When comparing liquid water content (LWC) one has to bear in mind that the bin particles may have a liquid water fraction of more than 90%, which is not included in the LWC. This is one reason why LWC is higher in the bulk scheme. The partitioning between the hydrometeor classes of frozen particles shows stronger differences though. But to decide how and when to transfer particles between the ice

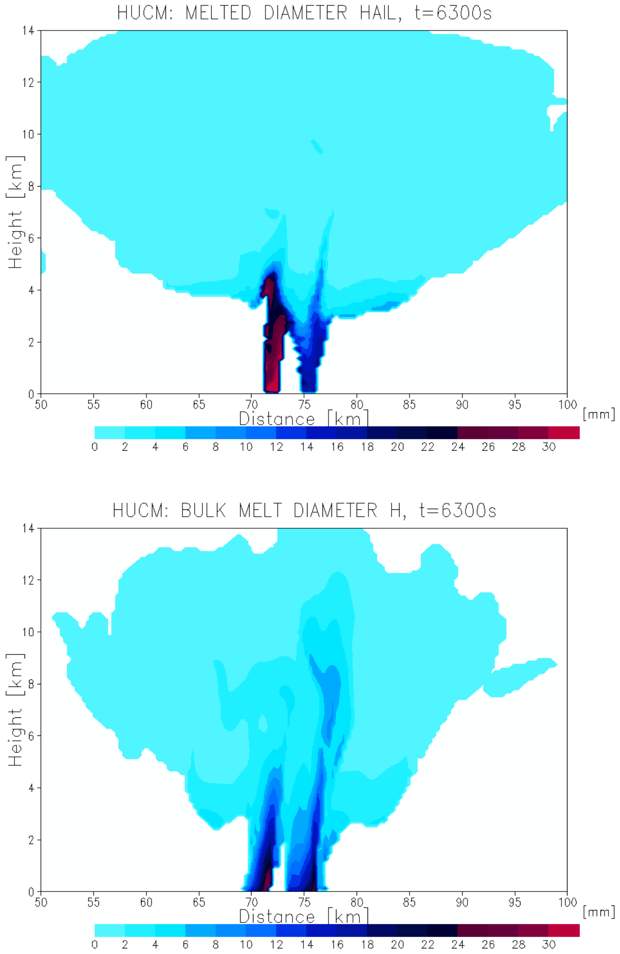

Fig. 6: Mass weighted mean diameter (mm) of hail particles in the bin scheme (top) and the bulk scheme (bottom) after 105 min simulation time for low CCN concentration.

classes, (e.g, from snow to graupel or from graupel to hail) is not trivial and the approaches to do that are different in both schemes. Hence, discrepancies have to be expected. For example, snow and graupel masses are higher in the bin scheme than in the bulk scheme, but hail mass is lower.

An important question is, whether the model is able to produce large hailstones, as they occur in strong convective storms. As an example, mass weighted mean particle diameters of hail after 105 min of the low CCN run are shown in Fig. 6. Generally, for high and low CCN concentration both schemes produce quite large hail particles with typical mean diameters of about 15 to 40 mm within the hail shaft, where values of more than 30 mm only occur in the bin scheme. Hailstones are much smaller at higher altitudes and tend to be a little bit larger in the bulk scheme. The results do not suggest any significant general impact of CCN concentration on mean hail particle diameter.

4 CONCLUSIONS AND OUTLOOK

Generally, the results of the bin and the 2-moment bulk microphysical scheme agree well (e.g., accumulated total precipitation and size of hailstones) indicating that the bulk scheme is in fact able to reproduce the microphysical processes within a convective storm.

The impact of CCN concentration on total accumultated precipitation is similar in both schemes. With regard to the amount of hail, both schemes show a significant CCN effect, though in opposite directions. To find the reason for this, further investigations will be necessary, including simulations with an updated version of the bin scheme, which includes shedding and a new approach to transfer snow to graupel.

REFERENCES

Blahak, U., 2008: Towards a Better Representation of High Density Ice Particles in a State-of-the-Art Two-Moment Bulk Microphysical Scheme. *15th International Conference on Clouds and Precipitation, July 7-11. 2008, Cancun, Mexico*

Khain, A., Pokrovsky, A, Pinsky, M., Seifert, A., Philips, V., 2004: Simulation of effects of tropospheric aerosols on deep convective clouds using a spectral microphysics mixed-phase cumulus cloud model: Part I. Model description and possible applications. *J. Atmos. Sci.*, **61**, 2963-2982.

Segal, Y. and Khain, A., 2006: Dependence of droplet concentration on aerosol condtions in different cloud types: Application to droplet concentration parameterization of aerosol conditions. *J. Geophys. Res.*, **111**, D15240, doi:10.1029/2005JD006561

Seifert, A., 2008: On the parameterization of evaporation of raindrops as simulated by a one-dimensional rainshaft model. *J. Atmos. Sci.* (accepted).

Seifert, A. and Beheng, K.D., 2006: A two-moment cloud microphysics parameterization for mixed-phase clouds. Part 1: Model description. *Meteorol. Atmos. Phys.*, **92**, 45–66.

Seifert, A., Khain, A., Pokrovsky, A. and Beheng, K.D., 2006: A comparison of spectral bin and two-moment bulk mixed-phase cloud microphysics. *Atmos. Res.*, **80**, 46–66.

Acknowledgements: The investigations presented above have been performed partly in the framework of the ANTISTORM project funded by the the EC-STREP project as part of FP6-2003-NEST-B1, and partly within a project funded by the German Federal Ministry of Education and Research (BMBF) under grant 02WT0536 in the framework of the joint German-Israeli Cooperation in Water Technology.

THE 7 TO 9 SEPTEMBER 2006 AMMA ANVIL-CIRRUS CLOUD CASE STUDY: NUMERICAL SIMULATION OF THE DYNAMICS, CLOUD MICROPHYSICS, AND SYNTHETIC OBSERVATIONS

G.PENIDE[1], V.GIRAUD[1], C.DUROURE[1], A.PROTAT[2], D.BOUNIOL[3], P.DUBUISSON[4]

[1] LaMP/CNRS, Université Blaise Pascal, 63177 Aubière, France
[2]CNRM, Centre National de Recherches Météorologiques, 31057 Toulouse, France
[3] BMRC, Bureau of Meteorology Research Centre, Docklands, VIC3008, Melbourne, Australia
[4] ELICO, Écosystèmes Littoraux et Côtiers, Université du Littoral Côte d'Opale, 62930 Wimereux, France

1. INTRODUCTION

AMMA campaign (African Monsoon Multidisciplinary Analysis) starts in 2002 and will end in 2010. The aims of this campaign are to better document and understand both spatial and temporal variability of African Monsoon and its impacts on Atmosphere-Earth-Ocean system. Different observation periods have been realized including Special Observing Periods (SOP) with intensively measurements from ground, aircraft and space to study processes (oceanic, dynamic, chemical, aerosols, convection and anvils).

In this framework, our stategies are focused on anvil-cirrus part of Mesoscale Convective Systems. We study their life cycle and impacts on monsoon based on observation analysis (acquired during SOP2a3) and numerical mesoscale simulations using the Brazilian version of RAMS-v5.2 (Regional Atmospheric Modeling System) tailored to the tropics (Cotton et al., 2003).

The strategy here was to simulate synthetic observations into 3-D fields mesoscale model outputs. We simulate active and passive instruments as seen from ground, aircraft and space and then compare them directly and statistically to real observations.

With such informations, we investigate a methodology to better quantify water and radiative budgets in the anvil part of MCSs and to better understand remote sensing observations.

2. OVERVIEW OF AMMA CASE

This work focus on September 8, 2006 (SOP2a3) case over Niamey region, Niger. This Mesoscale Convective System (MCS) was largely documented with both ARM mobile facility on ground and two flights of the French falcon with onboard RALI (RAdar: RASTA and LIdar: LNG) and microphysical measurements (2-DP, 2-DC, 1-D probes).

This MCS born North-East of Niamey September 7, near 12 am, and then move westward during the day to reach Niamey region at approximately 3 a.m. Then it stays several hours over Niamey developing itself to a maximum reached at 6 am, and then dissipates until 11 a.m.

3. STRATEGY

Synthetic observations are simulated with model output fields and will be compared directly and statistically to real measurements. This strategy is interesting because, thanks to numerical simulations, we dispose of all the variables to calculate radar reflectivity, lidar backscattering coefficient and brightness temperature. The best analysis will be done with the less hypothesis made. That's why a 2-moment scheme is at least necessary to achieve this method, otherwise one must keep in mind the hypothesis done to obtain mixing ratios or number concentrations of hydrometeors.

3.1. *NUMERICAL SIMULATION*:

Our simulation was set up on September 7, 2006 at 0h00 with ECMWF initialization fields and ends September 9, 2006 at noon. During the simulation a 6 hour nudging is applied at the lateral limits of the domain and no data assimilations have been done. We start the model with 2 nested grids with 25 and 5 km horizontal resolutions and 34 vertical levels centered on (10°N, 5°E). We add a third nested grid on September 8, centered on Niamey (13.5°N, 2.2°E) with 1 km horizontal resolution and 115 vertical levels stretched from 500 m resolution close to ground up to 100 m between 10 and 15 km.

Grell and Devenve, 2002 parameterization (a mass flux scheme exclusive to BRAMS) is used for the 2 coarser grids and the explicit calculation of deep convection is done for the finest one. The most sophisticated radiative scheme available in the model is used (Harrington 2-stream radiative scheme, J.Harrington, 2000). It takes into account for each condensate species as well as water vapor. We used the 2-moment microphysics scheme for this simulation, which permits to predict both mixing ratios and number concentrations for 7 hydrometeor species (Cloud droplets, Rain, Pristine ice, Snow, Aggregates, Graupel and Hail) and Water vapor. 5 different shapes are used for pristine ice and Snow, depending on the diagnostic of ambient temperature and saturation with respect to water. Mass and terminal falling velocity are parameterized with power laws function, $M=\alpha.D^{\beta}$ and $V=\gamma.D^{\delta}$, where D is the maximum diameter; α, β, γ and δ are coefficients depending on species (Meyers et al., 1997).

3.2 *SYNTHETIC OBSERVATIONS*

We simulate 95 GHz equivalent radar reflectivity factor (taking into account the attenuation), radar doppler velocity, Lidar backscattering coefficient (with the assumption of multiple scattering) and brightness temperature in the infrared thermal window at 8.7, 10.6 and 12 µm (as seen from the Imaging Infrared Radiometer (IIR) onboard Calipso).

3.2.1 *Radar Reflectivity*

95 GHz radars correspond to a wavelength of about 3.15 mm which is much smaller than the usual precipitation radar (3 cm). Because of hydrometeor sizes compared to radar wavelength, Rayleigh approximation failed. An exact calculation of optical properties for non spherical ice crystal is difficult and time consuming. Mie theory is more accessible but implies that all condensed hydrometeors are considered as spheres which is not realistic for most ice crystals. A lot of papers have shown different strategies to minimize this assumption, like the use of equivalent diameters in volume, mass and so on. Donovan et al, 2004 show that, for a 95 GHz radar, the best hypothesis was to represent ice crystals by a sphere with an equivalent maximum diameter and an adjusted density so that mass is conserved which can be done using Mass power laws.

3.2.2 *532 nm Lidar backscattering coefficient.*

Multiple scattering is important in the simulation of Lidar backscattering coefficient especially for space borne lidar observations because of the large instrument footprint (Hogan et al., 2006). The fast lidar forward model developed by Hogan et al., 2006 is used to simulate this instrument with the quasi small angle approximation. This model was chosen for its good compromise between speed and accuracy compare to other methods more accurate like Monte Carlo calculations but not fast enough.

3.2.3 *IIR simulations: Brightness temperatures.*

FASDOM, a fast radiative transfer code developed for simulating the IIR radiances is used (Dubuisson et al., 2005). Multiple scattering is taking into account with the Discrete Ordinates Radiative Transfer (DISORT) code developed by Stamnes et al., 1988. In terms of brightness temperature, it appears that this code is accurate to about 0.1 K.

Hydrometeors optical properties (used for the calculation of both lidar and radiometer) are retrieved from Ping Yang tables using effective diameter which can be calculate accurately with a 2-moment microphysics scheme.

4. FIRST SIMULATION ANALYSIS

4.1 *MODEL DYNAMIC ANALYSIS*

As a first validation of dynamics we used classical turbulent tool like time evolution (September 8, in the morning) of the first three moments of vertical velocity extracted from horizontal cross sections in grid 3.

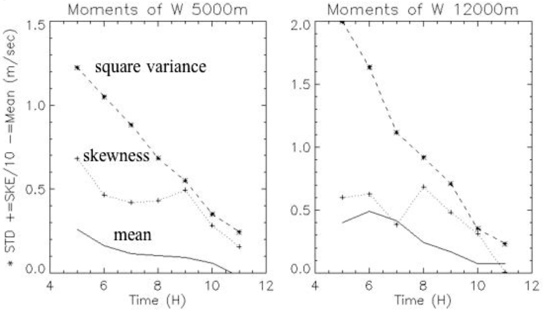

Figure 1: Time evolution of the first three moments of $\vec{W}$ field at 5 and 12 km.

Figure 1 shows that at 5 km, squared variance is decreasing linearly in time which is realistic with 3D turbulent convection theory in well mixed layers. Furthermore we see that on higher levels it decreased more rapidly during a couple of hours, certainly due to buoyancy effects in more stratified regions. This is a first step to conclude on the realism of dynamics in this model. We have also good results concerning time evolution of density energy of $\vec{W}$ Fourier spectra (on poster).

Concerning September 8 case, it appears that the simulated MCS is correctly represented in space and is a late by 2 hours in time. Nevertheless BRAMS model represents very well monsoon conditions as it simulates a good wind field in agreement with measurements (radio soundings near Niamey) a strong monsoon flux in lower layers associated with a dry harmattan above and easterly jets (African and Tropical) are realistic too.

4.2 *SYNTHETIC OBSERVATIONS*

Figure 2 shows simulated and observed MSG brightness temperatures at 12 µm. We can see that too much cloud are simulated on the whole domain (larger cold region in the model) but as we will focus on the MCS and its structure in the 3rd grid, MCS is well simulated (same magnitude of brightness temperatures).

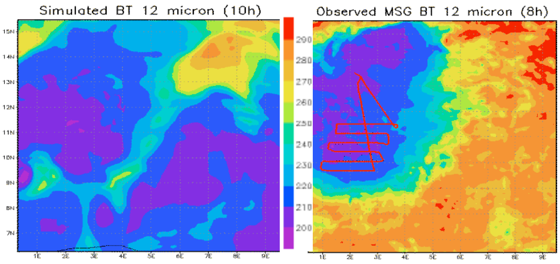

Figure 2: Comparison between simulated brightness temperature at 12 micron (left) and measures with MSG. Red line indicates the trajectory of the French falcon in MCS.

Simulation of radar reflectivity factor on ground with 5 minutes resolution is now compared to ARM mobile facility (Figure 3).

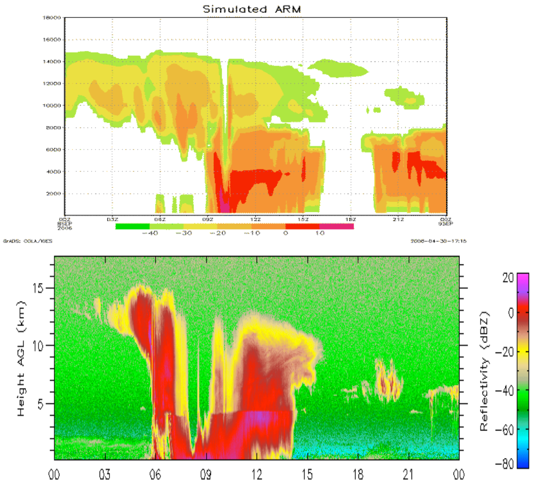

Figure 3 : Comparison with ARM radar reflectivity and simulated reflectivity obtained with 5 min temporal resolution

We can see that high altitude clouds are present before MCS which may be due to the previous convective system for one part (before 4 am) and due to the coming of the next one for the other part. We can note that when the main cores overpass Niamey, there is an important attenuation of radar signal because of the presence of large hydrometeors (effective diameter ~850 μm). This attenuation is present in our simulated reflectivity and the magnitude of reflectivity factors are similar with about 15-20 dBZe for the higher values in precipitating regions and less than -20 dBZe for anvil part. We can note that cloud top in the model reach 14 km altitude and decreases very slowly compared with ARM radar measurements in anvil region. Moreover we see that timing for the end of MCS in ARM simulations is well represented at 3 pm but still too much lower clouds are presents.

As ARM radar is strongly affected by attenuation maybe it can not reach cloud top because of lower limit of detection. One way to theoretically investigate this, would be to simulate geostationary space borne radar and lidar.

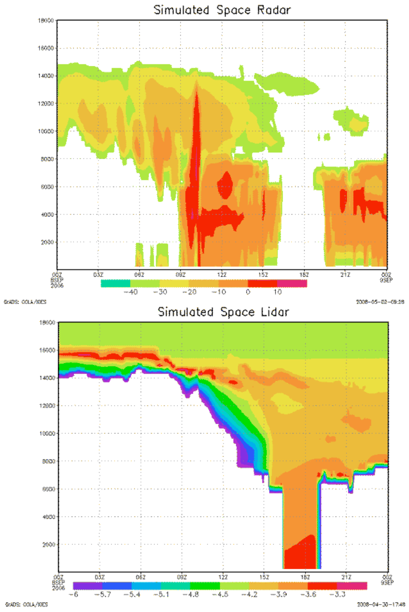

Figure 4 : Simulated Radar Reflectivity (dBZe) and Lidar backscattering coefficient (log (km-1.sr-1)) as seen from space with 5-min temporal resolution.

Lidar simulation in this case exhibit thin clouds invisible to radar measurements (ground or space based) above 14 km due to very small particle with effective diameter smaller than 50 μm and cloud coverage after 15 pm is greater than observed with ARM. These instruments and their different fields of view are complementary.

5. CONCLUSION AND OUTLOOKS

We have realized MCS simulation with important horizontal and vertical resolutions. Simulated MCS is well represented (spatially and temporally) and numerical simulation is sophisticated enough (mass flux scheme for convection 2-moment scheme for microphysics) to simulate synthetic observations without adding external parameterization. These new tools are now used to better constrain the model, remote sensing algorithm, and interpret physical processes.

Simulated and real measurements will be compared more statistically. First we will investigate this issue using comparisons between Rasta reflectivity and reflectivity calculated from microphysic probes to test different mass power laws.

6. BIBLIOGRAPHY

Cotton W.R., Pielke R.A.,Walko R.L., Liston G.E., Tremback C., Jiang H., McAnelly R.L., Harrington J.Y., Nicholls M.E., Carrio G.G., McFadden J.P., 2003 : RAMS 2001: Current status and future directions,. *Meteorol. Atmos. Phys.*, 82, 5–29.

Dubuisson P., Giraud V., Chomette O.,Chepfer H., and Pelon J., 2005 : Fast radiative transfer modeling for infrared imaging radiometry. *J. Quant. Spectrosc. Rad. Transfer*, 95, 201-220.

Harrington J.Y., Olsson P.Q., 2001 : A method for the parameterization of cloud optical properties in bulk and bin microphysical models. Implications for arctic cloudy boundary layers, *J. Atmospheric Research*., 57, 51-80.

Hogan R.J., 2006 : Fast approximate calculation of multiply scattered lidar returns, *Applied Optics*, 45, 5984-5992.

Ping Yang, Liou K.N., Wyser K., Mitchell D., 2000 : Parametrisation of the scattering and absorption properties of individual ice crystals. *J. Geophys. Res*,. 105, 4699-4718.

Meyers M.P., Walco R.L., Harrington J.Y., Cotton W.R., 1997 : New RAMS cloud microphysics parameerization. Part II : The two-moment scheme, *J. Atmospheric Research*, 45, 3-39.

Stamnes K., Tsay S.C. Wiscombe W., and Jayaweera K., 1988: Numerically stable algorithm for Discrete-Ordinate-Method radiative transfer in multiple scattering and emitting layered media. *Appl. Opt.*, 27, 2502-2509.

AN EXPLORATORY ANALYSIS OF THE POTENTIAL FOR RAINFALL ENHANCEMENT IN THE RANDOMIZED CONVECTIVE COLD CLOUD SEEDING EXPERIMENT IN EXTENDED AREAS IN CUBA (EXPAREX)

Carlos A. Pérez Sánchez[1], Daniel Martínez Castro[2], Petrov V.V [3], Ismael Pomares Ponce[1],
Koloskov, B. P.[3], Félix Gamboa Romero[1]

(1) Camagüey Meteorological Center, Camagüey, Cuba. C.P. 70100
Tel 5332 29-77-89; e-mail: carlos.perez@cmw.insmet.cu
(2) Institute of Meteorology, La Habana, Cuba. C.P. 11700
Tel-Fax: 537-881-3411 e-mail: daniel.martinez@insmet.cu
(3)Agency of Atmospheric Technologies (Agency ATTECH, ROSHYDROMET)
Novovagankovsky per. 8, Moscow, 123242, Russia.
Tel: +7(095)255-2372; Fax: +7(095)255-2134; e-mail: attech@mail.ru

1. INTRODUCCI0N

The Cuban Project for Artificial Weather Modification (PCMAT, in Spanish) began in 1979 in the Camaguey Meteorological Site (CMS) as part of scientific collaboration between Cuba and Russia. The earliest stage of the project included three major components: selection of appropriate site and period of the year to accomplish the experiment (1979-81); preliminary assessment of dynamical and microphysical characteristics of convective cold clouds in the site and an exploratory experiment (1982-1985).

The goal of this paper is to investigate the consistency of the behaviour of some properties of mixed phase convective clouds in CMS with the hypothesized precipitation enhancement as a response to dynamic seeding with silver iodide.

In the 1985 exploratory experiment, the hypothesis that the precipitation potential of clouds may be increased through dynamic seeding and a method for seeding convective clouds were both tested. This allowed us to draw some preliminary conclusions: the seeding of clouds with tops with height ranging from 6 to 8 km (-10 to -20 ºC) leads to enhanced growth, as they last longer and exhibit a higher radar reflectivity Suitable clouds must also have diameter between 2 to 5 km.

A confirmatory phase was designed for the period 1986 to 1990, including along with the seeding of individual convective clouds, clouds clusters extending over an area of 400-600 km². In conducting the confirmatory 1986-1990 experiment, a dynamical seeding conceptual model, which had been described and discussed by Wooddley and Sax (1976), was used. The treatment decision was randomized on a unit by unit basis and suitable convective cells were treated with AgI, in the case when the seed (S) decision was made, or were penetrated without being seeded in the case of no-seed (NS) decision. Neither the crews of instrumented aircraft nor of the service responsible for the monitoring of the seeding effect and the observation of experimental clouds, were informed about the results of randomization during the experiment.

In the confirmatory phase 46 individual convective clouds, 24 seeded and 22 not seeded and 82 clusters, 42 seeded and 40 not seeded, were studied. The analysis of radar data showed that the seeded clouds increases in lifetime, maximum height, area and rain volume by 120% for individual clouds and 65% for cloud clusters, as compared to unseeded ones, with a better than 5% level of significance.

On base of these encouraging results, a new phase was started in 1991, but in this case for extended areas with one or more cloud system. For this purpose, a floating experimental target with area of the order of 2000 km² was chosen as experimental unit. However in 1992 the experiment was interrupted due to funding problems.

At the beginning of 2005 the Cuban Government decided to support the resumption of the experiments in the CMS. As continuity of the PCMAT, a new experiment for the seeding of cold cumulus clouds in extended areas (EXPerimento aleatorizado de siembra de nubes en AReas EXtensas, EXPAREX), is being accomplished in CMS since 2005. The experiment was based on the revised dynamic–mode seeding conceptual model. Consequently, we have to answer the following question:

Do the dynamical and microphysical characteristics of cool cumulus clouds rising in CMS meet the criteria for the conceptual model?

The answer to this question is the main objective of this work.

2. FACILITIES

Two instrumented aircraft were used to collect the data, a twin engine IL-14 with ceiling of 3-3.5 km and cruising true airspeed of about 80 m s^{-1}, carried out measurement in the lower part of the clouds. For measurements in the upper part of clouds a twin engine AN-26 aircraft with maximum height of about 6 km and a cruising airspeed nearly 100 m s^{-1} was used. IL-14 was equipped with a large particle spectrometer (LPS) and Nevzorov LWC probe IVO-1 (Nevzorov 1996), aircraft load complex for the measurement of velocities of vertical drafts, mean temperatures fluctuation (Dmitriev and Strunin, 1983). A similar instrument set was installed in the AN-26 aircraft excluding LPS, but including a photoelectric ice crystal counter Mee-120 (WMO, 1977) and a total water content (TWC) probe IVO-2 similar to IVO-1, but capable to measure both, droplets and ice crystals. Currently, in the EXPAREX field measurements we have been using an a similarly instrumented AN-26, but including in this occasion a LPS and excluding Mee-120.

For the control and track of cloud was used the dual MRL-5 radar. With the radar and aircraft information, it was possible to follow the time evolution of cloud characteristics according to theirs development stage.

3. DESIGN

After 15 years without field experiment and with a limited research activity, a new design was necessary to consider the development in physic of clouds and concepts related with dynamic seeding mode achieved in last years.

The design of EXPAREX experiment (Pérez et al. 2005) was aided by the results of the experiment in Cuba (1985-1990), West Texas 1987-1990, Thailand 1987-1990 and achievements of FACE-I and FACE-II as dynamic cloud seeding concept (Simpson et al. 1965), mesoescale system growth through mergers and downdraft invigoration (Simpson et al. 1980), the use of floating target to provide a more sensitive measurement of the effects of seeding and the finding that the radar-estimate were accurate enough to make inference about seeding effect (Woodley et al. 1982). The EXPAREX design was addressed as continuity of above related experiment, thus it is based on the results of Cuban experiments conducted in CMS during 1985-1990 (Koloskov et al. 1996) and similar to the design of the Thailand cold-cloud seeding experiment (Silverman et al. 1994; Woodley et al. 1999). Consequently, the dynamic-seeding conceptual model as discussed by Rosenfeld and Woodley (1993) was adopted, including secondary seeding concept (Woodley and Rosenfeld, 2002).

According to the conceptual model, the glaciogenic seeding produces rapid glaciations in the updraft by freezing, preferentially the largest drops so that they can rime the rest of the cloud water into graupel. This seeding-induced graupel grows faster than rain drops of the same mass (Sednev et al. 1996), so that a large fraction as the cloud water is converted into precipitation before being lost due to other processes (Rosenfeld and Woodley, 1996). These processes results in increased precipitation and a stronger downdraft, increasing rainfall in the cloud cluster through downdraft interaction between groups of seeded and non-seeded clouds, increases their growths and mergers. Secondary seeding (Woodley and Rosenfeld, 2002) whereby non-seeded clouds ingest ice embryos from earlier seeding of separate clouds, have an important role in the propagation of seeding effect.

4. DYNAMICAL SEEDING-PROPER CLOUD CHARACTERISTICS

Over Cuba persistent Eastern winds blow from the Atlantic Ocean through all troposphere, so that the air mass in which CMS cumulus clouds are rising is basically maritime. According to that, this clouds may be good candidates to early freezing of the rain drops and ice multiplication (Woodley et al. 1993; Mossop 1976) and not suitable for dynamical seeding. In order to investigate the phase composition (Pérez et al. 1994), data from 58 clouds were used, penetrated at the level of 5600-6000 m (-7 to -10 ^{o}C in most of cases). All cumulus selected were experimental clouds which tops heights range between 6000-8000 m at the time of penetration. Only not-seeded clouds, or the first pass of seeded clouds, were included in the data set. To study the behaviour of the phase composition, the freezing coefficient K was defined as:

$$K = IWC / (IWC+LWC) *100 \qquad (1)$$

The coefficient K represents the fraction of frozen water and may be used to describe its evolution. IWC and LWC as measured with Nevzorov probe are given for particles with r < 120 µm. Ice particle concentration (N with r > 120 µm) was measured using Mee-120.

In Figure 1, the time evolution of solid phase, can be studied using simultaneous measurements of radar and aircraft. Cloud lifetime was defined as the time elapsed from first echo to dissipation. In order to describe the stage of cloud development at the time of penetration, a time scale was defined as t/t_0 were t is the time elapsed from the first echo to penetration and t_0 is the cloud lifetime.

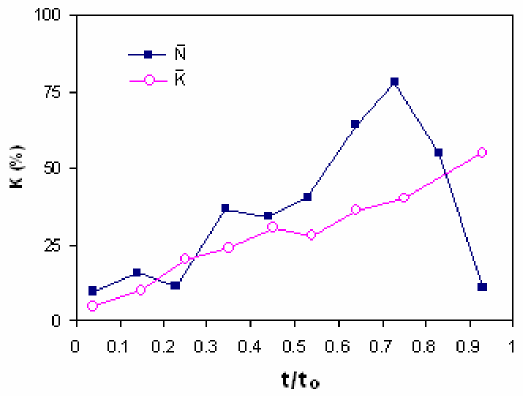

FIG.1. Time evolution of average crystal concentration (N ℓ^{-1}) and freezing coefficient

As can be appreciated, both parameters increase with the time, but in the first third of clouds lifetime N (2-6 ℓ^{-1}) and K (10-20 %) are small enough and begin to increase in the second third but not dramatically. We can see that in the first third of cloud lifetime the LWC budget is greater enough with respect to IWC and the onset of ice is not so rapid and no early glaciation of supercooled water is observed. Thus, the phase composition allows the alteration of clouds dynamic according to dynamic mode seeding conceptual model.

In the Table 1 we show natural and potential buoyancy enhancement (B and BE), calculated for a small sample of

15 updraft as defined by Czys (1991) as region of clouds with vertical velocities greater than 1 ms^{-1} for at least 3 continue seconds of flight.

To determine the buoyancy it was used the equation:

$$B = (\theta_v - \theta'_v) - Llwc - Liwc \qquad (2)$$

Where θ_v and θ'_v are the virtual potential temperature of cloud and environment respectively (Czys, 1991), Llwc and Liwc are the net loading of liquid water contents and ice water contents. The warming due to instantaneous isobaric freezing was obtained with the equation found in Orville and Hubbard (1973).

$$\delta T = T' - T = L_f/c_p\, Q_l + L_s/c_p\, [q_w\,(T) - q_l\,(T')] \quad (3)$$

Where T' and T are the parcel temperature after and before glaciation L_f and L_s the latent heat of fusion and sublimation, Q_l the liquid water expressed as kg of water per kg of air, q_w and q_l are the saturation mixing ratio with respect to water and ice.

As can be seen, when instantaneous isobaric freezing is simulated, more than 60 % of the cases with negative buoyancy, become positively buoyant. The isobaric freezing warming δT averaged 0.64 ℃ and ranged from 0.47 to 0.85 ℃.

Table 1. Buoyancy enhancement.

Diam (m)	LWC (g/m^{-3})	B (°C)	BE (°C)	δT_f (°C)	δTd (°C)
700	0.413	-0.429	-0.284	0,221	0.315
500	0,145	-0.253	0.374	0.078	0.394
400	0.291	-0.437	0.255	0.156	0.368
400	0.030	-0.292	0.314	0.016	0.441
1500	1.553	-1.421	-0.301	0.833	0.015
1200	1.278	-1.057	-0.021	0.685	0.099
1500	1.567	-1.662	-0.546	0.836	0.009
700	0.784	-0.332	0.574	0.419	0.269
500	0.673	0.483	1.403	0.360	0.341
1700	0.356	0.985	1.779	0.190	0.413
1600	0.683	-0.750	0.564	0.367	0.246
1100	0.204	-0.439	0.232	0.110	0.396
1400	0.989	-0.728	0.205	0.533	0.171
800	0.331	0.123	0.865	0.177	0.386
1800	0.713	0.024	0.895	0.381	0.280

Diam- Diameter of updraft; B – Buoyancy; BE – Buoyancy enhancement; δT_f - Warming due to freezing; δT_d – Warming due to depositional processes.

Therefore, though the sample presented herein is small, the response given for updrafts to the simulated instantaneous isobaric freezing, reinforces the physical possibilities of alteration of cloud dynamics by glaciogenic seeding.

On the other hand, maritime clouds with lower cloud droplet concentration and wider drop sizes distributions have active coalescence processes, producing glaciation at -10 ℃ or warmer. These clouds are not proper for glaciogenic seeding mode.

As illustration of the microstructure characteristics of CMS clouds, Figure 2 shows the droplet spectra for the measurements made in 12 cumulus clouds located over the Caribbean Sea (curve 2) and 5 located over CMS (curve 1). Maritime clouds were at a distance which ranged from 140 to 240 km offshore to the south (Pérez et al. 1992).

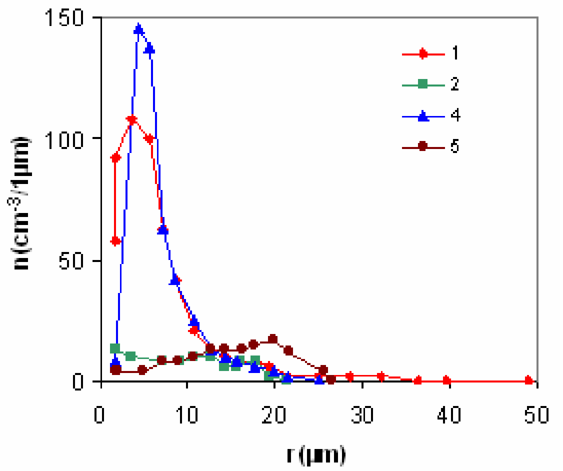

FIG. 2. Averaged size distribution of clouds drops.

Figure 2 shows also averaged size spectra as obtained by Hindman et al. (1992), in continental (curve 4) and maritime clouds (curve 5). The mean value for the concentration drops inside the clouds over Camagüey was 380 cm^{-3} and the mean droplet radius was 6,1 µm. At the same time, over the Caribbean Sea, the mean value of droplet concentration was 64 cm^{-3} and mean radius of 15,2 µm.

As can be appreciated, clouds developing over CMS can be considered as intermediate and closer to continental.

Clouds are suitable for an effective dynamic seeding when they have a proper coalescence process satisfying the presence of some rain and drizzle drops interspersed in high cloud water contents (Woodley and Rosenfeld, 2003).

Using radar information and airborne measurements made with a photoelectric spectrometer (D>200 µm) of cloud particles, from 139 penetration of not seeded cumulus clouds in their lower part and with tops between 3.7 and 11.4 km (Beleaev et al. 1994).

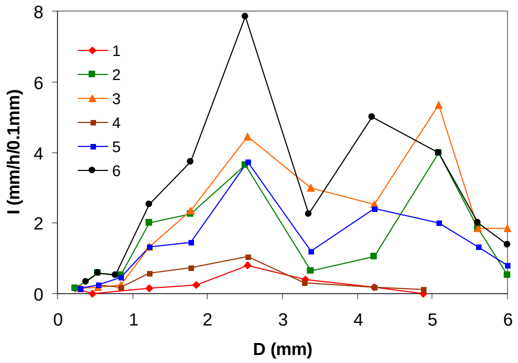

FIG. 3. Spectral rainfall intensities:

1- H ≤ 5 km; 2- 5< H ≤7 km; 3- H >7 km (clusters).
4- H ≤ 5 km; 5- 5< H <7 km; 6- H >7 km (isolated).
H: clouds top.

The behaviour of spectral rainfall intensities as calculated from the measured particle size distribution is shown in the Figure 3, where it is possible to appreciate that in the warm clouds having less than 5 km tops, with only coalescence mechanisms participating in rain formation, a unimodal distribution of precipitation intensities can be observed. For these cases, curve 1 (clusters) and 2 (isolated) are showing an active coalescence process, with peak at 2.5 mm raindrops diameter and some larger than 4mm. Two modes in the distributions were observed in clouds whose tops were above the freezing level. In such cases, both mechanisms, warm and cold, were likely to operate (Petrov et al. 2004).

In Figure 4 we show the frequency histogram for updrafts and downdrafts from measurements made at the levels of 5.6 – 6.1 km in the periods 1987-1990 and 2006-2007.

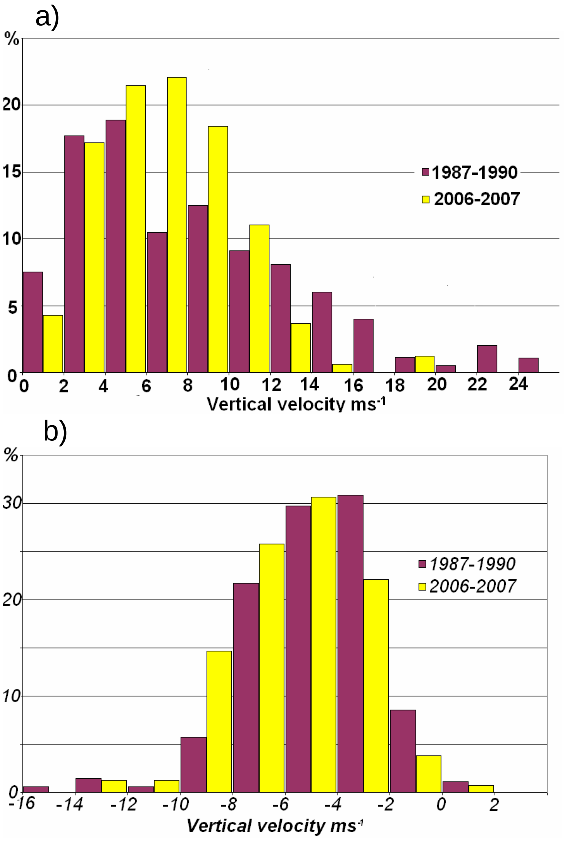

FIG. 4. Frequency of Maximum (a) and Minimum (b) velocity of vertical draft for the periods 1987-1990 and 2006-2007.

In the updraft cases, the most part (≈ 85 %) ranged up 2 to 17 ms^{-1} and some cases above 18 ms^{-1} (≈10%) for both periods. In 1987 -1990 cases ≈ 64% of the updraft are between 4 -16 ms^{-1} and 74% for 2006 -2007. Updrafts over passing 6 ms^{-1} are 56% and 57% in the first and second periods respectively. In considering downdrafts for both periods practically all case are grouped between 0 and -12 ms^{-1} (≈ 97%).

As we can see, in both periods experimental cloud properties meet the necessary criteria of strong updraft for dynamic seeding.

In the Figure 5 we can observe the same, because of the enough high quantities of clouds water at the seeding level.

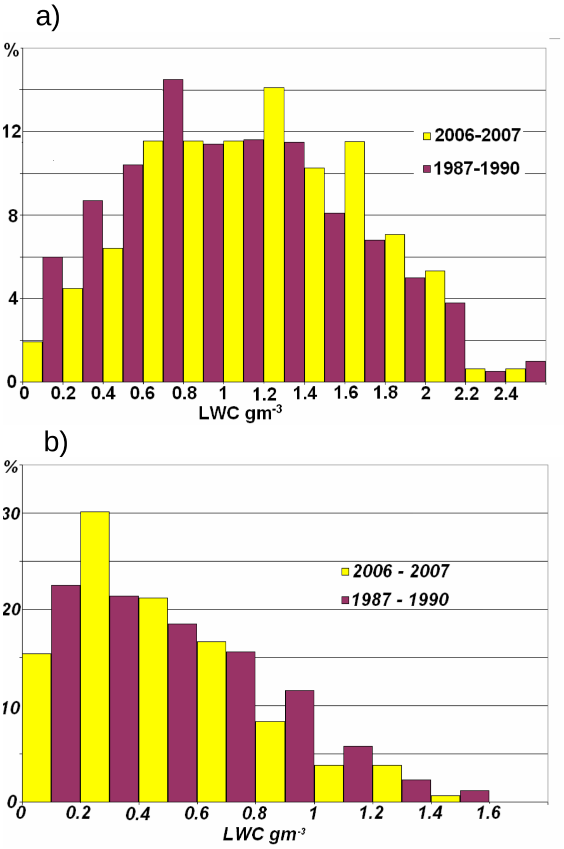

FIG. 5. Frequency of maximum (a) and averaged (b) liquid water content values.

Average for maximum values for 1986 - 1990 was 1.025 gm^{-3} and for 2006 – 2007 it was 1.12 gm^{-3}. In the first period, 85% of LWC values are above 0.4 gm^{-3} and in the second the 87%.
The behaviour of frequency distribution for mean values of LWC in both periods result practically the same. Average for 1987 - 1990 was 0.486 gm^{-3} and for 2006 – 2007 0.488 gm^{-3}.

According to the behaviour of the phase composition, without glaciated up to -10 ℃ or warmer levels and considering the values of LWC and vertical velocities in updraft, we can express that the cold convective clouds developing in CMS are suitable for the application of the conceptual model of dynamical seeding.

Nevertheless, in the absence of particle measurement probe in Cuban experiments, it is not possible to obtain directly, spectral characteristics of solid and liquid phase at seeding level. However considering the behaviour of clouds characteristics given in the Figures 3 and 4 for both periods, is possible to considerer that we are working with similar process in similar clouds. These condition allows the comparison between the measurements of ice particles (D>200 µm) made with the Mee-120 in the 1986-1990 period and measurements of cloud particles (solid and liquid) made with a photoelectric spectrometer for large (D>200 µm) cloud particles in the period 2006-2007. The comparison showed the presence of raindrops at the level of seeding, with concentration ranged between 0 to 11 ℓ^{-1} and an exception with concentration up 21 ℓ^{-1}. The values of concentration obtained are comparable with measurements in South Africa (Mather et al, 1986) and Illinois (Czys and Scott, 1993).

The comparison made with two different devices, in order to obtain raindrop concentration at the seeding level, may be inexact and should be use carefully. The future use of a laser bean particle measuring system, wich allows to discern the phase of the particles, is essential to accurately asses the presence of supercooled raindrop.

5. CONCLUSIONS

The design of EXPAREX experiment was based in results from the experiments in Cuba (1985-1990), West Texas 1987-1990, Thailand 1987-1990 and facets of FACE-I and FACE-II. The EXPAREX design was addressed as continuity of above related experiments period, and is similar to the design of the Thailand cold-cloud seeding experiment. As conceptual model guiding, the dynamic-seeding, the revised conceptual model as developed and discussed by Rosenfeld and Woodley (1993) was adopted.

The following arguments show that the towers of cold convective cumulus clouds developing over CMS satisfy the conceptual model for dynamic-seeding:

- The behaviour of the freezing coefficient and ice crystal concentration showed that, the LWC was greater than IWC and the crystal concentration was small enough, providing suitable conditions for seeding with glaciogenic reagents. The time evolution showed that in the first third of cloud lifetime the development of solid phase is slow and it increases in the second third but not dramatically, allowing a seeding window for the CMS clouds.
- The results of simulation of isobaric freezing in some updrafts, suggest that most of negatively buoyant ones would have become nearly neutral, or positively buoyant if they had been seeded. This reinforce the possibilities of alteration of cloud dynamic by glaciogenic seeding.
- In the analysis of droplet spectra measurements made over ground and sea, in the same day an during two consecutive days with the same synoptic conditions, it was found that spectra obtained for clouds over land are radically different from those for offshore clouds. That allows to conclude that clouds growing over CMS are nearly continental by their microstructural properties.
- The form of the raindrop size distributions obtained for the lower part of the clouds show an active coalescence process, showing, peaks at nearly 2.5 mm in raindrop diameter and the presence of some drops larger than 4mm for warm clouds having tops less than 5 km, for which the ice processes had no participation in rain formation.

Data of LWC, ice crystal concentration, vertical in clouds air motions and the suggestion of the presence of raindrops at the seeding level, provide a consistent picture of cloud structure in the supercooled region which indicate that is possible a proper application of glaciogenic seeding, within the vigorous supercooled updraft with enough high LWC and some raindrops interspersed, generated from below by coalescence. That is according with the dynamic-seeding revised conceptual model as adopted by the design of EXPAREX.

6. ACKNOWLEDGEMENTS

The authors thank the Cuban Government and particularly the Institute for Civil Aeronautic for coordinating and financing EXPAREX.

We thank the EXPAREX research team for their discussion, suggestions and helpful comments. The authors also wish to thank engineers, technicians, pilots and flight personnel for their efforts in the accomplished measurements.

7. REFERENCES

Beliaev, V. P., B. P. Koloskov, A.V. Koldaev, V.V. Petrov, Y.A. Seregin., A.A. Chernikov and C.Perez, 1994: A physical evaluation of the suitability of convective clouds for seeding. Proc. Sixth WMO Scientific Conf. on Weather Modification, Paestum, Italy, World Meteor. Org., 349-352.

Czys R. R., 1991: A Preliminary Apraisal of The Natural Struture and Seedability of Updrafts in Midwestern Cumulus At The – 10 ^{0}C. Jour. Wea. Mod., **23**, 1 – 17.

-----and R. W. Scott, 1993: A simple objective method used to forecast convective activity during 1989 PACE cluod-seeding experiment. J. Appl. Meteor., **32**, 996-1005

Dmitriev V. K., Strunin M.A., 1983: Aircraft measurements of the vertical components of wind speed fluctuations. Trudy CAO, issue 147, 39-51.

Hindman E. E., Kong K. Y., Borys R. D., 1992: Initiation of long – term cloud droplets measurements for climate change studies. Proceeding os Symposium on Planned and Inadvertent Weather Modification. Atlanta, USA.

Koloskov B., Zimin B., Beliaev V., Seregin Yu., Chernikov A., Petrov V., Valdes M., Martinez D., Perez., Puente G., 1996: Results of Experiments on Convective Precipitation Enhancement in the Camaguey Experimental Area, Cuba. Journal of Applied Meteorology, **35**, 1524-1534.

Mather G. K., B. J, Morrison, and G. M. Morgan Jr., 1986: A preliminary assessment of the importance of coalescence in convective clouds. J. Climate Appl. Meteor., **20**, 29-47.

Mossop S. C., 1976: Productionof secondary ice particle during the grought of graupel by riming. Quart. J. Roy. Meteor. Soc., **102**, 45-57.

Nevzorov A. N., 1996: CAO aircraft instrumentation for cloud physics. 12th international Conf. on Cloud Phys. and Precipitation. Aug. 19-23, V.1, Zurich, Switzerland, pp. 371-374.

Orville, H. D. and K. Hubbard, 1973: On the freezing of liquid water in cloud. J. Appl. Meteor., **12**, 671-676.

Pérez C., Martínez D. and Petrov V. (1992): Microstructure, mixing and turbulence in cumulus clouds over Cuba and the Caribbean Sea. In: Proceedings WMO Workshop on Cloud Microphysics and Aplication to Global Change, Toronto, 1992. WMP Report No. 19 WMO/TD 537. pp. 245-256.

Pérez C., Oms M., Martínez D. and Petrov V. (1994): Phase composition and seedability of cumulus clouds in the Camaguey Meteorological Site, Cuba. Sixth WMO Scientific Conference on Weather Modification, Paestum. WMP Report No. 22. WMO/TD No. 596. Vol. 2, pp.379-282.

Petrov V. V., D. Martínez, and C. A. Pérez, 2004:The Microphysical And Thermodynamic Characteristics of Tropical Convective Clouds by Results of Measurements on Cuba. WMO International Conference on Clouds and Precipitation. 18-24 July 2004, Bologna Italy.

Rosenfeld, D. and W. L. Woodley, 1993: Effects of cloud seeding in west Texas: Additional results and new insights. Journal of Applied Meteorology, **32**, 1848-1866.

Rosenfeld D. and Willian L. Woodley, 1996: Microphysical response of summer convective clouds in West Texas to AgI ‘dynamic' seeding. Proceedings of 12. th. International Conference on Clouds and Precipitation. (ICCP), Zurich, Switzerland.

Sednev I. L., M. B. Pinsky, A. P. Khain and D. Rosenfeld, 1996: The role oo ice generation in precipitation formation as seen from the results obtained using a mixed – phase cloud model with spectral microphysics. Proceedings of 12. th. International Conference on Clouds and Precipitation. (ICCP), Zurich, Switzerland.

Silverman, B. A., C. L. Hartzell, W. L. Woodley and D. Rosenfeld, 1994: Thailand Applied Atmospheric Resources Research Program, Vol. 2. Demonstration Project Design. Rept. No. R-94-01, Bureau of reclamation, U.S. Dept. of Interior, 183 pp.

Simpson, J., R. H. Simpson, D. A. Andrews, and M. A. Eaton, 1965: Experimental cumulos dynamics. Rev Geophys., **3**, 387-431.

-----, 1980: Downdraft as linkages in cumulus seeding effect. J. Appl. Meteor., **19**, 477-487.

Wooley, W. L., and R. I. Sax, 1976: The Florida Area Cumulus Experiment: Rationale. Desing, Procedure, Results, and Future Course. NOAA Technical Report ERL 354-WMPO 6. Boulder, Colo. 204 pp.

-----, W. L., J. Jordan, J. Simpson, R. Biondini, J. A. Flueck, and A. Barston, 1982: Rainfall Results for the Florida Area Cumulus Experiment, 1970-1976. J. Appl. Meteor., **21**, 139-164.

-----, D. Rosenfeld, W. Kukamjanaset, P. Sudhikoses, S. Ruangsuttinaruparp and W. Khantiganan, 1999: The Thailand cold-cloud seeding experiment: 1. physical-statistical design. Proc. of 7th WMO Conf. on Wea. Mod., 16-22 Feb., 1999, Chiang Mai, Thailand.

-----, D. Rosenfeld, and B. A. Silverman 2003a: Results of on-top glaciogenic cloud seeding in Thailand. Part I: The demonstration experiment. J.Appl. Meteor., **42**, 920-938.

-----, D. Rosenfeld, and B. A. Silverman, 2003b: Results of on-top glaciogenic cloud seeding in Thailand. Part II: Exploratory analyses. J. Appl. Meteor., **42**, 939-95.

-----, and D. Rosenfeld, 2002: Secondary seeding as a means of propagating seeding effect in space and time. J. Wea> Modif., **34**, 31-38.

World Meteorological Organization, 1977: Aircraft instrumentation for cloud physics research on weather modification programmes. WMO Report No. 7, 78 pp

AN EXPLORATORY ANALYSIS OF THE POTENTIAL FOR RAINFALL ENHANCEMENT IN THE RANDOMIZED CONVECTIVE COLD CLOUD SEEDING EXPERIMENT IN EXTENDED AREAS IN CUBA (EXPAREX)

Carlos A. Pérez Sánchez[1], Daniel Martínez Castro[2], Petrov V.V [3], Ismael Pomares Ponce[1],
Koloskov, B. P.[3], Félix Gamboa Romero[1]

(1) Camagüey Meteorological Center, Camagüey, Cuba. C.P. 70100
Tel 5332 29-77-89; e-mail: carlos.perez@cmw.insmet.cu
(2) Institute of Meteorology, La Habana, Cuba. C.P. 11700
Tel-Fax: 537-881-3411 e-mail: daniel.martinez@insmet.cu
(3)Agency of Atmospheric Technologies (Agency ATTECH, ROSHYDROMET)
Novovagankovsky per. 8, Moscow, 123242, Russia.
Tel: +7(095)255-2372; Fax: +7(095)255-2134; e-mail: attech@mail.ru

1. INTRODUCCI0N

The Cuban Project for Artificial Weather Modification (PCMAT, in Spanish) began in 1979 in the Camaguey Meteorologicval Site (CMS) as part of scientific collaboration between Cuba and Russia. The earliest stage of the project included three major components: selection of appropriate site and period of the year to accomplish the experiment (1979-81); preliminary assessment of dynamical and microphysical characteristics of convective cold clouds in the site and an exploratory experiment (1982-1985).

The goal of this paper is to investigate the consistency of the behaviour of some properties of mixed phase convective clouds in CMS with the hypothesized precipitation enhancement as a response to dynamic seeding with silver iodide.

In the course of the 1985 exploratory experiment, the hypothesis that precipitation potential of cloud may be increased through dynamic seeding and method for seeding convective clouds were both tested, this allowed us to draw some preliminary conclusions: the seeding of clouds with tops high ranged from 6 to 8 km leads to enhanced growth, longer-lasting and exhibit a higher radar reflectivity, according to preliminary criteria for determine the suitability of convective clouds for AgI treatment, suitable clouds, must be in growth stage whose tops have risen at the level of 6-8 km (-10 to -20º C) and have diameter between 2 to 5 km. A confirmatory phase was designed for the period 1986 to 1990, including along with the seeding of individual convective clouds, clouds clusters extending over an area of 400-600 km². In conducting the confirmatory 1986-1990 experiment, a dynamical seeding conceptual model, which had been described and discussed by Wooddley and Sax (1976). The treatment decision was randomized on a unit by unit basis and suitable convective cells were treated with AgI, in the case when the seed (S) decision was made, or were penetrated without being seeded in the case of no-seed (NS) decision. Neither the crews of instrumented aircraft nor of the service responsible for the monitoring of the seeding effect and the observation of experimental clouds, were informed about the results of randomization during the experiment.

In the confirmatory phase 46 individual convective clouds, 24 seeded and 22 not seeded and 82 clusters, 42 seeded and 40 not seeded, were studied. The analysis of radar data showed that the seeded clouds increase in lifetime, maximum high, area and rain volume by 120% for individual clouds and 65% for cloud clusters, as compared to unseeded ones a better than 5% level of significance.

On base of these encouraging results, a new phase was started in 1991, but in this case for extended areas with one or more clouds system. For this purpose, a floating experimental target with area of the order of 2000 km² was chosen as experimental unit. However in 1992 the experiment was interrupted due to funding problems.

At the beginning of 2005 the Cuban Government decided to support the resumption of the experiments in the CMS. As continuity of the PCMAT, a new experiment for the seeding of cold cumulus clouds in extended areas (EXPerimento aleatorizado de siembra de nubes en AReas EXtensas, EXPAREX), is being accomplished in CMS from 2005. The experiment was based around the revised dynamic – mode seeding conceptual model. Consequently with this selection we have to respond the following question:

The dynamical and microphysical characteristics of cold cumulus clouds rising in CMS meet the criteria for selected conceptual model?

Response to this question is the main objective of this work.

2. FACILITIES

Two instrumented aircraft was used to collect the date, a twin engine IL-14 with ceiling of 3-3.5 km and cruising true airspeed of about 80 ms^{-1}, carried out measurement in the lower part of the clouds. For measurements in the upper part of clouds a twin engine AN-26 aircraft with maximum height of about 6 km and a cruising airspeed nearly 100 ms^{-1} was used. IL-14 was equipped with a large particle spectrometer (LPS) and Nevsorov LWC probe IVO-1 (Nevsorov 1996), aircraft load complex for the measurement of velocities of vertical drafts, mean temperatures fluctuation (Dmitriev and Strunin, 1983). A similar instrument set was installed in the AN-26 aircraft excluding LPS but including a photoelectric ice crystal counter Mee-120 (WMO, 1977) and a total water content probe IVO-2 similar to IVO-1, but capable to measure both, droplets an ice crystals. Currently in the EXPAREX field measurements we have been used and instrumented AN-26 but including in this occasion a LPS and excluding Mee-120.

For the control and track of cloud was used the dual MRL-5 radar. With the radar and aircraft information, was possible to follow the temporal evolution of clouds characteristics according to its development stage.

3. DESIGN

Afterwards 15 years without field experiment and with a limited research activity, it have been necessary a new design in order to consider the development in physic of clouds and related concepts with dynamic seeding mode achieved in last years.

The design of EXPAREX experiment (Pérez et al. 2005) was aided by results from experiment in Cuba (1985-1990), West Texas 1987-1990, Thailand 1987-1990 and facets of FACE-I and FACE-II as dynamic cloud seeding concept (Simpson et al. 1965), mesoescala system growth through mergers and downdraft invigoration (Simpson et al. 1980), the use of floating target to provide a more sensitive measurement of the effects of seeding and the finding that the radar-estimate were accurate enough to make inference about seeding effect (Woodley et al. 1982). The EXPAREX design was addressed as continuity of above related experiment and it is based on the results of Cuban experiments conducted in CMS during 1985-1990 (Kalaskov et al. 1996) and similar to the design of the Thailand cold-cloud seeding experiment (Silverman et al. 1994; Woodley et al. 1999). As conceptual model guiding, the dynamic-seeding conceptual model as discussed by Rosenfeld and Woodley (1993) was adopted, including secondary seeding concept (Woodley and Rosenfeld, 2002). According to the conceptual model the glaciogenic seeding produce rapid glaciations in the updraft by freezing, preferentially the largest drop, so they can to rime the rest of the cloud water into graupel. This seeding-induced graupel grows faster than rain drops of the same mass (Sednev et al. 1996) so that a large fraction as the cloud water is converted into precipitation before being lost to other processes (Rosenfeld and Woodley, 1996).

These processes result in increased precipitation and a stronger downdraft, increasing rainfall in the cloud cluster through downdraft interaction between groups of seeded and non-seeded clouds, increases their growths and mergers. Secondary seeding (Woodley and Rosenfeld, 2002) whereby non-seeded clouds ingest ice embryos from earlier seeding of separate clouds, have an important role in the propagation of seeding effect.

4. DYNAMICAL SEEDING-PROPER CLOUD CHARACTERISTICS

Over Cuba persistent Eastern winds blow from the Atlantic Ocean through all troposphere, so that the air mass in which CMS cumulus clouds are rising, is prevailing maritime. According that, this clouds may be good candidate to early freezing of the rain drops and ice multiplication (Woodley et al. 1993; Mossop 1976) and not suitable for dynamical seeding. In order to investigate the phase composition (Pérez et al. 1994), data from 58 clouds were used, penetrated at the level of 5600-6000 m (-7 to -10 ^{o}C in most of cases). All cumulus selected were experimental clouds which tops heights range between 6000-8000 m at the time of penetration. Only not-seeded clouds, or the first pass of seeded clouds, were included in the data set. To study the behaviour of the phase composition, the freezing coefficient K was defined as:

$$K = IWC / (IWC+LWC) *100 \qquad (1)$$

The coefficient K represents the fraction of frozen water and may be used to describe its evolution. IWC and LWC as measured with Nevzorov probes are given for particles with r < 120 µm. Large ice particle concentration (N with r > 120 µm) was measured using Mee-120.

In Fig.1 can be appreciated the time evolution of solid phase accomplished using simultaneous measurements of radar and aircraft. Cloud lifetime was defined as the time elapse from first echo to dissipation. In order to describe the stage of cloud development at the time of penetration, a time scale was defined as t/t_0 were t is the time elapsed from the first echo to penetration and t_0 is the cloud lifetime.

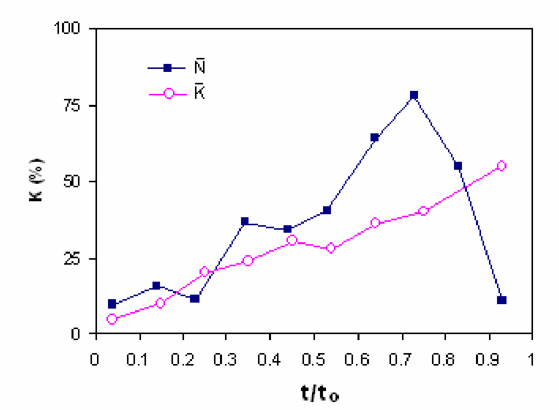

FIG.1. Time evolution of average crystal concentration and freezing coefficient.

As can be appreciated both parameters increase with the time, but in the first third of clouds lifetime N (2-6 l^{-1}) and K (10-20 %) are small enough and begin to increase in the second third but not dramatically. We can see that in the first third of cloud lifetime the LWC budget is greater enough with respect to IWC and the onset of ice is not so rapid and not early glaciations of supercooled water is observed. Thus the phase composition allows the alteration of clouds dynamic according to dynamic mode seeding conceptual model.

In the Table 1 we show natural and potential buoyancy enhancement (B and BE), calculated for a small sample of 15 updraft as defined by Czys (1991) as region of clouds with vertical velocities greater than 1 ms^{-1} for at least 3 continues second of flight.

To determine the buoyancy was used the equation:

$$B = (\theta_v - \theta'_v) - Llwc - Liwc \qquad (2)$$

Where θ_v and θ'_v are the virtual potential temperature of cloud and environment respectively (Czys, 1991), Llwc and Liwc are the net loading of liquid water contents and ice water contents. The warming due to instantaneous isobaric freezing was obtained with equation found in Orville and Hubbard (1973).

$$\delta T = T' - T = L_f/c_p\, Q_l + L_s/c_p\, [q_w(T) - q_l(T')] \quad (3)$$

Where T' and T are the parcel temperature after and before glaciations L_f and L_s the latent heat of fusion and sublimation, Q_l the liquid water expressed as kg of water per kg of air, q_w and q_l are the saturation mixing ratio with respect to water and ice.

As can be seen, when instantaneous isobaric freezing is simulated more than 60 % of the cases with negative buoyancy, become positively buoyant. The isobaric freezing warming δT averaged 0.64 ℃ and ranged from 0.47 to 0.85 ℃.

Table 1. Buoyancy enhancement.

Diam (m)	LWC (g/m^{-3})	B (°C)	BE (°C)	δT_f (°C)	δT_d (°C)
700	0.413	-0.429	-0.284	0,221	0.315
500	0,145	-0.253	0.374	0.078	0.394
400	0.291	-0.437	0.255	0.156	0.368
400	0.030	-0.292	0.314	0.016	0.441
1500	1.553	-1.421	-0.301	0.833	0.015
1200	1.278	-1.057	-0.021	0.685	0.099
1500	1.567	-1.662	-0.546	0.836	0.009
700	0.784	-0.332	0.574	0.419	0.269
500	0.673	0.483	1.403	0.360	0.341
1700	0.356	0.985	1.779	0.190	0.413
1600	0.683	-0.750	0.564	0.367	0.246
1100	0.204	-0.439	0.232	0.110	0.396
1400	0.989	-0.728	0.205	0.533	0.171
800	0.331	0.123	0.865	0.177	0.386
1800	0.713	0.024	0.895	0.381	0.280

Diam- Diameter of updraft; B – Buoyancy; BE – Buoyancy enhancement; δT_f - Warming due to freezing; δT_d – Warming due to depositional processes.

Therefore, though the sample presented herein is small, the response given for updrafts to the simulation instantaneous isobaric freezing reinforces the physical possibilities of alteration of cloud dynamics by glaciogenic seeding.

In another hand, maritime clouds with lower clouds droplets concentration and their wide drop sizes distributions have active coalescence processes, producing glaciations at -10 ℃ or warmer. These clouds are not proper for glaciogenic seeding mode.

As microstructure characteristic illustration of CMS clouds, Figure 2 shows the droplets spectra for the measurements made in 5 cumulus located over CMS (curve 1) and 12 cumulus clouds located over the Caribbean Sea (curve 2). Maritime clouds were at a distance ranged from 140 to 240 km offshore to the south (Pérez et al. 1992).

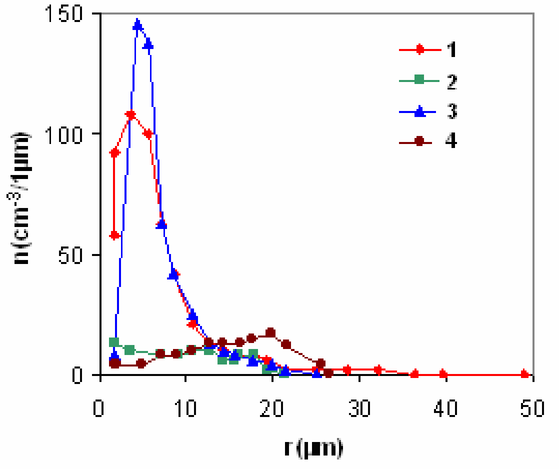

FIG. 2. Averaged size distribution of clouds drops.

Figure 2 gives also averaged size spectra as obtained by Hindman et al. (1992), in continental (curve 3) and maritime clouds (curve 4). The mean value for the concentration drops inside the clouds over Camagüey was 380 cm^{-3} and the mean droplets radius was 6.1 µm. At the same time over the Caribbean Sea the mean value of droplets concentration was 64 cm^{-3} and mean radius of 15.2 µm.

As can be appreciated, clouds developing over CMS can be considered as intermediate and closer to continental.

Clouds are suitable for a effective dynamic seeding when it have a proper coalescence process satisfying the presence of some rain and drizzle drops interspersed in high cloud water contents (Woodley and Rosenfeld, 2003).

Using radar information and airborne measurements made with a photoelectric spectrometer (D>200 µm) of cloud particles, from 139 penetrations of not seeded cumulus clouds in their lower portion and with tops between 3.7 and 11.4 km (Beleaev et al. 1994).

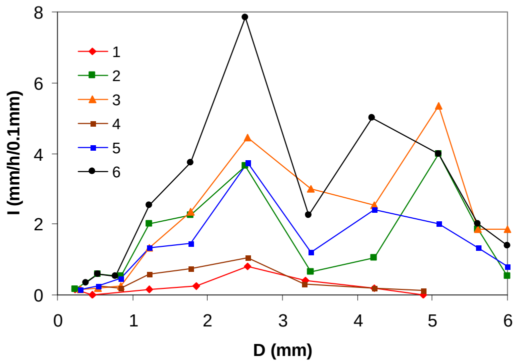

Figure 3. Spectral rainfall intensities:

1- H ≤ 5 km; 2- 5< H ≤7 km; 3- H >7 km (clusters)
4- H ≤ 5 km; 5- 5< H <7 km; 6- H >7 km (isolated).
H: clouds tops.

The behaviour of spectral rainfall intensities as calculated from the measured particle size distribution is shown in the Figure 3, where it is possible to appreciate that in the warm clouds having tops less than 5 km, with only coalescence mechanisms participating in rain formation, a unimodal distribution of precipitation intensities can be observed. For these cases, curve 1 (clusters) and 4 (isolated) are showing an active coalescence process, with peak at 2.5 mm raindrops diameter and some larger than 4 mm. Two modes in the distribution were observed in clouds whose tops were above the freezing level. In such cases both mechanisms, warm and cold, were likely to operate (Petrov et al. 2004).

In Figure 4 we show the frequency histograms for updrafts and downdrafts from measurements made at the levels of 5.6 – 6.1 km in the periods 1986-1989 and 2006-2007.

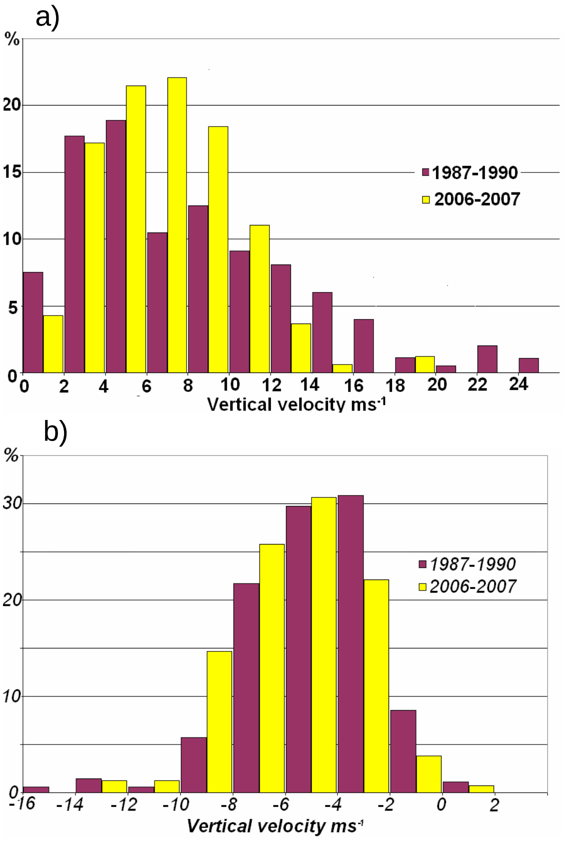

Figure 4. Frequency of Maximum (a) and Minimum (b) velocity of vertical draft for the periods 1987-1990 and 2006-2007.

In the updrafts cases the most part (≈ 85 %) ranged up 2 to 17 ms^{-1} and some cases above 18 ms^{-1} (≈10%) for both periods. In 1987 -1990 cases ≈ 64% of the updraft are between 4 -16 ms^{-1} and 74% for 2006 -2007. Updrafts over passing 6 ms^{-1} are 56% and 57% in the first and second periods respectively. In considering downdrafts for both periods practically all cases are grouped between 0 and -12 ms^{-1} (≈ 97%).

As we can to see, in both periods experimental clouds properties meet the necessary criteria of strong updraft for dynamic seeding.

In the Figure 5 we can to observe the same, because of the enough high quantities of clouds water at the seeding level.

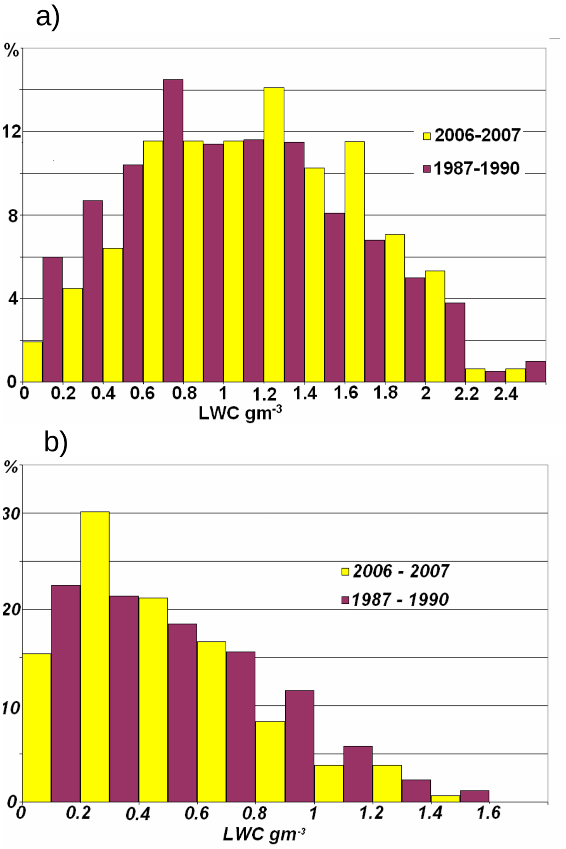

Figure 5. Frequency of maximum (a) and averaged (b) liquid water content values.

Average for maximum values for 1986 - 1990 was 1.025 gm^{-3} and for 2006 – 2007 it was 1.12 gm^{-3}. In the first period, 85% of LWC values are above 0.4 gm^{-3} and in the second the 87%. The behaviour of frequencies distribution for mean values of LWC in both periods result practically the same. Average for 1987 -1990 was 0.486 gm^{-3} and for 2006 – 2007 0.488 gm^{-3}.

According to the behaviour of the phase composition, without the presence of glaciate clouds to -10 ℃ or more warmer levels and the values of LWC jointly with vertical draft magnitudes, we can to express that the cold convective clouds rising in CMS are suitable for the application of conceptual model of dynamical seeding.

Nevertheless in absence of particle measurement probe in Cuban experiments, it is not possible to obtain directly spectral characteristics of solid and liquid phase at seeding level. However considering the behaviour of clouds characteristics given in the Figures 3 and 4 for both periods, is possible to considerer that we are working with similar process in similar clouds. These condition allow the comparison between the measurements of ice particles (D>200 µm) made with the Mee-120 in the 1986-1990 period and measurement of cloud particles (solid and liquid) made with a photoelectric spectrometer for large (D>200 µm) cloud particles in the period 2006-2007. The comparison showed the presence of raindrops at the level of seeding, with concentration ranged between 0 to 11 ℓ^{-1} and an exception with concentration up 21 ℓ^{-1}. The values of concentration obtained are comparable with measurement in South Africa (Mather et al, 1986) and Illinois (Czys and Scott, 1993).

The comparison made using two different devices, in order to obtain raindrop concentration at the seeding level, may be very inexactly and should be use carefully. It is essential the using of a PMS in order to assess with more accuracy the presence of supercooled raindrop.

5. CONCLUSION

The design of EXPAREX experiment was aided by results from experiment in Cuba (1985-1990), West Texas (1987-1990), Thailand (1987-1990) and facets of FACE-I and FACE-II. The EXPAREX design was addressed as continuity of above related experiment and it is based on the results of

Cuban experiments, conducted in CMS during 1985-1990 and similar to the design of the Thailand cold-cloud seeding experiment. As conceptual model guiding, the dynamic-seeding revised conceptual model as discussed by Rosenfeld and Woodley (1993) was adopted.

Tower of cold convective cumulus clouds developed over CMS, satisfies conceptual model for dynamic-seeding:

- The behaviour of the freezing coefficient and ice crystal concentration showed that, the LWC was greater than IWC and the crystal concentration was small enough to provide suitable condition for seeding with glaciogenic reagents. The time evolution showed that in the first third of cloud lifetime the development of solid phase is slow, increase in the second third but not dramatically allowing a seeding window for the CMS clouds.

- The results of simulation of isobaric freezing in some updrafts, suggest that most of negatively buoyant ones would have become nearly neutral, or positively buoyant if they had been seeded. These reinforce the possibilities of alteration of cloud dynamic by glaciogenic seeding.

- In the analysis of droplets spectra measurements made over ground and sea in the same day and during two consecutive days with the same synoptic condition, it was found that spectra obtained for clouds over land are radically different from those for offshore clouds. That allow conclude that clouds growing over CMS nearly continental by their microestructural features.

- In base to the data obtained in the lower parts of clouds, spectral rainfall intensities was calculated from the measured particle size distribution, where it is possible to appreciate an active coalescence process in the lower part of clouds with peak at 2.5 mm raindrops diameter and some larger than 4 mm, in the warm clouds having less than 5 km tops, without ice participation in rain formation.

Date of LWC, ice crystal concentration, vertical in clouds air motions and the suggestion of the presence of raindrops at the seeding level, provide a consistent picture of cloud structure in the supercooled region which indicate that is possible the proper application of glaciogenic seeding within the vigorous supercooled updraft with enough high LWC and some raindrops interspersed, generated from below by coalescence. That is according with the dynamic-seeding revised conceptual model as adopted by the design of EXPAREX.

6. ACKNOWLEDGEMENTS

The authors thank the Cuban Government and particularly Institute for Civil Aeronautic, for coordinating and financing EXPAREX.

Our thanks are given to the EXPAREX research team for discussion, suggestion and their helpful comments. The authors also wishes to thank, engineers, technician, pilots and flight personal for their efforts in the measurements accomplished.

7. REFERENCES

Beliaev, V. P., B. P. Koloskov, A.V. Koldaev, V.V. Petrov, Y.A. Seregin., A.A. Chernikov and C.Pérez, 1994: A physical evaluation of the suitability of convective clouds for seeding. Proc.Sixth WMO Scientific Conf.on Weather Modification, Paestum, Italy, World Meteor. Org., 349-352.

Czys R. R., 1991: A Preliminary Apraisal of The Natural Structure and Seedability of Updrafts in Midwestern Cumulus At The – 10 ^{0}C. Jour. Wea. Mod., **23**, 1 – 17.

-----and R. W. Scott, 1993: A simple objective method used to forecast convective activity during 1989 PACE cloud-seeding experiment. J. Appl. Meteor., **32**, 996-1005

Dmitriev V. K., M.A. Strunin, 1983: Aircraft measurements of the vertical components of wind speed fluctuations. Trudy CAO, issue 147, 39-51.

Hindman E. E., K. Y. Kong, R. D. Borys, 1992: Initiation of long–term cloud droplets measurements for climate change studies. Proceeding of Symposium on Planned and Inadvertent Weather Modification. Atlanta, USA.

Koloskov B., B. Zimin, V. Beliaev, Yu. Seregin, A. Chernikov, V. Petrov, M. Valdés, D. Martínez, C. Pérez, G. Puente, 1996: Results of Experiments on Convective Precipitation Enhancement in the Camagüey Experimental Area, Cuba. Journal of Applied Meteorology, **35**, 1524-1534.

Mather G. K., B. J, Morrison, and G. M. Morgan Jr., 1986: A preliminary assessment of the importance of coalescence in convective clouds. J. Climate Appl. Meteor., **20**, 29-47.

Mossop S. C., 1976: Production of secondary ice particle during the growth of graupel by riming. Quart. J. Roy. Meteor. Soc., **102**, 45-57.

Nevzorov A. N., 1996: CAO aircraft instrumentation for cloud physics. 12th International Conf. on Cloud Phys. and Precipitation. Aug. 19-23, V.1, Zurich, Switzerland, pp. 371-374.

Orville, H. D. and K. Hubbard, 1973: On the freezing of liquid water in cloud. J. Appl. Meteor., **12**, 671-676.

Pérez C., D. Martínez and V. Petrov (1992): Microstructure, mixing and turbulence in cumulus clouds over Cuba and the Caribbean Sea. In: Proceedings WMO Workshop on Cloud Microphysics and Application to Global Change, Toronto, 1992. WMP Report No. 19 WMO/TD 537. pp. 245-256.

Pérez C., M. Oms, D. Martínez and V. Petrov (1994): Phase composition and seedability of cumulus clouds in the Camagüey Meteorological Site, Cuba. Sixth WMO Scientific Conference on Weather Modification, Paestum. WMP Report No. 22. WMO/TD No. 596. Vol. 2, pp.379-282.

Pérez C. A., D. Martínez, F. Gamboa, V. Petrov, B. Kalaskov and B. Daneilan: Design of the Cuban Experiment for Artificial Enhancement of Rain In Extended Areas. III Cuban Congress of Meteorology. La Habana, Dec., 2005.

Petrov V. V., D. Martínez, and C. A. Pérez, 2004 The Microphysical and Thermodynamic Characteristics of Tropical Convective Clouds by Results of Measurements on Cuba. WMO International Conference on Clouds and Precipitation. 18-24 July 2004, Bologna, Italy.

Rosenfeld, D. and W. L. Woodley, 1993: Effects of cloud seeding in West Texas: Additional results and new insights. Journal of Applied Meteorology, **32**, 1848-1866.

Rosenfeld D. and W. L. Woodley, 1996: Microphysical response of summer convective clouds in West Texas to AgI ‘dynamic' seeding. Proceedings of 12th. International Conference on Clouds and Precipitation. (ICCP), Zurich, Switzerland.

Sevnev I. L., M. B. Pinsky, A. P. Khain and D. Rosenfeld, 1996: The role of ice generation in precipitation formation as seen from the results obtained using a mixed – phase cloud model with spectral microphysics. Proceedings of 12th. International Conference on Clouds and Precipitation. (ICCP), Zurich, Switzerland.

Silverman, B. A., C. L. Hartzell, W. L. Woodley and D. Rosenfeld, 1994: Thailand Applied Atmospheric Resources Research Program, Vol. 2. Demostration Project Design. Rept. No. R-94-01, Bureau of Reclamation, U.S. Dept. of Interior, 183 pp.

Simpson, J., R. H. Simpson, D. A. Andrews, and M. A. Eaton, 1965: Experimental cumulus dynamics. Rev Geophys., **3**, 387-431.

-----, 1980: Downdraft as linkages in cumulus seeding effect. J. Appl. Meteor., **19**, 477-487.

Wooley, W. L., and R. I. Sax, 1976: The Florida Area Cumulus Experiment: Rationale. Design Procedure, Results, and Future Course. NOAA Technical Report ERL 354-WMPO 6. Boulder, Colo. 204 pp.

-----, J. Jordan, J. Simpson, R. Biondini, J. A. Flueck, and A. Barston, 1982: Rainfall Results for the Florida Area Cumulus Experiment, 1970-1976. J. Appl. Meteor., **21**, 139-164.

-----, D. Rosenfeld, W. Kukamjanaset, P. Sudhikoses, S. Ruangsuttinaruparp and W. Khantiganan, 1999: The Thailand cold-cloud seeding experiment: 1. physical-statistical design. Proc. of 7th WMO Conf. on Wea. Mod., 16-22 Feb., 1999, Chiang Mai, Thailand.

-----, D. Rosenfeld, and B. A. Silverman 2003a: Results of on-top glaciogenic cloud seeding in Thailand. Part I: The demostration experiment. J.Appl. Meteor., **42**, 920-938.

-----, D. Rosenfeld, and B. A. Silverman, 2003b:

Results of on-top glaciogenic cloud seeding in Thailand. Part II: Exploratory analyses. J.Appl. Meteor., **42**, 939-95.

-----, and D. Rosenfeld, 2002: Secondary seeding as a means of propagating seeding effect in space and time. J. Wea> Modif., **34**, 31-38.

World Meteorological Organization, 1977: Aircraft instrumentation for cloud physics research on weather modification programmes. WMO Report No. 7, 78 pp.

NUMERICAL STUDY OF CONVECTIVE SUPERCELL EVENTS OBSERVED IN CRIMEA

Ganna Pirnach and Vitalii Shpyg
Ukrainian Hydrometeorological Research Institute

1. INTRODUCTION

A recent work continued many years of theoretical investigation of the dynamic and microphysics of cloud and precipitation on the mesoscale of atmospheric fronts and fulfilled in UHRI and other scientist community. Numerical models of the frontal cloud systems passing over Crimea have been used for theoretical interpretation of the field measurements in cumulus clouds that were carried out on the Hail Suppression Proving Ground. Field investigation has been conducted in the eastern Crimea. System “Antigrad” was used for radar measurements. Cases with a severe storm on July 22, 2002 and a super cell on September 27, 2002 will be presented.

2. METHODOLOGY

Formation and development in space and time of atmospheric front and its cloud system are simulated by integration of the set of the full equations for dynamic and thermodynamic and kinetic equations for the cloud particle sizes distribution functions:

The 3-D nowcasting and forecasting models that have been developed in UHRI for modeling of the winter and summer frontal cloud systems were modified by orography and carried out for numerical simulation of warm-season frontal clouds (see Pirmach, 1998, Pirnach, 2004, Pirnach and Shpyg, 2007, etc.). Cartesian coordinates and terrain-following sigma coordinates have been used. Coordinates named as (x, y, z) for all cases directed in east, north and vertical directions.

Features of the vortex movement in cumulus clouds and their nearest environment were basically investigated. A process of spout formation has been investigated by means of analyses of the vorticity and components its equation. Cyclonic and anticyclonic whirls that developed in investigated spout-dangerous region were modeled for different frontal cumulonimbus.

3. NUMERICAL RESULTS

Numerical models of the frontal cloud systems passing over the Crimea were used for theoretical interpretation of the field measurements in cumulus clouds that were carried out on the Hail Suppression Proving Ground (HSPG). For modeling of the supercell evolution the calculated scheme developed in (Pirnach and Shpyg, 2007) was used. This scheme sometime increase updraft, and downdrafts and precipitation but that let more clearly found the location, and formation, and development of deep convective cell features and heavy precipitation. The prognostic models were used in recent runs for founding of key parameters and processes leading to formation deep convective cell, and supercell, and heavy rainfall events, and damaging event observed in Crimea.

Case of September 27. Numerical modeling of cloud evolution with initial stage t = 0 at 1100 GMT depicted that most strong vertical motion, clouds and precipitation were in region of observed supercell centred at point (x, y)=(75, 40 km). Synoptical situation and details of the field experiment observations see in (Pirnach and Shpyg, 2007). Location of the real supercells and their vertical sizes is shown in Fig.1. During field measurements the supercell was fixed nearby the proving ground area in north-east about 10-20 km farther it in moment of field experiment starting and move in named direction.

Mesoscale convective systems with heavy precipitation were identified by strong updraft and downdraft columns, intensive rotor movement of both signs, heterogeneous distribution of equivalent potential temperatures, positive kinetic energy, cell structure of pressure, etc.

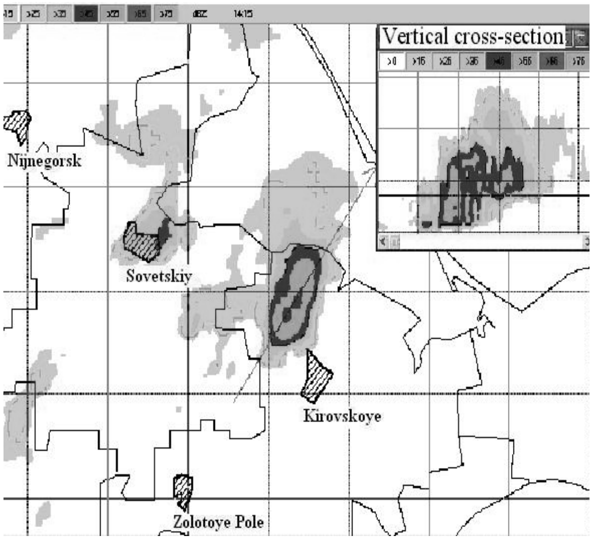

Figure 1. Horizontal (5 km height) and vertical cross-sections of the convective cloud reflectivity (1115 GMT). Sizes of grid cell are 10 km and 5 km in horizontal and vertical section respectively.

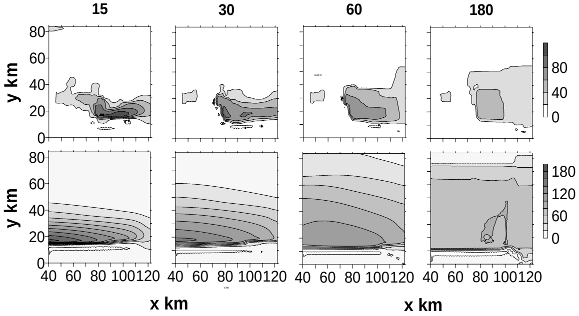

Figure 2. Spatial and temporal distribution of z-maximum updrafts. Numbers on top are t min. First row presented a run with orography, second row presents the run without including relief.

Fig.2 presented calculating of cloud cells for complex relief with and without topography. Comparison between both rows on fig.2 is clearly confirming a key role of relief on development of cloudiness in mountain region.

Disturbance zones promoted formation of cells and bands of frontal ascending movement and were responsible for transportation mechanism of moisture. High updraft columns caused appearance of deep *Cb* clouds with crystal tops (seeder zones) and mixed layers under (feeder zones) (see Figs. 2, 3).

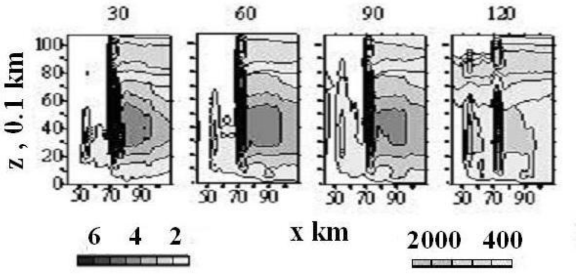

Figure 3. Vertical cross-sections of cloudiness at different calculated time, t, min; numbers on tops). First scale presents water content, $q_{w,}$ g/kg; numbers near second scale are ice concentration, N_i, 1/g.

Number falling crystals seeded the feeder zones, grown to size of precipitation particles and resulted in heavy precipitation. Vortical features in cumulus clouds and nearest environment were investigated basically. Theoretical interpretation of field experiments by numerical modeling has shown that appearance of new cyclonic cells predicted a new convective cells formation. Cyclonic vortical cells correspond to the initial stage and stage of maximal development of convective cells. An existence of the coupled cyclonic and anticyclonic vortexes is possible at the stage of maximal development of convective cloud. Decomposition of convective cells was followed by reduction of angular rotation and anticyclonic vortex.

Case of July 22. In this case the possible reasons of formation such interesting and dangerous atmospheric phenomenon as a convective severe storm is considered. Time t = 0 corresponds to 1100 GMT. Inspection of an operative range of spouts in village Vypasne has shown, that in a zone of villages Tomashivka-Vypasne operated four spouts, in a zone of village Lobanove one spout operated (see Fig.4). Here it has not been genetically connected to the others. It has been connected to other cloudy system and moved it toward. The exact times of spouts action (1250 GMT). In more detail, description of this phenomena see in Leskov at al., 2008.

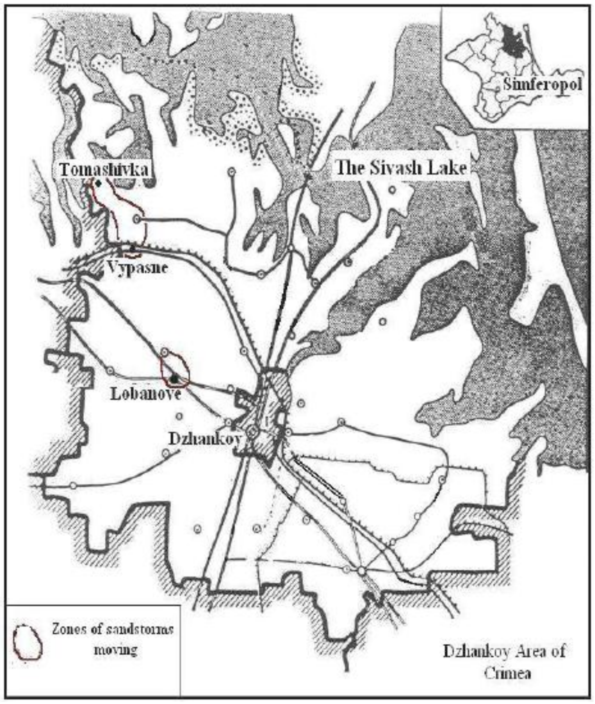

***Figure 4*. T**he scheme of Dzhankoy Area and zones of spout moving.
Coordinates (x; y): Simferopol(0; 0 km), Dgankoy (19; 113 km), Lobanove(9; 120 km), Vypasne (3; 132 km), Tomashivka (-1; 139 km).

Spout was formed under powerful Cb which tops have reached to tropopause. Passage of spout was accompanied by thunder-storms and showers, and the area occupied with these phenomena, there were more than zones with spouts. Numerical simulation were conducted with aim to determine key parameters and processes leading to formation deep convective cells and observed damaging events. Three series of numerical runs have been conducted with aim of investigation of key parameters of spout development: (Case 1) runs with clouds for complex relief; (Case 2) runs without clouds; (Case 3) runs for flat terrain. In Fig.5 presented those cases for pressure, temperature and vertical component of vorticity as named as rotor (rot) at 12 45 GMT.

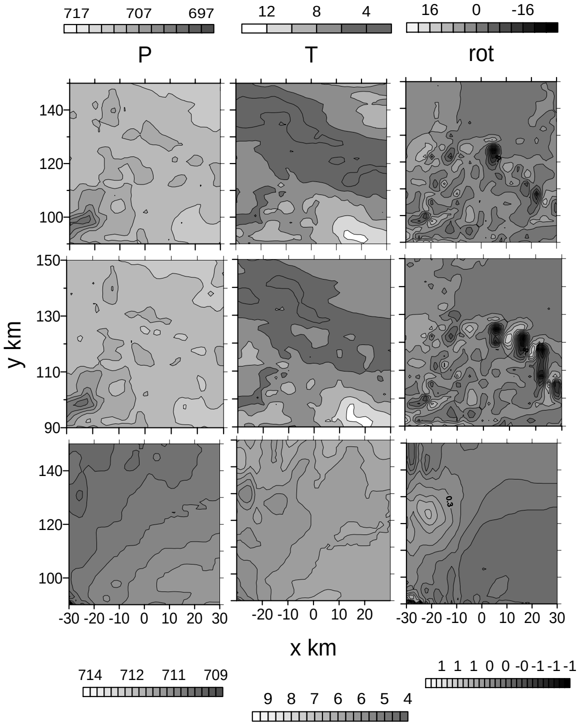

***Figure 5**.* Pressure (p, mb), temperature (T^o, C), rotor (rot, 10^{-3}/s) at t=105 min (1245 GMT) and z = 3 km. First row shows results of run with clouds for complex relief; second row presents the run without including cloudiness; third row shows a case with clouds and flat relief.

Cell structure of pressure, and rotor, and band of cold air mass has place in investigated regions for first and second cases and directed from north-west to south-east. In first case cyclonic rotor cells dominate in north-west and anticyclonic cells dominate in east part area in second case. Those cells surrounded the area with anticyclonic movement. In Case 3 presented features have more regular structure and cyclonic rotor was clearly depicted in north-west part of the picture.
Vertical motions in spout-dangerous region were very strong and reached 15m/s and more sometime. Calculated updraft z-maximums (see Fig.6) for first and third cases corroborate the physical mechanism explaining the development of those storms. Prevalence of the topography is explained. It is intended also to corroborate the hypothesis that the storm can be classified

as a supercell from the point of view of the simulation.

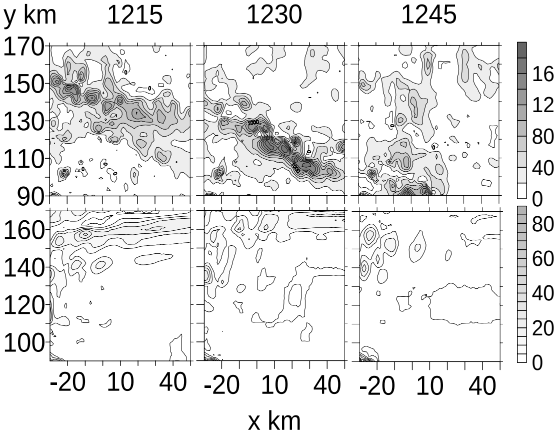

Figure 6. Space and time distribution of updraft z-maximums, w_{max}, during the spout activity. Digits near scale are w_{max}, cm/s. Digits in the picture tops note the time, GMT. First row: runs by terrain-following sigma coordinates. Second row: Cartesian coordinates were used.

Table 1 presented the highest w_{max} and mean w_{max} for target area included place of spout activity. At t=1h 30 min (1230 GMT) w_{max} reached 18 m/s for Case1.
It is time approached to time of dangerous spout described.

Table 1.
Time development of updraft z-maximum, w_{max} [cm/s] and mean updrafts, w_{mean} [cm/s] in area -20<x<30 km, 100<y<150 km

t, h	1	2	3	4
		w_{max}		
1.0	629	614	204	201
1.5	1773	1682	73	86
2.0	500	628	63	79
2.5	609	456	30	29
3.0	400	490	69	51
4.0	644	537	801	588
		w_{mean}		
1.0	184	190	63	64
1.5	386	355	15	16
2.0	138	159	17	23
2.5	135	109	7	7
3.0	108	114	10	11
4.0	127	112	97	162

In Case 1 and Case 2 vertical motions have difference distribution but convective values of updrafts and downdrafts maintained. Runs for flat relief decreased those motions fundamentally. Super cells disappeared.

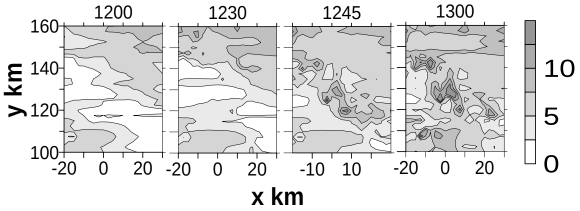

Figure 7. Space and time distribution of clouds, during the spout activity. Digits near scale are the total water content z-integral, s, mm.

During investigated time in cloud cover appeared convective cells with highest s exceeded 20 mm (see fig. 7).

4. CONCLUSION

Highiest gradient of pressure, and temperature, and rotor forced by orography caused development of cold stream of air, bands of strong updraft and downdraft, chain cyclonic and anticyclonic rotors and strong convective cells with updraft reached tens m/s.
Supercells disappeared if relief is flat.
Clouds modified the rotor and convective cells distribution but keep their power and existence.

5. BIBLIOGRAPHY

1. Leskov, B.N, Pirnach, A.M., Sirota, M.V., Shpyg, V.M., 2008: Spouts in Crimea of 2002, July 22. Trudy UHRI, **256**.
2. Pirnach, A.M., 1998: Construction and application of the various numerical models for study the cloud dynamics and structure of the frontal rainbands. J. Atmos. Res., **45-47**, 356- 376.
3. Pirnach, A.M., 2004: Numerical simulation of frontal clouds with heavy precipitation for flat and mountain relief. Trudy UHRI **251,** 31-50.
4. Pirnach, A.M., Shpyg V.M., 2007: Simulation the deep convective clouds. Geoinformatic, **4,** 86-94**.**

PRECIPITATION FROM TROPICAL CLOUDS SAMPLED DURING EPIC2001

G. B. Raga and D. G. Baumgardner
Centro de Ciencias de la Atmósfera, Universidad Nacional Autónoma de México

Background

The formation and evolution of precipitation is sensitive to the type and quantity of atmospheric aerosols under certain circumstances. Elevated concentrations of anthropogenic aerosols have been the focus of a number of studies related to precipitation formation. Some studies indicate suppression of precipitation while other suggest no change or even an enhancement (Yin et al. 2002; Khain et al. 2004; Khain et al. 2005; Seifert and Beheng 2005; Wang 2005; Lynn et al. 2005a,b; Levin et al. 2005). The relationship between the processes that produce precipitation and the nuclei, onto which water and ice hydrometeors are formed, is complex and remains an active topic of investigation.

In the present study, observations of aerosols and cloud particles are evaluated from measurements made in convective clouds that developed in the tropical East Pacific, on some days under conditions of no anthropogenic influence and on other days when there was clear evidence of pollution from manmade sources. These cases are analyzed to assess how much, if any, influence the aerosol particles had on the characteristics of the observed precipitation.

Methodology

Measurements of the size distributions of raindrops in convective clouds that developed in the inter-tropical convergence zone near Mexico were obtained during the East Pacific Investigation of Climate (EPIC) experiment in 2001. These measurements were made with optical spectrometers, the Forward Scattering Spectrometer Probe[1], Model 100, (FSSP-100) and the cloud and precipitation, two-dimensional optical array probes[1] (2D-C and 2D-P OAP) mounted on the C-130 research aircraft (National Science Foundation, operated by the National Center for Atmospheric Research). In addition to capturing shadow images of individual drops between 25 μm and 6400 μm, the OAPs also record the distance between each drop via a measurement of arrival times in the spectrometers' lasers. The separation distance, along with the drop size, provides detailed information about the microstructure of precipitation.

The aerosol particle properties were measured with a condensation nuclei counter[2] (CNC), a cloud condensation nuclei (CCN) counter[3] and a Passive Cavity Aerosol Spectrometer Probe[1] (PCASP). Details of the instrumentation and the nature of the project can be found in Baumgardner et al. (2005).

Results and Discussion

The measurements were taken in a region bounded by 8º to 12º N in latitude, 92º to 96º W in longitude, approximately 800 km from the coast of southern Mexico (Fig. 1).

The condensation nuclei clearly indicated two different conditions in the region related to the source of aerosols: a) clean maritime conditions when the winds were predominantly west/southwest and b) polluted air when the winds have a northerly component. As shown in Fig. 2 the CN concentrations (for particles larger than 0.05

---

[1] Droplet Measurement Technologies, Inc.
[2] TSI Model 3026
[3] University of Wyoming Model 100

µm) are on average four times larger under polluted conditions compared to the clean air case. The larger particles are also quite different as seen in the PCASP measurements, for particles with diameters larger than 0.1 µm and smaller than 3 µm.

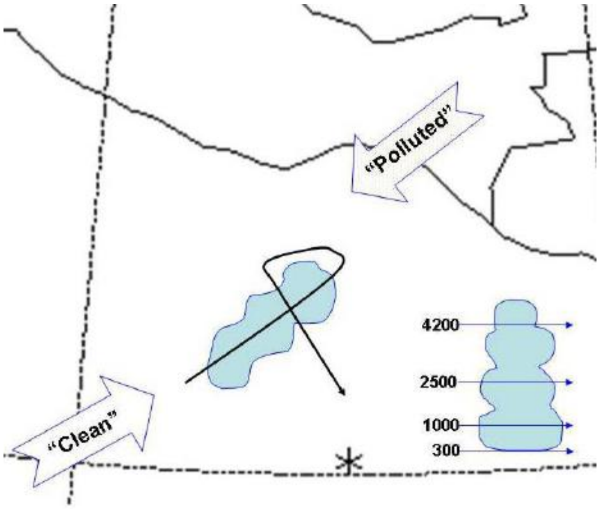

Figure 1

The average concentrations of particles in this size range are also four times higher in the polluted air masses.

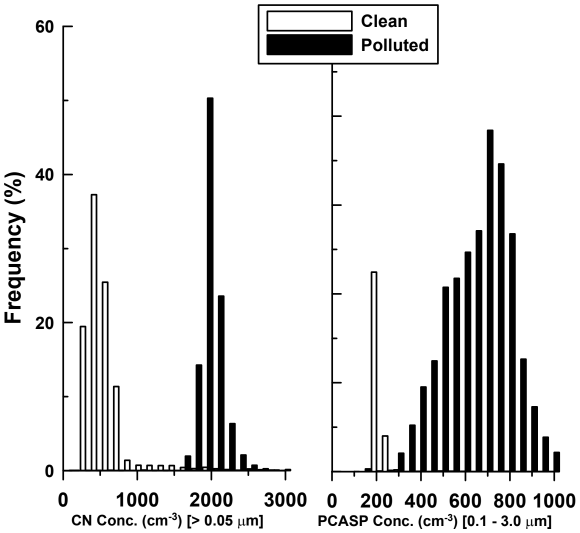

Figure 2

These large differences in the aerosol population lead us to hypothesize that the cloud microphysical properties would reflect the changes in CCN represented by the aerosol particles, i.e. that the cloud droplet concentrations should increase while the median volume diameters (DMVD) decrease leading to lower precipitation rates. The measurements were stratified according to where they were made in the cloud, separating updraft from downdraft regions, and by the aerosol properties, i.e. clean versus polluted. Figure 3 illustrates how the precipitation drop sizes and the FSSP and 2D measured concentrations vary with the changes in vertical velocity (top panel, black curve). Individual drop sizes are shown as blue filled circles and the FSSP concentrations with the red curve. In this particular illustration we see that the maximum FSSP concentrations are in the regions of maximum updraft whereas the precipitation maximizes in the downdraft regions where the largest drops are also found.

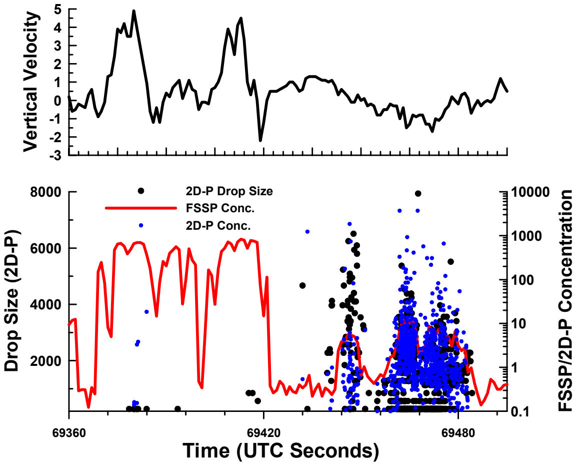

Figure 3

A comparison of the cloud droplet properties, represented by the concentrations, DMVDs and liquid water content (LWC, derived from the size distribution) shows that the differences in the droplet number concentrations between the clean and polluted air mass manifests itself only in the updraft regions and differences in the average DMVD are seen only in the downdrafts. As shown in the frequency distributions (Fig. 4), droplet concentrations are broadly distributed with values as large as 1000 cm^{-3} and a mode of 650 cm^{-3} in polluted air masses, whereas clouds formed in clean air had maximum concentrations of 400 cm^{-3} and a mode of 100 cm^{-3}. There is little difference in the DMVD between the two cases with both having the same mode at 20 µm and the clean air case has a somewhat longer tail towards larger DMVD. In the downdraft portions of the clouds, however, the mode of the DMVD frequency distribution is 28 µm in clean air clouds and 20 µm in polluted clouds. It should be noted that there is a second mode at 28 µm in the polluted case. The frequency distributions for the droplet number concentrations in clean clouds are almost identical in up and downdraft regions but the polluted clouds have distinctly different distributions. In the downdraft regions there is no difference between the clean and polluted clouds, whereas the updrafts showed much broader distributions for the polluted case.

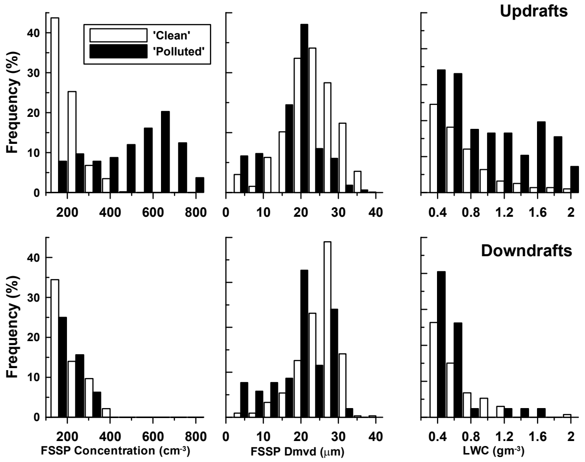

Figure 4

The LWC reflects a similar behavior as the number concentrations. In the downdrafts the majority of the LWC for both clean and polluted clouds is less than 0.8 g m^{-3}. In the updraft region, the clean cloud frequency distributions are similar to the downdraft regions but the polluted clouds have a uniform distribution from 0.8 up to almost 2 gm^{-3}. This larger LWC amounts are consistent with the much broader droplet number concentrations in the polluted clouds.

The frequency distributions of drizzle concentration (> 100 µm), rain rate and reflectivity derived from the 2D OAPs measurements also show marked differences based on vertical velocity and aerosol properties.

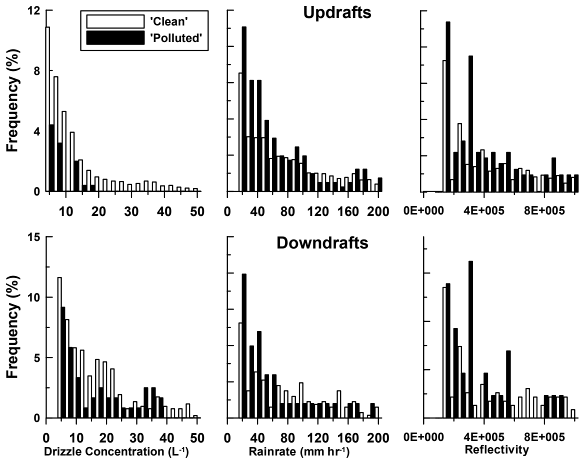

Figure 5

As illustrated in Fig. 5 in the downdraft regions the clean and polluted cases are relatively similar except that the clean clouds have a secondary maximum in their frequency distribution at around 20 l^{-1}. The polluted clouds have a secondary maximum at the same concentration, although at half the frequency as the clean case. The polluted clouds also show a tertiary maximum with the same frequency at 35 l^{-1}. In the updrafts, the polluted cloud frequencies are restricted to less than 15 l^{-1} whereas the clean clouds range up to 50 l^{-1}. The remarkable difference in the frequency distribution between clean and polluted clouds is related to the difference in the droplet number concentrations. This observation is consistent with the more effective coalescence occurring when fewer cloud droplets are present in the clean case (mode ~ 100 cm^{-3}), and suppressed autoconversion in the polluted case (mode ~ 700 cm^{-3})

The frequency distribution of rainrates shows no distinguishing features between the clean and polluted clouds that would indicate that the aerosol conditions were changing this precipitation property. Likewise the reflectivity distributions show no observable differences.

The explanation for the lack of difference in the rainrate and reflectivity when the cloud droplet concentrations, DMVD and drizzle concentrations show significant disagreement can be found in the frequency distribution of the large drop population, those larger than two millimeters. Figure 6 shows that in the updraft regions the distributions are similar with the clean clouds having a slightly longer tail towards larger sizes than the polluted case. In the downdraft region, however, the polluted clouds have a somewhat higher frequency of larger drops.

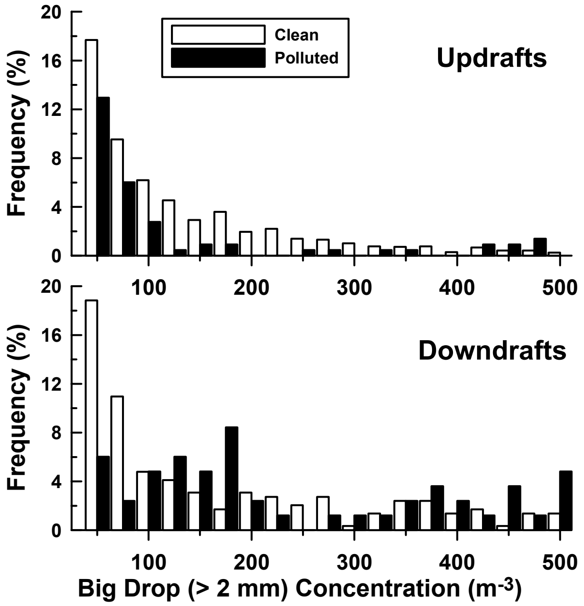

Figure 6

The convective clouds were sampled at mid- to lower levels, where temperatures were typically warmer than -5C. The clouds extended well beyond the -5C isotherm in depth, so that the cold rain processes were active in them. The big raindrops shown in Fig. 6 would have likely been melted frozen hydrometeors produced higher up in the clouds. Larger concentrations of big drops are observed in the polluted case, which would contradict the hypothesis that more rain should fall from clean clouds. In reality, in the polluted clouds there are many more cloud droplets in the updrafts, so that more LWC could be transported to the super-cooled regions of the clouds, where they would be available for interaction with the ice crystals at those levels. In contrast, the clean clouds would have less supercooled water at higher levels, and reduced growth rate of precipitating ice particles.

The rainrate and reflectivity are linearly proportional to the concentration but proportional to the fifth and sixth power of the drop diameter, respectively. This indicates that the population of large drops in the clouds will dominate the perceived precipitation reaching the ground and also that which is detected by radar.

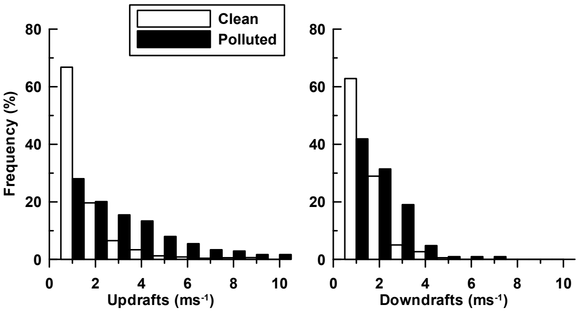

Figure 7

Figure 7, showing the frequency distribution of vertical winds in the clouds at flight levels between 1000 and 3000 m, provides further insight on why both clean and polluted clouds produce large drops. The majority of updrafts in the clean clouds were small, less than 2 ms^{-1} whereas the polluted clouds had more frequent stronger updrafts. Thus, although the droplets in the clean clouds may have grown faster leading to larger drops through coalescence, the polluted clouds were probably deeper with more time for droplets to grow in the updrafts. While individual days displayed a certain amount of variability in the convective available energy for convection, the soundings for the whole EPIC period showed consistent vertical profiles of entropy, with only small vertical shear (Raymond et al, 2003).

Summary

A comparison of measurements in clouds that developed under clean and polluted conditions in the Eastern Mexican Pacific show that the frequency of large drops and the derived rainrates and reflectivities are similar even though the background aerosol population and cloud droplet concentrations are quite different. The conclusion is that the large drops are being formed from different processes: coalescence for the clean clouds and ice phase for the polluted. These results show that cloud dynamics are as important as the background CCN for the processes that lead to precipitation.

Acknowledgements

The authors would like to thank the US National Science Foundation for supporting their participation in EPIC and the flight crew of the Research Aviation Facility, National Center for Atmospheric Research, for their support of the aircraft and instrumentation. This research was also funded under CONACYT Grant # 33319.

References

Baumgardner, D., G.B. Raga, J.C. Jimenez, J.C., K. Bower, **2005**: Aerosol particles in the Mexican East Pacific part I: Processing and vertical redistribution by clouds, *Atmos. Chem. Phys.*, 5, 3081–3091.

Khain A. and A. Pokrovsky, 2004: "Effects of atmospheric aerosols on deep convective clouds as seen from simulations using a spectral microphysics mixed-phase cumulus cloud model Part 2: Sensitivity study". J. Atmos. Sci. 61, 2983-3001

Khain, A. D. Rosenfeld and A. Pokrovsky 2005: Aerosol impact on the dynamics and microphysics of convective clouds. Q. J. Roy. Meteor. Soc. 131, 2639-2663.

Levin, Z., A. Teller, E. Ganor, and Y. Yin, 2005: On the interactions of mineral dust, sea-salt particles, and clouds: A measurement and modeling study from the Mediterranean Israeli Dust Experiment campaign. J. Geophys. Res., 110.

Lynn B., A. Khain, J. Dudhia, D. Rosenfeld, A. Pokrovsky, and A. Seifert 2005a: Spectral (bin) microphysics coupled with a mesoscale model (MM5). Part 1. Model description and first results. Mon. Wea. Rev., 133, 44-58.

Lynn B., A. Khain, J. Dudhia, D. Rosenfeld, A. Pokrovsky, and A. Seifert 2005b: Spectral (bin) microphysics coupled with a mesoscale model (MM5). Part 2: Simulation of a CaPe rain event with squall line. Mon. Wea. Rev. , 133, 59-71

Seifert, A. and K.D. Beheng, 2005: A two-moment cloud microphysics parameterization for mixed-phase clouds. Part II : Maritime vs. continental deep convective storms. Meteorology and Atmospheric Physics, 92, 67-82.

Raymond, D, R. B. Raga, C. Bretherton, J. Molinari, C. Lopez-Carrillo and Z. Fuchs, 2003: Convective forcing in the Intertropical Convergence zone of the Eastern Pacific. J. Atmos. Sci., 60, 2064-2082.

Wang C., 2005: A modeling study of the response of tropical deep convection to the increase of cloud condensational nuclei concentration: 1. Dynamics and microphysics. J. Geophys. Res.,110; D21211, doi:10.1029/2004JD005720.

Yin, Y., S. Wurzler, Z. Levin, T. G. Reisin, and S. Tzivion, 2002: Interactions of mineral dust particles and clouds: Effects on precipitation and cloud optical properties, J. Geophys. Res., 107, doi:10.1029/2001JD001544.

INDIRECT IMPACT OF ATMOSPHERIC AEROSOLS ON DEEP ORGANIZED CONVECTION: RESULTS FROM A PRESCRIBED-FLOW MODEL WITH A TWO-MOMENT BULK MICROPHYSICS SCHEME

Joanna Slawinska[1], Wojciech W. Grabowski[2]*, and Hugh Morrison[2]

[1] Institute of Geophysics, University of Warsaw, Warsaw, Poland
[2] National Center for Atmospheric Research, Boulder, Colorado

1. INDIRECT AEROSOL EFFECTS AND DEEP CONVECTION

Modification of cloud microphysics through changes of nucleating aerosols (e.g., due to anthropogenic emissions) is commonly referred to as the indirect aerosol effect on climate, in contrast to the direct effect due to absorption and scattering of radiation by aerosols in cloud-free air. The indirect effect is an uncertain aspect in climate change (IPCC 2007) and it is traditionally associated with two effects: the impact on the size of cloud particles which changes optical properties of clouds (most importantly, cloud albedo); and the impact on precipitation processes which can potentially affect abundance, extent, and lifetime of some types of clouds.

The indirect effects for warm shallow clouds (such as trade-wind cumulus and subtropical stratocumulus) have been the subject of vigorous theoretical and observational studies. For deep convection, studies concerning indirect effects are in their infancy, not least because of uncertainties associated with the modeling of ice processes. For instance, Wang (2005) found in his simulations that clouds developing in environments with higher concentration of CCN result in convection being stronger, reaching higher levels, and producing more precipitation. This was argued to occur through the interaction between warm-rain and ice processes, with less effective warm-rain processes in high-CCN environments resulting in more condensed water arriving at the freezing level and resulting in more latent heating aloft due to increased freezing. However, Cui et al. (2006) found the opposite result when modeling convection which occurred during CCOPE. In their simulations, increased aerosol led to the inhibition of cloud development and suppression of precipitation.

A significant fraction of precipitation on Earth falls from organized convection, i.e., mesoscale convective systems (e.g., Houze 2004). A classical example of such a system is a squall line, a large (horizontal extent of up to several hundreds km), fast-propagating system, characterized by the leading edge deep convection and trailing anvil cloud with extensive stratiform precipitation. Understanding aerosol effects on precipitation in such systems is arguably of significant importance and can involve contrasting effects (e.g., reduction or enhancement of the total precipitation) depending on environmental conditions such as environmental temperature or moisture profiles, or system dynamics (e.g., the convective updraft strength). In this paper we present preliminary results of an investigation of indirect aerosol effects in such systems using an idealized two-dimensional framework with prescribed flow (i.e., using the kinematic model). Such a framework allows separating indirect effects on cloud microphysics from those associated with cloud dynamics (i.e., when the changes in cloud microphysics affect the flow which is not possible in the kinematic model). Moreover, a kinematic framework offers an inexpensive way to explore the relevant parameter space for both the flow and representation of cloud microphysics. Arguably, once indirect effects are understood in such a relatively simple system, results from subsequent dynamic model simulations will be easier to interpret. Kinematic models have been used in the past (e.g., Rutledge and Hobbs 1984; Morrison and Grabowski 2007; 2008a) and the current study extends such an approach to the organized convection.

2. THE MODEL AND MODELING SETUP

The kinematic model used here represents microphysical processes using a double-moment warm-rain scheme (i.e., predicting number concentrations

---

* *Corresponding author address*: Dr. Wojciech W. Grabowski NCAR, PO Box 3000, Boulder, CO 80307; e-mail: grabow@ncar.ucar.edu.

and mixing ratios of cloud water and rain; Morrison and Grabowski 2007; 2008a) combined with a novel approach to represent ice processes (Morrison and Grabowski 2008b). In this approach, the ice particle mass-dimension and projected-area-dimension relationships vary as a function of particle size and rimed mass fraction. The rimed mass fraction is predicted locally by separately predicting the ice mixing ratios acquired through water vapor deposition and through riming. The third ice variable is the number concentration of ice particles. This approach allows representing in a natural way gradual transition from small to large ice particles due to growth by water vapor deposition and aggregation, and from unrimed crystals to graupel due to riming. See Morrison and Grabowski (2008b) for more details.

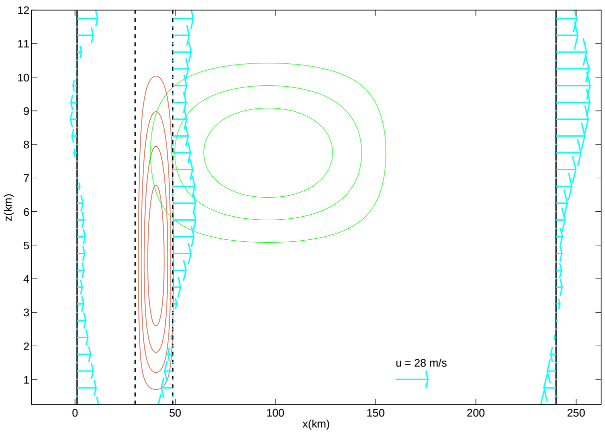

Figure 1: Computational domain and the flow pattern for the kinematic model simulations. The vertical velocity is shown using different contur intervals for the convective region (3.25 m s^{-1}; red color) and the stratiform region (0.33 m s^{-1}; green color). The convective region is for $30 \leq x \leq 48$ km with its boundaries shown as dashed lines in the figure. The stratiform region is for $48 \leq x \leq 240$ km. Horizontal velocity vectors (blue color) are shown at the lateral boundaries and at the boundary between convective and stratiform regions.

The prescribed-flow pattern includes a strong deep ascent in the convective part and relatively weak upper-tropospheric ascent in the stratiform part. The flow pattern is a combination of convective and stratiform flow regimes applied independently in kinematic-model simulations discussed in Grabowski (1999, section 3 therein). The model solves conservation equations for the hydrometeors (four variables for warm-rain processes and three variables for ice) as well as equations for the potential temperature and water vapor mixing ratio. These equations include advective transport (including hydrometeor sedimentation) and sources/sinks due to phase changes and latent heating. Transport in the physical space is calculated using the 2D version of the MPDATA scheme (e.g., Smolarkiewicz and Margolin 1998).

In current simulations, the computational domain is 240 km long (x direction) and 12 km deep (z direction). It is covered with a uniform grid with horizontal/vertical gridlength of 750/250 m. The boundary conditions are free-slip rigid lid in z. For scalars, the inflow lateral boundary conditions are taken from the initial sounding, whereas vanishing horizontal gradient is assumed for the outflow points. Velocities on lateral boundaries come from the initial sounding modified by the assumed flow perturbations (see Fig. 1). Model time step is 1 sec and simulations are run until nearly-steady-state conditions are achieved, typically after several hours (see Fig. 2).

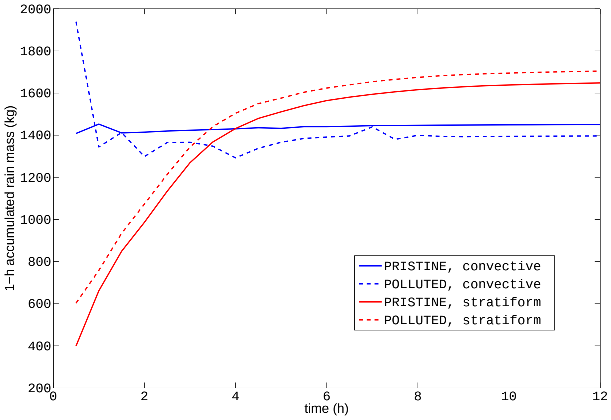

Figure 2: Evolution of time- and area-integrated surface precipitation separated into convective and stratiform regions for PRISTINE and POLLUTED simulations.

3. EXAMPLE OF RESULTS

We focus on the differences in model results when CCN characteristics are changed from PRISTINE to POLLUTED as in simulations described in Morrison and Grabowski (2007; 2008a). These changes modify the number of cloud droplets activated in the convective part (typical values close to 100/1000 cm^{-3} for the PRISTINE/POLLUTED), and thus they have significant impact on warm-rain processes. Similarly to simulations of Wang (2005) and Cui et al. (2006), ice nucleation is not affected by CCN changes (see Morrison and Grabowski 2008b for details of the ice nucleation; here, the number concentration of ice nuclei follows Meyers et al. 1992).

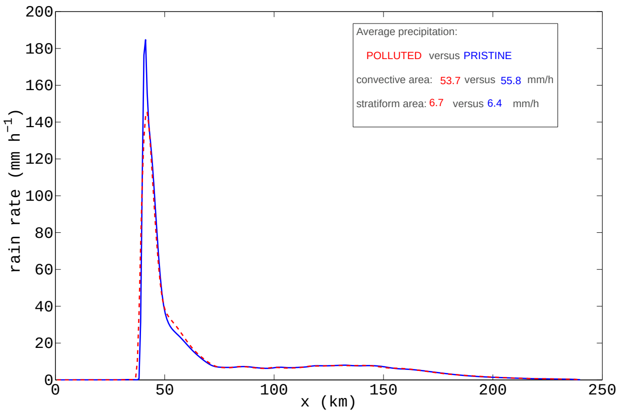

Figure 3: Spatial distribution of the steady-state surface precipitation for PRISTINE and POLLUTED simulations. Average surface precipitation rates separated into convective and stratiform regions are listed in the upper right corner.

Figure 1 shows the vertical velocity field and horizontal velocities at inflow boundaries in particular simulations discussed in this paper. The figure also shows the horizontal flow along the vertical line separating the convective region to the left ($30 \leq x \leq 48$ km) and stratiform region to the right ($48 \leq x \leq 240$ km). The prescribed flow is associated with the low-level convergence into the system and upper-level divergence, in general agreement with numerous observations of squall lines. The horizontal velocity between convective and stratiform regions is responsible for the mid- and upper-level transport of hydrometeors from the former into the latter.

Figure 2 shows evolutions of the one-hour accumulated rain, defined as the surface precipitation rate integrated over the area of interest and over one-hour time, separated into convective and stratiform regions for the PRISTINE and POLLUTED cases. The figure shows that the quasi-steady state is reached quite rapidly for the convective region, but it takes several hours for the stratiform precipitation to reach the steady state. The convective and stratiform regions contribute approximately equally to the total accumulated surface precipitation, in agreement with numerous observations of tropical and continental squall lines. Interestingly, the differences between PRISTINE and POLLUTED cases are rather minor, with almost perfect compensation between changes of surface precipitation in convective and stratiform regions when CCN is changed from PRISTINE to POLLUTED.

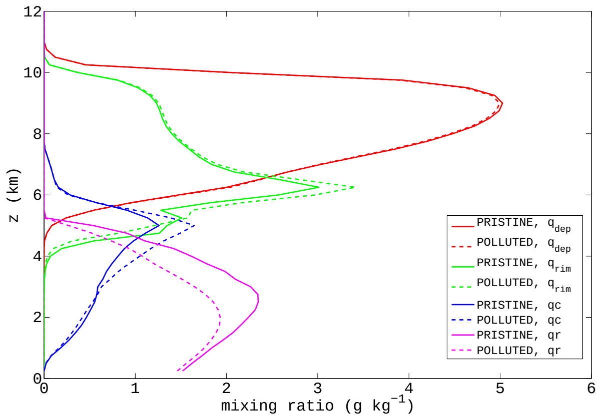

Figure 4: Profiles of conditionally-sampled mixing ratios for cloud water q_c, rain water q_r, mass of the ice field acquired by depositional growth q_{dep} and by riming q_{rim} for PRISTINE and POLLUTED cases. Data for the convective region. Conditional sampling includes only points with nonvanishing values of a given variable.

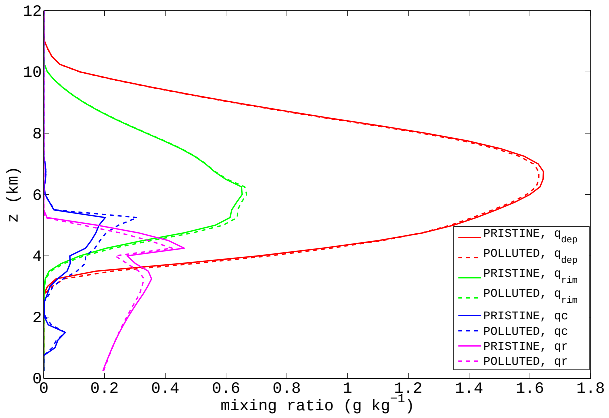

Figure 5: As Fig. 4, but for the stratiform region. Note a different scale on the horizontal axis.

Spatial distributions of the steady-state surface precipitation rate for PRISTINE and POLLUTED cases are shown in Fig. 3. As expected, large values of the surface precipitation rate are present in the convective region (average precipitation rate 55.8 and 53.7 mm h^{-1} for PRISTINE and POLLUTED, respectively) and much lower rates occur in the stratiform region (6.4 versus 6.7 mm h^{-1}). The figure also shows that the compensation of surface precipitation between the convective and stratiform regions is related to the changes of surface precipitation in the part of the stratiform region immediately adjacent to the convective region (and thus it depends on the arbitrarily-selected boundary between the two regions). In the steady-state, the low-level inflow of water vapor at the left boundary contributes about two-thirds of the total water inflow into the system; the remaining one-third comes from the low-level inflow from behind the system (i.e., at the right boundary). Water leaves the domain as surface rain (about 80%) and as the upper-tropospheric outflow out of the stratiform anvil (about 20%).

Figures 4 and 5 show conditionally-averaged profiles of mixing ratio for all hydrometeors for convective and stratiform regions, respectively, for PRISTINE and POLLUTED cases. The mixing ratios are generally higher in the convective region because of higher updraft velocity and thus higher condensation and deposition rates. It implies higher rates of other microphysical processes resulting in precipitation formation, like the autoconversion, accretion, ice-rain and ice-cloud water collection, etc. As already pointed out above, microphysical processes in the convective region have a significant impact of the stratiform region because of the transport of water and ice out of the convective region and into the stratiform region.

In the convective region (Fig. 4), surface rain mixing ratios for the two simulations (and thus the surface precipitation rates, see Figs. 2 and 3) are similar. Above the ground, however, the rain mixing ratio is higher in the PRISTINE case. This is because of the higher autoconversion and accretion rates (the latter being main source/sink of rain/cloud water) in this case, combined with the smaller mean rain drop size and hence smaller mean terminal fallspeed than POLLUTED. Condensation, similar for both cases, is the main source of cloud water and the differences in the cloud water profiles are because of different autoconversion and accretion rates in both simulations. Because of the strong updraft, cloud water and rain are carried upward in the center of the convective region and are involved in the initiation and further growth of the ice phase. The notable difference aloft is a lower ice mixing ratio acquired through riming q_{rim} (the dominant sink of rain aloft) for the PRISTINE case. Because rain is carried upward and falls toward the ground mostly at the downwind (i.e., right in Fig. 1) periphery of the updraft, larger rain production below the freezing level in the PRISTINE case is compensated by more efficient removal of rain by collisions between raindrops and ice crystals above the freezing level.

Rainfall in the stratiform region comes mainly from melting of snow grown in the area of the stratiform ascent. The initial ice crystals are either advected from the convective region or nucleated in-situ. The rime fraction changes across the stratiform region, with the highest values in the center of the ascent (not shown). Although the surface precipitation rate seems unaffected by CCN characteristics, there are subtle effects resulting in slightly different profiles of hydrometers in both simulations. Precipitation growth mechanisms differ significantly across the stratiform region. For instance, transport of ice crystals from the convective region is important in the water budget of the stratiform region close to the the convective updraft, but its role diminishes when one moves further downstream.

In conclusion, in the model with prescribed flow mimicking a squall line and in the particular modeling setup considered here, the total surface precipitation in PRISTINE and POLLUTED cases are almost exactly the same. This is because of the compensation of warm-rain and ice processes within the convective and stratiform regions. Simulations using modification of the modeling setup presented here (e.g., including changes of the updraft strength, position of the stratiform ascent with respect to the convective updraft, large-scale vertical shear, humidity profile, ice nucleation, etc) will be discussed at the conference to see how robust the above conclusion is. Dynamic model simulations will follow.

BIBLIOGRAPHY

Cui, Z., K. S. Carslaw, Y. Yin, and S. Davies, 2006: A numerical study of aerosol effects on the dynamics and microphysics of a deep convective cloud in a continental environment, *J. Geophys. Res.*, **111**, D05201, doi:10.1029/2005JD005981.

Grabowski, W. W., 1999: A parameterization of cloud microphysics for long–term cloud–resolving modeling of tropical convection. *Atmos. Res.*, **52**, 17–41.

Houze, R. A., 2004: Mesoscale convective system. Rev. Geophys. 42, RG4003, doi:10.1029/2004RG000150.

IPCC 2007: IPCC Fourth Assessment Report (AR4) Working Group I Report "The Physical Science Basis" (available from the International Panel on Climate Change web site at http://www.ipcc.ch/).

Meyers, M. P., P. J. DeMott, and W. R. Cotton, 1992: New primary ice nucleation parameterization in an explicit model. *J. Appl. Meteor.*, **31**, 708-721.

Morrison, H., and W. W. Grabowski, 2007: Comparison of bulk and bin warm rain microphysics models using a kinematic framework. *J. Atmos. Sci.*, **64**, 2839-2861.

Morrison, H., and W. W. Grabowski, 2008a: Modeling supersaturation and subgrid-scale mixing with two-moment bulk warm microphysics. *J. Atmos. Sci.*, **65**, 792-812.

Morrison, H., and W. W. Grabowski, 2008b: A novel approach for representing ice microphysics in models: description and tests using a kinematic framework. *J. Atmos. Sci.* (in press).

Rutledge, S. A., and P. V. Hobbs, 1984: The mesoscale and microscale structure and organization of clouds and precipitation in midlatitude cyclones. XII: A diagnostic modeling study of precipitation development in narrow cold-frontal rainbands. *J. Atmos. Sci.*, **41**, 2949-2972.

Smolarkiewicz, P. K. and L. G. Margolin, 1998: MPDATA: A finite-difference solver for geophysical flows. *J. Comput. Phys.*, **140**, 459-480.

Wang, C., 2005: A modeling study of the response of tropical deep convection to the increase of cloud condensation nuclei concentration. 1. Dynamics and microphysics. *J. Geophys. Res.*, *110*, D21211, doi:10.1029/2004JD005720.

Acknowledgments.
This work was partially supported by the NOAA Grant NA05OAR4310107. The National Center for Atmospheric Research is operated by the University Corporation for Atmospheric Research under sponsorship of the National Science Foundation.

"A QUANTITATIVE PRECIPITATION FORECAST ON FLASH FLOODING PRODUCING TROPICAL STORM"

V.Spiridonov[1], T.Sampan [2] and M.Curic[3]

[1] Hydrometeorological Service Skopje, Macedonia, [2]Thai Meteorological Department, Bangkok, Thailand and [3]Department of Meteorology, Faculty of Physics, Belgrade Serbia

1. Introduction

A major challenge associated with flash flooding is the quantitative character of the forecast: the task is not just to forecast the occurrence of an event, which is difficult enough by itself, but to anticipate the magnitude of the event. The physical processes associated with heavy convective precipitation are generally well understood, but the conditions which produce them still involve some uncertainness and can challenge the best meteorological science can offer. With some exceptions, most flash flood-producing convection is from more or less unremarkable thunderstorms, where multiple convective cells pass over a confined regions, with successive cells reaching forming, reaching maturity, and dissipating at about the same locations. Our ability to predict and understand these storms is very limited because they occur at a scale too small to be resolved by conventional observations and because there are so many uncertainties in our computerized weather prediction models. Thus, this paper has focused on the potential use of cloud resolving model in understanding of fundamental processes taking place in convective storms, and on the improvement of quantitative precipitation forecasts and flash flooding warnings.

2. THE MODEL

2.1 Model characteristics

Only few basic characteristics of the model are summarized here. The present version of the model is a three-dimensional, non-hydrostatic, time- dependant, compressible system which is based on the Klemp and Wilhelmson (1978) dynamics, Lin et. al. (1983) microphysics, Orville and Kopp (1977) thermodynamics.For the parameterization of the microphysical processes we use the integrated (bulk) water parameterization Lin et al. (198)], with significant improvement of hail growth parameterization. In front of using the hail spectrum from zero to infinity (idealized spectrum), Curic and Janc, (1995, 1997) proposed considering the hail size spectrum which includes only hail sized particles (larger than 0.5 cm in diameter; hereafter called realistic hail spectrum). The equivalent radar reflectivity factors for hail and rain are computed on the equations given by Smith et. al. (1975) and empirical equation for snow by Sekhon and Srivistava (1970). The radar measurements are carried out using a Doppler radar system Gematronik and Mitsubishi RC 34A radar system.

2.2. Boundary conditions

The normal component of the velocity is assumed to vanish along the top and bottom boundaries. In order to remove suspicions that the vertical oscillations in the numerical simulation are caused by the rigid top boundary in a model, the model is upgraded by a radiative upper boundary condition, according to suggestions given by Klemp and Duran, (1983). The lateral boundaries are opened and time-dependant, so that disturbances can pass through with minimal reflection.

2.3 Numerical technique

Model equations are solved on a semi staggered grid. All velocity components u_i are

defined at one-half grid interval $0.5\Delta x_i$ while scalar variables are defined at the mid point of each grid. All velocity components The horizontal and vertical advection terms are calculated by the centered fourth-and second-order differences, respectively. Since the model equations are compressible, a time splitting procedure is applied, to achieve numerical efficiency.

Since the model equations are compressible, a time splitting procedure is applied, to achieve numerical efficiency.

2.4. Initial conditions and initialization

Initial impulse for convection is an ellipsoidal warm bubble with the maximum temperature perturbation in the bubble center ($T_0 =$2.8°C). The model domain is 45 km x 45 km x 16 km. The horizontal resolution of the model is 0.5 km; the vertical one is 0.2 km. The temporal resolution of the model is 10 s time step for integration of the dynamics, microphysics and chemistry and a smaller one is (2 s) for solving the sound waves.

2. QPF OF STORM FLOODING USING CLOUD MODEL

The proposed method is focused on study the fundamental processes occur in convective storms over Thailand, developing a basic framework for understanding the occurrence of heavy precipitation and on the improvement of quantitative precipitation forecast and severe warnings. The main approach is to develop a physical basis for understanding the character on heavy convective precipitation expressed through implementation of QPF scheme based on cloud-resolving model simulations output and definition on have rainfall parameters. Numerical simulations are performed using different single meteorological profiles for initialization, obtained from five upper air sounding stations located in different areas in Thailand. The basic approach is to define the main individual model output parameters representing the storm intensity and structure under the potential instability atmospheric conditions in selected area. The next step is to determine the processes governing heavy precipitation such as total accumulated rainfall at the ground, rainfall duration, intensity and efficiency together with maximum radar reflectivity. Knowing these parameters is a good initial input for determination of the character of potential storm anticipated in the selected area and definition of heavy rainfall indexes.

4. NUMERICAL EXPERIMENT OF TROPICAL STORM ON 25 JULY, 2007

Initial data and model initialization are taken from the upper air sounding for five representative areas in Thailand for or 25 July 2007. The selected domain for a 2-d model run is 251km x 1km x 16km with horizontal and vertical grid steps Δx=1km and Δz=0.5km, respectively. Two-dimensional numerical simulations were performed under five different atmospheric environments. Table 1 shows the heavy rainfall parameters at different simulation time. The total accumulated rainfall at the ground is 74.2 mm. The maximum computed rainfall intensity is 2.18 mm/min (or 70.34 mm h^{-1}), average rainfall rate of 0.09 mm/min, maximum expected rainfall duration of 100 min., with time for rain to reach ground after initial convection of 33.5 min. The maximum radar reflectivity is 74.5 dBz. A three dimensional simulation is done on a smaller model domain of 61km x 61km x 16km that is consistent with a radar range. A 3-d model run has shown that case-specific simulation is able to more realistic represent the storm structure and dynamics and better interpretation of radar reflectivity and precipitation fields, wind speed and direction, and outflow heights.

Comparison of total simulated accumulated rainfall at the ground (left panel on Fig. 1) has shown a relatively good agreement with observed rainfall, where a three isolated rainfall peaks are quite well reproduced near Bangkok area (right panel). According to the results listed in Table 2, the most representative conditions for development and evolution of multicellular convection with radar reflectivity reaching > 50 dBZ and appearance of extreme convective rainfall are simulated to occur into Bangkok area, where maximum flood warning index is expected.

Table 1. Rainfall parameters during simulation time for Bangkok on 25 July, 2007

	Simulation time (min)																	
	10	**20**	**30**	**40**	**50**	**60**	**70**	**80**	**90**	**100**	**110**	**120**	**130**	**140**	**150**	**160**	**170**	**180**
Rainfall Rate (mm/min)			0.007	**2.18**	1.7	0.95	0.27	0.9	1.04	0.29	0.05	0.009	0.0	0.0	0.0	0.0	0.0	0.0
Tot. acc. Rainfall (mm)			0.26	22.1	39.1	48.6	51.3	60.3	70.7	73.6	74.1	74.19	**74.2**	74.2	74.2	74.2	74.2	74.2
Ref. (dBz)	22.9	53.8	45.8	38.6	44.7	36.9	38.3	41.9	38.6	40.3	42.0	40.0	39.3	40.5	39.5	42.0	38.2	38.3

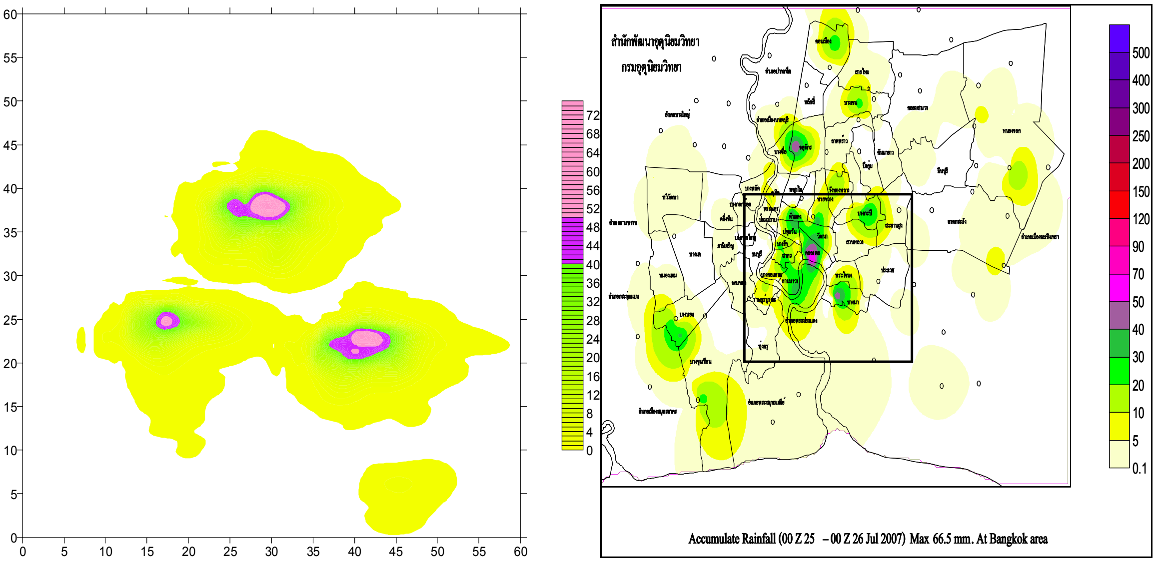

Fig. 1 Comparison of the total accumulated rain (00 Z 25 – 00 Z 26 July, 2007 in Bangkok area. Model computed accumulated rainfall at the ground for 180 min. simulation time (left panel) and observed total rainfall (right panel).

3. SUMMARY AND CONCLUSIONS

A three-dimensional cloud model has been used in order to simulate the main characteristics of tropical air mass thunderstorm, observed on 25 July, 2007 over Thailand. An attempt has been made in the present study to use the cloud model as potential tool for quantitatative rainfall forecast. It is done using model outputs for definition of corresponding convective rainfall parameters such as: rainfall rates, total amount of precipitation, duration and flood warning indexes.

Table. 2 Convective rainfall parameters and flood indexes simulated on 25 July, for Thailand

AREA	Initial rainfall (min)	Rainfall rate(mm $h^{-1)}$	Total acc. rainfall (mm)	Rainfall time duration (min)	Reflect. (dBz)	Character rainfall	Flood warning index
Chiang Mai	30	11.5	14.0	33	28.2	Heavy	3
Ubon Ratchathani	25	13.2	15.9	45	43.1	Heavy	3
Bangkok	**35**	**70.7**	**74.2**	**100**	**53.8**	**Extreme**	**5**
Phuket	No	0.0	0.0	0.0	0.0	No	0
Sonekhia	No	0.0	0.0	0.0	0.0	No	0

A 2-d numerical simulations have shown the dominant conditions for convectiion and associate extreme rainfall to occur near Bangkok area. The comparative analysis has shown good coinciding between simulated and registered rainfall. Numerical modeling of convective scale weather for operational purposes soon will be technically possible. However the convective cloud model should not be designed to produce improving forecasts of severe weather associated with deep convection..and associated rainfall directly, but rather to provide guidance for meteorologists to produce weather forecasts or warnings.

Acknowledgements

We are kindly acknowledged to Thai Meteorological Department for provision of analyzed data.

REFERENCES

Curic, M. and Janc, D.: On the sensitivity of the continuous accretion rate equation used in bulk-water parameterization schemes. Atmos. Res., 39, 313-332, 1995.

Curic, M. and Janc, D.: On the sensitivity of hail accretion rates in numerical modeling. Tellus, 49A, 100-107, 1997.

Durran, D. R.: The effects of moisture on mountain lee waves. Ph.D. Thesis, Massachusetts Institute of Technology Boston, MA(NTIS PB 82126621),1981.

Klemp, J. B. and Durran, D. R.: An upper boundary condition permitting internal gravity wave radiation in numerical mesoscale models. Mon. Wea. Rev., 11, 430-444, 1983.

Klemp, J. B. and Wilhelmson, R. B.: The simulation of three-dimensional convective storm dynamics. J.Atmos.Sci. 35, 1070-1096, 1978.

Lin, Y. L. Farley, R. D. and Orville, H. D.: Bulk water parameterization in a cloud model. J.Climate Appl. Meteor., 22, 1065-1092, 1983.

Smith, P.L, G.G. Myers and H.D. Orville: Radar reflectivity calculations on numerical cloud models using bulk parameterization of precipitation. J. Appl. Meteor., 14, 1156-1165, 1975.

Orville, H. D. and Kopp, F. J.: Numerical simulation of the history of a hailstorm. J.Atmos. Sci., 34, 1596-1618, 1977.

Sekhon, R.S. and Srivistava: Snow size spectra and radar reflectivity. J. Atnos. Sci., 27, 299-307, 1970

ON THE ROLE OF THE ALGORITHM OF CONVECTIVE CLOUD LOWER BOUNDARY DETERMINATION FOR DANGEROUS CONVECTIVE EVENT FORECAST AND NUMERICAL SIMULATION OF CONVECTIVE CLOUDS

Elena N. Stankova
Institute for High Performance Computing and Integrated Systems,
Kolomenskaja 35-37, liter A, 6H,
191119, St. Petersburg, Russia
lena@csa.ru, elenastankova@mail.ru

1. INTRODUCTION

Up to now forecasting of the dangerous events connected with the convective cloud development (thunderstorms, hails, storms) in the airports of CIS (Commonwealth of Independent States) countries is provided with the help of semi-empirical methods (Peskov, Yagudin, Reshetov and etc.) based upon the calculation of complex coefficients which are the functions of some cloud parameters (e.g.a temperature and a height of a cloud upper boundary, a temperature on a level of a certain isobar and so on). All these parameters are usually determined with the help of aerological diagram, where the possible cloud development is traced from a condensation level. The small shift of condensation level height is often resulted in several kilometer shift of the cloud upper boundary level and essential change of other cloud parameters. Forecast result is changed consequently.

We provided a comparative analysis of the effectiveness of several thunderstorm forecast methods using different approaches to the cloud lower boundary height calculation. The best results were obtained with the help of Lebedeva's method [1], where the way of condensation level height calculation is depended upon the type of convection. The method proposes to analyze three types of convection (thermal, free and forced), each characterized by the specific temperature and dew point temperature stratifications. Condensation level is determined taking into account height and temperature difference at the boundaries of available isotherm and inverse temperature levels. Consequently their presence at the boundary layer does not automatically prevent further convection development. The fact is especially important when numerical simulating of convection using real atmospheric soundings. In that case to maintain the instability, real temperature lapse rate in the boundary layer is arbitrarily modified to dry adiabatic one. Lebedev's method proposes more sound approach. We applied the method for preprocessing while numerical simulating convective cloud development with the help of 1-D and 1.5-D models which were used for on-line operation analyses and obtained much better thunderstorm forecast effectiveness.

2. COMPARATIVE ANALYSIS OF THE EFFECTIVENESS OF THE THUNDERSTORM FORECAST METHODS

During for more than ten years the author took part in the development of the software for airport information system intended for dangerous event forecasting [1]. The task was to adapt the semi-empirical methods used for thunderstorm, hail and storm forecasting for computer calculations and to provide new technologies connected with the usage of the simple (1-D and 1.5-D) numerical models.

The information system was installed in Moscow, Perm, Ekaterinburg, Kiev and during the period from 1996 till 2005 comparative analyses of the forecasting method effectiveness was provided. It was shown that the best results were obtained with the help of Lebedeva's method [1]: the forecast scored 93% in case of thunderstorm occurrence and 94% in case of its absence. To our mind the reason is in more accurate prediction of the condensation level resulted in more accurate prediction of the convective cloud parameters for which threshhold values of convective phenomena occurrence are established. It can be illustrated by Fig. 1-3, where the example of condensation and convection level calculation using the real sounding is presented.

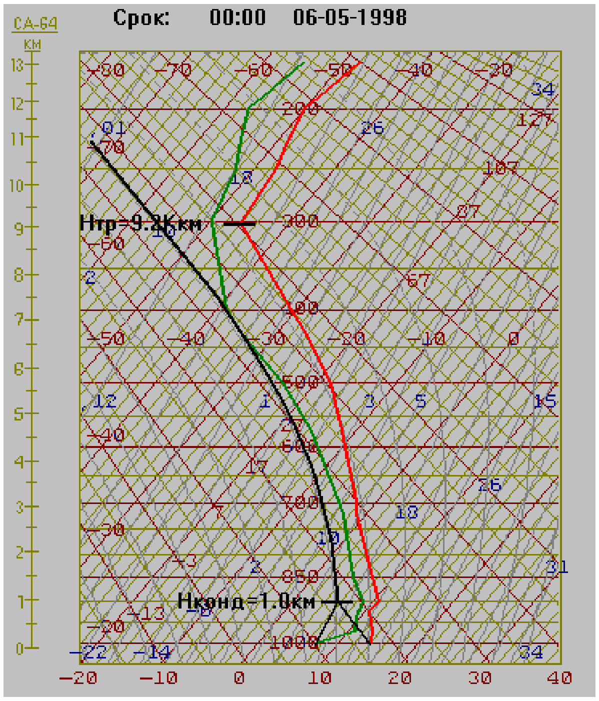

Fig.1 Real sounding example with the condensation level height (Нконд) obtained using true values of the temperature (red curve) and due point temperature (green curve) on the surface.
(Нтр is tropopause level height, black line – state curve)

Fig.1 shows the ordinary method of condensation level height obtaining using the true values of the temperature and dew point temperature. In this case no convection development is envisaged. The sounding is taken for 00 UTC. So to make true convection forecast we should modify it taking into account diurnal heating of the surface.

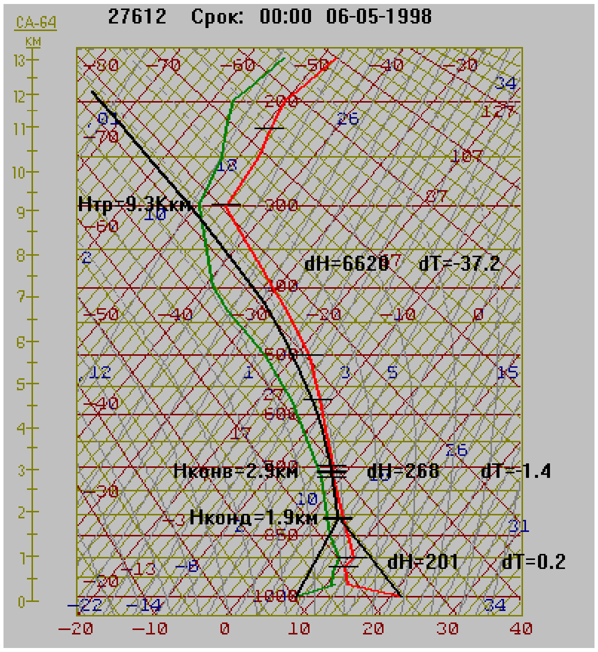

Fig.2 Real sounding example with the condensation level (Нконд) obtained using modified values of the temperature (red curve) and due point temperature (green curve) on the surface. (Нтр is tropopause level height; black line – state curve, Нконв – convection level height; dH,dT – the height and the temperature differece on the boundaries of the isotermal or inverse levels)

Fig.2 shows the method of condensation level height obtaining using the prognostic values of the temperature and dew point temperature. Prognostic values are obtained as a functions of a month and cloud amount [1], In this case we can expect only week convection development (the prognostic convection level height is only 2.9 km). Nearly the same result was obtained using another methods of prognostic surface temperature and due point temperature values obtaining. For example in case of Peskov method [3] the height of the condensation level was also equal 1.9 km, and convection level height – 3.2 km. Meanwhile the forecast result contradicts with the experimental both radar and surface data, which shows thunderstorm presence.

Fig. 3 shows the same sounding but the condensation level is predicted with the help of methodology suggested by Lebedeva, which included the preliminary analyses of convection type, estimation of the height of convection unstable layer and the presence of the isotherm and inverse temperature levels. As a result the height of the condensation level becomes equal to 1.5 km, the height of convection level – 8.3 km. These values together with the other convection parameters (cloud height, temperature on the upper cloud boundary, the mean deviation of the state curve from temperature stratification curve) show the possibility of the thunderstorm development, that is consistent with the experimental data.

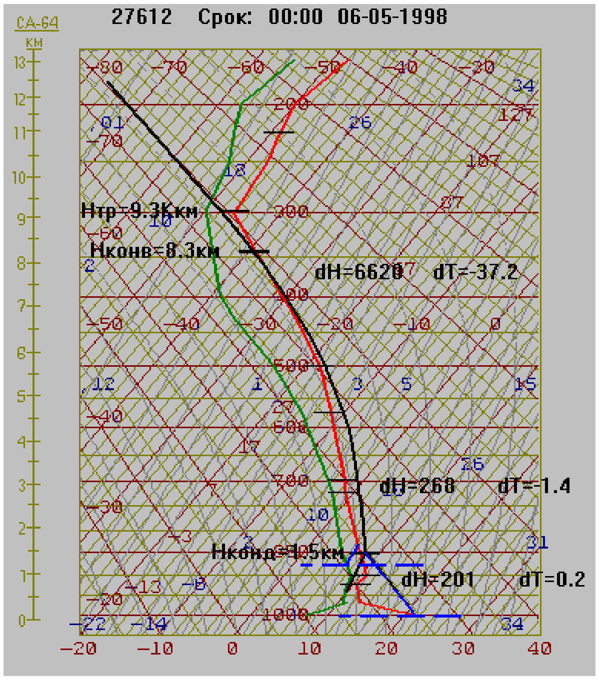

Fig.3 Real sounding example with the condensation level (Нконд) obtained with the help of Lebedev's method. (Нтр is tropopause level; black line – state curve, Нконв – convection level; dH,dT – the height and the temperature difference on the boundaries of the isotermal or inverse levels, blue lines mark the boundaries of the convective unstable level)

3. THUNDERSTORM FORECASTING USING 1-D AND 1.5-D CLOUD MODELS

1-D stationary cloud model [4] and 1.5-D time dependent cloud models [5] were used for thunderstorm prediction using the same sounding and experimental data.

1-D model uses the height and temperature of condensation level as an initial parameters and sounding data as boundary conditions. Testing results shows that the effectivness of the forecasting method increases by 20% in case of using Lebedeva's method of condensation level height definition.

!.5-D cloud model does not need the values of the height and temperature of the condensation level height explicitly, but is very sensitive to the temperature and due point lapse rates in the surface boundary layer and inverse and isotermal layer presence. Usage of the Lebedeva's method of condensation level height definition provides numerical simulation results much better consistent with the experimental data and in some cases only with the help of Lebedev's method we can obtain convection development in case of real atmospheric sounding.

Fig.4, 5 show the water content fields obtained with the help of 1.5-D cloud model using the soundings presented in fig. 2 and 3 consequently. As it can be seen, using the sounding, modified taking into account convection type and the height of convectin unstable layer (Lebedeva's method) provides much more intense convection than in the case when only surface temperature and due point temperature were modified.

The experience shows that using real sounding data for numerical simulation of convective clouds often produces a lot of difficulties connected with the presence of the isotermal and inverse temperature layers and the necessity of modification of the real temperature lapse rate in the boundary layer to a dry adiabatic one in order to maintain the instability. The methodology produced by Lebedeva provided the way of promt sounding modification resulted in good experimental data consistency.

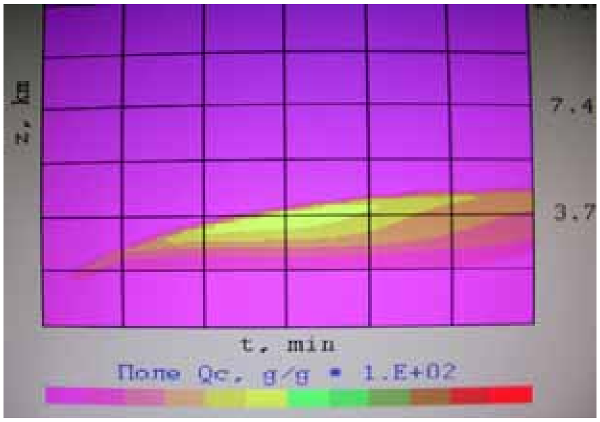

Fig.4 Water content field obtained with the help of 1.5-D cloud model using the sounding presented in fig. 2

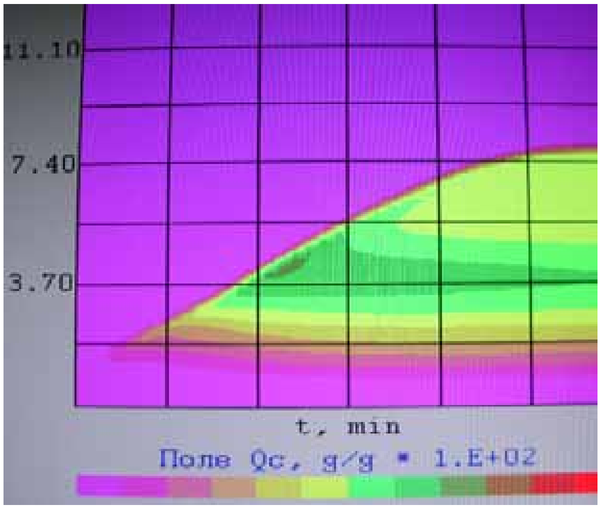

Fig.5 Water content field obtained with the help of 1.5-D cloud model using the sounding presented in fig. 3

4. CONCLUSIONS

Real soundings and real airport data of the thunderstorm events were used for the comparative analyses of dangerous event forecast methods. It was shown that forecast effectiveness is crucially depended upon the algorithm of convective cloud lower boundary determination. The method providing the best algorithm is defined. It was obtained that the algorithm can be of much importance for convective cloud numerical simulation.

7. BIBLIOGRAPHY

[1] Ponomarenko S.I., Lebedeva I.V., Chistyakov A.D., Instructional guidenlines. Estimation of the thunderstom forecasting methods and recommendations for their application. (in Russian), Moscow, 1971

[2] Institute for Radar Metheorology. Automated Information System "MeteoExpert" http://www.iram.ru/pexp.html

[3] Peskov B.E., Potapova L.V., Some practical recommendations to thunderstorm forecasting, Metodological letter N 13, Moscow, 1976, p. 15.

[4] Bocharnikov N.V. The usage of the jet model of the convective cloud in radar storm forecasting system operation Radar Meteorology, Leningrad, 1982, p. 35 (in Russian)

[5] Dovgaluk Yu.A., Veremei N.E., Sinkevich A.A. Application of the 1.5 model for the solution of the fundamental and applied problems of cloud physics.

Acknowledgments

The author expresses gratitute to all former colleagues from the Institute for Radar Meteorology and Main Geophysical Observatory for the permission to provide numerical experiments using the necessary experimental data. Figures 4 and 5 were obtained using the software developed by Zatevakhin M.A.

NUMERICAL INVESTIGATION OF COLLISION-INDUCED BREAKUP OF RAINDROPS. PART II: PARAMETERIZATIONS OF COALESCENCE EFFICIENCIES AND FRAGMENT SIZE DISTRIBUTIONS

Winfried Straub†, Jan Schlottke∗, Klaus D. Beheng† and Bernhard Weigand∗

† Institut für Meteorologie und Klimaforschung, Universität Karlsruhe / Forschungszentrum Karlsruhe
Hermann-von-Helmholtz-Platz 1, 76344 Eggenstein-Leopoldshafen, Germany

∗ Institut für Thermodynamik der Luft- und Raumfahrt, Universität Stuttgart
Pfaffenwaldring 31, 70569 Stuttgart, Germany

1 INTRODUCTION

Up to now, collision-induced breakup of raindrops has only been investigated in laboratory experiments with very limited sample of colliding drops of different sizes. McTaggart-Cowan and List (1975), Low and List (1982a) [abbreviated by LL82a] and Low and List (1982b) [abbreviated by LL82b], for example, derived coalescence efficiencies and numbers and size distributions of fragment drops resulting from collision-induced breakup from laboratory experiments with ten different pairs of large raindrops. Ochs et al. (1986) deduced coalescence efficiencies from experiments with ten different pairs of small precipitation drops and Ochs et al. (1995) and Beard and Ochs (1995) [abbreviated by BO95] investigated collision-induced breakup from experiments with four different pairs of drops. From their laboratory experiments, LL82a,b and BO95 developed parameterizations of coalescence efficiencies and size distributions of breakup fragments that are the one most frequently applied in meteorological cloud simulation models.

Recently, Beheng et al. (2006) [abbreviated by BE06] applied the VOF (Volume-of-Fluid) code FS3D (free surface 3D) model developed at the Institute of Aerospace Thermodynamics in Stuttgart, Germany to perform direct numerical simulations of collision-induced breakup of raindrops enlarging the database of LL82a,b to some 18 different pairs of colliding raindrops. The present study proceeds with the work of BE06 expanding the database to some 32 different pairs of drops. The model and setup as well as first results are explained in detail and compared with the findings of LL82a,b in Schlottke et al. (2008).

2 SIMULATION RESULTS

Overall, 32 drop pairs of sizes d_L (large drops) and d_S (small drops) are investigated. The drop pairs and sizes are listed in Tab. 1. The first ten drop pairs are identical to those investigated by LL82a,b and the first 18 drop pairs are identical to those of BE06. For each drop pair, six simulations are carried out. The simulations for each drop pair differ in the initial horizontal distance of the colliding drops, described by the excentricity ε that is the ratio of the horizontal distance δ of the droplet centers to the arithmetic mean of their diameters $\varepsilon = 2\delta/(d_L + d_S)$. Excentricities $\varepsilon = 0.05, 0.2, 0.4, 0.6, 0.8, 0.95$ have been chosen. Each simulation represents the collision results occuring in an individual segment of the cross section of size $\varepsilon\Delta\varepsilon$. The appropriate intervals $\Delta\varepsilon$ are $\Delta\varepsilon = 0.1, 0.2, 0.2, 0.2, 0.2, 0.1$. From this, the average number $\overline{f}$ of droplets is given as a weighted mean $\overline{f} = \sum n\,\varepsilon\Delta\varepsilon / \sum \varepsilon\Delta\varepsilon$ where n denotes the overall number of resulting drops per simulation. Similarly, coalescence efficiency E_c is given as fraction of the sum of cross section segments in which only coalescence occur to the sum of all cross section segments $E_c = \sum \delta_c\,\varepsilon\Delta\varepsilon / \sum \varepsilon\Delta\varepsilon$. In case of coalescence, that is, only one drop results from collision, $\delta_c = 1$, else $\delta_c = 0$. Now, the mean number $\overline{f_b}$ of breakup fragments is obtained from $\overline{f} = \overline{f_b}(1 - E_c) + E_c$. The results for E_c and $\overline{f_b}$ for all 32 drop pairs are also displayed in Tab. 1.

Besides this, the average number $\overline{p}_j(D_j)\Delta D_j$ of resulting droplets in the jth diameter intervall is needed. Here, $\overline{p}_j(D_j)$ denotes the average spectral number of drops in the jth diameter intervall with mean diameter D_j and ΔD_j denotes the width of the jth diameter intervall. As above, we have $\bar{p}_j(D_j)\Delta D_j = \sum n_j \varepsilon \Delta\varepsilon / \sum \varepsilon \Delta\varepsilon$ with the overall number n_j of resulting drops per simulation within the jth diameter intervall. The average number $\bar{p}_{b,j}(D_j)\Delta D_j$ of breakup fragments is obtained from $\bar{p}_j(D_j)\Delta D_j = \bar{p}_{b,j}(D_j)\Delta D_j(1-E_c) + \delta(D_c)E_c$ with diameter of the coalesced drop $D_c = (d_L^3 + d_S^3)^{1/3}$. $\delta(D_c) = 1$ if D_c lies within the jth diameter intervall $|D_c - D_j| \leq \Delta D_j/2$, $\delta(D_c) = 0$ in all other cases.

			Simulated		Calculated	
No.	d_L [cm]	d_S [cm]	E_c	$\bar{f}_b$	E_c	F_b
1	0.18	0.0395	0.49	2.00	0.60	2.00
2	0.40	0.0395	0.81	2.00	0.77	2.00
3	0.44	0.0395	0.81	2.00	0.80	2.00
4	0.18	0.0715	0.25	2.00	0.24	2.00
5	0.18	0.10	0.25	2.00	0.23	2.00
6	0.30	0.10	0.25	3.28	0.11	3.36
7	0.36	0.10	0.25	5.20	0.13	4.26
8	0.46	0.10	0.25	5.84	0.21	5.32
9	0.36	0.18	0.00	4.95	0.07	6.40
10	0.46	0.18	0.00	8.21	0.06	11.23
11	0.06	0.035	1.00	0.00	0.89	2.00
12	0.12	0.035	0.49	2.00	0.68	2.00
13	0.12	0.06	0.25	2.00	0.46	2.00
14	0.25	0.0395	0.49	2.00	0.65	2.00
15	0.24	0.09	0.25	2.00	0.14	2.07
16	0.27	0.15	0.09	2.79	0.11	3.12
17	0.32	0.0395	0.81	2.00	0.71	2.00
18	0.41	0.14	0.09	8.59	0.07	7.64
19	0.24	0.06	0.30	2.00	0.33	2.00
20	0.30	0.07	0.30	2.86	0.27	2.02
21	0.36	0.07	0.42	3.00	0.33	2.41
22	0.45	0.07	0.49	3.00	0.43	2.81
23	0.12	0.10	0.49	2.00	0.84	2.00
24	0.41	0.10	0.25	6.48	0.17	4.86
25	0.25	0.12	0.09	2.53	0.10	2.68
26	0.30	0.12	0.09	3.85	0.08	3.95
27	0.36	0.12	0.09	3.49	0.08	5.25
28	0.46	0.12	0.25	6.16	0.13	6.84
29	0.36	0.14	0.09	4.90	0.06	6.24
30	0.18	0.16	1.00	0.00	0.87	2.00
31	0.41	0.16	0.01	9.60	0.06	8.62
32	0.25	0.18	0.25	2.75	0.34	2.00

Table 1: *Coalescence efficiencies E_c and average numbers of breakup fragments $\bar{f}_b$, F_b as simulated with FS3D and calculated through the parameterization schemes developed in the following sections. Simulated and calculated coalescence efficiencies are correlated with correlation coefficient $r = 0.92$, simulated and calculated fragment numbers are correlated with $r = 0.93$.*

3 COALESCENCE EFFICIENCIES

Coalescence efficiency is defined as the ratio of the number of collisions resulting in a permanent unification to the number of all collisions. In case of coalescence, the total energy E_T of coalescence must be dissipated by the coalesced drop, where E_T is the sum $E_T = CKE + \Delta S$ of the collision kinetic energy CKE and the energy ΔS resulting from net loss of surface area during unification with the incident drops. Collision kinetic energy CKE is given as

$$CKE = \frac{\pi}{12}\rho_l \frac{d_L^3 d_S^3}{d_L^3 + d_S^3}(v_L - v_S)^2 \qquad (1)$$

where ρ_l is the bulk density of water and v_L and v_S are the terminal fall velocities of the large and small drops. ΔS denotes the decrease of surface energy $\Delta S = S_T - S_C$. S_T denotes the total surface energy $S_T = \pi\sigma(d_L^2 + d_S^2)$ of the colliding drops and S_C is the surface energy $S_C = \pi\sigma(d_L^3 + d_S^3)^{2/3}$ of the coalesced system, σ is the surface tension of water.

For small d_S-values, the total energy E_T is small too, that is, in case of coalescence only a small amount of energy has to be dissipated. Thus, in this case we may assume that coalescence efficiency is large. Furthermore, numerical simulations with FS3D have shown that coalescence occurs much more often in case of small excentricities ε but only if the collision kinetic energy CKE is not too large. In case of large CKE almost all collisions result in breakup, i.e. coalescence efficiency tends to zero. The third case we have to pay attention for is the one occuring when the large and small incident drops are almost equal in size. In this case, CKE disappers but ΔS does not. We may assume that ΔS can be dissipated by the coalesced drop and we have coalescence. Simulations No. 11 and

30 support this argument. On the other hand, it is not clear if in this case we have to expect rebound that may not be simulated properly by the employed VOF method.

Taking the previous arguments into account, we approximate the simulated coalescence efficiencies by the exponential function $\exp(-We)$ where We denotes the Weber number

$$We = \frac{CKE}{S_C} \tag{2}$$

Now, the exponential function is equal to one for $CKE = 0$ and tends to zero for large Weber numbers. The best fitting expression is

$$E_c = \exp(-1.15We) \tag{3}$$

and is displayed in Fig. 1 and 2. In Fig. 1, the experimental results from LL82a are also included.

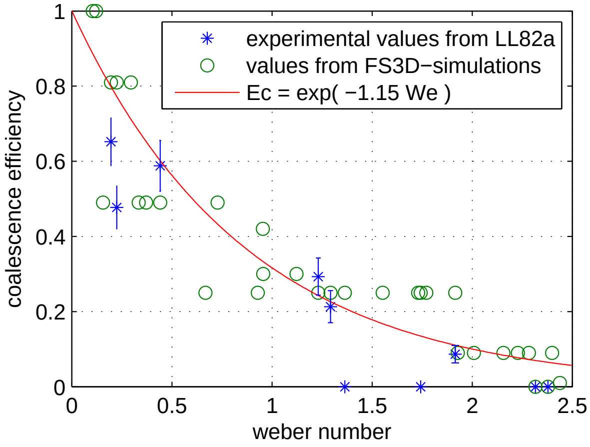

Fig. 1: *Coalescence efficiency E_c as function of the Weber number We. The correlation coefficient between the values from FS3D-simulations and the new parameterization is $r = 0.92$.*

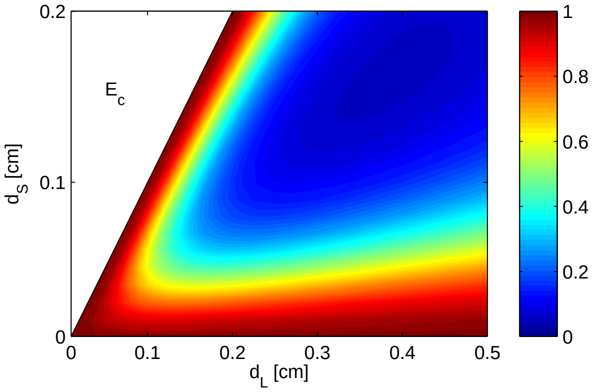

Fig. 2: *E_c-isolines (values see color bar) as function of colliding drop pairs with diameters d_L and d_S.*

4 SIZE DISTRIBUTIONS

In this chapter, a parameterization is developed to calculate the size distributions of breakup fragments as function of fragment diameters for several collisions of drops of sizes d_L and d_S. From the simulation results, four different modes of breakup fragments are identified.

- The first mode denoted by 'i' characterizes drops of sizes near d_L,
- the second mode 'ii' contains drops of sizes near d_S,
- the third mode 'iii' describes slightly smaller drops and
- the fourth mode 'iv' contains drops of smallest sizes.

The average number of drops found in each mode is given through $A_j = \bar{p}_{b,j}(D_j)\Delta D_j$ with the average spectral number $\bar{p}_{b,j}(D_j)$, the mean diameter D_j and the width ΔD_j of each mode as explained in chapter 2. Histograms for each collision of drops of sizes d_L and d_S are depicted in Fig. 6.

In our new parameterization, the fourth mode is characterized through a log-normal distribution reading

$$p_{\text{iv}}(D) = \frac{1}{D\sigma_{\text{iv}}\sqrt{2\pi}} \exp\left(-\frac{(\ln(D)-\mu_{\text{iv}})^2}{2\sigma_{\text{iv}}^2}\right) \tag{4}$$

where

$$\int_0^\infty p_{\text{iv}}(D)\,dD = 1 \tag{5}$$

From this, the average spectral number $P_{\text{iv}}(D)$ of fragments of the fourth mode is given as

$$P_{\text{iv}}(D) = A_{\text{iv}}\, p_{\text{iv}}(D) \tag{6}$$

The parameters σ_{iv} and μ_{iv} can be expressed as

$$\sigma_{\text{iv}}^2 = \ln\left(\frac{Var}{E^2}+1\right) \tag{7}$$

$$\mu_{\text{iv}} = \ln(E) - \frac{\sigma_{\text{iv}}^2}{2} \tag{8}$$

where E and Var denote the mean and variance of the log-normal distribution. On the other hand,

E and Var can be derived from the simulation results as $E = D_{\text{iv}}$ and $Var = \Delta D_{\text{iv}}^2/12$. From the simulations D_{iv} is approximated by a constant value = 0.04 cm and A_{iv} and ΔD_{iv} are approximated as

$$A_{\text{iv}} = \begin{cases} 0.75(E_T - 2.4) & \text{for} \quad E_T \geq 2.4\mu J \\ 0 & \text{for} \quad E_T < 2.4\mu J \end{cases} \tag{9}$$

$$\Delta D_{\text{iv}} = \begin{cases} k\left(\sqrt{E_T^2/S_C} - 1\right) & \text{for} \quad E_T^2/S_C \geq 1\mu J \\ 0 & \text{for} \quad E_T^2/S_C < 1\mu J \end{cases} \tag{10}$$

where $k = 1.7 \times 10^{-2}$ and E_T and S_C are given in μJ, ΔD_{iv} is given in cm. Simulated and calculated A_{iv} and ΔD_{iv} are correlated with correlation coefficients $r = 0.91$ and $r = 0.93$. The dependencies of simulated and calculated A_{iv} and ΔD_{iv} from E_T and E_T^2/S_C are shown in Fig. 3.

The third mode is characterized through a normal distribution

$$p_{\text{iii}}(D) = \frac{1}{\sigma_{\text{iii}}\sqrt{2\pi}}\left(-\frac{1}{2}\left(\frac{D - \mu_{\text{iii}}}{\sigma_{\text{iii}}}\right)^2\right) \tag{11}$$

where

$$\int_{-\infty}^{\infty} p_{\text{iii}}(D)\, dD = 1 \tag{12}$$

Now, the average spectral number $P_{\text{iii}}(D)$ of fragments of the third mode is given as

$$P_{\text{iii}}(D) = A_{\text{iii}}\, p_{\text{iii}}(D) \tag{13}$$

Here, $\mu_{\text{iii}} = D_{\text{iii}}$ and $\sigma_{\text{iii}}^2 = \Delta D_{\text{iii}}^2/12$. Again, from simulations D_{iii} is approximated as a constant with value $D_{\text{iii}} = 0.095$ cm and A_{iii} and ΔD_{iii} are approximated as

$$A_{\text{iii}} = 2.7 \times 10^{-6}\left(E_T^2/S_C\right)^4 \tag{14}$$

$$\Delta D_{\text{iii}} = 8.4 \times 10^{-8}\left(E_T^2/S_C\right)^4 \tag{15}$$

E_T and S_C are given in μJ, ΔD_{iii} is given in cm. In both cases, simulated and calculated A_{iii} and ΔD_{iii} are correlated with correlation coefficients $r = 0.96$. The dependencies of simulated and calculated A_{iii} and ΔD_{iii} from E_T^2/S_C are shown in Fig. 4.

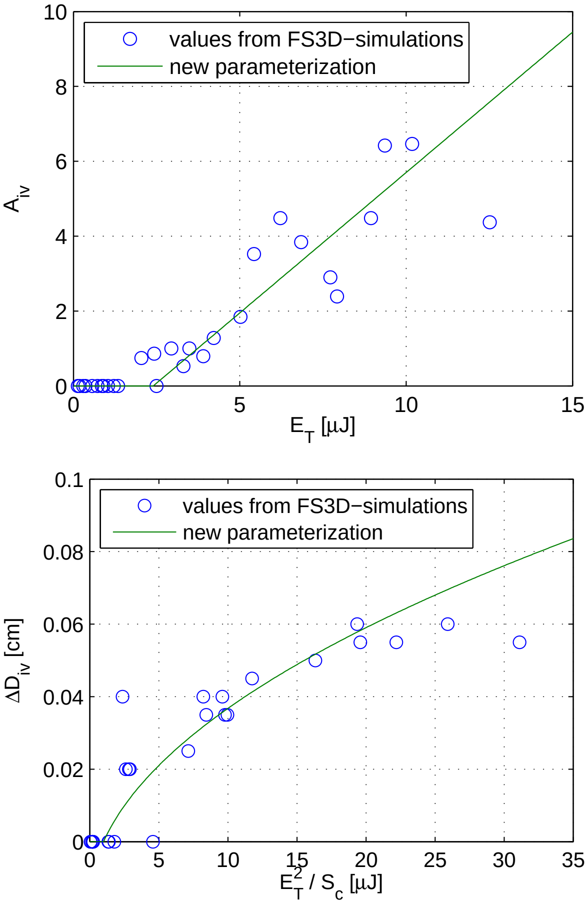

Fig. 3: *Parameters A_{iv} and ΔD_{iv} from simulations as well as from parameterization equations* (9) *and* (10) *as functions of E_T and E_T^2/S_C. The correlation coefficients between the values from FS3D-simulations and the new parameterization are $r = 0.91$ and $r = 0.93$.*

As for the third mode, the second mode is characterized through a normal distribution again

$$p_{\text{ii}}(D) = \frac{1}{\sigma_{\text{ii}}\sqrt{2\pi}}\left(-\frac{1}{2}\left(\frac{D - \mu_{\text{ii}}}{\sigma_{\text{ii}}}\right)^2\right) \tag{16}$$

In this case, the average spectral number $P_{\text{ii}}(D)$ of fragments of the second mode is

$$P_{\text{ii}}(D) = A_{\text{ii}}\, p_{\text{ii}}(D) \tag{17}$$

From simulations the mean diameter is approximately $D_{\text{ii}} = d_S - 0.01$ cm. A_{ii} and ΔD_{ii} are approximated as

$$A_{\text{ii}} = \begin{cases} 1 - h\left(E_T^2/S_C\right)^4 & \text{for} \quad E_T^2/S_C \leq 32{,}0\mu J \\ 0 & \text{for} \quad E_T^2/S_C > 32{,}0\mu J \end{cases} \tag{18}$$

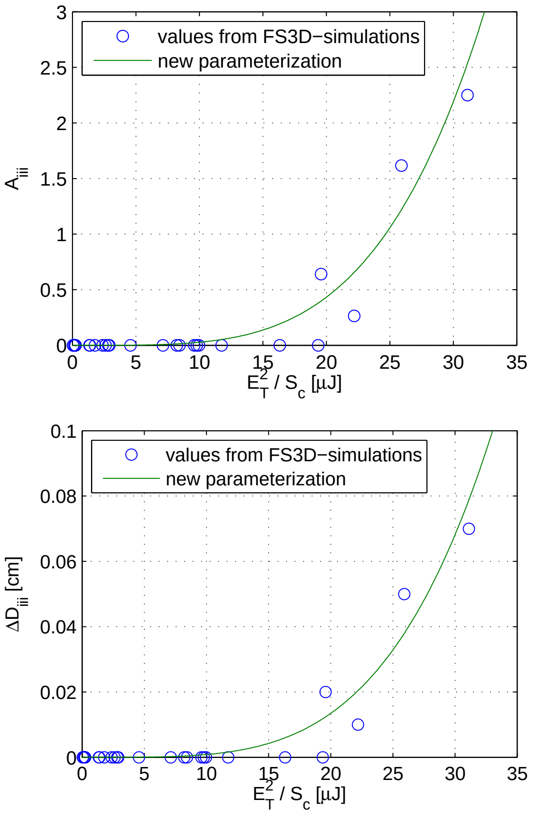

Fig. 4: *Parameters A_{iii} and ΔD_{iii} from simulations as well as from parameterization equations* (14) *and* (15) *as functions of E_T^2/S_C. The correlation coefficients between the values from FS3D-simulations and the new parameterization are $r = 0.96$ in both cases.*

with $h = 9.5 \times 10^{-7}$ and

$$\Delta D_{\text{ii}} = 1 \times 10^{-2} \left(0.22 E_T^2 / S_C + 1\right) \qquad (19)$$

with E_T and S_C in μJ and ΔD_{ii} in cm. Simulated and calculated A_{ii} and ΔD_{ii} are correlated with correlation coefficients $r = 0.73$ and $r = 0.91$. The dependencies of simulated and calculated A_{ii} and ΔD_{ii} from E_T^2/S_C are shown in Fig. 5.

The first mode is characterized through a Dirac delta function $\delta(D - D_{\text{i}})$ the integral of which is

$$\int_{-\infty}^{\infty} \delta(D - D_{\text{i}})\, dD = 1 \qquad (20)$$

and the average spectral number $P_{\text{i}}(D)$ of drops is $P_{\text{i}}(D) = A_{\text{i}} \delta(D - D_{\text{i}})$. This results from the simulations showing that, in general, $A_{\text{i}} = 1$. In order to ensure mass conservation D_{i} is derived from $D_{\text{i}} = M_{3,\text{i}}^{1/3}$ with $M_{3,\text{i}}$ calculated as the residual of the masses of the two initial drops minus the masses of the drops from modes 'ii', 'iii' and 'iv':

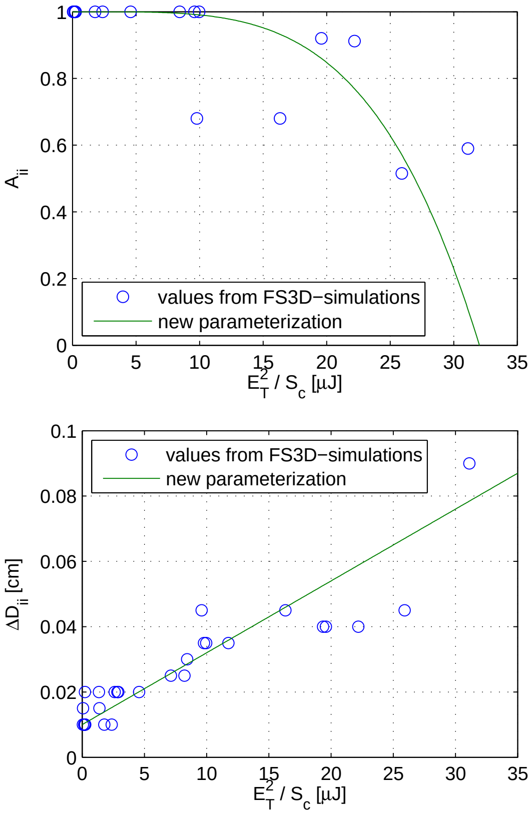

Fig. 5: *Parameters A_{ii} and ΔD_{ii} from simulations as well as from parameterization equations* (18) *and* (19) *as functions of E_T^2/S_C. The correlation coefficients between the values from FS3D-simulations and the new parameterization are $r = 0.73$ and $r = 0.91$.*

$$M_{3,\text{i}} = d_L^3 + d_S^3 - M_{3,\text{iv}} - M_{3,\text{iii}} - M_{3,\text{ii}} \qquad (21)$$

where the moments M_3 on the r.h.s. are given according to their distribution functions assumed by

$$M_{3,\text{iv}} = A_{\text{iv}} \exp\left(3\mu_{\text{iv}} + \frac{9\sigma_{\text{iv}}^2}{2}\right) \qquad (22)$$

$$M_{3,\text{iii}} = A_{\text{iii}} \left(\mu_{\text{iii}}^3 + 3\mu_{\text{iii}}\sigma_{\text{iii}}^2\right) \qquad (23)$$

$$M_{3,\text{ii}} = A_{\text{ii}} \left(\mu_{\text{ii}}^2 + 3\mu_{\text{ii}}\sigma_{\text{ii}}^2\right) \qquad (24)$$

Note that in this way a single drop remains with a diameter only slightly smaller than d_L.

Now, the overall spectral number of breakup fragments is given as

$$P_b(D) = P_{\text{iv}}(D) + P_{\text{iii}}(D) + P_{\text{ii}}(D) + P_{\text{i}}(D) \qquad (25)$$

and is displayed in Fig. 6 at the end of the paper for all 30 cases of different drop pairs of sizes d_L

and d_S (in two cases coalescense efficiency is one, that is, no breakup fragments has been simulated). According to chapter 2, the average number of resulting drops is given by

$$P(D) = P_b(D)(1 - E_c) + \delta(D_c)E_c \qquad (26)$$

where $\delta(D_c) = 1$ if $D = D_c$ and $\delta(D_c) = 0$ in all other cases.

The average number F_b of all breakup fragments for each initial drop pair of size d_L and d_S is now obtained from

$$F_b = \int_0^\infty P_b(D)\,dD \qquad (27)$$

and is given in Tab. 1. The overall number F of all resulting drops is then $F = F_b(1 - E_c) + E_c$.

5 SUMMARY AND CONCLUSIONS

In the present study, collision-induced breakup is investigated by application of the numerical simulation code FS3D. New parameterizations of coalescence efficiency as well as size distributions of fragment drops are developed on an extended basis of 32 different pairs of colliding drops of sizes $0 < d_L < 0.5$ cm and $0 < d_S < 0.2$ cm. Additionally, the new parameterization of coalescence efficiency fits quite well to the data of LL82a.

To increace accuracy of the parameterizations, further investigation should focus on increasing the number of simulations for each drop pair. Furthermore, it is needed to clarify the collision process for initial drop pairs of nearly the same size and to adjust the parameterization of coalescence efficiency to the new findings.

Acknowledgement

The authors gratefully acknowledge support by the German Science Foundation (DFG) under grants BE 2081/7-1 and WE 2549/17-1 in the framework of the priority program Quantitative Precipitation Forecast.

References

Beard, K. V. and H. T. Ochs (1995): Collisions between Small Precipitation Drops. Part II: Formulas for Coalescence, Temporary Coalescence, and Satellites. *J. Atmos. Sci.*, **52**, 3977–3996.

Beheng, K. D., K. Jellinghaus, W. Sander, N. Roth and B. Weigand (2006): Investigation of Collision-induced Breakup of Raindrops by Numerical Simulations: First Results. *Geophys. Res. Lett.*, **33**, L10811, doi:10.1029/2005GL025519.

Low, T. B. and R. List (1982a): Collision, Coalescence and Breakup of Raindrops. Part I: Experimentally Established Coalescence Efficiencies and Fragment Size Distributions in Breakup. *J. Atmos. Sci.*, **39**, 1591–1606.

Low, T. B. and R. List (1982b): Collision, Coalescence and Breakup of Raindrops. Part II: Parameterization of Fragment Size Distributions. *J. Atmos. Sci.*, **39**, 1607–1618.

McTaggart-Cowan, J. D. and R. List (1975): Collision and Breakup of Water Drops at Terminal Velocity. *J. Atmos. Sci.*, **32**, 1401–1411.

Ochs, H. T., K. V. Beard, R. R. Czys, N. F. Laird, D. E. Schaufelberger and D. J. Holdridge (1995): Collisions between Small Precipitation Drops. Part I: Laboratory Measurements of Bounce, Coalescence, and Temporary Coalescence. *J. Atmos. Sci.*, **52**, 2258–2275.

Ochs, H. T., R. R. Czys and K. V. Beard (1986): Laboratory Measurements of Coalescence Efficiencies for Small Precipitation Drops. *J. Atmos. Sci.*, **43**, 225–232.

Schlottke, J., W. Straub, K. D. Beheng and B. Weigand (2008): Numerical Investigation of Collision-induced Breakup of Raindrops. Part I: Methodology as well as Dependencies on Collision Energy and Excentricity. *15th International Conference on Clouds and Precipitation, July 7-11, 2008, Cacun, Mexico*.

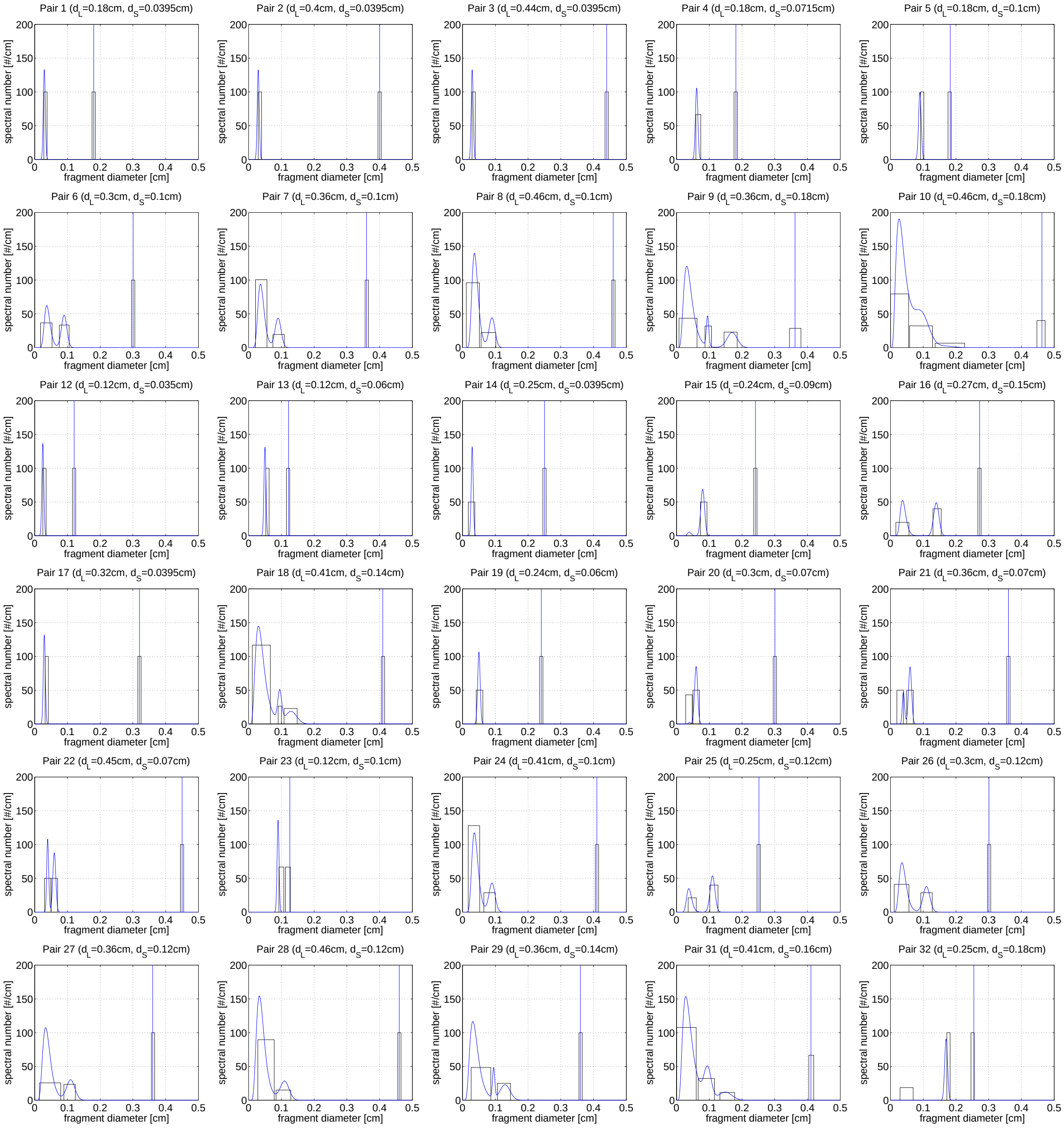

Fig. 6: *Spectral number of fragments as function of fragment diameter for d_S and d_L as indicated. Black boxes refer to the simulation results (cf. fig. 11 of the companion paper of Schlottke et al. (2008), this volume) and blue lines to the parameterizations for 30 different drop pairs. The first 10 pairs are the same as in LL82b. In case of pair 11 and pair 30 coalescence efficiency is one, that is, in these cases no breakup occurs.*

MESOANALYSIS OF THE INTERACTIONS OF PRECIPITATING CONVECTION AND THE BOUNDARY LAYER

Ruiyu Sun and Steven K. Krueger*
University of Utah, Salt Lake City, Utah, USA

1. INTRODUCTION

The DOE ARM program has promoted understanding of cumulus convection by producing high-quality "single-column model" observational datasets that allow one to run and evaluate single-column models and cloud-resolving models based on observed large-scale conditions (Xie and Zhang, 2000; Xie and Coauthors, 2002; Xu et al., 2002). The cloud and radiation fields produced by such simulations can then be compared to measurements by an ARM cloud profiling radar, as well as to satellite-based measurements (Luo et al., 2003; Luo and Krueger, 2004, 2005; Yang et al., 2006). This is an excellent evaluation method for stratiform cloud systems, but not for convective cloud systems, whose updrafts and downdrafts are inadequately sampled by the cloud profiling radars, and not detectable from space except by the TRMM precipitation radar, which has limited sampling at a given location (daily at its northern limit of 36 deg latitude). However, the existing observational systems at the ARM Southern Great Plains (SGP) Atmospheric Climate Research Facility (ACRF) can be used to provide a much more extensive statistical characterization of updrafts and downdrafts in convective cloud systems. The relevant datasets include the 5-minute Oklahoma Mesonet data and the hourly Arkansas Basin River Forecast Center (ABRFC) gridded precipitation data. Because convective cloud systems generally have strong interactions with boundary layer circulations and thermodynamics, the boundary layer wind and thermodynamic fields contain a great deal of information about convective cloud systems.

We are trying to produce a number of datasets based on Oklahoma Mesonet data and gridded precipitation data for mutiple warm seasons that should be very useful for evaluating cumulus parameterizations in GCMs, and also for evaluating the representation of cumulus convection and the boundary layer in cloud-resolving models (CRMs). As the first step, we report in this extended abstract our preliminary results about how to estimate the *mesonet-averaged* cloud base updraft and downdraft mass fluxes from the surface divergence field.

2. DATA SOURCES

Two datasets are used in our analyses, the Oklahoma Mesonet dataset and the Arkansas-Red River Basin Forecast Center hourly–gridded precipitation dataset. The Oklahoma Mesonet (sponsored by University of Oklahoma and Oklahoma State) provides 5-minute averaged surface meteorological data in quality assured data files. The Oklahoma Mesonet network consists of over 100 automated observing stations located throughout the state. Data are available from 1/1/1994 to 4/21/2007 (present). Data used in the current analysis are from May to August, 1997 and 2000.

The Arkansas-Red River Basin Forecast Center (ABRFC) produces an hourly gridded (4 km x 4 km) precipitation amount over the river basin. This field is a combination of both WSR-88D Nexrad radar precipitation estimates and rain gauge reports. The ABRFC performs extensive quality control on these data. The data are used for the ARM constrained variational analysis. Data are available from 6/24/1994 to 4/27/2007 (present). Data used in the current analysis are also from May to August, 1997 and 2000.

The locations of the various data referred to above are shown in Fig. 1. The Oklahoma Mesonet region is about 5 deg in longitude by 3 deg in latitude in size. Evaluating GCMs using

---

[*] *Corresponding author address:* Department of Meteorology, University of Utah, Salt Lake City, UT 84112. E-mail: steve.krueger@utah.edu

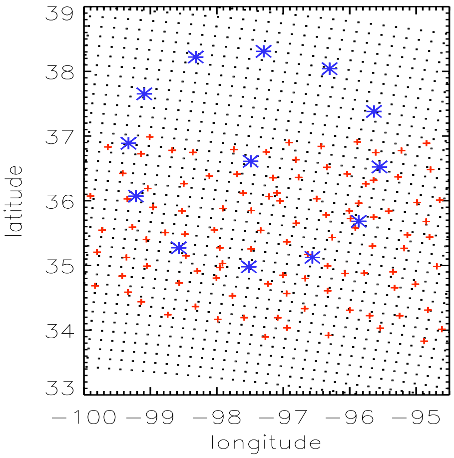

Figure 1: Map of SGP with every 4th grid point of the 4-km by 4-km hourly precipitation grid (dots), the Oklahoma Mesonet stations (red $+$), and constrained variational analysis domain (enclosed by blue stars). AERI profiles were retrieved at the Central Facility (central blue star) and at the blue stars at 12, 4, 6, and 8 o‘clock.

our proposed data products would be straightforward. In this report focus is given to the results produced based on data in 1997.

3. METHOD OF ANALYSIS AND PRELIMINARY RESULTS

Our goal is to estimate the *mesonet-averaged* updraft and downdraft cloud-base mass fluxes, $M_{c,u}$ and $M_{c,d}$, from the *mesoscale* surface divergence field.

The triangle method was used to calculate the mesoscale horizontal divergence field (div$\equiv \partial u/\partial x+\partial v/\partial y$) directly from the mesonet station wind measurements (Dubois and Spencer, 2005; Davies-Jones, 1993).

Figure 2 shows the horizontal divergence obtained from the Oklahoma Mesonet station data for a fair weather day, while Figure 3 shows the same for a day with precipitation. In the figures, each triangle formed from 3 stations is colored according to its divergence value: blue indicates weak divergence (divergence $>$ 0), purple indicates strong divergence ($> 10^{-4}$ s^{-1}), yellow indicates weak convergence (divergence $<$ 0), and red indicates strong convergence ($> 10^{-4}$ s^{-1}).

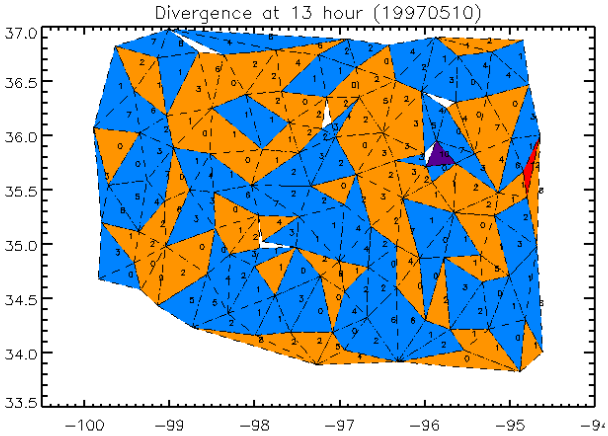

Figure 2: Divergence with colored triangles (see text for explanation; values are shown in units of 10^{-5} s^{-1}) and precipitation contours of 2 mm hr^{-1} (thick black line) at 13 UTC on May 10, 2007.

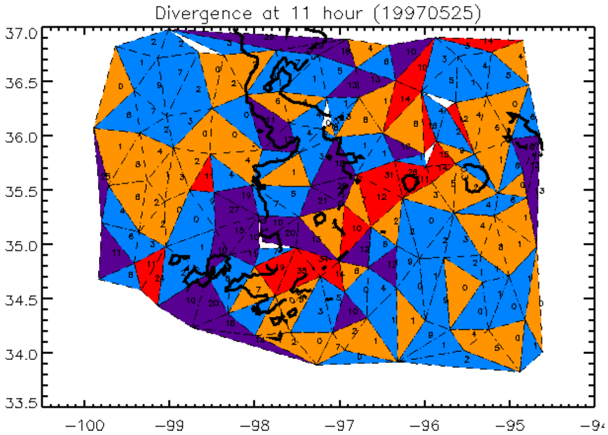

Figure 3: Divergence with colored triangles (see text for explanation; values are shown in units of 10^{-5} s^{-1}) overlaid with precipitation rate contours (2 mm hr^{-1}) at 11 UTC on May 25, 2007.

In Figure 3, the thick black contours delineate regions with precipitation rates greater than 2 mm h^{-1}.

When resolved at a scale of 100 m or less, the surface divergence field is obviously related to *boundary layer* updrafts and downdrafts because div $= -\partial w/\partial z$, neglecting density variations. If cloud-base updrafts and downdrafts are related to boundary layer updrafts and downdrafts, then we would expect that the surface divergence *averaged over regions of convergence only* (div < 0) would be related to $M_{c,u}$, and that the surface diver-

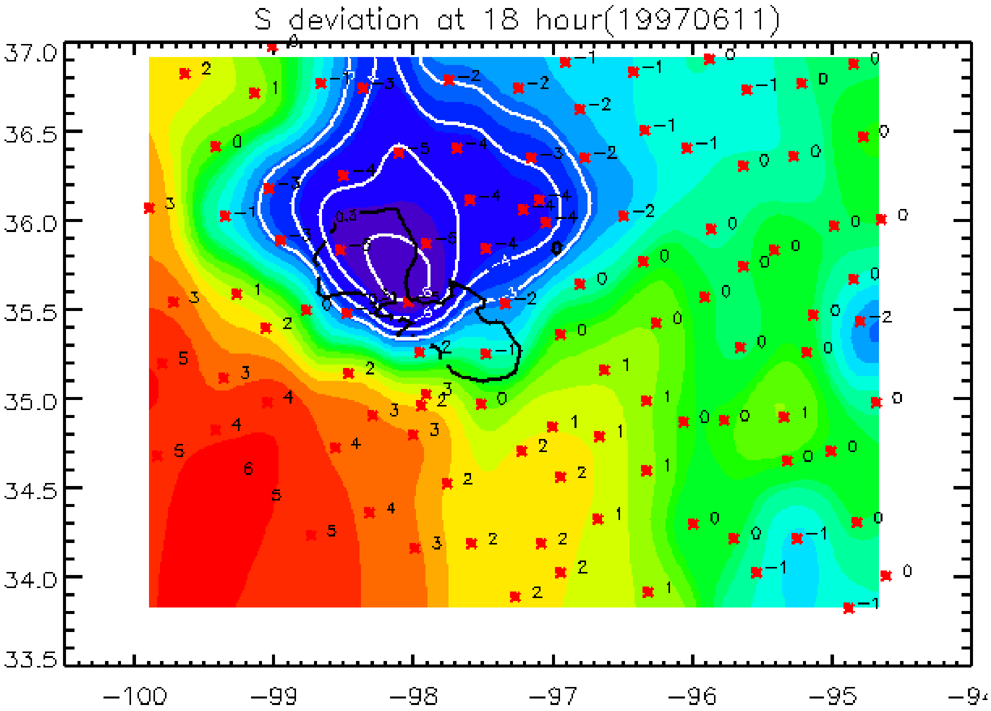

Figure 4: A cold pool represented by deviation of $s/c_p = T + gz/c_p$ (station values and white contours in K) from the Oklahoma Mesonet mean at 18 UTC, June 11, 1997. Precipitation rate (2 mm h^{-1}) contour is overlaid. Barnes (Barnes, 994a,b) analysis was used to produce this figure.

gence *averaged over regions of divergence only* (div > 0) would be related to $M_{c,d}$.

The average station spacing of the Oklahoma Mesonet is about 30 km. This means that the mesonet very poorly resolves the divergence fields associated with individual boundary layer eddies. However, the mesonet can resolve to varying degrees the mesoscale circulations associated with cumulus and cumulonimbus clouds and with mesoscale convective systems. Therefore we define M_u, the mesonet analog of the surface divergence averaged over regions of convergence only, and M_d, the mesonet analog of the surface divergence averaged over regions of divergence only as

$$\begin{aligned} M_u &= \frac{-\sum_i A_i \,\text{div}_i\, H(-\text{div}_i)}{\sum_i A_i} \\ M_d &= \frac{\sum_i A_i \,\text{div}_i\, H(\text{div}_i)}{\sum_i A_i} \qquad (1) \end{aligned}$$

where div$_i$ is the horizontal divergence of the ith triangle, which has area A_i, and $H(x)$ is the Heaviside step function.

M_u and M_d are typically nonzero due to convective boundary layer circulations even when there is no precipitating convection. Figure 2 is an example. Therefore, we also define M_u^+, the mesonet surface divergence averaged over regions of convergence $> 10^{-4}$ s^{-1}, and M_d^+, the mesonet surface divergence averaged over regions of divergence $> 10^{-4}$ s^{-1}. We have found that regions (triangles) with $|\text{div}_i| > 10^{-4}$ s^{-1} tend to be associated with regions of precipitating convection. Figure 3 is an example. We calculated the time series of hourly values of M_u, M_d, M_u^+, M_d^+.

It is well known that convective downdrafts and cold pools tend to increase the variances of winds (u and v components), temperature (T), and water vapor mixing ratio (q) in the boundary layer (e.g., Zulauf and Krueger, 1997; Zulauf, 2001). Figure 4 shows a cold pool more than 100 km in diameter that was observed within the Oklahoma Mesonet.We used a 3D CRM simulation in a 128 km by 128 km domain with a 1-km horizontal grid size to compare the variances resolved

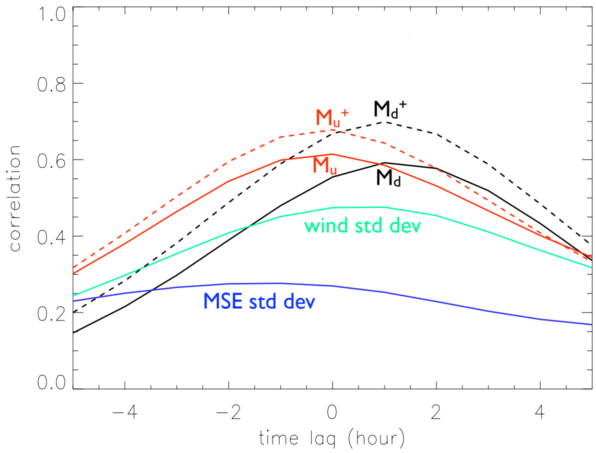

Figure 5: Lagged correlations of P with M_d, M_u, M_u^+, M_d^+, and standard deviations of moist static energy and wind for May–August 1997.

by a mesonet with a 32-km grid with those resolved by the 1-km grid. Our results indicate the mesoscale grid resolves more than 90 percent of the variance during periods with mesoscale convective systems. We calculated the time series of hourly values of the mesonet variances of u, v, T, q, and of related quantities including moist static energy, $h \equiv c_pT + Lq + gz$.

We correlated the divergence–related time series with the time series of hourly area-averaged precipitation rate (P), which represents to some degree the cloud–base mass fluxes. Figure 5 shows the lagged correlations of P with M_d, M_u, M_u^+, and M_d^+, and standard deviations of moist static energy and wind obtained from the hourly times series for May–August 1997. The figure shows that (1) M_d, M_u, M_u^+, and M_d^+ are correlated with P, (2) M_u^+ and M_d^+ are better correlated with P than are M_u and M_d, and (3) M_d and M_d^+ lag P and M_u and M_u^+ by about 1 h. These features are just what we would expect for convective precipitation and indicate that it is possible to retrieval cloud–base mass fluxes from surface divergence and other properties. The weak correlation between the standard deviation of h and P are mainly due to the contamination of the correlation by the variation of h induced by synoptical scale events and topographical effect.

4. EVALUATION OF THE 'RETRIEVAL' METHOD USING MODEL SIMULATION DATA

We tested our cloud base–mass–fluxes 'retrieval' methodology by using results from a 54-hour simulation of maritime tropical convective cloud systems observed during KWAJEX. The 3D simulation was performed with the UU LES with a horizontal grid size of 1 km and a horizontal domain size of 128 km by 128 km. We assumed that mesonet stations were located on a regular square grid with 32 km spacing.

Both updraft and and downdraft mass fluxes are calculated at 1050 m. Updraft mass flux occurs in cloudy grid cells with upward vertical velocity, while downdraft mass flux occurs in cloudy and/or precipitating grid cells with downward vertical velocity. Figure 8 shows the time series of cloud-base updraft and downdraft mass fluxes.

M_u and M_d are calculated at lowest model grid level (36 m) using (1). Two different methods are used to calculate div$_i$ for each 32-km square. In the first method, u and v at all the points on the boundary of the 32-km square are used to calculate the true value of div$_i$ for the square. In the second method, only u and v at the four corners of the 32-km square (representing mesonet stations) are used to estimate div$_i$. M_u and M_d calculated using the first method are called *true* M_u and M_d, represented by $M_{u\ \mathrm{true}}$ and $M_{d\ \mathrm{true}}$. M_u and M_d calculated by using the second method are called *meso* M_u and M_d, represented by $M_{u\ \mathrm{meso}}$ and $M_{d\ \mathrm{meso}}$. Large scale divergence is added to the true and meso div$_i$ before true and meso M_u and M_d are calculated.

How well can we estimate $M_{c,u}$ and $M_{c,d}$ from true and meso M_u and M_d for a 32-km mesonet grid size? Figure 6 shows a scatter plot of both $M_{u\ true}$ and $M_{u\ meso}$ versus $M_{c,u}$. The correlation of $M_{c,u}$ and the $M_{u\ true}$ is 0.82. The correlation of $M_{c,u}$ and $M_{u\ meso}$ is 0.79. Figure 7 shows a scatter plot of both $M_{d\ true}$ and $M_{d\ meso}$ versus $M_{c,d}$. The correlations of $M_{c,d}$ and $M_{d\ true}$ and $M_{u\ meso}$ are 0.90 and 0.89, respectively. For comparison, the correlations of P and $M_{c,u}$ and $M_{c,d}$ are 0.77 and 0.93, respectively.

If we assume the following linear relationship

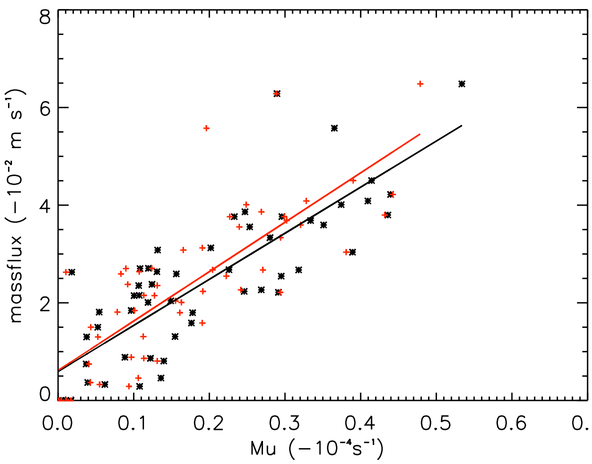

Figure 6: $M_{c,u}$ (m s^{-1}) at 1050 m AGL versus $M_{u\ true}$ (black stars) and $M_{u\ meso}$ (red crosses). Black and red lines are linear fits of $M_{c,u}$ and $M_{u\ true}$ and $M_{u\ meso}$.

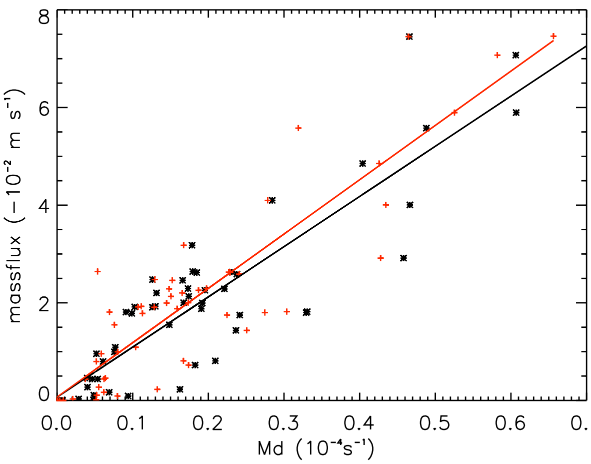

Figure 7: $M_{c,u}$ (m s^{-1}) at 1050 m AGL versus $M_{d\ true}$ (black stars) and $M_{d\ meso}$ (red crosses). Black and red lines are linear fits of $M_{c,d}$ and $M_{d\ true}$ and $M_{d\ meso}$.

between $M_{c,u}$ and M_u,

$$M_{c,u} = A + BM_u, \tag{2}$$

then we obtain the coefficients A, B, and RMS error listed in Table 1. Similarly the coefficients and RMS error for the linear fit of $M_{c,d}$ using M_d are listed in Table 2. The differences in correlations and RMS errors between true and meso methods are small. The results strongly suggest that it is possible to estimate $M_{c,u}$ using either $M_{u\ true}$ or $M_{u\ meso}$, and to estimate $M_{c,d}$ using either $M_{d\ true}$ or $M_{d\ meso}$.

Figure 8 shows the time series of $M_{c,u}$ and $M_{c,d}$ at 1050 m and $M_{c,u}$ estimated using $M_{u\ meso}$ and $M_{c,d}$ estimated using $M_{d\ meso}$. There is generally good agreement but with a slight time lag in the estimated values. Figure 9 shows the corresponding lagged correlations of P with $M_{c,u}$, $M_{c,d}$, M_d, and M_u. We see that M_u, M_d, and P lag the cloud-base updraft and downdraft mass fluxes, $M_{c,u}$ and $M_{c,d}$, by about 1 h on average, and that $M_{c,d}$ is more highly correlated with P than is $M_{c,u}$.

It is instructive to compare Fig. 9 with Fig. 5, which shows the lagged correlations of P with M_u and M_d obtained from the Oklahoma datasets. The most relevant aspect is that, taken together, these results imply that M_u and M_d are most correlated with $M_{c,u}$ and $M_{c,d}$ for lags of 1 to 2 h. We also see that both Oklahoma and KWAJEX have a maximum correlation between P and M_u at zero lag. However, the maximum correlation between P and M_d occurs at 1 h in Oklahoma, and at 0 h for KWAJEX. This difference is not surprising. There are several potential explanations. A good candidate is that the mesoscale cold pools that contribute to M_d are larger and more intense in Oklahoma, due to higher cloud bases and drier boundary layer air, and therefore M_d takes longer to maximize.

The maximum correlations between M_u and precipitation are similar for Oklahoma and KWA-

Table 1: Least squares linear fit coefficients and RMS errors for $M_{c,u}$.

	A	B	RMS
$M_{u\ true}$	0.0059	940	0.0088
$M_{u\ meso}$	0.0061	1010	0.0094

Table 2: Least square linear fit coefficients and RMS errors for $M_{c,d}$.

	A	B	RMS
$M_{d\ true}$	0.0007	1030	0.0081
$M_{d\ meso}$	0.0007	1110	0.0084

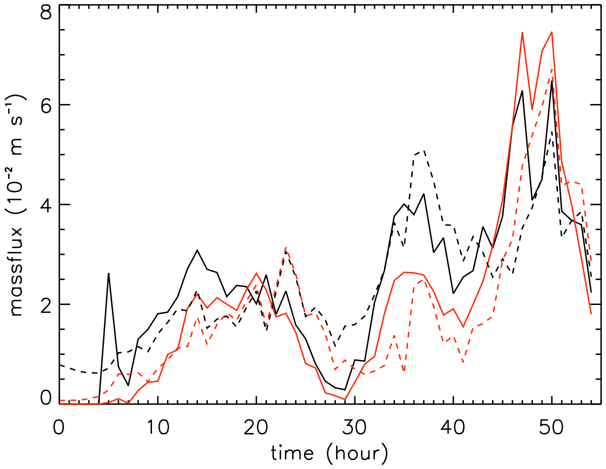

Figure 8: Time series of $M_{c,u}$ (black solid line) and $M_{c,d}$ (red solid line) at 1050 m AGL and $M_{c,u}$ estimated using $M_{u\ meso}$ (black dashed line) and $M_{c,d}$ estimated using $M_{d\ meso}$ (red dashed line).

JEX (0.67 vs 0.69) but for M_d and precipitation, the correlation is significantly larger for KWAJEX (0.92 vs 0.70). These results suggest that the relationship between updrafts and precipitation may be more universal than that between downdrafts and precipitation.[1]

5. SUMMARY

Two observational datasets, the Oklahoma Mesonet data and the hourly ABRFC gridded precipitation data from May to August in 1997, were used to test the 'retrieval' of the *mesonet-averaged* cloud base updraft and downdraft mass fluxes from the surface divergence field. It is shown that (1) M_d, M_u, M_u^+, and M_d^+ are correlated with P, (2) M_u^+ and M_d^+ are better correlated with P than are M_u and M_d, and (3) M_d and M_d^+ lag P and M_u and M_u^+ by about 1 h. This indicates that it is possible to retrieval cloud–base mass fluxes from surface divergence and other properties.

To examine how well this mass fluxes 'retrieval' method works data from a 54-hour CRM simulation of maritime tropical convective cloud systems observed during KWAJEX were used, along with the similar methods as in the Oklahoma Mesonet analysis. The results strongly suggest the possibility of estimates $M_{c,u}$ ($M_{c,d}$) using either $M_{u\ true}$ ($M_{d\ true}$) or $M_{u\ meso}$ ($M_{d\ meso}$). A generally good agreement was shown between the true and estimated $M_{c,u}$ ($M_{c,d}$) by using $M_{u\ meso}$ ($M_{d\ meso}$). However there is a slight lag in the estimated values.

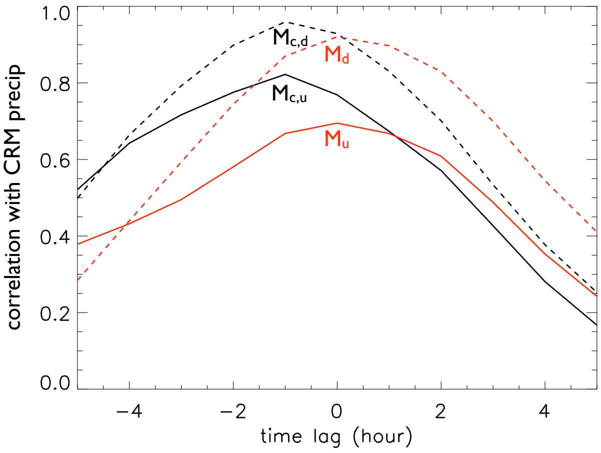

Figure 9: Lagged correlations of P with $M_{c,u}$, $M_{c,d}$, M_d, and M_u for the KWAJEX simulation.

Since the CRM simulation was performed over ocean not land, the results from KWAJEX simulation analysis should be applied with caution over land. This might be one of the possible reasons why our defined M_u^+ and M_d^+ are not significantly better correlated with $M_{c,u}$ and $M_{c,d}$ than M_u and M_d do. Other possible reasons may include short simulation time and small simulation domain.

ACKNOWLEDGMENTS. This research was supported by the National Science Foundation Science and Technology Center for Multi-Scale Modeling of Atmospheric Processes, managed by Colorado State University under cooperative agreement No. ATM-0425247. James Kelly at the Australian Bureau of Meteorology provided the IDL code for the Barnes analysis.

---

[1] The critical role of downdrafts in determining the structure of convective systems is well-known.

REFERENCES

Barnes, S. L., 1994a: Applications of the Barnes objective analysis scheme Part I: Effects of undersampling, wave position, and station randomness. *J. Atmos. Oceanic Technol.*, **11**, 1433–1448.

Barnes, S. L., 1994b: Applications of the Barnes objective analysis scheme Part II: Improving derivative estimates. *J. Atmos. Oceanic Technol.*, **11**, 1449–1458.

Davies-Jones, R., 1993: Useful formulas for computing divergence, vorticity, and their errors from three or more stations. *Mon. Wea. Rev.*, **121**, 713–725.

Dubois, J. A., and P. L. Spencer, 2005: Computing divergence from a surface network: Comparison of the triangle and pentagon methods. *Wea. Forecasting*, **20**, 596–608.

Luo, Y., and S. K. Krueger, 2004: Cloud types simulated by the NCEP GFS single-column model. *Proceedings of the Fourteenth Atmospheric Radiation Measurement (ARM) Science Team Meeting*, U.S. Department of Energy, Albuquerque, NM, Extended Abstract: `http://www.arm.gov/publications/proceedings/conf14/extended_abs/luo3-y.pdf`.

Luo, Y., and S. K. Krueger, 2005: Cloud properties simulated by a single-column model. Part 1: Comparison to cloud radar observations of cirrus clouds. *J. Atmos. Sci.*, **62**, 1428–1445.

Luo, Y., S. K. Krueger, G. G. Mace, and K.-M. Xu, 2003: Cirrus cloud properties from a cloud-resolving model simulation compared to cloud radar observations. *J. Atmos. Sci.*, **60**, 510–525.

Xie, S. C., and Coauthors, 2002: Intercomparison and evaluation of cumulus parameterizations under summertime midlatitude continental conditions. *Quart. J. Roy. Meteor. Soc.*, **128**, 1095–1136.

Xie, S. C., and M. H. Zhang, 2000: Impact of the convection triggering function on single-column model simulations. *J. Geophys. Res.*, **105**, 14983–14996.

Xu, K.-M., R. T. Cederwall, L. J. Donner, W. W. Grabowski, F. Guichard, D. E. Johnson, M. F. Khairoutdinov, S. K. Krueger, J. C. Petch, D. A. Randall, C. J. Seman, W.-K. Tao, D. Wang, S. C. Xie, J. J. Yio, and M.-H. Zhang, 2002: An intercomparison of cloud-resolving models with the Atmospheric Radiation Measurement summer 1997 Intensive Observation Period data. *Quart. J. Roy. Meteor. Soc.*, **128**, 593–624.

Yang, F., H.-L. Pan, S. K. Krueger, S. Moorthi, and S. J. Lord, 2006: Evaluation of the NCEP Global Forecast System at the ARM SGP site. *Mon. Wea. Rev.*, **134**, 3668–3690.

Zulauf, M. A., 2001: *Modeling the effects of boundary layer circulations generated by cumulus convection and leads on large-scale surface fluxes*. PhD thesis, University of Utah, Salt Lake City, UT 84112, 177 pp.

Zulauf, M. A., and S. K. Krueger, 1997: Parameterization of mesoscale enhancement of large-scale surface fluxes over tropical oceans. *Preprints, 22nd Conf. on Hurricanes and Tropical Meteorology*, Fort Collins, CO. Amer. Met. Soc., 164–165.

A Preliminary Study on the Techniques of Convective Clouds Rainfall Enhancement Seeding Effect Test

Tang Renmao (1) Ye Jianyuan(1) Xiang Yuchun(1) Xiao Yanjiao(2)
Liu Jian(1) Yuan Zhengteng(1) Chen Yingying(1)
(1) Weather Modification Office of Hubei Province, Wuhan 430074, China
(2) Wuhan Institute of Heavy Rain, China Meteorological Administrator 430074, China

1. Indexes of seeding condition on convective cloud

A set of indexes of seeding condition on convective cloud is built on the products of radar, satellite, sounding and numerical model for instructing precipitation enhancement operation.

1.1 Sounding stratification indexes

1) Convective instability;
2) Potential instability;
3) Showalter index: < 1.5

1.2 National operation model indexes

1) Precipitation forecasting from model (3 hours): 1-10 mm;
2) Total hydrometeors content (400hpa) : >= 0.01 g/kg;
3) Ice crystal water content (400hpa) : >= 0.01 g/kg;
4) Ice crystal quantity concentration (400hpa) : >= 1 /L;
5) Total hydrometeors content (500hpa) : >= 0.01 g/kg;
6) Ice crystal water content (500hpa) : >= 0.01 g/kg;
7) Ice crystal quantity concentration (500hpa) : >= 1 /L;
8) Cloud-top temperature: < -10

1.3 Three-dimension convective cloud model indexes

1) Precipitation: > 5 mm;
2) Precipitation enhancement present: > 0

1.4 Radar echo parameters indexes

1) Echo intensity: > 30 dbz;
2) Echo-top height: > 5 km;
3) Vertical integrated liquid water content: 2 kg/m^2

2. Method of selecting contrast cloud automatically

A method of selecting contrast cloud automatically and analyzing the seeding effect according to radar echo parameters is brought forward, aiming at physical test of convective cloud precipitation enhancement. Basing on the Doppler radar data products, the contrast cloud is selected automatically in all convective cells at the very time when seeding by comparing their birth time, distance, and varying characteristics of echo parameters before seeding with those of seeded cloud. Then, it is presented that the variation of echo parameters of seeded cloud and comparison between echo parameters of seeded cloud and that of contrast cloud.

In the view of this method, a set of seeding effect analysis software of convective cloud rainfall enhancement with radar products has been designed and developed. Its four modules include data transforming, radar products searching and displaying, contrast cloud automatically selecting and effect analyzing. It can identify the contrast cloud in real-time, trail and note the echo parameters of seeded cloud and contrast cloud during their existing period, present curve charts of the variation of the echo parameters of seeded cloud and comparison between seeded and contrast cloud.

3. Experiment and analyses

The experiment was performed in eastern Hubei province during August and September, 2007. In every operation, seeding was carried out severely by conforming to the seeding indexes and the dual-radar including Cinrad WSR-98D radar and 3-cm dual-linear polarization and entire-phase-parameter radar detected in high consistency.

3.1 Analyses on observation data with Doppler radar

1) The variation of echo parameters of seeded cloud

Analyzing echo parameter variation characteristic of seeded cloud in three cases, the life of the seeded clouds span in 72, 132, 126 minutes respectively, 59, 90, 61minutes after seeding which account for 82%, 68%, 48% respectively. It's explained that seeding is done respectively in prophase, metaphase and anaphase of convective cloud life in three operations.

From table 1, it's shown that after seeding, the echo intensity reaches the maximum value in 9-13 minutes, increases by 5-7dbz, accounted for 9%-13%; and the strong echo area reaches the maximum value in 21 minutes, increases by 30%-110%; the echo-top reaches the maximum value in 9-13 minutes, increases by 4 km greatly, accounted for 32%-40%; the liquid water content reaches the maximum value in 9-25 minutes, increases by 21kg/m^2 greatly, 40%-117%.

From figure 1, it's shown that the echo intensity increases by 3dbz before seeding, and increases by 5dbz to the maximum value rapidly in 12 minutes after seeding and then decreases slowly; the echo-top increases by 1.5km gradually in 12 minutes before seeding, and increases by 1.8km in some times after seeding; the liquid water content rises rapidly, increases by 11kg/m2 to the maximum in 24min and then decreases fleetly.

Table 1: the variation of echo parameters of seeded cloud and contrast cloud

No.	Cloud	Intensity		Strong echo area		Echo-top height		VIL.		Life (min)	Life after seeding (min.)
		Time (min.)	Increase percent	Time (min)	Increase percent	Time (min)	Increase percent	Time (min)	Increase percent		
1	Seeded -	9	9%	21	30%	9	33%	15	52%	72	59
	Contrast -	3	4%	6	16%	15	12%	0		48	35
2	Seeded -	13	13%	13	33%	7	32%	25	117%	132	90
	Contrast -	13	11%	13	18%	7	28%	Decrease		54	12
3	Seeded -	9	11%	21	110%	15	51%	9	40%	126	61
	Contrast -	9	4%	Decrease		Decrease		21	25%	96	31

Note: In the table "Time" means: the time which parameters getting strongest spend after the seeding.

2) The comparison between echo parameters of seeded cloud and that of contrast cloud

From table 1, it's shown that the increase percent of echo parameters of seeded cloud are larger than that of contrast cloud after seeding. The statistical results show that the seeded clouds' the echo intensity is 5%, the strong echo area is 46%, the echo-top height is 12%, the liquid water content is 61% and cell life 44 minutes more than those of contrast clouds.

From figure 1, it's shown that the echo intensity and echo-top of contrast cloud are similar to those of seeded cloud before seeding, which have a small scale rise, and increase by smaller scale than those of seeded cloud after seeding, the liquid water content does not increase, but reduces rapidly. It is explained that the artificial seeding makes a good progress.

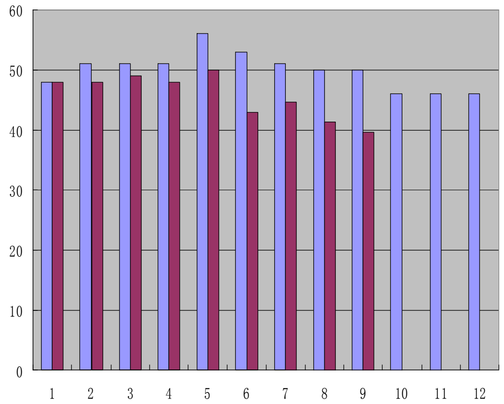

(a) The variation of echo intensity

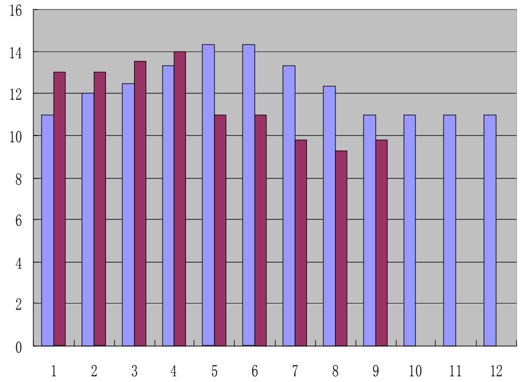

(b) The variation of echo-top height

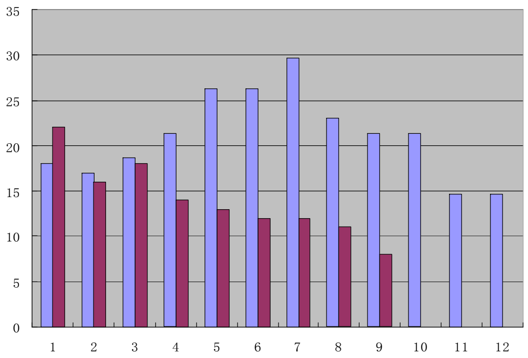

(c) The variation of VIL

Figure 1: the variation of echo parameters of seeded cloud and contrast cloud

3.2 Analyses on observation data with Dual-polarization radar

By analyzing the echo data from Dual-polarization radar, it’s shown that after seeding, the echo center intensity obviously strengthens, the echo-top rises, the strong echo area increases, and after maintaining a period of time, then begin to reduce, the minimum linear depolarization ratio decreases and region area of lower value increases, it reaches the extreme value in 23 minutes after seeding, and after lasting a period of time, the minimum starts to increase and the area starts to reduce, which explains that the precipitation granule gets bigger after operation; the bigger zero delay correlation coefficient's area also has increases, the related coefficient value discrimination is not obvious, but the greater value’s area increases and then reduces, which explains that the quantity of precipitation granule increases.

4. Discussions

The results of analyses show that the method of selecting contrast cloud automatically can eliminate errors causing by man-made judging and make the effect analysis on convective cloud rainfall enhancement more scientific practically. Analyzing operation cases, radar echo parameters and Dual-polarization factors take certain changes after seeding, which are used as radar observation evidence for seeding effect.

Some problems are as following: 1) there are fewer operation cases; 2) more further analyses with the Dual-polarization radar data are needed. Two experiment regions including the northwestern and eastern Hubei province will be set up to catching more operation opportunities and further development of application software will be taken for the future.

ON THE EVOLUTION OF THE STRUCTURE OF A BOW-ECHO OVER NORTHEASTERN ARGENTINA

Marcela M. Torres Brizuela*[(1)] and Matilde Nicolini[(1)]
[(1)] Centro de Investigaciones del Mar y la Atmósfera (CONICET-UBA) - Departamento de Ciencias de la Atmósfera (FCEyN-UBA), Argentina

1. INTRODUCTION

During the months of spring/summer mesoscale convective systems (MCS) move and develop through the northeastern of Argentina, producing severe weather generally in the form of strong winds, heavy precipitation, large hail and occasionally develop tornadoes (Velasco and Fritsch 1987, Conforte 1997, Laing and Fritsch 1997, Torres and Nicolini, 1999, Silva Dias 1999, Nicolini et al., 2002, Torres, 2003, Mota, 2003, Nieto Ferreira et al. 2003, Salio et al 2007, among others).

Since the late 1980s and early 1990s, it has been recognized that bow echoes, a well-known mode of severe convection, often produce damaging downburst winds and tornadoes. Numerous studies (Rotunno et al. 1988, Weisman et al. 1988, Lee et. al. 1992, Johns 1993, Weisman 1993) were dedicated to describe and explain a long-lived mesoconvective structure that takes the form of a 60-200 km long bow-shaped segment of cells that evolves from a unique cell or as a part of a larger scale multicellular convective system (line or MCCs). Weisman and Davis (1998) found that the Coriolis effect is not a necessary forcing for bow-echo generation but is responsible for enlarging the northern cyclonic end of the squall line as is observed in actual Northern Hemisphere bow echoes.

It is worth to mention that the typical morphology of radar echoes and wind damages associated with this bow structure was first depicted by Fujita (1979) in his well-known conceptual diagram reproduced in Figure 1. He was the first to hypotesize that downburst winds in a descending rear-inflow jet (**RIJ**) were responsible for the observed wind damage swaths preferably poleward of the bow apex.

This convective structure more frequently evolves within an environment associated with elevated moisture (surface dew-point greater than 20C), moderate to strong CAPE values and with a moderate to strong vertical wind-shear in the lowest 2.5km AGL.

A previous study of a multicellular storm (Torres Brizuela and Nicolini, 2006) developed over the area of Resistencia (27°27'S, 59°03'W), Province of Chaco, Argentina during the morning of 19 October 2000, concluded that this storm had strong evidences of the typical conditions leading to bow-echo development and the numerical simulations performed in this study also evidenced the genesis of this system in the area. The satellite images of this system displayed the evolution with a pattern and time length similar to the expected for bow-echoes.

The aim of this work is to study the role of the Coriolis force on the evolution structure of a bow echo produced over northeastern Argentina.

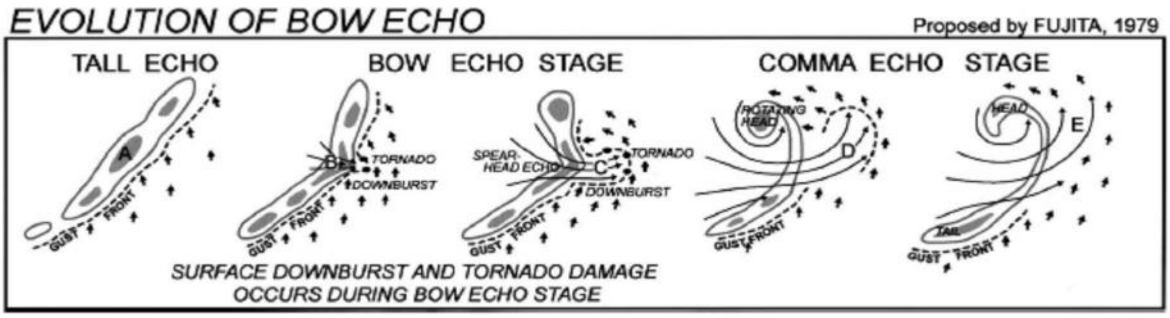

Figure 1: Schematic diagram illustrating bow-echo evolution in the northern hemisphere. Figure adapted from Fujita (1979).

2. METHODOLOGY

The numerical tool used for the numerical experiments is the Advanced Regional Prediction System (ARPS), a non-hydrostatic mesoscale model developed by the University of Oklahoma and completely described by Xue et al. (2000).

The following is a brief description of the configuration implemented in the model for this study. A bulk water, mixed-phase cloud microphysics, following Lin et al. (1983) is used. A 1.5 order prognostic turbulent kinetic energy equation option is used for subgrid scale turbulence parameterization. A Rayleigh friction absorption layer is activated near the top, and open lateral boundary conditions follow Klemp and Wilhemson (1987a). The horizontal domain was 340 km by 340 km with a 1 km grid spacing and the vertical grid spacing varied in a streched way from 150m near the surface to 600 m at the top of 18 km AGL. For the acoustic terms in the equations a "small" time step of 1 s is used and increased to 6 for the other terms.

The model is initialized within an horizontally homogeneous environment given by the Resistencia 12UTC radiosounding (shown in Figure 2), launched within a warm Θ_e air mass (> 355K) with strong vertical wind shear in the first 2.5km AGL.

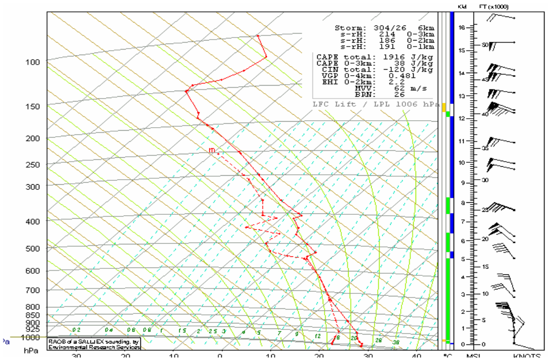

Figure 2: Radiosounding at Resistencia, 12UTC

Two different numerical experiments have been performed aimed to understand the role of the Coriolis force in organizing the convective structure of this particular event. The first one (**E1**) was run without Coriolis force, a second one with the Coriolis force included (**E2**) where the base state is geostrophically balanced, and the Coriolis force is acting only on the wind perturbations.

3. NUMERICAL RESULTS

Until 90 min of integration time, the evolution of convection in both numerical experiments, exhibits a clear multicell structure arranged in a line and the displacement of the system is quite similar.

Advancing in time, both simulations acquire the features of a typical bow-echo configuration owning to the book-end vortices with a stronger rotational downdraft in the poleward (southern) apex of the convective line.

Allthough at 120 min of simulated time, both experiments start to display differences in arrangement and also in their displacement, these differences are substantially slight.

The cold pool and the stronger winds in the rear part are clearly evident since 150 min. of simulated time for both experiments, with the **RIJ** becoming stronger in **E1**. Also for this experiment, the convective line is shorter and its displacement has a stronger southerly component.

Table I summarizes the evolution of characteristic parameters for both experiments as the extension of the convective line and the location of the central point of the convective line in order to account for the differences in system displacement.

TIME (min.)	**E1** Line length (km)	**E2** Line lenght (km)	**E1** Central point, Coord. x,y (km)	**E2** Central point Coord. x,y (km)
90	35	40	(80,205)	(80,210)
120	50	55	(100,180)	(105,180)
150	60	70	(120,150)	(130,150)
180	70	90	(140,120)	(150,140)
210	80	120	(165,100)	(175,95)
240	90	160	(185,70)	(210,90)

Table I. Values RUN **E1** and **E2**.

In the same way as Table I, Table II exhibits the maximum magnitude of the horizontal wind and the minimum vertical vorticity related with the descending motion located in the southern vortex apex of the bow convective line at a significant level in the lower troposphere.

TIME (min)	**E1** V 2.7km (ms^{-1})	**E2** V 2.7km (ms^{-1})	**E1** ζ z=2.7km $x10^{-3}s^{-1}$	**E2** ζ z=2.7km $x10^{-3}s^{-1}$
180	36	35	-10	-12
195	40	36	-12	-12
210	36	33	-10	-12
225	40	30	-10	-10
240	36	33	-12	-10

Table II. Values RUN **E1** and **E2**.

Wind speeds in the rear flank for the experiment **E1** are stronger than in **E2** whereas significant differences in the vertical vorticity are not apparent at 2.7km (see Table II). During the whole simulation the differences in cold pool height are negligible for both experiments.

At the end of the simulation (240min), figures 3a and 3b displays the wind pattern, the cores of the ascent motion jointly with the minimum vorticity related with the downdraft at the southern apex of the bow echo. Both experiments reproduced the **RIJ**, stronger in **E1**, and an intense downdraft related with a minimum in the vertical vorticity, but in **E2** the rotation is localized in a slightly smaller area.

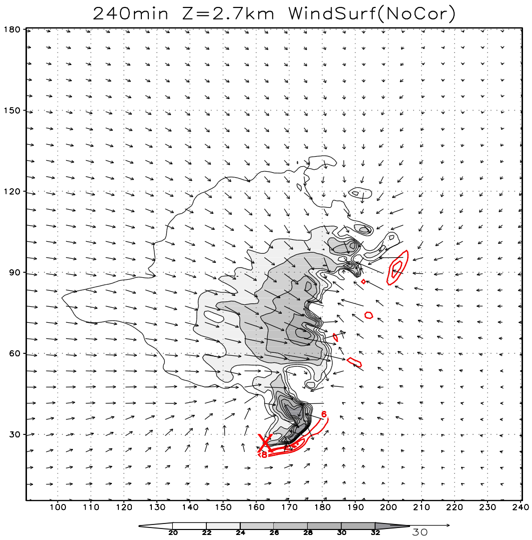

Figure 3a: Horizontal field of velocity maximum (ms^{-1}, shaded), updraft motion (w>5 ms^{-1}, __), superimposed V*(arrows) and X indicates minimum vertical vorticity related with descending motion for **E1** at 240min and Z=2.7km.

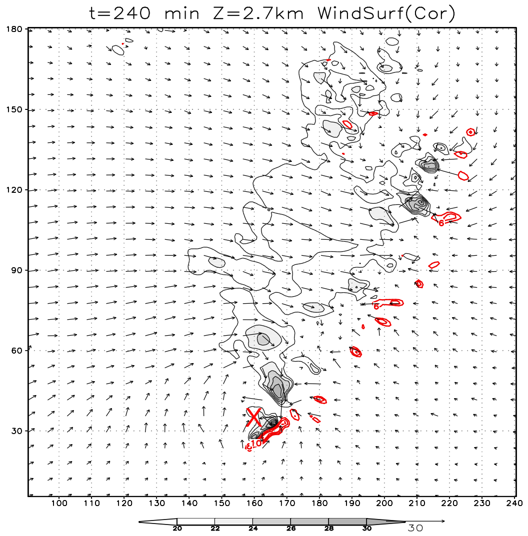

Figure 3b: Horizontal field of velocity maximum (ms^{-1}, shaded), updraft motion (w>5 ms^{-1}, __), superimposed V* (arrows) and X indicates minimum vertical vorticity related with descending motion for **E2** at 240min and Z=2.7km

More distinguishable differences between experiments are apparent in the total precipitating (qt>1gkg^{-1}) fields and location of strong winds at low levels (Figures 4a and 4b). Different patterns in terms of arrangement and extension lenght of the convective line are evident for both experiments.

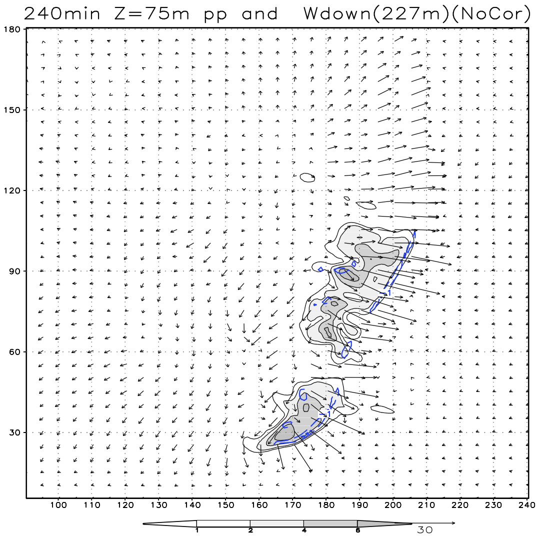

Figure 4a: Horizontal field of precipitating categories (qt>1gkg^{-1}, shaded), V(arrows) at Z=75m and superimposed w (<-1ms^{-1} at Z=227m, __) for **E1** at 240min.

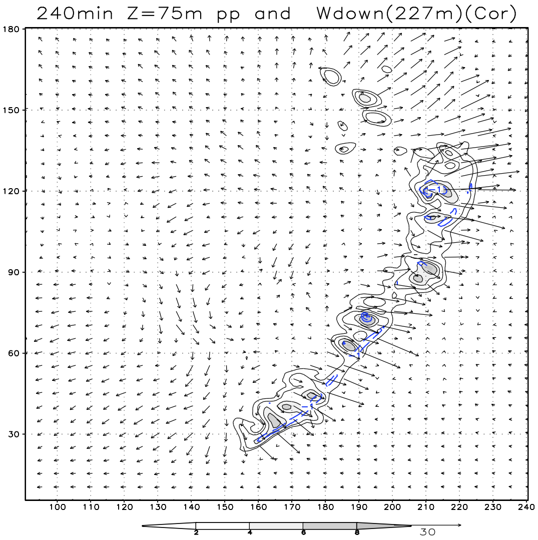

Figure 4b: Horizontal field of precipitating categories (qt>1gkg^{-1}, shaded), V(arrows) at Z=75m and superimposed w (<-1ms^{-1} at Z=227m, __) for **E2** at 240min.

4. SUMMARY AND FUTURE WORK

Numerical simulations of the 19 October 2000 convection using ARPS reproduced correctly the significant features and arrangement of a bow-echo structure. This "bow convective line" comes up more clearly in the **E2** experiment. In terms of vertical vorticity, related with descending motion the southern apex of the system becomes dominant for both experiments. The rotation in this apex is defined in a smaller area for **E2** experiment.

In terms of a stronger magnitude of the **RIJ**, **E1** reproduces it better, but in terms of characteristical lenghts of a typical bow-echo **E2** shows a better representation (see Table I). A remarkable pattern of **E2** simulation is that mesovortices are insinuated, result already found by different authors (Weisman and Trapp 2003, Trapp and Weisman 2003, Atkins 2006).

Future work will proceed in two aspects: a) a) enlarge the horizontal domain to enable a longer simulation with the system remaining inside in order to allow a better study of the coriolis effects b) Include the terrain and soil type to account for their effects on the bow-echo and c) In a longer simulation, study the evolution of the mesovortices and its relationship with the Coriolis force.

Acknowledgments This work was supported by the grants of: Agencia Nacional de Promoción Científica y Tecnológica ANPCyT PICT 2003 N° 07-14420, the University of Buenos Aires UBACYT X266, and by the Consejo Nacional de Investigaciones Científicas y Técnicas CONICET PIP 5582.
We are grateful to the National Weather Service to provide the Resistencia radiosounding.

REFERENCES

Atkins, N. T., 2006: On the genesis and strength of mesovortices formed within bow echoes. Preprints of 23rd Conference on Local and Severe Storms. St Lous, MO, USA, November 2006. P4.4. 4pp.

Conforte J.C., 1997: Um estudo de complexos convectivos de mesoescala sobre a América do Sul. [A study of mesoscale convective complexes over South America]. Doctoral dissertation. INPE.

Fujita, T. T., 1979: Objectives, operation and results of project NIMROD. Preprints 11th Conf. on Local and Severe Storms, Kansas City, MO. Amer. Met. Soc., 208-213.

Johns, R. H., 1993: Meteorological conditions associated with bow-echo development in convective storms. *Wea. Forecasting*., **8**, 294–299.

Klemp J.B. and R.B Wilhelmson, 1978a: The simulation of a three dimensional convective storm dynamics. *J. Atmos. Sci.*, **35**, 1070-1096.

Laing, A. G., J. M. Fritsch, 1993a: Mesoscale Convective Complexes over the Indian Monsoon Region, *J. Climate*, **6**, 911–919.

Lee, W. R. W. Wakimoto and R. Carbone, 1992: The evolution and structure of a "bow-echo-microburst event. Part II: The bow echo. *Mon. Wea. Rev.* **120**, 2211-2225.

Mota, G.V., 2003: Characteristics of rainfall and precipitation features defined by the Tropical Rainfall Measuring Mission over South America. *Ph.D. Dissertation, University of Utah*, 215 pp.

Lin, Y.L., R. D. Farley and H. D. Orville. 1983: Bulk Parameterization of the Snow Field in a Cloud Model. *J. Appl. Meteor*:, **22**, 1065–1092.

Nicolini, M., A. C. Saulo, J. C. Torres, and P. Salio, 2002: Enhanced precipitation over southeastern South América related to strong low-level jet events during austral warm season. Meteorologica, Special Issue for the SouthAmerican Monsoon System, 27, 59-69.

Nieto Ferreira, R. T. Rickenbach, D. Herdies and L. M. Carvalho, 2003: Variability of South American convective cloud systems and tropospheric circulation during January- March 1998 and 1999, Mon. Wea. Rev., 131, 961-973.

Rotunno, R., Klemp, J. B and M. L. Weisman, 1988: A theory for strong, long-lived squall lines. *J. Atmos. Sci.*, **45**, 463-485.

Salio, P., Nicolini, M. and E. J. Zipser 2007: Mesoscale Covcetive Systems over Southeastern South America and their relationship with the South American Low Level Jet. *Mon. Wea. Rev*., **135**, 4, 1290-1309.

Silva Dias, M.A.F., 1999: Storms in Brazil. In: Hazards and Disasters Series, Storms Volume II, R. Pielke Sr. , R. Pielke Jr., Eds., Routledge. pp.207-219.

Torres, J:C., 2003: Sistemas convectivos en mesoescala altamente precipitantes en el centro y norte de Argentina. [Heavily precipitating mesoscale convective systems over Central and Northern Argentina]. PhD dissertation, University of Buenos Aires, Argentina, 132 pp.

Torres, J. C. and M. Nicolini, 1999: "Analysis of a mesoscale convective system centered over the Río de la Plata". *Australian Meteorological Magazine*, Vol. 48, 261-272.

Torres Brizuela, M and M. Nicolini, 2006: Numerical simulation of a real case of multicell storm over Northeastern Argentina. Proceedings of 8th International Conference on Southern Hemisphere Meteorology and Oceanography, Foz do Iguaçu, Brazil, April 24-28, 2006, 2081-2084.

Trapp, R.J. and M.L. Weisman, 2003: Low-level mesovortices within squall-lines and bow echoes: Part II: Their genesis and implications. *Mon. Wea. Rev*.,**131**, 2804-2823.

Velasco, I. and J.M. Fritsch, 1987: Mesoscale convective complexes in the Americas. *J. Geophys. Res*., **92**, 9591-9613.

Weisman, M. L., Klemp, J. B and R. Rotunno, 1988: Structure and evolution of numerically simulated squall lines. *J. Atmos. Sci.*, **45**, 1990-2013.

Weisman, M. L., 1993: The genesis of severe, long-lived bow echoes. *J. Atmos. Sci.*, **50**, 645-670.

Weisman, M.L. and C. Davis, 1998: Mechanisms for the generation of mesoscale vortices within quasy-linear convective systems. *J. Atmos. Sci.*, **55**, 2603-2622.

Weisman, M.L. and R. J. Trapp, 2003: Low-level mesovortices within squall-lines and bow echoes: Part I. Overview and dependence on environmental shear. *Mon. Wea. Rev*.,**131**, 2779-2803.

Xue, M., K. K. Droegemeier y V. Wong, 2000: The advanced regional prediction system (ARPS) – A multiscale non-hydrostatic atmospheric simulation and prediction model. Part I: Model dynamics and verification. *Meteorol. Atmos. Phys.*, **75**, 161-193.

DENSITY CURRENTS IN THE SAHARA: SENSITIVITY TO EVAPORATION OF RAINDROPS

J. Trentmann[1], P. Knippertz[1], A. Seifert[2]
[1]Institute for Atmospheric Physics, Johannes Gutenberg
University Mainz, Germany
[2]German Weather Service, Offenbach, Germany

1. INTRODUCTION

Density currents are common atmospheric features. Evaporation of hydrometeors that sediment into sub-saturated air results in local cooling and moistening. These cold and moist air masses (commonly termed 'cold pool') can propagate in the form of a density current into undisturbed regions. Such atmospheric density currents are a well-known phenomenon, and their properties have been compared with results from theoretical and laboratory studies (Simpson 2000). Under unstable conditions, convection can be triggered by the forced uplift at the head of density currents. Depending on the ambient wind shear these convective cells can become organized in the form of a squall line (e.g., Weisman and Rotunno (2004)).

Over desert regions the deep, hot and dry boundary layer allows for a substantial amount of latent cooling by evaporation from sedimenting hydrometeors and the formation of large cold pools. These cold pools are accelerated by the substantial density and thus pressure differences to the environment. Because of the dry desert air and the stable stratification, no deep convection is initiated ahead of these density currents.

During the Saharan Mineral Dust Experiment (SAMUM), that took place between 11 May and 10 June 2006 in Marocco, density currents have been frequently observed and documented (Knippertz et al. 2007). These density currents in the North-Western Sahara are a result of the evaporation of hydrometeors formed in deep convection over the Atlas Mountains. The high wind speed at the leading edge of these density currents ('gust front') efficiently mobilizes desert dust. Figure 1 shows an example of such a dust-filled density current that originates from deep convection over the Atlas mountains and propagates into the Sahara. This situation defines an excellent testbed for the investigation of atmospheric density currents, because the Atlas Mountains serve as a hot-spot for the initiation of deep convection, evaporation of rain is very efficient over the desert, and no new convection is initiated along the leading edge of the density currents.

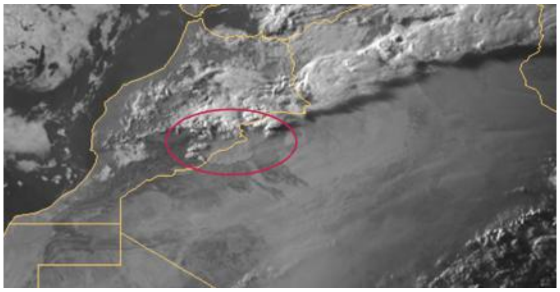

Figure 1: MSG visible image taken on 31 May 2006, 18 UTC. The red circle marks the location of the density current formed by melting and evaporation of hydrometeors.

Here we focus on the situation on 3 June 2006, when another density current was formed by evaporation of sedimenting hydrometeors from convection along the Atlas Mountains. We present model simulations

---

[1] Corresponding author's address: Jörg Trentmann, Institute for Atmospheric Physics, Johannes Gutenberg University Mainz, Becherweg 21, 55099 Mainz, Germany, jtrent@uni-mainz.de

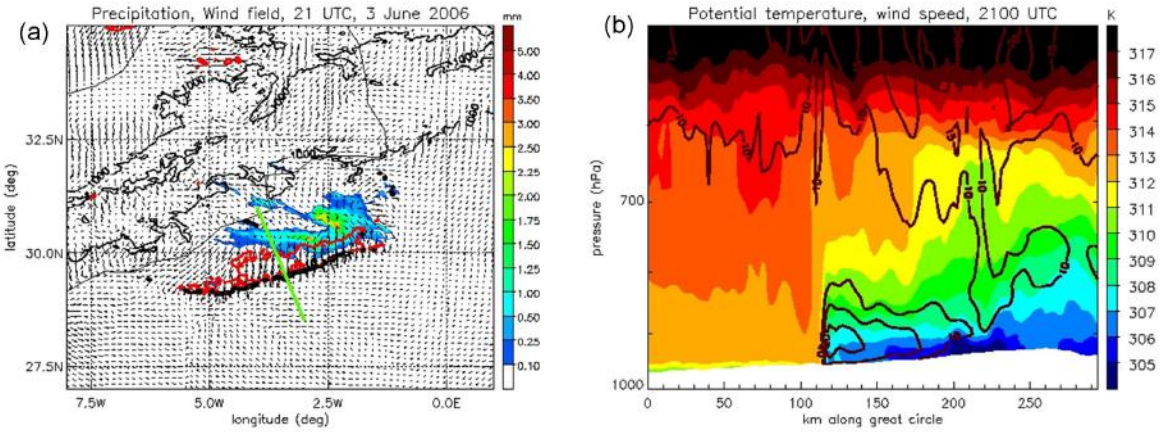

Figure 2: Two-dimensional structure of the simulated cold pool at 21 UTC on 3 June 2006. (a) Hourly precipitation (color coding), 10-m horizontal wind speed (arrows), 10-m s^{-1} isotach (red contour), leading edge of the density current (black contour). The green line represents the location of the cross section in Fig. 2b. (b) Vertical cross section along the green line in Fig. 2a, potential temperature (color coding) and horizontal wind speed (black contour).

with a numerical weather prediciton model (COSMO model) at high spatial resolution to allow for the explicit simulation of deep convection. The results from the model simulation are evaluated against surface and satellite observations (to be presented at the conference). The sensitivity of the density current on the evaporation of rain is explored.

2. MODEL SIMULATIONS

Model simulations were conducted using the COSMO model (Steppeler et al. 2003; Schättler et al. 2005), a non-hydrostatic atmospheric model used for operational weather forecast (e.g., at the German Weather Service, DWD) and for academic research. For the current investigation, the horizontal resolution was set to 0.025°, corresponding to approx. 2.8 km. This spatial resolution allows the explicit description of the processes associated with deep convection and no parameterization of this process was employed (Seifert et al. 2008). Initial and boundary conditions for these simulations were provided by a COSMO model simulation using a spatial resolution of 0.0625 (approx. 7 km), which was driven by analysis data from the global GME model. The high-resolution model simulations started on 3 June 2006 at 00 UTC.

The COSMO model includes numerous parameterizations to describe physical processes, like radiation, turbulence, and cloud microphysics. The results presented here were obtained using a single-moment bulk microphysics scheme that includes five classes of hydrometeors including graupel. Additional results obtained using a double-moment microphysics scheme (Seifert and Beheng 2006) with an updated description of rain evaporation (Seifert 2008) will be presented at the conference. Here, the results from the reference simulation will be shown. In Section 4, we introduce and compare results from sensitivity studies where the evaporation of rain was modified in the cloud microphysics.

3. MODEL RESULTS

In the following, we present results from model simulations designed to reproduce the situation on 3 June 2006.

Figure 2a presents the simulated hourly precipitation and the surface wind speed at 21 UTC on 3 June 2006. The location of the density current can easily be recognized by high wind speeds in SSE direction. The gust front was identified by vertical velocities larger than 3 m s^{-1} below 700 hPa. This dynamical feature only occurs along the gust front as can be seen in Figure 3. The vertical cross sec-

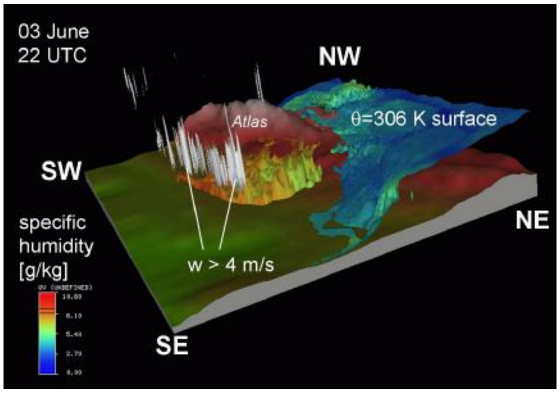

Figure 3: Three-dimensional structure of the cold pool as seen looking from SE towards NW. The simulated 306 K-isosurface of the potential temperature is shown at 3 June on 22 UTC on the topography. The color code represents specific humidity. White colors represent regions with a vertical velocity exceeding 4 m s^{-1}.

tion of the potential temperature, θ, (Fig. 2a) highlights the sharp and substantial horizontal gradient of θ in the lower troposphere (characteristic of a density current) between the background desert air ($\theta \approx$ 312 K) and the density current ($\theta \approx$ 306 K). The vertical extend of the density current is about 200 hPa, the wind speed near the gust front exceeds 20 m s^{-1}.

The three-dimensional structure of the density current is presented in Figure 3. Shown is the 306 K-isosurface of the potential temperature color-coded with the specific humidity. The cold air towards the north-east is associated with a synoptic-scale baroclinic zone, which is not directly related to the density current. However, such a synoptic situation with cold air mass advection favours the initiation of deep convection over the Atlas Mountains and, hence, the formation of density currents. Located SE of the Atlas the density current is clearly separated from the baroclinic zone. It is significantly moister (with specific humidities in the range of 7 – 10 g kg^{-1}) than the cold air towards the NE, because of the evaporation of rain drops that is a moisture source for the density current. The leading edge of the density current can be identified by enhanced vertical velocity, which results from the forced lifting of desert air by the propagating density current.

An evaluation of the model simulation with observations, e.g., from satellite and from ground based synoptic stations, will be presented at the conference. Overall, the model is able to satisfactorily simulate the occurrence, the propagation, and the characteristic features of this density current. In the following, we present model results to evaluate the impact of the description of evaporation of rain on the density current.

4. IMPACT OF EVAPORATION OF RAIN ON THE DENSITY CURRENT

Evaporation of sedimenting hydrometeors drives the formation and the propagation of density currents. In bulk microphysical schemes evaporation of rain is highly parameterized. Especially the choice of an appropriate droplet size distribution is crucial for the parameterization of evaporation. Typically, an exponential distribution, such as the Marshall-Palmer distribution, is assumed for rain drops. A more general expression is the gamma distribution given by

$$N(D) = N_0 \, D^{\mu} \, \exp(-\lambda D) \qquad (1)$$

Here, $N(D)$ is the drop size distribution, D is the drop diameter, N_0 the intercept parameter, λ the slope, and μ the shape parameter. In single-moment microphysical schemes, N_0 and μ are set constant and the slope parameter, λ, is a unique function of the rain water mixing ratio. With some additional assumptions, the evaporation rate can then be calculated from the rain water mixing ratio.

In the following we evaluate the impact of the choice of the shape parameter, μ, in a single-moment microphysical scheme on the evaporation and evolution of the density current. In the standard version of the COSMO model microphysics, a value of 0.5 is used for the shape parameter. The intercept parameter N_0 is parameterized as a function of μ using Eq. (27) of Ulbrich (1983), see also Schlesinger et al. (1988) who suggest $\mu \cong 0.4$ as best estimate based on radar observations of evaporation of rain. Here, we present results from model simulations using values of

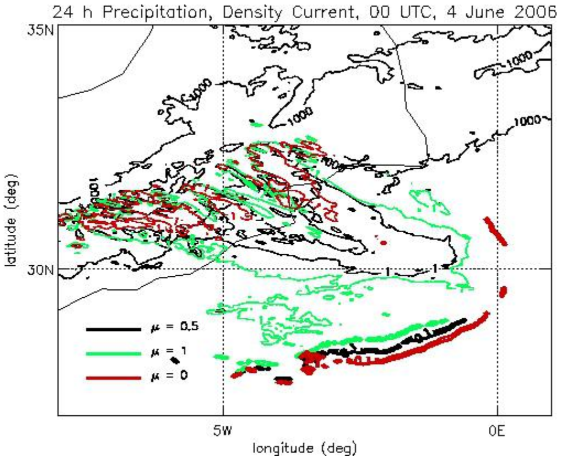

Figure 4: Simulated 24-h precipitation (thin lines mark the 1 mm-isolines) and location of the density current (thick lines) at 00 UTC on 4 June 2006 for three simulations employing different value for the shape parameter μ (see text for details).

zero (corresponding to a Marshall-Palmer distribution) and unity for the shape parameter.

Figure 4 presents results from the reference and the sensitivity simulations. Shown is the 24 h-precipitation sum and the location of the density current leading edge at 00 UTC on 4 June 2006. In all simulations, the precipitation is realistically initiated along the crest of the Atlas Mountains. The impact of the shape parameter on the simulated surface precipitation is huge. A small value for μ results in enhanced evaporation of rain drops and reduced surface precipitation. While a shape parameter of zero results in nearly no precipitation in the Algerian Sahara (thin red line in Fig. 4), setting the shape parameter to unity the band of precipitation stretches well into the desert region (thin green line in Fig. 4).

The location of the leading edge of the density current is also affected by the choice of the shape parameter. Enhanced evaporation (by reducing the shape parameter) results in an intensification of the density current. This can be seen in Fig. 4 by comparing the locations of the density current in the three simulations (thick lines). In the case of high evaporation (μ = 0, red line) the density current has propagated substantially faster than in the simulations with lower evaporation (compare the locations at 00 UTC in Fig. 4). Also the length of the gust front and the maximum wind speed is higher in this case.

Overall, there is a substantial impact of evaporation of rain on surface precipiation, while the impact on the density current can be considered moderate. This is consistent with the square-root dependency of the propagation speed of density currents on the horizontal gradient of the potential temperature (e.g., Weisman and Rotunno (2004)).

5. CONCLUSIONS

Density currents initiated by evaporation of hydrometeors in dry and hot desert environments have the potential to mobilize large amounts of dust. During spring and early summer, deep convection is regularly initiated along the crest of the Altas Mountains in Marocco resulting in the formation of density currents that propagate into the Saharan desert. Here, high resolution model simulations of such an event in June 2006 were presented. The COSMO model is able to realistically reproduce the initiation of convection, and the formation and propagation of the density current into the desert region. It was shown that the evaporation of rain drops has a substantial impact on the simulated surface precipitation and the density current. We conclude that high-resolution numerical models are capable of realistically reproducing convectively-induced density currents. The north-western African Saharan region is especially well suited for such investigation, since synoptic scale conditions (e.g., cold air advection), which are typically well represented in weather forecast models, determine the initiation of convection along the Atlas Mountains. The evaluation of the model simulations would benefit from ground observations (e.g., surface precipitation, synop stations) in the Algerian Sahara.

6. ACKNOWLEDGMENTS

J.T. thanks the DWD for providing and supporting the use of the COSMO model.

We acknowledge Bodo Ritter and Van Tan Nguyen (DWD) for providing the external parameters used in the model simulations. We thank EUMETSAT for providing the satellite image. P.K. is funded through the DFG Emmy Noether program (grant KN 581/2-3).

References

Knippertz, P., C. Deutscher, K. Kandler, T. Müller, O. Schulz, and L. Schütz, 2007: Dust mobilization due to density currents in the Atlas region: Observations from the Saharan Mineral Dust Experiment 2006 field campaign. *J. Geophys. Res.*, **112**, doi:10.1029/2007JD008774.

Schättler, U., G. Doms, and C. Schraff, 2005: A description of the nonhydrostatic regional model LM, Part VII: User's Guide. Technical report, Consortium for Small-Scale Modelling.

Schlesinger, M. E., J.-H. Oh, and D. Rosenfeld, 1988: A parameterization of the evaporation of rainfall. *Mon. Weath. Rev.*, **116**, 1887–1895.

Seifert, A.: 2008, On the parameterization of evaporation of raindrops below cloud base. *Proc. 15th Int. Conf. Clouds and Precip.*, Cancun, Mexico.

Seifert, A., M. Baldauf, K. Stephan, U. Blahak, and K. Beheng: 2008, The challenge of convective-scale quantitative precipitation forecasting. *Proc. 15th Int. Conf. Clouds and Precip.*, Cancun, Mexico.

Seifert, A. and K. D. Beheng, 2006: A two-moment cloud microphysics parameterization for mixed-phase clouds. Part 1: Model description. *Meteorol. Atmos. Phys.*, **92**, 45–66, doi:10.1007/s00703-005-0112-4.

Simpson, J., 2000: *Gravity Currents in the Environment and the Laboratory*. Halsted, Chichester, U.K.

Steppeler, J., G. Doms, U. Schättler, H. W. Bitzera, A. Gassmann, U. Damrath, and G. Gregoric, 2003: Meso-gamma scale forecasts using the nonhydrostatic model LM. *Meteorol. Atmos. Phys.*, **82**, 75–96.

Ulbrich, C. W., 1983: Natural variations in the analytical form of the raindrop size distribution. *J. Climate and Appl. Meteorol.*, **22**, 1764–1775.

Weisman, M. and R. Rotunno, 2004: ”A Theory for Strong Long-Lived Squall Lines” revisited. *J. Atmos. Sci.*, **61**, 361–382.

CONVECTIVE CLOUD MICROPHYSICS IN A HIGH-RESOLUTION NWP MODEL

J. Trentmann[1], A. Seifert[2], H. Wernli[1]

[1]Institute for Atmospheric Physics, Johannes Gutenberg
University Mainz, Germany
[2]German Weather Service, Offenbach, Germany

1. INTRODUCTION

Forecasting convective precipitation remains a challenge for numerical weather prediction. In April 2007 a convection-permitting version of the COSMO (Consortium for Small Scale Modeling) model has become operational at the German Weather Service, DWD – COSMO-DE. This model operates with a horizontal grid point distance of 0.025° ($\approx$2.8 km) and resolves the dominant spatial scales involved in deep convection. No parameterization of deep convection is employed. Such a model setup allows to evaluate and to investigate the description of cloud microphysical processes within deep convective clouds under realistic conditions, e.g., without the application of an artificial trigger mechanism for convection.

Here, we present model simulations for a case of localized deep convection that occurred on 12 July 2006 in South-West Germany.

2. OBSERVATIONS

Summertime precipitation in the low-mountainous region in South-West Germany is dominated by convective precipitation. On 12 July 2006, under weak synoptic-scale forcing, several convective cells formed in the early afternoon in mountainous regions across Europe including the Black Forest in South-West Germany (Fig. 1). While the Rhine-Valley remained free of convective activity, different stages of convective clouds can be identified over the German (Black Forest and Swabian Alb) and the French (Vosgue) low mountain ranges. The convective cell in the Northern Black Forest (marked by the yellow square) is in its active, growing phase. Its top has already reached the level of neutral buoyancy (i.e, the tropopause) and ice has formed in the anvil. In the southern Black Forest, a mature convective cloud is present with a huge ice anvil, while along the Swabian Alb (towards the NE) mainly shallow convection prevails. The mixture of different stages of cloud developments highlights the high spatial and temporal variability of convective clouds under weak synoptic forcing. Here we focus on the convective cell that formed around local noon in the Northern Black Forest.

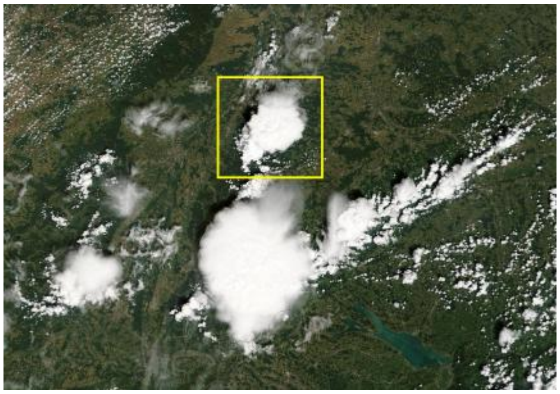

Figure 1: Visible image derived from MODIS at 1030 UTC, 12 July 2006, the yellow rectangle marks the convective cell of interest.

The precipitation field derived from gauge-

---

[1] Corresponding author's address: Jörg Trentmann, Institute for Atmospheric Physics, Johannes Gutenberg University Mainz, Becherweg 21, 55099 Mainz, Germany, jtrent@uni-mainz.de

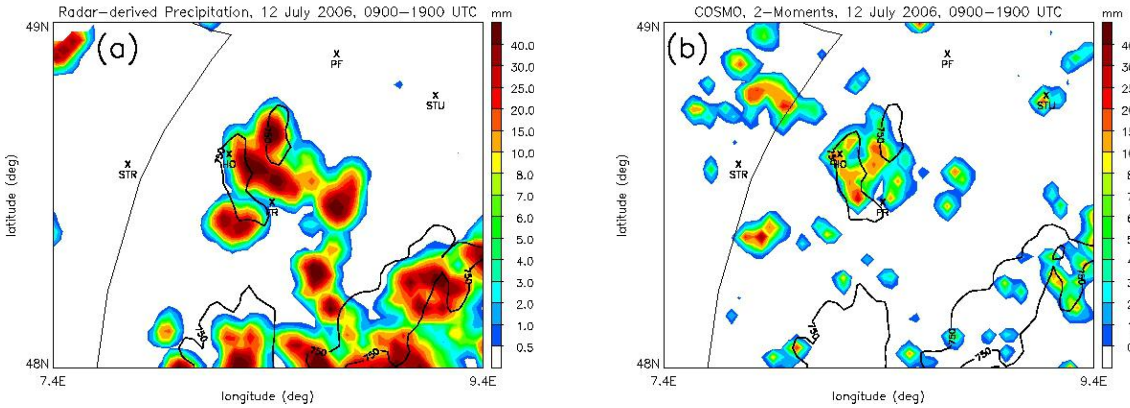

Figure 2: (a) Gauge-adjusted radar-derived precipitation between 9 and 19 UTC on 12 July 2006 provided by DWD; (b) model simulated precipitation between 9 and 19 UTC, 12 July 2006, thick black contour lines mark the topography, the thin black contour line marks the German-French border.

adjusted radar measurements between 09 and 19 UTC shows an area of convective precipitation in the Murg Valley north of Freudenstadt (8.42 °E, 48.47 °N) with a maximum precipitation amount of 58 mm within 10 hrs (Figure 2a). Ground-based wind-LIDAR measurements (not shown) obtained at Hornisgrinde (1177 m asl, the highest peak in the Northern Black Forest) revealed that horizontal wind convergence along the mountain crest, presumably due to thermally-induced mountain wind systems, was responsible for the initiation of these convective cells. Afternoon values of CAPE derived from radiosoundings exceeded $2000\,\mathrm{J\,kg^{-1}}$. Further information on the experimental results obtained within the PRINCE (Prediction, identification, and tracking of convective cells) field experiment can be found in Groenemeijer et al. (2008).

3. MODEL SIMULATIONS

Model simulations were conducted using the COSMO model (Steppeler et al. 2003; Schättler et al. 2005), an atmospheric model used for operational weather forecast and for academic research. For the current investigation, the horizontal resolution was set to 0.025°, corresponding to approx. 2.8 km. This spatial resolution allows the explicit description of the processes associated with deep convection and no parameterization of deep convection was employed (Seifert et al. 2008). Initial and boundary conditions for these simulations were provided by hourly COSMO-EU analysis with a spatial resolution of 0.0625° (approx. 7 km). The simulations were started on 12 July 2006 at 07 UTC. In the standard operational COSMO model setup, cloud microphysics is parameterized using a one-moment bulk microphysical scheme. Here, we will present results from simulations that employ a two-moment microphysical scheme that predicts the mass and the number concentrations of six classes of hydrometeors, including hail (Seifert and Beheng 2006; Blahak 2008). Nucleation of cloud droplets is parameterized using the method from Segal and Khain (2006); evaporation of rain drops is considered using the parameterization of Seifert (2008).

In the following we present results from model simulations designed to reproduce the situation on 12 July 2006.

3.1 Surface Precipitation

Figure 2b shows the simulated precipitation accumulated between 9 and 19 UTC on 12 July 2006 that can be compare to the radar-derived precipitation field presented in Figure 2a. The location and the amount of precipitation is satisfactorily captured by the model simulation. In the model the

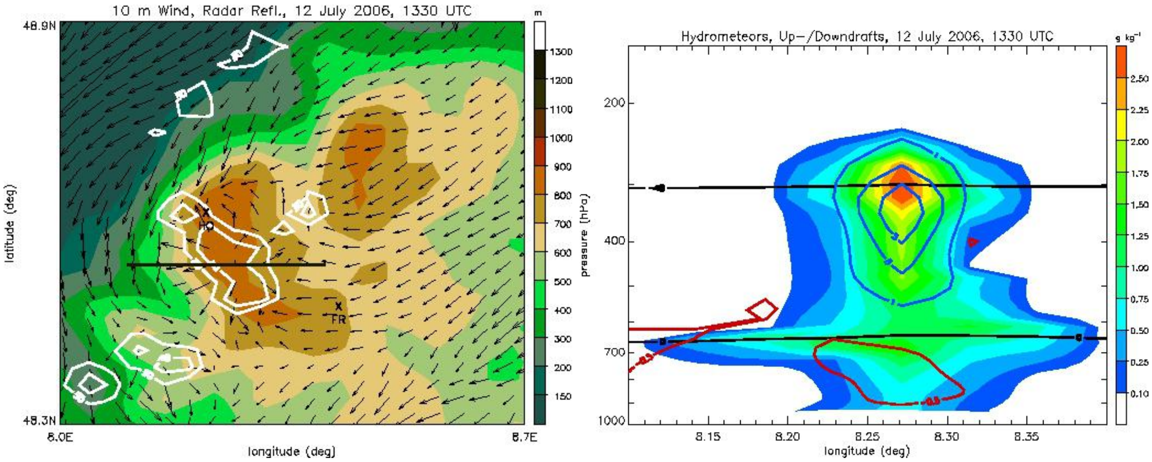

Figure 3: Visualisation of the model results for 1330 UTC on 12 July 2006. (a) The color coding represents the topography. White contour lines correspond to the 30- and 40-dbz isoline of the vertical maximum radar refelctivity derived from the model simulation. Black arrows represent the 10-m wind. The black line indicates the location of the cross section shown in Figure 3b. (b) Mass concentration of hydrometeors along the cross section depicted by the black line in Figure 3a. Blue contour lines represent positive vertical velocity (updraft), red contour lines correspond to negative vertical velocity (downdraft). Black contour lines correspond to the 0- and 40-°C isoline.

precipitation is also tied to the Murg valley in the Northern Black Forest suggesting that the process leading to the initiation of the convective cell is realistically described in the model simulation. The amount of precipitation is underestimated compared to the radar-derived precipitation (The simulated maximum precipitation is 30 mm.), however, the quantification of surface precipitation from radar observations is also associated with some uncertainty. An analysis of the diurnal precipitation cycle (not shown) reveals that the simulated precipitation is delayed compared to the radar observations by about 2 hrs. Overall, the good comparison between the observed and the simulated accumulated precipitation fields allows an investigation of the microphysical processes that are responsible for the formation of precipitation in the model simulations.

3.2 Cloud Microphysics

In the following we will present a more detailed view into the model results from the simulation presented in Section 3.1 focussing on the hydrometeors in the convective cloud.

Figure 3a presents the vertical maximum of the simulated radar reflectivity and the 10-wind field at 1330 UTC. The main convective activity is along the mountain crest of the Black Forest. The high spatial resolution allows to explicitly resolve the dynamical processes associated with the convective cell. The impact of the convective scale dynamics, e.g., downdrafts, cold air outflow, on the 10-m wind field is clearly visible. In Figure 3b a vertical cross section through the convective cloud along the black line depicted in Figure 3a is shown. The convection reaches the local tropopause at about 200 hPa. The updraft speed in this convective cell exceeds $9\,\mathrm{m\,s^{-1}}$, the water/ice mass mixing ratio reaches up to $5.5\,\mathrm{g\,kg^{-1}}$, and the downdraft exceeds $-5\,\mathrm{m\,s^{-1}}$. The main low level inflow region into this convective cell is slightly further towards the SE and not depicted in this cross section (see Figure 3a).

Figure 4 shows the simulated number concentration of hydrometeors by the two-moment scheme along the cross section indicated by the black line in Figure 3a. Also indicated are the regions with mainly liquid, with mainly frozen, and with a mixture of frozen and liquid hydrometeor mass. Significant parts of the cloud, mainly associated

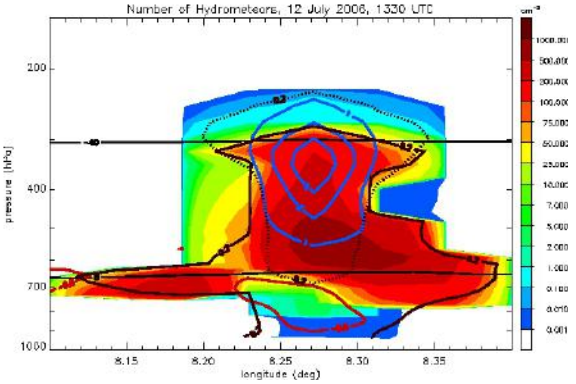

Figure 4: Simulated total number concentration of hydrometeors along the cross section depicted by the black line in Figure 3a. Note the huge range of the color colding, from 0.001 cm^{-3} (= 1 l^{-1}) to 1000 cm^{-3}. The solid black contour shows the 0.2-g kg^{-1} isoline of liquid hydrometeors, the dotted black contour represents the 0.2-g kg^{-1} isoline of frozen hydrometeors. Blue contour lines represent positive vertical velocity (updraft), red contour lines correspond to negative vertical velocity (downdraft). Black contour lines correspond to the 0- and 40-°C isoline.

with the updraft, involve a mixed phase between liquid and frozen hydrometeors. The hydrometeor number concentration in the cloud is extremely variable, ranging from 0.001 cm^{-3} to more than 1000 cm^{-3}. The precipitating downdraft region exhibits the lowest number concentration associated with large rain droplets (compare with the mass concentration in Figure 3b). Overall the number and the mass concentration of hydrometeors in the convective cloud are very realistic suggesting that the COSMO model with the two-moment microphysical scheme allows an in-depth investigation of microphysical processes in convective clouds.

4. SUMMARY AND CONCLUSIONS

We presented results from a model simulation using the COSMO model with a sophisticated two-moment cloud microphysical scheme. The model is used with a spatial resolution of about 2.8 km without a parameterization of deep convection and is driven by analysis data. No artificial initiation of convection is employed.

Model results were presented for the situation on 12 July 2006 when local convection occurred along mountainous regions in Central Europe. Focus was given to the convective cloud that formed in the Northern Black Forest in South-West Germany. The model reproduces the initiation and the lifecylce of the convection, but underestimates the surface precipitation compared to radar data. The dynamical processes (updraft, downdraft, outflow) in the cloud seem to be realistically described by the model. A significant fraction of the convective clouds is composed of a mixture between liquid and frozen hydrometeors with maximum total number concentration exceeding 1000 cm^{-3}. Surface precipitation is composed of large rain droplets with a number concentration in the order of 0.01 cm^{-3} (corresponding to 10 l^{-1}). Overall, the COSMO model with the two-moment cloud microphysics scheme allow detailed investigations of convective clouds and their microphysical processes.

5. ACKNOWLEDGMENTS

J.T. thanks the DWD for providing and supporting the use of the COSMO model.

References

Blahak, U.: 2008, Towards a better representation of high density ice particles in a state-of-the-art two-moment bulk microphysical scheme. *Proc. 15th Int. Conf. Clouds and Precip.*, Cancun, Mexico.

Groenemeijer, P., C. Barthlott, A. Behrendt, U. Corsmeier, J. Handwerker, , M. Kohler, C. Kottmeier, H. Mahlke, S. Pal, M. Radlach, J. Trentmann, A. Wieser, and V. Wulfmeyer: 2008, Multisensor measurements of a convective storm cluster over a low mountain range: Adaptive observations during PRINCE, submitted to *Mon. Wea. Rev.*

Schättler, U., G. Doms, and C. Schraff, 2005: A description of the nonhydrostatic regional model LM, Part VII: User's Guide. Technical report, Consortium for Small-Scale Modelling.

Segal, Y. and A. Khain, 2006: Dependence of droplet concentration on aerosol conditions in different cloud types: Application to droplet concentration parameterization of aerosol conditions. *J. Geophys. Res.*, **111**, doi:10.1029/2005JD006561.

Seifert, A.: 2008, On the parameterization of evaporation of raindrops below cloud base. *Proc. 15th Int. Conf. Clouds and Precip.*, Cancun, Mexico.

Seifert, A., M. Baldauf, K. Stephan, U. Blahak, and K. Beheng: 2008, The challenge of convective-scale quantitative precipitation forecasting. *Proc. 15th Int. Conf. Clouds and Precip.*, Cancun, Mexico.

Seifert, A. and K. D. Beheng, 2006: A two-moment cloud microphysics parameterization for mixed-phase clouds. Part 1: Model description. *Meteorol. Atmos. Phys.*, **92**, 45–66, doi:10.1007/s00703-005-0112-4.

Steppeler, J., G. Doms, U. Schättler, H. W. Bitzera, A. Gassmann, U. Damrath, and G. Gregoric, 2003: Meso-gamma scale forecasts using the nonhydrostatic model LM. *Meteorol. Atmos. Phys.*, **82**, 75–96.

A MODELING STUDY OF THE RELATIONSHIP BETWEEN ELECTRIFICATION AND MICROPHYSICS IN A TYPICAL THUNDERSTORM

Tuanjie Hou, Hengchi Lei

Institute of Atmospheric Physics, Chinese Academy of Sciences, Beijing, China 100029

1. INTRODUCTION

Some numerical models with charging parameterizations have been used to study charges accumulation in thunderstorms. However, a large-than-usual lower positive charge center exists in the thunderstorm of the Tibetan Plateau in China, which has been revealed by the research of Qie et al. (2005). But they were concerned more about lightning characteristics and less about microphysical processes. Hence, the goal of present work is to use a three-dimensional hailstorm model including inductive and noninductive charging mechanisms to investigate the relationship between electrification and microphysics.

2. THE NUMERICAL MODEL

The model used is the three-dimensional compressible hailstorm numerical model of the Institute of Atmospheric Physics, Chinese Academy of Sciences. It contains eight classes of hydrometeors. Microphysical processes are described in mass mixing ratio and number concentration. The noninductive charging mechanism is based on the experimental studies of Saunders et al. (1991) and Brooks et al. (1997), with charge separation between ice (snow) and graupel (frozen drops or hail). Discharge parameterization is considered at some grid points when the electric field magnitude exceeds a threshold. As systematic measurements of lightning characteristics were conducted in thunderstorms of the Tibetan Plateau, a typical thunderstorm in that area was simulated using the model.

3. RESULTS

3.1 The sounding and cloud scale characteristics

Field measurements of thunderstorms and lightning characteristics were conducted in Qinghai province, China in 2002(Zhang et.al., 2007). According to field observation, lightning flashes occurred between 0800UTC and 0928UTC. Therefore, simulation was initiated based on the sounding in Xingning at 0000UTC. The simulation is considered as idealized cloud modeling of an isolated cumulus cloud.

The temperature, dew point and environmental wind profiles of the sounding is shown in Fig.1.

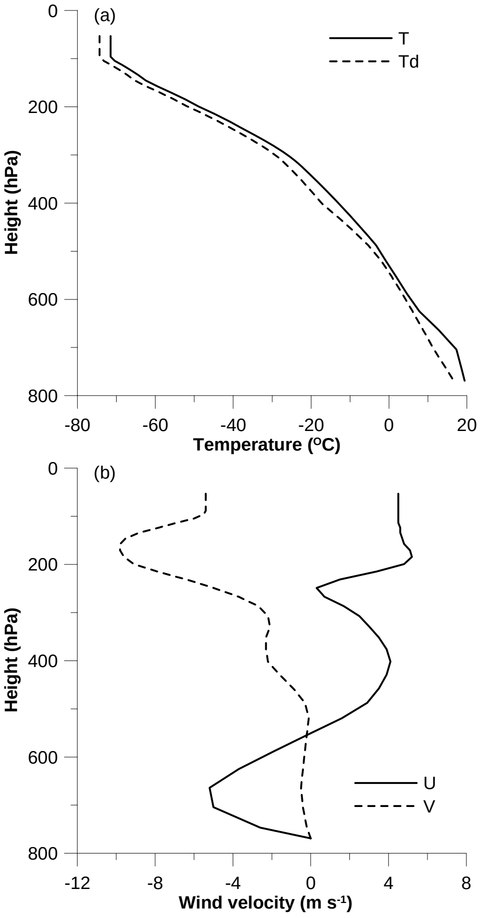

Fig. 1: The temperature, humidity, and wind sounding

The relative humidity near the surface is quite high, especially at the level between 500 hPa and 600 hPa, reaching over 90%. Form Fig.1(b) we can see that it is cold advection at the height of 550 hPa, as wind blew backing from the direction of northeasterly to northwesterly.

Total mixing ratios at 15 min and 23 min are shown in Fig.2. Affected by strong wind shear, the cloud dips towards east. At 15 min, the height of cloud base is only 1.5 km, at the temperature of 12℃, which is warm cloud base. And the maximum total mixing ratio is about 3.0 g m^{-3}, which is at 4.0 km. Rain started to fell to the surface at 23 min. At 24 min, the maximum total mixing ratio reaches over 4.0 g m^{-3}, only at the height of 0℃, as the level of the maximum updraft velocity is not very high.

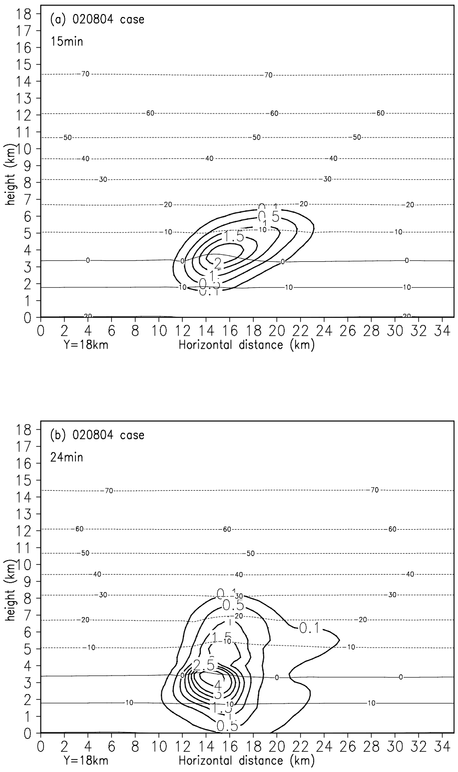

Fig. 2: Distributions of total mixing ratio (units: kg m^{-3}) at 15 min and 24 min

3.2 Total charge structure and main charge carriers

The charge separation starts at the center of liquid water content (LWC) after 12 min of integration. At the stage, charges are separated mainly by the non-inductive rebounding collisions between graupel and cloud ice at the height of below -10℃.

At 15 min, a small weak positive charge region forms at the -5℃ level. Later, the charging region moves upward. But due to slow upward development of updraft velocities, the main charging region is still around -10℃ before rain felling to surface. By 21 min, an inverted dipolar structure with the maximum charge density of -1 nC m^{-3} and 0.2 nC m^{-3} has been produced (Fig. 3a). And the lower positive charge carrier is graupel (Fig. 3b).

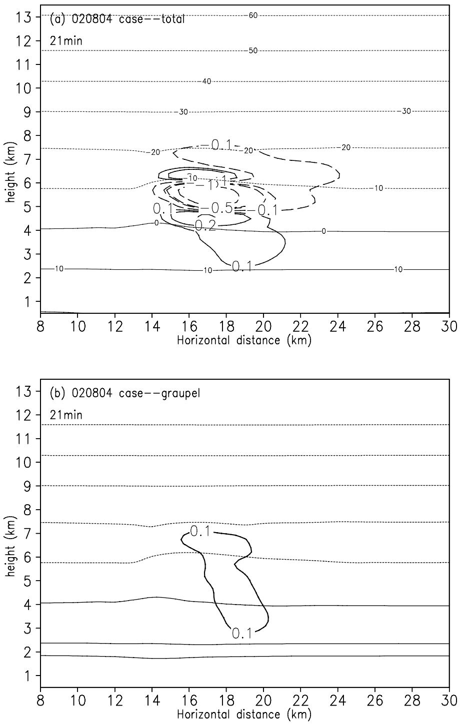

Fig. 3: Contours of total charge density

(units: nC m^{-3}) and charge density on graupel in the X-Z plane while Y=18 km, at 21 min. Solid contours represent positive values, and dashed contours show negative values. The horizontal lines are isotherms (units: ℃).

By 30 min, the cloud have developed a tripole, with a large vertically extended lower positive charge region. At that time, the lower positive charge carriers are frozen drops falling or melting from higher level, while the main charge carriers of upper negative charge region are positively charged cloud ice and negatively charged graupel.

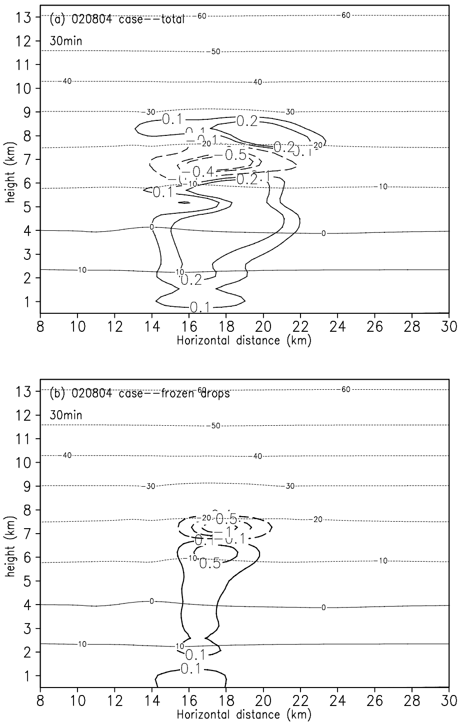

Fig. 4: Contours of total charge density (units: nC m^{-3}) and charge density on frozen drops in the X-Z plane while Y=18 km, at 30 min.

At 35 min, the charge structure is a dipole. And the lower positive charge region gradually disappears with precipitation.

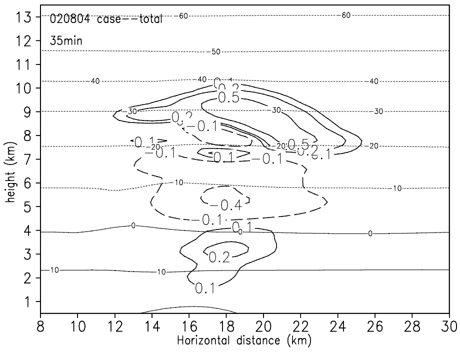

Fig. 5: Contours of total charge density (units: nC m^{-3}) in the X-Z plane while Y=18 km, at 35 min.

3.3 Frozen drops, graupel and lower positive charge region

Apart from non-inductive charging rate itself, transportive forcing including airflow and terminal velocity also plays a role to the distribution of charges. From Fig. 6, we can see that supercooled raindrops are formed at 12 min, reaching the maximum value of 2.6 g m^{-3} at 18 min. After that, the maximum mixing ratio of supercooled raindrops starts to decrease due to higher location of updraft core and transformation of supercooled raindrops to other ice particles. For the case in the present study, the amount of graupel is obviously larger than that of frozen drops.

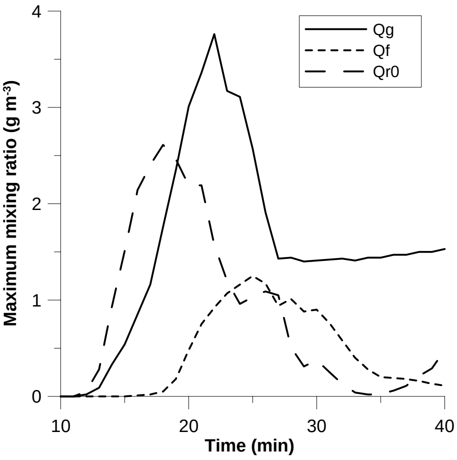

Fig. 6: Evolution of the maximum mixing ratio of graupel (Qg), frozen drops (Qf) and supecooled rain drops (Qr0)

To have insights into the role of transportive forcing, the evolution of the vertical transport of graupel and frozen drops at different levels are presented in Fig. 7. The absolute value of vertical transports increase with height for both graupel and frozen drops, but have different charge signs. For graupel, the value is negative as positively charged graupel fell to the surface at first and later negatively charged graupel sedimented from higher level. But for frozen drops, the transport mainly results from sedimentation of positively charged frozen drops at higher level.

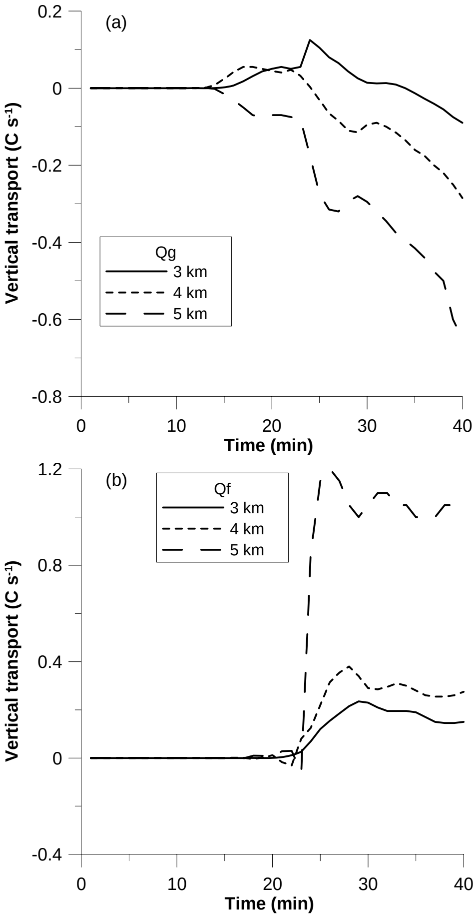

Fig. 7: Evolution of the vertical transport (units: C s^{-1}) of graupel and frozen drops at various levels

4 CONCLUSION

The numerical results show that an inverted dipole is produced at the initial stage of electrification. Later, a tripolar structure with a large lower positive charge region is formed and the lower charge region gradually becomes smaller with the falling of precipitation particles. On the whole, the lasting of lower positive charge center is greatly dependent on the sedimentation of positively charged graupel and frozen drops at the higher level, while the influence of them depends on the amount of supercooled raindrops, cloud base temperature and the core of maximum updraft velocity.

ACKNOWLEGEMENTS

The authors are grateful to WMO, IUGG, IAMAS and ICCP for providing financial support. Support was also provided by the National Natural Science Foundation of China (Grant No. 40537034).

REFERENCES

Brooks, I. M., C. P. R. Saunders, R. P. Mitzeva, and S. L. Peck, 1997.The effect on thunderstorm charging of the rate of rime accretion by graupel, J. Atmos. Res., 43, 277-295

Qie, X. S., Zhang, T. L., Chen, H. B., Zhang, G. S., 2005. The lower positive charge center and its effects on lightning discharges on the Tibetan Plateau. Geophys. Res. Lett. 32, L05814, doi: 10.1029/2004GL022162

Saunders C P R. , Keith W D , Mizeva R P., 1991. The effect of liquid water on thunderstorm charging. J .Geophys .Res . , 96 :11007-11017

Zhang, T. L., Qie, X. S., Yuan, T., et al., 2007. The charge structure of a typical thunderstorm in Chinese inland plateau. Proc.13th.Int. Conf. on Atmos. Electricity, Beijing, China, 194-197

Potential cloud formation over heterogeneous land surfaces

Chiel C. van Heerwaarden and Jordi Vilà-Guerau de Arellano
Meteorology and Air Quality Section, Wageningen University, The Netherlands
e-mail: chiel.vanheerwaarden@wur.nl

1. Introduction [1]

Convective cloud formation over land is a complex phenomenon due to the strong interaction between the land surface and the atmospheric boundary layer (ABL) (Kang et al., 2007). Previous studies (e.g. Ek and Mahrt, 1994; Ek and Holtslag, 2004) described the underlying physics of these interactions over homogeneous land surfaces. However, it has been suggested (e.g. Crook, 1997; Pielke, 2001; Kang et al., 2007) that the timing and location of cloud formation are sensitive to heterogeneous forcings at the land surface, which depend on the spatial variability of land use, soil moisture content and topography.

Heterogeneous forcings occur over a wide range of scale levels, but the strongest effects on ABL properties are found when the heterogeneities are in the meso-γ scale (2-20 km) (Mahrt, 2000), since they modify the horizontal and vertical structure of the ABL by inducing circulations. A consequence is that the effects of heterogeneity-induced circulations are difficult to be represented well by mesoscale and large-scale models, as these flows are mostly in the subgrid scales of the models. To date we lack adequate parameterizations, because the effects of circulations on cloud formation in the meso-γ scale are not fully understood.

By using an LES model, we studied the spatial distribution of entrainment and compared the total entrainment for cases with varying heterogeneity amplitudes and inversion strengths for potential temperature and specific humidity. By applying a statistical decomposition between turbulent and mesoscale components, we investigate the contribution of the heterogeneity-induced circulation to entrainment. Later, we connect our findings about the ABL height and entrainment processes to the thermodynamic changes in the ABL by studying the specific humidity and the RH. We analyzed the spatial structure of temperature, moisture and RH near the top of the ABL for different heterogeneity amplitudes and inversion strengths of potential temperature and specific humidity. Vertical profiles of the RH and the variances of potential temperature and specific humidity were analyzed in order to study the modification of the horizontally averaged profiles by heterogeneous forcings.

2. Numerical methods

2.1 *Model description*

The study is based on numerical experiments performed using the Dutch Atmospheric LES (DALES) model, which was initially developed by Nieuwstadt and Brost (1986), improved by Cuijpers and Duynkerke (1993) and updated to a parallel-processing version by Dosio et al. (2005). DALES solves the filtered Navier-Stokes equations with the Boussinesq approximation applied.

DALES has periodic boundary conditions in the horizontal plane. At the land surface the surface fluxes for heat $\overline{w'\theta'}$ and moisture $\overline{w'q'}$ and the friction velocity u_* are prescribed. There is a sponge layer in the top of the model, which prevents the reflection of gravity waves back into the model domain.

2.2 *Experimental setup*

For this study we discretized our LES-domain into 256 x 192 x 192 grid cells on the x, y and z axes. The grid length is 25 m in x and y and 12.5 m in z and our domain is thus 6400 x 4800 x 2400 m. All cases are dry convective boundary layers with prescribed surface heat fluxes. There is no background wind ($U_g = V_g = 0$ m s^{-1}) and the friction velocity u_* is fixed at 0 m s^{-1} i.e. free local convection. The initial profiles and surface forcings correspond to the temperature and moisture conditions of a typical early summer day in The Netherlands. All simulations have an initial potential temperature profile that is constant with height for the first 800 m. On top of this layer we prescribe a temperature jump (case dependent) and after this jump the stratified free atmosphere has a temperature lapse rate equal to 0.006 K m^{-1}. The initial specific humidity profile in the mixed layer is constant with height (0.005 kg kg^{-1}), with a jump on top of the mixed layer and a constant value in the free atmosphere (case dependent). The selected value for the potential temperature jump ($\Delta\theta$) determines the growth rate of the ABL. In case of a small jump, the ABL grows fast and and due to the pressure decrease at the top, the ABL top cools in terms of absolute temperature, which has a positive effect on the RH$_{zi}$. On the other hand, if the jump is small, a large amount of free atmospheric air enters the ABL. For this air the specific humidity jump (Δq) determines the dryness and thus in what extent the cooling can be compensated by drying.

In order to create heterogeneous forcings, the land surface is divided in two parts along the x-axis. All grid cells in the left patch (cells 1 to 128) are characterized by a Bowen ratio below the average Bowen ratio (the cold patch) and the cells in the right patch (grid cell 129 to 256) have an above average Bowen ratio (the warm patch). The length of the heterogeneity (one cycle of a cold and a warm patch) is therefore 6400 m. As the ABL heights vary between 1000 and 1100 m, the ratio between the heterogeneity length and the ABL height is in the range that AV98 and PA05 specify for the strongest mesoscale contribution to the flow.

---

[1] This abstract is a summary of Van Heerwaarden and Vilà-Guerau de Arellano (2008). Further details can be found in this manuscript.

Table 1: Initial conditions for all LES simulations. θ_{ML} is the initial mixed layer potential temperature, $\Delta\theta$ is the temperature jump at 800 m, Δq is the temperature jump at 800 m.

simulation	θ_{ML} [K]	$\Delta\theta$ [K]	Δq [kg kg^{-1}]
$Case1$	293.0	2.0	0.000
$Case2$	293.0	2.0	0.000
$Case3$	293.0	2.0	0.000
$Case4$	293.0	2.0	0.000
$Case5$	293.0	2.0	0.000
$Weak1$	294.5	0.5	0.000
$Weak5$	294.5	0.5	0.000
$Case1dry$	293.0	2.0	-0.004
$Case5dry$	293.0	2.0	-0.004
$Weak1dry$	294.5	0.5	-0.004
$Weak5dry$	294.5	0.5	-0.004
$Case1large$	293.0	2.0	0.000
$Case5large$	293.0	2.0	0.000

We performed a sensitivity analysis on the heterogeneity amplitude, which is defined as the Bowen ratio difference between the cold and the warm patches. In all cases, for every location at the land surface, the sensible H and latent LE heat flux add up to 360 W m^{-2}, but the Bowen ratios for the cold and the warm patch differ among the simulations (see Table 2). For the three other regimes we simulated the homogeneous and the largest amplitude case.

All cases were initially integrated for three hours. After three hours of spin-up, the three components of the wind, the potential temperature and specific humidity were recorded for each grid cell every five seconds for one hour. The statistics are thus based on 720 time steps.

2.3 *Statistical methods*

To calculate the turbulent statistics of our model runs we used a method based on phase averaging (Hussain and Reynolds, 1970). A similar method was previously employed in the LES study of heterogeneous land surfaces by PA05. Our model forcings are heterogeneous only on the x-axis and thus homogeneous on the y-axis. Therefore, we assume that a local spatial average can be calculated by averaging over y. We decompose an arbitrary space- and time-dependent turbulent variable $\phi_{x,y,z,t}$ in two components.

$$\phi_{x,y,z,t} = \langle\phi\rangle_{x,z,t} + \phi'_{x,y,z,t} \qquad (1)$$

We name the first term on the right hand side the local average, which is the spatial average of all values on the y-axis that share the same x, z and t-coordinates. Under homogeneous conditions $\langle\phi\rangle_{x,z,t}$ equals the slab average as there are no variations in local spatial averages in a horizontal plane. The difference between the local average and the slab average is thus a measure of advection and therefore of the contribution of the heterogeneous surface forcings to the statistics. This contribution we call the meso scale component from now on. The turbulent fluctuation $\phi'_{x,y,z,t}$ is the second term. In the further analyses we denote spatial averages in the y-direction as $\langle\phi\rangle$ and in the x-direction as $[\phi]$. Temporal averages are denoted as $\overline{\phi}$.

3. Results

3.1 *Entrainment processes and ABL growth*

3.1.1 STRUCTURE OF THE ABL TOP AND ENTRAINMENT

Our first objective was to study the influence of the heterogeneity amplitude on entrainment processes and on the evolution of the ABL height. Figure 1 shows the 1-h averaged ABL height as a function of space along the x-axis. The heights are derived using the maximum potential temperature gradient following the procedure in Sullivan et al. (1998). For every x, y-coordinate the ABL height is calculated for each time step and these values are averaged over y and time. The values in the figure are scaled by the horizontally averaged ABL height.

Figure 1 shows that the presence of horizontal variability in the surface forcings results in a spatial variability of the ABL height z_i along the heterogeneity. The homogeneous case ($Case1$) has an ABL height that is $z/z_i = 1.0$ with small fluctuations around this value, whereas in all heterogeneous cases a clear spatial pattern is visible, with a deeper boundary layer over the warm patch. Therefore, we corroborate the earlier findings of AV98 and PA05 who showed ABL height variations for different heterogeneity lengths.

Slight variations in this pattern are visible, caused by differences in the heterogeneity amplitude. For instance, above the warm patch (x/λ = 0.5), there is an increase in ABL height related to the larger heterogeneity amplitude. $Case2$ has a height that is 4 per cent larger than the average ABL height ($z/z_i = 1.04$), whereas $Case5$ attains values up to 5 per cent larger ($z/z_i = 1.05$) than the average. Over the cold patch, the opposite effect is visible, with a decreasing ABL height for increasing heterogeneity amplitude. In spite of the small variations caused by the heterogeneity amplitude, the main variations in ABL height are due solely to the presence of a heterogeneity-induced circulation. For cases with weak inversions (not shown), we found for $Case5dry$ the same relative increase over the warm patch ($z/z_i = 1.05$).

Figure 2 shows the spatial distribution of entrainment and contains the cross sections of the 1-h averaged values of the normalized turbulent heat flux $\overline{\langle w'\theta_v'\rangle}/\left[\overline{\langle w'\theta_v'\rangle_0}\right]$ for $Case2$ and $Case5$. The overlying vector plot shows the wind that is driven by the differential heating of the domain. Before analyzing the figure, it is worth mentioning that the average subgrid scale contribution to the heat flux at z/z_i = 0.95 is 5.6 % for $Case5$ (subgrid flux 0.0011 K m s^{-1}, resolved 0.0183 K m s^{-1}), which indicates that the resolved part largely exceeds the subgrid part, thus that the flow is resolved accurately.

A stronger heterogeneity amplitude results in stronger surface winds towards the center of the warm

Table 2: Surface boundary conditions for all LES simulations. H_L is the sensible heat flux of the cold patch, H_R is the sensible heat flux of the warm patch, LE_L is the latent heat flux of the cold patch, LE_R is the latent heat flux of the warm patch, β_L is the Bowen ratio of the cold patch, β_R is the Bowen ratio of the warm patch.

simulation	H_L [W m^{-2}]	H_R [W m^{-2}]	LE_L [W m^{-2}]	LE_R [W m^{-2}]	β_L [-]	β_R [-]
$Case1$	120	120	240	240	0.50	0.50
$Case2$	105	135	255	225	0.41	0.60
$Case3$	90	150	270	210	0.33	0.71
$Case4$	75	165	285	195	0.26	0.85
$Case5$	60	180	300	180	0.20	1.00
$Weak1$	120	120	240	240	0.50	0.50
$Weak5$	60	180	300	180	0.20	1.00
$Case1dry$	120	120	240	240	0.50	0.50
$Case5dry$	60	180	300	180	0.20	1.00
$Weak1dry$	120	120	240	240	0.50	0.50
$Weak5dry$	60	180	300	180	0.20	1.00
$Case1large$	120	120	240	240	0.50	0.50
$Case5large$	60	180	300	180	0.20	1.00

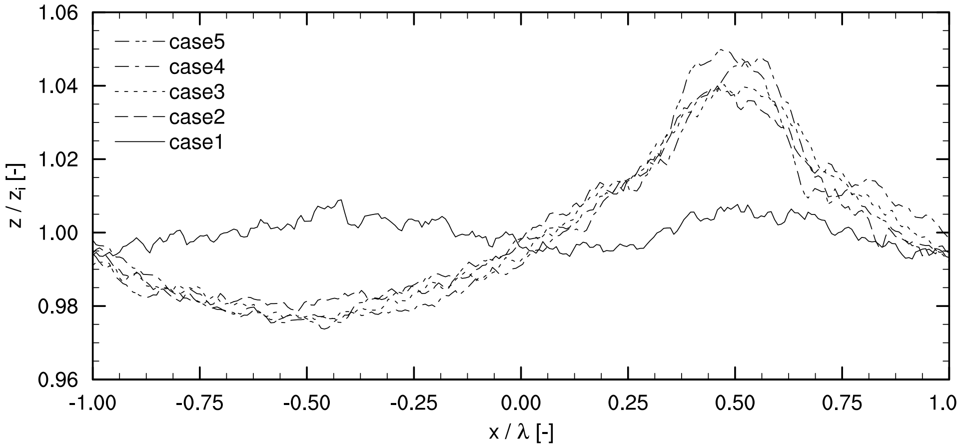

FIG. 1: Averaged ABL height along the x-coordinate during 1 h. Horizontal coordinates are scaled by the patch size λ, vertical coordinates are scaled by the time- and area-averaged ABL height $\left[\overline{\langle z_i \rangle}\right]$.

patch where thermals are merged. $Case2$ has, for instance, a wind of approximately 1 m s^{-1} at $x/\lambda = 0.3$ and $z/z_i = 0.05$, whereas $Case5$ has more than 2 m s^{-1} at the same location. The strongly buoyant thermals that are the product of the merging can penetrate the entrainment zone more vigorously, thereby locally enhancing entrainment, for instance at $x/\lambda = 0.5$ and $z/z_i = 1.0$. The normalized entrainment minima found for $Case2$ are -0.4 and -0.6 times the surface flux, while in $Case5$ the values have a range from -0.8 to -1.0 times the surface flux. These local values largely exceed the ratio of -0.2 times the surface flux that is widely used in parameterizations of the entrainment flux. Although the ABL heights over the warm patch are only slightly sensitive to heterogeneity amplitude, the entrainment minima increase greatly with increasing amplitude. In the next section we discuss the effects of this local entrainment enhancement on the total area averaged entrainment over the heterogeneous land surfaces.

In contrast to the warm patch, over the cold patch thermals are surpressed by the downward wind of the induced mesoscale circulation (downward motions x/λ = -1.0 to 0.0). At the top of the ABL winds are directed towards the cold patch (x/λ = 0.2 and 0.8). Convergence of air occurs here and the warm air is advected downwards towards the land surface. This downward-moving warm air does not allow thermals generated over the cold patch to reach the ABL top and thereby prevents entrainment over the cold patch. The line at which the turbulent flux becomes zero is located at z/z_i = 0.7 for $Case2$ and at z/z_i = 0.5 for $Case5$. The surpression of upward moving thermals is thus enhanced as heterogeneity amplitude increases. Above the warm patch we find strong upward motions (more than 3 m s^{-1} for $Case5$) over a small area, while the cold patch has gentle downward motions (less than 1 m s^{-1}) over the whole cold patch.

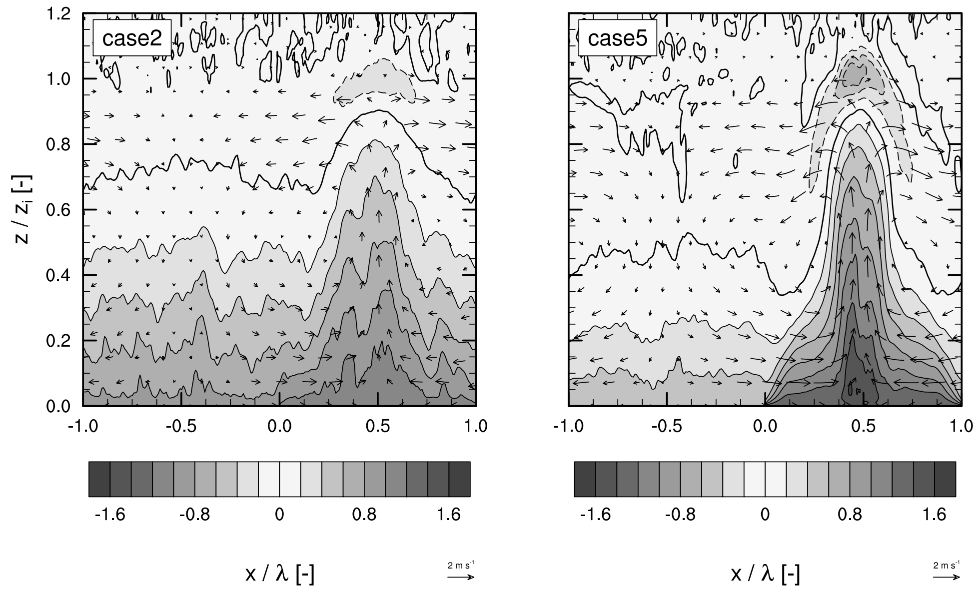

FIG. 2: Cross-section of the 1-h-averaged normalized turbulent heat transport $\overline{\langle w'\theta'_v\rangle}/\left[\overline{\langle w'\theta'_v\rangle_0}\right]$ for $Case2$ (left) and $Case5$ (right). Vectors indicate the wind direction and magnitude. The horizontal coordinates are scaled by the patch size λ and the vertical coordinates are scaled by the ABL height $\left[\overline{\langle z_i\rangle}\right]$.

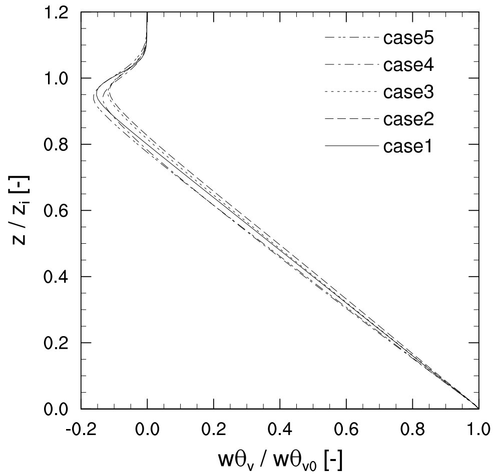

FIG. 3: Vertical profiles of the 1-h-averaged total heat transport $\left[\overline{w\theta_v}\right]$. Horizontal coordinates are scaled by the surface sensible heat flux $\left[\overline{\langle w'\theta'_v\rangle_0}\right]$, vertical coordinates are scaled by the ABL height $\left[\overline{\langle z_i\rangle}\right]$.

3.1.2 AREA AVERAGED ABL GROWTH AND ENTRAINMENT

Here, we further discuss the effects of surface variability on the thermodynamic vertical profiles. To address these effects, the vertical profiles of the homogeneous $Case1$ are compared with the four heterogeneous cases. Just as a reminder, notice that all cases have the same area-averaged sensible and latent heat flux and initial thermodynamic profiles. Consequently, differences among the simulations must be induced by the heterogeneous forcings and by the subsequent local effects on entrainment.

Figure 3 shows the 1-h area averaged heat flux profiles for all the simulations. In spite of the large structural changes that heterogeneity induces, there are only small differences between the homogeneous and heterogeneous cases, although as we show later, the distribution between mesoscale and turbulent contributions to the heat flux varies considerably. All cases show a linear heat flux profile in the ABL (z/z_i = 0 - 0.8) and an area of negative heat flux at the top of the ABL which is characterizing the entrainment zone (z/z_i = 0.8 - 1.1). The curved profiles of the heat flux that AV98 found for heterogeneous cases are not present in our cases. We found linear profiles similar to those in PA05. Therefore, we assume that heterogeneous cases should yield linear profiles and that AV98 results are the effect of the low resolution of their model runs.

Figure 4 shows the temporal evolution of the area-averaged ABL height for all five cases computed following the maximum temperature gradient method (Sullivan et al., 1998). After three hours of spin-up, the ABL heights of $Case4$ (1000 m) and $Case5$ (1010 m) are the largest, but the growth rate of all five cases, which is the entrainment velocity, has a similar magnitude (approximately 70 m h^{-1}). If all cases have the same entrainment velocity, the entrainment differences found in the previous section can not exist. Therefore, the suggested enhancement found in Figure 3 may be the result of the horizontal averaging, where the strongest amplitude cases have a deeper negative area due to the greater variability in ABL height over the domain. This connects with the findings of Lilly (2002) who suggest that the smooth heat flux profiles in the entrain-

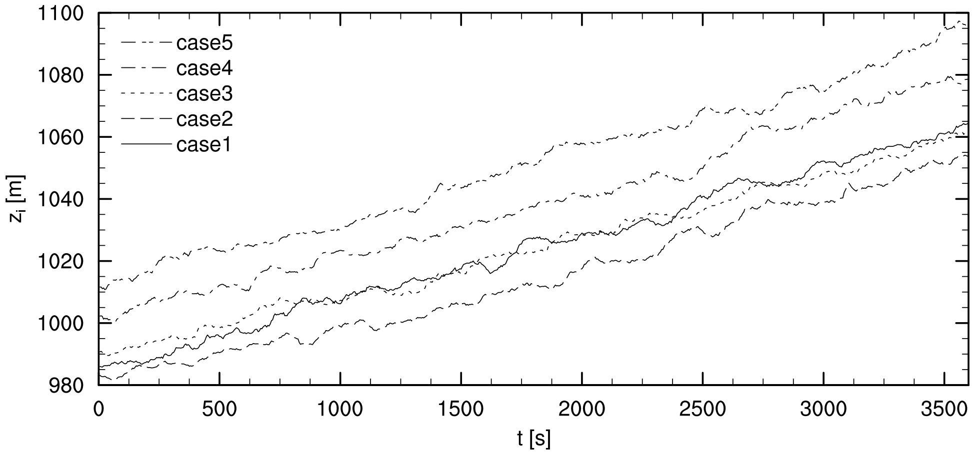

FIG. 4: Domain-averaged ABL height $[\langle z_i \rangle]$ during the hour of data recording.

ment zone found in LES are mostly an effect of horizontal averaging and the that link to the entrainment rate should be made carefuly. PA05 found no significant enhancement of entrainment when they performed a sensitivity analysis of the effect of the heterogeneity length, but they did not vary the heterogeneity amplitude. We showed by varying the amplitude that the results of PA05 are correct and we thus disagree on previous suggestions of AV98 and Letzel and Raasch (2003) that the area averaged entrainment is enhanced.

3.2 *Relative humidity in the ABL*

3.2.1 SPATIAL DISTRIBUTION OF RELATIVE HUMIDITY

Relative humidity is the indicator that links the results of the boundary layer growth and temperature analyses with the findings on the moisture structure. Here, we include the simulations that are performed for the regimes with weaker temperature inversions and a drier upper atmosphere to investigate the importance of the thermodynamic structure of the entrainment zone. Figure 5 shows the 1-h-averaged cross-section of $\overline{\langle RH \rangle}$ for $Case5dry$. The ABL top over the warm patch reaches values up to RH = 55 % (x/λ = 0.5, z/z_i = 0.95), while the cold patch does not exceed RH = 30 %. At the center of the cold patch, there is a dry area at x/λ = -0.5, z/z_i = 0.9 caused by the entrained dry air that is transported downwards here (see vectors in Figure 5). Above the center of the cold patch (x/λ = 0.5), the RH is the minimum for that height. The effects of dry air entrainment extend down to the land surface, as the surface RH at x/λ = -0.5 is less than 30 per cent, while over the warm patch at x/λ = 0.5, the RH exceeds 35 per cent.

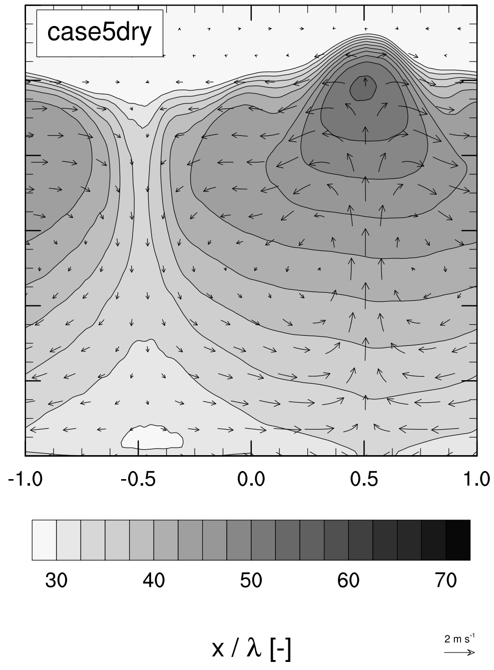

FIG. 5: Cross section of the 1-h-averaged relative humidity $\overline{\langle RH \rangle}$ for $Case5dry$. The horizontal coordinates are scaled by the patch size λ and the vertical coordinates are scaled by the ABL height z_i. Vectors indicate the wind direction and magnitude.

The maximum RH over the warm patch (RH = 62.5 %) of $Case5$ exceeds the value found over a homogeneous land surface sharing the same area-averaged fluxes (RH = 59 %, see Figure 7). In the cases characterized by a drier upper atmosphere, the RH-enhancement effect is still important, despite the intense dry air entrainment, since this air is horizontally advected towards the cold patch and does not directly influence the RH over the center of the warm patch (see Figure 5). As RH is our chosen indicator for cloud formation (Ek and Mahrt, 1994), we therefore expect that in free convective conditions cloud formation may occur earlier over heterogeneous land, independent of temperature and moisture inversion strengths. This finding provides a more complete explanation of previous studies (Avissar and Liu, 1996) that found that cloud formation is enhanced over areas that are warmer and drier than their environment.

3.2.2 VARIABILITY OF AREA AVERAGED RELATIVE HUMIDITY

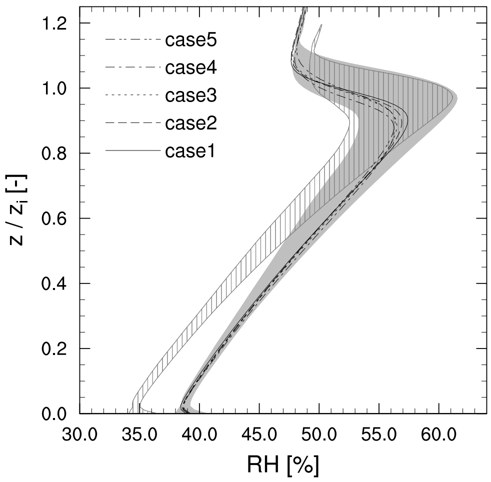

FIG. 6: Vertical profile of the spatial- and time-averaged value of the relative humidity $\left[\overline{\langle RH\rangle}\right]$ for all cases (left). The gray shading shows the range of time-averaged values of relative humidity $\overline{\langle RH\rangle}$ within the domain of $Case5$. The gray hatched area shows the same range but for $Weak5$.

Figure 6 shows the 1-h-averaged vertical profiles of the relative humidity. In the left figure, the shaded area is the range of the 1-h-average relative humidities found in $Case5$, the hatched area is the range of temporal averaged RHs in $Weak5$. This figure shows that the mean profiles of RH are nearly identical, with the maximum RH at $z/z_i = 0.95$. The large-amplitude cases are characterized by a deeper entrainment zone (see Figure 3), which tend to distribute the moisture over a larger region. The RH peak in the homogeneous case is thus slightly higher (RH = 57 %) than in the heterogeneous cases (RH = 55 %). Notice that the area averaged RH is not enhanced by heterogeneity, which is supported by the fact that we have identical surface fluxes and entrainment velocities for all amplitudes (see Figure 4).

The large RH-variability of $Case5$ (grey shaded area) indicates the importance of variability on possible cloud formation. The mean profiles of $Case1$ and $Case5$ are very similar, but in $Case1$ there is hardly any variability within the domain (not shown). In $Case5$ we find a range of 7 % (RH = 54 - 61 %) within the domain. This variability range is even larger (9 %, RH = 52 - 61 %) if the temperature inversion strength becomes weaker, caused by the extra dry air entrainment that sinks over the cold patch.

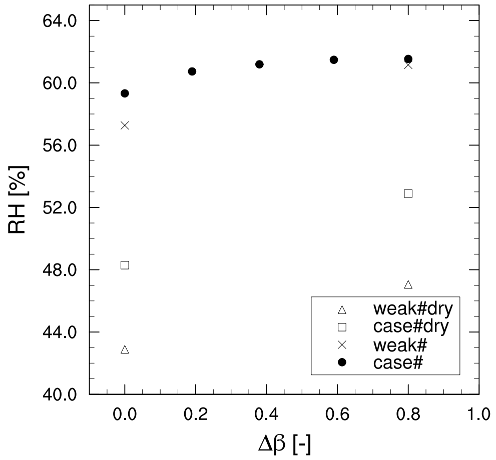

FIG. 7: Relation between the maximum time averaged relative humidity $\overline{\langle RH\rangle}_{max}$ per domain versus the heterogeneity amplitude, $\Delta\beta$ for all regimes. The # can be substituted by the number of the case.

Figure 7 shows the maximum time-averaged $\overline{\langle RH\rangle}$ found in the entrainment zone for all cases. The maximum value of RH increases with heterogeneity amplitude for the four defined regimes of potential temperature and specific humidity inversion strengths. For the numerical experiments with a strong inversion, the values range from 59.4 % ($Case1$) to 61.8 % ($Case5$) for a moist upper atmosphere and from 48.5 % ($Case1dry$) to 51.0 % ($Case5dry$) in the dry case. The weak inversion cases show a slightly stronger correlation between the maximum RH and the heterogeneity amplitude ($Weak1$ = 57.4 %, $Weak5$ = 61.3 %, $Weak1dry$ = 43.0 %, $Weak5dry$ = 47.0 %), which is in agreement with our previous finding that in weak inversions the ABL height variability is relatively larger compared to the strong inversion cases. Although a difference of 3 - 4 % between the homogeneous and strongest heterogeneous case is small, Ek and Mahrt (1994) found that in the afternoon the typical RH$_{zi}$ tendency per hour has similar values. Therefore, there might be a difference in cloud onset between the homogeneous and heterogeneous cases in the order of an hour, if we would take initial conditions for the LES simulations closer to saturation.

4. Summary and conclusions

We investigated the effect of heterogeneous forcings on the potential formation of convective clouds using relative humidity as an indicator. This was done by analyzing numerical experiments using a large eddy simulation model. A sensitivity analysis was performed on the heterogeneity amplitude and the inversion strengths of potential temperature and specific humidity for a land surface that is heterogeneous in the meso-γ scale (2 - 20 km). The cases are integrated for four hours of which the last hour was used to record statistics. We analyzed the height of the ABL, the specific and relative humidity structure near the ABL top for a free convective boundary layer that was forced by a sensible and latent heat flux that added up to 360 W m^{-2} for all simulations. The land surface was divided in 2 patches, one with a low Bowen ratio (cold patch) and one with a high Bowen ratio (warm patch). Different heterogeneity amplitudes were simulated by varying the difference between the

Bowen ratios of the two patches.

An analysis of entrainment and ABL growth of the heterogeneously forced ABL indicated that under heterogeneous conditions the ABL increases over the warm patch, and decreases over the cold patch. The greater ABL heights over the warm patch lead to lower absolute temperatures over the center of the warm patch. Due to the mesoscale circulation that is induced by the heterogeneous forcings, moisture is advected to the center of the warm patch. Low absolute temperatures in combination with high specific humidity over the warm patch lead to a situation which has a relative humidity that is higher under heterogeneous condititions than under homogeneous forcings. These are the first indications in this study that cloud formation may be favorable over the warm patches of a heterogeneous landscape.

The comparison of vertical heat flux profiles of homogeneous and heterogeneous cases sharing the same area-averaged forcings revealed that entrainment in low-amplitude heterogeneous cases appears to be less than in homogeneous cases, whereas the entrainment of large amplitude cases exceeds the entrainment of homogeneous cases. Nevertheless, this finding is rejected by the analysis of the time evolution of the ABL height, as identical entrainment velocities for all cases are found here.

Mean vertical profiles of relative humidity are very similar in all cases, but the variability in the time-averaged RH near the top of the ABL (RH$_{zi}$) is largely enhanced by the presence of heterogeneity. This finding is proven to be true for all cases with strong and weak potential temperature inversions and with moist and dry upper atmospheres. In all situations the RH$_{zi}$ over the warm patch is larger than over the cold patch and than in homogeneous conditions. By conditionally sampling the data, we show that thermals over heterogeneous surface conditions are more effective in transporting moisture upwards, due to their larger volume to surface ratio. In addition, the RH cross sections show that dry air that is entrained is transported downwards mostly over the cold patch and low values of RH are found over this patch. In cases with a drier free atmospheres, these effects can be more pronounced and dry entrainment events extend to the land surface. Therefore, we conclude that the mean RH profile shows incomplete information with regard to RH modifications by heterogeneity. It is highly relevant to calculate the variability of RH as a function of the amplitude of the heterogeneity, as this variable contains the influence of heterogeneity on the maximum RH that occurs in the domain.

All of the above findings suggest that land surface heterogeneity plays a significant role in the stucture and value of the RH$_{zi}$. Cloud formation may be enhanced over heterogeneous landscapes as the maximum RH and the specific humidity variance in the entrainment zone are larger than in homogeneous conditions.

Acknowledgments. The authors acknowledge the helpful comments of Ned Patton, Stephan de Roode and Joel Schröter. This study was supported by a grant from the Netherlands Organisation for Scientific Research (NWO TopTalent). This work was sponsored by the National Computing Facilities (NCF project SG132).

REFERENCES

Avissar, R. and Y. Liu, 1996: Three-dimensional numerical study of shallow convective clouds and precipitation induced by land surface forcing. *J. Geophys. Res.*, **101**, 7499–7518.

Crook, N. A., 1997: Sensitivity of moist convection forced by boundary layer processes to low-level thermodynamic fields. *Mon. Wea. Rev.*, **124**, 1767–1785.

Cuijpers, J. W. M. and P. G. Duynkerke, 1993: Large-eddy simulation of trade-wind cumulus clouds. *J. Atmos. Sci.*, **50**, 3894–3908.

Dosio, A., J. Vilà-Guerau de Arellano, A. A. M. Holtslag and P. J. H. Builtjes, 2005: Dispersion of a passive tracer in buoyancy- and shear-driven boundary layers. *J. Atmos. Sci.*, **42**, 1116–1130.

Ek, M. B. and A. A. M. Holtslag, 2004: Influence of soil moisture on boundary layer cloud development. *J. Hydrometeor.*, **5**, 86–99.

Ek, M. B. and L. Mahrt, 1994: Daytime evolution of relative humidity at the boundary layer top. *Mon. Wea. Rev.*, **122**, 2709–2721.

Hussain, A. K. M. F. and W. C. Reynolds, 1970: The mechanics of an organized wave in turbulent shear flows. *J. Fluid Mech.*, **41**, 241–258.

Kang, S.-L., K. J. Davis and M. LeMone, 2007: Observations of the abl structures over a heterogeneous land surface during ihop2002. *J. Hydrometeor.*, **8**, 221–244.

Letzel, M. O. and R. Raasch, 2003: Large eddy simulation of thermally induced oscillations in the convective boundary layer. *J. Atmos. Sci.*, **60**, 2328–2341.

Lilly, D. K., 2002: Entrainment into mixed layers. part i: Sharp-edged and smoothed tops. *J. Atmos. Sci.*, **59**, 3340–3352.

Mahrt, L., 2000: Surface heterogeneity and vertical structure of the boundary layer. *Bound.-Layer Meteor.*, **96**, 33–62.

Nieuwstadt, F. T. M. and R. A. Brost, 1986: The decay of convective turbulence. *J. Atmos. Sci.*, **43**, 532–546.

Pielke, R. A., 2001: Influence of the spatial distribution of vegetation and soils on the prediction of cumulus convective rainfall. *Rev. Geophys.*, **39**, 151–178.

Sullivan, P. P., C. H. Moeng, B. Stevens, D. Lenschow and S. D. Mayor, 1998: Structure of the entrainment zone capping the convective atmospheric boundary layer. *J. Atmos. Sci.*, **55**, 3042–3064.

van Heerwaarden, C. C. and J. Vilà-Guerau de Arellano, 2008: Relative humidity as an indicator for cloud formation over heterogeneous landscapes. *J. Atmos. Sci.*, **in press**.

THE FORECAST ERRORS OF GEM AND RUC MODELS FOR CONVECTIVE AND NONCONVECTIVE DAYS

Zlatko Vukovic
Environment Canada, Toronto, Ontario, Canada

1. INTRODUCTION

For operational purposes it is very useful to compare forecasts on convective and non-convective days. This is especially of use for convective now-casting since more than one model is available and preference needs to be given to one.

In this study forecast errors for convective available potential energy (CAPE) for the GEM (Regional, 15km resolution) and Rapid Update Cycle (RUC) 13km resolution model data are compared for two subsets of data, convective and non-convective days.

The CAPE values calculated from the radio-sonde data for 00 and 12 hour observations from Maniwaki (YMW) and Buffalo (BUF) locations from Jun to August 2007 are compared against the two models.

The intention of this paper is to get the preliminary evidence as to whether or not the convective conditions of the atmosphere significantly change the models forecast accuracy.

2. DATA SET

The forecast accuracy of the temperature (T), relative humidity (RH) and wind speed (WS) as a function of height were taken for the comparison.

The GEM model provides 36 hour forecasts in 58 eta levels (run operationally at 00 and 12Z daily) with forecast variables outputted every 30 minutes as instantaneous values at each time step. In considering GEM model spin up time, a 3 hour spin time was selected.

The RUC model data is available hourly, and they are extracted from the isobaric grid version of the model (i.e. 3-D variables given at 37 isobaric levels: 25 hPa, 1000-100 hPa). In this study, four forecast periods were analyzed: the 3 hour (RUC03), 6 hour (RUC06), 9 hour (RUC09) and 12h (RUC12).

The selections and number of the vertical levels for the radio-sonde and the models is different. Therefore, the first step was to standardize all three vertical profiles. Arbitrarily 15 referent pressure levels where chosen (925, 850, 700, 500, 400, 300, 250, 200, 150, 100, 70, 50, 30, 20, 10 hPa) for which the measured and forecasted values of T, RH, and WS were obtained for the YMW and BUF locations for 00 and 12 UTC time. From the radio-sonde data, using all vertical levels, CAPE values were calculated for both locations and hours.

The radio-sonde and the models T, RH, and WS sets of data for the 15 pressure levels were grouped in five subsets with regard to the CAPE value:

i) The referent set of data is all data regardless of the CAPE value;
ii) CAPE =0 J/kg;
iii) 0<CAPE<1000 J/kg;
iv) 1000J/kg<CAPE<2000 J/kg;
v) CAPE>2000 J/kg.

To estimate the models forecast error, the radio-sonde data was subtracted from the model data and the mean road square root (rms) was calculated.

3. ANALYSE

3.1. Temperature

The graphical presentation of the temperature rms variation with pressure levels for the GEM and RUC models for the Buffalo and Maniwaki locations for different CAPE values are shown in the Figure 1. From the data of one summer, a minimum of 16 up to a maximum of 161 data points was collected per level. It looks as if the models forecasts have a similar accuracy regardless of the CAPE value. The temperature rms difference between the most unstable atmosphere condition (red line, CAPE > 2000J/kg) and the referent case when all the data was included (black line) is inside the measured error or statistical significance, ie. less than 0.5 C.

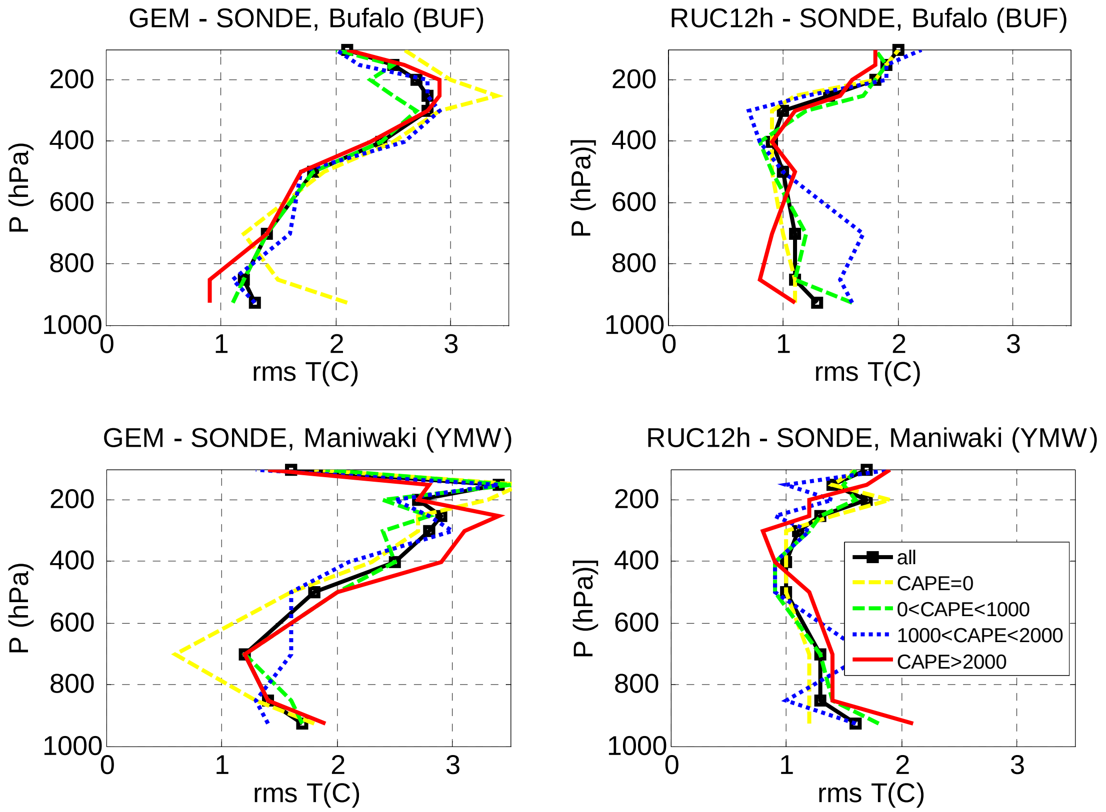

Figure 1. The temperature rms variation with pressure levels for GEM-Sonde (left) and RUC-Sonde (right) data for Bufalo (up) and Maniwaki (down) locations for all data (black color) and different CAPE values: yellow for 0, green for the 0-1000J/kg range, blue for the 1000-2000J/kg range, and red for CAPE greater than 2000J/kg.

A similar comparison for the RUC model for four forecast periods (3, 6, 9, and 12h) is shown in Figure 2. There is also no significant dependence of the temperature rms with the atmosphere instability.

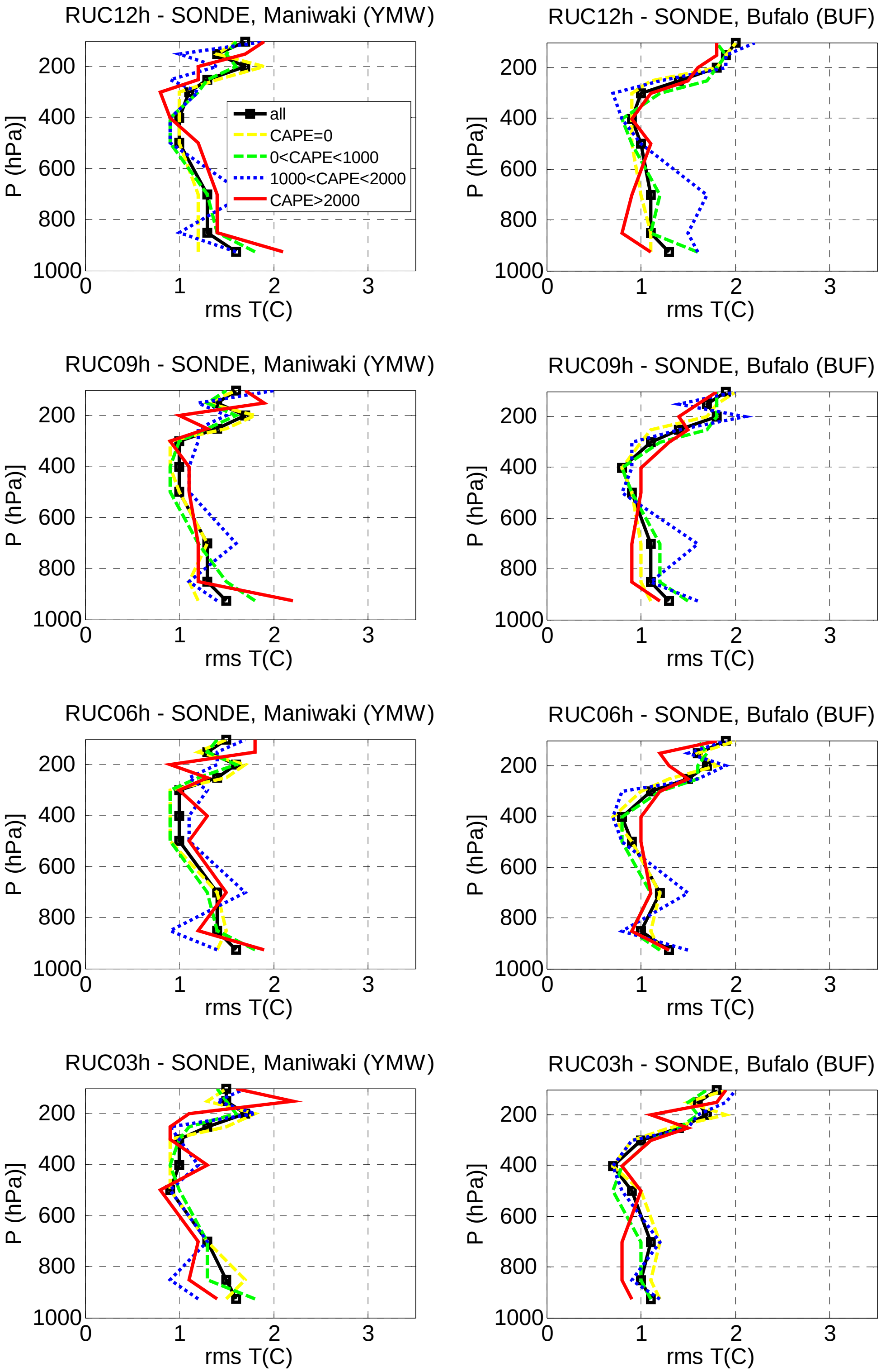

Figure 2. The temperature rms variation with pressure levels for RUC-Sonde data for Maniwaki (left) and Bufalo (right) locations for 3,6,9 and 12h forecast periods (from the top to the bottom) for all data (black color) and different CAPE values: yellow for 0, green for the 0-1000J/kg range, blue for the 1000-2000J/kg range, and red for CAPE greater than 2000J/kg.

3.2. Relative Humidity

The graphical presentation of the relative humidity rms is shown in Figure 3. It appears that the GEM model for more unstable atmosphere conditions (red line) has a better forecast accuracy when compared to all data regardless of the CAPE value, for both locations. The RH rms is about 25% for CAPE>2000J/kg compared to the 30 -35% for all data. While for the RUC model the RH rms is almost unchanged,
About 20-25%.

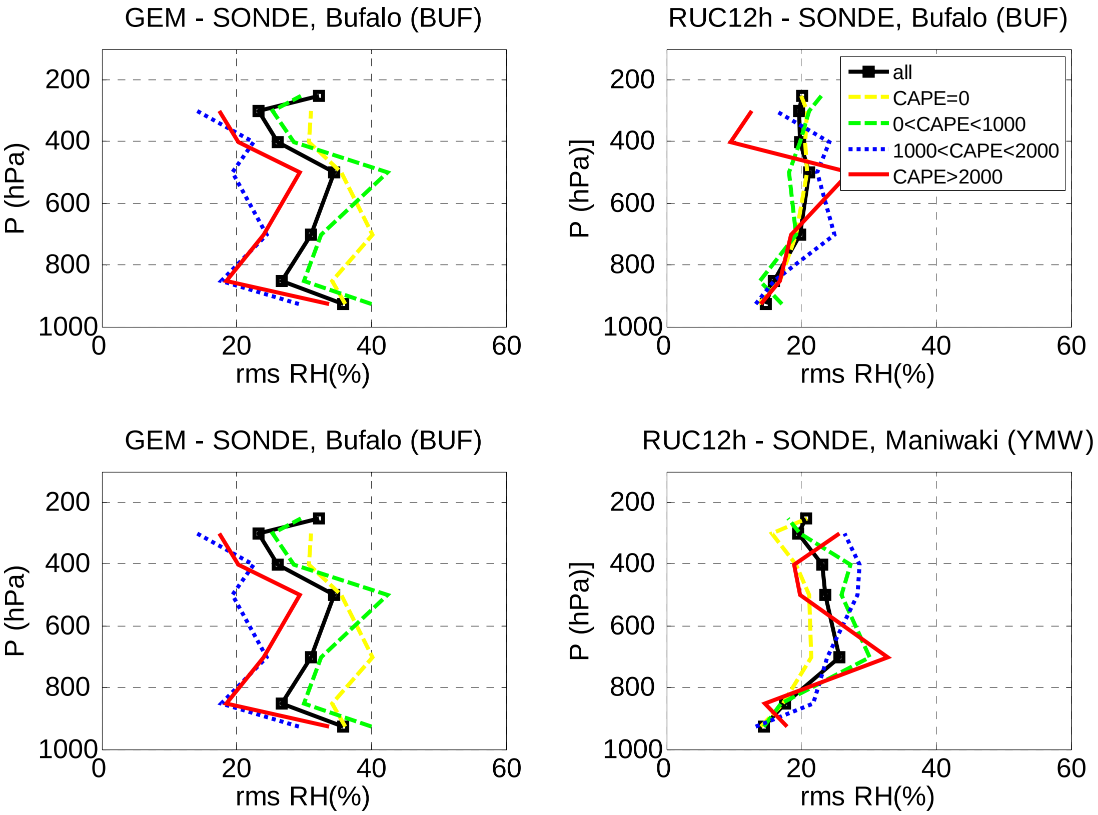

Figure 3. The relative humidity rms variation with pressure levels for GEM-Sonde (left) and RUC-Sonde (right) data for Bufalo (up) and Maniwaki (down) locations for all data (black color) and different CAPE values: yellow for 0, green for the 0-1000J/kg range, blue for the 1000-2000J/kg range, and red for CAPE greater than 2000J/kg.

3.3. Wind Speed

For wind speed (Figure 4) in very unstable atmosphere, the rms for the GEM model is slightly smaller in all levels for the Buffalo location, while for the RUC-12h it is almost unchanged.

For the Maniwaki site, in the upper troposphere the rms for the GEM model is bigger, which also applies to the RUC12h model.

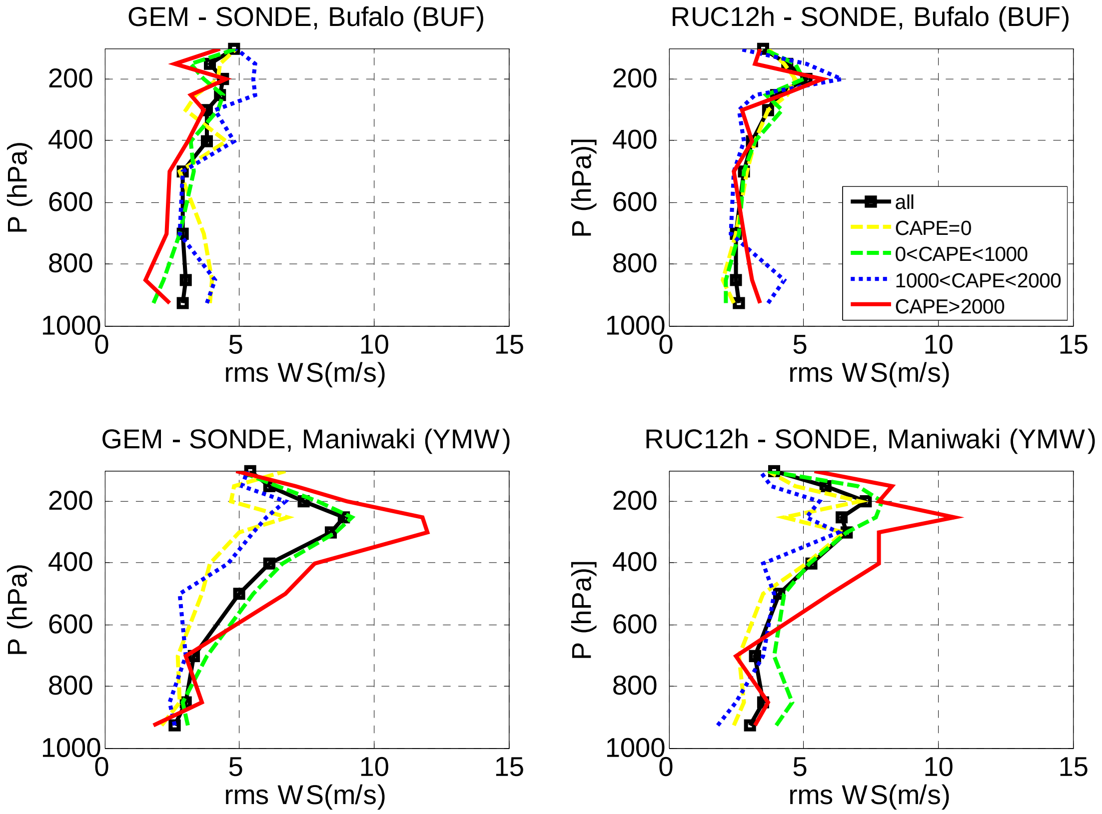

Figure 4. The wind speed rms variation with pressure levels for GEM-Sonde (left) and RUC-Sonde (right) data for Bufalo (up) and Maniwaki (down) locations for all data (black color) and different CAPE values: yellow for 0, green for the 0-1000J/kg range, blue for the 1000-2000J/kg range, and red for CAPE greater than 2000J/kg.

4. DISCUSION AND CONCLUSSIONS

The results of the analysis are for a relatively small data set, one summer, show that the convective conditions of the atmosphere have different influences on the model accuracy for different variables and locations.

The temperature forecast accuracy is practically unchanged for both models and locations.

The relative humidity accuracy, for both locations, is better for the GEM model when the atmosphere is more unstable. The relative humidity forecast for the RUC model is almost unchanged regardless of the location.

In very unstable atmospheric conditions the wind speed forecast error in the upper troposphere is bigger for the Maniwaki location, while for the Buffalo location it is effectively the same.

Before the obtained results can be used, analysis of a much larger data set is necessary.

NUMERICAL STUDY OF CONVECTION CLOUD BY RAIN ENHANCEMENT

WEN Ji-fen[1] ,HUANG Hao-juan[1], LUO Ning[2] and ZHOU li-na[1]
1:Guizhou Weather Modification Office, Guiyang, 550002,China
2:Guizhou Meteorological Bureau, Guiyang, 550002,China

1. INTRODUCTION

Cloud seeding activities for convection cloud by rain enhancement using cannon are carried out In Weining, the western area of Guizhou province of China. In thconvectione area the hailstone affects the agrarian production seriously, and causes substantial damages to agriculture every year. One of the main characteristics of the zone is that the convection clouds are those which originate after the noon; it is relatively easy to find that the reflectivity measured by the radar reach values of over 30 dbz. The purpose of convection cloud by rain enhancement is to affect the micro-physical structure of convection cloud by inducing artificial freezing nuclei to the clouds. The principle of convection cloud by rain enhancement by seeding is to produce a large of ice crystals by inducing artificial freezing nuclei to the supercooled clouds to consume supercooled water, so hail growth is restrained because of no enough water. According to this principle, some numerical simulations for supercooled cloud seeding are done. It is very important to study mechanisms of convection cloud by rain enhancement by seeding using the three-dimensional model of convection cloud because convection clouds have three-dimensional structure. Especially in China, convection cloud by rain enhancement work is blind and has no objective criterion on selecting seeding methods.In this paper, using the three-dimensional fully elastic numerical model of convection cloud developed by Institute of Atmospheric Physics(IAP),a convection cloud occurred in Guizhou province, is simulated seeding by AgI and no seeding for this convection. This study can supply optimal seeding scheme, it is beneficial to development of convection cloud by rain enhancement.

2. MODEL

The model contains more detail bulk-water parameterized microphysics, including forty-six warm and ice phase micro-physical processes such as condensation (sublimation), collection, nucleation, multiplication, melting, melting-evaporation and auto-conversion. The model contains vapor、cloud water、rain、cloud ice、snow、graupel and hail. The simulation area moves with the simulation convection cloud simultaneously to enable the convection cloud located in the central area of the simulation area. The time-splitting numerical integral technique is adopted to improve computation efficiency of fully elastic model. The model contains eighteen equations which predict motion field, atmospheric pressure, temperature, mixing ratios (vapor, cloud water, rain, cloud ice, snow, graupel, hail and AgI particles), concentrations of rain and ice phase particles. The standard spatially staggered mesh system is used in the model where three components of velocity are located in normal boundary center of mesh unit and others in the center of mesh unit. Radiation lateral and rigid top boundary conditions are adopted and sponge zone is added in the top boundary to restrain vertical fluctuation of internal gravity wave. The influence of underlying surface ignored, the value of turbulent exchange item is assumed to zero. The model uses the fourth order difference scheme for advection terms and second order leapfrog scheme for time terms andother space terms. The formation mode of initial convection includes thermodynamic disturbance and humidity disturbance et. al. The mechanisms by which AgI can produce the ice phase are as follows:1)Deposition nucleation: by converting vapor to solid at ice supersaturation.2)Contact freezing nucleation(including immersion freezing nucleation):by converting cloud water and rain to cloud ice and graupel.

3. NUMERICAL STUDY

The numerical study of convection cloud by rain enhancement by AgI shows that the principle of hail formation and growth conforms to the theory of accumulation zone. The basic theory of convection cloud by rain enhancement by seeding is “competitive principle”. A series of seeding experiments are done to seek optimal seeding methods.

3.1 SIMULATION OF CONVECTION CLOUD

The seeding and natural (no seeding) experiment is a simulation of moist convection initiated by a warm, moist bubble. The integration domain is 40 km in both horizontal directions and 14.0 km in vertical, with grid intervals△x=△y=1000m and △z=500m.The sounding data is used as the initial fields of temperature, moisture and velocity. To initiate disturbance, a warm moist bubble is inserted in the center of the domain at a height of 2 km. The initial impulse is 10km wide and 4km deep, with a maximum disturbance temperature of 4.5℃. Fig.1(omitted). shows Vertical cross section of total water content in natural simulation through the center of convection at t = 2, 4,8,12,16,20,28,48 min. The convection derived from simulation is similar to that measured by radar (radar map omitted). From Fig.1, it can be seen that the center of water content of convection is located 2km high at two minutes from the beginning of the developing convection and it is becoming higher with the developing convection. Seven minutes later, it is 3km high, ten minutes, 4 km. Then sixteen minutes later, the convection becomes weaker. In addition, during the period of convection developing, the total water content is always located in the maximum updraft area. In simulation, the top of convection reach 14.0 km high, the body of convection leans southwest, rain begin on surface at thirteen minutes, the total rainfall on surface is 956.48 ton.

3.2 SIMULATION OF CONVECTION CLOUD BY RAIN ENHANCEMENT

On the basis of the simulation of convection on 20,May,2007, A series of experiments simulated seeding by AgI for this convection has been done. In this paper, the seeding effect (E) is defined by the percentage of decreasing of rainfall on surface.The simulation of convection cloud by rain enhancement are shown in Fig.2(omitted)., from which it can be seen the seeding effectat second minute at height 2km, 3km, 4km, 5km and 6km separately (shadow area denotes E>8%). Shown as Fig 2, seeding activities with different height, or different site, or different amount of agents can all get the effect more than 50%. For the same seeding agents, the shadow area increases with height from 2km to 4km, while decreases from 4km to 6km. But it is possible for the total rainfall to increase at height 6km. The shadow area extends to southwest, it has the consistency with the convection southwest leaning. At the same height, the shadow area by 300g AgI seeding is larger than that by 50g. The convection cloud by rain enhancement can be taken with the best effect of 16%.

$$\frac{AgI}{\text{催化}}\begin{Bmatrix} 5.5\% & 36\% \\ TQ_i\uparrow & TQ_s\uparrow \\ TN_i\uparrow & TN_s\uparrow \\ 3.5\% & 83\% \end{Bmatrix} - \begin{Bmatrix} 42\% \\ TNCL_{rig}\uparrow \\ TNCL_{srg}\uparrow \\ 124\% \end{Bmatrix} - \begin{Bmatrix} 7\% \\ TQ_g\uparrow \\ TN_g\uparrow \\ 52\% \end{Bmatrix} - \begin{matrix} 49\% \\ P_{gh}\downarrow \end{matrix} - \begin{Bmatrix} 31\% \\ TQ_h\downarrow \\ TN_h\downarrow \\ 29\% \end{Bmatrix} \Rightarrow E \quad 16\%$$

This formula indicates that:

1)Because of seeding by AgI for the convection cloud, in the 21 minute, the quantity and the quality of ice in the simulation cloud have a little change. The ice changes to graupel become more and more weak and to snow become more and more strong.

2) The number of the snow is increasing, and the quality of the snow is decreasing.

3) The number of the graupel increase obviously.and its quality have a little change .The collision of the super-cooled water with ice and the super-cooled water with the snow is more than the ice and the snow change to graupel; this is the reason of the increasing quantity and quality of the graupel.

4) By the reason of the quantity increasing more than the quality increasing of the graupel, the graupel change to hail is weak, so the rainfall on surface is increasing.

4. CONCLUSION

The simulation results of convection cloud by AgI seeding with cannon are as follows: The simulation results of rain enhancement by AgI seeding are as follows: the optimal seeding position is located at 3-5km height in the updraft area.and the optimal seeding time is made at 2-6 minutes before a intense echo centre formation, Other things being equal, rain enhancement ratio increases with seeding amount of AgI. This study can supply optimal seeding strategy of rain enhancement.

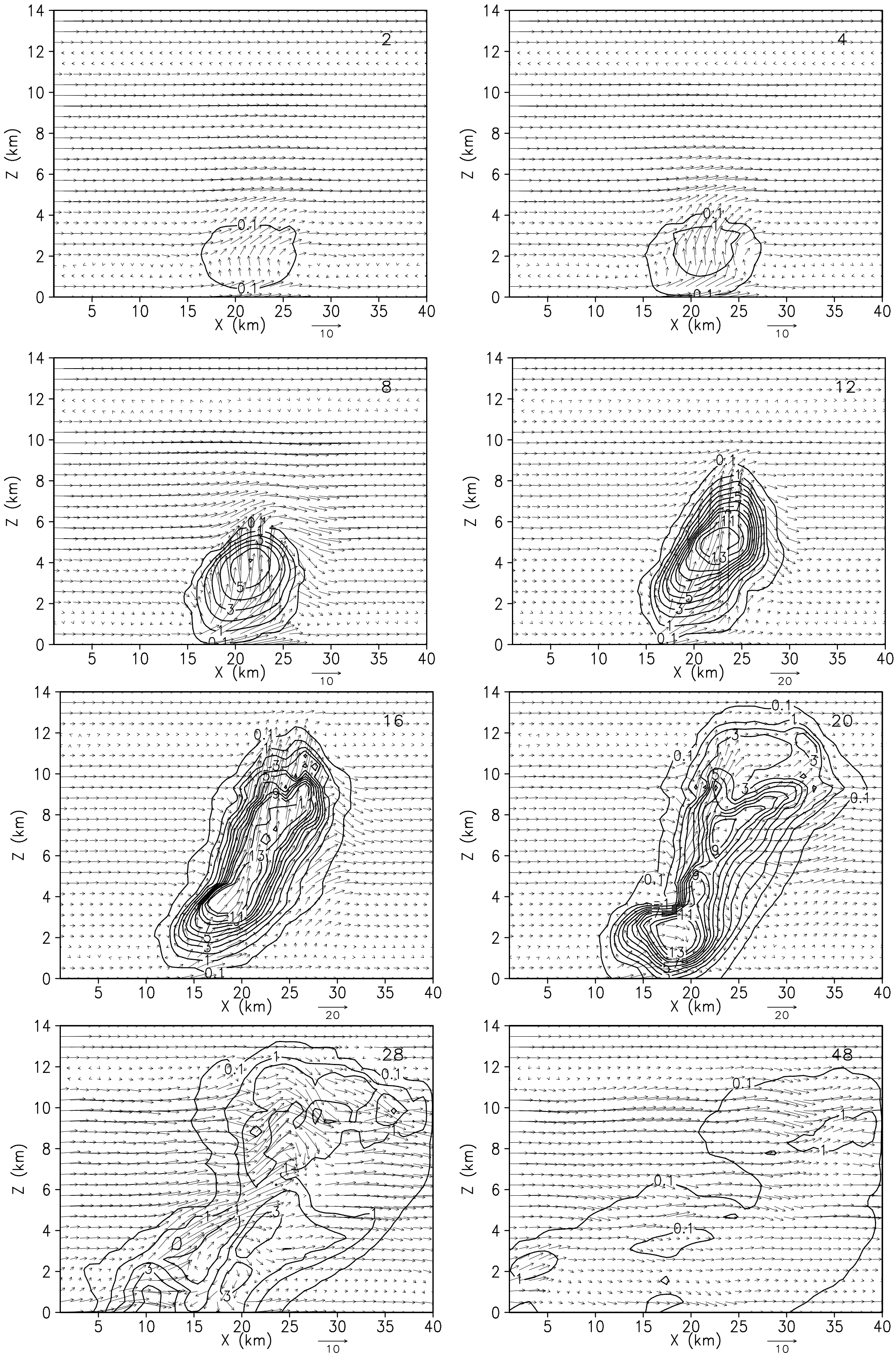

FIG.1. Vertical cross section of total water content in natural simulation through the center of hail cloud at t=2,4,8,12,16,20,28,48 min

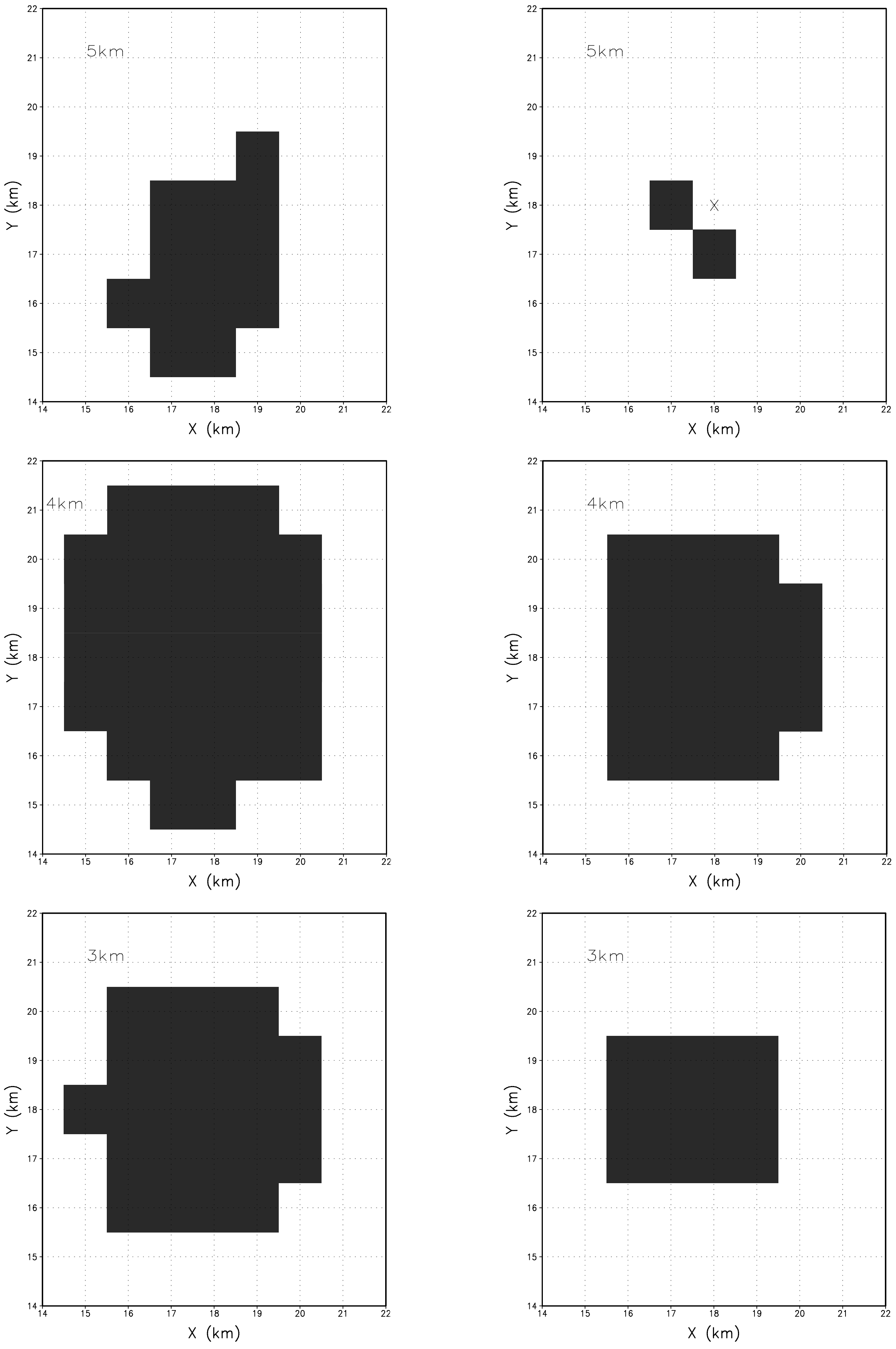

Fig.2 simulation of hail suppression by AgI seeding at two minutes (different height, different location and different amount of seeding agents, 300g in maps of left column, 50g in right, shadow area denotes E>8%)

UNIVERSAL FUNCTIONS FOR POST-FRONTAL SHOWERS - GEOMETRICAL CHARACTERISTICS AND RAIN RATE DEVELOPMENT

Tanja Weusthoff[1] and Thomas Hauf[1]

[1] *Institute for Meteorology and Climatology, Leibniz Universität Hannover, Germany*

1 INTRODUCTION

The study deals with the well-known convective cloud and precipitation patterns in the rear of cold-fronts passing Central Europe, typically in south-easterly directions. The structure and temporal development of those post-frontal shower fields were analysed aiming for a quantitative analytical description of that precipitation field as displayed in Figure 1. In this paper, we present a summary of ongoing work, comprising analyses of the geometrical structure and investigations on the temporal development of individual rain areas. The *geometrical structure* was analysed following the procedure of THEUSNER (2007) (in the following referred to as THEU) and MESNARD AND SAUVAGEOT (2003) (in the following referred to as MESN). We refined those studies by using a higher resolution radar product to calculate the diurnal cycle of the whole precipitation area and evaluate the individual rain areas within the precipitation field, e.g. with respect to area size. In addition, the *temporal development of individual rain areas* was investigated in a Lagrangian-type analysis. The information for this analysis was derived from a tracking of individual rain areas performed earlier by WEUSTHOFF AND HAUF (2008b) (in the following referred to as WEUS). The analysis includes determination of the life time and the total rain amount contained in the rain areas.

The data set used in the current study comprises radar data from 17 days in 2004 and 2006 (listed in WEUS). We employed the radar data from the radar composite RZ, which is available since 2004. An example of the composite is shown in Figure 1. For the RZ composite, the measured radar reflectivities were already converted into rain rates using an advanced Z-R-relationship. The latter was developed within the German Weather Service's (DWD) project RADOLAN (BARTELS ET AL., 2004). The composite has a temporal resolution of 5 minutes and a horizontal resolution of 1 km × 1 km. The rain rates are given in a resolution of 0.01 mm / 5 min. For the subsequent analyses, we used only radar

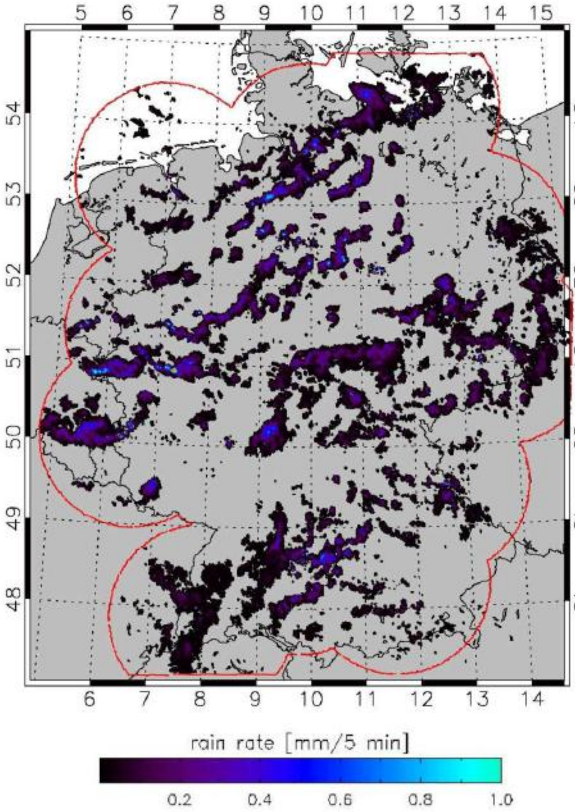

Figure 1. Image of radar composite RZ of 6 March 2006, 14:30 UTC.

data with values larger than 0.05 mm / 5 min, which corresponds to a reflectivity value of about 20 dBZ (calculated with the standard Z-R-relationship $Z = 256 \cdot R^{1.42}$). This value was found by THEU to be sufficient for an identification of convective structures within the precipitation field.

The radar data was analysed in terms of individual rain areas. A rain area, which we also refer to as a *cluster*, is defined as a contiguous region in the radar data where the rain rate R is larger than a given threshold, which is in this study the cut-off 0.05 mm / 5 min. Each cluster consists of n embedded convection cells, identified by local maxima of rain rates. We then address the cluster size in terms of cell number (n-cell cluster). The individual clusters were tracked over time and the temporal development in terms of cell number, size, rain rate, etc. was analysed. The whole set of clusters that belong together, such that they are precursors or successors of each other, are referred to as a *track*. Each track has a specific life span, which ist the time from the genesis of the first cluster of the track to the disappearance of the last member of the track. Altogether, about 82.000 such tracks, with a mean length of about 30 minutes, were identified. Three types of tracks are distinguished:
(1) Single-cell-tracks (53 500 tracks = 66 %, Fig. 2 (a)), i.e. rain areas that remain single cells over their whole life time. This means, growth occurs only with respect to the area and the rain rate, but not with respect to the number of cells within the rain area.
(2) Single-cluster-tracks (10 500 tracks = 13 %, Fig. 2 (b)): Rain areas, which develop only by internal growth and decay, respectively. They have no interaction with other clusters, but the number of embedded cells varies.
(3) Multi-cluster-tracks (17 000 tracks = 21 %, Fig. 2 (c)) are all those tracks where interactions among rain areas occur, namely merging and splitting. Those tracks often have a long duration and a rather complex life cycle.

In a first instance, we concentrated on single-cell tracks. The results are presented in WEUSTHOFF AND HAUF (2008a). The other two track types are subject of a current PhD study by WEUSTHOFF.

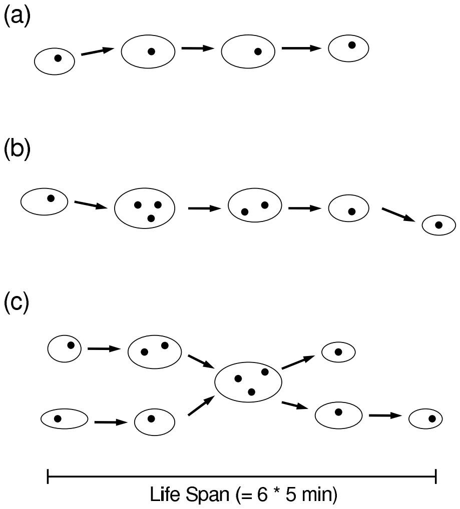

Figure 2. Three different track types: (a) single-cell-tracks, (b) single-cluster-tracks and (c) multi-cluster-tracks.

2 GEOMETRICAL STRUCTURE

The geometrical structure was intensively investigated by THEU. Those analyses were based on the PC radar composite of the DWD with a temporal resolution of 15 minutes and a horizontal resolution of 2 km x 2 km. We recalculated the results with the higher resolution RZ composite and can confirm them so far with that new data (e.g. WEUS). Three examples are presented here.

2.1 Diurnal Cycles

The mean diurnal cycle of the total precipitation area, that is the sum over all clusters within the post-frontal shower field, shows a sinusoidal shape with a maximum around 15 UTC and a minimum at night (Fig. 3). In the same plot, the diurnal cycle of the area per cell is displayed, which shows only slight variations with a maximum in the afternoon and a minimum in the morning. Thus, the cells are larger in the time around maximum convective activity. The mean area per cell is about $30\,\mathrm{km}^2$, respectively the mean equicircle diameter is $4\,\mathrm{km}$. THEU found a value of $230\,\mathrm{km}^2$ per cell for a cut-off of 19 dBZ, which corresponds with a diameter of 12 km. This is three times the value we found and probably due to the difference in the resolution of the radar data (THEU: PC composite with $2\,\mathrm{km}\,\mathrm{x}\,2\,\mathrm{km}$, here: RZ composite with $1\,\mathrm{km}\,\mathrm{x}\,1\,\mathrm{km}$), resulting, for example, in different numbers of detected cells inside a rain area and different areal coverage. As the single cells are the most frequent one, Theusner was missing the majority of all cells and thus his mean value was larger. The values agree quite well with those of MESN, who also used a high resolution radar, but a higher cut-off, and detected a mean value of about $2-3\,\mathrm{km}$ equicircle diameter per maximum.

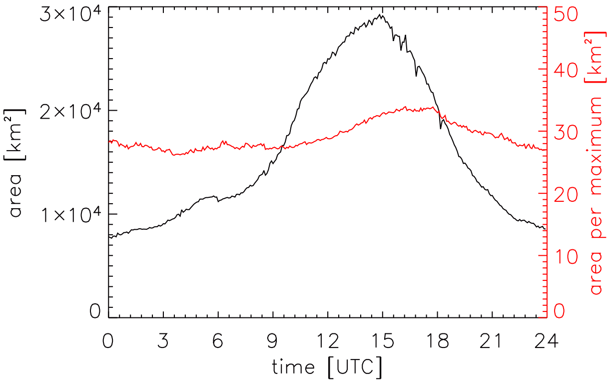

Figure 3. Diurnal cycle of total precipitation area and area per cell.

A similar shape of the diurnal cycle was found for the number of rain areas as well as for the total cell number. The ratio of those two quantities gives the number of cells per rain area, which is in average about 2.3, staying nearly constant over the day with a slight maximum in the afternoon. THEU also found a nearly constant value for that quantity, but a lower value, which lies slightly below 2.

2.2 Cell number distribution

The cell number distribution (CND) for the whole data set as depicted in Figure 4 can be fitted by a power law of the form

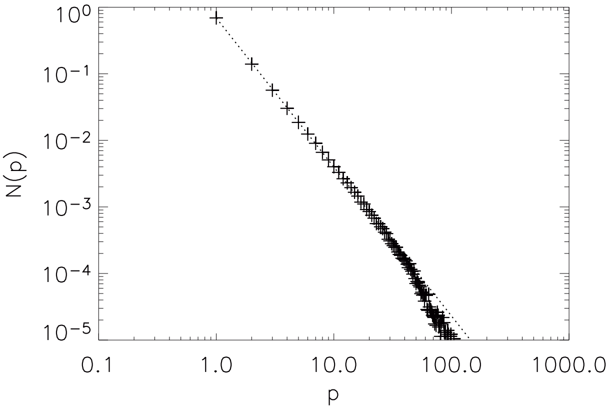

Figure 4. Cell number distribution for the whole set of analysed days. The regression is calculated with a power law.

$$N(p) = a \cdot p^b \tag{1}$$

The slope b of the regression for a cut-off of 0.05 mm / 5 min is -2.23, ranging from -1.92 to -2.50 for individual days. The difference to the result of THEU, who found a slope of -2.46 for a comparable cut-off of 19 dBZ, may be explained with the different resolution of the data again. While the PC composite differentiates 6 reflectivity classes, the RZ composite has a resolution of 0.01 mm / 5 min. Thus, we detected more maxima within the rain areas, each maximum corresponding to an individual convection cell. A lower absolute value of the slope means fewer clusters with a low cell number, which is the case with our data. MESN calculated slopes of e.g. -2.48 (Bordeaux) and -1.78 (Toulouse) for a cut-off of 23 dBZ and smaller regions covered by only one radar each. It needs to be mentioned that the investigations of MESN were not restricted to one specific synoptic situation and cover diverse periods. Despite those differences, the slope parameter lies for all three studies in a similar range.

In our case, this power law was found for the average of all days as well as for single days with slight variations from day to day. A closer look on the diurnal cycle of that slope based on the 17 days revealed, however, a diurnal cycle of the slope of the CND with a minimum in the morning, which means less small clusters

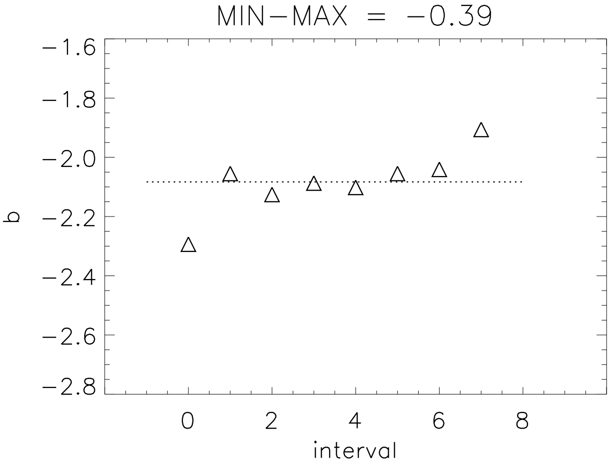

Figure 5. Diurnal variation of the slope b of the cell number distribution calculated for 3h-intervals.

and a maximum in the evening, which indicates more smaller and less larger clusters. However, the diurnal variation of the average CND (here about 0.4) is lower than the day-to day variation (here about 0.6) and shows a nearly constant behaviour in the daytime when convective activity has its maximum. The deviation in the morning and in the evening may also be caused by the lower number of maxima in those times of the day.

2.3 Rain area size distribution

For each fixed cell number p, the area size distribution was calculated (Fig. 6). The size is hereby represented by the equicircle diameter D. The data for each cell number could well be fitted by a lognormal distribution. This was already shown by MESN for a smaller investigation area and by THEU with the lower resolution radar composite data and could be confirmed here. The parameters of the distribution, σ and μ, depend on the cell number and can - like in previous studies - be described by power laws. While μ is well represented by a simple power law with a correlation coefficient of R = 1.00 (fit for p = 2 to 10, else: R = 0.97), we varied the power law for the fit with σ as it apperently is not best represented by a simple power law giving a straight line in the double logarithmic presentation. Despite a correlation coefficient of 0.98 for the simple power law, the modified power law (Equation 4) fits best with a correlation coefficient of 1.00. The constants are given in Table 1. THEU also applied a modified power law, but that one did not change the correlation coefficient in our case, while the addition of another factor did.

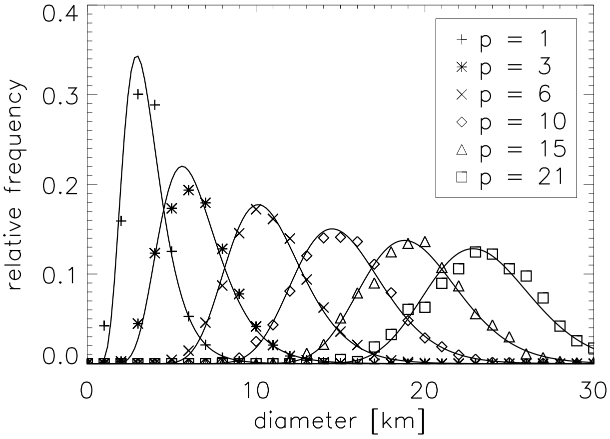

Figure 6. Rain area size distribution with respect to cell number p. The size is given in terms of the equicircle diameter D.

$$F(p) = \frac{e^{\left(-\frac{(ln(p)-\mu)^2}{2\cdot\sigma^2}\right)}}{\sqrt{2\pi}\cdot p\cdot\sigma} \qquad (2)$$

$$\sigma = a_1 \cdot p^{b_1} \qquad (3)$$

$$\mu = a_2 \cdot p^{b_2} \cdot x \qquad (4)$$

$$x = 1 - a_3 \cdot p^{b_3} - \frac{a_4}{p}$$

a_1	a_2	a_3	a_4
0.38	4.32	0.61	0.14
b_1	b_2	b_3	
-0.33	0.33	0.06	

Table 1. Constants of Equations 3 and 4.

3 GROWTH PROCESSES AND RAIN AREA DEVELOPMENT

The main part of the study deals with the growth processes of individual rain areas and associated rain rates. Cluster growth is hereby related

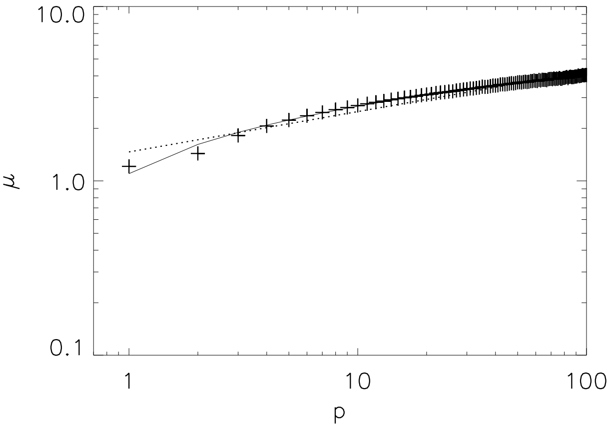

Figure 7. Parameter μ of the area size distribution, approximated modified power law (solid line, Eq. 4). Also shown is the fit to a standard power law (dotted line)

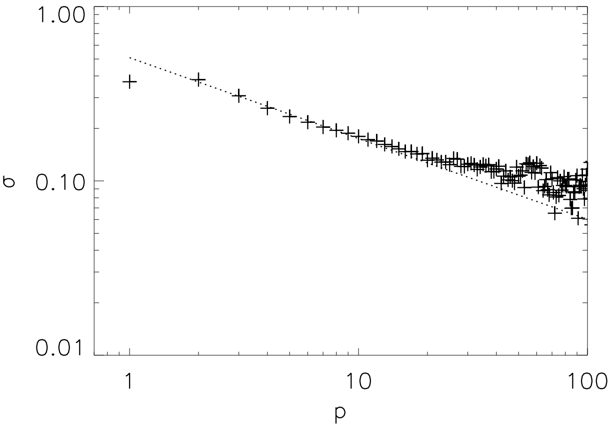

Figure 8. Parameter σ of the area size distribution, approximated by a power law (Equation 3).

to the number of embedded cells. A cluster develops within a time step of five minutes from an n-cell cluster to an m-cell cluster. The whole life cycle of convective rain areas comprises five different life stages, which can be identified immediately by visual inspection (Weus):

(i) genesis ($n = 0$),

(ii) growth ($n < m$),

(iii) stagnation($n = m$),

(iv) decay ($n > m$) and

(v) dissolving ($m = 0$).

Genesis means that the cluster appears for the first time in the radar data. *Growth* is defined as an increase in the number of cells inside a cluster. *Decay* is accordingly a decrease in the number of cells inside a cluster. When *stagnating*, a cluster does not change its size with respect to the cells included. *Dissolving* means the disappearance of a cluster within one time-step.

3.1 Transition probabilities

We applied two different approaches to the growth process (Weus). The first of them differentiates directly internal growth and merging or splitting processes (*cluster-based approach*), while the other, which is considered here, concentrates on the transitions ($n \rightarrow m$), without distinguishing between internal processes and interactions (*transition-based approach*). This way, we have for each transition from the initial cluster n to any successor m one individual transition process. Genesis ($n = 0$) and dissolving ($m = 0$) are also counted as a transition process. All transitions from a cluster with cell number n to one with cell number m were counted and inserted in a two-dimensional array, the transition matrix (Figure 9), of size $n_{max} \times n_{max}$, with n_{max} being the maximal number of cells taken into account. The total number of transitions from n to m maxima is shown as a hundredth. The diagonal colored in dark grey represents the stagnating clusters. Growth can be found below that line, decay above it. In both parts, above the diagonal and below it, the highest values are marked in light grey. Within the growth part, highest values can always be found in the transition from n to $m = n + 1$. In the decaying part, the picture is more variable: clusters of all sizes develop mainly to single cells ($m = 1$), while the second most likely transition is n to $m = n - 1$. As a conclusion, we may state that growth and decay take place preferably by one cell within a time step of five minutes (Weus).

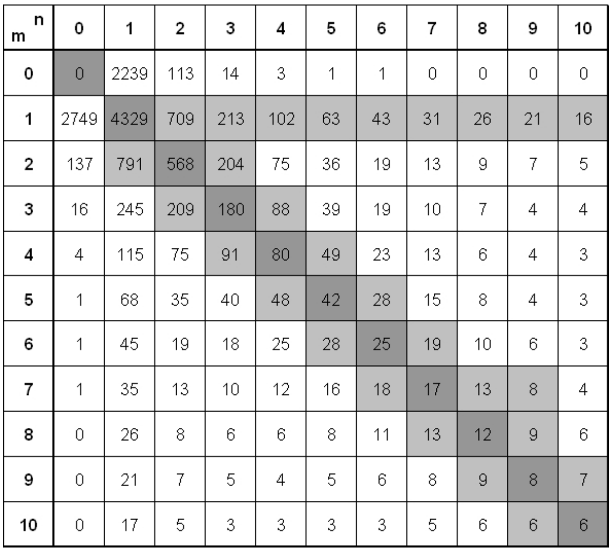

n m	0	1	2	3	4	5	6	7	8	9	10
0	0	2239	113	14	3	1	1	0	0	0	0
1	2749	4329	709	213	102	63	43	31	26	21	16
2	137	791	568	204	75	36	19	13	9	7	5
3	16	245	209	180	88	39	19	10	7	4	4
4	4	115	75	91	80	49	23	13	6	4	3
5	1	68	35	40	48	42	28	15	8	4	3
6	1	45	19	18	25	28	25	19	10	6	3
7	1	35	13	10	12	16	18	17	13	8	4
8	0	26	8	6	6	8	11	13	12	9	6
9	0	21	7	5	4	5	6	8	9	8	7
10	0	17	5	3	3	3	3	5	6	6	6

Figure 9. Transition matrix for all 17 analysed days. Displayed are the numbers of transitions $n \rightarrow m$ in hundredth.

3.2 Life span distribution

The life span of a track is defined as the time from genesis over all growth processes till the dissolving of the cluster. Because of the various interactions, the life span is not related to a specific cluster, but rather to a set of clusters that belong together in such a manner that they are successors or precursors of each other. A cluster has to be tracked at least once to be referred to as a track. The minimum life span is consequently 15 minutes, as each transition process is assigned to a 5-minutes interval (e.g. genesis, growth, dissolving). About 10 % of all clusters have neither precursor nor successor, they could not be tracked and, thus, have a life span of just ten minutes comprising genesis and dissolving. The frequency distribution of the life span of a track can again be fitted to a power law (Fig. 10, Eq. 1) with a correlation of R ≅ 1.00. The absolute value of the parameter $b = -2.26$, which is the slope of the double logarithmic representation, indicates that the short life spans are dominant. About 80 % of the tracks have a life span of 15 to 35 minutes. This dominance of short life spans is even more obvious if considering only single-cell-tracks. The regression calculated for all life spans with a frequency of more than $5 \cdot 10^{-5}$ yields a value of b = -3.95 with a correlation coefficient of R ≅ 1.00.

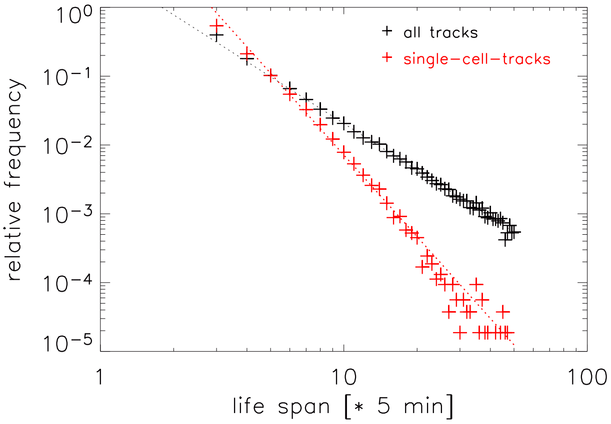

Figure 10. Life span distribution for all days and all tracks as well as for only single-cell tracks.

3.3 Time-series of single-cell-tracks

Conerning the temporal development, we, in a first instance, concentrated on single cells, which represent the majority of all tracks. The mean temporal development of the area integrated rain rate (AIRR) was investigated and an analytical description was found, which only depends on the life span of the track.

The AIRR time series, normalised with the total life span l_d and the maximum amplitude A_{l_d}, is plotted in Figure 11. It reveals the basic structure of the AIRR temporal development. The data was fitted both by a sinus function and a parabola. Details can be found in WEUSTHOFF AND HAUF (2008a). This was done for life spans lower than $16 \cdot 5\,\mathrm{min}$ as longer time spans occur rather seldom (cf. Figure 12). The parabola was identified to describe the time series best with a correlation coefficient of R = 0.96. The resulting function only depends on the life span:

$$\begin{aligned} \bar{r}_{l_d}(t) &= \frac{4 \cdot \beta}{l_d} \cdot \left(l_d \cdot t - t^2\right) \qquad (5) \\ \beta &= 0.28\,mm\,/\,(5\,min)^2 \end{aligned}$$

The integral of that function over the whole life span yields the area and time integrated rain sum (ATIRS). The ATIRS, plotted against

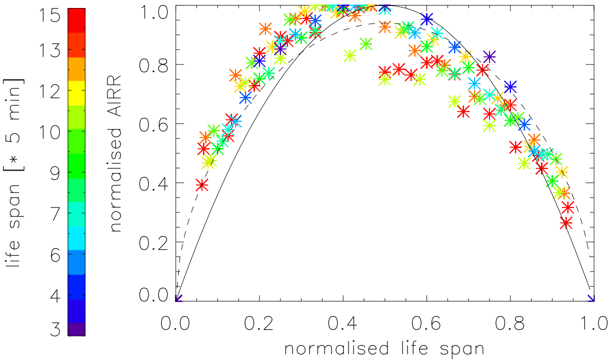

Figure 11. Temporal development of area integrated rain rate of single cells, normalized, fit to sinus (dashed line) and parabola (solid line).

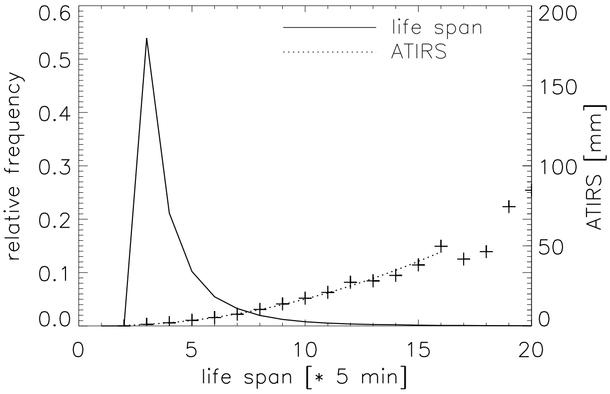

Figure 12. Life span distribution for single-cell tracks and area and time integrated rain sum (ATIRS) of a track with respect to life span.

life span in Figure 12, can be described by a quadratic function of life span:

$$\begin{aligned} R(l_d) &= \frac{2}{3} \cdot \beta \cdot l_d^2 \\ &= 0.19 \cdot {l_d}^2 \end{aligned} \qquad (6)$$

Thus, we found a surprisingly simple analytical description for the mean life cycle of post-frontal, precipitating convective clouds. As stated above, the analysis is currently extended by the other two track types. Preliminary results show, that those more complex track types can be described by comparable simple analytical functions of life span.

4 CONCLUSIONS

In this paper, we present exemplarily results of an extensive analysis of post-frontal precipitation fields over Central Europe. Simple analytical functions and distributions were found which describe the basic characteristics of the precipitation structures in terms of a) the geometrical structure and b) the temporal development of individual rain areas and their properties. Those are in detail:

(i) The rain area size distribution, which can be described by a lognormal function for each cell number (Eq. 2). The parameters σ and μ follow a power law with respect to the cell number (Eqs. 3 and 4).

(ii) The time series of the area integrated rain rates (AIRR) of single-cell-tracks, which can be described by a parabola as a function of life span (Eq. 5).

(iii) The area and time integrated rain sum (ATIRS) of single-cell-tracks, which is a quadratic function of only the life span (Eq. 6).

(iv) Transition probabilities derived by the transition matrix for transitions $n \rightarrow m$.

Thus, the main parameters to describe the post-frontal precipitation field are the cell number of the rain areas and the life span of the tracks. The cell number distribution follows a power law (Eq. 1), as does the life span distribution for all tracks and for only single-cell-tracks. Together with the results from previous studies (THEU, WEUS), the basis is given for a stochastic modelling of the precipitation field in that specific synoptic situation. Besides the possibility to forecast precipitation probabilities, such a model can provide relevant information for hydrological models (e.g. areal precipitaion, rain duration).
The results concerning the geometrical structure based on radar data are well in line with those of other authors like MESN and THEU, whose studies lead to the current work. Similar investigations are performed by GRYSCHKA

ET AL. (2008), who analysed the size distribution of cumulus clouds due to shallow and deep convection by means of radar data, satellite pictures and LES model results. The temporal development of individual shower structures, in contrast, has not been addressed so far in a comparable way. The results are promising as they reveal a simple underlying law for an apparent chaotic precipitation process.

Acknowldgements

The *German Research Foundation* (DFG) funded this work through its priority program *Quantitative Precipitation Forecast* under grant number HA 1761/5-2. The RZ composite used in this study was provided by the *German Weather Service* (DWD), which is kindly acknowledged.

5 BIBLIOGRAPHY

BARTELS, H., E. WEIGL, T. REICH, P. LANG, A. WAGNER, O. KOHLER AND N. GERLACH, 2004: *Projekt RADOLAN - Routineverfahren zur Online-Aneichung der Radarniederschlagsdaten mit Hilfe von automatischen Bodenniederschlagsstationen (Ombrometer)*, Abschlussbericht, Deutscher Wetterdienst, Offenbach, 111 S.

GRYSCHKA, M., B. WITHA AND D. ETLING, 2008: *Scale analysis of convective clouds*, Meteorol. Z., submitted

MESNARD, F. AND H. SAUVAGEOT, 2003: *Structural characteristics of rain fields*, Journal of Geophysical Research, **108**(D13), 4385, dOI:10.1029/2002JD002808

THEUSNER, M., 2007: An Investigation on Small Scale Precipitation Structures, Dissertation, Institut für Meteorologie und Klimatologie, Universität Hannover, 95 pp.

WEUSTHOFF, T. AND T. HAUF, 2008a: *Basic characteristics of post-frontal shower precipitation rates*, Meteorol. Z., submitted

—, 2008b: *The life cycle of convective shower cells under post-frontal conditions*, Quarterly Journal of the Royal Meteorological Society, accepted

THE MICROPHYSICS OF TROPICAL OCEANIC DEEP CONVECTION

Paul T. Willis[1], Heymsfield, A. J.[2], Bansemer, A.[2], Pilson, B.[3]

[1] CIMAS-NOAA/HRD-U of Miami, Miami, FL 33149
[2] NCAR/MMM, Boulder, CO 80301
[3]SPEC, Inc, Boulder, CO 80301

1.0 INTRODUCTION

The importance of convective clouds over the tropical oceans has come to the fore in recent times. Their role in the heat budget of the atmosphere, and their importance as the building blocks of mesoscale and larger scale systems, continues to be widely appreciated. In the fall of 2006 NASA mounted a field campaign where one of the goals was to obtain airborne measurements of the vertical structure, and the evolution of the cloud and hydrometeor microphysics and precipitation in tropical oceanic convective clouds. The experiment was called NAMMA and the NASA DC-8 aircraft was a primary research tool. It is the purpose of this study to accomplish a detailed examination of a series of aircraft transects of a specific case study cloud. We will attempt to convey to you the extraordinary exquisite detail of the microphysical measurements made in this cloud.

2.0 INSTRUMENTATION

The pertinent instrumentation on the NASA DC-8 used in this study included the aircraft navigation and state parameters. The high resolution vertical, ad horizontal air velocities are from the MMS system. The cloud structure and context from the JPL APR-2 radar system. The microphysical instrumentation included the SPEC 2DS(stereo) probes measuring particle size distributions and black and white images from vertical orientation (V) and horizontal orientation (H) photodiode arrays of 128 elements of 10 um. The DMT CAPS probe and PIP probes include a scattering spectrometer for cloud droplet, and small ice concentrations, the CIP probe array – 64elements of 25 um, and the PIP array 64 elements of 100 um. Further details on the instrumentation can be found at http://namma.msfc.nasa.gov.

3.0 DESCRIPTION OF CLOUD AND SAMPLING

The subject cloud of this study is a deep convective cloud complex nominally at 9.9 degrees north latitude, and 29.5 west longitude at 1815 UTC. The measured updraft/downdraft velocities, and the sampling temperatures of the cloud transect series are plotted in Fig. 1. The total sampling timefor the three cloud transects is 1000 s, or about 17 minutes. Cloud pass 1 is at +10.7 deg C, passes 2 – 3 at -3 deg C, pass 4 at -11.3 deg C, and pass 5 at -21.3 deg c. The updrafts are typically +10 m/s and the downdrafts -3 m/s. A dropwindsonde taken in the environment of the cloud is plotted on a skew-T in Fig. 2. The cloud base is near 950 mb, and the the positive buoyancy at 300 mb is still several deg C, indicating that the convection probably extends to near the tropopause-definitely deep convection.

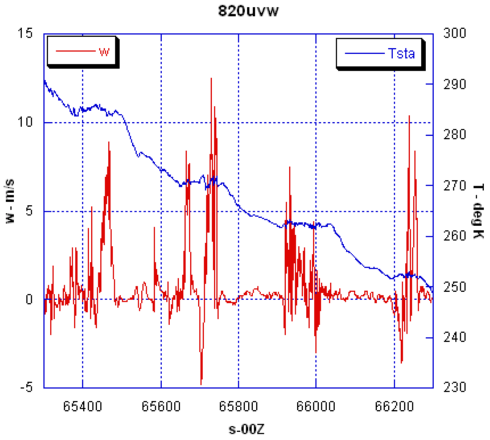

Fig.1 Vertical air velocity and temperature

The radar height slice (Fig. 3) indicates that the upshear side of the cloud is generally to the north, and downshear to the south. The environmental wind profile of Fig2 indicates upshear generally to the north. The shear between the wind at cloud base to 450 mb is from NNE to SSW. The sampling flight track is plotted in Fig. 4, with the cloud locations marked. The sampling was approximately along the shear vector (N-S line).

We think that the four, or five passes over a range of temperatures sample the same equivalent location in the structure of the cloud system. Each cloud pass with the microphysical instruments samples a one dimensional thread at particular location and time in the cloud system. This is far from a full four dimensional sample. The convective cloud is obviously not steady state, nor homogenous, nor stationary, yet at any given instant the components of the cloud system (i.e. updraft-downdrafts, spent cells, etc.) all coexist within the cloud structure. We feel that the sampling done here represents nearly the best that can be done presently. Even with the sampling limitations, these data provide a real data point for the complete microphysics of a deep tropical oceanic convective cloud, that can be compared with statistical and modeling results.

4.0 CONCEPTUAL MODEL

The following outlines the essential features of our conceptual model of this tropical oceanic deep convective cloud system. The updrafts are initiated below cloud base by boundary layer features, and extend as entities to near the tropopause. Between cloud base and 0 deg C, there is a deep layer of warm rain processes. The condensate made available by the updraft forms cloud droplets on the marine CCN aerosol. Drops form by stochastic coalescence balanced by collision breakup as the rain distributions develop. A fraction of the large drops start to fall out, since the peak updrafts are of the same order as the terminal velocities of the larger drops. Condensation feeds the cloud droplet spectrum, fallout and collision breakup and stochastic collision coalescence form the large hydrometeor spectra.

Even small amounts of vertical shear of the horizontal wind serves to organize the cloud. and impacts the details of the evolution of the microphysics. Fresh updrafts form on the upshear side of the cloud, and as the convective instability is spent, move downshear thru the cloud. Older cells. And hydrometeors with trajectories higher in the cloud are downshear of the active new updrafts. Even active updrafts tend to detrain hydrometeors on the downshear side of the updraft. Once the convective buoyancy of a cell is spent, often near the tropopause, large volumes of hydrometeors are detrained downshear. The entire spent cell moves downshear.

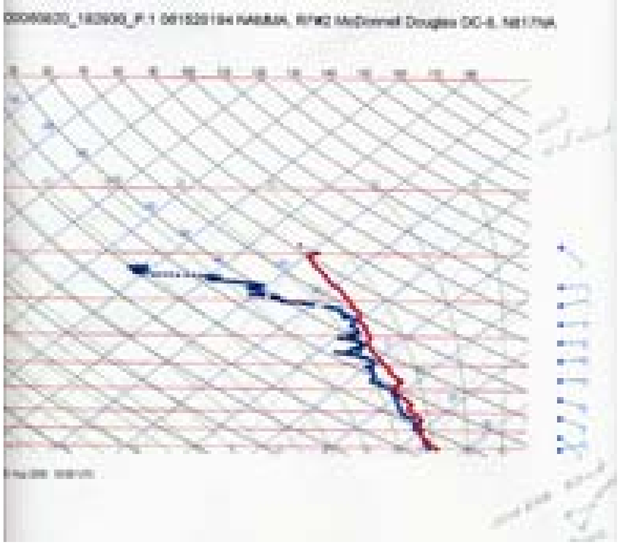

Fig. 2 Dropwindsonde through cloud environment

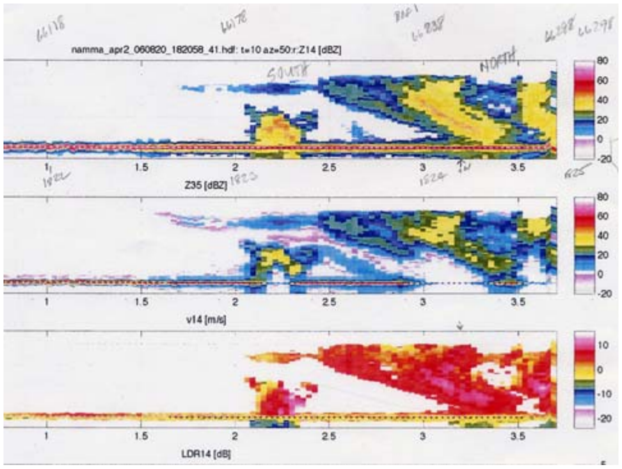

Fig.3 2 wavelength radar and LDR thru cloud

5.0 RESULTS

This section will present the results of an analysis of the particle images and the resulting particle size distributions for three cloud transects – 2C, -11C, and -21C. The focus will be on what is the cloud makeup as the updraft arrives at -2C, and then what happens in the updraft and in other parts of the cloud at higher colder levels.

5.1 cloud transect at -2C

The detailed temperature and vertical air velocity are plotted in Fig. 5 for this cloud transect at -2C. There are two updraft parts to this cloud and the six locations of detailed imagery and size distributions are marked with solid triangles. The first location is at 65624 in the cloud (Fig. 6). Keep in mind that the sampling temperature is -3C or warmer, and this location in the cloud is clearly nearly all ice. This series of detailed figures are all constructed the same way, the (a) frame plots the one second distributions from the PIP, CIP, and the particle spectrometer on a log-log format with a sample strip of CIP and PIP images. Frame 6b is a 1 sec size distribution composite for three probes – 2DS-vertical ,CIP, and PIP in a semi-log format, so that exponential distributions plot as a straight line. The image samples from the three probes in 6c, 6d, and 6e are completely raw data, i.e. no shattering or other artifact removal. The collapse of the out of depth of field particles to a donut shape can be seen. In the 2DS probe processing an adjustment to the sample volume was made for these particles. The agreement between the 2DS and the CIP is excellent from 20 -1100 um. There is a 2 – 3 decade mismatch between the small end of the 2DS and CIP imaging probes and the large end of the FSSP like small particle spectrometer. In all cases the abscissa diameter is a maximum dimension. The remarkable feature of the particles at this location is the intricacy of the surface , or edge, features of the large aggregates. At this older downshear location in the cloud, these hydrometeors must have had a trajectory from higher colder regions of the cloud.

Fig 7 presents data from a region of medium size (2-3 mm graupel). The surface of the graupel is smooth, though there is evidence some hydrometeors are aggregates of two, or more, near spheres to form a single larger graupel. At this location downshear from an updraft, there are virtually no smaller particles present in the 2DS sample frame, even though the distributions show some smaller particles (possibly breakup artifacts on probe tips?). The two decade mismatch also appears in Fig. 7a.

The data in Fig. 8 are from a location just on the downshear edge of a significant updraft. This location is a transition from large graupel in an environment of no smaller cloud particles to graupel collocated with very high concentrations of smaller droplets. Or, aregion where collection is complete, to a region where the supply of cloud droplets by the updraft is much greater than the collection on the graupel The graupel distribution is near exponential from 5 mm down to 0.4 mm, then a knee to a steeper exponential distribution to very high concentrations of small cloud droplets. There is clear evidence in the CIP images of drop fracture upon freezing. The 2+ decade small end mismatch still exists. This transition region to small droplet supplied by updraft may not be homogenous, even over the one s sampling.

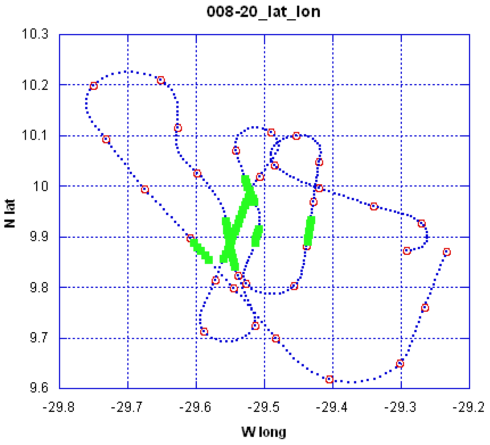

Fig 4 Sampling flight track 1 min ticks-red, six active convection areas, in green

Fig. 9 and Fig 10 are in a significant downdraft region downshear of another updraft. The distributions from 0.3 mm to 2 mm are quite flat exponentials, with fairly low concentrations of cloud droplets, virtually noneappearing in the 2DS sample image. Fig 10 in the downdraft, but closer to an active updraft is similar, but with a higher concentration of 0.4 mm droplets appearing. Still a 2-3 decade mismatch appearing, particularly in Fig. 10.

Fig11 is taken in the peak of the updraft (12 m/s) and, unlike the previous locations, is characterized by completely liquid water coming up from below. There is almost perfect agreement between the three probes from 1. mm down to 50 um. There is some problem with adequate sample volume, and artifact (splash) rejection in the sampling of larger raindrops.

There appears to be one exponential distribution from 5 mm down to 0.8 mm, and then a much steeper distribution in cloud droplets to 30 um and below. There is almost a perfect match between the 2DS and the cloud spectrometer. Since this section of cloud is all water the water content calculations are unambiguous, Fig. 12 shows the contribution of each size interval to the liquid water content from the 2DS and a composite of the CIP and PIP probes. The liquid water content from this composite is about 4 g/m3, and the adiabatic water content is 7 g/m3. There is a significant contribution at 150 um, and a second range of significant contribution from 900 um to larger sizes. The plot for the 2DS shows the same result, but it can not show any contribution beyond it's size range of 2 mm. The contribution around 100 um is largely due to the condensation supply from the updraft, and the larger diameter contributions are due to the efficient collision coalescence process. The conversions to ice, of course, will change this picture.

5.2 cloud transect at -11C

Fig. 14 is taken in the upshear edge of the updraft. The updraft on this pass is not quite as strong as on the previous pass, possibly not centered precisely on the center of the updraft. Graupel is still present but is typically about 0.5mm in size. Aggregates do not appear in the rising updraft parcels, The surface of the graupel is fairly smooth, but is just starting to show slight surface features. There is evidence of fragments of drops shattered upon freezing. There are copious quantities of cloud droplets (and possibly small ice particles). There is almost a perfect match at the large end of the cloud droplet spectrometer and the small end of the CIP and 2DS. The updraft is evidently supplying condensate droplets faster than the small graupel can deplete them. Fig 15 is located in the strongest part of the updraft and shows essentially the same features as Fig. 14. The graupel may be slightly larger. Fig 16, also in the main updraft region, is fairly similar, but shows some evidence of ice of more pristine ice habits, i.e. capped columns. Fig. 17 is located right on the downshear edge of the primary updraft region. The concentration of cloud droplets is still similar to the fresher updraft regions. The surface of the graupel is starting to display significant surface features and texture, some spicules.

Fig. 18 and Fig. 19 slightly further downshear from the fresher updrafts signal several major changes in the character of the particles and the size distributions. First, all of the cloud droplets (and/or very small ice) are completely gone. This is obvious in the images, and in the size distributions. The graupel, and rimed hydrometeors are replaced by aggregates. The surface features are now very pronounced, spicules and needle like protuberances are ubiquitous on the larger rimed hydrometeors (graupel). Second, pristine ice habits have become almost predominant - columns and capped columns. The ice particle generation and growth mechanism has changed from one involving drops in the active updrafts, to one involving deposition growth of more pristine habits. The terminal velocities of most of these ice particles could not support particle growth and evolution trajectories from very much higher, and colder, in the cloud; particularly for the 200 um columns and capped columns. Fig. 20 is located on the downshear edge of the cloud, far removed from the other figures presented for this cloud transect. Many of the larger hydrometeors exhibit a lot of linear structure and very complex structural features. There is less evidence here of pristine recognizable ice habits. Though we would classify these as aggregates, or rimed aggregates, it is a somewhat open question what evolution led to this complex structure and convoluted surface features.

Note that the size distributions of the cloud spectrometer, plotted as a blue line in the first panel of each of the composite figures, do not really change much in the figures across this cloud pass. This is true even when the concentrations of small particles present in the images of the 2DS change radically, and the small end of the imaging probes matches the large sizes of the cloud spectrometer curve. Also, particularly in Fig. 20, the first few bins on the small end of the 2DS size distributions often seem inordinately high. Drop breakup on the cloud droplet spectrometer, and the sample volume used in the first few bins of the 2DS may need to be revisited.

5.3 cloud transect at -21C

The temperature trace and the vertical air velocity trace are plotted in Fig.21. The updraft maxima in this transect look similar to the maxima in the first pass (Fig. 5), so the pass is well centered on the active updrafts. This analysis examines the microphysical particle makeup downshear of the active updrafts, on the downshear edge of the active updrafts, in the active updrafts, and in a weakness between the active updrafts.

Fig. 22 shows data from a downdraft region on the downshear edge of the cloud. The hydrometeors are complex very large aggregates, as well asmore pristine habits (columns and capped columns. Stellar dendrites, that might be expected here seem absent. The distributions may be characterized by one exponential slope for the large complex aggregates, and a steeper slope for the small ice of more pristine habits. Fig. 23on the downshear edge of the updraft, displays similar characteristics, but the aggregates possibly are not as large overall as in the older downdraft.

Fig. 24 just into the active updraft shows possibly the return of more nearly spherical graupel like hydrometeors. Small stellar particles appear here. The particle at the bottom of the 2DS images just to the left of center is interesting, a small stellar attached to an assemblage of connected columns (or needles). This structure, like an H, seems to be quite common. Are these capped columns always viewed edge on, or are they some assemblage of needles and columns?

Fig 25 is at the peak of the active updraft. The aggregates in the 2DS image data selected do not appear to be as large, but the PIP image distributions may contradict this. In this updraft the concentrations of small ice are considerably higher than outside the strong updrafts, Fig 26 shows considerable change just one second later, The aggregates in the 2DS are larger, and the small ice concentrations not quite as high.

Fig. 27 is located in a weakness between two active updrafts. The large aggregates in the2DS imagery are considerably larger and more complex, than in previous sections of this cloud transect. The more pristine habits of small ice are not as prevalent. Fig. 28 is right at the peak of the most upshear strong updraft. The surface of the larger ice particles is characterized by spicules and protuberances. The parallel needle and column assemblages are in evidence. No stellar crystals are in evidence.

5.4 relevant microphysics

The updraft parcels arrive at 0 deg C with small to medium raindrops; and with substantial concentrations of smaller cloud droplets (<100 um), sustained by the condensation from the updraft and collision breakup. By -3 to -5 deg C drops begin to freeze and fracture. These frozen drops quickly form graupel in the high concentrations of large cloud droplets. The freezing of the large hydrometeors stops the size limiting effect of collision breakup, and the graupel can grow quickly. This larger graupel is not lofted much higher in the cloud above it's formation level, as the fall velocities are of the same order as the updraft velocities. By the time the updraft reaches -10 deg C, virtually all of the liquid water is gone, except possibly in the very strongest updraft. The large graupel has fallen out and only small graupel is evident (< 500 um). By -20 deg C, the particle makeup is characterized by less rimed, more pristine habits, none, or very little, evidence of any liquid water droplets, essentially no graupel, and large particles with very complex surface structure .

6.0 SUMMARY AND CONCLUSIONS

The very detailed microphysics of a deep convective cloud over the tropical ocean has been examined in relation to the updraft structure at three important temperatures. This should serve as an adjunct to statistical compilations and cloud model microphysics statistics.

A significant amount of ice is found on this cloud transect –at -2C, albeit not in the active updrafts. This ice undoubtedly originated at higher slightly colder temperatures in the cloud, and evolved on trajectories to this level. The strong active updrafts are ice free at -2C. By -10C the ice is well developed in the updrafts, though some liquid small cloud droplets remain. There is evidence that the proto ice is involved with drop freezing and shattering upon freezing. At this point we can not unambiguously distinguish water from ice at the sizes of small cloud droplets. Graupel formation is prolific and rapid, probably starting with drop freezing. The graupel formation and rapid growth is limited to a fairly limited layer warmer than -10C. Although hydrometeors continue to rime, only fairly small graupel is lofted (present) at -10C and colder. By -20C more pristine ice is dominant, and the growth of ice has apparently shifted from something involving drop freezing to some other mechanism, possibly deposition deposition growth on more pristine ice habits.

The study will be expanded in the future utilizing radar data to define the context of the sampling. One warmer level (+10C) and one colder level (-30C) will be added, as well as statistics from other cloud samples. Emphasis will be placed on the water content coherence at the various temperature levels.

Acknowledgements

We acknowledge the NAMMA mission Director Dr. Ramesh Kakar, the NASA Earth Sciences Division, and all of the aircraft flight crews, scientists and engineers that made the collection of these data possible. Partial funding was provided from NASA #NNX06AC67G. Special thanks to S. Paul Bui from NASA Ames who made the MMS updraft data possible, and Dr Eastwood Im from JPL for the APR-2 radar data.

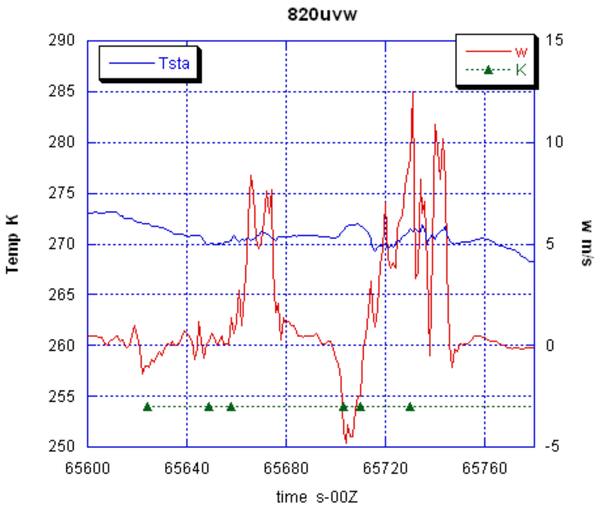

Fig. 5 vertical air velocity and temperature for cloud transect at -2C. locations of microphysics summation figures are indicated in green.

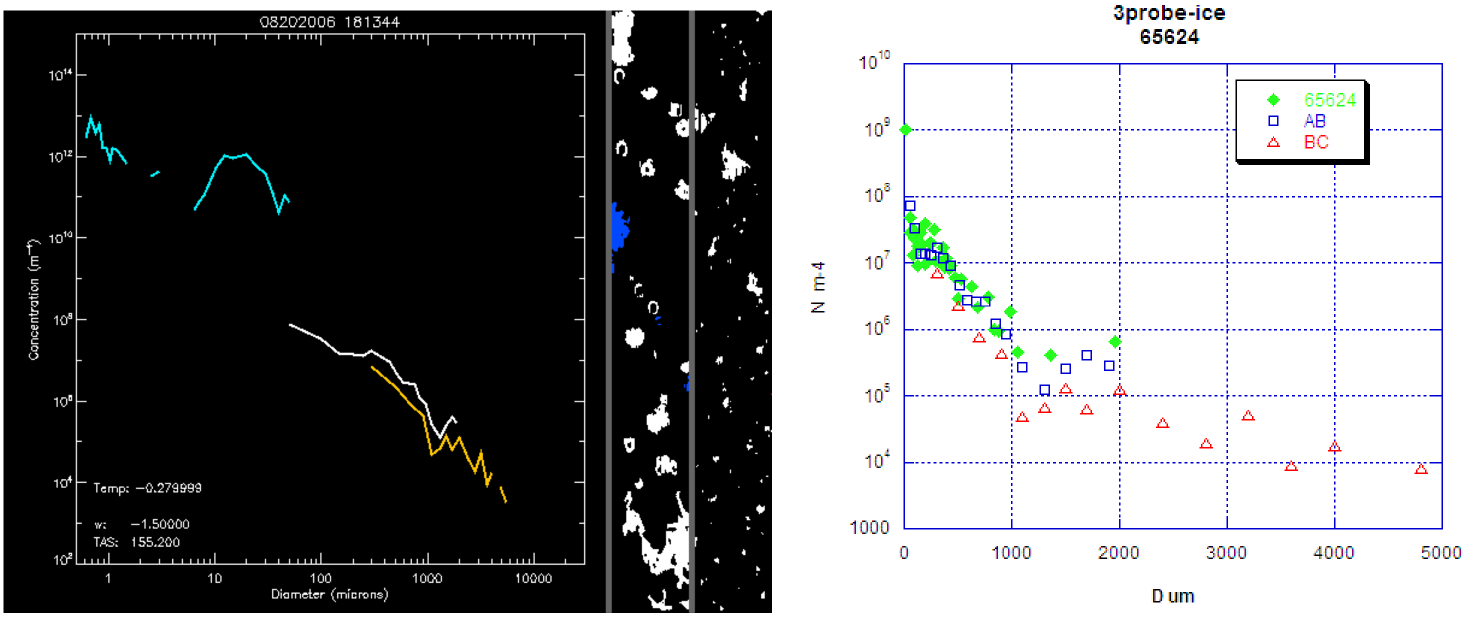

Fig. 6 a & b : left – composite size distributions, scattering particle spectrometer – blue, CIP – white, PIP yellow, image sample strips, width – CIP – 1.625 mm, PIP – 6.4 mm; 3 probe semi-log plot of size distributions, 2DS-V – green diamonds, CIP – blue squares, PIP – red triangles

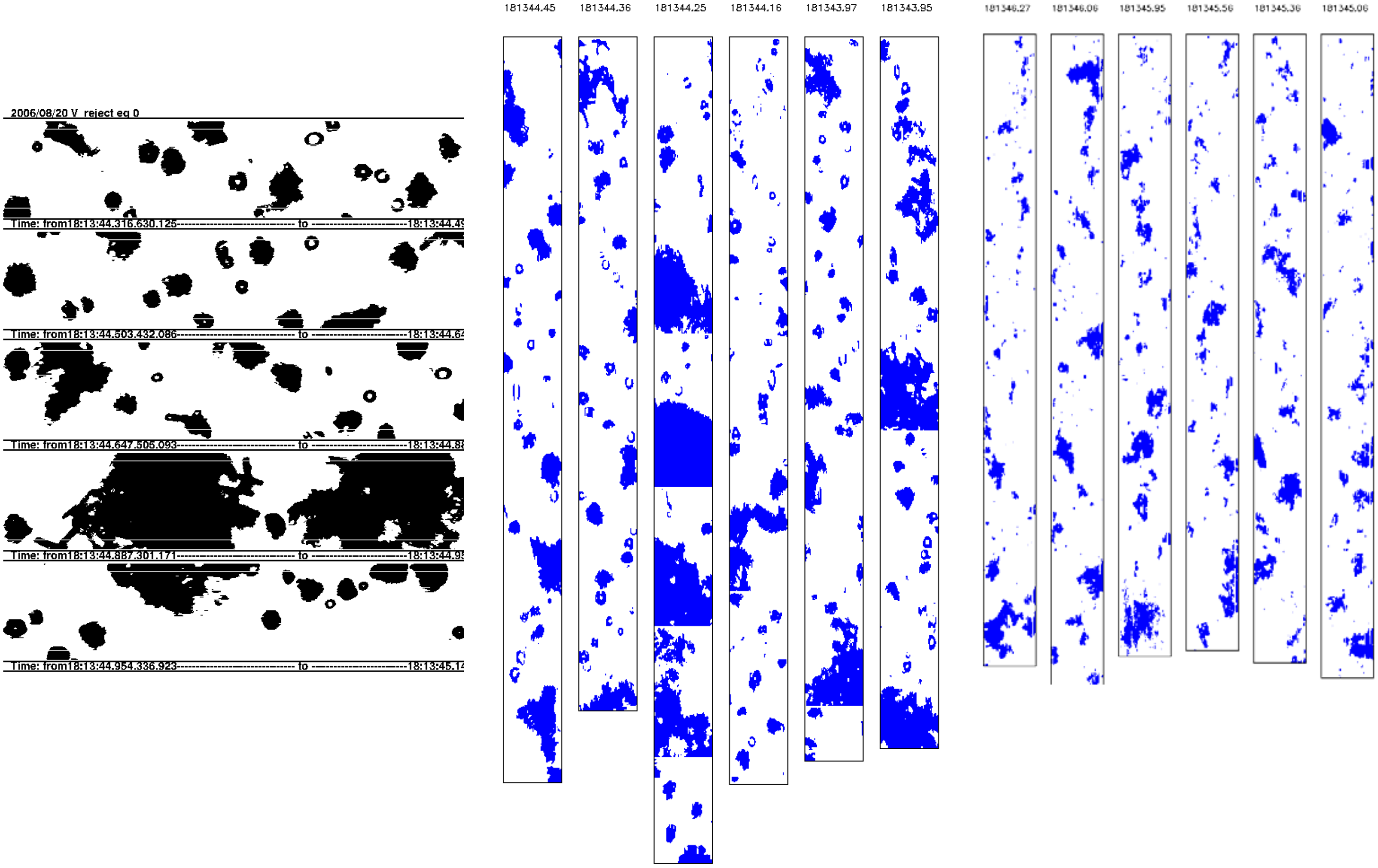

Fig. 6c, 6d, & 6e :2DS-V width – 1,28 mm, CIP width – 1.625 mm, PIP width – 6.4 mm

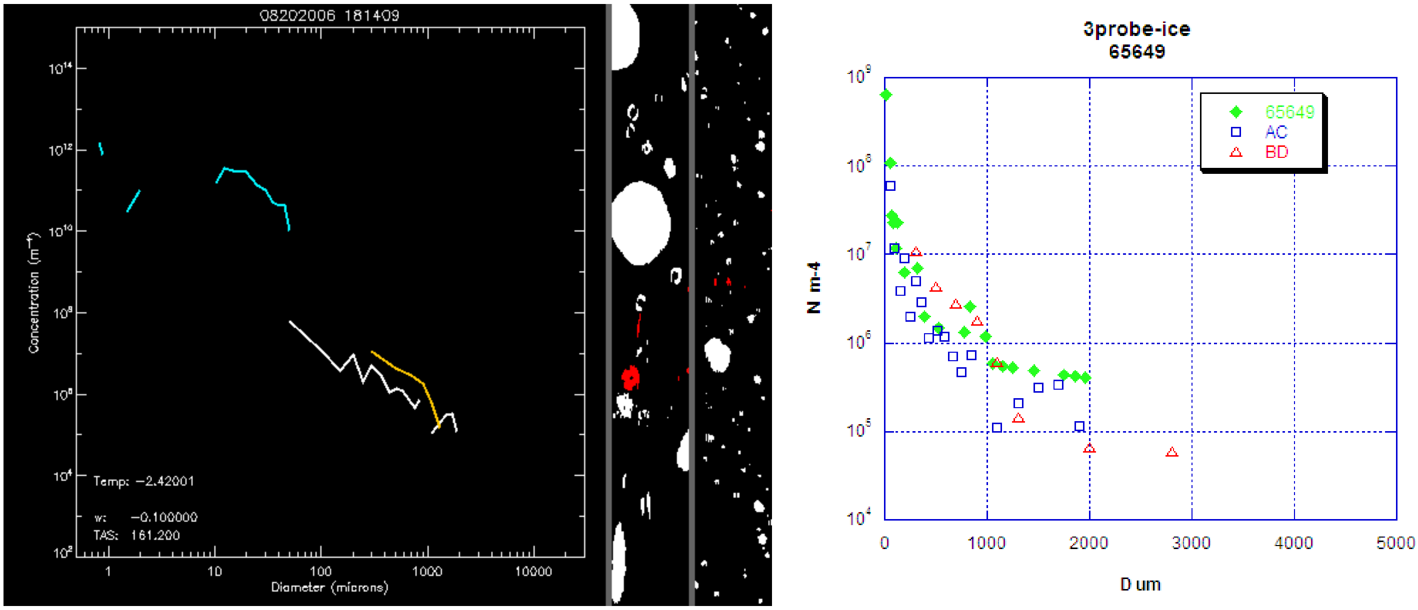

Fig. 7 a & b : left – composite size distributions, scattering particle spectrometer – blue, CIP – white, PIP yellow, image sample strips, width – CIP – 1.625 mm, PIP – 6.4 mm; 3 probe semi-log plot of size distributions, 2DS-V – green diamonds, CIP – blue squares, PIP – red triangles.

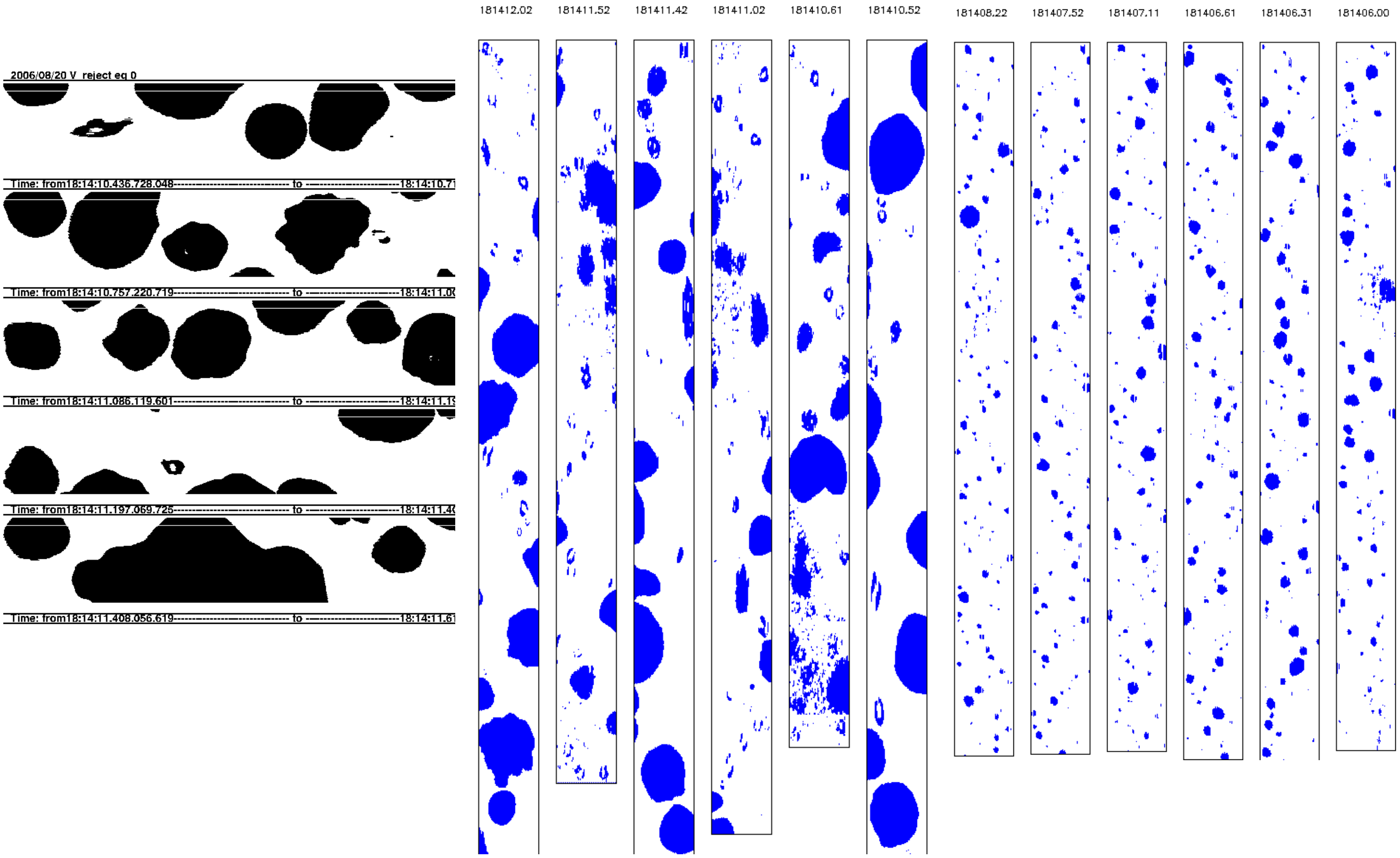

Fig. 7c, 7d, & 7e :2DS-V width – 1,28 mm, CIP width – 1.625 mm, PIP width – 6.4 mm

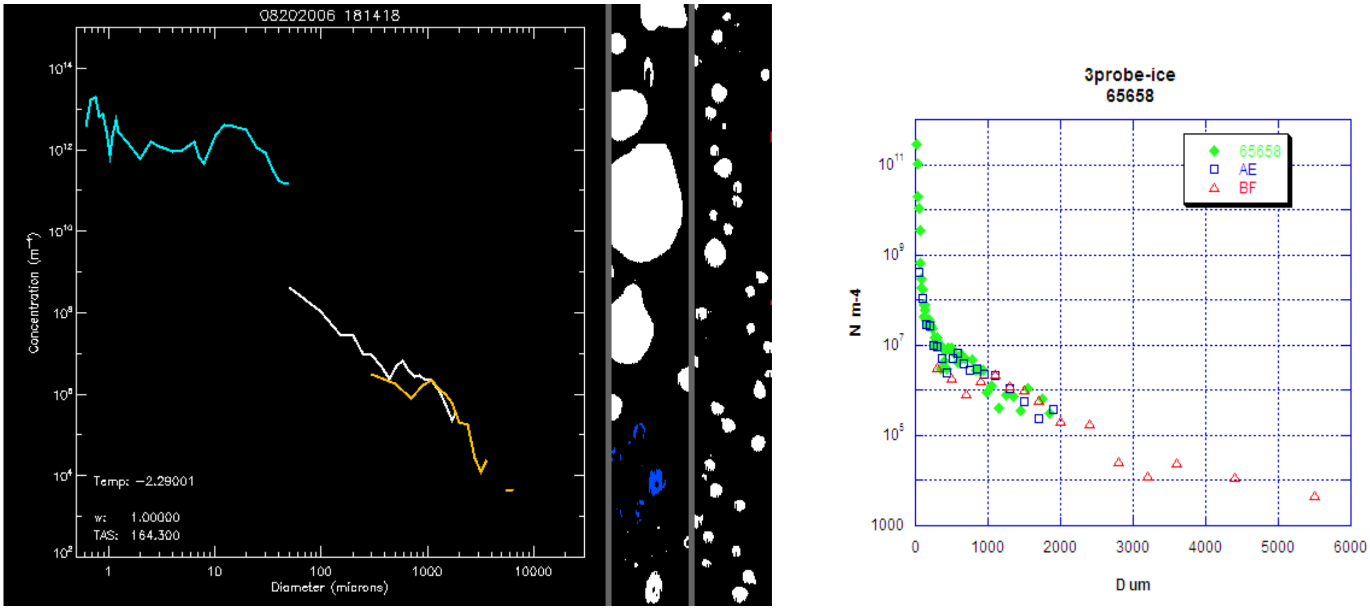

Fig. 8 a & b : left – composite size distributions, scattering particle spectrometer – blue, CIP – white, PIP yellow, image sample strips, width – CIP – 1.625 mm, PIP – 6.4 mm; 3 probe semi-log plot of size distributions, 2DS-V – green diamonds, CIP – blue squares, PIP – red triangles

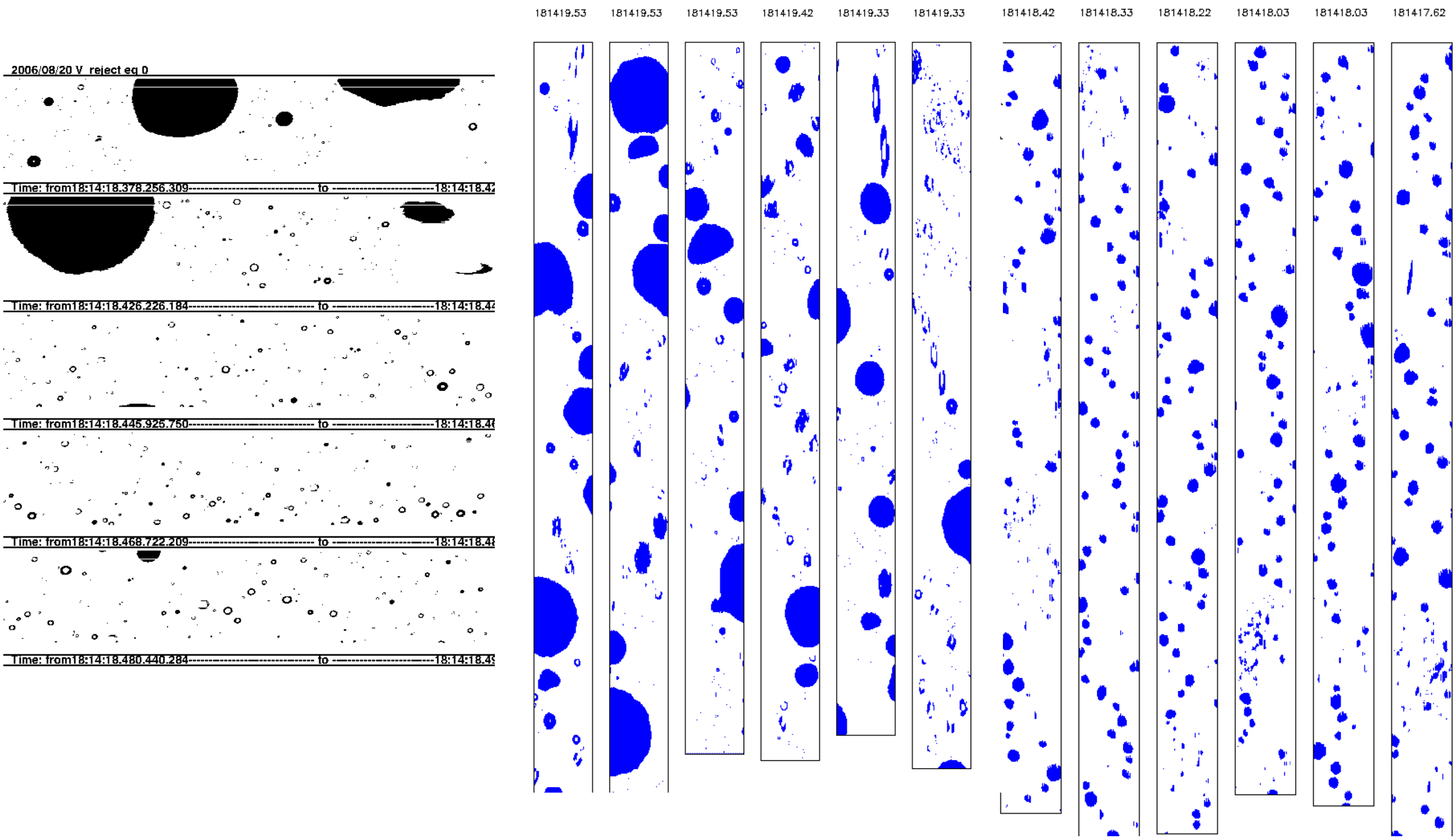

Fig. 8c, 8d, & 8e :2DS-V width – 1,28 mm, CIP width – 1.625 mm, PIP width – 6.4

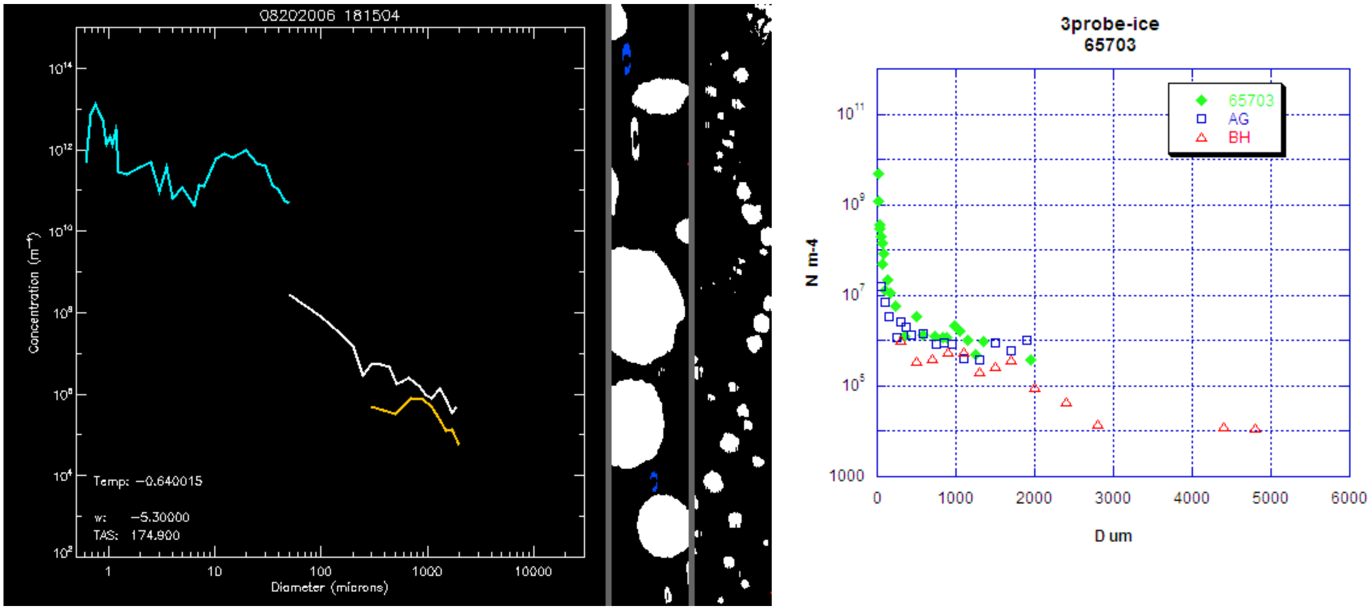

Fig. 9 a & b : left – composite size distributions, scattering particle spectrometer – blue, CIP – white, PIP yellow, image sample strips, width – CIP – 1.625 mm, PIP – 6.4 mm; 3 probe semi-log plot of size distributions, 2DS-V – green diamonds, CIP – blue squares, PIP – red triangles

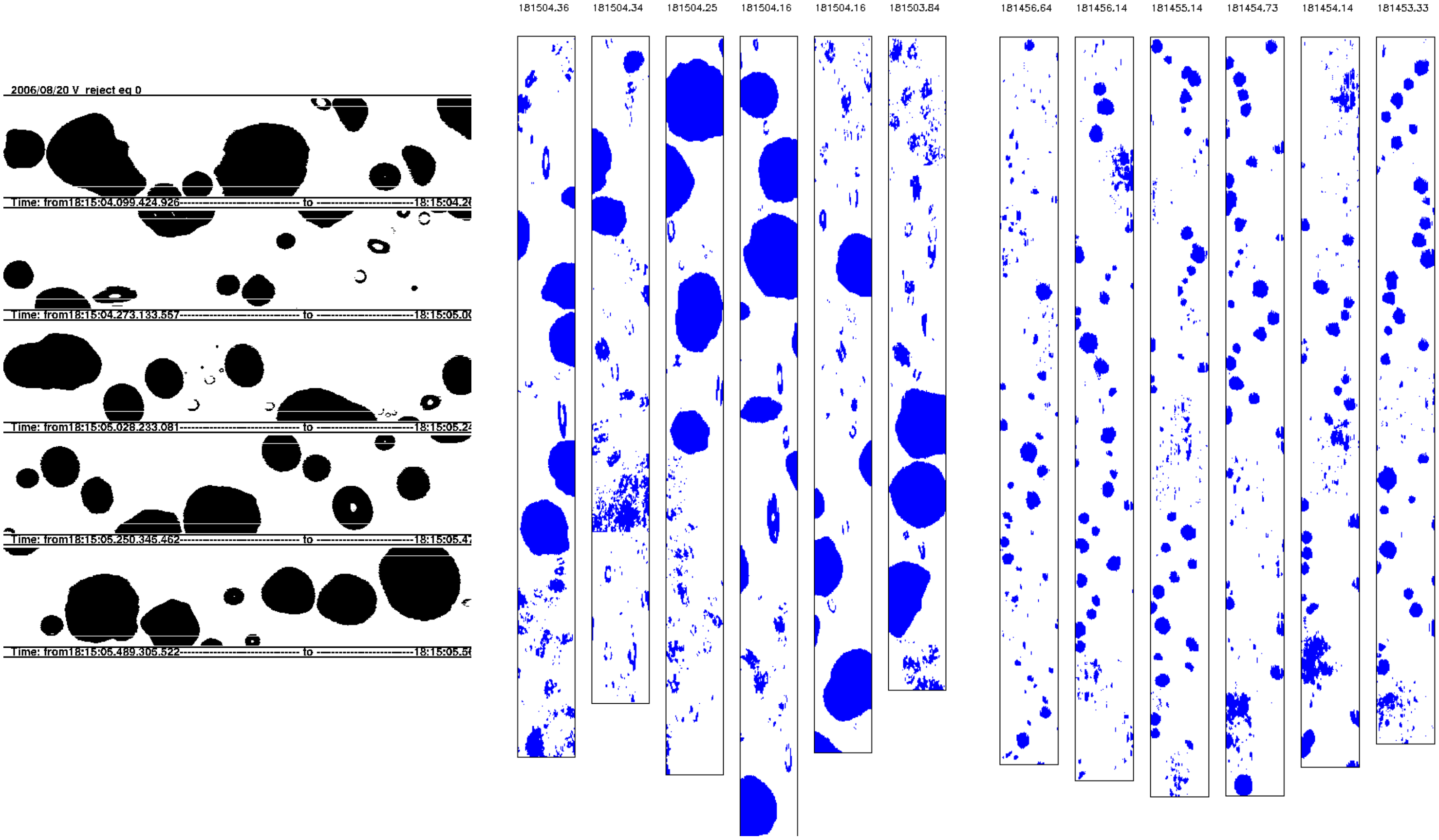

Fig. 9c, 9d, & 9e :2DS-V width – 1,28 mm, CIP width – 1.625 mm, PIP width – 6.4 mm

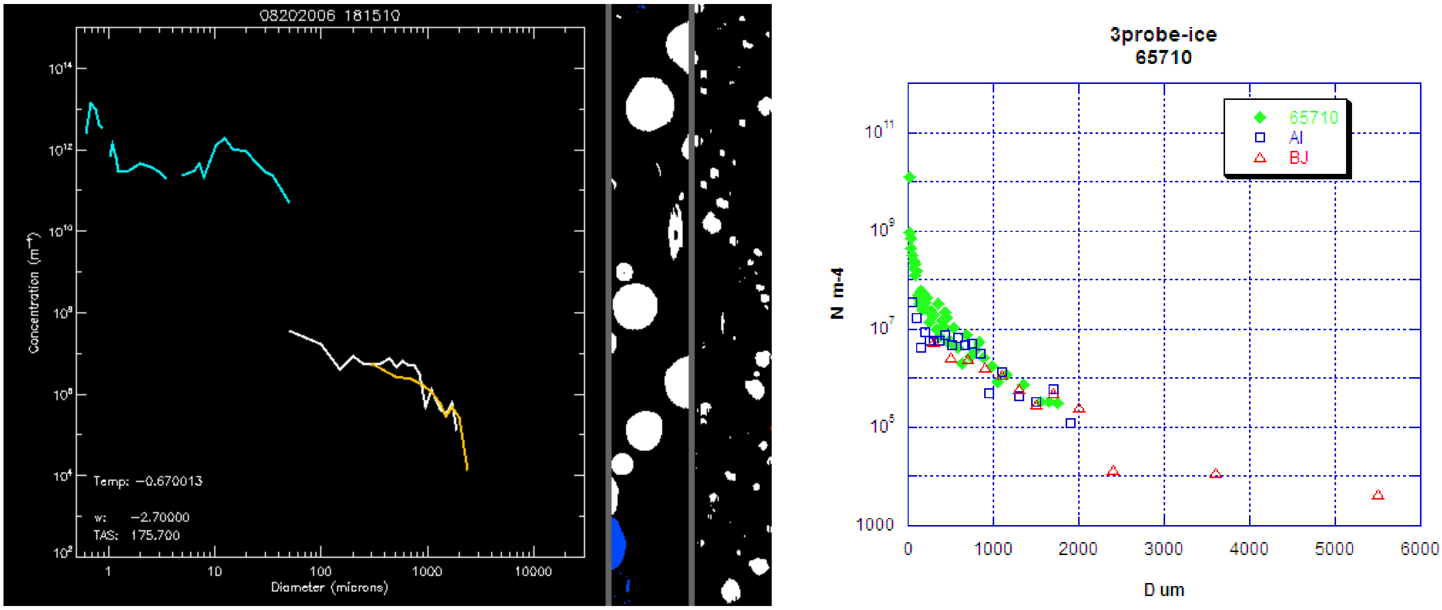

Fig. 10 a & b : left – composite size distributions, scattering particle spectrometer – blue, CIP – white, PIP yellow, image sample strips, width – CIP – 1.625 mm, PIP – 6.4 mm; 3 probe semi-log plot of size distributions, 2DS-V – green diamonds, CIP – blue squares, PIP – red triangles

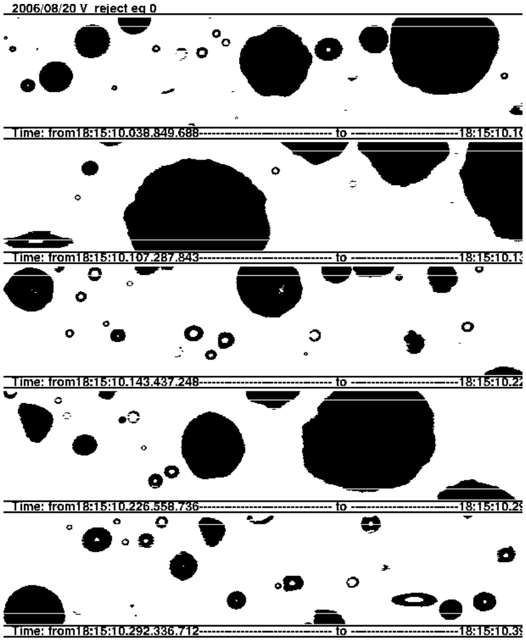

Fig. 10c:2DS-V width – 1,28 mm

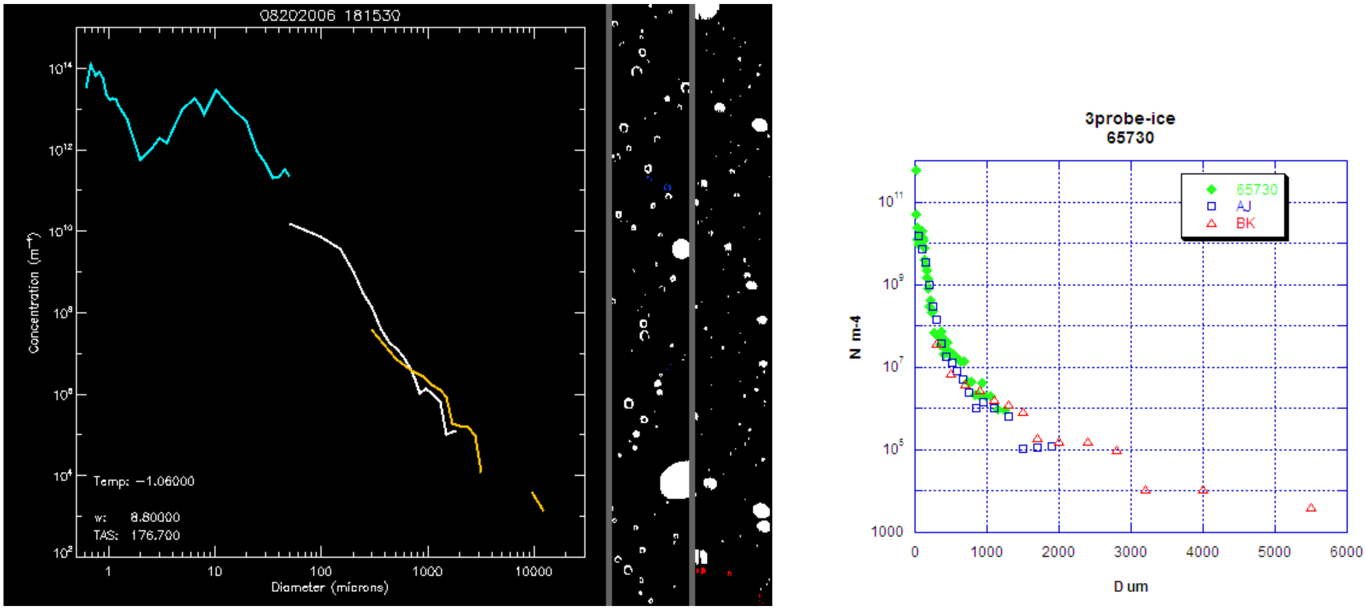

Fig. 11 a & b : left – composite size distributions, scattering particle spectrometer – blue, CIP – white, PIP yellow, image sample strips, width – CIP – 1.625 mm, PIP – 6.4 mm; 3 probe semi-log plot of size distributions, 2DS-V – green diamonds, CIP – blue squares, PIP – red triangles

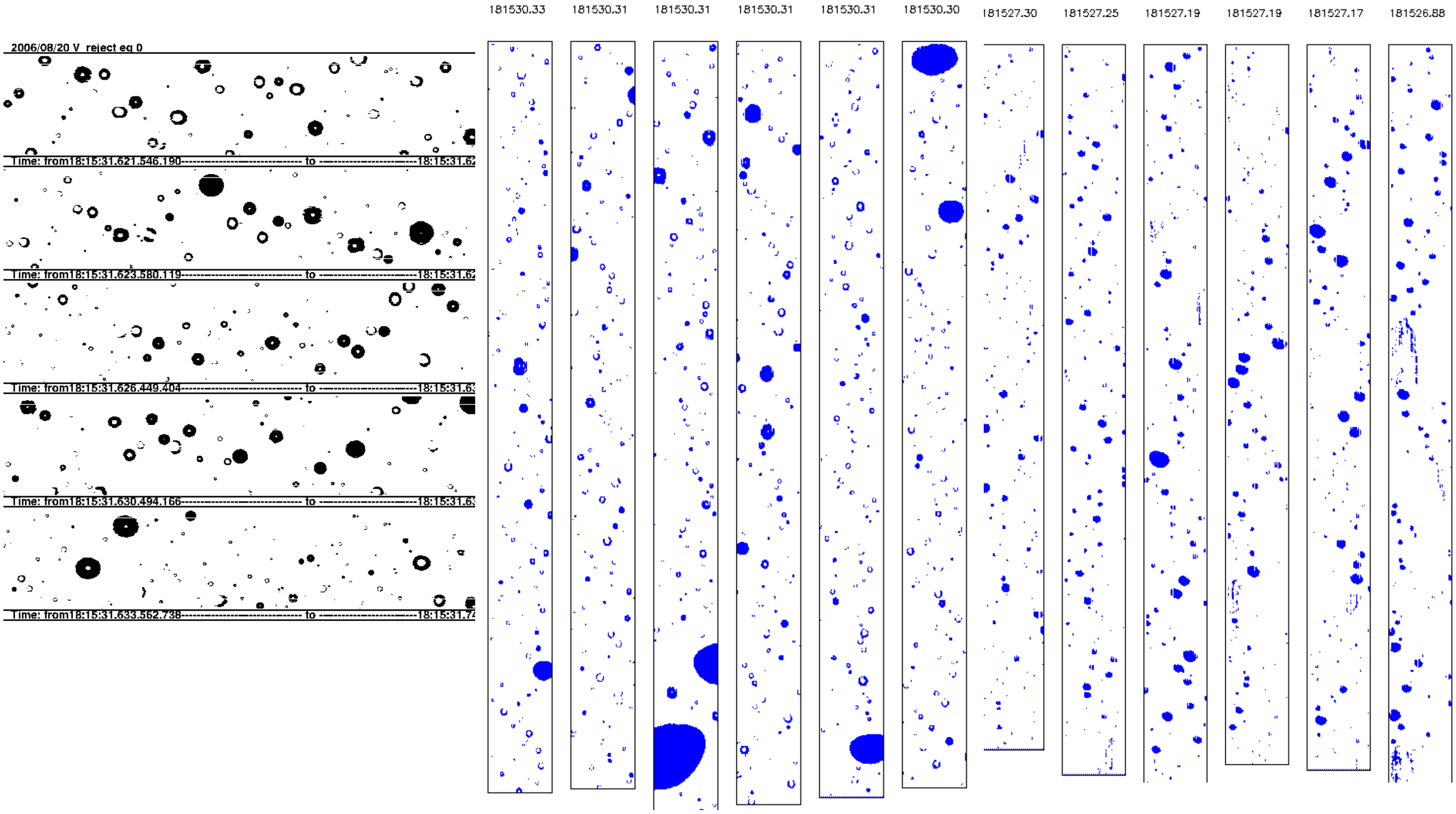

Fig. 11c, 11d, & 11e :2DS-V width – 1,28 mm, CIP width – 1.625 mm, PIP width – 6.4 mm

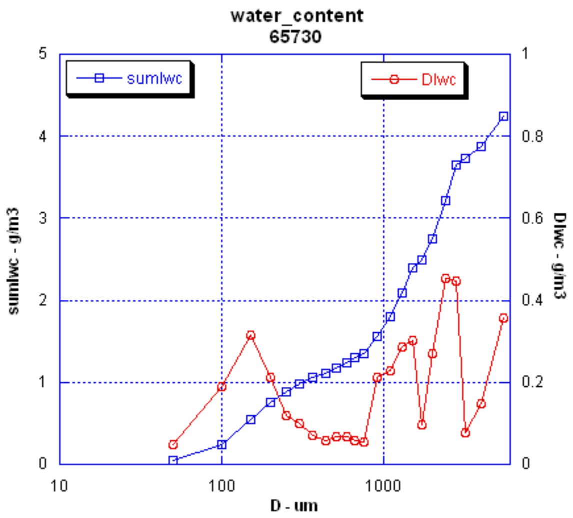

Fig.12a contribution by size interval to water content – combo CIP + PIP

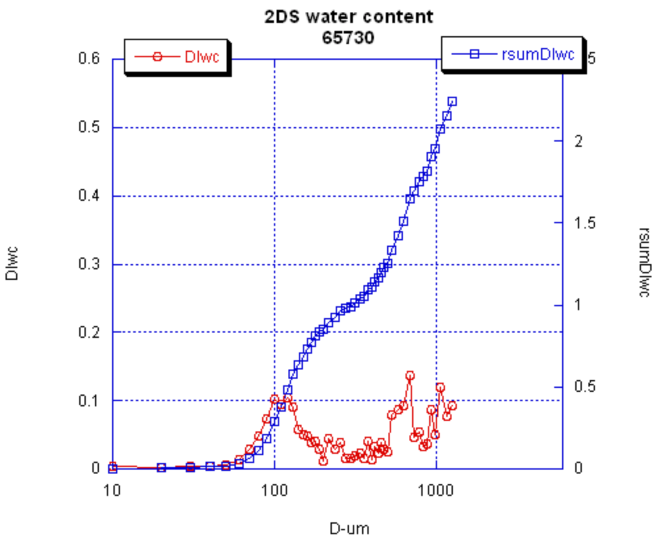

Fig. 12b as in a, but from 2DS size distribution

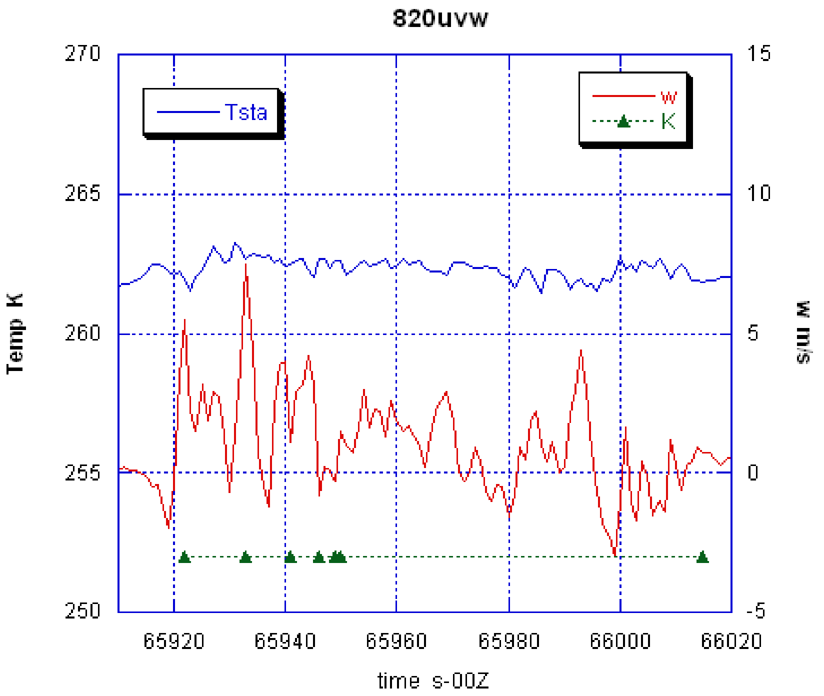

Fig 13 Detailed vertical air velocity and temp for -11C transect – microphysics figs in green

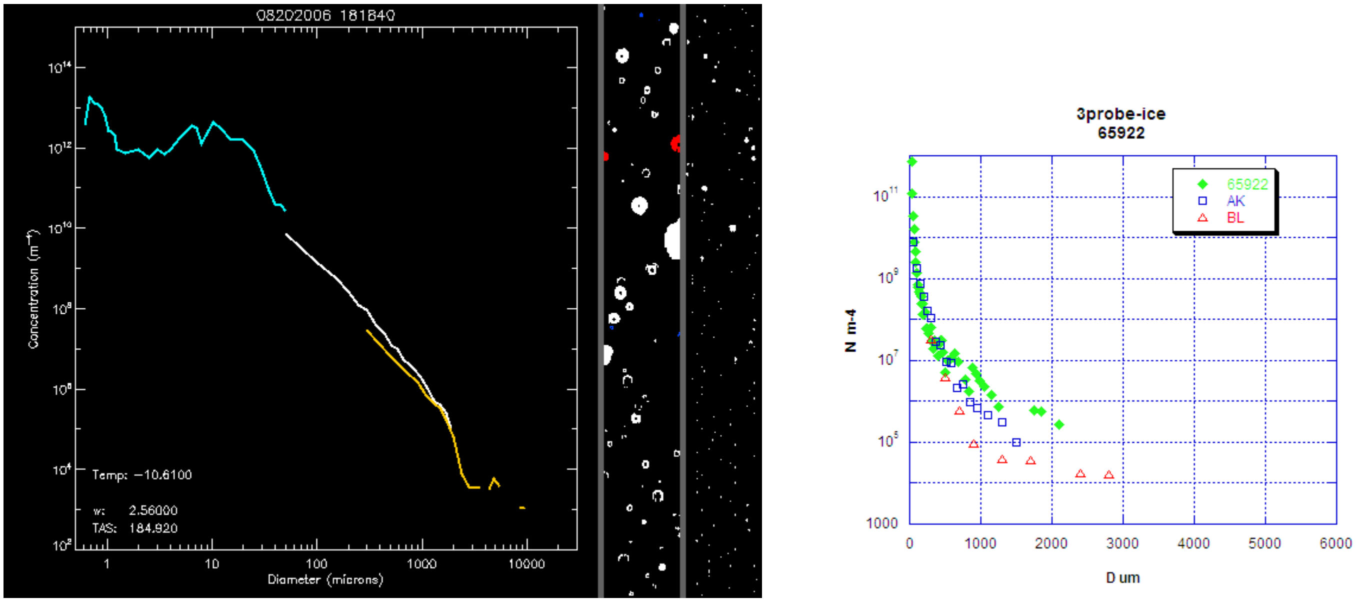

Fig. 14 a & b : left – composite size distributions, scattering particle spectrometer – blue, CIP – white, PIP yellow, image sample strips, width – CIP – 1.625 mm, PIP – 6.4 mm; 3 probe semi-log plot of size distributions, 2DS-V – green diamonds, CIP – blue squares, PIP – red triangles

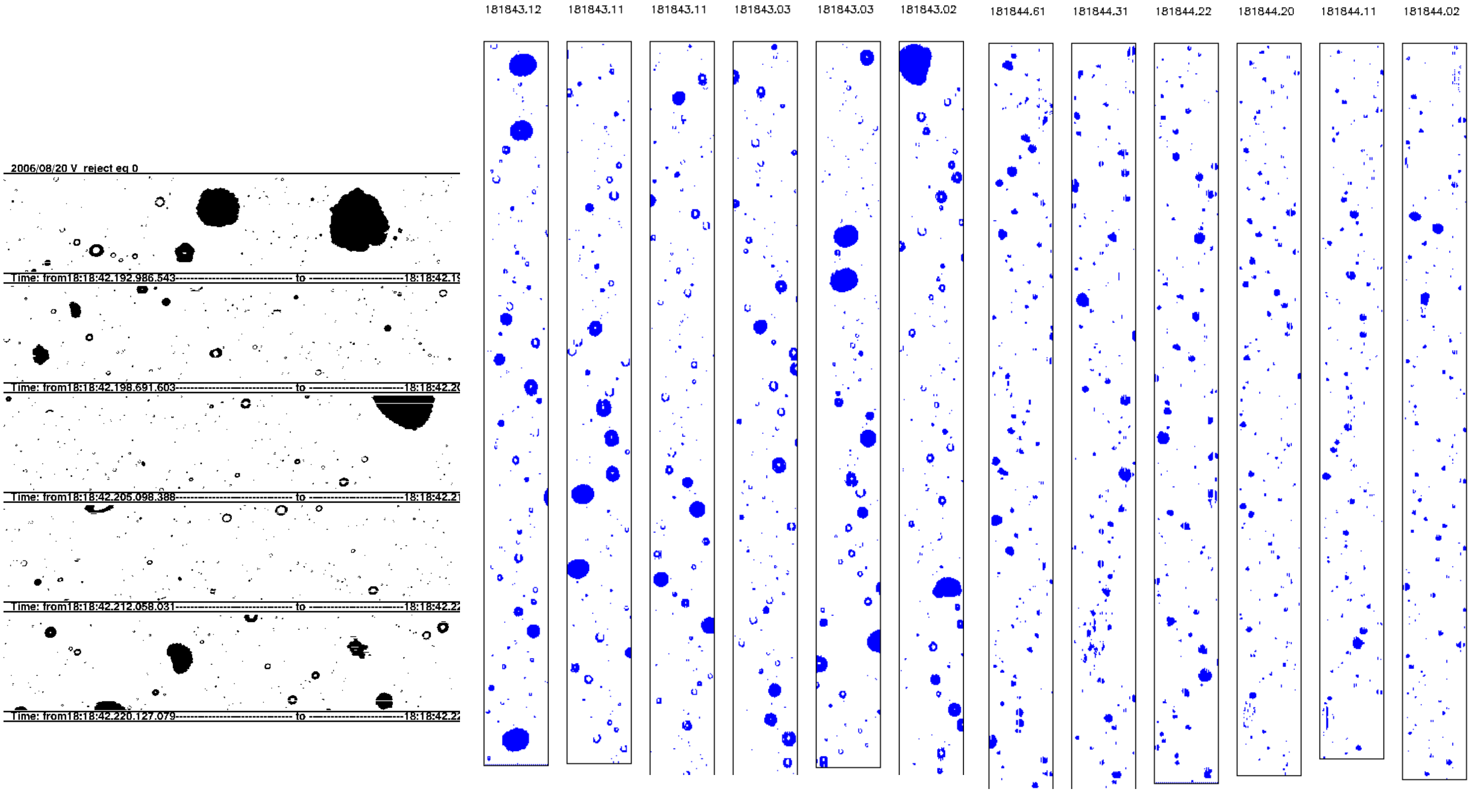

Fig. 14c, 14d, & 14e :2DS-V width – 1,28 mm, CIP width – 1.625 mm, PIP width – 6.4 mm

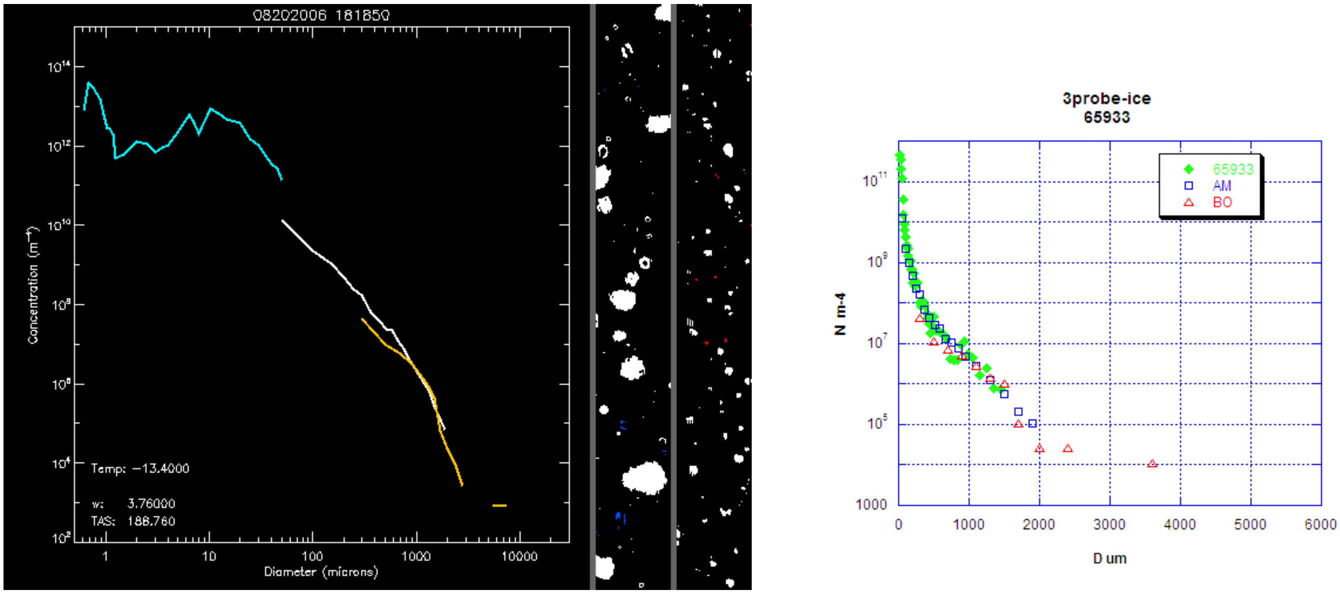

Fig. 15 a & b : left – composite size distributions, scattering particle spectrometer – blue, CIP – white, PIP yellow, image sample strips, width – CIP – 1.625 mm, PIP – 6.4 mm; 3 probe semi-log plot of size distributions, 2DS-V – green diamonds, CIP – blue squares, PIP – red triangles

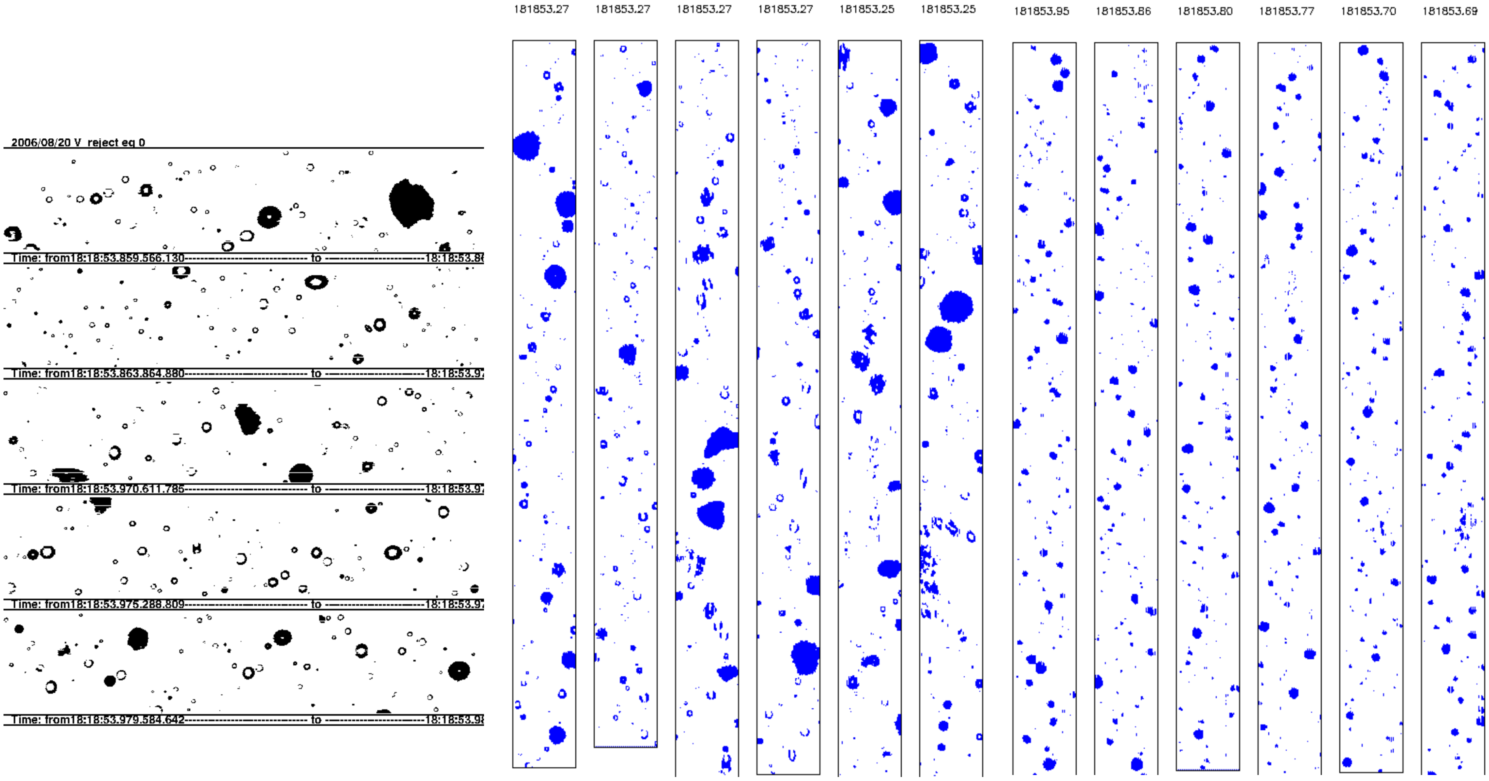

Fig. 15c, 15d, & 15e :2DS-V width – 1,28 mm, CIP width – 1.625 mm, PIP width – 6.4 mm

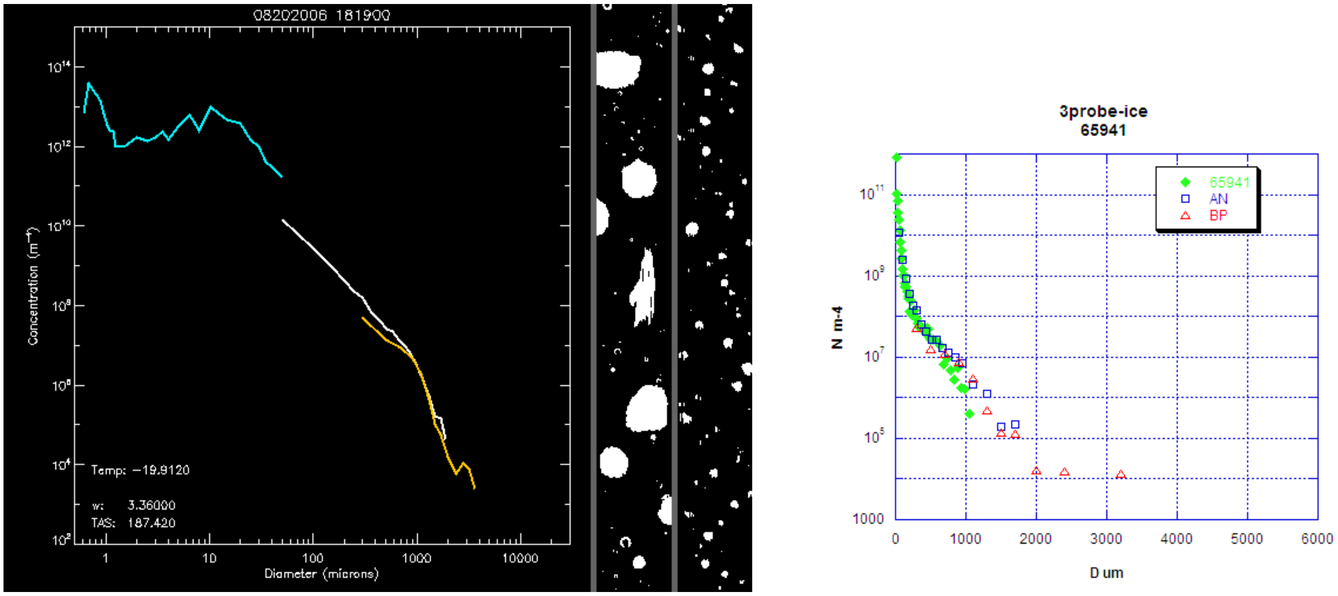

Fig. 16 a & b : left – composite size distributions, scattering particle spectrometer – blue, CIP – white, PIP yellow, image sample strips, width – CIP – 1.625 mm, PIP – 6.4 mm; 3 probe semi-log plot of size distributions, 2DS-V – green diamonds, CIP – blue squares, PIP – red triangles

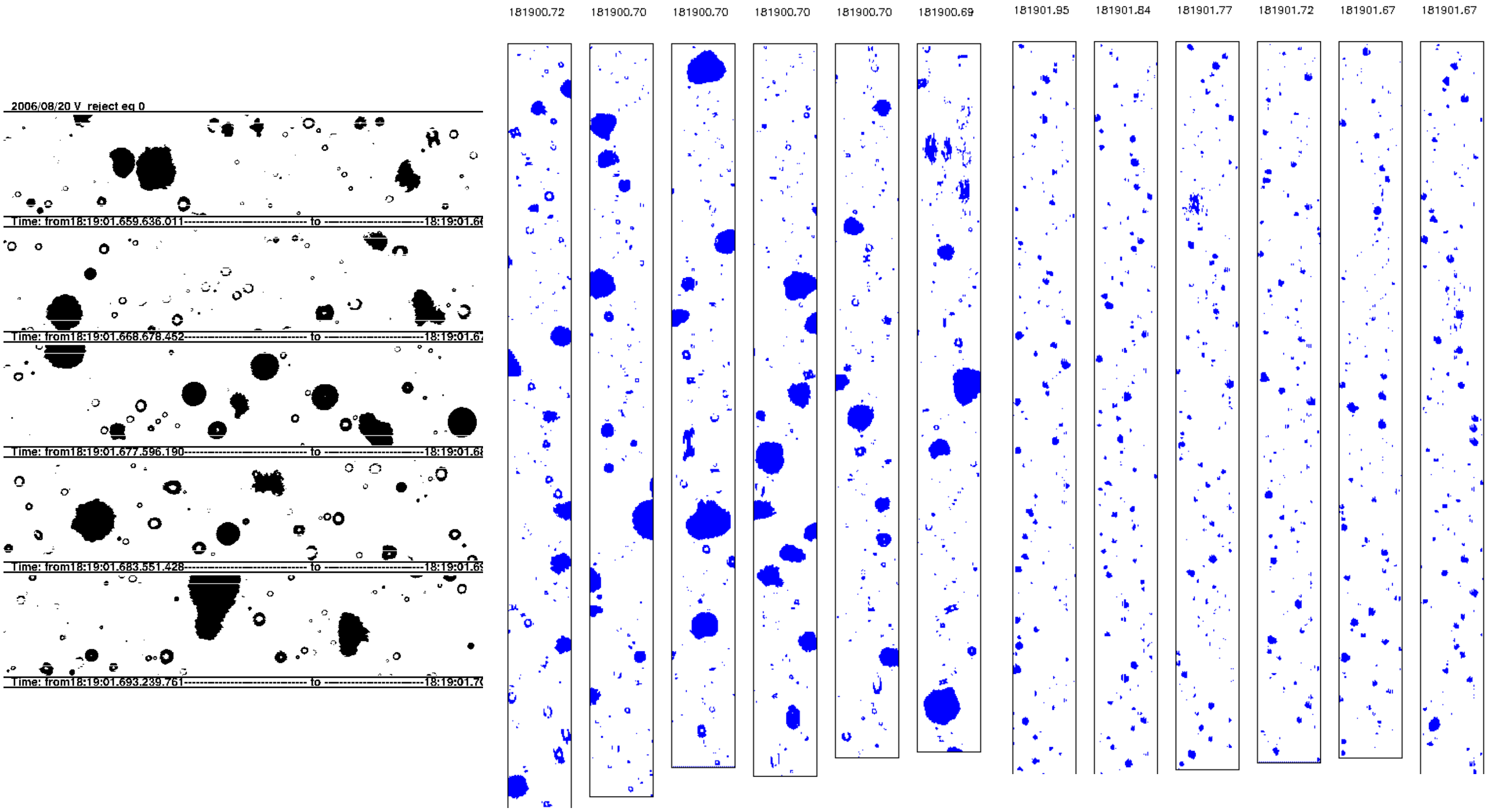

Fig. 16c, 16d, & 16e :2DS-V width – 1,28 mm, CIP width – 1.625 mm, PIP width – 6.4 mm

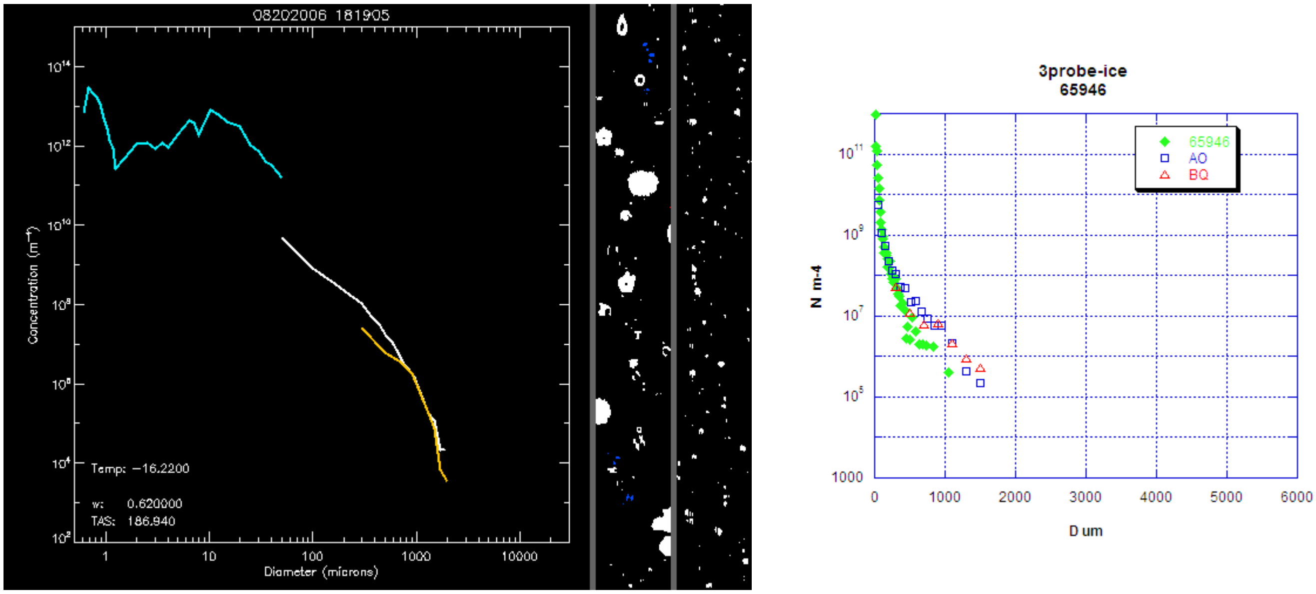

Fig. 17 a & b : left – composite size distributions, scattering particle spectrometer – blue, CIP – white, PIP yellow, image sample strips, width – CIP – 1.625 mm, PIP – 6.4 mm; 3 probe semi-log plot of size distributions, 2DS-V – green diamonds, CIP – blue squares, PIP – red triangles

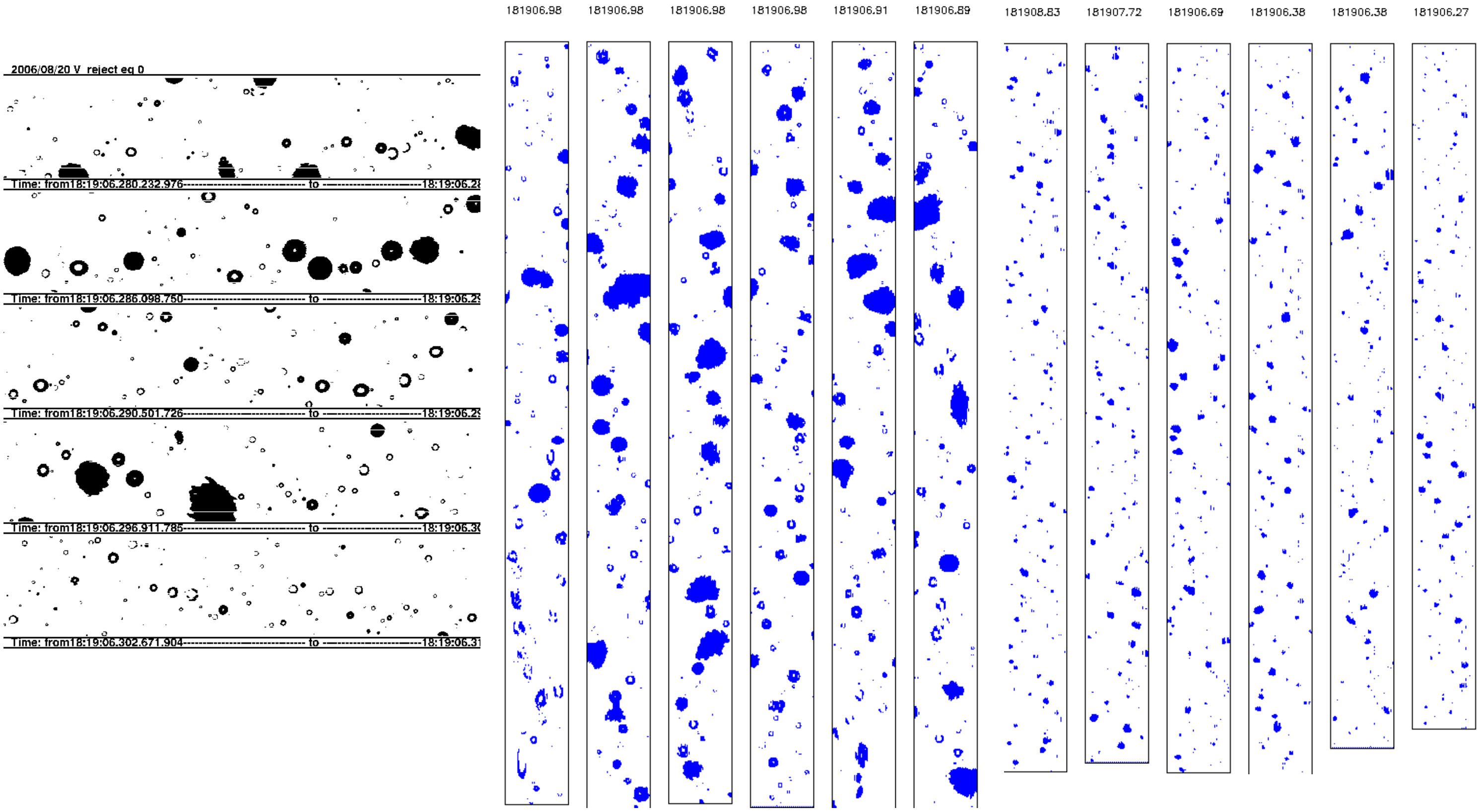

Fig. 17c, 17d, & 17e :2DS-V width – 1,28 mm, CIP width – 1.625 mm, PIP width – 6.4 mm

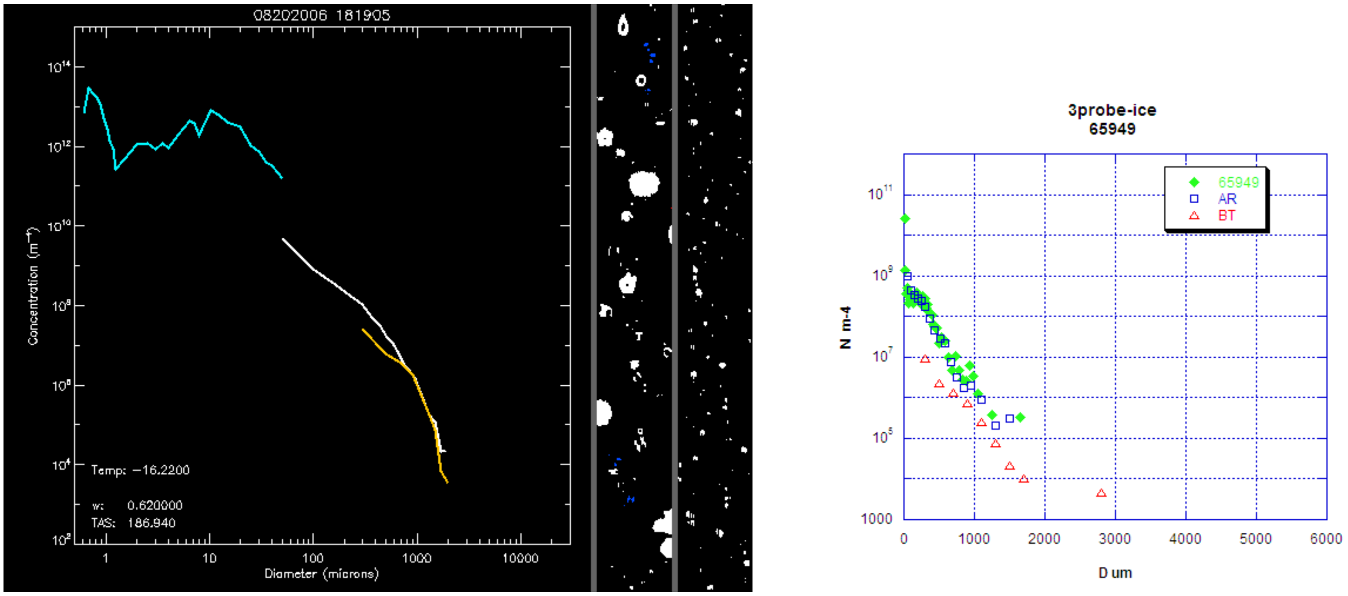

Fig. 18 a & b : left – composite size distributions, scattering particle spectrometer – blue, CIP – white, PIP yellow, image sample strips, width – CIP – 1.625 mm, PIP – 6.4 mm; 3 probe semi-log plot of size distributions, 2DS-V – green diamonds, CIP – blue squares, PIP – red triangles

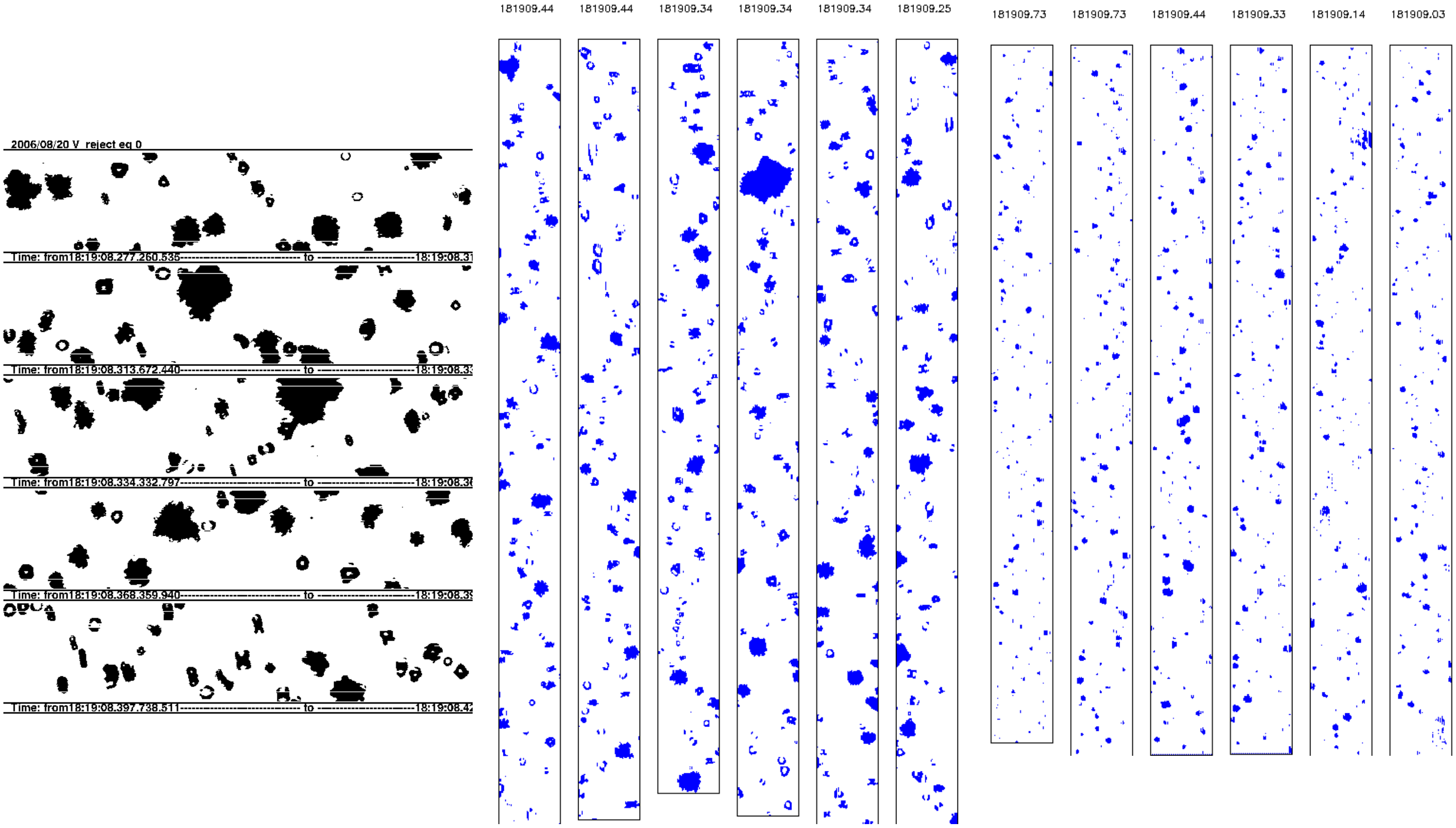

Fig. 18c, 18d, & 18e :2DS-V width – 1,28 mm, CIP width – 1.625 mm, PIP width – 6.4 mm

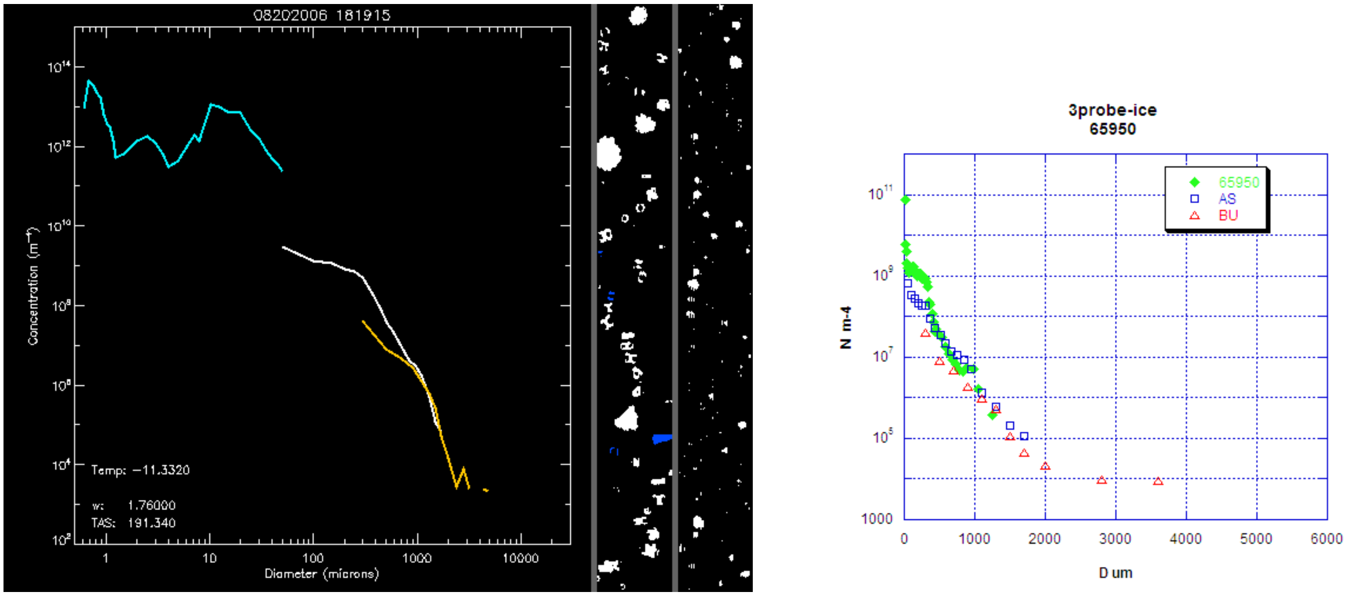

Fig. 19 a & b : left – composite size distributions, scattering particle spectrometer – blue, CIP – white, PIP yellow, image sample strips, width – CIP – 1.625 mm, PIP – 6.4 mm; 3 probe semi-log plot of size distributions, 2DS-V – green diamonds, CIP – blue squares, PIP – red triangles

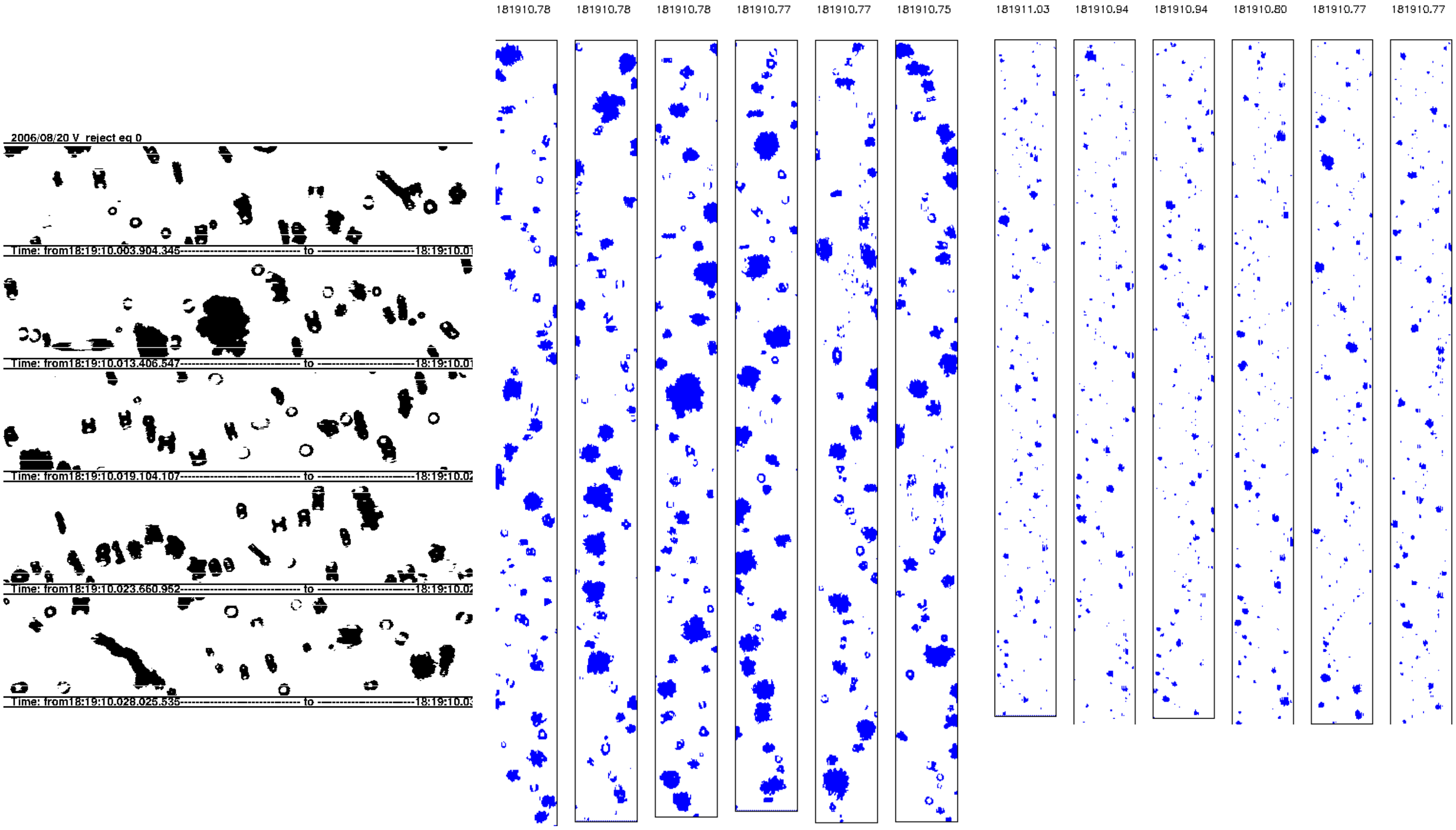

Fig. 19c, 19d, & 19e :2DS-V width – 1,28 mm, CIP width – 1.625 mm, PIP width – 6.4 mm

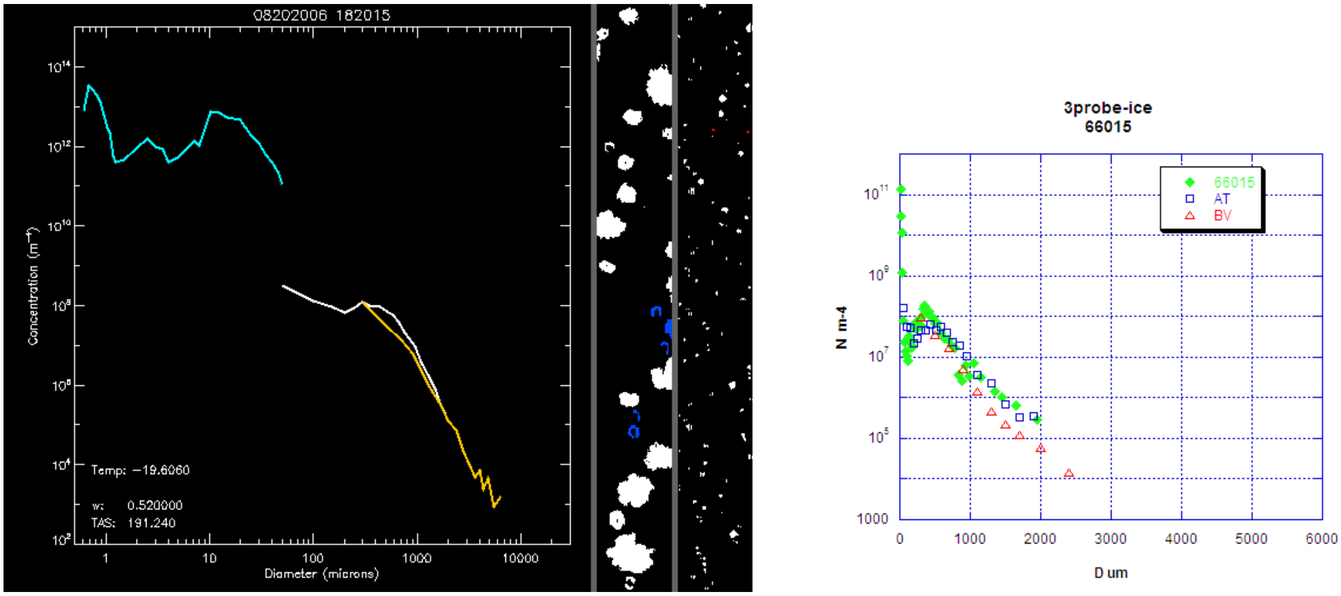

Fig. 20 a & b : left – composite size distributions, scattering particle spectrometer – blue, CIP – white, PIP yellow, image sample strips, width – CIP – 1.625 mm, PIP – 6.4 mm; 3 probe semi-log plot of size distributions, 2DS-V – green diamonds, CIP – blue squares, PIP – red triangles

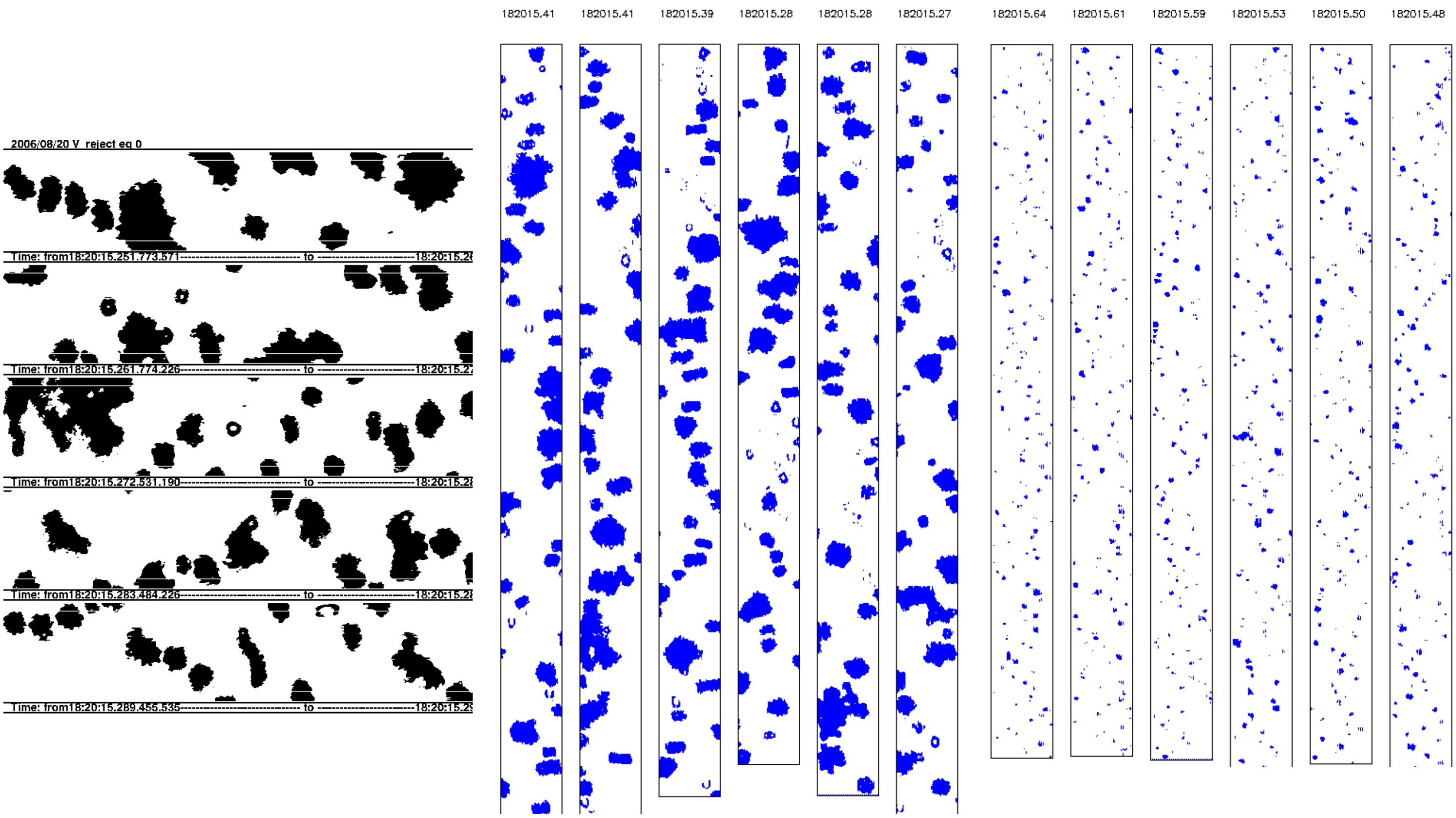

Fig. 20c, 20d, & 200e :2DS-V width – 1,28 mm, CIP width – 1.625 mm, PIP width – 6.4 mm

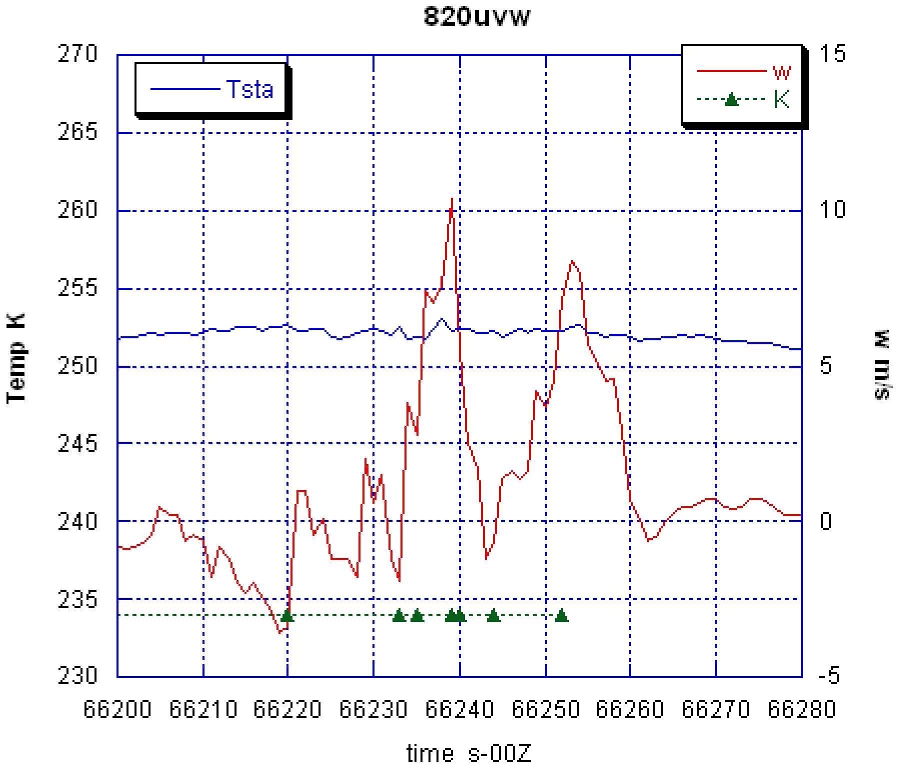

Fig 21 Detailed vertical air velocity and temp for -20C transect – microphysics figs in green

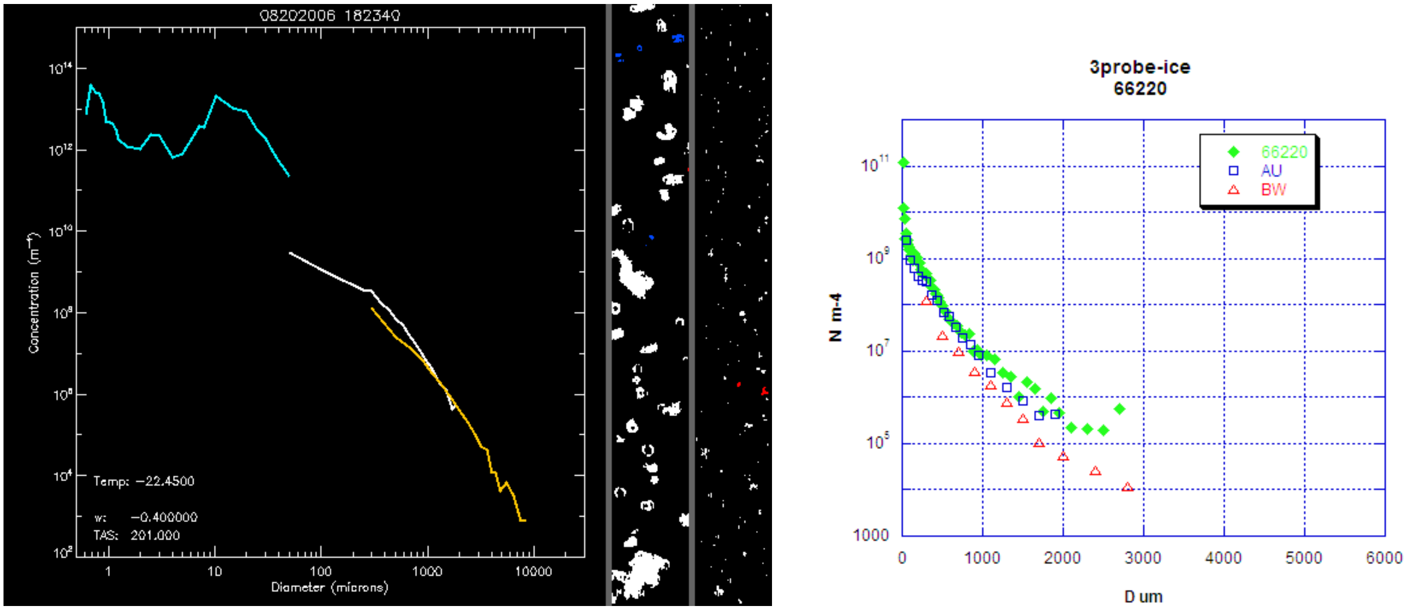

Fig. 22 a & b : left – composite size distributions, scattering particle spectrometer – blue, CIP – white, PIP yellow, image sample strips, width – CIP – 1.625 mm, PIP – 6.4 mm; 3 probe semi-log plot of size distributions, 2DS-V – green diamonds, CIP – blue squares, PIP – red triangles

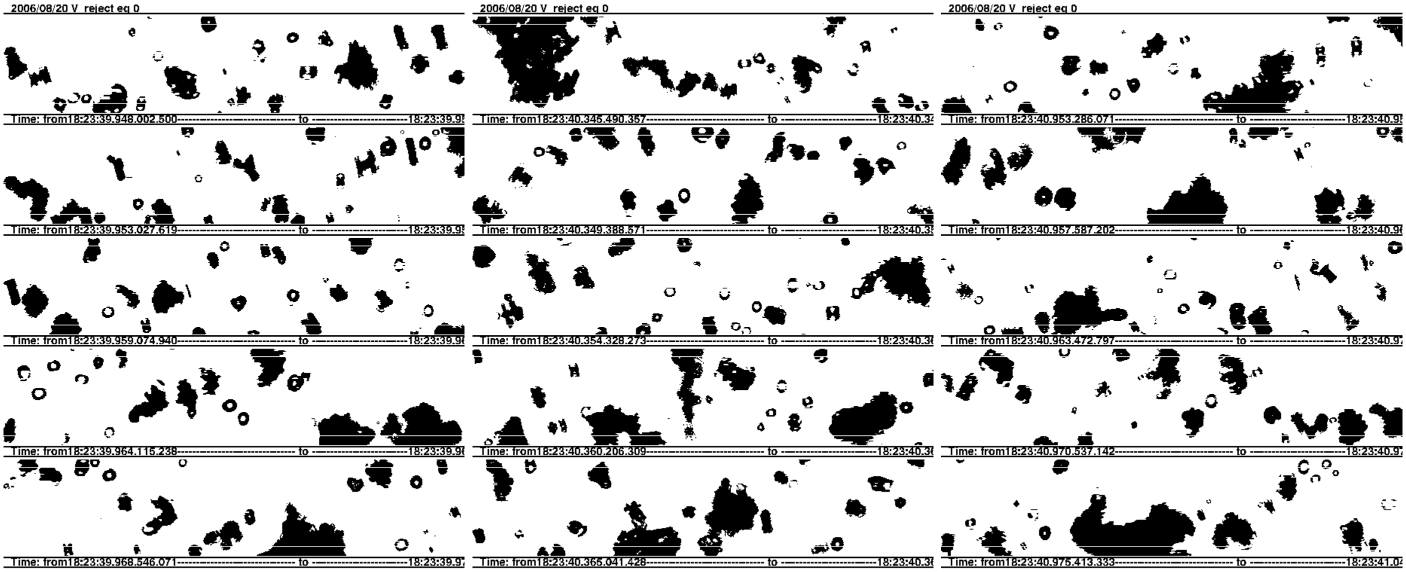

Fig. 22c, 22d, 22e, 2DS-V sample images, width of strip 1.28 mm.

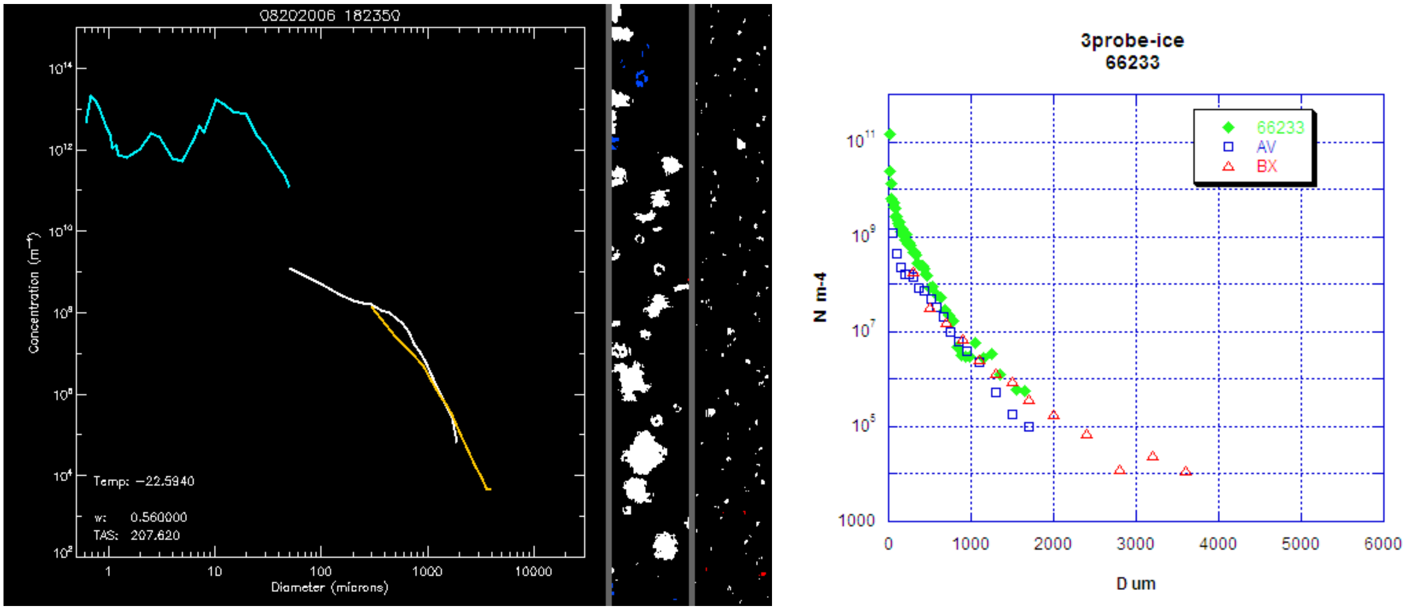

Fig. 23 a & b : left – composite size distributions, scattering particle spectrometer – blue, CIP – white, PIP yellow, image sample strips, width – CIP – 1.625 mm, PIP – 6.4 mm; 3 probe semi-log plot of size distributions, 2DS-V – green diamonds, CIP – blue squares, PIP – red triangles

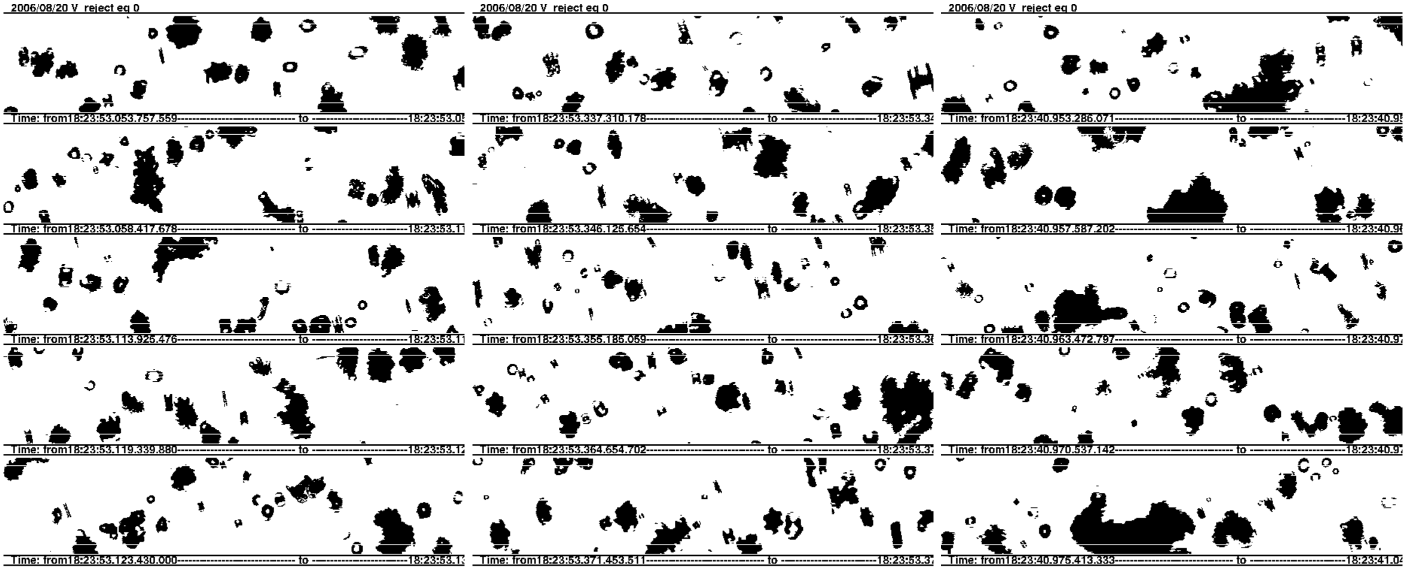

Fig. 23c, 23d, 23e, 2DS-V sample images, width 1.28 mm.

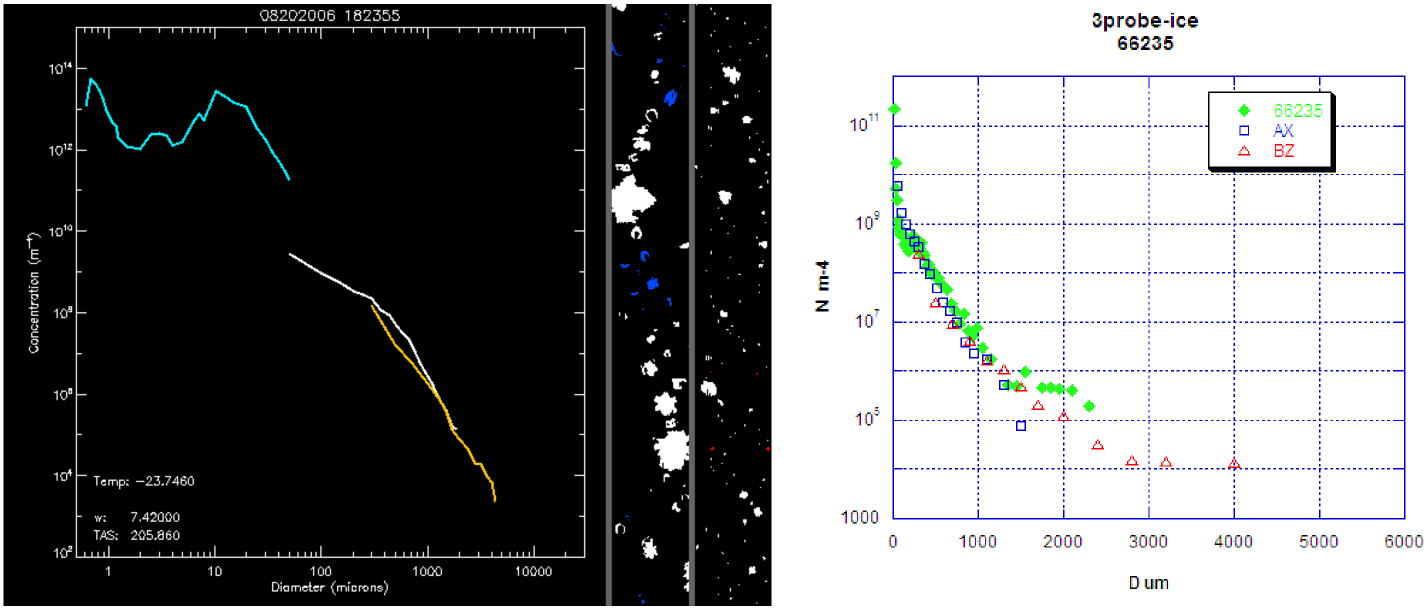

Fig. 24 a & b : left – composite size distributions, scattering particle spectrometer – blue, CIP – white, PIP yellow, image sample strips, width – CIP – 1.625 mm, PIP – 6.4 mm; 3 probe semi-log plot of size distributions, 2DS-V – green diamonds, CIP – blue squares, PIP – red triangles.

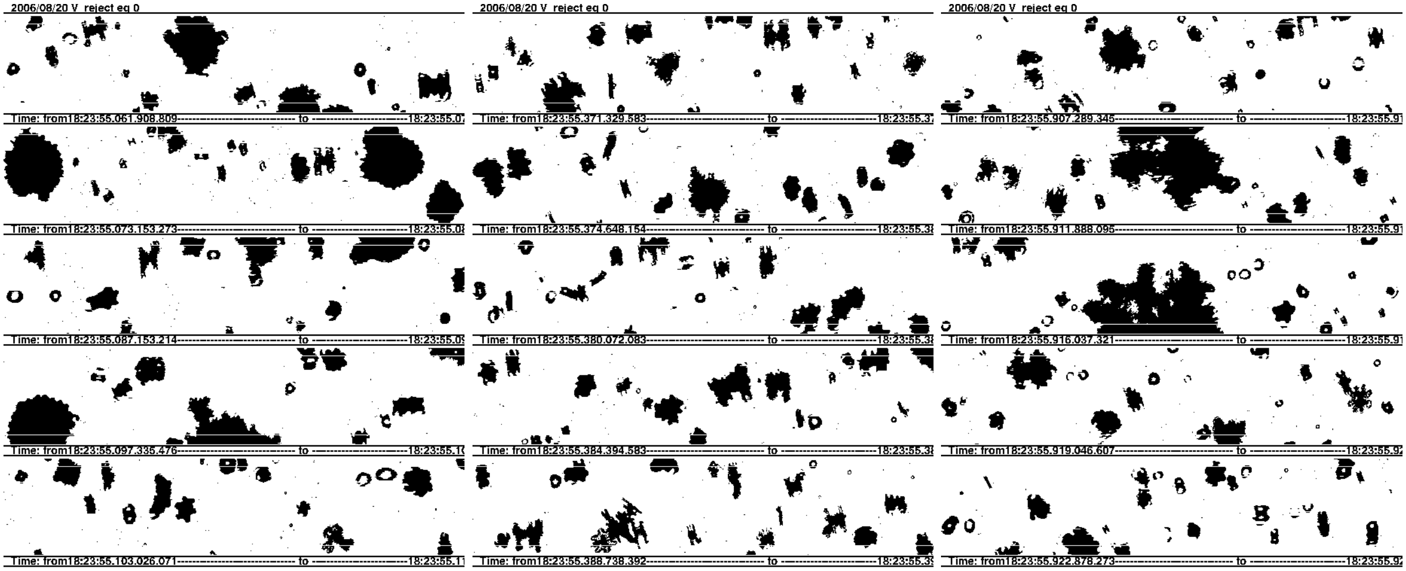

Fig. 24c, 24d, 24e, 2DS-V sample images, strip width 1.28 mm.

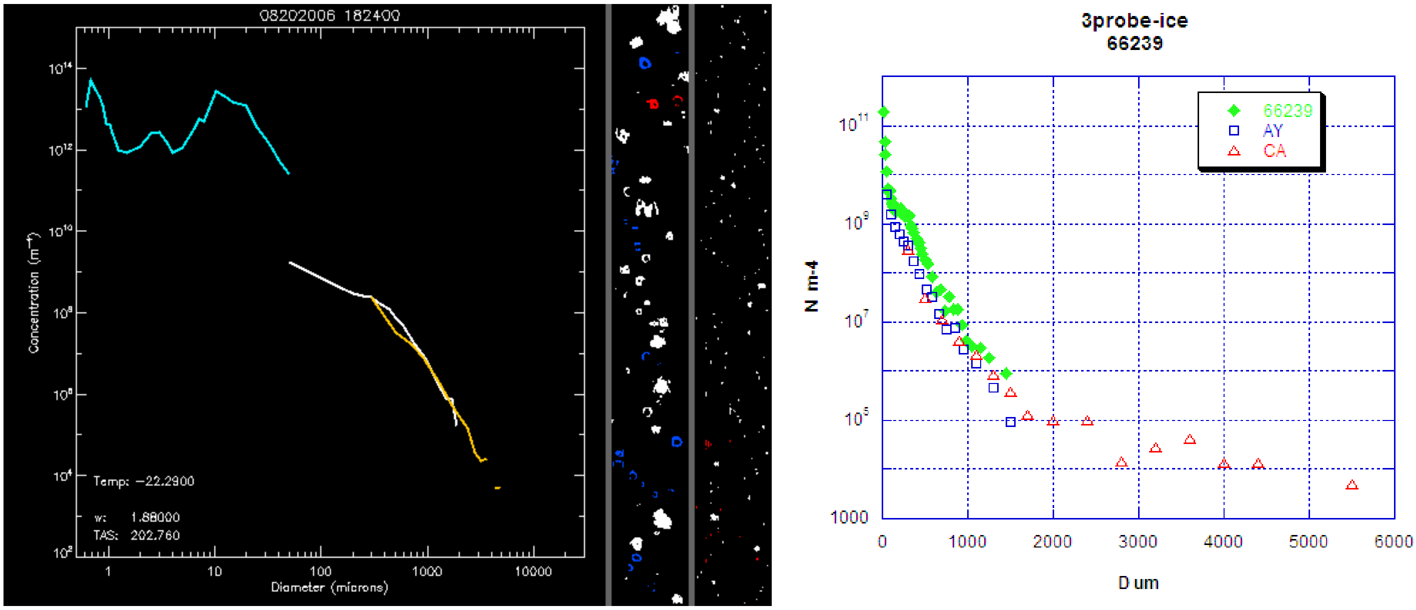

Fig. 25 a & b : left – composite size distributions, scattering particle spectrometer – blue, CIP – white, PIP yellow, image sample strips, width – CIP – 1.625 mm, PIP – 6.4 mm; 3 probe semi-log plot of size distributions, 2DS-V – green diamonds, CIP – blue squares, PIP – red triangles.

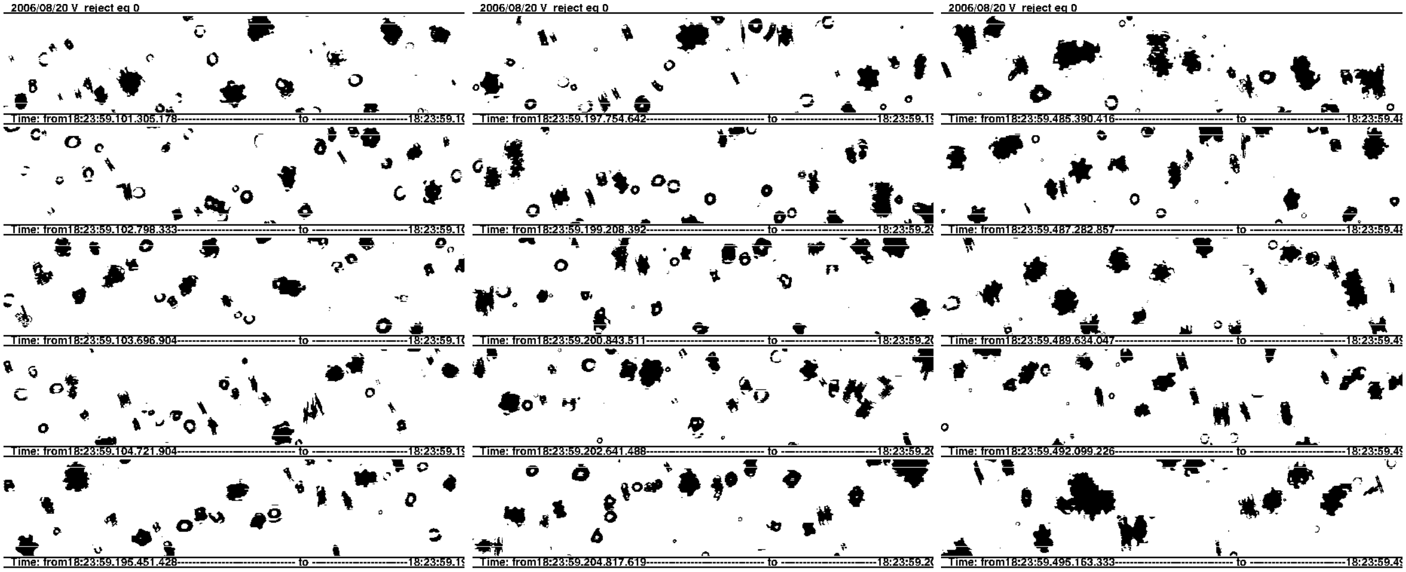

Fig. 25c, 25d, 25e, 2DS-V sample images, strip width 1.28 mm.

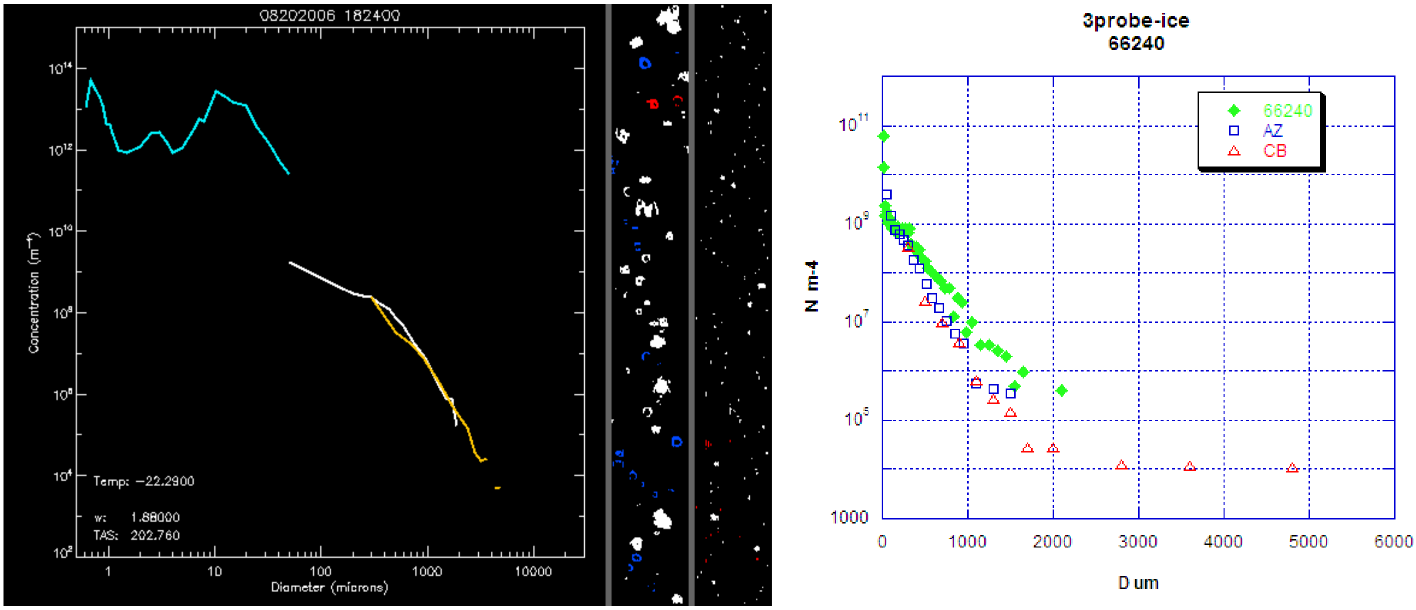

Fig. 26 a & b : left – composite size distributions, scattering particle spectrometer – blue, CIP – white, PIP yellow, image sample strips, width – CIP – 1.625 mm, PIP – 6.4 mm; 3 probe semi-log plot of size distributions, 2DS-V – green diamonds, CIP – blue squares, PIP – red triangles

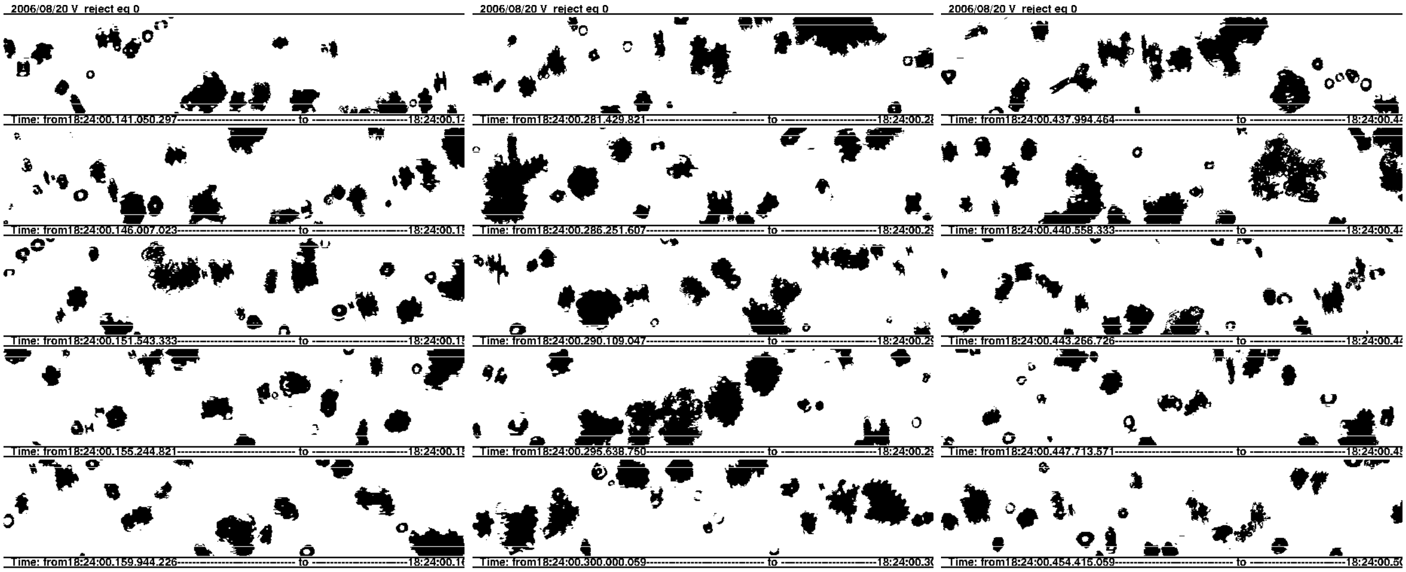

Fig. 26c, 26d, 26e, 2DS-V sample images, strip width 1.28 mm.

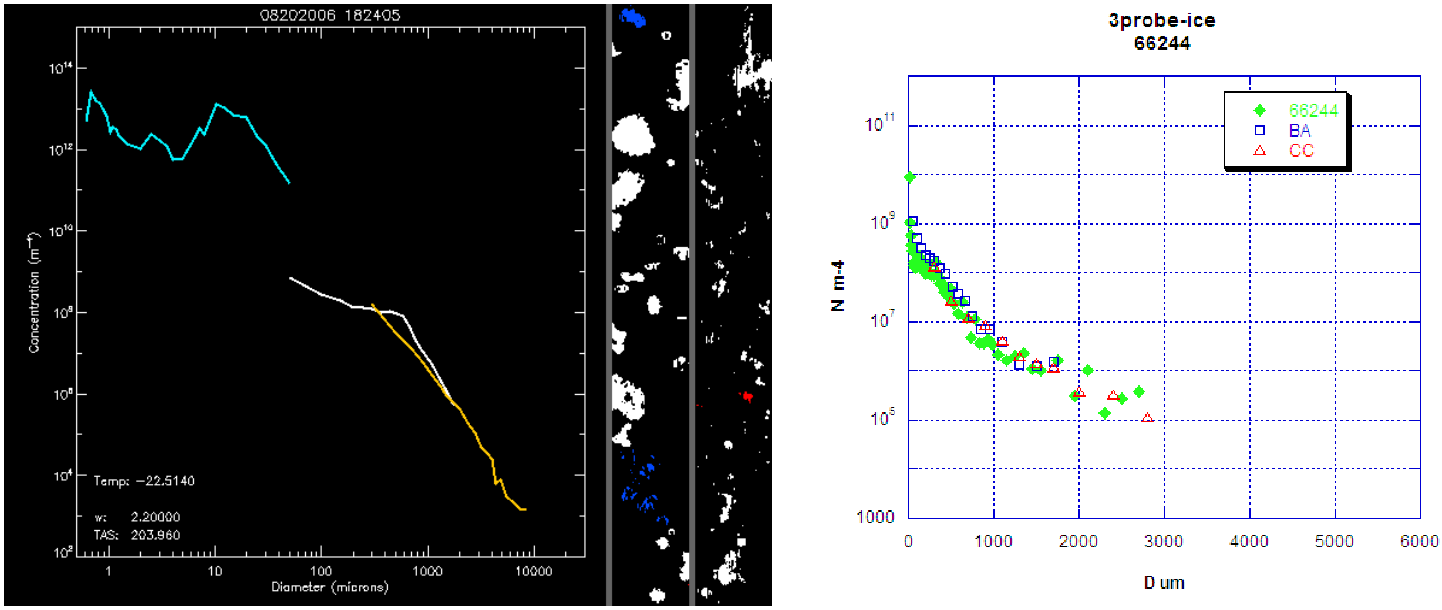

Fig. 27 a & b : left – composite size distributions, scattering particle spectrometer – blue, CIP – white, PIP yellow, image sample strips, width – CIP – 1.625 mm, PIP – 6.4 mm; 3 probe semi-log plot of size distributions, 2DS-V – green diamonds, CIP – blue squares, PIP – red triangles

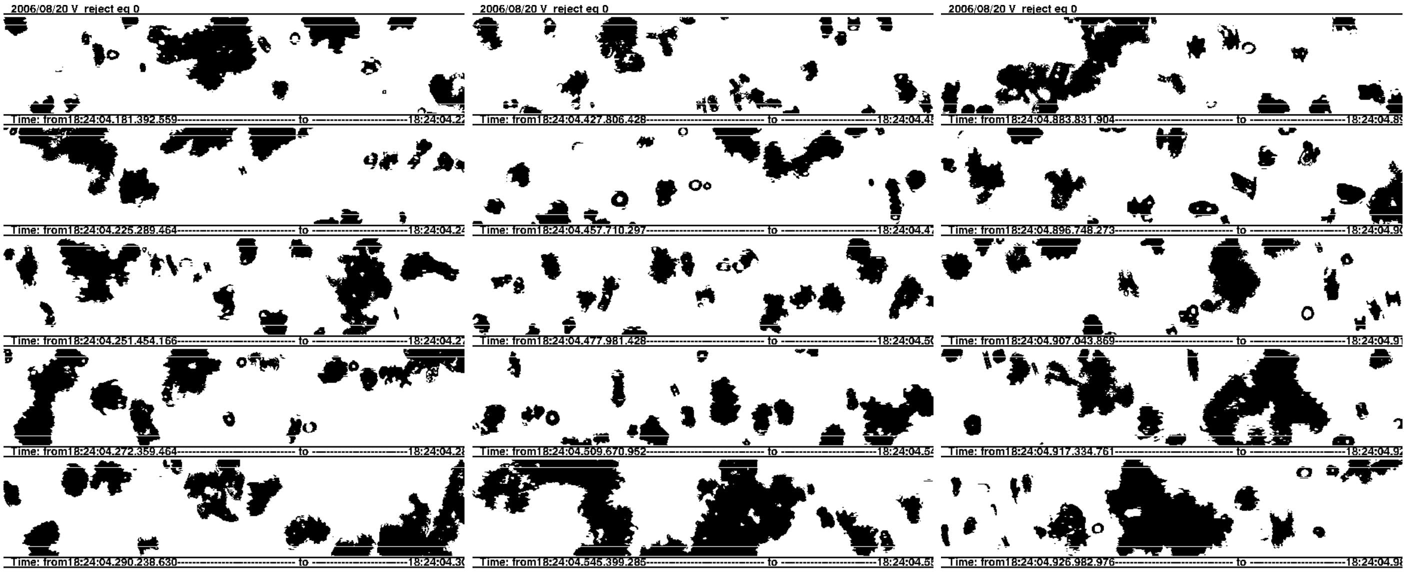

Fig. 27c, 27d, 27e, 2DS-V sample images, strip width 1.28 mm.

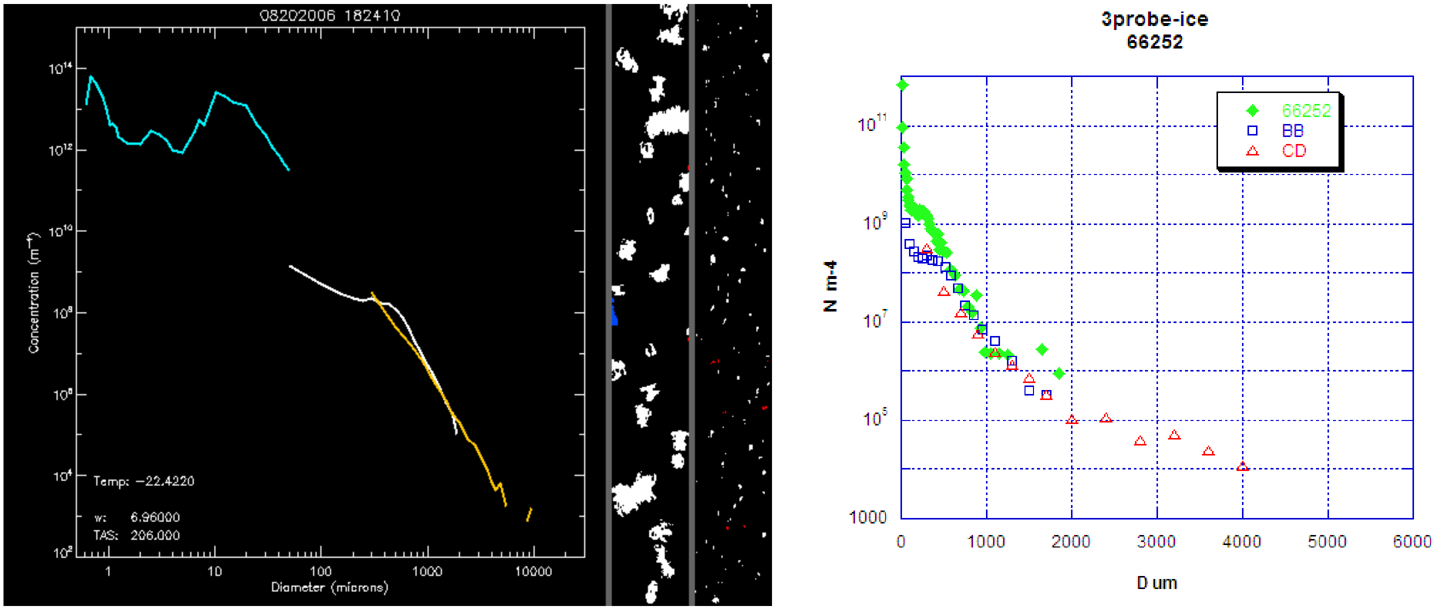

Fig. 28 a & b : left – composite size distributions, scattering particle spectrometer – blue, CIP – white, PIP yellow, image sample strips, width – CIP – 1.625 mm, PIP – 6.4 mm; 3 probe semi-log plot of size distributions, 2DS-V – green diamonds, CIP – blue squares, PIP – red triangles

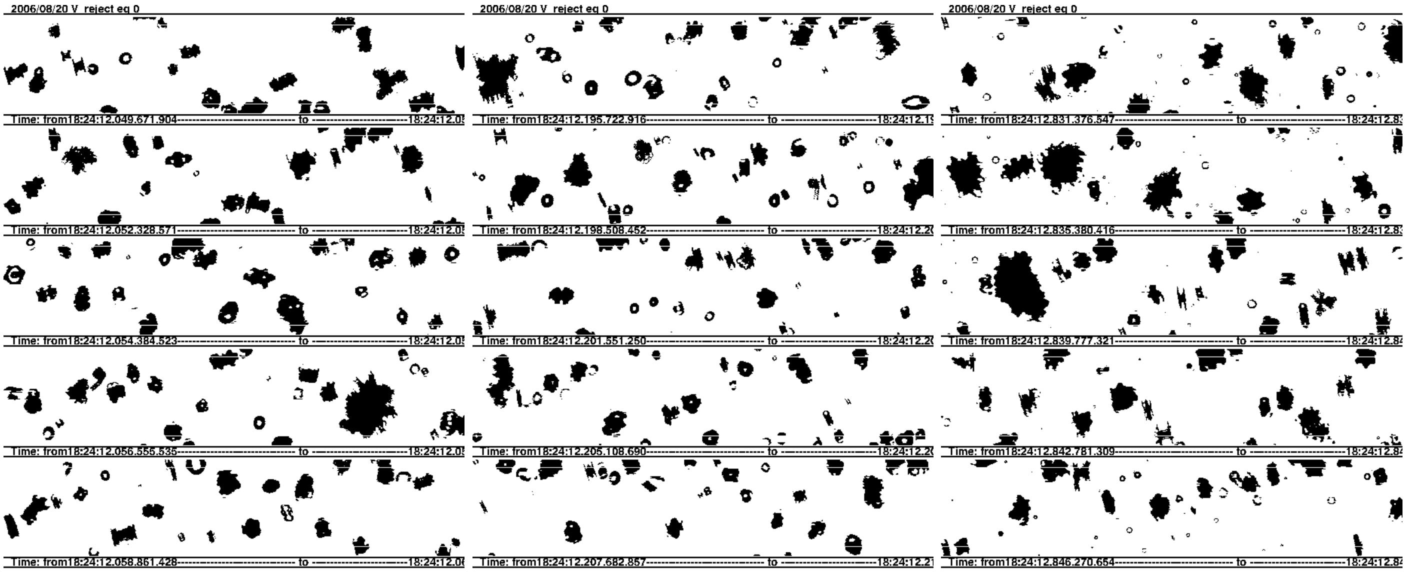

Fig. 28c, 28d, 28e, 2DS-V sample images, strip width 1.28 mm.

A Detective Analysis on the Effect of a Seeding Operation Test on Convective Cloud

Xiang Yuchun Tan Renmao Ye Jianyuan Liu Jian Yuan Zhengteng
(Weather Modification Office of Hubei Province, Wuhan 430074)

1. Seeding conditions and the seeding operation

The eastern part of Hubei Province was under the control of the southwest warm and humidity air flows, with plenty of water vapor on August 31st, 2007 ,especially 500hPa low trough from Nanyang to Yichang and 850 hPa Jianghuai shear line were suitable for the instability energy assembling and the convection developing. The weather-prognostics were good for rainfall enhancement seeding test.

The experimental station Yangxin County belongs to the Southeast Hubei hilly areas and lies at the transition area from Mufu Mountain to the Yangtze River Alluvial Plain. At 3pm on August 31st, over the experimental station, the cloud parameters inversed by the FY-2C data showed that the super cooled water was abundant, the thickness of the super cooled layer was between 5-5.5km and cloud top was over 9km. The Cinrad-WSR98d weather radar in Wuhan and dual-linear polarization and entire-phase-parameter weather radar (on 3cm wave-band) in Huangshi observed that there was a strong echo center of which the intensity maximum was more than 45dbz and the area of higher intensity was approximately $50km^2$ in the east-north direction of the experimental station. All of above showed that the seeding conditions were ripe. So the seeding operation was carried out by 3 WR rocket shells by 60 degrees elevation angles to the northeast direction, the effective coring rate of the catalyst this rocket shell amounts to 1.8×1015 /gram, each rocket carries 10 grams catalyst , maximum of altitude range is 6km and maximum of range distance is 8km.

2. Changes of Cinrad WSR-98D radar echo parameters

Using the first and second data products of Wuhan operational Cinrad WSR-98D weather radar scanning by VCP21 mode every 6 minutes, including composite reflectivity, echo top, the vertical integration of liquid water, storm(intensity >45dbz) tracking information, and so on, parameters(in Tab 1) of catalytic cell around the seeded cloud were analyzed.

Tab1: parameters of echo cells of seeded cloud

Observe time	Maximum intensity （dbz）	Area of intensity >45dbz（km^2）	Area of intensity >50dbz(km^2)	VIL （kg/m^2）	Area of vil >10 （km^2）	Area of Extreme VIL （km2）	Echo top （km）
15:46	53	46	4	18	160	16	9.2
15:49*	53	46	4	18	168	24	9.2
15:52	53	46	4	18	176	32	9.3
15:58	53	48	13	18	112	48	9.4
16:04	49	54	0	15	64	16	12.9
16:10	47	48	0	11	8		9.4
16:16	46	25	0	6	0		7.6
16:22	46	17	0	9	0		8
16:29	45	13	0	6	0		6.3

Note:* represents that the values of the time is got by linear interpolation

It can be seen from the radar image products(omitted)that the objective-echo came into being at about 14:40,when the echo intensity maximum was about 35dbz and the area was 10 km^2. It developed rapidly into a strong echo of which the maximum echo intensity was 53dbz and the stronger area of which the echo intensity was over 50dbz was about 4km^2 till 3:46pm.After the seeding time（3:49pm）, the maximum echo intensity had not significant augmentation ,but the area of stronger echo of which the echo intensity was over 50dbz was about 13km^2 at 3:58 pm (9min after seeding), enlarging 225% while the area of which the intensity was more than 45dbz increased by 17% in 15 minutes. The echo top before seeding was 9.2km and, it began to heighten after seeding. It reached the maximum of 12.9km at 4:04pm (15min after seeding), heightening 51%, after that, it fell rapidly. The value of VIL did not enlarge, but the area of higher VIL enlarged, the area of maximum VIL appeared at 3:58pm, 9min after seeding, increased by 100%.

In addition, according to the variation characteristics of echo parameters of the seeded cells from initial forming to the operation time, based on the methods in reference 1, contrast cloud, which was apart from the seeded cloud about 35km, was selected. The lifespan of the seeded cloud is longer than that of the contrast cloud. The characteristics of the stronger echo area of the seeded cloud presents two peaks before and after the seeding, but the contrasts cloud has only one crest value. The maximum of the echo top of the seeded cloud maintains approximately 26 minutes, longer than that of the contrast cloud.

3. Changes of dual-polarization factors

The linear depolarization ratio (Ldr) is defined as the ratio of vertical reception echo power and horizontal reception echo power when emitting horizontal pulse. Generally speaking, the greater the particle precipitation, the less the Ldr. At 3:49 pm, the minimum Ldr of the seeded cloud was about -25 dB, then, the minimum Ldr decreased and the area of lower Ldr enlarged, by 4:12pm, The Ldr minimum reached the extreme value about -34db, decreased by 36% in 23minutes and the area of lower Ldr continue to increase until 4:48 pm, then it began to decrease. The value of coefficient of zero delaying horizontal and vertical cross-signal correlation (ρ_{hv}) did not vary obviously, but the area of the higher value increased first then decreased.

4. Changes of lightning parameters

Data observed by Lightning location net are counted around the center of operation station in 400Km^2. There were 279 times of lighting in one hour after the catalytic action, in which two positive lightning. The intensities were among 27.2KA-35.3KA, and 277 times of negative lightning, the intensities were among -127.7KA--19.7KA. The maximum of intensity appears at 11th minute after the catalytic action. No lightning emerges after 48th minute. There were at least one lightning in the former 29 minutes after the operation and the period when more times of lightning occur was in the earlier 20 minutes. The most was 20 times at the 18th minute.

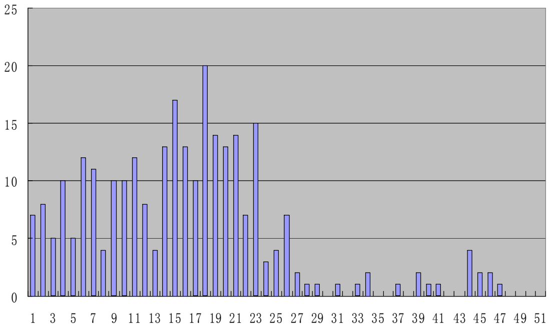

Fig.1　times of　lighting from 3：49pm to 4：40pm by minute

5. Precipitation observed by automatic weather station

The initial time of precipitation caused by Yangxin seeded cloud was at 4pm. The rainfall was 10mm in the one hour from 4pm to 5pm. The main occurs in the former half period, in which the rainfall was 8.7mm, 87% of the total. In this period, precipitation averaged 0.29mm/min, and the maximum was 1.2mm/min at 4:02 pm, the 13th minute after catalytic action. It was small array of precipitation I in the latter half period of the hour. It is just 0.2mm in the period from 5pm to 6pm.

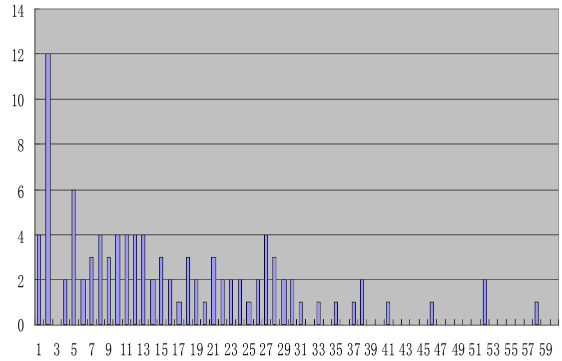

Fig.2 precipitation observed by the leeward side station from 4pm to 5pm by minute(X-time spot, Y-value of precipitation)

6. Discussions

(1) The physical effect of seeding convective clouds appears in the former 30mins after seeding from the above analysis based on data observed by Cinrad WSR-98D weather radar, dual-linear polarization and entire- phase- parameter weather radar and lighting location nets. Through comparing with the contrast cloud, seeding operation has received some positive effect. The precipitation and precipitation time is closely related to the variation of radar echo parameters and lighting parameters.

(2) Because convective precipitation presents the characteristics of lasting short time and rapidly developing, in order to track changes in cloud more accurately, density of observation should be increased. At the same time, the dual-polarization radar data should be further inversed and analyzed, including precipitation particle shape and size, phase distribution, spatial orientation, and other more specific, which can directly reflect the catalytic effect.

NUMERICAL SIMULATIONS OF THE FORMATION OF MELTING-LAYER CLOUD

Kazuaki YASUNAGA*[1], Akihiro HASHIMOTO[2], and Masanori YOSHIZAKI[1]
[1]Institute of Observational Research for Global Change, JAMSTEC Yokosuka headquarters , Kanagawa, Japan
[2] Meteorological Research Institute, 1-1, Nagamine, Tsukuba, Ibaraki, Japan

1. Introduction

A number of previously published observational studies have reported the common occurrence of cloudy layers at around 5 km elevation within the tropics. Mapes and Zuidema (1996) analyzed radiosonde data obtained during the Tropical Ocean Global Atmosphere Coupled Ocean–Atmosphere Response Experiment (TOGA COARE) and discovered that cloudy layers indirectly inferred from relative humidity profiles commonly occur around the melting level (approximately 550 hPa). Sugimoto et al. (2000) used ground-based Mie scattering lidar to observe the vertical distribution of clouds at Jakarta, Indonesia, over a period of 2 years and found that the height of the cloud base has a notable maximum at an altitude of approximately 5 km, especially during the wet season. Yasunaga et al. (2003) identified a mid-level peak in the cloud vertical distribution from aircraft lidar data obtained during the NASA Pacific Exploratory Mission-Tropics B (PEM-Tropics B). Yasunaga et al. (2006) used cloud profiling radar and lidar to determine the frequency distribution of the base heights of cloudy layers with little (or no) falling condensate particles. The observed clouds have base heights predominantly in the range 4.5–6.5 km, and most of the clouds are less than 500 m in thickness. The occurrence of thin cloudy layers at the 0°C level is frequent, especially during the Madden-Julian Oscillation (MJO) active phase when the coverage of stratiform-type radar echoes is much greater than that of convective-type radar echoes.

Johnson et al. (1996) described prominent stable layers at heights of 2, 5, and 15–16 km observed during TOGA COARE. Johnson et al. (1999) also found that maxima in the vertical distributions of radar echo (cloud) tops occur in the vicinity of these three stable layer heights. Environmental static stability influences the vertical profiles of detrainment from cumulus convection as well as the top heights of cumulus convection (e.g., Bretherton and Smolarkiewicz 1989; Taylor and Baker 1991; Zuidema 1998; Mapes 2001; Takayabu et al. 2006). It has therefore been considered that the commonly observed mid-level cloud layers mainly originate via detrainment from cumulus convection that is promoted by the stable layer

---

*Corresponding author address: Kazuaki Yasunaga, Institute of Observational Research for Global Change, JAMSTEC Yokosuka headquarters, 2-15, Natsushima-Cho, Yokosuka-city, Kanagawa, 237-0061, Japan: E-mail: yasunaga@jamstec.go.jp ("detrainment shelves" of Mapes and Zuidema 1996).

On the other hand, condensation can occur within a layer that contains melting ice particles because ice particles can melt within the regions of high relative humidity around 100% above the temperature of 0°C and melting diabatic cooling increases relative humidity. Rutledge and Hobbs (1983) used a numerical model to investigate the enhancement of precipitation in a “seeder-feeder” situation within warm-frontal rainbands. From the simulations, it was found that condensation occurs due to strong cooling associated with melting of snow from the seeder cloud and that the maximum cloud liquid water content in the feeder cloud is located just below the 0°C level. Stewart et al. (1984) took measurements from an aircraft flown through the melting layer of stratiform clouds over the California Valley and identified an isothermal layer at the 0°C level as well as large amount of cloud liquid water slightly below the 0°C level. It was inferred that the melting process within the stratiform precipitation region is possibly associated with the production of cloud liquid water and consequent enhancement of precipitation. Szyrmer and Zawadzki (1999) used a numerical model to demonstrate that the non-uniformity of snow content causes horizontal variability in various atmospheric properties within the melting layer and that this in turn leads to the generation of convective cells. Consequently, the possibility exists that diabatic cooling due to the melting process might be responsible for the formation of mid-level thin cloud that is commonly observed in the tropics, especially the cloud at the 0°C level.

Yasunaga et al. (2006) showed that thin clouds and layers with high relative humidity appear just below the 0°C level several hours after stratiform precipitation becomes active. The stable layer does not predate the appearance of the layer with high relative humidity. In contrast, the enhanced stability layer is simultaneously observed with high relative humidity and is located just above the level of high relative humidity. Moreover, the weakened stability layer is also synchronously found below the level of high relative humidity. Melting diabatic cooling can account for the simultaneous appearance of layers with high relative humidity and enhanced and weakened stability layers (e.g., Stewart et al. 1984; Johnson et al. 1996). Therefore, Yasunaga et al. (2006) suggested that the cloudy layer (and the layer with high relative humidity) around the 0°C level is brought about by the melting process within the stratiform precipitation region rather than detrainment of surface-based convection; this type of cloud was named “melting-layer cloud.”

As described above, there are two candidate processes that are able to explain the common occurrence of cloudy layers around the 0°C level in the tropics: cloud detrainment promoted by the stable layer and enhanced condensation to compensate melting cooling. Although both processes are plausible, little attention has been paid to diabatic cooling associated with the melting process. Therefore, in the present study, we use a two-dimensional cloud-resolving model, and conduct numerical simulations of a squall-line in order to examine: (1) whether mid-level thin cloud is able to form within an environment without a stable layer, and (2) what causes the mid-level thin cloud to form, especially at the 0°C level—the presence of a stable layer or melting cooling.

2. Model descriptions and experimental design

Numerical simulations were performed using version 2.1 of the Weather Research and Forecasting (WRF) model, which solves fully compressible nonhydrostatic equations. The basic equations and a description of the numerics can be found in Skamarock et al. (2001) and Wicker and Skamarock (2002). A third-order-accurate Runge-Kutta scheme is used for the time integration. Fifth- and third-order schemes are utilized for spatial discretization in the horizontal and vertical directions, respectively. A 1.5-order scheme using a prognostic equation of turbulent kinetic energy (TKE) is applied to represent subgrid-scale effects (Klemp and Wilhelmson 1978). Cloud microphysical parameterization includes five categories of water condensates (cloud water, rainwater, cloud ice, snow, and graupel), and is based on Lin et al. (1983) and Rutledge and Hobbs (1984). Although the original code of the WRF model does not allow evaporation from rain, snow, and graupel at values of relative humidity above 90%, in the present study we modify the cap on evaporation to 100% relative humidity. Radiation and land-surface schemes are not employed in the present study.

The model domain is limited to two dimensions (horizontal and vertical). The horizontal grid size is 250 m with the domain covering an area of 500 km (2000 grid points). The model has 95 layers in the vertical and a top boundary at 24 km, corresponding to a grid size of about 250 m. The model employs the time-splitting method proposed by Klemp and Wilhelmson (1978). In the present study, the large time step is set to 3 s, with 6 small time steps within each large step. Rayleigh damping is imposed near the upper boundary, and open lateral boundary conditions are specified. The Coriolis parameter is set to zero.

Environmental conditions prior to the initiation of convection are set to be horizontally homogeneous. While the sounding is based on a composite analysis by LeMone et al. (1994), some modifications are introduced. The original profile analyzed by LeMone et al. (1994) is used in the Global Energy and Water Cycle Experiment (GEWEX) Cloud System Study (GCSS) model intercomparisons, and is thought to be characteristic of the environment prior to the development of a squall-line (see Redelsperger et al. 2000, hereafter R2000). The profile of horizontal wind is shown in Fig. 1a. Low-level shear provides favorable conditions for the development of long lasting squall-lines (Rotunno et al. 1988). To eliminate the influence of fluctuations in humidity, temperature and horizontal wind profiles, we assume constant relative humidity (85%) above 2 km height (with respect to ice saturation below 0°C), a pseudo-adiabatic lapse rate between heights of 2 and 10 km (Fig. 1b), and constant vertical shear of horizontal wind above 2 km (Fig. 1a).

Deep convection is initiated in the numerical simulation by placing a 20 km surface-based cold temperature anomaly at time = 0. The 1.2 km-deep cold pool has temperature and moisture deficits of 3.5 K and 3.5 g kg^{-1} from the environmental sounding, respectively. To keep the convective system within the simulation domain, the model domain is translated at a constant speed of 12 m s^{-1} along the x direction. The model is integrated up to 17 hours (h).

3. Formation of melting-layer cloud in the numerical simulation

A cloudy grid box is defined as one in which the mixing ratio for those hydrometeors with small terminal velocity (cloud water, cloud ice, and snow) exceeds 0.05 g kg^{-1}. At the early stage of the squall-line, clouds reach a height of 15 km (Fig. 2a) with the cloud top height decreasing to 10 km at 5 h. Although the initial temperature profile does not show a mid-level stable layer (Fig. 1b), there is a notable peak in cloud coverage just below the 0°C level. If snow is excluded from the “cloud” variables, the peak in the middle level is still prominent (not shown), and does not depend on the “cloud” definition. Enhanced and weakened stability layers simultaneously appear above and below the peak level of cloud coverage (Fig. 2b), which is in agreement with the situation where melting-layer cloud was observed (Yasunaga et al. 2006). As most of the two-dimensional experiments in R2000 show a maximum in total hydrometeor content at the melting level (e.g., Fig. 17 in R2000), mid-level thin cloud would be robust regardless of the chosen models.

To clarify the process responsible for the mid-level thin cloud observed in Fig. 2a, changes in the cloud mixing ratio due to dynamic process (advection and diffusion) and cloud microphysics (condensation, evaporation, coalescence, aggregation, riming, etc.) are averaged over the model domain for a 17-hour period (Fig. 3). As the majority of condensates associated with the squall-line remain within the computational domain at 17 h, the domain-averaged changes of condensates by dynamic process in Fig. 3 result from vertical advection and vertical diffusion.

Although both profiles of the change in the cloud mixing ratio have a pronounced maximum around the height of 5 km (Fig. 3), the peak level of cloud microphysics is closer to the peak level of cloud coverage (Fig. 2a). In addition, the peak value of cloud microphysics is much greater than that of the dynamic process. Therefore, it can be said that cloud microphysics is responsible for the occurrence of mid-level thin cloud.

While the mid-level thin cloud is associated with cloud microphysics, total diabatic heating via cloud microphysics shows no notable peak around the height of 5 km (Fig. 4a); however, intense heating associated with the vapor-liquid or vapor-ice phase change occurs at the 0°C level, which approximately balances the strong melting cooling. The approximate balance between condensation or sublimation heating and melting cooling is locally maintained (not shown).

In the convective region near the leading edge (395–450 km), condensation or sublimation heating is the main contributor to the total diabatic heating (Fig. 4b). In the rear region of the squall-line (300–395 km), melting cooling and condensation or sublimation heating are approximately canceled, while total heating shows a typical profile of the stratiform region and no notable feature at the 0°C level (Fig. 4c). Therefore, the mid-level thin cloud is formed in the rear region of the squall-line.

It is possible that the enhanced condensation or sublimation is the cause of the intensified melting cooling. Condensation heating is, however, much larger than sublimation heating at the 0°C level, and the heating due to the phase change from liquid to ice above the 0°C level is much smaller than the cooling from ice to liquid in Fig. 4. In addition, the intensified melting cooling should be located in the rear of the enhanced condensation heating, if ice formation following the enhanced condensation intensifies melting cooling. The condensation heating region, however, coincides with the melting cooling region, and the approximate balance is locally attained. The coincident location indicates that strong melting cooling is the cause of the enhanced condensation at the 0°C level. In other words, ice formation following the enhanced condensation does not produce a notable peak of melting cooling at the 0°C level, but melting cooling enhances condensation. The simulated mid-level thin cloud is the “melting-layer cloud” suggested by Yasunaga et al. (2006).

Figure 5 represents the evolution of the simulated squall-line from 6 to 10 h at 30 minute intervals. The domain is subjectively partitioned into three regions (R1, R2, and R3), according to the stage of convective cells. At 6 h, active convective cells develop in the leading region of the squall-line (R1 in Fig. 5a), mature at 7 h (R2 in Fig. 5c), and gradually decay after 7 h and 30 min (R2 in Figs. 5d and 5e, and R3 in Figs. 5f and 5g). After the development of several weaker convective cells from 7 to 8 h near the leading edge of the squall-line (R1 in Figs. 5c, 5d and 5e), even more vigorous convective cells appear at 8 h and 30 min (R1 in Fig. 5f), and reach the height of 15 km at 10 h (R2 in Fig. 5i). In the trailing part of the active convective cells which develop from 6 h, thin cloud is found around 5 km at 8 h and 30 min (R3 in Fig. 5f), is left behind from the front part of the convective cells at 9 h (R3 in Fig. 5e), and then, is overlapped by the following weaker convective cells at 9 h and 30 min and 10 h (R3 in Figs. 5h and 5i).

Figure 6 shows condensation rate profiles averaged over each region in Fig. 5 from 6 to 10 h at 30 minute intervals. In the leading region of the squall-line (R1), condensation occurs most vigorously, and the peak of the condensation rate is located around the height of 2–3 km. In the rear region of the squall-line (R2 and R3), the condensation peak is prominent at the height of 5 km (around the 0°C level). Although mid-level thin cloud is not identified in the R2 region of Fig. 5, condensation is pronouncedly enhanced at the height of 5 km within the R2 region, even when convective cells mature in the R2 region (e.g., Figs. 5c, 5i, 6c, and 6i).

References

Bretherton, C. S., and P.K. Smolarkiewicz, 1989: Gravity waves, compensating subsidence and detrainment around cumulus clouds, *J. Atmos. Sci.*, **46**, 740-759.

Johnson, R.H., P.E. Ciesielski, and K.A. Hart, 1996: Tropical inversions near the 0°C level, *J. Atmos. Sci.*, **53**, 1838-1855.

-, T. M. Rickenbach, S. A. Rutledge, P. E. Ciesielski, and W. H. Schubert, 1999: Trimodal characteristics of tropical convection, *J. Climate*, **12**, 2397-2418.

Klemp, J. B., and R. B. Wilhelmson, 1978: The simulation of three dimensional convective storm dynamics, *J. Atmos. Sci.*, **35**, 1070-1096.

LeMone, M. A., D. P. Jorgensen, and B. F. Smull, 1994: The impact of two convective systems of sea-surface stresses in COARE. Preprints, *6th Conference on Mesoscale Processes*, Amer. Meteor. Soc., Portland, 40-44.

Lin, Y.-L., R. D. Farley, and H. D. Orville, 1983: Bulk parameterization of the snow field in a cloud model. *J. Appl. Meteor.*, **22**, 1065–1092.

Mapes, B. E., and P. Zuidema, 1996: Radiative-dynamical consequences of dry tongues in the tropical troposphere, *J. Atmos. Sci.*, **53**, 620-638.

-, 2001: Water's two height scales: the moist adiabat and the radiative troposphere, *Q. J. R. Meteor. Soc.*, **127**, 2353-2366.

Redelsperger, J. L., P. R. A. Brown, R. Guichard, C. Hoff, M. Kawasima, S. Lang, Th. Montmerle, K. Nakamura, K. Saito, C. Seman, W.K. Tao, and L.J. Donner, 2000: A GCSS model intercomparison for a tropical squall line observed during TOGA-COARE. Part I: Cloud-resolving models, *Q. J. R. Meteor. Soc.*, 126, 823-863.

Rotunno, R., J. B. Klemp, and M. L. Weisman, 1988: A theory for strong, long-lived squall lines, *J. Atmos. Sci.*, **45**, 463-485.

Rutledge, S. A., and P. V. Hobbs, 1983: The mesoscale and microscale structure and organization of cloud and precipitation in midlatitude cyclones. VIII: A model for the “Seeder-Feeder” process in warm-frontal rainbands, *J. Atmos. Sci.*, **40**, 1185-1206.

-, and -, 1984: The Mesoscale and microscale structure and organization of clouds and precipitation in midlatitude cyclones. XII: A diagnostic modeling study of precipitation development in narrow cold-frontal rainbands. *J. Atmos. Sci.*, **41**, 2949–2972.

Skamarock, W. C., J. B. Klemp, and J. Dudhia, 2001: Prototypes for the WRF (Weather Research and Forecasting) model. Preprints, *9th Conf. on Mesoscale Processes*, Fort Lauderdale, FL, Amer. Meteor. Soc., J11-J15.

Stewart, R. E., J. D. Marwitz, J. C. Pace, R. E. Carbone, 1984: Characteristics through the melting layer of stratiform clouds, *J. Atmos. Sci.*, **41**, 3227-3237

Sugimoto, N., I. Matsui, A. Shimizu, M. Pinandito, S. Sugondo, 2000: Climatological characteristics of cloud distribution and planetary boundary layer structure in Jakarta, Indonesia revealed by lidar observation, *Geophys. Res. Lett.*, 27(18), 2909-2912, 10.1029/2000GL011544.

Szyrmer, W., and I. Zawadzki, 1999: Modeling of the melting layer. Part I: Dynamics and microphysics, *J. Atmos. Sci.*, **56**, 3573-3592.

Takayabu, Y. N., J. Yokomori, and K. Yoneyama, 2006: A diagnostic study on interactions between atmospheric thermodynamic structure and cumulus convection over the tropical western Pacific Ocean and over the Indochina peninsula. *J. Meteor. Soc. Japan*, 84A, 151-169.

Taylor, G.R., and M.B. Baker, 1991: Entrainment and detrainment in cumulus clouds, *J. Atmos. Sci.*, **48**, 112-121.

Wicker, L. J., and W. C. Skamarock, 2002: Time splitting methods for elastic models using forward time schemes. *Mon. Wea. Rev.*, **130**, 2088-2097.

Yasunaga, K., H.Kida, and T. Satomura, 2003: The 600-750 hPa relative humidity minimum observed during PEM-Tropics B, *Geophysical Research Letters*, 30(24), 2282, doi: 10.1029/2003GL018739.

-, -, -, and N. Nishi, 2004: A Numerical Study on the Detrainment of Tracers by Cumulus Convection in TOGA COARE, *J. Meteor. Soc. Japan,* **82**, pp861-878.

-, K., K. Yoneyama, H. Kubota, H. Okamoto, A. Shimizu, H. Kumagai, M. Katsumata, N. Sugimoto, and I. Matsui, 2006: Melting-layer cloud observed during MR01-K05 cruise of Res/V Mirai, *J. Atmos. Sci.*, **20**, pp1061-1072.

Zuidema, P., 1998: The 600-800-mb minimum in tropical cloudiness observed during TOGA COARE, *J. Atmos. Sci.*, **55**, 2220-2228.

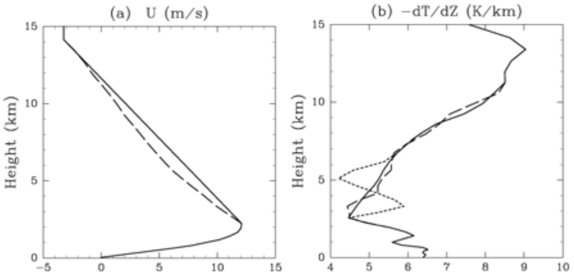

Fig. 1: (a) Initial profile of the horizontal wind (solid line). (b) Lapse rate calculated from initial temperature profile (solid line). Dashed lines in (a) and (b) represent the original profiles analyzed by LeMone et al. (1994). Dotted line in (b) indicates lapse rate calculated from initial temperature profile used in the sensitivity test (see Section 4a).

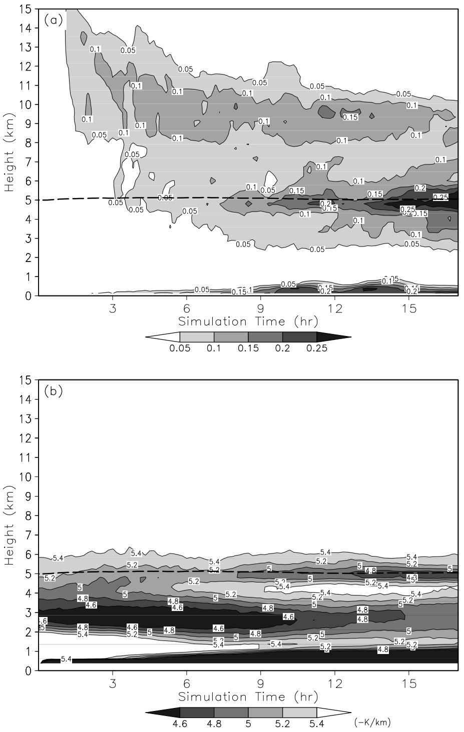

Fig. 2: Temporal record of vertical profiles of cloud fraction (a) and temperature lapse rate averaged over the model domain (b). A dashed line in each panel indicates the 0°C level.

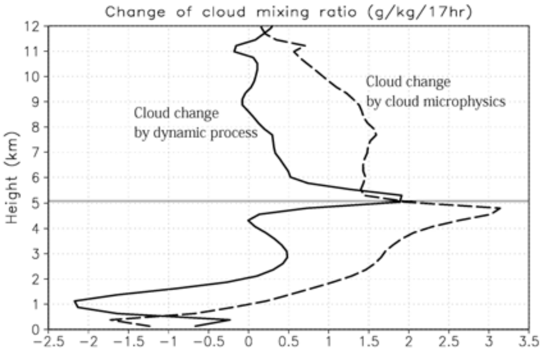

Fig. 3: Vertical profile of domain-averaged changes in the cloud (cloud water + cloud ice + snow) mixing ratio due to dynamic process (solid line) and cloud microphysics (dashed line) during the 17–hour period of the simulation.

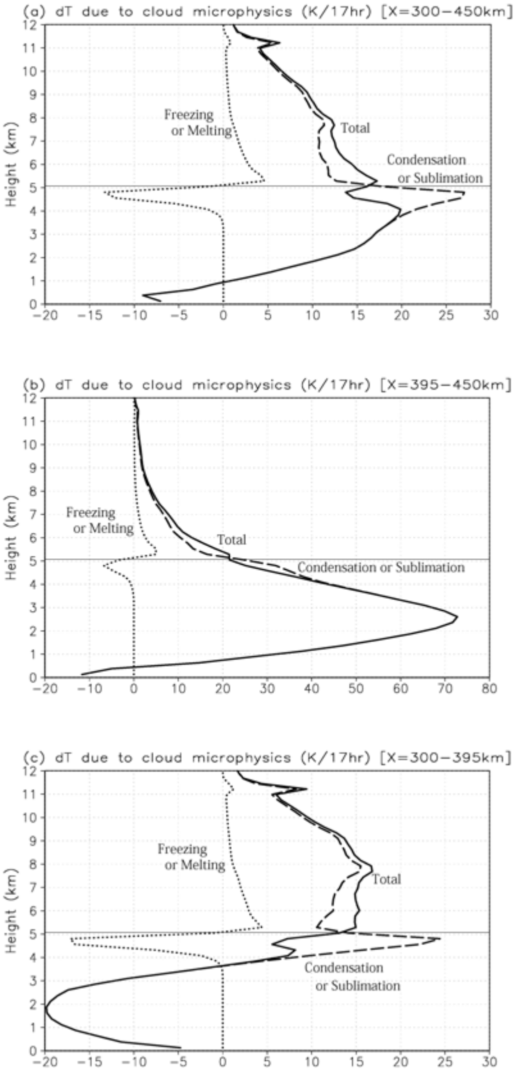

Fig. 4: Vertical profile of diabatic heating associated with cloud microphysics averaged over 300–450 km (a), 395–450 km (b), and 300–395 km (c) of the model domain. A solid line indicates total heating. Dashed and dotted lines represent heating due to phase changes between vapor and condensates (liquid or ice), and between liquid and ice, respectively.

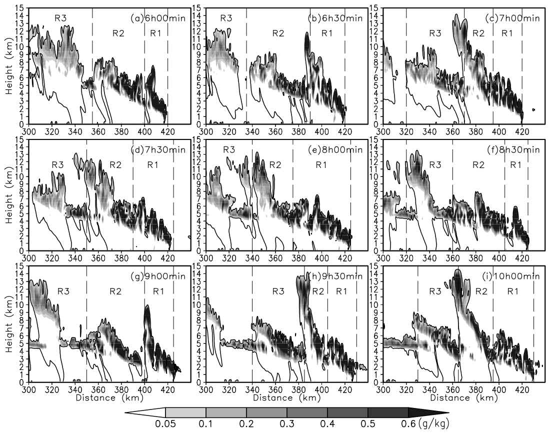

Fig. 5: Vertical cross sections of the cloud (cloud water + cloud ice + snow) mixing ratio from 6 to 10 h at 30 minute intervals. Contoured area represents the area exceeding the total hydrometeor of 0.05 g kg^{-1}. Only part of the simulation domain is shown.

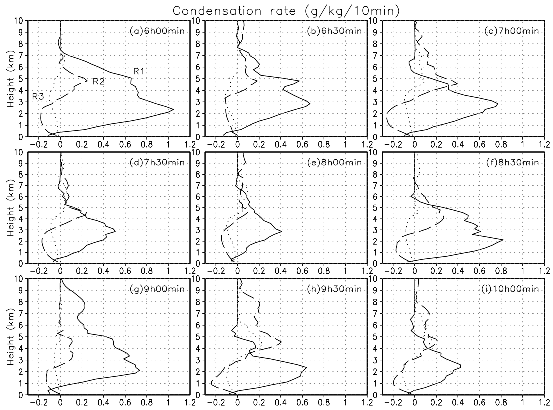

Fig. 6: Vertical profiles of condensation rate from 6 to 10h at 30 minute intervals. Solid, dashed, and dotted lines represent profiles averaged over R1, R2, and R3 regions in Fig. 5 during 10 minutes, respectively.

ORGANIZATIONAL MODELS AND DISASTER ANALYSES OF MESOSCALE CONVECTIVE SYSTEMS IN THE WEIBEI REGION OF SHAANXI PROVINCE

Zhi-Guo YUE[1,2], Sheng-Jie NIU[1*] , Gu LIANG[2]
1. Laboratory for Atmospheric Physics& Environment of China
Meteorological Administration, Nanjing University of Information Science & Technology,
Nanjing 210044, P.R.China;
2. Weather Modification Office of Shaanxi Province, Xi’an 710015, P.R.China

1. INTRODUCTION

The agricultural region of Weibei in Shaanxi province is a famous area for apple orchards, where there almost 800 thousand acres with a yearly yield of over 5 million tons. Weather disasters such as drought, low temperature, hail, strong wind etc, seriously influence the yield and quality of apple. The regional hail storms can cause tremendous loss in Weibei Region and seriously affect the fruit industry economy.

The regional severe storm weather is often caused by Mesoscale Convective Systems (MCS) that are a major focus for disaster research and mitigation. In the past 20 years, a lot of work (Bluestein; Parks 1983, Bluestein; Jain 1985; Bluestein et al. 1987; Jirak et al. 2003; Parker; Johnson 2000, 2004a, 2004b, 2004c) has been invested worldwide on modeling MCS coupled with field projects to measure their characteristics with ground based radar and satellite. Unfortunately, convective lines were often the only types of MCS considered in the radar studies. The classification presented in this paper includes a wide variety of MCS.

2. DATA AND METHODS OF ANALYSIS

There are four 711-digital weather radars and two Doppler weather radars in the Weibei region. The Radar of Luochuan county(35.49°N, 109.30°E, elevation 1159.1 m) located in the central part of Weibei region. During the annual May to September, there is regular observation every three hours a day, or a strong convection Echo detection, or clouds development report of continuous observation. Because Luochuan radar data has better integrity and long time accumulation, and this paper mainly use Luochuan radar data between May and September from 2000 to 2006, with other radar data, hail facts observations and hail disaster collections.

The entire occurrence, development and dissipation process of convective cloud Echo was defined one case. The convections on the same day in different period of time were respectively recorded for different cases.

We investigated seven years radar data, select 335 cases of convective clouds integrated development for classification analysis, incomplete case out of the 19 cases, accounting for a total of convective clouds case of 5.3%. We believe that the remove of these cases will not introduce a large bias into the study.

3. ORGANIZATIONAL MODELS OF MCS

Following Bluestein and Jain (1985), Parker and Johnson (2000), and Jirak et al.’s (2003) study, the terms line, areal, embedded, broken, merger, non-merger, TS(trailing stratiform), LS(leading stratiform), PS(parallel stratiform) were implemented into this paper.

According to PPI echo isolated

---

[*] Correaponding author.
E-mail address: niusj@nuist.edu.cn

convective cells or linear convection composed of a number of convective cells or group, the 335 MCS of May-September from 2000 to 2006 were classified into three basic categories: cell MCS, linear MCS, and areal MCS. Based on stratiform cloud spread to the location again, whether mobile, and the characteristics of the merger, these MCS were further defined nine subcategories (Fig.1).

Accordingly, the taxonomy presented here is based solely upon the radar reflectivity structures of the MCS, not upon their dynamics, velocity fields, or other observable properties.

a. Cell MCS

1) Unmoving cell

We deem a unmoving cell MCS to have only a convection cell in the 60 km zone if one cell’s position is little change. The change of the classification position is less than 5km throughout its life cycle.

2) Moving cell

The moving cell MCS in the newborn and the stage of development is the same features as unmoving cell MCS. However, the type has been in moving from newborn, development to dispersion, and Changes in the location of more than 5 km.

3) Merger cell

In the initial stage, the merger cell MCS has a series of little cell within the 10 to 30 km, and these cell is slowly approaching development, and ultimately merged into a centre of a strong echo of the convective cells, around 60 km range no other convection echo development.

b. Linear MCS

1) Trailing stratiform

2) Leading stratiform

3) Parallel stratiform

A convective line with trailing stratiform, leading stratiform, and parallel stratiform precipitation (simply TS, LS, and PS) was described by Parker and Johnson (2000), we follow the definition that they presented.

4) Broken Linear

The broken linear MCS was deemed a number of small cells arranged in a convection line, with a direction to the movement, with a series of intense reflectivity cells solidly isolation without connected. These convective cells in the process of development were mutual separation, but always maintain for the whole of the fracture line.

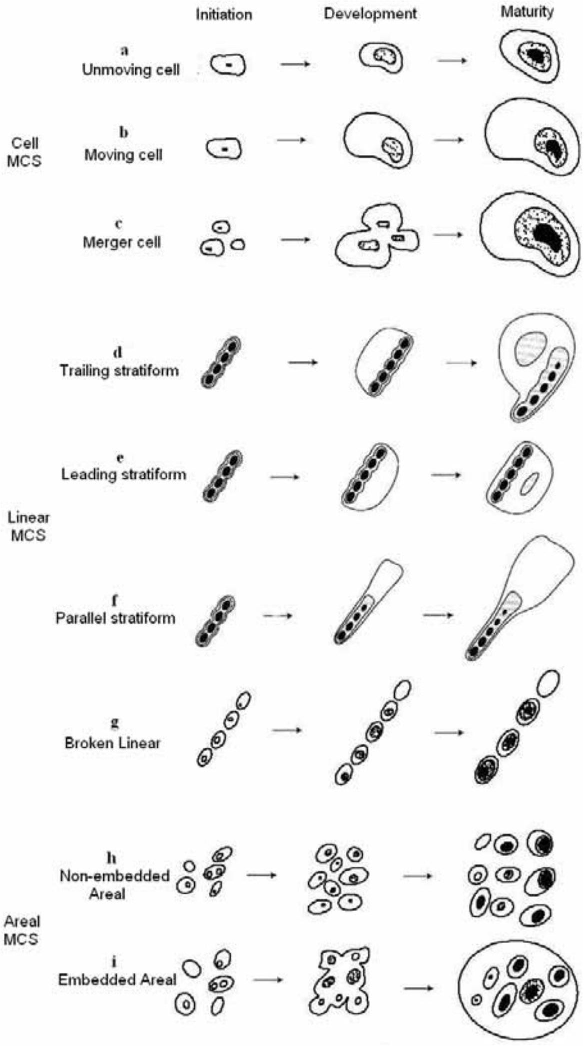

Fig.1 Idealized depiction of the classification scheme used to categorize MCS development as seen by radar in Weibei region of Shaanxi province. （Levels of shading roughly correspond to 20, 40, and 50 dBz. TS, LS and PS linear convective

systems from Parker 2000)

c. Areal MCS

1) Non-embedded Areal

We define non-embedded areal MCS who contains several dozens of disordered convective cells, the each cell's scale of 5 to 20 km, which have no apparent linear convection, and the cell cluster has an area of 40 km×60km to 80km×120km. The convective cells in the cluster are respective separation, and moving the same direction, generating new convective cells in the moving ahead. The cells are isolation without connected to the weak echo.

2) Embedded Areal

The embedded areal MCS type was described with a series of intense reflectivity cells (45～70dBz) solidly connected by echo of stratiform cloud, which have no apparent linear convection, exists melting layer and Strong convective cells of the top 8~10 km on RHI.

4. ANALYSES OF MCS CHARACTER

a. Examples of Classes

Of the 335 cases in the study domain between May and September from 2000 to 2006,cell MCS, linear MCS and areal MCS were 117, 71, and 147 cases, then it is obvious that cell MCS and areal MCS are the most prevalent of the two classes (accounting for 33% and 41% of the 335 total MCS). The non-embedded areal MCS was found to be the dominant mode in all MCS organization. The cell MCS and linear MCS were the greater the frequency of changes, and even don't appear in some years.

b. Diurnal Variability

The frequency of times of MCS initiation is displayed that most of the systems were initiated between 1100 and 2100 BST, which corresponds to the afternoon and evening hours of the China. The linear MCS cases occurred between 1300 and 2100 BST, with a smaller case in linear MCS between 0200 and 1200 BST. The areal MCS have occurred any times in a day, but the main initial time between 1000 and 1700 BST. Clearly, the strong afternoon solar radiation is the main factors to the development of various types of MCS. the linear MCS and areal MCS Occurred at the end of the morning often associated with the large-scale synoptic system.

c. Mean Duration, Scale and Speed

The unmoving cell MCS has the smallest mean duration(1.6h) and the smallest mean scale (7.42km) in nine subcategories, and the non-embedded areal MCS with the greatest mean duration (4.4h) and the greatest mean scale (102.98km). The moving speed of the TS MCS was the most, an average of 33 km/h.

5. DISASTER ANALYSES

a. Cell MCS

The unmoving cell MCS has the smallest probability of hail (6%), and the scope of surface hail was very small with about 5mm in hail diameter, very small disaster. The transmission paths of moving cell MCS were often more than 100km and there were almost hail in path with serious disaster. The probability of the moving cell MCS was 31%. The merger cell MCS was the least number of cell MCS (11 cases), but the highest probability of hail (36%) in cell MCS.

b. Linear MCS

The TS has the greatest probability of hail (62%) in nine subcategories, 5 times regional severe hail weather (May 15, June 28, July 2, 2002, May 30, 2005, June 25, 2006) which were the most destructive weather. The hail cases number of LS, PS, and broken linear were 2, 7 and 13.

c. Areal MCS

There were 26 hail cases in the total of the non-embedded areal MCS which have 26% probability of hail, and the most number of regional severe hail weather, with generally hail diameter between 5 and 15 mm, a very small number of hail diameter over 50 mm. The probability of the embedded areal MCS was 30%, which hail disaster and hail zone were less than non-embedded.

6. SUMMARY

This study cataloged and analyzed 335 MCS from the region of Weibei in Shaanxi province between May and September from 2000 to 2006. These conclusions are found include the following.

- The taxonomy is proposed that comprises three-levels (cell, linear and areal MCS) and nine sub-classes (unmoving cell, moving cell, merger cell, trailing (TS), leading (LS), parallel (PS) stratiform precipitation, broken Linear, non-embedded areal, and embedded areal MCS).
- The areal MCS was found to be the dominant mode in all MCS organization, the cell and linear MCS composed 53% of the population that was evaluated.
- The frequency of times of MCS initiation is displayed that most of the systems were initiated between 1100 and 2100 BST.
- The unmoving cell MCS was the smallest mean duration (1.6h) and the smallest mean scale (7.42km), and the non-embedded areal MCS was the greatest mean duration (4.4h) and the greatest mean scale (102.98km).
- The linear MCS has the highest probability of hail, and cell MCS has the least, TS MCS tends to have more severe weather reports and regional severe hail weather.

7. BIBLIOGRAPHY

Bluestein, H. B., and C. R. Parks, 1983: A Synoptic and Photographic Climatology of Low-Precipitation Severe Thunderstorms in the Southern Plains. *Mon. Weather. Rev.*, **111,** 2034-2046.

Bluestein, H. B., and M. H. Jain, 1985: Formation of Mesoscale Lines of Pirecipitation: Severe Squall Lines in Oklahoma during the Spring. *J. Atmos. Sci.*, **42,** 1711-1732.

Bluestein, H. B., G. T. Marx, and M. H. Jain, 1987: Formation of Mesoscale Lines of Precipitation: Nonsevere Squall Lines in Oklahoma during the Spring. *Mon. Weather. Rev.*, **115,** 2719-2727.

Jirak, I. L., W. R. Cotton, and R. L. McAnelly, 2003: Satellite and Radar Survey of Mesoscale Convective System Development. *Mon. Weather. Rev.*, **131,** 2428-2449.

Parker, M. D., and R. H. Johnson, 2000: Organizational Modes of Midlatitude Mesoscale Convective Systems. *Mon. Weather. Rev.*, **128,** 3413-3436.

——, 2004a: Simulated Convective Lines with Leading Precipitation. Part I: Governing Dynamics. *J. Atmos. Sci.*, **61,** 1637-1655.

——, 2004b: Simulated Convective Lines with Leading Precipitation. Part II: Evolution and Maintenance. *J. Atmos. Sci.*, **61,** 1656-1673.

——, 2004c: Structures and Dynamics of Quasi-2D Mesoscale Convective Systems. *J. Atmos. Sci.*, **61,** 545-567.

ACKNOWLEDGEMENT

Key Technology and Instrument Development in Weather Modification （2006BAC12B02）from MOST of P.R.China, and National Natural Science Foundation of China (Grant No. 40537034) supported this research.

THREE-DIMENSIONAL NUMERICAL SIMULATION OF A STRONG CONVECTIVE STORM

Hua-Ying YU[1,2], Sheng-Jie NIU[2 *], Song-Shan GU[1]

1. China-America Cooperative Remote Sensing Center, Nanjing University of Information Science & Technology, Nanjing 210044, P.R.China;
2. Laboratory for Atmospheric Physics& Environment of China Meteorological Administration, Nanjing University of Information Science & Technology, Nanjing 210044, P.R.China

1. ABSTRACT

A fully elastic, three-dimensional, convective storm model (IAP-CSM3D) was used to simulate a strong convective storm that occurred in Hunan province on Apr.23th, 2004. The temporal and spatial evolution of macro and microphysical variations and the formation mechanism of hailstones in the storm were analyzed. The primary results are: 1) The condition in the lower atmosphere of warm temperatures and high humidity combined with the wind shear to produce the resulting high precipitation intensity, 2) the changing with height of horizontal divergence, observed by radar, is consistent with the wind field structure of the simulation, 3) the maximum water content simulated by the model corresponds with the strong echo measured by the radar and both appear near to the region of the highest vertical velocities, 4) the high water content center was located near the freezing layer, 5) the auto-conversion of frozen drops and graupel is the main source of the hailstones in this particular strong convective storm but the contribution of frozen drops is greater than that of graupel.

2. ACTUAL WEATHER

On Apr.23th, 2004 a squall line crossed through the center and south area of Hunan province producing heavy rainfall in much of the area. The maximum 3-hour precipitation exceeded 50mm and there was hail damage, as well.

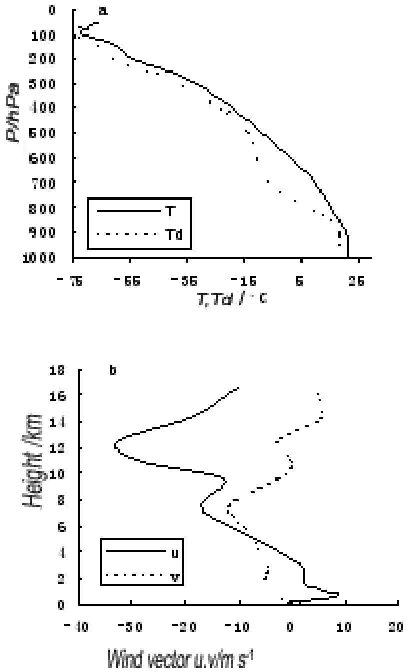

Fig.1 Initial conditions.
(a) Temperature profile. (b) Wind profile.
Positive value is east wind and north wind

3. THE SIMULATION OF THE SIMULATION OF THE WIND FIELD STRUCTURE

---

[*] Correaponding author.
E-mail address: niusj@nuist.edu.cn

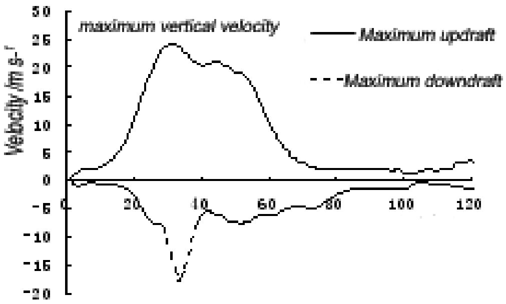

Fig. 2 The changing of maximum vertical velocity with time
(Solid line is updraft; dashed line is downdraft)

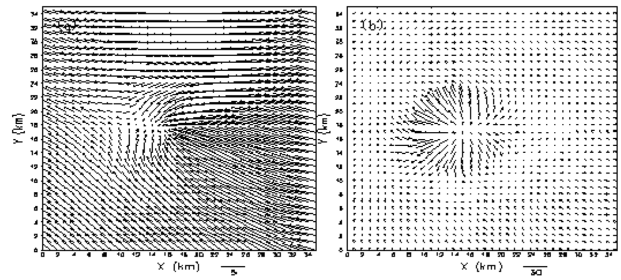

Fig. 3 The distribution of stream field at 18min (a) and 34min (b) on the surface z=0.5km

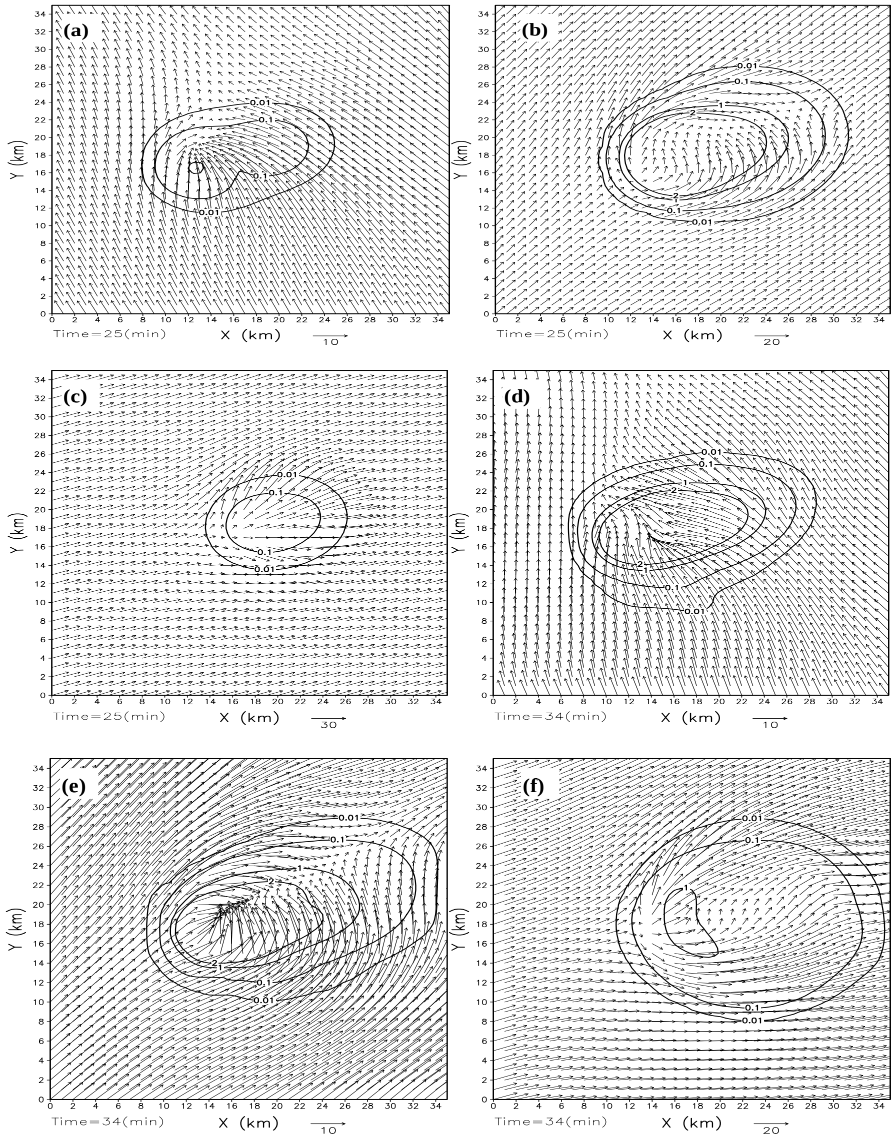

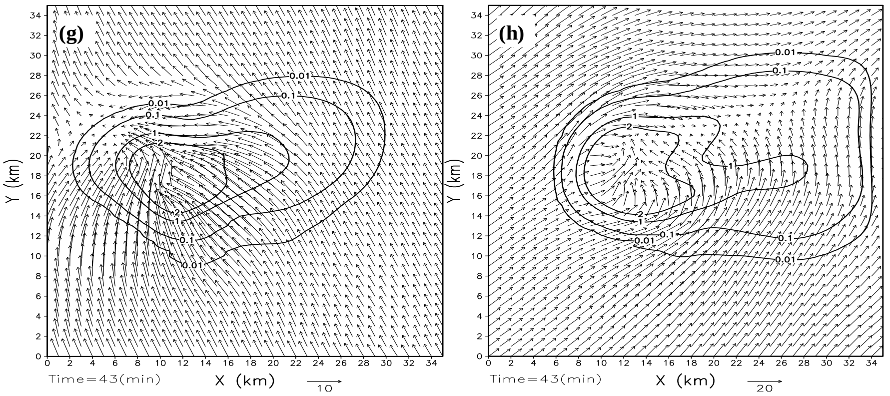

Fig. 4 Cross-sections of wind vector and Qt(solid curve) along Z axis at 25min 34min and 42min.

a. 25min, 2km; b. 25min, 5km; c. 25min, 9km; d. 34min, 2km; e. 34min, 5km; f. 34min, 9km; g. 43min, 2km; h. 43min, 5km; i. 43min, 9km.

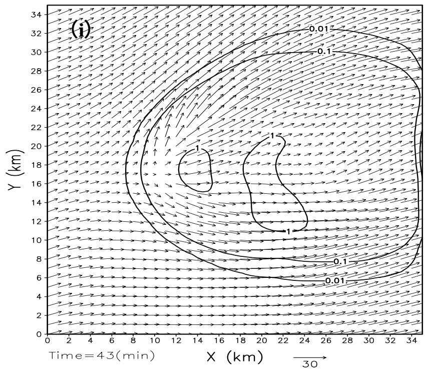

4. THE SIMULATION OF THE RADAR ECHO AND WATER CONTENT

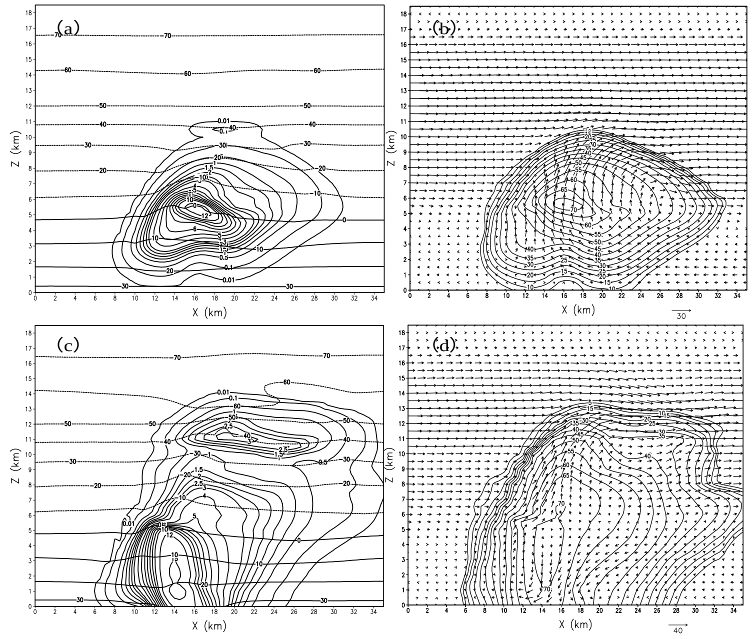

Fig.5 Cross-sections of total water content (Left) and radar reflectivity (Right) along x axis. (y=17km)

a. 25min; b. 25min; c. 34min; d. 34min.

5. THE FORMATION MECHANISM OF HAILSTONES

Hailstones mainly depend on the processes of collecting super cooled water to grow. The change of water content centered in hailstones was consistent with the changing trend of the water content first being centered on frozen drops. From this, the following result can be given from the macroscopic point: frozen drops mainly played the role as embryo during the course of the hailstone growing and then the water content centering on frozen drops could explain the forming and the distribution of the subsequent region of hailstones.

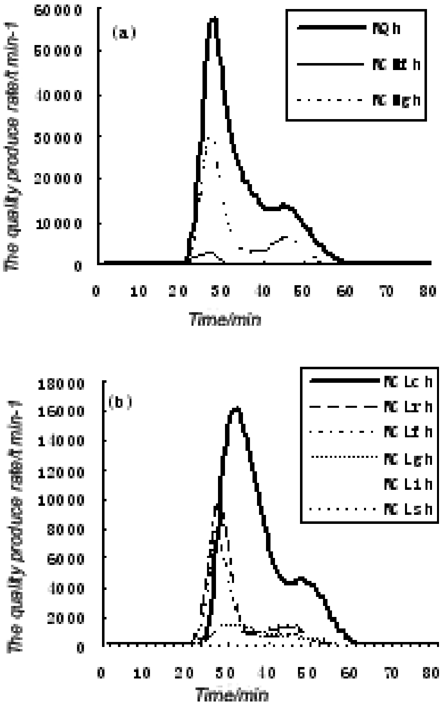

Fig.6 The quality produce rate of the hail's formation and increasing with time a. The quality produce rate of hail's formation ; b. The quality produce rate of hail's increasing

6. BIBLIOGRAPHY

Steiner J T. A three-dimensional model of cumulus cloud development [J]. Atmos Sci,1973,30(3):141-435.

Klemp J B,Wilhelmson.R B The simulation of three-dimensional convective storm dynamics[J]. Atmos Sci,1978,35(6):1070-1096.

Kong F.Y., Huang M.Y, Xu H.Y. Three-dimensional numerical simulations of iceing process in storms Ⅰ: Parameterized in cold cloud. Chinese Journal of Atmospheric Sciences, 1990, 14(4). pp. 441-453

Kong F.Y., Three-Dimensional Mumerical Simulations of Hailstorms [D]. Doctoral Disscrtation of Institute of Atmospheric Physics, Chinese Academy of Sciences, 1991

Hong Yanchao. A 3-D Hail Cloud Numerical Seeding Model. Acta Meteorologica Sinica, 1998, 56(6). pp.641-653

Zhou Ling, Chen B.J., Li Z.H. A Numerical Simulation of Hailstorm Accumulation Zone and Hail Formation. Chinese Journal of Atmospheric Sciences, 2001,25(4). pp.536-550

Xiao Hui, Wang X.B., Zhou F.F.A Three-Dimensional Numerical Simulation on Microphysical Processes of Torrential Rainstorms. Chinese Journal of Atmospheric Sciences, 2004, 28(3). pp.385-404

ACKNOWLEDGEMENT

Key Technology and Instrument Development in Weather Modification（2006BAC12B02）from MOST of P.R.China, and Nanjing University of Information Science & Technology Research Foundation Y652 supported this research. In this work, the quantitative analysis experiments are made using the Doppler radar data from Hunan province.

A COMPARISON OF CLOUD RESOLVING MODEL SIMULATIONS OF TRADE WIND CUMULUS WITH AIRCRAFT OBSERVATIONS TAKEN DURING RICO

Steven J. Abel, B. J. Shipway, C. J. Smith
Met Office, Exeter, UK, steven.abel@metoffice.gov.uk

1. INTRODUCTION

Trade wind cumulus clouds are prevalent over the subtropical oceans and are commonly observed to precipitate. Whilst detailed cloud resolving model (CRM) simulations have been shown to be a valuable tool for guiding parametrization development of moist convection within GCMs, the importance of precipitation from trade wind cumulus on the global climate remains poorly diagnosed, in part due to the crude representation of the warm rain process within current models. There is therefore the need to establish that CRMs are able to simulate realistic water budgets within the trade wind cumulus regime in order to ascertain their usability in developing parametrizations of precipitation fluxes.

The Rain In Cumulus over the Ocean (RICO) field campaign (Rauber et al., 2007) took place between November 2004 and January 2005 in the Caribbean around the islands of Antigua and Barbuda. A comprehensive suite of in-situ observations were made during RICO, providing an excellent tool for characterizing trade wind cumulus on scales ranging from the microphysical to the cloud field ensemble. This paper presents comparisons of some cloud field statistics derived from the three research aircraft that participated in RICO with those derived from numerical simulations performed with the Met Office CRM. The variation of updraft velocities, cloud liquid water content, and precipitation loading as a function of altitude above cloud base are shown, and the sensitivity of the simulations to different cloud microphysical configurations examined, focusing on the sensitivity to

- the complexity of the microphysics; single-moment (1M) versus double moment (2M) schemes.
- variations in the background aerosol conditions.

2. MODEL SET-UP

The model description and set-up are detailed in Abel and Shipway (2007). In brief, the horizontal domain spans 40 x 40 km with a resolution of 250m. In the vertical a stretched grid is used, consisting of 100 layers with 40m resolution in the boundary layer, increasing to 100m in the mid-troposphere and then further degraded to 200m at the top of the domain at 10 km. The sea surface temperature was fixed at 298 K and the Coriolis parameter set appropriate for a latitude of 18°N. Environmental profiles based on radiosonde and aircraft dropsonde measurements from the 19th January 2005 are chosen to initialise the model. The profiles show a fairly moist layer below the trade wind inversion at 600 - 650 hPa ($\sim$ 4 km) and above the sub-cloud boundary layer at 950 hPa. Above the inversion the air is much drier and stable, indicative of high level subsidence. Examination of radar imagery from the period of the observed profiles show towering cumulus with extensive rain shafts. The area-averaged surface rain rate derived from the radar data was 0.691 mm day^{-1} (Nuijens, 2005). The simulations tended to reach a quasi-equilibrium after around 10-12 hours and the results presented here are from 18 hours onwards[1].

3. WARM RAIN MICROPHYSICS

The Met Office CRM treats cloud and rain as two mutually exclusive categories and has previously been run using a 1M cloud scheme

---

[1] The model set-up varied slightly for the preliminary 2M cloud runs presented here. A smaller domain of 16x16km was used and the results represent a snapshot at hour 16.

in combination with both 1M and 2M representations of precipitation sized droplets (Swann, 1998; Abel and Shipway, 2007). In the 1M cloud/rain schemes the cloud/rain mass mixing ratio is the only prognostic variable. A more realistic representation of the precipitation is allowed with the addition of a prognostic rain drop number concentration variable in the 2M rain scheme. In both cases the cloud droplet number concentration (n_l) is fixed throughout the cloud. To assess the sensitivity of the simulated clouds to ambient aerosol conditions n_l is varied from 50 to 240 cm^{-3}. To put this into context, measurements of the sub-cloud concentration of cloud condensation nuclei (CCN) at a supersaturation of 1$\%$ made during the RICO field experiment varied from 54 to 200 cm^{-3}, with a mean value of 112±35 cm^{-3} (Hudson and Mishra, 2007).

In addition a 2-M cloud and rain scheme based on Seifert and Beheng (2006) has also been included into the CRM, which carries the cloud droplet number concentration as an additional prognostic variable. The activation of cloud droplets is calculated with a new parametrization detailed in Shipway et al. (2008). The aerosol conditions are included in the parametrization with a representation of the CCN spectra based on a log-normal size distribution and chemical components of the dry aerosol (Khvorostyanov and Curry, 2006).

The model is initialized by varying these aerosol parameters to best fit the observed CCN spectra. Figure 1 shows the cumulative CCN spectra derived from measurements made in the sub-cloud layer on the 19th January 2005. The number concentration of CCN, N_{CCN}, is shown to increase from 0.3 to 66.3 cm^{-3} at supersaturations of 0.02 to 1.5 $\%$. At a supersaturation of 1 $\%$ N_{CCN} is 57±13 cm^{-3}, indicative of some of the cleanest maritime conditons obseved during RICO (Hudson and Mishra, 2007). Figure 1 also shows the model fit (solid black) using the aerosol characterized with a monomodal log normal size distribution with a dry radius of 0.022 μm, standard deviation of 2.12 and total aerosol concentration of 73 cm^{-3}. The soluble component of the aerosol is assumed to consist of ammonium sulfate as detailed in Khvorostyanov and Curry (2006). To test the sensitivity to aerosol loading a simulation is also performed with the total aerosol concentration increased to 251 cm^{-3}, which corresponds to a N_{CCN} of 200 cm^{-3} at 1$\%$ supersaturation (dashed line in figure 1), indicative of the highest daily averaged CCN concentrations measured during RICO.

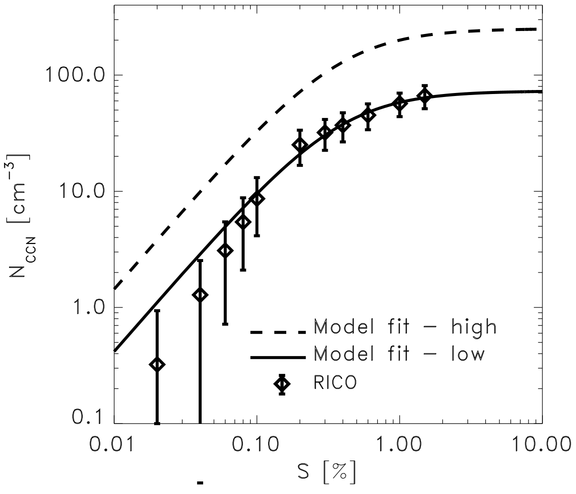

Figure 1: The observed mean sub-cloud CCN spectra from the 19th January 2005 is shown with diamonds. The error bars represent one standard deviation. The black line shows the model fit to the CCN spectra. The dashed line shows the model fit with an increase in aerosol loading.

4. SIMULATION FEATURES

Table 1 summarises the microphysics used in the different simulations and presents some area-averaged properties such as surface rain rate, liquid water path (LWP), rain water path (RWP) and cloud cover. Note that the area-averaged properties are not included for the preliminary 2M cloud simulations presented in this abstract which only represent a snapshot at hour 16 into the simulation. It is clear from table 1 that irrespective of the microphysics set-up, increasing the aerosol concentration acts to decrease the surface rain rate and RWP, whilst increasing the LWP and cloud cover. This is primarily due to a lower rate of cloud water being converted to rain in the autoconversion scheme. The surface rain rate for the simulations is within $\sim$ 30$\%$ of the radar derived value of 0.691 mm day^{-1}.

Run label	Cloud	Rain	n_l [cm^{-3}]	Rain rate [mm day^{-1}]	LWP [g m^{-2}]	RWP [g m^{-2}]	Cloud cover [%]	Microphysics
RUN-1Mc-1Mr-50n	1M	1M	50	0.813	9.0	4.6	10.8	S98
RUN-1Mc-1Mr-240n	1M	1M	240	0.522	13.9	3.6	11.3	S98
RUN-1Mc-2Mr-50n	1M	2M	50	0.887	8.2	6.9	10.7	S98
RUN-1Mc-2Mr-240n	1M	2M	240	0.700	13.5	5.0	12.0	S98
RUN-2Mc-2Mr-58n	2M	2M	*58*	–	–	–	–	SB06/S08
RUN-2Mc-2Mr-200n	2M	2M	*200*	–	–	–	–	SB06/S08

Table 1: Summary of the different simulations performed. n_l for the 2M cloud is the N_{CCN} at a supersaturation of 1 $\%$. S98 = Swann (1998), SB06 = Seifert and Beheng (2006), S08 = Shipway et al. (2008). Area-averaged properties are from 18 hours onwards.

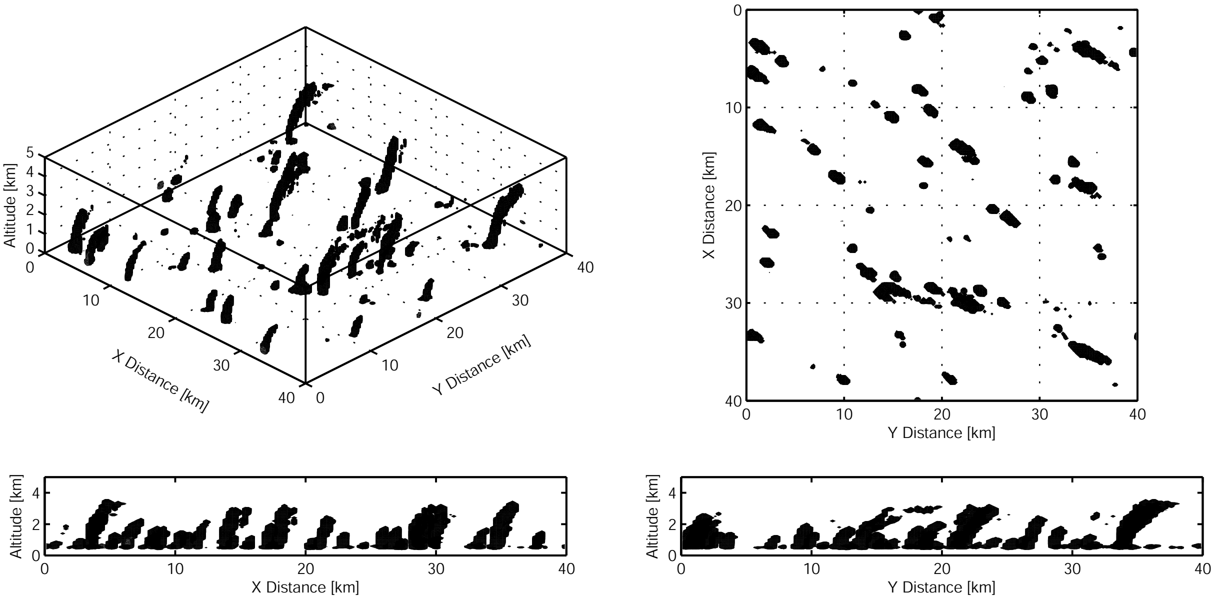

Figure 2: Example of the cloud field simulated in RUN-1Mc-2Mr-50n. Black regions indicate cloud LWC $\geq$ 0.01 g kg^{-1}.

A typical example of the simulated cloud field is shown in figure 2. The imposed horizontal velocities and wind shear act to tilt the clouds in the horizontal plane. The clouds are capped by a strong inversion and are forced to spread out in the horizontal. These effects lead to elongated cloud shapes when looking down as from a satellite view, and a subsequent increase in cloud cover when compared to simulations under more benign shear.

5. COMPARISON WITH AIRCRAFT OBSERVATIONS

Vertical profiles of updraft core vertical velocity, cloud and rain LWC simulated in the CRM are compared to that measured by the three research aircraft that participated in RICO. We define an updraft core as a region where the cloud LWC exceeds 0.05 g m^{-3} and the vertical velocity 1 m s^{-1} for a flight path length of at least 500 m. For the model 'simulated flight tracks' are made through the model domain, and are composed of straight legs along both of the horizontal grid directions (north-south and east-west) corresponding to approximately the along- and across-wind shear directions. Aircraft profiles are derived from each aircraft using data from the whole of the field experiment, and by combining the data from all aircraft on the simulated day (19th January 2005).

Figure 3 compares the model simulations to the aircraft observations. The vertical velocity increases from $\sim$ 1 m s^{-1} at cloud base to about 2.5 - 3 m s^{-1} at 2 km altitude and there is good agreement between the aircraft data and the majority of the model simulations. The model is fairly insensitive to the microphysics

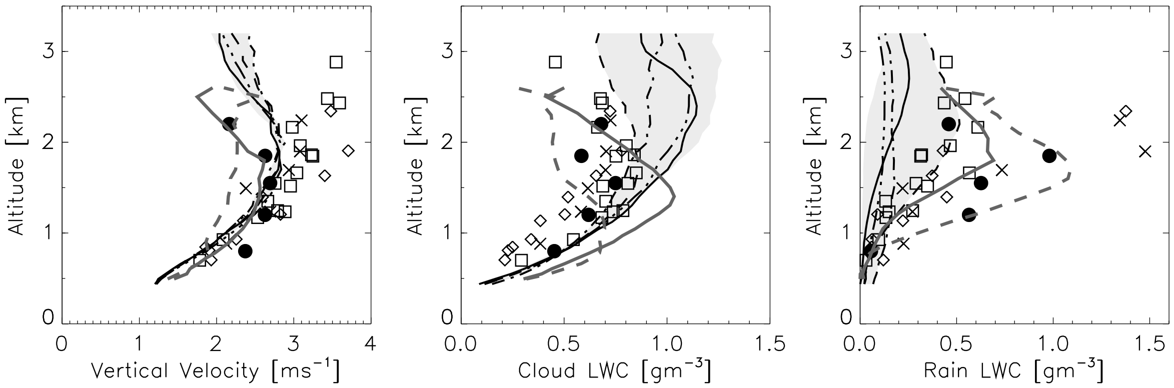

Figure 3: Vertical profiles of updraft core vertical velocity, cloud and rain LWC. The light grey shaded area represents the sensitivity of the simulations performed by Abel and Shipway (2007). Highlighted simulations are RUN-1Mc-1Mr-50n (dash-triple-dot), RUN-1Mc-1Mr-240n (dash-dot), RUN-1Mc-2Mr-50n (dash), RUN-1Mc-2Mr-240n (solid), RUN-2Mc-2Mr-58n (grey dash), RUN-1Mc-2Mr-200n (grey solid). Aircraft profiles using all data from RICO are shown by crosses (FAAM BAe 146), diamonds (C-130) and squares (King Air). The filled circles combine the data from all aircraft on the 19th January 2005.

set-up although it is clear that the preliminary simulations using the 2M cloud representation tend to have a lower vertical velocity. This is related to the increase in precipitation falling back through the cloud (see below), which acts to suppress the updraft strength. Above 2 km the aircraft profiles using all flight days from RICO continue to increase with altitude to $\sim$ 3.5 ms^{-1} at 3 km, whereas the model data tends to decrease. However, although the statistics are poorer, a reduction in the vertical velocity in the aircraft profile is also evident when updraft penetrations from the 19th January 2005 only are used. This suggests that the CRM is producing reasonable updraft speeds for the day that is simulated.

In contrast there is a large sensitivity in the model profiles of cloud and rain LWC when varying both the microphysics and the aerosol loading. The aircraft data show that the cloud LWC tends to increase to around 2.5 km altitude and then decrease above this. It is notable that differences in the model runs largely appear only above $\sim$ 1.3 km, where the effect of precipitation leads to a significant depletion in cloud LWC. For the rain LWC profiles, the aircraft data suggest a general increase with altitude. Using measurements from the whole of RICO the BAe 146 and C-130 aircraft show larger values of rain LWC at altitudes around 2.5 km than the King Air. It is evident that large values of rain LWC were present in the updrafts on the simulated day in the LEM when using aircraft data from the 19th January 2005 only.

Both of the simulations that use 1M rain do not generate sufficient amounts of rain LWC in the cloudy updrafts when compared to the observations, irrespective of the aerosol loading. Furthermore, they are not able to generate the shape of the rain LWC profile, with a peak at 2 - 2.5 km. By better representing the rain drop size distribution with 2M rain much better agreement with the observations is found with the model run with the lower aerosol loading (RUN-1Mc-2Mr-50n), which is more representative of the measured CCN concentrations on the simulated day. For the run with an increase in the cloud droplet concentration (RUN-1Mc-2Mr-240n) there is a clear overestimation of the cloud LWC and underestimation of the rain LWC.

The preliminary results from the simulations with 2M cloud show a further increase in the rain LWC and a decrease in cloud LWC, particularly above 1.5 km altitude. The simulation initialized with observations of the sub-cloud CCN distribution (RUN-1Mc-2Mr-58n) shows peak rain LWC values in agreement with the aircraft profiles on the 19th January 2005, although the cloud LWC appears to be underestimated. As the aerosol concentration is increased from 73 to 251 cm^{-3} the peak in the rain LWC drops off by approximately a factor of two and the cloud LWC comes into slightly better agreement with the observed profiles. Whilst the initial 2M cloud results are promising, it is important to realise that they represent a snapshot of the cloud field whereas the results from the other simulations are averaged over much longer time periods.

6. SUMMARY

The comparisons show that the model is unable to represent the observed variation in the water content of precipitation sized droplets when using a single-moment bulk cloud and rain scheme. Treating the precipitation sized droplets in a double-moment sense brings the model into better agreement with the observations. However, the simulations are highly sensitive to the prescribed cloud droplet concentration used in the autoconversion process, highlighting the importance of quantifying the aerosol conditions of the regime under investigation. A new double-moment cloud droplet scheme is developed and is initialized with observations of the sub-cloud CCN spectra. This new scheme can be used to explore the sensitivity of the model to different physical and chemical properties of the aerosol and to different aerosol loadings. Preliminary results shown in this abstract indicate that the scheme produces more precipitation in the updrafts than the 1M cloud simulations, which in turn acts to suppress the updraft strength. More comprehensive results with the new 2M cloud paremetrization will be presented at the conference.

7. BIBLIOGRAPHY

Abel, S. J. and Shipway, B. J., 2007. A comparison of cloud resolving model simulations of trade wind cumulus with aircraft observation taken during RICO. *Quart. J. Roy. Meteorol. Soc.*, **133**, 781-794.

Hudson, J. G. and Mishra, S., 2007. Relationships Between CCN and Cloud Microphysics Variations in Clean Maritime Air. *Geophys. Res. Lett.*, **34**, L16804, doi:10.1029/2007GL030044.

Khvorostyanov, V. I. and Curry, J. A., 2006. Aerosol size spectra and CCN activity spectra: Reconciling the lognormal, algebraic, and power laws. *J. Geophys. Res*, **111**, D12202, doi:10.1029/2005JD006532.

Nuijens, L., 2005. ‘Estimating precipitation from radar observations in the trade-wind cumulus region’. MSc thesis, Wageningen University and Research Center, The Netherlands.

Rauber, R. M., Stevens, B. et al., 2007. Rain in (shallow) cumulus over the ocean–The RICO campaign. *Bull. of the American Meteorol. Soc.*, **88**, 19121928.

Seifert, A. and Beheng, K. D., 2006. A two-moment cloud microphysics parametrization for mixed-phase clouds. Part 1: Model description. *Meteorol. Atmos. Phys.*, **92**, 45-66.

Shipway, B. J., Abel, S. J. and Smith, C. J., 2008. Nucleation of cloud liquid water in a double moment bulk microphysics scheme: Comparison with RICO observations. 15th International Conference on Clouds and Precipitation, Cancun, 7-11 July.

Swann, H., 1998. Sensitivity of the representation of precipitating ice in CRM simulations of deep convection. *Atmos. Res.,* **48**, *415-435.*

A NEW THREE-DIMENSIONAL VISUALIZATION SYSTEM FOR COMBINING AIRCRAFT AND RADAR DATA AND ITS APPLICATION TO RICO OBSERVATIONS

Dan K. Arthur[1], Sonia Lasher-Trapp[1], Ayman Abdel-Haleem[2], Nicholas Klosterman[2],
and David S. Ebert[2]

[1]Department of Earth and Atmospheric Sciences, Purdue University, West Lafayette, IN, USA
[2]Purdue University Rendering and Perceptualization Laboratory, West Lafayette, IN, USA

1. INTRODUCTION AND MOTIVATION

Meteorological field studies often provide researchers with diverse data sets gathered from different sources. The Rain In Cumulus over the Ocean (RICO) field campaign (Rauber et al. 2007) was such a study; along with the use of satellite observations, three research aircraft, a research vessel, surface observations, and the NCAR SPolKa radar were deployed to the Caribbean on and around the islands of Antigua and Barbuda for several weeks in December 2004 – January 2005. The observational strategy of RICO was to gather data on shallow maritime convection and trade wind cumuli at a wide range of scales. One goal of the project was to gain a better understanding of the warm rain process, as traditional theory has been unable to explain how the growth of cloud droplets by condensation alone proceeds to large enough drop sizes to begin the coalescence process and produce precipitation as rapidly as has been observed (Beard and Ochs 1993).

Examination of such data has generally involved using separate applications, often specific to the type of data being analyzed, making determination of correlations and synthesis of information between data sets extremely challenging. For example, during RICO, the aircraft conducted statistical sampling of cloud dynamic, thermodynamic, and microphysical properties along one-dimensional transects through clouds, while the radar gathered data on larger scales of cloud and hydrometeor motion and evolution. C130 aircraft measurements ranged from roughly 4 m to 100 m in spatial resolution, depending on sampling rate of the instrumentation, at constant altitude for a particular field of clouds, on a GPS-based lat-lon coordinate system. One-dimensional C130 data in netCDF files traditionally have been used with an application to produce time series plots such as that shown in Fig. 1. Radar measurements are based in a polar coordinate system with resolution decreasing with distance from the radar site. Radar scans during RICO were conducted primarily at successive constant elevation angles over an azimuthal sector of at least 180°, with a set of increasing elevation scans comprising one volume scan. The half-power beam width of the radar was 0.91° (Keeler et al. 1991), with 150 m a range resolution between samples. The S-Pol data, in its own format, can be viewed in successive two-dimensional slices for example with SOLO II (Oye et al. 1995). Figure 2 depicts a portion of an elevation scan within the same time period as that in Fig. 1.

Although useful in their own right, such traditional analysis tools force the investigator to spend significant amounts of time trying to collocate the data, and synthesize it into some conceptual picture, before being able to use it to test hypotheses. Here we present a new tool for combining multi-source, multi-scale data in three dimensions, allowing users to make queries from the combined data sets, applied toward the effort of attaining a better understanding of precipitation development in trade wind cumuli. In this work we examine microphysical probe data collected by aircraft simultaneously with radar data viewed in three dimensions. The new tool

---

Corresponding author's address: Dan K. Arthur, Dept. of Earth & Atmos. Sciences, Purdue University, West Lafayette, IN, 47907;
E-Mail: dkarthur@purdue.edu.

facilitates data organization and synthesis and may be of use in both individual case studies and in the statistical analysis of the properties of the entire cloud field.

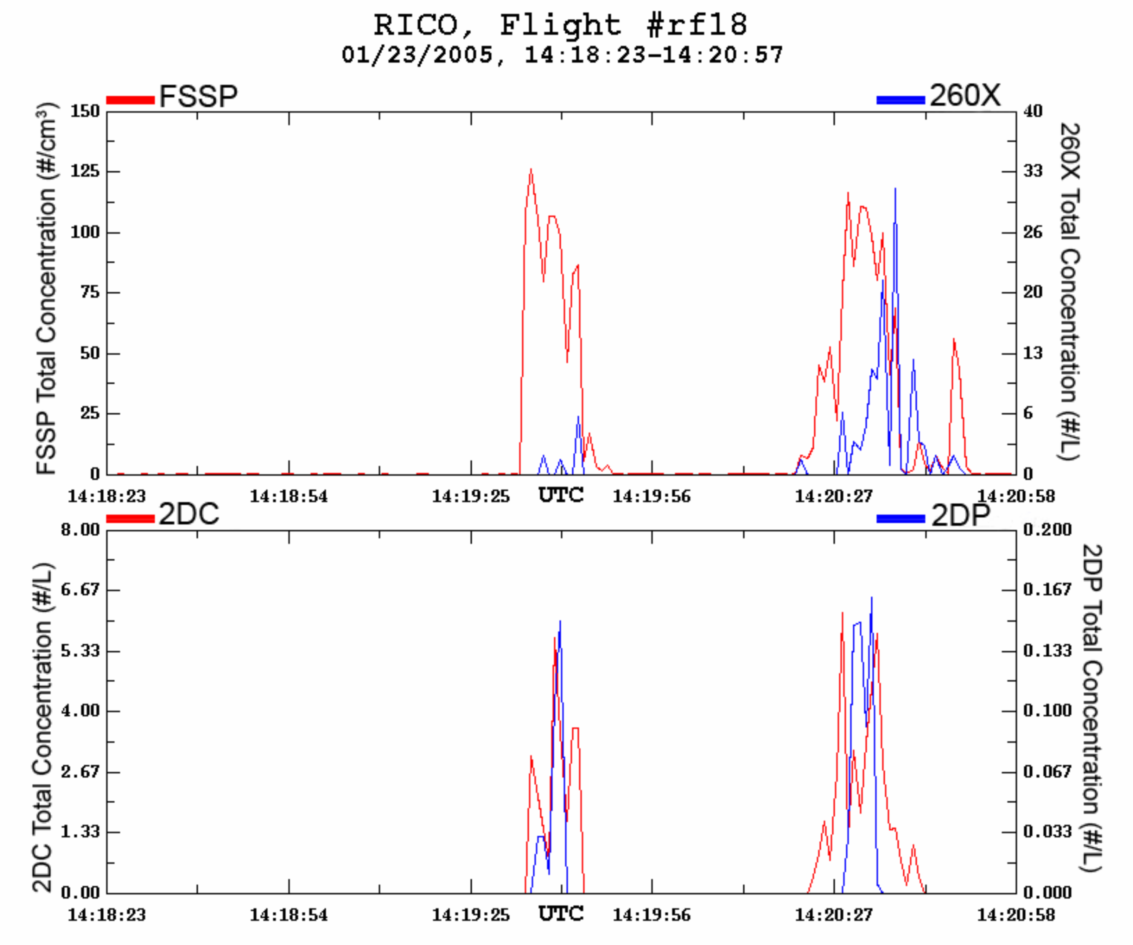

Fig. 1. A segment of aircraft time series data from four cloud droplet and precipitation probes during the 23 Jan 2005 RICO flight, using ncplot *(Webster 2007). Time is indicated along the abscissa, and total drop concentrations are plotted on the ordinates.*

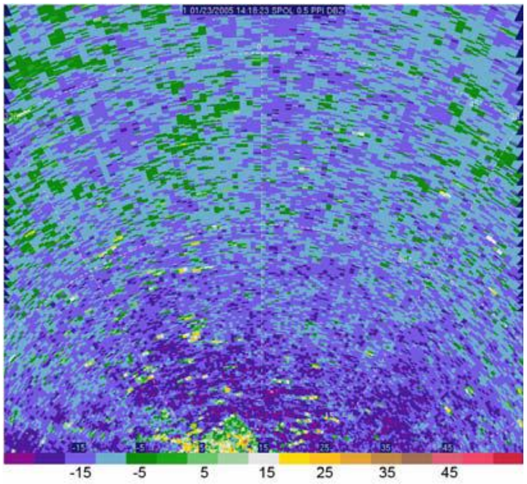

Fig. 2. A portion of one radar elevation scan during 23 Jan 2005, displaying reflectivity factor (Z_e). Color scale along bottom indicates increasing ranges of Z_e in colors toward the right (in dBZ, scale labels duplicated below colors for clarity). Ground clutter from the northern end of the island of Barbuda is visible near the bottom center of the figure. A field of small cumuli is indicated by the green clusters.

2. SYSTEM DESCRIPTION

Previous radar visualization packages capable of 3D output have been based on generation of isosurfaces (e.g., Johnson and Edwards 2001). For microphysical research applications, however, isosurface-based 3D products can present serious drawbacks. Specific values of multiple parameters in the 3D domain are often difficult to obtain from isosurface representations, and navigation of the 3D space, particularly when viewing multiple values in translucent surfaces, can be disorienting and confusing without clear reference coordinates.

Overcoming the challenge of collocating and synthesizing microphysical data such as that in Fig. 1 with larger-scale radar data such as in Fig. 2 is one goal of the application described herein. Collocation of the 3D polar coordinate radar volume with the lat-lon coordinate aircraft data is achieved via calculation of geodesics between the S-Pol site latitude, longitude, and altitude and the same values from GPS data for each aircraft data point (Vincenty 1975).

Once combined, the data sets can be queried to look for correlations between aircraft microphysical probe variables and radar data where they are spatially and temporally collocated. Such correlations can be used to make inferences across the field of trade wind cumuli where radar histories are well-documented but microphysical probe data are lacking due to the statistical sampling nature of the aircraft flights.

Our system uses netCDF data, in order to maintain standardization and transferability, so files from the RICO C130 flights needed no advance preparation. In order to use the radar data, a file translator that is part of the SOLO II software package (Oye et al. 1995) was used on the S-Pol files to convert them to netCDF. Any single radar variable and multiple 1-D aircraft variables can then be visualized simultaneously. The system uses a transfer function scheme to plot data quantitatively by color and/or opacity (Fig. 3). The user can set limits on what range(s) of values can be viewed by controlling the limits of this function.

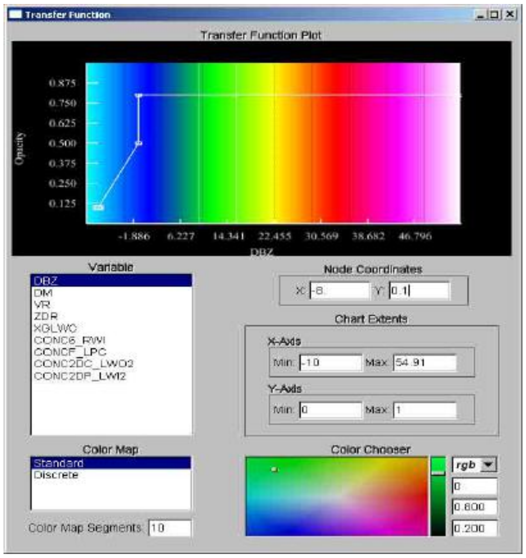

Node Coordinates X: -8 Y: 0.1

X-Axis Min: -10 Max: 54.91

Y-Axis Min: 0 Max: 1

Color Map Segments: 10

rgb: 0, 0.800, 0.200

Fig. 3. Transfer function for converting numerical data into color and opacity values for 3D plotting. Function shown displays Z_e > -1 dBZ at 75% opacity, decreasing from 50% to 10% opacity for Z_e between -1 dBZ to -8 dBZ.

A portion of one set of S-Pol elevation scans (one radar volume scan) is shown in Figs. 4, 5, and 6, from three different views. Using the PC mouse and keys, the investigator can rotate, pan, and zoom within the 3D view in order to examine any particular region more clearly. Coordinates can be input to define the data that is displayed in 3D to be within desired absolute geographic (lat-lon), relative Cartesian (in kilometers, centered on the radar site), or polar (also centered on the radar site) coordinate extents. User-defined Cartesian and polar grids can be overlaid onto the data in the 3D view if desired.

After setting color scales via transfer functions for at least one aircraft probe data variable, these data can be displayed in the system's 3D view along with the radar data using either of two schemes: aircraft-centric time or radar-centric time. The former displays the portions of the path of the aircraft that occurred within the space defined in the 3D view for the entire flight/data file, while the latter limits display of the aircraft variable(s) to those which correspond to the time of the currently-displayed radar volume scan (Fig. 7).

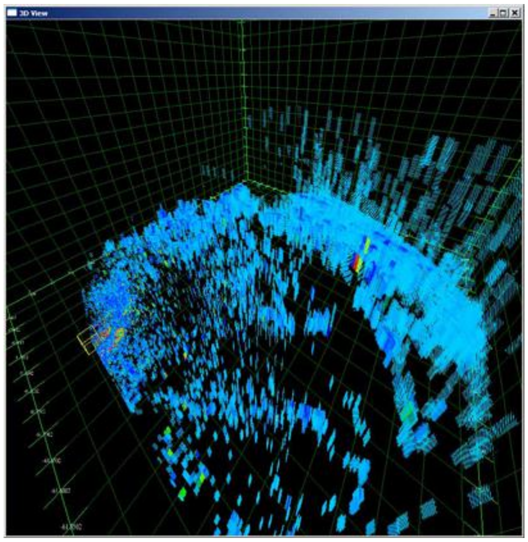

Fig. 4. Sample 3D view looking down obliquely onto portion of a 23 Jan 2005 volume scan, showing Z_e based on the transfer function described in Fig. 3. A Cartesian grid is overlaid onto the boundaries of the 3D space. Longitude scale is visible along the edge of the grid (lower left). Bluish clusters are likely fields of small cumulus, with some brighter colored regions more dense cloud regions, and the bright red to the right of center is a "skin paint" (direct detection of the aircraft by the radar, e.g. Bringi et al. 1991).

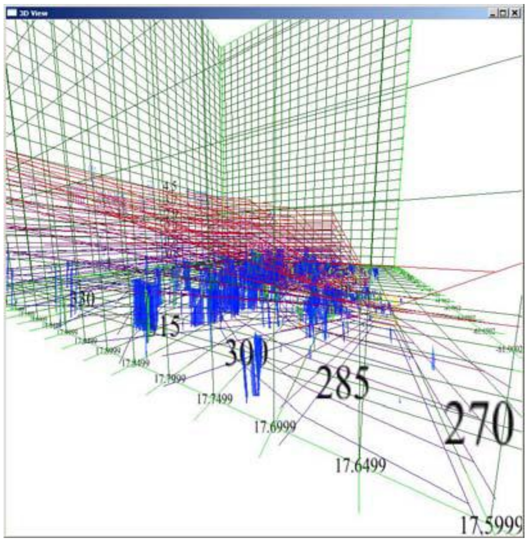

Fig. 5. A different view of the same volume as in Fig. 4, also demonstrating polar grid overlay and ability to alter background and coordinate scale value colors. Latitudes are smaller numbers along bottom, azimuthal scale accompanying polar grid are larger numbers above the latitude scale.

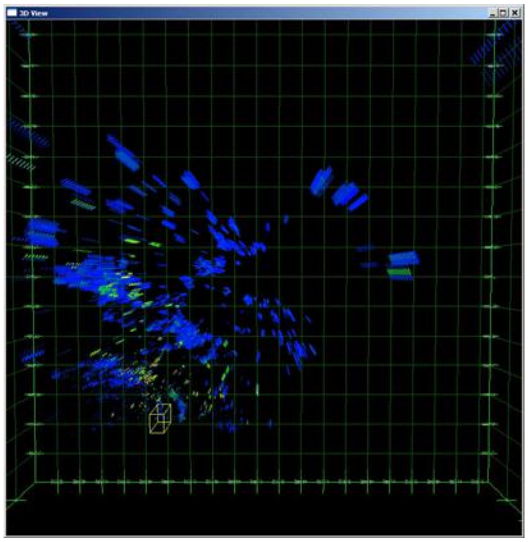

Fig. 6. Looking down onto the same volume as shown in Figs. 4 and 5, with a transfer function set for higher minimum Z_e. North is toward top of figure. Clouds are visible as the blue regions, and more dense/more developed clouds or skin paints of the aircraft are the brighter colors.

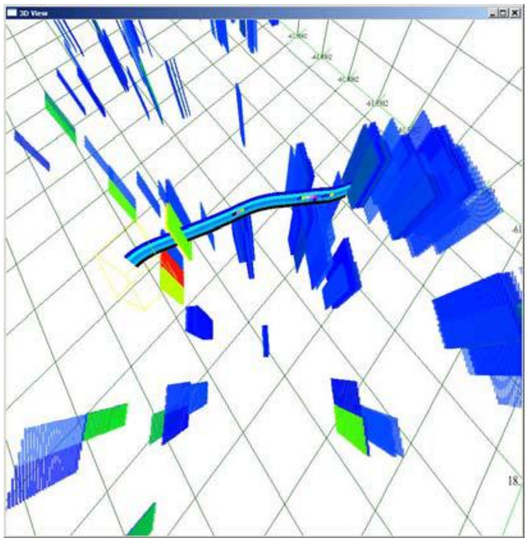

Fig. 7. Close-up of radar volume showing the aircraft track in radar-centered time mode. The aircraft track corresponding to

the entire time of the displayed radar volume scan is indicated by the ribbon near the center of the figure. Each color band on the ribbon represents a different aircraft data variable, and color changes along a band indicate greater values based on that variable's transfer function (i.e., color scale). The bright colored cluster of radar data penetrated by the left end of the aircraft track is a skin paint.

Along with the visual presentation of collocated multi-source data for qualitative analysis, the system contains quantitative tools useful in determining correlations not easily done when using separate applications for each data set. Visible in Figs. 4 and 6 is a distinct 3D cube shape; this cube is a "data probe" that can be sized and moved throughout the 3D view space by the user. It displays values for selected variables collocated at its center point, including the sample time. Also, as shown in Fig. 8, it is accompanied by a display window of basic statistical information on values contained within it. If desired, the probe can be locked onto the aircraft track contained in the displayed timeframe, and scrolled along the track in order to display the values of collocated radar and aircraft data points easily.

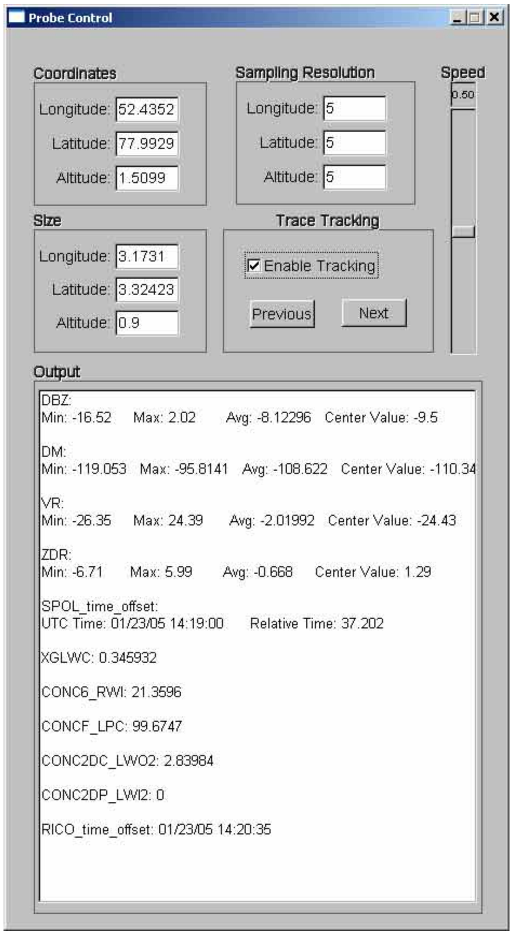

Coordinates
Longitude: 52.4352
Latitude: 77.9929
Altitude: 1.5099

Sampling Resolution
Longitude: 5
Latitude: 5
Altitude: 5

Speed
0.50

Size
Longitude: 3.1731
Latitude: 3.32423
Altitude: 0.9

Trace Tracking
☑ Enable Tracking

Output

```
DBZ:
Min: -16.52     Max: 2.02      Avg: -8.12296   Center Value: -9.5

DM:
Min: -119.053   Max: -95.8141   Avg: -108.622   Center Value: -110.34

VR:
Min: -26.35     Max: 24.39      Avg: -2.01992   Center Value: -24.43

ZDR:
Min: -6.71      Max: 5.99       Avg: -0.668     Center Value: 1.29

SPOL_time_offset:
UTC Time: 01/23/05 14:19:00     Relative Time: 37.202

XGLWC: 0.345932

CONC6_RWI: 21.3596

CONCF_LPC: 99.6747

CONC2DC_LWO2: 2.83984

CONC2DP_LWI2: 0

RICO_time_offset: 01/23/05 14:20:35
```

Fig. 8. Data probe control window, displaying its center location, size, minimum, maximum, and average values for radar data within, as well as values from both data sets collocated at the center. Control of data probe size, sampling resolution, and/or scroll speed (the latter when not locked to an aircraft track) are possible.

In addition to the information available from the data probe, 2D time series plots of the user's choice can be generated along the aircraft flight track, either within the application as a quick-look (Fig. 9), or, alternatively, variable values from both data sets along the flight track are exported to a text file and can be subjected to further analysis with other tools.

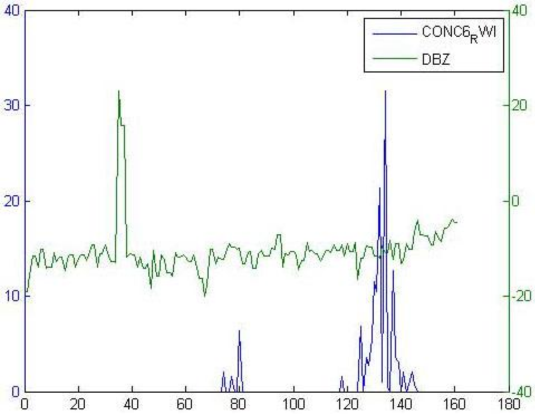

Fig. 9. Sample 2D plot of one aircraft variable (drizzle number concentration per liter – blue curve) and one radar variable (Z_e – green curve) along the aircraft track for one radar volume scan. Abscissa is time in seconds relative to start of volume scan. Peak toward the left on the green curve is the same skin paint visible in Fig. 7, Peak in blue curve corresponds to drizzle values visible along the aircraft track ribbon (yellow, red pixels) shown in Fig. 7.

Time is another important consideration in collocating radar and aircraft probe data. The aircraft is not always in the same place at the same time as the radar beam, and if the two do exactly coincide temporally as well as spatially, the radar values must be discarded as a "skin paint" (direct detection of the aircraft by the radar, e.g. Bringi et al. 1991). In order to attempt to account for the movement of radar echoes between the time the associated clouds were sampled by the aircraft and scanned by the radar, the system has a flexible advection adjustment mechanism (Fig. 10). The user can input an advection time, around which the radar is advected based on a user-input wind speed and direction. Radar samples after this time are advected along the direction of the wind, the distance depending on the wind speed and the difference between the sample time and the advection time. Radar samples occurring before the advection time are advected opposite the wind direction in a similar manner. This is admittedly a simplistic approach, and may introduce some errors in resulting collocations, but because the radar echoes evolve in time as well as in space, no advection scheme will achieve perfectly collocated results.

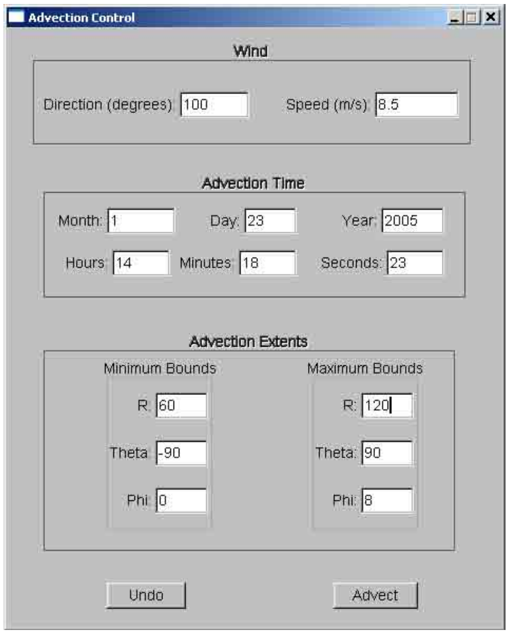

Direction (degrees): 100
Speed (m/s): 8.5
Month: 1
Day: 23
Year: 2005
Hours: 14
Minutes: 18
Seconds: 23
R: 60
Theta: -90
Phi: 0
R: 120
Theta: 90
Phi: 8

Fig. 10. Advection control window. To reduce calculation time, the user can limit the extent of advected radar data to be within a region of interest.

The application also includes the ability to perform multi-parameter database queries (Fig. 11). These can be executed to define a data set to locate echo regions of interest in any radar volume scan accessible by the database. For example, specific collocated Z_e and Z_{DR} pairs within user-defined limits accompanying radial velocity data (also within defined limits) could be located. Once found, these echo regions could be visually tracked across multiple radar volume scans to observe their evolution.

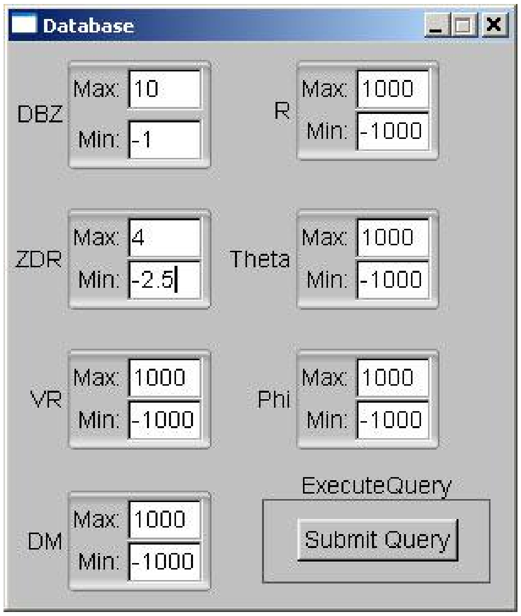

DBZ Max: 10 Min: -1

R Max: 1000 Min: -1000

ZDR Max: 4 Min: -2.5

Theta Max: 1000 Min: -1000

VR Max: 1000 Min: -1000

Phi Max: 1000 Min: -1000

DM Max: 1000 Min: -1000

Fig. 11. Sample screenshot of the database query interface. Future expansion will add the ability to query several aircraft variables in addition to the radar variables shown.

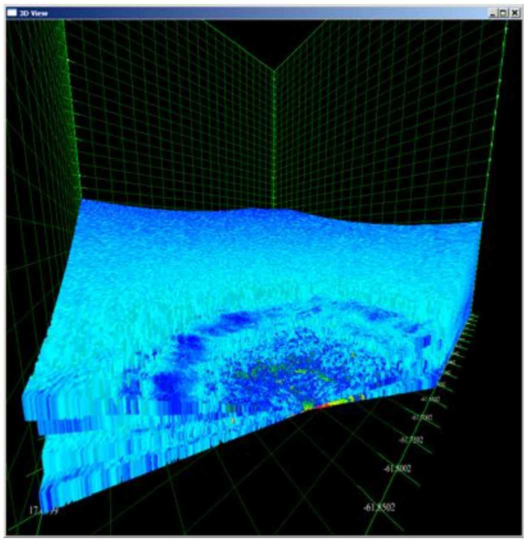

Fig. 12. A drastic example of a 3D radar volume scan viewed before selection of data by a database query. Values shown are -20 < Z_e *< 55 dBZ, so much of the echo filling the view is outside of cloud (cf. the 2D slice in Fig. 2).*

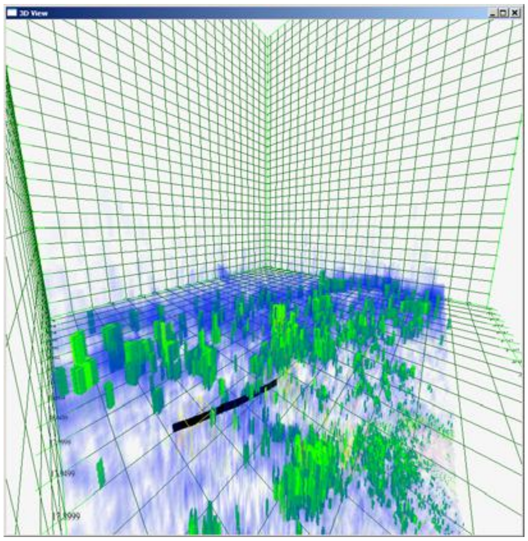

Fig. 13. 3D radar plot of a volume scan after selection of data by query: -1 < Z_e *< 10 dBZ and -0.5 <* Z_{DR} *< 0.5 dB. Aircraft track (dark stripe) is now visible. Background color was changed from Fig. 12 to emphasize differences between selected and unselected data.*

In order to display query results in 3D, the user can switch the 3D rendering mode from using transfer functions exclusively for color scales and opacity to "context mode". In this mode, the currently defined transfer function controls color and opacity of the selected data, and non-selected data can still be viewed using the same colors of the transfer function, at a different opacity controlled by the user. For example, as shown in Figs. 12 and 13, non-selected data is still visible after execution of the query. In this example, the opacity of non-selected data was set to 0.3, which is multiplied by the opacity of the current transfer function (90%), resulting in an opacity of 2.7%. The ability to view non-selected data along with selected data can aid keeping that data in context, to see possible cloud edges, areas of fractocumulus, Bragg scattering, and other weak echoes. Although Figs. 12 and 13 show a drastic example of the use of this feature, the "context mode" can easily help the investigator focus on a particular set of clouds within the entire field, based on the strength of their radar echoes, for example.

3. APPLICATION

Although it is difficult to convey the utility of the new software in a 2D medium, because its greatest advantages are in displaying the data in 3D and manipulating the view interactively, an initial application is presented here with a subset of the RICO data.

The initial task in examining the S-Pol and C130 aircraft data as a combined set in 3D involved finding peaks in drizzle/raindrop number concentration from the 260X, 2DC, and 2DP optical array probes[1] mounted on the C130 aircraft, and studying the radar echoes closest to the cloud penetration times where the peaks occurred. Because the clouds evolve and travel through the radar volume in time, the maximum Z_e and Z_{DR} values detected in a particular cloud may not be collocated with the peaks in drizzle/raindrop number concentrations detected by the aircraft at the same spatial location. This offset is easily detectible with the new software described here. From 42 volume scans across three different days during RICO, only 10% of the clouds sampled by the aircraft had peaks in drizzle/raindrop number concentration collocated with a maximum in Z_e, and only 7% with a maximum in Z_{DR}. In addition, only 57% of the maxima in Z_e were collocated with the maxima in Z_{DR} within the clouds. Although this latter estimate requires analysis of additional cases to generalize these percentages as an overall trend in the trade wind cumuli observed during RICO, it is in accord with analysis of the RICO radar data by Knight et al. (2008). In an earlier study by Knight et al. (2002), the authors examined early development of Z_e and Z_{DR} in Florida cumuli, and speculated that separation of the greatest Z_e and Z_{DR} signals in the cloud may result from larger drops appearing in weaker areas of clouds, before coalescence begins in earnest in regions often indistinguishable from Bragg scattering.

The new software is also useful for studying individual clouds and gaining perspective on the time a cloud was sampled by the aircraft versus its stage of evolution on the radar. Figures 14 through 17 show the aircraft track (or a portion thereof) within a given radar volume. It can be seen in these figures that the relative peak radar values are not collocated with the peak drizzle/raindrop concentrations measured by the aircraft. Due to the time differences between drop detection by the 260X and/or 2DC and scanning by the S-Pol, the maximum radar echoes are located *below* the aircraft tracks in Figs. 14 through 17. The aircraft wind measurements indicated that downdrafts were present at the time of cloud penetration in Figs. 14 through 16, and thus the maximum radar echoes were detected at lower levels by the radar than the flight level at which the aircraft sampled the clouds. In Fig. 17, the radar scanned the cloud well *before* aircraft penetration, and the entirety of the cloud echo appears below the sampling altitude of the aircraft. Aircraft measurements in this case indicated a cloud was penetrated at this location and an updraft was present at this time, so the drizzle sampled by the aircraft must have developed from lower altitudes that were scanned earlier by the radar. These examples demonstrate the ease with which the aircraft data and radar data can be combined, thus allowing the investigator to focus upon the precipitation evolution occurring within the cloud. Simple calculations constrained by the aircraft and radar observations, with the understanding of their spatial and temporal relationships, can then be used to provide insight into the possible mechanisms influencing precipitation development in these cases. Such analysis is planned, over the entire RICO data set.

---

[1] Manufactured by Particle Measurement Systems, Inc., Boulder, CO, USA.

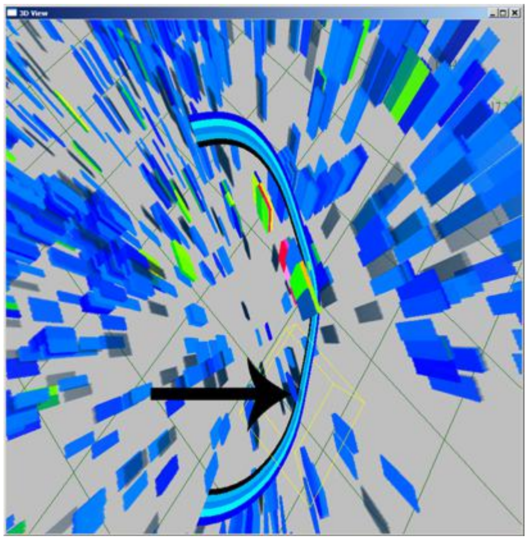

Fig. 14. Example of aircraft penetration before radar scanning of a cloud, from radar volume scan beginning at 17:56:20 UTC on 20 Dec 2004, viewed from above. Arrow highlights position along track of 260X peak value and cloud echo below track. Peak 260X concentration is 10.7 L^{-1}, with collocated radar values of Z_e = -12.9 dBZ and Z_{DR} = 0.8 dB. Below the aircraft track, Z_e = 1.51 dBZ and Z_{DR} = 0.01 dB. Z and Z_{DR} calculated from all aircraft droplet probes are 1.47 dBZ and 0.03 dB, respectively.

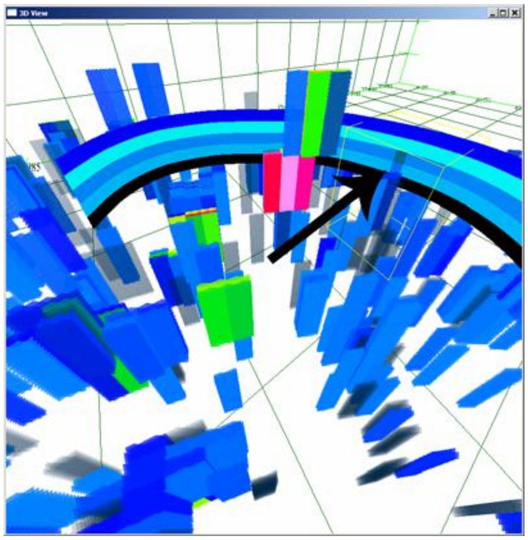

Fig. 15. As in Fig. 14, side view, arrow highlighting maximum 260X concentration point along aircraft track.

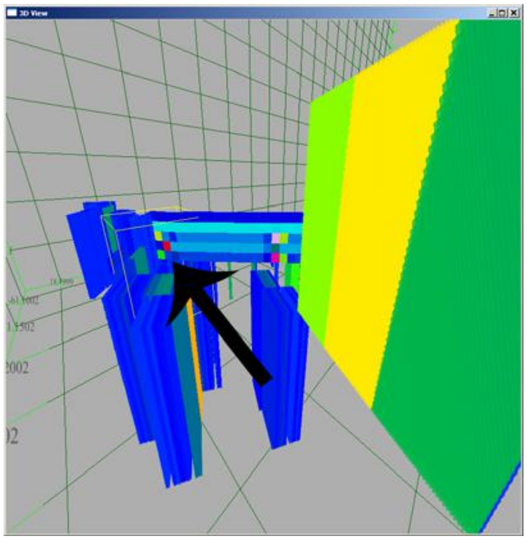

Fig. 16. As in Figs. 14 and 15, for radar volume scan beginning at 14:05:48 UTC 23 on Jan 2005. Peak 260X concentration (red pixel) is 189 L^{-1}, collocated Ze = 6.61 dBZ. Z calculated from aircraft probes is 18.51 dBZ. High values on the right side foreground are part of a skin paint of the C130.

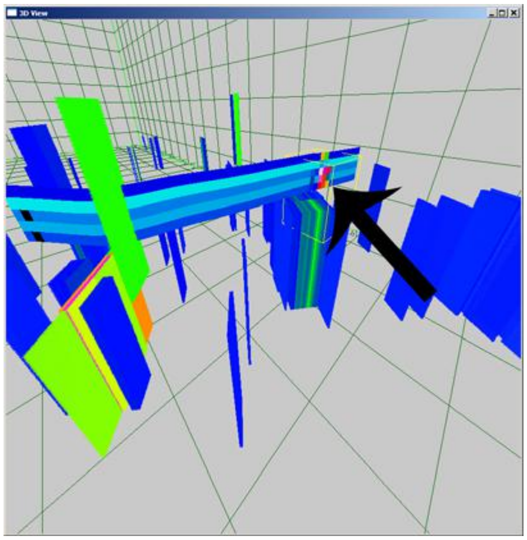

Fig. 17. Example of aircraft penetration after the radar scanned the cloud, from radar volume scan beginning at 14:33:48 UTC 23 on Jan 2005. Arrow highlights peak 2DC concentration of 242 L^{-1}, with collocated Z_e = -6.4 dBZ. Below the aircraft track, Z_e = 11 dBZ. Z calculated from aircraft probes is 23.68.

4. FUTURE WORK

As discussed previously, approximately half of the examined maximum Z_e echoes were not collocated with the max Z_{DR} echoes. Past studies have suggested that size-sorting of raindrops within the clouds may cause such a spatial disparity in these echoes [e.g., Knight et al. (2002, 2008)]. Such size sorting also suggests that the earliest raindrops falling from such clouds may result from a different microphysical path (for example, giant aerosol particles, or earlier thermals) than the bulk of the later rainfall. It is our intent to examine this dislocation of Z_e and Z_{DR} more closely with this 3D visualization system and the combined RICO datasets.

Analysis of cloud evolution across entire cloud fields, as mentioned above, will be conducted to determine if precipitation development occurs differently across the cumulus field on different days. The new visualization system can aid in easily detecting differences in cloud number, depth, width, spatial separation, organization, cloud lifetime, etc., across different days within the RICO field campaign that can be related to precipitation development.

5. ACKNOWLEDGEMENTS

The authors wish to acknowledge the National Center for Atmospheric Research (NCAR) for the use of the *ncplot* and SOLO II software, and Robert Rilling and Scott Ellis of the NCAR Earth Observing Laboratory for assistance with the NCAR S-Polka radar data. NCAR is sponsored by the National Science Foundation. We would also like to thank the participants of RICO for their data collection efforts, Amanda Sheffield for general statistical analysis of C130 data from each RICO flight, and the Purdue Cloud Microphysics Group for numerous helpful discussions and suggestions. Support for this project was provided by NSF grant IIS-0513464.

6. REFERENCES

Beard, K., V., and H. T. Ochs, 1993: Warm-rain initiation: an overview of microphysical mechanisms. *J. Appl. Meteor.*, **32**, 608-625.

Bringi, V. N., D. A. Burrows, and S. M. Menon, 1991: Multiparameter radar and aircraft study of raindrop spectral evolution in warm-based clouds. *J. Appl. Meteor.*, **30**, 853-880.

Johnson, S. G., and J. Edwards. "Vis5d+ Home Page." *Vis5d+*. 2 April 2001. SourceForge. 1 May 2008 http://vis5d.sourceforge.net/.

Keeler, R. J., W. Lutz, and J. Vivekanandan, 2000: S-Pol: NCAR's polarimetric Doppler research radar. IGAARS-2000, Honolulu, HI, 24-28 July, 2000, 4 pp.

Knight, C. A., J. Vivekanandan, and R. A. Rilling, 2008: Structural and evolutionary aspects of trade wind cumulus determined from dual-polarization measurements. *J. Atmos. Sci.*, in press.

______, ______, and S. G. Lasher-Trapp, 2002: First radar echoes and the early Z_{DR} history of Florida cumulus. *J. Atmos. Sci.*, **59**, 1454-1472.

Oye, R., C. Mueller, and S. Smith, 1995: Software for radar translation, visualization, editing, and interpolation. *Preprints, 27th Conference on Radar Meteorology*, Vail, CO, Amer. Meteor. Soc., 359-361.

Rauber, R. M., et al., 2007: Rain in shallow cumulus over the ocean: the RICO campaign. *Bull. Amer. Meterol. Soc.*, **88**, 1912-1928.

Vincenty, T., 1975: Direct and inverse solutions of geodesics on the ellipsoid with application of nested equations. *Survey Review XXII*, **176**, 88-93.

Webster, C. "EOL/CDS Aircraft Platform Software Product Guide." *Research Aviation Facility*. 27 Feb. 2007. NCAR Earth Observing Laboratory. 23 Apr. 2008 http://www.eol.ucar.edu/raf/Software/.

THE EFFECTS OF ENTRAINMENT AND MIXING ON DROPLET POPULATIONS: A COMPARISON OF NUMERICAL MODELING AND AIRCRAFT OBSERVATIONS

Jennifer L. Bewley and Sonia Lasher-Trapp
Dept. of Earth and Atmospheric Sciences, Purdue University, West Lafayette, IN, USA

1. INTRODUCTION

Many investigators (e.g. Mason and Chien 1962, Bartlett and Jonas 1972, Warner 1973, Mason and Jonas 1974, Latham and Reed 1977, Baker et al. 1980, Telford et al. 1984, and others) have noted the inability of an adiabatic parcel model to reproduce observed droplet size distributions, specifically the presence of small drops at heights far above cloud base, the droplet distribution width, and the locations of peaks within the droplet size distribution. It is likely that interactions between the cloud and its environment are important in determining the characteristics of the droplet size distribution; this interaction is lacking in the classical adiabatic model for a rising air parcel. Numerous investigators (e.g. Stommel 1947, Squires 1958, Warner 1969, Warner 1973, Blyth et al. 1980, Paluch and Knight 1984, Paluch 1986, Paluch and Knight 1986, Blyth et al. 1988, Politovich 1993, Lasher-Trapp et al. 2005, and others) have suggested that entrainment and mixing, which is not included in an adiabatic parcel model, is the key missing interaction that can help to explain the discrepancy between the characteristics of observed and modeled droplet size distributions.

While the use of microphysical observations is important to understanding the effects of entrainment and mixing on the broadening of droplet size distributions, advanced modeling techniques that can capture the many scales of cloud-droplet interactions are also needed. Lasher-Trapp et al. (2005) presented such a modeling technique that includes the use of a three-dimensional cloud model and a Lagrangian microphysical parcel model. The parcel model is run along trajectories derived from the cloud model; it complements the three-dimensional cloud model by performing calculations of droplet growth by condensation directly, using the kinematic and thermodynamic variables prescribed by the three-dimensional cloud model. The present study extends that of Lasher-Trapp et al. (2005) by comparing the predicted droplet size distributions from that modeling framework to observed droplet size distributions from the Rain In Cumulus over the Ocean (RICO) field campaign. Here, high-rate microphysical observations collected at multiple levels in trade wind cumuli on a single day during the field campaign are compared to the characteristics of the simulated droplet size distributions, to conduct the first quantitative assessment of the ability of the modeling framework to reproduce droplet size distributions representative of a field of small cumuli.

2. OBSERVATIONAL ANALYSIS OF THE RICO 10 DECEMBER CASE

The present study uses data collected on 10 December 2004 off the coast of Antigua during the RICO field campaign. Readers are referred to Rauber et al. (2007) for a complete review of the RICO field campaign and sampling strategies. Shallow trade wind cumuli approximately 1.5 km wide and 1 km deep with cloud bases located at approximately 500 m were penetrated by the NCAR C-130 aircraft at three primary altitude levels. The microphysical features of 52, 43, and 23 developing clouds were sampled at 650 m, 980 m, and 1300 m, respectively.

High-rate (10 samples per second) microphysical data were collected in the trade wind cumuli by various instruments onboard

---

Corresonding author's address: Jennifer Bewley, Dept. of Earth & Atmos. Sciences, Purdue University, West Lafayette, IN, 47907; email: jlbewley@purdue.edu

the NCAR C-130 aircraft. Those used here include cloud droplet concentration and size recorded by the Forward Scattering Spectrometer Probe (FSSP-100)[*], liquid water content (LWC) recorded by the PVM-100 Liquid Water Content Probe[†], and updraft speed recorded by the vertical gust component of the GPS-corrected wind vector. Cumulus clouds targeted for this study were identified by FSSP values greater than 20 cm^{-3} and positive updraft speeds. Decaying clouds (clouds with low liquid water content and slow updraft speed) were not included in the analysis, nor were clouds having raindrop concentrations greater than 0.1 L^{-1} (as detected by the 2DP[‡], a 2D optical array probe) to prevent the possibility of raindrop shattering on the instrument probes being considered as a locally high value of cloud droplets (Baker and Mo 2006). A value of 0.1 L^{-1} detected by the 2DP is a highly conservative estimate since values as high as 120 L^{-1} were recorded by the probe while specifically targeting rain shafts during the field campaign. The flight video from the forward-facing camera was then used to visually inspect each of the clouds identified by the aircraft observations. Maximum values for each of the microphysical probes were recorded for each cloud penetration, as well as the observed droplet size distributions.

Overall, the observed trade wind cumuli can be described as shallow cumulus clouds with sub-adiabatic liquid water content (LWC) (FIG. 1) and rather weak updraft speeds (not shown) rarely exceeding 7 m s^{-1}. The maximum cloud droplet number concentrations (FIG. 2) were observed to increase with height on this day, with the mean maximum value of 100 cm^{-3} observed at 1300 m. This observed trend is contrary to classical theory, which states that the maximum supersaturation and cloud droplet number should occur just above cloud base, and is currently under investigation.

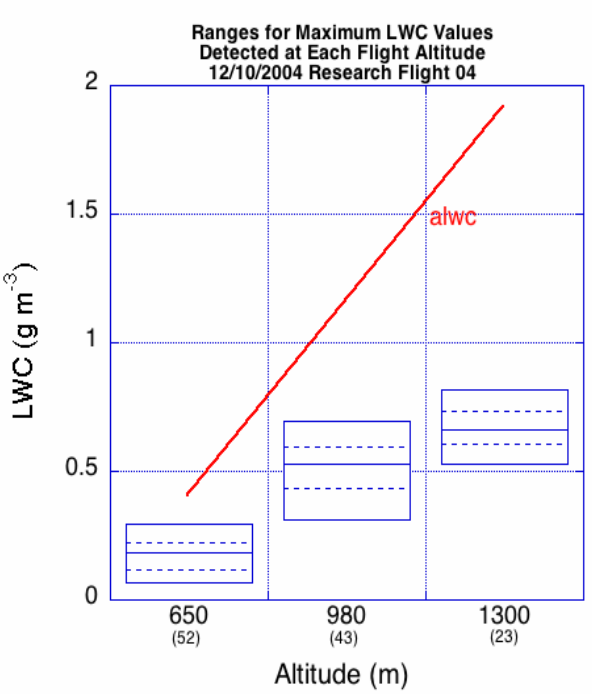

FIG. 1. Range of LWC values observed at each of the three flight levels on 10 December 2004. Solid box encloses 90% of the data: top and bottom bounds of each box represent 5th and 95th percentiles, dashed lines represent 25th and 75th percentiles, and solid center line is the median value (50th percentile). Adiabatic liquid water content (ALWC- red line) and number of clouds sampled at each level (number noted in parentheses under each altitude) also shown.

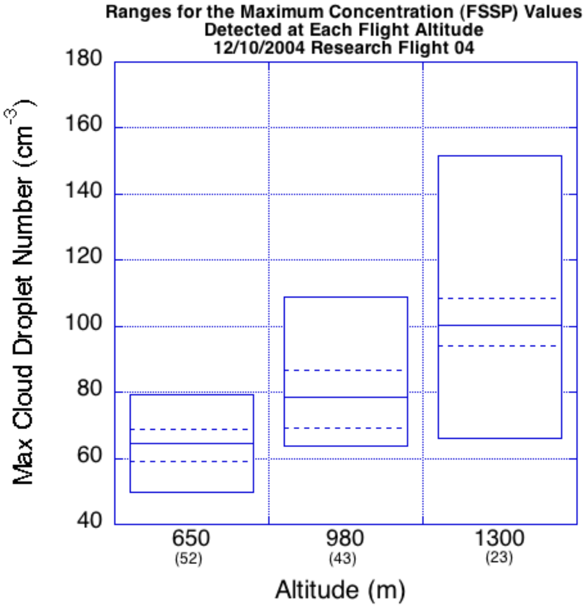

FIG. 2. As in FIG. 1, except ranges shown for the observed values of maximum cloud droplet number concentration across a cloud penetration.

---

[*] Manufactured by Particle Measurement Systems Inc.
[†] Manufactured by Gerber Scientific Inc.
[‡] Manufactured by Particle Measurement Systems Inc.

3. THE MODELS

3.1 3-D Cloud Model and Simulation

The Straka Atmospheric Model (Straka and Anderson 1993) as modified by Carpenter et al. (1998) was used to create a three-dimensional simulation representative of the trade wind cumuli observed on 10 December. The model uses the bulk condensation scheme of Soong and Ogura (1973) to produce condensate and has prognostic equations for the three wind components, potential temperature, water vapor mixing ratio, cloud-water mixing ratio, and turbulent kinetic energy. Autoconversion of cloud water to rain is not included here; calculations are truncated before significant rain forms. Specific model details can be found in Carpenter et al. (1998) and Lasher-Trapp et al. (2001).

The model domain for this simulation was 2.73 km x 2.73 km x 3.06 km with a grid spacing of 30 m. The model calculations were executed with a 0.3 s time step. Because the small trade wind cumuli of concern in the present study are found over the ocean, the Straka Atmospheric Model has been modified to allow cloud initialization by the convergence of prescribed surface winds, resulting for example by the horizontal convective rolls observed over the ocean during RICO. The prescribed surface winds are at a maximum (here, 4.25 m s^{-1}) at a distance from the center of the model domain (here, 690 m), and decrease to zero at the center of the domain. The magnitude of these prescribed winds approaches zero at a height of 30 m from the surface. When the winds converge toward the center of the domain, they are forced to rise, forming the updraft for the cloud. The surface convergence is held constant throughout the model integration time of one hour.

The 10 December dropsonde released at 1501 UTC by the NCAR C-130 aircraft was used to represent the atmospheric conditions for this simulation. Environmental winds were not used for initializing the model. The winds were light on this day (15 knots) in the cloud layer, with little vertical wind shear, so the neglect of these winds would not be expected to substantially affect the simulation.

The goal of this study is to produce a simulation that is representative of an average cloud observed during the flight, and not to reproduce any particular cloud. The model produces a small cumulus cloud with three successive pulses during the two hour simulation. Following Carpenter et al. (1998), a later pulse (FIG. 3) is analyzed because the turbulence is better developed than in the initial pulses.

Table 1. Simulated vs. observed range (5th to 95th percentile values) of cloud characteristics

	650 m	
	Simulated	Observed
Maximum Updraft Speed (m s^{-1})	1.94	0.9-3.1
Maximum Liquid Water Content (g m^{-3})	0.25	0.075-0.3
	980 m	
	Simulated	Observed
Maximum Updraft Speed (m s^{-1})	3.55	1.3-4.7
Maximum Liquid Water Content (g m^{-3})	1.45	0.3-0.68
	1300 m	
	Simulated	Observed
Maximum Updraft Speed (m s^{-1})	4.6	1.8-6.9
Maximum Liquid Water Content (g m^{-3})	2.4	0.53-0.82

The model produces reasonable cloud top and cloud base heights and cloud width when compared to the observations. The base of the modeled cloud is at 600 m and cloud top at 1620 m, both near the observed values of 500 m and 1500 m, respectively. The maximum simulated cloud width of 1800 m was only slightly greater than the observed value of 1500 m. The liquid water content and updraft speed were also compared to the observations taken at 3 different flight levels (650 m, 980 m, and 1300 m; see Table 1). At

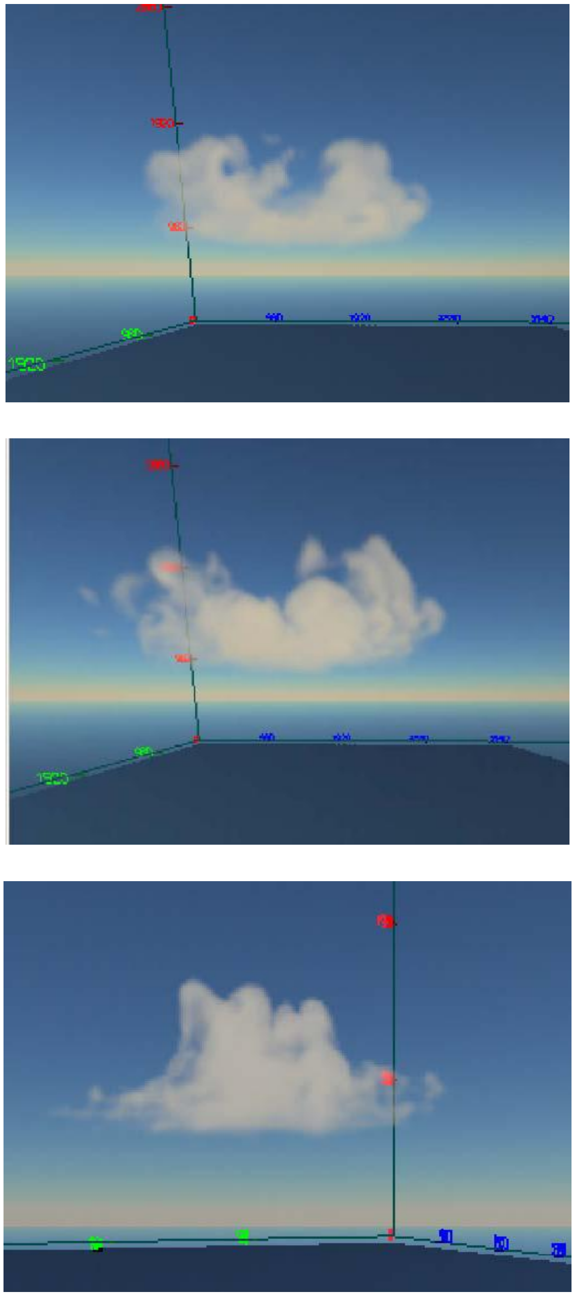

FIG. 3. Photorealistic rendering of the simulated trade wind cumulus meant to be representative of those observed on 10 Dec 2004. Renderings are at 7 (middle) and 14 (bottom) minutes after the beginning of cloud development associated with the second thermal (top). The second thermal (shown here) originates after the collapse of the first thermal (not shown), and ascends through remnants of the previous the cloud.

650 m the simulated cloud values falls easily into the range of observed values. At 980 m, the simulated maximum updraft speed falls into the observed range, but the simulated liquid water content is nearly double the maximum values observed, indicating that the simulated cloud is underestimating the amount of entrainment. At 1300 m, the simulated maximum updraft speed again falls into the range of those observed, but here too the simulated maximum liquid water content is greater than that observed.

3.2 The Trajectory Model

The three-dimensional cloud simulation was combined with microphysical calculations along trajectories derived from the cloud simulation using the method of Lasher-Trapp et al. (2005). Trajectories were computed backward in time, initiated across a line through the simulated cloud at a given altitude to mimic an aircraft penetration, hereafter referred to as “target points” (FIG. 4). Variability in the trajectories results from the subgrid-scale turbulence estimated using the turbulent kinetic energy from the cloud simulation. The condensation calculations were then run forward in time along the trajectories starting at cloud base up to the target points. The microphysical model is that of Cooper et al. (1997) that includes activation of CCN and growth or evaporation of droplets as the droplets move along the trajectories through the cloud, according to the ambient simulated conditions. Since entrainment and mixing are occurring in the cloud simulation, the properties of the air parcel traveling along each trajectory is forced to match those of the cloud simulation. The amount of environmental air entrained at each level is determined by the wet equivalent potential temperature (θ_q) prescribed by the cloud simulation. If the air parcel experiences a region of the simulated cloud where θ_q decreases, then environmental air and CCN are entrained into the parcel and mixing occurs either inhomogeneously or homogeneously depending on the method predefined by the user. If θ_q increases or stays constant, no entrainment is considered within the parcel. All calculations in the present study considered only homogeneous mixing, so that all droplets in the parcel experience the same resulting supersaturation after a mixing event. At the ending point (i.e. the target point), the trajectories (approximately 500 trajectories per target point, spaced 30 m apart) are averaged together to generate one average droplet size distribution for that target point at a given altitude. The features of the droplet size distributions (maximum total drop number concentrations, modal concentration, modal diameter, maximum droplet size, mean diameter, standard deviation from mean diameter, and dispersion) can be calculated along a line for a given altitude and then compared to those observed at a similar altitude across the real clouds observed during the 10 December flight. Further details of the calculation of trajectories and droplet size distributions are given by Lasher-Trapp et al. (2005).

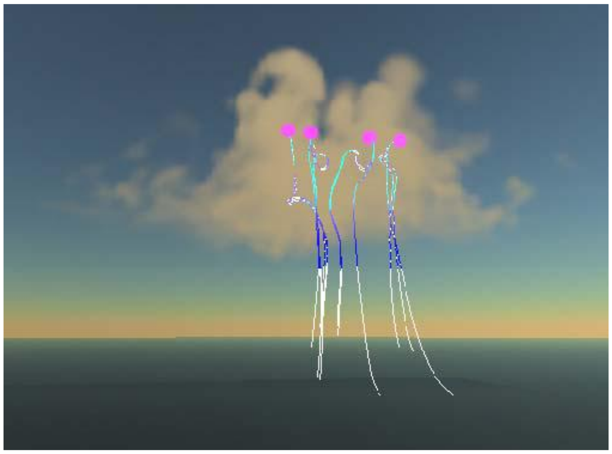

FIG. 4. Photorealistic rendering of the simulated trade wind cumulus at 54 minutes into the simulation, displayed with only a small subset of trajectories for multiple target points (pink dots). Color scale along trajectories represents ambient cloud water mixing ratio experienced by droplets with cool colors indicative of regions with less cloud water, and warm colors indicative of regions with more cloud water.

4. PRELIMINARY RESULTS

In order to quantitatively evaluate the ability of the modeling framework to produce realistic droplet size distributions for the trade wind cumuli observed during RICO, a comparison of the calculated values of total concentration, mean diameter, standard deviation, and dispersion with the observed values at similar altitudes was conducted. For this analysis, all of the observed values for each parameter are binned, producing a frequency distribution of observed values across the cloud field at a given altitude. The values from several transects across the modeled cloud are also binned, producing frequency distributions characteristic of the single simulated cloud. The modeled results can then be compared to the range of observations to see if the modeling framework is able to replicate the main trends in the observed values.

The model appears to be capable of representing the main trend in the observed total concentrations (FIG. 5a), although the mode for the modeled droplet size distributions is located at a slightly larger value than the secondary mode located at 70 cm^{-3} in the observations. Thus, the modeling framework appears to overestimate the maximum droplet concentrations found in the cloud. The model also appears to underestimate the number of parcels in the cloud that would have very low drop concentrations. This feature is most likely an artifact of the analysis technique, in that the observational data include more cloud penetrations when compared to the number of transects taken from the simulated cloud at this level (23 cloud penetrations compared to 3 transects through the simulated cloud) and as a result more cloud edges and regions of low liquid water content and cloud droplet concentration (i.e. holes in the clouds) are included in the observational sampling. It is also much more difficult to determine the edge of a cloud from observational data, while the edges of a simulated cloud are very distinct, and therefore there is a sharp gradient between the cloud and the environment. The observational analysis also includes all of the observed clouds matching the criteria established in Section 2, including clouds with weaker updraft speeds and lower maximum cloud droplet concentrations when compared to the updraft speed and maximum cloud droplet concentrations of the simulated cloud. Considering all of these effects, the underrepresentation of the frequency of areas of lower droplet concentration by the model appears to be an artifact of the analysis

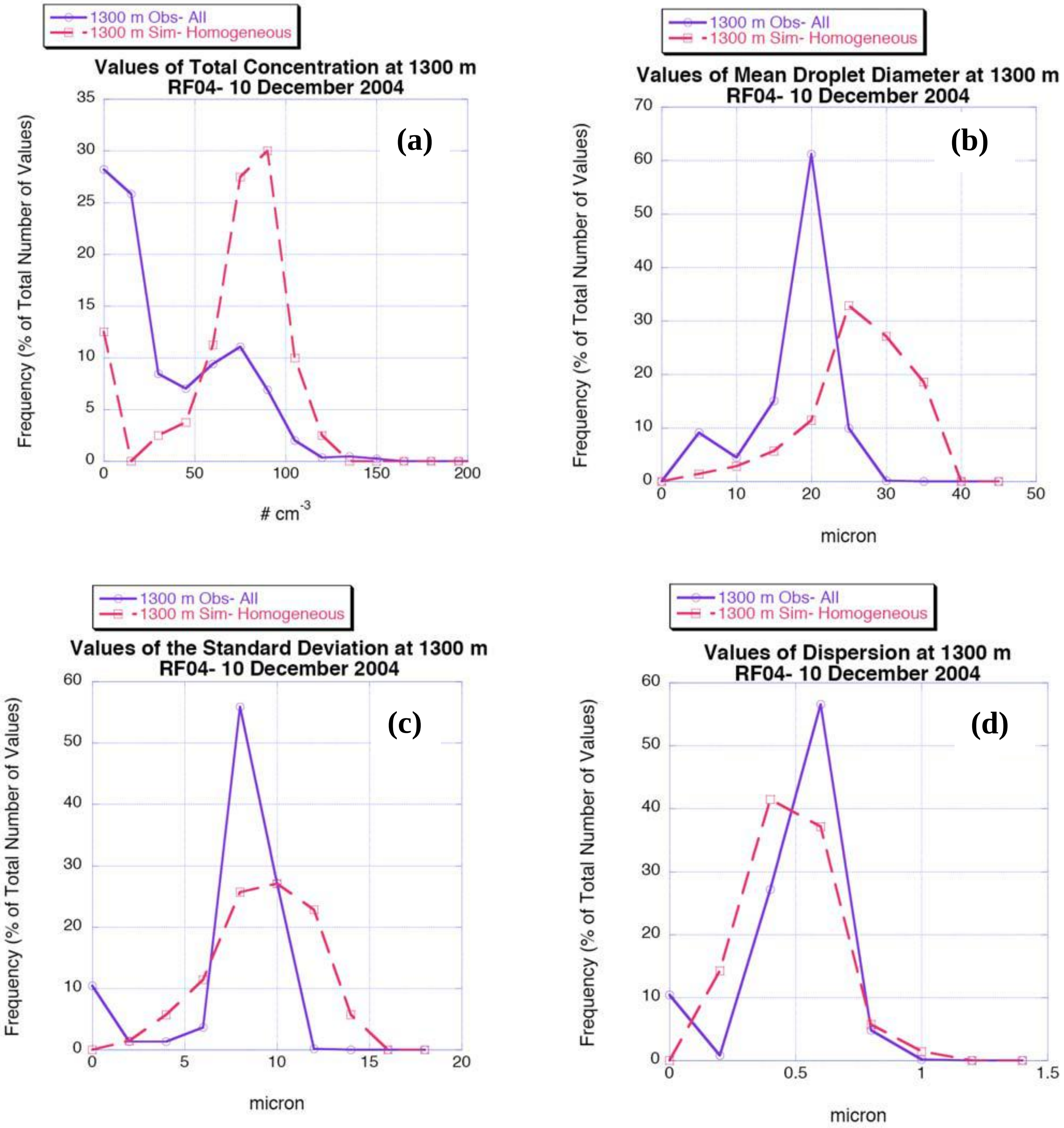

FIG. 5. The relative frequency (expressed as a percentage of the total number of values) distribution of (a) total concentration, (b) mean droplet diameter, (c) standard deviation in the mean droplet diameter and (d) dispersion for the observations (purple) and the simulated cloud when considering homogeneous mixing (pink) at 1300 m. The circles and squares plotted on each curve represent the maximum value for each bin.

technique.

From FIG. 5b, one can see that the modeling framework tends to overestimate the mean droplet diameter by at least 5 μm. It is also evident from the figure that the model produced mean droplet diameters as large as 35 μm, when the observed values are rarely ever greater than 25 μm, and are never greater than approximately 30 μm. One possible explanation for this discrepancy is the fact that although the model is producing broadened droplet size distributions, it still produces some rather ‘adiabatic’ droplet size distributions, evident when comparing the simulated mean droplet diameters to the calculated adiabatic droplet size of approximately 38 μm at this altitude. These narrow droplet size distributions are a result of the fact that most of the trajectories are taking a similar path to get to the target point, and thus little variation in the supersaturation histories is experienced among the trajectories. As a result the ending average droplet size distribution is not very broad, and the droplets grow rapidly, producing a narrow distribution with a larger, virtually adiabatic, mean diameter. This feature could possibly be avoided if the turbulence was better developed in the simulation so that the trajectories reaching the target point experience more variability.

The standard deviation of the droplet size distribution from its mean diameter, i.e., the width of the distribution (FIG. 5c), suggests that the model is able to represent substantial variability in the supersaturation histories of the droplets following different trajectories. The broadness of the droplet size distributions observed in these trade wind cumuli is substantial, and the model is able to replicate such broadness. Although the peaks in the two frequency diagrams overlap, it is evident that the model is also producing droplet size distributions that are wider than those observed. The breadth of the modeled size distributions is a result of the overestimation of the maximum drop diameters in the model as compared to the observations (not shown).

FIG. 5d displays the results for dispersion, i.e., the standard deviation normalized by the mean diameter. Because this value is derived from two other quantities, some errors can be cancelled by the division of the two terms. In this case, the dispersion for the simulated droplet size distributions matches the dispersion for the observed droplet size distributions well, but is a result of the modeling framework overestimating both the standard deviation and the mean diameter. This variable has thus proven to be of limited use in this analysis, but is shown for comparison with past studies where its use has been extensive.

5. FUTURE WORK

From the analysis in the previous section, the modeling framework appears to produce droplet size distributions that can replicate some features of those observed, but has a tendency to overestimate the number concentration of droplets, the mean diameter, and the width in these small maritime cumuli. It is not yet clear how transferrable these results are to deeper continental clouds such as that modeled by Lasher-Trapp et al. (2005).

Future work will include investigating the effects of inhomogeneous mixing, and allowing the parcels to mix with other undiluted parcels in the cloud, the latter not currently represented in the modeling framework. Also, testing the sensitivity of the results to the size and number concentration of the entrained CCN will be evaluated. Finally, the modeling framework will be used with new visualization software to investigate relationships between the timing of entrainment events relative to the evolution of the drop size distribution, and its influence on the drop size distributions afterward.

6. ACKNOWLEDGEMENTS

The authors would like to thank the participants of the RICO field campaign for the collection of the RICO data, Al Cooper for the use of the Lagrangian microphysical parcel model adapted to work with this modeling framework, Jerry Straka for the use of the Straka Atmospheric Model, and the

Purdue University Rendering & Perceptualization Lab (PURPL) for providing support for the visualization of model output. This study was funded by NSF grants ATM-0342421 and IIS-0513464. Computing support was supplied by the National Center for Atmospheric Research's (NCAR) Scientific Computing Division, and RICO observations were analyzed using the NCAR Research Air Facility's software. NCAR is sponsored by the National Science Foundation. Ms. Amanda Sheffield also supplied the statistical analysis shown in Figs. 1 and 2.

7. REFERENCES

Baker, B. and Q. Mo, 2006: The spurious effects of splashing precipitation on droplet measurements and the lack of natural cloud droplets in a RICO rain shaft. *12th Conference on Cloud Physics*, Madison, WI, USA.

Baker, M. B., R. G. Corbin, J. Latham, 1980: The influence of entrainment on the evolution of cloud droplet spectra: I. A model of inhomogeneous mixing. *Quart. J. R. Meteorol. Soc*., **106**, 581-598.

Bartlett, J. T. and P. R. Jonas, 1972: On the dispersion of the sizes of droplets growing by condensation in turbulent clouds. *Quart. J. R. Meteorol. Soc*., **98**, 23-38.

Blyth, A. M., T. W. Choularton, G. Fullarton, J. Latham, C. S. Mill, M. H. Smith and I. M. Stromberg, 1980: The influence of entrainment on the evolution of cloud droplet spectra: II. Field experiments at Great Dun Fell. *Quart. J. R. Met. Soc*, **106**, 821-840.

-----, W. A. Cooper, and J. B. Jensen, 1988: A study of the source of entrained air in Montana cumuli. *J. Atmos. Sci*., **45**, 3944-3964.

Carpenter, R. L., Jr., K. K. Droegemeier, and A. M. Blyth, 1998: Entrainment and detrainment in numerically simulated cumulus congestus clouds. Part I: General results. *J. Atmos. Sci*., **55**, 3417-3432.

Cooper, W. A., Bruintjes, R. T. and Mather, G. K., 1997: Calculations pertaining to hygroscopic seeding with flares. *J. Appl. Meteorol.*, **36**, 1449-1469.

Lasher-Trapp, S. G., W. A. Cooper and A. M. Blyth, 2005: Broadening of droplet size distributions from entrainment and mixing in a cumulus cloud. *Quart. J. Roy. Met. Soc*., **131**, 195-220.

-----, C. A. Knight and J. M. Straka, 2001: Early Radar Echoes from Ultragiant Aerosol in a Cumulus Congestus: Modeling and Observations. *J. Atmos. Sci.*, **58**, 3545-3562.

Latham, J. and R. L. Reed, 1976: Laboratory studies of the effects on the evolution of cloud droplet spectra. *Quart. J. R. Meteorol. Soc.*, **103**, 297-306.

Mason, B. J. and C. W. Chien, 1962: Cloud-droplet growth by condensation in cumulus. *Quart. J. R. Meteorol. Soc*., **88**, 136-142.

Mason, B. J. and P. R. Jonas, 1974: The evolution of droplet spectra and large droplets by condensation in cumulus clouds. *Quart. J. R. Meteorol. Soc.*, **100**, 23-38.

Paluch, I. R. and C. A. Knight, 1984: Mixing and the evolution of cloud droplet size spectra in a vigorous continental cumulus. *J. Atmos. Sci.*, **41**, 1801-1815.

-----, 1986: Mixing and the cloud droplet size spectrum: Generalizations from the CCOPE data. *J. Atmos. Sci.*, **43**, 1984-1993.

----- and C. A. Knight, 1986: Does mixing promote cloud droplet growth? *J. Atmos. Sci*., **43**, 1994-1998.

Politovich, M. K., 1993: A study of the broadening of droplet size distributions in cumuli. *J. Atmos. Sci.*, **50**, 2230-2244.

Soong, S. and Y. Ogura, 1973: A comparison between axisymmetric and slab-symmetric cumulus cloud models. *J. Atmos. Sci*., **30**, 879-893.

Squires, P., 1958: The spatial variation of liquid water and droplet concentration in cumuli. *Tellus*, **10**, 372-380.

Rauber, R. M., B. Stevens, H. T. Ochs III, C. Knight, B. A. Albrecht, A. M. Blyth, C. W. Fairall, J. B. Jensen, S. G. Lasher-Trapp, O. L. Mayol-Bracero, G. Vali, J. R. Anderson, R. A. Baker, A. R. Bandy, E. Burnet, J.-L. Brenguier, W. A. Brewer, P.

R. A. Brown, P. Chuang, W. R. Cotton, L. Di Girolamo, B. Geerts, H. Gerber, S. Goke, L. Gomes, G. G. Heikes, J. G. Hudson, P. Kollias, R. P. Lawson, K. K. Krueger, D. H. Lenschow, L. Nuijens, D. W. O'Sullivan, R. A. Rilling, D. C. Rogers. A. P. Siebesma, E. Snodgrass, J. L. Stith, D. C. Thornton, S. Tucker, C. H. Twohy, and P. Zuidema, 2007: Rain in shallow cumulus over the ocean: The RICO campaign. *Bull. Amer. Meteor. Soc*., **88**, 1912-1928.

Stith, J. L. and M. K. Politovich, 1989: Observations of the effects of entrainment and mixing on the droplet size spectra in a small cumulus. *J. Atmos. Sci.*, **46**, 908-919.

Stommel, H., 1947: Entrainment of air into a cumulus cloud. *J. Meteor*., **4**, 91-94.

Straka, J. M., and J. R. Anderson, 1993: Numerical simulations of microburst-producing storms: Some results from storms observed during COHMEX. *J. Atmos. Sci.*, **50**, 1329-1348.

Telford, J. W., T. S. Keck, and S. K. Chai, 1984: Entrainment at cloud tops and the droplet spectra. *J. Atmos. Sci.*, **41**, 3170-3179.

Warner, J., 1969: The microstructure of cumulus cloud. Part I. General features of the droplet spectrum. *J. Atmos. Sci.*, **26**, 1049-1059.

-----, 1973: The microstructure of cumulus cloud: Part IV. The effect on the droplet spectrum of mixing between cloud and environment. *J. Atmos. Sci.*, **30**, 256-261.

MICRO-SCALE DATA ASSIMILATION EXPERIMENTS

Gustavo G. Carrió, William Y. Cheng, and William R. Cotton

Colorado State University, Fort Collins, Colorado

1. INTRODUCTION

We performed a series of data assimilation experiments based on maritime boundary-layer (B-L) cloud cases documented during the RICO project. The fact that high spatial resolution observations are rarely available introduces unique difficulties to data assimilation into Large Eddy Simulation (LES) and cloud resolving models (CRMs). Moreover, the complexity and non-linearity of the microphysical processes interacting with the micro-scale circulations makes the optimization of the structure of these eddies a rather unrealistic goal. However, unlike typical applications of data assimilation on the mesoscale and synoptic-scale, our approach does not focus on spatial location and intensity of individual flow/cloud features. Conversely, it sees the 3-D or 2-D domain of the forecast (FCST) model as a column model capable of generating a realistic statistical perspective of the in-cloud small-scale inhomogeneities that govern the temporal evolution of the horizontally-averaged vertical profiles of the microphysical variables. We developed a method for the estimation of ice forming and cloud condensation nuclei (IFN and CCN) using the aforementioned approach (Carrió et al., 2006, 2008). We have already tested this modeling framework with simple observational operators. This abstract briefly summarizes recently performed experiments examining the response of the simulated cloud microstructure to periodic data assimilation while using more complex observational operators (i.e., for satellite radiances)

2. THE COUPLED MODEL

The Maximum Likelihood Ensemble Filter (MLEF) algorithm (Zupanski, 2005; Zupanski and Zupanski, 2005, Zupanski, et al, 2006) is used for this study. The algorithm calculates optimal estimates of the model state, error (bias) and empirical parameters. It also calculates uncertainties of all estimates in terms of analysis and forecast error covariance. This algorithm presents an important advantage (compared to the classical ensemble Kalman filter) as it does not make any assumption about the shape in the probability density function of the model state. A schematic description of this assimilation algorithm is given in Fig. 1.

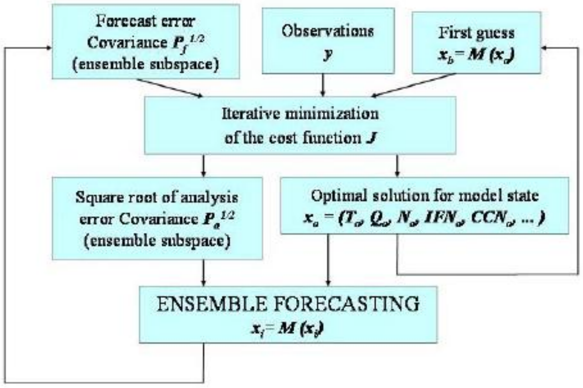

Figure 1. Maximum likelihood ensemble filter.

Several interface routines have been developed to include the MLEF algorithm into the LES version of the Regional Atmospheric Modeling System, developed at Colorado State University (RAMS@CSU;

Corresponding author: Gustavo G. Carrió, Atmospheric Science Dept., Atmospheric Science Bldg., Colorado State University, Fort Collins CO 80523, USA; e-mail: carrio@atmos.colostate.edu

Cotton et al, 2003). Several routines were added to consider as model state variables, the IFN, CCN , and giant CCN (GCCN) concentrations, and the number concentration and mixing ratio of all eight water species considered by RAMS@CSU (cloud droplets, drizzle drops, rain drops, pristine ice crystals, snow crystals, aggregates, graupel, and hail). Several other routines had to be added to deal with algorithmic issues related to the specifics of the LES model (see section 2). For the purposes of the present study, new observational operators were implemented to assimilate satellite-based observations.

3. THE BASIC APPROACH

The basic modeling framework we have used for the cloud-nucleating aerosol retrieval method is based on the assumption that periodical assimilation of observations into a LES (or high resolution CRM) leads to an improved estimation of the model state vector that contains all microphysical (prognostic) variables. As mentioned in Section 1, the 3-D or 2-D domain of the FCST model is seen as a column model capable of generating a realistic statistical perspective of microphysical processes governing the temporal evolution of the horizontally-averaged vertical profiles. These vertical profiles are seen by the data assimilation algorithm as a 1-D version of the state vector linked to the data assimilation algorithm. Consequently, the observations are considered valid for the entire horizontal extension of the forecast model domain.

When the model is initialized, the first ensemble of LES simulations is randomly designed. Larger-scale tendencies (as well as any other aspect not resolvable within the framework of the micro-scale model) are applied to each member until an assimilation time is reached. Then, observational data are assimilated and an *optimal* state of the model is computed by minimization of a cost function. After each assimilation cycle, new ensemble of LES simulations is generated adding to the optimal state perturbations (now based on error covariance matrices).

Each ensemble member needs a (spin-up) time to develop stable turbulence statistics physically consistent to the new vertical profiles. During these spin-up periods preceding the FCST runs, the horizontally-averaged vertical profiles are not allowed to change. A Newtonian relaxation technique (nudging) is used to preserve this 1-D version of the state vector while the 2-D/3-D model develops an eddy distribution consistent with these updated vertical profiles. During spin-up period, time "*freezes*" and L-S tendencies are *not* applied.

When the spin-up period ends, *time* starts evolving and then, L-S tendencies are applied to the ensemble of FCST runs until another assimilation time is reached. An schematic representation of the applied methodology is given in Fig 2.

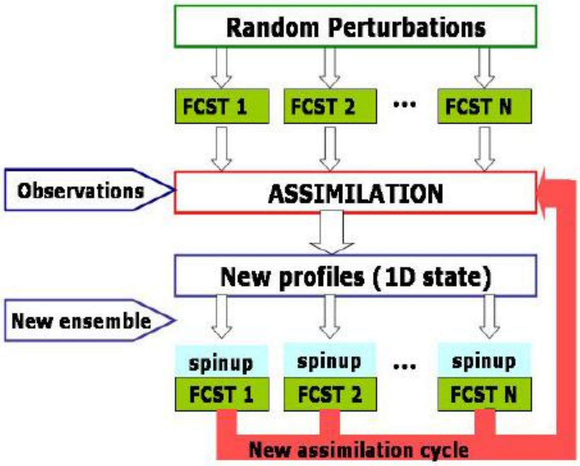

Figure 2. Assimilation into a LES model

4. SIMULATION CONDITIONS

We performed a free run and a series of data assimilation experiments based on a maritime B-L case documented during the RICO project (RF12). For all experiments, the FCST model domain represented a column with a base of 5000m and 20000m of height, and centered at ~ 15N, 61.5W. A constant horizontal grid spacing of 50m and a time step of 2s were used. The vertical grid was stretched (above the inversion) using the relationship $\Delta z(k+1) = 1.05 \Delta z(k)$, with a constant spacing of 30m within the B-L. The lateral boundary conditions were cyclic and the domain top is a rigid lid. Rayleigh damping was used in the five highest levels of the domain to prevent the reflection of vertically traveling gravity waves off this rigid lid. We used a two-moment bin-emulating microphysics framework (Meyers et al., 1997; Saleeby and Cotton, 2004) that assumes that the size distributions of the eight hydrometeor spectra follow gamma distributions (with two degrees of freedom). The prognostic microphysical variables include not only the number concentration and mixing ratio of water species, but also the IFN, CCN, and GCCN concentrations.

The free run was initialized on January 11 2005 00:00 UTC with a simulation period of 33h. One main objective of these experiments was to explore the feasibility of using satellite radiances to estimate (low level) CCN concentrations in regions covered by this type of clouds. The implemented observational operators (GOES-12) were applied to hourly model outputs of the free run to obtain a temporal series of radiances in the 3.9 and 6.7mm bands. This series of synthetic observations was used to define two series with higher (+10%) and lower (-10%) radiances to perform the assimilation experiments. If clouds were absent in the free run for a specific output time, the corresponding radiances were not modified.

5. RESULTS

The model state vector was configured to include the variables controlling the size spectra of the condensed water species (in this warm cloud, the number concentrations of cloud droplets, drizzle drops, and rain drops), the CCN concentration, the ice-liquid potential temperature, and the total water mixing (the sum of the mixing ratios corresponding to water vapor and all condensed species). Ensemble simulations were also initialized on January 11 2005 00:00 UTC, although, no assimilation was performed during the first 6 hours. We considered different ensemble sizes 25, 50, and 100 members and two infrared (IR) bands, however, results presented in this abstract correspond to ensemble simulations of 50 members and the 3.9-micron IR band.

Results show a clear response of the microstructure to the raw radiances assimilated in the 3.9-micron band. The behavior of the cloud droplet (and CCN) concentration indicates the potential of this modeling framework to retrieve those concentrations. To illustrate the latter, Fig. 3 gives the time evolution of the horizontally-averaged cloud droplet number concentrations for the 21 hourly cycles (with data assimilation). The central panel gives the results of the free run, and the upper and lower panels give those corresponding to the assimilation of decreased and increased radiances, respectively. Larger number concentrations (of smaller particles) correspond to lower radiances as the simulated cloud becomes a better shield of the higher temperatures below. A similar behavior was observed for the simulated *total* (activated+available) CCN concentration and optical depth, and liquid water contents did not show significant changes (not shown).

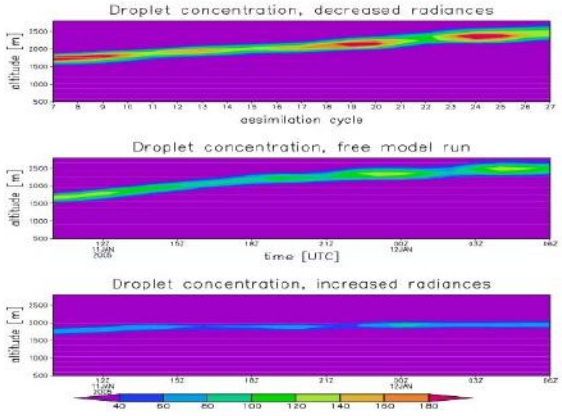

Figure 3. Horizontally-averaged cloud droplet concentrations [cm^{-3}].

Figure 4 is analogous to Fig. 3 but for the horizontally-averaged cloud droplet mean diameter.

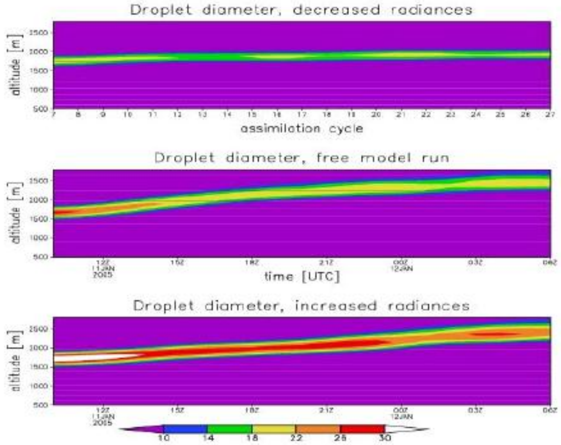

Figure 4. Horizontally-averaged cloud droplet mean diameters [μm].

As expected, approximately the same water mass distributed in larger (and fewer) particles resulted from assimilating a time series of increased satellite radiances.

Finally, we performed another series of numerical experiments using the 6.7μm band. Results are not conclusive although, they suggest a possible response of the second mode of cloud droplet (drizzle).

6. SUMMARY AND CONCLUSIONS

The MLEF algorithm has been adapted to assimilate data into the LES version RAMS@CSU. This abstract extends a previous study of ours that tested this modeling configuration for Arctic B-L clouds using simple observational operators.

Results indicate a clear response of the microstructure of the simulated maritime B-L clouds to the raw radiances assimilated in the 3.9-μm IR band. The behavior of the concentration of liquid particles (and CCN) suggests the potential of this approach to retrieve of these concentrations.

We are now performing a study assimilating real satellite observations for this and other RICO cases. By evaluating the coupled model performance in simulating independent observations, we will select its optimal configuration (e.g., bands/products to be assimilated, number of ensemble members and minimization iterations, assimilation frequency, etc).

ACKNOWLEDGEMENTS

This project has been funded by NASA (NNG04GD75G) and by NSF under grant ATM-0526600 (amd 002).

REFERENCES

Carrió, G.G, Cotton, and Zupanski, D 2008: Development of an Aerosol Retrieval Method Part I: Description and Preliminary Tests. *J.A.M.C., accepted.*

Carrió, G.G, Cotton, W.R. and D. Zupanski *Data assimilation into a LES model: Retrieval of IFN and CCN concentrations*. Presented at the 12th Conference on Cloud Physics - 12th Conference on Atmospheric Radiation. 10-14 July 2006, Madison (1.4A).

Cotton,W. R., R.A. Pielke, Sr., R.L. Walko, G.E. Liston, C. J. Tremback, H. Jiang, R. L. McAnelly, J. Y. Harrington, M.E. Nicholls, G. G. Carrió and J. P. Mc Fadden 2003: RAMS 2001: Current Status and future directions. *Meteor. Atmos. Phys.*, **82**, 5-29.

Meyers, M. P. Walko, R. L., Harrington J. Y. , Cotton, W.R., 1997: New Rams cloud microphyisics parameterization : Part II. The two-moment scheme. *Atmos. Res.*, **45**, 3-39.

Saleeby, S. M., and W.R. Cotton, 2004: A large-droplet model and prognostic number concentration of cloud droplets in the RAMS@CSU model. Part I: Module descriptions and Supercell test simulations. *J. Appl. Meteo,* **43**, 182-195.

Zupanski D. and M. Zupanski, 2005: Model error estimation employing ensemble data assimilation approach. *Mon. Wea. Rev*., **134**, 1337-1354.

Zupanski, M., 2005: Maximum likelihood ensemble filter: Theoretical aspects. *Mon. Wea. Rev,* **133***,* 1710-1726*.*

Zupanski, M., S. J. Fletcher, I. M. Navon, B. Uzunoglu, R.P. Heikes, D. A. Randall, T. D. Ringler, and D. Daescu, 2006: Initiation of ensemble assimilation. *Tellus*, **58A,** 159-170.

AEROSOL SIZE DISTRIBUTION VARIABILITY NEAR CARIBBEAN TRADE WIND CUMULUS CLOUDS

Marilé Colón-Robles[1*], Robert M. Rauber[1], Jørgen B. Jensen[2] and Larry Di Girolamo[1]

[1]Department of Atmospheric Sciences, University of Illinois at Urbana-Champaign, Urbana, IL, USA
[2]National Center for Atmospheric Research, Broomfield, CO, 80021 USA

1. INTRODUCTION

Shallow maritime cumuli continually modify aerosol size distributions in the trade wind regime, which leads to sampling problems due to this continual aerosol-cloud interaction. Because of the ubiquity of trade wind clouds across the world's tropical oceans, understanding the relationship between trade wind cumuli and aerosol spectra in the trade wind layer is required to evaluate the role of aerosols in Earth's radiation balance and climate. Studies in the past typically select either cloudy or cloud free areas to obtain aerosol size distributions. However, conclusions of past studies point to the fact that distance to cloud is an important parameter to consider when reporting aerosol size distributions.

In this work, data collected from the National Center for Atmospheric Research Hercules C-130 during the Rain in Cumulus over the Ocean (RICO) field campaign, which took place during November 2004 - January 2005 in the trades over the western Atlantic, is used to study the variations of deliquesced and dry particle size distributions of sub-micron (dry radius, $r = 0.05 - 2.0$ μm) and giant ($2 < r \leq 10$ μm) particles as function of distance to cloud and altitude above the ocean surface

2. METHODS AND RESULTS

Aerosol size distributions where collected during 11 research flights using aircraft-mounted probes, FSSP-100 (2 – 47 μm) and PCASP (SPP-200; 0.1 – 3.0 μm) between 600m and 3000m above the ocean surface. The size spectra were divided into areas inside or outside of regions of enhanced relative humidity. The identification of these regions of enhanced relative humidity or humidity halos were selected following the methods specified by Perry and Hobbs (1996). Additional constraints where used to avoid the influence of droplet splattering on the concentrations of particles measured by the FSSP-100.

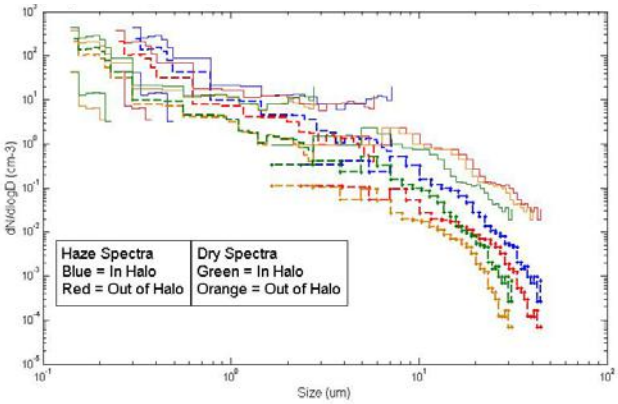

Figure 1: Variation of dry and deliquesced particle size distributions inside (dry – green; deliquesced – blue) and outside (dry – orange; deliquesced – red) humidity halos for 11 research flights. The thin lines represent one standard deviation from the average concentration for each spectrum plotted.

Corresponding author address: Marilé Colón-Robles, Univ. of Illinois at Urbana-Champaign, Dept. of Atmos. Sciences, 105 S. Gregory, Urbana, IL 61801;
e-mail: mcolon2@atmos.uiuc.edu

Figure 1 shows the average deliquesced and dry particle size distributions for regions inside and outside humidity halos. Results show that larger particles are found inside regions of enhanced humidity. Also, variations in spectra between dry and deliquesced radii were observed for regions inside and outside humidity halos. Larger particle sizes were observed for deliquesced spectra. This difference in radii is observed to be larger for giant particles.

Variations in concentrations between regions inside and outside of halos were also observed. Larger concentration of particles was observed inside of halos with a greater difference in the giant particle size range. Regions inside humidity halos were then divided into upshear and downshear halos by comparing the location of the halo, the location of the cloud producing the halo, and the mean wind shear observed for each flight. No significant differences were observed between upshear and downshear averaged spectra (see Fig. 2).

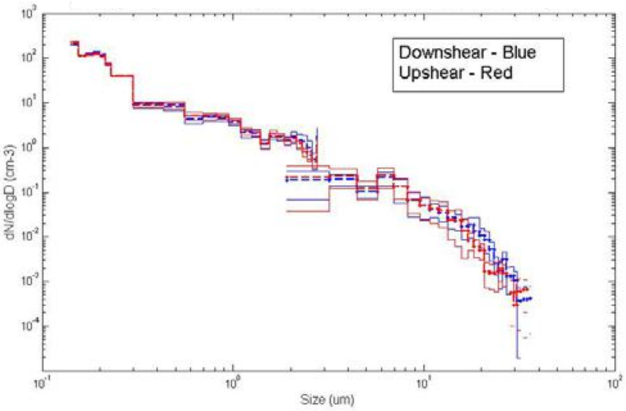

Figure 2: Variation of dry particle size distributions inside humidity halos divided into upshear (red, - -) and downshear (blue, - -) regions for 11 research flights. The thin lines represent one standard deviation from the average concentration for each spectrum plotted.

3. DISCUSSION

Particle spectra observed around trade wind cumuli were divided into regions inside and outside humidity halos for 11 research flights. Aerosols with larger diameters were observed within halos (see figure 1). Giant particle size range exhibits a larger difference between dry and deliquesced spectra compared to submicron particles, which do not exhibit such a pronounced difference. Larger concentrations of aerosols were observed inside humidity halos for both submicron and giant particles, with no difference between upshear and downshear halos.

Satellite studies typically use “cloud free” areas to obtain aerosol size distributions remotely. The data in Figure 1, point to the fact that aerosol size distributions change as a function of distance to cloud. This distance is an important parameter to consider when reporting aerosol size distributions derived from spaceborne platforms.

4. REFERENCES

Perry, K.D. and P.V. Hobbs (1996) Influences of isolated cumulus clouds on the humidity of their surroundings, J. Atmos. Sci., 53, 159-174.

BOUNDARY LAYER STRUCTURE AND TURBULENCE ASSOCIATED WITH FAIR WEATHER CUMULUS CLOUDS DURING RICO 2005

Shaunna Donaher[1], Bruce Albrecht[1], Chris Fairall[2], Sara Tucker[2] and Alan Brewer[2]
[1] University of Miami, RSMAS
[2] NOAA ESRL

1. INTRODUCTION

During the last four decades, marine fair weather cumulus clouds have been the focus of theoretical/modeling studies (e.g. Albrecht 1981; Albrecht 1993, Bretherton and Park 2008) and field experiments (e.g. Holland and Rasmusson 1973; Augstein et al. 1973). Shallow, oceanic cumulus convection is one of the most prevalent cloud types on Earth, although only a small percentage of these clouds may be considered active (contain active updrafts) at any given time (Albrecht 1989). Fair weather cumuli (FWC) typically exist in the trade wind regime of steady northeast winds in the tropics, are closely tied to surface fluxes through thermals in the boundary layer, and are dominated by warm rain processes (cloud tops below 0 ℃). Advection, convection, and radiation maintain a characteristic thermodynamic structure with a cloud layer that is often capped by an inversion of sufficient strength to inhibit deep convection (Albrecht 1993). Fair weather cumuli are present over much of the tropical oceans, and characterizing their properties is important towards understanding the global energy balance and climate, improving large-scale climate and weather forecast models, and even for basic and highly idealized cloud models that rely on information about entrainment and precipitation processes (Kollias et al. 2001).

In the Northern Hemisphere, typical trade wind conditions involve east or northeast wind directions as winds blow from the high-pressure area in the horse latitudes (30-35^{o}N) towards the low-pressure area around the equator. During the winter season, this flow is generally uninterrupted by strong convective events and is only varied by troughs, high pressure air masses and small systems embedded in the trade wind flow. During the summer months, tropical systems and deep convection can disrupt the “typical” trade wind zonal flow along the southern parts of the subtropical highs.

A good area to study FWC is the tropical Atlantic, especially to the east of the Leeward Islands. In this area, FWC develop, evolve and dissipate in a pure oceanic environment away from land or human effects. The large area of open Atlantic Ocean under this trade wind regime extends from the western coast of Africa westward to about 61.5^{o}W and from about 10^{o}N to 25^{o}N in latitude.

In this study, data collected during the Rain In Cumulus over the Ocean (RICO, Rauber et al. 2007) research cruise are used to study oceanic FWC and boundary layer structures in their purest uninfluenced form. The main objectives in this study are to characterize the boundary layer structure and use Doppler lidar observations in the upward facing mode to study subcloud layer turbulence and examine the relationship between subcloud turbulence, convection and precipitation.

2. DATA COLLETION

The RICO field experiment took place during November 2004-January 2005 off the Caribbean Islands of Antigua and Barbuda within the Northeast Trades of the western Atlantic. This time period was specifically selected to study trade wind clouds while avoiding hurricanes and deep convection (Rauber et al. 2007). There were many observational components of RICO, though this study focuses on ship-based instrumentation onboard the *R/V Seward Johnson* collected during the official RICO portion of the cruise, from 1/09/05- 1/14/05 (Leg 1) and 1/16/05-1/24/05 (Leg 2).

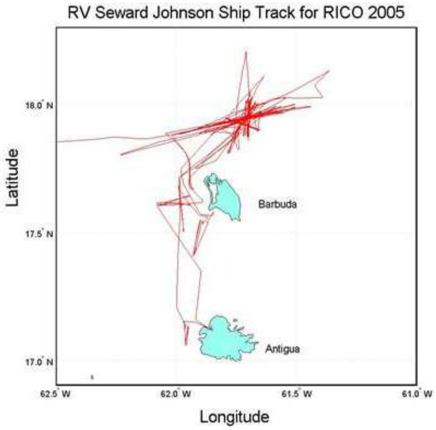

Figure 2.1: Ship Track for R/V Seward Johnson during RICO 2005 cruise (1/09 – 1/23).

Figure 2.1 illustrates the ship track during RICO. The typical observing strategy was to spend two hours traveling continuously into the trade winds and then quickly return to the starting point and repeat this track. This was done since a continuous upwind journey lasting at least 2 hours was needed for high quality averages of flux tower data. Other than a one-day port stop in Antigua between two legs of the experiment, the ship sampled NE (upwind) of Barbuda to avoid land effects.

An extensive suite of instruments was deployed onboard the research vessel for making measurements of boundary layer clouds and thermodynamic structure, as well as surface fluxes and meteorology. The NOAA Earth Science Research Laboratory (ESRL) Doppler lidar (light detection and range) is the principal remote sensing observing system used in this analysis because of its ability to measure small-scale vertical velocity variations in the subcloud layer. The lidar is a master-oscillator, power-amplifier Doppler lidar with a line tunable wavelength between 9.2-11.3 µm, pulse length of 600 ns, low pulse energy (2 mJ) and a high pulse rate (up to 300 Hz, normally operated at 120 Hz). The instrument provides wideband signal to noise ratio (SNR) and line-of-sight velocity estimates (Brewer et. al 1998). For the vertical stare scans, the laser pulse width was shortened from 1 µs to 450 ns, resulting in improved vertical resolution. Data were averaged into 1 Hz temporally and 60 meter vertical gates spatially.

During RICO, the Doppler lidar operated in several modes (PPI, RHI, sector, zenith, stare). In this study, we use the zenith (or vertically staring mode) data, which is extremely useful for calculating turbulence statistics during RICO, although this mode was only operated for the last 10-15 minutes of each hour that the lidar was operating. Since the lidar was located on the bow of the ship and experienced the roughest conditions and is a very sensitive machine, it was only operated for 8-12 hours per day as deemed most useful to the experiment. Thus, on the best days there is only about 2.5 hours of combined vertical data, which limits aspects of a statistical analysis.

3. BOUNDARY LAYER STRUCTURE, SYNOPTIC CONDITIONS AND CLOUDINESS

The temporal and spatial variability of the boundary layer and cloud properties during RICO are examined and are classified into four periods of similar conditions. For each observing period, the composite profiles and time series of cloud and boundary layer parameters are presented. The diurnal cycle of some key cloud properties (e.g. fractional cloudiness) is also examined. All of this is done in an attempt to better comprehend the processes occurring in the boundary layer and how they might be related to observed variations in subcloud turbulence.

3.1 RICO Synoptic Periods

A first look at several meteorological variables, such as cloud base height, moisture content and wind speed and direction, indicated a few striking shifts during different periods of RICO ship observations that all seemed to coincide in time. For example, Figure 3.1 shows the cloud base height from the ceilometer coupled with the LCL calculated from temperature and moisture measurements from the flux tower. Around January 20th, the cloud base height increases significantly and remains at this height for the duration of the cruise. Since the LCL stays nicely coupled with the ceilometer during this increase, we believed that the change was caused by a larger synoptic-scale variation.

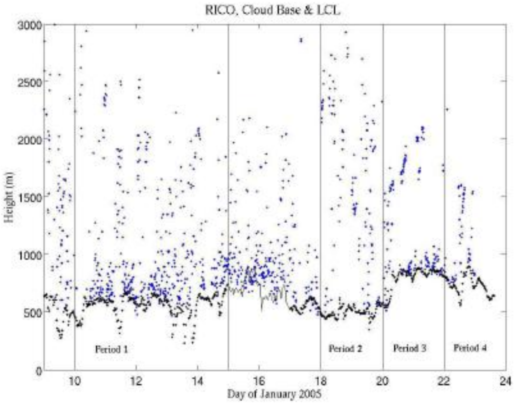

Figure 3.1: Cloud base height (blue dots) from ceilometer and LCL (black dots) from surface fluxes. The four synoptic periods are outlined.

Since synoptic conditions may affect the subcloud turbulence, the meteorological parameters and weather conditions over the entire cruise were classified into four periods identified in Fig. 3.1. Each period was analyzed in detail through NCEP Reanalysis (NCEP Reanalysis data provided by the NOAA/OAR/ESRL PSD, Boulder, Colorado, USA, from their Web site at http://www.cdc.noaa.gov/) and the overall synoptic conditions influencing each period were categorized and are described below.

Period 1: January 10th-14th (hereafter referred to as SP1)

Winds were strong and mostly zonal over the entire region, with the strongest easterly winds to the east of the islands. This period was very moist throughout the BL and experienced frequent rain showers with the passage of a surge line and a weak trough. Clouds were occasionally convective in nature. The most apparent variable separating this period from the others was the strong, constant easterly winds. A low level easterly wind maximum (LLEWM) occurred on the 11th along with a line of convection. Above 500mb, northwest winds advected dry air into the higher levels (Ceaser 2005).

Period 2: January 18th-20th (hereafter referred to as SP2)

This was a period of transition between the unsettled conditions of SP1 and the more "typical" trade wind conditions of SP3. On January 18th, a strong cold front approached from the NW, but as it came closer to the region it became more of a shear line. This increased low level moisture and instability and caused clouds to thicken into bellowing cumulus or overcast stratocumulus. Very dry air aloft limited any significant convective development. Winds were still easterly to the east of the islands, but took on a northeasterly component to the west of the islands. Wind speed decreased in magnitude significantly from SP1 (Fig. 3.2). Sea level pressure lowered with the approach of the shear line, and there were many rain showers from 18th-20th.

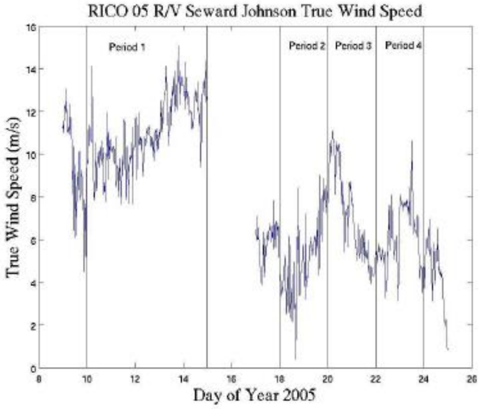

Figure 3.2: Surface true wind speeds taken from the flux tower (14 m) during RICO. The jump in data is due to a port call in Antigua on January 15th-16th, so that data is not included in the set.

Period 3: January 20th-22nd (hereafter referred to as SP3)

The shear line passed over the region on the 20th with increased clouds but very little shower activity due to strong subsidence aloft and the lack of low-level moisture. Westerly winds lowered to 700 mb and the trade wind inversion fell below freezing level for the remainder of the experiment, providing a very stable environment. During this period, we experienced the most “typical” trade wind conditions- namely light to moderate easterly winds and very little convection or precipitation. Overall, the wind direction remained from the NE. High pressure built in from the NW; clouds were very small and shallow and there was no measurable rainfall. The most striking change during this period was the drying of the air aloft.

Period 4: January 22nd-24th (hereafter referred to as SP4)

This period is very similar to SP3 as cloud bases continued to be high and the winds remained light over the islands. Strong inversions existed at 850 mb and 670 mb and maintained stable conditions. The wind direction has gained more of an easterly component back again. The high pressure system has passed to east, keeping the conditions mostly suppressed, with only one light rainfall occurrence. However, this period cannot be classified as part of SP3 due to increasing temperatures, humidity, and cloud activity.

3.2 Moisture Structure

A view of the moisture structure in the BL can be seen by averaging the soundings in each synoptic period, as done in Fig. 3.3. From this figure, the similarities in the moisture structure between SP1 and SP2 are obvious, as well as the decrease in moisture by 2-3 g/kg during SP3. SP4 shows a rebound in moisture content at the surface, but still lower values near the LCL. When averaging the soundings over a few days, the various layers of the BL tend to be blurred, but this kind of analysis is crucial for understanding the variations between various time intervals during RICO so that we can determine if any shifts in lidar turbulence statistics can be related to synoptic scale influences.

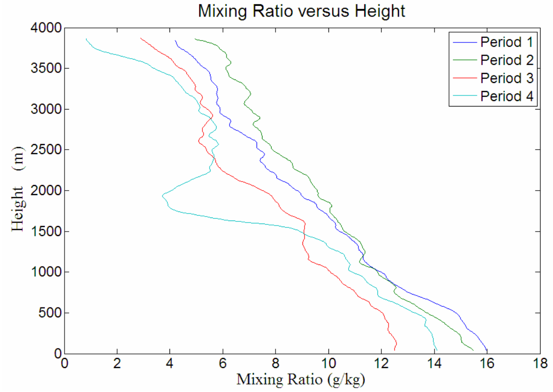

Figure 3.3: Average mixing ratio with height during each of the 4 Synoptic Periods.

3.3 Wind Speed and Direction

The winds observed from the ship are examined using time-height mappings made from the soundings. The wind speed is shown in Fig. 3.4, and the most striking feature in this figure is the area of high the wind speeds observed during the first leg of the cruise (January 9th-14th). During this time, wind speeds of 13-20 m/s are found throughout the first 2 km of the BL. Above this height, the winds are reduced to 2-5 m/s, except from January 12th-14th, when the high winds are present up to 3.5 km. During Leg 2 (January 16th-24th) of the cruise, there is a decrease in wind speeds from the surface to 2.5 km. In this time frame, the highest wind speed throughout the BL is only 10 m/s. There is an interesting feature of higher wind speeds from 3-4 km on January 20th-24th, which is actually related to the return of stronger westerlies aloft, which have lowered in height down to 5 km (Caesar 2005). This figure shows the drastic decrease in wind speeds between SP1 and the later 3 periods. The wind speeds that occurred from January 17th-24th are much more typical of the winter trade wind regime and will provide a nice comparison of “standard” turbulence conditions vs. the convective conditions seen during SP1 later on in this study.

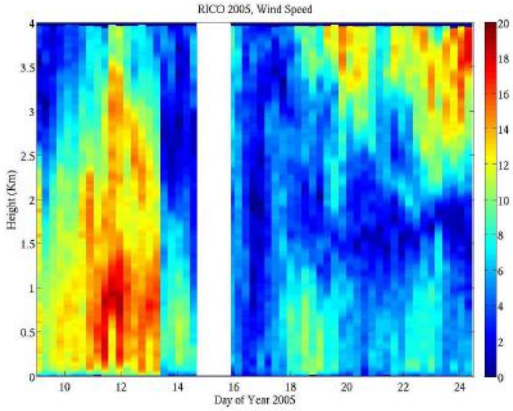

Figure 3.4: Time-height mapping of wind speeds (m/s) from sounding launched during RICO. White spaces indicate missing or bad data.

Winds in the tropical trades are usually easterly at lower levels and westerly above the TWI. During the winter months, weaker easterly winds are observed at the surface compared with those during the summer months. The time-height mapping of wind direction taken from the soundings during RICO is shown in Fig. 3.5. During Leg 1, easterly winds are present from the surface up to 4 km, except for a small area of southwesterly winds around 3.5 km on January 10th. During Leg 2 easterly winds only extend from the surface up to about 1.5 km during the majority of this period. Above this level the wind direction ranges from SW to NW up to 4 km.

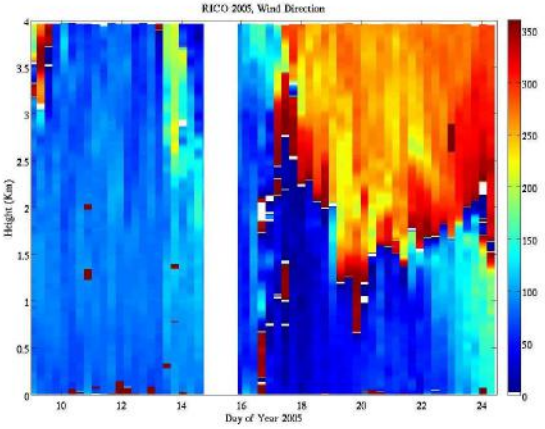

Figure 3.5: Time-height mapping of wind direction (0 is due north) from sounding launched during RICO. White spaces indicate missing or bad data.

3.4 Convective Velocity Scale

The convective velocity scale w* (Eq. 3.1, also known as the Deardorff velocity) is given as:

$$w^* = [g\overline{T}^{-1}\overline{(w'T_v')}_0 h]^{1/3} \quad \text{(Eq. 3.1)}$$

where g is gravity, T is surface temperature, $(w'Tv')_o$ is the virtual heat flux at the surface and h is subcloud layer depth (assumed to be cloudbase height).

This variable is related to buoyancy production of turbulence in the boundary layer and is a useful scaling parameter for convective boundary layers. A plot of w* is shown in Fig. 3.6, and the values will be used to scale turbulence profiles to compare synoptic periods in section 4.

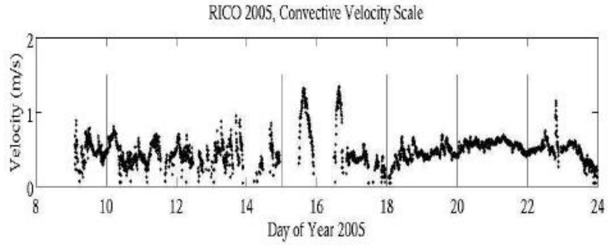

Figure 3.6: Time mapping of Convective Velocity Scale during RICO.

3.5 Fractional Cloudiness and Precipitation Occurrence

The ceilometer backscatter can be used to estimate the height of the cloud base with a temporal resolution of 30 seconds and a spatial resolution of 15 m as was seen in Fig. 3.1 (blue dots). Fig. 3.7 shows a histogram of cloud base height from the ceilometer over the entire RICO cruise. The main peak is seen around 700 meters, which is the average cloud base height from SP1 and SP2. A second, less dramatic, peak is seen between 1400-2000 meters, and is related to the higher cloud bases during SP3 and SP4.

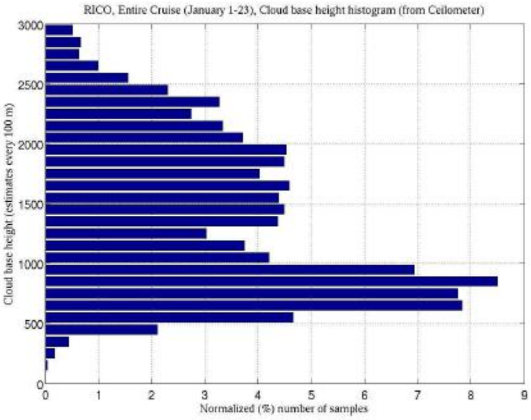

Figure 3.7: Histogram of cloud base height during RICO 2005.

Fractional cloudiness was highly variable during the RICO experiment. Fig. 3.8 shows the averaged fractional cloudiness by day. Typical fractional cloudiness in the tropical Atlantic trade wind winter regime is around .25-.30 (LeMone and Pennell 1976); 7 of the days that were encountered during RICO were significantly above this value. These days were associated with enhanced convection and the passage of a surge line, which explains the additional cloud cover. Another way to look at fractional cloudiness is by hour. Fig. 3.9 shows the diurnal cycle of cloud fraction during RICO. Contrary to other studies (such as ATEX, Augstein et al. 1973) which saw a 20% higher cloud fraction during the night, RICO had the highest cloud fraction between 6-10 AM local time. Overall, there is not much diurnal variation in fractional cloudiness. Thus, even though the lidar was only operating during the daytime, the turbulence statistics will most likely be representative of the entire day.

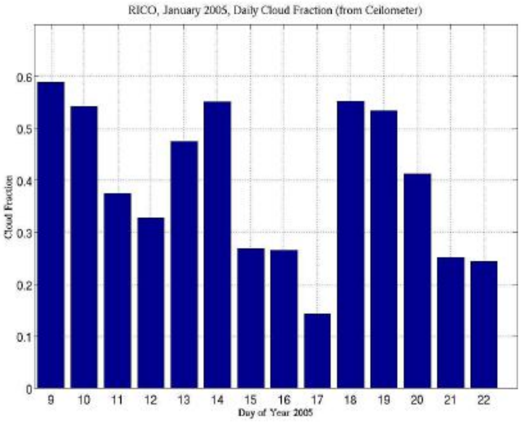

Figure 3.8: Daily averaged fractional cloudiness (from ceilometer) during RICO 2005.

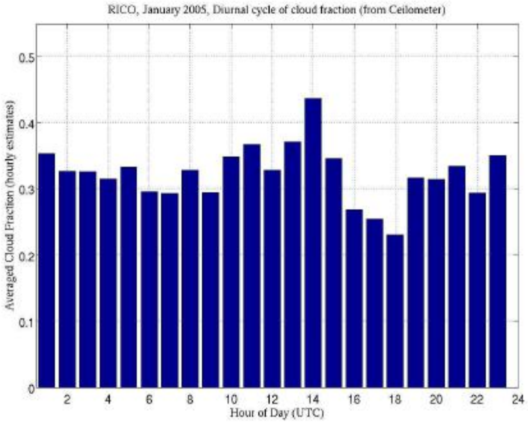

Figure 3.9: Histogram of hourly cloud fraction (from ceilometer) during RICO. Local time on the ship was 4 hours behind UTC.

4. LIDAR OBSERVATIONS

4.1 Data Processing

The motion-corrected vertically pointing lidar data were subjected to further post-processing before calculating any statistics. Examples of this post-processing are shown here for the same 15 minute case on January 11, 2005, from 14.75-15 UTC. To eliminate outliers from the data, all vertical velocities less than -5 m/s or greater than 5 m/s are removed. Further, any SNR values less than -5 dB and the corresponding velocities were removed. To remove the mesoscale variability, the perturbation velocity (w’) at a given point is obtained by subtracting the mean velocity at that level for the time period from the observed w. An example of the w’ field is shown in Fig. 4.1, where red colors (positive values) represent updrafts and blue colors (negative values) represent downdrafts.

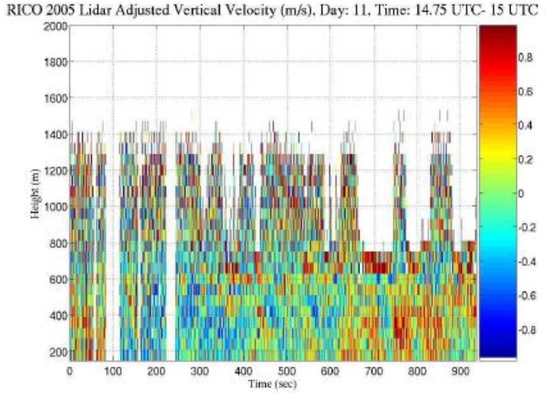

Figure 4.1: Lidar adjusted vertical perturbation velocity from January 11, 2005. Red colors (positive values) represent updrafts while blue colors (negative values) represent downdrafts.

For all of the data sets, we needed to find a cloud threshold SNR to determine if a cloud was present above the lidar at a particular time. After several trials, a SNR of 15 dB was determined to be the best threshold for finding the true cloud and thus the true cloud base. Using the 15 dB threshold, each one-second record is evaluated to see if the SNR exceeds 14 dB anywhere in the lowest 2 km. If so, that entire column is tagged as a “cloud column”, otherwise it is labeled a “no-cloud column.” This classification is done so that statistics can be calculated as cloud vs. no cloud conditions to see the effect the cloud has on the subcloud region. A similar classification was also done for updrafts, where the maximum velocity in each one second column (again below 2 km) is plotted and any velocities exceeding 1 m/s are tagged as strong updrafts.

One final correction that was made was the removal of the first five samples (or first five seconds) of each file. This was done because as the lidar switches to a new scanning mode (in this case the zenith mode), it takes a few seconds to stabilize and faulty velocity values can be returned. Such artifacts were removed from every data set.

4.2 Coupling Turbulence with Synoptic Periods

4.2.1 Cloudy vs. Clear Conditions

The mean vertical velocity and variance are good general indicators of boundary layer turbulence, and using the cloud threshold, the total variance can be separated into the components associated with clouds and clear areas. To better understand how various synoptic conditions affected the turbulence profiles, the lidar data were grouped into the four Synoptic Periods described in section 3. The height used for this analysis is the actual height normalized by the height of the LCL so that 0 is the surface and 1 is cloud base. Cloud base influences are seen in most of the profiles beginning around z/z_{LCL} = z*=0.8 due to averaging of the files over each day and using LCL as a scaling height rather than the cloud base height defined by the lidar SNR. The large jumps in the turbulence profiles between 0.8 and 1 may include some cloud sampling as indicated by the increase in the SNR. This cloud sampling may introduce artifacts due to the lidar chirp effect discussed earlier. Since it is useful to normalize the height axis to effectively compare results from different days and under different weather conditions, the LCL scaling is maintained, although the actual cloud base may be in the range of z* = 0.8 and 1.

Each composite synoptic period file was used to calculate mean and standard deviation of w’ for clouds vs. clear sky. Fig. 4.2 shows turbulence results in the form of σ_w/w^* vs. height, where the red profiles represent conditions under clouds, the blue profiles represent clear sky and the black profiles are an average of all conditions. For SP1, we see that the variance of w’ under clear sky decreases with height, while under clouds it decreases at first and then increases into cloud base. This is most likely due to the influence of both updrafts and downdrafts just under cloud base as SP1 had the most convective conditions with very active clouds, an ill-defined TWI, cloud tops penetrating 2-3 km and frequent rainfall.

Normally in the tropical Atlantic trade wind regime under clear skies or very weak, shallow cumulus clouds, you would expect to see a profile similar to that found by Nicholls and LeMone during GATE (see Fig. 4.6). The clear sky variance profile that we see during SP1 seems to follow the same shape as the upper half of the Nicholls and LeMone curve, but since the lidar does not collect accurate data in the lowest 150 meters of the atmosphere, it is difficult to know if our clear sky curve would follow their curve in the lower subcloud layer. To get a better idea of this, the green symbol in Fig. 4.2 shows the flux tower value of σ_w/w^* for SP1. An extrapolation from the lidar observations to the flux tower turbulence would give a turbulence structure similar to GATE during RICO suppressed conditions. The deviation from this profile only occurs with convective conditions and active clouds overhead.

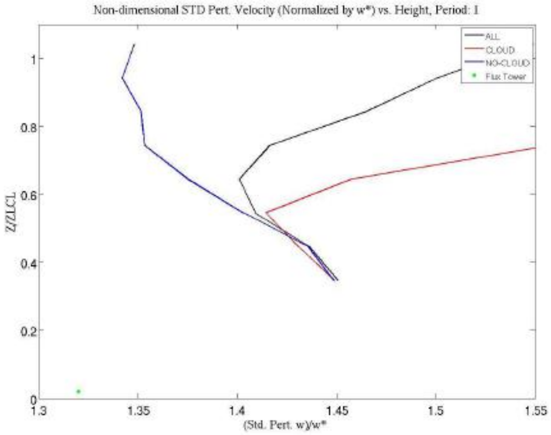

Figure 4.2: Standard Deviation of w' normalized by w for SP1 (January 10th-14th). Red curve represents columns under clouds, the blue curve represents clear sky and the black curve is a mean of all conditions. Green star represents* σ_w/w^* *from the flux tower (14m height) for all conditions in the same time period.*

Figure 4.3 shows the turbulence profiles for SP2. As seen for SP1 (Fig. 4.2), our clear sky variance profile and flux tower observations follow those of Nicholls and LeMone, while the CLOUD variance profiles increase in height towards cloud base. The increasing variance with height is due to the presence of strong updrafts and downdrafts from clouds, while the decrease just below base is most likely caused by the increase in downdrafts just beneath the clouds associated with the heavy precipitation observed on the 18th. The mean w' under clouds is positive in the middle of the subcloud layer but decreases with height, becoming negative as it approaches cloud base (not shown). This is due to the influence of downdrafts and rainfall out of the clouds.

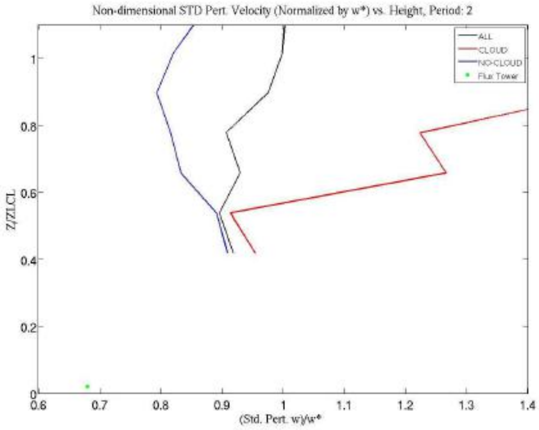

Figure 4.3: As in Figure 4.2, except for SP2 (January 18th-20th).

Figure 4.4 shows the turbulence profiles for SP3, which had the most suppressed conditions observed during RICO. While clouds were still present, they were very weak and shallow and typical of the wintertime trade wind regime. For this reason, we expect that our velocity variance curves should most closely follow those of Nicholls and LeMone, which they do as all three profiles decrease with height from the middle of the subcloud layer to cloud base.

A subjective interpolation of the curve from the lowest lidar height down to the flux tower point would give the same inverted ‘C’ shape curve as shown in Fig. 4.6.

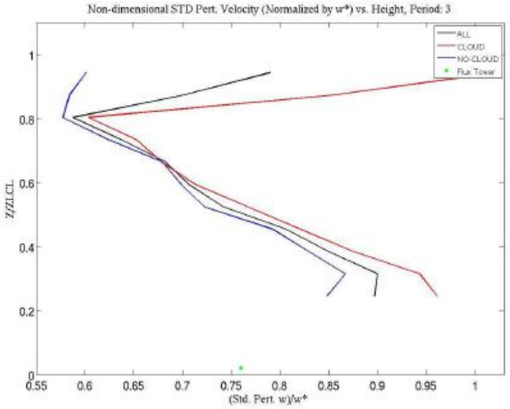

Figure 4.4: As in Figure 4.2, except for SP3 (January 20th-21st).

Figure 4.5 shows turbulence results for SP4, which was had mostly suppressed weather conditions similar to SP3 although the cloud interaction with the subcloud layer was increasing and cloud tops started to penetrate the strong TWI. As in the previous four periods, the variance of w’ under clear sky decreases with height, while under clouds it decreases at first and then increases just below cloud base. The clear sky curve in Fig. 4.5 again follows that of Nicholls and LeMone, as do the lower parts of the ALL and CLOUD profiles, although they increase with height just below cloud base. This is most likely due to the influence of increasing updrafts and downdrafts associated with the increasing cloud activity during this period, showing again how convection alters the expected turbulence curve.

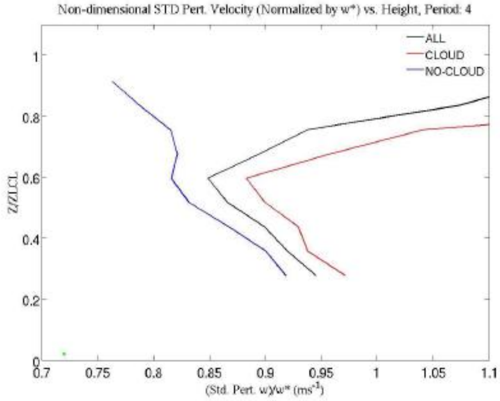

Figure 4.5: As in Figure 4.2 except for SP4 (January 22nd-24th).

Figure 4.6 shows the turbulence profiles of all conditions by each Synoptic Period (solid lines). Normalizing each profile by w* allows for days with different types of weather conditions to be compared on the same image. Here we see that SP2, SP3 and SP4 all have profiles that collapse together when normalized by w*. These three profiles are similar to the results seen during GATE, shown here as magenta stars. Adding the normalized flux tower values from each period to this image shows how the lidar curves could be interpolated to the surface and follow a similar shape as the GATE curve. It appears that the peak variance in the RICO curves occurs at a lower height then the GATE curve, but since the lowest height returns for the lidar are not very reliable, it is hard to say exactly where the peak would be located. Also, if we assume that due to averaging the cloud base is located closer to 0.8 Z/Z_{LCL}, then the upper portion of the lidar curves would be stretched relative to the GATE curve. The turbulence curve and flux tower point from SP1 are slight outliers on this figure, which is expected due to the drastically different convective conditions observed during this period. Also, this period had the most days of all of the Synoptic Periods (5 compared with 2 from SP2 and SP3 and 3 from SP4), and averaging over more days provides more samples and leads to more opportunity for an increased standard deviation.

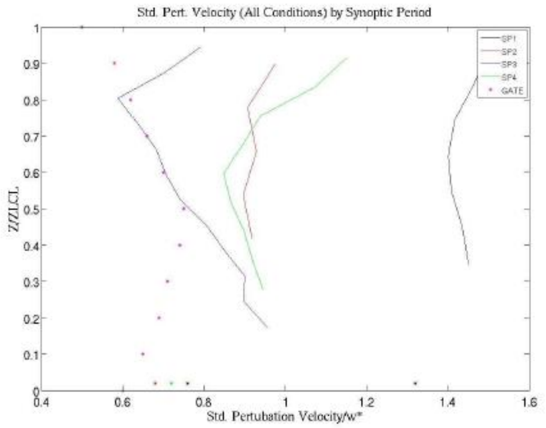

Figure 4.6: Standard deviation of w' for all conditions. Each Synoptic Period is shown as a solid line and is normalized by the mean w during that period. The flux tower σ_w/w^* observations are shown as stars (black for SP1, red for SP2, blue for SP3 and green for SP4). Observations collected during GATE by Nicholls and LeMone (1980) are shown as magenta stars for comparison purposes.*

4.2.2 Updrafts

Each synoptic period composite file was used to calculate mean and standard deviation of w' for strong updrafts vs. downdrafts. Strong updrafts are classified as any column that has w>1m/s below cloud base. The results are shown as a set of two images for each synoptic period where the top image is the mean w' and the bottom is the standard deviation of w'. Due to the scaling of height by LCL and averaging over several days, cloud base is probably closer to 0.8 Z/Z_{LCL} than 1.0 Z/Z_{LCL} for these figures. Figure 4.7 shows these results for SP1 where the red profiles represent conditions under strong updrafts, the blue profiles represent profiles under weak updrafts or downdrafts and the black profiles are an average of all conditions. For SP1, we see that the mean w' for updrafts is always positive (which is expected), though it does decrease slightly with height, leading to the conclusion that the updrafts are stronger in the middle of the subcloud layer than they are just under cloud base. The variance of w' for updrafts decreases with height in the lower subcloud layer, then increases with height into cloud base. This is due to the fact that just below cloud base some updrafts become stronger while profiles that have an updraft at lower levels may see a downdraft just below cloud base as seen by the decreasing values of w' in the UPDRAFT profile.

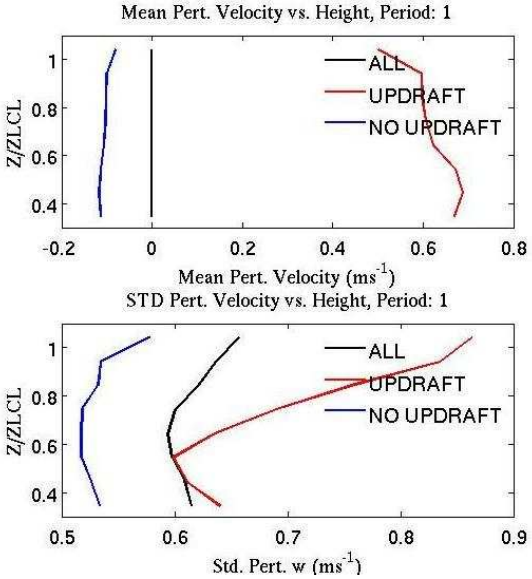

Figure 4.7: Turbulence profiles from SP1 (January 10th-14th). Upper panel: Mean w'; Lower panel: Standard Deviation of w'. In all plots, the red curve represents columns with an updraft of 1 m/s or greater, blue curves represent columns without a strong updraft and black represents all columns.

Figure 4.8 shows these results for SP2 where again we see that the mean w' for updrafts is always positive and decreasing towards cloud base, though now the velocity values are weaker than SP1. The variance of w' for updrafts again decreases with height in the lower subcloud layer, then increases with height in the middle of the subcloud layer before decreasing into cloud base. The increase in variance in the middle of the subcloud layer is most likely due to varying strengths of updrafts and vertical transports depending on whether or not a cloud is present overhead.

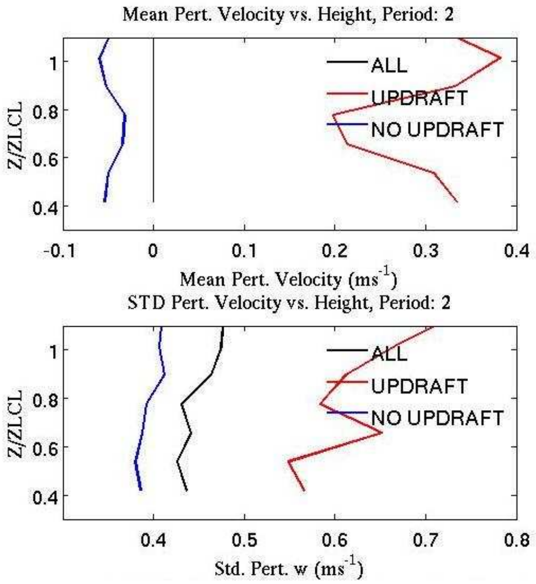

Figure 4.8: As in Figure 4.7, except for SP2 (January 18th-20th).

Figure 4.9 shows these results for SP3 where yet again the mean w' for updrafts is always positive. During this period it increases in strength in the lower subcloud layer before decreasing dramatically up to cloud base. This increase again implies that the updrafts are stronger in the middle of the subcloud layer than they are just under cloud base, as only the surface fluxes seem to be affecting the subcloud layer during this period. The overall variance of w' for updrafts decreases with height, though it does have a couple of jumps of increasing variance, one in the lower subcloud layer and one just below cloud base. The jump in variance below cloud base is probably caused by strong updrafts occurring at the same time as weak updrafts or downdrafts out of the clouds.

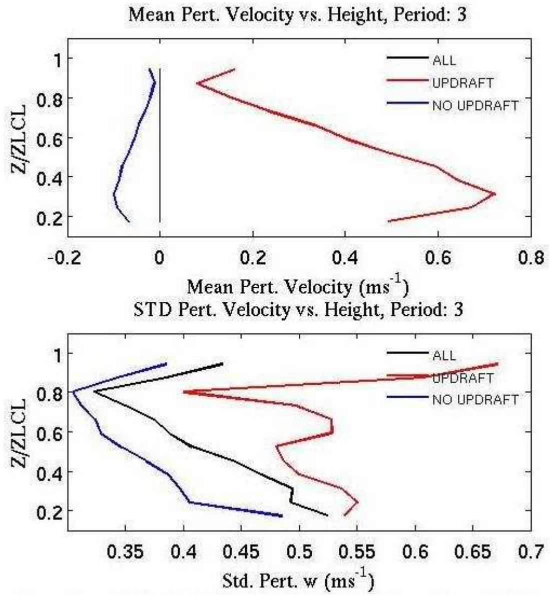

Figure 4.9: As in Figure 4.7, except for SP3 (January 20th-22nd).

Figure 4.10 shows these results for SP4 where we see that the mean w' profile for updrafts is similar to that seen during SP2, as it is positive but decreasing up to cloud base (here seen around 0.6 Z/Z_{LCL}). The variance of w' for updrafts decreases with height until just below cloud base and then increases going into cloud base due to the presence of both updrafts and downdrafts under the clouds.

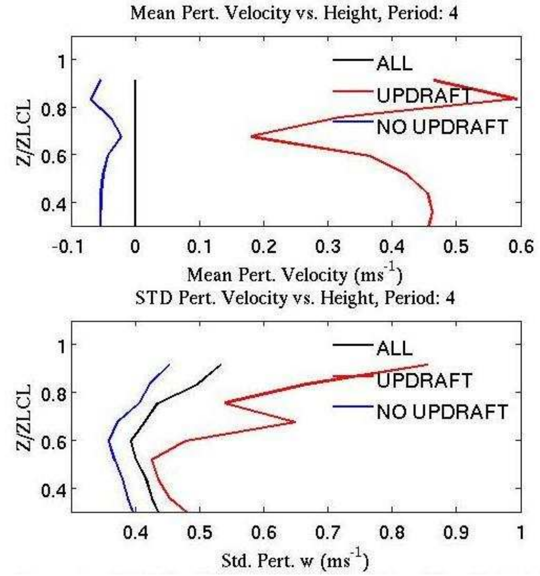

Figure 4.10: As in Figure 4.7, except for SP4 (January 22nd-24th).

5. CONCLUSIONS AND FUTURE WORK

Ship-based observations of marine fair weather cumulus clouds during RICO have been used to classify the boundary layer structure in the tropical Atlantic trade wind regime. RICO was the first field experiment to focus on this environment in several decades and provided new data sets about the region using new or improved technology. It was also the first experiment in this region in which a lidar was included in the ship instrumentation, which allowed for a detailed view of the small-scale variations in the subcloud layer. Here, observations from the soundings launched during RICO are used to document the structure and variability of the boundary layer and observations from the flux tower are used to provide a description of surface variables and rainfall throughout the cruise. Vertically pointing lidar data are used to study the subcloud vertical velocities and calculate turbulence statistics for clouds, clear-sky and strong updrafts. These results may be useful for future implementation in Large Eddy Simulation (LES) Models as the detailed lidar observations can accurately describe the spatial extent of the subcloud eddys.

The winter months in the Northern Hemisphere typically provide the best time to sample marine fair weather cumulus clouds without the influence of intense convection or organized tropical systems. While RICO was planned to study the typical suppressed conditions, the first half of the cruise encountered disturbed conditions. This turned out be useful as the disturbed period turbulence statistics were compared to the typically observed suppressed statistics and a different turbulence structure was found to be present during convective conditions. The documentation of these results along with the overall observed variability in the MABL and clouds is an important step in understanding the physical processes that contribute to the formation, maintenance and dissipation of marine FWC.

Our current understanding of marine FWC and the MABL in the trade wind regime comes from experiments that took place during the 1970s. Since that time, the majority of progress in understanding the processes occurring in this region came from modeling. The RICO data set will provide a new comparison for these modeled results. But, parameterization schemes, model evaluations and general assessments based solely on the findings from RICO may be valid only for specific cases or time periods and not the entire trade wind regime. This is especially true for the convective conditions encountered as this type of weather is generally expected to occur in the late fall or early spring as transitions to or from the suppressed wintertime conditions. Future experiments in the marine environment of the tropical Atlantic trades would be helpful to determine if the convective conditions encountered during RICO are truly more common during the winter months than previously thought. It would also be helpful to have a lidar on an experiment solely devoted to vertical stares to calculate more robust vertical velocity and turbulence statistics.

Some of the results obtained in this study can be directly correlated to satellite data or model parameterization for boundary layer structures and turbulence processes in the subcloud layer. A deeper analysis of the data should reveal even more interesting features, and could be used for evaluating specific satellite products and boundary-layer model simulations. For instance, Zhao and Di Girolamo (2006) found that the Advanced Spaceborne Thermal Emission and Reflection Radiometer (ASTER) saw a cloud fraction of only 0.08 during RICO. They filtered out all clouds except trade wind cumuli so the overall cloud fraction should be lower than that shown in thesis, but this result is significantly lower, which bears further studying. As other data sets from RICO are processed and analyzed in the next few years, a better understanding of marine FWC should emerge and new results can be implemented into models.

6. BIBLIOGRAPHY

Albrecht, B. A., 1981: Parameterization of trade-cumulus cloud amounts, *J. Atmos. Sci.,* **38**, 97-105.

——, 1989: Aerosols, cloud microphysics, and fractional cloudiness. *Science*, **245**, 1227-1230.

——, 1993: Effects of precipitation on the thermodynamic structure of the trade wind boundary layer. *J. Geo. Res.,* **98**, 7327-7337.

Augstien, E., H. Riehl, F. Ostapoff and V. Wagner, 1973: Mass and energy transports in an undisturbed Atlantic tradewind flow. *Mon. Wea. Rev*., **101**, 101-111.

Brewer, W. A., R. M. Hardesty, W. L. Eberhard, and B. J. Rye, 1998: Combined wind and water-vapor measurements using the NOAA Mini-MOPA Doppler lidar. Proceedings of the 19th International Laser Radar Conference, NASA Langley Research Cent., Hampton, VA, pp. 565-568.

Bretherton, C. S. and S. Park, 2008: A new bulk shallow cumulus model and implications for penetrative entrainment feedback on updraft buoyancy. Accepted by *J. Atmos. Sci,* in press.

Caesar, K.A.: Summary of the weather during the RICO project- December 8th, 2004 and January 24th, 2005. *Caribbean Institute for Meteorology and Hydrology*, January 2005.

Holland, J. S., and E. M. Rasmusson, 1973: Measurements of the atmospheric mass, energy and momentum over 500-kilometer square of tropical ocean. *Mon. Wea. Rev*., **101**, 44-55.

Kollias, P., B.A. Albrecht, R. Lhermitte, A. Savtchenko, 2001: Radar Observations of Updrafts, Downdrafts, and Turbulence in Fair-Weather Cumuli. *JAS*, **58**, 1750-1765.

LeMone, M. A., and W. T. Pennell, 1976: The relationship of trade wind cumulus distribution to subcloud layer fluxes and structure, *Mon. Wea. Rev*., **104**, 524-539.

Nicholls, S. and M. A. LeMone, 1980: The fair weather boundary layer in GATE: The relationship of subcloud fluxes and structure to the distribution and enhancement of cumulus clouds. *J. Atmos. Sci.,* **37**, 2051-2067.

Rauber, R. M., B. Stevens, H. T. Ochs III, C. Knight, B. A. Albrecht, A. M. Blyth, et al., 2007: Rain in (shallow) cumulus over the ocean- the rico campaign. *Bull. Amer. Meteor. Soc.*, 18, 1912-1928.

Zhao, G., and L. Di Girolamo, 2006: Cloud fraction errors for trade wind cumuli from EOS-Terra instruments. *Geophys. Res. Lett*., **33**, L20802, doi: 10.1029/2006GL027088.

Acknowledgments

The data from the lidar were generously provided by NOAA ESRL. This research was supported by NSF grant ATM 342623.

ANTHROPOGENIC AND MINERAL DUST AEROSOLS OVER THE WESTERN ATLANTIC OCEAN AND THEIR ROLE IN REGULATING CLOUD CONDENSATION NUCLEI

L. Gomes[1], O. L. Mayol-Bracero[2], F. Morales[2], G. Frank[3], J. J. N. Lingard[4] and J. McQuaid[4]

[1]Centre National de Recherches Météorologiques, Météo-France, Toulouse, France,
[2]Institute for Tropical Ecosystem Studies, University of Puerto Rico, San Juan, Puerto Rico,
[3]Department of Biogeochemistry, Max Planck Institute for Chemistry, Mainz, Germany,
[4]Institute for Atmospheric Science, University of Leeds, Leeds, UK

1. INTRODUCTION

The indirect effect of aerosols that refers to their ability to influence cloud radiative properties is considered to be one of the larger uncertainties in climate prediction. Indeed, the effect of CCN concentrations on climate is still very poorly determined [Anderson et al., 2003], but because there is a possibility that it is large, a correct description of the sources, evolution and properties of the remote marine aerosol is essential. This study is part of the *Rain In Cumulus over the Ocean Experiment* (RICO, www.joss.ucar.edu/rico/) whose primary objective was to characterize and understand the properties of trade wind cumulus with particular emphasis on determining the importance of precipitation. The specific objectives of this study are to determine the origin of the sampled air masses, the physical and chemical properties of the aerosol particles in those air masses, and the potential of the aerosol particles to act as CCN by direct and indirect methods. CCN concentrations are usually determined by direct measurement using a diffusion cloud chamber. Alternatively, CCN concentrations can be modeled via Köhler theory from the aerosol properties. Regarding the aerosol properties, we are interested in composition, sizes and concentrations of both the inorganic and organic fractions of marine aerosols. If marine aerosols contribute significantly to the CCN concentrations in the tropics, they could play an important role in indirect radiative forcing by modifying cloud's response when they encounter anthropogenic or Saharan influences altering the earth's radiative balance, hence having an impact on climate.

2. EXPERIMENTAL METHOD

All measurements were performed during the RICO experiment. Sampling occurred from 5 to 23 January 2005, at a ground site (17.03N, 61.48W; 25 m above sea level) located at Dian Point, on the east coast of the Caribbean island of Antigua. Aerosol instrumentation included stacked-filter units (SFUs) to collect fine particles ($D_p < 2$ μm), a condensation particle counter (CPC) to obtain total aerosol concentrations, a scanning mobility particle sizer (SMPS) to measure number distributions from 10 to 700 nm in diameter, a passive cavity aerosol spectrometer probe (PCASP) for measuring size distributions of single dry particles from 0.1 to 10 μm, a volatility system (ASASP-X) to estimate the time and size resolved aerosol composition for particles within the range $0.1 < D_p < 3$ μm, and a static thermal-gradient chamber (CCNC) to measure cloud condensation nuclei concentrations at various supersaturations (SS) between 0.2 and 2 %. Gravimetric analysis was done by weighing each filter before and after sampling to determine the total aerosol mass collected. The mass concentrations of the water-soluble ions were determined by ion chromatography, and the mass concentrations of total carbon (TC), organic carbon (OC), and elemental carbon (EC) were determined by a thermal/optical EC/OC analyzer. Analytical details are presented by Mayol-Bracero et al. [2008].

3. RESULTS AND DISCUSSION

3.1 Meteorological data

Meteorological data were collected by a local meteorological station and were supplemented by measurements at the experimental site where frequent rain showers occurred during the sampling period. Isentropic backward air mass trajectories (BT) indicate that our site was affected by Saharan and anthropogenic sources during the sampling period. From 11 to 18 January, surface air masses originated from the northeast to east and had traveled over the North Atlantic Ocean. A Saharan dust event was detected on 13-14 January. Then, from 21 to 24 January, surface air masses originated from North America. BTs together with AVHRR aerosol optical thickness (AOT) satellite images allowed the identification of three distinct influences: Saharan dust (SD) from Africa, clean marine air (CM), and anthropogenic pollution from North America (AP).

3.2 Particle size distributions

The SMPS measurements show typical submicron aerosol size distributions in the MBL with a bimodal structure. This feature is known as the result of a cloud processing [Hoppel et al., 1986]. An interstitial mode of particles too small to be activated peaks around 40 nm while an accumulation mode around 200 nm represents the residue of evaporated cloud droplets.

The PCASP measurements show that these distributions are also characterized by a significant enhancement in the coarse mode (>1 μm) during the SD period, which is coherent with the presence of dust particles, and an increase in particle number in the accumulation mode during the AP period, in agreement with the transport of particles from anthropogenic sources [Mayol-Bracero et al., 2008].

3.3 Chemical composition

The aerosol chemical properties and the impact by the different air masses have been discussed in details by Morales-Garcia et al. [2006] and Mayol-Bracero et al. [2006; 2007; and 2008]. These results showed that Cl^-, Na^+, SO_4^{2-}, and particulate organic matter (POM). constitute the predominant aerosol species at the sampling site. Samples with SD influence show an increase in Ca^{2+}, Mg^{2+} and K^+ concentrations, while the particle size distribution-volatility spectra show a low contribution by OC and ammonium sulfate aerosol, a significant contribution of NaCl (sea salt aerosol), and the presence of a significant residual refractory material (probably silicates). Samples with AP influence from North America show a significant increase of SO_4^{2-}, NH_4^+, NO_3^-, and POM, sea-spray acidification, and the highest $nssSO_4^{2-}$ concentrations. The particle size distribution-volatility spectra show a significant decrease in particle number due to the loss of SO_4^{2-} particles, and some evidence of OC particles. At 730°C, almost all particles >0.3 μm are volatilized. Based on the concentrations of EC, OC, and $nssSO_4^{2-}$, and despite these changes in concentrations, the local anthropogenic activity at Dian Point was very low.

3.4 Observed CCN concentrations

Total aerosol concentrations at Dian Point were typically between 200 and 500 cm^{-3} with a mean value of 300 cm^{-3}. CCN number concentrations were low and resulted in a spectrum resembling those typical of MBL environments. The CCN/CN ratio was strikingly very high during the SD period (0.5 and 0.75 at 0.4 and 1% SS, respectively), and then rather low during the AP period (0.15 at 1% SS) following the clean period (see figure 1).

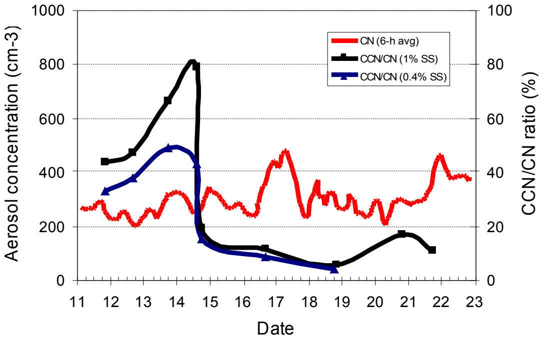

Figure 1. Aerosol concentration and CCN/CN ratio measured at Dian Point from January 11 to 23.

On January 14, the rain and drizzle drops washed out only a fraction of the aerosol population but a large part of the CCN was removed. The low CCN concentrations observed after the rain suggest that some modifications have occurred that can be due to the production of new organic particles as shown in previous works [Novakov et al., 1997; Krämer et al., 2000; Mayol-Bracero et al., 2001].

3.4 Modeled CCN concentrations

When compared to clean air masses, aged pollution (SD and AP) changes size distributions and chemistry, affecting the CCN concentrations in the MBL. Thus, results of CCN measurements were then compared to CCN concentrations predicted on the basis of the measured size distribution of the aerosol and assuming the aerosol was a mixture of 3 components: NaCl, $(NH4)_2SO4$, and insoluble constituents. With this simple approach, the modified Köhler equation [Pruppacher and Klett, 1978] was used to relate dry particle size to particle's critical supersaturation (Sc) and to determine critical diameters for integration of the measured number size distribution to model CCN concentrations at 0.4 and 1% SS. Since the DMA size distributions were taken at relative humidity below about 55%, we assumed that the particles were at their dry size.

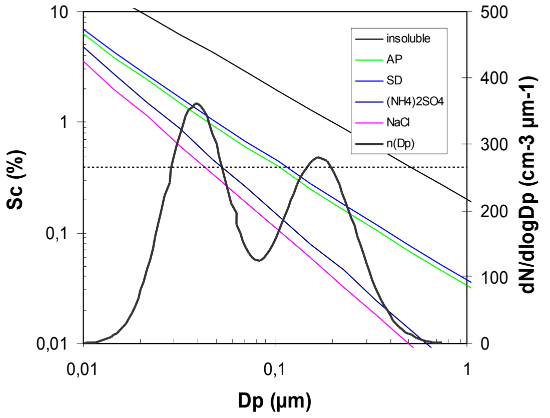

Figure 2. Number distribution and critical supersaturation versus dry particle diameter for several aerosol compositions.

The resulting relationships between Sc and Dp are shown in Figure 2 for the aerosol compositions found during SD and AP influences, and for the limiting cases for pure NaCl, pure $(NH4)_2SO4$ and insoluble aerosol.

These relationships between Sc and Dp were then combined with the number distribution (also shown in Figure 2) to yield the calculation of CCN concentration. The resulting CCN concentrations (figure 3) calculated at 0.4 and 1% SS with the simplified 3-component model are in good agreement with the measured results reported in figure 1.

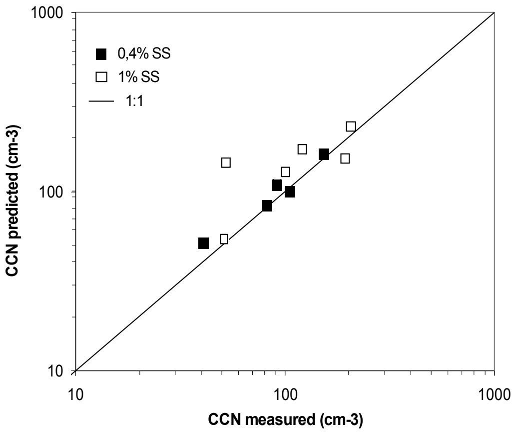

Figure 3. Comparison of modeled versus measured CCN concentration

The modeled CCN concentration was 10 to 40% larger than the directly measured CCN concentration. This result is consistent with the presence of insoluble or partially soluble material in the particles or externally mixed particles. The greatest discrepancies occurred with air masses from clean marine or anthropogenic origin which is consistent with an effect due to organic compounds that is not taken into account in this study. On the other hand, the study shows that the mixture of mineral dust and sea salt particles are very efficient CCN. As already shown in previous experiments [Levin et al., 1996; Trochkine et al., 2003], the chemical composition of insoluble mineral dust particles change during their transport as they are coated with sea salt and sulfate. These interactions cause the aerosols to be more soluble and increase their chance to serve as CCN.

REFERENCES

Anderson, T. L., et al., Climate forcing by aerosols - A hazy picture, Science, 300, 1103-1104, 2003.

Hoppel, W.A., G.M. Frick, and J.W. Fitzgerald, Deducing droplet concentration and supersaturation in marine boundary layer clouds from surface aersol measurements, J. Geophys. Res. 101, 26,553-26,565, 1996.

Krämer, M., et al., cloud processing of continental aerosol particles : experimental investigations for different drop sizes, J. Geophys. Res., 105, 11739-11752, 2000.

Levin, Z., Ganor, E., and Gladstein, V.: The effects of desert particles coated with sulfate on rain formation in the eastern Mediterranean. J. Appl. Meteorol., 35, 1511–1523, 1996.

Mayol-Bracero, O.L., et al., Chemical characterization of submicron organic aerosols in the tropical trade winds of the Caribbean using gas chromatography / mass spectrometry, Atmos. Environ., 35, 1735-1745, 2001.

Mayol-Bracero, O. L., F. Morales-García, M.H. Repollet, D. Ortiz-Montalvo, A. Kasper-Giebl, L. Gomes, G.P. Frank, U. Dusek, M.O. Andreae, J. Allan, J.J.N. Lingard, J.B. McQuaid, S. Decesari, J. R. Anderson, Chemical and Physical Characterization of Atmospheric Particles in the Caribbean Region: Clean Marine Air, Saharan Dust, and Anthropogenic Pollution, Joint IGAC/CACGP/SOLAS/WMO Symposium: Atmospheric Chemistry at the interfaces, Cape Town, South Africa, September 2006.

Mayol-Bracero, O.L., F. Morales-García, M.H. Repollet, J.J.N. Lingard, J.B. McQuaid, L. Gomes, G.P. Frank, M.O. Andreae, L. Di Girolamo, A. Kasper-Giebl, H. Puxbaum, The Impact of Aged Pollution on the Physical and Chemical Properties of Caribbean Aerosols: African Dust and Pollution from North America, Conference «Les Ouragans de l'Atlantique Nord et le Réchauffement Climatique : Exemple de la Caraïbe», Guadeloupe, May 2007

Mayol-Bracero O.L., F. Morales-García, M.H. Repollet, A. Kasper-Giebl, H. Puxbaum, A. Limbeck, C. Ramirez Santa Cruz, J.J.N. Lingard, L. Gomes, G.P. Frank, U. Dusek, M.O. Andreae, S. Decesari, J. R. Anderson, L. Di Girolamo, *The Impact of Transport on the Physico-Chemical Properties of Caribbean Aerosols during RICO: African Dust and Pollution from North America,* manuscript in preparation, 2008.

Morales-García, F., O. L. Mayol-Bracero, H. Caro-Gautier, M. H. Repollet, D. Ortiz-Montalvo, A. Kasper-Giebl, L. Gomes, M. O. Andreae, G. Frank, J. Allan, D. Baumgardner, G. Raga, J. J. N. Lingard, J. B. McQuaid, S. Decesari, J. Anderson Chemical and Physical Properties of Marine Aerosol during the RICO-PRACS Experiment: Evidence of a Clean Period, Saharan Dust, and Anthropogenic Pollution, 12th Cloud Physics Conference, Madison, Wisconsin, July 2006.

Novakov, T., et al., Organic aerosols in the Carribean trade winds: a natural source?, J. Geophys. Res., 102, 21307-21313, 1997.

Pruppacher, H.R., and J.D. Klett, Microphysics of clouds and precipitation, pp146-147, D.Reidel, Norwell, Mass., 1978.

Trochkine, D., et al.: Mineral aerosol particles collected in Dunhuang, China, and their comparison with chemically modified particles collected over Japan. J. Geophys. Res., 108, doi :10.1029/2002JD003268, 2003.

SCALINGS FOR PRECIPITATION AND COALESCENCE SCAVENGING OBTAINED FROM SIMULATIONS OF TRADE CUMULUS

David B. Mechem*[1] and Yefim L. Kogan[2]
[1]Department of Geography
University of Kansas, Lawrence, KS U.S.A.
and
[2]Cooperative Institute for Mesoscale Meteorological Studies
University of Oklahoma, Norman, OK U.S.A.

1. INTRODUCTION

Recent observational studies of stratocumulus have identified the existence of robust scalings relating cloud properties and microphysical processes. Pawloska and Brenguier (2003) found a drizzle rate that scaled as H^4N^{-1}, where H and N are cloud depth and mean droplet concentration respectively. Comstock et al. (2004) found a scaling of $(\text{LWP}/N)^{1.75}$ in subtropical eastern Pacific stratocumulus, and VanZanten et al. (2005) showed that cloud base drizzle rate during the DYCOMS-II project scaled with H^3N^{-1}. Wood (2005a) compares these various scalings.

Recent studies have also hinted at scalings for the reduction of cloud condensation nuclei or cloud droplets as a function of cloud properties. We term this reduction of droplet number by collision-coalescence either "depletion" or "coalescence processing." Employing a theoretical framework, Wood (2006) found a scaling for coalescence processing based on the product of droplet concentration and drizzle rate (N_cR). Using a mesoscale model and large eddy simulation, Mechem et al. (2006) found a similar scaling behavior. Wood (2005b) found that the coalescence processing represented by the bulk microphysical parameterization of Khairoutdinov and Kogan (2000) compared favorably with the stochastic collection equation applied to aircraft particle probe data.

The Rain in Cumulus over the Ocean (RICO) field campaign and the GCSS community modeling effort provides the opportunity to explore similar scalings appropriate to the trade cumulus boundary layer. Here we show preliminary results, including simple scalings, from a series of large eddy simulation runs employing size-resolving microphysical processes.

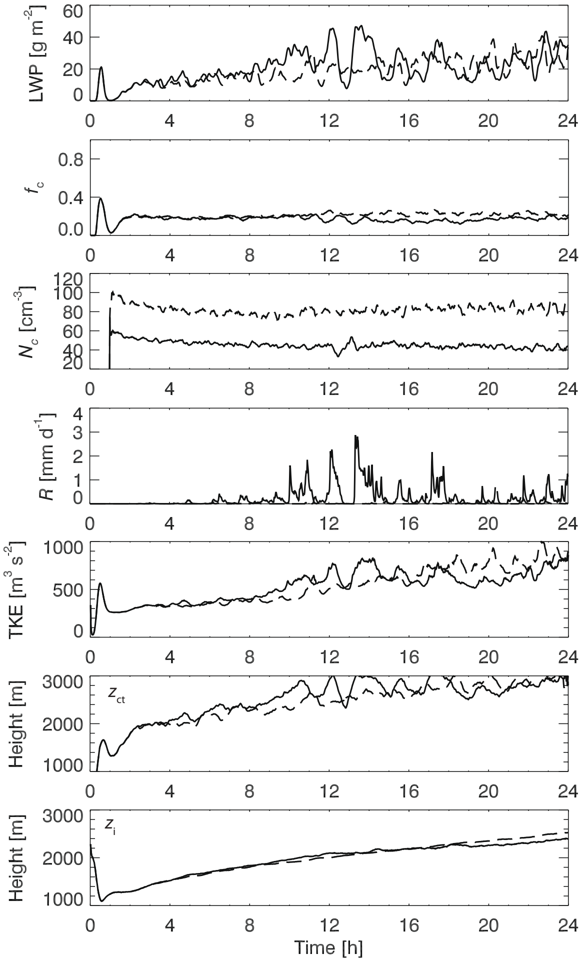

Fig. 1. Time series of liquid water path, cloud fraction, droplet concentration, surface precipitation rate, turbulent kinetic energy, maximum cloud top height, and inversion height for the 105 cm^{-3} (solid) and 211 cm^{-3} (dashed) simulations.

---

*Corresponding author address: David B. Mechem, Department of Geography, University of Kansas 1475 Jayhawk Blvd., 213 Lindley Hall, Lawrence, KS 66045-7613; email: dmechem@ku.edu.

2. METHODOLOGY

We analyze a series of simulations based on the GCSS RICO intercomparison case (Van Zanten et al., manuscript in preparation). Our simulations are based on SAMEX (System for Atmospheric Modeling — EXplicit microphysics), which is based on the dynamical core of SAM (Khairoutdinov and Randall 2003) and size-resolving microphysics of Kogan (1991), Kogan et al. (1995), and Khairoutdinov and Kogan (1999).

The control simulation is initialized from a bimodal CCN spectrum with a total concentration of 105 cm^{-3}. CCN were varied in a series of sensitivity simulations in order to produce variations of precipitation rate and cloud structure. With CCN concentrations of 90, 140, 175, and 211 cm^{-3}, a total of five simulations were completed.

3. RESULTS

Figure 1 shows an overview of two "bookend" simulations, which include a weakly and a strongly precipitating case. Mean liquid water path (LWP) is similar between the two cases, though LWP in the strongly precipitating case tends to exhibit greater variability. Increasing precipitation tends to slightly increase cloud fraction. In these simulations, the strongly precipitating case has at times higher and lower TKE, with predictable effects on the inversion height.

Trade cumulus dynamics are notably different from stratocumulus, so we should not expect the stratocumulus scalings discussed above to be applicable to trade cumulus. The experiment suite does support the simple scaling in Fig. 2, where precipitation rate is proportional to LWP$/N_c$. This particular scaling is very "bulk" in nature, in that it is an average of quantities over a long, 8-hour period. Given that cloud lifetime is short $(< \ 1\ h)$, taking hourly averages results in many more data points that can be considered independent realizations. The scalings from these independent realizations (Fig. 3) are more complicated than the bulk scalings collected from 8-hour averages. In fact, Fig. 3 hints at the existence of two different scalings, a weak dependence on LWP$/N_c$ for small precipitation rates, and then a stronger dependence for precipitation rates greater than 0.1 mm d^{-1}.

The simple scaling based on N_c in Fig. 4 is unsurprising, given that LWP is so similar between the two simulations. In other words, differences in N_c alone explain the variability in precipitation rate. This does not mean that cloud thickness or LWP is unimportant, as the LWP still constrains the drizzle rate; however, for given thermodynamic conditions, the LWP is largely invariant under different CCN concentrations.

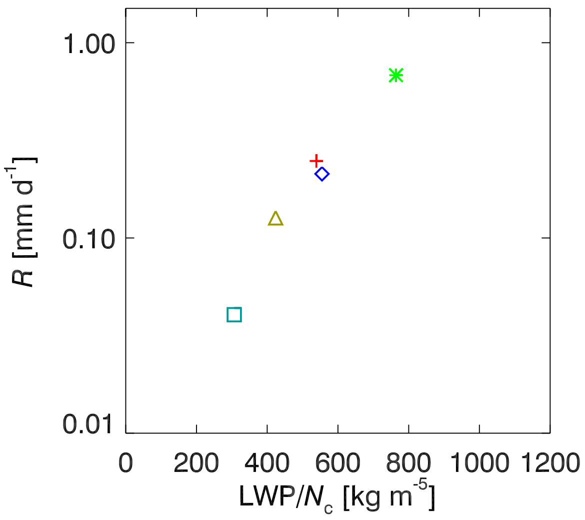

Fig. 2. Surface precipitation rate as a function of LWP$/N_c$ for the five simulation series. Quantities are averages taken over the last eight hours of the simulations.

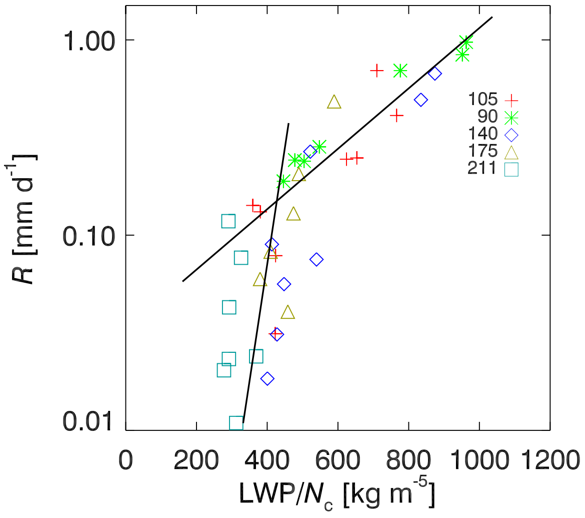

Fig. 3. As in Fig. 2 but averages are calculated hourly for the last eight hours of the simulations. Black lines indicated approximate scalings for two different precipitation rate regimes.

The relationship between precipitation rate and inversion height is less clear in the RICO case than for stratocumulus. In stratocumulus, precipitation tends to reliably decrease entrainment rate (and hence z_i, relative to a control simulation). Here, that general trend is confirmed in Fig. 5, but in reality, z_i is very sensitive to the averaging period and is closely tied to the boundary layer energetics (see the joint behavior of z_i and TKE in Fig. 1).

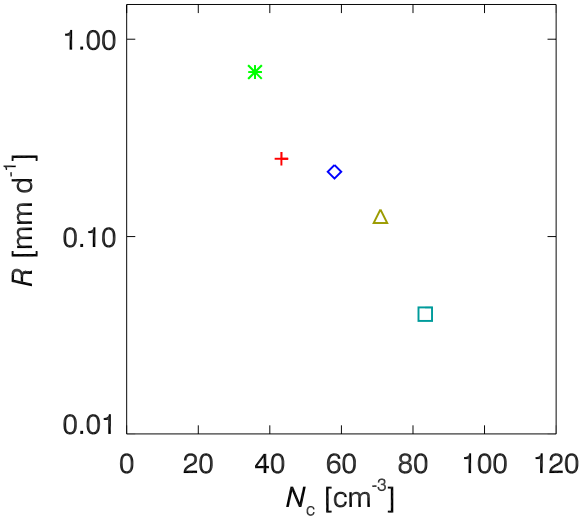

Fig. 4. Surface precipitation rate as a function of N_c for the five simulation series.

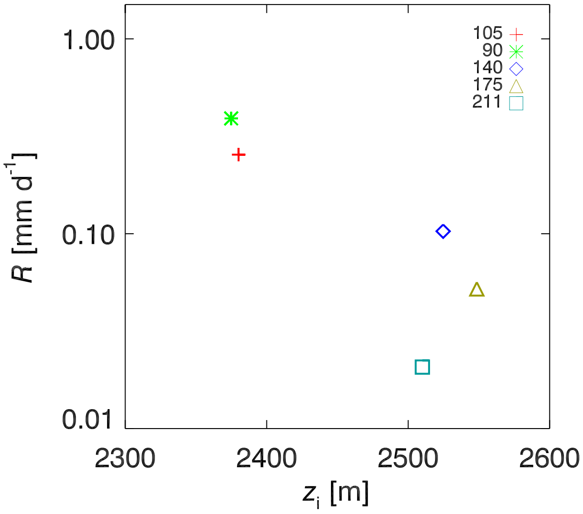

Fig. 5. Relationship between surface precipitation rate averaged over the entire simulation and the final inversion height z_i.

4. CONCLUSIONS

Preliminary analysis of a series of large eddy simulation runs of RICO trade cumulus hints at a scaling behavior fundamentally different than those found previously for marine stratocumulus. This is not terribly surprising, given the significant difference in dynamics for the two boundary layer cloud types. Mean LWP was very similar in all the simulations, so the majority of the precipitation rate differences between cases was explained by variations in N_c. This is evident both in plots of LWP$/N_c$ and N_c.

Our future plans include more in-depth analysis of the precipitation rate scaling and exploration of coalescence processing of trade cumulus. This will include conditional sampling of the precipitating cloud structures themselves, since in the low cloud fraction regime, these discrete features are responsible for the precipitation, the coalescence processing, and the entrainment.

Acknowledgements

This research was supported by the Office of Science (BER), U.S. Department of Energy, grant DE-FG02-05ER64062, by ONR grants N00014-05-1-0550 and N00014-03-1-0304, and by NOAA/Office of Oceanic and Atmospheric Research under NOAA-University of Oklahoma Cooperative Agreement #NA17RJ1227, U.S. Department of Commerce. Some of the computing for this project was performed at the OU Supercomputing Center for Education and Research (OSCER) at the University of Oklahoma.

References

Comstock, K. K., R. Wood, S. E. Yuter, and C. S. Bretherton, 2004: Reflectivity and rain rate in and below drizzling stratocumulus. *Quart. J. Roy. Meteor. Soc.*, **130**, 2891–2918.

Khairoutdinov, M. F. and Y. L. Kogan, 1999: A large eddy simulation model with explicit microphysics: Validation against aircraft observations of a stratocumulus-topped boundary layer. *J. Atmos. Sci.*, **56**, 2115–2131.

— 2000: A new cloud physics parameterization for large-eddy simulation models of marine stratocumulus. *Mon. Wea. Rev.*, **128**, 229–243.

Khairoutdinov, M. F. and D. A. Randall, 2003: Cloud-resolving modeling of the arm summer 1997 iop: Model formulation, results, uncertainties and sensitivities. *J. Atmos. Sci.*, **60**, 607–625.

Kogan, Y. L., 1991: The simulation of a convective cloud in a 3-d model with explicit microphysics. part I: Model description and sensitivity experiments. *J. Atmos. Sci.*, **48**, 1160–1188.

Kogan, Y. L., M. P. Khairoutdinov, D. K. Lilly, Z. N. Kogan, and Q. Liu, 1995: Modeling of stratocumulus cloud layers in a large eddy simulation model with explicit microphysics. *J. Atmos. Sci.*, **52**, 2923–2940.

Mechem, D. B., P. C. Robinson, and Y. L. Kogan, 2006: Processing of cloud condensation nuclei by collision-coalescence in a mesoscale model. *J. Geophys. Res.*, **111**, D18204, doi:10.1029/2006JD007183.

Pawloska, H. and J.-L. Brenguier, 2003: Microphysical properties of stratocumulus clouds during ACE-2. *Tellus, Ser. B*, **52**, 867–886.

VanZanten, M. C., B. Stevens, G. Vali, and D. H. Lenschow, 2005: Observations of drizzle in nocturnal marine stratocumulus. *J. Atmos. Sci.*, **62**, 88–106.

Wood, R., 2005a: Drizzle in stratiform boundary layer clouds. part I: Vertical and horizontal structure. *J. Atmos. Sci*, **62**, 3011–3033.

— 2005b: Drizzle in stratiform boundary layer clouds. part II: Microphysical aspects. *J. Atmos. Sci*, **62**, 3034–3050.

— 2006: The rate of loss of cloud droplets by coalescence in warm clouds. *J. Geophys. Res.*, **111**, D21205, doi:10.1029/2006JD007553.

Pulsation of Trade Wind Clouds and Effects on Precipitation Development

[1*]Hilary A. Minor, [1]R. M. Rauber, [2]S. Göke, and [1]M. Freer
[1]Department of Atmospheric Sciences, University of Illinois at Urbana-Champaign, Urbana, IL
[2]Division of Atmospheric Sciences, University of Helsinki, Helsinki, Finland

1. Introduction

Shallow, maritime cumuli are ubiquitous over much of the tropical oceans, and characterizing their properties is important to understanding weather and climate. One of the classical unsolved problems in cloud physics is the explanation of the observed short time between initial cloud formation and the onset of precipitation in warm clouds. Using data collected by the National Center for Atmospheric Research S-PolKa radar, which was operated continuously on Barbuda during the Rain In Cumulus over the Ocean (RICO) field campaign, the microphysical evolution of trade wind cumuli will be characterized focusing on the potential role of giant nuclei in influencing the ZDR signal, and the pulsed nature of the updrafts**.**

2. Methodology

During the Rain In Cumulus over the Ocean Experiment, the National Center for Atmospheric Research S-Pol radar was operated continuously on Barbuda in order to observe the evolution of trade wind cumuli and precipitation fields. The scanning strategies were designed to optimize observations of cloud lifetimes. Specifically, PPI volume scans were able to track the complete life cycles of a large number of trade wind clouds by collecting a volume every 3 to 4 minutes with 11 elevations. Individual trade wind cumuli were tracked using the computer program Soloii, which allows the data from one cloud to be cut out of the entire domain of radar data and analyzed individually over its entire life cycle. The maximum radar reflectivity factor (Z) and maximum differential reflectivity (ZDR) within the cloud were calculated, and Z and ZDR were spatially correlated for each scan within the cloud boundary. Precautions have been taken to filter out any artifacts that are not hydrometeors so that only the maximum values of the variables for rain are calculated.

3. Time-Height Diagrams

A large number of clouds can be analyzed using the time-height section approach. Figure 1 & 2 are time-height cross-sections that show the temporal evolution of the radar reflectivity factor, Z (top plot), differential reflectivity, ZDR (middle plot), and the spatial and temporal correlation between Z and ZDR (bottom plot). The black dots are the irregular grid of actual data points of

---

*Corresponding author address: Hilary A. Minor, Univ. of Illinois at Urbana-Champaign, Dept. of Atmos. Sciences, 105 S. Gregory St., Urbana, IL 61801;
Email: hminor@atmos.uiuc.edu

the maximum Z (top), maximum ZDR (middle), and correlation coefficient (bottom) for a specific time and height.

4. Statistics

The degree to which the Z and ZDR signals are correlated across the cloud provide information on the type of nucleation process that might occur. Giant nuclei can produce large drops (high ZDR) but weak reflectivity (Z). Growth processes on smaller nuclei should produce Z and ZDR that increase systematically, and are therefore more directly correlated. In this paper, we will examine precipitation initiation in these clouds, focusing on the observed pulsed nature of the updrafts composing the clouds, and the statistical correlations between Z and Z_{DR} and how these correlations are altered as successive pluses develop.

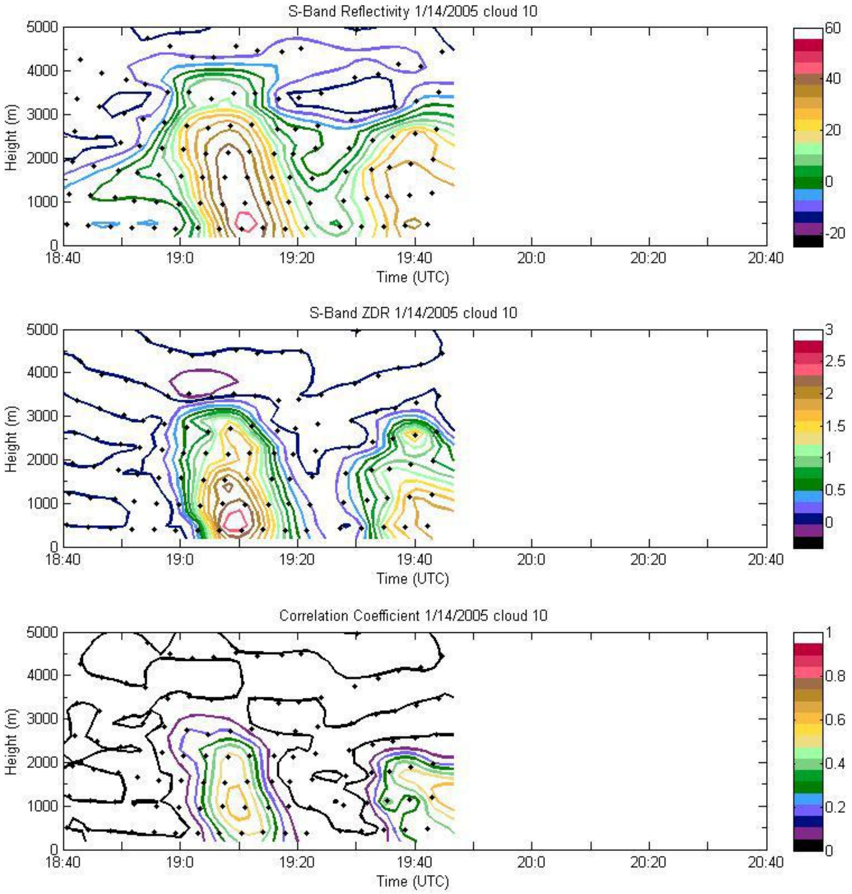

S-Band Reflectivity 1/14/2005 cloud 10

S-Band ZDR 1/14/2005 cloud 10

Correlation Coefficient 1/14/2005 cloud 10

Figure 1. Time-height cross-section for a cloud that developed on 14 January 2005 between 18:43 and 19:48 UTC.

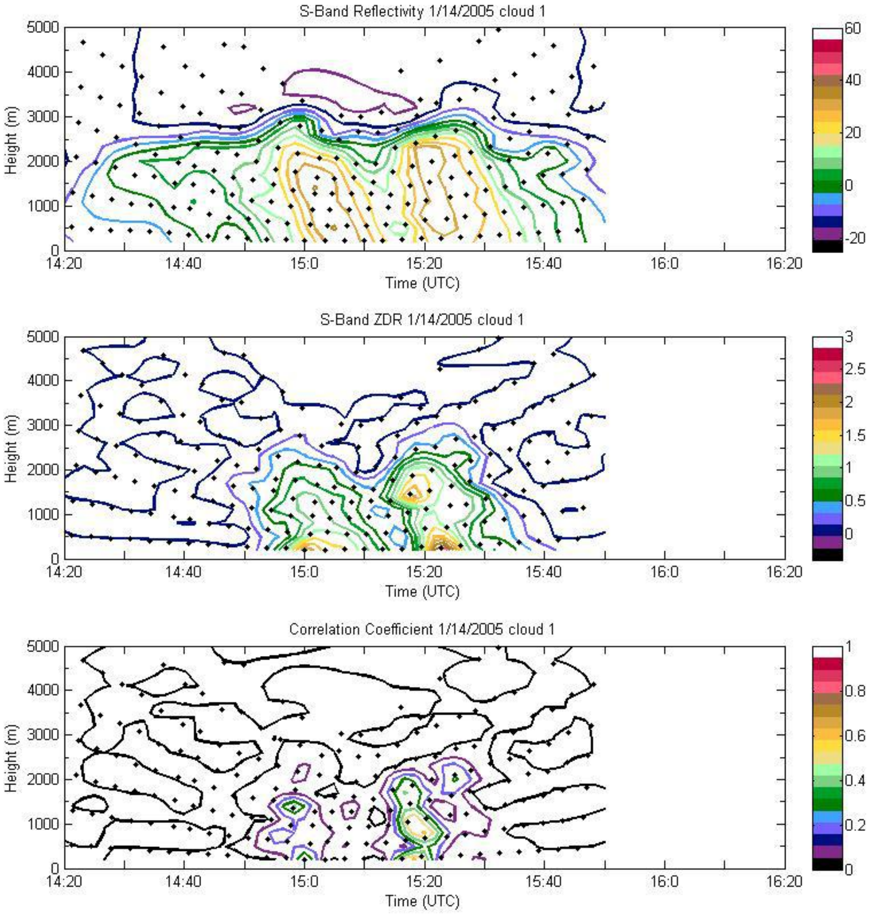

S-Band Reflectivity 1/14/2005 cloud 1

S-Band ZDR 1/14/2005 cloud 1

Correlation Coefficient 1/14/2005 cloud 1

Figure 2. Time-height cross-section for a cloud that developed on 14 January 2005 between 14:25 and 15:53 UTC.

The Power Law and the Scale Break in the Echo Size Distribution of Shallow Cumulus Field.

Trivej, Panu

February 23, 2008

0. Abstract

Based on radar data from the RICO campaign, during November 2004 to January 2005 over the Caribbean Islands of Antigua and Barbuda, the size distributions of radar echoes associated with shallow cumuli is explored. It appears to be a double power law upto 100 km^2 with the scale break around 10 km^2. This echo size distribution is qualitatively similar to what we have learned of cloud size distributions from previous studies. The main difference is that the scale break for echo fields is larger than that of cloud fields. Above 100 km^2, the echo size distribution departs noticeably from the double power law. This raises the question as to whether the law is a useful description of shallow cumuli statistics. Further analysis suggests that the deviations from the proposed power laws are likely artifacts of insufficient radar resolution and composition of data composition from differing meteorological regimes.

PARAMETERIZATION OF CIRRUS CLOUD FORMATION IN LARGE SCALE MODELS: HOMOGENEOUS NUCLEATION

Donifan Barahona[1] and Athanasios Nenes[1, 2]

[1] Chemical and Biomolecular Engineering, Georgia Institute of Technology, Atlanta, GA, USA
[2] Earth and Atmospheric Sciences, Georgia Institute of Technology, Atlanta, GA, USA

Keywords: Cirrus, Parameterization, Homogeneous, Freezing, Ice Nucleation

The effect of aerosols on clouds and climate is one of the major uncertainties in anthropogenic climate change assessment and prediction. Cirrus clouds are one of the most poorly understood systems, yet they can strongly impact climate. Cirrus are thought to have a net warming effect because of their low emission temperatures and small thickness (Liou, 1986). They also play a role in regulating the ocean temperature and affect the water vapor budget of the upper troposphere and lower stratosphere (Hartmann *et al.*, 2001) Concerns have been raised on the effect of aircraft emissions and long-range transport of pollution changing the properties of upper tropospheric clouds, i.e., cirrus and anvils, placing this type of clouds in the potentially warming components of the climate system (Lin *et al.*, 2002).

Introducing ice formation microphysics in large scale simulations requires a physically-based link between the ice crystal size distribution, the precursor aerosol, and the dynamics of cloud formation. To address the need for improved ice cloud physics in large scale models, we have developed a physically-based parameterization for cirrus cloud formation (Barahona and Nenes, *in press*), which is robust, computationally efficient, and links chemical effects (e.g., water activity and uptake effects) with ice formation via homogenous freezing. This was accomplished by tracing back the growth of ice crystals to their point of freezing, in a given ice saturation profile, connecting their size to their freezing probability. Using this approach, an expression for the crystal size distribution is derived, the integration of which yields the number concentration and size distribution of ice crystals. In its final form, the parameterization expression for crystal concentration, N_c, formed in the cirrus cloud is given by,

$$f_c \approx \frac{\rho_a}{\rho_i}\frac{[k(T)]^{1/2}}{\beta N_o}\left[\frac{2\alpha V S_{i,\max}}{\pi\overline{\Gamma}(S_{i,\max}-1)}\right]^{3/2}$$

$$N_c = N_o e^{-f_c}(1-e^{-f_c})$$

where N_o is the concentration of deliquesced aerosol particles; all other symbols are defined in *Barahona and Nenes* (*in press*).

The parameterization is evaluated against the predictions of a detailed numerical parcel model also developed by *Barahona and Nenes* (*in press*). The parcel model equations were integrated using a novel Lagrangian particle tracking scheme; the evolution of the ice crystal size distribution is described by the superposition and growth of monodisperse crystal populations generated by the freezing of single classes (of same size and composition) of supercooled droplets. The relative error of the parameterization in its final form is 1 ± 28%, which is remarkable given the simplicity of the final expression obtained for N_c, the broad set of conditions tested, and the complexity of the original parcel equations.

The prediction skill of the parameterization is robust across a wide range of parameters (e.g., deposition coefficient, aerosol characteristics) of atmospheric relevance. The parameterization successfully reproduces the effect of the aerosol number on ice crystal number concentration with a simple framework that explicitly links the variables that control the freezing time scale of the particles.

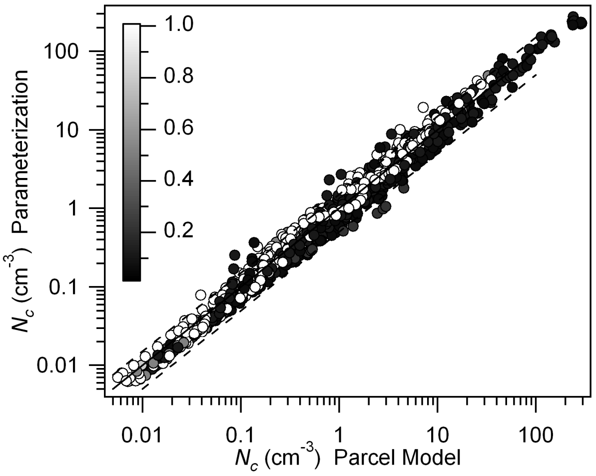

Figure 1. Ice crystal number concentration calculated by the parcel model and the parameterization. Gray scale represents the value of deposition coefficient used in the calculations; dashed lines represent the ± 50 % difference.

Acknowledgments

This study was supported by NASA MAP, NASA EOS-IDS-CACTUS, and a NASA New Investigator Award.

References

Barahona D., and A. Nenes, *J. Geoph. Res.*, in press

Hartmann, D. L., J. R. Holton, and Q. Fu (2001), *Geophys. Res. Lett.*, *28*, 1969-1972.

Lin, R., D. Starr, P. J. DeMott, R. Cotton, K. Sassen, E. J. Jensen, B. Kärcher, and X. Liu (2002), *J. Atmos. Sci.*, *59*, 2305-2328.

Liou, K. (1986), *Mon. Weather Rev.*, *114*, 1167-1199.

IN-SITU MEASUREMENTS OF ICE CRYSTALS IN THE TROPICAL STRATOSPHERE

M. de Reus[1], A. Bansemer[2], W. Frey[1], A.J. Heymsfield[2], S.M.F. Raupach[1], C. Schiller[3],
N. Sitnikov[4], H.J. Vössing[1] and S. Borrmann[1,5]

[1] Institute for Atmospheric Physics, Mainz University, Germany
[2] NCAR, Boulder, USA
[3] Research Centre Jülich, Germany
[4] Central Aerological Observatory, Russia
[5] Max Planck Institute for Chemistry, Particle Chemistry Department, Germany

1. INTRODUCTION

Cirrus clouds play a significant role in regulating the radiation balance of the earth-atmosphere system and are, hence, an important component of the Earth's climate system [e.g. *Lynch et al.,* 2002]. Moreover, cirrus clouds are involved in vertical transport and the (de)hydration of air masses. Slow radiatively driven transport from the free troposphere into the stratosphere can cause a dehydration of the airmass by condensation and subsequent sedimentation of ice particles [*Sherwood and Dessler,* 2001]. Overshooting convection penetrating directly into the stratosphere, however, might hydrate the stratosphere [*Chaboureau et al.,* 2007; *Corti et al,* 2008] and thereby contribute to the observed increase in stratospheric water vapour concentrations [*Oltmans et al.,* 2000].

In order to quantify the radiative effect of cirrus clouds and their influence on the water budget, detailed information about its microphysical properties are necessary.

Here microphysical properties of ice crystals in the tropical troposphere and lower stratosphere are presented from in-situ measurements onboard the Russian high altitude research aircraft M55 "Geophysica".

2. EXPERIMENT

During November and December 2005 four aircraft were stationed in Darwin, Australia for a combined mission of the SCOUT-O3 and ACTIVE projects. The main goal of the mission was to investigate the transport and transformation of water vapour, aerosol and trace gases in deep convection. Darwin was chosen as aircraft base for the mission because of the Hector storm system, which appears on an almost daily basis over the Tiwi Islands, north of Darwin during the pre-monsoon season.

As part of the SCOUT-O3 project nine flights were performed with the high altitude research aircraft M55 "Geophysica".

Ice crystal size distributions were measured onboard the "Geophysica" using two instruments: a Forward Scattering Spectrometer Probe (FSSP-100) and a Cloud Imaging Probe (CIP). The FSSP determines the scattering cross section of ice crystals by measuring the forward scattering of single crystals and was operated in the size range 2.7 – 31 µm diameter. The CIP provides two dimensional shadow images of ice crystals with diameters between 25 µm and 1.6 mm. By combining the data of both instruments cloud particle size distributions can be obtained for particles between 2.7 µm and 1.6 mm diameter.

Figure 1. The research aircraft M55 "Geophysica"

3. RESULTS

From the entire data set, 90 encounters with ice clouds could be selected between 10 and 19 km altitude. The ice crystal size distributions for these encounters were divided into potential temperature bins of 10K in order to be able to separate tropospheric and stratospheric air masses and are displayed in Figure 2. Ice crystals observed at potential temperatures exceeding 385 K are clearly situated in the stratosphere. The region between 365 and 385 K is influenced by tropospheric and stratospheric air masses and is referred to as tropopause region, while air masses below 365 K are tropospheric.

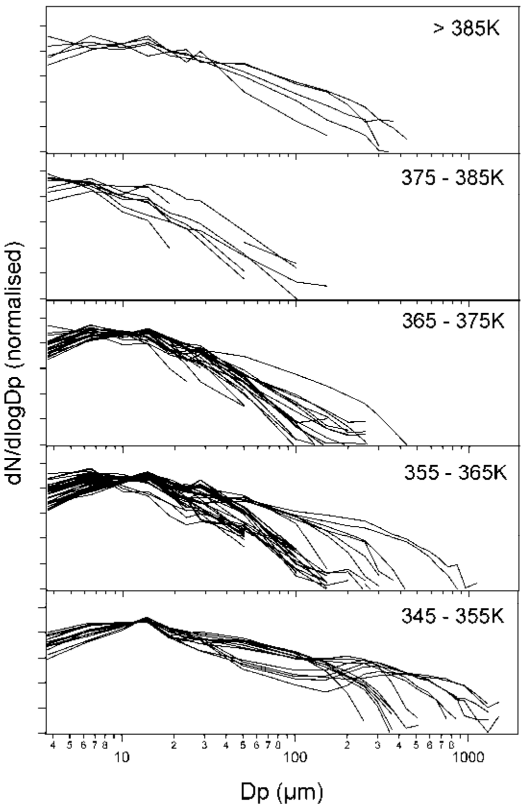

Figure 2. Normalised ice crystal size distributions for 90 ice clouds encounters.

From Figure 2 it can be seen that the largest particles, up to 1 mm maximum dimension, are observed in the lowest potential temperature bin. While ascending to the tropopause region the size of the largest observed ice crystal decreases. In the stratosphere, however, particles, with a maximum dimension up to 400 µm, are observed. Moreover, the shape of the stratospheric size distributions is similar to those observed in the upper troposphere.

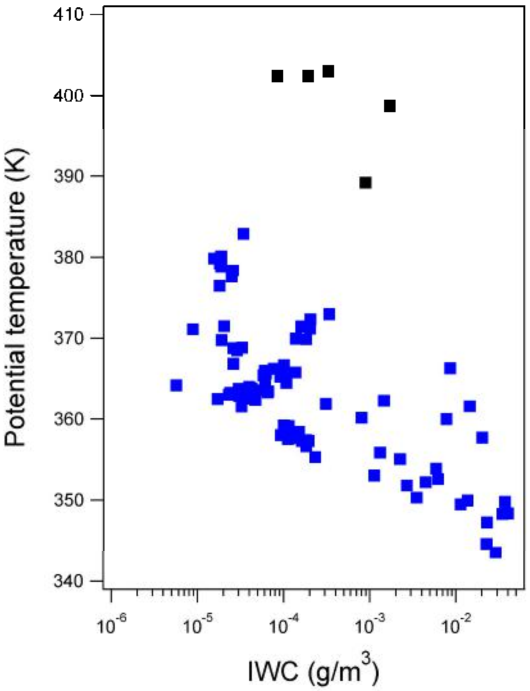

Figure 3. Ice water content calculated from the observed ice crystal size distributions.

The ice water content calculated from the observed ice crystal size distributions is shown in Figure 3. For this calculation, the ice crystals with a diameter smaller than 100 µm are assumed to be solid spheres with a density of 0.917 g/cm^3. For larger particles the relation between mass and ice crystal maximum dimension of *Brown and Francis,* [1995] is used. A decrease in IWC with potential temperature (and altitude) can be observed, which is mainly determined by a decrease in effective radius with altitude. Also from this Figure it can be seen that the IWC from the stratospheric ice clouds (black markers) is comparable with the IWC observed in the upper troposphere.

Ice crystals in the stratosphere were encountered during a flight on November 30, 2005. This flight was performed to investigate the Hector convective system. A large part of the flight was conducted in the stratosphere above the Hector system. The ice crystals were observed between 0.7 and 1.4 km above the local tropopause. Simultaneously with the observations of ice crystals, a sudden decrease in temperature and an increase in CO mixing ratio could be observed, indicating transport from the troposphere via overshooting convection.

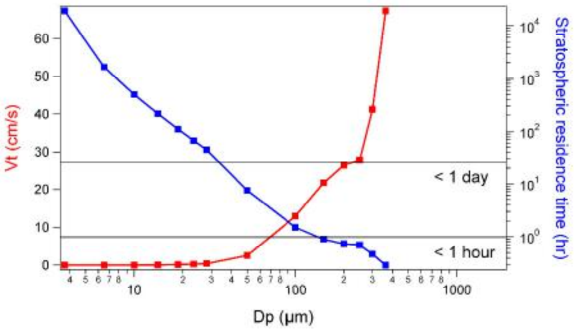

Figure 4. Terminal settling velocity (Vt) for the ice crystals in the stratosphere and the corresponding stratospheric residence time, given that the ice crystals were observed 0.7 km above the local tropopause.

Calculations of the terminal settling velocity (after *Mitchell and Heymsfield,* [2005]) of the ice crystals in the stratosphere and the corresponding stratospheric residence time (Figure 4) indicate that crystals with a size smaller than 100 µm will remain in the stratosphere for over an hour, and thereby will have time to evaporate and potentially humidify the stratosphere.

ACKNOWLEDGEMENTS

This work was supported by the SCOUT-O3 project funded by the European Commission. Financial support by the Max Planck Society is also gratefully acknowledged.

REFERENCES

Brown, P. R. A. and P. N. Francis: Improved measurements of the ice water content in cirrus using a total water probe, *J. Atmos. Oceanic Technol., 12*, 410-414, 1995.

Chaboureau, J. P., J. P. Cammas, J. Duron, P. J. Mascart, N. M. Sitnikov and H. J. Vössing: A numerical study of tropical cross-tropopause transport by convective overshoots during the TROCCINOX golden day, *J. Atmos. Chem. Phys., 7*, 1731-1740, 2007.

Corti, T., B. P. Luo, M. de Reus, D. Brunner, F. Cairo, M. J. Mahoney, G. Martucci, R. Matthey, V. Mitev, F. H. dos Santos, C. Schiller, G. Shur, N. M. Sitnikov, N. Spelten, H. J. Vössing, S. Borrmann and T. Peter: Unprecedented evidence for overshooting convection hydrating the tropical stratosphere, *Geophys. Res. Lett.,* submitted, 2008.

Lynch, D. K., K. Sassen, D. O. Starr, G. Stephens (Eds.): *Cirrus*, Oxford Univ. Press, New York, 2002.

Mitchell, D. L. and A. J. Heymsfield: Refinements in the Treatment of ice particle terminal velocities, highlighting aggregates, *J. Atmos. Sci., 62*, 1637-1644, 2005.

Oltmans, S. J., H. Vömel, D. J. Hofmann, K. H. Rosenlof and D. Kley: The increase in stratospheric water vapour from balloonborne, frostpoint hygrometer measurements at Washington D.C. and Boulder, *Geophys. Res. Lett., 27*, 3453-3456, 2000.

Sherwood, S. C. and A. E. Dessler: A Model for transport across the tropical tropopause, *J. Atmos. Sci., 58*, 765-779, 2001.

MESOCALE CIRRUS CLOUD MODELING AND COMPARISONS AGAINST REMOTE SENSING DATA COLLECTED FROM SPACE AND AIRCRAFT DURING THE CIRCLE CAMPAIGN

V. GIRAUD[1], G.PENIDE[1], A. PLANA[2], P.DUBUISSON[3], A.PROTAT[4], J.PELON[5] and JF.GAYET[1]

[1] LaMP/CNRS, Université Blaise Pascal, 63177 Aubière, France
[2]CETP, Centre d'Etudes des Environnements Terrestre et Planétaires, 78140 Velizy, France
[3]LOA, Laboratoire d'Optique Atmosphérique, 59655 Lille, France
[4]BMRC, Bureau of Meteorology Research Centre, Docklands, VIC3008, Melbourne, Australia
[4] SA, Service d'Aéronomie, 75252 Paris, France

1. INTRODUCTION

The properties and the persistence of cirrus clouds strongly depend on key dynamical and microphysical processes as well as interactions between microphysics, radiation and dynamic. Some major advances in the knowledge of cirrus cloud layers arise from coupling in situ observations with active and passive remote sensing that should described cloud structures at several scales.

The capability of the Brazilian Regional Atmospheric Modeling System (BRAMS) to simulate the dissipation phase of frontal cirrus cloud layers is evaluated. The simulation results are compared to aircraft and satellite observations acquired on may 16, 2007, during the CIRCLE-2 campaign.

2. THE MODEL AND THE STRATEGY OF ITS EVALUATION

Remote sensing observations revels cloud microphysical properties and their structures. Simultaneous observations at different wavelengths, or by active or passive instruments give access to different cloud characteristics. Our strategy is to simulate a large variety of instruments from the output fields of our model. Then, both real observations signatures and synthetic observation ones are compared to depict the lack (or the realism) of the model simulation. To be as efficient as possible, the calculations of the synthetic observations must be made with only the information, and the assumption, available from the model. In our study, the BRAMS model is used with the more complete microphysical scheme as possible (Cotton et al., 2001). The cloud microphysics parameterization with two-moment scheme has been activated and the characteristics of the shapes of particles for each species have been take into account (Harrington et al., 2001; Meyers et al., 1997).

From model outputs, and with only the hypothesis and parameterizations used in the model, we are able to simulate : radar reflectivity (with the Mie approximation and with absorption, Donovan et al., 2003); radar Doppler signal; lidar backscattering ratio (with multiple scattering, Hogan, 2006) and brightness temperature in the infrared window for classic instruments (with both aborption and diffusion, Dubuisson et al., 2005). Each instrument is simulated for satellite, airborne and ground based observatories. The single-scattering properties reported by Yang et al. (2005) for nonspherical ice particles have been used in the present radiative transfert calculations. Five ice crystal habits namely columns, plates, needles, dendrites and aggregates are considered for pristine and snow species. Crystal habits depend on the diagnostic of ambient temperature and saturation with respect to water.

2. THE CIRCLE-2 CAMPAIGN

The validation of CALIPSO/CLOUDSAT products dedicated to clouds has been performed within the frame of the PAZI/CIRCLE-2 project from DLR (Institute for Atmospheric Physics in Oberpfaffenhofen) in May 2007. During this campaign the LaMP operated a unique combination of cloud in-situ probes on the DLR F20 aircraft including a Polar Nephelometer, a Cloud Particle Imager (CPI) as well as standard PMS probes (FSSP and 2D-C) to measure cloud particle properties in terms of scattering characteristics, particle morphology and size, and in-cloud partitioning of ice and water content. During the CIRCLE-2 campaign, the DLR F20 flights were co-ordinated with the INSU F20 equipped with remote sensing instrumentation (RALI : combination of cloud radar and 3-λ lidar, IR radiometer CLIMAT…) representing an optimum configuration for CALIPSO/CLOUDSAT validation for cirrus clouds studies. The experimental strategy of the combined observations consisted to coordinate the flight plans with the CALIPSO/CLOUDSAT overpass, including the overall objective to validate the retrieved vertical profiles of cloud parameters (backscattering coefficient, extinction, thermodynamic phase including ice and/or liquid water content, effective diameter, …).

3. SITUATION OBSERVED ON MAY 16, 2007.

From MetOffice analyses: the situation on may 16 is characterized with a warm front extending southeastward from low pressure in the middle of North Atlantic. This warm front reached the West French coast at 12 UTC; nearly two hours before take-off aircrafts and the overpass of the A-train constellation.

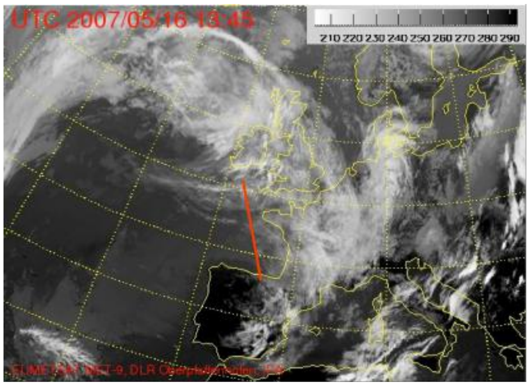

Figure 1: Eumetsat brightness temperature observed on may 16, 2007 at 13:45 UTC over the CIRCLE campaign area. The red line correspond to the ground track of the simultaneous A-train overpass.

The meteorological situation is confirmed by the EUMETSAT 9 observations at 13:45 UTC. Cloudiness draws the warm front that is at this time above the continent. The red line on satellite image (figure 1) shows the ground track of Aqua-train simultaneous observations. Falcon 20 trajectories are superposed to the MODIS image on figure 2. The first aircraft leg is spatially and temporally coordinated with the A-train overpass.

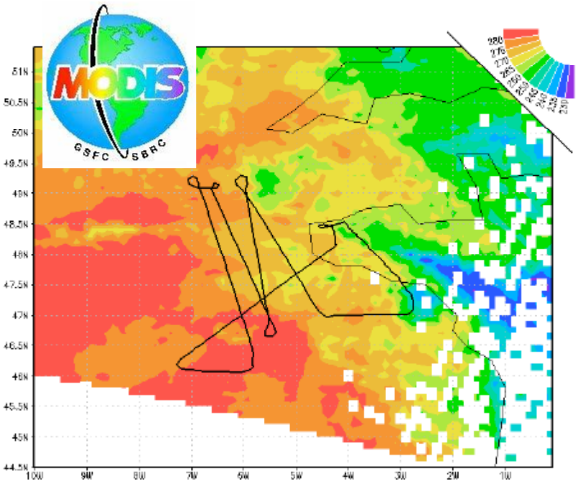

Figure 2: MODIS Brightness Temperatures observed at 12µm channel. Black line shows the FALCON-20 trajectory.

It is clear that the warm front passed over the observed area few hours before the intensive observations. Cirrus clouds have been generated by the warm front and are probably in a dissipative phase when the observations have been acquired.

3. SIMULATION PROTOCOL

Our simulation was set up on May 16 at 0h00 with ECMWF initialization fields and ends at noon the 17. A nudging has been applied every 6 hours from ECMWF analysis at the lateral boundaries of the simulated domain. The model has been configured with 3 nested grids with respectively 25, 5 and 1 km horizontal resolutions. There are 34 vertical levels for the larger grids. The 3th grid, with the higher resolution, was setup with 115 vertical levels extended from ground to 20 km altitude. The vertical resolution of the thinner grid was stretched from 500 m close to ground to 100 m at 10 km altitude (cloud levels). The 3 grids have been centered on 48°N and 5°W. The simulated areas for the 3 grids are represented by the rectangles on figure 3.

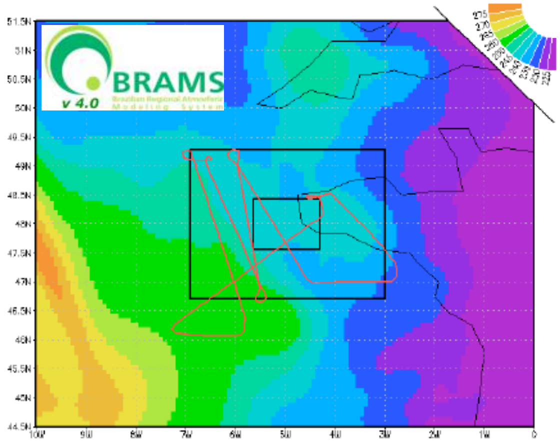

Figure 3: Brightness temperature as seen from MODIS channel at 12µm simulated from simulation at 14UTC. The three rectangles represent the domains covered by the 3 different grids of the model. The red line correspond to the aircraft trajectory

4. PRELIMINARY RESULTS:

Firstly, the infrared signatures of the simulations have been evaluated. Figure 3 shows the synthetic brightness temperature as should be observed from MODIS channel 32 (centered at 12 µm) on-board Aqua. A direct comparison of figures 2 and 3 shows that simulated temperatures are cooler than those observed. The difference in average throughout the area is close to 20 K. Analysis of the lidar profiles shows that cloud base and cloud top altitudes are correctly simulated. The temperature differences are due to a quantity of ice too important in the simulated cloud. Comparing the arches represented on Figures 4 and 5 corroborates this. These figures correspond to the observations acquired by the radiometer CLIMAT aboard FALCON 20 and the synthetic observations on the same wavelengths

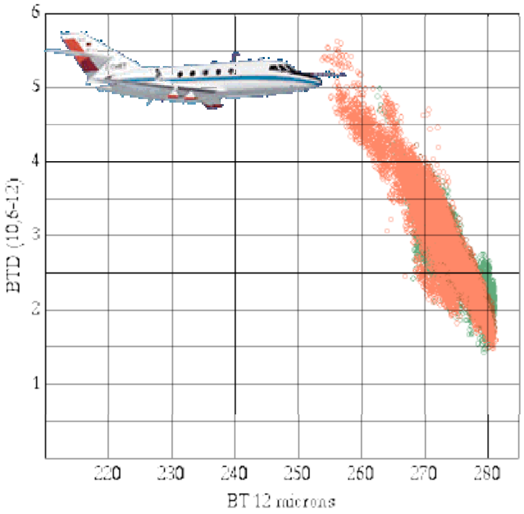

Figure 4 : Brightness temperatures measured by the CLIMAT radiometer aboard FALCON 20. The colours refer to different legs. The brightness temperature differences (between channels focused respectively to 10.6 and 12 microns) are drawn depending on the brightness temperature in the channel centred at 12 µ m.

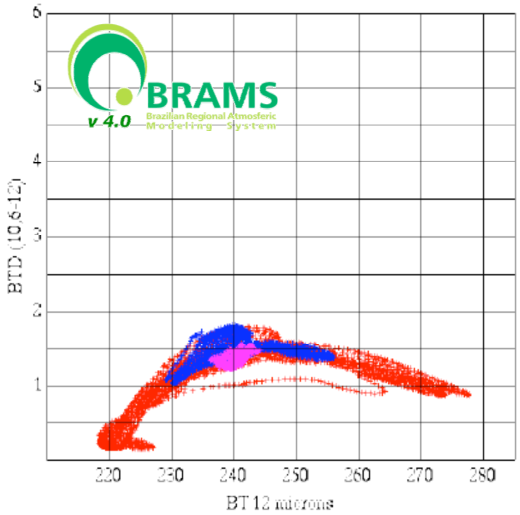

Figure 5 : Same as Figure 4 but for synthetic brightness temperatures. The colors correspond to the different grids of the model. Red, blue and magenta correspond respectively to grids 1, 2 and 3.

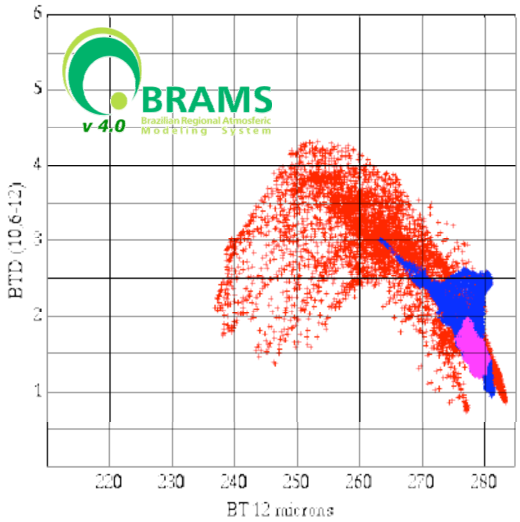

Figure 6 : Same as Figure 5 but for the simulation with terminal fall speed of pristine and snow multiplied by a factor 5.

Figure 4 shows that cirrus overflown by aircraft are optically thin. They are semi-transparent to ground infrared radiation. The simulated cirrus has more varied optical thickness since one can identify an entire arch. In particular, the coldest temperatures, associated with brightness temperature differences closed to zero, correspond to the temperature of the cloud top emission. They therefore correspond to areas of thick clouds.

Throughout the simulation domain, differences in brightness temperatures are still less than 2 K. Observations show that, contrary to the simulations, BTD may exceed 5 K. The arch signature on Figure 4 corresponds to small ice particles (Giraud et al., 1997).

These initial comparisons show that there are still too many ice in the simulated cirrus. In addition, ice particles are too large.

As the first test, we conducted a new simulation by changing only the terminal fall speed velocity of the primary ice and snow. These speeds have been multiplied by a factor of 5. They remain realistic.

Figure 6 shows the results with this new simulation. The colder brightness temperatures have disappeared, and brightness temperature differences have increased. The infrared signature of the simulated cirrus clouds is more realistic, compared to the observed ones.

Increasing the speed of falling ice particles increases the rate of sedimentation. Ice water contents decrease. The larger particles are disappearing, resulting in a decrease of the effective particle size and therefore an increase of the brightness temperature differences.

5. CONCLUSIONS AND PERSPECTIVE

Our simulation shows that the dissipation of the cirrus cloud is not sufficiently effective. A first test shows that the fall speed velocity of the ice particles impacts strongly the dissipative phase. Others key parameterization evaluations will be shown. All the observations made during the campaign will be used to constrain the choice of parameterizations and improve the dissipation of cirrus clouds in BRAMS.

6. BIBLIOGRAPHY

Cotton W.R., Pielke R.A.,Walko R.L., Liston G.E., Tremback C., Jiang H., McAnelly R.L., Harrington J.Y., Nicholls M.E., Carrio G.G., McFadden J.P., 2003 : RAMS 2001: Current status and future directions,. *Meteorol. Atmos. Phys*., 82, 5–29.

Donovan, D. P., 2003: Ice-clouds effective particle size parameterization based on combined lidar, radar reflectivity, and mean Doppler velocity measurements. JGR, 108, D18, 4573.

Dubuisson P., Giraud V., Chomette O.,Chepfer H., and Pelon J., 2005 : Fast radiative transfer modeling for infrared imaging radiometry. *J. Quant. Spectrosc. Rad. Transfer*, 95, 201-220.

Giraud V., J_C Buriez, Y. Fouquart, F. Parol and G. Sèze, 1997 : Large scale analysis of cirrus clouds from AVHRR data: Assessment of both a microphysical index and the cloud top temperature. J. Appl. Meteor., 36, 664-675.

Harrington J.Y., Olsson P.Q., 2001 : A method for the parameterization of cloud optical properties in bulk and bin microphysical models. Implications for arctic cloudy boundary layers, *J. Atmospheric Research*., 57, 51-80.

Hogan R.J., 2006 : Fast approximate calculation of multiply scattered lidar returns, *Applied Optics,* 45, 5984-5992.

Ping Yang, Liou K.N., Wyser K., Mitchell D., 2000 : Parametrisation of the scattering and absorption properties of individual ice crystals. *J. Geophys. Res*,. 105, 4699-4718.

Meyers M.P., Walco R.L., Harrington J.Y., Cotton W.R., 1997 : New RAMS cloud microphysics parameerization. Part II : The two-moment scheme, *J. Atmospheric Research*, 45, 3-39.

Acknowledgements : This work was partially supported by CNES (Centre National d'Etudes Spatiales) and INSU (Institut National des Sciences de l'Univers). The data collected during the experimental campaign were a joint effort of the other partners involved in this project (IPSL, DLR). The researchers of these groups are acknowledged for this work.

SIMULATION OF OROGRAPHIC CIRRUS IN THE GLOBAL CLIMATE MODEL ECHAM5

Hanna Joos[1]*, **Peter Spichtinger**[1] **and Ulrike Lohmann**[1]

[1] ETH Zurich, Institute for Atmospheric and Climate Science, Switzerland

A comparison of satellite data with simulations from global circulation models shows that there is a lack of cirrus cloud amount in large-scale models above and in the lee of mountains. The formation of orographic cirrus clouds due to gravity waves is usually not parameterized in large-scale models. To improve the simulation of such orographically excited cirrus clouds a coupling of the gravity wave dynamics and the cloud microphysics has been implemented in the climate model ECHAM5. As homogeneous freezing of solution droplets strongly depends on the vertical velocity, an increased vertical velocity due to gravity wave activity in the upper troposphere leads to the formation of cirrus clouds with higher ice crystal number densities. A comparison of the new parameterization with measurements shows a better agreement with observations.

1 INTRODUCTION

Cirrus clouds play an important role in the climate system. They cover approx. 30% of the earth and can influence the radiative budget of the earth in two different ways. Ice crystals scatter part of the incoming solar radiation back to space. This leads to a cooling of the underlying atmosphere (albedo effect of clouds). On the other hand, ice crystals reduce the outgoing longwave radiation and can lead to a warming (greenhouse effect of clouds). Which process is dominant depends on the properties of the cirrus cloud like ice crystal number density, thickness of the cloud and ice water content. In general it is thought that optically thin cirrus have a warming effect and optically thick cirrus a cooling effect. Thus, a net global warming of the Earth-atmosphere system due to cirrus clouds is possible (Chen et al., 2000). However, an estimate of the global influence of cirrus clouds on the radiative budget is very complex as the formation processes and the life cycle of cirrus clouds are not very well known (Spichtinger et al., 2005a,b) and especially the transition from the cooling to the warming regime is not yet completely understood. Recent studies indicate that the ice crystal number density plays a crucial role for the transition from warming to cooling due to cirrus clouds (Fusina et al., 2007).

An important factor for triggering the formation of ice is the vertical velocity. It induces adiabatic cooling and thus an increase of the relative humidity with respect to ice. Mesoscale velocity fluctuations in the range of 10-50 cm/s amplify homogeneous nucleation (Haag and Kärcher, 2004; Hoyle et al., 2005). Amongst others, these mesoscale fluctuations in the vertical velocity can be induced by gravity waves. One important source of gravity waves are mountains producing orographic waves. There are lots of mountainous regions in the world,

---

*hanna.joos@env.ethz.ch

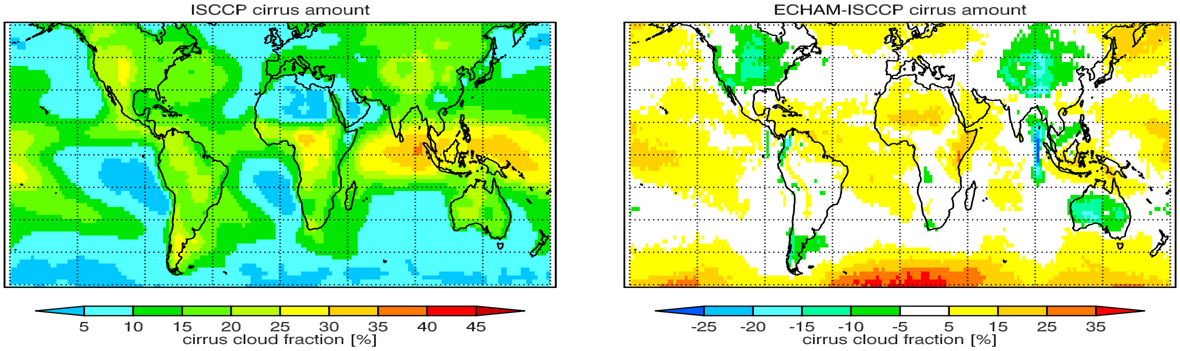

Fig. 1: Annual mean ISCCP Cirrus cloud amount (percentage of a gridbox covered with cirrus) for the years 1983-2005 (left) and the difference between a three year ECHAM5 simulation and ISCCP. Cirrus clouds are defined as clouds above 440 hPa and an optical depth $\tau < 3.6$.

where an influence of the gravity waves on the formation of clouds has to be considered (Kärcher and Ström, 2003). Dean et al. (2005) analyzed satellite data from the ISCCP project and compared them with the results of the 19-level HadAM3 version of the United Kingdom Met Office Unified Model. They showed that the model does not simulate sufficient high cloud cover over land especially in the regions of the mountains. Therefore they proposed a parameterization of orographic clouds described in Dean et al. (2007).

The comparison of the cirrus cloud cover simulated with the ECHAM5 model used in this study (Lohmann et al., 2007) with observations from the International Satellite Cloud Climatology Project (ISCCP) (Rossow and Schiffer, 1999) also shows a lack of cirrus cloud cover over continents and in the mountainous regions, as shown in figure 1. We therefore present a new concept of coupling the gravity wave dynamics and cloud microphysics in the climate model ECHAM5 (Roeckner et al., 2003). In our parameterization we explicitely calculate a vertical velocity induced by gravity waves which is used directly in the parameterization of homogeneous freezing. Since a double-moment scheme for the ice phase is implemented in ECHAM5, the new scheme influences not only the ice water content but also the ice crystal number concentration.

2 PARAMETERIZATION OF CIRRUS CLOUDS: HOMOGENEOUS FREEZING

Homogeneous freezing of supercooled solution droplets plays an important role for the formation of cirrus in the upper troposphere. The lack of efficient ice nuclei, high ice crystal number densities frequently measured in young cirrus clouds and the frequently observed high relative humidities with respect to ice indicate the importance of homogeneous freezing as an important mechanism for the formation of cirrus (Sassen and Dodd, 1989). The formation of gravity waves with high vertical velocities leads to very high supersaturations with respect to ice and one can assume that homogeneous freezing is the dominant freezing mechanism, although heterogeneous nucleation could modify homogeneous freezing events (Kärcher and Ström, 2003).

Kärcher and Lohmann (2002) developed a parameterization for the formation of cirrus due to homogeneous freezing of supercooled solution droplets. This parameterization is implemented in the version of ECHAM5 used for this study (Lohmann et al., 2007).

The number of newly frozen ice particles depends on a critical ice supersaturation S_{cr}, which only depends on temperature (Koop et al., 2000), the water vapor number density at ice saturation n_{sat} and the vertical velocity

w. Furthermore, the maximal number of newly frozen ice crystals cannot exceed the number of hygroscopic aerosol particles N_a. Hence, one can deduce the approximate scaling relationship for the number of newly frozen ice crystals due to homogeneous freezing N_i^{hom} as:

$$N_i^{hom} \propto w^{3/2} n_{sat}^{-1/2}. \quad (1)$$

The positive correlation between N_i^{hom} and w shows that the number density of freshly formed ice crystals increases with increasing vertical velocity. Higher vertical velocities lead to higher supersaturations allowing more ice crystals to form before the supersaturation is depleted efficiently. At lower temperatures the depositional growth is less efficient, thus the growing ice crystals need longer to take up the available water vapor and to reduce the supersaturation (Pruppacher and Klett, 1997). Therefore, the high supersaturations can exist over a longer time period and more ice crystals can be formed (Kärcher and Lohmann, 2002).

So far, the vertical velocity used in this parameterization consists of two parts: A large-scale, grid mean vertical velocity w_l and a contribution from the turbulent kinetic energy (TKE), in order to represent the subgrid-scale variabilities in the vertical velocity. The total vertical velocity used in this parameterization is then given by

$$w_{l+t} = w_l + 0.7\sqrt{TKE} = w_l + w_t. \quad (2)$$

3 CALCULATION OF THE VERTICAL VELOCITY

The calculation of the vertical velocity induced by gravity waves is based on the parameterization of orographic gravity waves from Lott and Miller (1997) which is part of the standard ECHAM5 model. Gravity waves can be excited when stably stratified air flows over mountains. Such waves can propagate to considerable altitudes before they dissipate (McFarlane, 1987). An important property of such vertically propagating waves is the transport of momentum from the Earth's surface to the regions where they dissipate. This transport of momentum significantly influences the large-scale circulation in the stratosphere (McFarlane, 1987).

The parameterization of the gravity wave drag is based on the linear theory for monochromatic waves in the hydrostatic regime. As a detailed derivation of the linear theory is beyond the scope of this work, only the main issues are explained here. For more details see e.g. Smith (1979). In order to derive a vertical velocity induced by gravity waves the 2-dimensional equations of motion for an incompressible atmosphere are considered. Additionally, Boussinesq approximation is used and the Coriolis force is neglected. Furthermore, it is assumed that the flow follows the shape of the terrain at the lower boundary which is described by $z = h(x) = h_m \sin(kx)$, whereas h_m is the height of the mountain. The maximal vertical velocity induced by gravity waves can then be calculated as

$$w_{gw} = k \cdot U \cdot \delta h(z) \quad (3)$$

where $\delta h(z)$ is the vertical displacement (amplitude) of the flow which depends on the air density ρ, the Brunt-Väisäla frequency N and the horizontal wind U projected in the plan of the gravity wave stress. To account for the breaking of gravity waves, an instability criterion based on Lindzen (1981) is defined: A minimum Richardson number Ri_{min} that includes the gravity wave influence on the static stability and wind shear is evaluated. It is assumed that instability occurs for $Ri_{min} < 0.25$. This condition takes into account the occurrence of both convective overturning and shear instability. If Ri_{min} reaches its critical value saturation occurs and the amplitude $\delta h(z)$ is restricted to the value at which instability occurs. For the new total vertical velocity we obtain

$$\begin{aligned} w_{ges} &= \underbrace{w_l}_{large-scale} + \underbrace{0.7\sqrt{TKE}}_{turbulence} + \underbrace{w_{gw}}_{gravity\ waves} \quad (4) \\ &= w_l + w_t + w_{gw}. \end{aligned}$$

The calculation of the vertical velocity contains a horizontal wavenumber k which describes the width of the mountain. In ECHAM5 the orography is represented as elliptical mountains (Baines and Palmer, 1990; Lott and Miller, 1997) with an aspect ratio $r = a/b$ where a and b are the semi axis of the ellipse. Thus, the horizontal wavelength of the excited gravity wave depends on the aspect ratio of the mountain and the angle between the incident flow and the orography. Furthermore flow can be blocked at the windward side of the mountain, such that only flow from the higher levels can flow over the mountains which reduces the effective height as seen by the flow and also the horizontal wavelength which is excited.

4 RESULTS

In order to investigate the influence of gravity waves on the formation of cirrus clouds simulations with the global climate model ECHAM5 (Roeckner et al., 2003) with a horizontal resolution of T63 (1.875° x 1.875°) and 31 vertical levels using a timestep of 12 minutes were carried out for three years after a spin-up time of three month. Climatological sea surface temperature and sea-ice extent were used. One reference run (REF) was performed, where the previous vertical velocity described by eq. (2) is used. In a second simulation (GWD) the original vertical velocity is replaced by the vertical velocity that contains a contribution from the gravity waves and is described by eq. (4).

Additionally, a nudged simulation was performed in order to compare the simulation to observations from the INCA (Interhemispheric differences in cirrus properties from anthropogenic emissions) campaign (Gayet et al., 2004), which took place during March/April 2000 at Punta Arenas, Chile and September/October 2000 at Prestwick, Scotland. Nudging is a special assimilation technique where the dynamical model variables are relaxed to observations or meteorological analysis (Davies, 1976; Jeuken et al., 1996).

4.1 GLOBAL SIMULATION

Figure 2 shows a three-year mean of the vertical velocities and the ice crystal number density for the REF and GWD simulation averaged over the upper troposphere from 165 - 285 hPa. In the REF simulation very low values for the vertical velocity are simulated with maxima up to 20 cm/s in the tropics. In the GWD simulation one can see a completely different distribution of the vertical velocities. There are high values in the range of 5 cm/s to 100 cm/s over the mountains where gravity waves can be excited. This leads to a completely new distribution of the vertical wind field which also influences the ice crystal number concentration. The ice crystal number concentration in the REF simulation lies between 1 and 6 cm^{-3}. Only in the tropics values of up to 15 cm^{-3} occur due to convection. There is a lack of cirrus over continents in general and especially over mountains. In the GWD simulation the model produces much higher concentrations due to the higher vertical velocities. Thus, ice crystals form over the mountains and the ice crystal number concentrations lie between 1-5 cm^{-3} over the oceans and up to 40 cm^{-3} over the mountains. Due to the development of orographic cirrus we can expect a higher cirrus cloud amount in this region and the lack of cirrus clouds over continents can be reduced. Furthermore we see slight advection of ice crystals formed in orographic waves downstream for example to the adjacent ocean at the tip of south America.

4.2 COMPARISON WITH MEASUREMENTS

In order to test the new parameterization, the results of the nudged simulation are compared with measurements taken during the INCA campaign. The INCA campaign took place in April 2000 in Punta Arenas, Chile and in October 2000 in Prestwick, Scotland. INCA was an aircraft field experiment with the DLR (German Aerospace Center) Falcon aircraft. Vertical velocities were measured with a 5-hole probe (Bögel and Baumann, 1991) only during constant altitude flight sections. The accuracy of

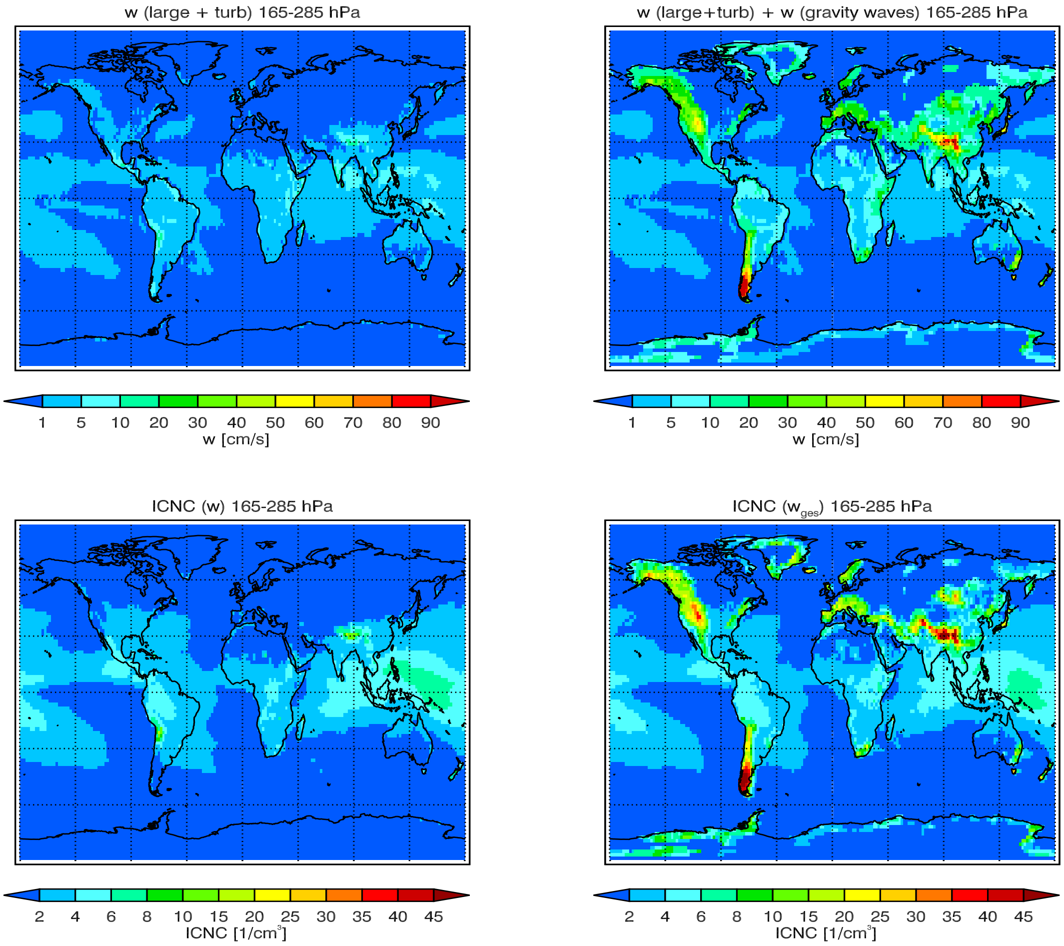

Fig. 2: Global distribution of the annual mean vertical velocity [cm/s] (upper panels) and annual mean of in cloud ice crystal number concentration [cm^{-3}] (lower panels) in the upper troposphere (165-285 hPa) for the REF simulation (left column) and the GWD simulation (right column).

the vertical velocity is estimated to be on the order of 0.1 m/s. Ice particle concentrations were measured during INCA with a combination of two instruments, the FSSP-300 and 2D-C optical probes (Gayet et al., 2002, 2004). The particle concentrations used for this comparison refer to the particle size range 3 – 800 micrometer in diameter. As a nudged simulation is used, one can assume that the large-scale flow in the model is similar to the observed one during the measurement period; thus, it makes sense to compare the simulated values with the measured ones. For comparison of the histograms of the vertical velocity and ICNC all values at altitudes higher than 280 hPa and temperatures less than 235 K measured during the southern and northern hemispheric campaign in the area of the measurements were taken. The experimental data represent about 40 flight hours taken during a 4 week period, in each hemisphere. Although these data do not represent climatological averages, their probability frequency distributions should be representative for this region and season and thus can be compared to the results from a nudged simulation. The two regions where measurements were taken are shown in Figure 3. The grey shaded areas in the map show the points where

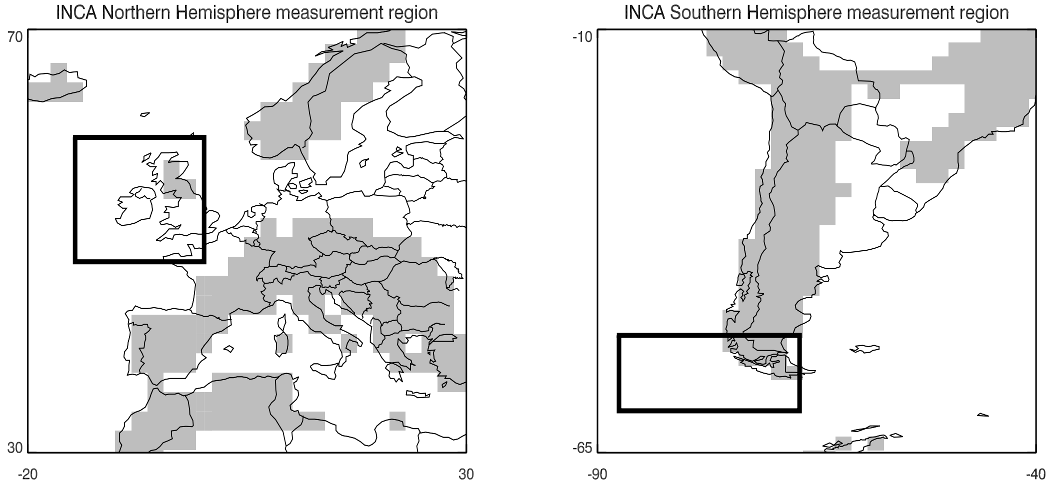

Fig. 3: Measurement region of the INCA campaign in the Northern and Southern Hemisphere. Grey shaded areas denote gridpoints where the gravity wave scheme can be activated.

the gravity wave scheme in the model can be activated. In the northern hemisphere there are only three gridpoints where the scheme can become activated and where gravity waves can develop. In the southern hemisphere there are nine active points. The histograms for the simulated values are calculated using data from a nudged simulation from March to May 2000 for the southern hemispheric case and from September to November 2000 for the northern hemispheric case for the upper troposphere from 165-285 hPa in the measurement regions. Figure 4 shows the comparison of the histogram for the measured and simulated values. For the northern hemispheric case one can see that the addition of a gravity wave induced vertical velocity leads to a better representation of the measured values. The values in the range of 0.2 to 2 m/s are shifted to a higher probability of occurrence but cannot reach the measured distribution. This could be due to the fact that in the measurement region there are only three gridpoints where the gravity wave scheme can be active and thus gravity waves can develop. We also should mention here that the development of turbulence in breaking gravity waves (i.e. nonlinear contributions) would lead to an additional vertical velocity which is not yet calculated. This lack of turbulence could lead to an underestimation of the probability of occurrence especially in the range of 10-100 cm/s. Using the new parameterization a higher probability of occurrence for the ice crystal number concentration in the range of 10 to 200 cm^{-3} can be simulated which is a better representation of the measured values. For the southern hemispheric case we also obtain an improvement due to the new parameterization. Gravity waves lead to enhanced vertical velocities which better represent the measurements especially in the range of 1 to 2 m/s, although it seems that the scheme produces too high vertical velocities. In this case an additional vertical velocity from turbulence also would enhance the probability of occurrence in the range of 10-100 cm/s. Higher ice crystal number concentrations are also simulated in better agreement with measurements.

5 SUMMARY AND CONCLUSION

A coupling of gravity wave dynamics and cloud microphysics has been implemented in

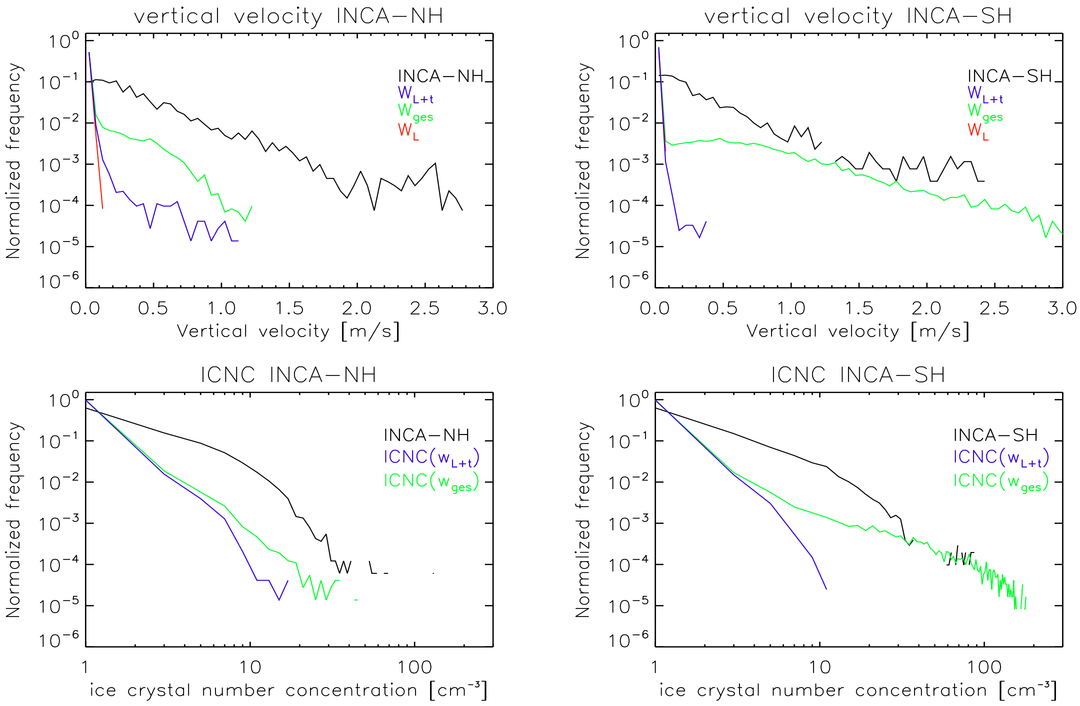

Fig. 4: Histogram of the measured and simulated vertical velocities [m/s] (upper panels) and ice crystal number concentration [cm^{-3}] (lower panels) sampled over the measurement regions in the Northern Hemisphere (left column) and the Southern Hemisphere (right column) shown in figure 3.

ECHAM5 in order to simulate sufficient amount of cirrus clouds in the lee of mountains. To account for the effect of gravity waves and to simulate the formation process of orographic cirrus an additional component for the vertical velocity has been added to the previously used formula in ECHAM5, which only contains a large-scale part and a contribution from TKE. The calculation of the vertical velocity induced by gravity waves is based on the parameterization of the gravity wave drag which calculates the momentum transfer from the earth surface to the atmosphere. The contribution of the vertical velocity from gravity waves leads to a much more realistic simulation of the vertical wind field. The probability of occurrence of the vertical velocity in the upper troposphere is enhanced in the range of 20-200 cm/s. This is exactly the range where a contribution due to gravity waves was expected. Good agreement with the measurements from the INCA campaign can be achieved in a direct comparison. Due to the new parameterization, the annual mean vertically integrated ice crystal number concentration could be enhanced from $1.5 \cdot 10^{10}$ m^{-2} to $1.67 \cdot 10^{10}$ m^{-2} which corresponds to an increase of $\sim$ 11%. Higher ice crystal number concentrations are simulated especially over mountains, which decreases the lack of cirrus over mountains.

Indeed, the new parameterization has a few limitations which should be mentioned here. Currently, the influence of the downdraft of a gravity wave on an orographic cirrus cloud is neglected. As the horizontal extend of an orographic cirrus cloud is limited by strong downdrafts, this limitation of the parameterization should be taken into account in a next step. Moreover, it has to be clarified whether the calculation of the vertical velocity based on a two-dimensional gravity wave scheme has to be modified as the vertical velocities seem to be slightly overestimated and the two-dimensional theory leads to an overestimation of the vertical velocities (Dörnbrack, 1998). Additionally,

it should be considered if the contribution from the TKE to the vertical velocity can be dropped or decreased whenever gravity waves occur.
The new distribution of the vertical velocity in the troposphere could also influence the formation of warm and mixed phase clouds via the activation of aerosols into cloud droplets. Thus, the calculation of a more realistic vertical wind field could therefore be of great importance for cloud processes in general.

ACKNOWLEDGEMENTS

We thank Andreas Minikin and Jean-Francois Gayet for the allocation of the INCA data and Marco Giorgetta, Andrew Orr and Johannes Quaas for helpful discussions and suggestions. Furthermore we thank the Deutsches Klimarechenzentrum (DKRZ) for computing time. This work contributes to the TH-project ”Orographic cirrus clouds in the climate model ECHAM5” (grant: TH-18 06-1) supported by ETH Research Fonds.

REFERENCES

Baines, P., Palmer, T., 1990. Rationale of a new physically based parameterization of sub-grid scale orographic effects. Tech. Rep. 169, European Centre for Medium-Range Weather Forecast.

Bögel, W., Baumann, R., 1991. Test and calibration of the dlr falcon wind measuring system by maneuvers. J. Atmos. Ocean. Tech. 8 (1), 5–18.

Chen, T., Rossow, W., Zhang, Y., 2000. Radiative effects of cloud-type variations. J. Climate 13, 264–286.

Davies, H., 1976. A lateral boundary fomulation for multilevel prediction models. Quart. J. R. Met. Soc. 102, 405–418.

Dean, S., Flowerdew, J., Lawrence, B., Eckermann, S., 2007. Parameterisation of orographic cloud dynamics in a gcm. Clim. Dyn. 28, 581–597.

Dean, S., Lawrence, B., Grainger, R., Heuff, D., 2005. Orographic cloud in a GCM: the missing cirrus. Clim. Dyn. 24, 771–780.

Dörnbrack, A., 1998. Turbulent mixing by breaking gravity waves. J. Fluid. Mech. 375.

Fusina, F., Spichtinger, P., Lohmann, U., 2007. The impact of ice supersaturated regions and thin cirrus on radiation in the mid latitudes. J. Geophys. Res.In press.

Gayet, J.-F., Auriol, F., Minikin, A., Ström, J., Seifert, M., Krejci, R., Petzold, A., Febvre, G., Schumann, U., 2002. Quantitative measurement of the microphysical and optical properties of cirrus clouds with four different insitu probes: Evidence of small ice crystals. Geophys. Res. Lett. 29,24, 2230.

Gayet, J.-F., Ovarlez, J., Shcherbakov, V., Ström, J., Schumann, U., Minikin, A., Auriol, F., Petzold, A., 2004. Cirrus cloud microphysical and optical properties at southern and northern midlatitudes during the inca experiment. J. Geophys. Res. 109.

Haag, W., Kärcher, B., 2004. The impact of aerosols and gravity waves on cirrus clouds at midlatitudes. J. Geophys. Res. 109.

Hoyle, C., Luo, B., Peter, T., 2005. The origin of high ice crystal number densities in cirrus clouds. J. Atmos. Sci. 62, 2586–2579.

Jeuken, A., Siegmund, P., Heijboer, L., Feichter, J., Bengtsson, L., 1996. On the potential of assimilating meteorological analyses in a global climate model for the purpose of model validation. J. Geophys. Res 101, 16939–16950.

Kärcher, B., Lohmann, U., 2002. A parameterization of cirrus cloud formation: Homogeneous freezing of supercooled aerosols. J. Geophys. Res. 107.

Kärcher, B., Ström, J., 2003. The roles of dynamical variability and aerosols in cirrus cloud formation. Atmos. Chem. Phys. 3, 823–838.

Koop, T., Luo, B., Tsias, A., Peter, T., 2000. Water activity as the determinant for homogeneous ice nucleation in aqueous solutions. Nature 406, 611–614.

Lindzen, R., 1981. Turbulence and stress due to gravity wave and tidal breakdown. J. Geophys. Res. 86, 9707–9714.

Lohmann, U., Stier, P., Hoose, C., Ferrachat, S., Kloster, S., Roeckner, E., Zhang, J., 2007. Cloud microphysics and aerosol indirect effects in the global climate model echam5-ham. Atmos.Chem.Phys. 7, 3425–3446.

Lott, F., Miller, M., 1997. A new subgrid-scale orographic parameterization: its formulation and testing. Q.J.R. Meteorol. Soc. 123, 101–127.

McFarlane, N., July 1987. The effect of orographically excited gravity wave drag on the general circulation of the lower stratosphere and troposphere. J. Atmos. Sci. 44 (14), 1775–1800.

Pruppacher, H., Klett, J., 1997. Microphysics of clouds and precipitation. Kluwer Academic Publisher.

Roeckner, E., Baeuml, G., Bonaventura, L., Brokopf, R., Esch, M., Giorgetta, M., Hagemann, S., Kirchner, I., Kornblueh, L., Manzini, E., Rhodin, A., Schlese, U., Schulzweida, U., Tompkins, A., 2003. The atmoshperic general circulation model ECHAM5. PART I: Model description, Report 349, Max Planck Institut of Meteorologie, Hamburg.

Rossow, W., Schiffer, R., 1999. Advances in understanding clouds from isccp. Bull Am Met Soc 80 (11), 2261–2287.

Sassen, K., Dodd, G., 1989. Haze particle nucleation simulation in cirrus clouds and aplication for numerical and lidar studies. J. Appl. Sci. 46, 3005–3014.

Smith, R., 1979. The influence of mountains on the atmosphere. Adv. Geophys. 21, 87–230.

Spichtinger, P., Gierens, K., Dörnbrack, A., 2005a. Formation of ice supersaturation by mesoscale gravity waves. Atmos. Chem. Phys. 5, 1243–1255.

Spichtinger, P., Gierens, K., Wernli, H., 2005b. A case study on the formation and evolution of ice supersaturation in the vicinity of a warm conveyor belt's outflow region. Atmos. Chem. Phys. 5, 1243–1255.

SUPERSATURATIONS IN CIRRUS:
FIELD AND LABORATORY OBSERVATIONS

M. Krämer^1, C. Schiller^1, A. Afchine^1, R. Bauer^1,
I. Gensch^1, A. Mangold^{1,7}, S. Schlicht^1, N. Spelten^1,
O. Möhler^2, H. Saathoff^2, V. Ebert^3, N. Sitnikov^4,
M. de Reus^5 S. Borrman^5 and P. Spichtinger^6

^{1} Research Center Jülich, Germany, ^{2} Research Center Karlsruhe, Germany,
^{3} University Heidelberg, Germany, ^{4} Central Aerological Observatory, Moscow Region,
Russia, ^{5} University Mainz, Germany, ^{6} ETH Zürich, Switzerland,
^{7} Royal Meteorological Institute, Bruxelles, Belgium

1. OVERVIEW

Upper tropospheric water vapor supersaturations over ice of up to unexplained 200% inside and outside of cold cirrus clouds are frequently reported from aircraft and ballons in recent years (Ovarlez et al. (2002), Gao et al. (2004), Jensen et al. (2005), Vömel and David (2007)). Such supersaturations may have significant impact on climate, since higher critical supersaturation for ice cloud formation than hitherto assumed will lead to a decrease in high cloud cover, which in turn feeds back to the radiation balance of the atmosphere Gettelman and Kinnison (2007). Supersaturations inside cirrus interact with the ice clouds microphysics and thus with the radiative properties of the cloud as well as the vertical redistribution of water vapor through sedimentation of ice crystals. Peter et al. (2006) summarised this 'supersaturation puzzle' and raise the question whether it maybe caused by a lack of understanding of conventional ice cloud microphysics or by uncertainties or flaws in the water instruments.

Here, we present high quality field observations of supersaturations in and outside of cirrus from 28 flights in ten field campaigns in Arctic, mid-latitude and tropical cirrus clouds. In our data set, no supersaturations larger than 200% are found.

In addition, the temporal evolution of supersaturations in ice clouds formed at the aerosol chamber AIDA by different types of aerosol particles are shown. Combined analysis of the field as well as the laboratory observations suggests that conventional ice cloud microphysics can explain our supersaturation observations.

2. EXPERIMENTALS

Water vapor measurements from several instruments operated on three different aircraft and in the AIDA chamber during the above mentioned campaigns are analyzed in the present study.

During field experiments with the Russian M55 Geophysica, water vapor was determined simultaneously with the FISH (Fast Insitu Stratospheric Hygrometer) and the FLASH (FLuorescent Airborne Stratospheric Hygrometer), both closed cell Lyman-α fluorescence hygrometers. The FISH is equipped with a forward facing inlet sampling total water, i.e. gas phase + ice water. Ice particles are oversampled with an enhancement depending on altitude and cruising speed of the aircraft. Corrections are applied during post-flight analysis. The FLASH uses a down-ward facing inlet that excludes ice particles and samples only gas phase water. Those experiments that used the German *enviscope*-Learjet or DLR Falcon em-

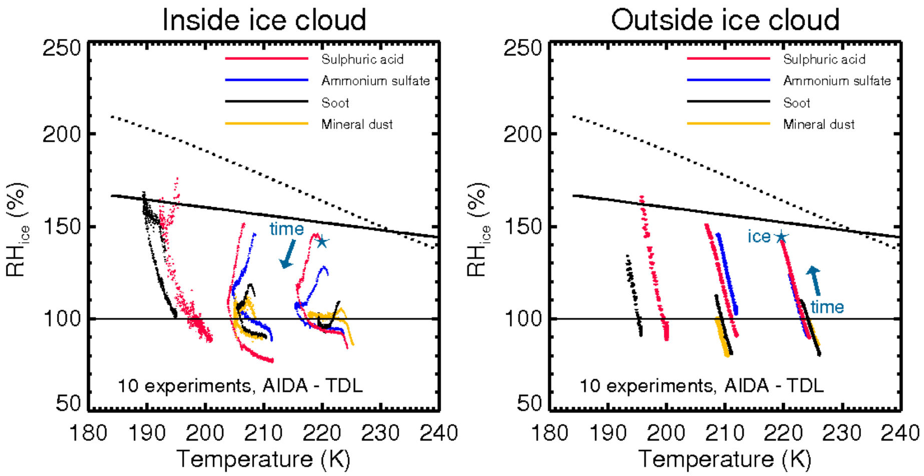

Figure 1: AIDA laboratory observations of RH_{ice} vs. temperature in- and outside of cirrus for 10 ice nucleation experiments initiated by different aerosol particles. The arrow shows the direction of time of the experiments, the star denotes for one examplary experiment the point where ice crystals appear for the first time. The black dotted line represents water saturation, the black solid line the homogeneous freezing threshold after Koop et al. (2000).

ployed versions of the FISH for the total water measurements, while gas phase water was measured with the open path TDL OJSTER (Open path Juelich Stratospheric Tdl ExpeRiment, MayComm Instruments. During laboratory campaigns at the AIDA chamber, gas phase water was also measured with an open path TDL.

The relative humidity with respect to ice, RH_{ice}, is calculated as $(H_2O_{gas}/H_2O_{sat,ice}) \cdot 100$ (H_2O_{gas}: gas phase water vapor, $H_2O_{sat,ice}$: water vapor saturation wrt ice after Marti and Mauersberger (1993)). The term 'supersaturation' refers to relative humidities with respect to that ice that exceeds 100%.

3. AIDA ICE NUCLEATION EXPERIMENTS

The ice nucleation experiments performed at the AIDA chamber offer the possibility to study the RH_{ice} evolution in cirrus life cycles (operation of the AIDA facility as an expansion cloud chamber for ice nucleation studies is described in detail by Möhler et al. (2003) or Mangold et al. (2005)).

RH_{ice} inside and outside of ice clouds generated at the AIDA chamber are shown in Figure 1 for ten ice nucleation experiments initiated by different aerosol particles. As homogeneously feezing aerosol sulfuric acid - water (red) and ammonium sulfate (blue) particles were injected in the AIDA chamber. In addition, as heterogeneously freezing particle types soot (black) and mineral dust (yellow) were used. These particle types are chosen because they are believed to be important components of the upper troposheric aerosol particle population, though the knowlegde of the aerosol in this altitude is very limited.

3.1 Outside AIDA ice clouds

In Figure 1 (right panel) RH_{ice} before ice formation is shown for aerosol particles with differing freezing thresholds. Each stroke represents one experiment and the freezing thresholds are the upper ends of the strokes (the star denotes for one examplary experiment the point where ice crystals appear for the first time).

During the homogeneous ice nucleation experiments with liquid sulfuric acid-water particles (red strokes) RH_{ice} increases up to around the homogeneous freezing threshold derived by Koop et al. (2000) (black solid line). Ammonium sulfate particles (blue), though liquid, nucleate below the homogeneous freezing threshold, because crystallization in the liquid droplets already starts during the cooling process (Mangold et al., 2005). Soot and mineral dust particles (black and yellow) freeze well below the homogeneous freezing threshold, mineral dust already at RH_{ice} only slighlty exceeding 100% (Mangold et al. (2005), Möhler et al. (2005)) . In addition to the dependence of the freezing tresholds on the aerosol type, it can be seen that ice nucleation occurs at higher supersaturations for lower temperatures.

3.2 Inside AIDA ice clouds

In the left panel of Figure 1 RH_{ice} after ice formation is shown for the same experiments as in the right panel, i.e. the coloured curves in the left panel continue the respective right panels strokes. Note here that the RH_{ice} development inside of the AIDA ice clouds is not directly comparable to the atmosphere because of the H_2O flux from the wall into the chamber during the existence of ice crystals. However, a qualitative picture of the evolution of RH_{ice} during an ice cloud cycle can be derived from the AIDA observations.

After ice crystal formation and continuous cooling RH_{ice} still rises up to a 'peak RH_{ice}'. This increase in RH_{ice} is because the ice crystals are so small in the beginning, that the water depletion of the gas phase is not large enough to compensate the increase of RH_{ice} caused by the further cooling. Consequently, the duration and the degree of the post-ice RH_{ice} increase depend on the number of ice crystals formed during the nucleation. A lower number of ice crystals appear for heterogeneously formed ice clouds. Thus, the few ice crystals consume the water vapour much slower and therefore RH_{ice} raises until a plateau after ice formation (see for example the yellow mineral dust experiments). In colder ice clouds, this behaviour becomes more pronouced and appears also for homogeneously forming ice clouds (see red and black experiments for sulfuric acid and soot, respectively). For the homogeneous sulfuric acid-water experiment (red) at the lowest temperature($<$200 K), it can be seen that after the ice nucleation at the homogeneous threshold RH_{ice} even shortly exceeds the homogeneous freezing line.

When cooling is stopped (the experiment curves turn to the right to higher temperatures), RH_{ice} immediately drops very quickly down to saturation and below, while ice crystals still exist. The part of the cirrus cycle where the crystals are evaporating is represented by the subsaturated part of the in-cloud observations.

4. CIRRUS FIELD OBSERVATIONS

4.1 Clear sky

Frequencies of occurence of RH_{ice} outside of cirrus in dependence on temperature are plotted in plotted in Figure 2 (top panel). From our clear sky observations, representing about 16 hours of aircraft flight time, it can be seen that RH_{ice} between nearly zero up to the homogeneous freezing thresholds are possible for temperatures $>$200 K. For lower temperatures, the highest frequencies of occurenc of RH_{ice} is enveloped by the dashed lines, representing RH_{ice} in dependence of temperature for a constant value of 2 and 3 ppmv, corresponding to the range of water vapour mixing ratios observed in the upper troposphere.

Although the AIDA experiments do not cover the complete temperature range observed during the field observations and more laboratory studies would be desirable, the general picture of the AIDA cloud free supersaturations matches that of the clear sky supersaturations observed in the upper troposphere .

No supersaturations close to or above water saturation are observed in our field measurements. Thus, from our data set we could not confirm the hypothesis of suppression of ice cloud formation.

4.2 In - cloud

The frequencies of occurence of in-cloud RH_{ice} observed in the field (Figure 2, bottom panel) show a pattern comparable to the AIDA measurements. Above about 200 K, values of $\mathrm{RH_{ice}}$ between around 50% and the homogeneous freezing thresholds are found, but most of the $\mathrm{RH_{ice}}$ observations group around 100%. Less frequent high supersaturations are probably observed in young cirrus directly after ice formation, while subsaturations are from old cirrus in the evaporation stage. This is a hint to short water vapour relaxation times in this temperature range, causing these parts of the clouds life cycle to be short compared to the time the clouds live around saturation.

At temperatures lower than about 200K, the grouping of the $\mathrm{RH_{ice}}$ frequencies of occurence around saturation broadens, pointing to longer water vapour relaxation times as for the warmer cirrus. There is no clear supersaturation cycle during the cirrus lifetime in this temperature range, as also seen from the AIDA experiments shown in Figure 1 (left panel).

No supersaturations above water saturation are observed in our field measurements, but, in the low temperature range, we observed few data points between the homogeneous freezing threshold and water saturation. By comparison with the AIDA observations, these measurements could be interpreted as the very first part of the cirrus life cycle, where $\mathrm{RH_{ice}}$ is between the freezing threshold and the 'peak $\mathrm{RH_{ice}}$'.

REFERENCES

Gao, R., Popp, P., Fahey, D., Marcy, T., Herman, R., Weinstock, E., Baumgardener, D., Garrett, T., Rosenlof, K., Thompson, T., Bui, P., Ridley, B., Wofsy, S., Toon, B., Tolbert, M., Kärcher, B., Peter, T., Hudson, P., Weinheimer, A., and Heymsfield, A.: Evidence That Nitric Acid Increases Relative Humidity in Low-Temperature Cirrus Clouds , Science, 303, 516 – 520, 2004.

Gettelman, A. and Kinnison, D. E.: The global impact of supersaturation in a coupled chemistry-climate model, Atmos. Chem. Phys., 7, 1629–1643, 2007.

Jensen, E., Smith, J., Pfister, L., Pittman, J., Weinstock, E., Sayres, D., Herman, R., Troy, R., Rosenlof, K., Thompson, T., Fridlind, A., Hudson, P., Cziczo, D., Heymsfield, A., Schmitt, C., and Wilson, J.: Ice supersaturations exceeding 100% at the cold tropical tropopause: implications for cirrus formation and dehydration, Atmos. Chem. Phys., 5, 851–862, 2005.

Koop, T., Luo, B., Tsias, A., and Peter, T.: Water activity as the determinant for homogeneous ice nucleation in aqueous solutions, Nature, 406, 611 – 614, 2000.

Mangold, A., Wagner, R., Saathoff, H., Schurath, U., Giesemann, C., Ebert, V., Krämer, M. ., and Möhler, O.: Experimental investigation of ice nucleation by different types of aerosols in the aerosol chamber AIDA: implications to microphysics of cirrus clouds, Meteorol. Z., 14, 485 – 497, 2005.

Marti, J. and Mauersberger, K.: A survey and new measurements of ice vapor pressure at temperatures between 170K and 250K, Geophys. Res. Lett., 20, 363–366, 1993.

Möhler, O., Stetzer, O., Schaefers, S., Linke, C., Schnaiter, M., Tiede, R., Saathoff, H., Krämer, M., Mangold, A., Budz, P., Zink, P., Schreiner, J., Mauersberger, K., Haag, W., Kärcher, B., and Schurath, U.: Experimental investigation of homogeneous freezing of sulphuric acid particles in the aerosol chamber AIDA, Atmos. Chem. Phys., 3, 211–223, 2003.

Möhler, O., Büttner, S., Linke, C., Schnaiter, M., Saathoff, H., Stetzer, O., Wagner, R., Krämer, M., Mangold, A., Ebert, V., and Schurath, U.: Effect of sulfuric acid coating on heterogeneous ice nucleation by soot aerosol particles, J. Geophys. Res., 110, 2005.

Ovarlez, J., Gayet, J.-F., Gierens, K., Ström, J., Ovarlez, H., Auriol, F., Busen, R., and Schumann, U.: Water vapour measurements inside cirrus clouds in Northern and Southern hemispheres during INCA, Geophys. Res. Lett., 29, 1813, doi: 10.1029/2001GL014440, 2002.

Peter, T., Marcolli, C., Spichtinger, P., Corti, T., Baker, M., and Koop, T.: When dry air is too humid, Science, 314, 1399 – 1401, 2006.

Vömel, H. and David, D.E.and Smith, K.: Accuracy of tropospheric and stratospheric water vapor measurements by the cryogenic frost point hygrometer: Instrumental details and observations, J. Geophys. Res., 112, doi: 10.1029/2006JD007224, 2007.

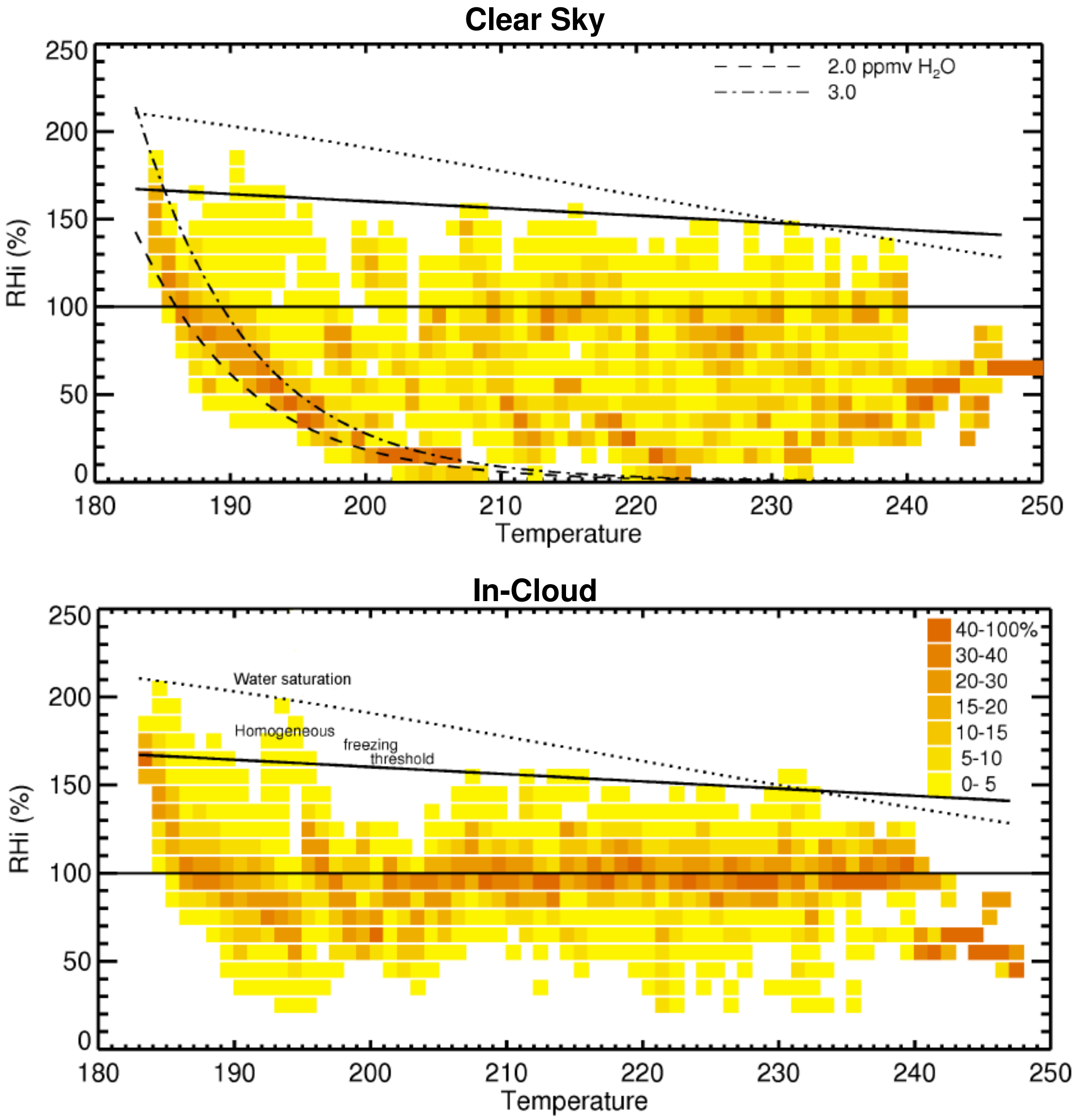

Figure 2: Frequencies of occurence of supersaturations vs. temperature, observed during 28 flights in Arctic, mid-latitude and tropical cirrus (data are sorted in 1K temperature bins; solid line: homogeneous freezing threshold, dotted line: water saturation line). **Top panel**: Outside of cirrus (16 h flight time); dashed lines: RH_{ice} calculated for constant water vapor mixing ratios of 2 and 3 ppmv, rspectively. **Bottom panel**: Inside of cirrus (13 h flight time).

MICROPHYSICAL ROOTS OF CIRRIFORM CLOUDS: ROLE OF CRYSTAL-GROWTH KINETICS

Dennis Lamb, Alfred M. Moyle, Jerry Y. Harrington, and Lindsay M. Sheridan

Meteorology Department, The Pennsylvania State University
University Park, Pennsylvania 16802, USA

1. INTRODUCTION

Cirriform clouds can be viewed as a visible manifestation of a complex set of physical phenomena interacting over a broad range of spatial scales in the upper troposphere. At some times, synoptic-scale pressure patterns force air to rise slowly over denser airmasses, yielding a uniform shield of cirrostratus cloud (Cs) composed of small ice crystals. At other times, mesoscale waves induce more local, but stronger updrafts that stimulate the formation of cirrus clouds (Ci) with clear evidence of large particles that sediment. The visible distinctions between cirrostratus and cirrus clouds result in part from the different forcing scales, but the microphysical responses (e.g., ice nucleation and crystal-growth kinetics) to the respective external forcings also differ and need to be clarified. Ultimately, our ability to predict the type and evolution of cirriform clouds depends on how well numerical models are able to capture the relevant physics on all scales.

This paper focuses on the microphysics of ice crystal growth under cirriform conditions. We explore the possibility that the observed forms and behavior of cirriform clouds are rooted partly in the detailed, molecular-scale processes responsible for ice crystal growth. After reviewing some of the processes involved, we present early computational results aimed at clarifying the issue.

2. HYPOTHESIS AND MOTIVATION

The limited efficiency with which ice grows from the vapor phase is hypothesized to control, at least in part, the macrostructure of ice clouds in the upper troposphere. An important visible distinction between the two main genera (Cs and Ci) is the presence or absence of visible fall streaks. The fibrous appearance of *cirrus uncinus*, for instance, is due to the sedimentation of relatively large ice particles. These fall streaks may become distorted by the wind shear, but it is the evidence of large, precipitating crystals that characterizes *Ci uncinus*. By contrast, the uniform appearance and lack of detail of *Cs nebulosus* suggests a uniform population of much smaller crystals. How much of the distinction in crystal size is driven by the macroscopic setting for cloud formation (updraft speed, cloud depth, temperature, etc.) and how much can be ascribed to different growth microphysics?

That a link might exist between ice crystal growth and the morphology of cirriform clouds stems from both theory and laboratory experiments. Theory shows that ice crystals respond to supersaturated environments by building some of the excess vapor molecules into the lattice at steps on individual facets. Each facet advances at a rate that increases monotonically with increased supersaturation, but the dependence on supersaturation is not linear. The involvement of steps in the growth process causes this nonlinearly and ultimately the potential for effects on cloud morphology.

Corresponding author's address: Dennis Lamb, 503 Walker Bldg., Penn State University, University Park, PA 16802 USA; E-Mail: lno@ems.psu.edu

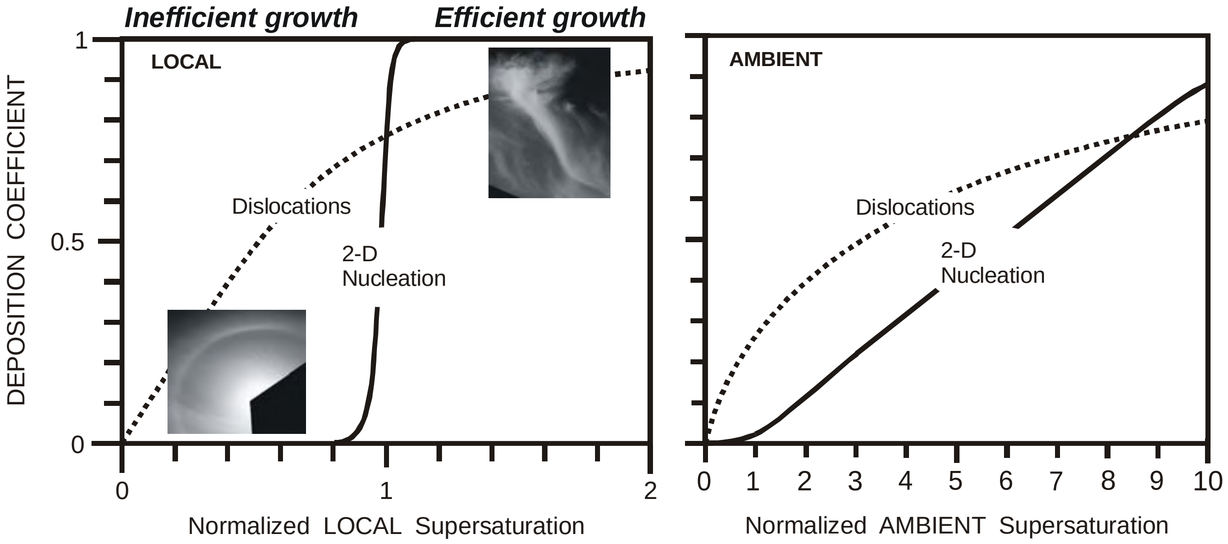

Fig. 1. Dependence of deposition coefficient on supersaturation and its possible link to the morphology of cirriform clouds. Left panel: Dependence on the LOCAL supersaturation immediately over a facet. Photos of Cs (low s_i) and Ci (high). Right panel: Dependence on AMBIENT supersaturation.

A parameter that accounts for the complicated and as yet uncertain surface processes responsible for ice growth is the deposition coefficient, α. Being the ratio of the actual growth rate to the maximum possible, α is a measure of the efficiency with which vapor molecules incorporate into the crystal lattice and contribute to the growth of the ice particle. This coefficient can be both calculated from theory and measured in the laboratory, so it affords a rich physical interpretation, as well as serving as a useful parameter in cloud models.

Recent lab measurements give evidence that ice particles may grow very slowly under cirriform cloud conditions. Libbrecht (2003) found α values of only a few per cent over a range of temperatures and supersaturations. Magee et al. (2006) found particle-average mass deposition coefficients to vary between about 0.004 and 0.008 in the temperature range -60 to -40 °C. Such low values suggest extremely inefficient growth and the likelihood of impacts on the properties of cirriform clouds (Gierens et al. 2003).

Theory gives an expectation that the deposition coefficient depends on conditions in the environment, so these low deposition coefficients may not hold universally. Supersaturation, s_i, in particular, seems to be a variable that plays an important role in the mechanism of growth. Indeed, measurements of individual facets show that α increases significantly with s_i (Sei and Gonda 1989; Libbrecht 2003). The functional form of $\alpha(s_i)$ is contingent on the assumed mechanism of step formation, which is still under debate (Frank 1982; Nelson and Knight 1998; Lamb 2000).

Figure 1 shows the range of possibilities for steps arising at the sites of emerging screw dislocations and for new layers initiated by 2-D nucleation (Nelson and Baker 1996; Lamb 2000). The left panel shows the theoretical dependences of α on the supersaturation immediately over the ice surface, whereas the right panel gives the expected dependence when air is present and ambient supersaturation is used (Lamb and Chen 1995). Because of the need for steps on facets, ice crystals can be expected to grow inefficiently at low supersaturations, but more efficiently once the supersaturation exceeds the critical supersaturation (unity on the abscissa). The inset photos indicate the hypothesized connection between the two genera of cirriform clouds and the kinetic coefficients of crystal growth. Do the crystals of Cs grow in an inefficient growth regime, whereas those of Ci grow efficiently?

3. TESTING AND FINDINGS

The suggestion that ice particles grow from the vapor with different efficiencies in cirrostratus and cirrus clouds was examined using a simplified cloud model (Lebo et al. 2008). The model was used as a tool for sensitivity studies rather than as means for simulating clouds.

Computations were performed with a parcel model using prescribed dynamics (constant updraft speed). The cloud particles were assumed to be spherical and distributed in size by a gamma distribution with initial radii between 1 and 40 μm. No explicit nucleation took place; rather, the concentration of particles (100 L^{-1}) was specified to be ice once ice saturation was reached during uplift. The model was initialized by specifying the temperature (-30 °C) and pressure (350 hPa) at cloud base. Two sets of runs were made by specifying the updraft speed to be 15 cm s^{-1} (to represent Cs) and 75 cm s^{-1} (Ci).

Within each model set, the parameter representing the growth microphysics (α) was varied to test different microphysical options. Several fixed values of α were used between 0.001 and 1. Also, several cases of variable α were tried to represent the supersaturation dependence shown in Fig. 1. The variable α was calculated by iteration for each supersaturation according to

$$\alpha = \left(\frac{x}{1+K\alpha}\right)^m \tanh\left[\left(\frac{1+K\alpha}{x}\right)^m\right],$$

where $x \equiv s_{amb}/s_1$ is the ratio of ambient and critical supersaturations (with respect to ice), and where K ~ 10 is the ratio of transport resistances due to vapor diffusion and surface kinetics (Lamb and Chen, 1995). The parameter m was set to 1 to represent spiral growth ("dislocations") and to 30 to represent 2-D nucleation of new layers, a suggestion offered by Nelson and Baker (1996). Each choice of α was used in the adaptive parameterization of Chen and Lamb (1994).

Examples of output from the model applied over a layer 2 km in depth are shown in Fig. 2 (low updraft speed, Cs) and Fig. 3 (larger updraft, Ci). Each panel presents the indicated variable as a function of height above cloud base. Each curve arises from the selected choice of α, as identified in the legend. Results from using three constant values of α are shown, as are three sets of variable α distinguished by the chosen value of critical supersaturation (s_1). Each set of variable-α curves is further distinguished by the step-origin mechanism. The mean radius of the ice particles is shown in Figs. 2a and 3a, respectively, for Cs and Ci situations. The ambient supersaturations for each case is given in Figs. 2b and 3b, while the computed α values for the variable-α cases are shown in Figs. 2c and 3c, respectively. We are aware of the limitations of this parcel model, in particular the fact that crystals having fallspeeds in excess of the given updraft speed are not able to be lifted, so the estimated cut-off radius is shown.

Noteworthy features of the model output include the grouping of curves for certain ranges of α. To first approximation, it makes little difference what the value of α is for $\alpha >$ 0.01, a result consistent with the fact that the dominant resistance to mass transport is vapor diffusion, not surface kinetics in such cases. Values of $\alpha < 0.01$ severely limit crystal growth and let the supersaturation rise, in some cases, unrealistically. Critical supersaturations of $s_1 = 10$ are unreasonable and so could be eliminated in future work. Large distinctions arise from the assumption of step origin, especially in the case $s_1 = 1$. It seems unlikely that crystals could grow at $s_1 =$ 1 by 2-D nucleation, but spiral growth can not be excluded by these results.

The hypothesis that ice crystals in cirriform clouds grow with variable α was explored with limited success. The variations in α with altitude for the variable-α cases (Figs. 2c and 3c) are large, but they are important only when $\alpha < 0.01$. It appears that the constant-α case, with $\alpha = 0.01$, allows sufficient growth in both Cs and Ci situations.

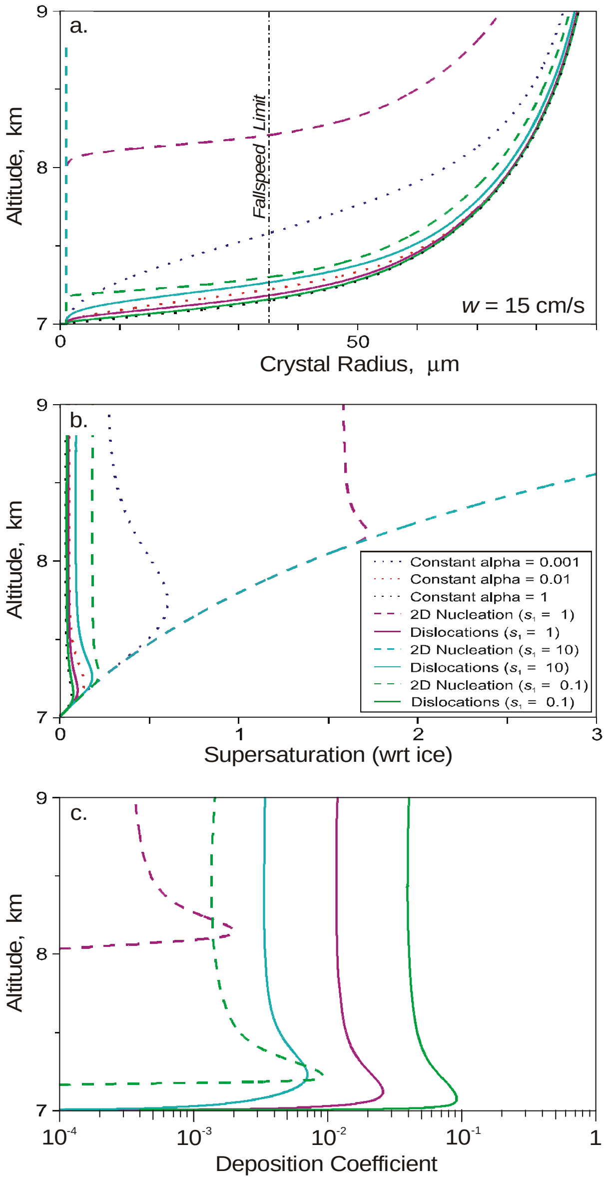

Fig. 2. Model results representing a Cs cloud with updraft speed w = 15 cm/s. a. Crystal radius. b. Supersaturation. c. Deposition Coefficient.

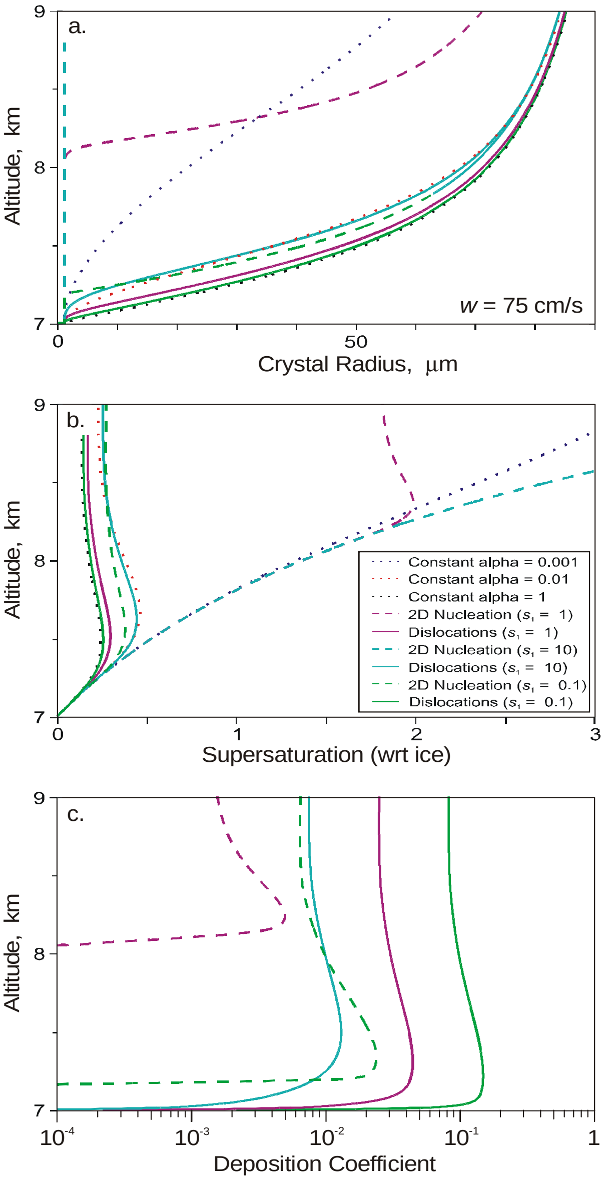

Fig. 3. *Model results representing a Ci cloud with updraft speed w = 75 cm/s. a. Crystal radius. b. Supersaturation. c. Deposition Coefficient.*

4. TENTATIVE CONCLUSIONS

The basic level of modeling used for this study allows a few tentative conclusions to be drawn. We can eliminate certain possibilities as being physically unrealistic, but further study with a more complete model would be needed to refine the conclusions. We cannot yet say with any certainty what, if any, role the growth kinetics play in distinguishing Cs and Ci clouds.

The step origins (dislocations or 2-D nucleation) greatly impact the development of ice particles in these model clouds. The mechanisms of step formation are tied to each other through a common edge energy (Lamb 2000), so one might not have expected to find such large effects. The findings of the model also show that critical supersaturations as large as 10 are not physically realistic; in fact, they are more likely to be in a range about 0.1 (Burton et al. 1951).

This study also highlights the need for new laboratory measurements of ice particle growth under cirriform conditions. In the near term, models may be run with appropriate constant values of α, perhaps, but this representation of surface processes leading to molecular incorporation is almost certain to depend on the supersaturation and on the areas of the facets. We must therefore learn how to identify the likely origins of steps on the low-index facets of complex crystals, and we must learn how to measure the critical super-saturation, which probably varies with temperature and with the crystallographic orientations of the facets.

5. BIBLIOGRAPHY

Burton, W. K., N. Cabrera, and F.C. Frank, 1951: The growth of crystals and the equilibrium structure of their surfaces. *Phil. Trans. Roy. Soc. London*, **243,** 299-358.

Chen, J.-P., and D. Lamb, 1994: The theoretical basis for the parameterization of ice crystal habits: Growth by vapor deposition. *J. Atmos. Sci.*, **51,** 1206-1221.

Frank, F. C., 1982: Snow crystals. *Contemp. Phys.*, **23,** 3-22.

Gierens, K. M., M. Monier and J-F. Gayet, 2003: The deposition coefficient and its role in cirrus clouds. *J. Geophys. Res.*, **108,** 4069, doi:10.1029/2001JD001558, AAC.

Lamb, D., 2000: Crystal growth: 2-D or not 2-D? *13th International Conf. on Clouds and Precipitation*, Reno, NV, 14-18 August 2000, International Assn. of Meteorology and Atmospheric Sciences, 752-755.

Lamb, D., and J.P. Chen, 1995: An expanded parameterization of the growth of ice crystals by vapor deposition. *Conf. on Cloud Physics*, Dallas, Texas, 15-20 January 1995, AMS, Boston, 389-392.

Lebo, Z. J., N.C. Johnson, and J.Y. Harrington, 2008: Radiative influences on ice crystal and droplet growth within mixed-phase stratus clouds. *J. Geophys. Res.***,** in press.

Libbrecht, K. G., 2003: Growth rates of the principal facets of ice between -10 ^{o}C and -40 ^{o}C. *J. Cryst. Growth*, **247,** 530-540.

Magee, N., A.M. Moyle, and D. Lamb, 2006: Experimental determination of the deposition coefficient of small cirrus-like crystals near -50 ºC. *Geophys. Res. Lett.***,** L17813, doi:10.1029/2006GL026665.

Nelson, J., and M.B. Baker, 1996: New theoretical framework for studies of vapor growth and sublimation of small ice crystals in the atmosphere. *J. Geophys. Res.*, **101,** 7033-7047.

Nelson, J., and C. Knight, 1998: Snow crystal habit changes explained by layer nucleation. *J. Atmos. Sci.*, **55,** 1452-1465.

Sei, T., and T. Gonda, 1989: The growth mechanism and the habit change of ice crystals growing from the vapor phase. *J. Cryst. Growth*, **94,** 697-707.

Acknowledgements.

This work was sponsored in part by NSF Grant ATM-0639542. The authors gratefully acknowledge the help of Zach Lebo with development of the model.

ESTIMATION OF THE DEPOSTION RATE IN CIRRUS USING RAMAN LIDAR AND CLOUD RADAR

Ruei-Fong Lin[1,2], Jennifer M. Comstock[3], David O'C. Starr[2]

1 - Goddard Earth Sciences and Technology Center, University of Maryland, Baltimore County, Baltimore, Maryland, USA
2 - Laboratory for Atmospheres, NASA Goddard Space Flight Center, Greenbelt, Maryland, USA
3 - Pacific Northwest National Laboratory, Richland, Washington, USA

1. INTRODUCTION

The deposition rate, $\dot{\chi}$, (in units of mass of condensate per mass of air per unit time) is an essential component in cirrus evolution. If the deposition rate is known, we could explain the evolution of the observed moisture field in a more quantitative fashion. The goal of this research is to present a new method for estimating the deposition rate using ground-based remote sensing measurements.

2. MEASUREMENTS

We use measurements of the extinction coefficient, $b_{ext,L}$, from a Raman lidar (RL) and the equivalent radar reflectivity factor, Z_e, from a 35 GHz Millimeter-wave Cloud Radar (MMCR) to derive $\dot{\chi}$. Both instruments are located at the ARM Climate Research Facility (ACRF) Southern Great Plains (SGP) site. The different but complimentary operating wavelengths (Donovan and van Lammeren, 2001) make the retrieval of $\dot{\chi}$ possible. Details for both the ARM RL and MMCR can be found at http://www.arm.gov.

The parameter $b_{ext,L}$ is computed from the ARM RL nitrogen channel using a procedure described in Ansmann et al. (1992). The water vapor mixing ratio q_v is computed using the ratio of the lidar signals at 408-nm (water vapor scattering) and at 387-nm (nitrogen scattering). Temperature profiles are interpolated between four times a day radiosonde profiles.

3. METHOD

In this study, we consider columns and bullet rosettes because we are mostly interested in the upper tropospheric cirrus formed in situ.

The modified Gamma function has been widely used to describe the size distribution of ice particles in cirrus clouds, i.e., $N(D)dD = \frac{N_t}{\Gamma(\nu)}(\frac{D}{D_*})^{\nu-1}\exp(-\frac{D}{D_*})\frac{dD}{D_*}$, where D is the particle maximum dimension, N_t is the number of particles per unit volume, ν is a parameter controlling the width of the distribution and D_* is a characteristic length. Note that $D_*(\nu-1)$ is the modal length. An advantage of this practice is that a simple formula results for the moments. Thus, if a particle property can be formulated or approximated by a power-law function (i.e. $x = \alpha D^{\beta}$), its integrated property over the entire size distribution can be obtained easily.

The extinction coefficient $b_{ext,L}$ is a moment of the particle size distribution (PSD), $b_{ext,L} \approx 2\int A(D)N(D)dD$, where A is the particle cross section and $N(D)$ is the size distribution function. The power-law relationship between A and D has been observed from various studies and is summarized in Heymsfield and Miloshevich (2003).

Analogously, Z_e is also a moment of the PSD, $Z_e = \frac{\lambda^4}{\pi^5 |k_w|^2} \int \sigma_R(D) N(D) dD$, where σ_R is the backscatter cross section, λ is the wavelength, and $|k_w|^2$ is the dielectric constant for water particles. The power-law relationship between σ_R and D has been given in Aydin and Walsh (1999).

The power law relationship is suitable to describe the relationship between the ice crystal growth and its maximum dimension because the approximation error is within 10% when using 2 or 3 segments to capture the full parameter range. In this work, the capacitances of bullet rosettes and columns are formulated according to Chiruta and Wang (2003) and the spheroid approximation, respectively. The actual value of the deposition coefficient, β_i, is still a debatable question. Thus, we use a sensitivity test approach to examine its effect. It is set to 0.006 (slow growth, e.g., Magee et al., 2006), 0.1, or 1 (fast growth) in the calculations.

The flowchart of the procedure is briefly illustrated in Figure 1. First, R, the ratio of $b_{ext,L}$ and Z_e times a constant, is used to obtain D_*, which is then used to acquire N_t. The parameter ν is set to 2 after tests confirm a less than 10% sensitivity to the parameter by varying its value between 1 and 3. Note that in the procedure, the incomplete gamma function is used to account for segments of power-law relationship. A similar approach has been adopted to retrieve ice water content (IWC) and mass median size using the zeroth and first moments of the Doppler spectrum from a millimeter-wavelength Doppler radar (Mace et al., 2002).

4. RESULTS

A cirrus observed on 7 December 1999 is examined in this study. A modeling study of the same cloud system is reported in Comstock et al. (2008). The RL and MMCR measurements are plotted in Figure 2. Note that the uncertainty for the RL measured q_v increases from ~10% at z = 8.5 km to ~30% near the cloud top. Roughly 25% of cloudy pixels in the upper cirrus are highly ice supersaturated (RHI>120%).

Spotty high extinction ($b_{ext,L}$) regions are located near the cloud top. From our calculations, these bright spots contain many small particles (Figure 3). Nevertheless, 80% the cloudy pixels contain N_t between 5 and 500 L^{-1} where only 10% of the cloudy pixels contain N_t greater than 500 L^{-1}.

Also shown in Figure 3 is a decreasing trend of D_* with respect to height, indicating the importance of sedimentation-growth in this cloud. 90% the cloudy pixels contains PSDs of D_* less than 100 micron.

$\dot{\chi}$ in Figure 3 is calculated assuming column particles and β_i =1, which is the fastest growth scenario. The results indicate that, if those assumptions on the particle shape and the deposition coefficient are adequate, particles are uptaking water vapor very efficiently in those high ice supersaturation regions. However, this seems to directly contradict the frequent (25%) and non-spotty occurrence of high ice supersaturation in this cloud. Does this contradiction imply that β_i should be smaller than 1? It is yet too premature to make such a conclusion. More studies are needed to understand this issue.

One naturally wonders whether the significance of latent heat release in the cirrus evolution might change with β_i. From Figure 3, persistent high positive deposition rate occurs in the upper cloud between 0300 and 0400 UTC. The hourly averaged latent heating rate profiles computed from six scenarios for this period of time are compared in Figure 4. As the figure indicates, the differences are enormous. Latent heat release in the fast growth scenario would contribute significantly to buoyancy production and local circulation whereas it plays a minor role in the cloud dynamics in the slow growth scenario.

The last panel in Figure 3 shows that a moderate (as compared to the local moisture tendency) magnitude of sublimation takes place near the cloud base. Does particle sedimentation and local sublimation result in the downward development of the cloud observed by the ground-based instruments? To answer this question, we need to examine the local q_v tendency first. Most of the pixels below z = 8.2 km has a random error less than 10%. According to our estimate, the local tendency calculated from two consecutive pixels in time has an error less than 20% when their difference is greater than 20%. We've found the uncertainty in the measured q_v does not hamper our analysis because this cloud base experiences a fast moistening that is within the measurement limit. According to our calculations, even the fastest growth scenario is not able to explain the drastic moistening near the cloud base. The moistening should have been a result of sub-grid (relative to the large-scale data derived from the constrained variational analysis) q_v forcing, i.e., likely the unresolved horizontal advection.

5. SUMMARY

A new method that estimates the deposition rate using data collected from Raman lidar and the millimeter wave cloud radar is developed to provide a more quantitative explanation of the observed water vapor evolution in the upper troposphere. In the selected case, regions with largest ice supersaturation ratios and deposition rates located were found near cloud top where plenty of small particles are present. This suggests a nucleation process in action. Moreover, a small particle regime is particularly sensitivie to specification of the deposition coefficient in terms of deposition rate and latent heat release. This implies that the cirrus dynamics and its evolution time scale may be closely linked to the deposition coefficient. Therefore, more studies to reduce the uncertainties in the deposition coefficient are warranted.

6. BIBLIOGRAPHY

Aydin, K., and T. M. Walsh, Millimeter wave scattering from spatial and planar bullet rosettes. IEEE Transactions on Geoscience and Remote Sensing, 37, 1138-1150, 1999.

Ansmann, A. U., Wandinger, M. Riebesell, C. Weitkamp, and W. Michaelis, Independent measurement of extinction and backscatter profiles in cirrus clouds by using a combined Raman elastic-backscatter lidar, App. Opt., 31, 7113-7131, 1992.

Chiruta, M. and P. K. Wang, The capacitance of rosette ice crystals. *J. Atmos. Sci., 60,* 836-846, 2003.

Comstock, J. M., R.-F. Lin, D. O'C. Starr, Understanding ice supersaturation, particle growth, and number concentration in cirrus clouds. *The 15th International Conference on Clouds and Precipitation,* Cancun, Mexico, July 7-11, 2008.

Donovan, D. P., and A. C. A. P. van Lammeren: Cloud effective particle size and water content profile retrievals using combined lidar and radar observations. I. Theory and examples. *J. Geophys. Res.,* 106 (D21), 27 425- 27 448, 2001.

Heymsfield, A. J., and L. M. Miloshevich, Parameterization for the cross-sectional area and extinction of cirrus and stratiform ice cloud particles. *J. Atmos. Sci., 60,* 936-956, 2003.

Mace, G. G., A. J. Heymsfield, M. R. Poellot, On retrieving the microphysical properties of cirrus clouds using the moments of the millimeter-wavelength Doppler spectrum. *J. Geophys. Res., 107,* doi:10.1029/2001JD001308, 2002.

Magee, N. A. M. Moyle, and D. Lamb, Experimental determination of the deposition coefficient of small cirrus-like ice crystals near -50°C. *Geophys. Res.*

Lett., 33, L17813, doi:10.1029/2006GL026665, 2006.

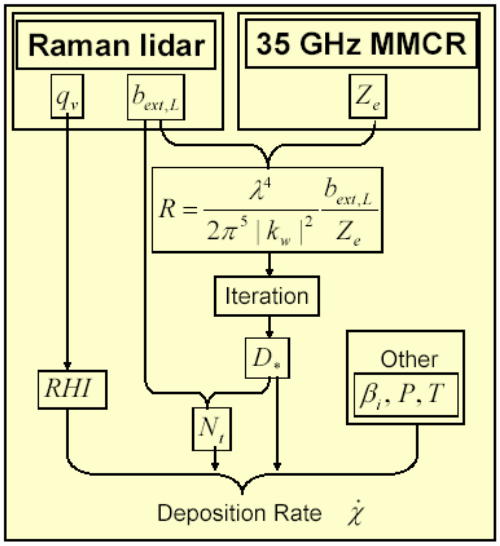

Figure 1. Flowchart.

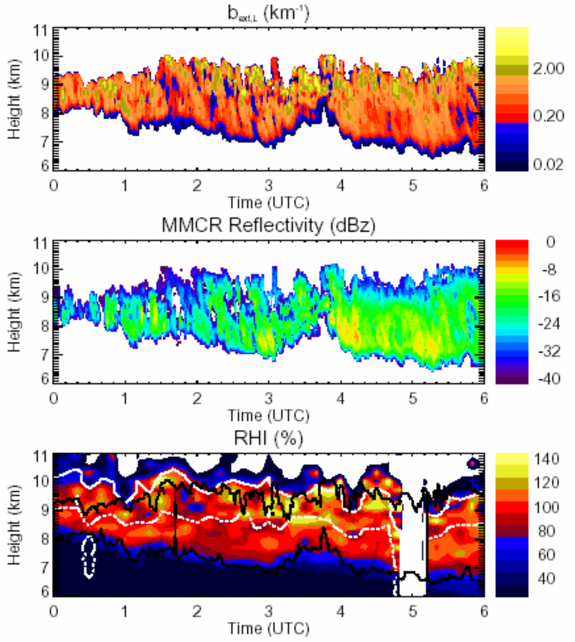

Figure 2. Height-time sections of the RL extinction coefficient, radar reflectivity, and RHI. In the last panel, the black, white solid, and white dash-dotted curves indicate the cloud boundaries, the 30% error contour, and the 10% error contour, respectively.

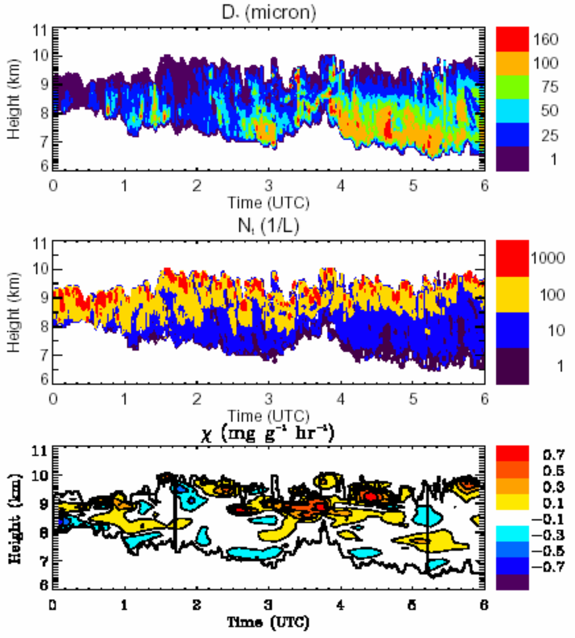

Figure 3. Height-time sections of the derived D_*, N_t, and $\dot{\chi}$. In this calculation, ν =2, β_i =1, particles are columnar.

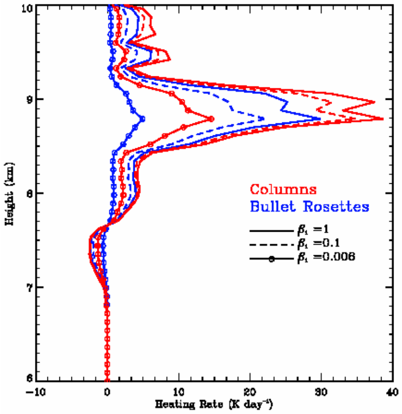

Figure 4. Heating rates due to latent heat release.

GROUND BASED REMOTE SENSING OF SMALL ICE CRYSTAL CONCENTRATIONS IN ARCTIC CIRRUS CLOUDS

Subhashree Mishra[1], David L. Mitchell[1], Daniel DeSlover[2] and Greg McFarquhar[3]

1. Desert Research Institute, Reno, NV
2. University of Wisconsin, Madison, WI
3. University of Illinois, Urbana, IL

1. INTRODUCTION

Measurement of small ice crystals (D < 60 μm) remains an unsolved and controversial issue in the cloud physics community. Concentrations of small ice crystals are hard to measure due to shattering of crystals at probe inlets. However, these small ice crystals alter cirrus cloud radiative properties and may affect the cirrus cloud feedback in global climate models. To facilitate better estimation of small ice crystal concentrations in cirrus clouds, a new ground-based remote sensing technique has been used in combination with in situ aircraft measurements. That is, data from the Mixed-Phase Arctic Cloud Experiment (M-PACE) conducted at Barrow on the north slope of Alaska (Fall 2004) is being used to develop an Arctic ice particle size distribution (PSD) scheme, that in combination with the anomalous diffraction approximation (for ice cloud optical properties), serves as the framework of the retrieval algorithm.

2. THEORY

Small ice crystals are evaluated using the properties of photon tunneling or wave resonance. Photon tunneling can be described as the process by which radiation beyond the physical cross-section of a particle is either absorbed or scattered outside the forward diffraction peak (Fig. 1). Tunneling is strongest when:

- The effective size of the particles and the wavelength of radiation are comparable.
- The particle is spherical or quasi spherical (an attribute of many small crystals)
- The real index of refraction is relatively large

Tunneling contributions to the absorption efficiency in the window region can reach 20% when particle size is less than 60 μm. Tunneling depends on the real refractive index, which changes abruptly for ice between 12 and 11 μm wavelengths. The corresponding emissivity difference at these wavelengths is only due to tunneling, which makes the tunneling signal an ideal signal for inferring the concentrations of small ice crystals. Historically this emissivity difference was attributed to differences in the imaginary refractive index, but in essence, it is the real refractive index that accounts for this difference in emissivity in ice clouds.

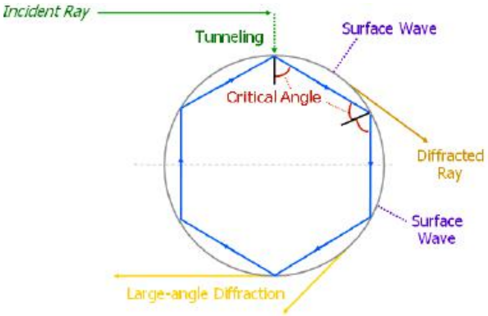

Figure1: Depiction of possible trajectories of an incident grazing ray after tunnelling to the drop surface.

Better understanding of remote sensing of small crystals by applying the tunneling technique is shown in Fig. 2. The solid curve shows absorption efficiencies (Q_{abs}) for a bimodal size distribution of quasi-spheres (droxtals) in the small mode and bullet rosettes in the large mode. Dashed curve is for the large mode, rosettes only. Bimodal PSD are shown in Fig. 3. Q_{abs} for wavelengths > 11 µm are greater for the complete PSD due to tunneling. Tunneling depends strongly on the real index of refraction, n_r. The reason Q_{abs} is greater at 12 µm than 11 µm when the full PSD is used is because n_r has a minimum near 11 µm but is substantial at 12 µm. Since tunneling is a measure of the small mode, and the 12 – 11 µm Q_{abs} difference is only from tunneling, this difference serves as a measure of the small mode of the cirrus PSD. These calculations are based on the optical property database given in Yang et al. (2005).

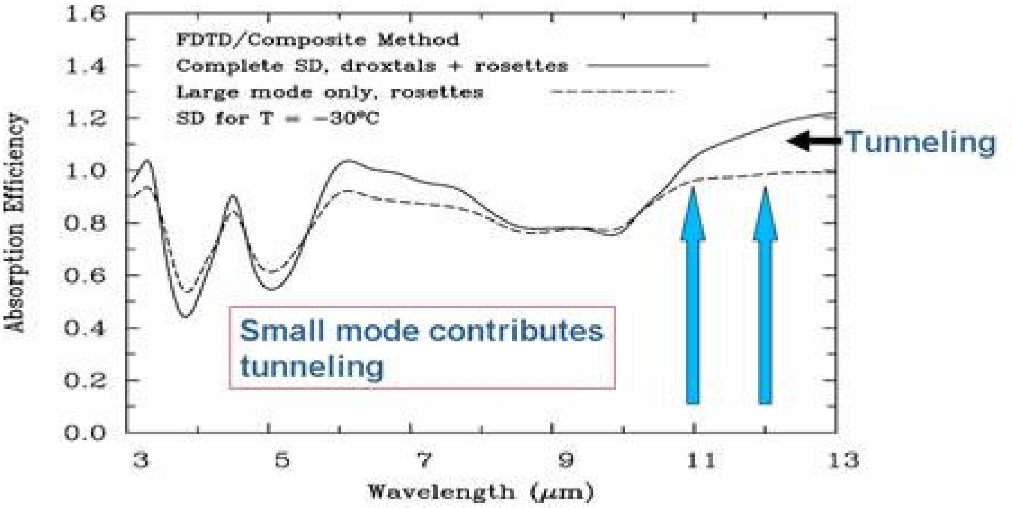

Figure 2: Absorption efficiencies (Q_{abs}) for a bimodal size distribution.

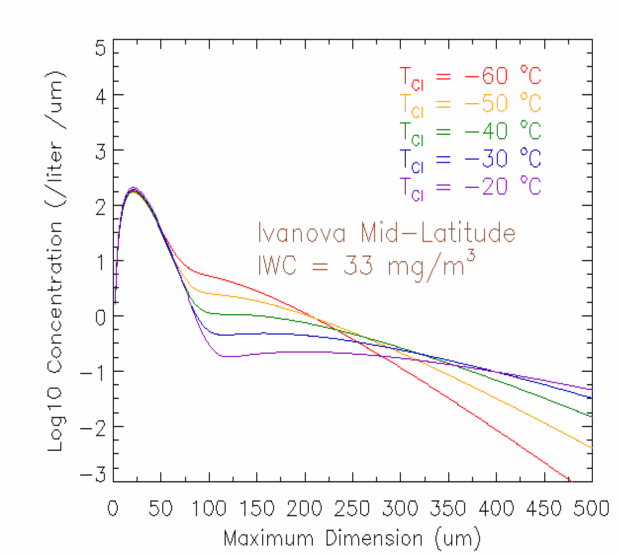

Figure 3. Examples of bimodal size distributions based on measurements from mid-latitude cirrus clouds (Ivanova et al. 2001).

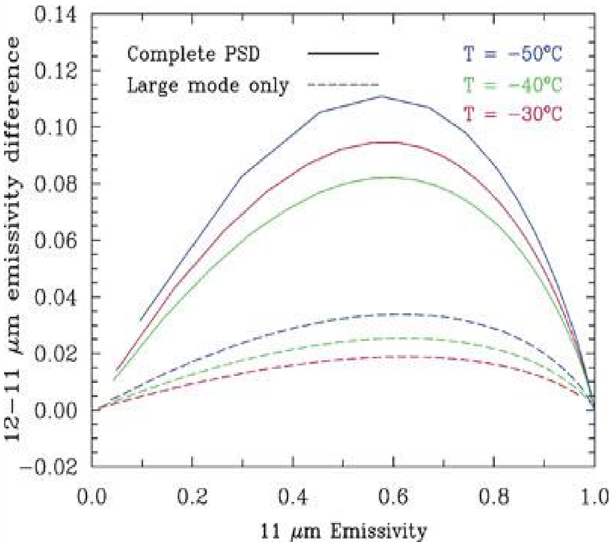

Figure 4. Theoretical curves denoting the large mode (dashed) and the complete PSD (solid) corresponding to 3 different temperatures.

3. ESTIMATING SMALL CRYSTAL CONCENTRATIONS

The small mode ice mass content can be estimated by the “arches” in Fig. 4 and also from the absorption optical depth ratio at 12 and 11 μm, referred to as β. Several studies have shown that β ≈ 1.08 for synoptic and anvil cirrus. The higher the small mode ice mass content (or ice crystal number concentration, N_{sm}), the higher the arches are. This principle is used to determine N_{sm} by matching theory with observations, as described below.

1. The first step is to begin with retrievals of cloud temperature and cloud emissivity (ε) at 11 and 12 μm wavelength channels from the ground based Atmospheric Emitted Radiance Interferometer (AERI), and from a corresponding sounding and cloud radar profile.
2. The cloud temperature can then be used to estimate PSD mean size (D) and dispersion for large and small mode. The difference between the solid and dashed curves results primarily from differences in the contribution of the small PSD mode to the ice water content (IWC). This also determines the effective diameter (D_{eff}). The dispersion parameter has little influence on the emissivities or emissivity differences.
3. Locate retrieved Δε (y-axis) and the 11 μm ε by (1) incrementing the modeled ice water path (IWP) to increase ε(11 μm) and (2) incrementing the small mode contribution to the cloud IWC, which elevates the curve.
4. If all IWC is in small mode and retrieved Δε and ε (11 μm) are still not located, then decrease small mode D to locate them.
5. If retrieved point lies below the “large mode only” curve (e.g. a dashed curve), then systematically increase D for large mode until a match is obtained. Negative Δε values correspond to maximum allowed D values.
6. This method retrieves IWP, $D_{eff,}$ and the small-to-large mode ice crystal concentration ratio. For a given IWC, it also estimates ice particle number concentration and the complete PSD, even when it is bimodal.

The modified anomalous diffraction approximation (MADA) was used to calculate ice and water cloud optical properties in this AERI retrieval algorithm since it couples explicitly with the cloud microphysics and its analytical formulation makes it computationally efficient (Mitchell et al. 2006; Mitchell 2000).

4. CASE STUDY ANALYSIS

The Ivanova et al. (2001) PSD scheme for mid-latitude synoptic cirrus was used in our retrieval algorithm, but soon we will replace this with a PSD scheme developed from M-PACE PSD data for ice clouds, based on ice water content (IWC) and temperature. Measurements made by the ground-based AERI are used to indicate the concentration of small ice crystals (D < 60 μm) relative to the larger ice particles.

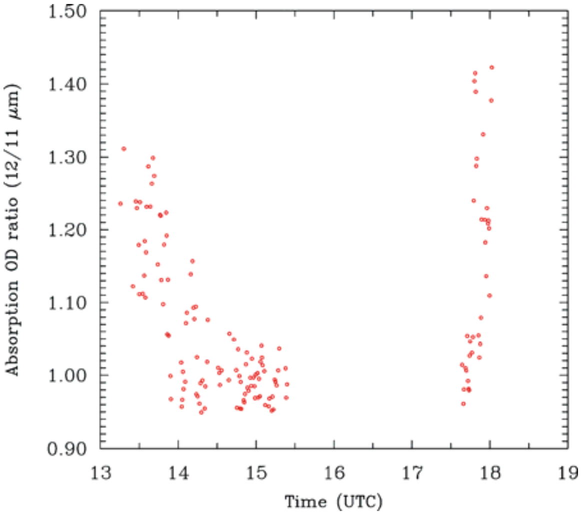

Figure 5: Ratio of the absorption optical depth between 12 μm and 11 μm as a function of hour of the day (UTC).

The absorption optical depth (AOD) of these clouds for three wavelengths (12.19 μm, 11.09 μm and 8.73 μm) are obtained from the AERI and the 12-to-11 μm AOD ratios are plotted in Fig. 5 above. Visible optical depth (OD) is less than 4.5 (to prevent emissivity saturation) and greater than 0.5. An AOD ratio above 1.1 suggests the presence of liquid water in the cloud (Giraud et al. 1997, 2001).

Figure 6 shows that the cloud temperature ranges between -27 °C and -39 ^{o}C. According to the homogeneous nucleation theory, super cooled water may be present along with ice in clouds at temperatures above -36 ^{o}C. This is supported by AERI AOD values that are higher than 1.1 (Fig. 5).

Combining the small crystal information (from AERI radiances) with the PSD scheme describing the larger particle concentrations yields the retrieved PSD. The products from this AERI retrieval scheme are the PSD and ice particle number concentration for a given IWC, as well as the ice water path, effective diameter and the ratio of the small mode-to-large mode number concentration. However this presumes that the cloud does not contain significant amounts of liquid water.

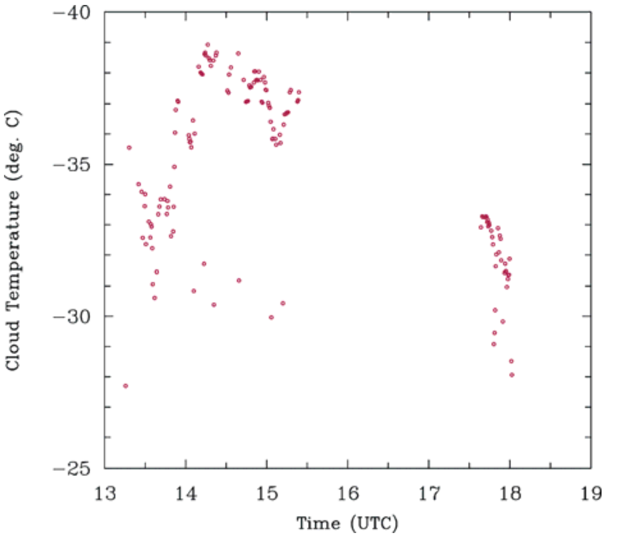

Figure 6: Plot of the cloud temperature in (deg. C) versus the hour of the day in UTC.

As noted, the AOD ratios in Fig. 5 and the radiance-weighted cloud temperatures in Fig. 6 suggest the presence of liquid water in the cirrus. In addition, recent findings shown on our website, http://www.dri.edu/Projects/Mitchell/ , indicate that the cirrus PSD is either monomodal or weakly bimodal (based on applying our retrieval algorithm to several published remote sensing studies, as well as a case study we recently analyzed). Therefore we have modified our retrieval algorithm to interpret all condensate in the small mode as liquid water. The small mode mean diameter, D_{sm}, and the dispersion parameter were assumed to be 7 μm and 9, respectively, which may be representative of droplet spectra in mixed phase conditions. Unfortunately, the cloud retrievals are sensitive to what one assumes for D_{sm}, and this is the major limitation of this retrieval method. For example, increasing D_{sm} from 7 to 10 μm

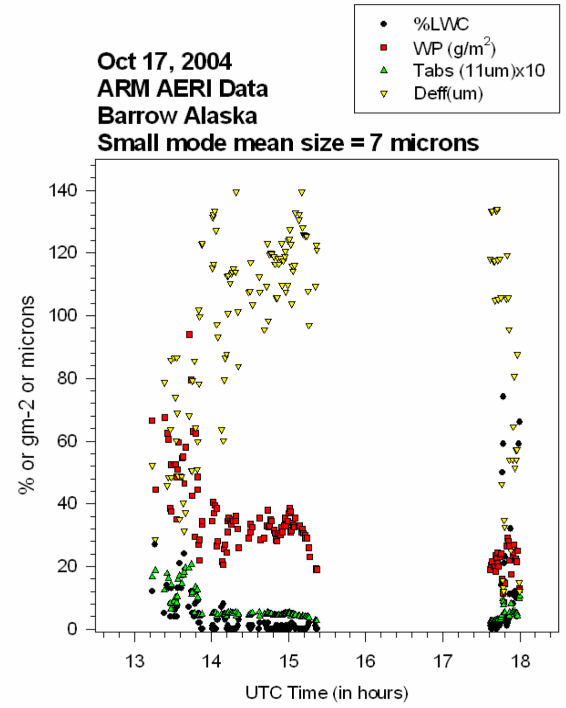

Figure 7: Retrieval results for M-PACE case study of 17 Oct. 2004.

can increase the retrieved percent liquid water content (LWC) by a factor of 3 and decrease the retrieved water path (WP) and D_{eff} by 40% and 32%, respectively.

Results from this analysis are shown in Fig. 7 for the M-PACE cirrus case study of 17 Oct. 2004. T_{abs} in Fig. 7 is the absorption optical depth at 11 μm multiplied by a factor of 10. Consistent with Figs. 5 and 6, the percentage of liquid condensate is significant from 13 to 14.2 UTC and from 17.6 to 18 UTC. If the mean cloud droplet size was assumed to be 5 μm instead of 7 μm, the %LWC would not exceed 26%. The effective diameter, D_{eff}, is for both liquid and ice fractions combined. Therefore D_{eff} is largest between 14.2 and 15.4 UTC when the cloud is glaciated (LWC is negligible), and these D_{eff} values are typical of the ice phase in general for this case study. At least over this time period, AERI radiances indicate the PSD is generally monomodal with ice particle concentrations of about 4 – 7 liter^{-1} when the IWC = 10 mg m^{-3} (see Fig. 8). For other time periods having significant liquid water, the cloud droplet number concentration N_d can exceed 30 cm^{-3}. When we changed the algorithm to assume the small mode is comprised of ice crystals (based on Ivanova et al. 2001) instead of cloud droplets, N_{ice} ranged from about 1 to 10 cm^{-3} in the regions where the AOD ratio exceeds 1.08. It seems unlikely that N_{ice} would change so abruptly, making the mixed phase explanation most reasonable. T_{abs} in Fig. 7 is minimum between 14.2 and 15.4 UTC, which corresponds to glaciated cloud conditions, lower N and larger D_{eff}.

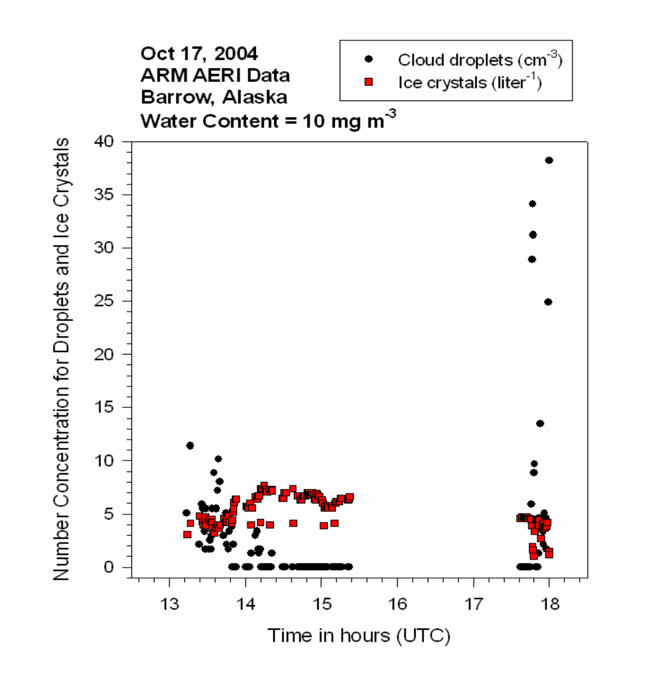

Figure 8. Retrieved cloud droplet and ice crystal number concentrations assuming a total water content (ice + liquid) of 10 mg m^{-3}.

Finally, Fig. 9 shows lidar depolarization ratios and Millimeter Cloud Radar (MMCR) backscatter for this case study. The high depolarization ratios indicate the dominance of the ice phase, and the MMCR backscatter provides more detail on cloud structure and position. Since we only used AERI data having visible OD between 0.5 and 4.5, the cirrus between 15.4 and 17.6 UTC was not included in this analysis. Note that the low patch of cloud near 18 UTC could be responsible for the higher percent LWC in Fig. 7.

The physics responsible for the differences in AOD at 12 and 11 μm are different for liquid water than for ice. Whereas tunneling produces the AOD differences in small mode ice crystals, the role of tunneling is relatively minor in water droplets since the real refractive index is similar for water at these wavelengths. For

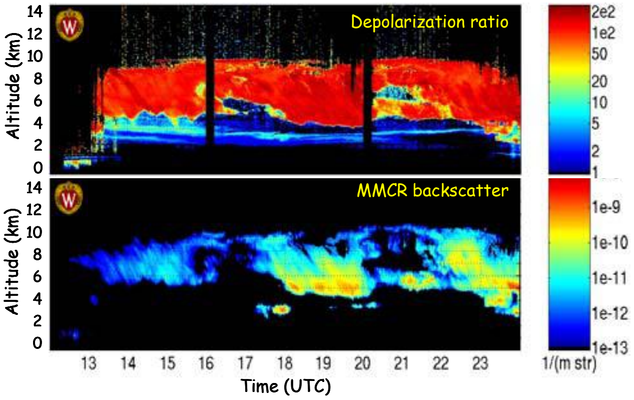

Figure 9. Lidar depolarization ratios and MMCR backscatter for the M-PACE 17 October case study at Barrow, Alaska, courtesy of Ed Eloranta (Univ. of Madison, WI).

cloud droplets, it is the transition from area dependent absorption to mass dependent absorption (as droplet size decreases for D < 10 μm) that causes the sudden changes in AOD ratio (see Mitchell and Arnott 1994 for a discussion of area and mass dependent absorption). This is why the retrieval algorithm is so sensitive to D_{sm}.

5. CONCLUDING REMARKS

By applying the principle of photon tunneling or wave resonance to radiances at 11 and 12 μm, we have found in previous work that the cirrus PSD tends to be monomodal or weakly bimodal, allowing us to infer that the small mode of the retrieved PSD, when present, is mainly comprised of liquid water. When the LWC was negligible, the retrieved ice particle concentrations appear consistent with known ice nucleation processes.

Acknowledgment: This research was sponsored by the Office of Science (BER), U.S. Dept. of Energy, Grant No. DE-FG02-06ER64201.

BIBLIOGRAPHY

- Giraud, V., O. Thouron, J. Riedi, and P. Goloub, 2001: Analysis of direct comparison of cloud top temperature and infrared split window signature against independant retrievals of cloud thermodynamic phase. *Geophys. Res. Let.*, **28**, 983-986.

- Giraud, V., J.C. Buriez, Y. Fouquart, and F. Parol, 1997: Large-Scale Analysis of Cirrus Clouds from AVHRR Date: Assessment of Both a Microphysical Index and the Cloud-Top Temperature. *J. Appl. Met.*, **36**, 664-674.

- Ivanova, D., D.L. Mitchell, W.P. Arnott and M. Poellot, 2001: A GCM parameterization for bimodal size spectra and ice mass removal rates in mid-latitude cirrus clouds. Atmos. Res., **59**, 89-113.

- Mitchell, D.L., and W.P. Arnott, 1994: A model predicting the evolution of ice particle size spectra and radiative properties of cirrus clouds. Part II: Dependence of absorption and extinction on ice crystal morphology. J. Atmos. Sci., **51**, 817-832.

- Mitchell, D.L., 2000: Parameterization of the Mie extinction and absorption coefficients for water clouds. J. Atmos. Sci., **57**, 1311-1326.

- Mitchell, D.L., A.J. Baran, W.P. Arnott and C. Schmitt, 2006: Testing and comparing the modified anomalous diffraction approximation. *J. Atmos. Sci.*, **63**, 2948-2962.

- Yang, P., H. Wei, H-L. Huang, B.A. Baum, Y.X. Hu, G.W. Kattawar, M.I. Mishchenko, and Q. Fu, 2005: Scattering and absorption property database for nonspherical ice particles in the near- through far-infrared spectral region. *Appl. Opt.*, **44**, 5512–5523.

MOLECULAR DYNAMICS SIMULATIONS OF CIRRUS-LIKE ICE CRYSTAL GROWTH AND SUBLIMATION

Erin Nugent[1], Steven Neshyba[1], Pavel Jungwirth[2]
[1]University of Puget Sound, Tacoma, Washington, USA
[2]Institute of Organic Chemistry and Biochemistry, Academy of Sciences of the Czech Republic

1. INTRODUCTION

Of particular interest (and controversy) in theories of vapor-deposited ice crystal growth is the vapor deposition coefficient, α, defined here as the fraction of incident vapor molecules in excess of equilibrium that contribute to ice growth. The value of α plays a significant role in several contexts of atmospheric interest. For example, very small values ($\alpha \approx 0.001$) have been used to explain in-situ observations of large ambient supersaturations and large concentrations of small crystals in cirrus clouds[1]. Other experiments[2] point to values of α close to the opposite extreme, $\alpha \approx 1$.

Nucleation theory offers one way of understanding processes that influence α in a facet-dependent way. In this picture,[3,4] adsorbed water molecules forming a quasi-liquid layer at the ice-vapor interface diffuse over that surface until either they find a nucleation site, or are ejected once again into the vapor phase. The molecular mechanisms of such processes, however, are still poorly understood.

Molecular dynamics simulations offer a way to gain insight into the molecular processes associated with α. As a step in that direction, we focus on assessing the equilibrium vapor pressure associated with rigid water molecules interacting via the NE6 intermolecular potential[5] at 250 K. We construct a constant-volume, constant-temperature model in which a slab of ice consisting of 1280 molecules is located next to an evacuated part of the simulation volume (figure 1). The lateral (x-y) dimensions of the model are 3.6x3.1 nm, with periodic boundary conditions designed to simulate infinite lateral extent. In the z-direction, the unit cell consists of ten layers. Periodic boundary conditions in the z-coordinate ensure that molecules ejected from one ice-vapor interface are captured within a few picoseconds by the other ice-vapor interface. The model therefore enforces quasi-equilibrium between the ice and vapor phases. By counting the number of ejections we are able to infer a vapor pressure, which we interpret as the equilibrium vapor pressure of the slab.

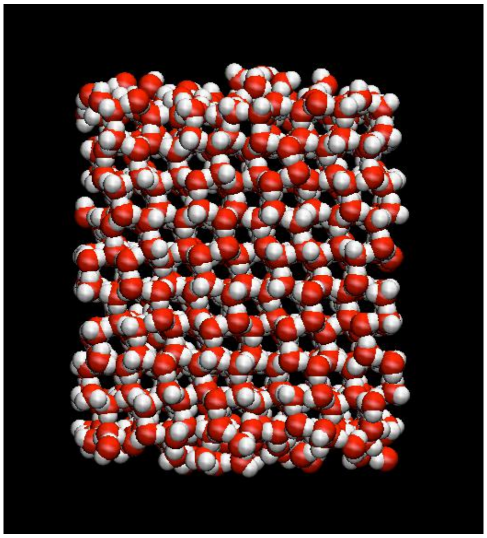

Figure 1. Lateral view of the ice slab. Quasiliquid layers (each consisting of O and O*, as defined in the text) are visible at the top and bottom of the figure.

2. THE QUASI-LIQUID LAYER

The quasi-liquid layer (QLL) that forms at the ice-vapor interface of real ice at 250 K is known to be 1-2 nm thick (i.e., a few layers).[6] Since this layer is likely to dominate surface-vapor exchange, it is important to characterize the QLL that occurs in the model. Figure 1 suggests that the model does develop a QLL, evidenced qualitatively as a reduction in the order of the outermost (top and bottom) layers. Beginning a simulation with perfectly crystalline ice, we find that the QLL develops fully in 2-3 ns of simulation time.

Quantifying the thickness of the QLL is criterion-dependent, but we can arrive at a reasonable estimate by examining density profiles, i.e., laterally integrated profiles of oxygen atom z-coordinates. The upper panel of figure 2 displays the density profile of a 10 ns simulation, summed over all 1280 oxygen atoms in the slab. Bilayer structure is evident in all ten layers. The bottom outermost surface, between 1.5 and 2 nm, consists of a degraded bilayer (labeled "O") and an additional, small layer extending farther into the vapor phase (labeled O*); similar structure is evident in the top outermost surface, between 5 and 5.5 nm.

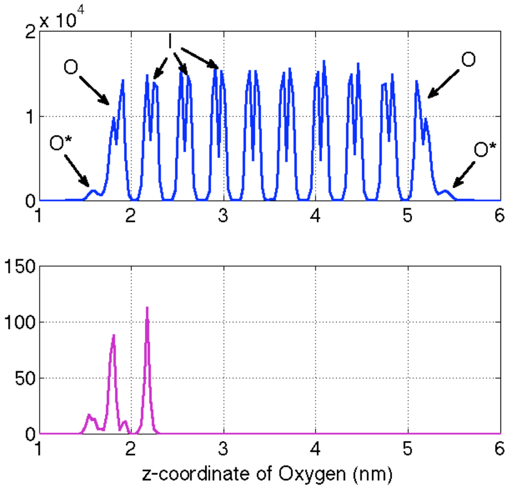

Figure 2. Density profiles of the z-coordinate of the Oxygen atom in a 10 ns simulation. Upper panel: all atoms. Layers "O*" and "O" are the outermost layers. There are eight inner layers, called "I" (three are marked). Lower panel: profile for a single oxygen atom in the QLL.

Tracking individual molecules, we find that $H_2O(I) \leftrightarrow H_2O(O)$ transitions occur rarely; the molecule shown in the lower panel of figure 2 is an exception. We interpret these results as suggesting that the QLL consists of the O and O* layers, and perhaps a small fraction of the first inner (I) layer. This implies a QLL thickness of 0.4-0.8 nm, slightly smaller than experimental values.

By integrating the areas of the peaks in the top panel of figure 2 corresponding to O* and O, we arrive at a free energy difference of $\Delta G°=6$ kJ/mol for $H_2O(O) \rightarrow H_2O(O^*)$.

In an effort to characterize the kinetics of exchange between layers O and O*, we examined z-coordinate trajectories of individual molecules in the QLL. One such trajectory is shown in figure 3. It is evident from trajectories such as these that the residence time for a molecule in O* is on the order of 100s of ps.

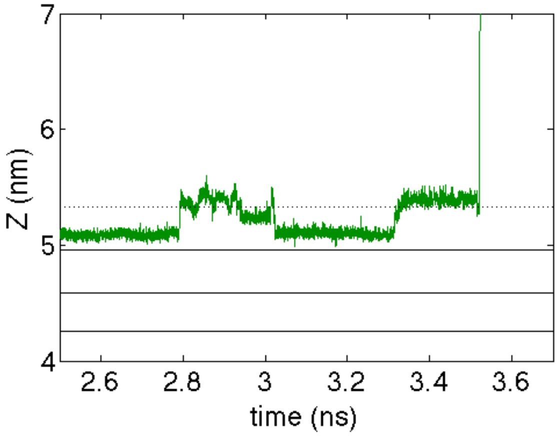

Figure 3. Z-coordinate trajectory of a molecule exhibiting three $H_2O(O) \leftrightarrow H_2O(O^*)$ transitions before leaving the surface at 3.5 ns. The boundary between O* and O is indicated by a dashed line.

3. VAPORIZATION FROM THE QLL

We have thus far analyzed trajectories spanning a total of 17.5 ps. Because this is too little time to achieve statistically meaningful results, the results we report here are preliminary. A total of six vaporization events were observed, corresponding to a departure rate of $3x10^{25}$ molecules/second/meter^2. The equivalent vapor pressure is obtained by

$$P = 2 \times Rate \times \sqrt{2kT\pi m} = 400\,Pa \qquad (1)$$

where T=250 K, m is the mass of a water molecule, and the factor of 2 comes from the presence of two ice-vapor interfaces in the model. The equilibrium vapor pressure of real ice at 250 K is much smaller, 77 Pa (assuming Clausius-Clapeyron behavior and ΔH_{sub}= 51 kJ/mol[7]). A vapor pressure of 400 Pa corresponds to that of real ice at 268 K.

We are unable at the present time to judge whether the above disagreement is due to statistical fluctuation, or to some underlying fault in the model. Nevertheless, some investigation into the molecular mechanism of vaporization is informative. Layers O*, O, and I have significantly different vertical binding energies (Table 1).

Table 1. Vertical binding energies (kJ/mol)

H_2O(I)	88
H_2O(O)	71
H_2O(O*)	43

The low binding energy of O* suggests that molecules in that layer will be most likely to evaporate. Detailed examination of z-coordinate trajectories of the six departing molecules confirms this hypothesis: prior to departing, each of the six molecules that departed did so from the O* layer, having spent 30-300 ps continuously in that layer immediately prior. For comparison, the energetic thermalization time for molecules entering the QLL from the vapor phase is ~3 ps.

4. REFERENCES

1. Gierens, K. M., M. Monier, and J-F. Gayet (2003), *J. Geophys. Res., 108(D2),* 4069, doi:10.1029/2001JD001558.
2. Haynes, D. R., N. J. Tro, and S. M. George (1992), *J. Phys. Chem., 96,* 8502-8509.
3. Libbrecht, K. G. (2003), *J. Crystal Growth*, *258*,168-175.
4. Wood, S. E., M. B. Baker, and D. Calhoun (2001), *J. Geophys. Res., 106,* 4845-4870.
5. Nada, H., and J. P. van der Eerden (2003), *J. Chem. Phys., 118*, 7401.
6. Doppenschmidt, A., and H-J. Butt (2000), *Langmuir, 16*, 6709-6714.
7. Murphy, D. M., and T. Koop (2005), *Q. J. R. Meteorol. Soc.*, *131,* 1539-1565.

BALLOONBORNE OBSERVATION OF CIRRUS CLOUD PARTICLES AND AEROSOLS MEASURED WITH HYDROMETEOR VIDEOSONDE, SNOW WHITE HYGROMETER, AND OPTICAL PARTICLE COUNTER

Narihiro Orikasa, Tetsu Sakai, Masataka Murakami, Atsushi Saito, Takuya Tajiri,
Katsuya Yamashita, and Tomohiro Nagai
Meteorological Research Institute, Tsukuba, Ibaraki, Japan

1. INTRODUCTION

It is well known that cirrus clouds play a significant role in regulating the radiation balance of earth-atmosphere system. However they have been identified as one of the major uncertain components on earth's climate system.

The ice nucleation process in cirrus clouds is one of the most important and fundamental issues required for better understanding of their formation and maintenance mechanisms. In order to examine the relationships between ice crystals and aerosols in cirrus, it is highly desirable to provide unique combination of instrumentation for in-situ simultaneous microphysical measurements.

We have developed the balloonborne observation system for in-situ measurements of cirrus cloud particles and aerosols, using a hydrometeor videosonde (HYVIS) and an optical particle counter (OPC) together with a Snow White (SW) hygrometer, attached to the same balloon. The motivation of this study is to examine how Asian mineral dust particles are relevant to ice formation in cirrus clouds. Two launches were conducted at Tsukuba (36.06°N, 140.13°E, 25 m), Japan, in the May of 2007. Concurrently, the Raman lidar at the Meteorological Research Institute (MRI) was also used to measure vertical distributions of the aerosols and cloud particles as well as the water vapor mixing ratio.

The purpose of this paper is to analyze microphysical properties in cirrus clouds measured with the HYVIS and SW. Detailed analysis on aerosol characteristics will be provided in a companion paper that utilizes the OPC data with the Raman lidar data.

2. INSTRUMENTATION

The HYVIS (Murakami and Matsuo 1990; Orikasa and Murakami 1997) has two video cameras with different magnifications (close-up and microscopic cameras) to take pictures of cloud particles larger than about 7 μm. After the launch of the HYVIS (typical ascent rate of about 5 m s^{-1}), the particle images are transmitted via a 1687 MHz microwave to a ground receiving station in real time.

In the present study, cirrus particles from the HYVIS imagery were classified into several habit categories by the human eye: column, bullet, plate, side plane, bullet rosette, and aggregation (combination) of column and plate. Particle images were analyzed by image processing software to obtain several parameters such as maximum dimension, perimeter, area, and aspect ratio.

The OPC provides particle number counts in 8 channels whose detection limit ranges from 0.15 to 3.5 μm in radius, assuming spherical particles with the refractive index of 1.4 (Hayashi et al. 1998; Iwasaki et al. 2007).

The SW (Meteolabor AG) sensor is a

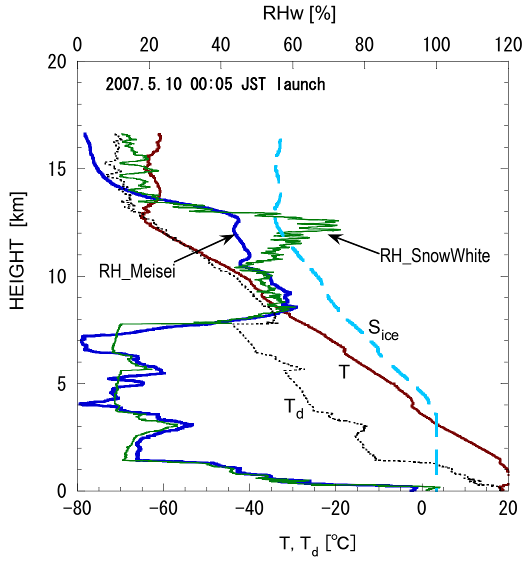

Fig. 1 Vertical profiles of ambient temperature, frost-point temperature, relative humidities with respect to water, and ice-saturation curve measured by the Snow White sensor and the Meisei RS-01G radiosonde launched at Tsukuba on 10 May 2007.

chilled-mirror hygrometer which measures the dewpoint or frost-point temperature during a flight (Fujiwara et al. 2003). We used a "day" type of SW whose sensor housing and radiator were enclosed in a Styrofoam box.

The RS-01G (Meisei Electric Co., Ltd.) is a radiosonde that collects meteorological data and that transmits data of various sensors to the ground station. In practice we used two units of RS-01G, because it was impossible for only one unit to serve for all transmission of meteorological data, the SW signals, and the OPC signals. The relative humidity is measured with the thin-film capacitive sensor.

The Raman lidar used in this study was developed by the MRI. The lidar system and the data analysis procedure are described in detail in Sakai et al. (2003). The lidar employs a Nd:YAG laser (wavelength of 532 nm) with 300–600 mJ at a pulse repetition frequency of 30 Hz.

3. SYNOPTIC FEATURES AND SOUNDING

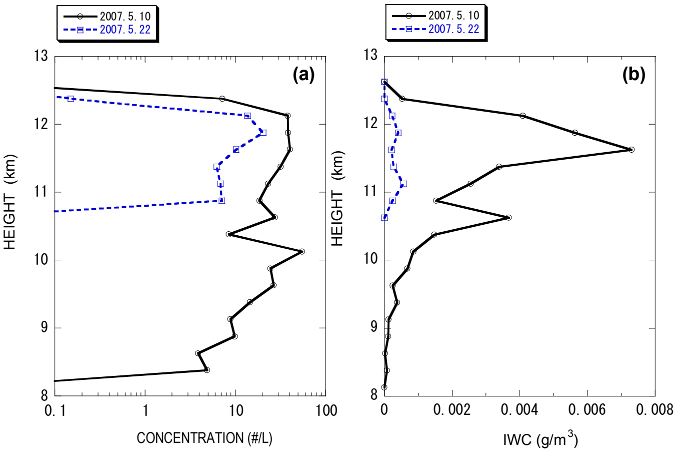

Fig. 2 Vertical profiles of (a) ice crystal number concentrations and (b) IWC measured with the HYVIS in two cases: May 10 (solid) and May 22 (dashed). A data point indicates an averaged value over 250-m-thick cloud layers.

Two sets of sondes were launched from Tsukuba: at 0005 JST (Japan Standard Time, UTC + 9 hours) on 10 May 2007 and at 0002 JST on 22 May 2007. The set included the HYVIS, the OPC, the SW, and two RS-01G sondes.

Figure 1 shows the vertical sounding measured with the radiosonde at the observation site on 10 May 2007. Ice particles measured with the HYVIS were located from –33°C (altitude: 8.4 km) to –63°C (12.5 km). In the cloud layers, the humidity was well below ice saturation according to the measurements of the RS-01G capacitive sensor. As described by Fujiwara et al. (2003), we determined which the SW measured dewpoint or frost point based on the housekeeping data.

On 9 May 2007, the developing low pressure system was approaching from the west. At the first launch time, cirrus clouds were covered all over the site with no low-level or mid-level intervening clouds, and the center of the cyclone was about 1,000 km west of the site.

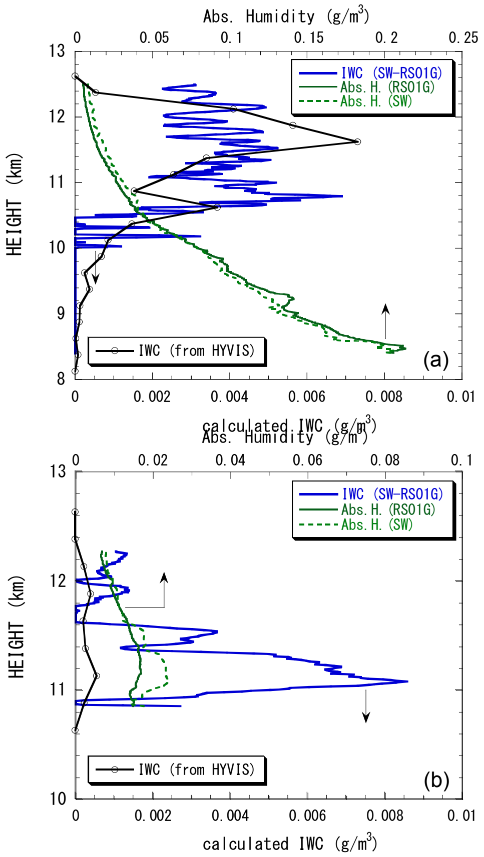

Fig. 3 Comparison of IWC profiles from the HYVIS with the profile of differences in absolute humidity derived from the two humidity sensors (SW – RS01G) in the two cases of (a) May 10 and (b) May 22.

The case of 22 May 2007 was thinner cirrus clouds, where ice particles were located from –50°C (10.9 km) to –62°C (12.3 km) and well below ice saturation (figure not shown). On 21 May 2007, the high pressure passed over the site and moved on eastward. The band of clouds associated with an upper trough moved south-eastward near the second launch time. As opposed to the first case, stratocumulus (spread over more than half of the sky) coexisted with cirrus covered all over the site.

4. RESULTS

Figure 2 shows the vertical distributions of the number concentration of ice particles and the ice water content (IWC) in two cases. They were analyzed from the particle imagery of the HYVIS and were based on the combined size distributions from close-up and microscopic images. The data point in Fig. 2 indicated an averaged value over 250-m-thick cloud layers. The number concentrations were on the order of 10s per liter in both cases, although the second (May 22) case had relatively low concentrations. The IWC had a peak of about 0.007 g m^{-3} near the cloud top in the first case, whereas there had no significant peak in the second case.

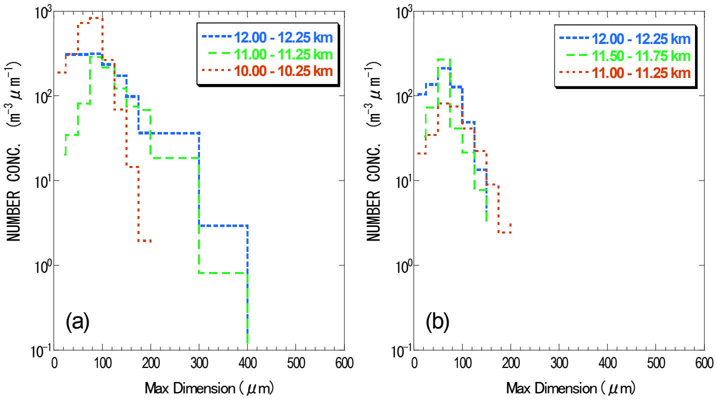

Fig. 4 Vertical evolution of ice particle size distributions from the HYVIS measurements in the two cases of (a) May 10 and (b) May 22.

Figure 3 presents the comparison of IWC profiles from the HYVIS with the profile of differences in absolute humidity derived from the two humidity sensors (SW and RS-01G). In Fig. 3a, both profiles were found to agree well with each other. This result is reasonable since the SW sensor should make total water measurements (Fujiwara et al. 2003). However the absolute humidity in Fig. 3b from the humidity sensors overestimated the IWC measured with the HYVIS. The SW hygrometer of the "day" type can be more sensitive for water vapor outgassing problem followed by particle contamination (via raindrops and/or cloud droplets) than the

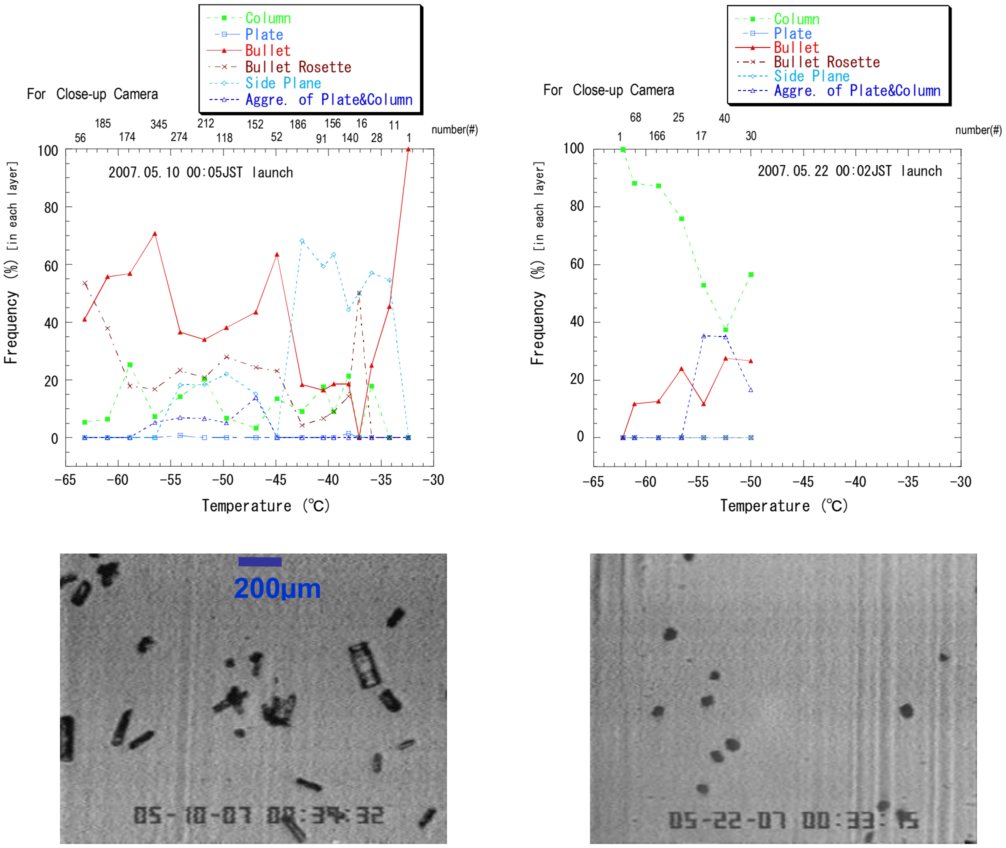

Fig. 5 Relative frequency of ice crystal habits vs ambient temperature (upper panel) and a sample of microscopic images from the HYVIS (lower panel) in two cases (left: May 10; right: May 22). The frequency of habit occurrence was normalized in each layer (~50-m thickness). The values in the upper panel indicate the number of ice particles detected in each layer.

"night" type because of the Styrofoam box with a duct for sensor housing. In the second case, there were significant amount of stratocumulus (water) clouds in lower level during the flight, so the above problems might seriously affect the humidity from the SW in the upper troposphere (in relatively low water vapor conditions).

The vertical evolution of the ice crystal size distributions measured with the HYVIS is shown in Fig. 4. In the first case, upper and middle layer of the clouds contained large particles (~400 μm) and lower clouds had particles smaller than 200 μm. On the other hand, size distributions did not change markedly over the whole layers in the second case.

Figure 5 shows the relative frequency of ice crystal habits as a function of ambient temperature, together with a sample of microscopic images in both cases; the frequency was normalized in each layer (~50-m thickness). The most dominant crystal type was bullet in the first case and column in the second case. In the first case, it was found from Fig. 5a that there was a shift in crystal habits from side plane to bullet (and bullet rosette) in the temperature ranges of –40° to –45°C.

5. CONCLUSIONS

At Tsukuba in Japan, we successfully conducted the balloonborne measurements of cirrus particles and aerosols using the HYVIS, the OPC, and the SW instruments. Two cases (on 10 and 22 May 2007) of data were presented in this paper.

The first (May 10) case had a peak of IWC (~0.007 g m^{-3}) near the cloud top, whereas the second (May 22) case had no clear peak of IWC. The cloud thickness was thinner in the second case (~1.5 km vs ~4 km). In both cases ice clouds were located well below the ice saturation in all levels.

In the first case there was a shift in dominant crystal habit occurrence from side plane to bullet (and bullet rosette) near the temperature of about –40°C. The result was consistent with recent laboratory studies (e.g., Bailey and Hallett 2004).

The IWC profile from the HYVIS was found to agree well with the profile in absolute humidity derived from the two humidity sensors (the Meteolabor SW and the Meisei RS-01G) in the first case. However, large gap in two profiles was found in the second case, which could be explained by the water vapor contamination and outgassing problems, caused by lower-level intervening clouds and enclosed Styrofoam box for sensor housing.

Those results combined with the OPC and the lidar measurements will help better understanding the microphysical and optical properties of cirrus clouds.

Acknowledgments

We gratefully acknowledge the staff of the Aerological Observatory for their help and cooperation in the balloon observation. We also thank Drs. Masatomo Fujiwara and Nawo Eguchi for helpful discussions about the Snow White hygrometer measurements and the data analysis. This study was partly supported by a grant from the Ministry of Education, Culture, Sports, Science and Technology of Japan.

REFERENCES

Bailey, M., and J. Hallett, 2004: Growth rates and habits of ice crystals between -20° and -70°C. *J. Atmos. Sci.*, **61**, 514-544.

Fujiwara, M., M. Shiotani, F. Hasebe, H. Vömel, S. J. Oltmans, P. W. Ruppert, T. Horinouchi, and T. Tsuda, 2003: Performance of the Meteolabor “Snow White” chilled-mirror hygrometer in the tropical troposphere: Comparisons with the Vaisala RS80 A/H-Humicap sensors. *J. Atmos. Oceanic Technol.*, **20**, 1534-1542.

Hayashi, M., and Coauthors, 1998: Size and number concentration of liquid PSCs: Balloon-borne measurements at Ny-Alesund, Norway in winter of 1994/95. *J. Meteor. Soc. Japan*, **76**, 549-560.

Iwasaki, S., and Coauthors, 2007: Characteristics of aerosol and cloud particle size distributions in the tropical tropopause layer measured with optical particle counter and lidar. *Atmos. Chem. Phys.*, **7**, 3507-3518.

Murakami, M., and T. Matsuo, 1990: Development of the hydrometeor videosonde. *J. Atmos. Oceanic Technol.*, **7**, 613-620.

Orikasa, N., and M. Murakami, 1997: A new version of hydrometeor videosonde for cirrus cloud observations. *J. Meteor. Soc. Japan*, **75**, 1033-1039.

Sakai, T., T. Nagai, M. Nakazato, Y. Mano, and T. Matsumura, 2003: Ice clouds and Asian dust studied with lidar measurements of particle extinction-to-backscatter ratio, particle depolarization, and water vapor mixing ratio over Tsukuba. *Appl. Opt.*, **42**, 7103-7116.

A SENSITIVITY STUDY ON LINEAR-CONTRAIL RADIATIVE FORCING

R. Rodríguez De León (1), D. S. Lee (1), Martina Krämer (2), J. C. Thelen (3)
(1)Centre for Air Transport and the Environment, Dalton Research Institute, Department of Environmental and Geographical Sciences, Manchester Metropolitan University, UK
(2)Institut für Chemie und Dynamik der Geosphäre I: Stratosphäre Forschungszentrum, Jülich, Germany
(3)Met Office, Exeter, UK.

1. ABSTRACT

We have derived a parameterization of the radiative forcing that may arise from persistent linear contrails as a function of their temperature. In order to produce representative micro-physical properties for persistent contrails, we have made use of cirrus ice water content (IWC) climatological data and middle latitude cirrus size distributions. This approach is based on the assumption that, despite their anthropogenic origin, the micro-physics of persistent contrails depends mainly on the atmosphere in which they develop.

We have assessed the impact of the observed wide variability of ice crystal shape, size and concentration on the optical properties of persistent-contrails was assessed, showing that IWC is the most significant factor for determining contrail radiative forcing.

2. INTRODUCTION

Persistent, line-shaped contrails induced by air traffic have been estimated to cover, on average, about 0.1% of the Earth's surface (IPCC, 1992). However, under favourable conditions of temperature and humidity conditions, these contrails can expand in their vertical and horizontal extent to become contrail-cirrus, potentially increasing their influence on the planet's radiative balance (IPCC, 1999). The best estimate of the global mean radiative forcing due to line-shaped contrails presented in the Special Report on Aviation IPCC (1999) for the year 1992 was +0.020 Wm^{-2}, but later studies (e.g. Marquart *et al.*, 2003; Fichter *et al.*, 2005; Stuber and Forster, 2006) have lowered this value by almost a factor of 10. The current IPCC best estimate (Table 2.9; Sausen *et al.*, 2005) for the radiative forcing of persistent linear contrails for aircraft operations in 2000 is +0.010 Wm^{-2}.

The large variability in particle concentration, size and shape observed in ice clouds complicates the calculation of their radiative properties and contributes to the large discrepancies between the estimates reported in the studies cited above.

Most radiative applications use two parameters to characterize ice clouds, i.e. IWC and a metric of the particle size spectrum, commonly the effective radius r_e. This two-parameter representation neglects the dependence of the radiative properties on the shape of the size distribution (De Leon and Haigh, 2007 and references therein) but requires accurate retrievals of the relative concentration of small and large crystals. It has recently been recognized that *in situ* measurements of cirrus particle concentrations may be severely biased by large ice particles shattering on probe inlets (Heymsfield, 2007), thereby overestimating the number concentration of small particles and contributing to the uncertainties about ice clouds' global radiative impact.

No representative statistics about contrail micro-physical evolution are available to date. For this reason it seems sensible, as a first approximation, to assume that the properties of persistent contrails will not be significantly different from those of natural cirrus under the same atmospheric conditions. We followed this approach in the present study although further research is needed to validate this assumption. Donovan (2003) developed a parameterization of cirrus size distributions based on five months of lidar/radar data retrieved in the Southern Great Plains site in Oklahoma, USA. The effective radius in Donovan's parameterization is treated as a function of temperature and IWC. These two variables have been correlated for tropical, middle and high latitudes by Schiller *et al.*, based on an extensive set of airborne field experiments. By combining the parameterizations produced by Schiller *et al.*, and Donovan, the microphysical properties of persistent contrails can be completely defined in terms of their temperature alone.

We recognize the fact that temperature is not the only variable determining the microphysical properties of ice clouds, but this one-variable approach allows a more transparent sensitivity analysis.

3. MODEL SETUP

We used the Edwards-Slingo (E-S) radiative transfer code (Edwards and Slingo, 1996). The optical properties of the contrail in the shortwave and longwave were represented using the parameterizations described in Fu *et al.* (1998) and Fu (1996) respectively, assuming randomly oriented hexagonal ice crystals in the reference case. In the shortwave we varied the solar zenith angle in steps of 5° to obtain daily averages. The size of the contrail particles was allowed to vary with the temperature and the IWC. The reference configuration uses a 100% contrail cover with a 200 m physical depth in an otherwise clear atmosphere. The altitude of the contrail was chosen as that of the layer with the maximum zonally averaged contrail cover at tropical, middle and high latitudes (see Table 1). Two layers were used in the high latitude winter case to allow for the presence of a second maximum at a lower altitude.

Latitude(°)	Altitude (km) Winter	Temperature (K) Winter	Altitude (km) Summer	Temperature (K) Summer
60-90 High latitude	11.0, 6.5	215.3, 233.3	10.0	232.2
30-60 Mid latitude	10.0	221.9	10.0	241.3
0-30 Tropics	11.0	241.3	11.0	240.8

Table 1. Contrail altitude and temperature used in the calculations.

The radiative properties of a contrail depend on its microphysics, height, and structure as well as on the surface albedo and the ambient temperature and humidity profiles. In order to represent the seasonal dependence of these variables and their impact on the contrail's radiative forcing, our calculations were performed using January and July as representative months, based on 30 years of ECMWF zonal averages in 5° increments of latitude. Mean global contrail coverage distributions were used for the same months. For simplicity only three values were used, defining continental, oceanic, and ice-covered surface albedos (0.2, 0.05, 0.7, respectively). Hexagonal crystals were assumed in the reference case, but spheres were also used in order to assess the sensitivity to the particle shape. The optical properties of randomly oriented hexagonal cylinders were taken from the Baran *et al.* (2002) database in the longwave and from that of Yang *et al.* (2000) in the shortwave.

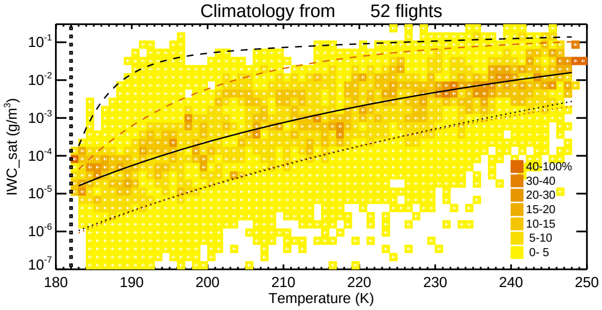

Fig. 1. Frecuency of IWC observed during 52 flights. The maximum, mean and minimum fits are shown by dashed, solid and dotted black lines respectively. The red lines correspond to the maximum and minimum fits in which the values with a frequency less than 5% were excluded.

The IWC and the effective size of the contrail were allowed to vary with temperature following Schiller *et al.*'s climatology of cirrus IWC and Donovan's (2003) effective radius parameterization. Schiller *et al.'s* parameterization is based on

IWCs measured *in situ* during 52 flights in tropical, middle and high latitudes. Figure 1 shows the frequency of IWCs at different temperatures with interpolation curves for the maximum, mean and minimum values (dashed, solid and dotted black lines respectively). In order to reduce the range between the minimum and maximum values, without losing their representativeness, new interpolation curves were calculated excluding the values with a frequency less than 5%. The fits of the maximum and the minimum for these core measurements are shown respectively by the dashed and dotted red lines in Fig. 1.

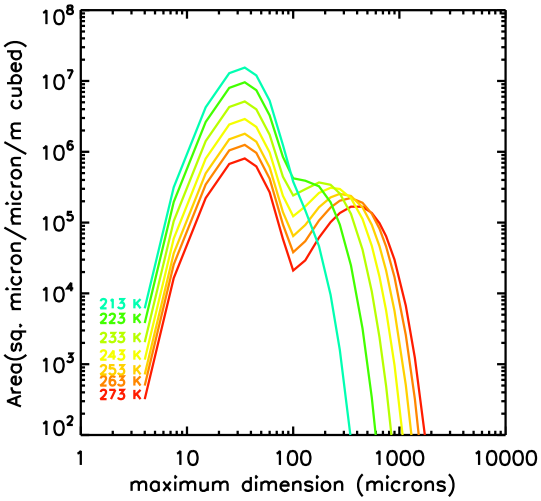

Fig. 2. Infrared absorption cross sectional area as a function of temperature from 213 K (blue) to 273 K (red).

Donovan parameterized the retrieved size spectrum of cirrus clouds observed at the Southern Great Plains site in Oklahoma, USA, in terms of the clouds' temperature and IWC. Fig. 2 shows the infrared absorption cross sectional area derived from Donovan's parameterization. By combining Schiller *et al.'s* parameterization with Donovan's we defined the IWC and the effective radius of a persistent contrail in terms of its temperature alone. This representation provides variable optical infrared and visible properties for tropical, middle and high latitudes defined by the contrail's temperature.

The details of the persistent linear-contrail coverage used in this study can be found in Fichter *et al.* (2005) and are based on a TRADEOFF inventory of aircraft-flown distance for 1992 and a parameterization (Ponater *et al.*, 2002) for line-shaped contrails. Contrails with optical depths less than the visibility criterion were not excluded.

4. RESULTS

The global radiative forcing calculated for different IWC values is shown in Table 2. The last row corresponds to the range corresponding to one standard deviation of the IWC database. The results for the assumptions of spherical particles or fixed size are also included, showing that the IWC variability is the most significant factor influencing contrail radiative forcing.

5. CONCLUSIONS

Variability of IWC is the most significant factor for determining contrail radiative forcing and is sufficient to explain the discrepancies between published estimates of contrail radiative forcing published estimates. It is important to consider the statistical distribution of IWC on contrail radiative forcing calculations in order not to assume unrepresentatively high values: this may occur when average values from satellite observations are used.

IWC	July (CC=0.032%)	January (CC=0.044%)
Max	10.7	18.8
Core Max	7.7	15.7
Mean (fixed size)	2.1	2.3
Mean (spheres)	2.3	2.3
Mean	1.4	1.5
Median	0.9	1.1
Core Min	0.2	0.2
Range (1 S.D.)	0.2-2.6	0.2-4.3

Table 2. Seasonal persistent linear contrail global radiative forcing (mW m^{-2}) for different IWC values.

REFERENCES

Baran, A.J., Havemann, S. and Mackowski, D., 2001. A database of hexagonal column optical properties for wavelengths ranging between 0.2 microns to 30 microns produced for ANNEX 7, Contract N° 4b/3/02. , DEFRA, UK.

de Leon, R.R. and J. Haigh (2007) Infrared properties of cirrus clouds in climate models. Quarterly Journal of the Royal Meteorological Society, 133 (623), pp. 273-282.

Donovan, D. P., Ice-cloud effective particle size parameterization based on combined lidar, radar reflectivity, and mean Doppler velocity measurements, (2003) J. Geophys. Res., 108(D18), 4573.

Edwards J.M., and Slingo A. (1996) Studies with a flexible new radiation code I: choosing a configuration for a large-scale model Q.J.R. Met. Soc., 122, pp689-719.

Fichter, C., S. Marquart, R. Sausen, D.S. Lee, (2005) The impact of cruise altitude on contrails and related radiative forcing. Meteorol. Z. 14, 563–572.

Fu, Q., (1996) An accurate parameterization of the solar radiative properties of cirrus clouds for climate models. J. Climate, 9, 2058-2082.

Fu, Q., P. Yang, and W.B. Sun. (1998) An accurate parameterization of the infrared radiative properties of cirrus clouds for climate models. J. Climate, 11, 2223-2237.

Heymsfield, A. J., On measurements of small ice particles in clouds. (2007) Geophys. Res. Lett., 34, L23812.

IPCC, 1999: see PENNER et al., 1999.

IPCC, 2001: Climate Change 2001. The Scientific Basis. Contributions of working group I to the Third Assessment Report of the Intergovernmental Panel on Climate Change. Cambridge University Press, Cambridge, UK and New York, NY, USA, 881 pp.

Marquart, S., M. Ponater, F. Mager, R. Sausen, (2003) Future development of contrail cover, optical depth and radiative forcing: Impacts of increasing air traffic and climate change. J. Climate 16, 2890–2904.

Penner, J.E., D.H. Lister, D.J. Griggs, D.J. Dokken, M. McFarland (Eds), 1999: Aviation and the global atmosphere. A special report of IPCC working groups I and III. Intergovernmental Panel on Climate Change. Cambridge University Press, Cambridge, UK and New York, NY, USA, 365 pp.

Ponater, M., S. Marquart, and R. Sausen (2002), Contrails in a comprehensive global climate model: Parameterization and radiative forcing results, J. Geophys. Res., 107(D13), 4164

R. Sausen et al.: Aviation radiative forcing in 2000: An update on IPCC (1999). (2005) Meteorol. Z., Vol. 14, No. 4, 555-561.

Schiller, C. M. Krämer, A. Afchine, N. Spelten. (submitted to JGR) An in-situ climatology of ice water content in Arctic, mid latitude and tropical cirrus.

Stuber, N. and P. Forster (2007). The impact of diurnal variations of air traffic on on contrail radiative forcing. Atmos. Chem. Phys., 7, 3153–3162.

Yang, P., Liou, K.N., Wyser, K. and Mitchell, D. (2000). Parameterization of the scattering and absorption properties of individual ice crystals. J. Geophys. Res. 105, pp. 4699–4718.

THE PROPERTIES OF LOW LATITUDE TROPOPAUSE SUBVISIBLE CIRRUS

C. G. Schmitt and A. J. Heymsfield
National Center for Atmospheric Research, Boulder, CO

1. INTRODUCTION

Low-latitude in-situ generated cirrus and convectively generated anvil cirrus are important due to their effect on the radiation budget of the planet. Accurate knowledge of the microphysical properties of these clouds is important to better understand their impact on climate. Low-latitude cirrus clouds have been a focus of several recent field campaigns. The 2002 Cirrus Regional Study of Tropical Anvils and Cirrus Layers - Florida Area Cirrus Experiment (CRYSTAL-FACE) and the 2004 Pre-Aura Validation Experiment (Pre-AVE) projects both targeted upper troposphere low stratosphere (UTLS) cirrus with the NASA WB-57 aircraft. During both of these experiments the NCAR Video Ice Particle Sampler (VIPS) probe (McFarquhar and Heymsfield, 1997) was used to provide particle size distribution and particle projected area information for particles from 10 to 350 microns in diameter. The microphysical characteristics of low latitude cirrus particles as small as 10 microns have rarely been measured reliably due to the limitations of electronic probes.

Observations show that low latitude cirrus clouds are ubiquitous and are therefore important for understanding the energy balance in the tropics. Using a delta-four stream model, McFarquhar et al (2000) calculated that sub-visible cirrus layers have heating rates of up to 1.0 K per day with a radiative forcing of 1.2 W m^{-2}. They point out that although the radiative effect of sub-visible cirrus in the tropics is relatively small, it should not be ignored due to the extent and frequency of occurrence of the clouds.

Global climate model (GCM) results would benefit from improved parameterizations of cirrus cloud properties. Mitchell et al (2006) showed that GCM model run results differed significantly when low latitude cirrus was parameterized to have slower fall speeds indicating that GCM results are highly dependant on mass weighted fall speed values (V_m). GCM values of V_m are commonly parameterized in terms of ice water content (IWC) or the ice water mixing ratio (Boville et al., 2006).

Particle terminal velocities are often calculated using the relationship between the Reynolds number and the Best number (Re-X). This method was refined by Mitchell and Heymsfield (2005) and is particle shape independent, depending only on particle mass and projected area in addition to the atmospheric state conditions. Common mass-dimensional and area-dimensional relationships do not treat particles smaller than 200 μm reasonably. Often mass and area relationships are expressed using power law functions which require an artificial truncation to avoid unreasonable values.

This study analyzes low-latitude cirrus cloud properties from aircraft measurements of in-situ and convectively generated cirrus at temperatures from -56 to -86C. Key particle parameters for the calculation of terminal velocities are emphasized in our analysis. Mass and projected area relationships are developed and compared to commonly used parameterizations.

2. LOW-LATITUDE CIRRUS DATASET

The NCAR VIPS probe was used to measure ice particle sizes from 10 to 350 microns for both CRYSTAL-FACE and Pre-AVE. The WB-57 was equipped with a Cloud Aerosol Precipitation Spectrometer (CAPS) probe which includes a Cloud

Imaging Probe (CIP), a 2-D optical array probe (OAP) used to measure the particle size distribution from 75 microns to several millimeters. When large particles were present, data from the CIP were processed as described in Heymsfield et al (2002) with additional processing to remove potential artifacts from particle breakup (Field et al 2006). In the overlap size range (75 to 200 microns), the CIP and VIPS probes were found to agree very well. For the Pre-AVE data used in this study, the VIPS was the only available instrument for particle size distribution (PSD) measurement. Given that the Pre-AVE flight was the coldest, it is believed that the VIPS accurately measured the entire size range present in the cloud, as the there were few particles larger than 150 microns.

The dataset is composed of measurements from three flights. The first part of the dataset is comprised of data from the 23 July 2002 CRYSTAL-FACE flight. During this flight, the WB-57 repeatedly sampled anvil cirrus in varying stages of development. The temperature during the passes was -56 to -65C at an altitude between 12 and 13 km. Initially, decaying anvil cloud was sampled, then later in the flight, more recently generated anvil clouds were intercepted as well as fresh convection.

The second part of the dataset is from WB-57 measurements from 26 July 2002, also during CRYSTAL-FACE. The WB-57 descended from 15 to 12 km (-75 to -60C) through a cloud suspected to have originated from gravity waves. Airborne Laser Infrared Absorption Spectrometer (ALIAS) HDO data suggest that the cloud particles were formed from vapor at the level of the sampling (Webster and Heymsfield, 2003) supporting the gravity wave formation conjecture.

The third dataset is from a Pre-AVE flight off the coast of Costa Rica on 24 January, 2004. The WB-57, while cruising at 15km, intercepted a high altitude cirrus layer that extended up to 17 kilometers in altitude. After ten minutes of sampling at 15 km, the aircraft began a slow ascent to the top of the cloud layer near 17km. The temperature of this layer was between -76 and -86C.

3. TERMINAL VELOCITIES OF LOW-LATITUDE CIRRUS PARTICLES

This section will focus on estimating the values of individual particle projected area (*A*) and mass (*m*) from the low latitude cirrus dataset to facilitate the calculation of V_t. Emphasis will be placed on sub-200 micron particles as they comprise the bulk of the low latitude cirrus dataset.

Area ratio to maximum dimension relationships are common in the literature (Mitchell, 1996). For this dataset, one area to maximum dimension relationship was determined and applied to the entire dataset. Figure 1 shows particle area ratio by size developed for this dataset compared to common parameterized values. The variability in the parameterizations for area ratio especially for small particles can lead to high uncertainty in fall speeds for individual particles.

An exponential fit was deemed more suitable for the area ratio to maximum dimension relationship for particles 200 microns and smaller. Power law parameterizations require an artificial limit to be placed on the area ratio so that it does not exceed 1.0 at small sizes. Exponential relationships automatically avoid this by allowing the y-intercept to be fixed. For particles larger than 200 microns a power law fit was fit to the CIP and CPI datasets. The equation for the fit to the low-latitude dataset for D<200 microns is given below:

$$Ar = e^{-38D} \qquad D<200\mu m$$

where *Ar* is the area ratio and *D* is the particle maximum dimension in cm.

Typical mass-Dimensional (m-D) relationships are power laws of the form

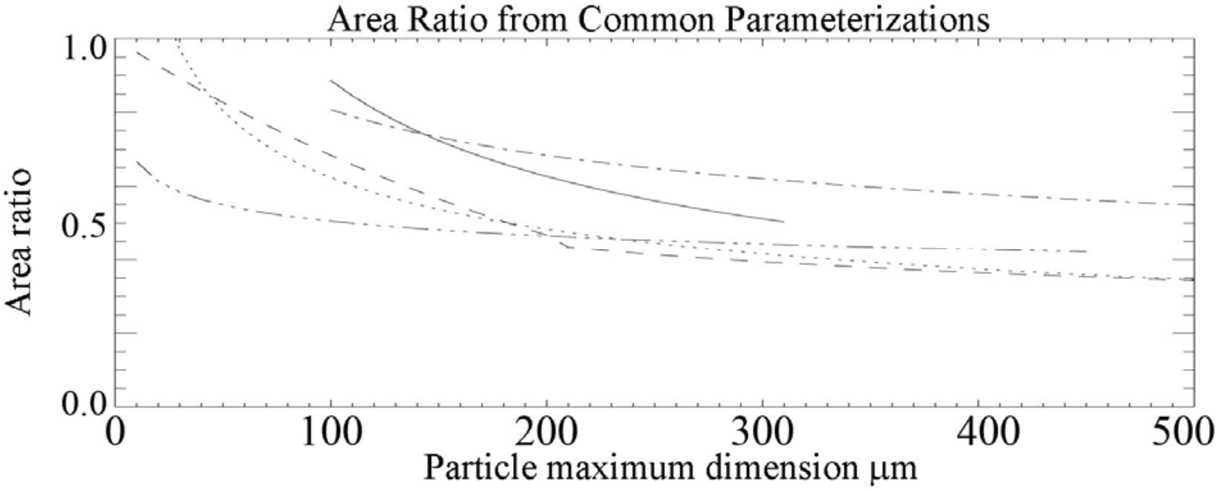

Figure 1: Area ratio to particle maximum dimension for low latitude dataset (dashed line) as well as commonly used parameterizations. Solid line: Columns from Mitchell and Arnott (1994). Dotted line: Cirrus CPI from Heymsfield and Miloshevich (2004). Dot-Dash: Broad branched crystals from Mitchell (1996). Dash-dot-dot-dot: Planar polycrystals in cirrus from Mitchell (1996).

$m=aD^b$ where m is the mass, a and b are constants, and D is the maximum measured dimension. m-D relationships are generally developed for broad size ranges and typically require that smaller particles (sub 100 micron) are solid ice spheres. Potential errors are often ignored as the mass in broad PSDs is often concentrated in the larger particles. For this dataset an exponential m-D relationship was chosen to estimate the mass of particles smaller than 200 microns.

The m-D relationship was calculated by varying the parameters of the exponential function to minimize the error between measured and calculated IWC for the dataset. The m-D relationship is shown in below and is plotted compared to some other representations in Figure 2:

$$m = 0.91\frac{\pi}{6}D^3e^{-92D} \qquad D<200\mu m$$

where m is the particle mass in grams and D is the particle maximum dimension in cm. It will be shown later that the mass of particles larger than 200 μm have very little influence on the results of this work.

The V_t values were calculated for the observed particle range using the Mitchell and Heymsfield (2005) Re-X relationships along with the particle areas and masses reported earlier. Fall speeds are normalized to 150 mb and -70C, typical values for the low-latitude cirrus dataset. Figure 3 shows V_t plotted with respect to particle size. The small particle fall speeds compare well to experimental measurements by Fukuta (1969) and Kajikawa (1973) for particles between 10 and 100 microns. For comparison, the dashed line represents V_t calculated using Brown and Francis (1995) particle mass values and the dotted line uses a parameterization for unrimed plane dendrites developed by Locatelli and Hobbs (1974). The Locatelli and Hobbs (1974) parameterization was not meant to be extrapolated to such small particle sizes and the errors in doing so are quite apparent. The Re-X fall speeds can be parameterized by two power-law expressions:

$$V_t=123000*D^{1.84} \qquad D<70\mu m$$

$$V_t=3830D^{1.15} \qquad 70<D<200\mu m$$

In contrast to parameterizations developed in recent publications (Ivanova et al, 2001, McFarquhar and Heymsfield, 1997, Mitchell

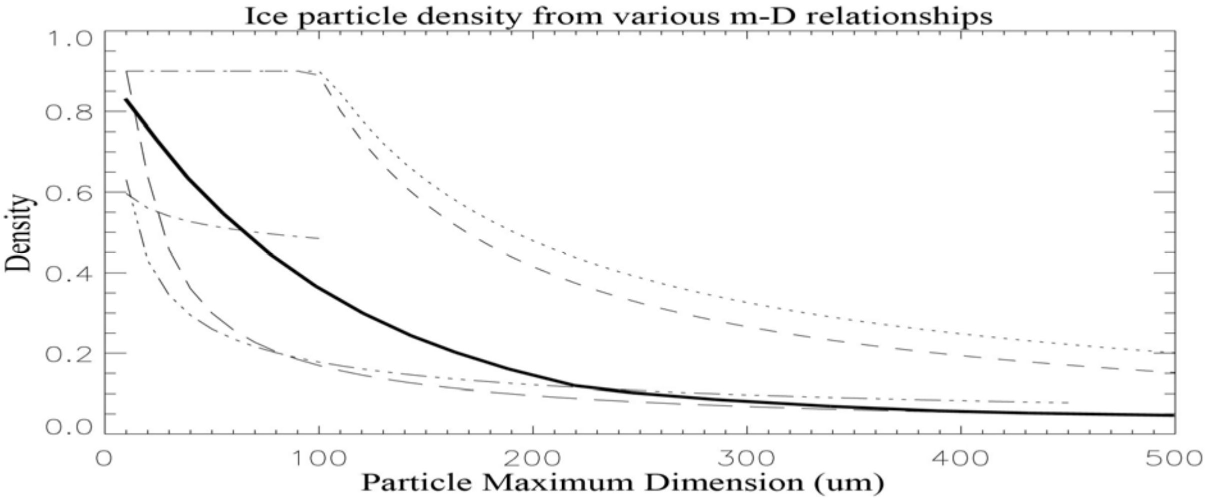

Figure 2: Particle density versus maximum dimension for various m-D relationships. Bold line: This study. Short dashes: Brown and Francis (1995). Dotted line: Heymsfield et al (2004). Long dash: Heymsfield et al (2002) 6 branch bullet rosettes. Dash dot dot dot: Mitchell et al (1996) Planar polycrystals in cirrus. Dot dash: Mitchell and Arnott (1994) hexagonal columns.

et al, 2006) the measured PSDs for the low-latitude cirrus dataset were mono-modal. PSDs have been typically measured with a 2-dimensional optical array probe and a forward scattering-type probe for particles smaller than 50 microns. Results from forward scattering probes have been shown to be contaminated by the breakup of large particles on the leading edges of the probes (Field et al, 2003, Heymsfield et al, 2006, McFarquhar et al, 2007). Particle breakup can lead to inflated concentrations in the presence of large ice particles giving the appearance of bi-modality. Ryan (2000) points out that the commonly observed transition from the small mode to the large

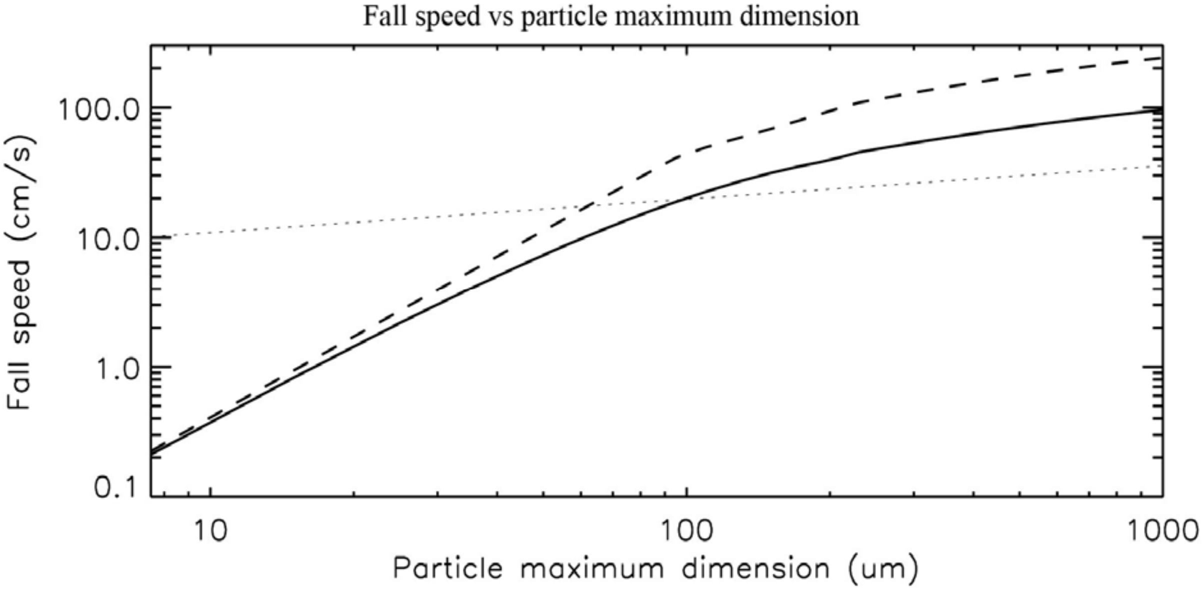

Figure 3: Particle fall speed plotted versus particle maximum dimension. The dashed line represents the fall speed using mass values calculated from Brown and Francis (1995). The dotted line is a parameterization from Locatelli and Hobbs (1974).

mode in a measured bimodal size distribution takes place at the cutoff point between different probes. In this study, the typical transition point between modes (50-100 μm) was well measured by the VIPS and no signs of bimodality were noted.

Figure 4 shows a representative PSD with parameterized fits using the McFarquhar and Heymsfield (1997) distribution, a gamma distribution and an exponential distribution. The gamma distribution is based on the function: $N = N_o D^{\mu} e^{-\lambda_{\Gamma} D}$ where N_o is the intercept, λ_{Γ} is the slope and μ is the dispersion and was calculated as in Heymsfield et al (2002). The exponential fit is of the form: $N = N_o e^{-\lambda D}$. The exponential fit was calculated by matching the second and third moments of the distribution as described in Zhang et al (2007).

4. MASS WEIGHTED FALL SPEED

Mass weighted fall speed (V_m) is calculated by totaling the V_t * IWC_{bin}, then dividing by the total mass for a size distribution (IWC_{bin} is the particle mass*concentration for each bin). To better understand the importance of different size particles in the calculation of V_m, the IWC_{bin}* V_t was calculated, then cumulatively summed, then normalized by total for each size distribution. Figure 5 shows the results with shading levels changing every 10th percentile. This shows that mass flux in these clouds is dominated by the 15-50 micron range and that particles larger than 200 μm are of little importance for calculating V_m for this dataset.

In GCMs, V_m is often parameterized by condensed water content mixing ratio (*w*). Figure 6 shows the calculated V_m values as well as a parameterization used in the CSU System for Atmospheric Modeling (SAM) GCM. Parameterized values are plotted with respect to *w*. The V_m results from the studied dataset are significantly slower than would be predicted by SAM. A parameterization relating V_m and mixing ratio for the measurements is:

$$V_m = 1150 w^{0.36}$$

where *w* is the mixing ratio in g/kg and V_m is in cm/s.

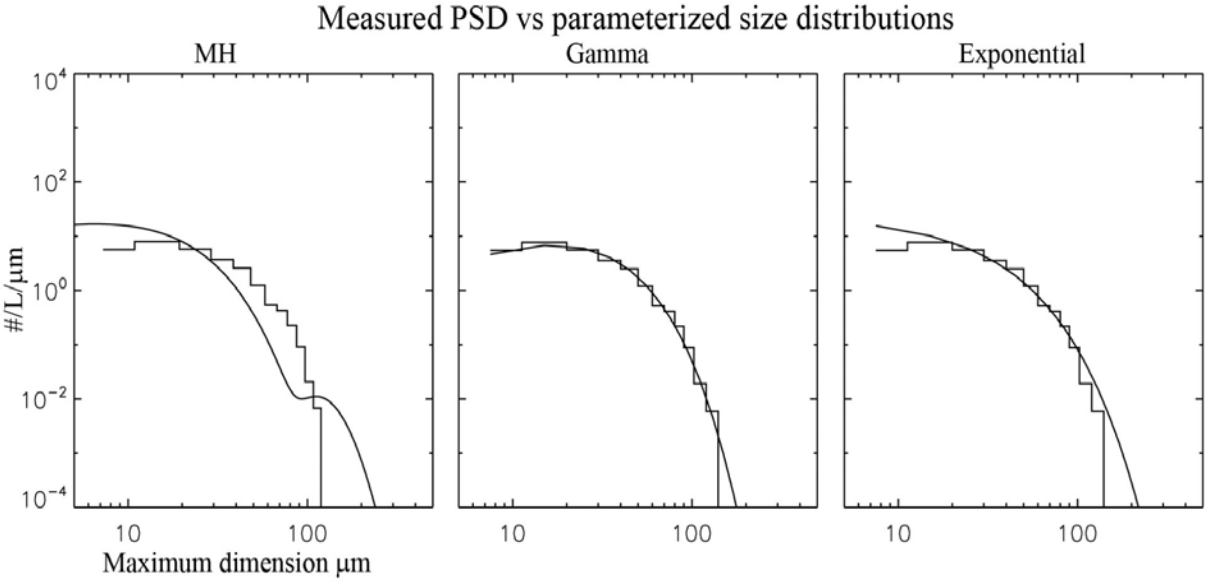

Figure 4: Typical PSD compared to three different parameterizations, the MH parameterization, a gamma function and an exponential function.

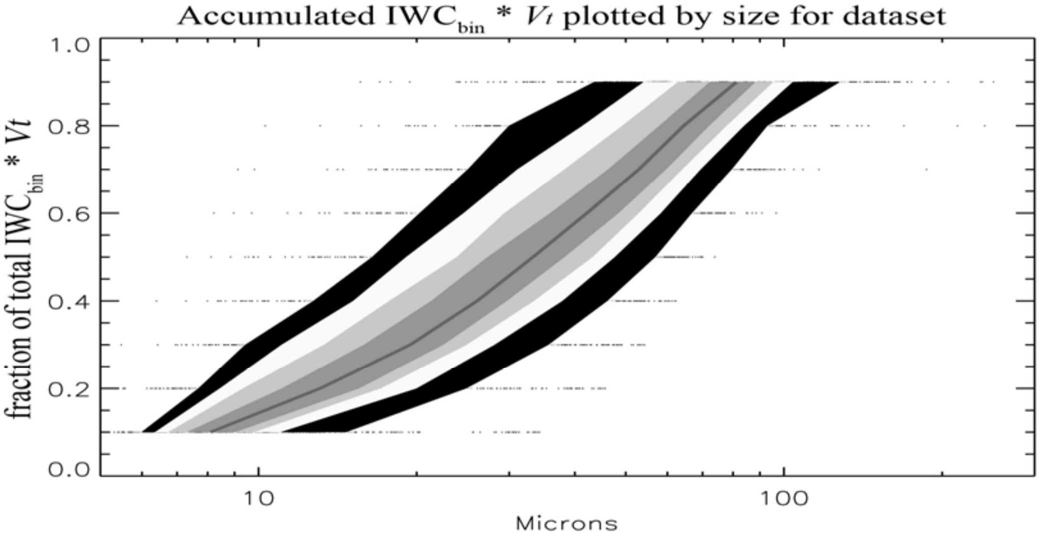

Figure 5: Accumulated IWC_{bin} * V_t for PSDs normalized by the total IWC_{bin} * V_t for the distribution are plotted for the dataset versus particle dimension. Shading indicates 10th through 90th percentiles of the data. Dots outside the shaded area represent where outliers intersect the percent levels.

5. CONCLUSIONS

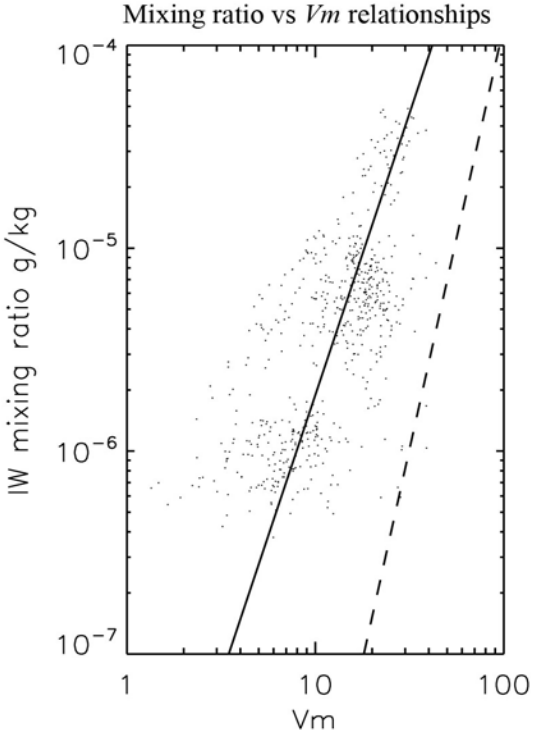

Figure 6: Mass weighted fall speed versus condensed water content mixing ratio for the dataset. The solid line is the parameterization and the dashed line represents the values used in the CSU SAM model.

This study has sought to improve our understanding of low-latitude cirrus cloud microphysics. High quality microphysical data measured by the VIPS probe during several flights to characterize cloud properties includes particle sizes in the size range poorly measured by other probe combinations. Cloud particle properties necessary for accurate estimates of particle fallspeeds have been thoroughly analyzed. It was found that common parameterizations were inadequate when applied to particle populations composed mainly of particles smaller than 200 microns. Size distributions measured by the VIPS were shown to be monomodal. Small particle mass was investigated using particle size distributions and total condensed water content measurements. Indications are that small particles should have lower mass values than commonly used parameterizations predict.

The area, mass and particle size distributions were used to calculate particle fall speeds. An exponential fit was found to better represent density and area functions by size for the smaller particles as the exponential fits do not require artificial assumptions to account for the unrealistic density and area values predicted for small particles by power law relationships. The exponential parameterizations led to fall speeds that were significantly lower than frequently used parameterizations would predict. Because the small particles were predicted to have lower fall speeds, V_m values were significantly lower than parameterizations currently used in climate models.

6. BIBLIOGRAPHY

Boville, B. A., P. J. Rasch, J. J. Hack, and J. R. McCaa, 2006: Representation of clouds and precipitation processes in the community atmosphere model version 3 (CAM3). *J. Clim.,* **19**, 2184-2198.

Brown, P. R. A., and P. N. Francis, 1995: Improved measurements of the ice water content of cirrus using a total-water probe. *J. Atmos. Oceanic Technol.,* **12**, 410-414.

Field, P. R., A. J. Heymsfield and A. Bansemer, 2006: Shattering and particle interarrival times measured by optical array probes in clouds. *J. Atmos. Oceanic Tech.,* **23**, 1357-1371.

Field, P., R., R. Wood, P. R. A. Brown, P. H. Kaye, E. Hirst, R. Greenaway, and J. A. Smith, 2003: Particle interarrival times measured with a Fast FSSP. *J. Atmos. Oceanic Tech.*, **20**, 249-261.

Fukuta, N. 1969: Experimental studies on the growth of small ice crystals. *J. Atmos. Sci.,* **26,** 522-531.

Heymsfield, A. J., A. Bansemer, P. R. Field, S. L. Durden, J. Stith, J. E. Dye, W. Hall and T Grainger, 2002: Observations and parameterizations of particle size distributions in deep tropical cirrus and stratiform precipitating clouds: Results from in-situ observations in TRMM field campaigns. *J. Atmos. Sci.*, **59**, 3457-3491.

Heymsfield, A. J., S. Lewis, A. Bansemer, J. Iaquinta, L. Milosovich, M. Kajikawa, C. Twohy, and M. Poellot, 2002: A general approach for deriving the properties of cirrus and stratiform ice cloud particles. *J. Atmos. Sci.*, **59**, 3-29.

Heymsfield, A.J., A.R. Bansemer, C.G. Schmitt, C.H. Twohy, and M. Poellot, 2004: Effective ice particle densities derived from aircraft data. *J. Atmos. Sci.,* **61**, 982-1003.

Heymsfield, A. J., and L. M. Miloshevich, 2003: Parameterizations for the cross-sectional area and extinction of cirrus and stratiform ice cloud particles. *J. Atmos. Sci.*, **60**, 936–956.

Heymsfield, A. J., C. Schmitt, A. Bansemer, G-J. Zadelhoff, M. J. McGill, C. Twohy, and D. Baumgardner, 2006, Effective radius of ice cloud particle populations derived from aircraft probes. *J. Atmos. Oceanic Technol.* **23**, 361-380.

Ivanova, D., D. L. Mitchell, W. P. Arnott, M. Poellot, 2001: A GCM parameterization for bimodal size spectra and ice mass removal rates in mid-latitude cirrus clouds. *Atmos. Res.*, **59-60**, 89-113.

Kajikawa, M. 1973: Laboratory measurements of falling velocity of individual ice crystals. *J. Meteorol. Soc. Japan,* **51**, 263-271.

Locatelli, J. D., and P. V. Hobbs, 1974: Fall speeds and masses of solid precipitation particles. *J. Geophys. Res.* **79**, 2185-2197.

McFarquhar, G. M., and A. J. Heymsfield, 1997: Parameterization of tropical cirrus ice crystal size distributions and implications for radiative transfer: results from CEPEX. *J. Atmos. Sci.*, **54**, 2187-2200.

McFarquhar, G. M., Heymsfield, A. J., Spinhirne, J., and Hart, B., 2000: Thin and subvisual tropopause tropical cirrus: Observations and radiative impacts. *J. Atmos. Sci.*, **57**, 1841–1853, 2000.

McFarquhar, G. M., J. Um, M. Freer, D. Baumgardner, G. L. Kok, and G. Mace, 2007: Importance of small ice crystals to cirrus properties: Observations from the Tropical Warm Pool International Cloud Experiment (TWP-ICE). *Geophys. Res. Lett.*, **34**, L13803, doi:10.1029/2007GL029865.

Mitchell, D. L., 1996: Use of mass- and area-dimensional power laws for determining precipitation particle terminal velocities. *J. Atmos. Sci.*, **53**, 1710-1723.

Mitchell, D. L., and W. P. Arnott, 1994: A model predicting the evolution of ice particle size spectra and radiative properties of cirrus clouds. Part II: Dependence of absorption and extinction on ice crystal morphology. *J. Atmos. Sci.,* **51**, 817-832.

Mitchell, D. L., P. Rasch, D. Ivanova, G. McFarquhar, T. Nousiainen, 2006: The impact of controversial small ice crystals on GCM simulations. *Proceedings of the 12th conference on cloud physics and radiation.* Madison Wisconsin.

Mitchell, D. L., and A. J. Heymsfield, 2005: Refinements in the treatment of ice particle terminal velocities, highlighting aggregates. *J. Atmos. Sci.*, **62**, 1637-1644.

Ryan, B. F., 2000: A bulk parameterization of the ice particle size distribution and the optical properties in ice clouds. *J. Atmos. Sci.,* **57**, 1436-1451.

Webster C. R., and A. J. Heymsfield, 2003: Water isotope ratios D/H, $^{18}O/^{16}O$, $^{17}O/^{16}O$ in and out of clouds map dehydration pathways. *Science*, **302**, 1742–1745.

Zhang, G., M. Xue, Q. Cao, and D. Dawson, 2007: Diagnosing the intercept parameter for exponential raindrop size distribution based on video disdrometer observations. *Proceedings 18th AMS NWP conference Park City, UT June 2007*.

ACKNOWLEDGEMENTS

This research was supported by CSU Contract G-3045-9 under the ATM Prime Award No. 0425247 and NASA Grant No. NNX07AQ85G.

TURBULENCE IN CIRRUS CLOUDS – IMPACT OF CRITICAL LAYERS

Peter Spichtinger[1*], **and Piotr K. Smolarkiewicz**[2]

[1] ETH Zurich, Institute for Atmospheric and Climate Science, Zurich, Switzerland
[2] National Center for Atmospheric Research, Boulder, Colorado, USA

We investigate the impact of gravity-wave induced turbulence in critical layers on the formation and evolution of cirrus clouds in ice-supersaturated regions. The anelastic non-hydrostatic computational model EULAG (http://www.mmm.ucar.edu/eulag) employs a recently developed ice microphysics scheme. An idealized framework includes time-dependent lower boundary for excitation of waves with prescribed wave number and amplitude, and arbitrarily specified ice–supersaturated layer in the vicinity of the critical level. The formation of ice crystals triggered by the laminar wave motion and turbulence in critical layer aloft are both captured in the simulation.

1 INTRODUCTION

Clouds are still one of the least understood components of the climate system. As stated in the IPCC report (IPCC, 2007) and during the recent international workshop at the Ernst Strüngmann Forum (http://fias.uni-frankfurt.de/esforum/clouds.html), cloud properties and their impact on the radiation budget in changing climate are not sufficiently known. Especially, the impact of high clouds consisting purely of ice crystals, viz. cirrus clouds, is known poorly, although a net warming is typically assumed (Chen et al., 2000). However, recent studies of the radiative properties of mid latitude cirrus clouds indicate that under certain conditions the transition between warming (i.e., for dominating absorption of thermal radiation) and cooling (i.e., for dominating reflection of solar radiation) strongly depends on the ice crystal number concentration, whereas the ice water content determines mainly the magnitude of warming or cooling (Fusina et al., 2007).

Generally, there are two distinct processes of ice crystal formation in the upper troposphere (Vali, 1985): a homogeneous freezing of aqueous solution droplets (Koop et al., 2000) or heterogeneous nucleation on aerosol particles — so-called ice nuclei, hereafter IN for brevity — (DeMott et al., 2003). At high temperatures ($T > 235$ K) ice crystals are formed via heterogeneous nucleation, whereas in the low temperature range ($T < 235$ K) homogeneous freezing is the dominant pathway (Kärcher and Ström, 2003); yet heterogeneous IN can modify homogeneous nucleation (Kärcher et al., 2006; Spichtinger and Gierens, 2008b). Homogeneous nucleation depends strongly on vertical velocity and temperature (Kärcher and Lohmann, 2002; Spichtinger and Gierens, 2008a). Variations of the updraft velocity inducing adiabatic cooling can easily effect in a few orders of magnitude change in the ice crystal concentration number. In consequence, these variations of vertical velocity have strong impact on radiative properties of the resulting cirrus clouds.

Although cirrus clouds appear quite homo-

---

[*] peter.spichtinger@env.ethz.ch

geneous from a satellite perspective (e.g., a warm-front cirrus), even a casual glance from the ground reveals an inhomogeneous, patchy structure of cirrus. Furthermore, in situ measurements (Schlicht et al., 2006; Gayet et al., 2004; Krämer, 2008) document that cirrus clouds have high internal variability. Inside cirrus, temperature and vertical velocity fluctuations are substantial, thus causing inhomogeneities in ice crystal number concentration and ice water content. Based on temperature and/or vertical velocity measurements in the upper troposphere (e.g. Gary, 2006; Gierens et al., 2007) an “ubiquitous” background of temperature fluctuations is often assumed. This feature is typically used for a random offset of box-model calculations of ice crystal formation in large-scale motions (Haag and Kärcher, 2004; Hoyle et al., 2005). However, these fluctuations (of temperature and/or vertical velocity) have a deterministic physical origin. In particular, small-scale variations can be related to turbulence generated by breaking internal gravity waves. Notably, measurements indicate that in the tropopause region, where cirrus clouds occur preferentially, turbulence is found frequently (Smith and Jonas, 1996; Worthington, 1999). One plausible source for turbulence are nonlinear interactions of orographic waves with sheared ambient wind within critical layers (Booker and Bretherton, 1967; Worthington and Thomas, 1996). As the gravity wave approaches the critical level, it becomes increasingly shorter, overturns and breaks; thus generating turbulence and mixing (Grubisic and Smolarkiewicz, 1997).

Herein, we study the impact of turbulence generated in critical layers on the formation and evolution of ice–supersaturated regions (i.e., latent regions of cirrus formation) and cirrus clouds. Our primarily tool of research is the anelastic nonhydrostatic computational model EULAG (Smolarkiewicz and Margolin, 1997; Prusa et al. 2008) combined with a recently developed ice microphysics scheme (Spichtinger and Gierens, 2008a). The vertically propagating wave and the associated critical layer effects are simulated using an idealized scenario.

In the next section, the computational model and ice microphysics scheme are briefly described. In section 3 the model setup and parameters of sensitivity studies are specified. In section 4 the simulation results are summarized, while section 5 concludes the paper.

2 MODEL DESCRIPTION

2.1 DYNAMICAL MODEL DESCRIPTION

The multiscale dynamic model EULAG has been broadly documented in the literature; see Prusa et al. 2008, for a recent review. For dry dynamics, the anelastic equations employed in the present study can be written in perturbation form as follows (cf. Smolarkiewicz et al., 2001)

$$\begin{aligned} \nabla \cdot \bar{\rho}\mathbf{u} &= 0 && (1)\\ \frac{D\mathbf{u}}{Dt} &= -\nabla\left(\frac{p'}{\bar{\rho}}\right) - \mathbf{g}\left(\frac{\theta'}{\bar{\theta}}\right) - \mathbf{f}\times\mathbf{u}' && (2)\\ \frac{D\theta'}{Dt} &= -\mathbf{u}\cdot\nabla\theta_e && (3) \end{aligned}$$

Here, $\mathbf{u}$ is the velocity vector; p, ρ and θ denote pressure, density and potential temperature, respectively; **g** and **f** denote vectors of, respectively, gravitational acceleration and Coriolis parameter; $\bar{\theta}$ and $\bar{\rho}$ are the anelastic reference-state profiles for potential temperature and density. The subscript $_e$ refers to balanced ambient profiles, not necessarily equal to the profiles of the reference state; cf. Smolarkiewicz et al., 2001 for a discussion. Primes denote deviations from the environmental state (e.g. $\theta' = \theta - \theta_e$), and $\frac{D}{Dt} := \partial/\partial t + \mathbf{u}\cdot\nabla$ is the total derivative.

The approximate solutions of the prognostic equations (2) and (3) are evaluated using the unified semi-Lagrangian/Eulerian approach broadly described in the literature (see Prusa et al. 2008 and the references therein). Let $\mathbf{\Psi}$ and $\mathbf{F}$ denote, respectively, the vectors of dependent variables (u, v, w, θ') and their associated forcings. With $\tilde{\mathbf{\Psi}} := \mathbf{\Psi}^n + 0.5\Delta t\mathbf{F}^n$ and the generalized forward-in-time non-oscillatory transport operator LE, the approximate solution can be compactly written as

$$\mathbf{\Psi}_{\mathbf{i}}^{n+1} = LE_{\mathbf{i}}\left(\tilde{\mathbf{\Psi}}\right) + 0.5\Delta t \mathbf{F}_{\mathbf{i}}^{n+1} \qquad (4)$$

whereby $\mathbf{i}$ and n denote, respectively, spatial and temporal location on the mesh. The forcing $\mathbf{F}^{n+1} = \mathbf{F}(\mathbf{\Psi}^{n+1})$, thus implying the trapezoidal-rule (implicit) integration of the governing equations. Inverting the implicit formulae (4) involves formulation and solution of the elaborate elliptic equation for the pressure perturbation, implied by the mass continuity in (1). For extensions to moist thermodynamics see Grabowski and Smolarkiewicz (2002).

The model outlined was used in many applications on different scales and for disperse problems of geophysical fluid dynamics (in particular, for stratified orographic flows and convectively generated gravity waves pertinent to this study). One noteworthy aspect of EULAG is its design around the non-oscillatory advection scheme MPDATA (for multidimensional positive definite advection transport algorithm; see Smolarkiewicz, 2006, for a recent overview).

2.2 ICE MICROPHYSICS DESCRIPTION

Here, we provide a brief overview of the parameterized microphysical processes employed in this study. For a detailed description the interested reader is referred to Spichtinger and Gierens (2008a).

A double-moment bulk microphysics scheme is utilized; i.e., prognostic equations are solved for ice crystal number and mass concentrations. Ice crystal mass (or equivalently size) is assumed to follow a lognormal distributions with time-dependent mean mass but fixed spectral width. Crystal shapes are droxtals (aspect ratio one) up to a diameter of 7.42 μm and columns with size–dependent aspect ratio for larger sizes. An arbitrary number of ice classes can be treated with this scheme. Each ice class is explicitly tied to an aerosol type that nucleates it, hence ice classes are distinguished by their formation mechanism (e.g., heterogeneously vs. homogeneously formed ice). The aerosol types are also characterized by their number and mass concentration.

The three microphysical processes parameterized to simulate cold cirrus are nucleation (homogeneous and heterogeneous), diffusional growth/evaporation and sedimentation. Ice crystal aggregation is neglected, because it is of minor importance for thermodynamics of cold cirrus ($T < 235$ K) as well as for the low vertical and terminal velocities (Kajikawa and Heymsfield, 1989) considered in our study.

For the representation of homogeneous freezing of aqueous solution droplets we prescribe lognormally-distributed sulfuric acid drops as a background aerosol. The water content of the solution droplets is computed using the Koehler theory. Freezing rates are calculated using the water activity based and temperature dependent parameterization of Koop et al. (2000). In this study we focus on the homogeneous nucleation. The heterogeneous nucleation is not addressed, although parameterizations for these formation mechanisms are available in the model (Spichtinger and Gierens, 2008b). For parameterizing the diffusional growth of ice crystals, we use a modified Koenig ansatz (Koenig, 1971) with corrections for small crystals (i.e., droxtals) and ventilation. This approach for single ice crystals was extend to the bulk quantity (the cloud ice mixing ratio). For the evaporation of ice crystals, both the ice mass concentration and number concentration decrease in relative proportion, as described in (Spichtinger and Gierens, 2008a, sec. 3.3). To simulate sedimentation we use mass and number weighted terminal velocities, respectively, with parameterizations for single crystals adopted from Heymsfield and Iaquinta (2000).

3 EXPERIMENTAL SETUP

Our idealized framework assumes a 2D domain in the xz vertical plane, with periodic boundary conditions in the x direction. The horizontal and vertical extent of the domain are $L_x = 10$ km and $L_z = 15$ km, respectively. The model domain is discretized with $n_x \times n_z = 224 \times 335$ grid points, thus resulting in grid resolution $dx \approx$

44.8 m and $dz \approx 44.9$ m, in the horizontal and the vertical, respectively.

In order to excite waves with prescribed wave number and amplitude we specify: i) the constant-stratification ambient profile of potential temperature (Clark and Farley, 1984) with surface value $\theta_s = T_s = 288.18$ K and Brunt-Väisälä frequency $N = 0.0097\mathrm{s}^{-1}$; and ii) the linear wind profile with the surface value $u_0 = 10\,\mathrm{m\,s}^{-1}$ and constant shear of $du/dz = -10^{-3}\mathrm{s}^{-1}$; fig. 1. Furthermore, we specify a single Fourier mode for the lower boundary profile

$$z_b(t, x) = a(t) \cdot \sin\left(\frac{2\pi x}{x_0}\right) \tag{5}$$

with $x_0 = 10$ km and the time dependent amplitude

$$a(t) = \begin{cases} a_0 \cdot t/t_0 & \text{for} \quad t \leq t_0 \\ a_0 & \text{for} \quad t > t_0 \end{cases} \tag{6}$$

with $t_0 = 405$ min. All simulations are for total time of $T_s = 720$ min, using temporal increment $dt = 2.5$ s. For the microphysics, we use a smaller time increment of $dt_{mp} = 0.25$ for vertical columns, only if homogeneous nucleation takes place somewhere in the column. Initial condition consists of the ambient wind and a Gaussian noise with standard deviation $\sigma_T = 0.1$ K for the perturbation potential temperature. Furthermore, a deep layer of ice supersaturation is specified in the altitude range $6 \leq z \leq 10$ km. As shown in fig. 1, this range is in the cold temperature regime ($T < 240$ K), so the cirrus may form by homogeneous nucleation.

4 RESULTS

The aim the simulation performed is to elucidate the overall impact of waves and turbulence occurring in critical layers on the moisture field and eventual ice crystal formation.

Figure 2 shows the time evolution of the vertical velocity in time intervals of 90 min, starting at 180 min. The time dependent lower boundary slowly forces the development of the orographic like gravity wave. The wave packet propagates in the vertical, and as it approaches the critical level at $z = 10$ km, the vertical component of the group velocity and the vertical wavelength tend to zero. The wave packet cannot reach the critical level, and is absorbed by the mean flow. The wave dissipates within the turbulent critical layer beneath $z_c = 10$ km. The corresponding fig. 3 illustrates the impact of waves and turbulence on the evolution of the moisture field and formation of ice crystals.

As the wave approaches the critical level, the associated updrafts and downdrafts cool down and warm up the environment adiabatically; thus correspondingly increasing/decreasing the initially prescribed supersaturation, depending on the position in the layer relative to the propagating wave. As the wave is developing, the supersaturation is increased in some regions, such that the thresholds for homogeneous nucleation are surpassed, and the ice crystals are formed. The cloud formation starts at the lower levels, due to the interplay of two distinct phenomena. First, because of the proximity to the forcing region, the magnitude of vertical velocity increases (chronologically) earlier

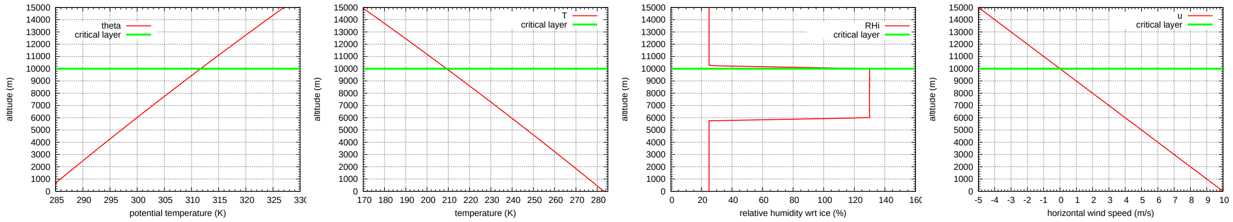

Fig. 1: Initial profiles for the idealized simulations. From left to right: potential temperature, temperature, relative humidity wrt ice and horizontal wind speed (red line). The theoretical position of the critical level (i.e., z at which $u = 0\,\mathrm{m\,s}^{-1}$) is indicated by the green line.

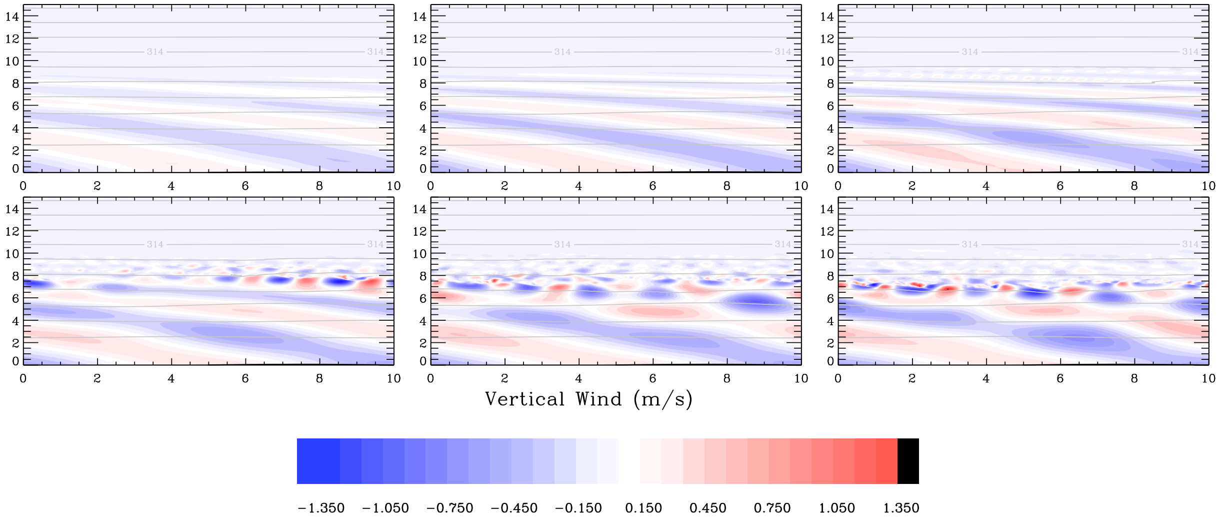

Fig. 2: Evolution of the vertical velocity forming a critical layer (time lag = 30 min), starting at simulation time $t_s = 270$ min (time lag = 90 min; upper panel:270/360/450 min, lower panel: 540/630/720 min). Grey lines indicate potential temperature.

in the lower part of the supersaturated layer. Second, the homogeneous nucleation thresholds (for different sizes of the aqueous solution droplets) are temperature dependent (Koop et al., 2000), such that the threshold for a fixed aerosol size increases with decreasing temperature. Hence, for the lower part of the supersaturation layer, nucleation can be triggered at lower thresholds; only a small uplift suffices to produce enough supersaturation for ice formation. In effect of the two mechanisms described, ice crystals form first in the lower part of the supersaturated layer, and subsequently the cirrus grows upward.

With the onset of turbulence near critical level, the vertical motions develop much stronger than in the laminar wave motion below. The larger updrafts can additionally trigger ice formation. However, the formation of ice crystals by the turbulent portion of the vertical velocity spectrum appears limited by some factors:

- In turbulent regions the spatial (and thus temporal) scale of updrafts is much smaller than in the laminar region below. For the ice crystal formation, the updrafts must be appreciated for some time, because ice supersaturation has to surpass the homogeneous nucleation thresholds and maintain the excess until a reasonable amount of ice crystals are formed.
- Here, the strongest updrafts driven by turbulence occur in the lower half of the ice supersaturated layer. However, depending on the environmental temperature and humidity, ice formation can be triggered by the wave motion even before the onset of the turbulence. In such a case, due to their diffusional growth, ice crystals act as a strong sink for the water vapor, thus reducing the local supersaturation. Moreover, as crystals reach adequate size, they fall out, and a local dehydration takes place. Hence, the eventual homogeneous nucleation in subsequent turbulent motions starts at lower supersaturation, thus reducing the ability to form ice crystals.

Figure 4 shows the probability density functions for the vertical velocity and the relative humidity, respectively, inside the layer ($4 \leq z \leq 10.5$ km). Here, a data point is labeled as cloudy if the ice crystal number density is larger than $0.1\mathrm{L}^{-1}$.

The vertical velocity spectrum is dominated by the small scale variations in the early time of the evolution, when the wave has not been

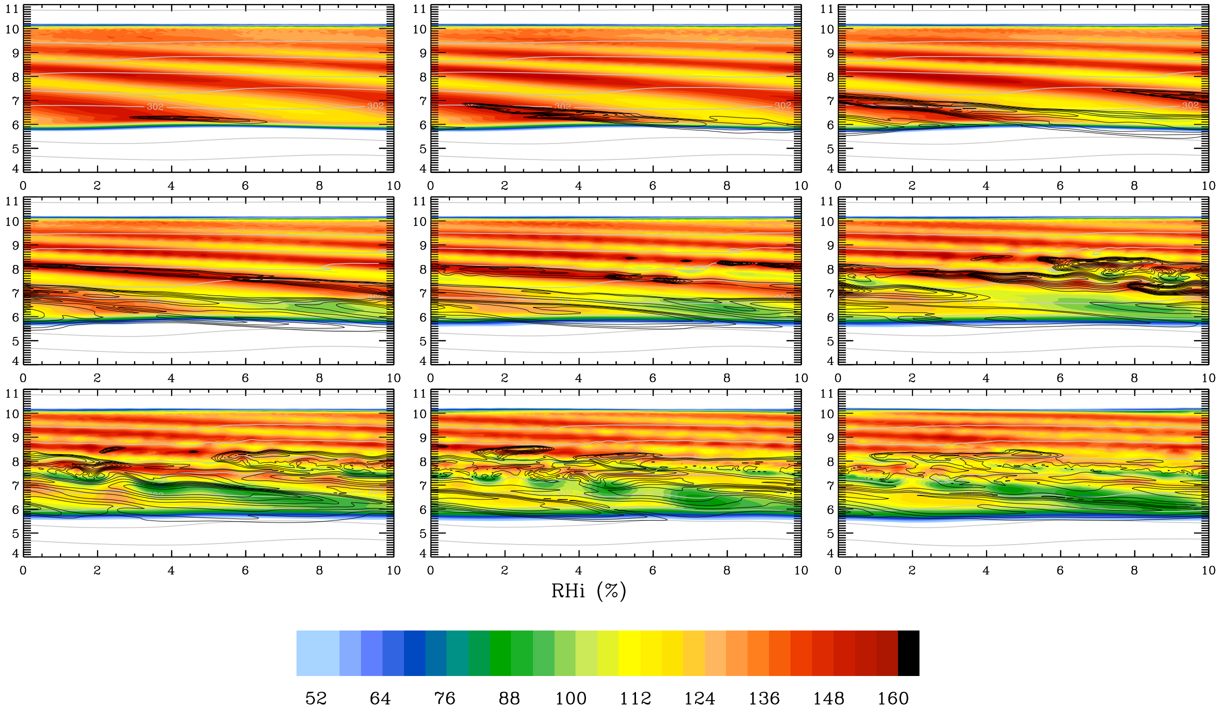

Fig. 3: Evolution of the moisture field due to the dynamical impact, starting at $t = 360$ min in time intervals of 36 min (upper panel: 360/396/432 min; middle panel: 468/504/540 min; lower panel: 576/612/648 min). Black lines indicate ice crystal number concentration of the formed cirrus clouds, grey lines indicate potential temperature.

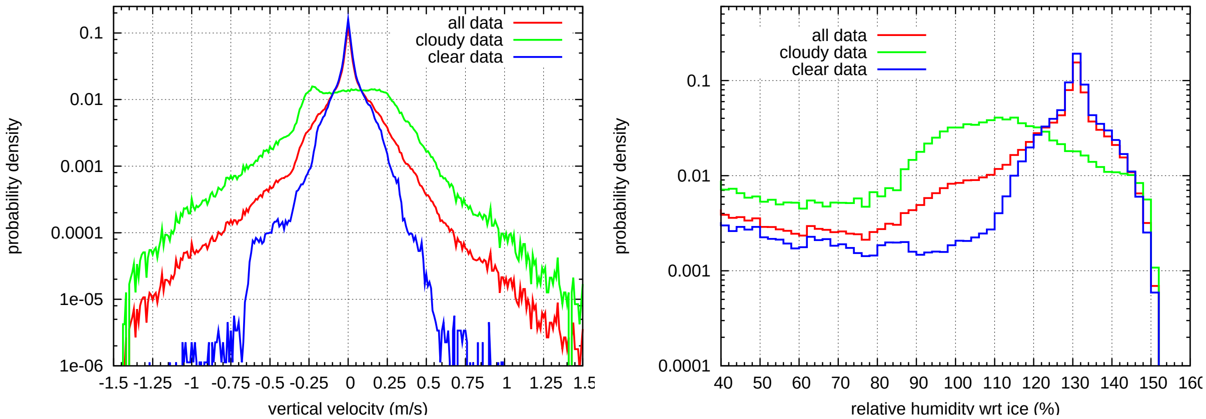

Fig. 4: Statistics of vertical velocity (left) and relative humidity wrt ice (right) inside the vertical layer $4 \leq z \leq 10.5$ km for all data (red), cloudy data (green) and clear air data (blue). A data point is labeled as cloudy if the ice crystal number density is larger than $0.1\mathrm{L}^{-1}$.

established in the upper altitude range beneath the critical level. However, the wave component (vertical velocities in the range $-0.25 \leq w \leq 0.25$) can be seen clearly (especially in the cloudy data), the long tails of the distribution are characteristic of turbulence. The relative humidity distributions are dominated by the initial values ($RHi = 130\%$), but the distributions are broaden by the vertical updrafts. The characteristic cut-off at $RHi \sim 150\%$ represents the homogeneous nucleation thresholds. For the cloudy data, high relative humidity values are relaxed to saturation, because ice crystals act as a strong sink for supersaturation. However, vertical velocity variations still present in the supersaturation layer, can modify this process leading to a broad maximum of relative humidity in the range $100 \leq RHi \leq 130\%$. This interpretation is corroborated by the vertical velocity distribution inside cirrus clouds (see fig. 4, left) indicating considerable updraft contributions leading to deviations of relative humidity from saturation.

Noteworthy, the vertical velocity distributions appear similar to the distributions of temperature fluctuations found by Gierens et al. (2007). This also supports our conjecture that variations in temperature/vertical velocity found in in situ measurements may originate from vertically propagating and dissipating waves.

5 CONCLUSIONS AND FUTURE WORK

We investigated the impact of turbulence formed by a dissipating wave near a critical level on the formation and evolution of cirrus clouds, using an idealized 2D setup with a prescribed wave length and amplitude. The vertically propagating wave and turbulence resulting from the wave breaking induce vertical updrafts which can trigger ice crystal formation; whereupon cirrus clouds can form nearby the critical level. These processes can be important for cirrus cloud formation in the natural atmosphere over mountainous terrain. Furthermore, inside cirrus clouds, the vertical velocity variations (resulting from wave and turbulence) broaden the relative humidity distribution; i.e., the relaxation to saturation is disturbed, whereupon higher relative humidities inside cirrus are possible.

The formation of ice crystals in the updraft regions of wave- and/or turbulent motions depend on the wave length and amplitude as well as on the environmental temperature and humidity. Herein, we only begun investigating the impact of the environment on the resulting cirrus. Our preliminary results indicate that initial supersaturation has a strong impact on the subsequent cloud evolution. For a drier supersaturated layer, the vertically propagating wave can only marginally trigger the ice formation, while the wave dissipating via turbulence can later induce much stronger updrafts leading to higher ice crystal number densities and, at later time, to longer life time of cirrus. Colder temperature may have a similar impact. Finally, it should be noted that the latent heat release from growing/evaporating ice crystals can modify the stability, thus changing the environment for the propagating waves. A thorough study of the sensitivity of cirrus evolution to the environmental conditions is a subject of the future work.

ACKNOWLEDGMENTS:

This work was partly supported by the European Commission within the framework of the Marie Curie Fellowship “Impact of mesoscale dynamics and aerosols on the life cycle of cirrus clouds” (IMDALCC). The numerical simulations were carried out at the European Centre for Medium–Range Weather Forecasts (special project “Ice supersaturation and cirrus clouds”).

REFERENCES

Booker, J. R. and F. P. Bretherton, 1967: The critical layer for internal gravity waves in a shear flow. Jour. Fluid Mech., 27, 513–539.

Chen T., W. Rossow, Y.Zhang, 2000: Radiative effects of cloud-type variations. J. Climate, 13, 264–286.

Clark T. L. and R. D. Farley, 1984: Severe downslope windstorm calculations in two and three spatial dimensions using anelastic interactive grid nesting: A possible mechanism for gustiness. J. Atmos. Sci., 41, 329–350.

DeMott, P. D. Cziczo, A. Prenni, D. Murphy, S. Kreidenweis, D. Thomson, R. Borys,

D. Rogers , 2003: Measurements of the concentration and composition of nuclei for cirrus formation. Proc. Nat. Acad. Sciences, 100, 14655–14660.

Fusina, F., P. Spichtinger, U. Lohmann, 2007: The impact of ice supersaturated regions and thin cirrus clouds on radiation. J. Geophys. Res., 112, D24S14, doi:10.1029/2007JD008449.

Gary. B. L., 2006: Mesoscale temperature fluctuations in the stratosphere, Atmos. Chem. Phys., 6, 4577–4589.

Gayet, J.-F., J. Ovarlez, V. Shcherbakov, J. Ström, U. Schumann, A. Minikin, F. Auriol and A. Petzold, Cirrus cloud microphysical and optical properties at southern and northern midlatitudes during the INCA experiment, J. Geophys. Res., 109, 2004.

Gierens, K., R. Kohlhepp, N. Dotzek, H. G. Smit, 2007: Instantaneous fluctuations of temperature and moisture in the upper troposphere and tropopause region. Part 1: Probability densities and their variability. Met. Z., 16, 221–231.

Grabowski, W.W. and P.K. Smolarkiewicz, 2002. A multiscale model for meteorological research. Mon. Weather Rev., 130, 939–956.

Grubisic, V. and P.K. Smolarkiewicz, 1997: The Effect of Critical Levels on 3D Orographic Flows: Linear Regime. J. Atmos. Sci., 54, 1943–1960.

Haag W. and B. Kärcher, 2004: The impact of aerosols and gravity waves on cirrus clouds at midlatitudes. J. Geophys. Res., 109, D12202.

Heymsfield, A. and J. Iaquinta, 2000: Cirrus crystal terminal velocities. J. Atmos. Sci., 57, 916–938.

Hoyle, C., B. Luo, T. Peter, 2005: The Origin of High Ice Crystal Number Densities in Cirrus Clouds. J. Atmos. Sci., 62, 2568–2579.

IPCC, 2007: Climate Change 2007: The Physical Science Basis. Contribution of Working Group I to the Fourth Assessment Report of the Intergovernmental Panel on Climate Change [Solomon, S., D. Qin, M. Manning, Z. Chen, M. Marquis, K.B. Averyt, M. Tignor and H.L. Miller (eds.)]. Cambridge University Press, Cambridge, United Kingdom and New York, NY, USA, 996 pp.

Kajikawa, M. and A. Heymsfield, 1989: Aggregation of ice crystals. J. Atmos. Sci., 46, 3108–3121.

Kärcher, B. and U. Lohmann, 2002: A Parameterization of cirrus cloud formation: Homogeneous freezing of supercooled aerosols. J. Geophys. Res., 107, 4010.

Kärcher, B., and J. Ström, The roles of dynamical variability and aerosols in cirrus cloud formation, Atmos. Chem. Phys., 3, 823–838, 2003.

Kärcher, B., J. Hendricks and U. Lohmann, 2006: Physically based parameterization of cirrus cloud formation for use in global atmospheric models J. Geophys. Res. , 111, D01205.

Koenig, L., 1971: Numerical modeling of ice deposition. J. Atmos. Sci., 28, 226–237.

Koop, T., B. Luo, A. Tsias, T. Peter, 2000: Water activity as the determinant for homogeneous ice nucleation in aqueous solutions. Nature 406, 611–614.

Krämer, M., 2008, pers. comm.

Prusa J.M., P.K. Smolarkiewicz, A.A. Wyszogrodzki, 2008: EULAG, a Computational Model for Multiscale Flows. Comput. Fluids; in press, doi:10.1016/j.compfluid.2007.12.001

Schlicht, S., P. Spichtinger, H. Vössing, C. Schiller, P. Konopka and M. Krämer, 2006:

A Cirrus Cloud Case Study in Frontal Systems over Norway using the Model EULAG. Geophysical Research Abstracts 8, 10535 (EGU General Assembly, Vienna).

Smith, S. and P. Jonas, 1996: Observations of turbulence in cirrus clouds. Atmos. Res., 43,, 1–29.

Smolarkiewicz P.K., 2006: Multidimensional Positive Definite Advection Transport Algorithm (MPDATA): An Overview. Int. J. Numer. Meth. Fluids, 50, 1123–1144.

Smolarkiewicz, P. and Margolin, L., 1997: On forward–in–time differencing for fluids: an Eulerian/Semi–Lagrangian non–hydrostatic model for stratified flows. Atmosphere–Oceans, 35, 127–152.

Smolarkiewicz, P., L. Margolin, A. Wyszogrodzki, 2001: A class of nonhydrostatic global models. J. Atmos. Sci., 58, 349–364.

Spichtinger, P. and K. Gierens, 2008a: Modelling Cirrus Clouds. Part 1: Model description and validation. Atmos. Chem. Phys. Diss., 8, 601–686.

Spichtinger, P. and K. Gierens: Modelling Cirrus Clouds. Part 2: Competition of different nucleation mechanisms. Atmos. Chem. Phys. Diss., accepted.

Vali, G, 1985: Nucleation terminology. J. Aerosol Sci., 16, 575–576.

Worthington, R.M., 1999: Tropopausal turbulence caused by the breaking of mountain waves. Jour. Atmos. Solar Terr. Phys., 59, 1543–1547.

Worthington, R. M. and L. Thomas, 1996: Radar measurements of critical–layer absorption in mountain waves. Quart. Jour. Roy. Meteorol. Soc., 122, 1263–1282.

MICROPHYSICAL CHARACTERISTICS OF TROPICAL CIRRUS FROM THE 2006 TROPICAL WARM POOL INTERNATIONAL CLOUD EXPERIMENT (TWP-ICE)

Junshik Um, Greg M. McFarquhar, and Matt Freer
Dept. of Atmospheric Sciences, University of Illinois at Urbana-Champaign, Urbana, IL 61801

1. INTRODUCTION

In situ cloud data acquired during the 2006 Tropical Warm Pool International Cloud Experiment (TWP-ICE) were used to determine if the microphysical properties of tropical cirrus formed under different conditions can be characterized in terms of prognostic variables used in large-scale models such as temperature and ice water content (IWC), or whether dependence on additional variables is required. To accomplish this, the spatial variability (horizontal and vertical) of microphysical properties (IWC, habit distribution, size distribution, median mass diameter D_{mm}) was examined and contrasted for different types of cirrus (convective vs. non-convective; aged vs. fresh)

2. IN SITU MEASUREMENTS

Data acquired by the Cloud Particle Imager (CPI) on the Scaled Composites Proteus in aged cirrus on 27 Jan. (Fig. 1) and 29 Jan. (Fig. 2) and in fresh anvils on 2 Feb. (Fig. 3) were examined in this study.

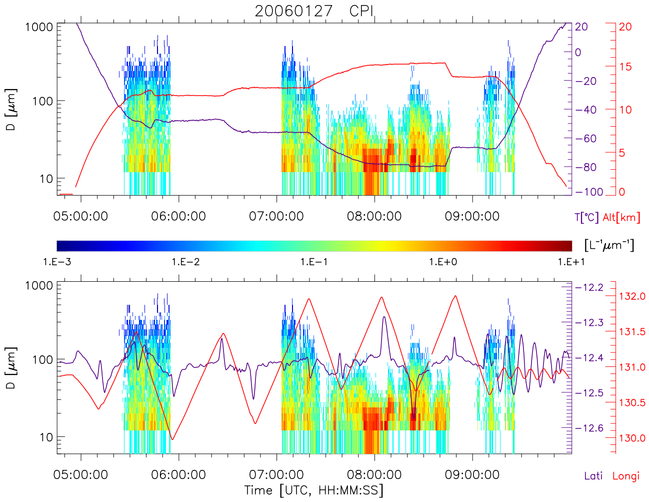

Fig.1. CPI number distribution function N(D), temperature (T), altitude (Alti), latitude (Lati), and longitude (Longi) for 27 Jan. flight during which horizontal east-west oriented legs were flown through aged cirrus bands of varying lifetime.

3. ICE CRYSTAL HABITS

Ice crystals imaged by the CPI were classified into 11 different habits (Fig. 4): small, medium, and large quasi-spheres, columns, plates, bullet rosettes, aggregates of columns, aggregates of plates, aggregates of bullet rosettes, capped columns, and unclassifiable. Quasi-spheres dominated the number concentration on all days (Fig. 5), but the fractional contributions of

---

Corresponding Author: Junshik Um, University of Illinois, Dept. of Atmospheric Science, 105 S. Gregory Street, Urbana, IL, 61801. junum@earth.uiuc.edu

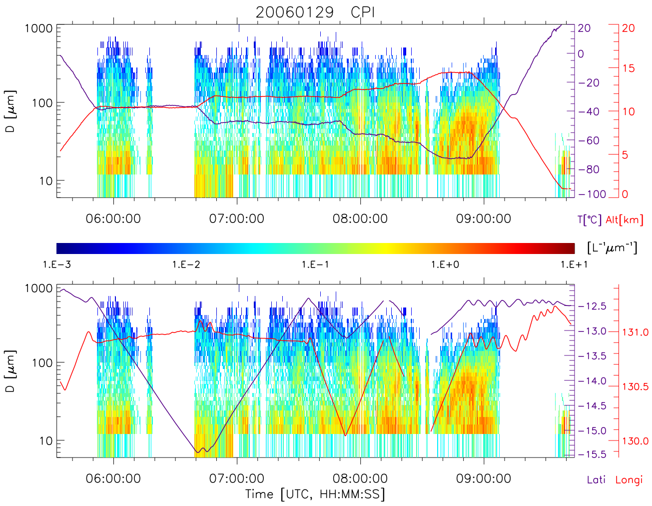

Fig.2. As in Fig. 1 except for 29 Jan. flight that may have sampled transition of anvil cirrus to more generic cirrus; north-south oriented legs sampled cirrus bands of varying age.

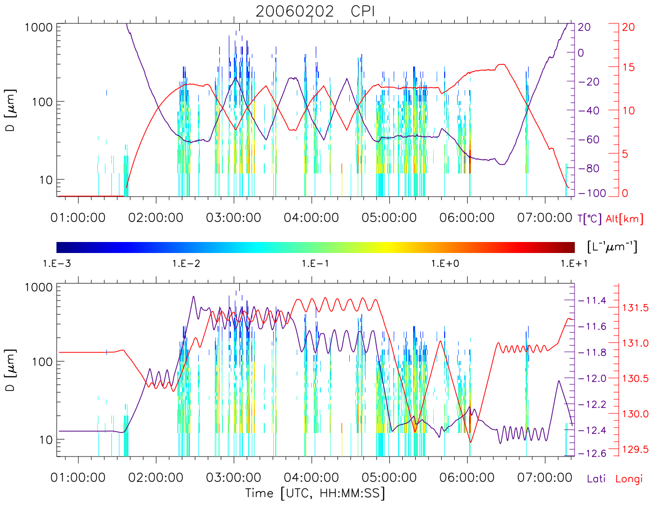

Fig.3. As in Fig. 2 except for 2 Feb. flight where spiral ascents/descents flown through rapidly dissipating fresh anvils behind a convective line over Tiwi Islands.

different habits to the total cross-sectional area for crystals with D > 200 μm varied for different days. For example, the area fraction from bullet rosettes and their aggregates was 48 % and 60 % for 27 and 29 Jan., respectively, when

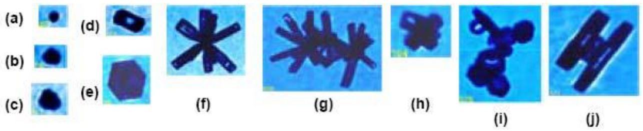

Fig.4. Example CPI images of (a) small quasi-sphere (SQS), (b) medium quasi-sphere (MQS), (c) large quasi-sphere (LQS), (d) column (COL), (e) plate (PLT), (f) bullet rosette (BR), (g) aggregates of bullet rosettes (ABR), (h) aggregates of columns (AC), (i) aggregates of plates (AP), and (j) capped column (CC). All images obtained during TWP-ICE.

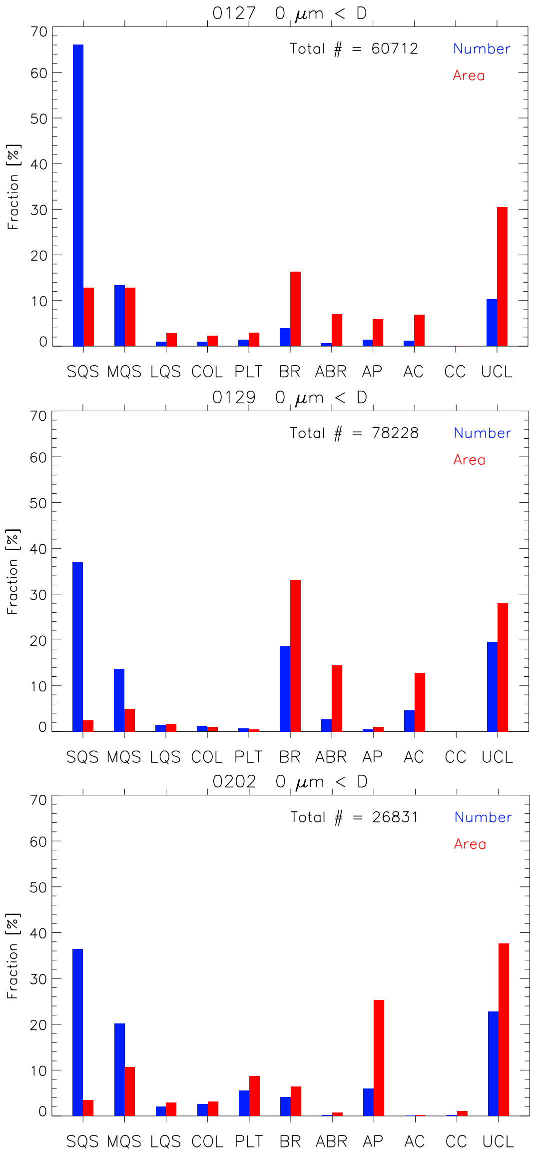

Fig.5. Fractional contribution of different ice crystal habits to total number and area for 27 and 29 Jan. and 2 Feb.

observations were acquired in aged cirrus but only 7 % for 2 Feb. when observations were made in a rapidly dissipating fresh anvil. On the other hand, the fraction of aggregates of plates is 46.2 % for 2 Feb. and only 7.2 % and 1 % for 27 and 29 Jan., respectively (Fig. 6). Further, the presence of capped columns for 2 Feb. is notable.

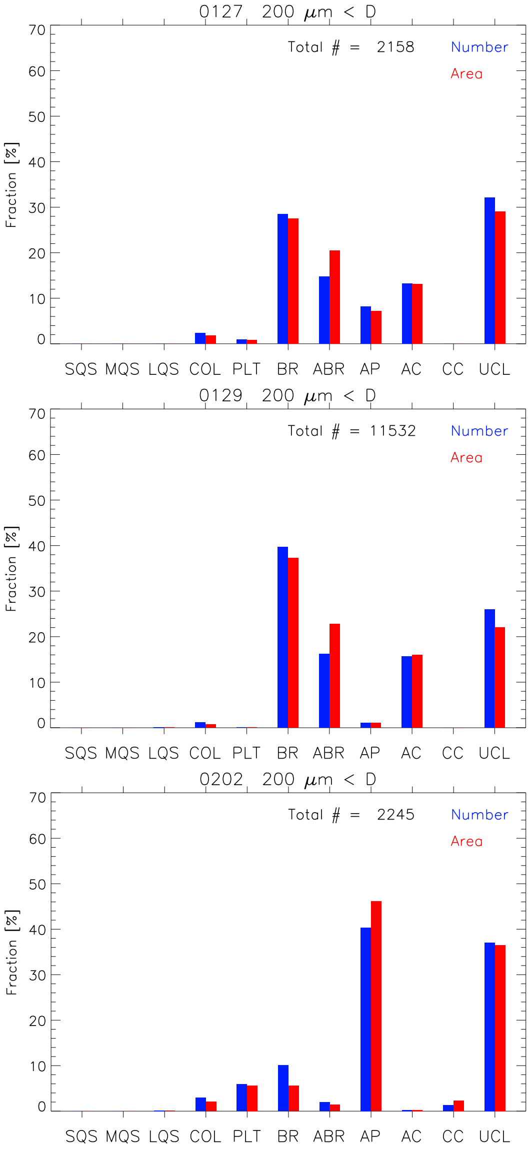

Fig.6. As in Fig. 5 except contributions from ice crystals with D > 200 μm displayed.

4. HORIZONTAL VARIABILITY

For a constant altitude (12km) horizontal leg (south to north leg, 64800-73500 UTC on 29 Jan., at -50 ºC) the dependence of N_o, μ, λ (variables of a gamma function fit to the observed size distributions, $N(D)=N_oD^{\mu}\exp(-\lambda D)$), D_{mm}, IWC, and habit distribution on latitude were determined. During this leg, the Proteus started from approximately 390 km away from the center of a deep quasi-stationary low over the central Northern Territory (Fig.7), which was called “Landphoon John” as it had a tropical-cyclone feature over land. As the Proteus moved north, it sampled cirrus of varying ages, the majority of which appeared to be aged.

Fig. 8 shows λ, IWC, D_{mm}, and the fractional contribution of different habits to the total cross-sectional area as a function of latitude. A distinct feature is the variation of the areal fraction of bullet rosettes with latitude, the fraction being a local maximum in the middle of the leg between -13.8 º and -13.7 º. At the southern edge of the leg, the Proteus passed through a thin cirrus band and there were some pristine crystals (i.e., bullet rosette), but many small unclassifiable crystals. Both the IWC and D_{mm} were smaller and λ larger, showing small crystals made larger fractional contributions to the bulk properties at the southern edge compared to the middle of this leg. The Proteus flew into a thicker cirrus band in the middle of the leg with higher IWC and D_{mm}, lower λ, and larger fractions of bullet rosettes. Approaching the edges of this cirrus band, there was clear sky at latitudes between -13.8 º and -13.7 º where D_{mm} and IWC decreased. After

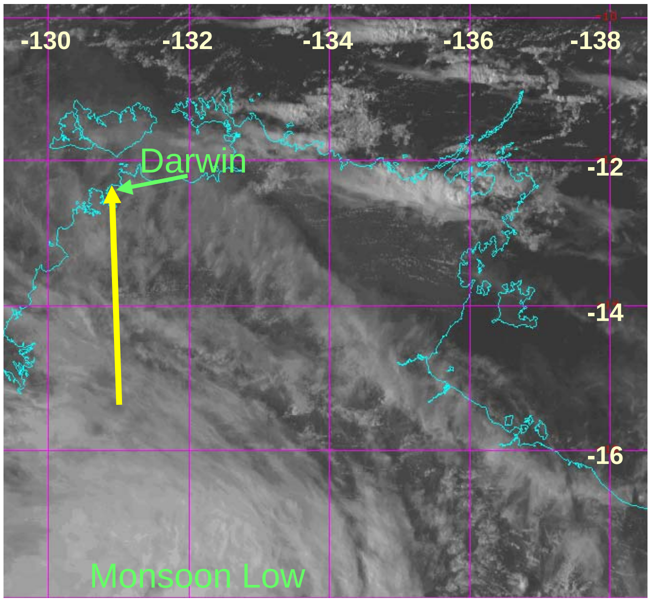

Fig.7. Proteus track (yellow arrow) during constant altitude leg overlapped on a visible satellite image taken at approximately 74800 UTC from TWP-ICE data browser (http://dods.bom.gov.au/twpice/browser/index.html).

passing this clear sky zone the Proteus entered another band of cirrus. In general, as the Proteus flew to the north, there were changes in the fractional distributions of habits. There were pristine bullet rosettes and aggregates at the southern half of the leg (-15.0º to -13.8 º), hollow bullet rosettes after passing clear sky between two bands (-13.7º to -13.2 º), and less pristine bullet rosettes with rounded edges and their aggregates at the end of the leg (-13.2º to -12.3º, Fig.9). A gradual decrease in D_{mm} with latitude occurred in the northern half of this leg (-13.3º to -12.3º). It is also noted that the areal fraction of aggregates of bullet rosettes exceeded that of bullet rosettes at the north end of leg (-13.2º to -12.3º, Fig.10), a trend different than that noted at the southern end of the leg. These trends

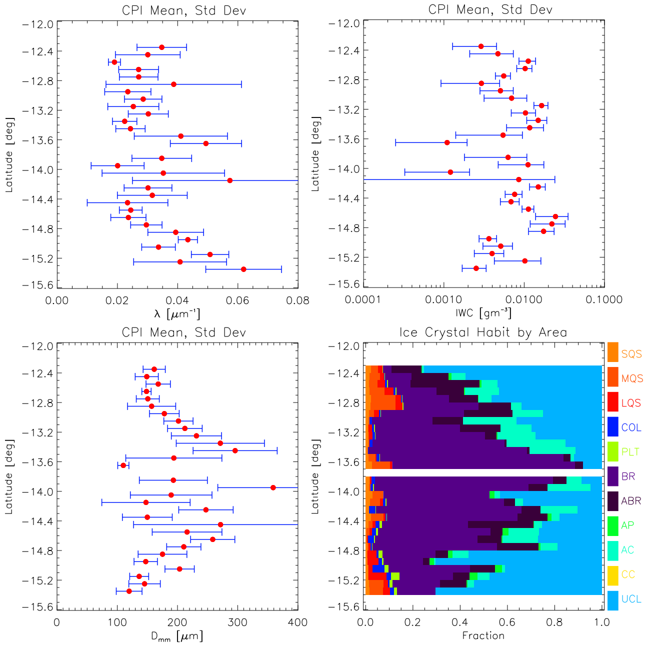

Fig.8. Mean (red) and standard deviation (blue) of λ, IWC, and D_{mm} as a function of latitude. Normalized fraction of different habits to total cross-sectional area as a function of latitude (right bottom).

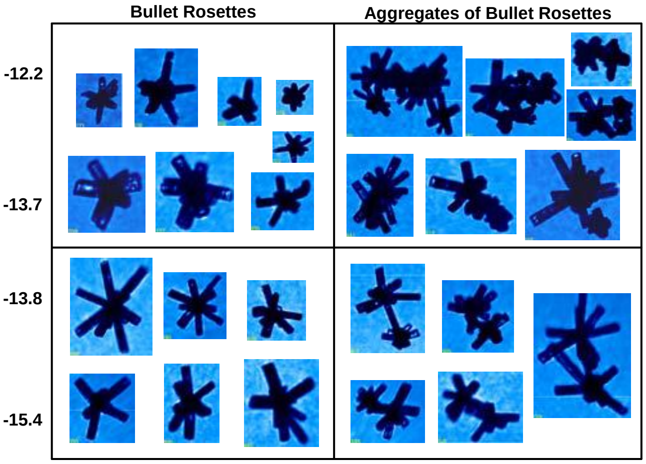

Fig.9. Selected CPI images of bullet rosettes and aggregates of bullet rosettes at southern (latitude between -15.4 º and -13.8 º) and northern (latitude between -13.7 º and -12.2 º) end of constant altitude leg.

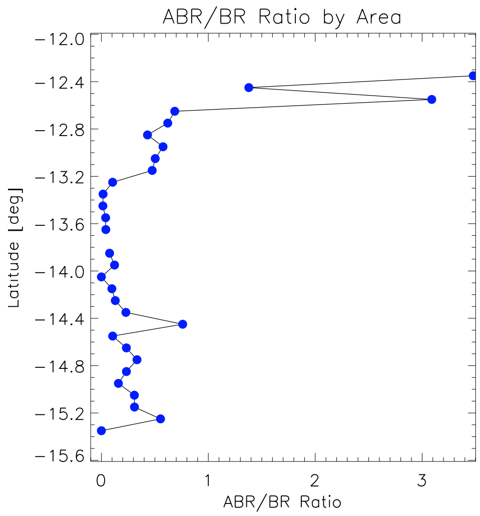

Fig.10. Ratio of areal contribution of aggregates of bullet rosettes to that of bullet rosettes as a function of latitude.

suggest that aggregation and sublimation may have been more prominent in the northern portion of the leg, whereas the presence of more pristine habits at the southern portion of the legs suggests the crystals there may have formed more recently.

5. VERTICAL VARIABILITY

The vertical dependence of λ, IWC, D_{mm}, and habit distributions are examined in Fig.11. The D_{mm} increased and the habits changed from quasi-spheres to either aggregates of plates or bullet rosettes for all days as altitude decreased. The smallest D_{mm} and IWC were seen on 2 Feb. in the rapidly dissipating fresh anvils, and the largest D_{mm} and IWC were seen on 29 Jan. in the aged cirrus bands. The habit distribution for 2 Feb. is distinct from other days as the aggregates of plates were the dominant large crystals on this day and capped columns appeared that were not seen on 27 and 29 Jan. In addition, the habit distribution for a given altitude range is distinct on 29 Jan. compared to other days with, for example, bullet rosettes more commonly observed between 13 and 15 km than on other days.

Larger D_{mm}, IWC, and smaller λ were also seen on 29 Jan. between 13 and 15 km. Fig.12 shows the range of λ as a function of IWC on each day. Here, it is not possible to distinguish the variation of λ with IWC seen on 29 Jan. from that seen on other days. This is also shown on Fig. 13 where the variation of λ with IWC in the temperature range -70 to -60 ºC (~13 to 14 km) is shown; there appears to be no systematic variation in how λ varies with IWC between days even though larger IWCs were observed on 29 Jan.

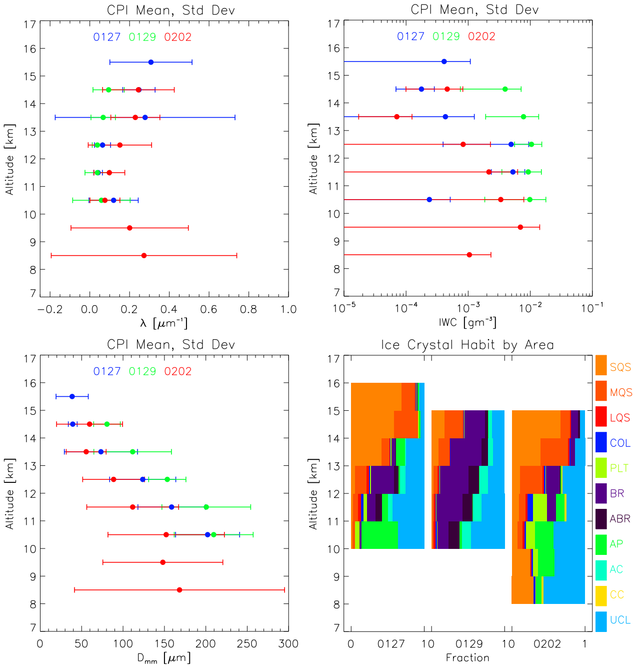

Fig.11. Mean and standard deviation of λ, IWC, and D_{mm} for 27 (blue) and 29 Jan. (green) and 2 Feb. (red) as a function of altitude. Vertical habit distributions (right bottom) for same three days as a function of latitude.

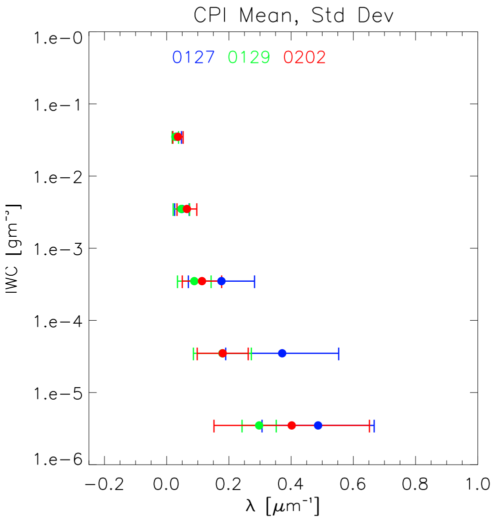

Fig.12. Mean and standard deviation of λ for 27 (blue) and 29 Jan. (green) and 2 Feb. (red) as a function of IWC.

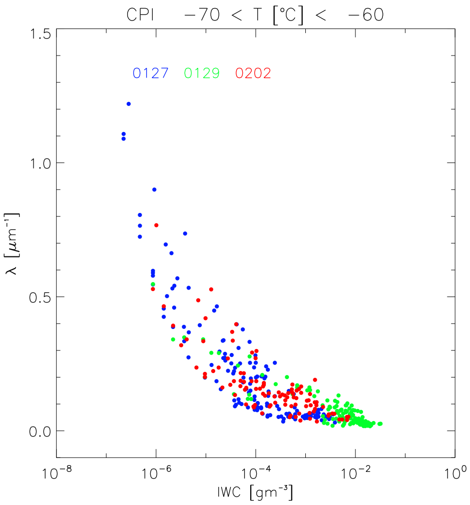

Fig.13. λ as a function of IWC for temperatures between -70 and -60 ºC for the three flights indicated in the legend.

Similarly, Fig.14 shows that the variation of λ with IWC for temperature between -50 and -40 ºC (~10 to 11 km), the λ on 29 Jan. cannot be distinguished from the other days; statistical tests are needed to confirm the robustness of these conclusions. Thus, to first order it appears that the slope of the size distributions may be function of prognostic variables such as the IWC and temperature; however, additional analysis of other cases is needed to determine if this trend is consistently realized in a wider range of conditions.

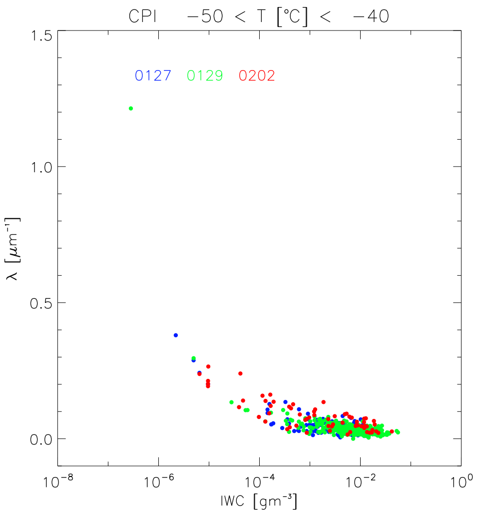

Fig.14. As in Fig.13, except for temperature between -50 and -40 ºC.

6. SUMMARY

In this study, data acquired by the CPI on 27 Jan., 29 Jan., and 2 Feb. were analyzed to determine if the bulk microphysical properties of tropical cirrus formed under different conditions could be characterized by the same relations in terms of prognostic variables used in large-scale models such as temperature and IWC. To accomplish this task, the horizontal and vertical variability of microphysical properties of tropical cirrus were examined.

For all three days, small quasi-spheres dominated the number concentrations and unclassifiable ice crystals represented at least 28 % of the total cross-sectional area. Ice crystal habits for 2 Feb. (aggregates of plates and capped column) were distinct from those observed on 27 and 29 Jan. (bullet rosettes and aggregates of bullet rosettes). This difference in ice crystal habits might be due to different age of cirrus as fresh anvils were sampled on 2 Feb. and aged cirrus on 27 and 29 Jan.

During a constant altitude (12km) horizontal leg (S-N leg, -50 ºC) on 29 Jan., there were significant changes in the habits of the ice crystals with latitude. The ratio of the cross-sectional area of aggregates of bullet rosettes to that of bullet rosettes increased with latitude suggesting that aggregation was more important for the cirrus bands towards the north of this leg.

The D_{mm} increased and the dominant habit changed from quasi-spheres to either aggregates of plates or bullet rosettes with decreasing altitude for all three days. The smallest D_{mm} and IWC were seen on 2 Feb., whereas the largest D_{mm} and IWC were noted on 29 Jan. However, when examining how the distributions of λ changed with temperature and IWC, the preliminary analysis suggested that λ could be characterized in terms of temperature and IWC. It remains to be seen whether this conclusion will persist if more robust statistical analysis and more cases are analyzed. In any event, the habit distributions of cirrus have been shown to depend on other variables in addition to just IWC and temperature.

Acknowledgements

This research was supported by the Office of Science (BER), U.S. DOE Atmospheric Radiation Measurement (ARM) Program Grant Numbers DE-FG02-02-ER63337 and DE-FG02-07ER64378.